The ESC Textbook of Cardiovascular Imaging

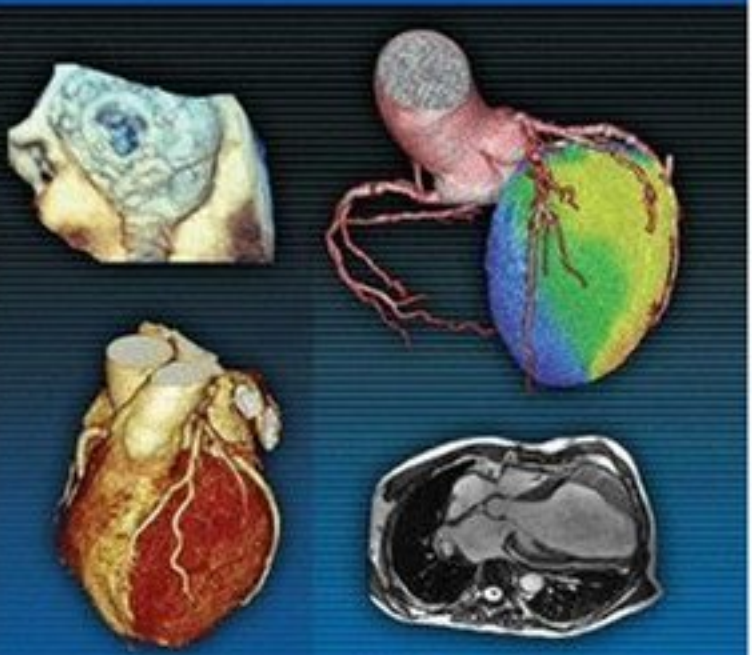

José-Luis Zamorano
Jeroen Bax
Frank Rademakers
Juhani Knuuti
Editors

Springer

The European Society of Cardiology Textbook of Cardiovascular Imaging

José Luis Zamorano
Jeroen J. Bax
Frank E. Rademakers
Juhani Knuuti (Eds.)

The ESC Textbook of Cardiovascular Imaging

Springer

Prof. José Luis Zamorano
Hospital Clinico San Carlos
Instituto Cardiovascular
C/Professor Martin Lagos, s/n
28040 Madrid
jlzamorano@vodafone.es
Jzamorano.hcsc@salud.madrid.org

Prof. Jeroen J. Bax
Leiden University
Medical Center
Dept. Cardiology
Albinusdreef 2
2333 ZA Leiden
Netherlands
j.j.bax@lumc.nl

Prof. Dr. Frank E. Rademakers
University Hospitals Leuven
Dept. Cardiology
Herestraat 49
3000 Leuven
Belgium
frank.rademakers@uzleuven.b

Prof. Dr. Juhani Knuuti
Turku University Hospital
Turku PET Centre
FI-20521 Turku
Finland
juhani.knuuti@tyks.fi

ISBN: 978-1-84882-420-1 e-ISBN: 978-1-84882-421-8
DOI: 10.1007/978-1-84882-421-8
Springer Dordrecht Heidelberg London New York

Library of Congress Control Number: 2009934506

Preface

Imaging is at the core of diagnostic procedures in cardiology. The idea of creating *The European Society of Cardiology Textbook of Cardiovascular Imaging* has, therefore, been in the air for quite a long time. We recognized the rapid development of cardiovascular imaging and the growth of the clinical use of cardiac imaging. Although there have been excellent books and reviews on the matter, the society experienced the need of a book representing the accumulated expertise of European cardiovascular imagers.

Our goal was to produce a clinically orientated book, which explained the utility of different imaging modalities in the diagnosis of all relevant major cardiovascular disorders. We invited the best specialists in the field to contribute with their expertise as authors.

The book is divided in sections that deal with specific themes involving theory and practice of cardiac imaging and its clinical use in all major cardiovascular diseases from coronary heart disease to cardiomyopathies.

We hope this book will become an ideal companion to all cardiologists, trainees, and cardiovascular imagers. There has been a lot of effort and hard work to develop this project. We are confident that this book will help to spread the expertise and knowledge available on cardiovascular imaging.

We thank all the authors who contributed long hours to develop the content of this book. Without their expertise and commitment, this book could not have been possible.

Madrid, Spain — José Luis Zamorano
Leiden, The Netherlands — Jeroen J. Bax
Leuven, Belgium — Frank E. Rademakers
Turku, Finland — Juhani Knuuti

Foreword

Images are a central part of our lives. Of the five senses, the eyes and vision have indeed triumphed over the others. We live, think, and dream through images.

Television captures our imagination and sends messages to us through images to the extent that there are now news reports in total silence. Television sound is often just a background noise. Newspapers, even the daily ones, communicate to us through catchy and colourful images. Often leaders and politicians care more about their image than their mission.

It is, therefore, not surprising that image has also invaded medicine and cardiology in particular. When I was a student, I thought that to be a good cardiologist one should have very good hearing to capture all of the abnormal heart sounds. This is no longer the case. The image of the echocardiogram has surpassed the stethoscope; the eyes have surpassed the ears. Today, technology is providing heart doctors with more and more sophisticated and fascinating images. So, to be a good cardiologist, you have to read this book!

I mean it. As it always happens in life, interaction is important. This is also true for cardiovascular images that need to be integrated within themselves and particularly with the patients. Without such interaction and integration even the most sophisticated image will be dull.

Interaction is what this book is about. Several European leaders explain to the reader, in a simple and comprehensive manner, the value and the benefit of different imaging modalities in the diagnosis of the most relevant cardiovascular diseases.

This book does something more as well. It describes a new subspecialty that we will all soon need: the imaging doctor, who will be able to interact with clinicians and help them resolve diagnostic dilemmas by choosing the right technique and by interpreting images in a patient-based manner.

As the president of the ESC, I thank the ECHO Association, the working groups, and the councils who are responsible for *The European Society of Cardiology Textbook of Cardiovascular Imaging.*

As a cardiologist, I thank all the authors and editors for contributing to develop the education of all cardiologists (myself included) through this book.

President Roberto Ferrari
European Society of Cardiology

Contents

Contributors

Stephan Achenbach, MD Medizinsche Klinik I, University of Erlangen, Erlangen, Germany

Luigi P. Badano, MD Echocadiography Laboratory, Cardiopulmonary Sciences, Azienda Ospedaliero-Universitaria, Udine, Italy

Helmut Baumgartner, MD Adult Congenital and Valvular Heart Disease Center, University of Muenster, Muenster, Germany

Prof. Jeroen J. Bax, MD, PhD Department of Cardiology, Leiden University Medical Center, Leiden, The Netherlands

Harald Becher, MD, PhD Department of Cardiovascular Medicine, John Ratcliffe Hospital, Oxford, UK

Frank M. Bengel, MD Division of Cardiovascular Nuclear Medicine, Johns Hopkins University Medical Institutions, Baltimore, MD, USA

Ruxandra T. Beyer, MD, PhD Cardiology-Intensive Care Unit, Heart Institute "N. Stancioiu", Cluy-Napoca, Romania

Amit Bhan, MD Department of Cardiology, King's College Hospital, London, UK

Jan Bogaert, MD, PhD Department of Radiology, Gasthuisberg University Hospital, Leuven, Belgium

Thomas Buck, MD Department of Cardiology, Division of Internal Medicine, West German Heart Center, University Clinic Essen, Essen, Germany

Peter Buser, MD Cardiology Department, University Hospital, Basel, Switzerland

Filippo Cademartiri, MD, PhD Radiology, Azienda Ospedaliero–Universitaria, Parma, Italy

Paolo Camici, MD Mrc Clinical Sciences Center, Imperial College School of Medicine Hammersmith Hospital, London, UK

Jean-Paul Carpenter, MD Royal Brompton Hospital, London, UK

Ignasi Carrio, MD Nuclear Medicine Unit, Hospital de Sant Pau, Barcelona, Spain

Pio Caso, MD Division of Cardiology, Monaldi Hospital, Naples, Italy

Paolo Colonna, MD Institute of Cardiology, Policlinico of Bari, Bari, Italy

Pim J. De Feyter, MD Radiology and Cardiology, Erasmus Medical Center, Rotterdam, The Netherlands

Genevieve Anne Derumeaux, MD Laboratre d'Echochardiographie, Hospital Louis Pradel, Lyon, France

Nuno Cortez Dias, MD Department of Cardiology, University Hospital Santa Maria, Lisbon, Portugal

Raimund Erbel, MD Department of Cardiology, West German Heart Center Essen, University Duiburg-Essen, Essen, Germany

Arturo Evangelista, MD Servei de Cardiologio, Hospital Vall d'Hebron, Barcelona, Spain

Frank Flachskampf, MD Universitaetsklinik Erlanger, Erlanger, Germany

Albert Flotats, MD Nuclear Medicine Department, Hospital Sant Pau, Barcelona, Spain

Miguel Garcia Fernandez, MD, PhD Department of Medicine, Universidad Compluterse de Madrid, Martinez Izquierdo 7 Bajo Deredro, Madrid, Spain

Covadonga Fernandez-Golfin, MD Cardiac Imaging Unit, Cardiovascular Institute Hospital Clinico San Carlos, Madrid, Spain

Mark Friedberg, MD Division of Cardiology, Hospital for Sick Children, Toronto, ON, Canada

Jerome Garot, MD Hospital Univesitaire Henri Mondor, Creteil, France

Michael A. Gatzoulis, MD, PhD Adult Congenital Heart Clinic, Royal Brompton Hospital, London, UK

Bernhard M. Gerber, MD Servize de Cardiologie, Cliniquis Univesitaires St. Luc, Woluwe St. Lambert, Belgium

Gilbert Habib, MD Service de Cardiologie B, C.H.U. de la Timone, Marseille, France

Rainer Hoffman, MD Aachen University, Prauwelsstrasse 30, Aachen, Germany

Majo Joseph, MD Department of Cardiovascular Medicine, Flinders Medical Center, Adelaide, Australia

Philipp Kaufmann, MD Cardiovascular Center, Nuclear Cardiology NUK C32, University Hospital Zurich, Zurich, Switzerland

Philip Kilner, MD Cardiovascular Magnetic Resonance Unit, Royal Brompton Resonance Unit, Royal Brampton Hospital, London, UK

Prof. Dr. Juhani Knuuti, MD, PhD Turku PET Centre, Turku University Hospital, Turku, Finland

Frederic Lamare, MD, PhD Division of Cardiovascular Nuclear Medicine, Johns Hopkins University Medical Institutions, Baltimore, MD, USA

Patrizio Lancellotti, MD, PhD Cardiology, University of Liege, Liege, Belgium

Paul Leeson, PhD, MRCP Department of Cardiovascular Medicine, John Radcliffe Hospital, Oxford, UK

Massimo Lombardi, MD MRI Laboratory, Clinical Physiology Institute, CNR National Research Council, Pisa, Italy

Erica Maffei, MD Department of Radiology, Erasmus Medical Center, Rotterdam, The Netherlands

Heiko Mahrholdt, MD Cardiology, Robert Bosch Medical Center, Stuttgart, Germany

David C. Maintz, MD Department of Clinical Radiology, University of Munster, Munster, Germany

Pedro Marcos-Alberca, MD, PhD Unidad de Imagen Cardiaca, Instituto Cardiovascular, Hospital Clinico San Carlos, Madrid, Spain

Chiara Martini, RT Radiology, Non-Invasive Cardio Imaging, Azienda Ospedaliera Di Parma, Parma, Italy

Thomas H. Marwick, MD Department of Medicine, Princess Alexandra Hospital, Brisbane, Australia

Julia Mascherbaur, MD Cardiology, Medical University of Vienna, Vienna, Austria

Luc Mertens, MD, PhD Cardiology, Hospital for Sick Children, Toronto, ON, Canada

Nico R. Mollet, MD, PhD Department of Radiology, Erasmus Medical Center, Rotterdam, The Netherlands

Mark Monaghan, MD Cardiology Care Group, Kings College Hospital, London, UK

Maric Moonen, MD Cardiology, University of Liege, Liege, Belgium

Denisa Muraru, MD Cardiology, Professor Dr. C.C. Iliescu Institute of Cardiovascular Diseases, Bucharest, Romania

Eike Nagel, MD Imaging Sciences, Rayene Institute, London, UK

Danilo Neglia, MD, PhD Cardiovascular PET Program, CNR, Pisa, Italy

Stefan Neubauer, MD Department of Cardiovascular Medicine, John Radcliffe Hospital, Oxford, UK

Ed Nicol, MD Cardiovascular Magnetic Resonance Unit, Royal Brompton Hospital, Sydney Street, London, UK

Petros Nihoyannopoulos, MD Imperial College School of Medicine, Hammersmith Hospital, London, UK

Alessandro Palumbo, MD, PhD Department of Radiology, Erasmus Medical Center, Rotterdam, The Netherlands

Dudley Pennell, MD Cardiovascular MR Unit, Royal Brompton Hospital, Sydney Street, London, UK

Leopoldo Perez de Isla, MD, PhD Unidad de Imagen Cardiovascular, Instituto Cardiovascular, Hospital Clinico San Carlos, Madrid, Spain

Pasquale Perrone-Filardi, MD Cattedra di Cardiologia, Universita Federico II, Naples, Italy

Luc Pierard, MD, PhD Cardiology, University of Liege,
Liege, Belgium

Fausto Jose Pinto, MD Department of Cardiology, Lisbon Cardiovascular Institute, Lisbon, Portugal

Don Poldermans, MD Department of Anesthesiology, Erasmus Medical Center, Rotterdam, The Netherlands

Björn Plicht, MD Cardiology Clinic, West German Heart Center, University Clinic Essen, Essen, Germany

Sanjay Prasad, MD CMR Unit, Royal Brompton Hospital, Sydney Street, London, UK

Prof. Dr. Frank E. Rademakers, MD, PhD Department of Cardiology, University Hospitals Leuven, Herestraat 49, 3000 Leuven, Belgium

Raphael Rosenhek, MD Department of Cardiology, Medical University of Vienna, Vienna, Austria

Michael Rubens, MD Cardiovascular Magnetic Resonance Unit, Royal Brompton Hospital, Sydney Street, London, UK

Juerg Schwitter, MD Department of Internal Medicine, University Hospital Zurich, Zurich, Switzerland

Roxy Senior, MD Department of Cardiology, Northwick Park Hospital, Harrow Middlesex, UK

Rosa Sicari, MD Echocardiography, CUR, Institute of Clinical Physiology, Pisa, Italy

Udo Sechtem, MD Abteilung Fuer Kardiologie Und Pulmologie, Robert Bosch Krankenhaus, Stuttgart, Germany

Joseph Selvanayagam, MD Department of Cardiovascular Medicine, Flinders Medical Center, Adelaide, Australia

Marta Sitges, MD Cardiology Department, Hospital Clinic-University of Barcelona, Barcelona, Spain

James Elliot Stirrup, MRCP, MB, BS, BSC Nuclear Medicine, Royal Brompton Hospital, Sydney Street, London, UK

Edgar Tay, MD Adult Congenital Heart Disease, Royal Brompton Hospital, London, UK

Frank Thuny, MD Service de Cardiologie B, Département de Cardiologie, C.H.U. de la Timone, Marseille, France

Stephen Richard Underwood, MA, MD Department of Nuclear Medicine, Royal Brompton Hospital, London, UK

Nico Van de Veire, MD, PhD Department of Cardiology, Leiden University Medical Center, Leiden, The Netherlands

Ernst E. van der Wall, MD, PhD Department of Cardiology, Leiden University Medical Center, Leiden, The Netherlands

Albert C. Van Rossum, MD Department of Cardiology, VU Medical Center, Amsterdam, The Netherlands

Jeremy J. Wright, MB, BS(Hons) Hearts 1st, Greenslopes Private Hospital, Greenslopes Brisbane, Australia

Ali Yilmaz, MD Abteiling fuer Kardiologie und Pulmologie, Robert Bosch Krankenhaus, Stuttgart, Germany

Prof. José Luis Zamorano, MD, PhD Cardiovascular Institute, Hospital Clinico San Carlos, Madrid, Spain

Section 1

Technical Aspects of Imaging

Chapter 1

ECHOCARDIOGRAPHY: BASIC PRINCIPLES

Miguel Angel García-Fernández and Pio Caso

CONTENTS

J. L. Zamorano et al. (eds.), *The ESC Textbook of Cardiovascular Imaging*
DOI: 10.1007/978-1-84882-421-8_1, © Springer-Verlag London Limited 2010

Introduction

Echocardiography is a useful technique for the examination of the heart of patients of all ages. Good-quality images are required and transducer positions must be adapted to each patient.

A variety of transducers are available with different widths, ultrasound emission frequencies, and focal characteristics. Transducer width is based on ultrasound emission frequency, and it is important to consider the relationship between resolution and penetration in order to choose frequencies appropriate for a given examination. Resolution is the ability to distinguish between adjacent structures, while ultrasound penetration measures the ability of the ultrasound beam to pass through different cardiac structures. An increase in ultrasound emission frequency leads to an increase in image resolution. If attenuation also increases, however, there is a reduction in ultrasound penetration.

Echocardiographic examination usually requires a frequency of at least 2.0 MHz, but it can change depending on the patient's chest characteristics. In a child or thin adult, a 3–5 MHz transducer can be used with good resolution and penetration. A 7–7.5 MHz transducer produces better-quality images in a newborn, while a 2–2.5 MHz transducer is optimal for an obese adult.

Second harmonic imaging is an echocardiographic tool used to improve technically difficult images. For example, a transducer with second harmonic echocardiography transmits ultrasound at 1.8 MHz (plus penetration) and receives a 3.6 MHz signal with improvement in image quality. Moreover, it is essential to set ultrasound emission frequency low when using Doppler technique, as lower frequencies are required to register high-velocity flows. Following the selection of an appropriate transducer, gray scale gains and depths are manually controlled to an adequate delineation of structures to be visualized.

Echocardiographic examination is usually performed with the patient in left lateral decubitus position and with 30° flexion of the chest in order to situate the heart nearer to the anterior chest wall. The patient's left arm is placed under the head so as to widen intercostal spaces. A different transducer position may be used during a conventional echocardiographic exam (Fig. 1.1).[1,2] The examination begins by placing the transducer on the third or fourth intercostal space of the left parasternal line (left parasternal window) and subsequently on the apex (apical window). Such images are obtained with the patient in left lateral position (Fig. 1.2).

Sub-costal and supra-sternal windows may be obtained with the patient in supine position. A sub-costal approach is useful for visualizing inferior vena cava, hepatic veins, and congenital abnormalities, as well as in patients with low diaphragm or bad acoustic window due to respiratory

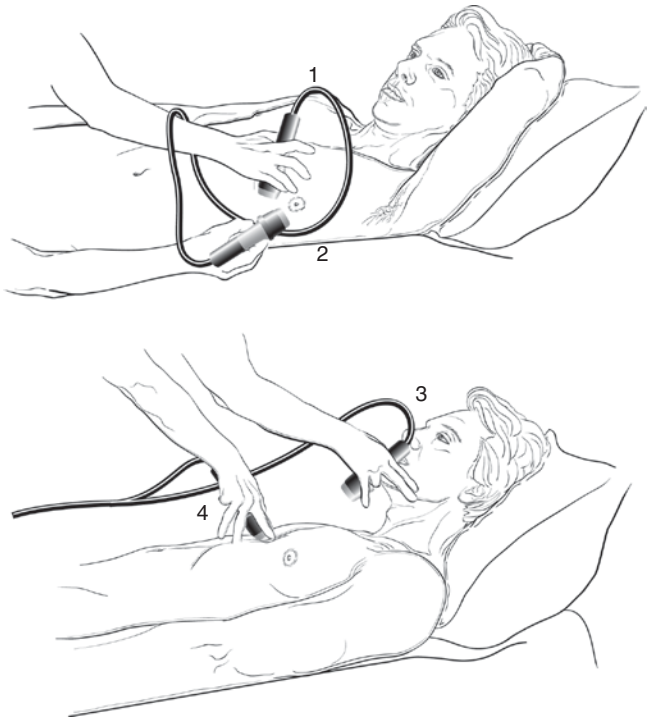

Fig. 1.1 Transthoracic transducer standard positions for obtaining different planes. Parasternal (*position 1*) and apical planes (*position 2*) are obtained with the patients in left lateral position. Supra-sternal (*position 3*) and subxiphoid planes are usually obtained with the patient in supine position (*position 4*)

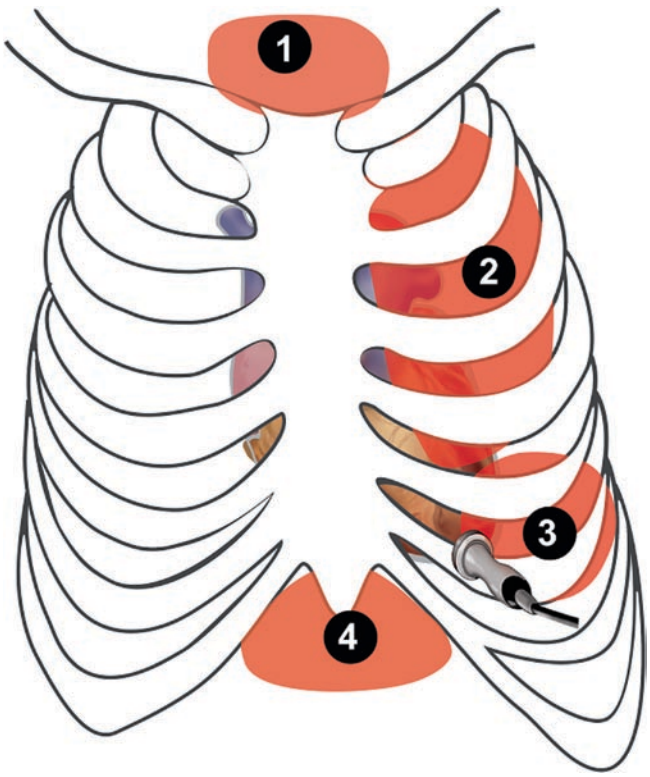

Fig. 1.2 Anatomic structures and transthoracic transducer positions for obtaining parasternal views (*position 2*), apical views (*position 3*), supra-sternal views (*position 1*), and subxiphoid views (*position 4*)

diseases.[3,4] The supra-sternal approach places the patient's head in retroflexion and permits an observation of the base of the heart and great vessels.[5] Finally, the right parasternal window is useful for visualizing the aorta and inter-atrial septum and is obtained by placing the patient in right lateral position.[6,7]

M-Mode Echocardiography

M-mode echocardiography was described at the end of the 1950s[8] and introduced into clinical practice at the beginning of the 1960s. M-mode was the only technique used during echocardiographic study for 20 years, but current echocardiographic study includes different techniques such as 2D, Doppler, and colour-flow Doppler imaging. M-mode, however, remains a very useful part of ultrasound examination. M-mode echocardiography is able to evaluate rapid motion of cardiac structures because sampling rate is higher than in 2D echo, and it can show movement in thin structures such as the cardiac valves. The method is based on transmission of echo in a single line. Returning echoes are displayed on a graph in which structural depth and movement in time are reliably represented.

The routine cardiac examination with M-mode shows images of four cardiac chambers and cardiac valves. A better evaluation is obtained with the probe guided by 2D echo image in parasternal view, perpendicular to cardiac structure. It is sometimes necessary to move the probe tip from a different intercostal space in order to determine the best position with perpendicular incident echoes through cardiac structures.

Aortic Valve

Aortic valve, left atrium, and aortic root are well evaluated when the cursor is perpendicular to the aortic root. An M-mode recording through the aortic root at the level of valve leaflets shows aortic walls in parallel moving anteriorly in systole and posteriorly in diastole. Aortic valve leaflet coaptation in M-mode is seen as a thin single line in diastole and a double line in systole that separate rapidly and completely, forming a box-like appearance (Fig. 1.3). It is possible to evaluate the pre-ejection time (from EKG q wave to beginning of aortic valve opening) and ejection time (period in which the aortic leaflets are opened). The left atrium is posterior to the aortic root and shows filling during atrial diastole (ventricular systole) and emptying in atrial systole (ventricular diastole). Anterior displacement of the aortic root is due to left atrial filling. This anterior movement is increased when there is increased filling (mitral regurgitation) or decreased in case of decreased cardiac output.

Mitral Valve

The mitral valve can be studied in parasternal view by placing the cursor perpendicular to the septum and mitral leaflets. The ultrasonic beam transverses the anterior thorax, right ventricle, inter-ventricular septum, anterior mitral leaflet, posterior mitral leaflet, posterior wall of left ventricle, and the pericardium (Fig. 1.4).

The leaflets of mitral valve separate widely with maximum early-diastolic motion of the anterior leaflet, termed E point. The leaflets move together in the centre of the left ventricle and then separate again after atrial systole (A wave).

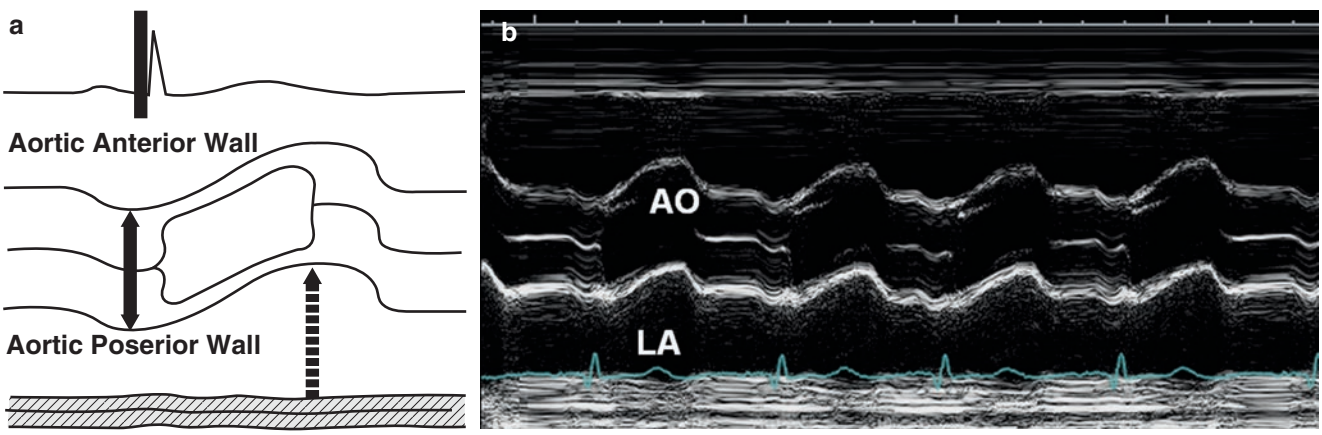

Fig. 1.3 **(a)** Diagram of aortic valve and left atrium. Cursor transects anterior aortic wall, aortic valve, posterior aortic wall, left atrium, and posterior wall of left atrium. **(b)** Aortic valve plane in M-mode. It is possible to show aortic leaflets as a box in systole and thin line in diastole. *AO* aorta; *LA* left atrium

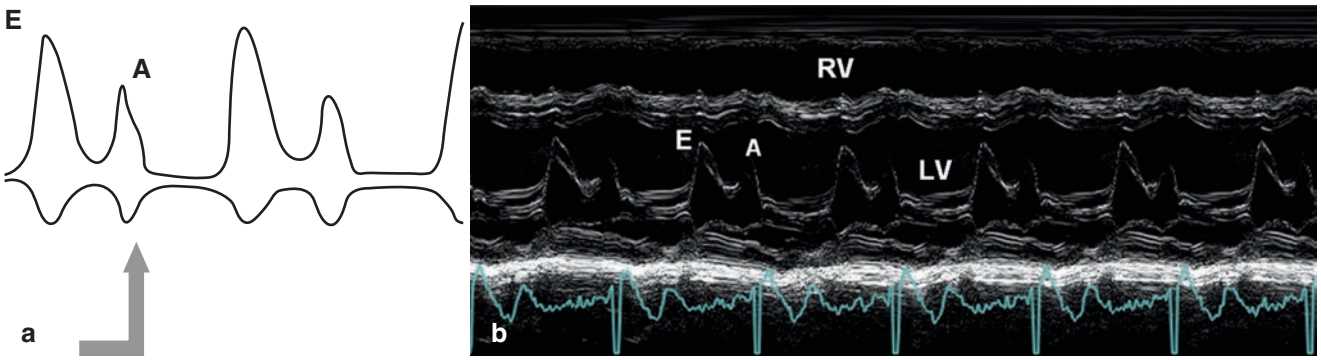

Fig. 1.4 **(a)** Diagram of mitral valve. **(b)** Mitral valve in M-mode, opening in diastole in the centre of left ventricle. The leaflets of mitral valve separate widely with maximum early-diastolic motion of anterior leaflet called E point. The leaflets move together in the centre of left ventricle and then separate again after atrial systole (A wave). *RV* right ventricle; *E* early mitral diastolic wave; *A* late diastolic mitral valve wave; *LV* left ventricle

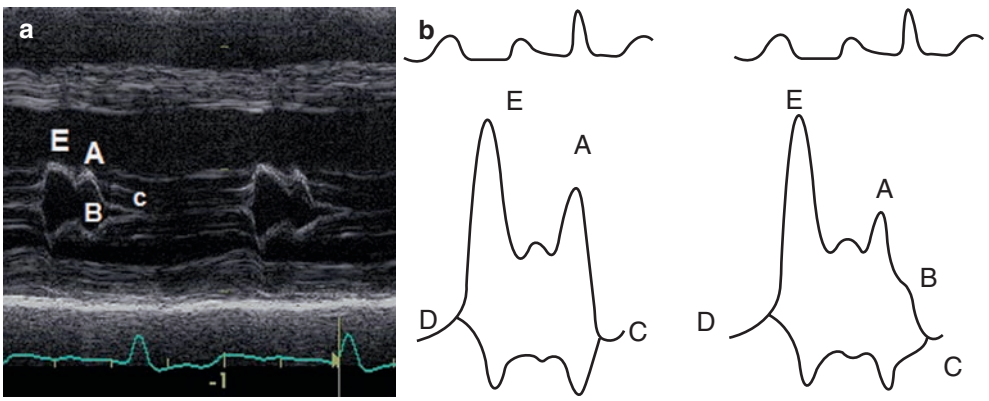

Fig. 1.5 Diagram of mitral valve opening in normal patient and in patients with ventricular dysfunction. In normal patients, the leaflets of mitral valve separate widely with maximum early-diastolic motion of anterior leaflet (E point). Distance between E point and septum is usually short. Leaflets move together in the centre of left ventricle and then separate again after atrial systole (A wave). The slope from A point to mitral closure (C point) is linear. In patients with left ventricular dysfunction and high left ventricular end-diastolic pressure, the slope from A to C presents a B bump or shoulder. M-mode (b) of a patient with left ventricular dysfunction and high end-diastolic pressure with characteristic shoulder on A-C line (B point). The distance between E wave and septum is greater. *D* opening point of mitral valve; *E* point is the maximum early-diastolic motion of anterior leaflet; *A* point is the late diastolic motion of anterior leaflet of mitral valve; *C* point is the closure of mitral valve; *B* point is the shoulder of A-C slope

The slope from A point to mitral closure (C point) is linear unless left ventricular end-diastolic pressure is elevated. In this case, a B bump or an A-C shoulder can be seen (Fig. 1.5). In systole, the leaflets of the mitral valve are seen as a thin line that moves slightly forward during systole.

Left Ventricle

Measurements of the left ventricular cavity dimensions, thickness of septum and posterior wall, volumes, and mass can be readily derived from M-mode recordings. These measurements are limited because they represent a single line evaluation through the septum and, in case of abnormal regional contraction, can be misleading.

For better reproducibility of M-mode evaluation, morphologic and temporal criteria have been established: (1) cursor perpendicular to septum and left ventricle, (2) diastolic measures at the beginning of QRS, and (3) systolic measures at highest excursion of posterior wall endocardium. The ventricular border of septum (as anterior line) and the ventricular border of posterior wall (as posterior line) can be used to evaluate left ventricular diameters. It is important to distinguish between mitral chordae and anterior border of the posterior wall (Fig. 1.6). The cavity dimensions can be used to calculate ejection fraction, but this measure involves assumptions that do not always hold (Tables 1.1–1.4). With the transducer placed along the left sternal border and in the third or fourth intercostal space, we can sweep the ultrasonic beam in a sector between the base of the heart and the apex (Fig. 1.7).

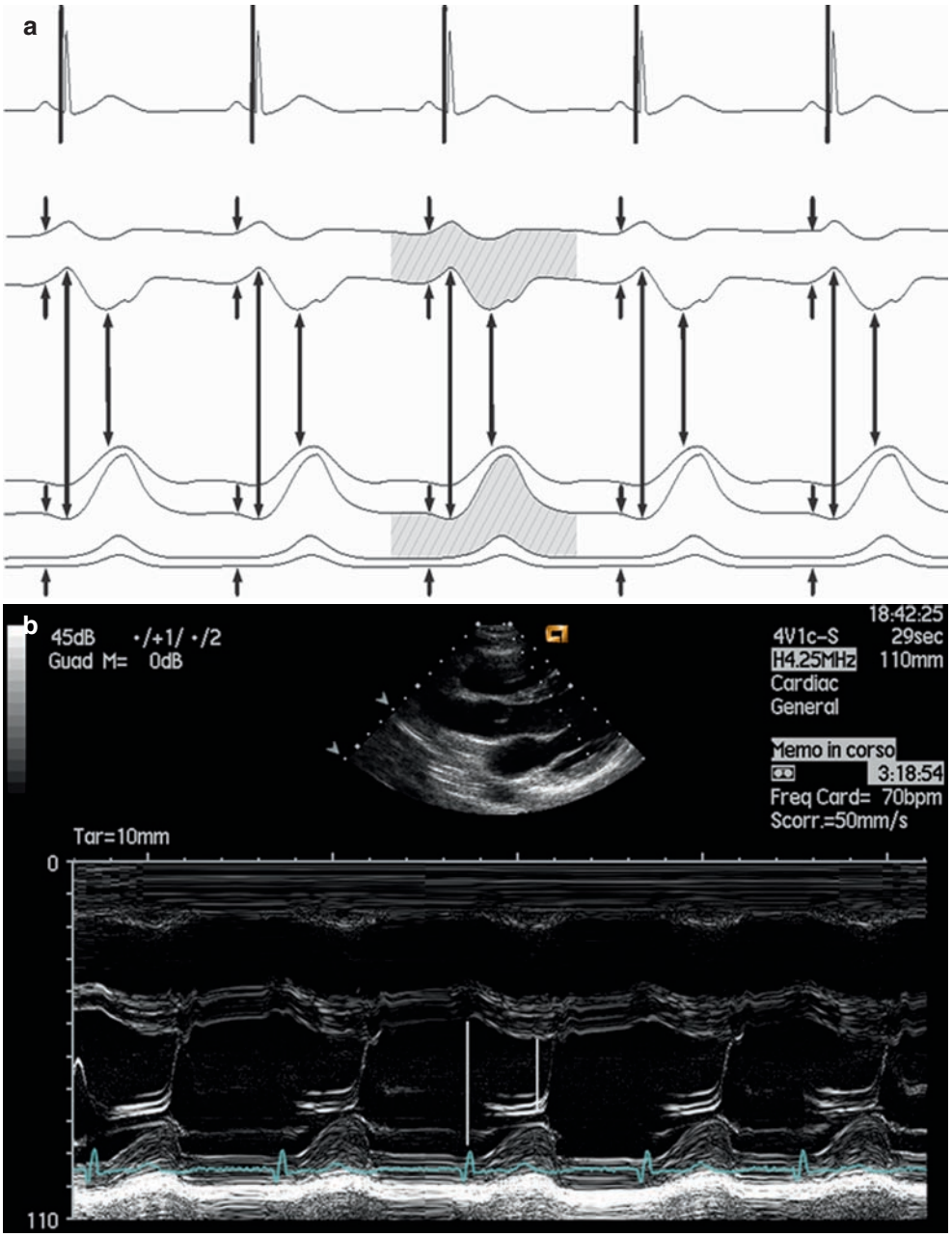

Fig. 1.6 **(a)** Diagram of left ventricle. The *arrows* show measures of end-systolic and end-diastolic diameters of left ventricle and thickness of septum and posterior wall. For evaluation of left ventricular diameters, the ventricular border of septum and ventricular border of posterior wall are used as *anterior line* and *posterior lines*, respectively. **(b)** Left ventricle measures in M-mode. Diastolic measures are taken at the beginning of QRS and systolic measures are taken where higher excursion of posterior wall endocardium can be seen. The *long and short lines* show left ventricle end-diastolic diameter and left ventricle end-systolic diameter, respectively

Table 1.1. Normal M-mode values[9,10]

	≤30 years	>70 years	M	F
			N = 288	*N* = 524
LVID (mm)	48 ± 5.6	45.3 ± 5.6	50.8 ± 3.6	46.1 ± 3
LVSS (mm)	30 ± 5.8	28.4 ± 5.8	32.9 ± 3.4	28.9 ± 2.8
IVS thickness (mm)	9.8 ± 1.7	11.8 ± 1.7	9.5 ± 3.5	8.5 ± 3
PW s (mm)	10.1 ± 1.4	11.8 ± 1.4	9.5 ± 2.5	8.5 ± 3.5
Aorta	27.4 ± 5.7	33.5 ± 5.7	32 ± 3	28 ± 3
Left atrium	34.3 ± 7	39.7 ± 7	37.5 ± 3.6	33.1 ± 3.2

LVID left ventricular internal dimension, end diastole; *LVSS* left ventricular internal dimension, end systole; *IVS* inter-ventricular septum; *PW* posterior wall; *M* male; *F* female

Table 1.2. Ventricular mass and myocardial dimension[33]

	n	g/m2	g/m	SIV (mm)	PP (mm)	LVID (mm)
Man						
Total	47	99 ± 15(129)	108 ± 17	10.2 ± 1.2	9.9 ± 1	51 ± 3
<50a	27	97 ± 14(124)	107 ± 15	10.1 ± 0.9	9.6 ± 0.8	52 ± 3
≥50a	20	102 ± 17(135)	111 ± 20	10.4 ± 1.5	10.2 ± 1.1	51 ± 3
Woman						
Total	64	88 ± 15(129)	89 ± 17	9.2 ± 1.2	8.9 ± 0.9	47 ± 4
<50a	34	82 ± 13(108)	83 ± 14	8.6 ± 0.7	8.6 ± 0.7	47 ± 3
≥50a	30	93 ± 16(124)	96 ± 18	9.8 ± 0.9	9.2 ± 0.9	47 ± 4

LVID left ventricular internal dimension, end diastole; *LVSS* left ventricular internal dimension, end systole; *IVS* inter-ventricular septum; *PW* posterior wall

Table 1.3. Left ventricular volumes[15]

	End-diastolic	End-systolic
Apical 4-chamber (cc)		
Man	112 ± 27	35 ± 16
Woman	89 ± 20	33 ± 12
Apical 2-chamber (cc)		
Man	130 ± 27	40 ± 14
Woman	92 ± 19	31 ± 11
Biplane (Simpson)		
Man	110 ± 22	34 ± 12
Woman	80 ± 12	29 ± 10

Right Ventricle

Diastolic diameter can be measured along the same lines as for left ventricular diastolic measures. The anterior border of right ventricle is not clearly visible in many cases and the position of right ventricle is sometimes oblique. The different alignment between the cursor and the right ventricle yields high measurement variability (Fig. 1.6).

Tricuspid Valve

The tricuspid valve can be recorded from the initial position and by angulating the transducer inferomedially. The tricuspid valve's M-mode image is similar to that of the mitral valve and uses the same nomenclature (Fig. 1.8).

Pulmonary Valve

The posterior leaflet of the pulmonary valve can be seen with the transducer in the initial position and by tilting slightly superiorly and laterally. The leaflet moves to a posterior position in systole and to an anterior position in diastole. *A wave* is the expression of atrial contraction and is signed after EKG *p wave. Point b* occurs at the beginning of systole. *Point c* marks maximal excursion. *Point d* occurs at the end of systole and posterior closure is labelled *Point e.* During diastole and just before atrial contraction, the leaflet moves posteriorly with maximum excursion and is denoted as *Point f.* As stated previously, slight displacement of the leaflet in diastole is referred to as *a wave.* This wave is increased when pulmonary stenosis is present, and decreased

Table 1.4. Left ventricular dimension and body surface (m^2)[11]

		1.4–1.6 m^2	1.61–1.8 m^2	1.81–2.0 m^2
Long axis (mm)	Diastole Systole	34–49 23–39	36–51 24–41	39–53 25–44
Short axis (mm)	Diastole Systole	35–55 23–39	38–58 24–40	41–61 26–41
Four chamber (mm)	Diastole Systole	59–83 45–69	63–87 46–74	66–90 46–79

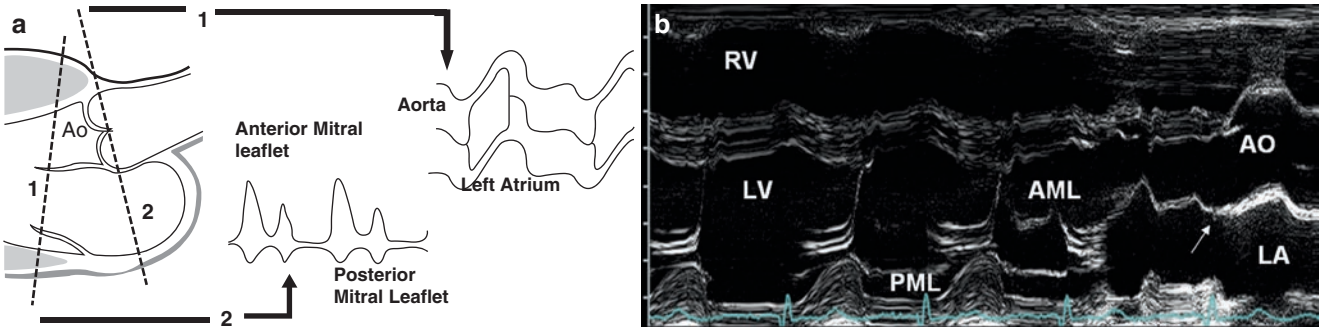

Fig. 1.7 Standard sweep from left ventricle and mitral valve to aorta and aortic valve. **(a)** Diagram of moving cursor line from left ventricle (*line 1*) to aorta (*line 2*). It is possible to measure all important diameters of the left and right ventricle, aorta, and left atrium. **(b)** M-mode of moving cursor line from left ventricle to mitral valve and aorta. The mitral valve appears in the centre of the left ventricle and aortic valve appears in the centre of the aorta. Line of continuity between AML and posterior aortic wall is evident. *Large arrow* in the diagram shows probe movement from mitral valve to aortic valve; thin arrow in M-mode shows continuity between anterior leaflet of mitral valve and posterior aortic wall. *AO* aortic valve; *LA* left atrium; *LV* left ventricle; *RV* right ventricle; *AML* anterior mitral valve leaflet; *PML* posterior mitral valve leaflet

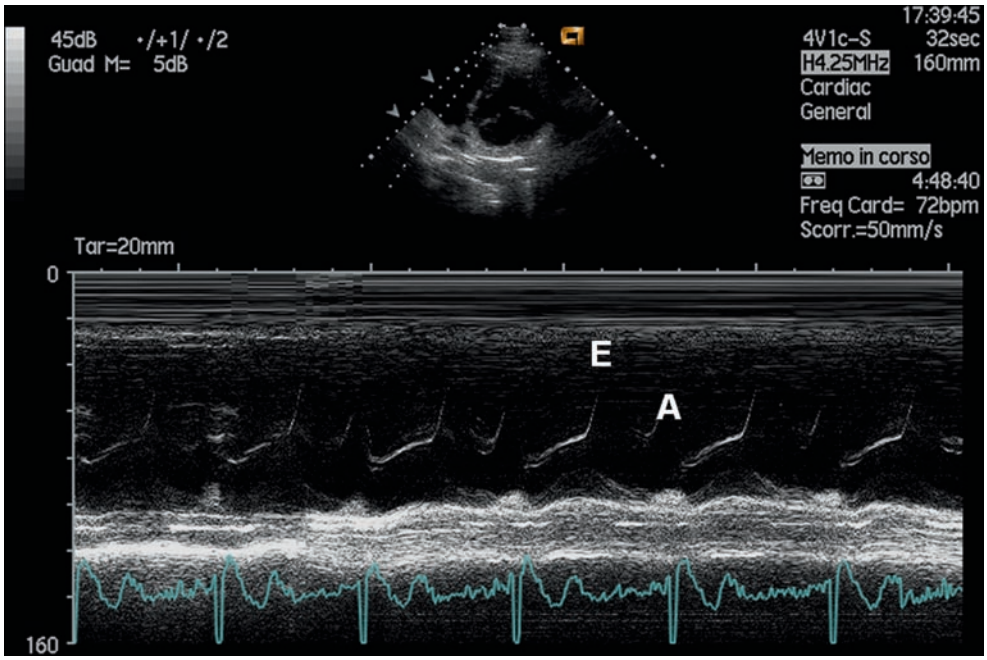

Fig. 1.8 Tricuspid valve M-mode image is similar to mitral valve image and uses the same nomenclature. E point is the maximum early-diastolic motion of tricuspid valve. A-point is the late diastolic motion of tricuspid valve

when pulmonary hypertension is present. In the latter case, midsystolic closure of the pulmonary valve is seen. Finally, it is possible to evaluate pre-ejection period from EKG *q wave* to *Point b,* and ejection period can be measured from *Point b* to *Point e* (Fig. 1.9).

Two-Dimensional Echocardiography

Two-dimensional echocardiography offers the possibility of real-time high resolution imaging of cardiac structure and function. It is the basis of the study of cardiac imaging with ultrasound, as it is the reference for analysis of cardiac flow with pulsed-wave Doppler (PWD), continuous-wave Doppler (CWD), and colour-flow Doppler.

Preference of image orientation in 2D echocardiography varies from one echo laboratory to another one. Recommendations for echocardiographic image orientation which were established by the American Society of Echocardiography[12] will be herein adhered to in the description of different echocardiograhic imaging planes. There are three basic imaging slices utilized for obtaining such images[13,14]: long axis (from the aorta to the apex), short axis, and 4-chamber (Fig. 1.10).

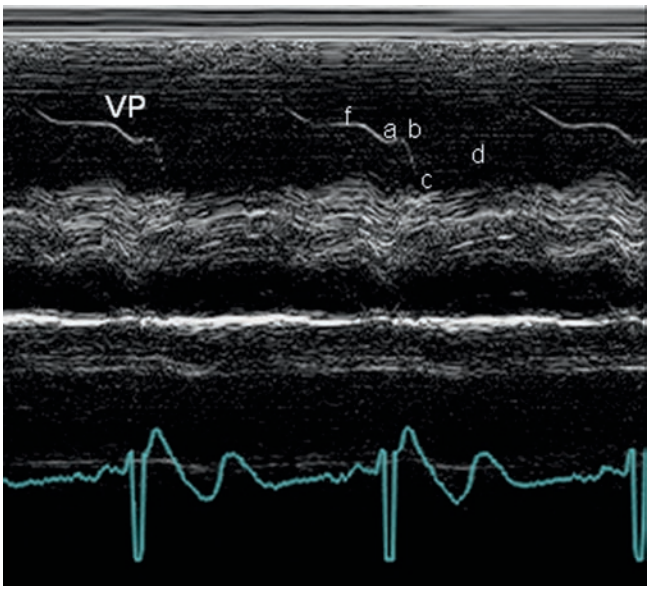

Fig. 1.9 The pulmonary valve is observed in short-axis parasternal view under the guide of 2D images. It is possible to follow the anterior and posterior excursions of the posterior leaflet in systole and diastole, respectively. *A wave* is atrial contraction (after EKG p wave); *b point* is at the beginning of systole; *point d* is the end of systole; *f point* is in diastole before atrial contraction and is maximum posterior displacement of the valve

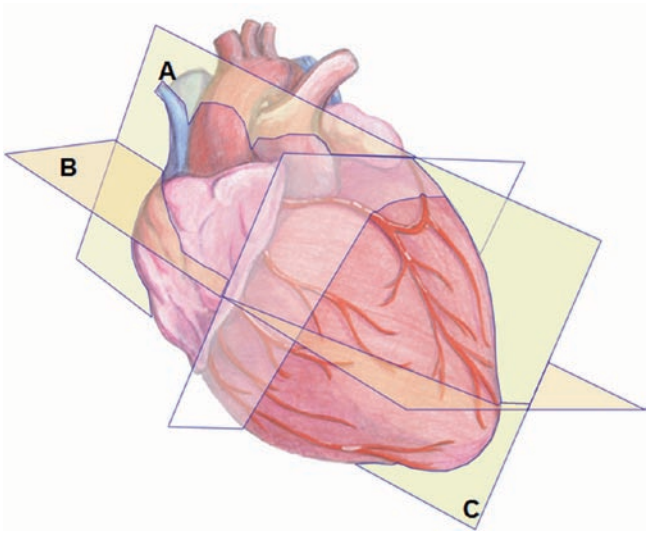

Fig. 1.10 Tomographic image planes used in a 2D echocardiographic study. *A* long axis; *B* short axis; *C* 4-chamber

Parasternal Long-Axis View

In this view (Fig. 1.11), the ultrasound scan plane intersects an imaginary line drawn from the right shoulder to the left hip and represents a long-axis section of the left ventricle. A large number of cardiac structures that do not lie precisely in the scan plane can be visualized at this level. Due to variations in patient anatomy, slight re-positioning of the transducer must be performed for image optimization.

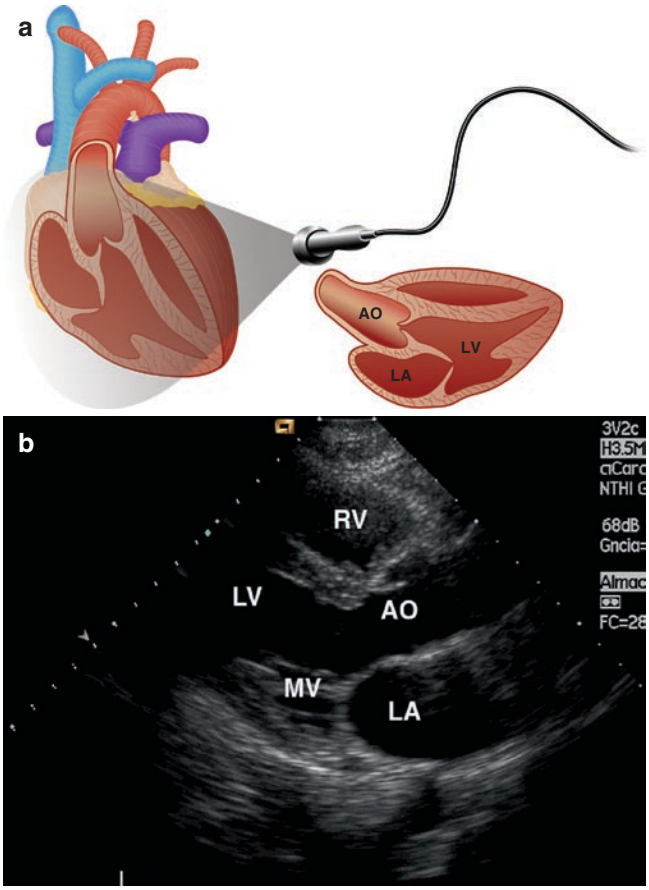

Fig. 1.11 **(a)** Schematic anatomic section of a parasternal long-axis view. **(b)** Corresponding still-frame of a 2D echocardiography of the parasternal long-axis view. *AO* aortic valve; *RV* right ventricle; *LA* left atrium; *MV* mitral valve; *LV* left ventricle

The *right ventricle* is located in the region closest to the transducer. The *left atrium* can be seen in the far right region of the image. In some cases, it is possible to visualize a round structure representing the left inferior pulmonary vein immediately posterior to left atrium. The *aortic valve* and *ascending thoracic aorta* can be viewed between left atrium and right ventricle. The aortic valve can be visualized during systole as two linear echocardiographic images parallel to the walls of the ascending thoracic aorta. The *right coronary cusp* and non-coronary cusp can be viewed in the regions closest to and farthest from the transducer, respectively. A linear echodense image can be observed at level of cusp closure during diastole. The *anterior* and *posterior leaflets* of the *mitral valve* can also be identified in this imaging plane, as well as the *tendinous chords* and their fusion with *papillary muscle.* The *left ventricular outflow tract* is situated between the inter-ventricular septum and anterior mitral leaflet, which are observed in the anterior and posterior positions of the image, respectively. The left ventricle is found in the left area of the image when the inter-ventricular septum and posterolateral wall are placed proximal and distal to the transducer, respectively. The *pericardium* appears at the lower edge of the image

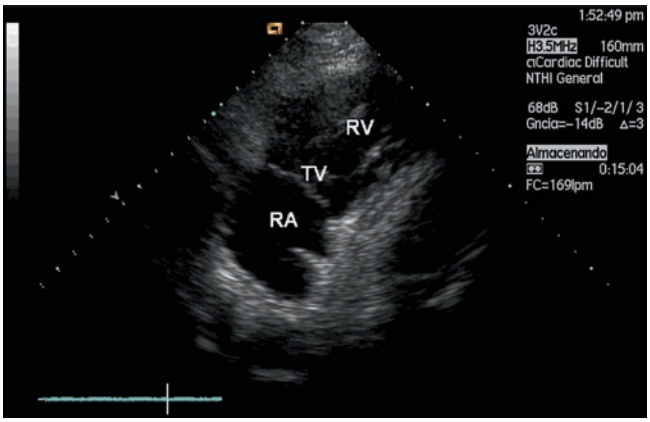

Fig. 1.12 Long-axis view of the right ventricle and right atrium. *RA* right atrium; *RV* right ventricle; *TV* tricuspid valve

where the descending thoracic aorta is also sometimes visible. The *coronary sinus* can be visualized as an echo-free structure at atrio-ventricular groove level and follows the motion of the atrio-ventricular ring.

Long-axis views of the *right ventricle* and *right atrium* are obtained upon slight inferomedial rotation of the transducer. In this view, the right atrium is observed in the right posterior region of the image, while the right ventricle apex appears in the extreme upper left-hand corner. It is also possible to detect the orifice of the inferior vena cava and Eustachian valve in the posterior wall of the right atrium. This image plane permits the assessment of *inferior* and *anterior right ventricle walls* and *inflow tract,* as well as of anterior and posterior leaflets of the tricuspid valve (Fig. 1.12).

Parasternal Short-Axis View

The parasternal short-axis view is obtained upon 90º clockwise rotation of the transducer from its initial position. The ultrasound scan plane now intersects an imaginary line drawn from the left shoulder to the right hip. Four different imaging planes are made possible by slightly tilting the transducer.

The base of the heart can be visualized by tilting the transducer towards the right shoulder within what is termed *parasternal short-axis plane at level of aorta* (Fig. 1.13). The aortic valve, located anterior to left atrium and posterior to right ventricle, is observed in the central region of the image along with its three leaflets (in a Y-shape configuration): right coronary at the lower left, coronary in the upper region, and non-coronary in the left region of the image. This imaging plane permits the measurement of aortic root size, detection of morphological alterations of Valsalva sinus (aneurysms, etc.), and diagnosis of proximal aortic dissection. Congenital anomalies of the aortic valve and valve leaflet abnormalities can also be assessed.

The *tricuspid valve* is observed to the left of the aortic valve. Coursing leftward and anterior to the aortic root is the right ventricular outflow tract. Rightward and anterior to the aortic valve, a portion of the *pulmonary valve* can be seen. The main *pulmonary artery* curves around the aorta and its two principal branches (*right* and *left pulmonary arteries,* respectively) can be observed. The left atrium is seen posterior to the aortic valve and separated from the right atrium by the atrial septum. In spite of the fact that the parasternal short-axis imaging plane was originally indicated for the assessment of septal defects (atrial septal defect, patent

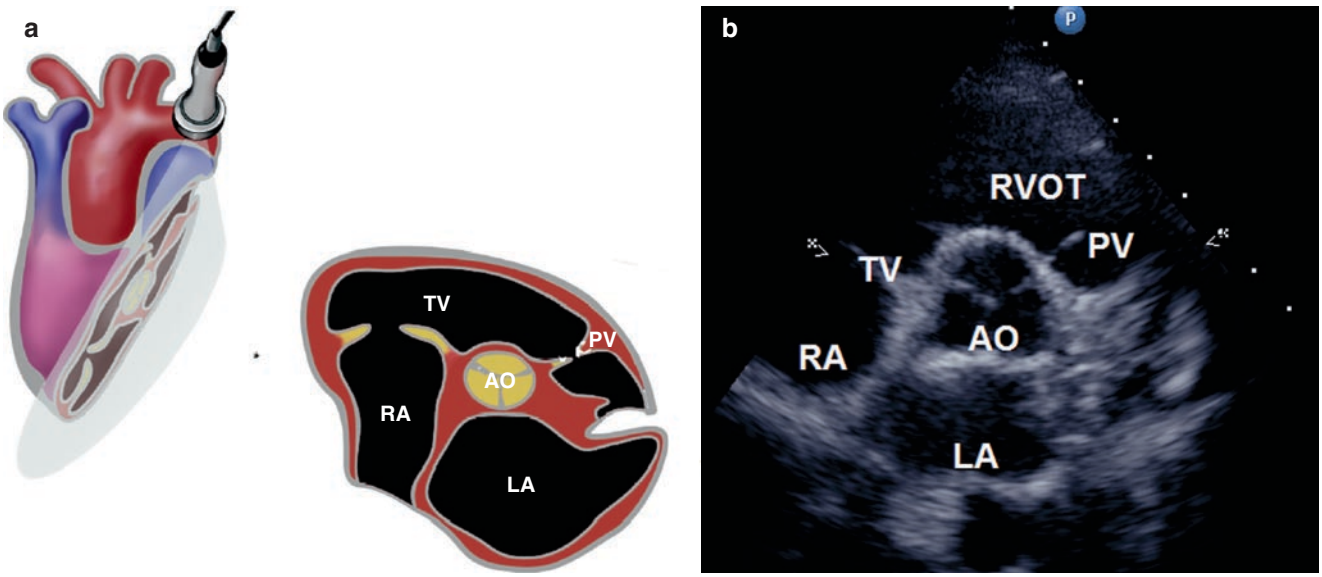

Fig. 1.13 **(a)** Schematic anatomic section of a parasternal short axis plane through the base of the heart. **(b)** Corresponding still-frame of a 2D echocardiography of parasternal short-axis plane at the base of the heart. *AO* aortic valve; *RA* right atrium; *RV* right ventricle; *LA* left atrium; *TV* tricuspid valve; *PV* pulmonary valve; *RVOT* right ventricular outflow tract

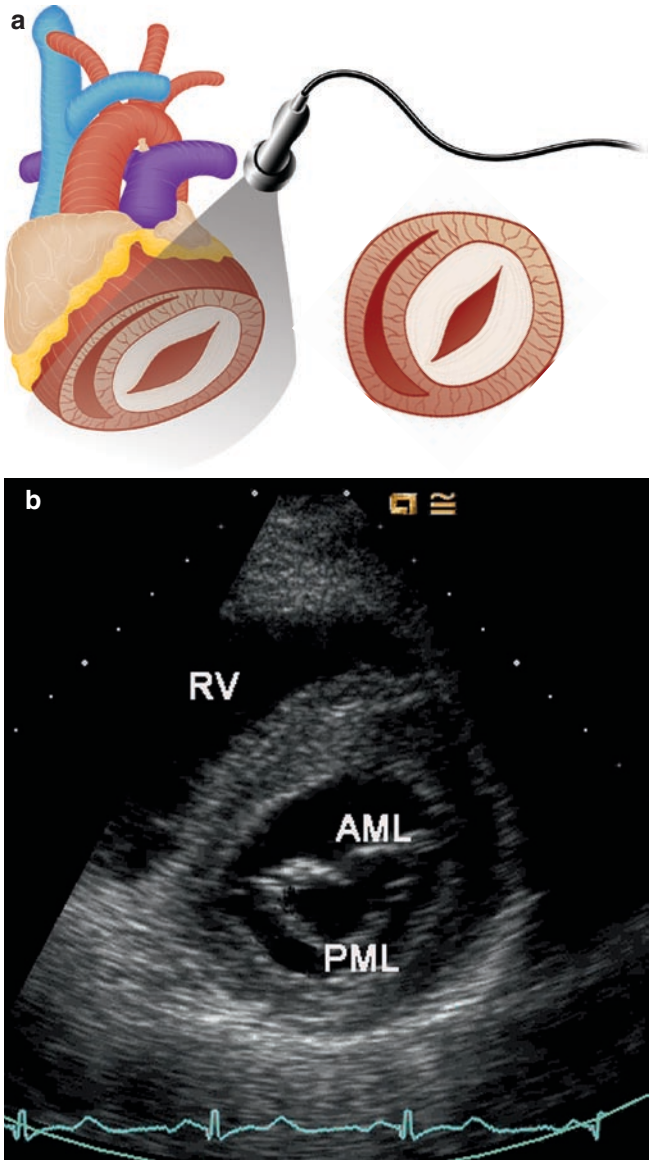

Fig. 1.14 **(a)** Schematic anatomic section of a parasternal short-axis plane through the mitral valve. **(b)** Corresponding still-frame of a 2D echocardiography of parasternal short-axis plane at the mitral valve level. *RV* right ventricle; *AMV* anterior mitral valve leaflets; *PMV* posterior mitral valve leaflets

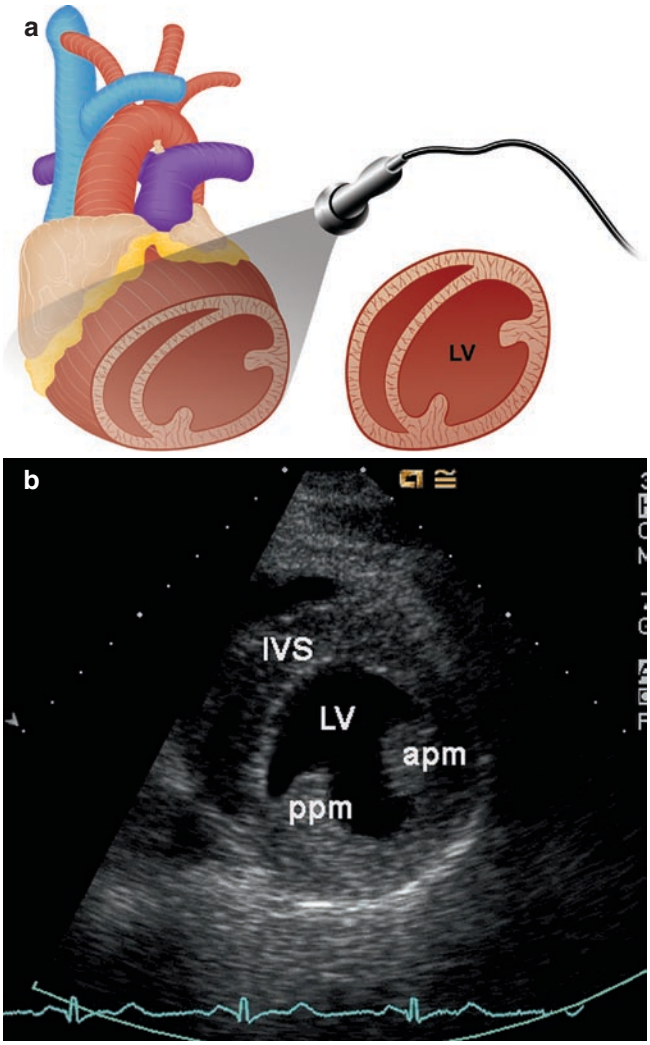

Fig. 1.15 **(a)** Schematic anatomic section of a paraesternal short-axis plane through papillary muscle level. **(b)** Corresponding still-frame of a 2D echocardiography of the parastenal short-axis plane at the papillary level. *IVS* inter-ventricular septum; *apm* anterior papillary muscle; *ppm* posterior papillary muscle

foramen ovale), these are analyzed more adequately with apical 4-chamber and sub-costal imaging.

An inferior and rightward tilting of transducer results in a *parasternal short-axis view at the level of the mitral valve* (Fig. 1.14). The mitral valve is observed with the septal leaflet in anterior position and posterior leaflet in the lower portion of the image (whose form has been commonly likened to a fish mouth). Tilting the transducer more parallel to the direction of blood flow, it is possible to identify the *left ventricle* as well as antero-lateral and postero-medial papillary muscles located inside the ventricular cavity at the 3 and 8 o′clock positions, respectively (Fig. 1.15). The right ventricle (anterior, lateral, and posterior segments) can be identified in the left anterior portion of the image and is separated from the left ventricle by the inter-ventricular septum. Figure 1.16 shows the different segments of the left ventricle, which can be observed in the short-axis view at mitral, papillary muscle, and apical levels.

Apical Views

The apical imaging plane is obtained with the patient in left lateral decubitus position. The ultrasound scan plane intersects an imaginary line that runs superiorly and medially from the left median axillary line to the right scapula of the patient. The transducer is placed tangentially in the fifth intercostal space along the median axillary line at apical level. It is useful in some patients to locate the cardiac apex and place the transducer nearest to the point of maximum apical impulse. Another way of locating the apex (in cases where palpitation is inadequate) consists of progressively sliding the transducer from parasternal short-axis plane position.

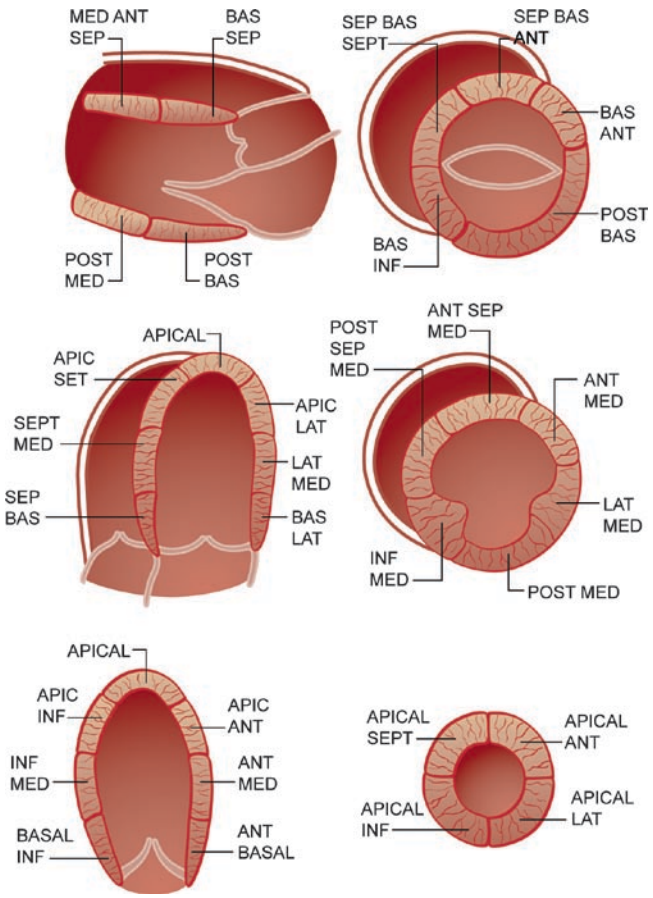

Fig. 1.16 Schematic diagram of the 16 segment model for regional wall motion analysis. The myocardium is divided into different levels: basal, mid-, or papillary muscle, and apical. The different segments can be analyzed from multiple tomographic planes

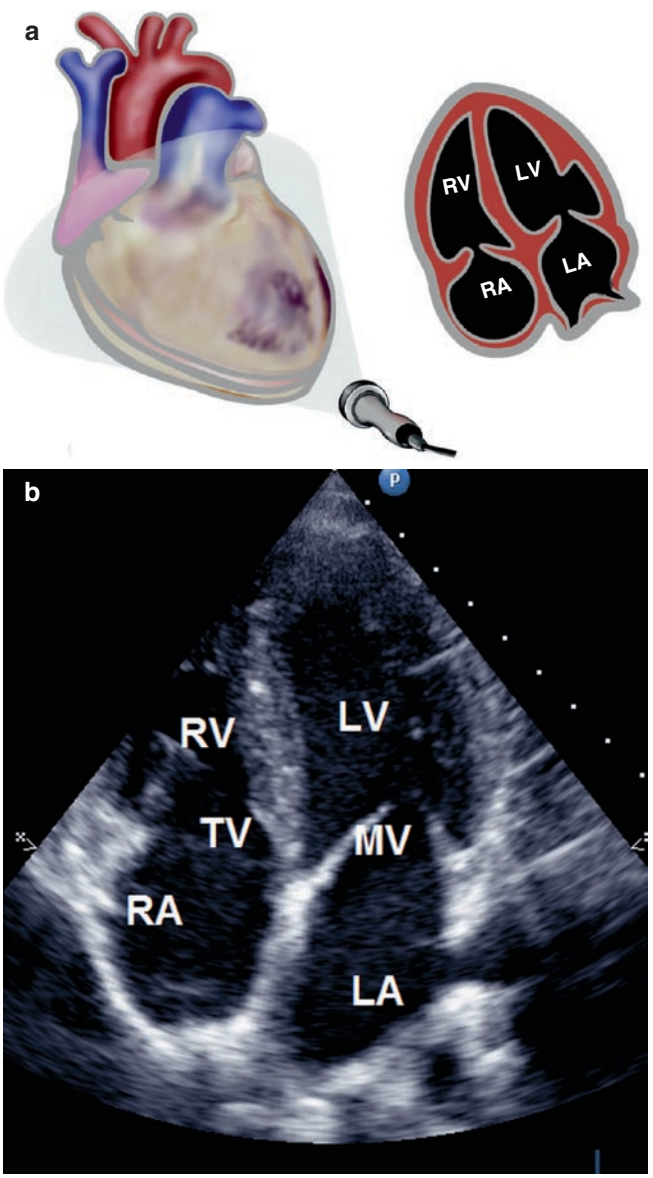

Fig. 1.17 **(a)** Schematic anatomic section of an apical 4-chamber view. **(b)** Corresponding still-frame of a 2D echocardiography apical 4-chamber view. *RV* right ventricle; *LV* left ventricle; *MV* mitral valve; *TV* tricuspid valve

Subsequent clockwise rotation of the transducer about its own axis and with a slight lateral tilt results in 4-, 5-, 2-, and 3-chamber views. Images obtained with the transducer in very high or very medial intercostal spaces should be avoided as they result in truncated ventricular cavity images in which it is not possible to evaluate the ventricular apex.

Apical 4-Chamber View

The apical 4-chamber view (Fig. 1.17) displays all four cardiac chambers, inter-ventricular and inter-atrial septums, mitral and tricuspid valves, and the crux of the heart. The apex and atriums are observed in the image's upper and lower regions, respectively. The right and left cavities of the heart along with their respective atrio-ventricular valves are found in the left and right regions of the image, respectively. In some patients it is possible to observe a transverse cross section of the descending thoracic aorta in the right bottom region of the image.

The mitral valve is usually at a position slightly higher than the tricuspid valve. The anterior mitral leaflet inserts into the left atrio-ventricular groove near the cephalic edge of the membranous septum, while insertion of the septal leaflet of the tricuspid valve occurs 5–10 mm below that of the anterior mitral leaflet. Such anatomical information is useful in identifying ventricular chambers. The entire atrial septum can be observed with a slight anterior re-positioning of the ultrasound beam; this must be done with care because any slight posterior deviation can truncate the image and prevent adequate visualization of the middle segment (region of the *fossa ovalis*). The pulmonary veins can be seen leading to the left atrium in the most posterior region of the image. The image makes possible an optimum analysis of the segmentary contractility of both ventricles through assessments of the lateral wall (in the right region of the image), septum, left ventricular apex, and lateral wall of the right ventricle (Fig. 1.17, Tables 1.3 and 1.4).

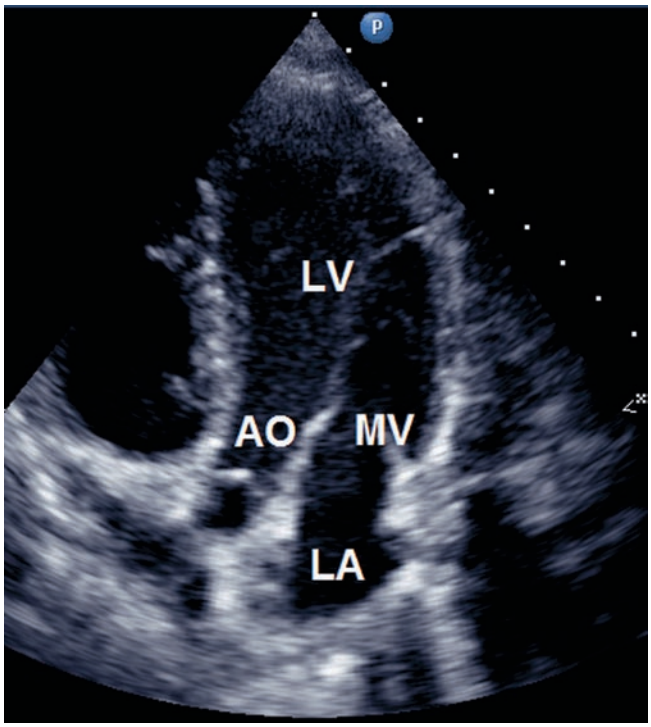

Fig. 1.18 Still-frame of 5-chamber view. We can detect the left ventricular outflow tract, aortic valve, and proximal segment of the ascending thoracic aorta. *MV* mitral valve; *AO* aortic valve; *L* left atrium; *LV* left ventricle

Apical 5-Chamber View

A slight counterclockwise tilt of the transducer makes possible an image of the left ventricular outflow tract, aortic valve, and proximal segment of the ascending thoracic aorta. This section corresponds to the 5-chamber view (Fig. 1.18). The aorta now lies in the position previously occupied by the crux cordis.

Apical 2- and 3-Chamber Views

A 90º counterclockwise rotation of the transducer results in an apical 2-chamber view (Fig. 1.19), in which it is now possible to make an assessment of the left atrium, mitral valve, and left ventricle (anterior and inferior walls in the right and left regions of the image, respectively). Both the apical 2- and 4- chamber views are fundamental in being able to assess segmentary wall motion and left ventricular ejection fraction using Simpson's method. Finally, an apical 3-chamber view can be obtained, in which the aortic valve and aortic root appear in the right portion of the image. This view is similar to the right anterior oblique angiographic projection and has also been called *right anterior oblique equivalent.*

Sub-costal Views

The sub-costal views make possible an assessment of the right and left sides of the heart, which is impossible to obtain

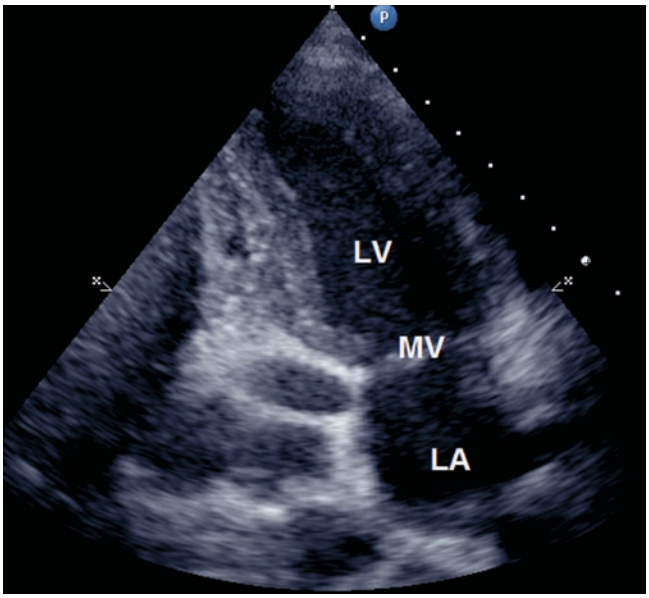

Fig. 1.19 Apical 2-chamber view. *LA* left atrium; *LV* left ventricle; *MV* mitral valve

with parasternal planes. To facilitate the sub-costal imagings, the patient is moved into supine position. Such images are particularly important in patients with chronic obstructive lung disease and emphysema. Figure 1.20 shows the different views obtained from this position: the *sub-costal 4-chamber view* (Fig. 1.20a) is achieved by placing the transducer at the centre of the epigastrium and tilting downward along an imaginary line drawn from the supra-sternal notch to the patient's left shoulder. The image is similar to that of the apical 4-chamber. The plane is especially useful for evaluating defects at the level of atrial septum. The liver is found in the upper region of the image, while below is the right ventricle with its apex directed towards the right. Contractility of the inferior and lateral walls and apex of the right ventricle, as well as the presence of pericardial effusion, can be analyzed.

The tricuspid valve and right atrium can be found to the left of the right ventricle. Wall motion can now be assessed at the septum and left ventricular inferoposterior level. A slight tilting of the transducer results in a 5-chamber view, which makes it possible to observe the left ventricular outflow tract and aortic valve. In the sub-costal view, it is also possible to obtain a section of the abdominal aorta.

An image showing the liver, suprahepatic veins, and transverse cross section of the inferior vena cava can be obtained if the transducer is pointed towards the patient's right side. In order to obtain a long-axis view, it is necessary to point the transducer to the patient's right flank (Fig. 1.20b). In some patients, a very prominent Eustachian valve can be seen in the junction of the inferior vena cava and right atrium.

The short-axis sub-costal view is similar to that of the parasternal. However, it is usually more favourable in the analysis of the right heart (Figs. 1.20c, d).

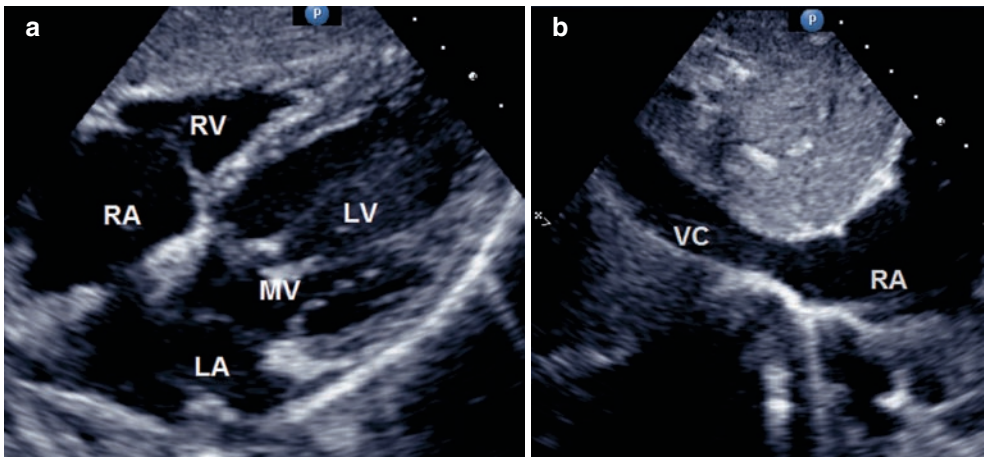

Fig. 1.20 2D echocardiographic images of the different sub-costal views. **(a)** Long-axis view allows a better definition of the atrial septum. **(b)** Entrance to the inferior vena cava to the right atrium. **(c)** Short axis at the basal level in which we can analyze simultaneously the right atrium and the inflow and outflow areas of the right ventricle and pulmonary valve and pulmonary trunk. **(d)** Sub-costal short-axis plane of the left ventricle. *RA* right atrium; *RV* right ventricle; *LA* left atrium; *TV* tricuspid valve; *PV* pulmonary valve; *LV* left ventricle; *MV* mitral valve

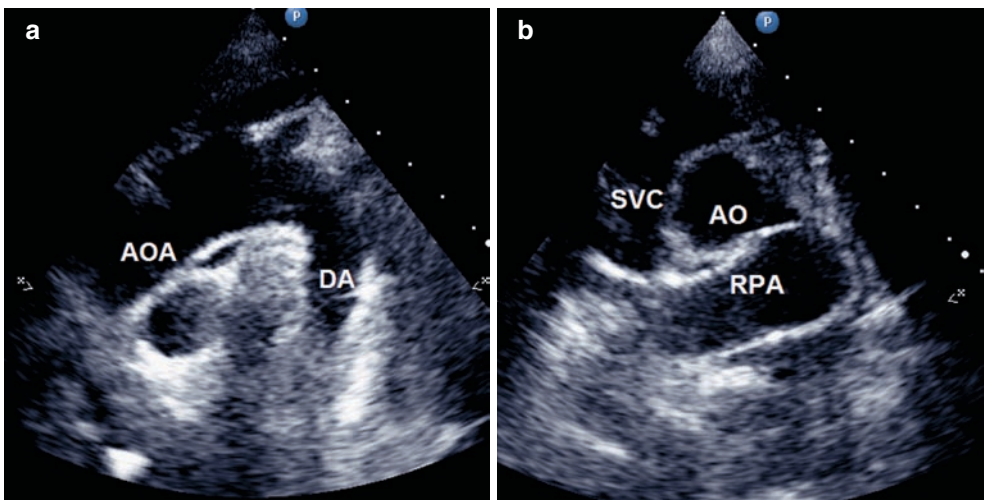

Fig. 1.21 The transducer position in the supraesternal notch allows the visualization of the ascending aorta, aortic arch, brachiocephalic vessel, and descending aorta. **(a)** Long-axis plane through the aorta from the supra-sternal position. **(b)** Short-axis view of the aortic arch. *SVC* superior vena cava; *RPA* right pulmonary artery; *DA* descending thoracic aorta; *AO* aorta

Supra-sternal View

Two different images of the aorta can be obtained if the transducer is placed over the supra-sternal notch (Fig. 1.21). Orientation of the transducer's long axis parallel to the trachea results in the supra-sternal long-axis view. The ascending aorta and aortic arch (with the brachiocephalic vessels) can be seen in the left region of the image, and descending thoracic aorta is found in the right region. The right pulmonary artery and left atrium are seen beneath the aortic arch. A 90º counterclockwise rotation of the transducer allows us a study of the aortic arc. The transverse cross section of the aortic arch is located in the upper region of the image with visualization of the right pulmonary artery in its long-axis format and located inferiorly. A section of the left atrium at the level of its posterior wall as well as the outflow orifice of the right

pulmonary veins can be observed in the extreme lower region of the image. Clockwise rotation of the transducer permits visualization of the superior vena cava appearing along the right side of the aorta.

Other Imaging Planes

It is sometimes necessary to employ unorthodox echocardiographic windows in order to assess certain physiological structures. A right parasternal window may be useful in some patients to permit an assessment of the aorta and inter-atrial septum.[16] A right apical window with the patient placed in the right lateral decubitus position may be useful in cases of dextrocardia.

Doppler Imaging

General Principles

Sound consists of waves. A wave represents the propagation of energy produced by the motion of some specified entity. Sound requires a particle medium, while light does not. Sound (just as any waveform) is defined by several parameters. Wavelength is defined as the distance between corresponding points on two consecutive waveforms (Fig. 1.22).[17,18] The number of waves within a specified unit of time is called the *frequency* and is measured in hertz (Hz or cycles per second). Frequency is inversely proportional to wavelength, i.e. a wavelength of 1 mm would correspond to a frequency of 2 MHz.

The velocity and attenuation of a sound wave depend on both the nature of the medium through which it is propagated and the inherent characteristics of the wave (amplitude and frequency). Transmission of sound in air requires waves of relatively larger amplitude than transmission in a liquid.

In his work of 1842, On the Coloured Light of the Binary Stars and Some Other Stars of the Heavens, Johann Christian Doppler described the changes that are produced in the reception of sound when objects emitting the sound waves are in motion with respect to the listener (Fig. 1.23). A sound's frequency increases and decreases as its source moves towards and away from the observer, respectively. Doppler's theory was initially poorly received. Buys Ballot, a contemporary of Doppler, published a thesis in which he tried to refute Doppler's concept. However, the experiments that he relied upon to do so only further confirmed Doppler's theory.

Doppler cardiac imaging utilizes the Doppler effect as a basis for measuring blood flow velocity in the heart and great vessels. Sound is transmitted through the human body at an almost constant speed. When an ultrasound beam of known frequency (f_0) is transmitted to the heart, a certain percentage of sound is reflected by red blood cells back to the transducer. The reflected wave (f_r) is then analytically compared to the wave originally transmitted. The Doppler Effect predicts that both frequencies will be identical if the red blood cells reflecting the wave are not in motion. The frequency of reflected waves proportionally increases and decreases when red blood cells are moving towards and away from the ultrasound source, respectively. The difference between transmitted and reflected frequencies, known as Doppler shift (Δf), is positive when

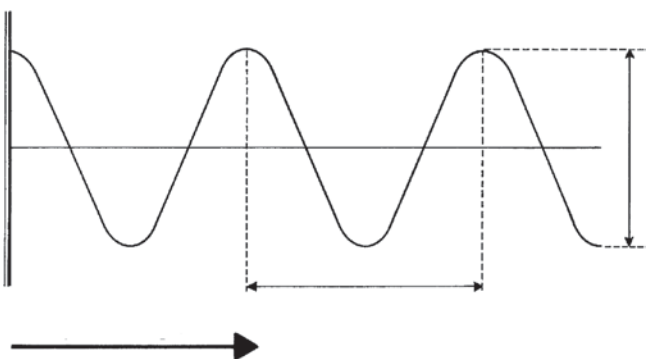

Fig. 1.22 Diagram illustrates the characteristic of sound waves. The frequency and amplitude of particle displacement are expressed as a sine wave

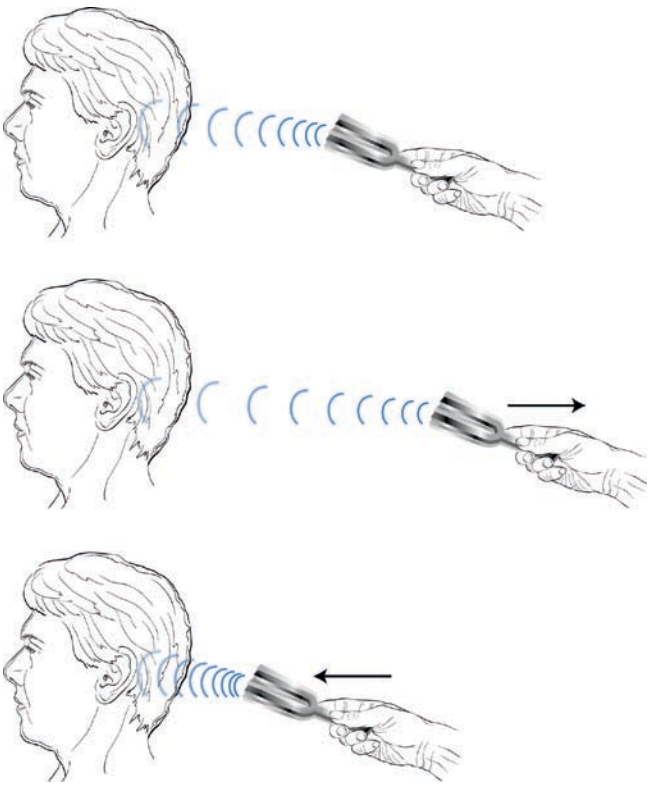

Fig. 1.23 Doppler Effect. A decrease in pitch is perceived as the source moves away from the listener. This is analogous to a reduction in frequency received by the ultrasonic transducer when blood is flowing away from it. An increase in pitch is perceived as the source moves towards the listener. This effect is analogous to an increase in frequency noted when blood moves at a given velocity towards the ultrasonic transducer

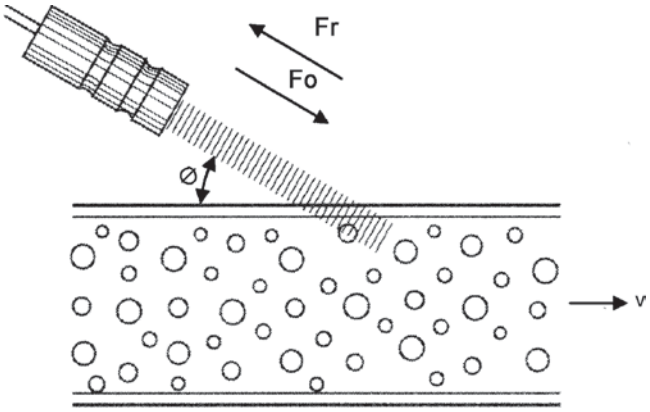

Fig. 1.24 Schematic representation of the Doppler equation

blood flow is towards the transducer and negative when it is away from the transducer. Doppler frequency shift depends on the frequency of ultrasound emission, blood flow velocity, and angle between ultrasound beam and blood flow (Fig. 1.24).

$$\Delta f = 2 f_0 \times v \times \cos\theta / c$$

v = red blood cell velocity, c = speed of sound in blood = 1.560 m/s, f_0 = frequency of transmitted wave, Δf = Doppler shift, θ = angle between ultrasound beam and blood flow. If θ is 0º (i.e. ultrasound beam parallel to blood flow), the cosine value is 1 and maximum blood flow velocity is recorded. Maximum blood flow velocity is progressively under-estimated as θ increases due to corresponding cosine values becoming progressively less than 1. This necessarily results in the under-estimation of Doppler shift, and consequently of peak velocity flow.

Pulsed-Wave Doppler

The two most common forms of Doppler imaging applied to cardiac study are PWD and CWD. In PWD, a single ultrasound crystal emits a short pulse of ultrasound and awaits its return. The pulse is emitted at a specific frequency known as the pulse repetition frequency (PRF) (Fig. 1.25). Although the emission is actually omni-directional in nature, the transducer produces a beam directed and focussed within a determined tri-dimensional area. PWD is accomplished electronically by range gating, which entails transmission of a tone burst at a certain PRF, with selection (gating) for in-line analysis of only those frequencies returning from a discrete portion *(sample volume)* of a cardiac chamber. Blood flow velocity may be determined in different regions by altering the position and size of the sample volume. Relatively larger sample volumes make it easier to detect regions of blood flow, but measurements are relatively non-specific. On the other hand, smaller sample volumes permit more precise spatial analysis of blood

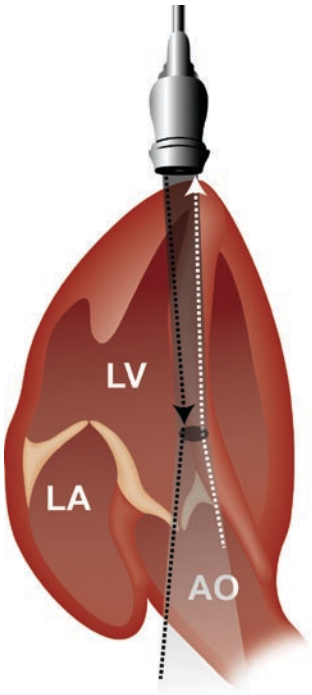

Fig. 1.25 With the pulsed-wave Doppler (PWD), a single ultrasound crystal emits a short pulse of ultrasound and awaits its return before the following pulse is transmitted

flow. The great advantage of PWD is its ability to analyze blood flow at any specific point in the heart cavities, while its chief disadvantage is the limited range of velocities that it can measure. The maximum frequency shift (velocity) that can be exactly measured using a certain PRF is determined by the Nyquist frequency limit, which corresponds to PRF/2. If frequency shift is higher than the Nyquist frequency, *aliasing* is said to occur (Fig. 1.26). The Doppler spectrum gets cut off at the Nyquist frequency limit, and the remaining portion of the signal is recorded on the opposite side of the baseline.

Continuous-Wave Doppler

CWD imaging utilizes a transducer containing two ultrasound crystals–one that continually emits ultrasound pulses and another that continually receives backscattered waveform (Fig. 1.27). Maximum recordable Doppler shift is, in this way, not limited by PRF. The recording can be done with the guidance of 2D echocardiogram or using a small non-imaging transducer (pencil probe). Unlike PWD, CWD measures all frequency shifts present along its beam path. The principal goal of CWD is the complete definition of maximal velocity. However, this advantage is conferred with one important trade-off. Because the wave forms are received and transmitted continuously, no time is allowed for the instrument to discriminate between reception and transmission of a

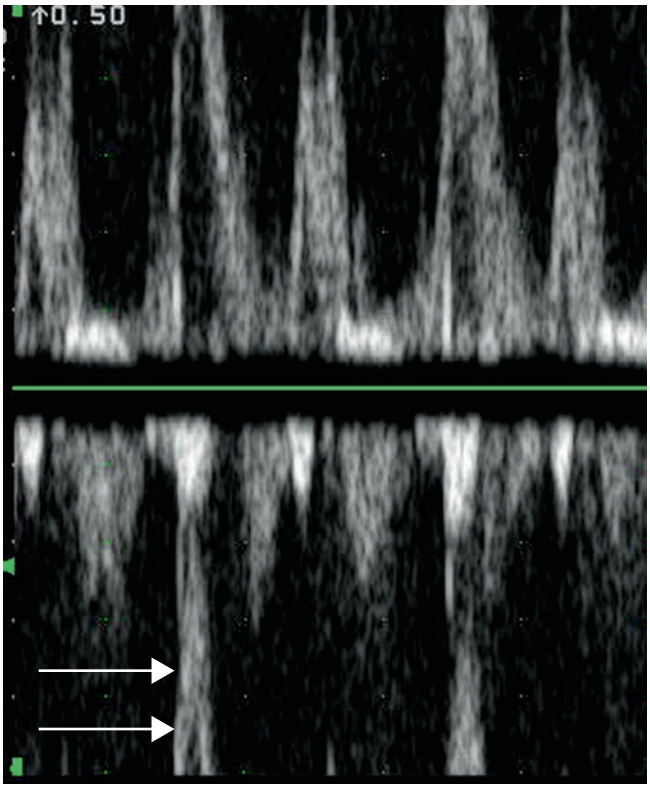

Fig. 1.26 Aliasing effect. Maximal velocity flow of the mitral valve is depicted above 0 baseline, but because of the presence of aliasing, the complexes appear blunted at the top and remaining frequencies are subtracted and plotted at the bottom of the tracing (*arrows*)

given portion of the signal. That means that the use of CWD does not allow localization of specific flow velocity information. Rather, it provides a composite of blood flow velocity information from all sites along the ultrasonic beam.

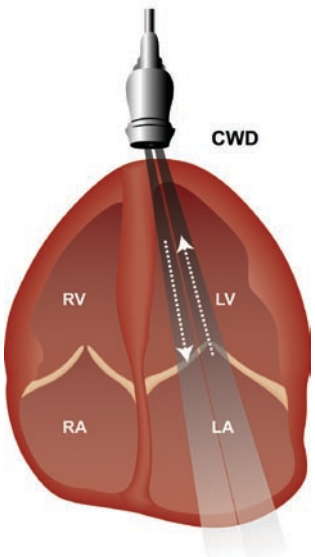

Fig. 1.27 Continuous-wave Doppler imaging utilizes a transducer containing two ultrasound crystals–one that continually emits ultrasound pulses and another that continually receives backscattered waveform

Most blood flow velocities in the normal heart are less than 1.5 m/s and can be measured with precision using PWD. In certain pathological conditions such as valvular stenosis, however, high velocity blood flow jets are common. In this case, it is mandatory to use CWD.

Colour-Flow Doppler

Both pulsed-Doppler and CWD are techniques in which ultrasound pulses are transmitted in a single line. In colour-flow Doppler, however, the ultrasound beam moves through an arc with Doppler shifts being recorded across the entire sector. At every point within the sector, frequency shifts between waves emitted by the transducer and those reflected by red blood cells are assigned certain colour. Colour-flow maps (based on combinations of red, blue, and green) utilizing bidimensional or M-mode images are then constructed in which blood flow velocities are colour coded in function of blood flow turbulence and direction (Fig. 1.28).[19, 20] Blood flow towards the transducer (positive Doppler shift) is represented in red, while blood flow away from the transducer is observed in blue. Maximum blood flow velocities measurable within the Nyquist limit are assigned maximum colour-intensity values. Velocities exceeding the limit produce aliasing and abrupt opposite colourations are observed. Abnormal flows marked by velocity changes and varying degrees of turbulence are represented as mixtures of colours.

Colour-flow Doppler is an important element in the study of cardiac haemodynamics. It not only permits the semi-quantitative estimation of degrees of valvular regurgitation and intra-cardiac shunt, but is also essential in calculations such as that of isovelocity surface area in the quantification of valvular regurgitation. Colour Doppler M-mode is useful in offering a display of abnormal blood flow locations over time.

Normal Colour-Flow Doppler Patterns

Two-dimensional imaging complemented by M-mode is initially assessed. Colour-coded flow imaging is then used for the analysis of intra-cardiac flow.[19–22]

Left Parasternal Long-Axis View

In this imaging plane, the ultrasound beam passes almost perpendicularly through the ventricular wall and aortic and mitral valves. As such, there is little possibility of obtaining good alignment with left ventricular inflow and outflow. The Doppler signal obtained is weak, and data acquired using this imaging plane are limited because colour-flow imaging systems are relatively insensitive to low-velocity blood flows and are consequently more dependent on insonation angles.

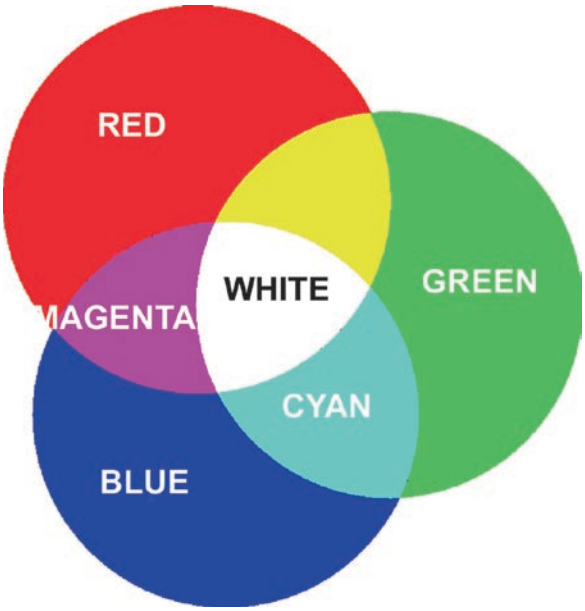

Fig. 1.28 Colour-flow maps (based on combinations of *red, blue,* and *green*) are then constructed in which blood flow velocities are colour-coded in function of blood flow turbulence and direction. Blood flow towards the transducer (positive Doppler shift) is represented in *red*, while blood flow away from the transducer is observed in *blue*

Ventricular and atrial flow is recorded in red during diastole (Fig. 1.29). In the initial phase of ventricular filling, blood flow velocity may be sufficient to cause aliasing and correspond to peak E-wave velocity in M-mode recording of the mitral valve. Retrograde blood flow directed towards the left atrium can be found during mid-diastole and contributes to valve closure. Aliasing disappears during this phase, but reappears following atrial contraction (A-wave). Analysis of this phenomenon over time is more precise upon M-mode rather than 2D images. During systole, a blue-coded column of blood flow can be observed from the left ventricle directed towards the aortic valve within which small aliasing regions can sometimes be detected.

Left Parasternal Short-axis View at Baseline

Left parasternal short-axis view at baseline is one of the most appropriate views for the blood flow analysis of the right cardiac cavities (Fig. 1.30). Blood flow in the right atrium appears in the image as a red-coded column directed towards the tricuspid valve. In the case of tricuspid insufficiency, a blue-coded column of systolic blood flow is observed and directed away from the valve. Right ventricular inflow during diastole is coded in red upon opening of the tricuspid valve and is better analyzed (as in the case of mitral blood flow) using colour M-mode. Blood flow in the right ventricular outflow tract is coded in blue and fills the main pulmonary artery (Fig. 1.31). During diastolic time, it is possible, in normal patients, to observe a small red-coded flow moving towards the right ventricle, which corresponds to a pulmonary insufficiency.

Apical Views

The *apical* views are fundamental (as are those of 2D echocardiography) to the Doppler analysis of intra-cardiac blood flow. A good ultrasound beam alignment with the valvular planes is essential for optimal analysis of Doppler blood flow data at levels of mitral and tricuspid valves, left ventricular outflow tract, and aortic valve.

Blood flow corresponding to atrial filling is observed in red throughout the entire cycle (Fig. 1.32). The blood flow column passes through the atrio-ventricular valvular planes at the onset of diastole and fills the ventricular cavities. Aliasing has been observed at this point in 63% of healthy patients. Colour M-mode inflow analysis permits an evaluation of the relationship between protodiastolic filling (E-wave) and late filling due to atrial contraction (A-wave). In the left ventricle, the blood flow column is directed first towards the lateral ventricular wall and afterwards towards the apex, inter-ventricular septum, and outflow tract. A small region of turbulent flow in contact with the atrial side of the mitral valve can be

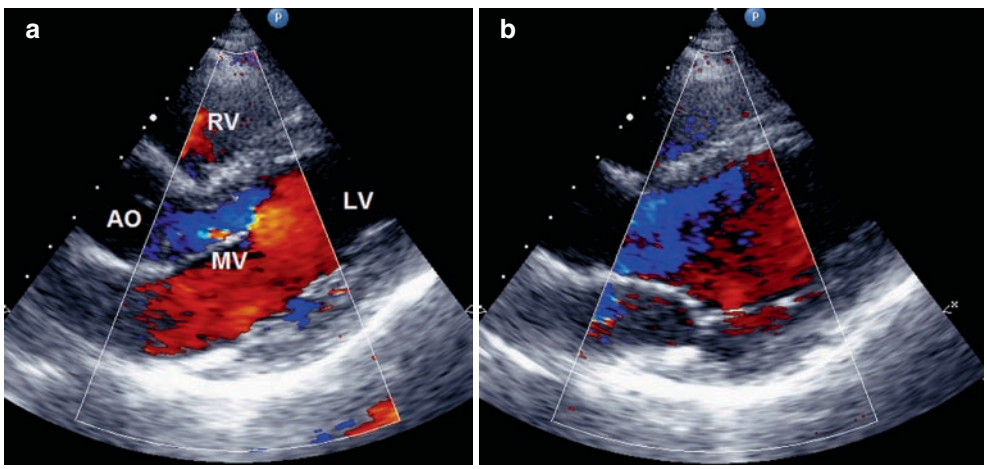

Fig. 1.29 2D echocardiography of the parestenal long-axis view with colour-flow Doppler during **(a)** diastolic frame and **(b)** systolic frame. *Red* flow indicates movement towards the transducer (diastolic filling), and *blue* flow indicates movement away from the transducer (systolic ejection). *AO* aortic valve; *RV* right ventricle; *LA* left atrium; *MV* mitral valve; *LV* left ventricle

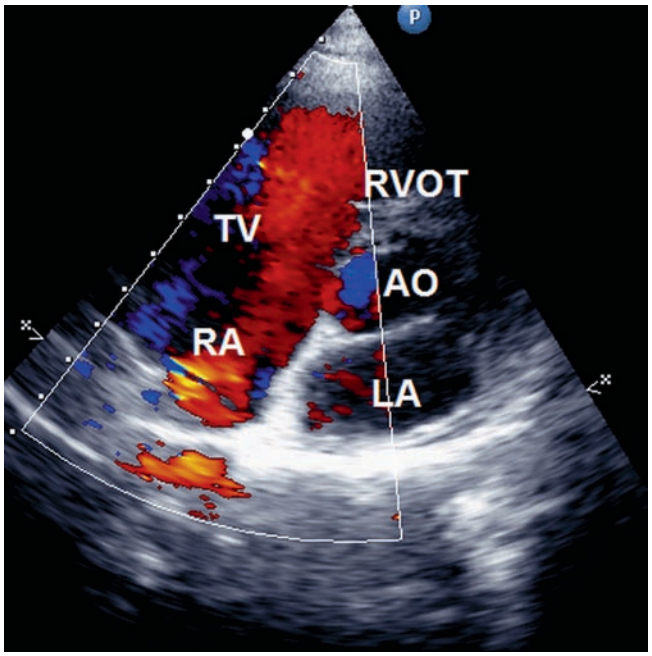

Fig. 1.30 Short-axis view of the aortic valve. The flow can be seen to emerge from the vena cava to the tricuspid valve into the right ventricle. *AO* aortic valve; *RV* right ventricle; *LA* left atrium; *MV* mitral valve; *RVOT* right ventricular outflow tract

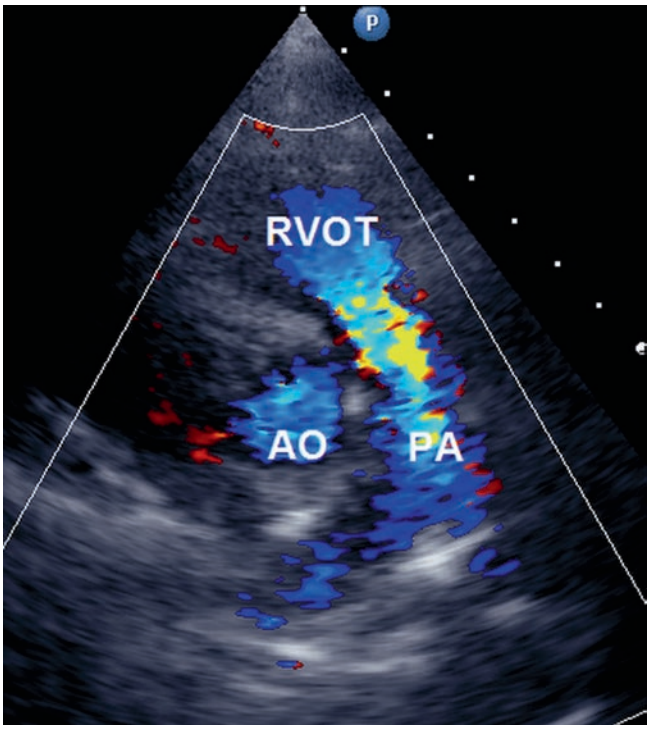

Fig. 1.31 Short-axis view of the aortic valve showing pulmonary outflow tract flow in systole as it fills the pulmonary artery to the bifurcation. *AO* aortic valve; *PA* pulmonary artery; *RVOT* right ventricular outflow tract

observed at the onset of the isovolumetric period.[12] When blood flow moves towards the outflow tract, the direction of motion is away from the transducer, and the column becomes blue-coded. The flow also shows a small region of aliasing near the aortic valve, especially in early systole.

Normal Patterns in Conventional Doppler

Once colour-flow Doppler study has been performed, pulsed-Doppler or occasionally continuous-flow Doppler must be used to study the characteristics of blood flow across the atrio-ventricular valves, great vessels, and heart chambers.

Mitral Valve Flow

Diastolic flow velocity through the mitral valve corresponds with mitral valve morphology as recorded in M-mode echocardiography (Fig. 1.33). There is an initial peak mitral inflow corresponding to passive rapid filling (E-wave) followed by another smaller telediastolic wave due to atrial

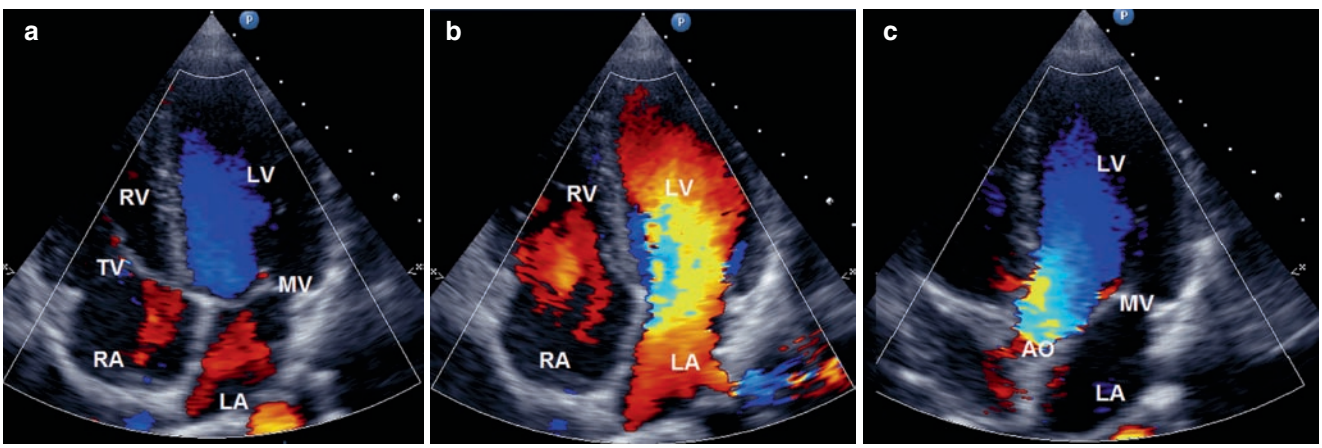

Fig. 1.32 2D echocardiography of the parestenal long-axis view with colour-flow Doppler during **(a)** protodiastole, **(b)** mesodiastole, and **(c)** systole. *Red* flow indicates movement towards the transducer (diastolic filling), and *blue* flow indicates movement away from the transducer (systolic ejection). *AO* aortic valve; *RV* right ventricle; *LA* left atrium; *MV* mitral valve; *LV* left ventricle; *TV* tricuspid valve

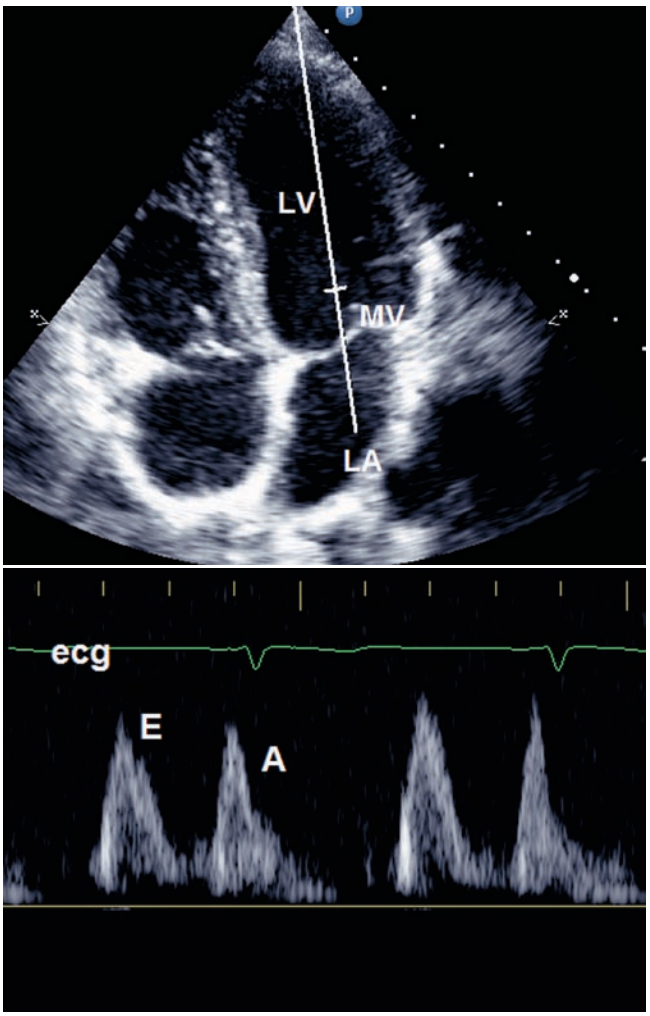

Fig. 1.33 PWD transmitral flow detected from apical approach characterized by early and late diastolic components of flow (E and A waves). *LV* left ventricle; *MV* mitral valve; *LA* left atrium

Table 1.5. Mitral and tricuspid valve flow[23]

	Mitral	Tricuspid
E wave (m/s)	0.86 (0.44–1.10)	0.64 (0.42–0.86)
A wave (m/s)	0.56 (0.28–0.60)	0.33 (0.19–0.47)
E/A	1.62 (1.31–1.93)	1.52 (1.25–1.79)
Desaceleration time	179 (150–240)	188 (150–210)
(DT) (ms)		
Isovolumic relaxation time	76 (60–110)	76 (60–440)
Integral(IVT) (cm)	(10–13)	

contraction (A-wave), which disappears during atrial fibrillation. Mitral inflow patterns do not always present the characteristic M-shape in normal patients. An added signal can be observed between E-wave and A-wave, especially in young patients or those with bradycardia (Table 1.5).

Tricuspid Valve Inflow

Flow velocities across the tricuspid valve are best detected using 4-chamber views. The morphological characteristics of right atrio-ventricular inflow are similar to those of mitral valve inflow, i.e. initial peak inflow corresponding to rapid filling (E- wave) and a lower-velocity second inflow produced by atrial contraction (A-wave) (Fig. 1.34).

The basic characteristic difference to mitral inflow is the important physiological change produced by respiration – maximum inflow velocity is substantially increased during

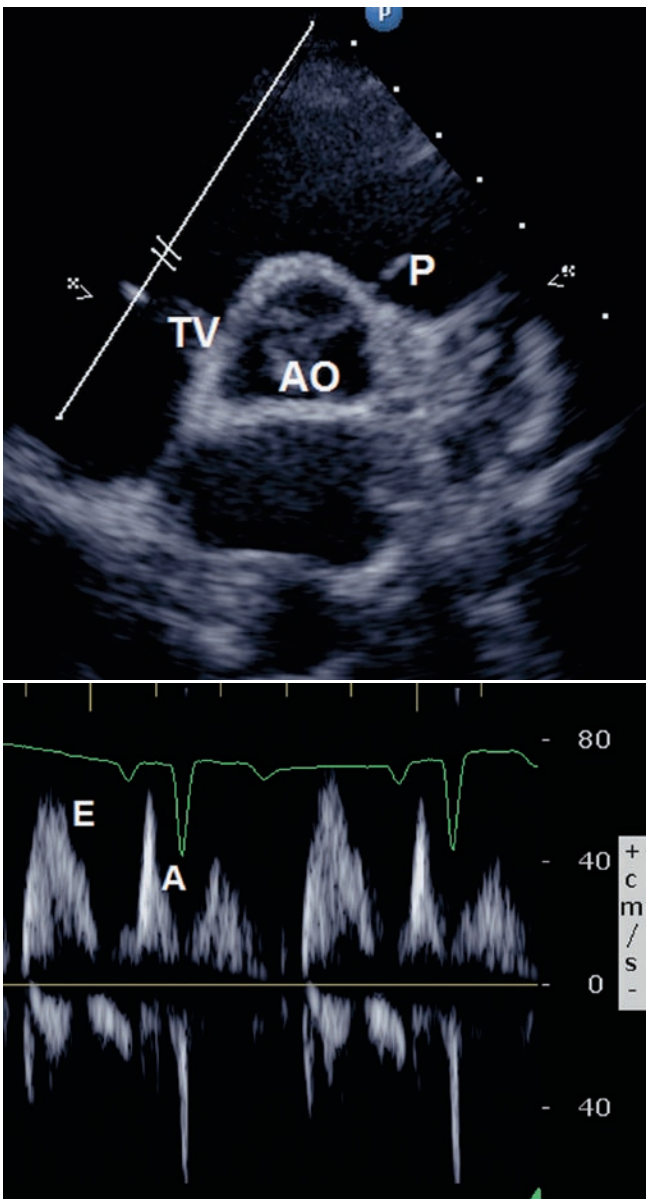

Fig. 1.34 Flow velocities across the tricuspid valve are best detected using apical 4-chamber view or paraesternal short axis. Flow velocity is recorded above 0 baseline with an early and much smaller late diastolic component. In some cases, a third signal also directed towards the transducer appears during mesosystole and is probably produced by displacement of the tricuspid plane towards the apex of the right ventricle. *AO* aortic valve; *TV* tricuspid valve; *P* pulmonary valve

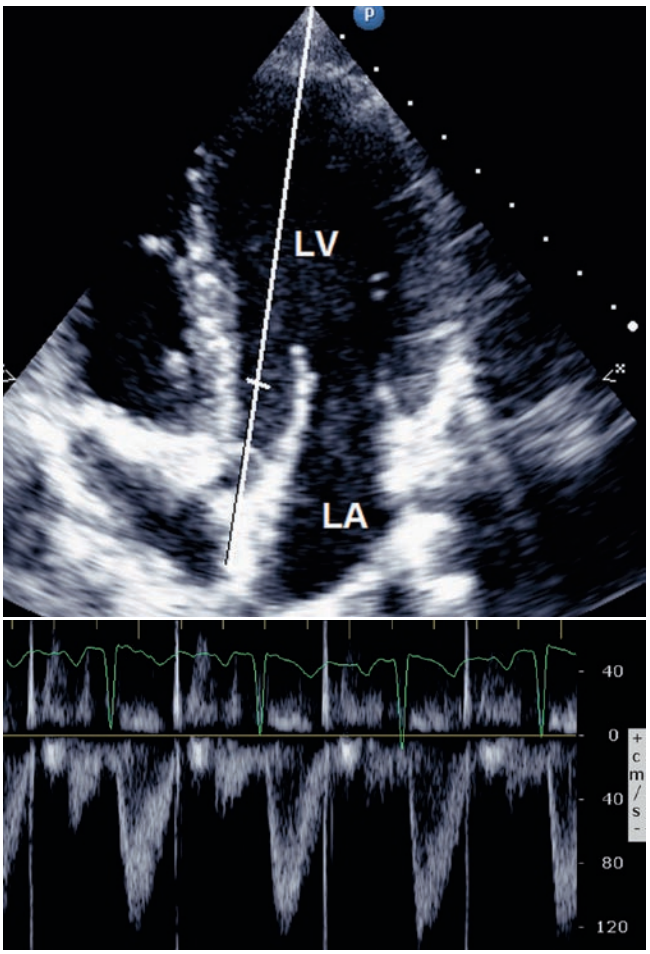

Fig. 1.35 Flow velocities of the aortic flow. The ejection flow is recorded as a negative systolic wave. *LV* left ventricle; *LA* left atrium

inspiration. In some cases, a third signal also directed towards the transducer appears during mesosystole. It coincides with motion towards the tricuspid valve plane and is probably produced by displacement of the tricuspid plane towards the apex of the right ventricle.

Table 1.5 shows normal values for young adults. Such values were calculated using the parasternal view. Calculations of inflow velocity using the apical view have been observed to be slightly lower with PWD and superimposable with CWD.

Table 1.6. Outflow tract velocities[23]

	LVOT	RVOT
Maximal velocity	0.88 (0.47–1.29)	0.72 036–1.08
Ejection time (m/s)	286 (240–332)	281 212–350
Acceleration time(m/s)	84 (48–10)	118 70–166
Acceleration (m/s^2)	11 (5–17) (5–17)	6.1 (3–9) (3–9)
Flow integral	20–25	

Left Ventricular Outflow Tract

In this view, left ventricular flow is recorded as a negative systolic wave with characteristics very similar to those of aortic blood flow but with a slightly lower velocity (Fig. 1.35). Table 1.6 shows quantitative data for blood flow in this region.

Ascending Aortic Blood Flow

If recorded from the supra-sternal or right parasternal positions, the ascending aortic blood flow is observed as a rapidly rising positive deflection corresponding to flow directed towards the

Table 1.7. Aortic flow and pulmonary flow: normal values[23]

	Ascending aortic blood flow	Descending aortic flow	Pulmonary artery flow
Maximal velocity	1.17	1.07	0.84
(m/s)	(0–1.75)	(0.50–1.79)	(0.56–1.33)
Ejection time	263	261	300
(TE) (m7s)	(216–310)	(202–302)	(197–403)
Acceleration time	79	91	122
(TA) (m/s)	(61–97)	(70–122)	(63–181)
Acceleration time	15	12	7.2
(m/s^2)	(7–23)	(5–19)	(4–10)
AT /ET	0.3	0.35	0.310
	(0.57–0.36)	(0.22–0.5)	(0.21–0.41)
(Integral cm)	18–22		

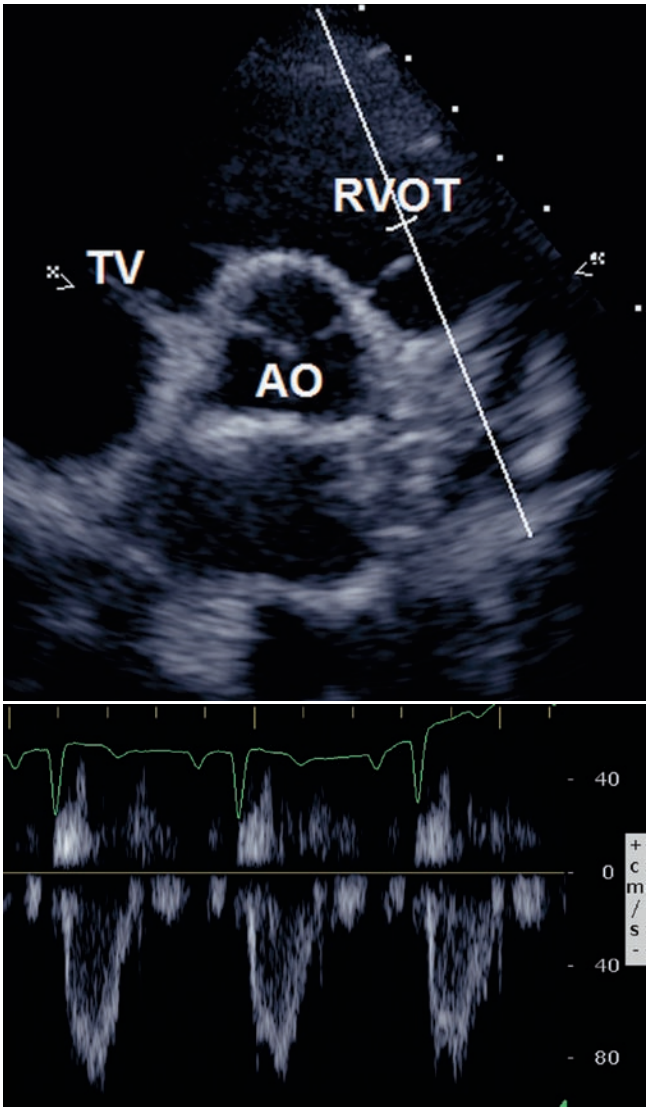

Fig. 1.36 Short-axis view represents the best approach for the analysis of the ejection flow of the right ventricle. *TV* tricuspid valve; *AO* aorta, *RVOT* right ventricular outflow tract

transducer. The descending portion of the signal, which corresponds to blood flow deceleration, shows spectral widening caused by a broader range of blood flow velocities. The velocity curve is an identical mirror image when the recording is made from the apical position. Table 1.7 shows values for normal adults obtained from the supra-sternal position.

Descending Aortic Flow

A blood flow signal with characteristics similar to those of the ascending aorta except for direction (directed away from rather than towards the transducer) is produced if recorded from a supra-sternal position. Average blood flow velocity is the same in the ascending and descending aortas. This implies that any loss of volume mostly to supra-aortic trunks is exactly compensated by lessening of vessel caliber. Normal values are shown in Table 1.7.

Right Ventricular Outflow Tract

Recordings from the parasternal position show a negative systolic blood flow (Fig. 1.36). Maximum velocity through the region is slightly less than that obtained when blood flow has already passed through the pulmonary valve. Table 1.6 shows normal values for young adults. It is not uncommon (13%) to detect a holodiastolic flow due to a small pulmonary regurgitation.

Pulmonary Blood Flow

Pulmonary blood flow is morphologically similar to pulmonary outflow tract, but is of higher velocity. Spectral widening occurs at peak velocity and during deceleration phase, which follows an initial negative deflection corresponding to acceleration phase.

While maximum velocities are slightly inferior to those of the ascending aorta and average velocities are superimposable, blood flow acceleration in comparative terms is approximately twice that of the pulmonary artery.

Vena Cava Blood Flow

The recording of blood flow through the superior vena cava from the supra-sternal or supra-ventricular notch shows typical morphology of two waves directed away from the transducer. The first of these is larger in normal patients and appears during systole (S-wave) and the second (D-wave) appears during mesodiastole (Fig. 1.37). The velocity of these waves is affected

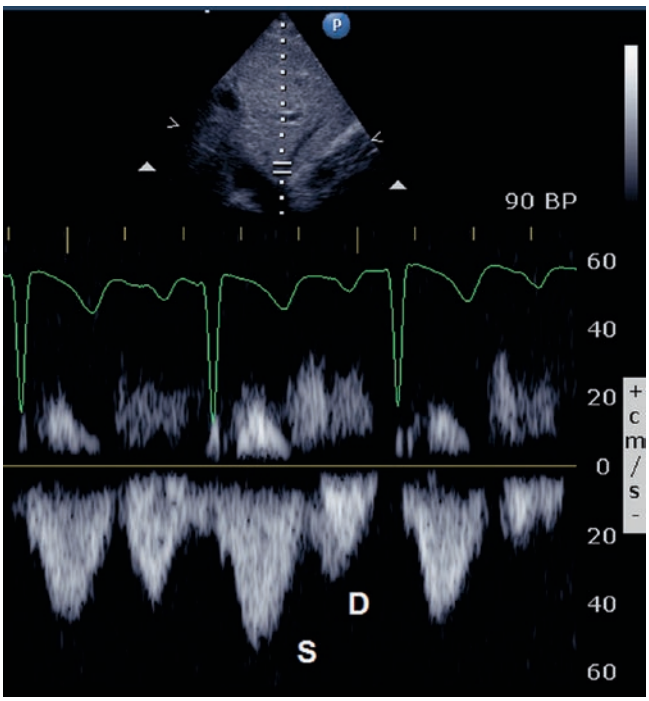

Fig. 1.37 PWD from the hepatic vein. Systolic forward flow (*S*) is greater than diastolic (*D*) forward flow

Table 1.8. Vena cava and pulmonary venous flow[23]

	<50 years	>50 years
Pulmonary venous flow (m/s)		
S wave	0.48 ± 0.09	0.71 ± 0.09
D wave	0.50 ± 0.10	0.38 ± 0.09
	0.19 ± 0.04	0.23 ± 0.14
Superior vena cava flow		
S wave	0.41 ± 0.09	0.42 ± 0.12
D wave	0.22 ± 0.05	0.22 ± 0.05
Auricular wave	0.13 ± 0.03	0.16 ± 0.03

Table 1.9. Normal values of pulmonary venous flow by TOE[23]

PVF – TOE	Media ± ED
Systolic Wave S (m/s)	0.59 ± 0.15
ITV S wave (cm)	14.7 ± 3.4
Diastolic wave D (m/s)	0.44 ± 0.13
TIV D (cm)	7.9 ± 2.7
S wave/ D wave	1.35 ± 0.24
TIV S/ TIV D	2.01 ± 0.62
A wave Ar (m/s)	0.23 ± 0.06
ITV ar	1.8 ± 0.67
desaceleration timeDT (ms)	168.6 ± 64

by respiratory cycle changes typically produced by venous return. Table 1.8 shows normal values for young adults.

Blood Flow in the Pulmonary Veins

The characteristics of blood flow in the pulmonary veins can be studied either with an apical 4-chamber view or from the trans-oesophageal position with placement of the Doppler sample volume in its interior. Normal flow is characterized by two waves, systolic (S) and diastolic (D) inflow with a smaller atrial reversal signal (A) (Fig. 1.42, Table 1.9).

Coronary Arterial Blood Flow

The sample volume of the PWD beam is placed in the central region of the left main trunk, which is where the recording is obtained in most patients. Coronary flow is measured as a double-peaked Doppler wave with higher velocity during diastole. Such coronary flow characteristics are compatible with patterns obtained using invasive methods (see Fig. 1.42b).

Table 1.10. Most frequent indications for TOE examination

Suspicion of endocarditis
Endocarditis evaluation
Native valvular disease
Prosthetic valve study
Cardiac sources of embolism
Left ventricle function
Critical patient evaluation
Precardioversion evaluation
Aorta study
Inter-atrial defect

Trans-oesophageal Echocardiography

In the last years, clinical use of TOE has increased and replaced other imaging techniques. TOE gives simultaneous anatomic, functional and haemodynamic information with great quality images. TOE can be used in different clinical situations such us outpatients care, critical care and for intra-operative evaluation.[24]

In 1976, Franzin described for the first time his experience with a coaxial cable connected to one crystal transducer.[16] In the 1980s, technology development permitted the creation of flexible probes with phased array transducers. With the first monoplane, TOE plane images were obtained using a single transverse plane ultrasound emission. The development of 2D probes with perpendicular and transversal crystals succession has permitted the evaluation of vertical structures as superior cava, inter-atrial septum, and left ventricle long axis. Further development of TOE has been associated with the introduction of 180° routable transducers that have allowed the acquisition of endless number of sections from transversal to longitudinal images. Finally, a 3D fully sampled matrix array TOE transducer was recently developed to allow real-time acquisition and online display of 3D images.[25] Most frequent clinical indications for TOE examination are listed in Table 1.10.

TOE Examination

TOE examination is considered a mini-invasive technique and requires some precautions. Four hours of fasting is

Table 1.11. TOE examination protocol

Precautions before the examination
Patient fasting for 4–6 h before TOE examination (except for extreme emergency)
Check all the necessary materials (drugs, physiological saline solutions, echocontrast agents, probe lubricant, plastic dental ring, O_2, pulse oximeter, aspiration pump and emergency kit)
Medical history of patient in order to determine any contraindications (dysphagia, oesophageal varices, allergy)
Detailed explanation of TOE examination and patient reassurance
Informed consent
Basal physical evaluation of patient, with EKG and continuous oxygen saturation monitoring if high-risk patient
Peripheral intravenous access
Removal of patient's partial denture or any other prosthesis
Patient in left lateral position with semi-flexion of head
Lubrication of probe
Optional: patient's sedation with mydazolam (2–3 mg IV to start)
Optional: saline solution
Examination
Introduction of plastic dental ring in order to protect the probe
Intubation of the oesophagus
Restraint from introducing the probe in a forced manner (should there be any resistance)
Introduction of the probe to approximately 30 cm from incisors
Physical evaluation and patient reassurance
End of the examination
Removal of peripheral IV line
Control of patient function if sedation had occurred; instructions for patient not to operate a motor vehicle during the next 12 h
Probe disinfection

necessary for all patients unless an urgent evaluation is required (i.e. diagnosed aortic dissection). Patients with pharmacological therapy should not discontinue it, especially on angina therapy.[17] During the examination, physical monitoring of patient is important, and for high-risk patients (COPD, heart failure), pulse oximetry is useful to identify hypoxia onset. In all TOE examination rooms, a complete kit for cardiopulmonary resuscitation with an aspiration pump should be present (Table 1.11).

The best position for TOE is left lateral unless the patient is intubated. Usually TOE is not performed with anaesthesia. For this reason, it is really important to communicate with the patient to explain the exam and ask for their collaboration.

In most TOE laboratories, almost all TOE are done without patient sedation. If necessary, a mild sedation can be obtained with mydazolam, a medium half-life benzodiazepine (2–3 mg IV). Although mydazolam can be rapidly antagonized with flumazenil (0.2 mg IV), this antagonist can cause hypertension and tachycardia. Lidocaine spray is sometimes used to anaesthetize the pharynx. Prophylaxis for endocarditis is not strictly necessary even in high-risk patients (i.e. previous endocarditis). Actually, bacteraemia is not considered common after TOE.[26, 27]

Before introducing the probe, the patient is asked to remove any partial dentures and is given plastic dental rings in order to avoid probe damage. Oesophagus intubation starts by placing the probe tip on the tongue and gently accompanying it with the left index finger. When it has passed over the tongue, the patient is instructed to swallow the probe and it is subsequently introduced approximately 30 cm from the incisors. It is better to use an endoscopic evaluation if the probe cannot be easily introduced. This usually occurs due to lack of patient collaboration or operator inexperience. If the patient is intubated, the probe can be introduced with the help of a second operator, who moves the jaw anteriorly.

It is important to record images during the TOE examination, as TOE cannot be easily repeated. The probe is disinfected in glutaraldehyde solution for at least 10 min after every TOE.

Complications and Contraindication

TOE is a semi-invasive technique with low risk of complication (<1%).[28] While most of these are minor, greater complications, such as patient death, may occur (<0.01% in major European centres). A careful scrutiny of the patient's medical history can avoid most complications. Complications in TOE can be classified on the basis of their underlying mechanism.

Mechanical Damage

The most common form is the persistence of pharynx irritation after TOE examination. Major complications are less common. Among 10,219 TOE examinations, studies in major European centre have found just one case of death for an oesophageal perforation. This patient had pulmonary cancer with oesophagus infiltration.

Near Organs' Compression

During prolonged intra-operative TOE examinations, vocal cord palsy can occur. It is due to recurrent laryngeal nerve compression between endotracheal tube and TOE probe.

Visceral Reflexes Induction

The introduction of the probe into the oesophagus can lead to sympathetic or parasympathetic nervous system reflexes due to nervous irritation. Sympathetic system activation can trigger sinus tachycardia, supra-ventricular tachycardia or ventricular tachycardia, while parasympathetic system activation can lead to sinus bradycardia, atrio-ventricular block, laryngeal or bronchial spasm and vomiting.

Other

Other worsening of aortic dissection and aneurysm rupture probably due to hypertensive response or mechanical compression of aorta has been described.

There are few absolute contraindications for TOE examination. It is usually performed in critically ill patients, and complications are infrequent. The only real contraindication is the presence of oesophageal disease that is resistant to probe transit.

Contraindications for TOE examination are the following:

- Oesophageal disease: oesophageal diverticula, oesophageal cancer and other causes of oesophageal stenosis
- Perforated bowel
- Previous chest radiotherapy
- Atlanto-occipital and atlanto-axial joints' disease with impossibility or reduced neck flexion

Sections in Multi-plane Study

Modified gastroscopic probes are currently used for TOE in adults (Fig. 1.38). Those probes have a 10–14 mm tip and allow good spatial resolution with high frequency transducers (3–7, 5 MHz). For paedriatic patients, smaller probes can be used (4–7 mm tip). Currently used TOE probes (mono, 2D and multi-plane) are flexible and enable easier progression through the oesophagus and complete rotation both clockwise and counterclockwise. Moreover, the presence of two wheels makes it possible for the operator to choose anterior and posterior flexion and lateral movement of the tip. The use of 180° rotatable transducers permits the acquisition of an infinite number of sections without transition from transversal to longitudinal images.

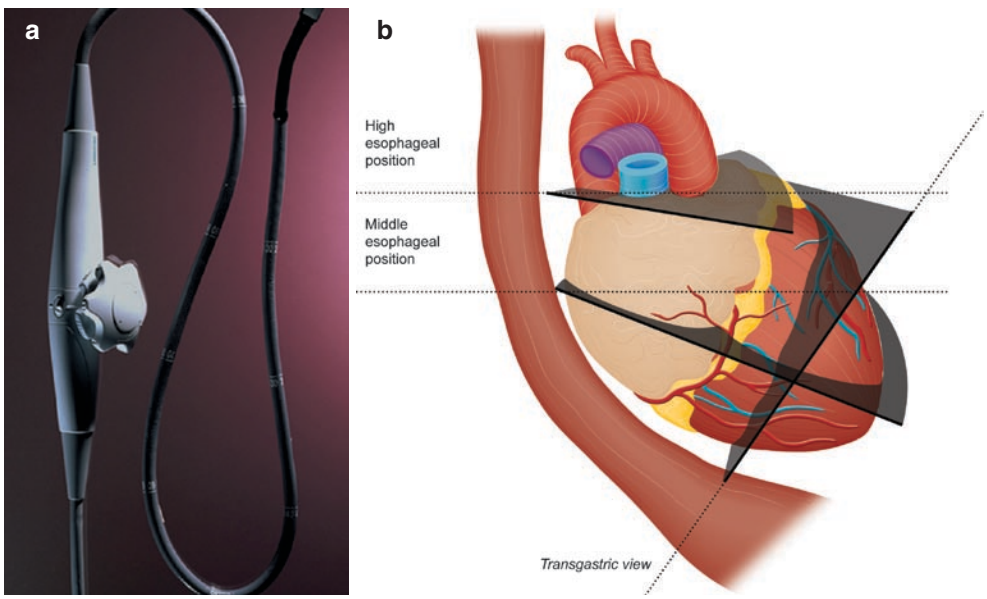

Fig. 1.38 **(a)** Trans-oesophageal multi-plane probe. The presence of two wheels allows the operator to decide the anterior and posterior flexion and lateral movement of the tip. Push bottom rotation allows both clockwise and counterclockwise rotation. **(b)** Multi-plane technique permits the acquisition of endless number of sections without transition from transversal to longitudinal images mainly due to 180° rotatable transducers. Three oesophageal positions are showed: high oesophageal position, middle oesophageal position and transgastric view

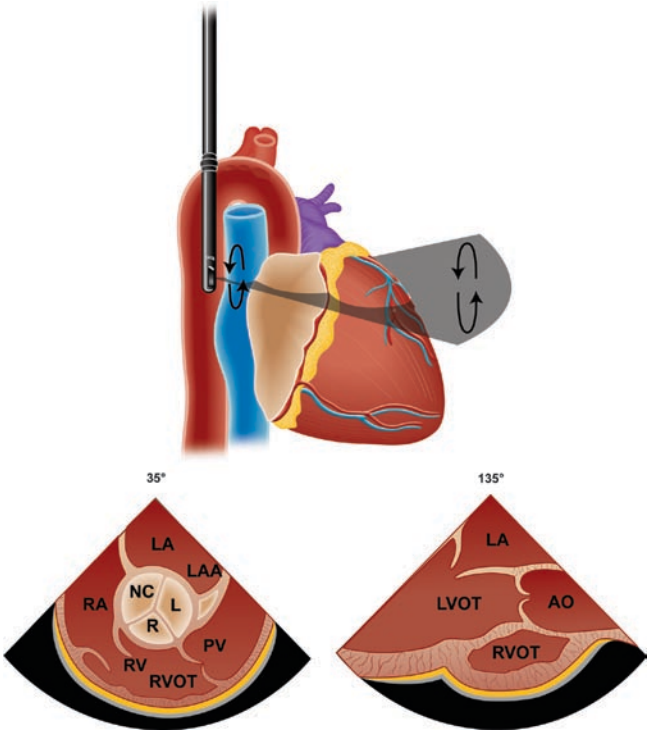

Fig. 1.39 High oesophageal position. This view is obtained advancing the probe to 28–30 cm from the incisors into the proximal oesophagus and rotating the transducer from 0 to 135°

Next, we will describe the different views we can obtain with multi-plane probes in TOE. These planes include sections obtained with monoplane and biplane probes (transversal or longitudinal and oblique by moving of the tip).

Three different positions can be described: high oesophageal level, middle oesophageal position and transgrastric view (Fig. 1.38).

High Oesophageal Position

These sections are obtained with transversal planes. The probe is advanced to 28–30 cm from the incisors into the proximal oesophagus; the transducer is rotated from 0 to 135° with some flexion of the probe (Fig. 1.39).

High oesophageal Position: Plane of Aortic Valve, Left Atrial Appendage, and Left Upper Pulmonary Vein

Transversal plane (0°): A short-axis view with an oblique view of basal heart structures and a short oblique view of aortic valve. This section allows the correct visualization of the left atrial appendage and left upper and lower pulmonary vein (Fig. 1.40).

Left atrial appendage: The complete echocardiographic study of the left appendage includes analysis of volume (or size) and function. While it can be measured with planimetry, variability is relatively high because of the anatomic

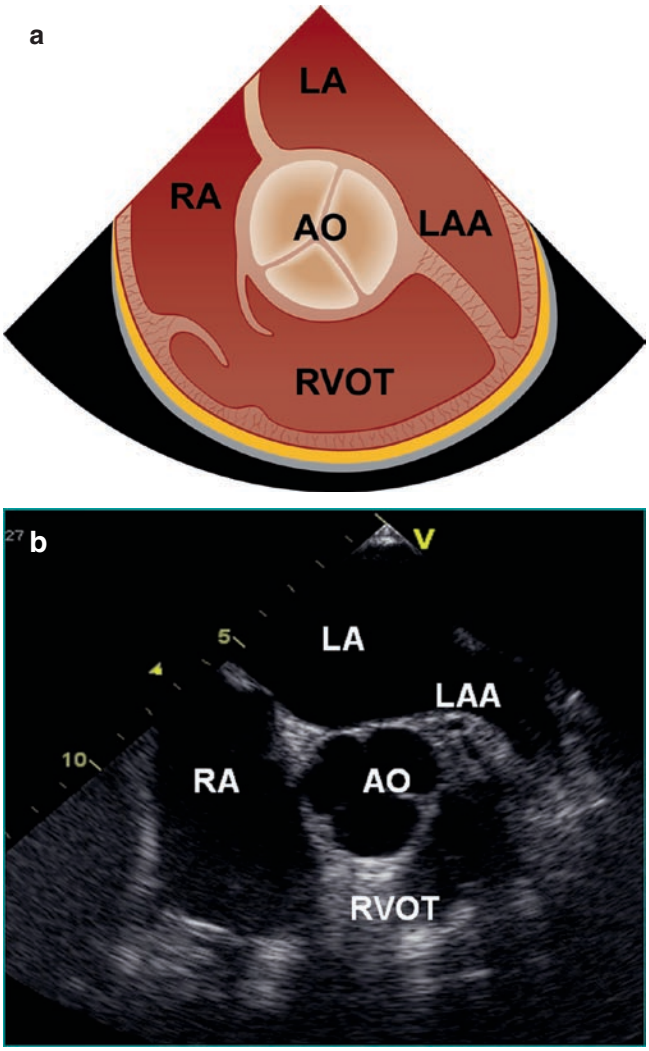

Fig. 1.40 High oesophageal position: plane of aortic valve and left atrial appendage. The section is obtained advancing the probe to 28–30 cm from the incisors into the proximal oesophagus and rotating transductor (0º). Schematic anatomical section **(a)** and 2D image **(b)**. In this plane, aorta is in the centre of the image and the three leaflets are visualized. Non-coronary leaflet is in upper left position, left leaflet in upper right position, and right leaflet in anteroinferior position. Around aortic valve, we can find right atrium, tricuspid valve, and right ventricle. *AO* aortic valve; *LA* left atrium; *LAA* left atrial appendage; *LV* left ventricle; *RV* right ventricle; *RA* right atrium

complexity of the atrium. When the sample volume is placed in the left atrial appendage, three different flow patterns can be detected:[31]

- Type I flow is characterized by a biphasic flow of clearly defined waves of filling and emptying (Fig. 1.41).
- Type II is a saw-tooth model corresponding to fast and well-defined filling and emptying waves described in patients with fibrillation or flutter.
- Type III is marked by the absence of identifiable waves, most frequently (though not exclusively) in atrial fibrillation, which reflects the presence of atrial contractile dysfunction.

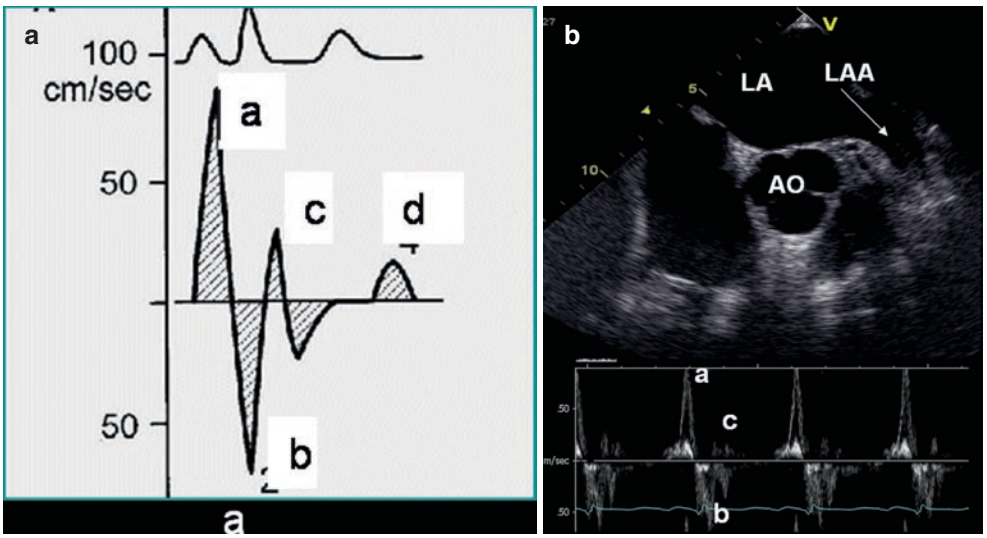

Fig. 1.41 High oesophageal position. Plane of aortic root and left atrial appendage flow and left upper pulmonary vein. **(A)** Schematic drawing of atrial appendage flow characterized by four waves. After P-wave, atrial contraction (a), atrial relaxation (b), systolic reflexion (c), and diastolic wave (d). **(B)** Doppler trace of left atrial appendage showing a wave depending on atrial contraction (a) after P-wave of EKG and the second of atrial relaxation, (b) one of systolic reflexion, and (c) diastolic wave is not evident. The normal velocity peak is about 40 cm/s. In the upper part of this 2D image of left appendage, the arrow shows left appendage position of the sample volume

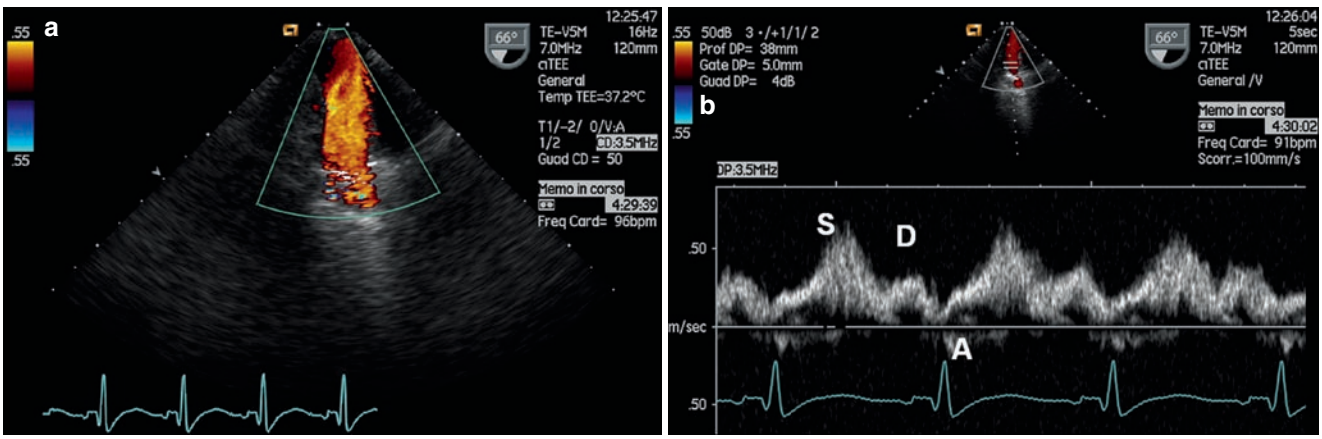

Fig. 1.42 High oesophageal position. Plane of aortic root and left atrial appendage and left upper pulmonary vein flow. **(a)** Flow from left upper pulmonary vein in left atrium; **(b)** Pulsed-Doppler recording of normal flow in left upper pulmonary vein characterized by systolic (S) and diastolic (D) inflow with a smaller atrial reversal signal (A). This pattern can be obtained also by middle oesophageal position 2-chamber view with sample volume positioned in left upper pulmonary vein 1 cm from the junction with body of left atrium

Pulmonary veins: The upper pulmonary veins are easier to detect than the lower veins. Colour-Doppler is helpful in appropriately positioning the sample for spectral Doppler (Fig. 1.42).

Left pulmonary veins: These can be visualized at 0°. The upper left vein is located near the left atrium. In order to visualize the lower left vein, the probe must be slightly advanced. It can be observed extending into the left atrium (Y-morphology). For this reason, the ideal viewpoint of the transducer is 110° together with a global counterclockwise rotation of the probe. This position provides good Doppler alignment.

Right pulmonary veins: The upper right pulmonary vein is usually seen in the transverse plane by positioning the probe at the same level as the upper left vein. It arrives at the left atrium with a horizontal orientation above the superior vena cava and adjacent to the inter-atrial septum. The image of the upper right vein can be seen in the transverse plane for up to approximately 110° rotation; it becomes more vertical so that alignment with spectral Doppler can improve. The lower right vein can be seen with small anterior-flexion of the probe or by advancing it slightly. In order to simultaneously detect right pulmonary venous outflow, the ideal angulation is that of the aortic valve short axis

(approximately 45–50°) followed by a clockwise rotation of the probe.

The pulmonary venous flow in the left upper pulmonary vein (systolic and diastolic flow followed by reversal peak of atrial contraction) can be studied. The pulmonary veins are located close to the transducer in TOE (which is not the case in TTE). This proximity helps obtain a high quality flow image. The pulmonary vein flow towards the left atrium occurs predominantly during systole through a suction effect caused by atrial relaxation. The diastolic flow is produced by the pressure relationship between left atrium and left ventricle and by the active relaxation of the latter. It is smaller than the systolic flow except in very young individuals.

High Oesophageal Position: Plane of Aortic Root and Coronary Arteries

Transversal plane (0°) Section of Coronary Arteries: The origin of coronary arteries can be identified by scanning up from the leaflet of aortic valve to their orifices at level of sino-tubular ring. The left coronary artery is located in the middle of left Valsalva sinus. It is possible to visualize the bifurcation of main left coronary artery in circumflex and anterior descending artery. The first can be seen laterally for several centimeters between left ventricle and left atrial appendage until it turns posteriorly. The proximal portion of left anterior descending coronary artery can also be visualized with a more oblique plane to permit its alignment with pulsed Doppler (Fig. 1.43).

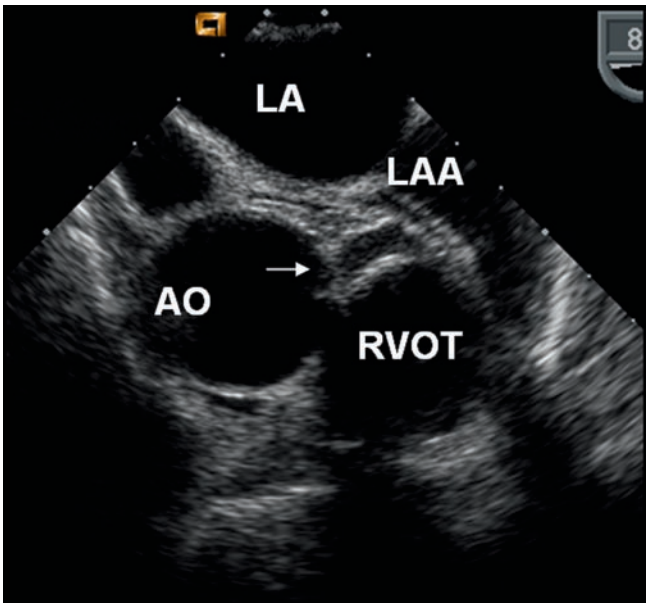

Fig. 1.43 High oesophageal position, plane of aortic root, and coronary arteries. The origin of left coronary artery can be identified by scanning up from the leaflet of aortic valve to its orifice at the level of sinutubular junction. The left coronary artery is located in the middle of the left Valsalva sinus. Left main coronary artery can be visualized (*arrow*). *AO* aortic valve; *LA* left atrium; *LAA* left atrial appendage; *RVOT* right ventricle outflow tract

High Oesophageal Position: Plane of Aorta and Main Pulmonary Artery

Transversal Plane (0–20°) for Main Pulmonary Artery and Its Bifurcation: Obtained with a slight further anteflexion of the probe. It is now possible to detect the pulmonary trunk long axis and right pulmonary arteries, short axis of superior vena cava situated anterior to right pulmonary artery and the proximal ascending aorta situated anteriorly and in the centre of image. The distal segment of the right upper pulmonary vein and its connection with the left atrium can be visualized at level of the superior vena cava–right atrium junction; the location of the oesophagus behind the right pulmonary artery makes it sometimes possible to see the bifurcation of this artery with its upper and lower branches. The initial portion of the left pulmonary artery (LPA) can be clearly observed due to the interposition of the left bronchus. These structures are visualized at 0° by removing the probe from the transverse plane of the left atrium. A counterclockwise rotation of the probe can improve the initial image of LPA, while a clockwise rotation reveals the long axis of the LPA (Fig. 1.44).

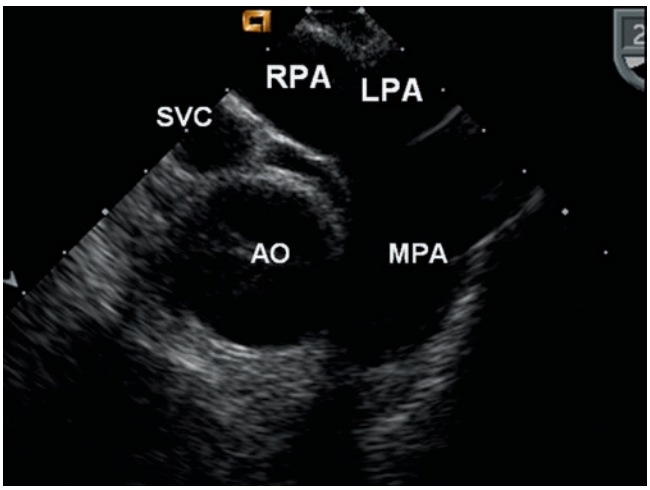

Fig. 1.44 High oesophageal position, plane of aorta and main pulmonary artery. This plane is obtained in the same position as the last plane with further anterior flexion of the probe. The section shows aorta and main pulmonary artery. *SVC* superior vena cava; *AO* aorta; *MPA* main pulmonary artery; *RPA* right pulmonary artery; *LPA* left pulmonary artery

High Oesophageal Position: Plane of Aortic Valve

Short-axis View of the Aortic Valve (35–45°) with Slight Advancement of Probe: Such yields a perpendicular plane of the aortic cusps (similar to parasternal short-axis view). It is important to find a circular section of the valve in order to properly

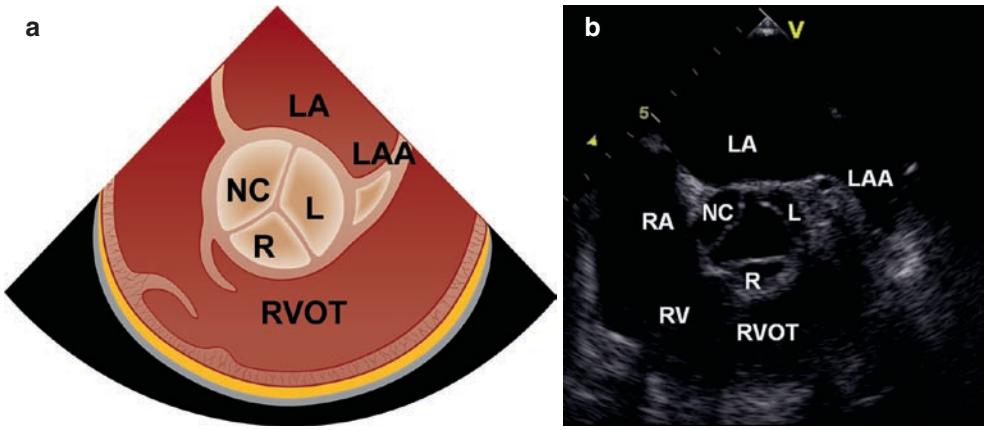

Fig. 1.45 High oesophageal position, plane of aortic valve. Schematic anatomical section **(a)** and 2D imaging **(b)**. Short-axis view of aortic valve (35–45°) with little advancement of probe: perpendicular plane of aortic cusps (similar to parasternal short-axis view). A circular section of the valve allows the detection of three leaflets: non-coronary leaflet in upper left position, left leaflet in upper right position, and right leaflet in anteroinferior position. *AO* aortic valve; *LA* left atrium; *LAA* left atrial appendage; *LV* left ventricle; *RV* right ventricle; *RA* right atrium; *NC* non-coronary aortic cusp; *R* right aortic coronary cusp; *L* left aortic coronary cusp; *RVOT* right ventricular outflow tract

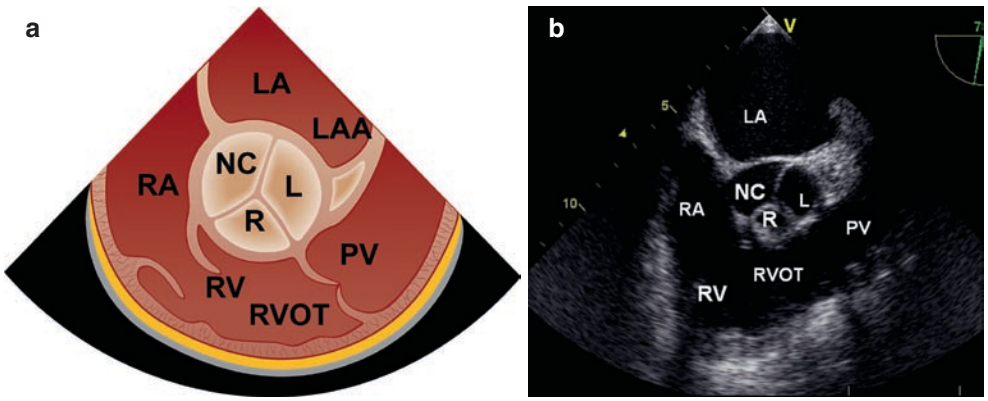

Fig. 1.46 High oesophageal position, longitudinal plane of right ventricular out flow tract (75°). Schematic anatomical section **(a)** and 2D imaging **(b)**. This section intersect the right atrium, tricuspid valve, right ventricle, and right ventricular out flow tract until pulmonary valve and pulmonary trunk with its bifurcation in right and left pulmonary arteries. *LA* left atrium; *RA* right atrium; *NC* non-coronary aortic cusp; *R* right aortic coronary cusp; *L* left aortic coronary cusp; *RV* right ventricle; *RVOT* right ventricular outflow tract; *PV* pulmonary valve

observe the three leaflets: non-coronary leaflet in upper left position, left leaflet in upper right position, and right leaflet in anteroinferior position. All around the aortic valve we can find right atrium, tricuspid valve, and right ventricle (Fig. 1.45).

High Oesophageal Position: Longitudinal Plane of Right Ventricular Out Flow Tract

Longitudinal Plane of Right Ventricular Out Flow Tract (75°). This plane intersects the right atrium, the tricuspid valve, right ventricle, and right ventricular out flow tract, until pulmonary valve and pulmonary trunk with bifurcation in right pulmonary artery and beginning of LPA (Fig. 1.46).

High Oesophageal Position: Oblique Images of Heart

Longitudinal Plane (90°): Oblique images of heart long axis and main axis of aortic root.

High Oesophageal Position: Longitudinal Plane of Left Atrium and Left Ventricle Outflow Tract (135°)

Longitudinal Plane (135°) of the Left Atrium and Left Ventricle Outflow Tract: Similar to parasternal long-axis view. The image is optimal for clearly visualizing the aortic root with a symmetrical view of both aortic leaflets

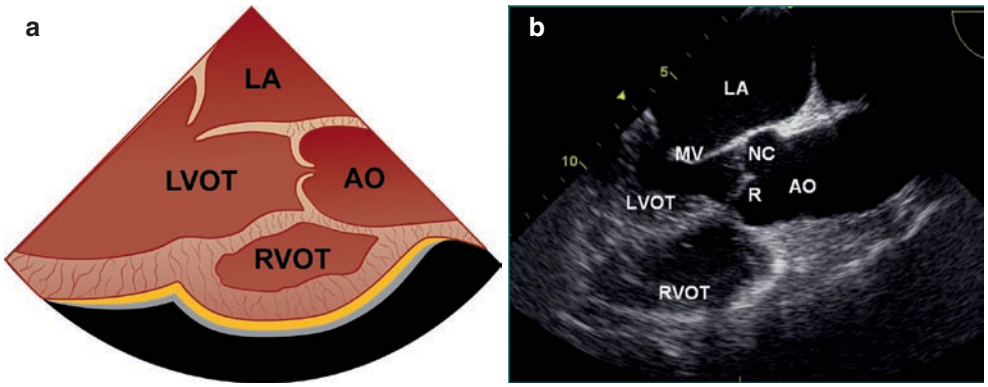

Fig. 1.47 High oesophageal position. Longitudinal plane of left atrium and left ventricle outflow the aortic root with a symmetric view of the two aortic leaflets (non-coronary leaflet in the upper part and right leaflet in the inferior part of echographic image). *LA* left atrium; *MV* mitral valve; *LVOT* left ventricular outflow tract; *NC* non-coronary aortic cusp; *R* right aortic coronary cusp; *RVOT* right ventricular outflow tract; *PV* pulmonary valve

(non-coronary and right leaflets in the upper and lower regions of the image, respectively) (Fig. 1.47).

Middle Oesophageal Position

From this position we obtain transversal and longitudinal planes from 0 to 135°. The probe is placed at 30–35 cm from the incisors (Fig. 1.48).

Middle Oesophageal Position: Transverse Plane, 4-Chamber View

With the transducer in 0° position, a 4-chamber view can be obtained by gently introducing the probe to 30–35 cm from the incisors and with slight retroflexion of the tip. Visualization of both atrium and left and right ventricles is obtained. The 4-chamber views are displayed with the apex oriented downward. The left and right atriums are at the top of the image; the left ventricle is in the right portion of the image, and right ventricle is in the left portion (Fig. 1.49).

The crux cordis is well visualized with septal leaflet of tricuspid valve lower than septal leaflet of mitral valve. The atrio-ventricular septum is between them.

A 5-chamber view can be obtained from the 4-chamber view with a mere anteflexion of the tip (Fig. 1.50). Slight advancement and extreme retroflexion of the tip from 4-chamber view will display the right ventricle inflow tract and long axis of the coronary sinus opening in the right atrium.

With the multi-plane probe, a complete study of the entire mitral valve can be made. The anterior mitral leaflets can be divided into three parts (A1, A2, A3) and the posterior in other three parts or levels (P1 or anterior-lateral, P2, P3 or middle-posterior).

In the middle oesophagus, starting from the transverse plane where A2 and P1 can be visualized, by rotating the

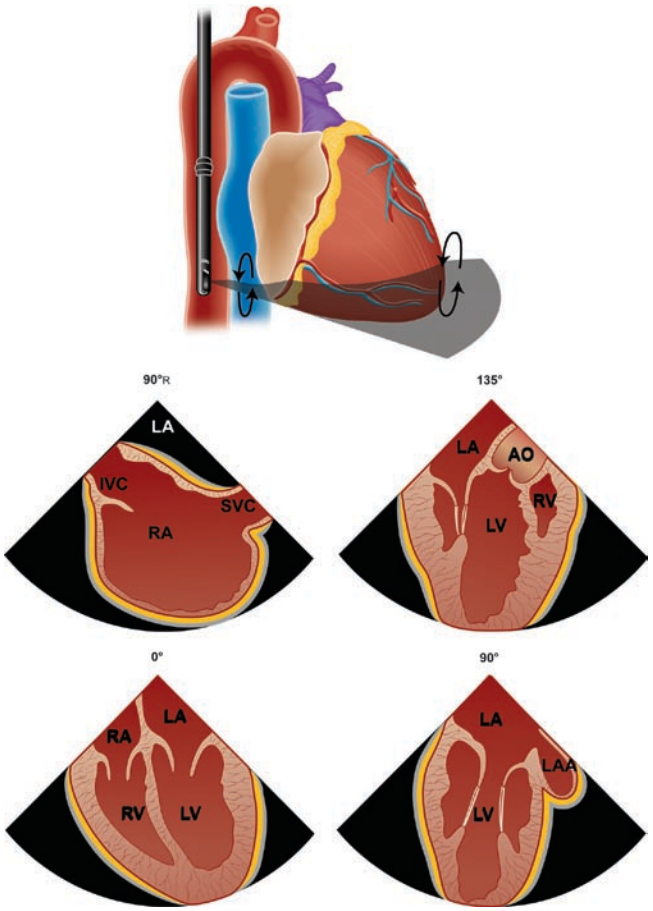

Fig. 1.48 Middle oesophageal position. Four main planes can be obtained from this position with rotation of the probe from 0° to 135 °. 4-chamber view can be obtained to 0°, 2-chamber view of left ventricle to 90°, and 3-chamber view of left ventricle with its outflow tract and aorta to 135°. Otherwise, from 2-chamber view to 90° when the probe is turned towards the patient's right (clockwise), we obtain a long-axis view of right atrium and inferior vena cava and superior vena cava. In some individuals, a Eustachian valve at inferior caval atrial junction can be seen. *IVC* inferior vena cava; *SVC* superior vena cava; *RA* right atrium; *LA* left atrium; *RV* right ventricle; *LV* left ventricle; *AO* aorta; *R* rotation to patient's right

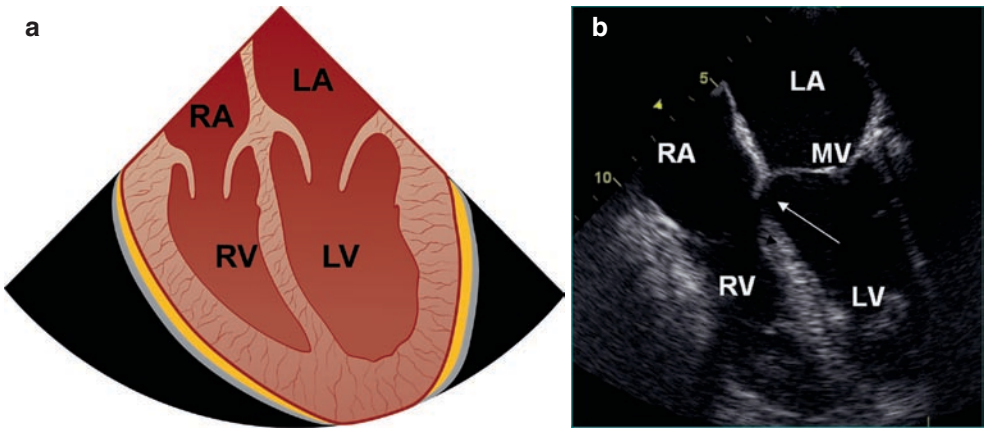

Fig. 1.49 Middle oesophageal position, 4-chamber view (0°). Schematic drawing **(a)** and 2D image of the 4-chamber views **(b)**: the apex is displayed *downward,* the left and right atriums are at the *top* of the image, left ventricle, and the right ventricle at the *bottom* of the image. The crux cordis is well visualized with septal leaflet of tricuspid valve lower than septal leaflet of mitral valve. *R* right atrium; *LA* left atrium; *RV* right ventricle; *LV* left ventricle

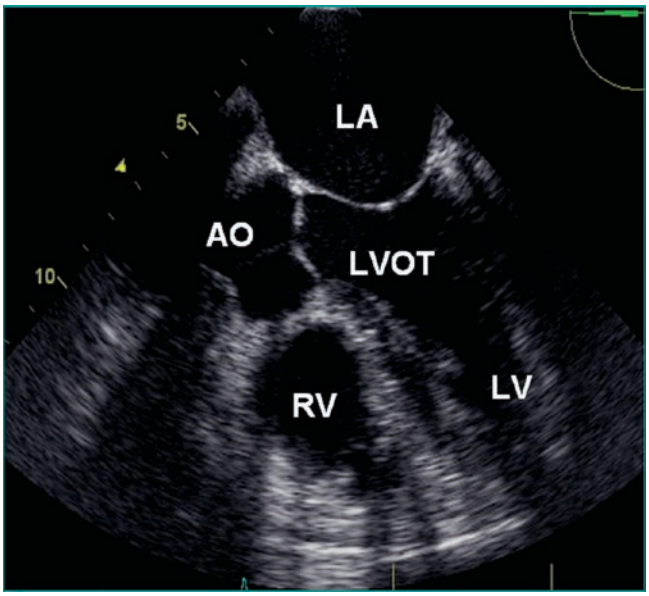

Fig. 1.50 Middle oesophageal position 5-chamber view. From 4-chamber view we can obtain a 5-chamber view with an anteroflexion of the tip of the probe. *RA* right atrium; *LA* left atrium; *RV* right ventricle; *LV* left ventricle; *AO* aorta; *LVOT* left ventricular outflow tract

transducer at 35°, we can observe the levels P1, A2, and P3. At 90° we can see the anterior valve cut along the long axis (A1, A2, and A3) and P3, as well as the central levels (A2 and P2) as 135°.

Middle Oesophageal Position: Longitudinal Planes of Superior Vena Cava and Inferior Vena Cava

Longitudinal planes can be obtained with probe tip at 30–35 cm from incisors and with 90° rotation of transducer. If the probe is rotated clockwise, the entrance of the two caval veins in right atrium can be visualized (two caval veins and inter-atrial septum plane) (Fig. 1.51). This plane allows the study of inter-atrial septum. The septum thickness in the

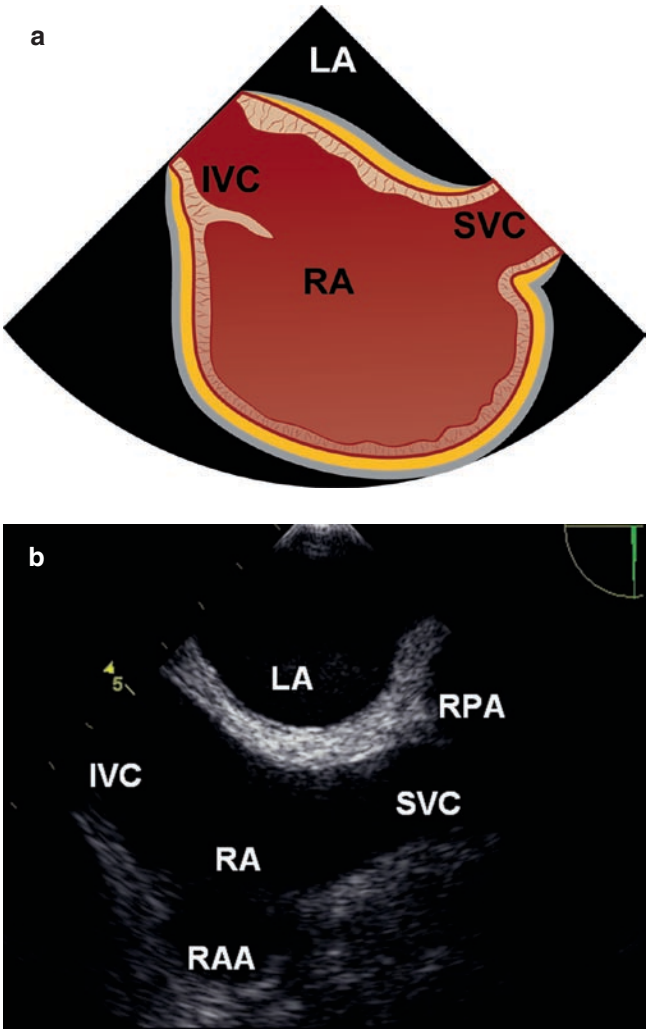

Fig. 1.51 Middle oesophageal position, long-axis view of right atrium and inferior and superior caval veins. Schematic section **(a)** and 2D imaging **(b)**. This plane can be obtained from 2-chamber view 90° for rotation of probe to patient's right; the entrance of the superior caval vein and inferior caval vein in right atrium can be visualized. Also the right pulmonary artery in short-axis view can be shown in upper and right of image near the superior vena cava. *IVC* inferior vena cava; *SVC* superior vena cava; *RA* right atrium; *RAA* right atrial appendage; *RPA* right pulmonary artery; *LA* left atrium

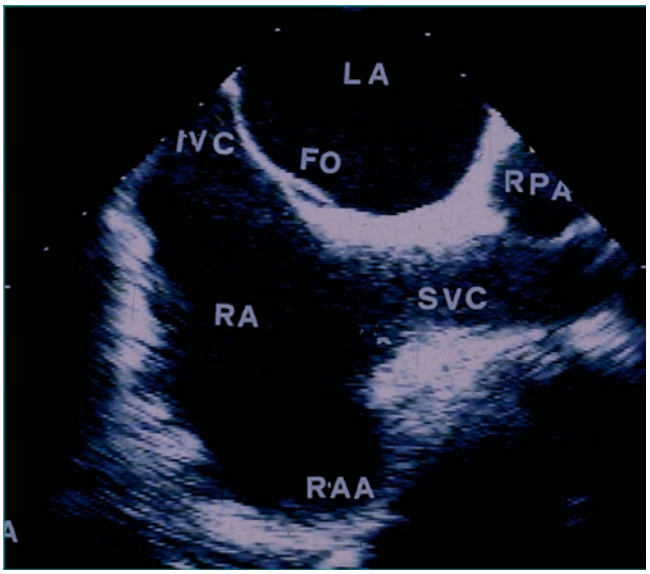

Fig. 1.52 Middle oesophageal position, long-axis view of right atrium and inferior and superior caval veins. The area of foramen ovale can be seen in the middle of the septum. *IVC* inferior vena cava; *SVC* superior vena cava; *RA* right atrium; *RAA* right atrial appendage; *RPA* right pulmonary artery; *LA* left atrium

periphery is almost constant and, in general, decreases rapidly in the region of the fossa ovalis (Fig. 1.52).

Middle Oesophageal Position: Longitudinal Planes, Right Ventricle, Right Ventricular Outflow Tract, and Main Pulmonary Artery

Right Ventricle Long Axis (35–55°): This plane intersects the right atrium, tricuspid valve, right ventricle, and right ventricular outflow tract until the pulmonary valve and pulmonary trunk (with its bifurcation into right pulmonary artery and initial portion of LPA); the aorta is seen in the centre of the image. This plane is similar to that of high oesophageal position for right ventricle and pulmonary artery as described in Fig. 1.46.

Middle Oesophageal Position: Longitudinal Planes, Left Ventricle 2-Chamber View

Left Ventricle 2-chamber View (90°): Visualization of left ventricle anterior and inferior walls, left atrial appendage, and left upper pulmonary vein. It is necessary to apply a slight retroflexion of the probe tip in order to see the left ventricle apex (Fig. 1.53).

The combination of middle oesophagus planes (at 0 and 90°) and long-axis plane (at 135°) permits an evaluation of the global and segmental contractile function of the left ventricle in such a way that the classification of ASE into 16 segments (originally conceived for TTE) can be applied. Contractility of the lower septum and lateral side can be evaluated in the 4-chamber plane; both anterior and inferior sides can be evaluated in the 2-chamber plane and contractility of the anterior septum and posterior part can be evaluated in the 3-chamber plane.

Middle Oesophageal Position: Longitudinal Planes Left Ventricle Outflow Tract and Aorta

Three-chamber View (135°): Plane that allows a perfect alignment of ultrasound with the left ventricle outflow tract and aorta; a long tract of ascending aorta can be seen. Two aortic valve leaflets are shown: non-coronary leaflet in the upper portion of the image and right leaflet in the lower portion (Fig. 1.54).

Middle and High Oesophageal Position: Thoracic Aorta

The thoracic aorta can be visualized in different planes. The aortic arch can be observed by slowly withdrawing the probe to approximately 18–20 cm. The aortic arch lies slightly anterior to the oesophagus, so that the operator should rotate the probe slightly clockwise or to the patient's right side

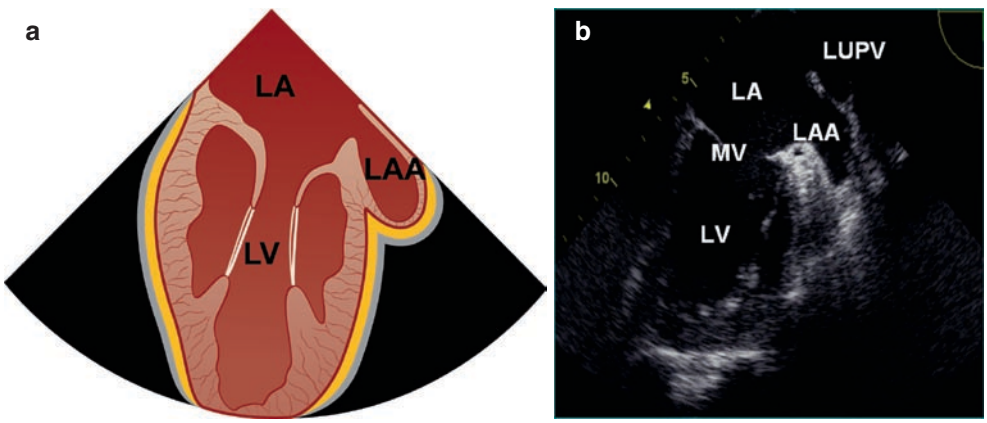

Fig. 1.53 Middle oesophageal position, 2-chamber view, long-axis view to 90°. Schematic drawing of the plane **(a)** 2D visualization **(b)**. This plane shows visualization of left ventricle's anterior and inferior walls and left atrial appendage, with left upper pulmonary vein. The pulmonary venous flow can be studied from left upper pulmonary vein. *LA* left atrium; *LV* left ventricle; *LAA* left atrial appendage; *LUPV* left upper pulmonary vein

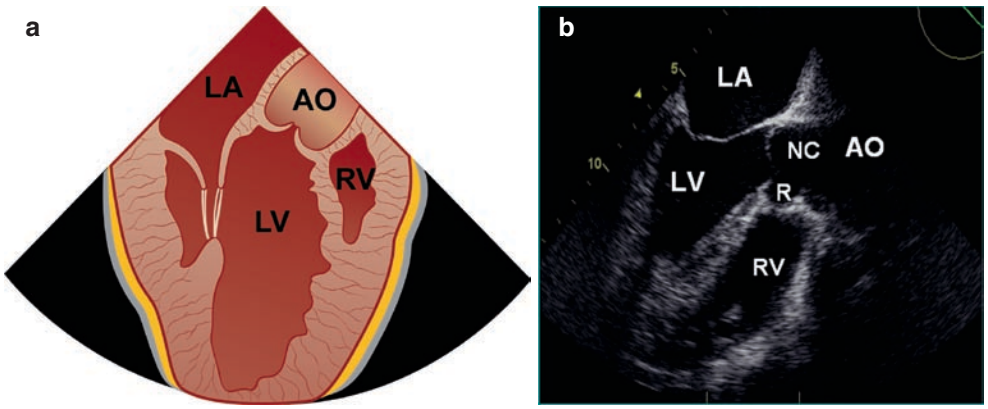

Fig. 1.54 Middle oesophageal position, 3-chamber view (135°). Schematic drawing **(a)** and 2D visualization image **(b)**. This plane allows a perfect alignment of ultrasounds with left ventricle outflow tract and aorta with left ventricle; a long tract of ascending aorta can be seen. Two aortic valve leaflets can be shown: non-coronary leaflet in the upper part and right leaflet in the inferior part of echographic image. *LA* left atrium; *AO* aorta; *LV* left ventricle; *RV* right ventricle; *NC* non-coronary aortic cusp; *R* right aortic coronary cusp

while withdrawing it. The transverse plane shows a long view of the arch. The left common carotid and proximal portion of the left subclavian artery may also be displayed in short axis. The right innominate artery cannot be seen because of the air-filled trachea. The thoracic aorta is posterior to the oesophagus. The thoracic aorta can be better seen in transverse plane (0°). The aorta appears as a circle upon withdrawing the probe from the stomach after a counterclockwise rotation. The probe is gradually withdrawn in 5 cm increments. In short-axis view, the anterior wall is displayed at the top of the screen and posterior wall at the bottom (Fig. 1.55).

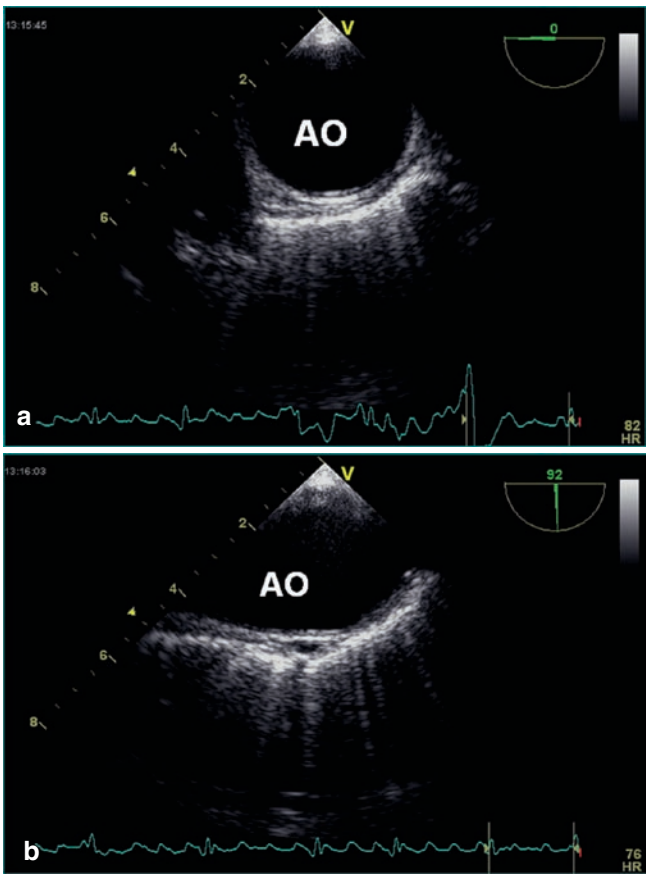

Fig. 1.55 Thoracic aorta can be displayed in short-axis view withdrawing the probe from stomach after count clockwise rotation. The aorta in transverse plane (0°) appears as a circle **(a)**, the aorta in 90° appears as a double line in long-axis view **(b)**. *AO* Aorta

Transgastric View

Transgastric planes can be obtained by introducing the probe tip to stomach fundus (40–45 cm from incisors) (Fig. 1.56). Rotation of the multi-plane transducer from 0 to 135° results in the following planes:

Transgastric View: Short Axis of Left and Right Ventricles

Transversal Plane (0°): Short axis of left and right ventricles. Anteflexion of the tip yields a more basal view of structures, whereas retroflexion of the tip produces images that tend to be apical. The left ventricle is displayed in the right portion of the image and the right ventricle in the left portion. Posterior structures are seen at the top of the video screen and anterior structures at the bottom. When the papillary muscles can be detected, antero-lateral and posterior medial muscles are distinguishable in the image at the 5 and 8 o′clock positions, respectively. The postero-inferior segments are closer to the transducer (Fig. 1.57).

Transgastric View: 2-Chamber View of Left Atrium and Left Ventricle

Longitudinal Plane (90°): A 2-chamber view of the left atrium and left ventricle. The left ventricle inferior wall is located

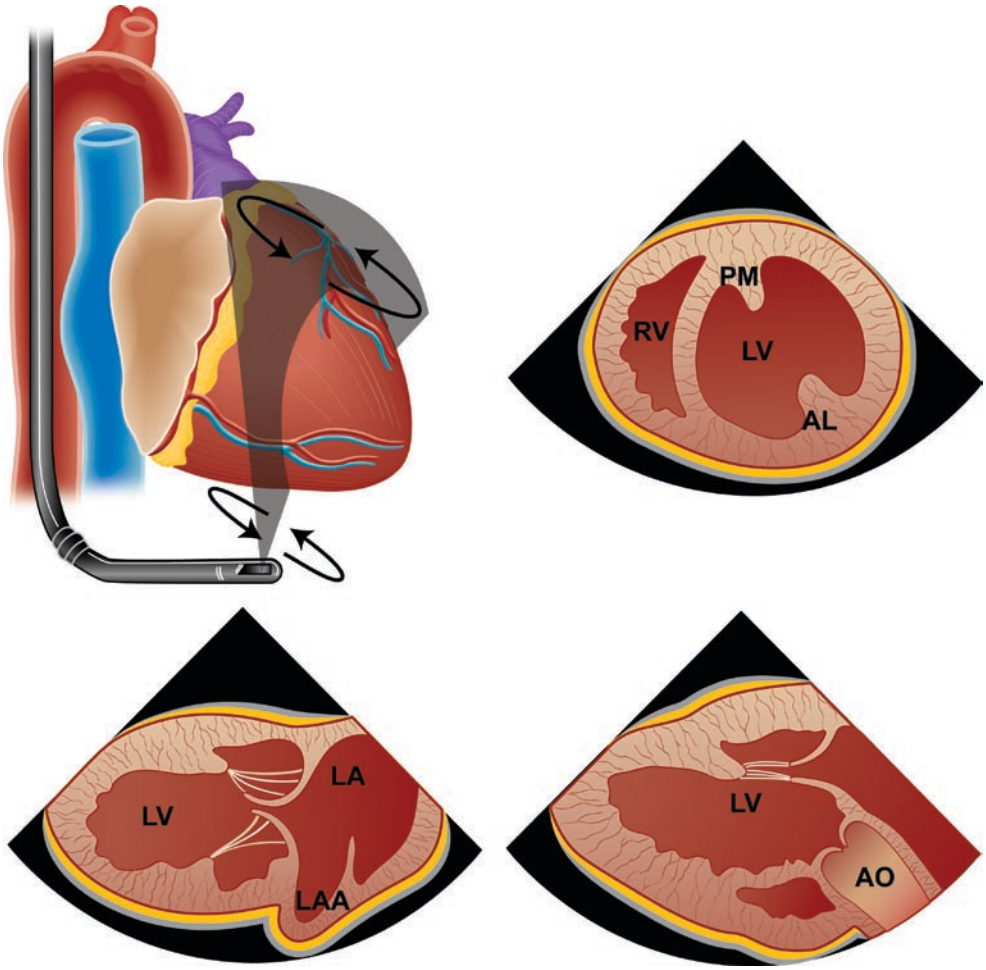

Fig. 1.56 Transgastric view. Schematic drawing of different view obtained with rotation by 0° to 135°. 0º: Short-axis view of left and right ventricle. 90º: 2-chamber view. 135°: Outflow tract of left ventricle and aortic valve. *LA* left atrium, *LAA* left atrial appendage; *AO* aorta; *LV* left ventricle; *RV* Right ventricle; *PM* posterior papillary muscle; *AM* anterior papillary muscle

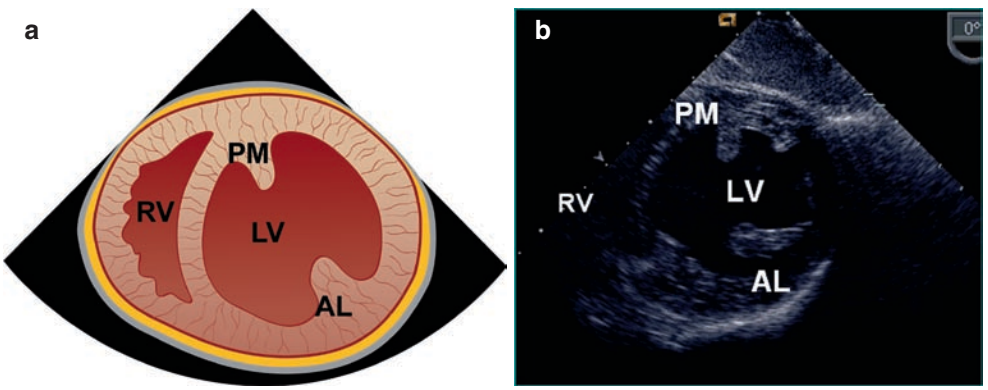

Fig. 1.57 Transgastric view. Transverse plane (0°). Schematic drawing and 2D visualization. The left ventricle is displayed to the viewer's right and the right ventricle to the viewer's left. Posterior structures are seen at the top of the video screen and anterior structures at bottom. The short-axis view of left ventricle at level of papillary muscles is showed. *LV* left ventricle; *RV* right ventricle; *PM* posterior papillary muscle; *AM* anterior papillary muscle

near the transducer and the anterior wall is directly opposite and at the bottom of the screen. The left atrium, medial scallop of the posterior mitral leaflet, and lateral segment of the anterior mitral leaflet can be observed. Two papillary muscles are visualized: postero-medial and antero-lateral. The left atrial appendage cannot usually be seen well. This view is very useful for obtaining a long-axis view of papillary muscles and mitral chordae (Fig. 1.58).

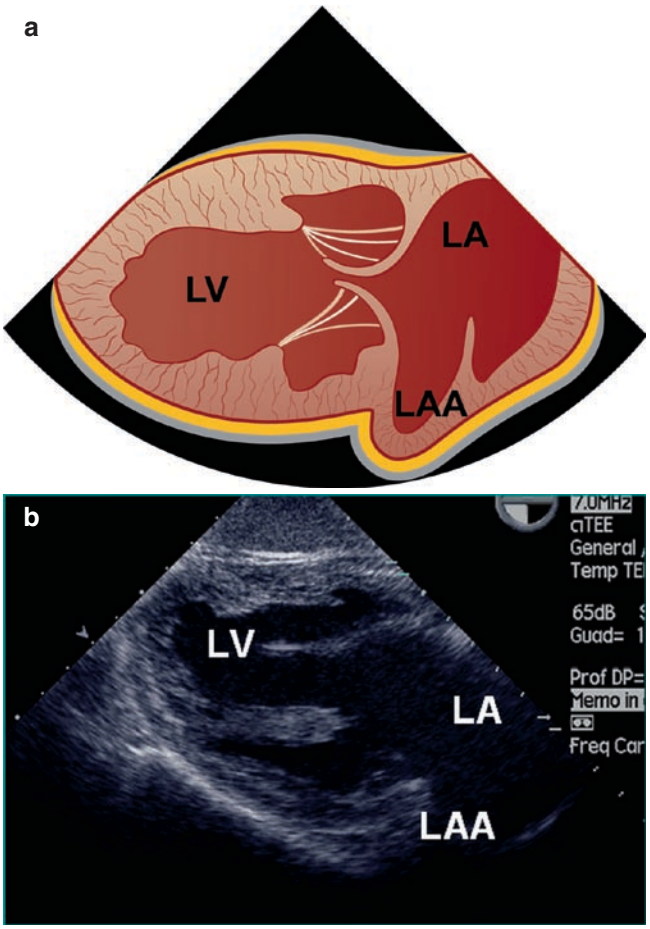

Fig. 1.58 Transgastric view. Longitudinal plane (90°). Schematic drawing and 2D visualization. The left ventricle appears in 2-chamber view with the appendage at the bottom and at the level of A–V junction. The papillary muscle and mitral cordae can be well visualized. *LA* left atrium; *LAA* left atrial appendage; *LV* left ventricle

Transgastric View: Left Ventricular Outflow Tract and Aortic Root

Longitudinal View (110–135°): Transgastric planes of left ventricular outflow tract (135°). This view allows us to see left ventricular outflow tract and aortic root. However, a deeper transgastric long axis or 5-chamber view can be useful in cases where the ascendant aorta cannot be observed adequately or accurate Doppler alignment is not possible. This plane is obtained by inserting the probe more deeply into the gastric fundus with maximum anteflexion of the tip and rotating the transducer (60–90°). Such movement of the probe tip will lead to a view similar to transthoracic apical 5-chamber view.

Other Transgastric Views

A short-axis view of the mitral valve can be obtained from the transversal plane by withdrawing the probe slightly. This is useful for the assessment of mitral valve prolapse. Rotating the probe and the transducer yields a right ventricle view (short axis of tricuspid valve at 30°, 2-chamber view of right atrium and right ventricle at 90°, and right ventricular outflow tract).

References

1. Henry WL, et al Report of the American Society of Echocardiography Committee on nomenclature and standards in two dimensional echocardiography. *Circulation*. 1980;62:212–216
2. Edwards WD, Tajik AJ, Seward JB. Standardized nomenclature and anatomic basis for regional tomographic analysis of the heart. *Mayo Clin Porc*. 1981;56:479–497
3. Weyman AE. *Principles and practice of echocardiography*. 3rd ed. Philadelphia: Lea and Febiger; 1994:99–123
4. Lange LW, Sahn DJ, Allen HD, Golberg SJ. Subxiphoid cross-sectional echocardiography in infants and children with congenital heart disease. *Circulation*. 1979;59:513–518
5. Goldberg BB. Supraesternal ultrasonography. *JAMA*. 1971;215:245–249
6. Feigenbaum H. *Echocardiography*. 5th ed. Philadelphia: Williams & Wilkins; 1994:68–123
7. Tei C, Tanaka H, Kashima T, Yoshimura H, Minagoe S, Kanehisa T. Real-time cross-sectional echocardiographic evaluation of the interatrial septum by right atrium–interatrial septum-left atrium direction of ultrasound beam. *Circulation*. 1979;60:539–543
8. Edler I. The use of ultrasound as a diagnostic aid and its effects on biologic tissues. *Acta Med Scand Suppl*. 1961;370:39
9. Oh JK. *Echo manual, Mayo clinic. Assessment of ventricular function*. Boston: Little Brown; 2000
10. Lauer MS, Larson MG, Levy D. Gender-specific reference M-Modevalues in adults: population-derived values with consideration of the impact of height. *J Am Coll Cardiol*. 1995;26:1039–1046
11. Pearlman JD, Triulzi MO, King ME, et al Limits of normal left ventricular dimensions in growth and development: analysis of dimensions and variance in the two-dimensional echocardiograms of 268 normal healthy subjects. *J Am Coll Cardiol*. 1988;12:1432–1441
12. American Society of Echocardiography Committee on Standards. Recommendations for quantification of the left ventricle by two dimensional echocardiography. *J Am Soc Echocardiogr*. 1989;2:358–367
13. Henry WL, et al Report of the American Society of Echocardiography Committee on nomenclature and standards in two dimensional echocardiography. *Circulation*. 1980;62:212
14. Tajik AJ, et al Two–dimensional real-time ultrasonic imaging of the heart and great vessels: Technique, image orientation, structure indentification, and validation. *Mayo Clin Proc*. 1978;53:271–303
15. Wahr DW, Wang YS, Schiller NB. Left ventricular volumes determinates by two dimensional echocardiography in a normal adult population. *J Am Coll Cardiol*. 1983;I:863–868

16. Franzin L, Talano JV, Stephanides L, Loeb HS, Kopel L, Gunnar RM. Esophageal echocardiography. *Circulation*. 1976;54:102–108
17. Hatle L, Angelsen B. *Doppler ultrasound in cardiology: physical principles and clinical applications*. 2nd ed. Philadelphia: Lea and Febiger; 1985
18. García Fernández MA. *Principios y práctica del doppler cardíaco*. Madrid: McGraw Hill; 1995:2–21
19. Omoto R, Kasai C. Physics and instrumentation of Doppler color flow zapping. *Echocardiography*. 1987;4:467–483
20. Kisslo J, Adams DB, Belkin RN. *Doppler color flow imaging*. New York: Churchill Livingstone; 1988
21. Wittlich N, Erbel R, Drexler M. Color Doppler flow mapping of the heart in normal subjects. *Echocardiography*. 1988;5:157–164
22. Garcia Fernandez MA, Zamorano J. *Procedimientos en ecocardiografía*. Madrid: McGraw Hill; 2004
23. Garcia Fernández MA. *Principios del Doppler cardíaco*. Interamericana: McGraw.Hill; 2005
24. Garcia Fernández MA, Moreno M, San Román D, Torrecilla E, Sousa RC, Decán JL. Ecocardiografía transesofágica multiplaza: Técnica, metodología y aplicaciones. Comparación con las técnicas monoplana biplana. *Rev Esp Cardiol*. 1994;47:26–33
25. Sungeng MD, Stanton K, Salgo I, et al Live 3-dimnsiona. Transesophageal echocardiography. Initial experience using the fully sampled matrix array probe. *J Am Coll Cardiol*. 2008;6:446–449
26. Khanderia BK. Prophylaxis or no prophylaxis before transesophageal echocardiography? *J Am Soc Echocardiogr*. 1992;5:285–297
27. Melendez LJ, Chan KL, Cheung PK, Sochowsli RA, Wong S, Austin TW. Incidence of bacteremia in transesophageal echocardiography: prospective study of 140 consecutive patients. *J Am Coll Cardiol*. 1991;18:1650–1654
28. Daniel WG, Erbel R, Kasper W, et al Safety of transesophageal echocardiography: a multicenter survey of 10419 examinations. *Circulation*. 1991;83:817–821
29. García Fernández MA, Torrecilla EG, San Román D, Bueno H, Moreno M, Delcán JL. Left atrial appendage. Doppler flow patterns: implications on thrombus formation. *Am Heart J*. 1992;124:955
30. Seward JB, et al Transesophageal echocardiography: technique, anatomic correlations, implementation, and clinical applications. *Mayo Clin Proc*. 1988;63:649–680
31. Seward JB, et al Multiplane transesophageal echocardiography: image orientation, examination technique, anatomic correlations, and clinical applications. *Mayo Clin Proc*. 1993;68:523–551

Chapter 2

NEW DEVELOPMENTS IN ECHOCARDIOGRAPHY

Mark Monaghan and Amit Bhan

CONTENTS

J. L. Zamorano et al. (eds.), *The ESC Textbook of Cardiovascular Imaging*
DOI: 10.1007/978-1-84882-421-8_2, © Springer-Verlag London Limited 2010

Contrast Echo

Mark Monaghan and Amit Bhan

Introduction

The use of contrast agents is widespread in most medical imaging modalities for enhancing image quality. In echocardiography, ultrasound contrast agents have found widespread applications for the opacification of the left ventricular cavity to enhance the endocardial border, improve cardiac Doppler signals, and provide an evaluation of myocardial blood flow. This section discusses the methodology and utility of contrast echocardiography.

Contrast Echo Technology

Ultrasound backscatter is created when sound waves are reflected from an interface between two media with very different acoustic densities. Consequently, fresh thrombus sitting in a cardiac cavity surrounded by blood with a similar density creates a weak backscattered signal (echo), whereas a calcified or even prosthetic valve in the same cavity creates a strong signal. Gas filled bubbles have a significantly different acoustic density to blood; hence, they are also strong acoustic reflectors. Consequently, it has been appreciated for a long time that venous injection of hand-agitated saline plus a small quantity of air can create very small or micro-bubbles, which act as tracers of blood flow through the right heart, and these can be readily visualized on both 2D and M-mode echocardiography as shown in Fig. 2.1. Since these bubbles have no shell and air is highly soluble in blood, these small bubbles only last a few seconds in the circulation and do not normally survive the pulmonary circulation. Appearance of bubbles in the left heart, very shortly after arrival in the right heart, can be used as a simple test for right to left shunting through a patient foramen ovale, atrial septal defect, or even a ventricular septal defect.

In order to opacify the left heart, micro-bubbles have to survive transpulmonary passage. This means that they need to be small enough to behave physiologically in the circulation and not obstruct flow, at even a capillary level. They also have to be robust enough to ensure that the encapsulated gas does not escape and/or diffuse into the circulation. As illustrated in Fig. 2.2, commercially manufactured ultrasonic contrast agents have adopted two main approaches to achieve this. They have either created a contrast micro-bubble using a thick, impermeable shell such as a lipid, or else the micro-bubble has been filled with a high molecular weight gas such as sulfur hexafluoride or a perflurocarbon.

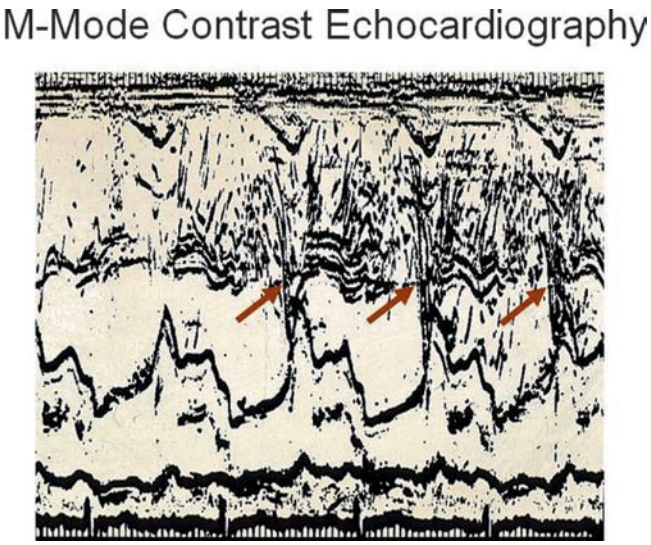

Fig. 2.1 M-mode echocardiogram of a hand-agitated bubble contrast study in a patient with a large ventricular septal defect. Bubbles can be seen (*arrowed*) crossing from the right ventricle to the left secondary to bidirectional shunting

Figure 2.3 lists the currently available or developing ultrasound contrast agents, their shell type, and contained gas.

In an ideal world, we would wish the intensity of backscattered (reflected) ultrasound from contrast micro-bubbles to be as large as possible. The ratio of incident (transmitted) to backscattered ultrasound intensity is dependent upon a number of factors, the most important being the fourth power

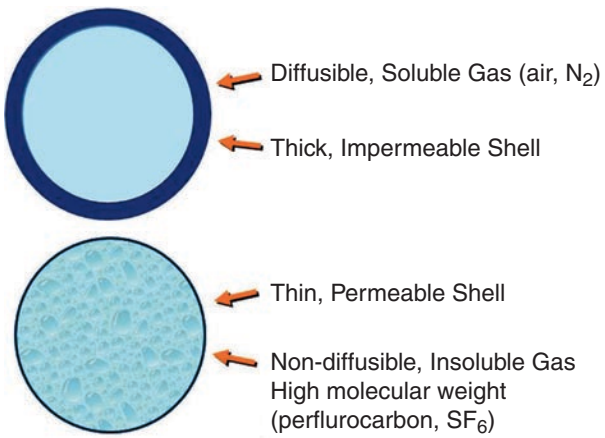

Fig. 2.2 Diagrammatic illustration of the different approaches taken with commercial contrast agents to enhance micro-bubble stability within the circulation. Micro-bubbles are covered with a relatively impermeable shell and/or filled with a non-soluble high molecular weight gas

Fig. 2.3 A list of commercially available contrast agents with their contained gas and shell types

AGENT	MANUFACTURER	SHELL TYPE	ENCAPSULATED GAS
Levovist	Schering	GalactosePalmitic Acid	Air
Luminity	Lantheus	Lipid Micro-bubble	Perfluoropropane
Imagify	Acusphere	Phospho-lipid	Perfluorocarbon
Optison	GE Medical Systems	Albumin Micro-sphere	Octafluoropentane
Sonovue	Bracco	Lyophilisate	SF6 & Air

of the micro-bubble diameter. So from that point of view, we would want the bubbles to be as large as possible. However, as previously mentioned, contrast agent micro-bubbles have to be small enough to behave physiologically in the circulation, which means that they need to be of similar size to red blood cells. In practice, this means that the mean size of commercial contrast micro-bubbles is around 4 μ. While this means that the backscatter from contrast is many times that from red blood cells, there are other confounding factors, the most important being that contrast micro-bubbles are fragile and are almost instantly destroyed by ultrasound delivered at diagnostic intensities. If the intensity of ultrasound is reduced to minimize destruction, the backscatter intensity can diminish to below the detection threshold of a standard 2D imaging system. Furthermore, it is desirable to have the ultrasound system working in a way that suppresses the tissue signal and enhances the contrast signal so that the contrast-enhanced blood pool in the ventricular cavities and myocardium can be easily seen.

Fortuitously, because contrast micro-bubbles are gas-filled and surrounded by a relatively soft and elastic shell, they have the ability to resonate and oscillate in a non-linear manner in a sound field. The frequency at which they resonate is dependent on the size of the micro-bubble. A large wine glass will "ring" when tapped at a lower frequency than a small wine glass. Micro-bubbles with a diameter of approximately 4 μ have a resonant frequency of approximately 2 MHz, which is within the frequency bandwidth of ultrasound used in echocardiography, and this is a very fortunate coincidence. The fact that contrast micro-bubbles exhibit non-linear oscillation in an echo ultrasound field and that they therefore have very different acoustic properties to tissue means that it is possible to process the backscattered signals in such a way as to suppress tissue and enhance the contrast signal.[1–3] Had this coincidence with respect to the resonant frequency of contrast micro-bubbles not existed, contrast echocardiography may not have existed!

Contrast-specific imaging technologies conveniently separate themselves into methods that rely on or cause micro-bubble destruction and those techniques that aim to preserve the micro-bubbles–non-destructive imaging. Some of the currently available contrast specific imaging techniques are listed in Table 2.1.

At higher MIs, the non-linear oscillation of contrast micro-bubbles within the ultrasound field results in the generation of harmonic signals and then destruction of the micro-bubble. Typically these harmonics will occur at multiples of the transmitted (fundamental) frequency, with the strongest response occurring at the second harmonic.

Although there is also a tissue signal at the second harmonic frequency, it is lower in amplitude than the contrast signal. So, if the received frequency filters on the scanner are set to only receive the second harmonic frequency (twice the transmitted fundamental frequency), the contrast signal amplitude will be greater than that of the tissue. Therefore, the all-important contrast to tissue signal ratio is increased. At even higher harmonics, the tissue signal will be negligible, but there will still be a contrast signal. These techniques are called ultraharmonics and essentially rely upon receiving selected higher frequencies. However, the received contrast signal amplitude is still very small at these higher harmonics,

Table 2.1. Destructive and non-destructive contrast-specific imaging modalities. As a general rule, destructive imaging techniques use an MI (output power) > 1.0, whereas non-destructive techniques need to use an MI < 0.3 in order to limit contrast destruction, as previously mentioned

Destructive Contrast Imaging Techniques
Second harmonic imaging
Ultraharmonics
Pulse inversion
Harmonic power Doppler (angio)
Non-destructive Contrast Imaging Techniques
Low MI real-time methods
Power modulation
Power pulse inversion
Cadence contrast imaging
Contrast pulse sequencing

making them susceptible to noise and artifacts. In addition, specially constructed broad-bandwidth transducers have to be utilized to detect these higher harmonics.

In summary, these high MI destructive techniques cause high amplitude resonance of the micro-bubbles, generation of harmonics, and, of course, bubble destruction. Although these techniques are sensitive for micro-bubble detection, they have to be used in an intermittent imaging mode.[4] This is to allow time for contrast micro-bubbles to replenish the myocardium following each destructive frame. In practice, this means that a frame is acquired every 1, 2, 3, or up to 10 cardiac cycles. Intermittent imaging is more difficult to use, and many consider this a significant disadvantage. Consequently, it is not currently a widely used contrast-specific imaging technique and is not discussed further in this chapter.

Non-Destructive Contrast Imaging Techniques

As previously mentioned, intermittent imaging does make destructive imaging techniques more difficult to use. Also the absence of any wall motion information is considered by many to be an important disadvantage. In order to provide wall motion information, the frame rate needs to be increased from 1 frame every few cardiac cycles to a minimum of 20 frames a second. If the frame rate is to be increased without causing bubble destruction, the MI needs to be decreased significantly and usually needs to be <0.3.

A low MI will minimize micro-bubble destruction, but, as previously mentioned, will generate only a very weak backscattered signal. Therefore, more sensitive contrast detection methods have to be used, which at the same time will suppress the tissue signal. These low MI methods are called real-time because the higher frame rates allow evaluation of wall motion and myocardial blood flow simultaneously.

All the non-destructive contrast-specific imaging techniques work on similar principles. They send multiple, low-amplitude pulses down each scan line. Each pulse varies from the preceding one in amplitude, phase, or a combination of both. Different manufacturers use one or more of these methods for their low MI real-time methods, and some of the proprietary names for these techniques are listed in Table 2.1.

Power modulation is one of the typical low MI real-time methods. With this methodology, alterations in signal amplitude are used. Multiple pulses are transmitted down each scan line; however, each alternate pulse is of 50% amplitude. The ultrasound scanner receives circuitry, doubles the received signals from the 50% amplitude pulses, and then subtracts that from the received signal from the 100% amplitude pulses. This means that, in theory, backscattered signals from a linear reflector, such as myocardial tissue, should cancel each other out, thereby suppressing the myocardial signal. Contrast micro-bubbles are non-linear reflectors, so the doubled backscatter signal from the 50% amplitude pulse does not cancel the signal created by the 100% amplitude pulse. The remaining signal indicates the presence of contrast within the scan plane.

Usually, the only image signals seen when utilizing low MI non-destructive real-time imaging are those derived from contrast micro-bubbles, and tissue signals are completely suppressed. At low contrast micro-bubble concentrations, there may be insufficient contrast within the myocardium to cause any enhancement, and the only contrast that can be seen is within the left ventricle (LV) cavity. Since the myocardium will be black and the cavity bright, this results in excellent endocardial definition. Frame rates of >30 Hz can be achieved, and this is satisfactory for use during stress echocardiography. Furthermore, the absence of contrast destruction allows much better visualization of the left ventricular apex than when conventional high MI second harmonic imaging is used with contrast. High MI second harmonic imaging also creates a significant tissue signal and this can make it more difficult to determine the endocardial boundary. If second harmonic imaging is to be used with contrast for left ventricular opacification, it is sensible to reduce the MI < 0.4 to limit the tissue signal and contrast destruction.

Figure 2.4 illustrates a pre-contrast and post-contrast (using power modulation) apical image where the right ventricle (RV) and the septal aspect of the LV can be clearly delineated. In the pre-contrast image, it is impossible to see either ventricle well. A video clip (Video 2.4) of this is available.

European and American guidelines on the use of ultrasound contrast agents have recommended their use for left ventricular opacification when two or more myocardial segments are not adequately visualized, or when delineation of left ventricular morphology and detection of thrombi are required. Contrast for left ventricular opacification is particularly useful during stress echocardiography where image quality is of prime importance. Obtaining high-quality images, especially at peak stress, can be extremely difficult in many patients, and contrast-enhanced imaging is required in at least 75% of patients during stress echo. Plana et al[5] have shown that the use of contrast agents during dobutamine stress echocardiography in patients with more than two myocardial segments not visualized significantly increases the accuracy of the technique when coronary angiography is used as the gold standard.

As the contrast micro-bubble concentration is increased in the blood, either by increasing the bolus volume or infusion rate, sufficient micro-bubbles will appear within the myocardium to cause myocardial enhancement. The myocardial contrast signal intensity is directly proportional to the number of micro-bubbles within a unit volume of myocardium, and this equates to the myocardial blood volume. As previously mentioned, the great advantage of this type of

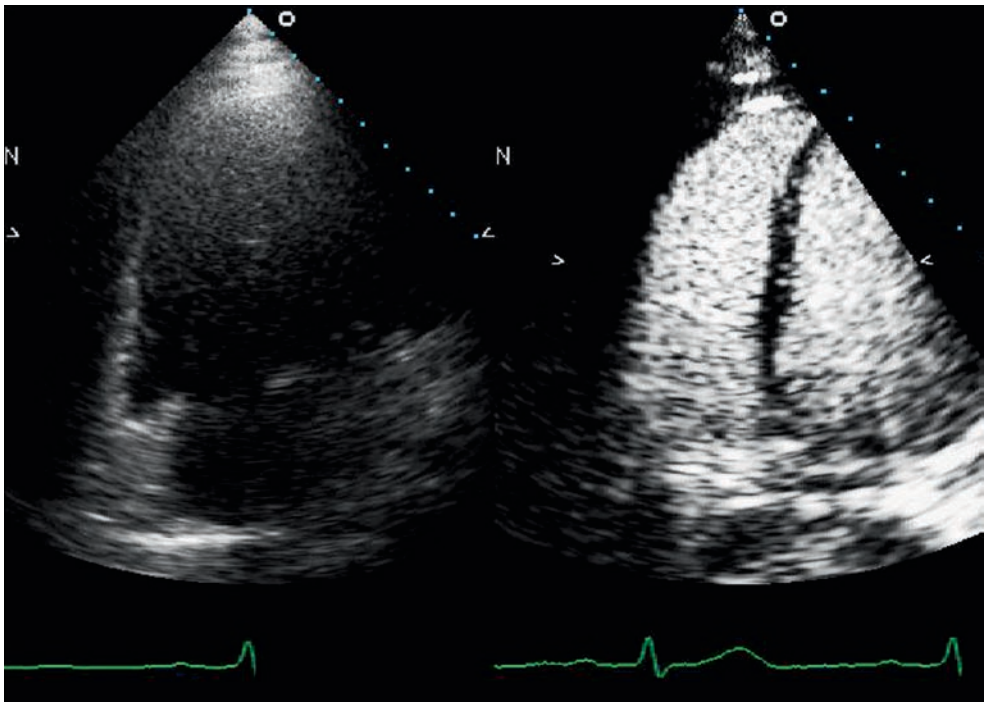

Fig. 2.4 Apical 4-chamber view obtained using a contrast-specific imaging modality before (*left*) and after (*right*) intravenous administration of contrast. Enhancement of the right and left ventricular endocardial borders are clearly seen

contrast imaging technique is that it potentially permits evaluation of both left ventricular wall motion with excellent endocardial definition and myocardial blood flow through evaluation of myocardial blood volume.

Evaluation of myocardial blood flow is achieved by firing a few frames of high MI ultrasound to destroy the contrast in the myocardium, where it is at much lower concentration than in the LV cavity. Once the contrast is destroyed within the scan plane, it will replenish over the next few cardiac cycles.[6,7] The rate at which it replenishes is dependent upon the capillary myocardial blood flow velocity. At rest, it will normally take about four cardiac cycles following complete destruction to plateau at the baseline level. During peak pharmacological (vasodilator or inotrope) stress, replenishment will occur in 1–2 cardiac cycles because blood flow velocity will normally increase by a factor of 4. As previously mentioned, the plateau level of backscattered contrast intensity is directly proportional to the concentration of contrast microbubbles within a unit volume of myocardium, which is a surrogate for myocardial blood volume. As illustrated in Fig. 2.5a, if a region of interest (ROI) is placed over a myocardial segment and we measure the contrast signal intensity from that region before, during, and after contrast destruction, we can construct a replenishment curve. The slope of the curve is proportional to blood flow velocity and the plateau to blood volume. The product of these two parameters will provide, in theory, a value equivalent to myocardial blood flow per unit volume of myocardium.

Figure 2.5b illustrates a real contrast replenishment curve created using commercially available software for the analysis of contrast images. While construction of such curves provides the potential for absolute quantification of blood flow at rest and stress, and therefore evaluation of blood flow reserve, it is currently a time-consuming process. From a routine clinical perspective, it is often sufficient to visually analyze contrast images following destruction and look at the timing of replenishment in terms of number of cardiac cycles post-destruction. As previously mentioned, at rest, replenishment will take about four cardiac cycles, and during stress, 1–2 cardiac cycles. Myocardial segments with reduced flow reserve, implying reversible ischaemia, will exhibit delayed replenishment post-destruction, and the myocardium will remain dark for a prolonged period. In less severe reversible ischaemia, this delayed replenishment may be confined to the subendocardial region, whereas in more severe cases, it may be trans-mural and the plateau contrast intensity may also be reduced.

An example of severe reversible ischaemia relating to the left circumflex territory is shown in Figs. 2.6 and 2.7 (Videos 2.6 and 2.7). This patient had a 95% proximal circumflex lesion with atypical symptoms. He had normal resting wall motion and thickening. Peak dobutamine stress demonstrated a minor wall motion abnormality in the posterior and lateral walls that was appreciated using the left ventricular opacification provided by contrast. The myocardial contrast echo demonstrated a clear trans-mural reduction in myocardial

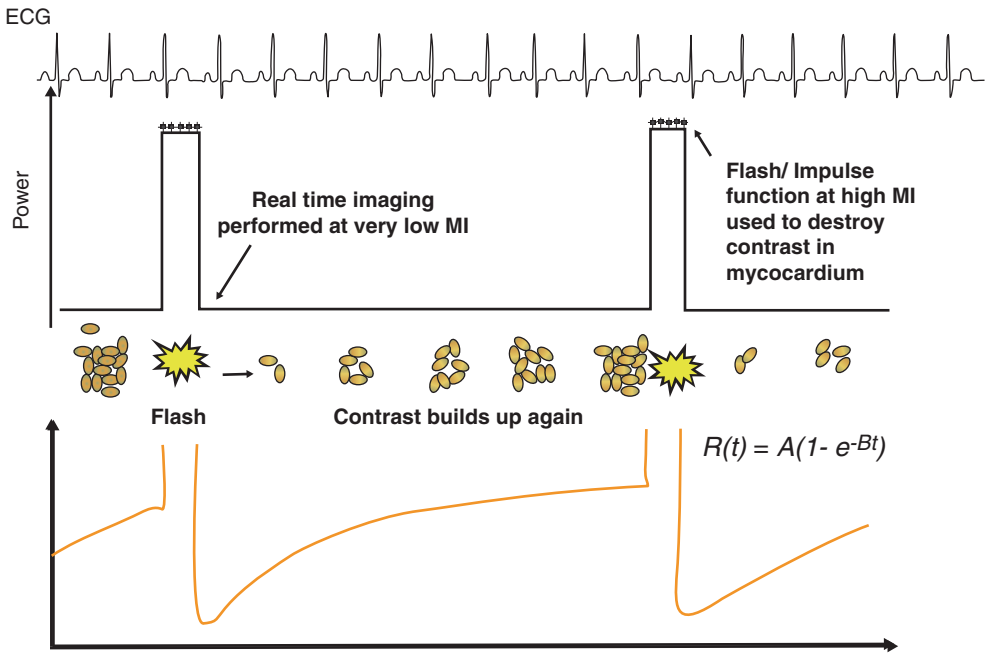
ECG
Power
Real time imaging performed at very low MI
Flash/ Impulse function at high MI used to destroy contrast in mycocardium
Flash
Contrast builds up again
R(t) = A(1- e-Bt)

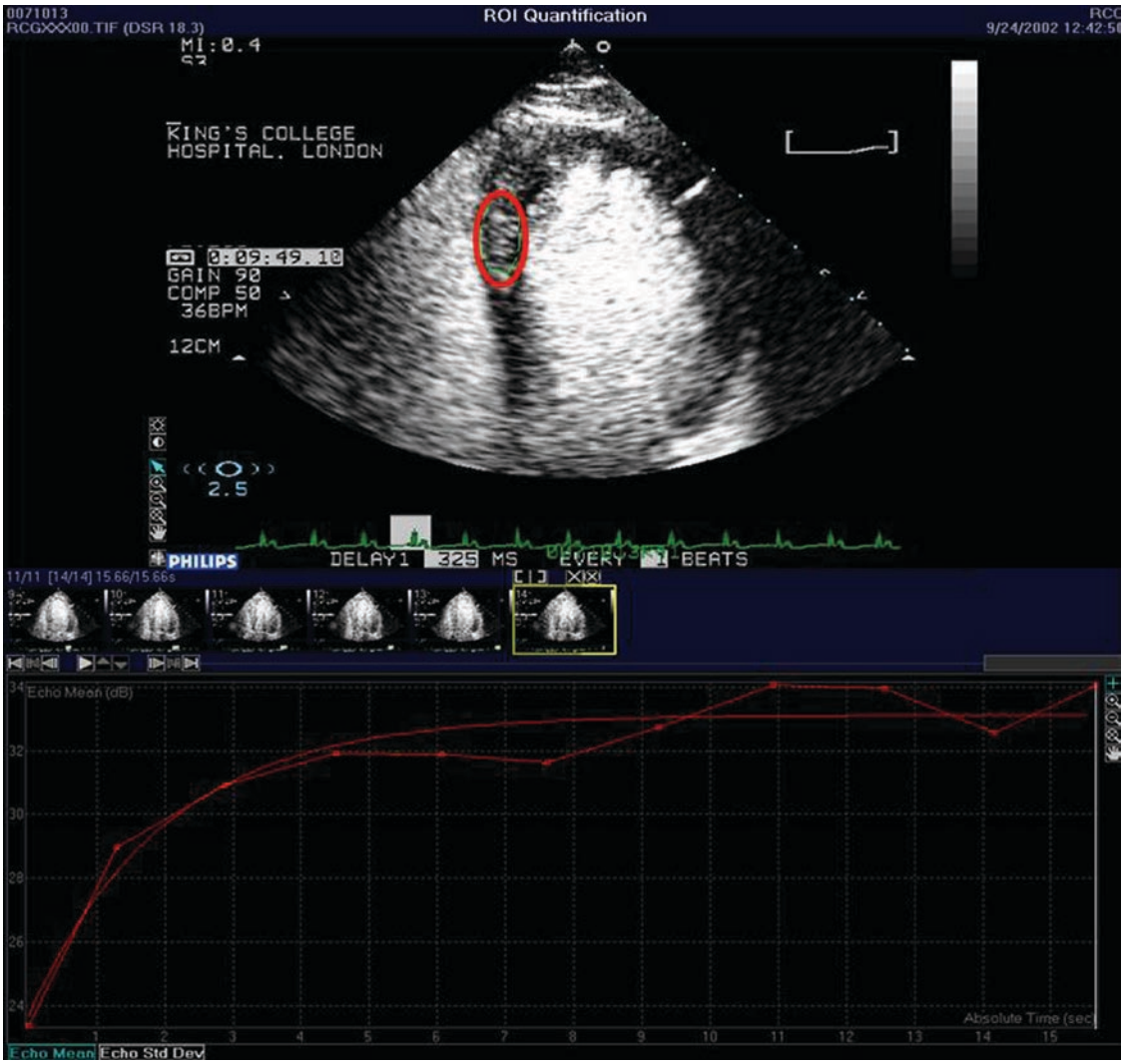
ROI Quantification
MI:0.4
KING'S COLLEGE HOSPITAL, LONDON
GAIN 90
COMP 50
36BPM
12CM
2.5
PHILIPS
DELAY1 325 MS EVERY 1 BEATS
Echo Mean (dB)
Absolute Time (sec)
Echo Mean
Echo Std Dev

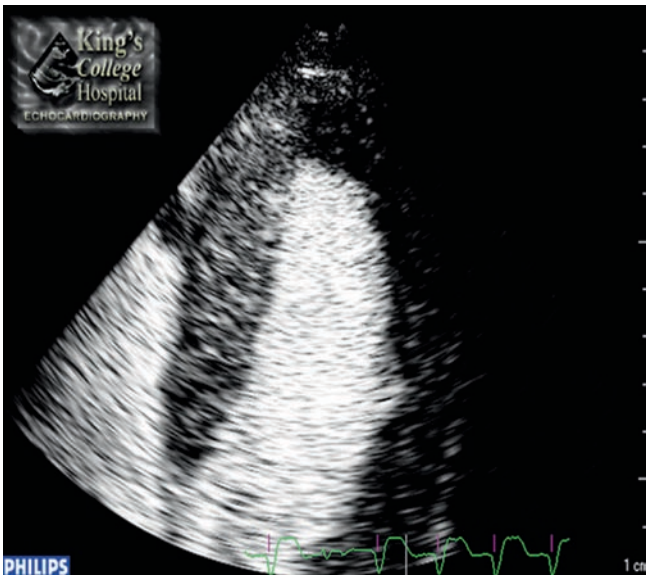

Fig. 2.6 Contrast-enhanced apical 4-chamber view at peak dobutamine stress in a patient with a 95% left cirmcumflex lesion. The still image is taken at two cardiac cycles post-destruction. The septum has fully replenished, whereas the lateral wall has not, indicating reversible ischaemia in this territory. The video clip shows a stress induced wall motion abnormality seen (with contrast enhancement) in the lateral wall together with a persisting perfusion defect post-destruction

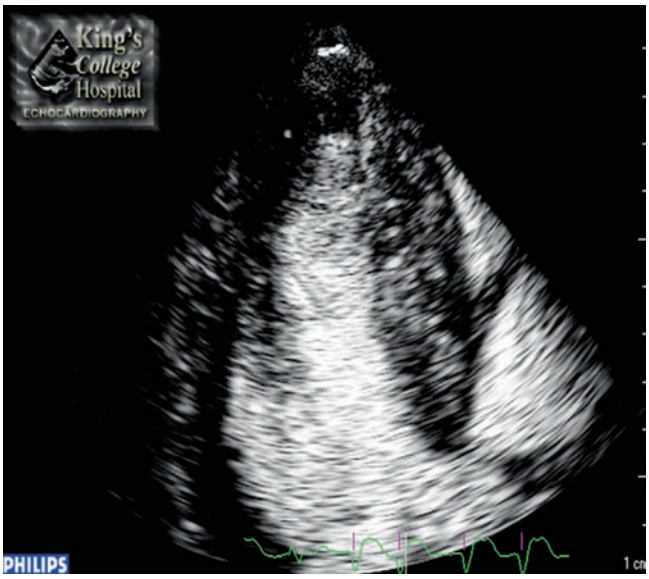

Fig. 2.7 Contrast-enhanced apical 3-chamber view at peak dobutamine stress in a patient with a 95% left cirmcumflex lesion. The still image is taken at two cardiac cycles post-destruction. The anterior septum has fully replenished, whereas the posterior wall has not, indicating reversible ischaemia in this territory. The video clip shows a stress induced wall motion abnormality seen (with contrast enhancement) in the posterior wall together with a persisting perfusion defect post-destruction.

blood flow within the entire circumflex territory, which remained dark for several cardiac cycles post-destruction and exhibited delayed replenishment. This confirmed the presence of reversible ischaemia in the left circumflex territory. In this example, contrast has provided enhanced assessment of wall motion during stress and also facilitated evaluation of myocardial blood flow, thereby increasing the accuracy of the test.

Safety of Ultrasound Contrast Agents

The European (EMEA) and North American (FDA) drug licensing agencies have previously raised concerns about the potential harmful side effects of ultrasound contrast agents. However, extensive post-marketing surveillance of more than 1 million contrast studies and detailed evaluation of adverse events have concluded that the risk of significant allergic reactions to most agents is less than 1:1,000. The conclusion of most experts in the field has been that they are safe and that the risk/benefit profile of ultrasound contrast agents is strongly in favour of their use in stable patients.[8–11] Patient care is more likely to be disadvantaged and additional investigations required if contrast agents are not used when appropriate, than if they are.

Contrast Echocardiography: Future Directions

At the time of writing this chapter, none of the commercially available contrast agents have a license for myocardial perfusion imaging. Although, as has been discussed, they can all provide acceptable myocardial contrast images. Consequently, some agents are now undergoing phase three

Fig. 2.5 **(a)** A region of interest (ROI) is placed over a myocardial segment, the contrast signal intensity is measured from that region before, during, and after contrast destruction, and a replenishment curve is constructed. The slope of the curve is proportional to blood flow velocity and the plateau to blood volume. The product of these two parameters will provide, in theory, a value equivalent to myocardial blood flow per unit volume of myocardium. **(b)** An example of a contrast destruction replenishment curve obtained using commercially available contrast evaluation software. The ROI is placed in the midseptum and the post-destruction replenishment curve is seen. The software can automatically calculate the slope, plateau, and derived myocardial blood flow parameters from the curve

studies and/or seeking regulatory approval as perfusion agents. These will be used in combination with vasodilator stress, and reversible ischaemia will be evident as a reduction in myocardial blood flow, with any stress induced wall motion abnormalities being a minor effect. A vasodilator stress echo is likely to be much quicker than one performed using an inotrope, and this will have obvious advantages. In addition, studies performed so far suggest at least equal accuracy to SPECT perfusion imaging for the detection of reversible ischaemia.[12,13]

Contrast-specific imaging modalities have now been incorporated into the latest 3D imaging systems so that it is possible to use contrast to both enhance left ventricular endocardial border detection[14] and the myocardial blood volume to obtain an assessment of perfusion.[15] Since contrast-specific imaging modalities, such as power modulation, are multipulse techniques, the effect on frame rate is even more marked with 3D as compared to 2D imaging. This may limit its applicability to use during 3D dobutamine or exercise stress echo where peak heart rates are high. However, 3D contrast perfusion imaging may be very useful during vasodilator stress, where heart rate does not increase and reduction in myocardial blood volume (perfusion defect) may be more evident. Figure 2.8 (Video 2.8) clip demonstrates a still image and rotating video clip of a patient with an acute antero-apical infarct. Contrast enhancement of the left ventricular cavity and normal myocardium is seen clearly, with a defect (hole) in the myocardial contrast enhancement seen at the apex, which represents the infarct zone. 3D contrast techniques such as this have the potential to facilitate measurement of perfusion defect volume rather than just area, which is all that can be appreciated from 2D contrast imaging.

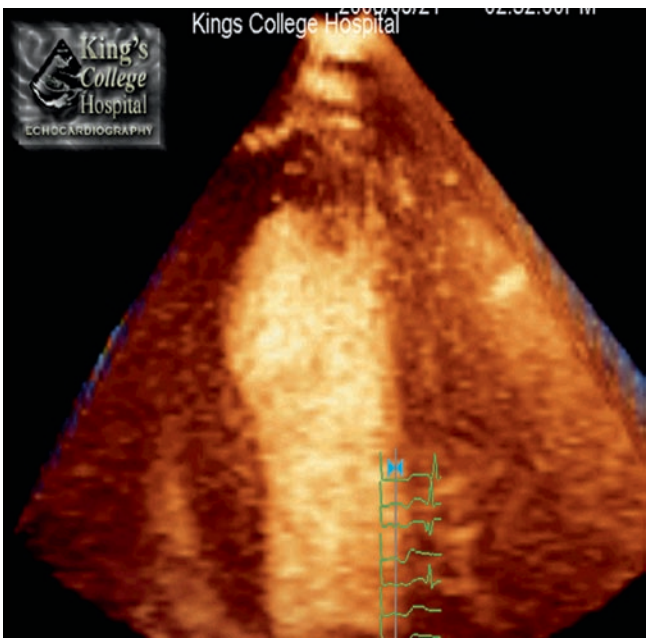

Fig. 2.8 Cropped 3D power modulation imaging during contrast infusion in a patient with an acute antero-apical infarct. The image is displayed in still and rotating formats. The rotating image demonstrates the 3D perspective of the image, which shows contrast opacification of the left ventricular cavity and also the myocardium. A contrast "defect" is seen in the antero-apical segment, which corresponds to the infarct zone. The volume of the defect can be appreciated and potentially quantified

The potential role of contrast micro-bubbles in therapy, rather than diagnostics, is now being actively explored. Ultrasound mediated contrast micro-bubble drug or gene delivery has been shown to be feasible. Contrast microbubbles can be loaded with the required drugs or genes and the micro-bubble provided with ligands, which can attach to specific receptors on cells allowing target delivery. This can be used in combination with spatially focussed high power ultrasound, which causes the bubbles to burst within the target zone. The rapid alteration in pressure caused by the bubbles bursting has been shown to increase transfection of drugs or genes across cell membranes and increase the amount of drug or gene delivery significantly. This is an exciting area of research that will take contrast echocardiography into an entirely new zone of applications. Unfortunately, it is out of the scope of this chapter to discuss this therapeutic application further.

Over the past few years, ultrasound contrast agents have become as important for the enhancement of echocardiography images as other types of contrast have become essential for the enhancement of X-Ray, CT, MRI, or nuclear imaging. Ultrasound has a major advantage of being portable and non-invasive, and when combined with contrast, it further strengthens the technique as a highly cost-effective and accurate imaging technique.[16]

3D Echocardiography

Amit Bhan and Mark Monaghan

Introduction

The concept of and, indeed the ability to perform three-dimensional echocardiography (3DE), has been around for some time now. It was back in 1974 that investigators first reported the acquisition of 3D ultrasound images of the heart,[17] but it has not been until the last decade that 3DE has started to enter clinical practice. The early attempts at this form of imaging were based around computerized reconstruction from multiple 2D slices achieved by carefully tracking a transducer

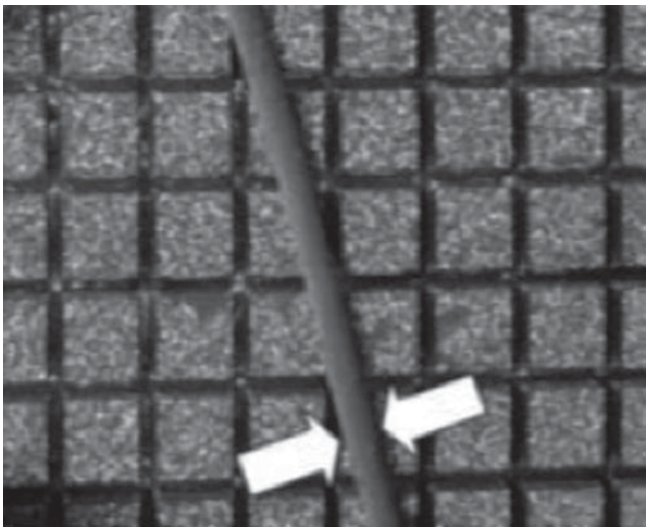

Fig. 2.9 A magnified photo of the grid-like arrangement of a matrix array transducer. A *human hair* is shown for size comparison

through a number of 2D acquisitions. Over subsequent years, this technique was gradually refined and improved; ECG gating was introduced, and free hand scanning gave way to motorized rotary transducers, whose location in space was continually tracked. This approach appeared to produce accurate volumes[18] and impressive images; however, the time involved for reconstruction and the labor intensive analysis, not to mention the requisite computing capabilities, meant that it was the preserve of dedicated research departments.

The advent of a sparse matrix array transducer in the early 1990s[19] represented a marked improvement in transducer capabilities and heralded a new era for 3DE. It was made up of 256 elements, arranged in a grid-like fashion (Fig. 2.9), and was capable of parallel processing, allowing the rapid acquisition of pyramidal datasets with a sector angle of up to 60 by 60°. It was now possible to obtain direct volumetric data at frame rates high enough to demonstrate cardiac motion. Images were presented as 2D orthogonal planes and both spatial and temporal resolution were low; nevertheless, it was used very effectively to investigate mitral valve disease, as well as left ventricular (LV) function and mass.

Since then, transducer technology has continued to advance, and fully sampled matrix array technology, with more than 2,000 and now more than 3,000 elements, has facilitated the integration of 3DE into clinical practice. These transducers (Fig. 2.10) allow rapid ECG gated image acquisition with temporal and spatial resolution sufficient for clinical applications.

Fig. 2.10 Two examples of current 3D transthoracic (*left*) and 2D transducers. Although the main body of the 3D transducer is significantly larger, in order to allow for preprocessing, the actual footprints are not that dissimilar in size

Matrix Array Technology

The current generation of widely available matrix phased array transducers allows five main types of image acquisition, each differing in spatial and temporal resolution profiles, as well as the number of cardiac cycles required for image capture. Furthermore, the exact capabilities and availability of each mode differ slightly from vendor to vendor. These modes are (Fig. 2.11a–e, Video 2.11):

- Multi-plane (biplane and tri-plane)
- Live 3D
- 3D zoom
- Full volume
- 3D colour Doppler

Although all these techniques are termed real-time, this is only strictly true for the multi-plane, live 3D, and 3D zoom. The other modes require capture of a number of ECG gated subvolumes, which are then rapidly reconstructed before viewing is possible.

Multi-plane imaging allows the simultaneous presentation of multiple 2D slices, be it two or three that can be captured in a single cardiac cycle. The exact angle of these slices can be adjusted, within certain limits, depending on the structures being imaged.

Live 3D allows a truly real-time beat-by-beat 3D image, which can be manipulated live. In order to enable this kind of imaging, the field sector is narrow and something in the order of 50 by 30°.

3D zoom mode provides a magnified dataset of a specific ROI, generally also allowing a sector angle of around 50 by 30°. This can be widened to around 90 × 90°, but at the expense of frame rates. Both live 3D and 3D zoom are ideal for imaging smaller structures, in particular valves.

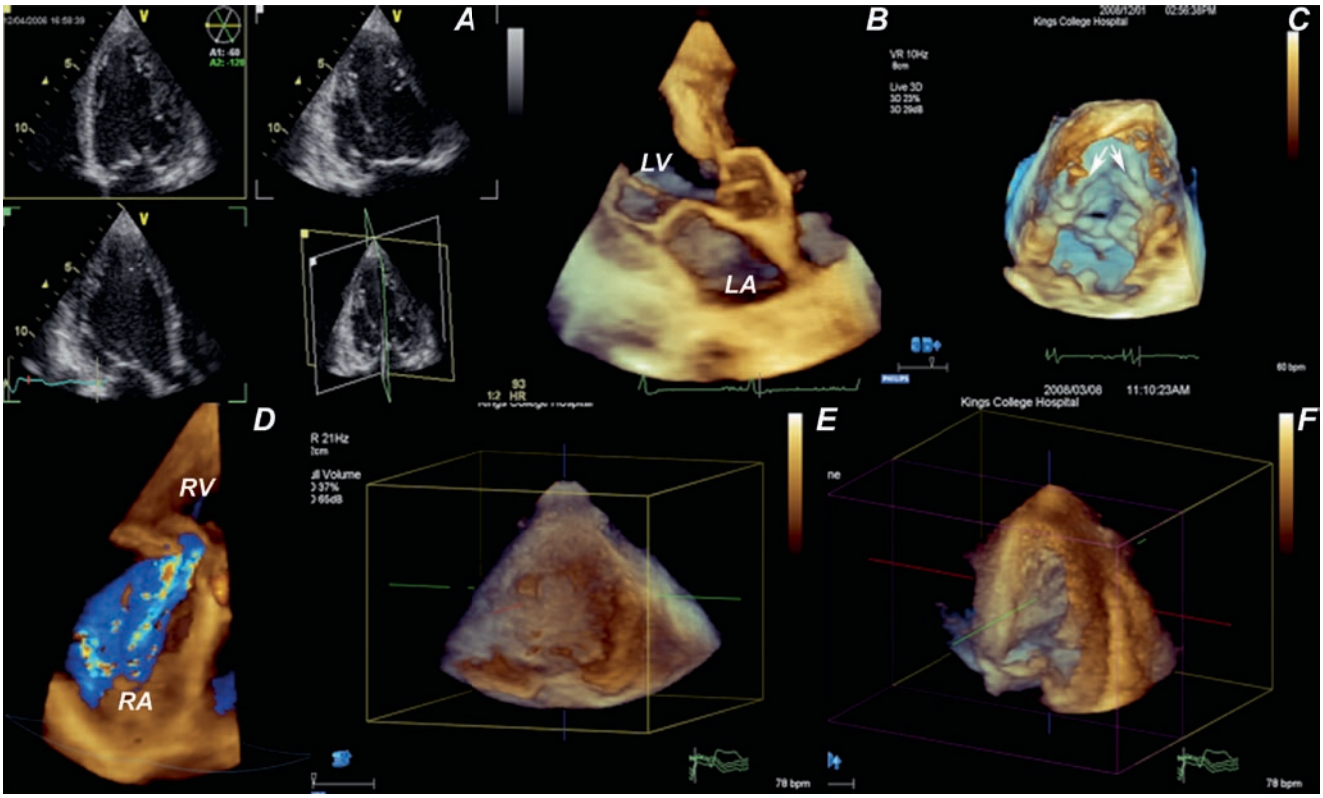

Fig. 2.11 **(a–e)** Examples of the possible modes available using 3DE. **(a)** Triplane view showing three apical views (4 chamber, 2 chamber, and 3 chamber), **(b)** parasternal long axis using live 3D mode. **(c)** 3D zoom showing the left ventricular aspect of the mitral valve (*arrows* = chords). A ruptured chord can also be seen attached to the anterior leaflet in the video clip. **(d)** 3D colour Doppler demonstrating significant tricuspid regurgitation. **(e, f)** A full volume dataset in uncropped format **(e)** and then cropped to reveal a 4-chamber view of the left ventricle **(f)**. *LA* left atrium; *LV* left ventricle; *RA* right atrium; *RV* right ventricle

However, for chamber visualization and quantification, a full volume is required. This mode allows a dataset of around 90 × 90°, although reducing the line density can widen this a little. Acquisition is performed over at least 4–7 cardiac cycles gated to the R-wave and with suspended respiration. Images can then be displayed in a number of ways in order to facilitate viewing and analysis (Fig. 2.12).

3D colour Doppler allows a small sector (around 50 by 50°) and takes at least seven cardiac cycles to complete an acquisition. It combines gray scale imaging with colour Doppler in 3D and is ideal for assessing valvular regurgitation.

One of the main limitations of the full volume and colour Doppler modes is the potential for thin "lines" to appear between the subvolumes after reconstruction. These lines, known as stitching artifacts, can be caused by an irregular R-R interval or any movement of the heart relative to the transducer during image acquisition. Stitching artifacts not only impair image quality, but also hinder analysis and make it challenging to image those with an arrhythmia. This is a problem that has been overcome by the latest generation of transducers, which have recently been released. Acquisition times have now been reduced to such an extent that they are capable of high frame rate and full volume 90 by 90° acquisitions, including 3D colour Doppler, all in one cardiac cycle (Fig. 2.13, Video 2.13). This abolishes the potential for stitching artifacts, making it easier to accurately image those with arrhythmias.

In 2007, the first fully sampled matrix array transoesophageal transducer (X72t, Philips Medical Systems, Andover, MA) with similar modes to those described above was introduced. This development was possible due to remarkable advancements in electronics and miniaturization of beam-forming technology. Not only is the transducer only marginally larger than a standard 2D probe, it is also capable of high-resolution 2D imaging and standard Doppler capabilities, unlike its transthoracic counterparts.

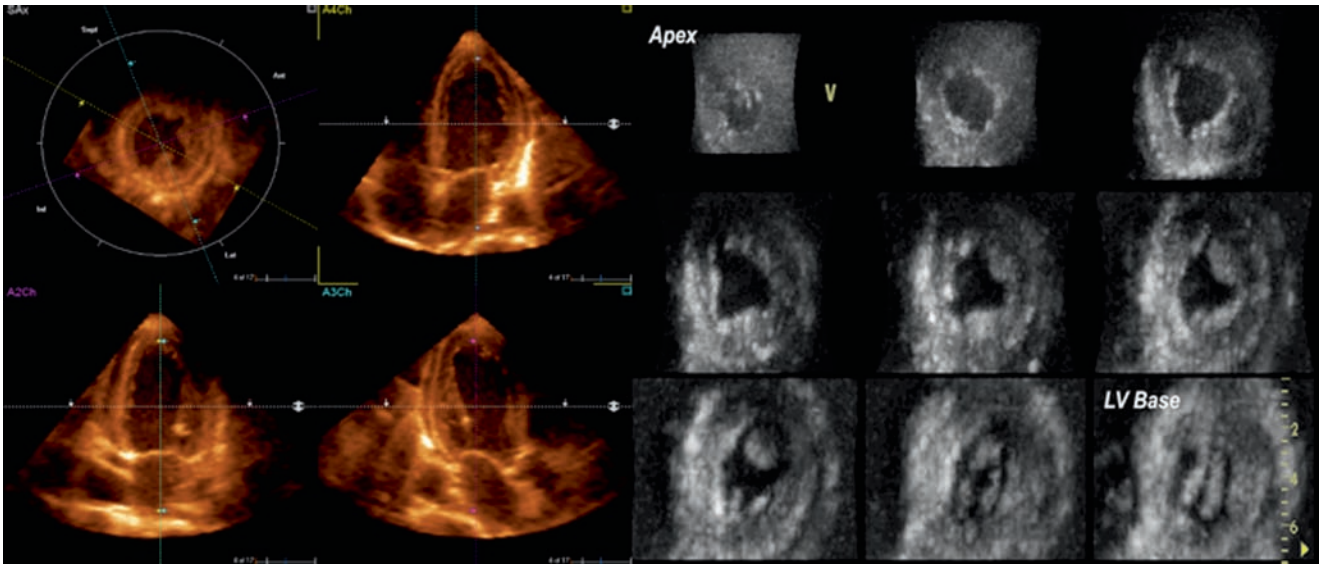

Fig. 2.12 In addition to the crop box display for full volumes (11 E + F), datasets can be presented as 2D apical planes (*left*) or a series of short-axis slices (*right*), in order to facilitate viewing and analysis

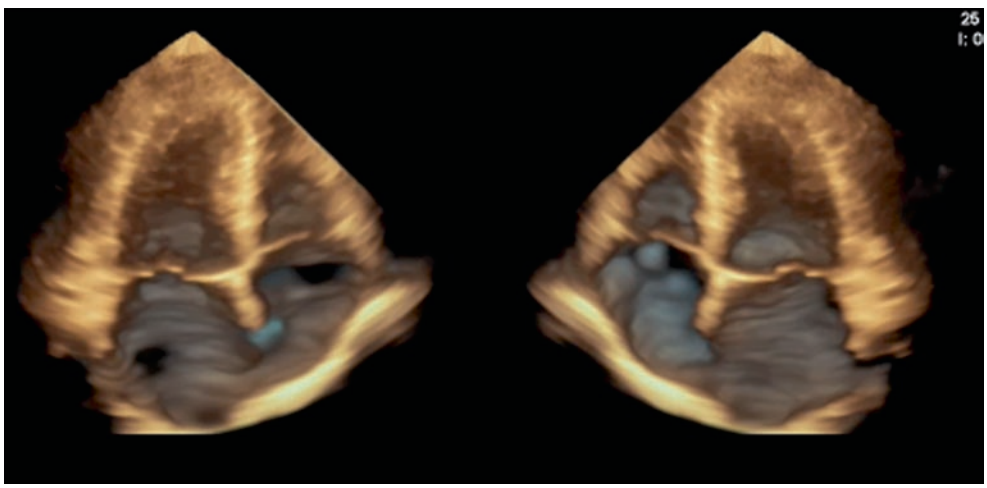

Fig. 2.13 An example of a single beat full volume acquisition from one of the new generation 3D transducers

Clinical Applications of Three-Dimensional Echocardiography

The main areas of clinical research in 3DE have unsurprisingly concentrated on chamber quantification, specifically that of the left ventricle, and also more recently on the RV, left atrium (LA), and valvular assessment. Direct volumetric acquisition allows for correction of the two most important sources of error from 2D and M-mode measurements: image foreshortening and the geometric assumptions that are needed for volume calculations.

Left Ventricle

One of the most important and widely researched current clinical applications of 3DE is LV quantification. The main forms of analysis that can be performed are LV mass, global function (volumes and ejection fraction), and regional function, for which a number of offline software packages are available. In addition, most vendors have some form of on-cart quantification package available.

3D LV mass analysis can be done from a full volume by using an anatomically corrected biplane technique and

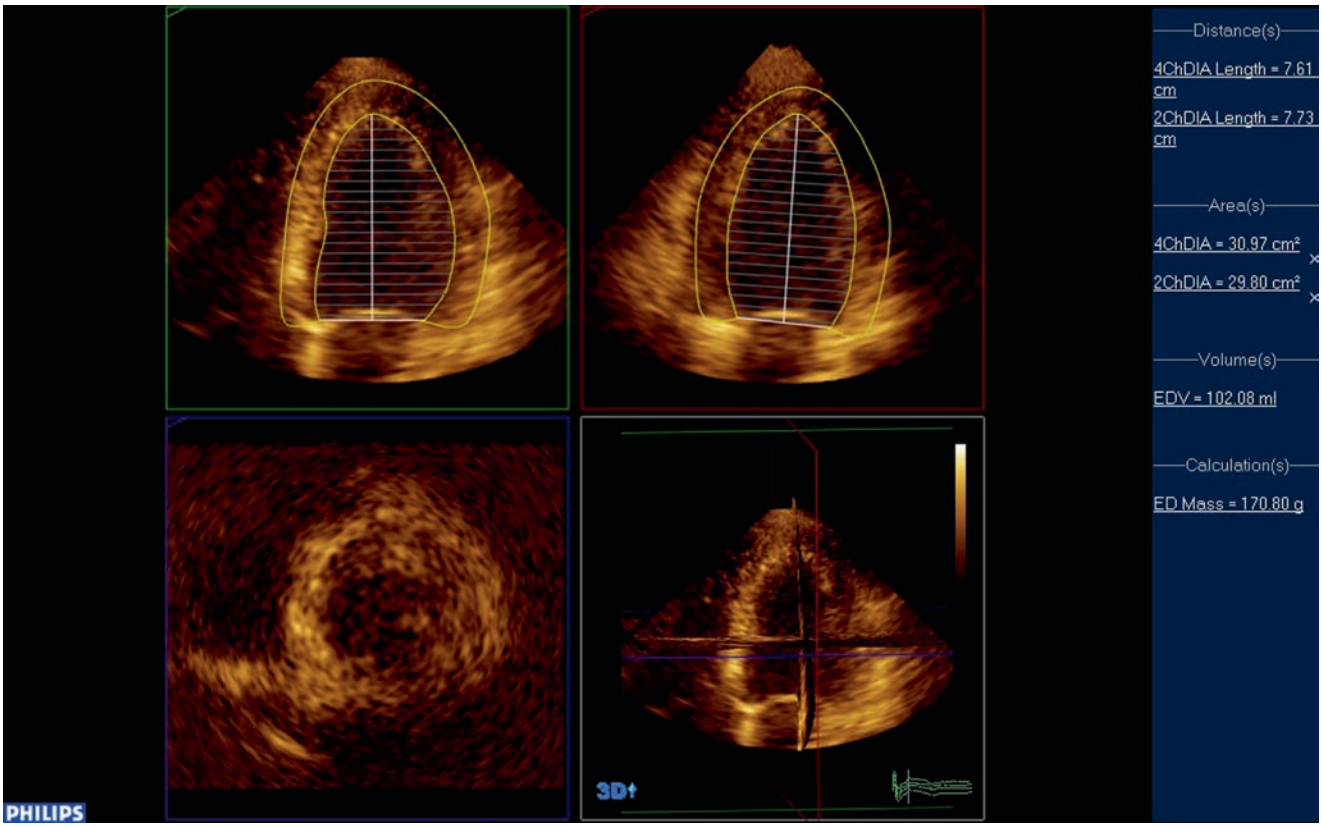

Fig. 2.14 A 3D-derived LV mass calculation

semi-automated border detection (Fig. 2.14). Not only is this technique relatively quick and easy, but has also been proven to be more accurate than 2D or M-mode calculations when compared to cardiac magnetic resonance imaging (CMR),[20,21] which is the current gold standard for mass and volumes.

In order to obtain global LV function, semi-automated border tracking software can be used to create a mathematical cast of the LV throughout the cardiac cycle from which volumes and ejection fraction are extracted, completely dispelling the need for geometric assumptions.

In this context, multiple research publications have proven the superiority of this technique over 2D and M-mode measurements when compared to CMR. Correlation has persistently been very good with the gold standard technique, albeit with a tendency for echocardiography to slightly underestimate volumes, probably because of the difference in endocardial border visualization.[22] Furthermore, 3DE has better inter-observer, intra-observer, and test–retest variability[23] than 2D and has elegantly been shown to have significant clinical impact when assessing patients for interventions.[24]

The mathematical cast described above can also be used to provide regional information. It can be divided into the American Society of Echocardiography 16- or 17-segment models, and for each segment, a regional ejection fraction can be obtained as well as a time to minimum volume (Fig. 2.15, Video 2.15). From this data, a systolic dyssynchrony index can be calculated,[25] which is the standard deviation of the time to minimum volume of all the segments corrected for the R-R interval. This technique gives a measure of the intra-ventricular mechanical dyssynchrony, and there is a growing body of evidence supporting its use in the selection of patients for cardiac resynchronization therapy (CRT).

Further subdivision of this model into more than 800 segments can be performed with the time to peak contraction of each one colour coded. This information can be merged to give a dynamic parametric image known as a contraction front map. This technique offers an intuitive display of mechanical contraction with an ability to rapidly demonstrate significant areas of myocardial delay (Fig. 2.16, Video 2.16).

Another important aspect of LV assessment is stress imaging, and this can now also be performed with 3DE, both with and without contrast enhancement. Analysis can be performed by manually cropping datasets to assess wall motion or by using parametric imaging such as contraction front mapping. While a single acquisition at each stage of stress seems appealing, it is currently not without its limitations. Frame rates are significantly reduced at peak heart rates, and the lack of high-resolution 2D imaging on 3D transducers

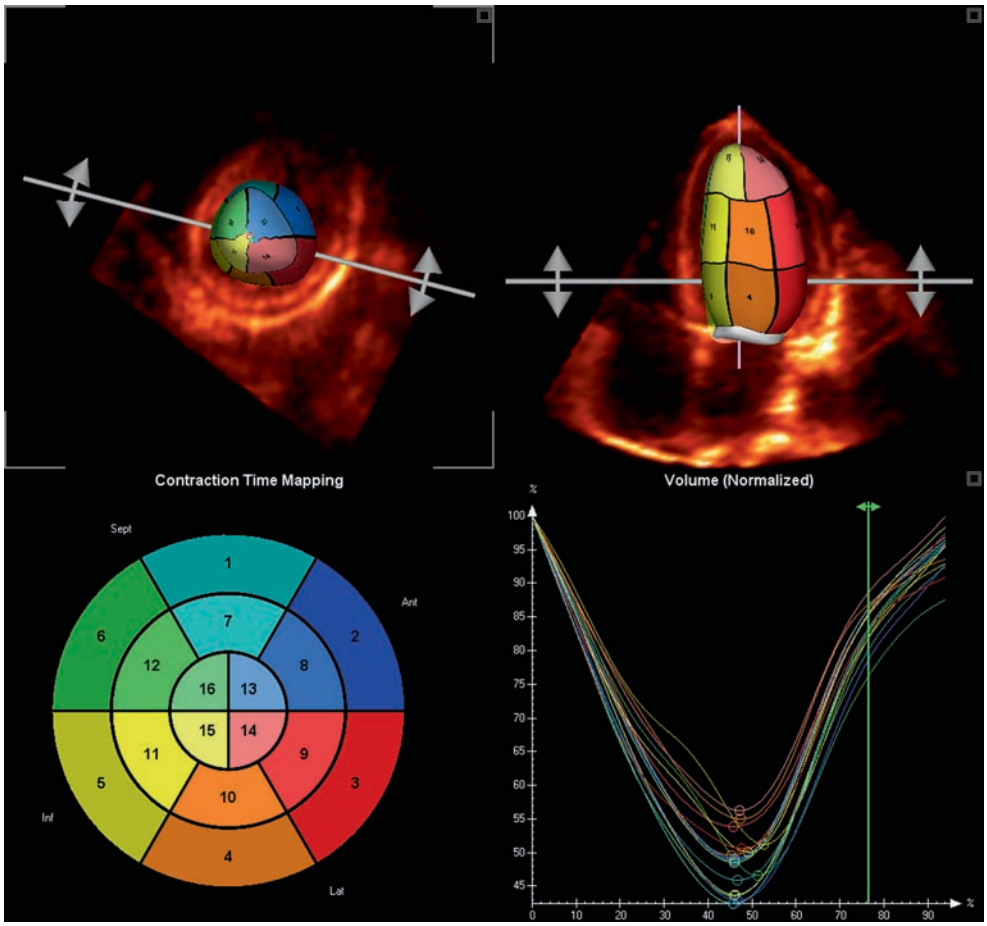

Fig. 2.15 Semi-automated border tracking software is used to create a mathematical cast of the left ventricle. This can then be segmented for regional analysis. Regional time volume curves are seen in the *bottom right*

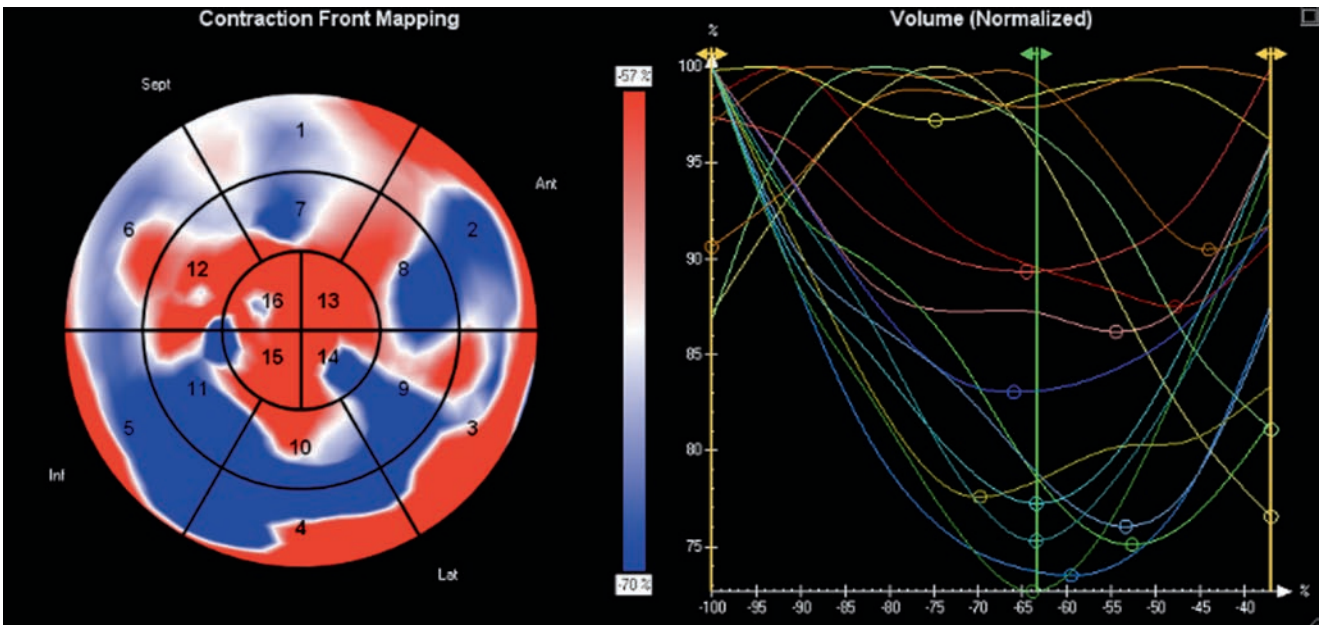

Fig. 2.16 Contraction front mapping in a patient with ischaemic LV dysfunction. The activation pattern is very heterogeneous with significant areas of delay (*red areas demonstrate delay*) and very abnormal time volume curves (*right side*)

means they have to be interchanged during an exam for any required 2D images. Furthermore, there is a lack of dedicated software packages allowing adequate visualization and anatomic orientation for analysis.

However, the latest generation of transducers, mentioned above, promises to help overcome some of these difficulties. Improved frame rates with single beat acquisitions are exciting, and new dedicated 3D stress viewers are now becoming available (Fig. 2.17). These developments may help 3D stress echo become more clinically attractive. Finally, 3D myocardial perfusion imaging is also clinically possible, although still very experimental.[15]

Right Ventricle

The complicated geometrical structure of the RV, both in health and disease, has significantly limited 2D quantification of size and function. As such, a volumetric ultrasound acquisition has long been desired and is now available. Newer offline 3D software packages allow a mathematical cast to be created with a global time-volume curve (Fig. 2.18, Video 2.18) similar to what can be done for the LV. Again, global volumes can be obtained, and ejection fraction calculated. This technique has been validated in vitro[26] and is accurate when compared to MRI.[27] Much work is ongoing to find its specific clinical benefits, but it is likely to involve surveillance of patients with pulmonary hypertension and those with congenital heart disease.

Left Atrium

Left atrial volumes can now also be calculated in a similar fashion (Fig. 2.19). It has been found that the difference between calculated volume from 2D and direct measurement using 3DE is minimal,[28] suggesting that this technique may be surplus to requirements. However, the 3D technique has better test–retest variability, indicating that it may be better for long-term follow up. It has also been suggested that it

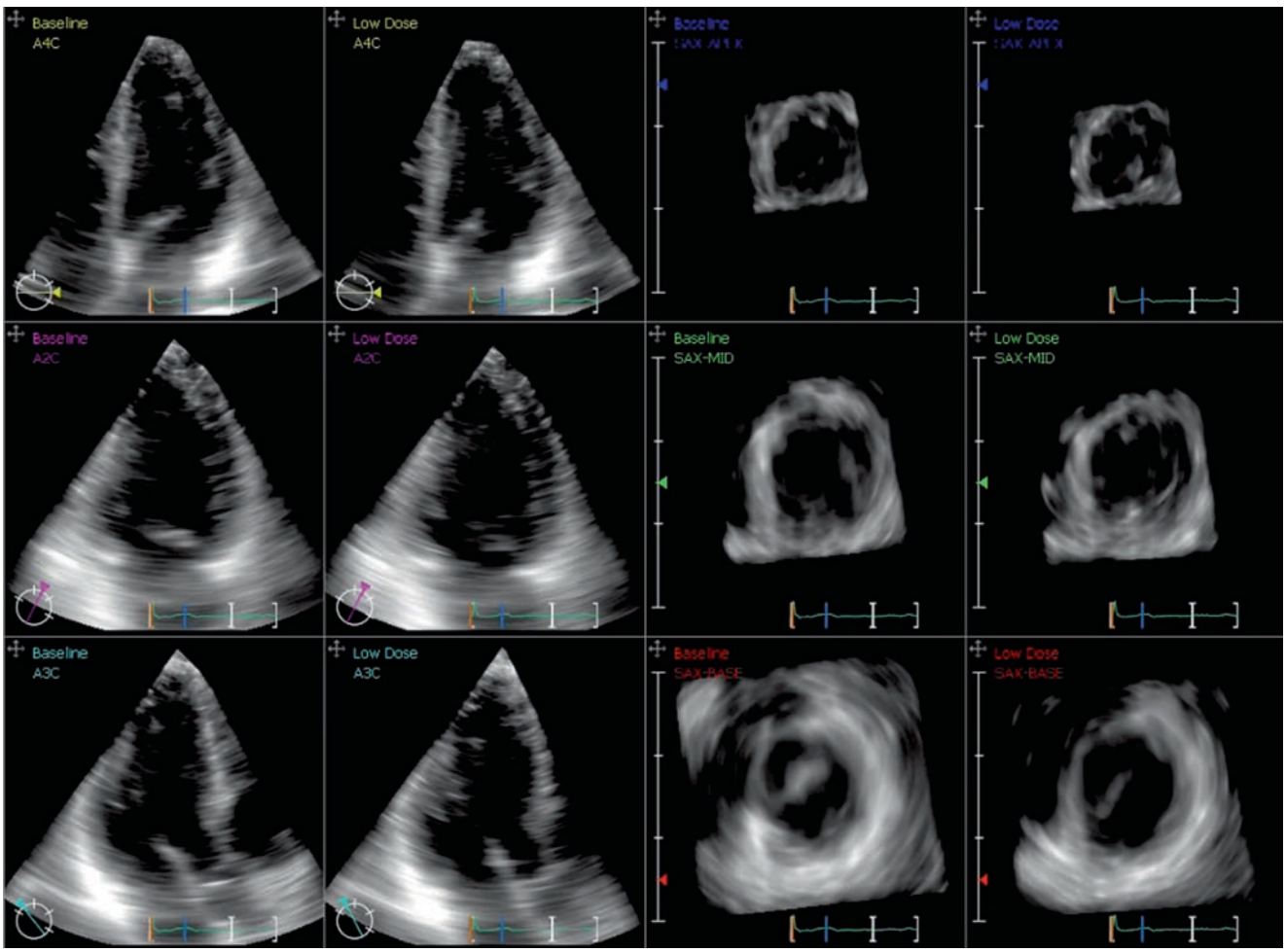

Fig. 2.17 An example of a dedicated 3D stress viewer. Baseline and low dose apical views are seen on the left, while short-axis slices are presented on the *right*. The video clip demonstrates manipulation of a dataset to ensure it is being viewed along its true long axis

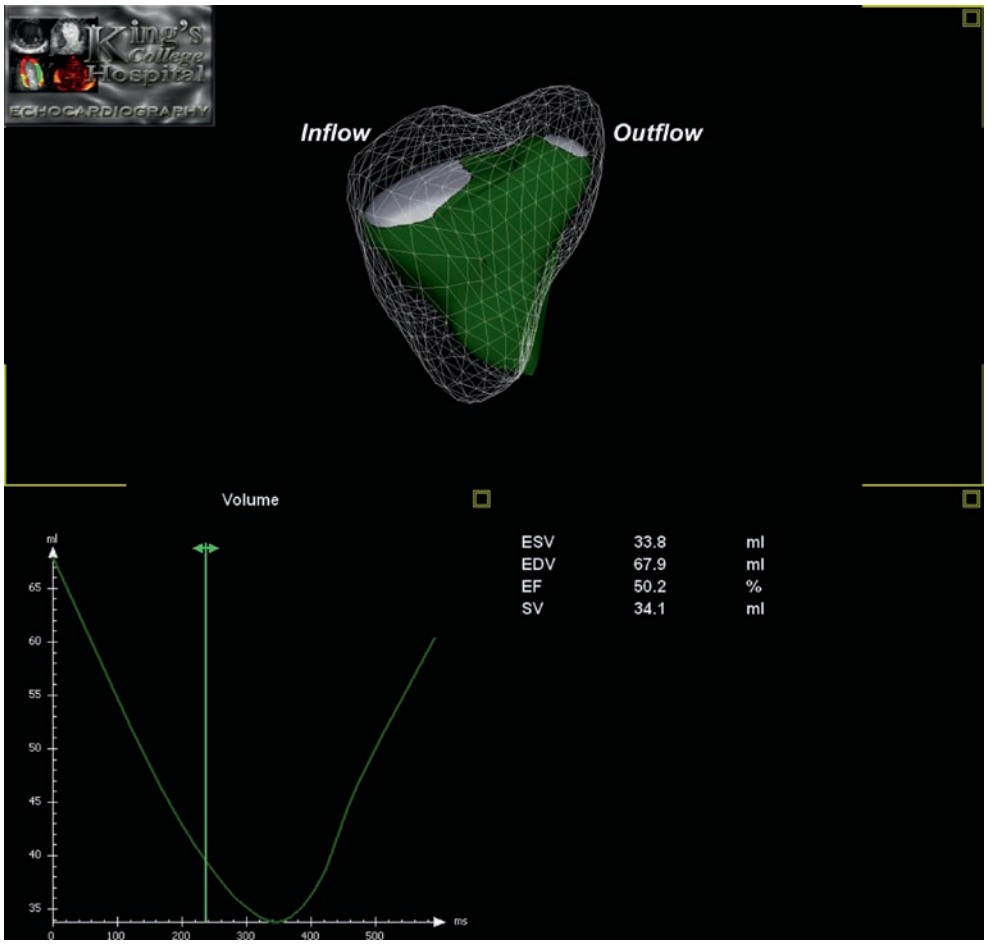

Fig. 2.18 A 3D right ventricular analysis. The mesh model represents the end-diastolic volume. Global time volume curve is seen on the *bottom left* and numerical volumes on the *bottom right*

may be more accurate in more dilated atria when geometrical assumptions become a larger source of error.

Valves

Most work into valvular assessment has been on the mitral valve. Its position in the chest lends itself well to 3DE. Gray scale images offer true anatomical data, and multi-plane reconstruction can be used to perform a segmental analysis of each of the scallops, or to line up an anatomically correct orifice area, while colour Doppler can give concomitant functional data. Work has suggested that good 3D transthoracic echo can abolish the need for 2D TOE in conditions such as mitral valve prolapse.[29]

Mitral valve quantification is also now available from a number of vendors, offering a multitude of measurements, such as annular areas, leaflet tenting volumes, and mitral aortic offset angle. Although very interesting, the clinical role of these measurements is yet to be established.

3D transthoracic assessment of aortic and tricuspid valves is considerably more challenging, primarily because of their locations and the thinness of the leaflets. Clinical roles have been researched, but they are much less well delineated.

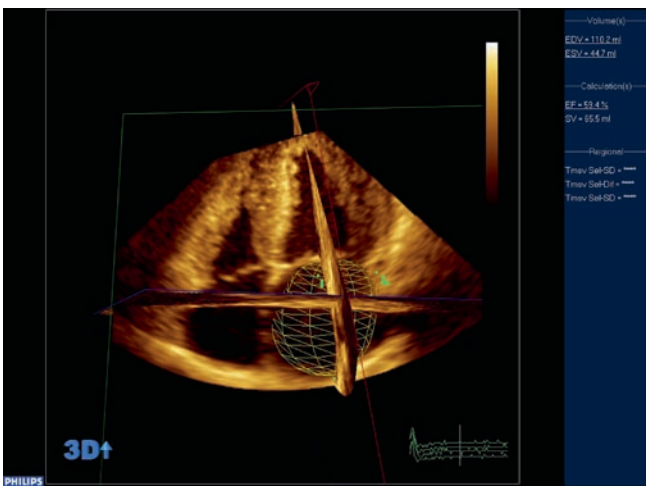

Fig. 2.19 A left atrial 3D analysis. Volumes and ejection fraction are given on the *right hand side*

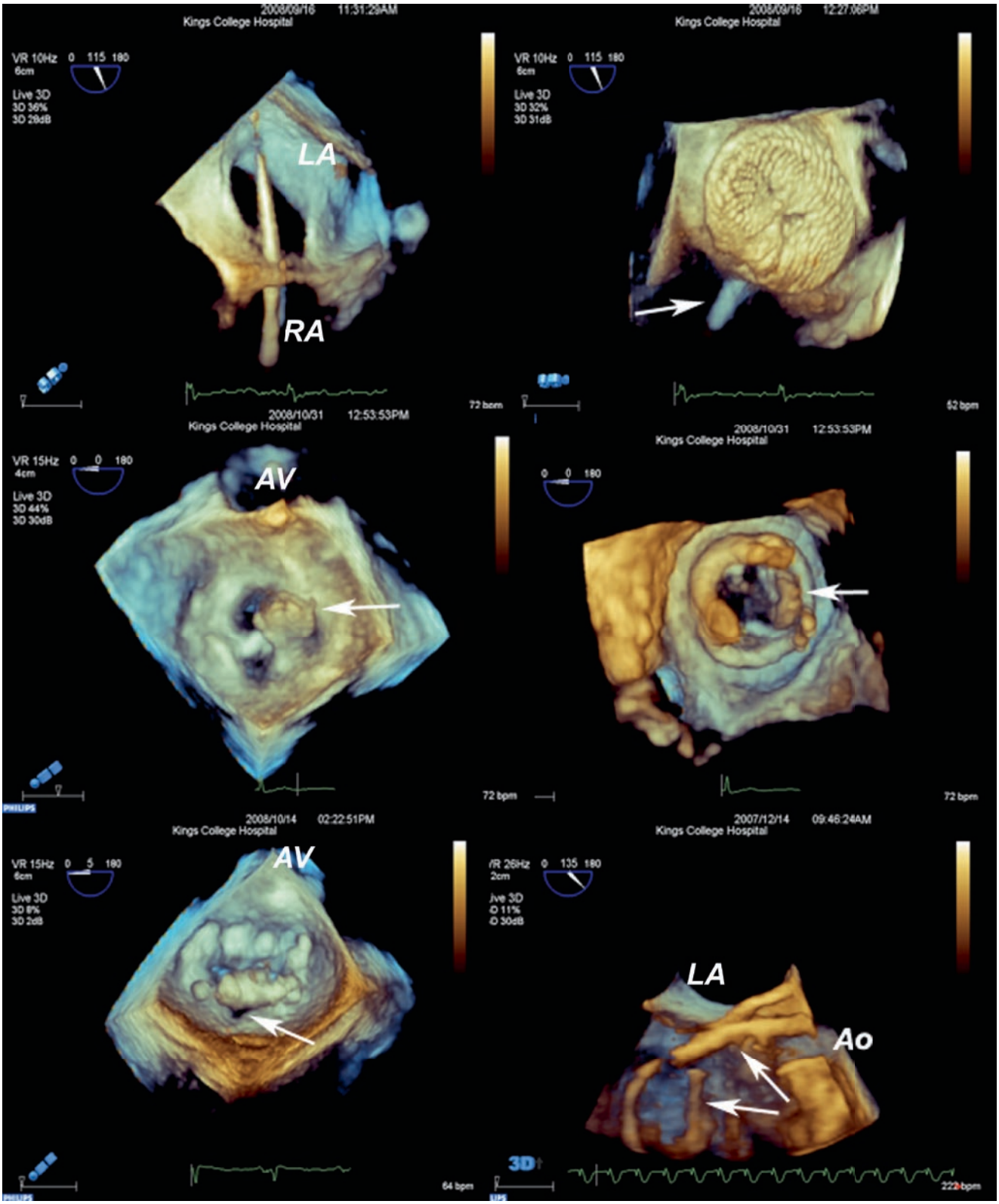

Fig. 2.20 A selection of 3D trans-oesophageal echo pictures. *Top left:* Clip during a percutaneous atrial septal defect closure. A catheter with a guide wire poking from the end is passed through the defect from right atrium (RA) to left atrium (LA). *Top right:* A view of the left atrial disc of an Amplatzer ASD occluder just before detachment. The delivery catheter is seen in the RA (*arrow*). *Middle row:* A patient with endocarditis of a mitral bioprosthesis. The large mobile vegetation (*arrows*) is seen from the left atrial side in systole (left and video clip) and the left ventricular side in diastole (*right*) AV- aortic valve. *Bottom left (+video clip):* A patient with significant mitral regurgitation post-mitral valve repair. The ring is clearly visualized from the left atrial side with a local area of dehiscence seen posteriorly (*arrow*). *Bottom right (+video clip):* 3D TOE guidance of a transfemoral transcatheter aortic valve implantation. A catheter is seen crossing the aortic valve with a wire curled up in the left ventricle. Note the ECG tracing. Rapid ventricular pacing is required during balloon inflation to avoid dislodgement of the prosthesis

Trans-oesophageal Imaging

The currently available matrix array trans-oesophageal probe offers unprecedented images of cardiac morphology, particularly that of the mitral valve. Although its clinical role is not yet fully established, it is likely to become the gold standard for imaging mitral valve pathology and invaluable in assessing prosthetic valve anatomy, structural heart disease, and guidance and planning of contemporary interventional procedures (Fig. 2.20).

Future Directions

The future will no doubt offer complete integration of 3DE with standard techniques. Single beat transducers are now available, but integration of high quality traditional 2D ultrasound techniques will mean only a single transducer will be necessary for a complete study.

Continued improvements in frame rates and resolution will improve image quality, and intelligent software promises fully automated analyses, potentially further reducing subjectivity.

The advent of dedicated stress viewing packages will facilitate the application of clinical 3D stress echo, and 3D perfusion offers the hope of volumetric quantification of perfusion defects. 3D speckle tracking has now also been developed and promises to give us true 3D myocardial deformation.

Direct volumetric acquisitions also allow the possibility of fusion imaging, for example, with CMR and computed tomography, which may offer superior assessment of structure and function.

It is important to remember that to encourage full integration of 3DE we must pay heed to the practical aspects. We are in need of systems for careful raw data storage that allow image manipulation, and guidelines/imaging protocols are helpful for those attempting to begin to incorporate 3D.[30]

Conclusion

3DE is a remarkable development in contemporary echocardiography that has required combined developments in ultrasound, electronics, and computer technology. The combination of real-time volumetric scanning in the context of cheap and safe ultrasound imaging is a powerful one. Investigation has not only proved the use of 3DE in a research base, but is also now proving its clinical benefits. Its accuracy for quantification of LV volumes and ejection fraction is beyond doubt, and evidence for its ability to assess more advanced regional function is strong and growing. There is also promising work in the quantification of other chambers, and it can be invaluable in valvular assessment.

Myocardial Deformation Imaging: From Tissue Doppler to 2D Speckle Tracking

Denisa Muraru and Luigi P. Badano

Non-invasive quantification of global and segmental left ventricular (LV) function plays a central role in clinical cardiology, but, in certain cases, it may be challenging on its own. Visual evaluation of wall motion is known to be highly subjective, at times insensitive, and requires significant training and mostly assesses only radial deformation component of the myocardium. However, the heart has a very complex motion pattern, and regional myocardial deformation occurs in three major directions: longitudinally, circumferentially, and radially (Fig. 2.21).

The novel technologies of myocardial deformation imaging both from tissue velocity imaging (TVI) and from 2D speckle tracking have been reported to be promising in quantifying regional and global cardiac function and to be able to provide new, detailed information about cardiac mechanics that are not easily obtainable using other imaging modalities.[31–33]

TVI, also known as *tissue Doppler imaging,* is currently accepted as a sensitive and accurate echocardiographic tool for quantitative assessment of cardiac function.[34] TVI provides information on the velocity of the myocardial motion in the direction parallel to the ultrasound beam. In contrast with blood-pool data, myocardium is characterized by high-intensity, low-velocity signals that can be distinguished from the blood by the implementation of appropriate thresholding and clutter filters.[35] The velocities can be

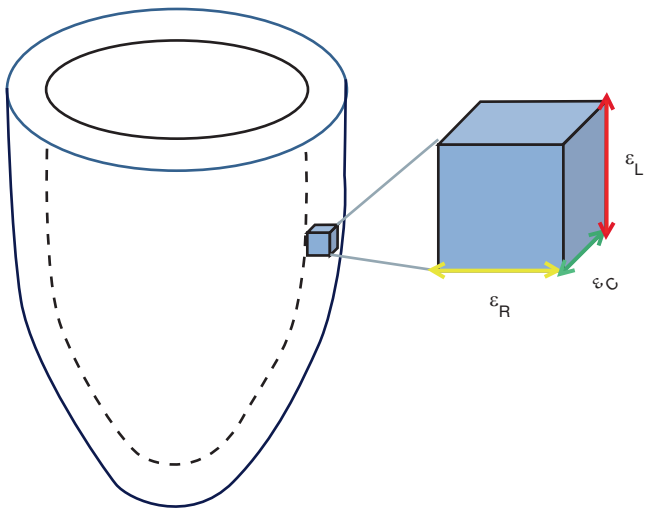

Fig. 2.21 Schematic representation of the main directions of myocardial deformation: longitudinal (ε_L, along the direction of chamber's long axis), radial (ε_R, towards the centre of the cavity), and circumferential (ε_C, along the chamber circumference)

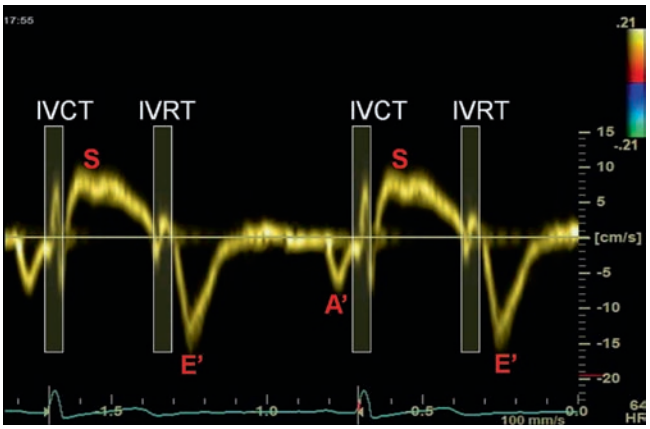

Fig. 2.22 Typical pulsed Doppler tissue velocity waveform from basal septum in a young normal subject. *IVCT* isovolumic contraction time; *IVRT* isovolumic relaxation time; *S* peak systolic myocardial velocity; *E'* early diastolic myocardial velocity; *A'* regional myocardial motion due to atrial contraction

measured and displayed online as a spectral profile (PW-TVI, Fig. 2.22) or as a colour-coded image (colour TVI, Fig. 2.23) in which each pixel represents the velocity relative to the transducer.

Of note, pulsed Doppler records peak myocardial velocities constantly higher (up to 20%) than colour Doppler imaging that yields mean velocities for the same segment (Fig. 2.24). This difference in amplitude is due to the fact that spectral Doppler is computed by Fast Fourier Transformation (FFT), while colour Doppler imaging uses the autocorrelation method.[36] A major advantage of colour Doppler TVI is that it allows a simultaneous, time-saving assessment of motion and deformation of all segments within that view (Figs. 2.25 and 2.6), avoiding the potential bias of comparing event timings on cardiac cycles with different R-R duration, as it may occur using PW-TVI wall-by-wall sampling. In contrast, the resolution of early diastolic or isovolumic events requires

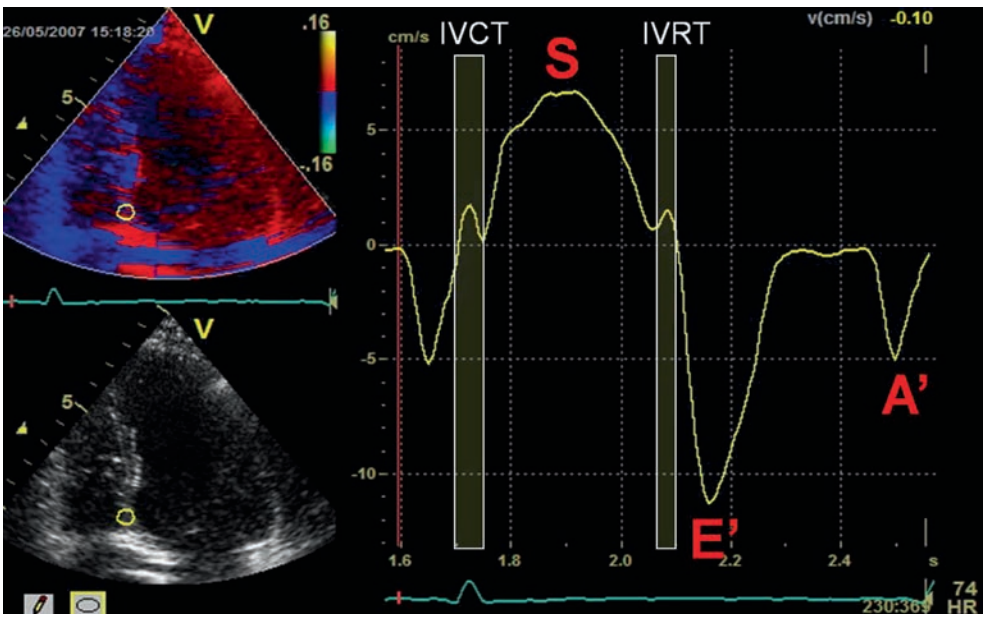

Fig. 2.23 Example of a colour tissue Doppler velocity profile from the basal part of the interventricular septum of a young normal subject. *IVCT* isovolumic contraction time; *IVRT* isovolumic relaxation time; *S* peak systolic myocardial velocity; *E'* early diastolic myocardial velocity; *A'* regional myocardial motion due to atrial contraction

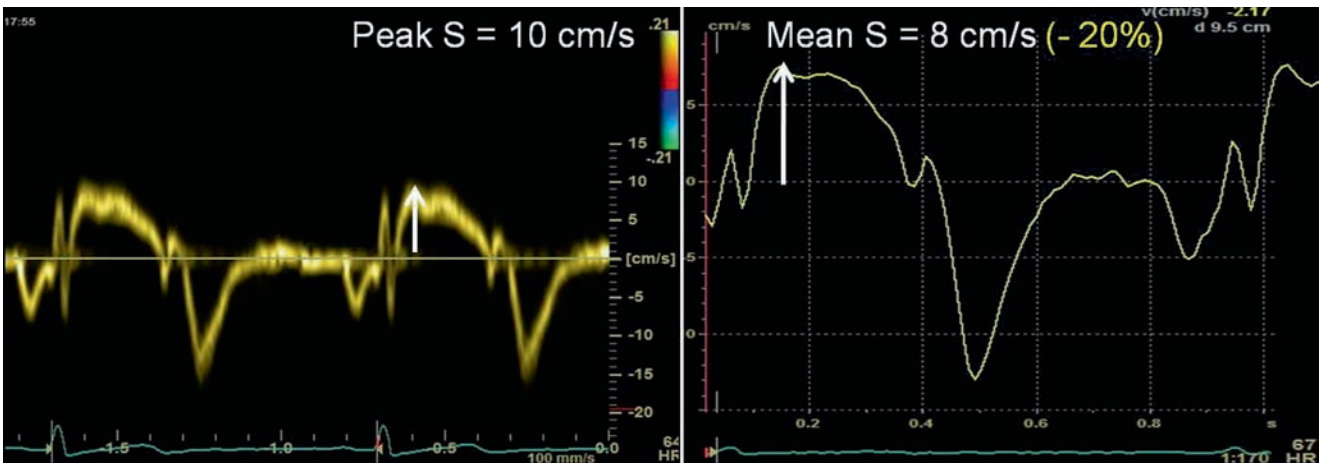

Fig. 2.24 Basal septal Doppler tracings from a normal subject recorded using pulsed-wave TVI (*left panel*) and colour Doppler TVI (*right panel*). Pulsed Doppler peak systolic myocardial velocities (S) are about 20% higher than mean velocities recorded by colour Doppler

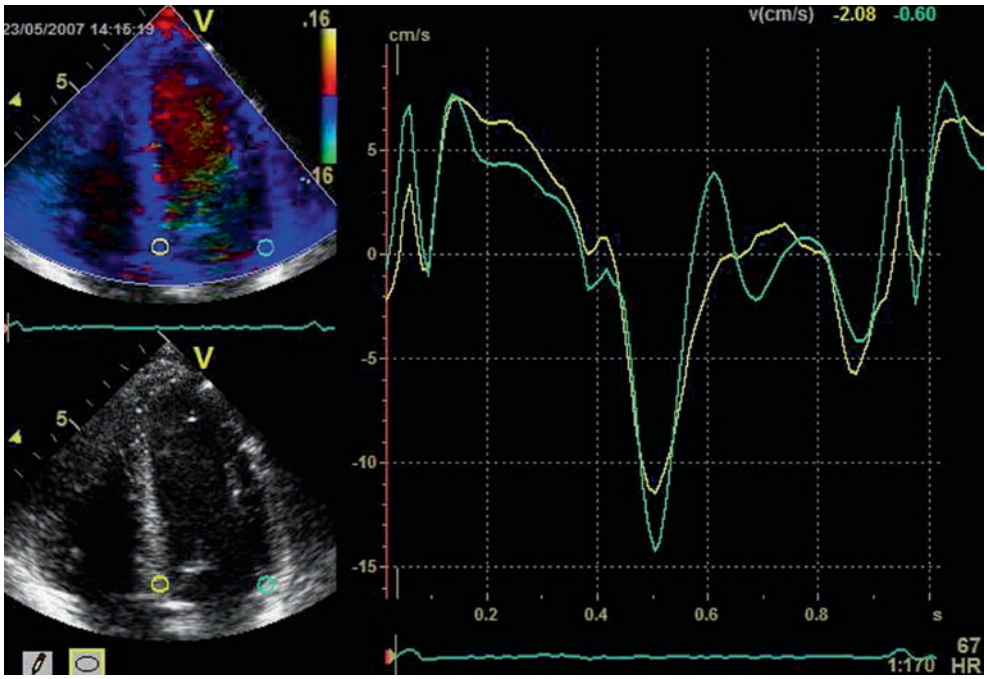

Fig. 2.25 Simultaneous display of regional velocities using colour Doppler TVI in basal septal and lateral LV wall on the same cardiac cycle. The synchronicity of systolic and diastolic peak waves in this healthy volunteer is evident

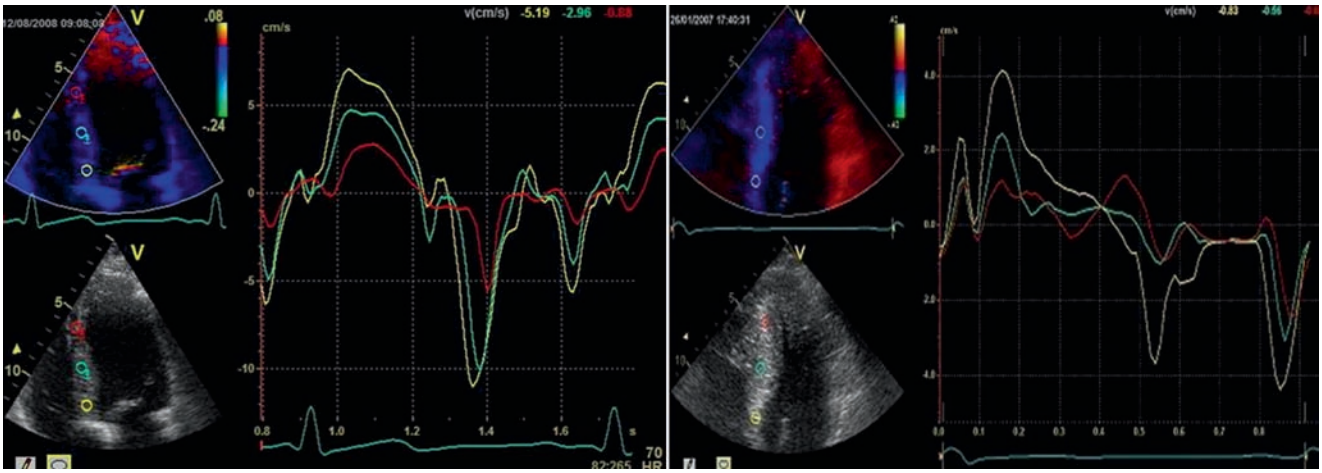

Fig. 2.26 Colour TVI velocity recordings at different levels of interventricular septum in a normal subject (*left panel*). The basal velocities are significantly higher than more apical ones. In a patient with hypertrophic cardiomyopathy (*right panel*), the velocities are significantly lower, but the basal-apical gradient still persists. This regional velocity gradient is used to derive strain rate

high frame rates (more than 200 and 400 FPS, respectively), in which case the superior temporal resolution of PW-TVI may be of use (Fig. 2.22). Assessment of regional myocardial function by TVI has two major drawbacks: angle dependency and influence of overall heart motion (rotation and contraction of adjacent myocardial segments) on regional velocity estimates. In order to overcome some of these limitations, ultrasonic deformation imaging has been developed by estimating spatial gradients in myocardial velocities.

Tissue-tracking (TT) is a new echo modality based on TVI that allows rapid visual assessment of the systolic basal-apical displacement in apical views for each LV segment by a graded colour display (Figs. 2.27 and 2.28). TT-derived mitral annular displacement correlates closely with mitral annular displacement determined by M-mode and with left ventricular ejection fraction measured by 2D echocardiography.[37] Therefore, the unique feature of TT is the rapid parametric display of LV systolic function from a single image, even in the setting of poor 2D image quality.

Tissue synchronization imaging (TSI) is a parametric imaging tool derived from tissue Doppler images that automatically calculates and colour codes the time from the

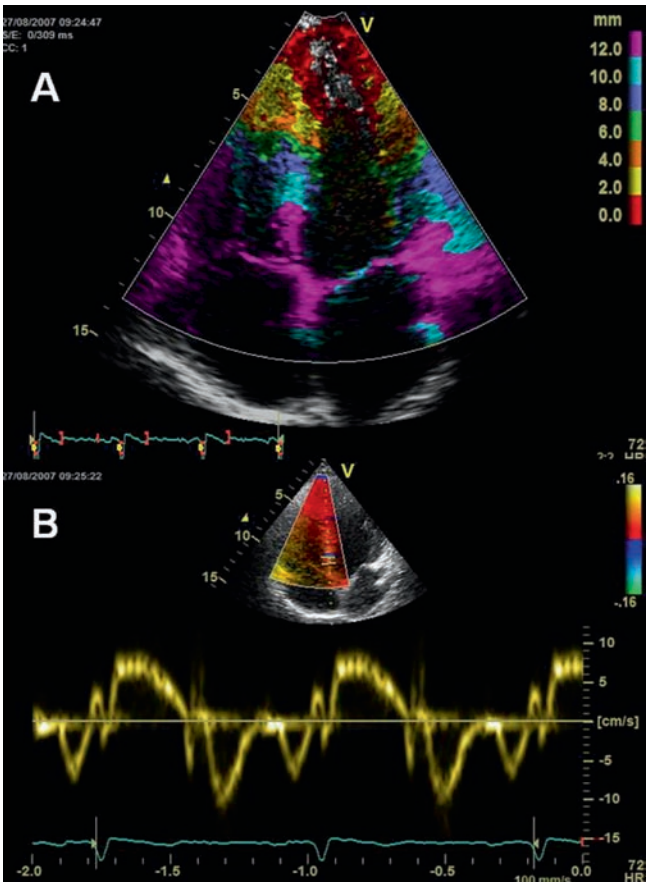

Fig. 2.27 **(a)** Example of a tissue tracking image in a normal subject, showing the colour-coded map of myocardial end-systolic displacement. Note the corresponding colour scale for displacement length, ranging from *purple* (12 mm) to *red* (no displacement) on the *upper left corner*. **(b)** The corresponding PW tissue velocity recording in basal septum, showing normal values

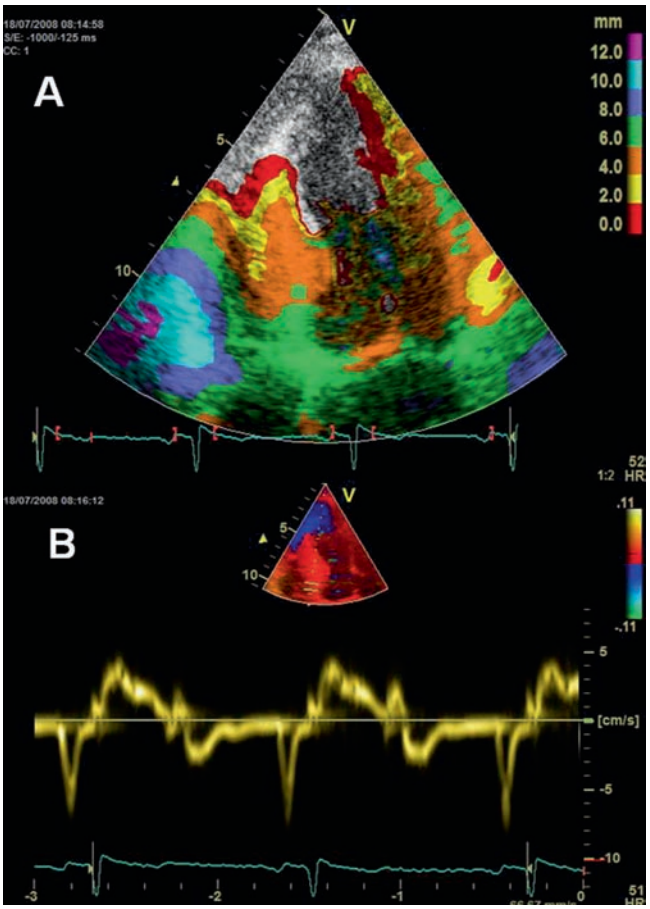

Fig. 2.28 **(a)** Tissue tracking image in a patient with critical aortic stenosis. Severely impaired longitudinal function marked as a shift of colour spectrum to lower values in contrast to the normal subject showed in Fig. 2.7 and to right ventricular free wall of the same patient. **(b)** The corresponding PW tissue velocity recording in basal septum, showing significantly reduced values of both S (systolic) and E′ (early diastolic) waves

beginning of the QRS complex to peak systolic velocity (Fig. 2.29). This method has been proposed to detect intraventricular dyssynchrony and predict the acute response to CRT[38–40] (Fig. 2.30).

Myocardial deformation (strain and strain rate) can be calculated non-invasively for both left and right ventricular or atrial myocardium, providing meaningful information on regional function in a variety of clinical settings. From a physical point of view, strain is a dimensionless parameter defined as the relative change in length of a material related to its original length (Fig. 2.31), whereas strain rate describes the temporal change in strain (rate of shortening or lengthening) and it is expressed as a percent (Fig. 2.32). While strain is a measurement of deformation relative to a reference state, strain rate is an instantaneous measurement. Strain rate seems to be a correlate of rate of change in LV pressure (dP/dt), a parameter that reflects contractility, whereas strain is an analogue of regional ejection fraction.[41] As ejection fraction, strain is a load-dependent parameter. In

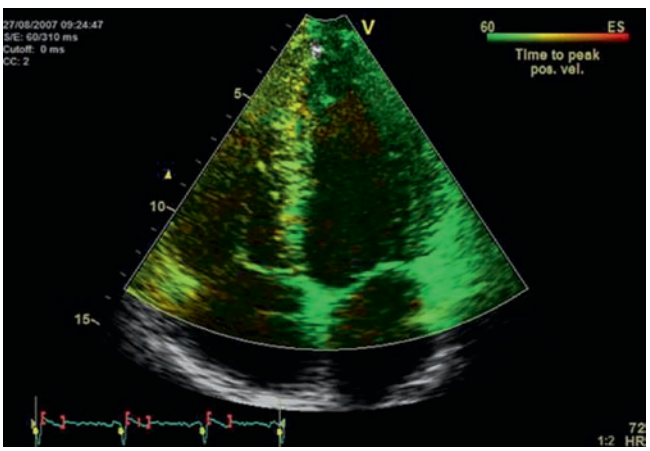

Fig. 2.29 Tissue synchronization imaging (TSI) colour map superimposed on apical 4-chamber view in a normal subject. In the *upper left corner*, the time-to-peak colour scale is showed. The time delay is coded into different colours according to the severity of the delay in the sequence *green*, *yellow*, *orange*, and *red*. The homogeneous *green* and *yellowish* colours in this patient show a synchronous mechanical activation in both ventricles

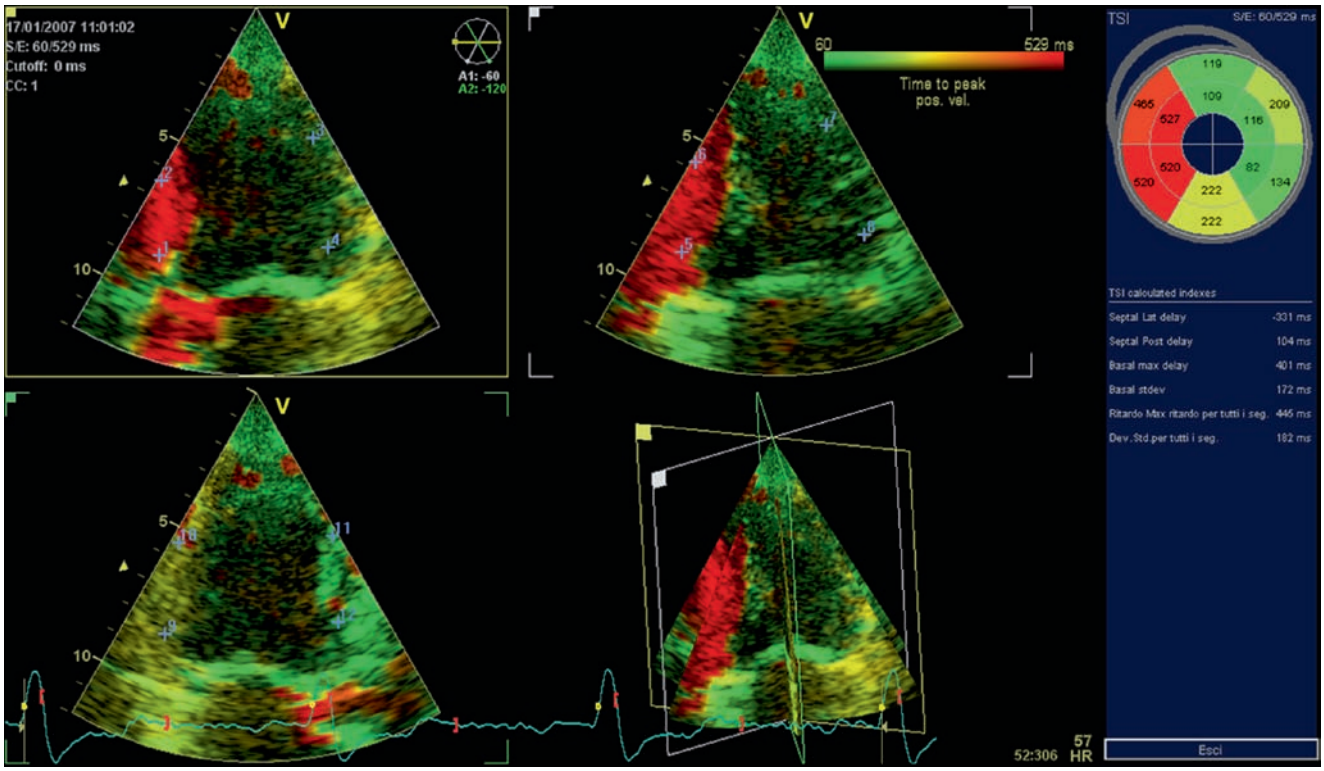

Fig. 2.30 TSI in a patient with dilated cardiomyopathy and significant intra-ventricular dyssynchrony. Delayed time-to-peak regional velocity is colour coded *red* in the Inferior and inferior septum segments. The bull's eye map displays regional time delays, and several indices of dyssynchrony are automatically calculated

contrast, strain rate is thought to be less dependent on loading conditions of the LV.

Among the main advantages of TVI and strain imaging, there are the quantitative assessment of wall motion with no more need of accurate endocardial border detection, high temporal resolution (> 200 fps) that allows to detail the complex motion (with multiple troughs and peaks) of the heart (Fig. 2.22), and the possibility to measure velocity and acceleration as better descriptors of cardiac motion than classical wall thickening. For example, short-lived events (such as isovolumic events) can be detected only by high temporal resolution techniques such as TVI, or detection of post-systolic shortening or thickening (a highly specific marker of dyssynchrony and/or viability) is feasible only by the high temporal resolution and quantitative nature of TVI-based techniques.

On the other end, TVI assessment of myocardial deformation, although based on great body of evidence, has several drawbacks. The amplitude of the TVI-derived strain rate or strain curves may be influenced by the insonation angle, yet in clinical practice, the influence of this angle dependency on the timing of events or on the curve profiles is probably less important. Angle dependency may adversely affect the inter-observer and interstudy reproducibility of the measurements. Since only axial strain component can be quantified using TVI, not all strain components (radial, longitudinal, and circumferential) can be measured for all myocardial segments. Tissue velocity and strain imaging are also affected by noise components, such as random thermal noise and reverberations, which may degrade the quality of the velocity and strain rate measurements. Despite all limitations listed, this technique has been validated with sonomicrometry and with magnetic resonance imaging.[42,43]

Speckle-tracking echocardiography (STE) is a newer non-Doppler (based on gray-scale images) echocardiographic technique in which ultrasound speckles within the image are tracked and strain is measured from the displacement of speckles in relation to each other, thereby providing an angle-independent parameter of myocardial function (Fig. 2.33). The acoustic markers, or speckles, are the result of backscattered ultrasound from neighbouring structures within the myocardial wall, which generate a unique pattern (acoustic fingerprint or "kernel") that can be tracked frame by frame.[44] Using a sufficiently high frame rate, it can be assumed that particular speckle patterns are preserved between subsequent image frames.[45] The geometric shift of each speckle represents local tissue movement. Tracking the relative motion of the various speckles during

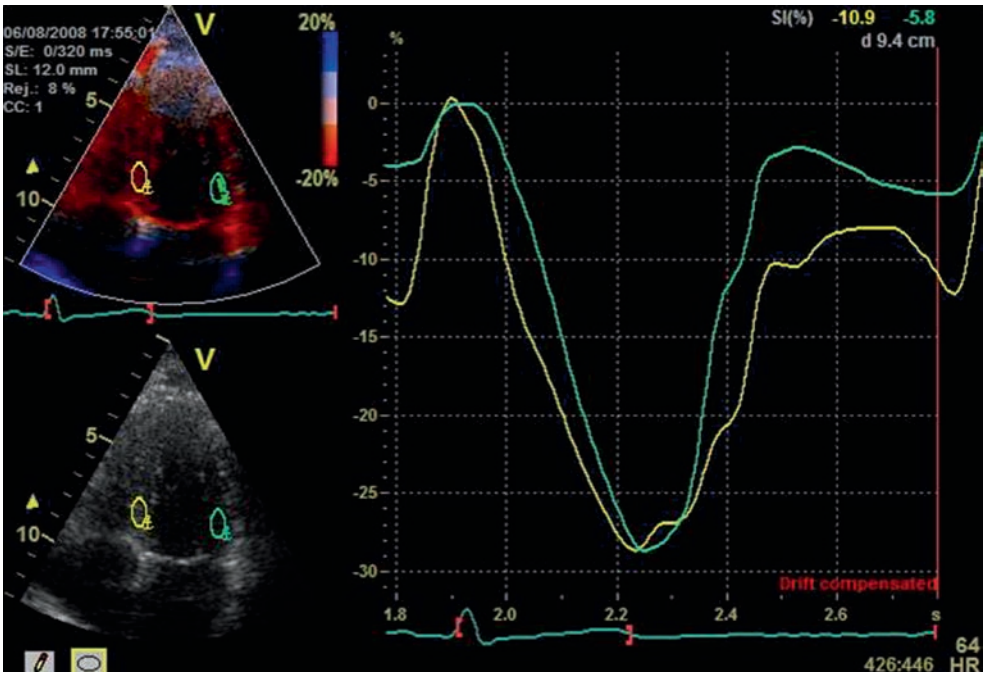

Fig. 2.31 TVI-derived longitudinal strain recorded in a normal subject. Strain colour-coded image (*upper left panel*) and the derived strain traces (*right panel*). The sample region for the traces (ROI) are shown in the basal septum and left ventricular lateral wall. In normal segments, longitudinal strain is negative during systole (segmental shortening) and reverses back to the 0 point during diastole

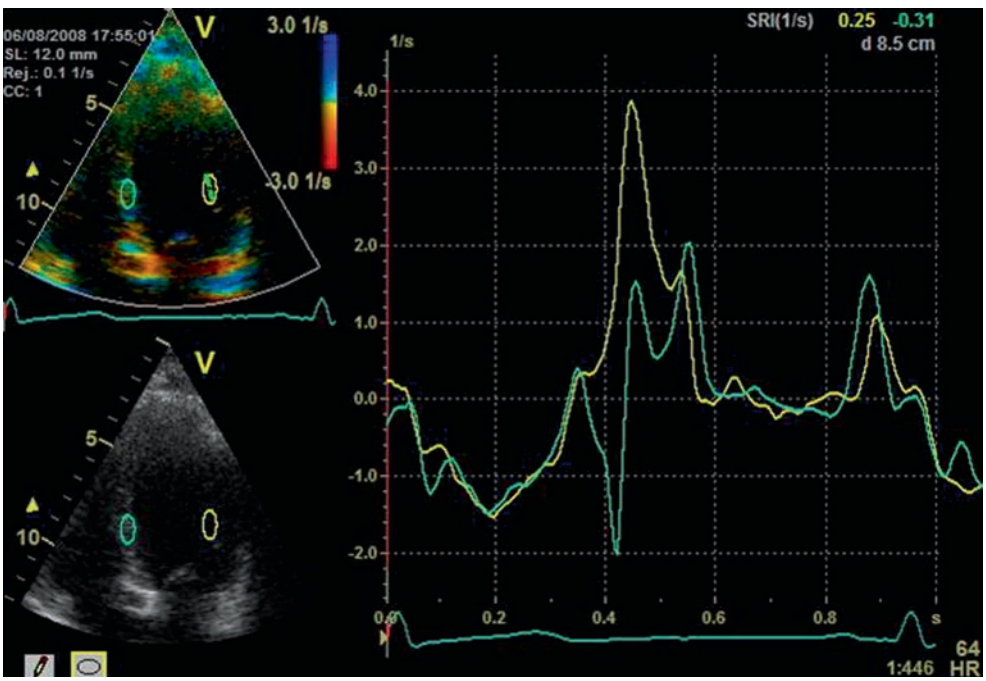

Fig. 2.32 TVI-derived longitudinal strain-rate in a normal subject. Strain rate colour-coded image (*upper left panel*) and the derived strain rate trace (*right panel*). The strain rate tracing mirrors the myocardial velocity profile, with a negative systolic wave and positive early and late diastolic waves

the cardiac cycle allows the generation of a 2D map of myocardial motion and deformation. From 2D strain, tissue velocity, displacement, and strain rate can be calculated (Fig. 2.34). In addition, the angle independent nature of STE allows the software to measure rotation and rotation rate at different left ventricular levels (Figs. 2.35 and 2.36; Videos 2.35A-D). The accuracy of STE has been validated against sonomicrometry and magnetic resonance tagging.[46]

The values of strain and strain rate obtained by TVI and STE are well correlated, yet the gray-scale approach of STE is more rapid and reproducible.[47–49]

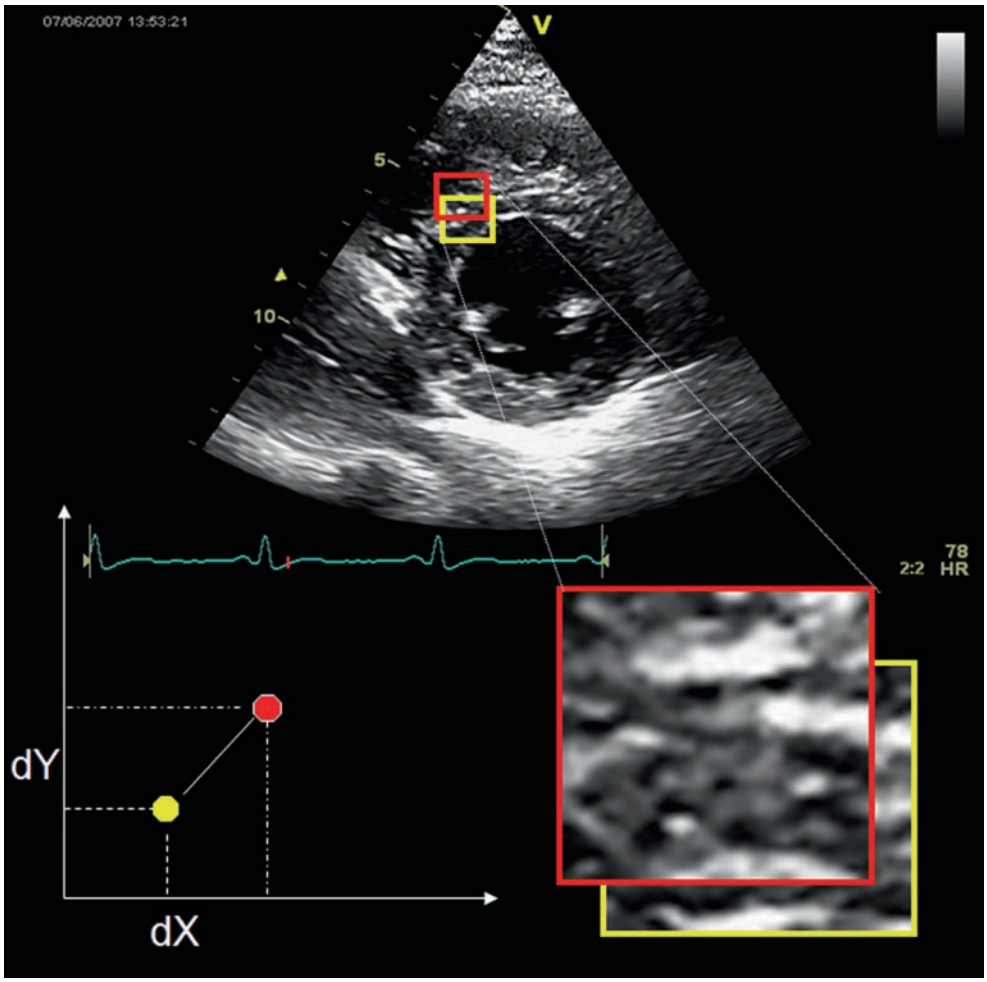

Fig. 2.33 Illustration of speckle-tracking principle. Stable random myocardial speckles from routine gray-scale 2D image create a unique acoustic "fingerprint" for each segment (kernel), allowing frame-by-frame tracking of individual kernels during cardiac cycle and measurement of their relative distance

The STE is also a practical tool for estimating LV torsion, which is defined as the difference in opposite rotation of the apical vs. the basal short-axis LV planes (Figs. 2.37 and 2.38). Torsion represents an important component of LV ejection and a pathophysiologic link between systole and diastole. Elastic energy is stored during systole, then abruptly released with sudden untwisting during isovolumic relaxation, generating intra-ventricular pressure gradients and allowing filling to proceed at low filling pressure.[50]

The advantages of STI over TVI method are numerous: use of routine gray-scale 2D images (provided they are acquired at an adequate frame rate, i.e. between 50 and 90 fps), angle-independency implying the possibility to assess all LV segments and to measure the different components of myocardial deformation in any desired view (Fig. 2.39, Videos 2.39; Fig. 2.40, Video 2.40), better spatial resolution, less time-consuming, and lower sensitivity to noise. There are, however, several shortcomings to the current STE approach. The software is inherently dependent on high-resolution 2D image quality with adequate endocardial border definition and use of second harmonic imaging. It requires manual tracing of the myocardium, which may be a tedious and time-consuming task, but *automated function imaging (AFI)* modality has been developed to compensate for this aspect.

Although STE provides the assessment of tissue deformation in two directions, the cardiac motion is, in fact, 3D, and the through-plane motion may adversely affect the accuracy of tracking, particularly at the basal level. The measurement reproducibility is also influenced by endocardial tracing manner, width, and placement of the ROI. For the assessment of rotation and torsion, one major issue is the lack of precise standardization of the LV short-axis levels, especially for the apex, which is the main contributor to LV torsional deformation. The future implementation of 3D speckle-tracking will obviate all these limitations.

Clinical Applications

The clinical utility of TVI, strain, and strain rate has been demonstrated in numerous experimental, animal, and

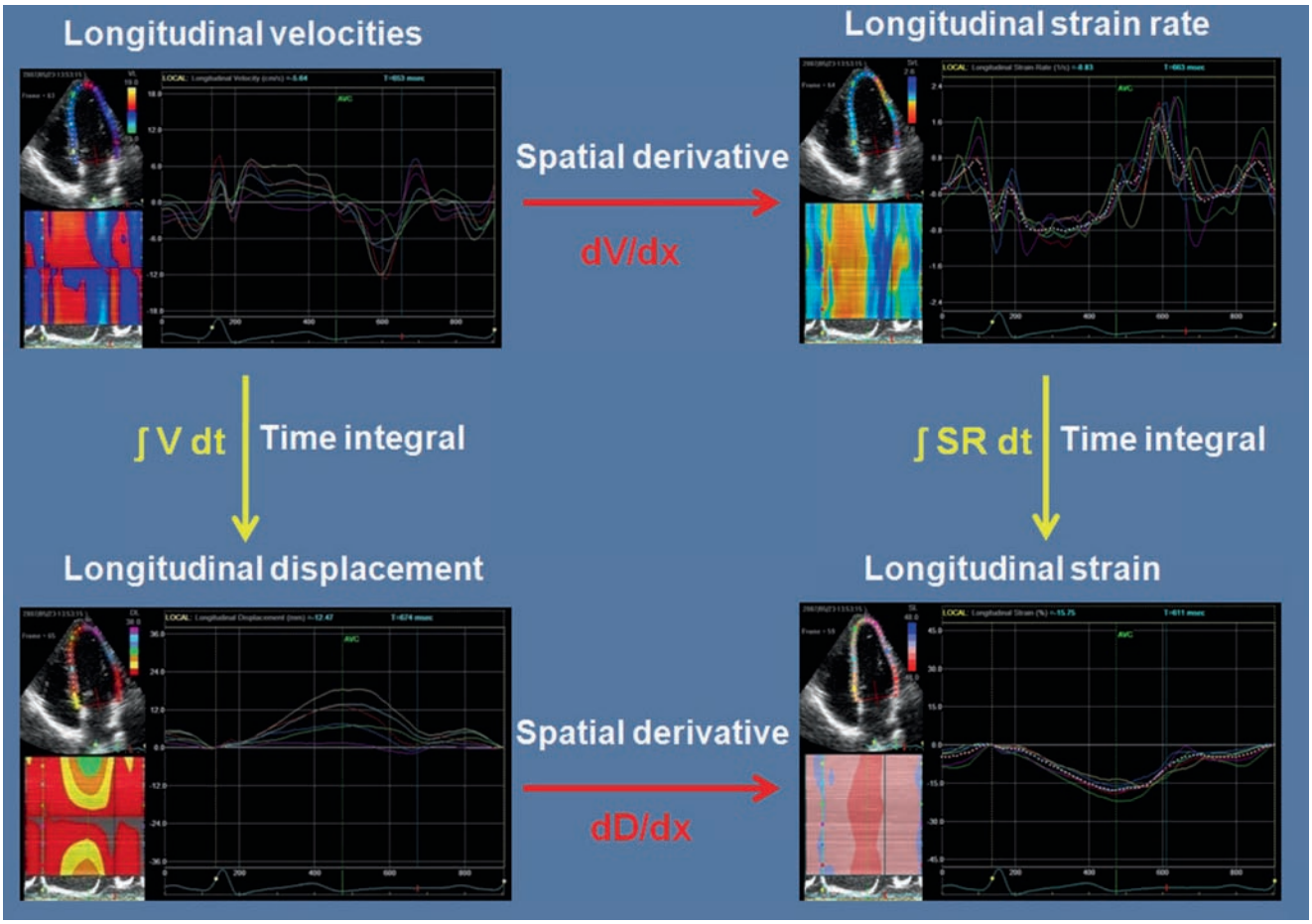

Fig. 2.34 Schematic representation of the calculations needed to obtain the different myocardial function parameters using deformation imaging techniques

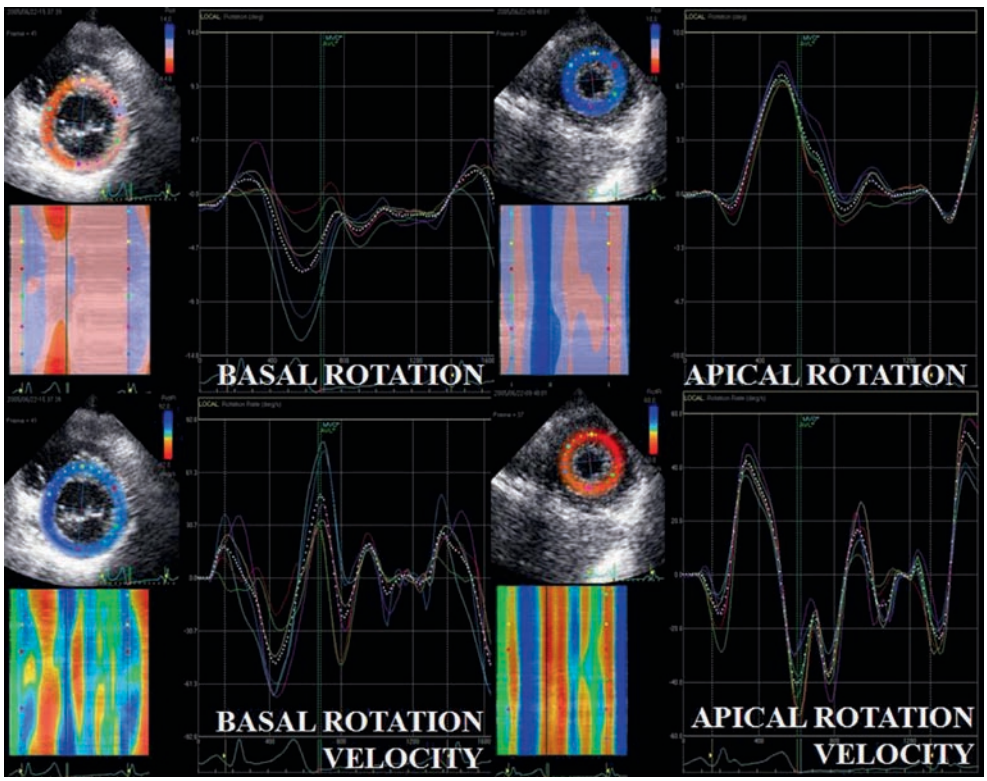

Fig. 2.35 Examples of rotation and rotation velocity curves at basal and apical left ventricular levels in a normal subject

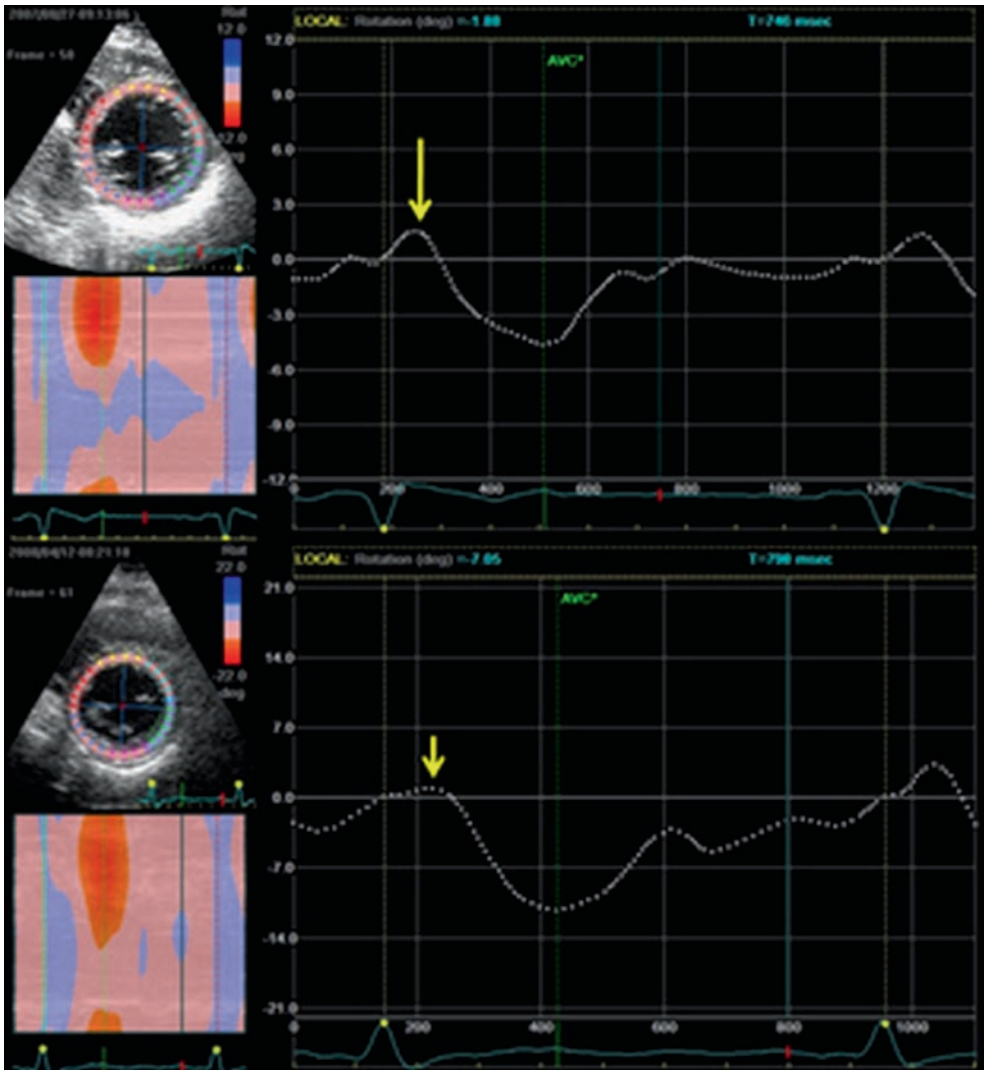

Fig. 2.36 Mean basal rotation vs. time plot in 24-year-old and 73-year-old normal subjects. Note the higher basal rotation angle and the smaller initial counter-clockwise rotation angle (*arrow*) in the old with respect to the young subject, possibly due to age-related subendocardial dysfunction

clinical studies. However, the role of these techniques to address management of patients remains to be clarified.

LV myocardial velocities measured by TVI may serve for non-invasive estimation of LV filling pressures. When the ratio between mitral inflow velocity (*E*) and the early diastolic mitral annular velocity (*E′*) is below eight, LV filling pressure is normal, while when the E/E′ ratio is greater than 15, LV filling pressure is increased.[51] The ratio *E*/*E′* is a key part of the proposed algorithm for diagnosing heart failure with preserved ejection fraction.[52] *E*/*E′* ratio has been validated for LV filling pressure assessment in the presence of preserved or poor LV systolic function,[51] sinus tachycardia,[3] atrial fibrillation,[54] heart transplant,[55] and hypertrophic cardiomyopathy,[56] and may serve as a prognostic marker of survival in hypertensive patients[57] or after myocardial infarction.[58] In addition, *E′* velocity can distinguish patients with constrictive pericarditis from those with a restrictive cardiomyopathy[59] or may discriminate between physiologic and pathologic hypertrophy (Fig. 2.41).[60]

Multiple TVI-based indexes have been proposed for quantitation of intra-ventricular dyssynchrony, from simpler time-delay between opposite LV walls (e.g. septal-lateral delay) to a more comprehensive 12 segments (6 basal and 6 mid LV) approach.[61, 62] STE may have a future application to quantify dyssynchrony in patients with heart failure and predict immediate and long-term response to CRT (Fig. 2.42, Video 2.42).[44] However, although the echocardiographic techniques discussed above (and several others, such as 3D echo) have been reported to be superior to ECG QRS width to assess dyssynchrony and predict response to CRT, evidence from the PROSPECT trial[63] and current practice guidelines[64] suggest that patients who meet accepted criteria for CRT should not have therapy withheld because of results of an echocardiography Doppler dyssynchrony study as recommended by the American Society of Echocardiography.[65]

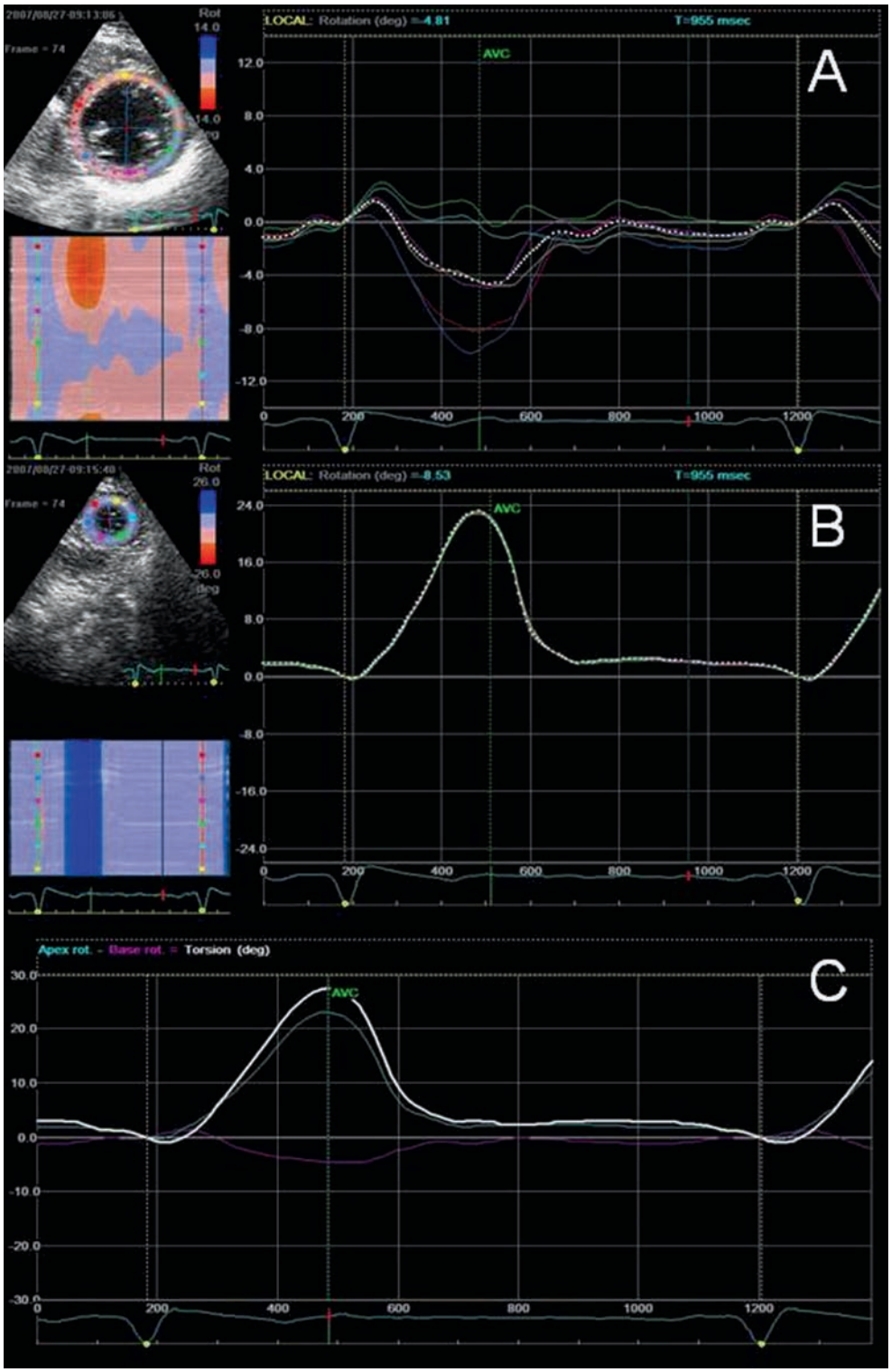

Fig. 2.37 Normal aspect of basal **(a)** and apical **(b)** rotation curves. Segmental rotation is colour-coded; dotted line represents average segmental rotation for each level. **(c)** Displays torsion vs. time plot (*white curve*), automatically computed by the software as the net difference between apical (*green curve*) and basal (*pink curve*) rotation for each time point of the cardiac cycle

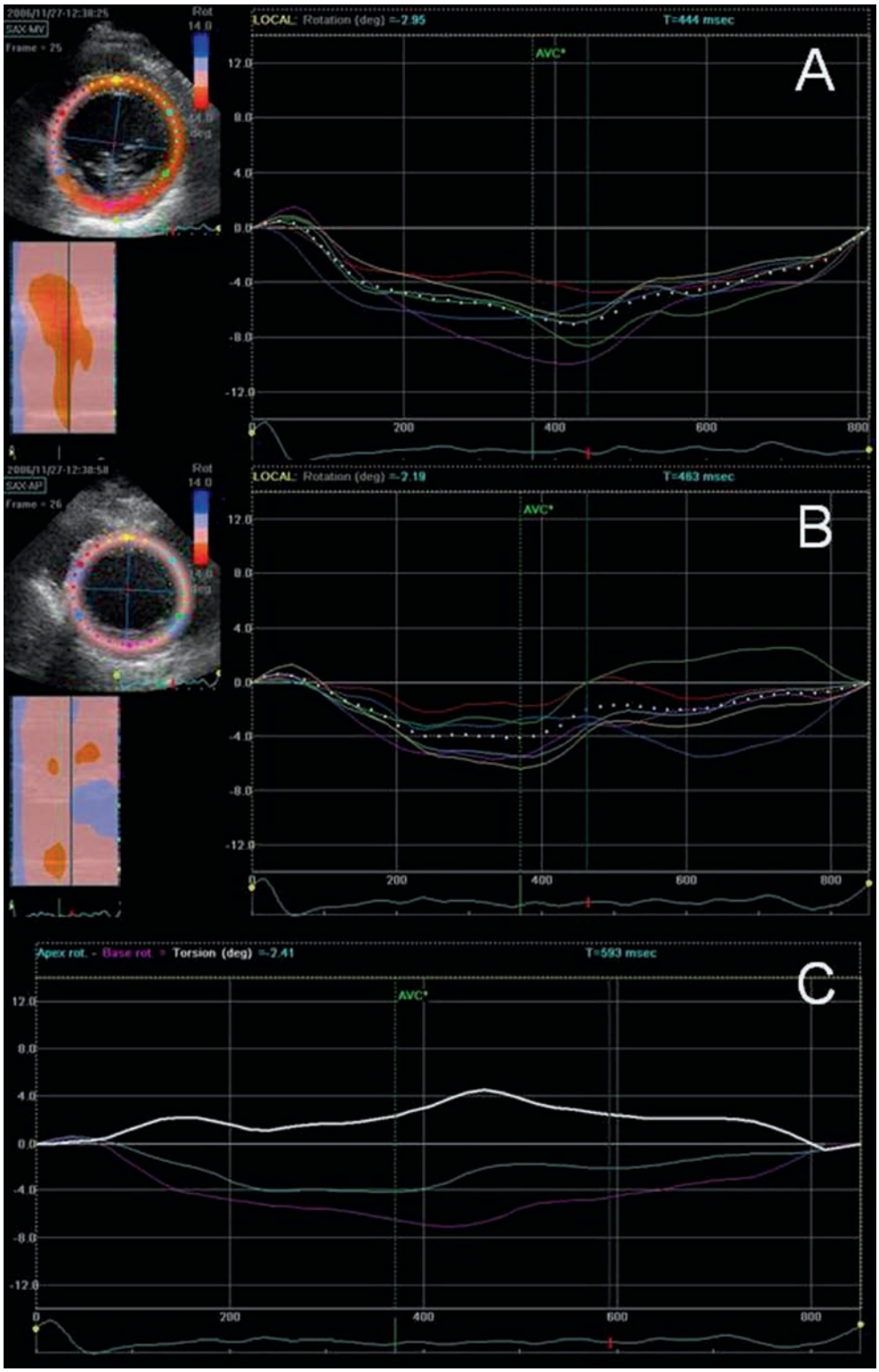

Fig. 2.38 Basal **(a)** and apical **(b)** rotation curves in a non-ischaemic dilated cardiomyopathy patient with severely dilated left ventricle, depicting "solid body" rotational profile (reversed rotation of the apex and normally oriented basal rotation) with markedly reduced amplitude in both levels. The "torsion" **(c)** is due to the small relative difference in the basal and apical same-directed rotational amplitude

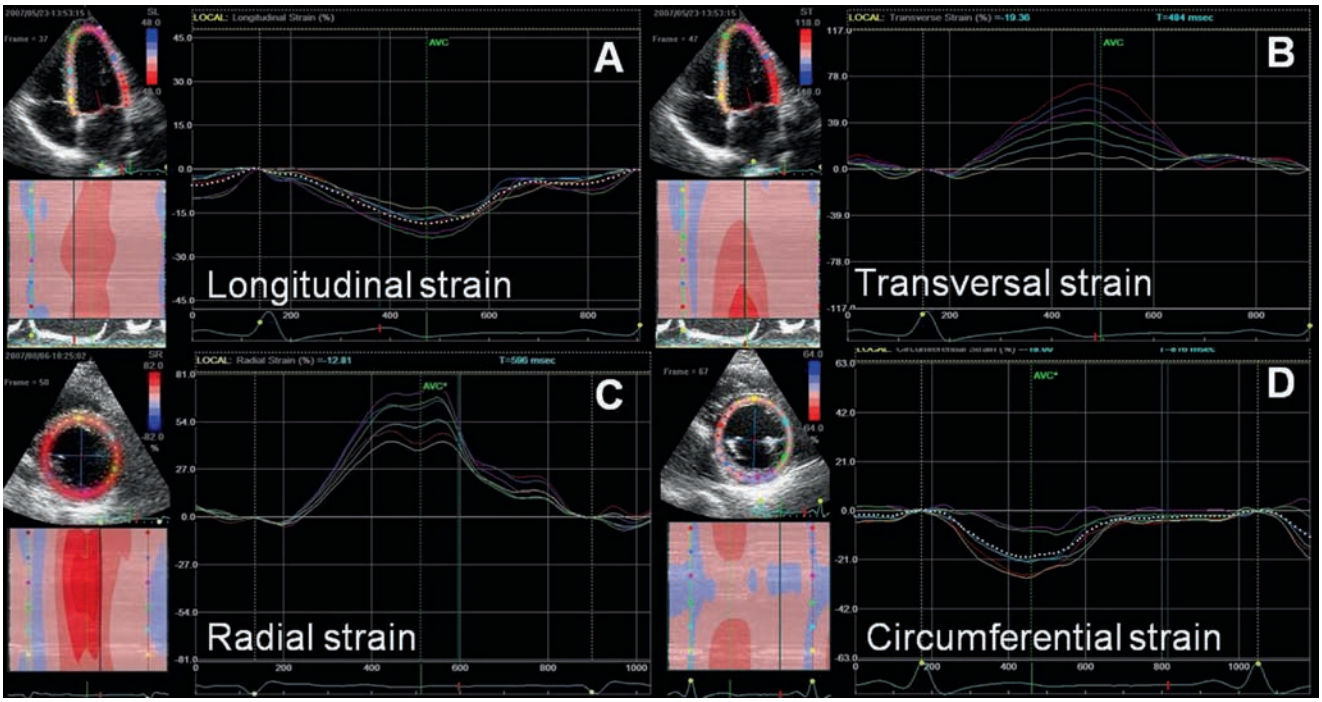

Fig. 2.39 Speckle tracking echocardiography allows the assessment of strain in various directions independently on the angle of insonation. From apical views, both longitudinal **(a)** and transversal **(b)** strain can be measured. From short-axis views both radial **(c)** and circumferential **(d)** strain can be measured

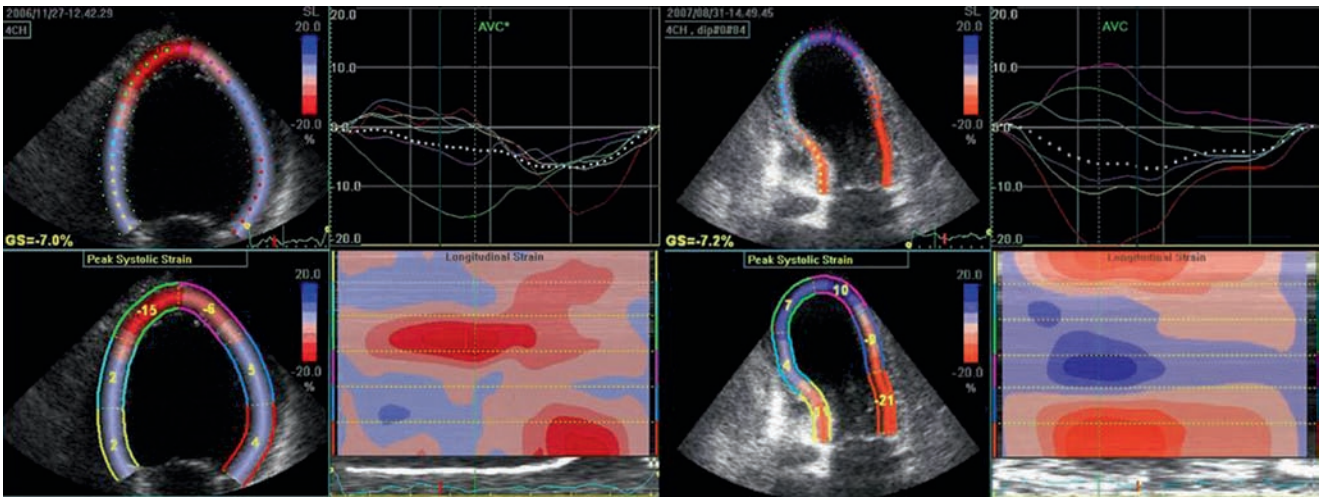

Fig. 2.40 The angle-of-insonation independency of speckle tracking assessment of strain allows to measure strain in severely dilated (*left panel*) and in abnormally shaped (*right panel*) ventricles in which correct alignment of the Doppler beam required by TVI would be difficult

Other emerging clinical settings in which these echocardiographic techniques are under clinical investigation are regional function assessment in coronary artery disease and during stress echocardiography (Fig. 2.43, Videos 2.43) to detect acute ischaemia (Fig. 2.44, Videos 2.44), or myocardial viability. However, more evidence is needed for these new echocardiographic technologies to be implemented in routine daily practice for these purposes. Thus, STE technique is likely to be superior to TVI for a more subtle analysis of myocardial mechanics and function[66, 67] or for the detection of infarct trans-murality, with possible implications for the reperfusion treatment.[38] Strain and strain rate measurements

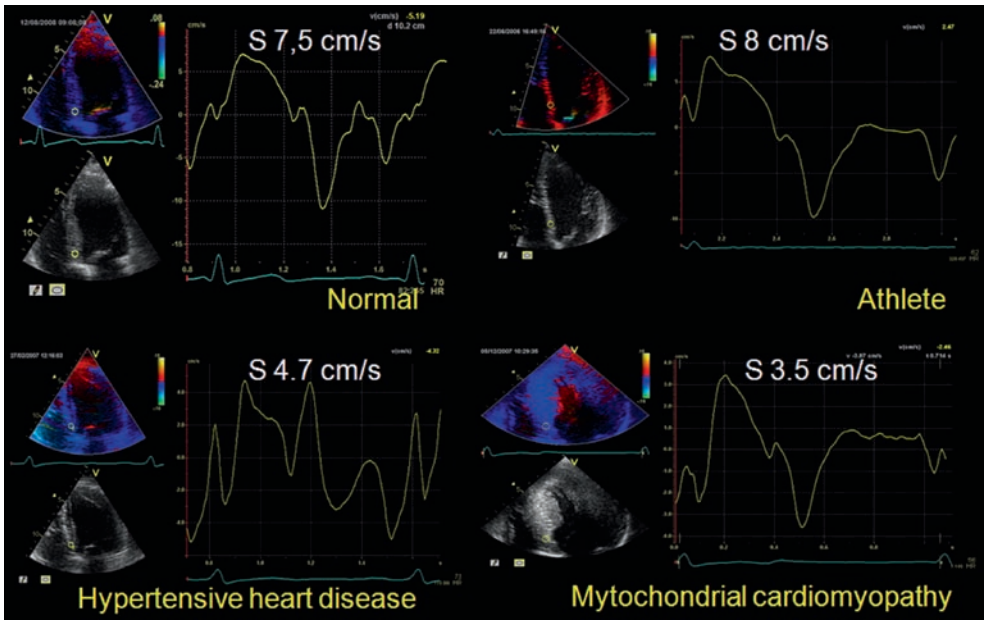

Fig. 2.41 Tissue Doppler recording in basal septum serves to discriminate pathologic and physiologic hypertrophy. The panel demonstrates various Doppler patterns in a normal and an athletic heart with normal systolic function, in contrast with reduced systolic velocity in a hypertensive heart disease or mytochondrial cardiomyopathy, despite normal left ventricular ejection fraction

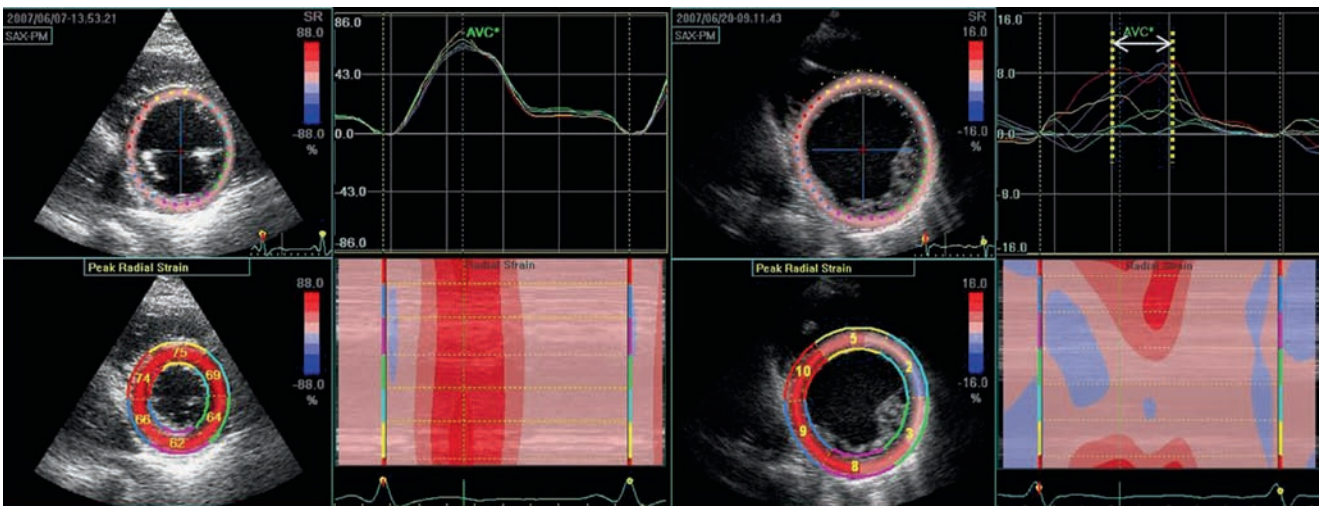

Fig. 2.42 *Left panel:* Quad view of 2D speckle-tracking radial strain in a normal subject showing normal strain values and simultaneous occurrence of peak radial strain values in all left ventricular segments. *Right panel:* Quad view of 2D speckle-tracking radial strain in a patient with dilated cardiomyopathy, showing significantly reduced strain values and wide dispersion of the time to peak radial strain due to intra-ventricular dyssynchrony (*dotted yellow lines* show the delay between the first and the latest activated segments)

by STE were found to be highly sensitive and specific for the diagnosis of MI and bull's eye map (Fig. 2.45) closely correlated with the specific coronary lesions demonstrated by coronary angiography.[68]

Detailed assessment of heart mechanics may provide a superior pathophysiological insight into the mechanism of cardiac dysfunction. Myocardial diseases, as well as ischaemia or LV hypertrophy in aortic stenosis (Fig. 2.46, Video 2.46), usually produce an early impairment of subendocardial function marked by a reduction in longitudinal LV function. In patients with hypertrophic cardiomyopathy, despite an apparently normal left ventricular systolic function based on conventional echocardiography, strain imaging may reveal an abnormal LV function (Fig. 2.47, Videos 2.47).[69, 70] Strain imaging may also reveal early signs of infiltrative cardiac disease in familial amyloidotic polyneuropathy.[71] Systolic longitudinal strain and strain rate are also accurate for detecting subtle LV dysfunction in patients with systemic

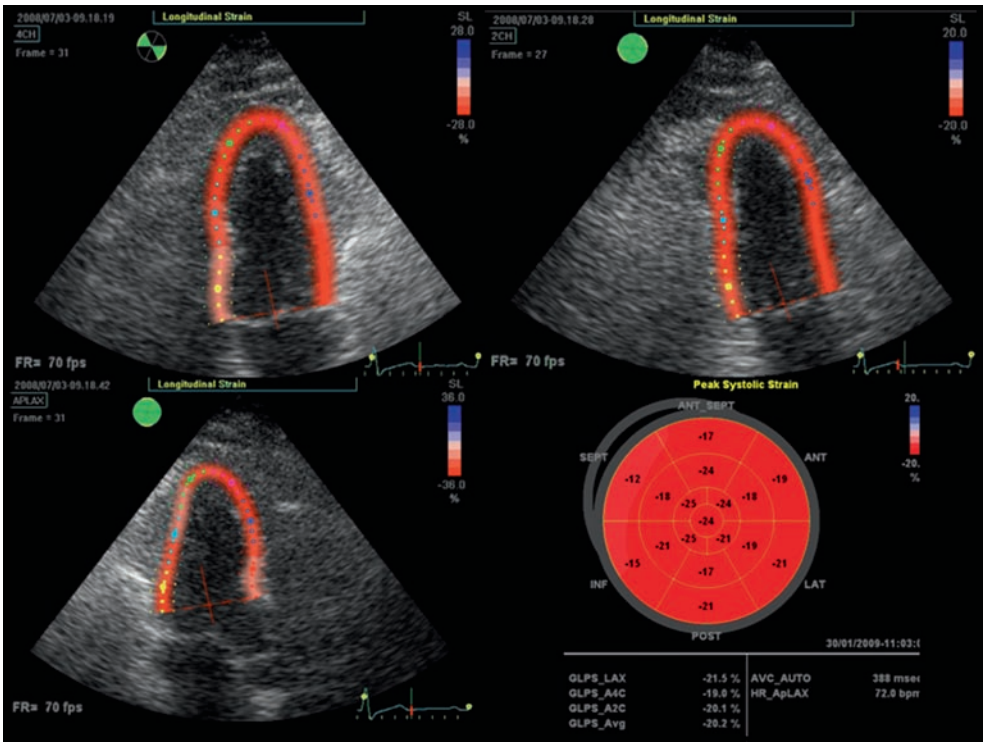

Fig. 2.43 Bull's eye map of longitudinal strain at rest, showing normal strain pattern across entire left ventricular myocardium

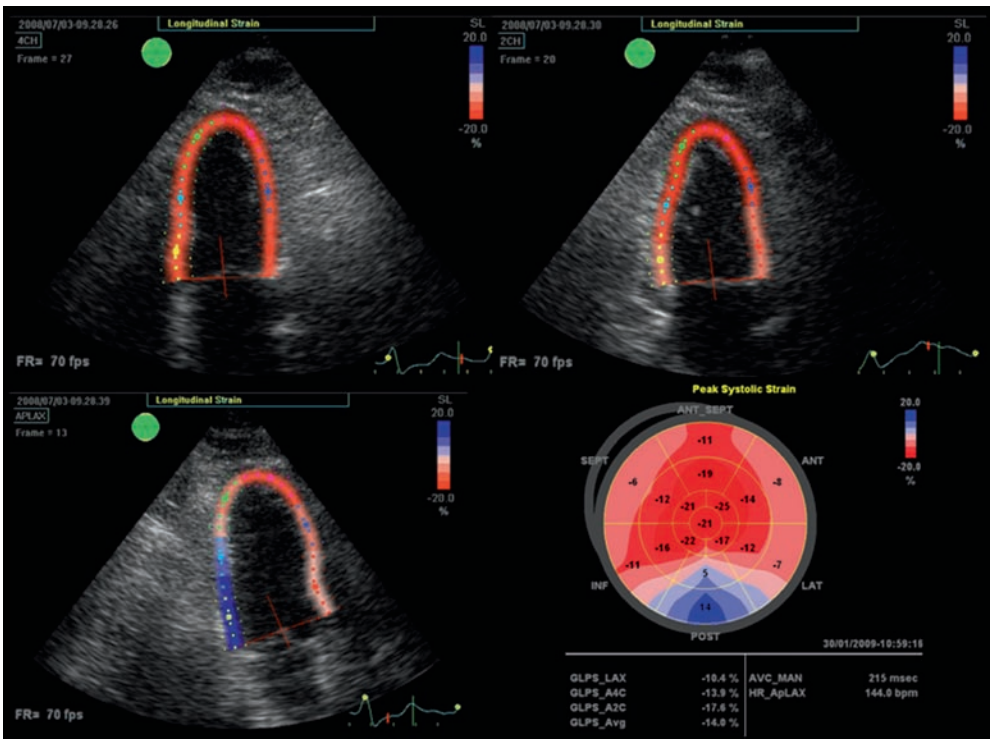

Fig. 2.44 Bull's eye map demonstrating inducible ischaemia at peak stress. Areas of decreased peak systolic strain are clearly demonstrated by different colour codes especially in the postero-inferior wall and all LV basal segments

amyloidosis and normal standard examination, possibly before the occurrence of diastolic dysfunction.[72]

In summary, TVI and strain imaging confer a more accurate quantification of cardiac function in different clinical settings that may supplement the diagnosis and prognosis in patient care routine, although the clinical applications and implications still need to be confirmed by future large-scale studies before implementing them in everyday practice.

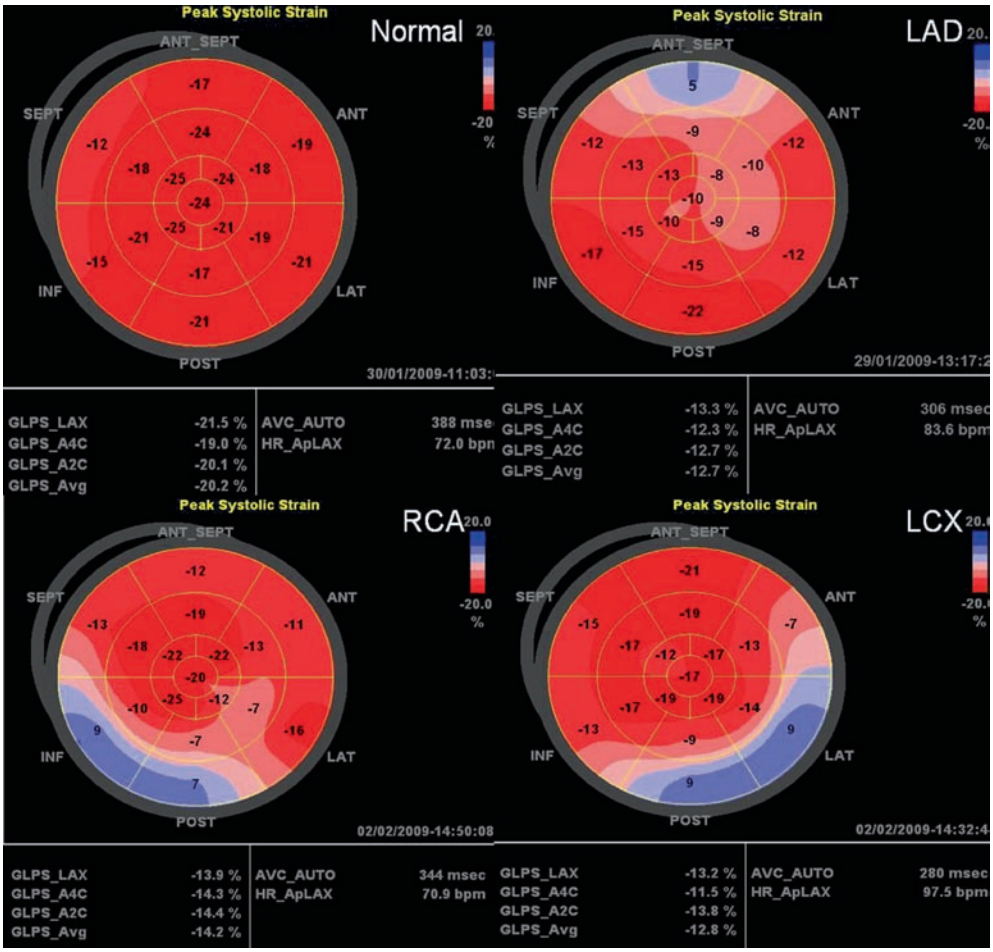

Fig. 2.45 Longitudinal strain rate assessed by speckle tracking echocardiography shows a close relationship with the coronary supply territory in patients with previous myocardial infarction or during induced ischaemia at stress echo

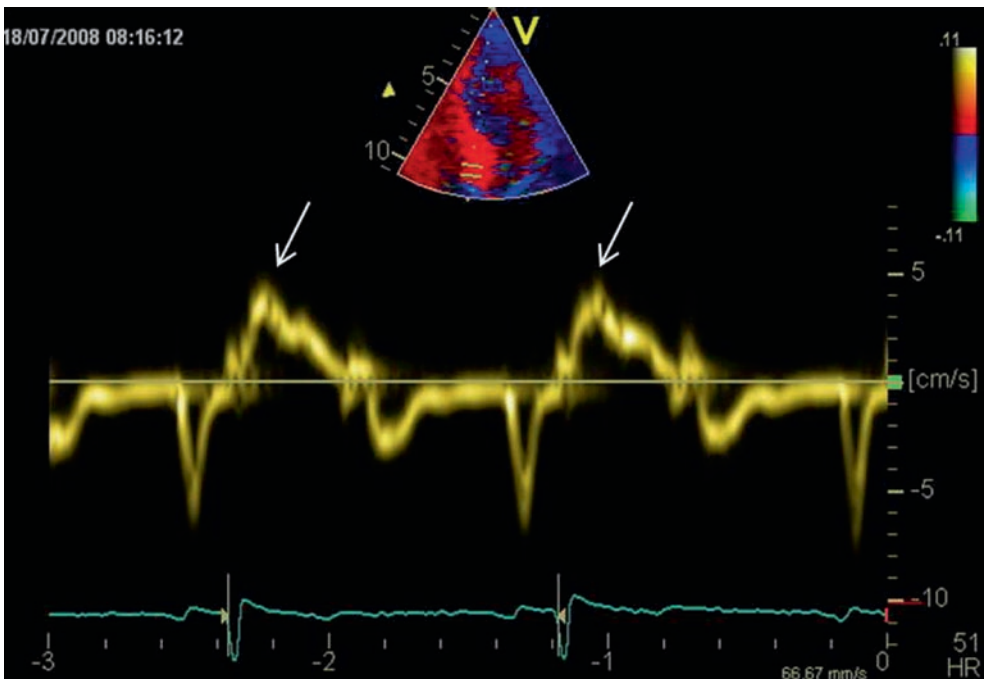

Fig. 2.46 Recording of pulsed tissue Doppler from septal mitral annulus in a patient with severe aortic stenosis. S wave velocity is significantly reduced signifying an impaired longitudinal function, despite a preserved global left ventricular ejection fraction

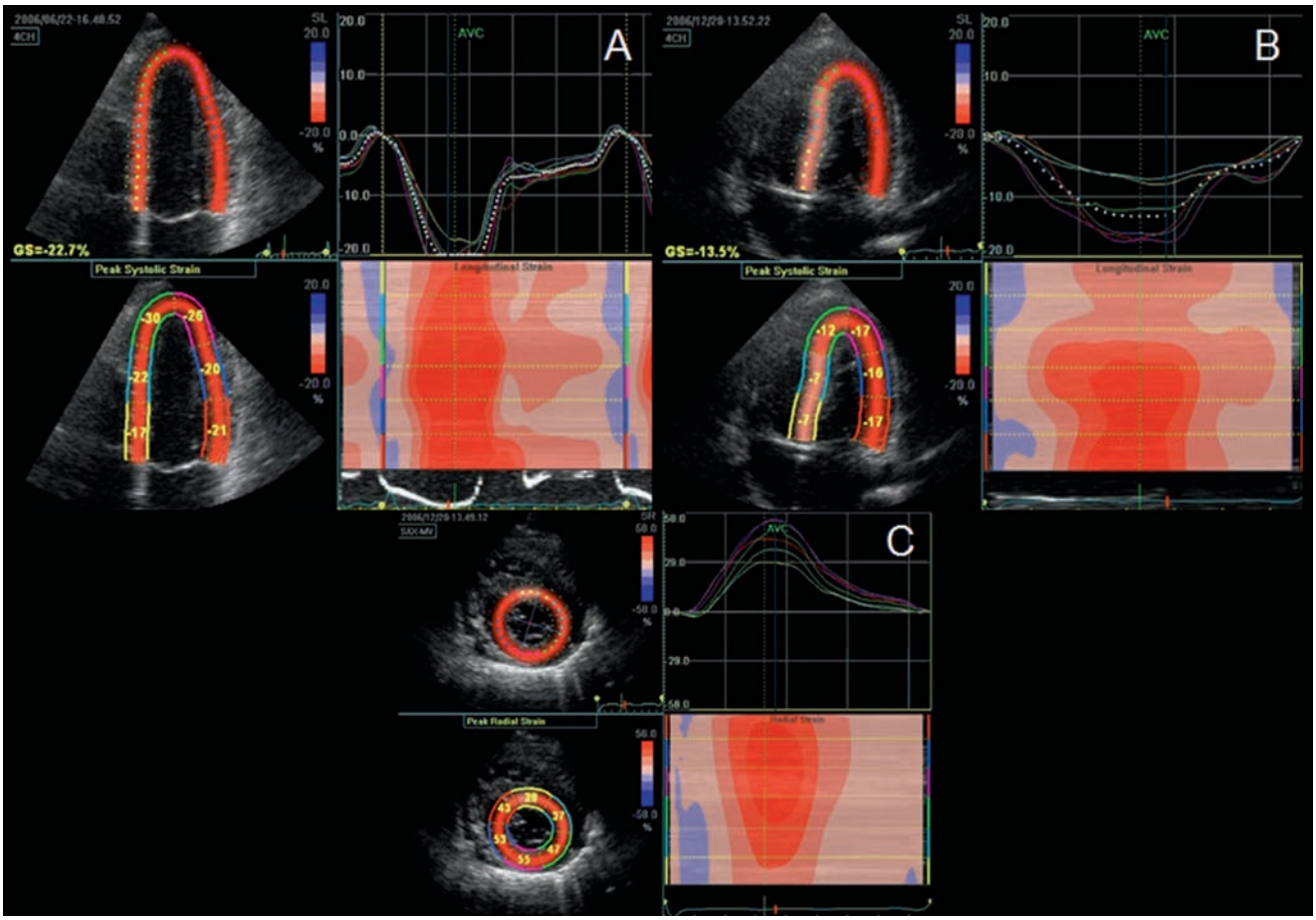

Fig. 2.47 **(a–c)** Speckle tracking detection of pathological hypertrophy. **(a)** Normal longitudinal strain in an athlete with physiologic hypertrophy. **(b)** Reduced longitudinal strain in a patient with hypertrophic cardiomyopathy. **(c)** Active basal radial strain and rotation in the same patient

References

1. Burns PN, Powers JE, Simpson DH, Brezina A, Kolin A, Chin CT, et al Harmonic power mode Doppler using microbubble contrast agents: an improved method for small vessel flow imaging. In: Levy M, Schneider SC, McAvoy BR, eds. *IEEE ultrasonics symposium proceedings: an international symposium*. Vol 3. New York: Institute of Electrical and Electronics Engineers; 1994:1547–1550
2. Powers JEBP, Souquet J. Imaging instrumentation for ultrasound contrast agents. In: Nanda NC, Schlief R, Goldberg BB, eds. *Advances in echo imaging using contrast enhancement.* 2nd ed. Dordrecht: Kluwer; 1997:139–1370
3. Simpson DHCC, Burns PN. Pulse inversion Doppler: a new method for detecting nonlinear echoes from microbubble contrast agents. *IEEE Trans Ultrason Ferroelectr Freq Control*. 1999;46:372–382
4. Porter TR, Xie F. Transient myocardial contrast after initial exposure to diagnostic ultrasound pressures with minute doses of intravenously injected microbubbles. Demonstration and potential mechanisms. *Circulation*. 1995;92:2391–2395
5. Plana JC, Mikati IA, Dokainish H, et al A randomized cross-over study for evaluation of the effect of image optimization with contrast on the diagnostic accuracy of dobutamine echocardiography in coronary artery disease. The OPTIMIZE Trial. *J Am Coll Cardiol Img*. 2008;1:145–152
6. Wei K, Jayaweera AR, Firoozan S, Linka A, Skyba DM, Kaul S. Quantification of myocardial blood flow with ultrasound-induced destruction of microbubbles administered as a constant venous infusion. *Circulation*. 1998;97:473–483
7. Kaul S, Jayaweera AR. Coronary and myocardial blood volumes: noninvasive tools to assess the coronary microcirculation? *Circulation*. 1997;96:719–724
8. Main ML, Goldman JH, Grayburn PA. Thinking outside the "box" – the ultrasound contrast controversy. *J Am Coll Cardiol*. 2007;50:2434–2437
9. Grayburn PA. Product safety compromises patient safety (an unjustified black box warning on ultrasound contrast agents by the Food and Drug Administration). *Am J Cardiol*. 2008;101:892–893
10. Vancraeynest D, Kefer J, Hanet C, et al Release of cardiac biomarkers during high mechanical index contrast-enhanced echocardiography in humans. *Eur Heart J*. 2007;28:1236–1241
11. Van Camp G, Droogmans S, Cosyns B. Bio-effects of ultrasound contrast agents in daily clinical practice: fact or fiction? *Eur Heart J*. 2007;28:1190–1192
12. Peltier M, Vancraeynest D, Pasquet A, et al Assessment of the physiologic significance of coronary disease with dipyridamole real-time myocardial contrast echocardiography. Comparison with technetium-99m sestamibi single-photon emission computed tomography and quantitative coronary angiography. *J Am Coll Cardiol*. 2004;43:257–264

13. Senior R, Monaghan M, Main ML, Zamarono JL, Tieman KL, Agati L, et al Detection of coronary artery disease with perfusion stress echocardiography using a novel ultrasound imaging agent: two phase 3 international trials in comparison with radionuclide perfusion imaging. *Eur J Echocardiogr*. 2009;10:26–35
14. Takeuchi M, Otani S, Weinert L, Spencer KT, Lang RM. Comparison of contrast-enhanced real-time live 3-dimensional dobutamine stress echocardiography with contrast 2-dimensional echocardiography for detecting stress-induced wall-motion abnormalities. *J Am Soc Echocardiogr*. 2006;19:294–299
15. Bhan A, Kapetanakis S, Rana BS, et al Real-time three-dimensional myocardial contrast echocardiography: is it clinically feasible? *Eur J Echocardiogr*. 2008;9:761–765
16. Shaw LJ, Monaghan MJ, Nihoyannopolous P. Clinical and economic outcomes assessment with myocardial contrast echocardiography. *Heart*. 1999;82(Suppl 3):III16–III21
17. Dekker DL, Piziali RL, Dong E. A system for ultrasonically imaging the human heart in three dimensions. *Comput Biomed Res*. 1974;7:544–553
18. Siu SC, Rivera JM, Guerrero JL, et al Three-dimensional echocardiography. In vivo validation for left ventricular volume and function. *Circulation*. 1993;88:1715–1723
19. von Ramm OT, Smith SW. Real time volumetric ultrasound imaging system. *J digit imaging*. 1990;3:261–266
20. Mor-Avi V, Sugeng L, Weinert L, et al Fast measurement of left ventricular mass with real-time three-dimensional echocardiography: comparison with magnetic resonance imaging. *Circulation*. 2004;110:1814–1818
21. Takeuchi M, Nishikage T, Mor-Avi V, et al Measurement of left ventricular mass by real-time three-dimensional echocardiography: validation against magnetic resonance and comparison with two-dimensional and m-mode measurements. *J Am Soc Echocardiogr*. 2008;21:1001–1005
22. Mor-Avi V, Jenkins C, Kuhl HP, et al Real-time 3-dimensional echocardiographic quantification of left ventricular volumes: multicenter study for validation with magnetic resonance imaging and investigation of sources of error. *J Am Coll Cardiol Img*. 2008;1:413–423
23. Jenkins C, Bricknell K, Hanekom L, Marwick TH. Reproducibility and accuracy of echocardiographic measurements of left ventricular parameters using real-time three-dimensional echocardiography. *J Am Coll Cardiol*. 2004;44:878–886
24. Hare JL, Jenkins C, Nakatani S, Ogawa A, Yu CM, Marwick TH. Feasibility and clinical decision-making with 3D echocardiography in routine practice. *Heart*. 2008;94:440–457
25. Kapetanakis S, Kearney MT, Siva A, Gall N, Cooklin M, Monaghan MJ. Real-time three-dimensional echocardiography: a novel technique to quantify global left ventricular mechanical dyssynchrony. *Circulation*. 2005;112:992–1000
26. Chen G, Sun K, Huang G. In vitro validation of right ventricular volume and mass measurement by real-time three-dimensional echocardiography. *Echocardiography*. 2006;23:395–399
27. Gopal AS, Chukwu EO, Iwuchukwu CJ, et al Normal values of right ventricular size and function by real-time 3-dimensional echocardiography: comparison with cardiac magnetic resonance imaging. *J Am Soc Echocardiogr*. 2007;20:445–455
28. Jenkins C, Bricknell K, Marwick TH. Use of real-time three-dimensional echocardiography to measure left atrial volume: comparison with other echocardiographic techniques. *J Am Soc Echocardiogr*. 2005;18:991–997
29. Gutiérrez-Chico JL, Zamorano Gómez JL, Rodrigo-López JL, et al Accuracy of real-time 3-dimensional echocardiography in the assessment of mitral prolapse. Is transesophageal echocardiography still mandatory? *Am Heart J*. 2008;155:694–698
30. Yang HS, Bansal RC, Mookadam F, Khandheria BK, Tajik AJ, Chandrasekaran K. Practical guide for three-dimensional transthoracic echocardiography using a fully sampled matrix array transducer. *J Am Soc Echocardiogr*. 2008;21:979–989; quiz 1081–1082
31. Sutherland GR, Di Salvo G, Claus P, D'hooge J, Bijnens B. Strain and strain rate imaging: a new clinical approach to quantifying regional myocardial function. *J Am Soc Echocardiogr*. 2004; 17 : 788–802
32. Bijnens B, Claus P, Weidemann F, Strotmann J, Sutherland GR. Investigating cardiac function using motion and deformation analysis in the setting of coronary artery disease. *Circulation*. 2007; 116: 2453–2464
33. Palka P, Lange A, Fleming AD, et al Differences in myocardial velocity gradient measured throughout the cardiac cycle in patients with hypertrophic cardiomyopathy, athletes and patients with left ventricular hypertrophy due to hypertension. *J Am Coll Cardiol*. 1997;30:760–768
34. Yu CM, Sanderson JE, Marwick TH, Oh JK. Tissue Doppler imaging a new prognosticator for cardiovascular diseases. *J Am Coll Cardiol*. 2007;49:1903–1914
35. Pavlopoulos H, Nihoyannopoulos P. Strain and strain rate deformation parameters: from tissue Doppler to 2D speckle tracking. *Int J Cardiovasc Imaging*. 2008;24:479–491
36. Kukulski T, Voigt JU, Wilkenshoff UM, et al A comparison of regional myocardial velocity information derived by pulsed and color Doppler techniques: an in vitro and in vivo study. *Echocardiography*. 2000;17:639–651
37. Pan C, Hoffmann R, Kuhl H, Severin E, Franke A, Hanrath P. Tissue tracking allows rapid and accurate visual evaluation of left ventricular function. *Eur J Echocardiogr*. 2001;2:197–202
38. Yu CM, Zhang Q, Fung JW, et al A novel tool to assess systolic asynchrony and identify responders of cardiac resynchronization therapy by tissue synchronization imaging. *J Am Coll Cardiol*. 2005;45:677–684
39. Gorcsan J III, Kanzaki H, Bazaz R, Dohi K, Schwartzman D. Usefulness of echocardiographic tissue synchronization imaging to predict acute response to cardiac resynchronization therapy. *Am J Cardiol*. 2004;93:1178–1181
40. Van de Veire NR, Bleeker GB, Ypenburg C, et al Usefulness of triplane tissue Doppler imaging to predict acute response to cardiac resynchronization therapy. *Am J Cardiol*. 2007;100:476–482
41. Teske AJ, De Boeck BW, Melman PG, Sieswerda GT, Doevendans PA, Cramer MJ. Echocardiographic quantification of myocardial function using tissue deformation imaging, a guide to image acquisition and analysis using tissue Doppler and speckle tracking. *Cardiovasc Ultrasound*. 2007;5:27
42. Urheim S, Edvardsen T, Torp H, Angelsen B, Smiseth OA. Myocardial strain by Doppler echocardiography. Validation of a new method to quantify regional myocardial function. *Circulation*. 2000;102:1158–1164
43. Edvardsen T, Gerber BL, Garot J, Bluemke DA, Lima JA, Smiseth OA. Quantitative assessment of intrinsic regional myocardial deformation by Doppler strain rate echocardiography in humans: validation against three-dimensional tagged magnetic resonance imaging. *Circulation*. 2002;106:50–56
44. Suffoletto MS, Dohi K, Cannesson M, Saba S, Gorcsan J III. Novel speckle-tracking radial strain from routine black-and-white echocardiographic images to quantify dyssynchrony and predict response to cardiac resynchronization therapy. *Circulation*. 2006;113:960–968
45. Leitman M, Lysyansky P, Sidenko S, et al Two-dimensional strain-a novel software for real-time quantitative echocardiographic assessment of myocardial function. *J Am Soc Echocardiogr*. 2004;17: 1021–1029
46. Notomi Y, Setser RM, Shiota T, et al Assessment of left ventricular torsional deformation by Doppler tissue imaging: validation study with tagged magnetic resonance imaging. *Circulation*. 2005;111: 1141–1147

47. Modesto KM, Cauduro S, Dispenzieri A, et al Two-dimensional acoustic pattern derived strain parameters closely correlate with one-dimensional tissue Doppler derived strain measurements. *Eur J Echocardiogr*. 2006;7:315–321
48. Perk G, Tunick PA, Kronzon I. Non-Doppler two-dimensional strain imaging by echocardiography - from technical considerations to clinical applications. *J Am Soc Echocardiogr*. 2007;20:234–43
49. Ingul CB, Torp H, Aase SA, Berg S, Stoylen A, Slordahl SA. Automated analysis of strain rate and strain: feasibility and clinical implications. *J Am Soc Echocardiogr*. 2005;18:411–418
50. Thomas JD, Popovic ZB. Assessment of left ventricular function by cardiac ultrasound. *J Am Coll Cardiol*. 2006;48:2012–2025
51. Ommen SR, Nishimura RA, Appleton CP, et al Clinical utility of Doppler echocardiography and tissue Doppler imaging in the estimation of left ventricular filling pressures: a comparative simultaneous Doppler-catheterization study. *Circulation*. 2000;102:1788–1794
52. Paulus WJ, Tschope C, Sanderson JE, et al How to diagnose diastolic heart failure: a consensus statement on the diagnosis of heart failure with normal left ventricular ejection fraction by the Heart Failure and Echocardiography Associations of the European Society of Cardiology. *Eur Heart J*. 2007;28:2539–2550
53. Nagueh SF, Mikati I, Kopelen HA, Middleton KJ, Quinones MA, Zoghbi WA. Doppler estimation of left ventricular filling pressure in sinus tachycardia. A new application of tissue doppler imaging. *Circulation*. 1998;98:1644–1650
54. Sohn DW, Song JM, Zo JH, et al Mitral annulus velocity in the evaluation of left ventricular diastolic function in atrial fibrillation. *J Am Soc Echocardiogr*. 1999;12:927–931
55. Sundereswaran L, Nagueh SF, Vardan S, et al Estimation of left and right ventricular filling pressures after heart transplantation by tissue Doppler imaging. *Am J Cardiol*. 1998;82:352–357
56. Nagueh SF, Lakkis NM, Middleton KJ, Spencer WH III, Zoghbi WA, Quinones MA. Doppler estimation of left ventricular filling pressures in patients with hypertrophic cardiomyopathy. *Circulation*. 1999;99:254–261
57. Wang M, Yip GW, Wang AY, et al Peak early diastolic mitral annulus velocity by tissue Doppler imaging adds independent and incremental prognostic value. *J Am Coll Cardiol*. 2003;41:820–826
58. Hillis GS, Moller JE, Pellikka PA, et al Noninvasive estimation of left ventricular filling pressure by E/e' is a powerful predictor of survival after acute myocardial infarction. *J Am Coll Cardiol*. 2004;43:360–367
59. Rajagopalan N, Garcia MJ, Rodriguez L, et al Comparison of new Doppler echocardiographic methods to differentiate constrictive pericardial heart disease and restrictive cardiomyopathy. *Am J Cardiol*. 2001;87:86–94
60. Vinereanu D, Florescu N, Sculthorpe N, Tweddel AC, Stephens MR, Fraser AG. Differentiation between pathologic and physiologic left ventricular hypertrophy by tissue Doppler assessment of long-axis function in patients with hypertrophic cardiomyopathy or systemic hypertension and in athletes. *Am J Cardiol*. 2001;88: 53–58
61. Yu CM, Fung JW, Zhang Q, et al Tissue Doppler imaging is superior to strain rate imaging and postsystolic shortening on the prediction of reverse remodeling in both ischemic and nonischemic heart failure after cardiac resynchronization therapy. *Circulation*. 2004; 110:66–73
62. Bax JJ, Abraham T, Barold SS, et al Cardiac resynchronization therapy: Part 1 - issues before device implantation. *J Am Coll Cardiol*. 2005;46:2153–67
63. Chung ES, Leon AR, Tavazzi L, et al Results of the predictors of response to CRT (PROSPECT) trial. *Circulation*. 2008;117: 2608–2616
64. Hunt SA, Abraham WT, Chin MH, et al ACC/AHA 2005 guideline update for the diagnosis and management of chronic heart failure in the adult: a report of the American College of Cardiology/American Heart Association Task Force on Practice Guidelines (writing committee to update the 2001 guidelines for the evaluation and management of heart failure): developed in collaboration with the American College of Chest Physicians and the International Society for Heart and Lung Transplantation: endorsed by the Heart Rhythm Society. *Circulation*. 2005;112:e154–e235
65. Gorcsan J, III, Abraham T, Agler DA, et al Echocardiography for cardiac resynchronization therapy: recommendations for performance and reporting - a report from the American Society of Echocardiography Dyssynchrony Writing Group endorsed by the Heart Rhythm Society. *J Am Soc Echocardiogr*. 2008;21:191–213
66. Jamal F, Strotmann J, Weidemann F, et al Noninvasive quantification of the contractile reserve of stunned myocardium by ultrasonic strain rate and strain. *Circulation*. 2001;104:1059–1065
67. Voigt JU, Exner B, Schmiedehausen K, et al Strain-rate imaging during dobutamine stress echocardiography provides objective evidence of inducible ischemia. *Circulation*. 2003;107:2120–2126
68. Zhang Y, Chan AK, Yu CM, et al Strain rate imaging differentiates transmural from non-transmural myocardial infarction: a validation study using delayed-enhancement magnetic resonance imaging. *J Am Coll Cardiol*. 2005;46:864–871
69. Serri K, Reant P, Lafitte M, et al Global and regional myocardial function quantification by two-dimensional strain: application in hypertrophic cardiomyopathy. *J Am Coll Cardiol*. 2006;47:1175–1181
70. Kato TS, Noda A, Izawa H, et al Discrimination of nonobstructive hypertrophic cardiomyopathy from hypertensive left ventricular hypertrophy on the basis of strain rate imaging by tissue Doppler ultrasonography. *Circulation*. 2004;110:3808–3814
71. Lindqvist P, Olofsson BO, Backman C, Suhr O, Waldenstrom A. Pulsed tissue Doppler and strain imaging discloses early signs of infiltrative cardiac disease: a study on patients with familial amyloidotic polyneuropathy. *Eur J Echocardiogr*. 2006;7:22–30
72. Al Zahrani GB, Bellavia D, Pellikka PA, et al Doppler myocardial imaging compared to standard 2-dimensional and doppler echocardiography for assessment of diastolic function in patients with systemic amyloidosis. *J Am Soc Echocardiogr*. 2009;22(3):290–298

Chapter 3

NUCLEAR CARDIOLOGY (PET AND SPECT): BASIC PRINCIPLES

Frank M. Bengel, Paolo Camici, and Frederic Lamare

CONTENTS

J. L. Zamorano et al. (eds.), *The ESC Textbook of Cardiovascular Imaging*
DOI: 10.1007/978-1-84882-421-8_3, © Springer-Verlag London Limited 2010

Introduction

Radionuclide imaging of the heart is well established for the clinical diagnostic and prognostic workup of coronary artery disease (CAD). Myocardial perfusion single photon emission computed tomography (SPECT) has been the mainstay of cardiovascular radionuclide applications for decades, and its usefulness is supported by a very large body of evidence.[1] Positron emission tomography (PET) is an advanced radionuclide technique that has also been available for decades. In contrast to SPECT, PET has long been considered mainly a research tool because of its methodological complexity. However, owing to several recent developments, cardiac PET is now increasingly penetrating the clinical arena.[2]

Nuclear cardiology techniques are considered robust, accurate, and reliable for clinical imaging of heart disease. They will thus continue to play a key role in the assessment of myocardial perfusion, function, and viability. At the same time, nuclear imaging technology is progressing towards higher sensitivity and resolution, and novel, highly specific radiotracers are being introduced.[3] These developments are indicators of a steady evolution of nuclear cardiology towards characterization of molecular events at the tissue level. In the competitive environment of cardiovascular imaging, it is therefore expected that radionuclide imaging will take a central role in the implementation of molecular imaging techniques for more specific, personalized, preventive, and therapeutic decision-making.

This chapter will outline the basic aspects of SPECT and PET as the two key nuclear cardiology techniques. The technical aspects of image acquisition will be discussed first. A brief overview on the current application of radionuclide imaging procedures will then be given, and the chapter will be concluded with an outlook on future developments of camera and tracer methodology.

Technical Aspects: Physics and Data Analysis

SPECT

Myocardial SPECT imaging is typically performed using a multi-detector gamma camera system, which rotates around the chest to obtain tomographic images of single emitted photons (Fig. 3.1). Collimators are used to balance detection sensitivity and optimize spatial resolution. For imaging, the patient is typically positioned supine on the table, although prone positioning has been shown to be useful for reducing attenuation artefacts.[4]

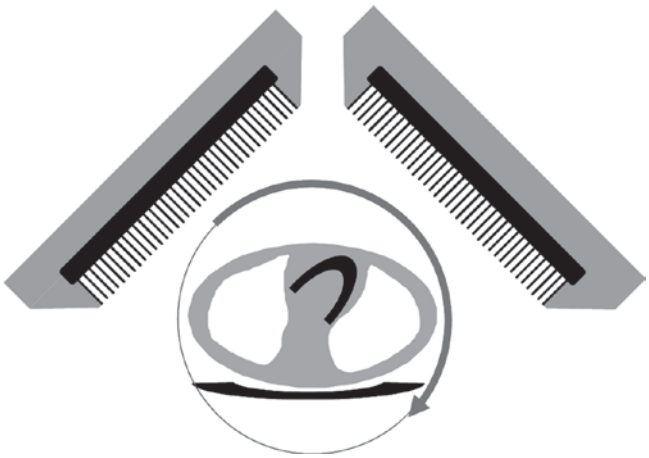

Fig. 3.1 Configuration of a single photon emission computed tomography (SPECT) system. Two gamma camera detector heads, equipped with collimators, rotate in a semi-circular fashion around the chest and create images in multiple positions ("step-and-shoot")

During acquisition, the system creates "raw" data that consist of multiple planar projection images at different angles. As for any other tomographic acquisition, the raw data must be transformed into tomographic images for subsequent analysis and interpretation. This process, known as reconstruction, produces an image that reflects, as closely as possible, the tracer's distribution in the organ/tissue of interest at the time of acquisition. This is achieved using either the standard filtered back-projection (FBP) or novel iterative reconstruction algorithms. The process of reconstruction is then followed by filtering to reduce image noise. The resulting tomographic data sets are reorientated along the left ventricular (LV) short and long axes to facilitate review of myocardial tracer distribution and comparison of rest and stress studies (Fig. 3.2a). Software tools have been developed which employ contour detection algorithms and circumferential profiles to create polar maps from the tomographic images.[5–8] These polar maps are a two-dimensional display of the three-dimensional (3D) tracer distribution throughout the myocardium which facilitate comparison of patient data with normal databases as well as semi-quantitative analysis of defect sizes (Fig. 3.2b).

Electrocardiographic (ECG) Gating

ECG-gated acquisition of perfusion SPECT studies has become a standard procedure, which has two major advantages over non-gated acquisition: First, ECG-gating allows quantitative measurement of LV ejection fraction (EF) and volumes, as well as regional evaluation of LV wall motion.[9] Second, ECG-gating may improve the diagnostic accuracy of perfusion imaging in the event of attenuation artefacts.[10]

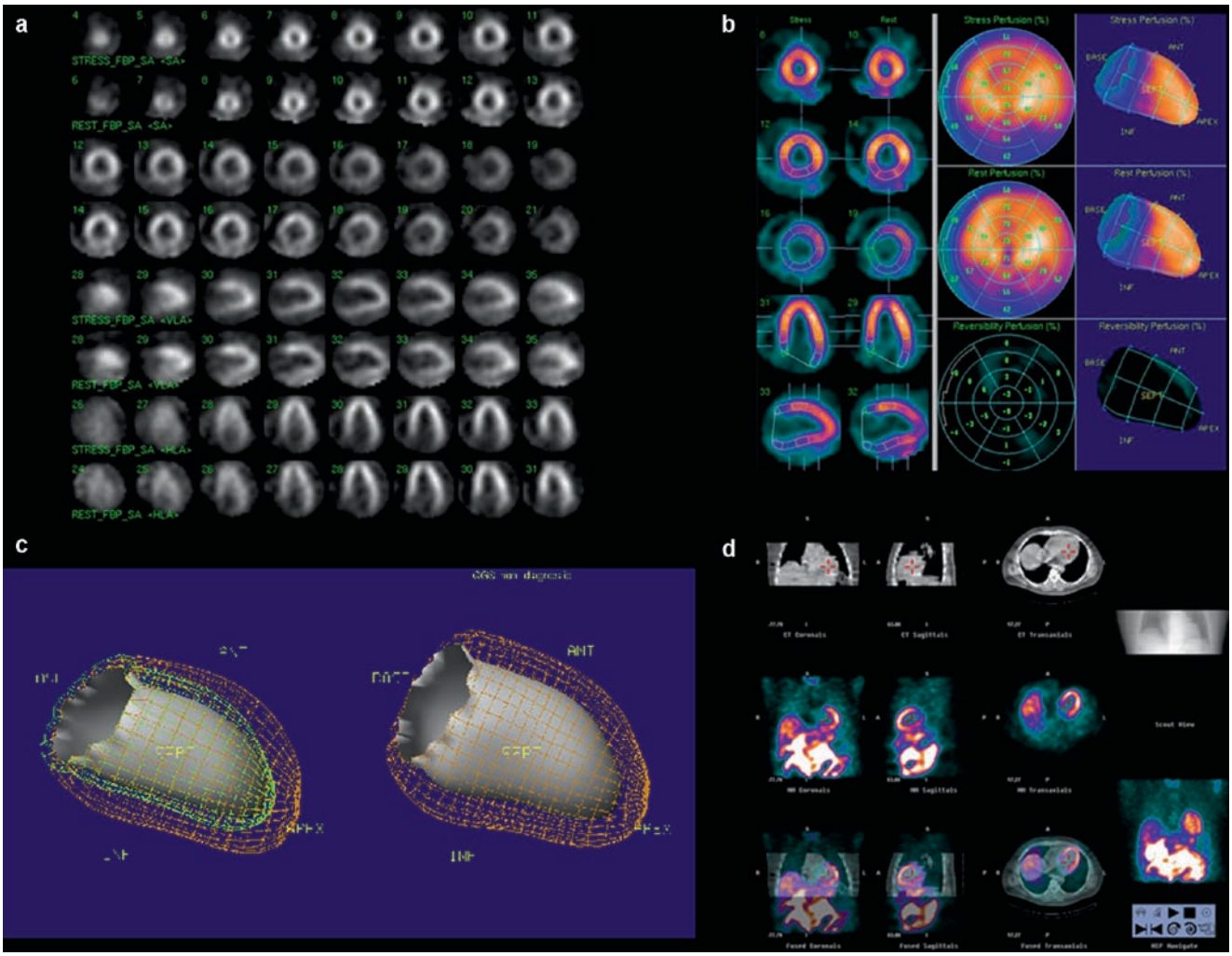

Fig. 3.2 State-of-the-art myocardial SPECT imaging. **(a)** Display of matched stress (*rows 1, 3, 5, 7*) and rest (*rows 2, 4, 6, 8*) tomographic images, reangulated along the short and long axes of the *left* ventricle for visual analysis. **(b)** Creation of two- (*middle column*) and three-dimensional (3D) polar maps (*right column*) using software-assisted detection of myocardial contours (*left column*), for semi-quantitative analysis of perfusion defects. **(c)** Three-dimensional display of endocardial contours throughout the cardiac cylce from gated SPECT acuisition, for visual and quantitative analysis of left ventricular (LV) function. **(d)** Creation of density maps from transmission images, for attenuation correction of SPECT data

Such artefacts may appear as apparently irreversible perfusion defects, but normal regional wall motion prevents a wrong interpretation, such as scar tissue.

It should be noted that functional gated SPECT acquired after stress shows the LV at rest, although sometimes, transient wall motion abnormality and possibly dilated LV and reduced EF (myocardial stunning) may persist and be observed during the acquisition phase, up to 90 min or even later after the resolution of ischaemia.[11]

For ECG-gating, the patient should have a fairly regular heart rhythm. The cardiac cycle is usually divided into 8, and sometimes into 12 or 16 gates (time bins). Based on the relative timing after the R-wave, counts in each projection image are then accumulated for each of the gates. For reproducible functional analysis, software products are available which semi-automatically generate 3D myocardial contours throughout the cardiac cycle. Volumetric data from the contours can then be used for 3D display and calculation of quantitative global parameters (Fig. 3.2c).

Attenuation Correction

Attenuation of radiation in the body can lead to a non-uniform reduction in the apparent activity in the myocardium and to the introduction of artefacts in the images. Additionally, scatter of radiation both within the body and in the detector degrades the image contrast and potentially affects the accurate quantification of activity and relative distribution of perfusion. Finally, resolution decreases with distance from the

collimator face, which can alter the apparent distribution of activity in the myocardium.

Among those factors, attenuation is considered to have the most significant effect. The amount of attenuation in a clinical study depends on the type of tissue (soft tissue, bone, or lung), the energy of the radiation, and the thickness of the body. Hence, compensation for soft-tissue attenuation requires exact knowledge of the attenuation characteristics for each patient. While many schemes for the generation of the attenuation characteristics have been reported,[12] nowadays the attenuation map of a patient is usually generated by transmission imaging, using either an external radiation source or the X-ray CT in hybrid systems (Fig. 3.2d). Software and hardware methods used in these systems vary significantly from one vendor to another, but it has been documented for several systems that attenuation correction improves image quality and image interpretation.[13–15]

Importantly, failure to incorporate effects of scatter into the attenuation compensation technique will result in introduction of artefacts so that a combination of attenuation and scatter correction is necessary. Additional corrections for depth-dependent resolution changes are being developed, but not yet broadly implemented.

Systematic Data Analysis

For adequate interpretation of myocardial perfusion images, a systematic visual review of raw data and reconstructed images on a computer screen is warranted.[16] The system of reviewing comprises several reviewing levels. First, raw projection data are reviewed to identify motion artefacts and assess tracer distribution in organs other than the heart. Next, reorientated tomographic images are reviewed without and, if available, with attenuation/scatter compensation and gated cine data. Then, software-derived semi-quantitative data are reviewed and used to strengthen the visual impression of tomographic image readout. Finally, the impression of the image readout is integrated with stress performance and with clinical data and should be reported in a standardized format.

PET

There are multiple methodological differences between conventional SPECT and PET. Most importantly, PET scanners have a different geometry and a different detection principle. Multiple corrective algorithms are routinely applied to yield images of absolutely quantitative tracer distribution within the body. In addition, much shorter-lived positron emitting radioisotopes are being utilized which increase the flexibility of imaging protocols and biologic targets, but at the same time increase complexity and limit availability of the methodology.

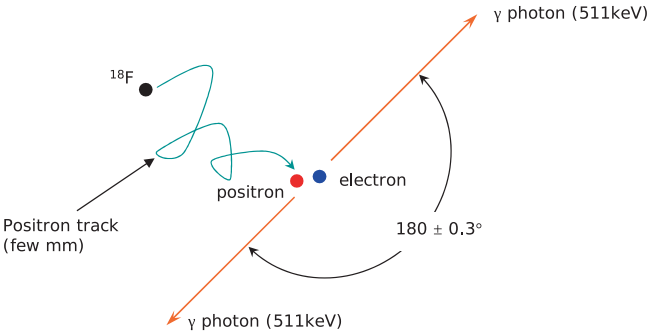

Fig. 3.3 Schematics of the annihilation process

Acquisition

The goal of PET scanning is to produce a 3D image volume, which is an accurate map of the distribution of tracer in the body. To allow absolute quantification, a series of such volumes is normally generated over time to describe the time–activity curves (TAC) and investigate the kinetics of tracer uptake and release from different tissues and blood.

Cyclotrons accelerate protons or deuterons, which interact with target atoms to produce "proton-rich" radioisotopes. During decay, a proton gets converted to a neutron and a positron is emitted. Under the influence of surrounding atomic electrons, the positron is slowed down until interaction with an electron results in the annihilation of both particles, and two photons are emitted (each with energy of 511 keV) in practically opposite directions (Fig. 3.3). Compared with radionuclides emitting single gamma-ray photons, the emission of pairs of 511 keV annihilation photons gives PET imaging higher detection efficiency, better uniformity of spatial resolution, and easier correction for attenuation (scattering) of photons in the tissue (Fig. 3.4).

Attenuation

In PET, the probability to detect a coincidence along a line, indicating that none of the two photons forming the coincidence have interacted with the matter, is independent of the position of annihilation along the detected line-of-response (LOR). This property is different from SPECT and is utilized to correct for photon attenuation in a robust manner.

Coincidence Detection

If photons interact with the detectors ring within a specified time period, known as the coincidence window, then an event is recorded and is termed a prompt coincidence. True coincidences, formed by the two photons detected within the coincidence window without having undergone any interaction

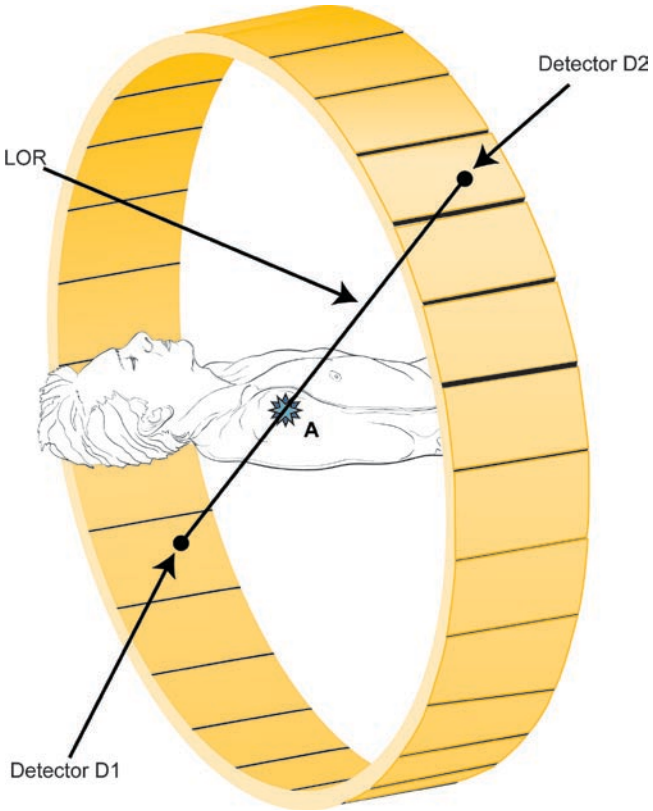

Fig. 3.4 Representation of the detection of the two emitted photons. Two photons arise from annihilation at point *A* and impinge on detectors *D1* and *D2*. A circular ring of individual detectors is shown here, but the same principles apply for other position-sensitive systems such as rings of planar detectors or rotating gamma cameras. Imposing a coincidence condition on the detection process, such that an event is only recorded when signals are produced from both detectors simultaneously, effects an automatic electronic collimation and enables the annihilation to be localized to the line *D1–D2*, conventionally termed a line-of-response (*LOR*). The width of the LOR is the intrinsic spatial resolution of the detectors. It can also readily be seen that the resolution will be quite constant along the LOR

with matter, need to be separated from scattered and random coincidences (Fig. 3.5).

3D Imaging

Figure 3.6 shows an axial section through a multi-ring PET tomograph. The 3D mode makes maximum use of the detectors available within all rings, as well as the same ring, allowing the use of lower doses of radioactivity. This seems the obvious solution, but registration of scattered and random coincidences complicates the situation and often leads to a retreat from 3D acquisition to a more conservative 2D mode. In the latter, tungsten annuli called Septa are placed between the detector rings.

Data Correction

To exploit the potential of PET to provide quantitative data a number of corrections need to be carried out.

Normalization

The geometry of a PET system introduces variation in the detection sensitivity. Normalization corrects this by measuring the count rate for each LOR using a source with predefined radioactivity.

Dead Time

The response time of a detector system is finite. Dead time is the period when a detector is unable to record an event.[17, 18]

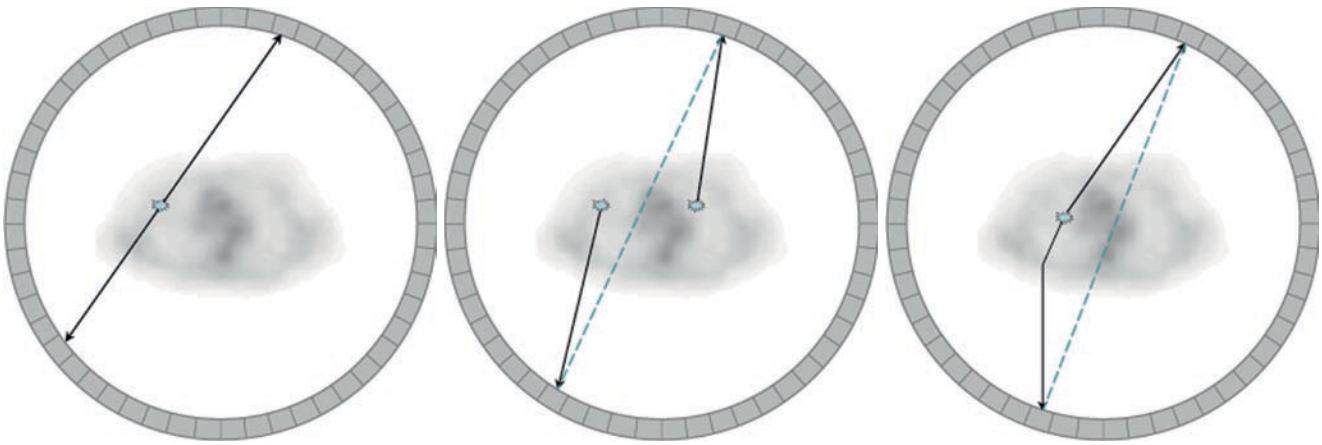

Fig. 3.5 Representation of the different types of coincidences. True coincidence (*left*), random coincidence (*middle*), scattered coincidence (*right*)

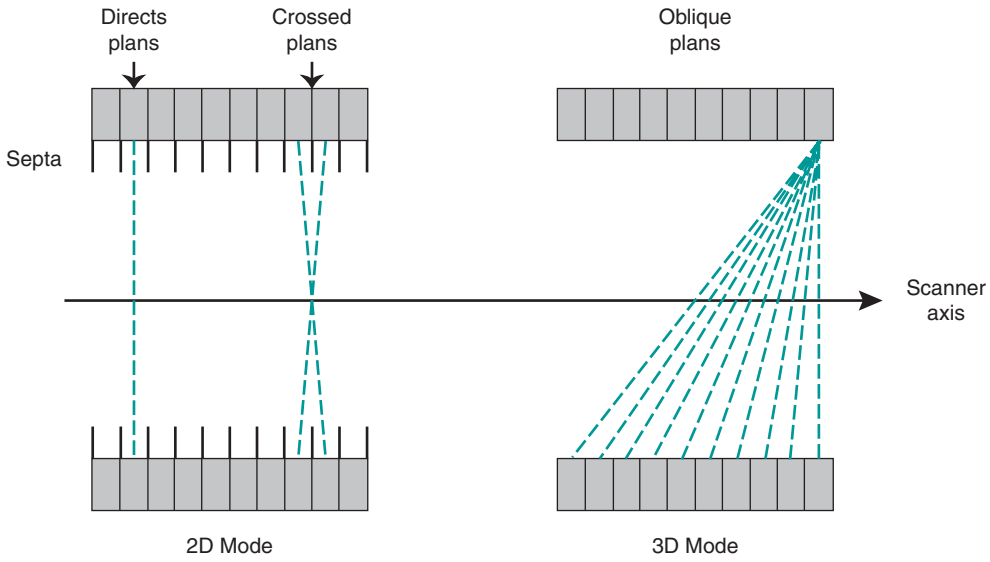

Fig. 3.6 Comparison of the two acquisition modes permitted by some positron emission tomography (PET) systems. In 2D mode, because of the use of lead septa reducing the transaxial acceptance angle, the device only detects photons in the direct or crossed plans, whereas in 3D mode, all the planes, direct or oblique, can be recorded

This might be because the electronics remains in a "busy" phase or when more than one photon strikes a detector within its resolving time and is rejected.

Attenuation

Traditionally, an external positron emitting source has been used to measure the attenuating factor before the administration of radioactivity.[19–21] This process results in an image representing the distribution of the density of the patient's organs. With the advent of hybrid PET-CT, a CT scan provides a substitute for the conventional PET transmission scan.[22] The duration of the CT scan is much less than the PET transmission scan, but a problem to overcome is the movement of the patient (cardiac, respiratory, and other voluntary and involuntary), resulting in misalignment of CT and PET.

Scattered Coincidences

Some correction methods employ mathematical modelling (e.g. using data from point sources in scattering media) to deconvolve scattered events from the total signal.[23] In the chest, however, scatter distribution is complex owing to the range of tissue densities. An alternative, but more challenging, approach is that of calculation of scattered photon distribution from raw image data, a process that can be repeated iteratively until satisfactory accuracy is achieved.[24] It should not be assumed that scatter correction methods are perfect and developments and improvements are still being actively pursued.

Random Coincidences

In cardiac scanning, the correction for and treatment of random coincidence events is very important. The most commonly used method estimates randoms using a delayed coincidence circuit,[25] which is employed with a temporal delay so that no true coincidences will be registered. Randoms are then estimated and can be subtracted online from the prompt events or stored separately for later processing.

Motion

A very important consequence of the high-timing resolution made possible by the data acquisition in list mode is that it makes effective motion correction possible. ECG-gating is a standard procedure for use with PET, and studies have also been carried out on respiratory gating, making feasible the monitoring of and the correction for both cardiac and respiratory movements of the patient.[26, 27]

Partial Volume

Despite the technological developments in PET, basic physical characteristics mean that its spatial resolution is limited and the signal in a particular region will be "diluted" due to the presence of surrounding tissues – there will be a "spill-over" of radioactivity between adjacent structures. The same is true for SPECT, which usually has an approximately two-fold lower spatial resolution compared with PET. Combination of transmission and emission data has been used to correct for this effect in the myocardium and PET, and CT or MRI images have been combined to enable corrections.[28]

Current Imaging Procedures and Applications

SPECT

SPECT is widely used for the clinical workup of suspected or known CAD. Its diagnostic and prognostic usefulness is supported by a large body of evidence.[1] Most importantly, SPECT-derived information is utilized as a gatekeeper to invasive procedures and as a guide for further clinical decision-making. Assessment of myocardial perfusion and function are the two major clinical applications.[16, 29]

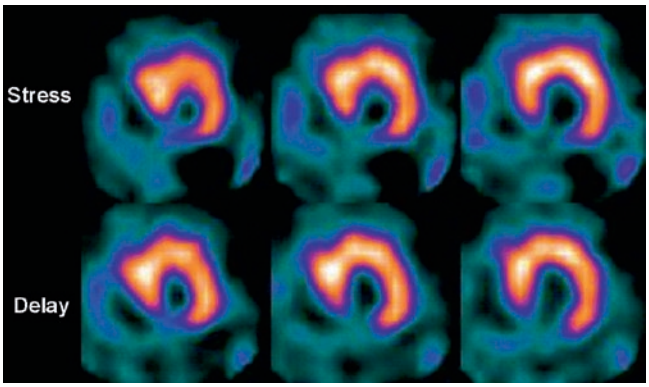

Fig. 3.7 Mid-ventricular short-axis myocardial perfusion SPECT images using ^{201}T1 in a patient with history of inferior wall myocardial infarction. Note the perfusion defect with lack of redistribution on delayed images in inferior wall, indicating absence of myocardial viability

Myocardial Perfusion

For perfusion imaging, thallium-201 (^{201}Tl)- and two technetium-99m (^{99m}Tc)-labelled radiopharmaceuticals (sestamibi and tetrofosmin) are commercially available.

^{201}Tl decays by electron capture to mercury-201, emitting 65–80 keV X-rays (88% abundance) and gamma photons of 135 and 167 keV (12% abundance). Following intravenous injection, first-pass extraction by the myocardium is 88% and uptake mostly occurs via the sodium–potassium ATPase. The uptake proportionally increases with perfusion over a relatively large range.[30] After initial uptake, prolonged retention depends on the sarcolemma integrity and hence on tissue viability. ^{201}Tl redistributes over several hours, thus allowing delayed images to be acquired that are independent of perfusion and reflect viability. ^{201}Tl has been used clinically for more than two decades, but does have certain limitations such as the long half-life associated with high radiation burden, low photon energy resulting frequently in attenuation artefacts, and low injected activity contributing to a low signal-to-noise ratio.

After an i.v. injection of ^{201}Tl at stress, the radiotracer is distributed in the myocardium according to myocardial perfusion, and SPECT images are obtained early after injection. Subsequently, redistribution images are acquired 2–4 h later which reflect the baseline perfusion and viability.[16] Comparison of stress and redistribution images allows for the identification of relative regional stress-induced ischaemia, while a fixed defect may indicate myocardial necrosis (Fig. 3.7). It has been observed that redistribution may be incomplete at 4 h and a second injection of ^{201}Tl or delayed imaging can be performed for a more accurate assessment of myocardial viability.[31]

Two ^{99m}Tc-labelled perfusion tracers, sestamibi and tetrofosmin, are commercially available. The higher energy of ^{99m}Tc- generally leads to better quality images (because of less attenuation and scatter) compared with ^{201}Tl. Moreover, the short half-life permits much higher activities to be administered, giving better counting statistics (Fig. 3.8) and results in lower radioactivity doses compared with ^{201}Tl. Furthermore, the use of ^{99m}Tc-labelled perfusion tracers allows LV ECG-gating or first-pass imaging, which provide additional functional information. However, tracer kinetic properties are somewhat inferior when compared with ^{201}Tl.[32] Uptake of

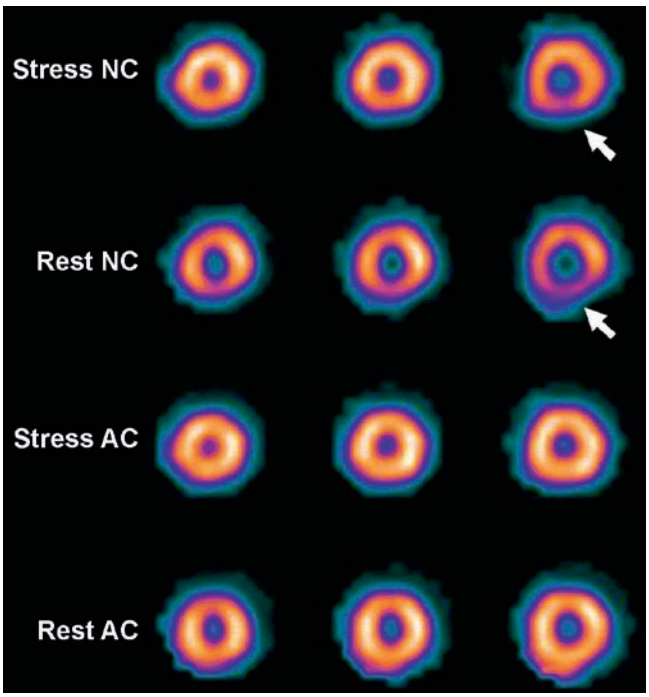

Fig. 3.8 Non-corrected (NC) and attenuation corrected (AC) mid-ventricular short axis myocardial perfusion SPECT images using ^{99m}Tc-sestamibi in an individual with suspected coronary artery disease (CAD). Note the inferior wall defect in NC images (*arrows*) which resolves after AC, indicating the presence of artefact rather than disease

both ^{99m}Tc-labelled tracers as a function of myocardial perfusion is less avid, and defects may be less profound.

^{99m}Tc-sestamibi is a cationic complex, which diffuses passively through the capillary and cell membrane, although less readily than ^{201}Tl, resulting in lower immediate extraction. Within the cell, it is trapped in the mitochondria. Retention is based on intact mitochondria, reflecting viable myocytes.[33, 34] Tetrofosmin is also cleared rapidly from the blood and its myocardial uptake is similar to that of sestamibi. Hepatic clearance is slightly more rapid than in the case of sestamibi.[35, 36] However, for both ^{99m}Tc -labelled tracers, splanchnic uptake and excretion are markedly higher than for ^{201}Tl, which may occasionally complicate assessment of the inferior LV wall. Importantly, the tracer molecules remain within cardiac myocytes and do not redistribute so that two injections are necessary to obtain stress and rest images. Two-day, same-day stress–rest or same-day rest–stress imaging protocols have been established.[37, 38]

SPECT imaging usually begins 30–60 min after injection to allow for hepatobiliary clearance. Longer delays are required for resting images and for stress with vasodilators alone, because of the risk of higher subdiaphragmatic activity. For improved assessment of myocardial viability, resting injections can be given following nitrate administration to avoid under-estimation in areas with reduced resting perfusion.[39]

Finally, a dual-isotope protocol, consisting of rest ^{201}Tl injection, followed immediately by stress and a ^{99m}Tc-compound injection, has been employed.[40] This shortens the duration of a full stress rest or stress redistribution protocol, and takes advantage of the superior ability of ^{201}Tl to assess myocardial viability at the same time as using technetium to provide functional information from ECG-gated imaging. Disadvantages are the high radiation burden of the two tracers, and the fact that changes between stress and rest mean that images of different tracers with different technical characteristics are compared.

Ventricular Function

Assessment of LV function and volumes is not only important for the assessment of prognosis in CAD. Addition of gating has also been shown to improve diagnostic and prognostic accuracy of myocardial perfusion SPECT.[10, 41] Additionally, assessment of the function of the right ventricle (RV) is recognized to be important in some diseases such as arrhyhmogenic RV and pulmonary hypertension. Finally, determination with equilibrium radionuclide ventriculography of LV-EF is recognized as one of the methods-of-choice for monitoring of cardiotoxicity of cytotoxic anti-cancer drugs.[42]

Functional radionuclide cardiac studies include several techniques, and ECG-gating with R-wave triggering is a key point in these methods.

First-pass radionuclide ventriculography comprises a short sequence of cardiac cycles acquired during the transit of a bolus of any radionuclide through the heart. It can be performed at rest and during stress,[43] provides high target to background ratio with temporal separation of the RV and LV, but imaging is possible in only one projection, and tomographic SPECT images cannot be obtained.[29]

Equilibrium radionuclide ventriculography is performed after ^{99m}Tc-labelling of red blood cells using different techniques.[29] It provides high-quality planar images and may even be performed as a SPECT study (Fig. 3.9) for accurate separation of RV and LV, and for accurate assessment of regional wall motion.[44]

Finally, as mentioned earlier, SPECT (and PET) perfusion studies can be acquired in ECG-gated mode in order to obtain parameters of LV function on top of myocardial perfusion.[45] This technique usually employs a smaller number of time bins than equilibrium radionuclide ventriculography, and is less well established for the assessment of diastolic function, but multiple studies have documented the usefulness to improve diagnostic accuracy or obtain incremental prognostic information.

PET

In contrast to SPECT, which is the clinical mainstay for the diagnostic workup of CAD by nuclear imaging techniques, PET offers deeper insights into myocardial pathophysiology and pathobiology. Although PET has the potential to probe a number of complex functions (including genes), the current

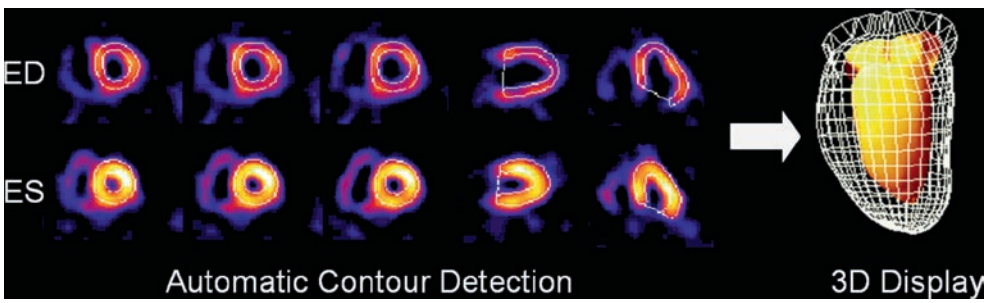

Fig. 3.9 Gated myocardial perfusion SPECT. Automated contour detection (*left*) is employed for creation of 3D displays (*right*) to review wall motion, volumes, and ejection fraction (EF). *ED* enddiastolic frame, *ES endsystolic frame*

clinical applications of PET imaging in cardiology can be divided into three main categories: studies of regional myocardial blood flow, metabolism, and pharmacology.

Myocardial Blood Flow (MBF)

Mainly three tracers are used for the measurement of MBF using PET: ^{15}O-labelled water ($H_2{}^{15}O$),[46, 47] ^{13}N-labelled ammonia ($^{13}NH_3$),[48–51] and the cationic potassium analogue, ^{82}Rubidium (^{82}Rb).[52]

Although kinetic models[53,54] have been proposed for quantification of MBF using ^{82}Rb,[49] these are limited by the dependence of the myocardial extraction of this tracer on the prevailing flow rate and myocardial metabolic state.[55] Furthermore, the high positron energy of ^{82}Rb results in relatively poor image quality and reduced spatial resolution due to its long positron track.

For $H_2{}^{15}O$ and $^{13}NH_3$ tracer kinetic models have been successfully validated in animals against the radiolabelled microsphere method over a wide flow range[46, 47, 51, 56]. The values of MBF determined in normal human volunteers using both tracers either at rest or during pharmacologically induced coronary vasodilatation are similar.[46, 51] Recent advances in image processing[57] have enhanced the quality of myocardial $H_2{}^{15}O$ images (Fig. 3.10) to match the quality of $^{13}NH_3$ images. Both tracers have short physical half-lives (2 and 10 min, respectively), which allow repeated measurements of MBF in the same session.[58]

The major regulatory site of tissue perfusion is at the level of arterioles of less than 300 μm diameter (i.e. the microcirculation). Information on this section of the coronary circulation in man in vivo can only be obtained indirectly by measuring parameters such as MBF and coronary flow reserve (CFR), i.e. the ratio of maximal MBF following pharmacologically induced coronary vasodilatation to resting MBF (Figs. 3.11 and 3.12).

The use of PET has highlighted the effects of age,[46, 51, 59, 60] gender,[61] and sympathetic tone[62] on MBF. The accuracy of PET has been used to detect impairments of MBF in asymptomatic subjects with cardiovascular risk factors,[63, 64] in the relatives of patients with CAD, in whom coronary arteriography is not justifiable on the basis of family history alone,[65] and in diabetic patients without symptoms of cardiac disease.[66]

In patients with CAD, the measurement of CFR is useful for the assessment of the functional significance of coronary stenoses.[67] In addition, PET is particularly effective in those circumstances where the CFR is diffusely (and not regionally) blunted, e.g. in patients with hypertrophic or dilated cardiomyopathy. The improved spatial resolution of the latest generation of 3D PET cameras has allowed the quantification of the trans-mural distribution of myocardial blood flow in patients with LV hypertrophy secondary to aortic stenosis, demonstrating a more significant reduction of subendocardial CFR which is directly related to the reduction of the aortic valve area.[68]

Myocardial Metabolism

In the post-absorptive state, the heart relies mainly on the oxidation of free fatty acid (FFA) as its main source of high-energy phosphates while glucose uptake and oxidation are low. In the fed state, glucose uptake is high and accounts for

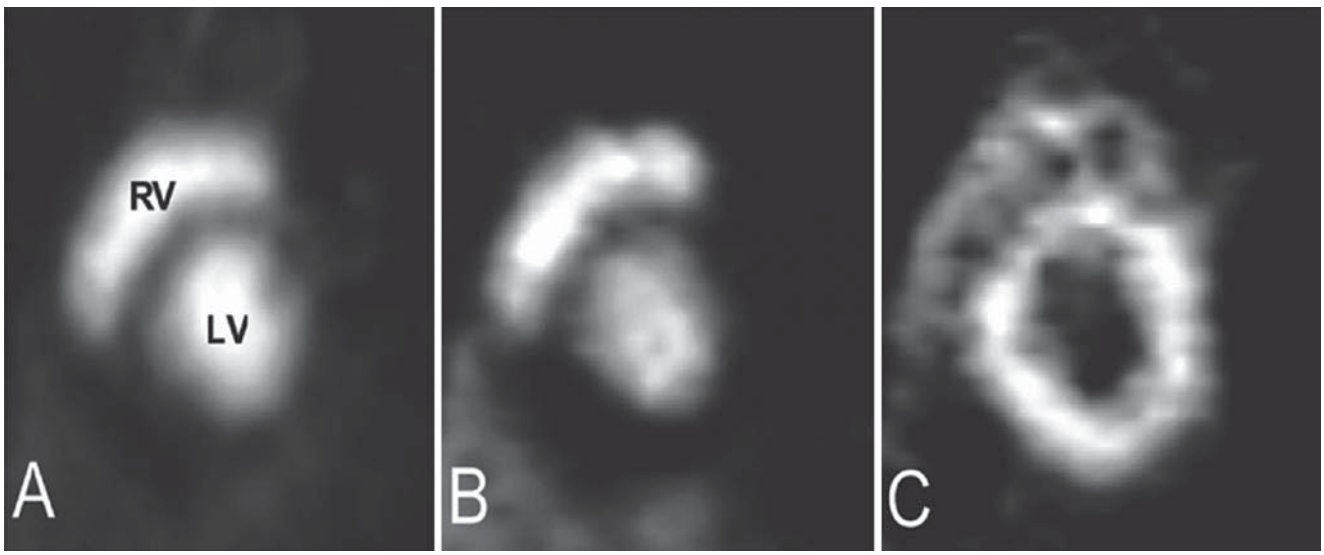

Fig. 3.10 Short-axis images obtained from one representative study showing the blood pool (**a**) measured with C^{15}O, which labels the erythrocytes through the formation of carboxyhaemoglobin, and the distribution of $H_2{}^{15}O$ separated in a blood (**b**) and myocardial tissue (**c**) component. (**b**) and (**c**) are both calculated by means of factor analysis. From.[57] *RV* right ventricle; *LV* left ventricle

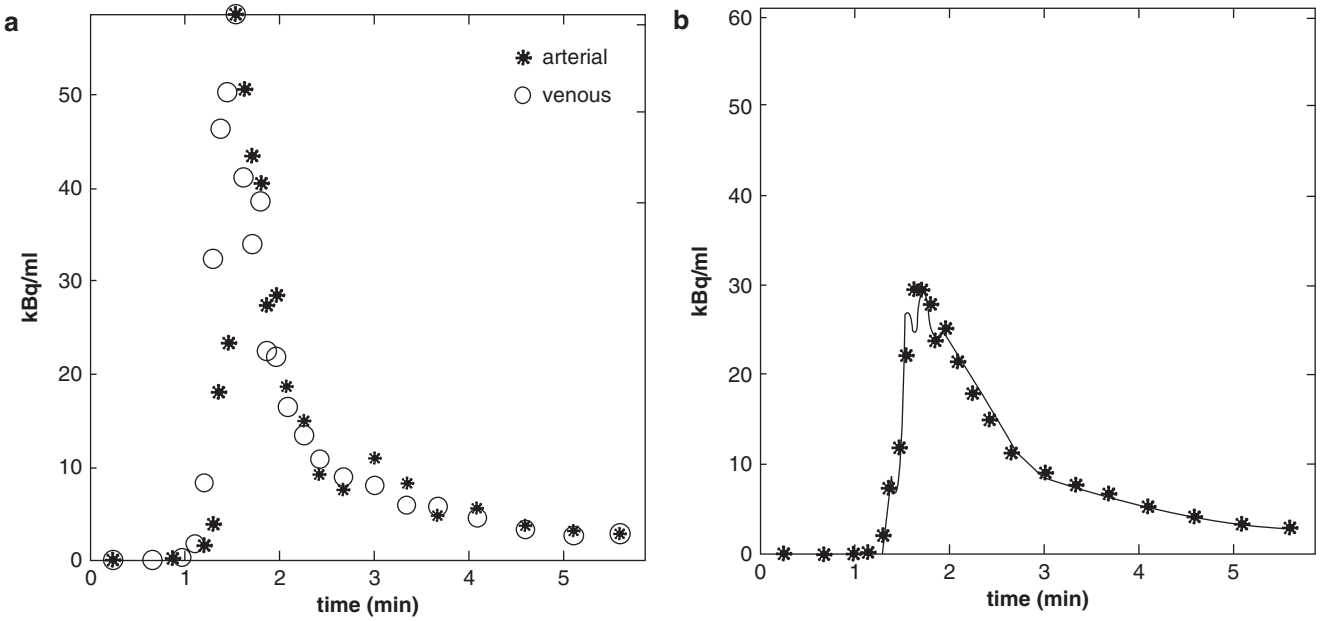

Fig. 3.11 **(a)** Blood (arterial and venous) and **(b)** tissue time–activity curves (TAC) measured from the dynamic scan sequence obtained after injection of $H_2{}^{15}O$. The arterial and venous TAC were obtained from regions of interest (ROI) drawn in the right and left ventricle, while the tissue TAC was obtained from an ROI placed in LV myocardium. These data are then used to compute myocardial blood flow (MBF) in mL/min/g

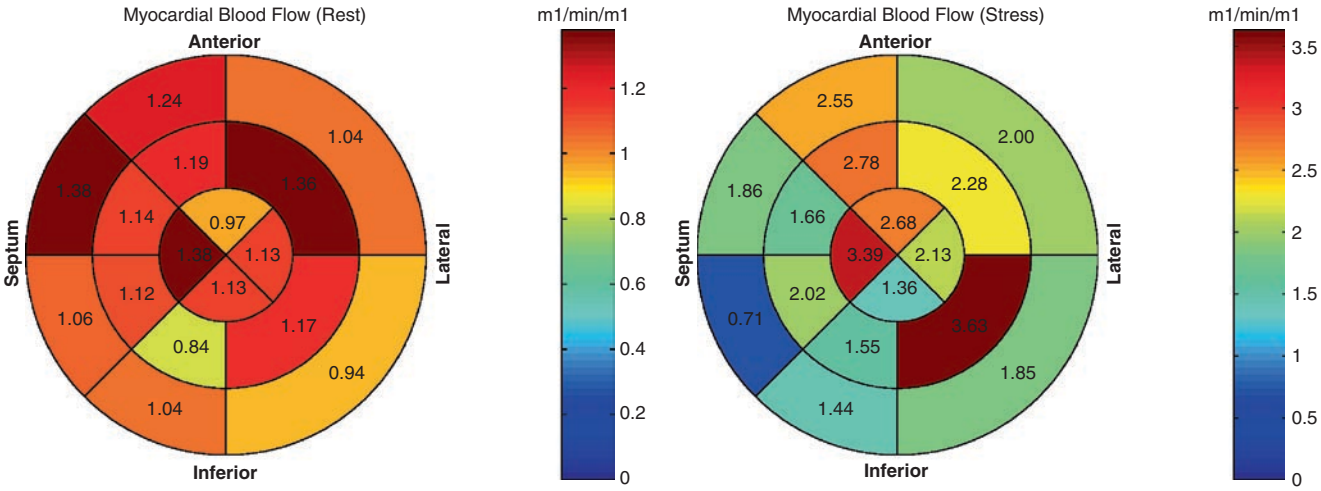

Fig. 3.12 Polar maps of MBF measured with $H_2{}^{15}O$ at rest and during adenosine stress in a patient with significant disease of the *left* anterior descending and *right* coronary arteries

virtually all the concurrent oxygen uptake.[69] The factors that regulate myocardial substrate utilization are complex and depend, in addition to substrate concentration, on the action of different hormones. Insulin that stimulates myocardial glucose uptake and utilization also inhibits adipose tissue lipolysis, so that during hyperinsulinemia, the circulating levels of FFA are low.[69] On the other hand, catecholamines decrease rather than increase glycolysis in the heart, together with a greatly increased uptake and oxidation of FFA.[69] Myocardial utilization of carbohydrates is also affected by cardiac workload, with oxidation of carbohydrates accounting for more than 50% of energy produced during conditions of maximal stress.[70] Finally, glucose utilization is increased during conditions of reduced oxygen supply; under these circumstances, exogenous glucose uptake and glycogen breakdown are increased, glycolysis is stimulated, and ATP can be produced from the anaerobic catabolism of glucose with the concomitant formation of lactate.[69]

To measure the flow through this pathway during normoxic and ischaemic conditions, PET imaging has been performed after i.v. administration of the natural FFA palmitate labelled with ^{11}C (^{11}C-palmitate).[71] Furthermore, ^{11}C-labelled acetate has been advocated as a tracer of tricarboxylic acid cycle activity[72] and used as an indirect marker of myocardial oxygen consumption (MVO_2) by PET in both experimental animals[73, 74] and humans.[75–77]

The utilization of exogenous glucose by the myocardium can be assessed using PET with ^{18}F-2-fluoro-2-deoxyglucose (FDG).[78] FDG is transported into the myocyte by the same trans-sarcolemmal carrier, as glucose and is then phosphorylated to FDG-6-phosphate by hexokinase. This is essentially a unidirectional reaction, as no glucose-6-phosphatase (the enzyme that hydrolyzes FDG-6-phosphate back to free FDG and free phosphate) has yet been identified in cardiac muscle.[78] Thus, measurement of the myocardial uptake of FDG is proportional to the overall rate of trans-sarcolemmal transport and hexokinase-phosphorylation of exogenous (circulating) glucose by heart muscle, but it does not provide information about the further intracellular disposal of glucose.

A number of kinetic modelling approaches have been used for the quantification of glucose utilization rates using FDG.[79] The major limitation of these approaches is that quantification of glucose metabolism requires the knowledge of the lumped constant (LC), a factor which relates the kinetic behavior of FDG to naturally occurring glucose in terms of the relative affinity of each molecule for the trans-sarcolemmal transporter and hexokinase. Unfortunately, the value of the LC in humans under different physiologic and pathophysiologic conditions is not known, thus making true in vivo quantification of myocardial metabolic rates of glucose very difficult.[80] Still, the quantification of the uptake of FDG (particularly if obtained under standardized dietary conditions such as during insulin clamp[81]) allows comparison of absolute values from different individuals and may help to establish the absolute rates of glucose utilization (in FDG units) in normal and pathologic myocardium.

Myocardial Pharmacology

Different tracers have been used to study the pre-synaptic sympathetic terminals: ^{18}F-labelled fluorometaraminol,[82, 83] ^{11}C-labelled hydroxyephedrine (^{11}C-HED),[84] and ^{11}C-labelled epinephrine,[85] which compete with endogenous noradrenaline for the transport into the pre-synaptic nerve terminal.

Several beta-blocker drugs have been labelled with ^{11}C to act as radioligands for the study of post-synaptic β-adrenoceptor.[86] ^{11}C-(S)-CGP 12177 is a non-selective β-adrenoceptor antagonist, which is particularly suited for PET studies owing to its high affinity and low lipophilicity, thus enabling the functional receptor pool on the cell surface to be studied.[87] Studies in patients have demonstrated diffuse downregulation of β-adrenoceptor density in hypertrophic cardiomyopathy[88, 89] and in congestive heart failure.[90–92]

In addition to studies of the sympathetic nervous system, the density and affinity constants of myocardial muscarinic receptors can be evaluated non-invasively with ^{11}C-MQNB (methylquinuclidinyl benzilate), a specific hydrophilic antagonist, in both experimental animals[93] and in man.[94, 95] In patients with congestive heart failure, mean receptor concentration (Bmax) was significantly higher compared with normal subjects,[94] a clear indication that congestive heart failure is associated with an upregulation of myocardial muscarinic receptors paralleling the downregulation of β-adrenoceptors.

Future Developments

Fast Acquisition

Present clinical, scientific, and financial needs require further improvements in hardware and software to continue the success of myocardial perfusion imaging (MPI) SPECT. It is difficult to realize improvements with the imaging hardware and software used in most nuclear imaging laboratories today. The basic SPECT camera design has been introduced decades ago.[96] Recently, the notion that SPECT acquisition can be optimized for more rapid cardiac acquisition, higher patient throughput, and potentially improved image quality has led to several advancements in imaging hardware and software.[97] The Anger Camera general-purpose design has been replaced by some manufacturers with systems with multiple detectors focussed on the heart yielding 5–10 times the sensitivity of conventional SPECT. Some novel designs also use advanced electronic detectors with superior energy resolution. Furthermore, there are significant innovations in reconstruction software incorporated into these newly designed systems that take into account the true physics of the SPECT reconstruction geometry to gain at least a factor of 2 in sensitivity. Some of these new systems are well suited for dynamic applications that may facilitate measurements of CFR. It is expected that SPECT nuclear cardiology procedures with these novel techniques will be faster and more accurate, while radiotracer dose and thus radiation exposure can be reduced.

Hybrid Imaging

Hybrid imaging is the merging of nuclear imaging systems with an X-ray CT. Based on its success in oncology, the

hybrid PET-CT technique is now the standard for all PET imaging systems. Likewise, SPECT is increasingly becoming SPECT-CT. Hybrid systems are increasingly equipped with fast, multi-slice CT components, opening up their application to multimodality, single-camera cardiac imaging. One advantage of these hybrid imaging systems is the feasibility to correct soft-tissue attenuation artefact with a brief CT scan before or after emission imaging.[98, 99] More importantly, the hybrid multi-slice CT system can provide comprehensive assessment of cardiac and coronary morphology in addition to the nuclear study.[100] The benefits and prospects of this new generation of scanners will be discussed in separate chapters of this textbook.

Molecular Imaging

The tracer principle – the attachment of a radioisotope to a biomolecule in order to follow its distribution throughout the body – is attractive not only for the imaging of physiologic mechanisms such as perfusion or contractile function. It is especially suitable for non-invasive detection of biologic processes at the level of tissue and cells.[3, 101–103] Myocardial metabolism and sympathetic innervation have emerged as the first applications of clinical biologic/molecular cardiac radionuclide imaging. While those are increasingly entering the clinical stage, a broad spectrum of other tracers for specific biologic targets in the cardiovascular system is being evaluated on the preclinical level. These targets include the renin–angiotensin system, integrins, matrix metalloproteinases, cell death, reporter genes, and transplanted stem cells. The goal is the visualization of key mechanisms involved in subjects of ongoing basic cardiovascular science, including early disease development and novel therapeutic interventions. It is expected that molecular imaging, early disease detection, and molecular therapy will progress hand-in-hand from the preclinical to the clinical level in the future. Radionuclides are very likely to play a key role in this paradigm.

Conclusion

Radionuclide imaging techniques are well established for imaging of myocardial function, perfusion, viability, and biologic mechanisms. While SPECT is the clinical workhorse for the workup of CAD, PET is an advanced technique that is utilized to obtain quantitative, more specific insights into disease mechanisms. Advances in imaging methodology aim at more rapid, more accurate acquisition and hybrid systems. Additionally, the advent of various molecular-targeted probes is expected to result in novel clinical applications of nuclear cardiology in the future.

References

1. Marcassa C, Bax JJ, Bengel F, et al Clinical value, cost-effectiveness, and safety of myocardial perfusion scintigraphy: a position statement. *Eur Heart J*. 2008;29:557–563
2. Le Guludec D, Lautamaki R, Knuuti J, Bax JJ, Bengel FM. Present and future of clinical cardiovascular PET imaging in Europe-a position statement by the European council of nuclear cardiology (ECNC). *Eur J Nucl Med Mol Imaging* 2008;35:1709–24
3. Higuchi T, Bengel FM. Cardiovascular nuclear imaging: from perfusion to molecular function: non-invasive imaging. *Heart*. 2008;94:809–816
4. Segall GM, Davis MJ. Prone versus supine thallium myocardial SPECT: a method to decrease artifactual inferior wall defects. *J Nucl Med*. 1989;30:548–555
5. Ficaro EP, Lee BC, Kritzman JN, Corbett JR. Corridor4DM: the Michigan method for quantitative nuclear cardiology. *J Nucl Cardiol*. 2007;14:455–465
6. Klein JL, Garcia EV, DePuey EG, et al Reversibility bull's-eye: a new polar bull's-eye map to quantify reversibility of stress-induced SPECT thallium-201 myocardial perfusion defects. *J Nucl Med*. 1990;31:1240–1246
7. Nekolla SG, Miethaner C, Nguyen N, Ziegler SI, Schwaiger M. Reproducibility of polar map generation and assessment of defect severity and extent assessment in myocardial perfusion imaging using positron emission tomography. *Eur J Nucl Med*. 1998;25:1313–1321
8. Slomka PJ, Nishina H, Berman DS, et al Automated quantification of myocardial perfusion SPECT using simplified normal limits. *J Nucl Cardiol*. 2005;12:66–77
9. Germano G, Kiat H, Kavanagh PB, et al Automatic quantification of ejection fraction from gated myocardial perfusion SPECT. *J Nucl Med*. 1995;36:2138–2147
10. Choi JY, Lee KH, Kim SJ, et al Gating provides improved accuracy for differentiating artifacts from true lesions in equivocal fixed defects on technetium 99m tetrofosmin perfusion SPECT. *J Nucl Cardiol*. 1998;5:395–401
11. Johnson LL, Verdesca SA, Aude WY, et al Postischemic stunning can affect left ventricular ejection fraction and regional wall motion on post–stress gated sestamibi tomograms. *J Am Coll Cardiol*. 1997;30:1641–1648
12. Corbett JR, Ficaro EP. Clinical review of attenuation-corrected cardiac SPECT. *J Nucl Cardiol*. 1999;6:54–68
13. Bateman TM, Cullom SJ. Attenuation correction single-photon emission computed tomography myocardial perfusion imaging. *Semin Nucl Med*. 2005;35:37–51
14. Hendel RC, Berman DS, Cullom SJ, et al Multicenter clinical trial to evaluate the efficacy of correction for photon attenuation and scatter in SPECT myocardial perfusion imaging. *Circulation*. 1999;99:2742–2749
15. Tonge CM, Manoharan M, Lawson RS, Shields RA, Prescott MC. Attenuation correction of myocardial SPECT studies using low resolution computed tomography images. *Nucl Med Commun*. 2005;26:231–237
16. Hesse B, Tagil K, Cuocolo A, et al EANM/ESC procedural guidelines for myocardial perfusion imaging in nuclear cardiology. *Eur J Nucl Med Mol Imaging*. 2005;32:855–897

17. Cranley K, Millar R, Bell T. Correction for deadtime losses in a gamma camera data analysis system. *Eur J Nucl Med*. 1980;5: 377–382
18. Daube-Witherspoon ME, Carson RE. Unified deadtime correction model for PET. *IEEE Trans Med Imaging*. 1991;10:267–275
19. deKemp RA, Nahmias C. Attenuation correction in PET using single photon transmission measurement. *Med Phys*. 1994;21: 771–778
20. Karp JS, Muehllehner G, Qu H, Yan XH. Singles transmission in volume-imaging PET with a 137Cs source. *Phys Med Biol*. 1995; 40:929–944
21. Yu SK, Nahmias C. Single-photon transmission measurements in positron tomography using 137Cs. *Phys Med Biol*. 1995;40:1255–1266
22. Burger C, Goerres G, Schoenes S, Buck A, Lonn AH, Von Schulthess GK. PET attenuation coefficients from CT images: experimental evaluation of the transformation of CT into PET 511-keV attenuation coefficients. *Eur J Nucl Med Mol Imaging*. 2002;29:922–927
23. Ollinger JM. A model-based scatter correction for fully 3D PET. *Phys Med Biol*. 1996;41:153–176
24. Watson CC, Newport D, Casey ME. Three-dimensional image reconstruction in radiology and nuclear medicine. In: Grangeat P, Amans JL, eds. Dordrecht, Kluwer Academic;1996:255–268
25. Dyson NA. The annihilation coincidence method of ocalizing positron-emitting isotopes, and a comparison with paralell counting. *Phys Med Biol*. 1960;4:376–390
26. Dawood M, Kösters T, Fieseler M, et al Motion correction in respiratory gated cardiac PET/CT using multi-scale optical flow. In: *Med Image Comput Comput Assist Interv Int Conf Med Image Comput Comput Assist Interv*; 2008:155–162
27. Lamare F, Teras M, Kokki T, et al Correction of respiratory motion in dual gated cardiac imaging. *J Nucl Med*. 2008;49(suppl 1):389P
28. Boussion N, Hatt M, Lamare F, Rest CC, Visvikis D. Contrast enhancement in emission tomography by way of synergistic PET/CT image combination. *Comput Methods Programs Biomed*. 2008;90:191–201
29. Hesse B, Lindhardt TB, Acampa W, et al EANM/ESC guidelines for radionuclide imaging of cardiac function. *Eur J Nucl Med Mol Imaging*. 2008;35:851–885
30. Grunwald AM, Watson DD, Holzgrefe HH Jr, Irving JF, Beller GA. Myocardial thallium-201 kinetics in normal and ischemic myocardium. *Circulation*. 1981;64:610–618
31. Dilsizian V, Smeltzer WR, Freedman NM, Dextras R, Bonow RO. Thallium reinjection after stress-redistribution imaging. Does 24-hour delayed imaging after reinjection enhance detection of viable myocardium? *Circulation*. 1991;83:1247–1255
32. Takahashi N, Reinhardt CP, Marcel R, Leppo JA. Myocardial uptake of 99mTc-tetrofosmin, sestamibi, and 201Tl in a model of acute coronary reperfusion. *Circulation*. 1996;94:2605–2613
33. Beanlands RS, Dawood F, Wen WH, et al Are the kinetics of technetium-99m methoxyisobutyl isonitrile affected by cell metabolism and viability? *Circulation*. 1990;82:1802–1814
34. Meerdink DJ, Leppo JA. Comparison of hypoxia and ouabain effects on the myocardial uptake kinetics of technetium-99m hexakis 2-methoxyisobutyl isonitrile and thallium-201 *J Nucl Med*. 1989;30:1500–1506
35. Jain D, Wackers FJ, Mattera J, McMahon M, Sinusas AJ, Zaret BL. Biokinetics of technetium-99m-tetrofosmin: myocardial perfusion imaging agent: implications for a one-day imaging protocol. *J Nucl Med*. 1993;34:1254–1259
36. Munch G, Neverve J, Matsunari I, Schroter G, Schwaiger M. Myocardial technetium-99m-tetrofosmin and technetium-99m-sestamibi kinetics in normal subjects and patients with coronary artery disease. *J Nucl Med*. 1997;38:428–432
37. Berman DS, Kiat HS, Van Train KF, Germano G, Maddahi J, Friedman JD. Myocardial perfusion imaging with technetium-99m-sestamibi: comparative analysis of available imaging protocols. *J Nucl Med*. 1994;35:681–688
38. Heo J, Kegel J, Iskandrian AS, Cave V, Iskandrian BB. Comparison of same-day protocols using technetium-99m-sestamibi myocardial imaging. *J Nucl Med*. 1992;33:186–191
39. Sciagra R, Bisi G, Santoro GM, Rossi V, Fazzini PF. Nitrate versus rest myocardial scintigraphy with technetium 99m-sestamibi: relationship of tracer uptake to regional left ventricular function and its significance in the detection of viable hibernating myocardium. *Am J Card Imaging*. 1995;9:157–166
40. Berman DS, Kiat H, Van Train K, Friedman JD, Wang FP, Germano G. Dual-isotope myocardial perfusion SPECT with rest thallium-201 and stress Tc-99m sestamibi. *Cardiol Clin*. 1994;12: 261–270
41. Sharir T, Germano G, Kang X, et al Prediction of myocardial infarction versus cardiac death by gated myocardial perfusion SPECT: risk stratification by the amount of stress-induced ischemia and the poststress ejection fraction. *J Nucl Med*. 2001;42:831–837
42. Klocke FJ, Baird MG, Lorell BH, et al ACC/AHA/ASNC guidelines for the clinical use of cardiac radionuclide imaging-executive summary: a report of the American college of cardiology/American heart association task force on practice guidelines (ACC/AHA/ASNC committee to revise the 1995 guidelines for the clinical use of cardiac radionuclide imaging). *Circulation*. 2003;108:1404–1418
43. Nichols K, DePuey EG, Gooneratne N, Salensky H, Friedman M, Cochoff S. First-pass ventricular ejection fraction using a single-crystal nuclear camera. *J Nucl Med*. 1994;35:1292–1300
44. Daou D, Van Kriekinge SD, Coaguila C, et al Automatic quantification of right ventricular function with gated blood pool SPECT. *J Nucl Cardiol*. 2004;11:293–304
45. Germano G, Berman DS. On the accuracy and reproducibility of quantitative gated myocardial perfusion SPECT. *J Nucl Med*. 1999;40:810–813
46. Araujo LI, Lammertsma AA, Rhodes CG, et al Noninvasive quantification of regional myocardial blood flow in coronary artery disease with oxygen-15-labeled carbon dioxide inhalation and positron emission tomography. *Circulation*. 1991;83:875–885
47. Bergmann SR, Herrero P, Markham J, Weinheimer CJ, Walsh MN. Noninvasive quantitation of myocardial blood flow in human subjects with oxygen-15-labeled water and positron emission tomography. *J Am Coll Cardiol*. 1989;14:639–652
48. Schelbert HR, Phelps ME, Hoffman EJ, Huang SC, Selin CE, Kuhl DE. Regional myocardial perfusion assessed with N-13 labeled ammonia and positron emission computerized axial tomography. *Am J Cardiol*. 1979;43:209–218
49. Huang SC, Williams BA, Krivokapich J, Araujo L, Phelps ME, Schelbert HR. Rabbit myocardial 82Rb kinetics and a compartmental model for blood flow estimation. *Am J Physiol*. 1989;256: H1156-H1164
50. Bellina CR, Parodi O, Camici P, et al Simultaneous in vitro and in vivo validation of nitrogen-13-ammonia for the assessment of regional myocardial blood flow. *J Nucl Med*. 1990;31:1335–1343
51. Hutchins GD, Schwaiger M, Rosenspire KC, Krivokapich J, Schelbert H, Kuhl DE. Noninvasive quantification of regional blood flow in the human heart using N-13 ammonia and dynamic positron emission tomographic imaging. *J Am Coll Cardiol*. 1990;15: 1032–1042
52. Herrero P, Markham J, Shelton ME, Weinheimer CJ, Bergmann SR. Noninvasive quantification of regional myocardial perfusion with rubidium-82 and positron emission tomography. Exploration of a mathematical model. *Circulation*. 1990;82:1377–1386
53. Anagnostopoulos C, Almonacid A, El Fakhri G, et al Quantitative relationship between coronary vasodilator reserve assessed by 82Rb PET imaging and coronary artery stenosis severity. *Eur J Nucl Med Mol Imaging*. 2008;35:1593–1601

54. Lortie M, Beanlands RS, Yoshinaga K, Klein R, Dasilva JN, DeKemp RA. Quantification of myocardial blood flow with 82Rb dynamic PET imaging. *Eur J Nucl Med Mol Imaging*. 2007;34:1765–1774
55. Araujo L, Schelbert HR. Dynamic positron emission tomography in ischaemic heart disease. *Am J Cardiac Imaging*. 1984;1:117–124
56. Shah A, Schelbert HR, Schwaiger M, Henze E, Hansen H, Selin C, Huang SC. Measurement of regional myocardial blood flow with N-13 ammonia and positron-emission tomography in intact dogs. *J Am Coll Cardiol*. 1985;5:92–100
57. Schaefers K, Spinks TJ, Camici PG, et al Absolute quantification of myocardial blood flow with $H_2{}^{15}O$ and 3-dimensional PET: an experimental validation. *J Nucl Med*. 2002;43:1031–1040
58. Kaufmann PA, Gnecchi-Ruscone T, Yap JT, Rimoldi O, Camici PG. Assessment of the reproducibility of baseline and hyperemic myocardial blood flow measurements with 15O-labeled water and PET. *J Nucl Med*. 1999;40:1848–1856
59. Czernin J, Muller P, Chan S, et al Influence of age and hemodynamics on myocardial blood flow and flow reserve. *Circulation*. 1993;88:62–69
60. Uren NG, Camici PG, Melin JA, et al Effect of aging on myocardial perfusion reserve. *J Nucl Med*. 1995;36:2032–2036
61. Chareonthaitawee P, Kaufmann PA, Rimoldi O, Camici PG. Heterogeneity of resting and hyperemic myocardial blood flow in healthy humans. *Cardiovasc Res*. 2001;50:151–161
62. Lorenzoni R, Rosen SD, Camici PG. Effect of alpha 1-adrenoceptor blockade on resting and hyperemic myocardial blood flow in normal humans. *Am J Physiol*. 1996;271:H1302-H1306
63. Kaufmann PA, Gnecchi-Ruscone T, di Terlizzi M, Schafers KP, Luscher TF, Camici PG. Coronary heart disease in smokers: vitamin C restores coronary microcirculatory function.[see comment]. *Circulation*. 2000;102:1233–1238
64. Kaufmann PA, Gnecchi-Ruscone T, Schafers KP, Luscher TF, Camici PG. Low density lipoprotein cholesterol and coronary microvascular dysfunction in hypercholesterolemia. *J Am Coll Cardiol*. 2000;36:103–109
65. Sdringola S, Patel D, Gould KL. High prevalence of myocardial perfusion abnormalities on positron emission tomography in asymptomatic persons with a parent or sibling with coronary artery disease. *Circulation*. 2001;103:496–501
66. Momose M, Abletshauser C, Neverve J, et al Dysregulation of coronary microvascular reactivity in asymptomatic patients with type 2 diabetes mellitus. *Eur J Nucl Med Mol Imaging*. 2002;29:1675–1679
67. Uren NG, Melin JA, De Bruyne B, Wijns W, Baudhuin T, Camici PG. Relation between myocardial blood flow and the severity of coronary-artery stenosis. *N Engl J Med*. 1994;330:1782–1788
68. Rajappan K, Rimoldi OE, Dutka DP, et al Mechanisms of coronary microcirculatory dysfunction in patients with aortic stenosis and angiographically normal coronary arteries. *Circulation*. 2002;105:470–476
69. Camici PG, Ferrannini E, Opie LH. Myocardial metabolism in ischemic heart disease: basic principles and applications to imaging by positron tomography. *Prog Cardiovasc Dis*. 1989;32:217–238
70. Camici PG, Marraccini P, Marzilli M. Coronary haemodynamics and myocardial metabolism during and after pacing stress in normal humans. *Am J Physiol*. 1989;257:E309-E317
71. Schelbert HR, Henze E, Schon HR. C-11 palmitic acid for the noninvasive evaluation of regional myocardial fatty acid metabolism with positron computed tomography. IV. In vivo demonstration of impaired fatty acid oxidation in acute myocardial ischaemia. *Am Heart J*. 1983;106:736–750
72. Buxton DB, Schwaiger M, Nguyen A, Phelps M, Schelbert HR. Radiolabeled acetate as a tracer of myocardial tricarboxylic acid cycle flux. *Circ Res*. 1988;63:628–634
73. Armbrecht JJ, Buxton DB, Schelbert HR. Validation of [1–^{11}C] acetate as a tracer for noninvasive assessment of oxidative metabolism with positron emission tomography in normal, ischemic, postischemic and hyperemic canine myocardium. *Circulation*. 1990;81:1594–1605
74. Buxton DB, Nienaber CA, Luxen A. Noninvasive quantitation of regional myocardial oxygen consumption in vivo with [1–^{1}C] acetate and dynamic positron emission tomography. *Circulation*. 1989;79:134–142
75. Bing RJ. The metabolism of the heart. In: *Harvey Lecture Series 50* Orlando, FL/New York: Academic; 1954:22–70
76. Armbrecht JJ, Buxton DB, Brunken R, Phelps M, Schelbert HR. Regional myocardial oxygen consumption determined noninvasively in humans with [1–^{1}C] acetate and dynamic positron tomography. *Circulation*. 1989;80:863–872
77. Walsh MN, Geltman EM, Brown MA. Noninvasive estimation of regional myocardial oxygen consumption by positron emission tomography with carbon-11 acetate in patients with myocardial infarction. *J Nucl Med*. 1989;30:1798–1808
78. Gallagher BM, Fowler JS, Gutterson NI, MacGregor RR, Wan C-N, Wolf AP. Metabolic trapping as a principle of radiopharmaceutical design: some factors responsible for the biodistribution of [^{18}F]2-deoxy-2-fluoro-D-glucose. *J Nucl Med*. 1978;19:1154–1161
79. Huang SC, Phelps ME. Principles of tracer kinetic modeling in positron emission tomography and autoradiography. In: Phelps ME, Mazziotta JC, Schelbert HR, eds. *Positron emission tomography and autoradiography. Principles and applications for the brain and heart*. New York: Raven; 1986:287–346
80. Botker HE, Bottcher M, Schmitz O, et al Glucose uptake and lumped constant variability in normal human hearts determined with [18F]fluorodeoxyglucose. *J Nucl Cardiol*. 1997;4:125–132
81. Ferrannini E, Santoro D, Bonadonna R, Natali A, Parodi O, Camici PG. Metabolic and hemodynamic effects of insulin on human hearts. *Am J Physiol*. 1993;264:E308-E315
82. Goldstein DS, Chang PC, Eisenhofer G, et al Positron emission tomographic imaging of cardiac sympathetic innervation and function. *Circulation*. 1990;81:1606–1621
83. Wieland DM, Rosenspire KC, Hutchins GD, Van Dort M, Rothley JM, Mislankar SG, Lee HT, Massin CC, Gildersleeve DL, Sherman PS, et al Neuronal mapping of the heart with 6-[18F] fluorometaraminol. *J Med Chem*. 1990;33:956–964
84. Schwaiger M, Kalff V, Rosenspire K, et al Noninvasive evaluation of sympathetic nervous system in human heart by positron emission tomography.[see comment]. *Circulation*. 1990;82:457–464
85. Munch G, Nguyen NTB, Nekolla SG, et al Evaluation of sympathetic nerve terminals with [^{11}C]Epinephrine and [^{11}C]hydroxyephedrine and positron emission tomography. *Circulation*. 2000;101:516–523
86. Syrota A. Positron emission tomography: evaluation of cardiac receptors. In: Marcus ML, Schelbert HR, Skorton DJ, Wolf GL, eds. *Cardiac imaging. A companion to Braunwald's heart disease*. Philadelphia: W B Saunders; 1991:1256–1270
87. Staehelin M, Hertel C. [3H]CGP-12177, a beta-adrenergic ligand suitable for measuring cell surface receptors. *J Recept Res*. 1983;3:35–43
88. Lefroy DC, de Silva R, Choudhury L, Uren NG, Crake T, Rhodes CG, Lammertsma AA, Boyd H, Patsalos PN, Nihoyannopoulos P, et al Diffuse reduction of myocardial beta-adrenoceptors in hypertrophic cardiomyopathy: a study with positron emission tomography. *J Am Coll Cardiol*. 1993;22:1653–1660
89. Schafers M, Dutka D, Rhodes CG, et al Myocardial presynaptic and postsynaptic autonomic dysfunction in hypertrophic cardiomyopathy. *Circ Res*. 1998;82:57–62
90. Bristow MR, Ginsburg R, Minobe W, et al Decreased catecholamine sensitivity and beta-adrenergic-receptor density in failing human hearts. *N Engl J Med*. 1982;307:205–211

91. Esler M, Kaye D, Lambert G, Esler D, Jennings G. Adrenergic nervous system in heart failure. *Am J Cardiol*. 1997;80:7L-14L
92. Merlet P, Delforge J, Syrota A, et al Positron emission tomography with 11C CGP-12177 to assess beta-adrenergic receptor concentration in idiopathic dilated cardiomyopathy. *Circulation*. 1993;87:1169–1178
93. Delforge J, Janier M, Syrota A, et al Noninvasive quantification of muscarinic receptors in vivo with positron emission tomography in the dog heart. *Circulation*. 1990;82:1494–1504
94. Le Guludec D, Cohen-Solal A, Delforge J, Delahaye N, Syrota A, Merlet P. Increased myocardial muscarinic receptor density in idiopathic dilated cardiomyopathy: an in vivo PET study. *Circulation*. 1997;96:3416–3422
95. Le Guludec D, Delforge J, Syrota A, et al In vivo quantification of myocardial muscarinic receptors in heart transplant patients. *Circulation*. 1994;90:172–178
96. Anger HO. A multiple scintillation counter in vivo scanner. *Am J Roentgenol Radium Ther Nucl Med*. 1953;70:605–612
97. Patton JA, Slomka PJ, Germano G, Berman DS. Recent technologic advances in nuclear cardiology. *J Nucl Cardiol*. 2007;14:501–513
98. Goetze S, Brown TL, Lavely WC, Zhang Z, Bengel FM. Attenuation correction in myocardial perfusion SPECT/CT: effects of misregistration and value of reregistration. *J Nucl Med*. 2007;48:1090–1095
99. Lautamaki R, Brown TL, Merrill J, Bengel FM. CT-based attenuation correction in (82)Rb-myocardial perfusion PET-CT: incidence of misalignment and effect on regional tracer distribution. *Eur J Nucl Med Mol Imaging*. 2008;35:305–310
100. Di Carli MF, Hachamovitch R. New technology for noninvasive evaluation of coronary artery disease. *Circulation*. 2007;115:1464–1480
101. Knuuti J, Bengel FM. Positron emission tomography and molecular imaging. *Heart*. 2008;94:360–367
102. Schwaiger M, Bengel FM. From thallium scan to molecular imaging. *Mol Imaging Biol*. 2002;4:387–398
103. Wu JC, Bengel FM, Gambhir SS. Cardiovascular molecular imaging. *Radiology*. 2007;244:337–355

Chapter 4

HYBRID IMAGING: PET–CT AND SPECT–CT

Juhani Knuuti and Philipp A. Kaufmann

CONTENTS

J. L. Zamorano et al. (eds.), *The ESC Textbook of Cardiovascular Imaging*
DOI: 10.1007/978-1-84882-421-8_4, © Springer-Verlag London Limited 2010

Introduction

Hybrid scanners combining PET or SPECT with high-resolution multi-detector CT are becoming the standard for almost all commercially available systems. Hybrid scanners offer the ability to assess the anatomy of the heart and coronary arteries and the functional evaluation either at stress (for assessment of induced ischaemia) or at rest (for viability) in association with the left ventricular systolic function. Therefore, combining functional information from PET or SPECT is appealing.[1]

Definition of Cardiac Hybrid Imaging

The term *cardiac hybrid imaging* has been proposed if images are fused combining two data sets, whereby both modalities are equally important in contributing to image information. Mostly, this refers to combining CT with a nuclear myocardial perfusion imaging technique. Some reports have referred to X-ray-based attenuation correction of perfusion imaging as hybrid imaging, raising confusion about its exact meaning because in such setting the CT data do not provide added anatomical information, but are simply used to improve image quality of the PET or SPECT modality. Similarly, the parametric maps obtained from low-dose CT do not provide image information beyond that needed for attenuation correction, although it could be used to obtain calcium scoring.[2,3]

Others have used the term hybrid imaging for the mere side-by-side analysis of perfusion and CT images. To avoid confusion, we suggest using the term hybrid imaging to describe any combination of structural and functional information beyond that offered by attenuation correction or side-by-side analysis, by fusion of the separate data sets, for example, from CT coronary angiography and from SPECT or PET into one image. Similarly, separate acquisition of structural information as well as functional data such as, for example, perfusion on two separate scanners or on one hybrid device would allow mental integration of side-by-side evaluation but only fusion of both pieces of information would result in what should be considered a hybrid image (Fig. 4.1).

Rationale for Cardiac Hybrid Imaging

The field of cardiac imaging has witnessed an enormous development in the past years and is now offering an ever-increasing spectrum of tools and options to the clinicians.

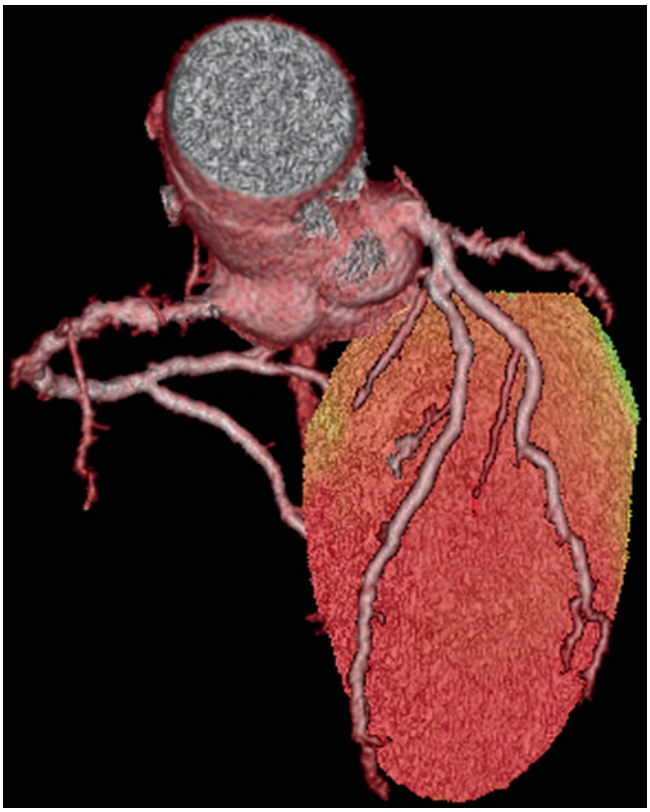

Fig. 4.1 Three-dimensional cardiac hybrid PET-CT image providing a panoramic view of stress perfusion MPI *(red* and *yellow colours* indicate normal perfusion) in relation to the coronary territories. Despite several calcifications in the proximal segments of the left and right coronary arteries there is no relevant ischaemia

The potential disadvantage is that the patients may now be exposed to multiple, sequential, time-consuming, and costly diagnostic test and procedures, which may deliver occasionally even contradicting results. This may have contributed to the fact that the majority of patients are referred to diagnostic invasive coronary angiography and consequently to percutaneous coronary interventions (PCI) in the absence of any sort of functional evaluation,[4,5] although professional guidelines call for objective documentation of ischaemia prior to elective PCI.[6–8] It is this background that has paved the way for the conceptual search of a non-invasive technique to assess coronary artery disease in which the detected perfusion abnormalities can be immediately and accurately associated with the individual's coronary anatomy.

Although CT coronary angiography with multi-detector scanners has proven to be a valuable alternative to diagnostic invasive coronary angiography for the evaluation of many subgroups of patient with known or suspected coronary artery disease, it only allows assessing coronary luminology, thus providing purely morphological information. The limitations of morphologic measures for delineating the physiologic implications of stenoses are well described.[9] The vasomotor

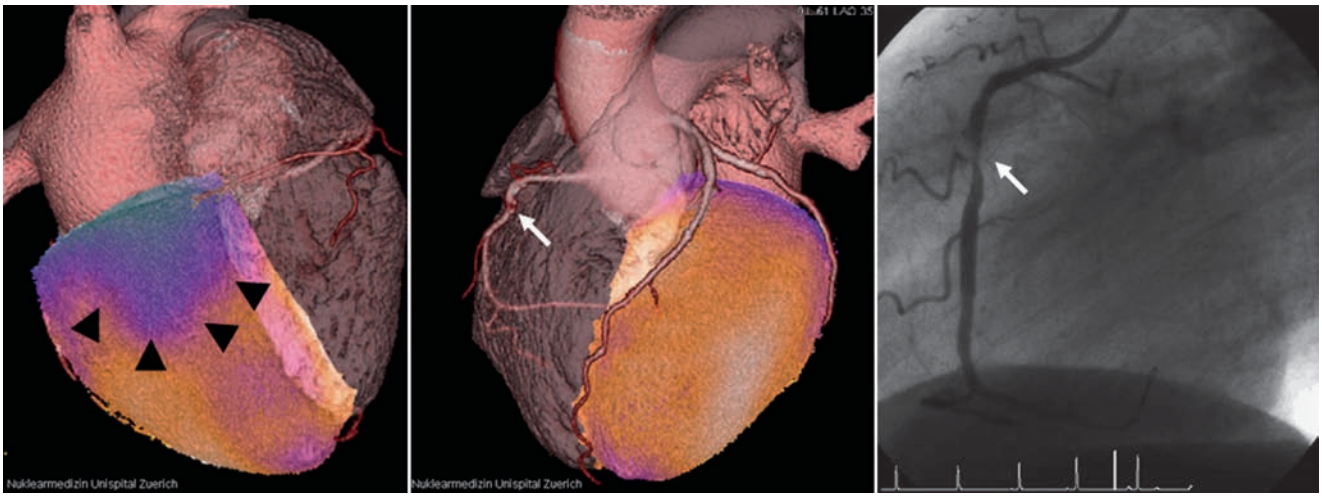

Fig. 4.2 Three-dimensional cardiac hybrid SPECT-CT image: a volume rendered CT coronary angiography image is fused with the stress perfusion SPECT. The *left panel* shows a basal inferior ischaemic area *(blue area, black arrow heads)*. The *middle panel* reveals a lesion in the right coronary artery *(white arrow)*, with otherwise unremarkable coronaries and normal perfusion. Invasive coronary angiography confirms a significant lesion in the RCA *(white arrow)*

tone and coronary collateral flow, both of which are known to affect myocardial perfusion, cannot be estimated by measures of stenosis severity. The percent diameter stenosis is only a weak descriptor of coronary resistance as it does not take into account the length and shape or stenoses. Lastly, CTA is limited in its ability to accurately define the severity of stenosis.

Accordingly, the major drawback of the CT has been found to be the relatively low positive predictive value and that the estimation of the haemodynamic significance of the detected stenosis is difficult.[9–11] In contrast, myocardial perfusion imaging provides a simple and accurate integrated measure of the effect of all of these parameters on coronary resistance and tissue perfusion, thereby optimizing selection of patients who may ultimately benefit from revascularization. This has triggered the idea of obtaining combined anatomic and functional non-invasive imaging of the coronary circulation in a single session through hybrid instrumentation.

Early studies conducted with image fusion of invasive coronary angiography and myocardial perfusion imaging from SPECT showed limited success due to the disadvantages inherent in warping planar 2D angiogram into a fusion with a 3D perfusion data set. Furthermore, the fusion process was time consuming and, therefore, not helpful for rapid decision making during an ongoing intervention.

Alternatively, combined information can be gained by mental integration of the information, e.g. from invasive of CT angiography and SPECT. However, the planar projections of coronary angiograms and axial slice-by-slice display of cardiac perfusion studies make a subjective integration difficult. This may lead to inaccurate allocation of the coronary lesion to its subtended myocardial territory, particularly in patients with multi-vessel disease and intermediate severity lesions. In addition, standard distribution of myocardial territories corresponds with the real anatomic coronary tree in only 50–60% of cases, which may cause misleading interpretation.

Therefore, the concept of hybrid imaging to deliver comprehensive integrated morphological and functional information is particularly appealing. In addition to being intuitively convincing, these images provide a panoramic view of the myocardium, the regional myocardial perfusion or viability, and the coronary artery tree, thus eliminating uncertainties in the relationship between perfusion defects, scar regions, and diseased coronary arteries in watershed regions (Fig. 4.2). This may be particularly helpful in patients with multiple perfusion abnormalities (Fig. 4.3, Video 4.3) and complex CAD, including situations after bypass surgery (Fig. 4.4). Combining anatomical information with perfusion also helps to identify and correctly register the subtle irregularities in myocardial perfusion (Fig. 4.5).

Integrated Scanners vs. Software Fusion

The potential added value of hybrid imaging originates from the spatial correlation of structural and functional information on the fused images, which facilitates a comprehensive interpretation of coronary lesions and their pathophysiologic relevance. An important prerequisite of hybrid imaging is accurate image coregistration because misalignment may result in erroneous allocation of perfusion defects to coronary artery territories. From a technical perspective, image coregistration can be achieved by a software-based or hardware-based approach.

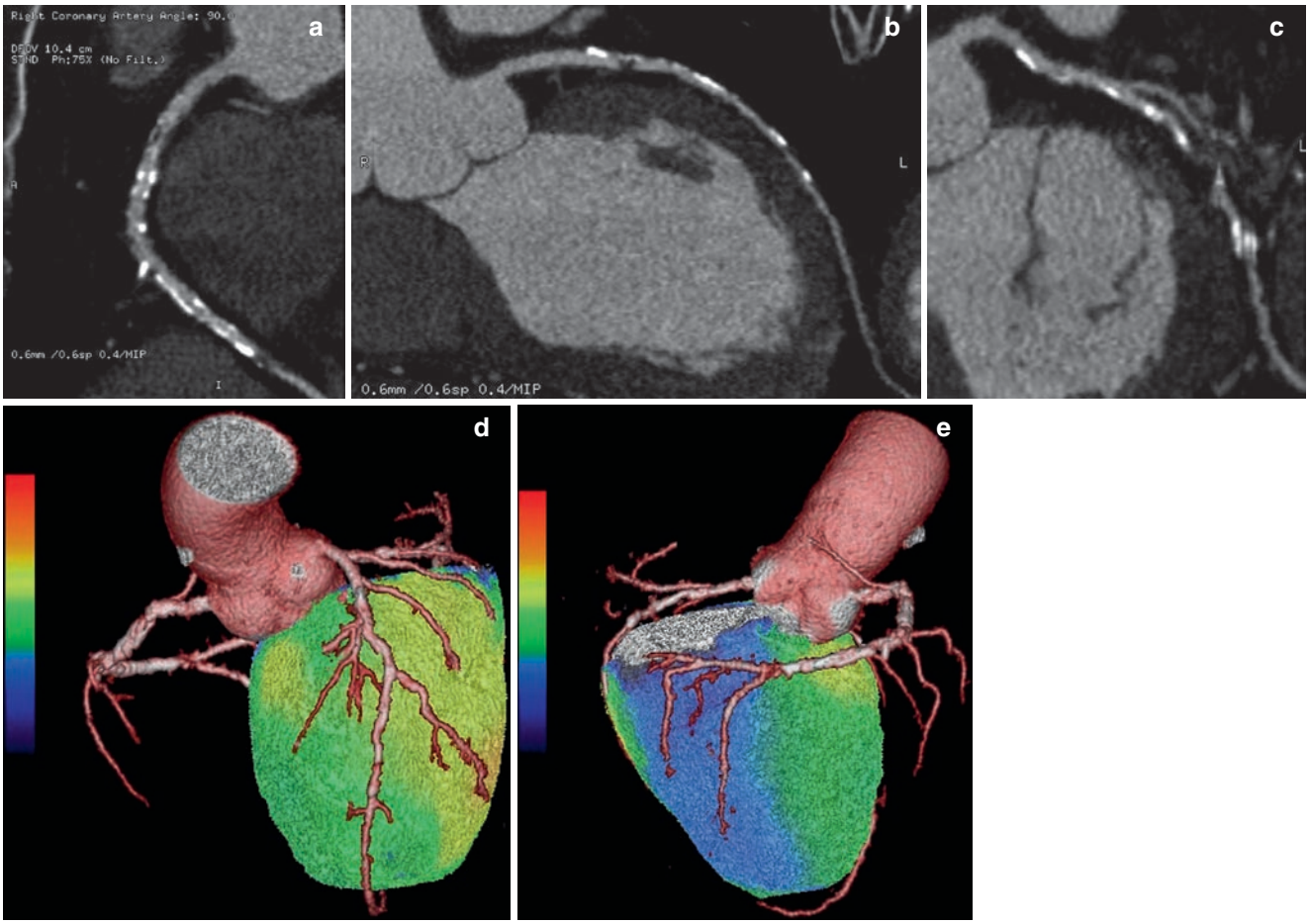

Fig. 4.3 CT coronary angiography images (curved multi-planar reconstructions) of a male patient with effort angina. The images of RCA **(a)**, LAD **(b)** and LCX **(c)** show several calcified and non-calcified plaques, which suggest significant multi-vessel disease. Three-dimensional cardiac hybrid PET-CT images of anterior **(d)** and right lateral view **(e)** shows very different stress perfusion patterns in each vessel region. The perfusion in region supplied by LCX was normal *(red and yellow colour)*, slightly reduced in region supplied by LAD *(green colour)*, and severely compromised in region supplied by RCA *(blue colour)*

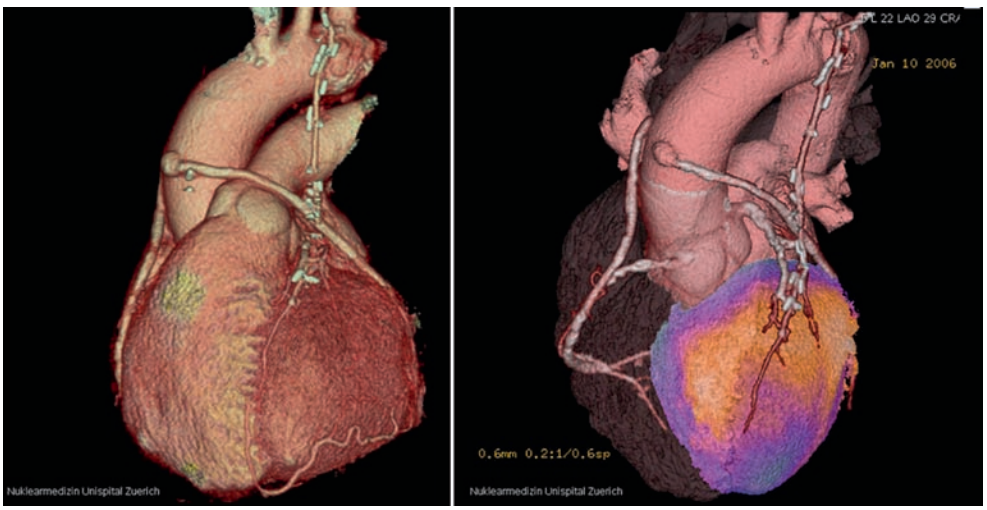

Fig. 4.4 In situations of complex coronary CAD and after bypass surgery hybrid cardiac imaging provides added value. CT coronary angiography may allow visualization of patent bypass grafts but the evaluation of the anastomoses remains difficult. A conclusion about haemodynamic relevant lesions can only be reached in conjunction with perfusion. The image documents residual ischaemia in the distal left anterior descending artery territory

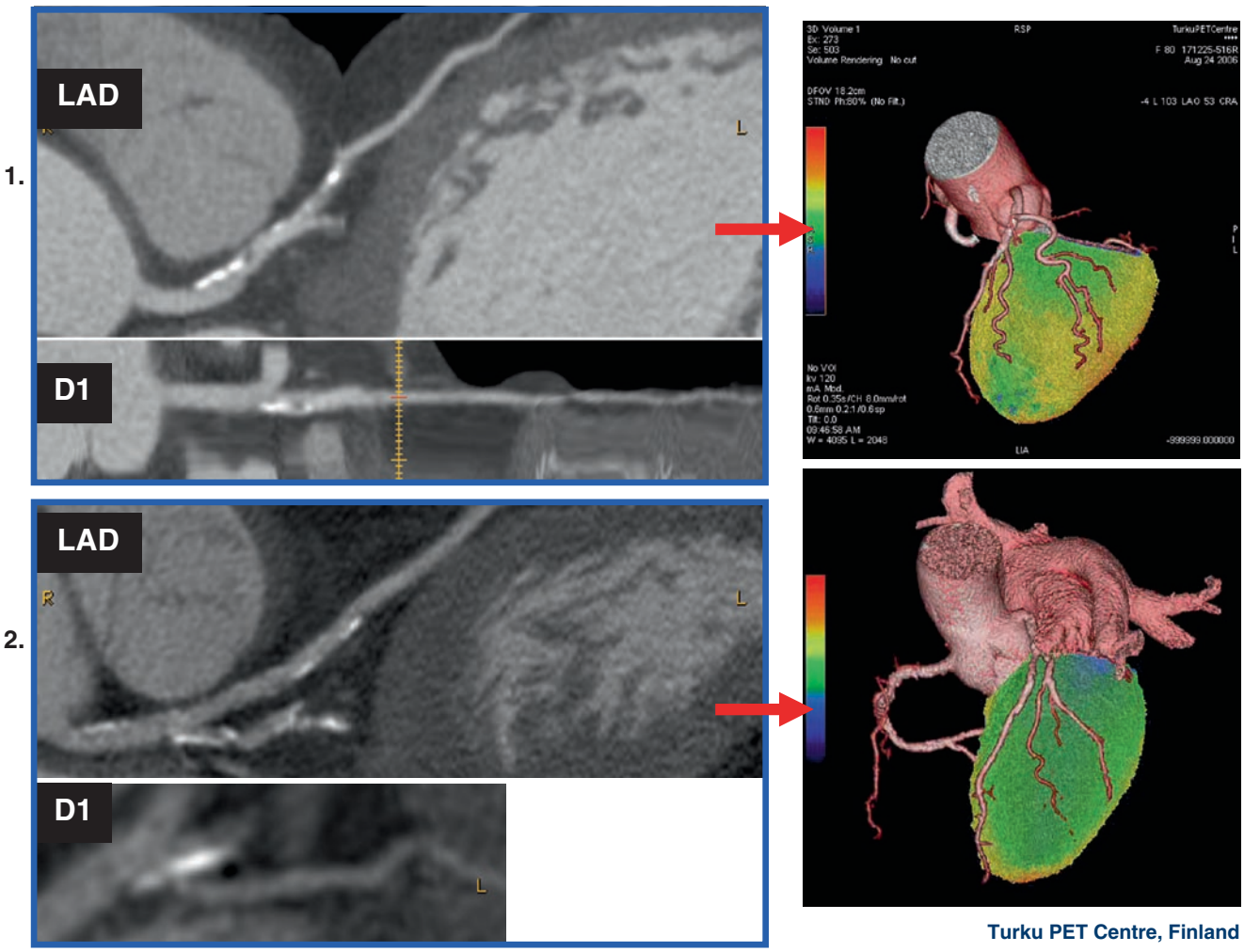

Fig. 4.5 Examples of two clinically similar symptomatic patients who had also similar findings in LAD and the first diagonal branch (D1) in CT angiography *(left panels)*. The patient 1 *(upper row)* showed in hybrid PET/CT imaging (right panel) only subtle reduction in territory supplied by D1. The patient 2 *(lower row)* showed large poorly perfused region covering whole anterior wall supplied by both LAD and D1

Hardware-based image coregistration permits the acquisition of fused anatomical and functional images using hybrid scanners (such as PET/CT or SPECT/CT devices) with the capability to perform nuclear and CT image acquisition, almost simultaneously with the patient's position fixed. Inherently, image fusion is performed fully or semi-automatically by superposition of image data sets. The real benefit of fusing different imaging modalities is also in the ability of using the anatomical information acquired *in situ* to improve the scan efficiency and to use the CT images for attenuation correction of the nuclear scan. Last but not the least, the very important benefit for the patient is that comprehensive study can be performed in short single session of scans. The drawback is that the sequential procedure requires careful planning of logistics to enable efficient patient throughput.

Alternatively, with software-based coregistration, image data sets can be obtained on stand-alone scanners and fused manually through the use of landmark-based coregistration techniques. Intuitively, the hardware-based approach appears preferable because manual coregistration may be hampered by issues of accuracy and user interaction. While the hybrid PET/CT device is the preferred tool for whole-body PET/CT imaging predominantly used in oncology, the routine use of fully automated hardware-based image coregistration for cardiac hybrid applications is challenged by certain organ-specific characteristics. First, minor beat-to-beat variations in the heart's position may interfere with accurate image coregistation despite fixation of the patient's position and orientation. Second, CT image acquisition and analysis requires electrocardiographical gating, and images are generally reconstructed in mid- to end-diastolic phases and acquired while holding one's breath. In contrast, SPECT and PET non-gated data sets are used resulting in a slight mismatch of ventricular size between the image sets. Furthermore, the position of the heart is susceptible to respiratory motion; SPECT and PET images are typically acquired during normal breathing.

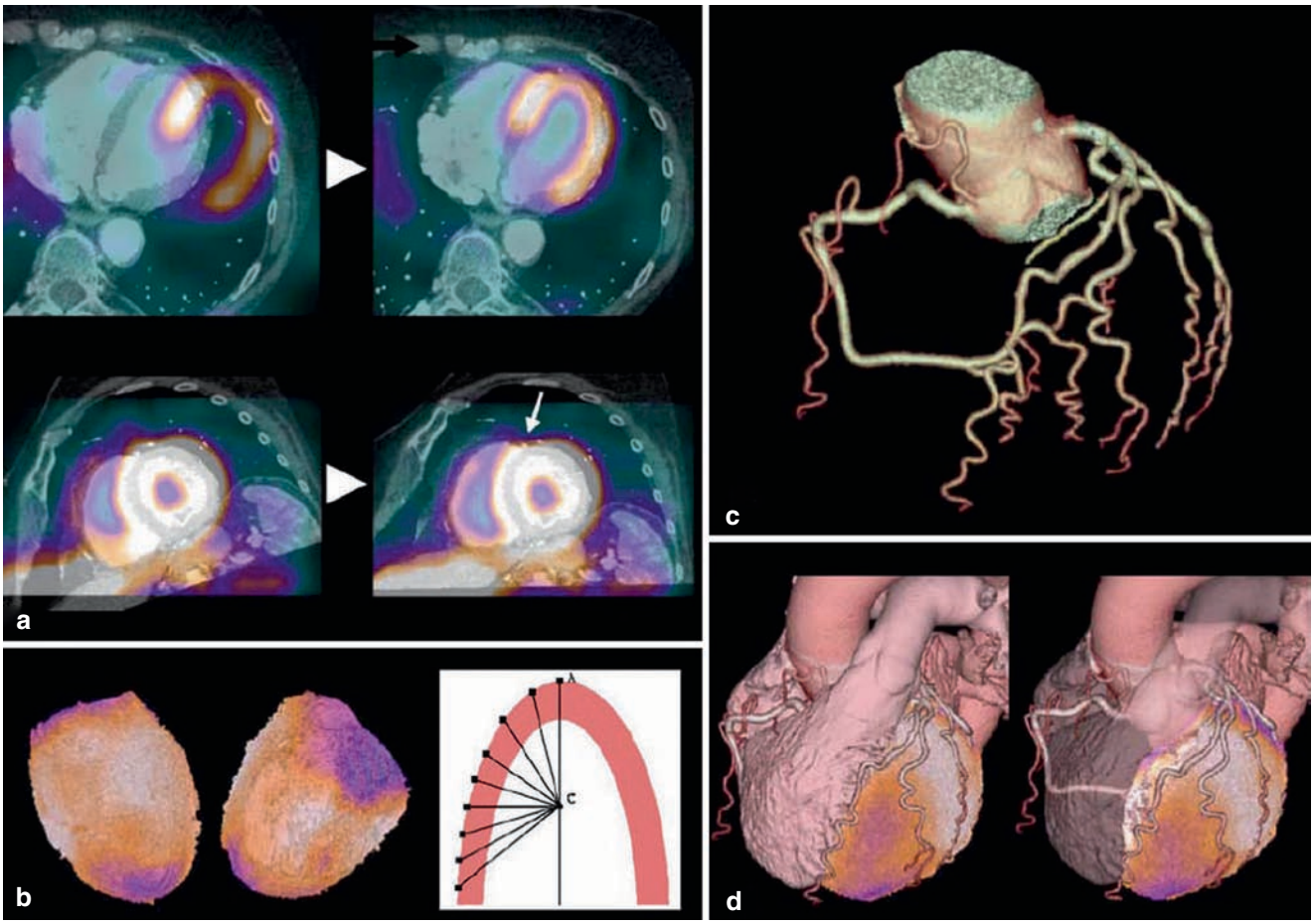

Fig. 4.6 Main steps for creating a cardiac hybrid SPECT-CT image from stand-alone systems. The main steps include **(a)** image coregistration, **(b)** epicardial contour detection, **(c)** coronary artery segmentation, and **(d)** MPI and CT image superposition (with permission from Gaemperli et al.[32] The same steps are also performed even if hardware-based hybrid imaging (PET/CT or SPECT/CT) device were used

These facts can result in misalignment of the heart between PET/SPECT and superimposed CT and can also lead to diagnostic errors.[12] Therefore, software realignment of cardiac image sets is performed even if the scans were acquired in a single session using hybrid device.

Despite the integration of high-end CT devices with nuclear scanners to form dedicated cardiac hybrid scanners, software-based image coregistration may still remain a common form of hybrid imaging. Dedicated cardiac fusion software packages are now commercially available, allowing hybrid imaging with an excellent inter-observer reproducibility and short processing durations. Image transfer processes to workstations performing coregistration are currently simple and fast. A recent validation study has documented that 3D SPECT/CT image fusion (Fig. 4.6) from image sets obtained on stand-alone scanners with such software package is feasible and reliable, allowing correct superposition of PET/SPECT segments onto cardiac CT anatomy. Such software is used irrespective of whether the images are acquired on a hybrid device or on two different stand-alone scanners.

Indeed, with SPECT the stand-alone scanner setting may appear favourable in view of the fact that with the latest generation of multi-detector CT scanners, coronary angiography is acquired within seconds, while emission scans for stress and rest gated SPECT with 99mTc-based radiotracers at standard doses take at least 45 min.[13] Thus, in a hybrid cardiac device the high-end CT facilities will be blocked during long emission scan periods and therefore operate at low capacity. Advances in nuclear medicine such as newly developed dedicated cardiac detectors systems[14] and novel image reconstruction algorithms[15] may contribute to reduce emission scan times considerably and may eventually help shifting the balance in favour of hybrid scanners in the future.

With PET there are several advantages of hybrid imaging using hardware-based image fusion. The efficiency of imaging is enhanced. The PET imaging protocols are short, allowing both CT angiography and perfusion imaging to be performed in a single session below 30 min of total scan duration. It is expected that PET/CT is increasingly used in traditionally difficult patient populations such as obese and diabetic patients.

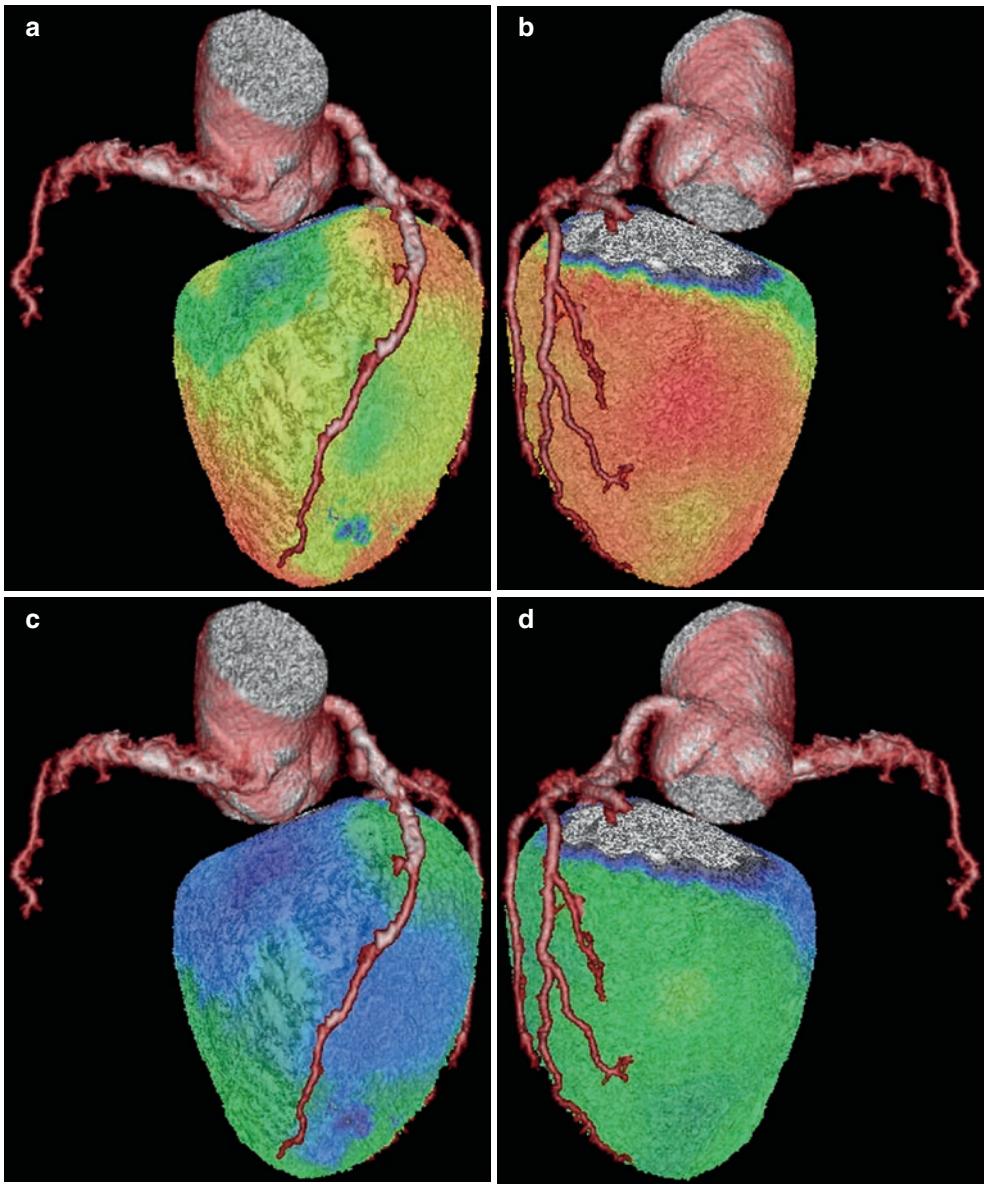

Fig. 4.7 Hybrid images from stress PET/CT with extensive coronary artery disease. The images **(a, b)** scaled to relative scale where the best perfused region is set to maximum and has the brightest colour (in rainbow scale lowest = blue and highest = red). The hybrid images of anterior **(a)** and posterior **(b)** views suggested only minor perfusion abnormalities in the anterior wall. The images scaled according to absolute scale **(c, d)** (0 mL/g/min = blue and 3.5 mL/g/min = red) uncovered global reduction of perfusion. The hybrid images of anterior **(c)** and posterior **(d)** views showed severely reduced stress perfusion in the anterior wall but also abnormally low perfusion in other myocardial territories *(green colour)*

There are also other promising future applications that involve molecular imaging of cardiac targets, and these may further enhance the clinical utility of hybrid imaging using PET/CT.

As explained in the earlier chapters, PET imaging offers the unique possibility to measure myocardial perfusion quantitatively in absolute terms. This is useful in patients with diffuse CAD or balanced disease where relative assessment of myocardial perfusion cannot uncover global reduction in perfusion (Fig. 4.7). Typically, in relative analysis of perfusion, only the regions supplied with the most severe stenosis are detected. Quantification of myocardial perfusion using dynamic PET provides a high performance level for the detection and localization of CAD.[16] The incremental value of quantitative analysis was also recently studied, and it was found that the accuracy of PET was further improved by quantitative analysis.[17–19]

Imaging Protocols for Hybrid Imaging

The patient preparation for hybrid study is mostly the same as for the individual scans. It is important that the patients heart rate is controlled for CT and that caffeine-containing drinks are avoided during the preceding 12 h because pharmacological stressors are commonly used in hybrid imaging. There are several options for hybrid imaging that have certain advantages and disadvantages.

In the protocols where the need of perfusion study is individually decided upon the findings in CT angiography, the protocol naturally starts with CT. This procedure is powerful because it utilizes the high negative predictive value of CT, and only that fraction of the patients that had suspicious findings in CT will continue with perfusion imaging. Depending on the selected patient population, this fraction is about 25–50% and, thus, on the average one perfusion session is needed for each three patients. The potential limitation is that the premedication needed for CT angiography may also affect the perfusion results, although this is likely less significant with pharmacological stressors such as adenosine and dipyridamole.

If perfusion study is performed first, the earlier-mentioned potential problem is avoided, but currently the analysis of perfusion images is not fast enough to be used for immediate decision whether to leave out CT angiography in the case of a completely normal perfusion result. Thus, in this protocol both studies are performed in all patients.

The positioning of the patient to the scanner bed is critical to prevent any motion artefacts. It is strongly recommended that hands are supported upright and not within the field of view. The calcium score study can be performed first followed by CT angiography study. The detailed protocol of CT angiography depends on the system used. Thereafter, low-dose CT for attenuation correction scan is performed if needed (in some systems, calcium score study can be used for this).

The perfusion imaging protocol depends on whether PET or SPECT or which tracer is used. In hybrid imaging, the stress study is performed using pharmacologic stressors such as adenosine, dipyridamole, or dobutamine. With PET tracers such as ^{82}Rb and ^{15}O-water studies (half-life 76 s and 112 s), the stress study can be performed practically without delay after the rest study. With ^{13}N-ammonia, stress testing is delayed for about 30 min to allow tracer decay. If a method to correct patient motion between stress and rest studies is not available, a second low-dose CT scan for attenuation correction is needed. In all studies quality control process is needed to ensure optimal alignment of the CT attenuation and PET emission scans, and, if necessary, misalignment needs to be corrected (Fig. 4.6).

If the system can list mode acquisition, the data can be collected as ECG-gated mode that allows the simultaneous assessment of regional and global left ventricular wall motion from the same scan data. This is particularly practical in Rb-82 studies. The total time required for whole study session depends on the tracer used. With ^{15}O-water and ^{82}Rb, the whole session can be finished in 30 min and with ^{13}N-ammonia in 80 min. The protocols may further shorten significantly since in hybrid approaches only single stress perfusion imaging may be needed especially when using quantification.[19]

If hybrid imaging is used to assess myocardial viability the standard patient preparations and procedures are used as in stand-alone imaging.

Image Analysis and Interpretation of Hybrid Imaging

The analysis of CT angiography includes standard processes and techniques such as visual assessment of original transaxial slices, multi-planar reconstructions, and utilization of quantitative tools available. The analysis of PET/SPECT studies also follows the standard procedures that have been explained in detailed guidelines.[20–22] However, to utilize the true power of hybrid imaging, an analysis system that is able to handle fused images and data also should be used. By doing so, the individual coronary anatomy can be visualized together with functional information enabling accurate association between coronary anatomy and, e.g. perfusion. The most advanced analysis also includes visualization of perfusion in diagnostic quality multi-planar reconstructions of CT. If quantitative measurement of flow has been performed, the absolute stress flow values also should be included in the analysis (Fig. 4.7).

Radiation Safety Aspects

Utilizing hybrid imaging, the patient radiation dose will further increase since the "additional" imaging techniques also utilize ionizing radiation. The dose for the patient from CT angiography has been reported to be in the range of 6–20 mSv depending on the system and protocol used. Recently, techniques that reduce patient dose have been developed and the doses have been reduced as low as 1–7 mSv.[23] The radiation doses from single SPECT perfusion imaging range from 5 to 8 mSv (^{99}mTc-based tracers). The radiation dose from PET perfusion studies is small, e.g. radiation dose from single PET perfusion study is 0.8 mSv ^{15}O-water and 1 mSv for ^{13}N-ammonia. Therefore, although the use of hybrid imaging obviously causes an increased radiation dose for the patient, the recent technical development has improved the radiation safety tremendously, and complete hybrid imaging can now be performed with a radiation dose below 10 mSv.[24–26]

Clinical Impact of Cardiac Hybrid Imaging

As mentioned before, it is well established that a comprehensive assessment of CAD requires not only morphologic information about coronary artery stenosis location and degree but also functional information on pathophysiologic lesion severity. Eventually, many factors that cannot fully

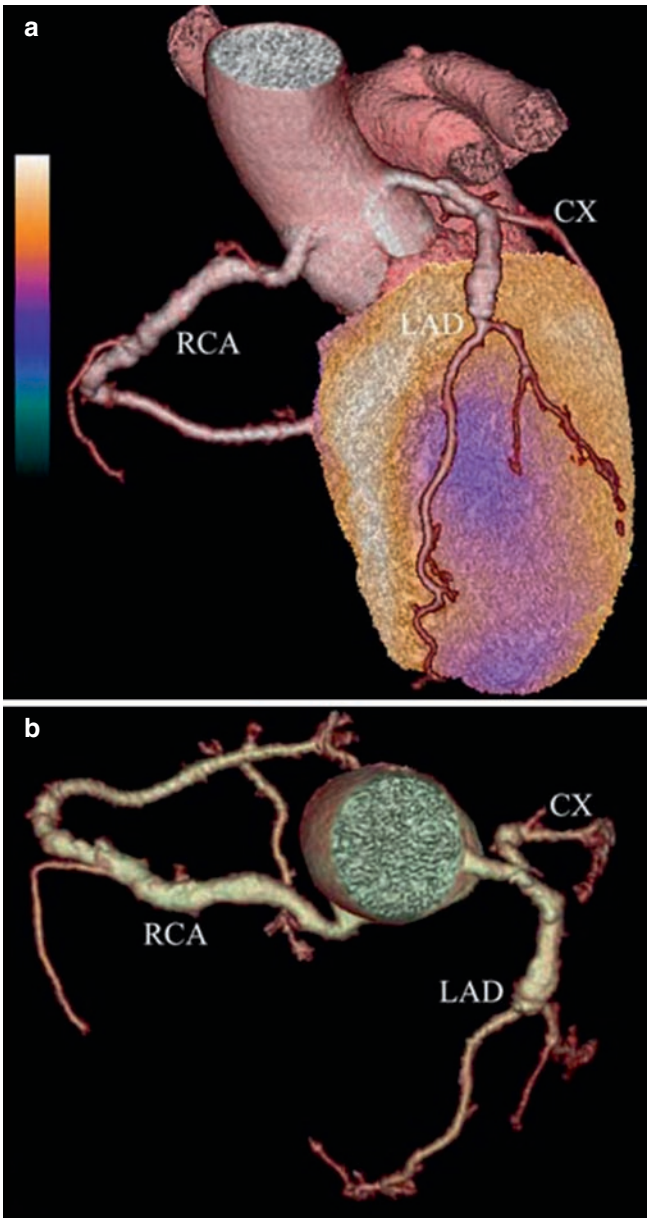

Fig. 4.8 **(a)** Hybrid images from stress SPECT MPI fused with the CT coronary angiography indicating that the territory subtended by the ectatic left anterior descending (LAD) is ischaemic *(blue area)*. **(b)** CT coronary angiography shows the extent of the ectatic coronary disease involving the right (RCA) and the circumflex (CX) coronary arteries. With permission from Husmann et al.[33]

be assessed with coronary luminology will determine whether a given lesion really induces a myocardial perfusion defect (Fig. 4.8; see also Figs. 4.3, 4.5, and 4.7). It has been repeatedly shown that only about half of the lesions classified as significant in CT are linked with abnormal perfusion.[9–11, 27]

In a study by Namdar et al.,[28] the concept was evaluated in patients with suspected CAD yielding a sensitivity and specificity of 90 and 98%, respectively, to detect important coronary lesions haemodynamically (as compared with the combination of stress-rest PET perfusion imaging and invasive coronary angiography). In a recent study using PET/CT systems with 64-slice CT scanner, it was found that the positive predictive value of stenosis in CT was low (around 50%) in predicting stress-inducible perfusion abnormalities in PET but the negative predictive value was over 90%.[29] This indicates that the assessment of functional consequences of coronary stenoses is difficult with CT, and that perfusion imaging provides useful complementary information.

Although these studies provide important clinical information about the performance of different imaging modalities, they do not directly show the incremental value of the hybrid imaging. Hybrid images may offer superior diagnostic information with regard to identification of the culprit vessel and therefore increase diagnostic confidence.[19,27] The initial experience that combined SPECT perfusion imaging and CT coronary angiography studies indicates that in almost one-third of patients the fused SPECT/CT analysis provided added diagnostic information on pathophysiologic lesion severity that was not obtained on side-by-side analysis.[29] The incremental value was most pronounced for functionally relevant lesions in distal segments and diagonal branches and in vessels with extensive CAD or substantial calcification on CT. Similar results also have been obtained using hybrid PET/CT imaging.[27,30] Because of the variant coronary anatomy in each individual and the complex disease pattern in these patients, correct allocation of perfusion defect and subtending coronary artery was only achieved by the hybrid images. As hybrid images offered superior information with regard to identification of the culprit vessel the diagnostic confidence for categorizing intermediate lesions and equivocal perfusion defects was significantly improved. Interestingly, most of the lesions that were originally found to be equivocal with regards to pathophysiologic severity on side-by-side analysis (due to the fact they could not be firmly assigned to a perfusion defect) were classified with high confidence by hybrid image evaluation. From these preliminary results one can conclude that the greatest added value appears to be the firm exclusion of haemodynamic significance of coronary abnormalities seen on CT coronary angiography, which might be useful to avoid unnecessary interventional procedure.

Other patients in whom hybrid imaging is likely clinically useful are those with multi-vessel CAD. Typically myocardial perfusion analysis is based on relative assessment of perfusion distribution. This technique, however, often uncovers only the coronary territory supplied by the most severe stenoses. In multi-vessel disease, coronary flow reserve may be abnormal in all territories, thereby reducing the heterogeneity of flow between “normal” and “abnormal” zones (Fig. 4.7, Video 4.7). This is obviously limiting the ability of relative perfusion analysis to delineate the presence of multi-vessel CAD.

There are several alternatives to solve this problem. The response of left ventricular ejection fraction to stress can be measured from perfusion data, and decrease in peak stress indicates multi-vessel disease.[31] PET has some benefit since the acquisition is done during stress, unlike with SPECT where post-stress imaging is performed. Another solution would be using quantification of myocardial perfusion in absolute terms (in mL/g/min), which is readily possible with PET[17–19] and provides independent information about all myocardial territories. In addition, integrated PET/CT offers an opportunity to assess the presence and magnitude of subclinical atherosclerotic disease burden and to measure absolute myocardial blood flow as a marker of endothelial health and atherosclerotic disease activity. Last but not the least, anatomical information from CT is able to identify the patients with severe balanced multi-vessel disease despite globally reduced but relatively homogenous myocardial perfusion.

Although assessment of myocardial viability using stand-alone systems is well established, the hybrid imaging provides clear benefits. The detected dysfunctional but viable or scar regions can be directly linked with the individual's coronary anatomy and linked with coronary stenoses. The limitation of hybrid approach in this patient group is that a substantial fraction of the patients have other diseases that prevent to use iodinated contrast agents.

Future Perspectives

Although the role of hybrid imaging in daily clinical routine remains to be determined, it appears that this approach may have the potential to become the central decision-making element in the future diagnostic and therapeutic strategy for patients with coronary artery disease. Studies assessing the prognostic value and cost-effectiveness of hybrid imaging are warranted.

Currently, the position of nuclear imaging in cardiovascular research and patient care is primarily based on its capacity to image perfusion and glucose metabolism. However, the methods allow for imaging and quantification of molecular interactions and pathways with picomolar sensitivity. Thus, the number of cellular processes can be studied, e.g. receptor density, enzyme activity, inflammatory processes, and gene expression.

Ruptures of vulnerable coronary atherosclerotic lesions account for one-third of all deaths worldwide and constitute a major source of disability and health care costs. Non-invasive techniques such as multi-slice CT can characterize morphologic criteria associated with high risk of atherosclerotic plaque rupture. In contrast, PET and SPECT utilize radiolabelled molecules designed to specifically target individual inflammatory activities in atherosclerotic plaques. This approach is possible only with high-resolution morphological imaging of the coronary arteries using hybrid imaging.

Conclusion

The newest generation of the hybrid imaging devices have matured to the level that they can be successfully used for clinical cardiovascular imaging. In addition, software-based image fusion has become readily available, allowing robust and fast image merging. It is likely that in the near future the primary clinical use of hybrid imaging is not only in the detection of coronary artery disease using CT coronary angiography and nuclear perfusion imaging but also in other long-term molecular imaging applications that are entering clinical cardiology.

References

1. Bax JJ, Beanlands RS, Klocke FJ, et al Diagnostic and clinical perspectives of fusion imaging in cardiology: is the total greater than the sum of its parts? *Heart.* 2007;93(1):16–22
2. Schepis T, Gaemperli O, Koepfli P, et al Use of coronary calcium score scans from stand-alone multislice computed tomography for attenuation correction of myocardial perfusion SPECT. *Eur J Nucl Med Mol Imaging.* 2007;34(1):11–19
3. Koepfli P, Hany TF, Wyss CA, Namdar M, Burger C, Konstantinidis AV, et al CT attenuation correction for myocardial perfusion quantification using a PET/CT hybrid scanner. *J Nucl Med.* 2004;45(4):537–542
4. Lin GA, Dudley RA, Lucas FL, Malenka DJ, Vittinghoff E, Redberg RF. Frequency of stress testing to document ischemia prior to elective percutaneous coronary intervention. *JAMA*. 2008;300(15):1765–1773
5. Topol EJ, Ellis SG, Cosgrove DM, Bates ER, Muller DW, Schork NJ, et al Analysis of coronary angioplasty practice in the United States with an insurance-claims data base. *Circulation.* 1993;87(5):1489–1497
6. Klocke FJ, Baird MG, Lorell BH, et al ACC/AHA/ASNC guidelines for the clinical use of cardiac radionuclide imaging – executive summary: a report of the American College of Cardiology/American Heart Association Task Force on Practice Guidelines (ACC/AHA/ASNC Committee to Revise the 1995 Guidelines for the Clinical Use of Cardiac Radionuclide Imaging). *Circulation.* 2003;108:1404–1418
7. Anderson HV, Shaw RE, Brindis RG, Klein LW, McKay CR, Kutcher MA, et al Relationship between procedure indications and outcomes of percutaneous coronary interventions by American College of Cardiology/American Heart Association Task Force Guidelines. *Circulation.* 2005;112(18):2786–2791
8. Boden WE, O'Rourke RA, Teo KK, et al Optimal medical therapy with or without PCI for stable coronary disease. *N Engl J Med.* 2007;356(15):1503–1516
9. Rispler S, Keidar Z, Ghersin E, et al Integrated single-photon emission computed tomography and computed tomography coronary angiography for the assessment of hemodynamically significant coronary artery lesions. *J Am Coll Cardiol.* 2007;49(10):1059–1067

10. Di Carli MF, Hachamovitch R. New technology for noninvasive evaluation of coronary artery disease. *Circulation*. 2007;115(11): 1464–80
11. Meijboom WB, Meijs MF, Schuijf JD, et al Diagnostic accuracy of 64-slice computed tomography coronary angiography: a prospective, multicenter, multivendor study. *J Am Coll Cardiol.* 2008;52(25): 2135–2144
12. Gould KL, Pan T, Loghin C, Johnson NP, Guha A, Sdringola S. Frequent diagnostic errors in cardiac PET/CT due to misregistration of CT attenuation and emission PET images: a definitive analysis of causes, consequences, and corrections. *J Nucl Med.* 2007; 48(7):1112–1121
13. Hansen CL, Goldstein RA, Berman DS, et al Myocardial perfusion and function single photon emission computed tomography. *J Nucl Cardiol.* 2006;13(6):e97–e120
14. Patton JA, Slomka PJ, Germano G, Berman DS. Recent technologic advances in nuclear cardiology. *J Nucl Cardiol.* 2007;14(4):501–513
15. Borges-Neto S, Pagnanelli RA, Shaw LK, et al Clinical results of a novel wide beam reconstruction method for shortening scan time of Tc-99m cardiac SPECT perfusion studies. *J Nucl Cardiol.* 2007; 14(4):555–565
16. Muzik O, Duvernoy C, Beanlands RS, et al Assessment of diagnostic performance of quantitative flow measurements in normal subjects and patients with angiographically documented coronary artery disease by means of nitrogen-13 ammonia and positron emission tomography. *J Am Coll Cardiol.* 1998;31(3):534–540
17. Yoshinaga K, Katoh C, Noriyasu K, et al Reduction of coronary flow reserve in areas with and without ischemia on stress perfusion imaging in patients with coronary artery disease: a study using oxygen 15-labeled water PET. *J Nucl Cardiol.* 2003;10(3):275–283
18. Parkash R, deKemp RA, Ruddy TD, et al Potential utility of rubidium 82 PET quantification in patients with 3-vessel coronary artery disease. *J Nucl Cardiol*. 2004;11(4):440–449
19. Kajander S, Ukkonen H, Joutsiniemi E, et al The clinical value of absolute quantification of myocardial perfusion in the detection of coronary artery disease. A study using positron emission tomography to detect multi-vessel disease. *Circulation.* 2008;118: S1010–S1011
20. Hesse B, Tagil K, Cuocolo A, et al EANM/ESC procedural guidelines for myocardial perfusion imaging in nuclear cardiology. *Eur J Nucl Med Mol Imaging.* 2005;32(7):855–897
21. Bacharach SL, Bax JJ, Case J, et al PET myocardial glucose metabolism and perfusion imaging: Part 1—Guidelines for data acquisition and patient preparation. *J Nucl Cardiol.* 2003;10(5):543–556
22. Schelbert HR, Beanlands R, et al PET myocardial perfusion and glucose metabolism imaging: Part 2 – Guidelines for interpretation and reporting. *J Nucl Cardiol.* 2003;10(5):557–571
23. Husmann L, Valenta I, Gaemperli O, et al Feasibility of low-dose coronary CT angiography: first experience with prospective ECG-gating. *Eur Heart J.* 2008;29(2):191–197
24. Husmann L, Herzog BA, Gaemperli O, et al Diagnostic accuracy of computed tomography coronary angiography and evaluation of stress-only single-photon emission computed tomography/computed tomography hybrid imaging: comparison of prospective electrocardiogram-triggering vs. retrospective gating. *Eur Heart J.* 2009;30(5):600–607
25. Herzog BA, Husmann L, Landmesser U, Kaufmann PA. Low-dose computed tomography coronary angiography and myocardial perfusion imaging: cardiac hybrid imaging below 3mSv. *Eur Heart J*. 2009;30(6):644
26. Kajander S, Ukkonen H, Sipilä H, Teräs M, Knuuti J. Low radiation dose imaging of myocardial perfusion and coronary angiography with a hybrid PET/CT scanner. *Clin Physiol Funct Imaging.* 2009; 29(1):81–88
27. Kajander S, Joutsiniemi E, Ukkonen H, et al Hybrid PET/CT imaging allows accurate detection of coronary atherosclerosis with assessment of functionally significant stenoses. *Eur Heart J.* 2008; 29:792–793, 4621
28. Namdar M, Hany TF, Koepfli P, et al Integrated PET/CT for the assessment of coronary artery disease: a feasibility study. *J Nucl Med.* 2005;46(6):930–935
29. Gaemperli O, Schepis T, Valenta I, et al Cardiac image fusion from stand-alone SPECT and CT: clinical experience. *J Nucl Med.* 2007; 48(5):696–703
30. Sampson UK, Dorbala S, Limaye A, Kwong R, Di Carli MF. Diagnostic accuracy of rubidium-82 myocardial perfusion imaging with hybrid positron emission tomography/computed tomography in the detection of coronary artery disease. *J Am Coll Cardiol.* 2007; 49(10):1052–1058
31. Dorbala S, Vangala D, Sampson U, Limaye A, Kwong R, Di Carli MF. Value of left ventricular ejection fraction reserve in evaluating the magnitude of myocardium at risk and the extent of angiographic coronary artery disease: a 82Rb PET/CT study. *J Nucl Med.* 2007; 48349–358
32. Gaemperli O, Schepis T, Kalff V, et al Validation of a new cardiac image fusion software for three-dimensional integration of myocardial perfusion SPECT and stand-alone 64-slice CT angiography. *Eur J Nucl Med Mol Imaging*. 2007;34:1097–1106. DOI 10.1007/s00259–006–0342–9
33. Husmann L, Herzog BA, Burkhard N, et al Coronary artery ectasia causing ischemia. *Eur J Nucl Med Mol Imaging*. 2008;35(11):2142. DOI 10.1007/s00259–008–0895-x

Chapter 5

CARDIAC CT: BASIC PRINCIPLES

Filippo Cademartiri, Erica Maffei, Alessandro Palumbo, Chiara Martini, and Nico R. Mollet

CONTENTS

J. L. Zamorano et al. (eds.), *The ESC Textbook of Cardiovascular Imaging*
DOI: 10.1007/978-1-84882-421-8_5,

Introduction

Cardiac CT is a fast developing technique. In 10 years, it developed from an investigative tool into a clinical reality. The technology drive has been the key to success for this technique, which is to date the only non-invasive clinical tool for coronary angiographic assessment. Technical background is quite complex and the newer solutions are aiming at reducing the scan time and the radiation dose while improving temporal resolution, contrast resolution, and ultimately image quality. The key technical development was in the late 1990s – the introduction of ECG triggering/gating techniques. Spatial resolution has also been improved reaching sub-millimeter performance. The latest innovations provide fast coverage with >64 slice detectors, high spatial resolution with 0.5 mm slice thickness, high temporal resolution with <100 ms in hardware, and higher contrast resolution with the forthcoming dual-energy solutions.

Now, multi-detector computed tomography (MDCT) scanners are available; they enable the simultaneous acquisition of 64 slices per rotation. The additional improvement in spatial and temporal resolution of these new devices has already provided excellent results in the field of cardiac imaging. In the future, the optimization of protocols will enable MDCT coronary angiography to reach levels of diagnostic accuracy similar to those of invasive techniques.

Basic Cardiac CT Technique

The most important components of a CT system are the X-ray tube and the system of detectors (Fig. 5.1). The combination of a fast rotation time and multi-slice acquisitions is particularly important for cardiac applications.[1, 2] The latest generation of 64-MDCT scanners meets these requirements. They are able to acquire 64 sub-millimeter slices per rotation and routinely achieve excellent image quality and visualization of small-diameter vessels of the coronary circulation, combining isotropic spatial resolution (0.4 mm^3) with gantry rotation speeds of 330 ms. They also redefine the MDCT methodology of analyzing coronary plaque and evaluating stent lumens.

Until a few years ago, CT systems had only a single row of detectors, which meant that for each rotation, they were able to acquire only one slice. These systems were followed by others known as multi-slice or multi-detector-row, featuring many detector rows positioned in a two-dimensional array. During a rotation, numerous contiguous slices are acquired. As a result, a broader region of the body can be acquired in the same time frame with an improvement in image quality. This also has the advantage of drastically reducing examination times, which is an important factor given that thoracic and abdominal examination require the patient to maintain breath-hold to guarantee that image quality is not compromised by chest motion. The clinical impact of the new technology lies in the improvement in image quality in terms of both spatial and temporal resolution. The improvement in spatial resolution regards numerous features of non-invasive coronary imaging:

- It increases the ability to visualize small-diameter vessels (e.g. the distal coronary branches).[3]
- It increases the ability to quantify calcium in that it reduces blooming artefacts.
- It enables the reduction of blooming artefacts in stents and therefore enables the visualization of the stent lumen.
- It improves the definition of the presence of coronary plaques and better quantifies their characteristics (volume, attenuation, etc.).

The improvement in temporal resolution influences many other aspects of non-invasive coronary imaging:

- It increases the ability to freeze images in the cardiac cycle.
- It enables additional reconstruction windows to be found within the cardiac cycle.

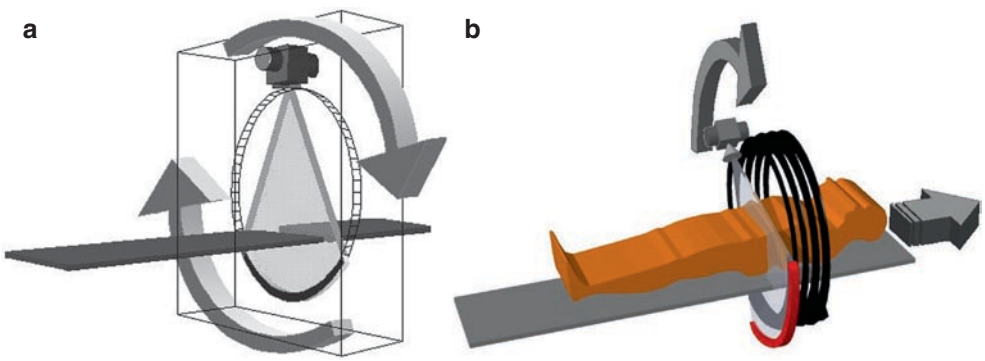

Fig. 5.1 Geometry of a CT scanner. A CT scanner is designed with an X-ray tube and a detector that rotate around the table **(a)**. During the rotation the table moves in order to generate the volume dataset **(b)**

- It increases the performance of the system when left ventricular function needs to be evaluated.
- It reduces scan time.

The technical characteristics of each scanner vary according to the model, and technological development is ongoing and rapid. The precise temporal resolution of the images obtained by MDCT scanners depends on many factors: gantry rotation speed, size and position of the field of view (FOV) in the scan volume, and the image reconstruction and post-processing algorithms. In reality, the data acquired at half a rotation of the gantry are sufficient to reconstruct a single tomographic image with retrospective or prospective ECG control (Fig. 5.2). The temporal resolution of the latest MDCT scanners, therefore, is approximately 165 ms.[4–6]

This is sufficient to obtain images of the heart during the diastolic phase (when cardiac motion is at a minimum), free of obvious motion artefacts if the heart rate (HR) is <70 beats per minute (bpm).

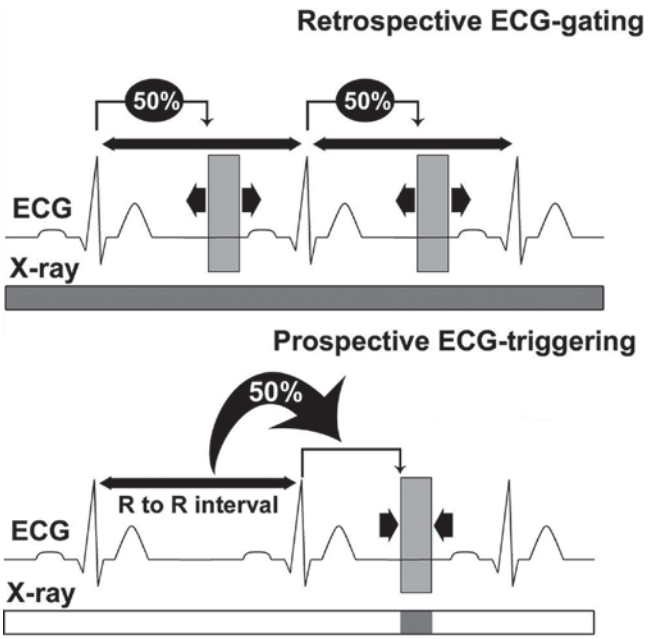

Fig. 5.2 Retrospective ECG gating vs. prospective ECG triggering. The two main techniques for cardiac CT ECG synchronization are displayed. In the upper panel, we can observe retrospective ECG gating. It is based on spiral continuous X-ray delivery at low pitch while recording the ECG track. Afterwards the operator is able to arbitrarily decide which phase of the cardiac cycle is worth reconstructing. In the lower panel, we can observe the prospective ECG triggering. It is based on sequential scanning (also called "step and shoot" mode). Radiation is delivered only within the phase of the cardiac cycle that has been decided prior to the initiation of the scan. It requires very low heart rate (HR) and/or very high temporal resolution to guarantee adequate image quality

Definition of CT Parameters

The following is a brief list of the main parameters used to create cardiac CT images.

- Spatial resolution represents the capability to separate two neighbouring points.
- Coverage resolution represents the minimum time required to complete a single volumetric acquisition.
- Temporal resolution represents the minimum time required to generate one single axial image.
- Contrast resolution represents the capability to separate two neighbouring attenuation values (Hounsfield Units) with a given background noise.
- Collimation (i.e. X-ray beam collimation) refers to the beam width along the longitudinal axis at the scanner isocentre.
- Pitch (Fig. 5.3) reflects the width of the helix that is created by the rotating gantry and table feed. Scan pitch is conventionally defined as the beam/volume pitch (table feed/slice collimation) and it is not affected by the number of detectors that characterizes the scanner.
- Table feed represents the speed of patient's translation along the *z*-axis. A fast table feed determines a faster scan speed.
- The X-ray tube current (mAs) corresponds to the number of photons that are produced and that actually run through the patient. A higher mAs improves the contrast-to-noise ratio (e.g. image quality).
- The X-ray tube voltage (kV) represents the energy of the photons (usually 120–140 kV for cardiac CT). Recently, it has been suggested that MDCT could be performed with a lower patient dose using protocols with 80/100 kV and increasing the mAs.
- Effective slice width refers to the thickness in the longitudinal axis from which the image is generated.
- Reconstruction increment is the distance between consecutive reconstructed axial slices. It mainly affects the spatial resolution in the longitudinal axis. Reconstruction increment is usually set in order to obtain 50% overlapping slices.
- FOV represents the size of the image that is going to be reconstructed.
- Image matrix represents the number of pixels that are reconstructed in one image and is generally constant for CT (i.e. 512 × 512 pixel). A small FOV increases in-plane spatial resolution.
- Interpolation is an algorithm by which the software estimates a missing value from known surrounding points. This operation is used for image reconstruction in spiral CT and in three-dimensional reconstruction.
- Kernels are convolution filters that modify the value of a voxel according to the values of the surrounding voxels.

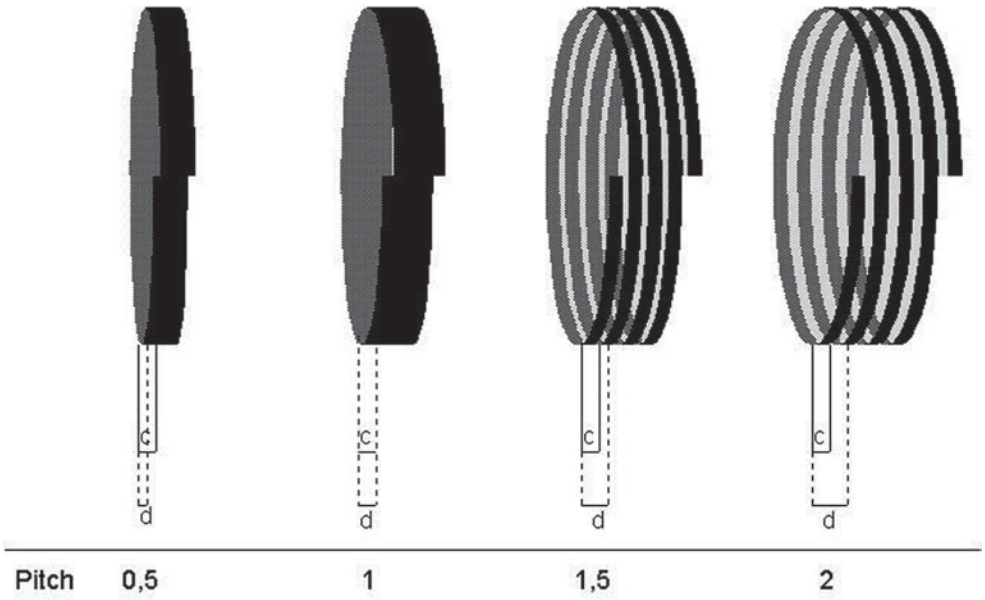

Fig. 5.3 *Pitch*. Several examples of increasing pitch. From the *left* to the *right,* we can see the unraveling of the helical geometry of volumetric CT acquisition. *c* slice thickness; *d* distance between two points at 360° rotation

Convolution kernels may smoothen or sharpen CT images. Sharp kernels and filters are used to enhance the edges of high-contrast structures (e.g. calcifications and stents).

Patient Selection

Inclusion Criteria

Normally, inclusion criteria for the scan are HR <65 bpm (spontaneous or induced by drugs) and the ability to maintain breath-hold for a period compatible with the scan time.[2, 3, 7] In the patients with high HR, beta-blocking agents are generally administered to optimize HR. These criteria are aimed at avoiding motion artefacts. Even though MDCT coronary angiography can be diagnostic with a higher HR, motion artefacts progressively reduce the number of segments that can be visualized correctly.[8] The second criterion aims at avoiding artefacts associated with respiratory motion.

Exclusion Criteria

Patients with a HR ≥ ³70 bpm, known allergies to iodinated contrast agent, renal insufficiency (serum creatinine >120 mmol/L), pregnancy, respiratory failure, unstable clinical conditions, and severe heart failure are excluded from the MDCT coronary angiography study. In case of mild renal failure, the administration of contrast agent may be better tolerated if the patient is adequately hydrated prior to contrast agent injection.[9]

Scan Parameters

The ideal protocol enables high spatial resolution (thin collimation), high temporal resolution (fast gantry rotation), and low radiation dose (prospective modulation of the tube current synchronized to the ECG[10] compatible with a good signal-to-noise ratio. The main scan parameters for 64-slice MDCT of the heart are presented in Table 5.1.

Regardless of the number of slices used, spatial and temporal resolutions need to be as high as possible, all the while remaining compatible with the other scan parameters. The final objective is to obtain a scan during an easily performed breath-hold. The duration of the scan is essentially linked to the number of slices and the pitch: generally <0.5 and more often <0.3 in retrospective gating. This allows for the oversampling of data that characterizes CT of the heart. Multi-segment reconstructions should be avoided, because there is no evidence to suggest that they are able to compensate for the lack of temporal resolution at higher HRs.

Retrospective Gating

The acquisition of image data during the MDCT coronary angiography scan is continuous during the cardiac cycle, such that the data corresponding to the phase when cardiac

Table 5.1. Scan and reconstruction parameters with 64-slice CT

Scan	Sensation 64
Detectors	64 (32 × 2)
Collimation	0.5–0.625 mm
Kilovolt	100–120
Milliampere/sec (range)	700–900
Rotation time	330 ms
Tube current modulation	Systolic
Effective temporal resolution	165 ms
Maximum temporal resolution	83 ms[a]
Effective spatial resolution	0.3 × 0.3 × 0.4 mm
Feed/rotation	3.84 mm (or adaptive)
Feed/second	11.63 mm
Pitch	0.2
Scan time	12 s
Reconstruction	
Effective slice width	0.5–0.75 mm
Reconstruction increment	0.3–0.4 mm
Temporal windows ("hot spots")	End-diastole/end-systole
Field of view (FOV)	140–180 mm
Filtro di convoluzione/kernel	Medium
Contrast Material	
Synchronization	Test bolus/bolus tracking
Region of interest (ROI)	Ascending aorta
Threshold in the ROI	+100–120 HU
Predelay	10 s
Transition time (breath-hold instructions)	4–6 s
CM volume	80–100 mL
CM rate	4–6 mL/s
Administration time	15–20 s
Iodine concentration	320–400 mgI/mL
Bolus chaser	40 mL @ 4–6 mL/s
Venous access	Antecubital
Total administration time	23–28 s

The table shows a simplified version of cardiac MDCT scan protocol. Parameters are adapted from the commonly used 64-slice MDCT scanners

[a]Multi-segment algorithm

motion is at a minimum need to be retrospectively extracted to minimize blurring and motion artefacts (Figs. 5.4 and 5.5).[5,6] This process is called *cardiac gating* (Fig. 5.2). Once the data have been acquired, they can be reconstructed with retrospective gating in any phase of the cardiac cycle by shifting the initial point of the image reconstruction window relative to the R-wave. Therefore, the combination of z-interpolation and cardiac gating enable generating a stack of parallel tomographic images that represent the heart in the

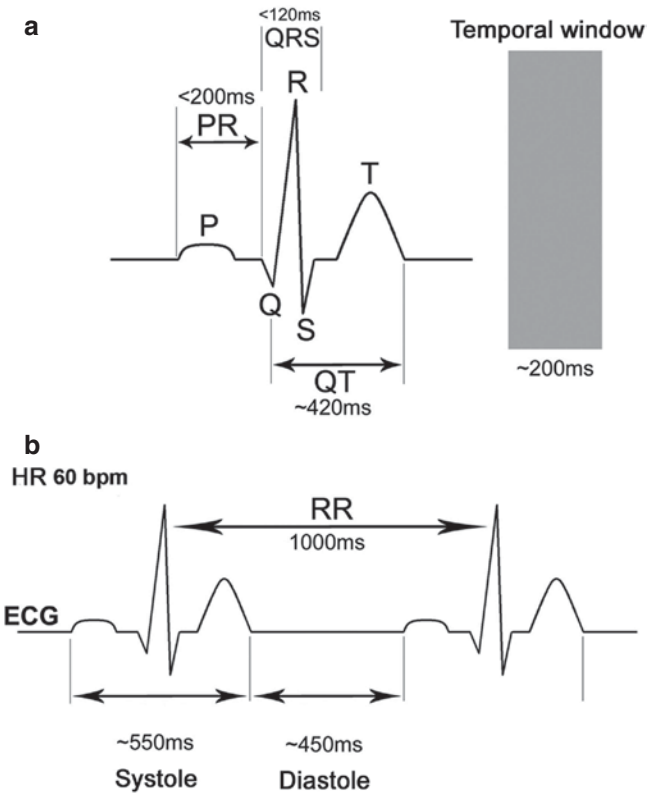

Fig. 5.4 Baseline ECG in multi-detector computed tomography (MDCT) coronary angiography. The cardiac cycle is composed of a systole and a diastole. Systole involves contraction of the atria, followed by contraction of the ventricles. The synchronized contraction is guided by a conducting system that arises from the sinoatrial node in the right atrium. The impulse then propagates to the atrio-ventricular node via the walls of the atria. From the atrio-ventricular node, the impulse is transmitted via the conducting system across the septum and the ventricular walls. This phenomenon is depicted by the ECG trace, which shows the typical sequence of waves **(a)** P-wave (atrial contraction), QRS complex (ventricular contraction), T-wave (ventricular repolarization). Normally, the P-R interval is <120 ms, the QRS complex is <80 ms, and the Q-T interval is ~320 ms. Therefore, the duration of a complete systolic contraction with repolarization wave is ~550 ms. The diastolic period is ~450 ms. This means that for a HR of 60 bpm, systole and diastole account for 55 and 45% of the cardiac cycle, respectively **(b)**. The ~200 ms windows for the ECG retrospectively gated reconstruction obtained with MDCT coronary angiography is generally placed in the diastolic phase **(a)**.The most generally favourable position extends from mid- to end-diastole just prior to the P-wave

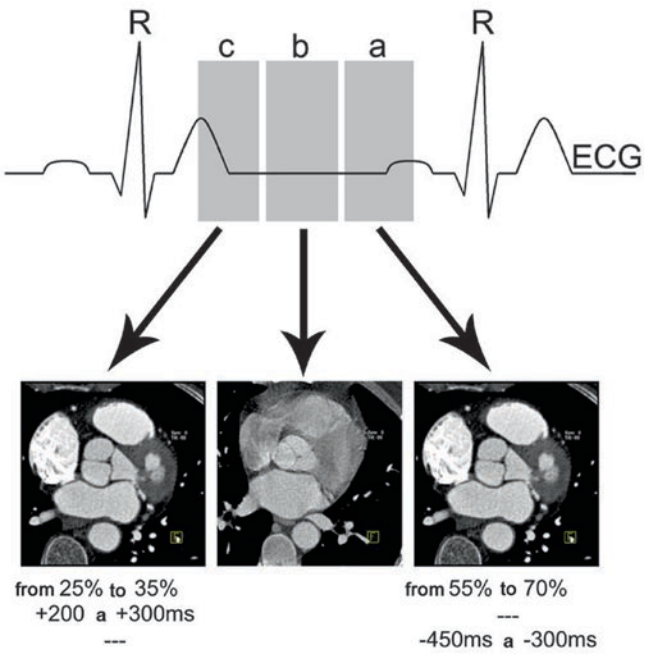

Fig. 5.5 Positioning the reconstruction time window. Several principles need to be borne in mind regarding the positioning of the time window when performing image reconstruction in MDCT coronary angiography. The operator should concentrate on three main areas of the ECG trace. The first **(a)** is the end-diastolic phase. In this phase, the ventricle has completed filling, just prior to atrial systole and motion is at a minimum. The second phase **(b)** is the early-mid diastolic phase. In this phase, the heart is filling and there is generally residual motion, which does not allow adequate coronary artery imaging. The third phase **(c)** is end-systole. In this phase, the heart is in isovolumetric contraction and motion is at a minimum. The images obtained in this phase can be just as valid as those obtained at end-diastole and in a number of cases, even better

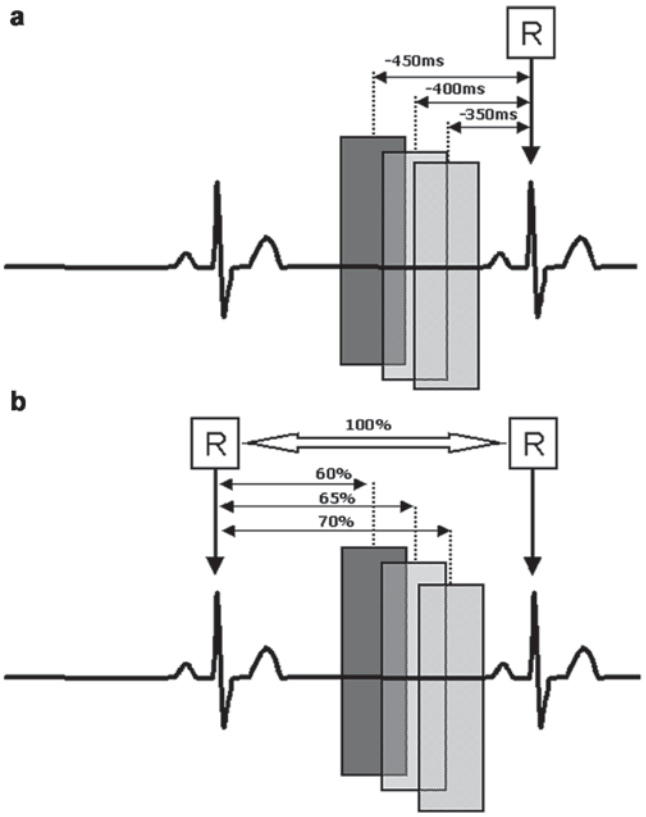

Fig. 5.6 End-diastolic positioning of temporal windows. In **a**, the temporal windows are positioned in the end-diastolic phase consecutively prior to the next R-wave at 50 ms distance each. In **b**, the temporal windows are positioned in the end-diastolic phase at 5% R-R interval distance

same phase of the cardiac cycle.[5, 6] A real optimization of retrospective gating is yet to be achieved.

To obtain images in the diastolic phase, some operators reconstruct the images in relation to the phase (i.e. a percentage) of the cardiac cycle (typically between 50% and 60% of the R-R interval), whereas others use the time window of the absolute interval prior to the peak of the next R-wave (typically 300–400 ms; Fig. 5.6).[11, 12] Multiple reconstructions are usually performed in different time windows, and the physician/operator successively selects the dataset where motion artefacts are minimal, paying particular attention to the visualization of the right coronary artery (RCA).[13] In MDCT, different coronary angiography time windows can be optimized and used in the same patient for the visualization of the left and right coronary arteries.[4, 12, 13] Improving the temporal resolution of the MDCT coronary angiography scan by increasing the gantry rotation speed is subject to obvious limitations. To overcome these difficulties, new data post-processing strategies have been proposed to further increase the temporal resolution. With the simultaneous acquisition of multiple slices using an MDCT coronary angiography scanner and the relative overlapping of the volume acquired, multi-segment reconstructions can be created.

In a multi-segment reconstruction, data acquired in the same cardiac phase but from different cardiac cycles are combined in a single image. In this case, the temporal resolution will depend on the number and size of the segments used for the creation of a single image, but it will be higher than that derived from a single segment.[5] This technique is sensitive to variations in beat-per-beat HR, and the current implementation of these algorithms does not always improve image quality.[14]

Prospective Triggering

The first geometry for ECG synchronization applied to tomographic equipments was prospective ECG triggering. In particular, this technique was applied to an older technology

(i.e. Electron Beam Computed Tomography) that could rely on a very high temporal resolution in the range of 50–100 ms. This technique suffered from low spatial resolution and the field of applications was mainly calcium score. In the last 2 years, CT technology has produced newer scanners with newer software and/or very high temporal resolution (i.e. dual-source CT with 83 ms temporal resolution). New software applications allow scanning prospectively using a "pad" (a temporal window that can be modified according to operator's experience and patient's HR). By combining these newer technologies with aggressive HR control it is possible to obtain diagnostic image quality with prospective ECG triggering (Fig. 5.2)

Radiation Dose

Radiation dose was one, if not the main, issue of cardiac CT since the first reports. The increase in spatial resolution and the intrinsic retrospective nature of scan geometry brought an inevitable increase in dose. With 64-slice CT and no special means for reduction, the range of dose was between 10 and 25 mSv. The first means to reduce radiation dose was applied to retrospective ECG gating and relied on ECG-controlled prospective tube current modulation (Fig. 5.7). Using this technique, it is possible to reduce radiation dose up to 50% depending on the patient's HR (the lower the HR, the lower the dose).

The recent implementation of prospective ECG triggering has lead to a dramatic reduction in radiation dose without significant deterioration of image quality (range: 1–4 mSv). This was achieved by exposing the patient to radiation only during the desired phase and performing acquisition without oversampling (pitch = 1.0).

Image Reconstruction

According to the literature, the techniques capable of providing diagnostic images are based on a few reconstructions concentrated from the mid- to end-diastole (the time windows are positioned at about 400 ms prior to the next R-wave or at 60–70% of the R-R interval). A variety of approaches can be used for the reconstructions. At least four different strategies can be listed (Fig. 5.8):

1. Relative delay strategy, whereby the delay time is a percentage of the R-R interval.[15]
2. Absolute delay strategy, whereby the delay time is constant after the previous R-wave.[15]
3. Absolute reverse delay strategy, whereby the delay time is constant prior to the next R-wave.[15]
4. End of the time window positioned at the peak of the P-wave.[16]

All four strategies can be used, but this will largely depend on the degree of experience of the operator, and to a lesser extent, on the capabilities of the software/hardware, the type of change in the HR, and the time available for the reconstructions.

Other reconstruction parameters are also relevant for obtaining an image of diagnostic quality. The effective slice thickness is usually slightly wider than the minimum possible collimation so as to improve the signal-to-noise ratio of the image. The reconstruction increment should be about 50% of the effective slice thickness, so as to improve the spatial resolution and the overlap in the *z*-axis. The FOV should be as small as possible to include the entire heart, so as to fully exploit the image matrix, which is constant (512 × 512 pixels). The convolution kernel should be half way between noise and image quality. In general, medium

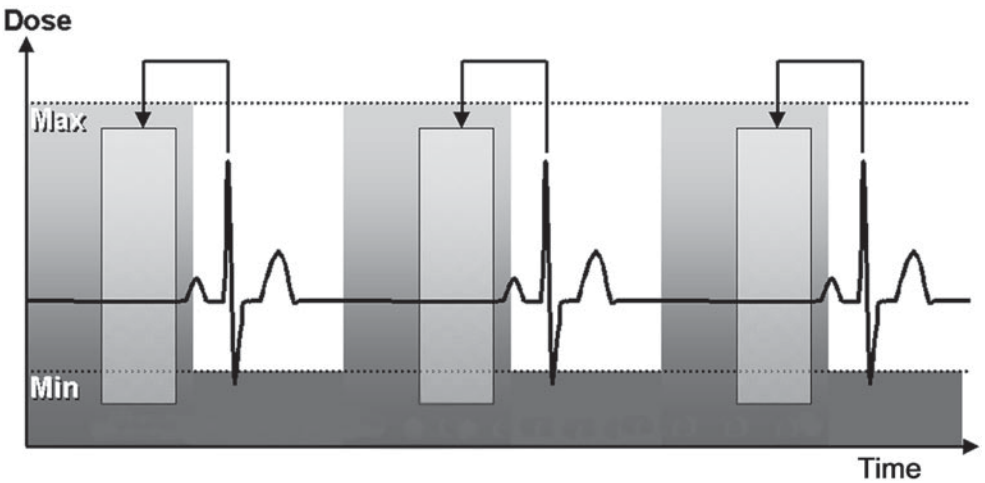

Fig. 5.7 Prospective tube current modulation. While the reconstruction can be reliably performed in the end-diastolic phase (especially at low and regular HRs), tube current can be modulated and reduced to 4–20% of the peak during the systolic phase

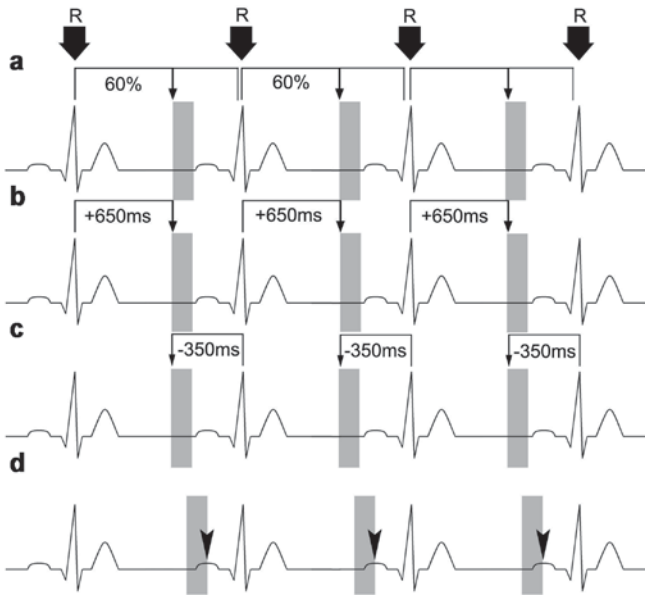

Fig. 5.8 Retrospective cardiac gating techniques. The figure depicts different strategies for cardiac gating in MDCT coronary angiography. **(a)** Probably, the most widely used strategy: percentage relative delay. The software calculates the distance from one R-wave to the next, and positions the time window at a defined point based on the percentage of the entire R-R interval. **(b)** Absolute delay. With this strategy, the time window is placed according to a fixed delay time after the previous R-wave. **(c)** Absolute reverse delay. With this strategy, the time window is placed with a fixed time delay prior to the next R-wave. **(d)** With this strategy, the final portion of the time window is positioned at the peak of the P-wave. The aim of this approach is to "strike" the final moment of cardiac akinesia prior to systolic contraction

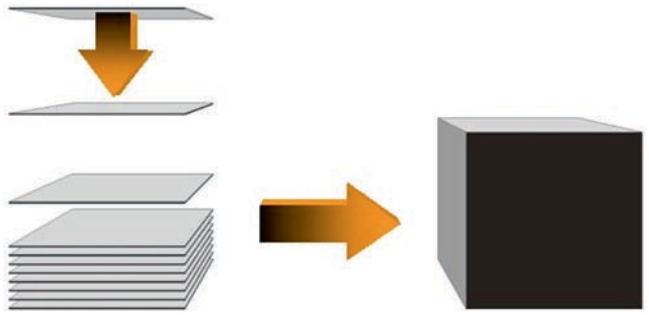

Fig. 5.9 Volume dataset. The stack of axial images derived from the reconstruction platform is interpolated (or "fused") into a continuous volume

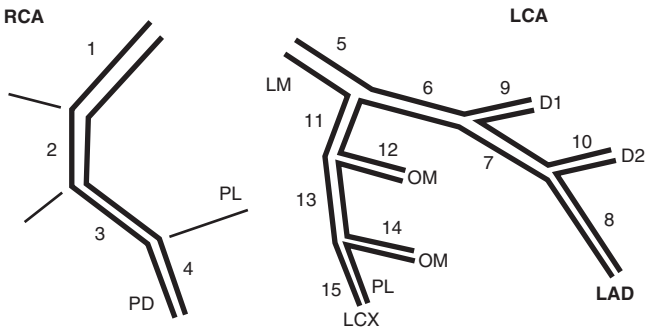

Fig. 5.10 Classification of coronary artery segments. The figure shows a diagram of the coronary tree divided into 15 segments according to the modified American heart association classification.[18] The classification includes most of the segments with diameter > 1.5 mm. *LCA* left coronary artery; *LCX* left circumflex coronary artery; *LAD* left anterior descending coronary artery; *LM* left main coronary artery; *OM* obtuse marginal branch; *RCA* right coronary artery; *D1* first diagonal branch; *D2* second diagonal branch; *PL* postero-lateral branch; *PD* posterior descending branch

convolution kernels are used for coronary artery imaging. When the coronary arteries are highly calcified or stents are present, sharper convolution kernels may be used; although they tend to increase image noise, they usually improve the visualization of the vessel wall or the structure of the stent and its lumen.

Image Evaluation

The stack of axial images resulting from the reconstruction will be fused into a continuous volume of data (Fig. 5.9). There is still no standardized technique for the evaluation of MDCT coronary angiography images. In terms of repeatability, the performance of MDCT coronary angiography is currently operator-dependent.[17] The evaluation is generally performed with the American Heart Association classification in 15 or 16 coronary segments.[18] With this classification in mind, the operator carefully observes the clinically more important segments (Fig. 5.10). The studies conducted till date have demonstrated the ability of MDCT coronary angiography to identify significant stenoses that are defined as a reduction in lumen diameter ≥ ³50%.[2, 3, 7] The evaluation is always done in a semi-quantitative fashion. The first step is to observe the axial images by scrolling the dataset to evaluate whether there are any pertinent findings that do not regard the coronary arteries. At the same time, the location of the cardiac structures can be checked (e.g. the great thoracic vessels, the cardiac valves, the atria, the ventricles, etc.), including the coronary arteries, to identify the presence of significant morphologic anomalies.

The next step involves the evaluation of the multi-planar reconstructions (MPR). For each vessel, there is a dedicated plane that facilitates its correct and complete visualization. The main planes for the evaluation of the coronary arteries are: (1) the plane parallel to the atrio-ventricular groove, which enables the longitudinal visualization of the RCA and the left circumflex artery and (2) the plane parallel to the

interventricular groove, which enables the visualization of the left anterior descending coronary artery (LAD). Once the best evaluation plane has been obtained, in the event the vessel has a tortuous course, the reconstruction algorithm for maximum intensity projections (MIP) can be used. If vascular calcifications are absent or present in only minimal quantities, an MIP with a thickness between 5 and 8 mm is usually excellent, whereas if the calcifications are present in great quantity, the slice thickness needs to be reduced. Manual or automatic tracing of the centreline of the vascular lumen to produce curved MPR reconstruction may be useful when the vessel is only partially visualized, but can also be employed when it can be completely visualized in a plane. When dedicated software is used, the resulting image may be rotated 360° on its own axis. At the same time, a cross-sectional plane of the vessel is visualized. This modality of visualization is particularly useful for the evaluation of stenoses with a semi-quantitative system. Volume rendering images are usually reconstructed to obtain a global view and for teaching purposes.

Limitations of MDCT Coronary Angiography

Patients with a HR > 70 bpm should not undergo MDCT coronary angiography. Only patients with slightly irregular cardiac rhythms can be included (e.g. early beat, atrial fibrillation, left bundle-branch block, prolonged QRS complex, HR < 40 bpm, etc.). In this case, the scan should not be performed with ECG-controlled tube current modulation.[10] In the presence of an abnormal HR, the location of the period with lowest dose will be variable and can be included within diastole. In addition, the presence of rhythm irregularities, with the exclusion of low HR (<40 bpm), does not allow the application of multi-segment reconstruction algorithms.[19, 20] This is owing to the variability in diastolic filling, which hampers the combination of data originating from contiguous cardiac cycles.

Future Developments and Outlook

The newer technical developments are all aiming to further reduce the radiation dose, improve image quality, and extend the spectrum of applications. The reduction of radiation exposure is already a reality, as the latest solutions allow an average dose of 1–2 mSv. We expect a further dose reduction by the implementation of dual-energy, with respect to sub-mSv cardiac CT. Image quality will increase owing to the improvement of detector technology (more sensitivity and speed). The final objective would be flat panel technology with 0.2 mm^3 resolution. The spectrum of applications will be enhanced again with the implementation of dual-energy. The possibility to obtain multi-parametric imaging of the heart with CT will enhance plaque characterization, delayed enhancement, and perfusion capabilities without significant impact on the radiation dose.

Conclusions

The recent development and technological research in cardiologic imaging with MDCT is integrating and profoundly changing the diagnostic protocol of the patient with suspected coronary artery disease for whom percutaneous coronary angiography has for long been the imaging modality of absolute diagnostic value. It should nonetheless be borne in mind that although MDCT coronary angiography is a promising technique, it is the sole domain of highly skilled operators. The clinical outcome of the technique is in fact closely associated with the optimization of each step of the procedure.

References

1. Flohr TG, Schoepf UJ, Kuettner A, et al Advances in cardiac imaging with 16-section CT systems. *Acad Radiol*. 2003;10:386–401
2. Nieman K, Cademartiri F, Lemos PA, et al Reliable noninvasive coronary angiography with fast submillimeter multislice spiral computed tomography. *Circulation*. 2002;106:2051–2054
3. Ropers D, Baum U, Pohle K, et al Detection of coronary artery stenoses with thin-slice multidetector row spiral computed tomography and multiplanar reconstruction. *Circulation*. 2003;107: 664–666
4. Achenbach S, Ulzheimer S, Baum U, et al Noninvasive coronary angiography by retrospectively ECG-gated multislice spiral CT. *Circulation*. 2000;102:2823–2828
5. Ohnesorge B, Flohr T, Becker C, et al Cardiac imaging by means of electrocardiographically gated multisection spiral CT: initial experience. *Radiology*. 2000;217:564–571
6. Kachelriess M, Kalender WA. Electrocardiogram-correlated image reconstruction from subsecond spiral computed tomography scans of the heart. *Med Phys*. 1998;25:2417–2431
7. Mollet NR, Cademartiri F, Nieman K, et al Multislice spiral computed tomography coronary angiography in patients with stable angina pectoris. *J Am Coll Cardiol*. 2004;43:2265–2270
8. Nieman K, Rensing BJ, van Geuns RJ, et al Non-invasive coronary angiography with Multislice spiral computed tomography: impact of heart rate. *Heart*. 2002;88:470–474
9. Aspelin P, Aubry P, Fransson SG, et al Nephrotoxic effects in high-risk patients undergoing angiography. *N Engl J Med*. 2003;348: 491–499

10. Jakobs TF, Becker CR, Ohnesorge B, et al Multislice helical CT of the heart with retrospective ECG gating: reduction of radiation exposure by ECG-controlled tube current modulation. *Eur Radiol*. 2002;12:1081–1086
11. Nieman K, Oudkerk M, Rensing BJ, et al Coronary angiography with multi-slice computed tomography. *Lancet*. 2001;357:599–603
12. Georg C, Kopp A, Schroder S, et al Optimizing image reconstruction timing for the RR interval in imaging coronary arteries with multi-slice computerized tomography. *Rofo Fortschr Geb Rontgenstr Neuen Bildgeb Verfahr*. 2001;173:536–541
13. Hong C, Becker CR, Huber A, et al ECG-gated reconstructed multi-detector row CT coronary angiography: effect of varying trigger delay on image quality. *Radiology*. 2001;220:712–717
14. Flohr T, Ohnesorge B. Heart rate adaptive optimization of spatial and temporal resolution for electrocardiogram-gated multislice spiral CT of the heart. *J Comput Assist Tomogr*. 2001;25:907–923
15. Cademartiri F, Luccichenti G, Marano R, et al Non-invasive angiography of the coronary arteries with multislice computed tomography: state of the art and future prospects. *Radiol Med (Torino)*. 2003;106:284–296
16. Sato Y, Matsumoto N, Kato M, et al Noninvasive assessment of coronary artery disease by Multislice spiral computed tomography using a new retrospectively ECG-gated image reconstruction technique. *Circ J*. 2003;67:401–405
17. Cademartiri F, Mollet NR, Lemos PA, et al Standard vs. user-interactive assessment of significant coronary stenoses with multislice computed tomography coronary angiography. *Am J Cardiol*. 2004; 94:1590–1593
18. Austen WG, Edwards JE, Frye RL, et al A reporting system on patients evaluated for coronary artery disease. Report of the Ad Hoc committee for grading of coronary artery disease, council on cardiovascular surgery, American heart association. *Circulation*. 1975;51(suppl 4):5–40
19. Dewey M, Laule M, Krug L, et al Multisegment and halfscan reconstruction of 16-slice computed tomography for detection of coronary artery stenoses. *Invest Radiol*. 2004;39:223–229
20. Halliburton SS, Stillman AE, Flohr T, et al Do segmented reconstruction algorithms for cardiac multi-slice computed tomography improve image quality? *Herz*. 2003;28:20–31

Chapter 6

CMR: BASIC PRINCIPLES

Jeremy Wright and Jan Bogaert

CONTENTS

J. L. Zamorano et al. (eds.), *The ESC Textbook of Cardiovascular Imaging*
DOI: 10.1007/978-1-84882-421-8_6, © Springer-Verlag London Limited 2010

Introduction

Cardiac magnetic resonance imaging (CMR) is one of the newer non-invasive cardiac diagnostic imaging modalities. Recent advances have enabled CMR to come close to the goal of a complete examination of the cardiovascular system by a single modality. It can provide relevant information on most aspects of the heart–structure, global and regional ventricular function, valve function, flow patterns, myocardial perfusion, coronary anatomy, and myocardial viability, all obtained non-invasively in a single study in 30–60 min.

The aim of this chapter is to describe the physics and practical aspects of CMR and then explore the available pulse sequences, so that the clinical utility of CMR can be maximized.

Introduction to MRI Physics

Magnetic resonance imaging (MRI), formerly called nuclear magnetic resonance (NMR), relies on the physical properties of hydrogen nuclei (protons). These protons, abundantly present in the human body, have an intrinsic "spin." When a patient is brought into a high-strength magnetic field, the "spins" of the human body align with the direction of the magnetic field.[1] Application of a radiofrequency (RF) pulse can excite the spins and perturb their alignment, with the vector components in line with the magnetic field (longitudinal magnetization) and perpendicular to the field (transverse magnetization). These spins gradually return to their resting state (relax) and in the process create RF signals that are used to create an image. The magnitude of signal arising from the tissue is mainly influenced by two relaxation times (T1 and T2), proton density, and movement of the protons (blood flow).[2]

T1 is the time constant describing the return of longitudinal magnetization to baseline, and T2 is the time constant describing the return of transverse magnetization to baseline. Note that T1 and T2 of a proton are independent and vary according to the local environment of the proton (i.e. the tissue). This phenomenon enables the excellent soft-tissue discrimination seen in MRI images. Fat and water are at the extremes of T1 and T2 relaxation times. Fat has short T1 and T2, whereas water has long T1 and T2 times. T1-weighted images exploit the differences in T1 relaxation behaviour among tissues. For instance, fat has a hyper-intense ("bright") appearance and fluid has a hypo-intense ("dark") appearance, while myocardial tissue is iso-intense ("gray"). In comparison, on T2-weighted images, fluid has a bright appearance, while fat has a less bright appearance.

Image formation also requires understanding of the origin of a particular signal in the patient. This is achieved by the application of magnetic field gradients in a process called spatial encoding, a detailed discussion of this can be found in any basic MR textbook. For any image "slice," the raw data acquired are called K-space[3] and consist of multiple lines of data (typically between 128 and 256). To generate an image, the K-space data undergo a complex mathematical process called Fourier transformation. The key concept of this transformation is that the centre of K-space contains image-contrast information, while image resolution is governed by the periphery of K-space.[4]

Contraindications to MRI

The main contraindications to MRI relate to the presence of metal within the patient. Non-magnetic material has a risk of heating and electric current induction, while ferromagnetic material may move in the magnetic field. Patients with permanent pacemakers, defibrillators, and other implanted devices (neurostimulator, insulin pump, cochlear implant, etc.) should not undergo MRI. Sternal wires, most prosthetic cardiac valves, coronary stents, orthopaedic implants, and surgical clips are NOT contraindications – though all should be verified as MRI compatible before the patient enters the scanner.

MRI Contrast Agents

Contrast agents are often used in assessing ischaemic heart disease patients with CMR.

The most commonly used contrast agents contain chelates of the lanthide metal element gadolinium with multi-dentate ligands (e.g. Gd-DTPA or Gd-DOTA). These are non-specific contrast agents that distribute throughout the extracellular space and are renally excreted in an unchanged form. They shorten the T1 relaxation times of tissues, and therefore result in an increase in signal intensity on T1-weighted images (lesser effect on T2). The typical dose is 0.1–0.2 mmol/kg (~15–30 mL). Side effects are very rare, and these contrast agents have proven to be much safer than the iodinated contrast agents used for conventional X-ray. However, precautions are still necessary. Gadolinium-containing contrast agents do not cause renal dysfunction, but should be avoided in patients with GFR < 60 mL/min/1.73m^2 because of the recently observed association with nephrogenic systemic fibrosis.[5] Gadolinium should be avoided in patients

with haemolytic and sickle cell anaemia, and use during pregnancy is discouraged. It is important to note that assessment of cardiac structure, global and regional myocardial function, valve function, coronary angiography, and flow quantification can be performed without administration of contrast.

Pulse Sequences

A pulse sequence is a carefully timed series of RF pulses and magnetic field gradients, and provides the raw information filling K-space - the "echo." The two broad families of pulse sequences are spin-echo and gradient-echo.

In spin-echo sequences, a 90° RF pulse is applied to the selected slice, so that the resting longitudinal magnetization (Z) is entirely flipped into the transverse (XY) plane. The transverse magnetization begins to dephase when a 180° RF pulse is applied. This causes the transverse magnetization to partially rephase and produce a spin "echo," filling one line of K-space. This rephasing 180° pulse can be repeated multiple times to acquire multiple lines of K-space, and this is known as fast or turbo-spin echo. Excellent quality images can be obtained with T1, T2, or proton-density weighting. The main drawback of these sequences is the long time required to fill K-space.

In contrast, gradient-echo pulse sequences utilize a smaller initial RF pulse (usually between 10 and 90°) and then apply magnetic field gradients to rephase the magnetic moments to produce a signal known as a "gradient" echo. These sequences can produce images with T1, T2, or proton density weighting. The main advantage of gradient echo sequences is that gradient-echoes can be generated very quickly, so that scan times are reduced. The main disadvantage is an increased susceptibility to artefacts.

Imaging speed is a key concern in cardiac MRI, and parallel imaging is often used to reduce scan times or improve temporal resolution.[6,7] The vendors have slightly different parallel imaging techniques - SENSE (Philips), ASSET (General Electric), GRAPPA (Siemens). They all rely upon multiple-element coils that allow under-sampling of K-space and allow for a 2–3-fold reduction in scan times. The main disadvantage of parallel imaging is a reduced signal-to-noise ratio (SNR).

Cardiac Motion

As with other imaging modalities, CMR data acquisition is synchronized to cardiac motion using the electrical activity of the heart. The magnetic field exerts a significant magneto hydrodynamic effect on the surface ECG, resulting in a voltage artefact in the ST segment of the ECG. Reliable R-wave detection is possible using a vector cardiogram[8] (VCG), but reliable ST/T-wave monitoring is not possible. The VCG can be used for either prospective triggering or retrospective gating.

Prospective triggering is typically used for single-phase acquisitions, i.e. a static image of the heart at a single point in the cardiac cycle. Information is acquired at a specific interval after the R-wave, usually chosen to coincide with diastases (when the heart is relatively still). Typically, the data for a single slice are obtained in a ~10 s breath-hold.

Multi-phase acquisitions are used to acquire dynamic information such as cine MRI. Typically, data is acquired throughout the cardiac cycle and is reconstructed with retrospective reference to the VCG. Usually, the cardiac cycle is divided into 20–30 phases. One image is reconstructed for each phase, and the resulting images are displayed as a cine loop. A single slice cine loop is acquired during a ~10 s breath-hold.

Real-time cine MRI images can be acquired by increasing the parallel imaging factor and reducing the spatial resolution. With these sequences, it is possible to obtain diagnostic images in patients who cannot breath-hold and in those with very irregular cardiac rhythms (when normal cine images are often sub-optimal).

Respiratory Motion

Most CMR images are obtained during breath-holds, typically of 10–15-s duration. In general, an end-inspiratory breath-hold is more comfortable and can be held longer. However, a breath-hold at the end of gentle expiration tends to be more consistent (minimizing slice misregistration) and is less likely to provoke ectopy. We generally commence with inspiratory breath-holds, but have a low threshold for changing to expiration. Administration of oxygen is helpful for patients experiencing shortness of breath.

The use of a navigator-echo during free breathing is an alternative method of image acquisition and is typically used for high-resolution imaging such as coronary angiography. The navigator-echo is typically positioned on the right hemidiaphragm to monitor respiratory motion. The patient is instructed to breathe regularly and consistently, and image information is only acquired when the diaphragm is in a predetermined position (e.g. end expiration). Depending on the scan prescribed and the navigator efficiency, these scans take 5–15 min to acquire.

We will now discuss the specific sequences used for the assessment of cardiac function, cardiac morphology, perfusion, viability, and MR angiography.

Cardiac Function

The balanced steady state free procession (b-SSFP) sequence is the mainstay of functional assessment.[9] There are several monikers; balanced FFE (Philips), FIESTA (General Electric), TrueFISP (Siemens). The resultant images are not T1- or T2-weighted; rather the signal intensity depends on the ratio of T2/T1 in addition to flow. Therefore, blood, water, and fat all appear bright.

First, a set of single-phase localizer scout views are obtained in the axial, coronal, and sagittal planes. Next, a cine sequence is obtained in the vertical long axis (VLA) - a plane prescribed on the axial images through the apex of the LV and the middle of the mitral valve (Fig. 6.1a). On this image, a second cine sequence is prescribed in the horizontal long axis (HLA) - transecting the LV apex and the middle of the mitral valve (Fig. 6.1b). Now, the LV short axis can be prescribed, perpendicular to both the VLA and HLA. The ventricles are encompassed in a stack of 10–12 contiguous slices in short-axis direction (Fig. 6.1c-d). The end-diastolic and end-systolic frames are selected, and then the endocardial and epicardial contours are delineated. This allows calculation of global functional parameters, end-diastolic volume (EDV), end-systolic volume (ESV), stroke volume (SV), ejection fraction (EF), and myocardial mass. This is the reference standard for in vivo assessment of myocardial volume, global function, and mass.[10–13] Regional function is assessed qualitatively and quantitatively. In addition to short-axis slices, the standard echocardiographic views can be prescribed; 2-chamber, 4-chamber, and apical long axis views. Qualitative evaluation of LV contractility is reported using the 17-segment model proposed by the American Society of Echocardiography.

It is also possible to perform volumetric quantification of the right ventricle (RV) on the stack of short-axis slices. However, it can be challenging to recognize the plane of the tricuspid valve. Therefore, we prefer to perform quantification of RV function on a stack of contiguous axial images that encompasses the heart.

Valvular function can also be assessed with cine imaging. The valve leaflets are easily seen (Fig. 6.2) and mechanisms

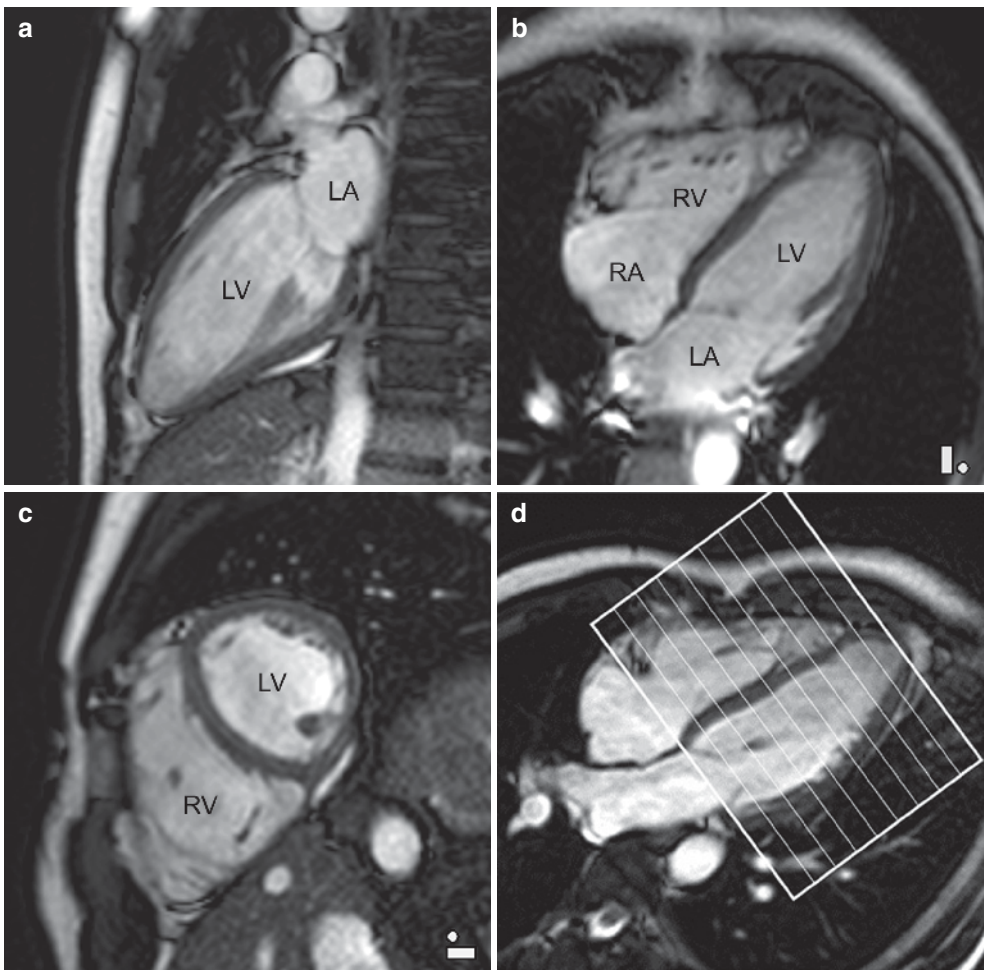

Fig. 6.1 Assessment of cardiac function. A b-SSFP cine sequence is used for functional assessment (only end diastolic frames are shown here). From the localizer scout images, the VLA plane is prescribed **(a)**. A plane perpendicular to the VLA produces the HLA **(b)**. The LV short-axis plane can now be prescribed, perpendicular to both the VLA and HLA **(c)**. The LV is encompassed by a stack of slices in the short-axis plane **(d)** to enable quantification of ventricular volumes and assessment of global and regional systolic function. *LV* Left ventricle; *LA* Left atrium; *RV* Right ventricle; *RA* Right atrium; *VLA* Vertical long axis; *HLA* Horizontal long axis

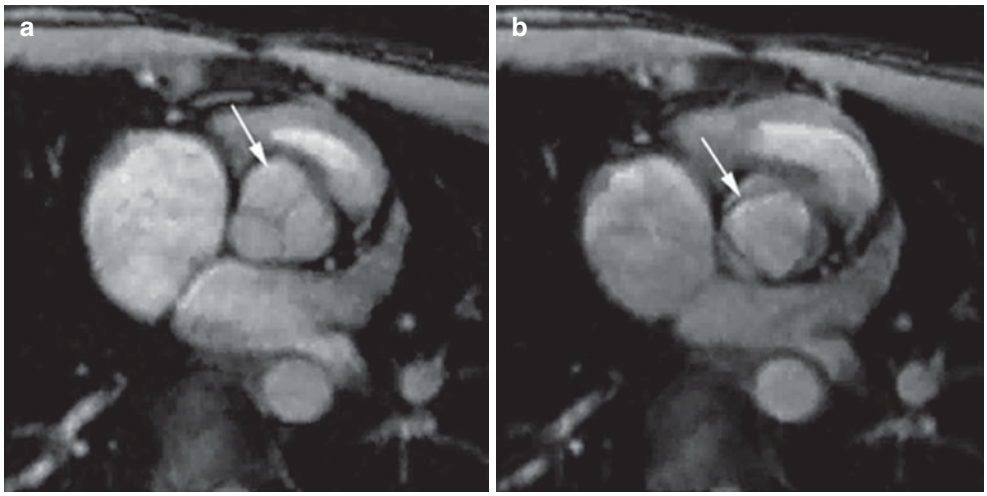

Fig. 6.2 Assessment of valve morphology. Valve morphology and function can be qualitatively assessed with b-SSFP cine imaging. Short-axis images of the aortic valve at end diastole **(a)** and mid-systole **(b)** demonstrate a tri-leaflet aortic valve with thin leaflets that open normally (*arrow*)

of dysfunction identified. Although the b-SSFP sequence is designed to be relatively flow "insensitive," turbulent flow through stenotic or regurgitant valves is visible. The regurgitant fraction of an isolated valve lesion can be calculated from the difference between LV and RV stroke volume. Further assessment of valve dysfunction will be discussed in the section on velocity-encoded CMR.

Myocardial tagging is another CMR technique useful in functional analysis.[14] A grid or tag of lines on the myocardium is transiently created, and these lines track the underlying myocardial deformation. These images can be analyzed qualitatively and quantitatively, e.g. strain analysis, but the elaborate post-processing required for quantitative analysis has largely limited it to the research setting.

Cardiac Morphology

In addition to cine MRI, additional information on cardiac morphology can be obtained using spin-echo sequences. These are typically used to produce images at a single phase of the cardiac cycle–usually mid-diastole. Optimal depiction of cardiac anatomy is achieved by making the flowing blood appear black by using two 180° inversion pre-pulses (double inversion recovery).[15] A third inversion pre-pulse can also be applied to suppress the signal arising from fat. The images can be T1- or T2-weighted. T1-weighted images typically provide excellent delineation of cardiac anatomy (Fig. 6.3a).

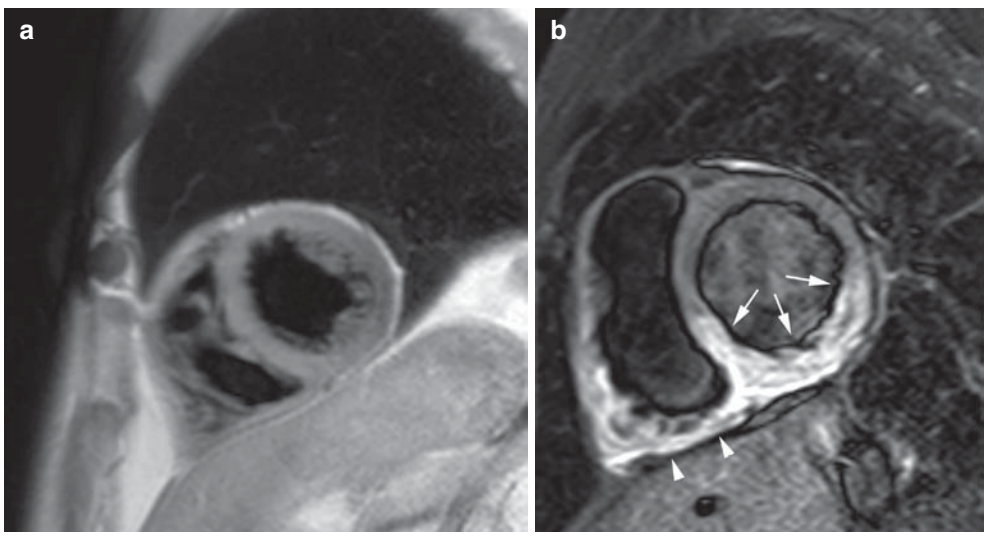

Fig. 6.3 Assessment of cardiac morphology with fast spin-echo. Cardiac morphology can be assessed with fast spin-echo sequences and "black-blood" pre-pulses. A single-phase image in mid-diastole is usually acquired, to minimize motion artefact. These images can be T1- or T2-weighted, with or without fat suppression. **(a)** T1-weighted short-axis image (without fat suppression) of a normal heart. **(b)** T2-weighted short-axis image (with fat suppression) of a patient with a large inferior myocardial infarction. Note the marked increase in signal intensity (*white*) in the inferior, inferolateral, and inferoseptal segments of the left ventricle (*arrows*) as well as the extensive involvement of the inferior wall of the right ventricle (*arrowheads*)

In contrast, T2-weighted images provide unique information about free water content and are highly useful to detect and quantify myocardial oedema, e.g. in patients with acute myocardial infarction[16] (Fig. 6.3b).

Another unique property of MRI is the ability to estimate tissue iron content.[17] This is possible because iron within tissue becomes "magnetized," and causes a reduction in the T2 and T2* relaxation times (T2* is the time constant reflecting T2 relaxation and dephasing owing to local magnetic field inhomogeneities). The technique has been validated for the assessment of iron content in the liver and myocardium. To measure myocardial T2*, a single-phase LV short-axis slice is acquired using 2–8 echo times, and a trend line is fitted to the plot of signal intensity vs. echo time.

Contrast-Enhanced CMR

Contrast-enhanced CMR - also called delayed contrast-enhanced, late gadolinium enhancement, or contrast-enhanced IR (CE-IR), is a key strength of CMR and is considered the reference standard for in vivo assessment of myocardial infarction in both the acute and chronic phase. It has been extensively evaluated in animal and human studies[18–20] and can accurately measure infarction within 1 g. The technique is called "late" or "delayed" because images are typically obtained 10–20 min after injection of contrast. This is the optimal time to discriminate between normal and abnormal myocardium, with the maximum difference in gadolinium-contrast concentration between normal and abnormal tissue. The usual dose of contrast is 0.15–0.2 mmol/kg.

The mechanism of accumulation of contrast within infarcted tissue is incompletely understood. Regarding acute infarction, it is thought that myocardial cell membrane rupture allows gadolinium to diffuse into the intracellular space (it must be noted that gadolinium is an extracellular contrast agent). The greater distribution area, concomitant myocardial oedema, and altered contrast kinetics result in hyper enhancement relative to the normal myocardium.[21] The mechanism of contrast accumulation within chronic infarcts is thought to be due to increased interstitial space between collagen fibres, combined with slower wash-in and wash-out contrast kinetics of infarct tissue compared with normal myocardium.[22]

The technique consists of first applying an inversion RF pre-pulse.[23] As the "spins" of a tissue "relax" towards their resting state, they pass through a point where they have 0 longitudinal magnetization. If image information is acquired at this point, no signal will arise from these spins, which are "nulled" and appear dark on the resultant image. This delay between the inversion pre-pulse and image acquisition is called the inversion time (TI). Typically, we choose to null the signal of normal myocardium, while infarcted or scarred myocardium has a bright signal because of the gadolinium within it (Fig. 6.4a). The TI to null normal myocardium is variable and depends on patient weight, contrast dose, renal function, and time-point after injection of the contrast. It is usually between 200–250 ms for the first images and 250–300 ms for later images. Choosing the correct TI is crucial to maximize the contrast between normal and abnormal myocardium and to prevent image artefacts. Experienced users can usually satisfactorily estimate the TI, but in difficult cases (and for inexperienced users), pulse sequences are available to help choose the ideal TI (Look Locker, TI-scouting). A new type of pulse sequence, called the phase-sensitive inversion-recovery (PS-IR), has been developed to overcome the difficulty of choosing TI.[24] These sequences are not available from all vendors, but they enable the TI to be arbitrarily chosen with no adverse effect on the resultant image.

2D and 3D acquisition schemes are available. 3D acquisitions enable imaging of the entire heart in a single breath-hold

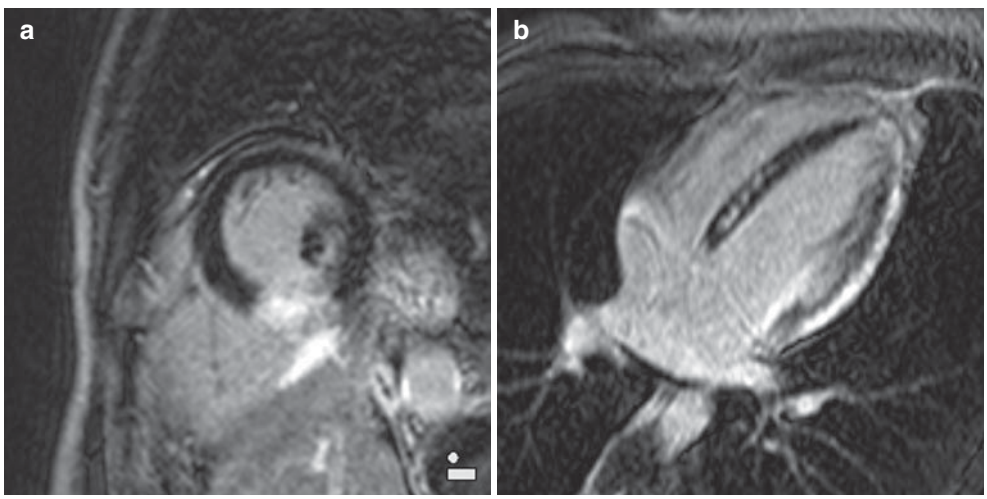

Fig. 6.4 Contrast-enhanced CMR. A short-axis slice of the left ventricle at mid-ventricular level showing trans-mural hyper-enhancement of the mid-inferoseptal segment owing to acute myocardial infarction **(a)**. Note that there is also enhancement of the inferior wall of the right ventricle owing to infarction. Contrast enhancement is not specific for ischaemic injury. **(b)** shows extensive sub-epicardial enhancement of the lateral wall with patchy mid-wall enhancement in the ventricular septum owing to myocarditis

with a high SNR, but are prone to image blurring.[25] In contrast, 2D sequences acquire one slice per breath-hold (more tiring for the patient) and have lower SNR. However, despite more image "noise," the 2D images usually provide greater spatial resolution. We recommend commencing with a 3D sequence and to examine abnormal areas with a 2D sequence.

It is important to emphasize that enhancement on contrast-enhanced CMR images is not specific for ischaemic injury; it can also be seen in myocarditis (Fig. 6.4b), infiltrative disorders (e.g. amyloid, sarcoid), and cardiomyopathies (e.g. hypertrophic, arrhythmogenic right ventricular dysplasia).[26] It is the pattern of enhancement that is used to distinguish the different etiologies.

Myocardial Perfusion

"First-pass" imaging after intravenous injection of a small dose of contrast is the standard CMR method of assessing myocardial perfusion (perfusion-CMR).[27] It is performed at rest and during pharmacologic vasodilator stress (Adenosine or Dipyridamole). Usually, 3–5 short-axis slices of the LV are obtained to encompass all myocardial segments. An ultrafast acquisition scheme is required, because each slice is imaged once per heartbeat immediately after gadolinium contrast (usually injected at 2 mL/s followed by a saline flush). The optimal dose of gadolinium is 0.03–0.1 mmol/kg, depending on the sequence used and whether visual analysis (higher dose) or semi-quantitative analysis is planned.

Visual analysis is the most frequently used approach. A perfusion defect is identified as a region of non-enhancing myocardium during the first pass of contrast (Fig. 6.5). A defect is most pronounced in the sub-endocardium and has variable trans-mural spread. It is critical to differentiate true defects from frequently encountered dark rim artefacts.[28] Semi-quantitative assessment is usually performed by the analysis of signal intensity-time curves. The myocardial perfusion reserve index (MPRI) is calculated by comparing the myocardial perfusion upslope between rest and stress.[29–31] Absolute quantitative assessment of perfusion can also be performed, but is largely confined to the research setting.

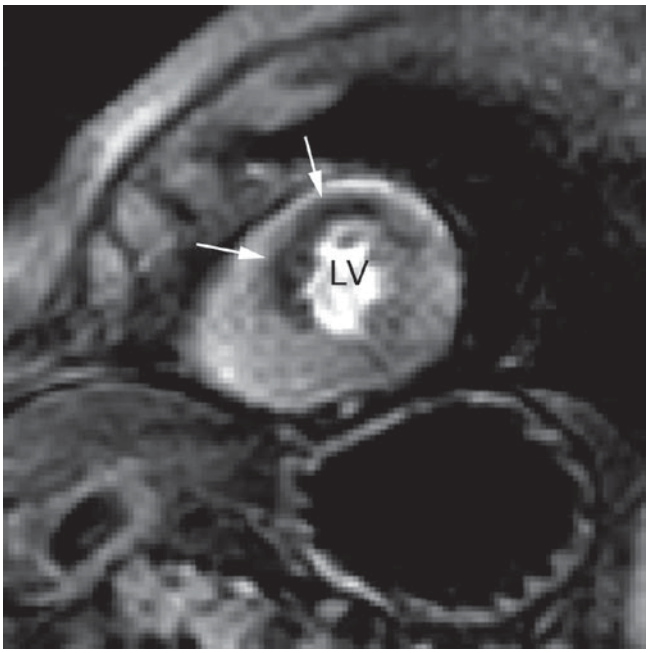

Fig. 6.5 Adenosine stress first-pass myocardial perfusion imaging. A short-axis slice of the left ventricle at mid-ventricular level is shown during the first pass of intravenous gadolinium during adenosine vasodilator stress. There is a large perfusion defect in the mid-anterior and antero-septal segments (*arrows*)

Velocity-Encoded CMR

Velocity-encoded CMR, also known as phase-contrast flow quantification, is an established fast and simple method of measuring blood flow.[32] It is based upon the phenomenon that as "spins" flow along a magnetic field gradient, they acquire a "shift" in their transverse (XY) magnetization. This shift is proportional to the strength of the magnetic field gradient as well as the flow velocity, which can thus be calculated. Comparisons with invasive measurements and phantom studies have demonstrated that the overall error in flow measurement is <10%.[33–35]

To measure flow through a vessel, first an image slice is prescribed perpendicular to the flow direction. It is important that this slice is within 15° of the true perpendicular plane; otherwise, flow will be significantly under-estimated (similar to the principle of Doppler line-up in echocardiography). Second, an appropriate encoding velocity (VENC) is selected, which must be greater than the highest velocity in the flow, otherwise aliasing will make the data unreliable. The images are acquired during a 15–20 s breath-hold, and minor post-processing produces flow and velocity data (Fig. 6.6). Flow in any vessel can be assessed, though in clinical imaging, vessels smaller than the pulmonary veins are rarely quantified.

There are many applications of flow quantification, including calculation of RV and LV stroke volumes, shunt quantification (Qp:Qs), calculation of valvular regurgitant fraction,[36] and assessment of diastolic function (mitral inflow, pulmonary vein flow, mitral annular velocities, tricuspid inflow, caval flow). In addition, velocity data enables assessment of gradients, which is crucial for the assessment of stenotic valvular lesions.[37]

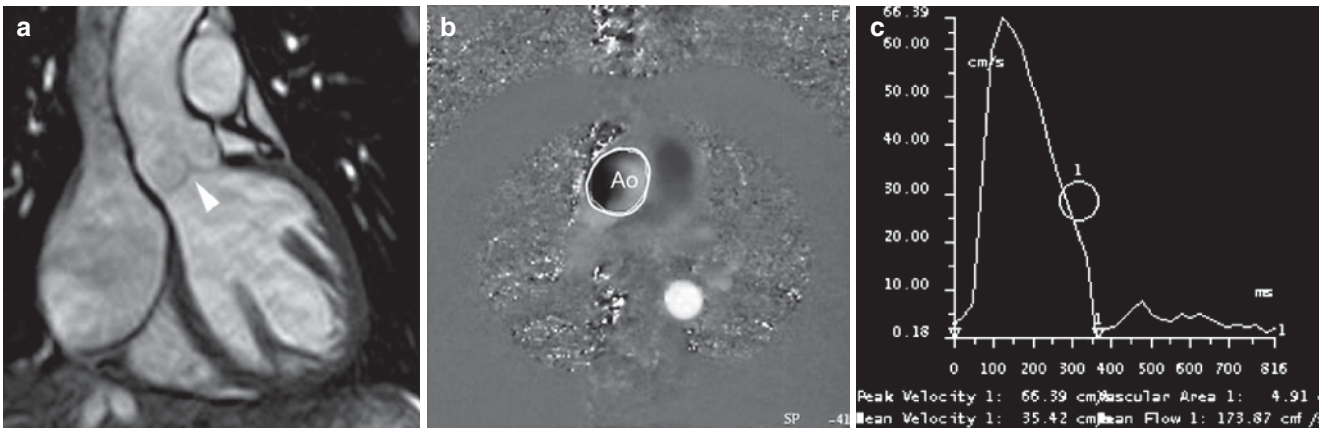

Fig. 6.6 Velocity-encoded CMR flow quantification. Velocity-encoded CMR flow quantification of aortic flow. A long-axis view of the aortic valve (*arrowhead*) **(a)** is used to prescribe an imaging plane perpendicular to aortic flow. On the resultant image, the vessel is delineated **(b)**. Flow through the vessel is calculated **(c)**. *Ao* Aorta

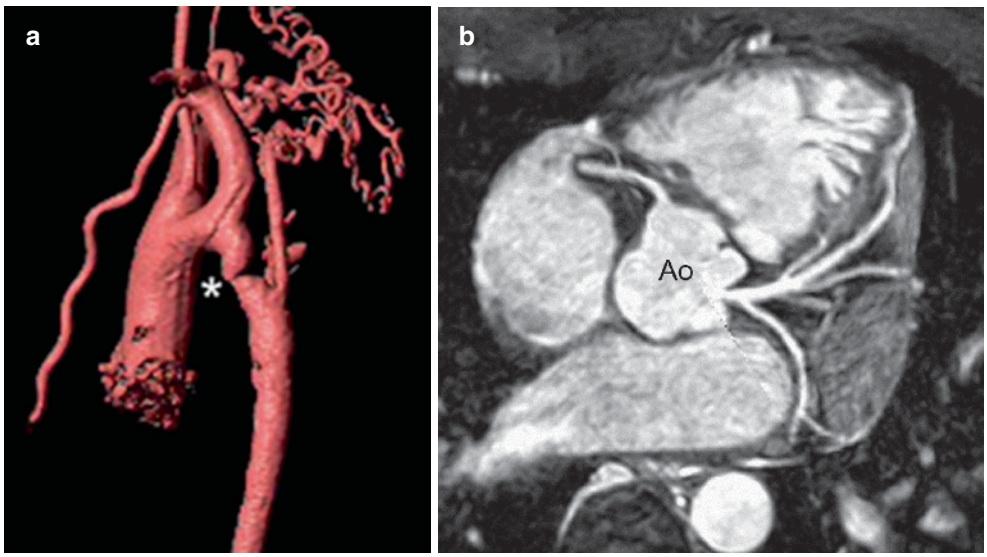

Fig. 6.7 Magnetic Resonance Angiography. 3D MRA was performed following injection of a gadolinium-containing contrast agent. Post-processing of the data with volume rendering **(a)** showing significant aortic coarctation (*asterisk*) with extensive collateral formation. **(b)** Magnetic resonance coronary angiography. A tangential view showing normal origin and proximal courses of the left and right coronary arteries. *Ao* Aorta

MR Angiography

Gadolinium contrast-enhanced MR angiography is widely used for evaluation of the great vessels of the thorax. The standard technique is a 3D gradient echo acquisition during the first pass of contrast, resulting in a 3D volume of high spatial-resolution images.[38] A "bolus-tracker" is used to ensure optimal timing of image acquisition relative to the arrival of contrast.[39] Usually, 0.1–0.2 mmol/kg of gadolinium is injected at 2 mL/s followed by a saline flush. Post-processing techniques can be used to explore the 3D datasets - including maximum intensity projections (MIP), multi-planar reformatting (MPR), and volume rendering (Fig. 6.7a).

Coronary artery imaging with MRI is much more challenging and has been investigated extensively. The principle challenges are the small size of the coronaries (2–5 mm), their long tortuous course, motion (respiratory, cardiac, and individual artery), and flow. Many techniques have been used, but despite promising results in the literature,[40] coronary artery imaging is usually only performed to assess the anomalous coronary origins and to follow the aneurysms of Kawasaki disease (Fig. 6.7b).

An important factor is the fast-growing availability of multi-detector computer tomography (CT) scanners, which offer fast and reliable imaging of the coronary arteries. The newest scanners equipped with 320 detectors can image the heart within a single beat with a substantially reduced radiation dose. This makes coronary CMR somewhat redundant,

though it remains an appealing option when nephrotoxic contrast agents must be avoided (e.g. severe renal dysfunction). Technical developments in the near future may renew the interest for this exciting field of cardiac imaging (e.g. coronary wall or plaque imaging).

Conclusions

MRI is a powerful tool for the assessment of the cardiovascular system; indeed, it is the reference standard for the assessment of many aspects of cardiac structure and function. A wide variety of pulse sequences are available, and the full potential of CMR is realized when data from all the relevant sequences are integrated in a comprehensive manner.

References

1. Hendrick RE. The AAPM/RSNA physics tutorial for residents. Basic physics of MR imaging: an introduction. *Radiographics*. 1994;14:829–846
2. Van Guens RJ, Wielopolski PA, de Bruin HG, et al Basic principles of magnetic resonance imaging. *Prog Cardiovasc Dis*. 1999;42:149–156
3. Petersson JS, Christoffersson JO, Golman K. MRI simulation using the K-space formalism. *Magn Reson Imaging*. 1993;11:557–568
4. Henning J. K-space sampling strategies. *Eur Radiol*. 1999;9: 1020–1031
5. Morcos SK. Nephrogenic systemic fibrosis following the administration of extracellular gadolinium based contrast agents: is the stability of the contrast agent molecule an important factor in the pathogenesis of this condition? *Br J Radiol*. 2007;80:73–76
6. Sodickson DK, Manning WJ. Simultaneous acquisition of spatial harmonics (SMASH): fast imaging with radiofrequency coil arrays. *Magn Reson Med*. 1997;38:591–603
7. Pruessmann KP, Weiger M, Scheidegger MB, Boesiger P. SENSE: sensitivity encoding for fast MRI. *Magn Reson Med*. 1999;42: 952–962
8. Fischer SE, Wickline SA, Lorenz CH. Novel real-time R-wave detection algorithm based on the vector cardiogram for accurate gated magnetic resonance acquisitions. *Magn Reson Med*. 1999;42:361–370
9. Thiele H, Nagel E, Paetsch I, et al Functional cardiac MR imaging with steady-state free precession (SSFP) significantly improves endocardial border delineation without contrast agents. *J Magn Reson Imaging*. 2001;14:362–367
10. Bogaert J, Bosmans H, Rademakers FE, et al Left ventricular quantification with breath-hold MR imaging: comparison with echocardiography. *MAGMA*. 1995;3:5–12
11. Sakuma H, Fujita N, Foo TK, et al Evaluation of left ventricular volume and mass with breath-hold cine MR imaging. *Radiology*. 1993;188:377–380
12. Grothues F, Smith GC, Moon JC, et al Comparison of interstudy reproducibility of cardiovascular magnetic resonance with two-dimensional echocardiography in normal subjects and in patients with heart failure or left ventricular hypertrophy. *Am J Cardiol*. 2002;90:29–34
13. Myerson SG, Bellenger NG, Pennell DJ. Assessment of left ventricular mass by cardiovascular magnetic resonance. *Hypertension*. 2002;39:750–755
14. Zerhouni EA, Parish DM, Rogers WJ, et al Human heart: tagging with MR imaging - a method for non-invasive assessment of myocardial motion. *Radiology*. 1988;169:59–63
15. Stehling MK, Holzknecht NG, Laub G, et al Single shot T1- and T2-weighted magnetic resonance imaging of the heart with black blood: preliminary experience. *MAGMA*. 1996;4:231–240
16. Friedrich MG, Abdel-Aty H, Taylor A, Schulz-Menger J, Messroghli D, Dietz R. The salvaged area at risk in reperfused acute myocardial infarction as visualised by cardiovascular magnetic resonance. *J Am Coll Cardiol*. 2008;51:1581–1587
17. Anderson LJ, Holden S, Davis B, et al Cardiovascular T2* magnetic resonance for the early diagnosis of myocardial iron overload. *Eur Heart J*. 2001;2001 22:2171–2179
18. Kim RJ, Fieno DS, Parrish TB, et al Relationship of MRI delayed contrast enhancement to irreversible injury, infarct age, and contractile function. *Circulation*. 1999;100:1992–2002
19. Wu E, Judd RM, Vargas JD, Klocke FJ, Bonow RO, Kim R. Visualization of presence, location, and transmural extent of healed Q-wave and non-Q wave myocardial infarction. *Lancet*. 2001;357:21–28
20. Wagner A, Mahrholdt H, Holly TA, et al Contrast-enhanced MRI and routine single photon emission computed tomography (SPECT) perfusion imaging for detection of subendocardial myocardial defects: an imaging study. *Lancet*. 2003;361:374–379
21. Judd RM, Lugo-Oliveri CH, Arai M, et al Physiological basis of myocardial contrast enhancement in fast magnetic resonance images of 2-day old reperfused canine infarcts. *Circulation*. 1995; 92:1902–1910
22. Lima JA, Judd RM, Bazille A, Schulman SP, Atalar E, Zerhouni EA. Regional heterogeneity of human myocardial infarcts demonstrated by contrast-enhanced MRI. Potential mechanisms. *Circulation*. 1993;92:1117–1125
23. Simonetti OP, Kim RJ, Fieno DS, et al An improved method for the visualization of myocardial infarction. *Radiology*. 2001;218: 215–223
24. Kellman P, Arai AE, McVeigh ER, et al Phase-sensitive inversion recovery for detecting myocardial infarction using gadolinium-delayed hyperenhancement. *Magn Reson Med*. 2002;47:372–383
25. Kuhl HP, Papavasiliu TS, Beek AM, et al Myocardial viability: rapid assessment with delayed contrast-enhanced MR imaging with three dimensional inversion-recovery prepared pulse sequence. *Radiology*. 2004;230:576–582
26. Bogaert J, Taylor AM, van Kerkhove F, Dymarkowski S. Use of inversion recovery contrast-enhanced MRI for cardiac imaging: spectrum of applications. *Am J Roentgenol*. 2004;182:609–615
27. Ishida N, Sakuma H, Motoyasu M, et al Non-infarcted myocardium: correlation between dynamic first-pass contrast-enhanced myocardial MR and quantitative coronary angiography. *Radiology*. 2003;229:209–216
28. Gerber BL, Raman SV, Nayak K, et al Myocardial first-pass perfusion cardiovascular magnetic resonance: history, theory, and current state of the art. *J Cardiovasc Magn Reson*. 2008;10(1):18
29. Wilke N, Jerosch-Herold M, Wang Y, et al Myocardial perfusion reserve: assessment with multisection, quantitative, first-pass MR imaging. *Radiology*. 1997;204:373–384
30. Cullen JHS, Horsfield MA, Reek CR, et al A myocardial perfusion reserve index in humans using contrast enhanced magnetic resonance imaging. *J Am Coll Cardiol*. 1999;33:1386–1394
31. Al-Saadi N, Nagel E, Gross M, et al Non-invasive detection of myocardial ischaemia from perfusion reserve based on cardiovascular magnetic resonance. *Circulation*. 2000;101:1379–1383
32. Spritzer CE, Pelc NJ, Lee JN, et al Rapid MR imaging of blood flow with a phase sensitive, limited flip angle, gradient recalled pulse sequence: preliminary experience. *Radiology*. 1990;176:255–262

33. Kondo C, Caputo GR, Semelka R, et al Right and left ventricular stroke volume measurements with velocity encoded cine MR imaging: in vitro and in vivo validation. *Am J Roentgenol*. 1991;157:9–16
34. Hoeper MM, Tongers J, Leppert A, et al Evaluation of right ventricular performance with a right ventricular ejection fraction thermodilution catheter and magnetic resonance imaging in patients with pulmonary hypertension. *Chest*. 2001;120:502–507
35. Lee VS, Spritzer CE, Caroll BA, et al Flow quantification using fast cine phase-contrast MR imaging, conventional cine phase-contrast MR imaging, and Doppler sonography: in vitro and in vivo validation. *Am J Roentgenol*. 1997;12:1952–1953
36. Kozerke S, Schwitter J, Pedersen EM, Boesiger P. Aortic and mitral regurgitation: quantification using moving slice velocity mapping. *J Magn Reson Imaging*. 2001;14:106–112
37. Eichenberger AC, Jenni R, von Schulthess GK. Aortic valve pressure gradients in patients with aortic valve stenosis: quantification with velocity-encoded cine MR imaging. *Am J Roentgenol*. 1993; 160:971–977
38. Prince MR, Narasimham DL, Jacoby WT, et al Three-dimensional gadolinium-enhanced MR angiography of the thoracic aorta. *Am J Roentgenol*. 1996;166:1387–1397
39. Riederer SJ, Bernstein MA, Breen JF, et al Three-dimensional contrast-enhanced MR angiography with real-time fluoroscopic triggering: design specifications and technical reliability in 350 patient studies. *Radiology*. 2000;215:584–593
40. Kim YW, Danias PG, Stuber M, et al Coronary magnetic resonance angiography for the detection of coronary stenoses. *N Engl J Med*. 2001;345:1863–1869

Section 2

Valvular heart disease

Chapter 7

VALVULAR STENOSIS

Raphael Rosenhek, Julia Mascherbauer,
David C. Maintz, and Helmut Baumgartner

CONTENTS

J. L. Zamorano et al. (eds.), *The ESC Textbook of Cardiovascular Imaging*
DOI: 10.1007/978-1-84882-421-8_7, © Springer-Verlag London Limited 2010

Introduction

Echocardiography is the method of choice for the diagnosis, assessment of morphology, and aetiology as well as quantification of valvular stenoses. It permits the additional evaluation of the consequences on atrial and ventricular size and function, myocardium, and pulmonary circulation. Haemodynamic assessment can be performed by Doppler echocardiography providing transvalvular gradients as derived from transvalvular velocities with the simplified Bernouilly equation. Depending on the site of disease, valve areas can be determined by the continuity equation, direct planimetry, or empirical formulas. Recently, MR and CT imaging have gained importance in the assessment of valve morphology, ventricular function, and aortic disease. In current practice, their role in quantifying the severity of valve disease, however, remains limited. Imaging techniques are also crucial for the identification of patients suitable for percutaneous interventions and actual guidance of these procedures. It is important to be aware of the specific limitations and pitfalls of the various measurements. Final judgment should be based on an integrated approach involving all available information. Finally, imaging techniques provide prognostic information in valvular stenosis and have a fundamental impact on the decision-making process in clinical practice.

Aortic Stenosis (AS)

Echocardiographic Assessment of Morphology and Severity with Its Pitfalls and Limitations

Assessment of Morphology

Site of Left Ventricular Outflow Obstruction

Aortic stenosis is most commonly valvular. Subvalvular AS can either be fixed in case of congenital malformation (discrete membrane or muscular band), or dynamic in case of hypertrophic obstructive cardiomyopathy. Supra-valvular AS is a rare congenital condition. Echocardiography allows distinction of these entities by morphologic assessment, Doppler determination of the site of velocity increase, and analysis of its time course (early, mid, late systolic peak, Fig. 7.4). Typical examples are shown in Fig. 7.1 (Videos 7.1 and 7.2).

Assessment of Valvular AS Aetiology

Calcific AS is the most common form and is characterized by thickened and calcified cusps (bicuspid or tricuspid valve) with reduced mobility.[1] *Congenital AS* most commonly presents with bicuspid, and less frequently with unicuspid, tricuspid, or quadricuspid valves. The two cusps of bicuspid valves are typically of different size, and the larger cusp often contains a raphe (fusion line of two cusps). Typically, the cusps are oriented either in an anterior/posterior (fusion of right and left coronary cusp; 80%) or right/left manner (fusion of right and non-coronary cusp). *Rheumatic aortic stenosis* is characterized by commissural fusion, thickening of the cusp edges, and sometimes, cusp retraction. It is commonly associated with aortic regurgitation and mitral valve involvement. Typical examples are shown in Fig. 7.2 (Videos 7.3–7.6).

In advanced disease stages, congenitally malformed and rheumatic valves develop calcification. Once the valve is extensively calcified, the exact determination of the underlying morphology and aetiology becomes difficult.

Assessment of Aortic Valve Calcification

Aortic valve calcification is best assessed in a short-axis view, although the presence of extensive calcification may also be noted in the 5-chamber view. The degree of calcification (Fig. 7.3) can be classified into mild (isolated, small spots), moderate (multiple bigger spots), and severe (extensive thickening/calcification of all cusps), and it has prognostic implications (see below).[2]

Assessment of the Aorta

Assessment of the ascending aorta is crucial as aneurysms are not uncommon. In particular, congenital AS is frequently associated with dilatation of the ascending aorta. However, its extent is not related to the haemodynamic severity of AS.

Additional Findings

The echocardiographic assessment should also include the determination of concomitant left ventricular (LV) hypertrophy and dysfunction, coexisting mitral valve disease, and pulmonary hypertension.

Quantification of Stenosis Severity

A normal aortic valve has an orifice area of 3–4 cm^2 and a laminar normal transvalvular flow with a peak velocity of <2 m/s. While several other parameters have been proposed for the AS quantification, peak transvalvular velocity, mean Doppler gradient, and effective orifice area as derived from the continuity equation have been best validated and are currently recommended for clinical assessment of AS.[3–5]

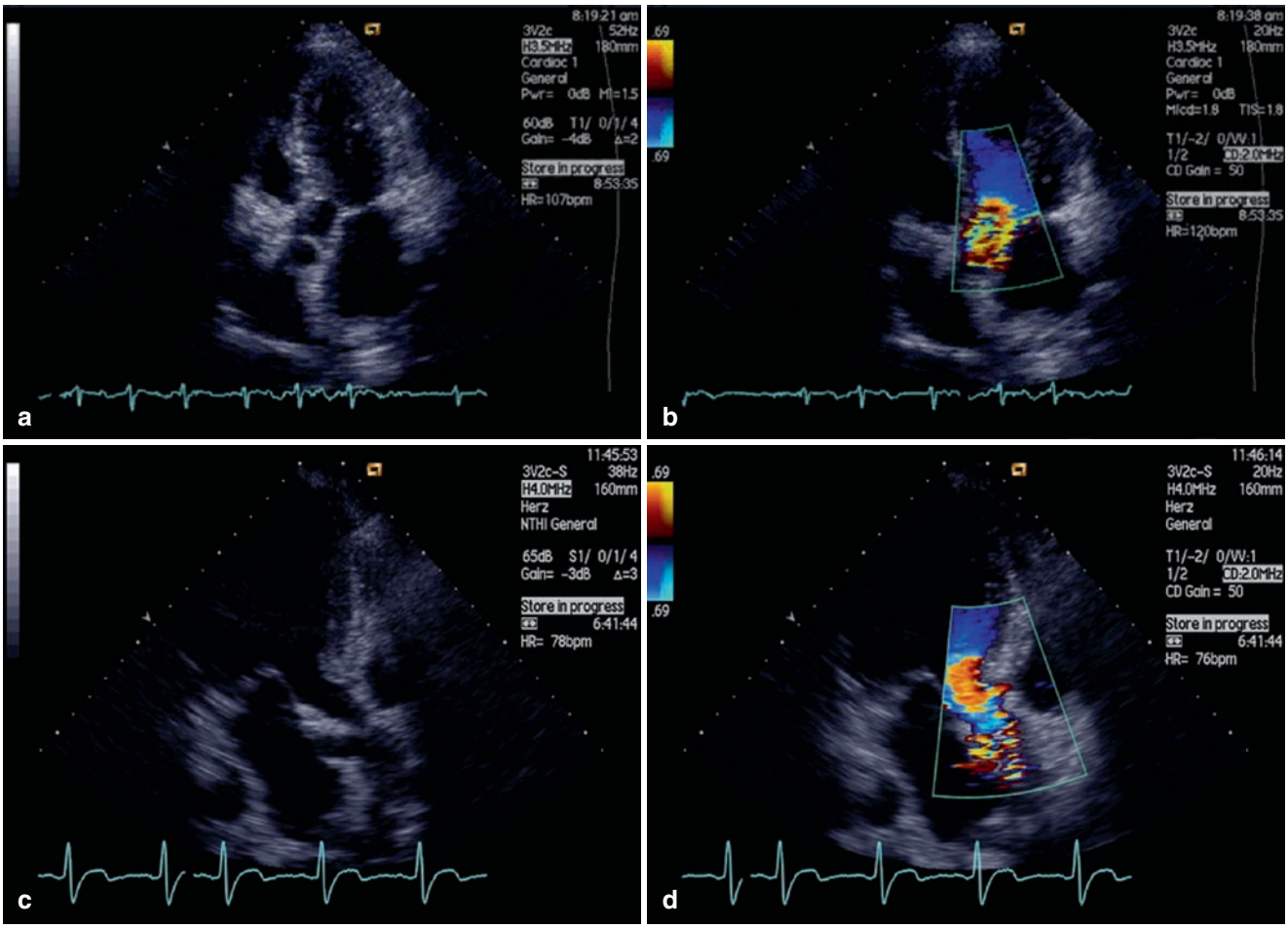

Fig. 7.1 Examples of subaortic stenosis and supra-valvular aortic stenosis (AS). **(a)** 5-chamber view of a patient with subaortic stenosis. *Arrows* indicate the subaortic membrane and the aortic valve. **(b)** Colour flow image of the same view **(a)**. *Arrows* again indicate the subaortic membrane and the valve. Flow convergence is observed in front of the subvalvular membrane helping to define the site obstruction. **(c)** Apical 3-chamber view of a patient with supra-valvular stenosis. Arrows indicate the hourglass-like obstruction at the level of the sinotubular junction. The aortic valve is also thickened. **(d)** Colour flow image of the same view **(c)**: turbulences occur downstream from the supra-valvular stenosis (*arrow*)

Transvalvular Velocity and Gradients

Transvalvular velocity continuously increases with AS severity, as long as the cardiac output is maintained.

Transvalvular gradients (ΔP) are calculated from continuous-wave Doppler-derived transvalvular velocities (v) using the Bernoulli equation, which is based on the conservation of energy principle. In clinical practice, the simplified Bernoulli equation $\Delta P = 4v^2$ that ignores viscous losses and the effects of flow acceleration is used.[6] It also ignores the flow velocity proximal to the stenosis, which is an acceptable assumption as long as the transvalvular velocity is significantly greater than the proximal flow velocity and, in particular, when ≤1 m/s. However, if proximal velocity is increased (narrow outflow tract or increased flow rate caused by high cardiac output or aortic regurgitation), the less simplified version $\Delta P = 4(v_2^2 - v_1^2)$ should be used, where v_2 and v_1 represent the transvalvular and proximal flow velocities, respectively.

The peak transaortic pressure gradient corresponds to the maximum instantaneous difference between the pressure in the aorta and in the ventricle. With increasing stenosis severity, the peak of the gradient occurs later during systole (Fig. 7.4). Note that the peak gradient is different from the "peak-to-peak" gradient that is determined by catheter, and corresponds to the difference between peak aortic pressure and peak LV pressure. The latter is not a physiologic measure, as these two peaks do not occur simultaneously and it cannot be determined by Doppler echocardiography.

The mean gradient is calculated by averaging the instantaneous gradients throughout the ejection period.

Technical Considerations and Pitfalls

Besides neglecting an increased subvalvular velocity (see above), a number of other sources of error may occur.

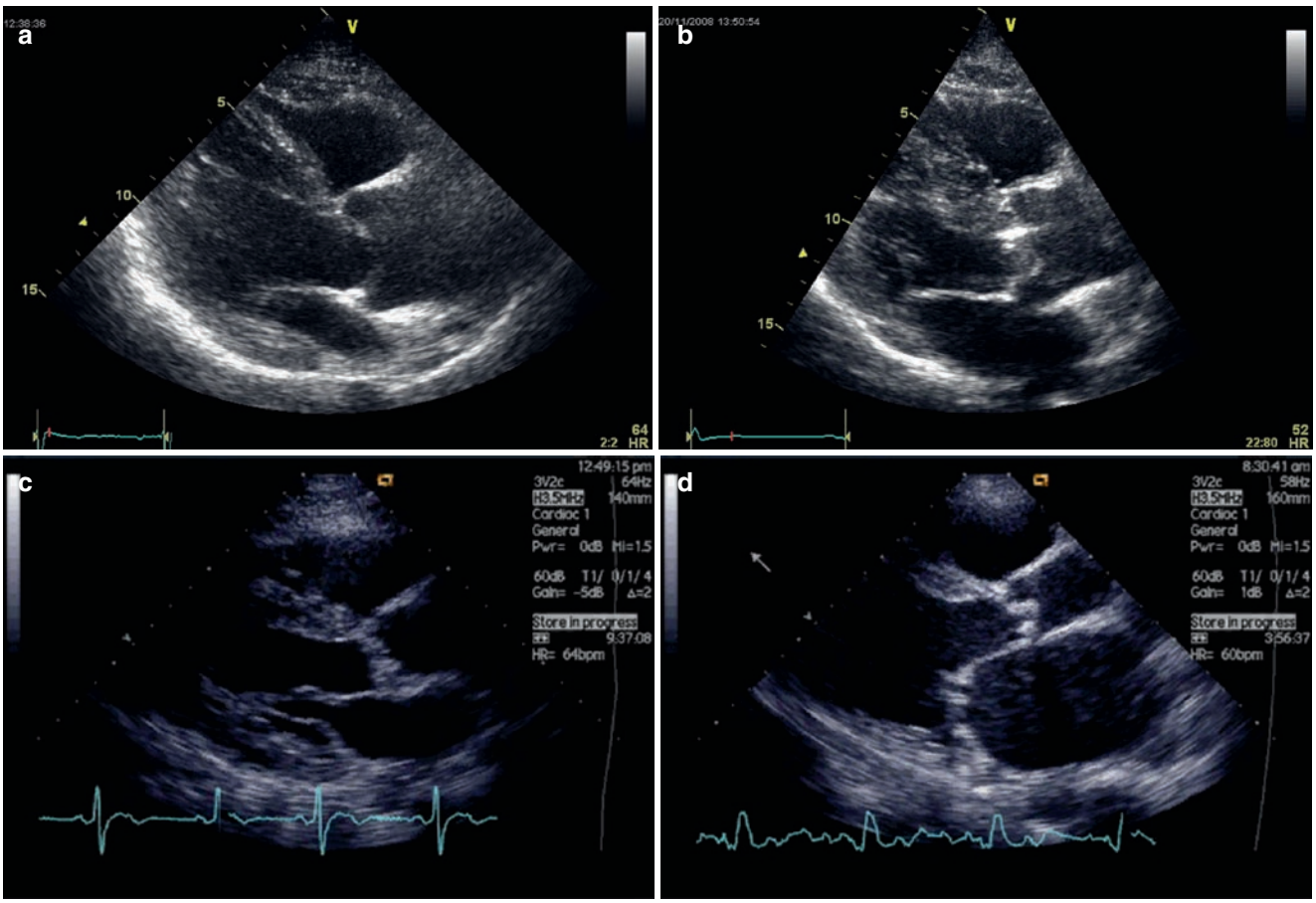

Fig. 7.2 Etiologies of AS (long-axis views). **(a)** Congenital AS: Thickened valve with doming and no calcification. **(b)** Bicuspid aortic valve with circumscript eccentric calcification. Doming of the cusps can still be appreciated. **(c)** Calcific AS with thickened and calcified rigid cusps. **(d)** Rheumatic AS: thickening, predominantly of the cusp edges, and concomittant affection of the mitral valve can be appreciated

A correct alignment of the Doppler beam with the direction of the stenotic jet is essential.

Malalignment leads to an under-estimation of the Doppler gradient and, hence, of the severity of AS. Multiple transducer positions (i.e. right parasternal, supra-sternal, apical, and sometimes even sub-costal) have to be used, to obtain the accurate velocity. For that purpose, the use of a small, dedicated continuous wave Doppler transducer (pencil probe) is mandatory (Fig. 7.5). When the rate of haemodynamic progression is determined, one has to make sure that measurements were recorded from the same window.

Another potential source of error that needs to be avoided is the confusion of the AS signal with a signal originating from another obstruction or from mitral or tricuspid regurgitation. In the presence of arrhythmias, such as atrial fibrillation, several consecutive beats have to be averaged, and beats after long RR-intervals or post-extrasystolic beats must be avoided.

The phenomenon of pressure recovery may also cause pitfalls and may explain discrepancies between catheter and Doppler-derived pressure gradients.[7] Obstruction of flow in any kind of stenosis causes flow velocity increase and pressure drop corresponding to a conversion of potential energy to kinetic energy. Pressure is lowest and velocity is greatest at the level of the vena contracta, the site of minimum cross-sectional flow area. The jet expands and decelerates downstream from the stenosis. Although some of the kinetic energy dissipates into heat owing to turbulences and viscous losses, some of it will be reconverted into potential energy, and pressure will increase again to some degree (=pressure recovery). The Doppler gradient corresponds to the maximum pressure drop from proximal to the vena contracta, and overestimates the net pressure drop as usually given by catheter measurement in the case of significant pressure recovery. In AS, the magnitude of pressure recovery is frequently small, as the abrupt widening from the small valve orifice to a generally normal-sized or enlarged aorta causes a lot of turbulences. However, the effects of pressure recovery may be significant in the presence of a small ascending aorta (<30 mm).[7]

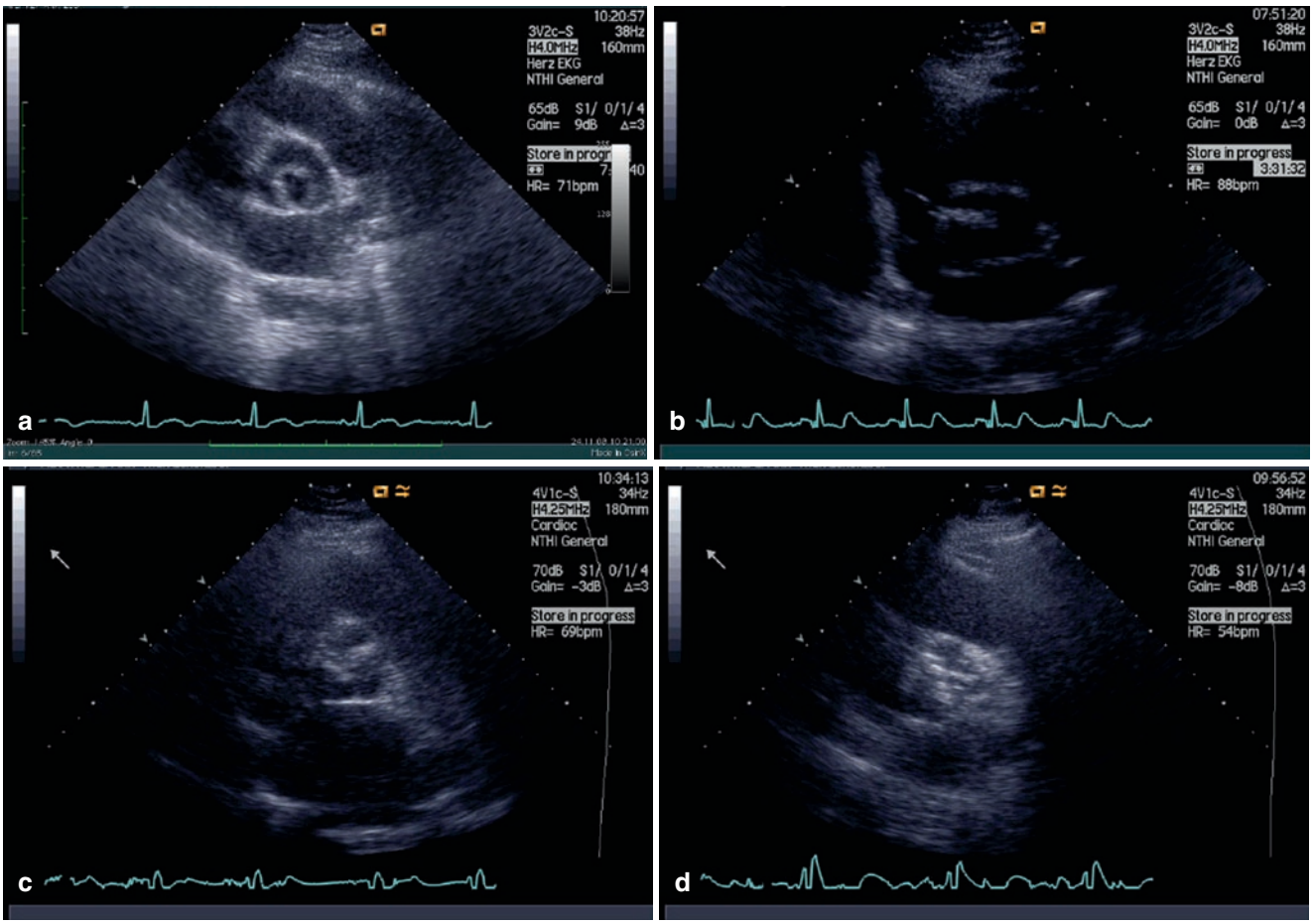

Fig. 7.3 Degree of aortic valve calcification. **(a)** Parasternal short-axis view of a unicuspid stenotic aortic valve without calcification. **(b)** Parasternal short-axis view of a bicuspid AS with minimal calcification. **(c)** Parasternal short-axis view of a moderately calcified stenotic aortic valve. **(d)** Parasternal short-axis view of a severely calcified stenotic aortic valve with extensive thickening and calcification of all cusps

Doppler velocities and pressure gradients are highly flow-dependent. In the presence of high cardiac output or significant aortic regurgitation, consideration of these measurements alone may cause significant overestimation of AS severity. On the other hand, in the presence of low flow rates, most commonly caused by an impaired LV function as well as, e.g. in the presence of mitral stenosis, AS severity may be under-estimated. Thus, valve area as a less flow-dependent parameter is required for appropriate AS quantification.

Valve Area Calculation by the Continuity Equation

The continuity equation has gained maximum acceptance for valve area calculation.[8,9] It is based on the fact that the stroke volume passing through the left ventricular outflow tract (LVOT) must be equal to the stroke volume crossing the stenotic aortic valve:

$$AVA \times VTI_{AS} = CSA_{LVOT} \times VTI_{LVOT}$$

where AVA is the aortic valve area, VTI_{AS} and VTI_{LVOT} are the velocity time integrals in the LVOT and effective valve orifice, respectively, and CSA_{LVOT} is the cross-sectional area of the LVOT (Fig. 7.6).

A simplified version of the continuity equation that uses peak aortic jet and outflow tract velocities instead of the velocity time integral has also been proposed.

The CSA of the LVOT is calculated using the formula:

$$CSA_{LVOT} = \pi (D/2)^2$$

where D is the diameter of the LVOT measured in the parasternal long-axis view. This assumption of a circular LVOT shape and the requirement for measuring LVOT size and velocity exactly at the same site are important limitations of the method that may cause error. The LVOT flow velocity is measured from an apical approach using pulsed Doppler ultrasound with the assumption of laminar flow and a flat velocity profile. The fact that these assumptions may not be fulfilled also limits the accuracy of the method.

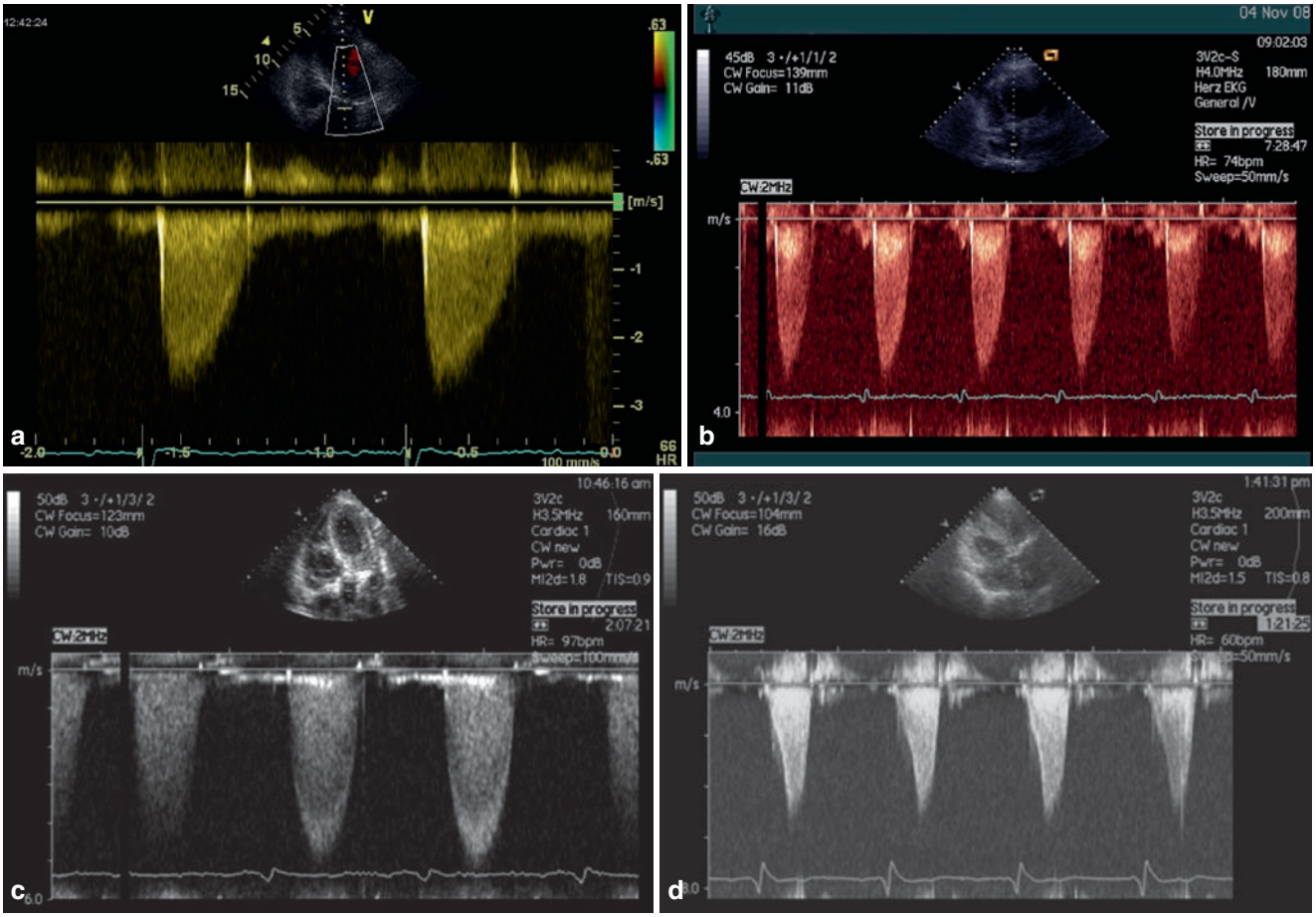

Fig. 7.4 CWD velocity spectrum. **(a)** Mild AS with immediate peak. **(b)** Moderate AS with early peak. **(c)** Severe AS with midsystolic peak. (**d**) Dynamic obstruction in the setting of a hypertrophic obstructive cardiomyopathy with late peak

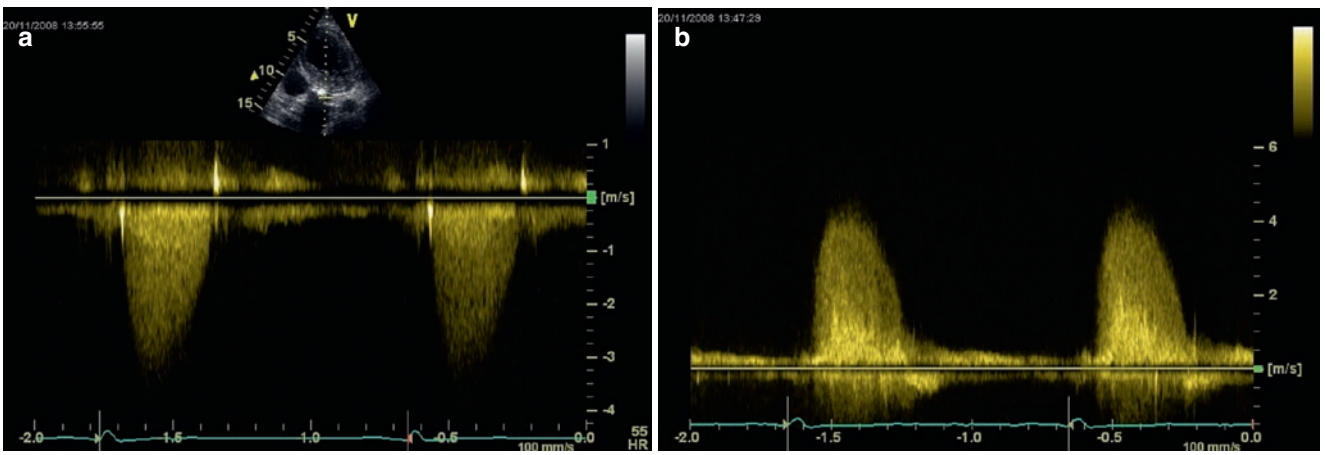

Fig. 7.5 CWD recordings of a patient with severe AS: the recording from the apical window provides a peak velocity of 3.4 m/s consistent with moderate AS **(a)**, whereas the right parasternal window provides 4.3 m/s consistent with severe AS **(b)**, emphasizing the importance of the use of multiple transducer positions

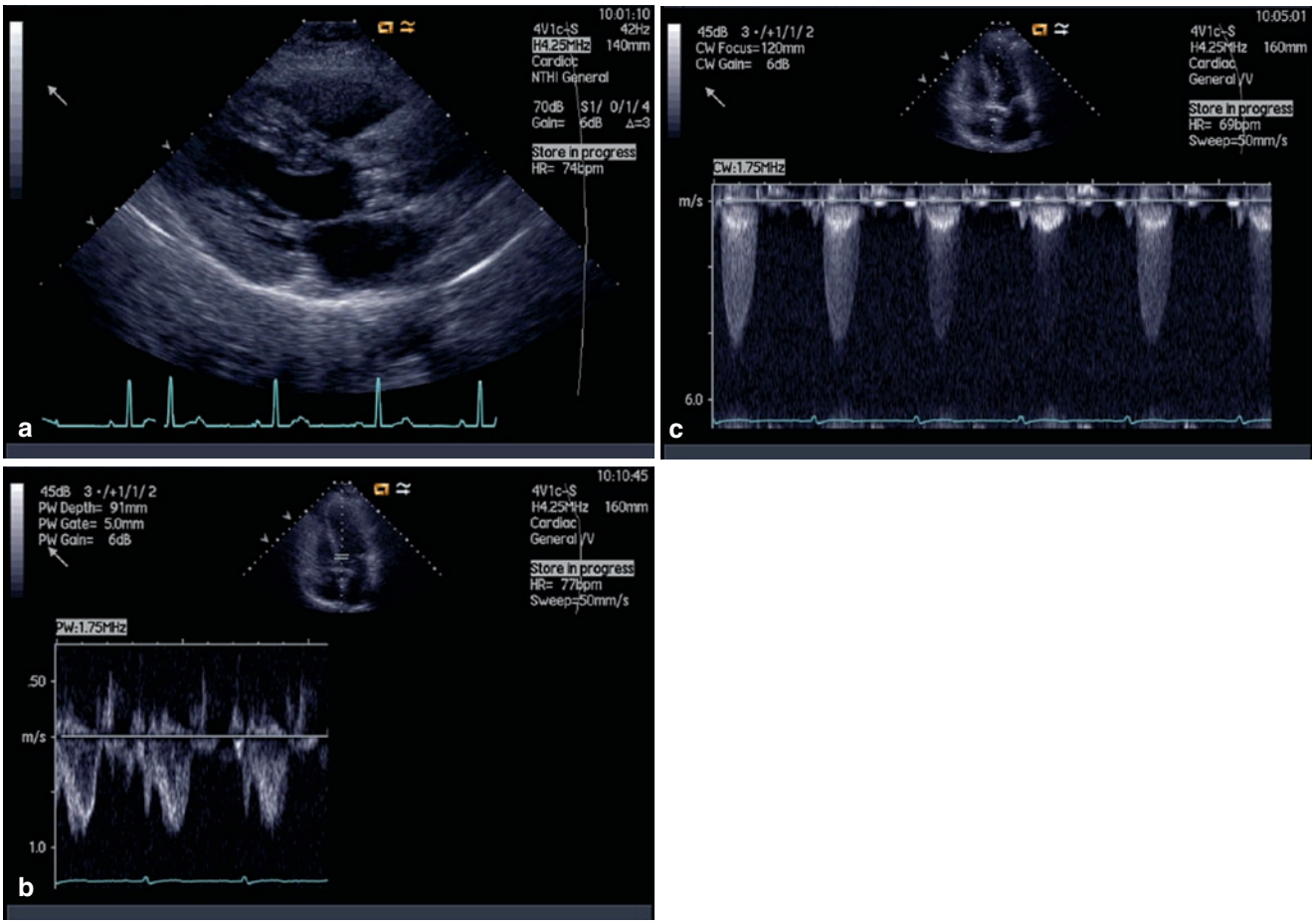

Fig. 7.6 Continuity equation: Required recordings. **(a)** Parasternal long-axis view with the LV outflow tract diameter measurement. **(b)** Pulsed-wave Doppler recording of LVOT velocity obtained from an apical 5-chamber view. **(c)** Continuous-wave Doppler recording of the aortic jet velocity (apical transducer position)

Despite these limitations, continuity equation has been shown to be currently the best technique of valve area estimation, and yields valuable measurements for AS quantification as a basis for patient decision-making when sources of error are carefully considered.

Velocity Ratio

To reduce the error related to LVOT measurements it has been proposed to remove it from the continuity equation. The so-determined dimensionless velocity ratio expresses the size of the effective valve area as a proportion of the CSA of the LVOT:

$$\text{Velocity ratio} = V_{\text{LVOT}}/V_{\text{AS}}$$

Both velocity time integrals and peak velocities have been used. Severe stenosis is present when the velocity ratio is ≤0.25, corresponding to a valve area 25% of the normal. To some extent, the velocity ratio normalizes for the body size, because it reflects the ratio of the actual valve area to the expected valve area in each patient, regardless of the body size. However, this measurement ignores the variability in LVOT size beyond variation in body size, and has gained less acceptance for routine use than the parameters mentioned earlier.

Valve Area Planimetry

Planimetry of the valve area, primarily by 2D TOE, has also been proposed. However, the orifice of a stenotic aortic valve frequently represents a complex 3D structure that cannot be reliably assessed with a planar 2D image. The presence of valvular calcification further limits an accurate delineation of the aortic valve orifice. Thus, this method has not been

accepted as a routine measurement. Nevertheless, it might be useful in selected patients when additional information is needed.[5]

3D echocardiography has been reported to allow valve area planimetry, but has not yet been sufficiently validated.

Dobutamine Echocardiography

Dobutamine echocardiography is indicated in the setting of low flow-low gradient AS, which is defined by a small calculated valve area (<1.0 cm^2) in the presence of a reduced transaortic gradient (<30–40 mmHg) and a reduced LV function.[10] It is performed at a low dobutamine dose that is gradually increased up to a maximum dose of 10–20 µg/kg/min.

It allows the determination of the presence of a contractile reserve (defined as an increase of cardiac output ≥20%), which has been shown to be of prognostic value. In the presence of a contractile reserve, it allows a further differentiation between pseudosevere stenosis (compared with baseline, the gradients remain small, whereas the valve area increases significantly with increasing flow indicating that AS is non-severe and LV dysfunction is caused by other disease) and true severe stenosis (gradients increase, whereas the valve area remains small indicating a fixed small valve orifice with a low gradient caused by secondary LV dysfunction and flow reduction).

Experimental Methods of AS Quantification

Several additional parameters such as valve resistance, stroke work loss, or the energy loss coefficient have been proposed to quantify AS severity. As their complexity adds sources of error, and as they lack prognostic validation, they are still considered experimental and not recommended for routine clinical use.[5]

Definition of AS Severity (Table 7.1)

By current recommendations, severity of AS is assessed by combining the aortic jet velocity, mean gradient, and valve area.[3–5] Because of prognostic implications, the differentiation between severe and non-severe stenosis is of particular importance. In several clinical studies, severe stenosis is considered with a peak aortic jet velocity of > 4 m/s. Current recommendations define severe AS by using a cutoff of <1 cm^2 for the valve area. It has also been suggested to index AVA to body surface area (cutoff 0.6 cm^2/m^2). However, there is no linear relation between body surface area and valve area, and there is a particular distortion at the extremes of the spectrum.

Role of MRI and CT

Although echocardiography remains the standard modality for the diagnosis and quantification of AS, MRI and CT are gaining importance, both for valve assessment and adjunct cardiovascular evaluation.

The role of *MRI* in patients with AS may be fourfold: (1) assessment of valve morphology, (2) assessment of valve function, (3) assessment of LV function, and (4) assessment of aortic disease.

For the assessment of valve morphology, CINE imaging is applied in at least two orthogonal planes through the aortic valve, usually in the orientation of the aortic ring and in the LVOT orientation. Usually, CINE imaging is performed using steady-state-free-precession sequences with an effective temporal resolution of approximately 35 ms. CINE images in LVOT orientation show a flow jet during systole, extending from the valve into the ascending aorta (Video 7.7). This jet is due to phase dispersion in increased flow velocities. To quantify the AVA by planimetry, systolic images through the aortic ring are needed (Fig. 7.7, Video 7.8). Computer programs are available to perform planimetry

Table 7.1. Recommendations for the classification of AS severity[3–5]

	Aortic sclerosis	Mild	Moderate	Severe
Aortic jet velocity (m/s)	≤2.5 m/s	2.6–2.9	3–4	>4
Mean gradient (mmHg)	–	<20 (<30[b])	20–40[a] (30–50[b])	>40[a] (>50[b])
AVA (cm^2)	–	>1.5	1.0–1.5	<1.0
Indexed AVA (cm^2/m^2)		>0.85	0.60–0.85	<0.6
Velocity ratio		>0.50	0.25–0.50	<0.25

[a]AHA/ACC Guidelines
[b]ESC Guidelines

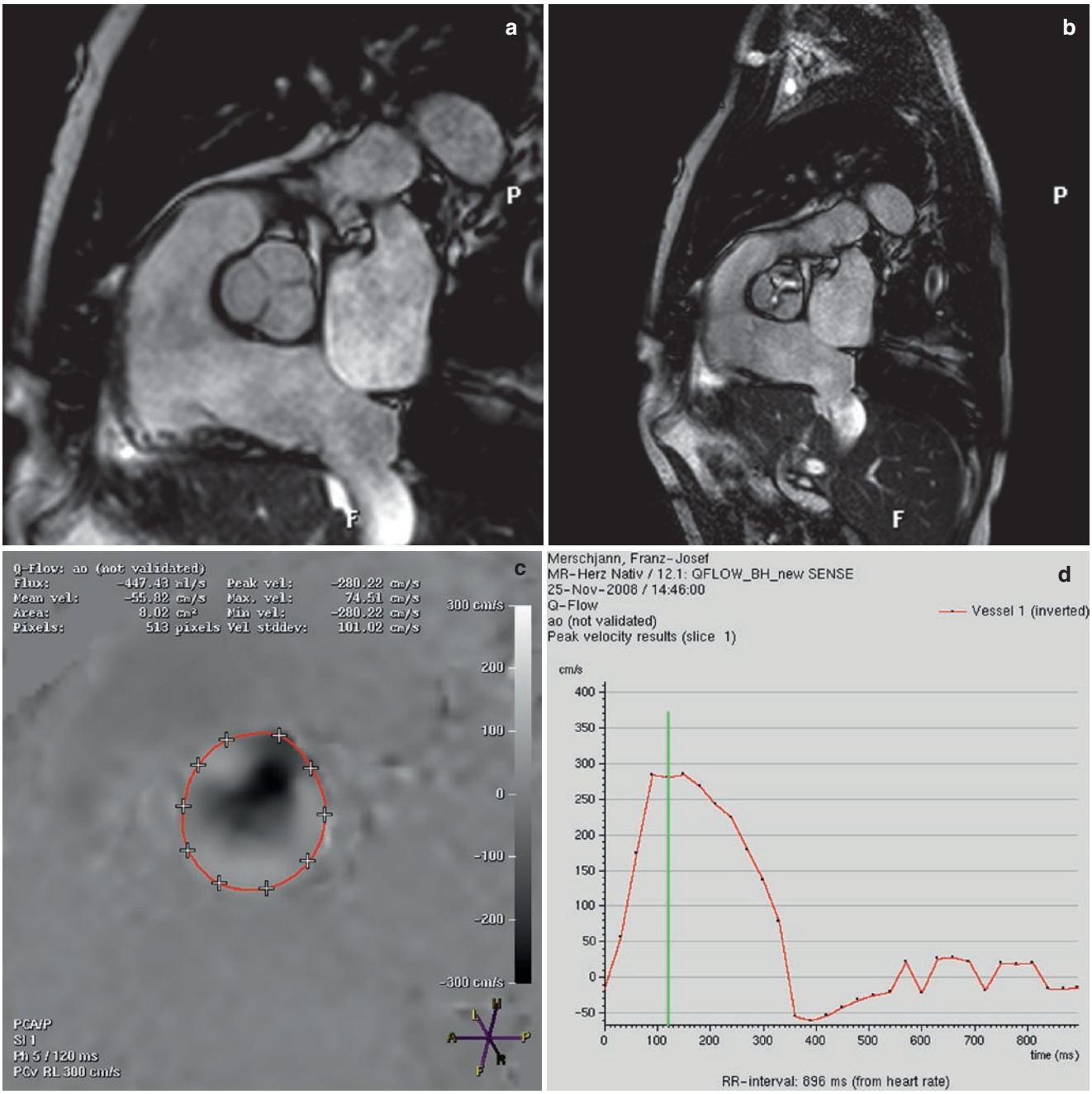

Fig. 7.7 MRI of AS: Steady-state-free-precession MR images in diastole **(a)** and systole **(b)** show impaired opening of the valve and reduced valve area. **(c)** shows a phase-contrast image at a level 2 cm above the valve, **(d)** a time curve of peak flow velocity measurements

semi-automatically on most work stations. Measurements of the AVA based on steady-state-free-precession images have been shown to correlate better with TOE than the conventional spoiled gradient echo images.[11]

One advantage of MRI (vs. CT) is that, in addition to the assessment of valve morphology in CINE images, flow can be measured in phase-contrast sequences. The background of these techniques is the fact that the phase shift in moving spins is proportional to their velocity. By measuring the peak velocity, one can derive the pressure gradient by the use of the Bernoulli equation (Fig. 7.7). Prerequisite for exact measurements in phase-contrast sequences is that the expected maximum velocity is provided, otherwise aliasing artefacts may occur. Valve area can also be calculated from MRI data using the continuity equation.

MRI is the method of highest accuracy for the assessment of LV function and LV mass. At the same time, the LV can be evaluated for the presence of fibrotic changes using late

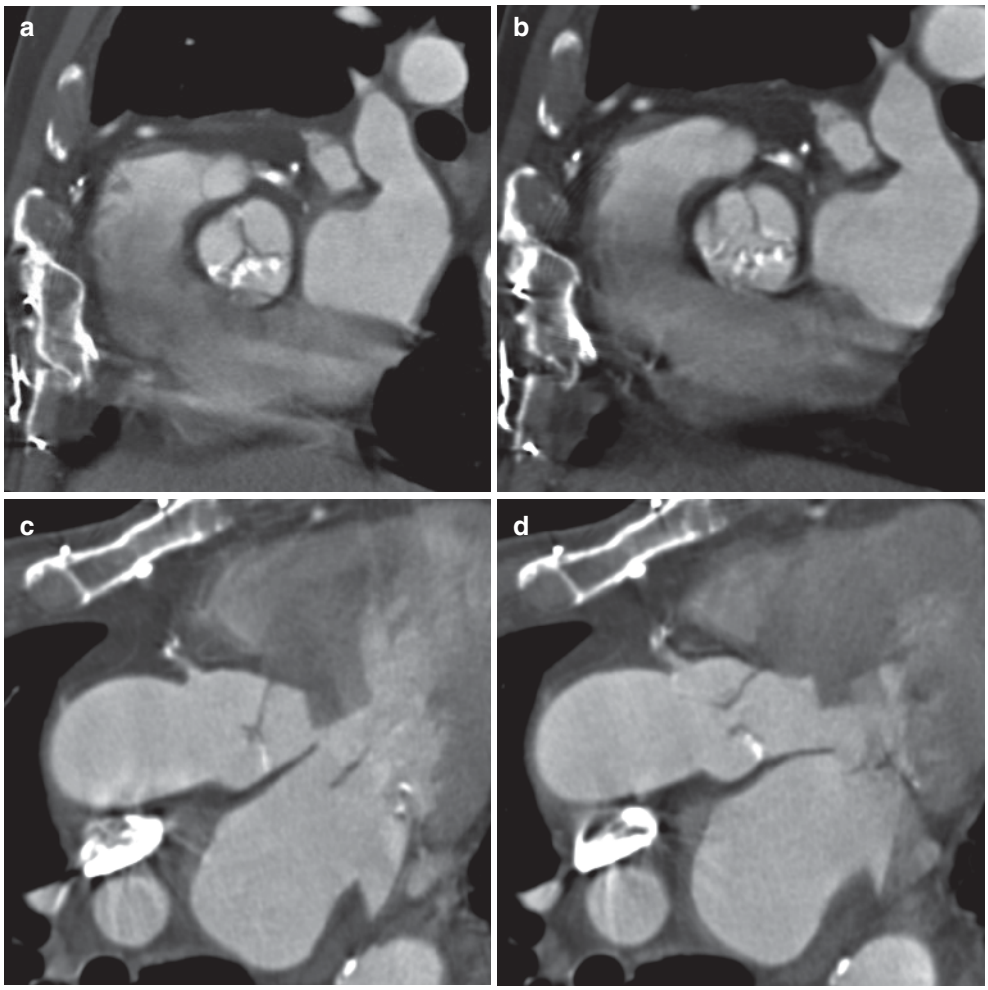

Fig. 7.8 Computed tomography of AS: Diastolic and systolic reformations through the aortic valve show impaired opening of the heavily calcified posterior and left cusp of the valve. **(a, b)** short-axis view. **(c, d)** 3-chamber view

enhancement imaging. Pathology of the aorta (aneurysm, coarctation) may be investigated using contrast-enhanced magnetic resonance angiography.

With the advent of 64 slice CT scanners, the assessment of valve morphology and function using *CT* has become feasible. CT has the advantage of a high spatial resolution and a very high sensitivity for the detection of calcific changes of the valves (Fig. 7.8). Despite its inferior temporal resolution compared with echo and MRI, CT is able to acquire systolic and diastolic images of the aortic valve, which allow for the assessment of valve morphology as well as planimetry of the AVA. In recent comparisons of CT and echocardiography, a good correlation of both methods was found, with a tendency of CT to measure larger values for AVA.[12,13]

While it cannot provide haemodynamic data, CT has the important advantage over MRI and echo in the fact that it can also assess the coronary arteries in the same scan. The method has been shown to detect significant coronary artery disease in patients prior to valve surgery.[14]

Prognostic Information Provided by Imaging

Severity of AS

Imaging techniques allow the detection and quantification of AS. Even the presence of aortic sclerosis without haemodynamic obstruction is associated with an increased morbidity and mortality. With an increasing severity of AS, the outcome is further impaired. In fact, peak aortic jet velocity is an important predictor of outcome in asymptomatic patients with AS. With increasing velocity, subsequent necessity of an aortic valve replacement becomes more likely[15] (Fig. 7.9).

Haemodynamic Progression

Faster rates of haemodynamic progression are associated with an increased event rate, both in patients with severe and mild-to-moderate AS.[2,16] Haemodynamic progression is

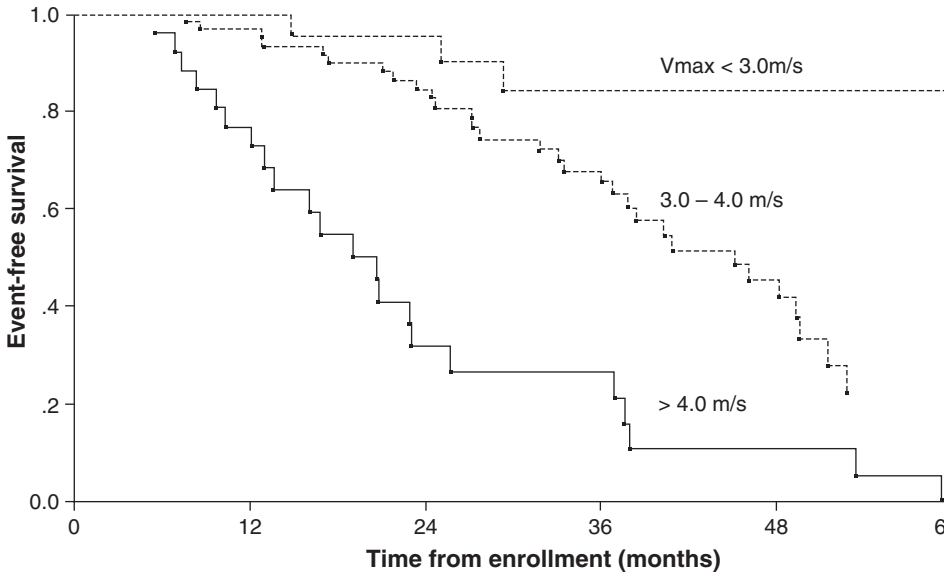

Fig. 7.9 Cox regression analysis showing event-free survival in 123 initially asymptomatic adults with AS, defined by aortic jet velocity at entry ($p < 0.0001$ by log rank test). Modified from ref [15]

actually indirectly related to AS severity. While there is great inter-individual variability in the rates of haemodynamic progression, the presence of a calcified aortic valve has been shown to predict faster haemodynamic progression.

Calcification of the Aortic Valve

The presence of a moderately-to-severely calcified aortic valve is a significant predictor of outcome in patients with mild-to-moderate AS[16] (Fig. 7.10). More importantly, in patients with severe AS, the presence of a moderately-to-severely calcified aortic valve is associated with an event rate of 80% within 4 years, with events defined as the symptom onset warranting aortic valve replacement or death[2] (Fig. 7.10). The presence of a calcified aortic valve in combination with a rapid haemodynamic progression (defined as an increase in peak aortic jet velocity of > 0.3 m/s within 1 year) identifies a high-risk population with an event rate of 79% within 2 years (Fig. 7.10).

Exercise Haemodynamics

In a recent study, an exercise-induced increase in the mean transaortic gradient of >18 mmHg was proposed as a predictor of poor outcome; this finding, however, needs confirmation in larger studies[17] (Fig. 7.11).

Dobutamine Echocardiography in Low Flow–Low Gradient AS

The absence of contractile reserve in low flow–low gradient AS is a predictor of poor outcome[10] (Fig. 7.12). When patients with contractile reserve have true severe AS, they generally benefit from aortic valve surgery. However, although they have a markedly higher operative mortality, even patients without contractile reserve may frequently improve in LV function after surgery. Management decisions remain difficult in this patient population and must be taken on an individual basis.

New Interventions and Imaging

Recently, percutaneous aortic valve implantation has become an increasingly used option in the elderly with high operative risk owing to co-morbidities.[18] Imaging modalities such as echocardiography, MR angio, and CT angio have gained major importance for the safe performance of this procedure.

Aortic Valve Ring

For the choice of valve size, the assessment of aortic valve ring dimension is of critical importance. So far, echocardiography has been most widely used and current recommendations for valve-size choice refer to TOE measurements. These are in general slightly larger (on average 1 mm) than TTE measurements. CT and MRI can also be used. However, it appears that they yield slightly larger measurements than TOE. Optimal standards still need to be defined.

Vascular Access

As the intervention requires still large introducer sheaths (18–24 F depending on the device type and size), the assessment of femoral and iliac vessel size and quality are of

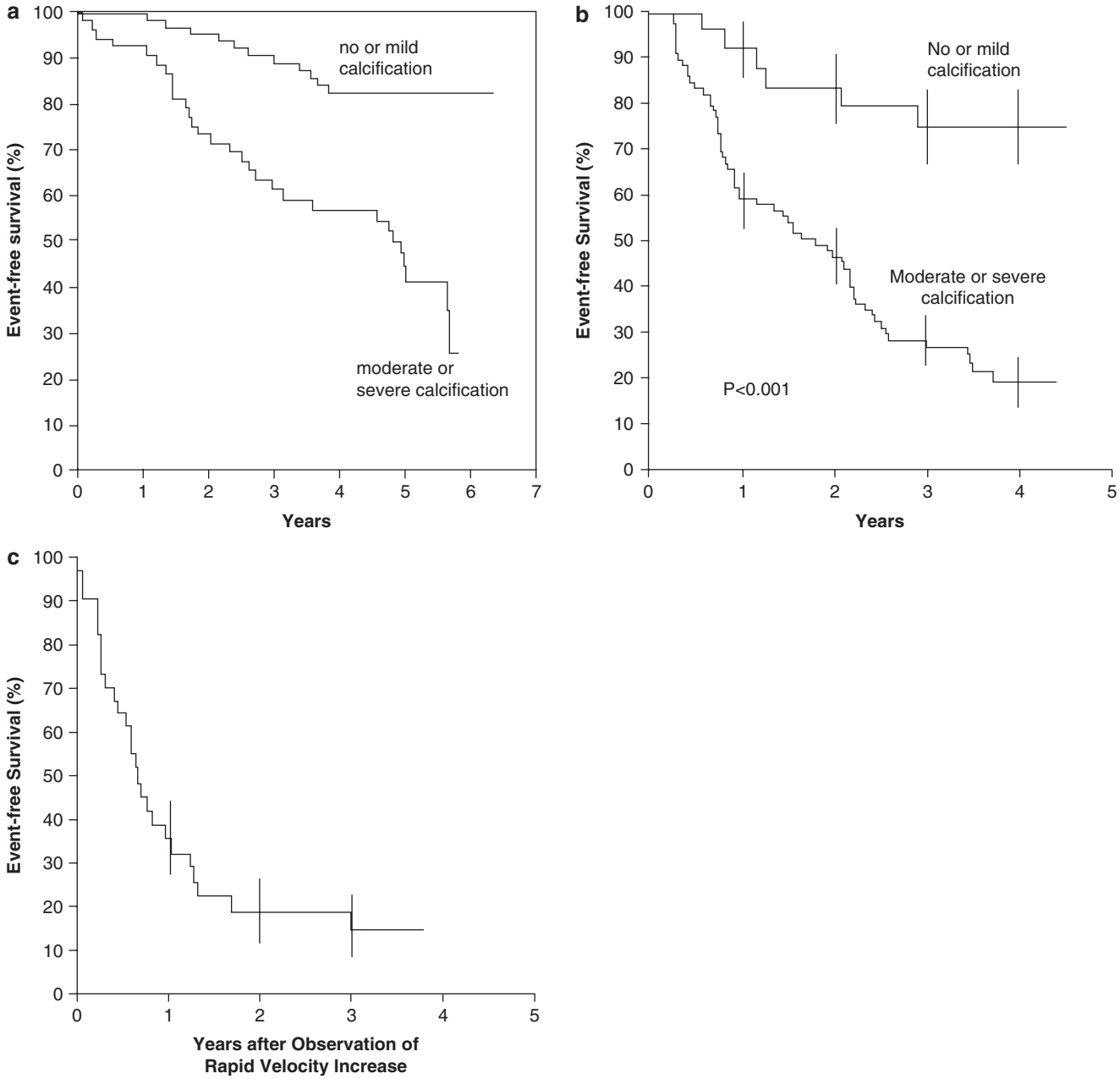

Fig. 7.10 (a) Kaplan–Meier analysis of event-free survival for patients with mild or moderate AS having no or mild calcification compared with patients having moderate or severe aortic valve calcification ($p = 0.0001$). Modified from ref [16] **(b)** Kaplan-Meier analysis of event-free survival for patients with severe AS (aortic jet velocity of at least 4 m/s at study entry) having no or mild aortic valve calcification compared with patients having moderate or severe calcification ($p < 0.001$). The vertical bars indicate standard errors. Modified from ref [2] **(c)** Kaplan–Meier analysis of event-free survival patients with moderate or severe calcification of their aortic valve and a rapid increase in aortic jet velocity of at least 0.3 m/s within 1 year. In this analysis, follow-up started with the visit at which the rapid increase was identified. The vertical bars indicate standard errors. Modified from ref [2]

critical importance for patient selection. Although MR angio can be used as an alternative, CT angio is, in general, the preferred method. Vessel diameter, extent of calcification, and vessel tortuosity are the required informations. 3D reconstruction is extremely helpful for procedure planning (Fig. 7.13).

Additional Information Provided by Imaging

MRI and CT are helpful in evaluating additional anatomic details that may be important for procedure planning and risk assessment. Complex plaques in the aorta may increase the risk of embolic events. Detailed assessment of the aortic

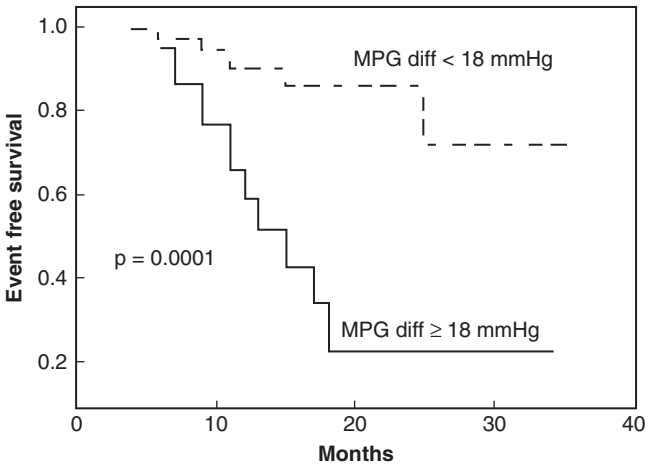

Fig. 7.11 Event-free survival curves according to exercise-induced changes in mean transaortic pressure gradient (MPG) in 69 consecutive patients with severe AS ($p = 0.0001$). Modified from ref [17]

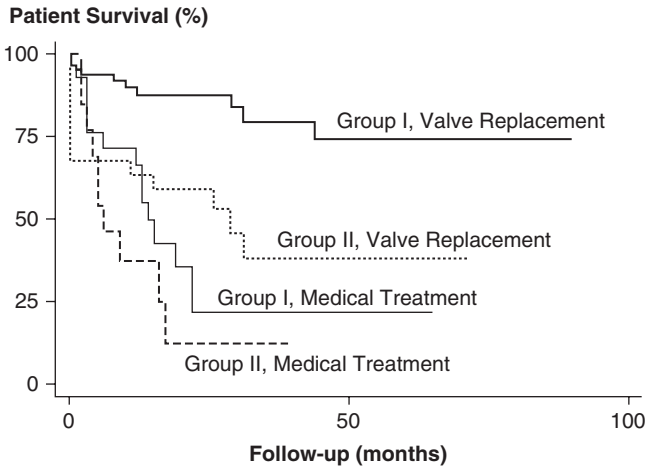

Fig. 7.12 Kaplan–Meier survival estimates of 136 consecutive patients with low flow-low gradient AS. Group I ($n = 92$) represents patients with contractile reserve determined by low-dose dobutamine echocardiography, and Group II represents the group of patients with absent contractile reserve ($n = 44$). Survival estimates are represented according to contractile reserve and treatment strategy (aortic valve replacement vs. medical therapy). Modified from[10]

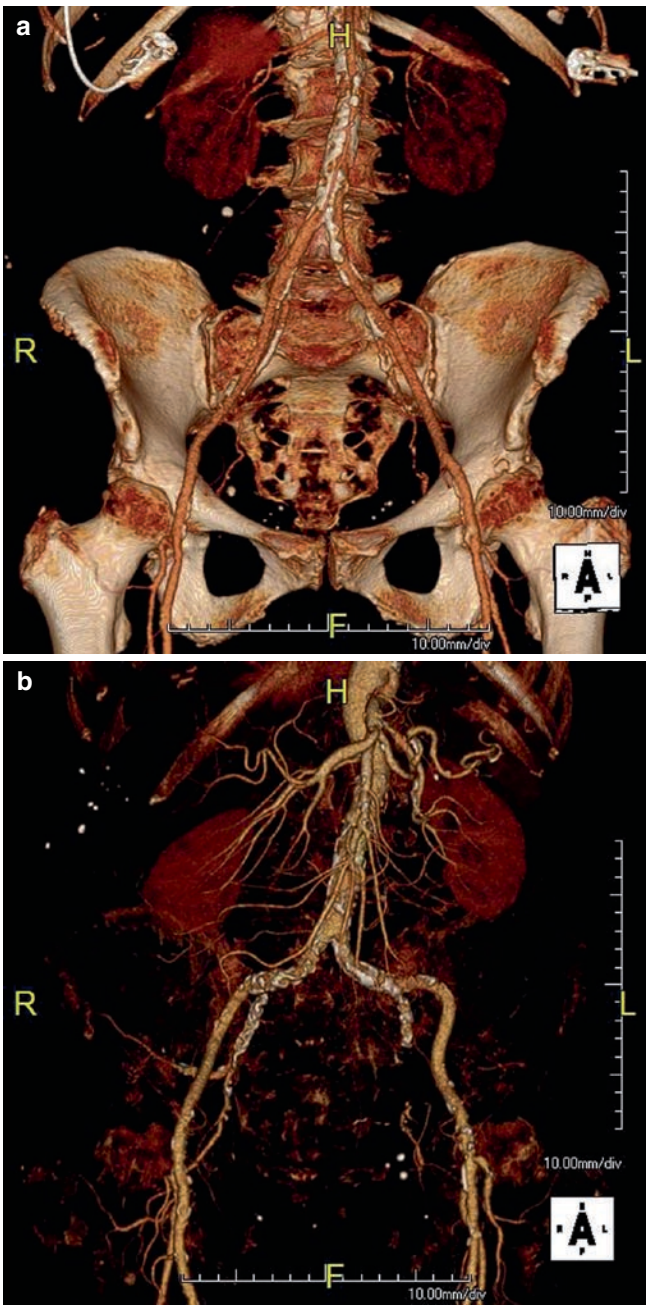

Fig. 7.13 Evaluation of femoral access prior to transfemoral aortic valve implantation using 3D reconstruction of CT-angiography. **(a)** Patient with no tortuosity and little calcification of iliac arteries (particularly on the right side). **(b)** Patient with significant tortuosity and marked calcification of iliac arteries

root with geometry and relation between aortic valve and coronary artery take off, as well as the extent and distribution of valve calcification may gain more importance in the future.

Monitoring of the Procedure

Currently, positioning of the valve mostly relies on aortic root angiography. CT may be helpful to define the best projection plane prior to the procedure. TOE is frequently used during the procedure, but has difficulties to precisely define the stent ends. Real-time 3D echo has been reported to be superior with this regard. TOE is useful in assessing residual perivalvular aortic regurgitation. In addition, complications such as pericardial effusion or aortic

dissection and interference with the mitral valve can be quickly recognized.

Imaging in Clinical Decision-making

Indications for Surgery

Echocardiography is the gold standard for diagnosis and quantification of AS as the basis for the decision-making process in this disease. The strongest indication for valve replacement is given by the occurrence of symptoms in the presence of severe AS. In asymptomatic patients, unexplained LV systolic dysfunction as detected by echo is considered as an indication for surgery.[3, 4] Exercise testing has been shown to be helpful for selecting patients who might benefit from surgery while still reporting to be asymptomatic. The incremental valve of exercise echo when compared with regular stress testing still requires validation. However, the echocardiographically provided criterion of moderate to severe aortic valve calcification and a rapid haemodynamic progression (increase in peak aortic jet velocity of > 0.3 m/s within 12 months) is considered a class IIa indication for elective surgery in asymptomatic patients.

Scheduling Follow-up Intervals

Intervals for the follow-up visits of asymptomatic patients with AS can be scheduled based on the severity of AS. Generally, patients with a severe stenosis should be followed up every 6 months and those with moderate AS, on a yearly basis. In addition, factors such as the previous rate of haemodynamic progression and the degree of valve calcification (important: calcification is associated with more rapid disease progression) help to optimize the timing of follow-up visits.

Mitral Stenosis (MS)

Echocardiographic Assessment of Morphology and Severity with its Pitfalls and Limitations

The mitral valve area (MVA) normally ranges between 4.0 and 5.0 cm^2. An area <1.5 cm^2 is considered moderate MS, and <1.0 cm^2 severe MS. Routine echocardiographic evaluation of MS should always include assessment of valve morphology and planimetry of valve area, as well as measurement of mean gradient and pressure half-time. In patients with good imaging quality, planimetry is the reference method for the grading of MS severity. MS affects the left atrial size and pulmonary artery pressure (PAP), which should be included in the assessment. Associated mitral regurgitation has to be evaluated with great care, especially in view of potential balloon valvulotomy.

Transthoracic echocardiography enables complete evaluation in most cases. Trans-oesophageal echo is only recommended in patients with insufficient imaging quality and when left atrial thrombi or endocarditis (vegetations) are suspected.

Valve Morphology

MS is mostly of rheumatic origin, which is characterized by thickening of the leaflet tips and commissural fusion resulting in the typical doming appearance of the anterior leaflet (Figs. 7.14 and 7.15). Degenerative MS is characterized by pronounced annular calcification and rarely reaches haemodynamic significance (Fig. 7.16). Complete fusion of both commissures generally indicates severe MS. However, the lack of commissural fusion does not exclude significant MS,

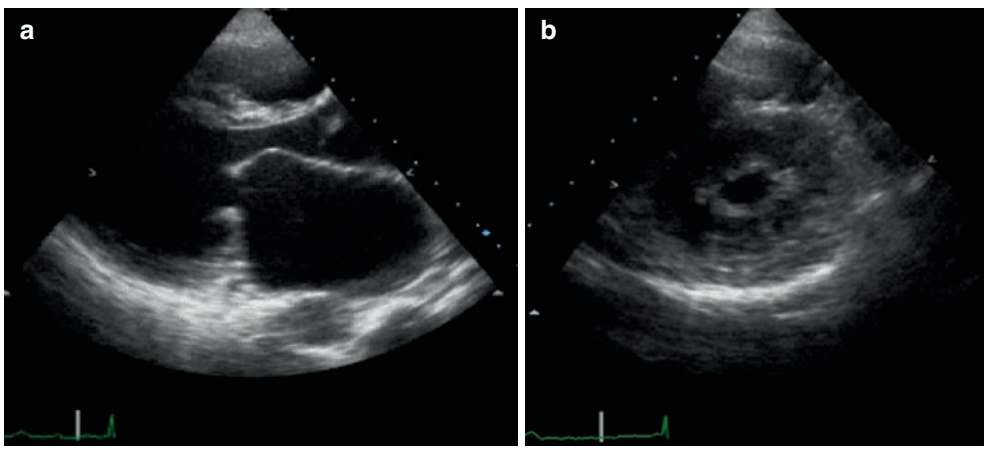

Fig. 7.14 Typical example of rheumatic mitral stenosis (parasternal views). **(a)** Parasternal long-axis view with typical diastolic doming of the anterior mitral leaflet and anterior displacement of the posterior leaflet. **(b)** Parasternal short-axis view showing the mitral valve orifice

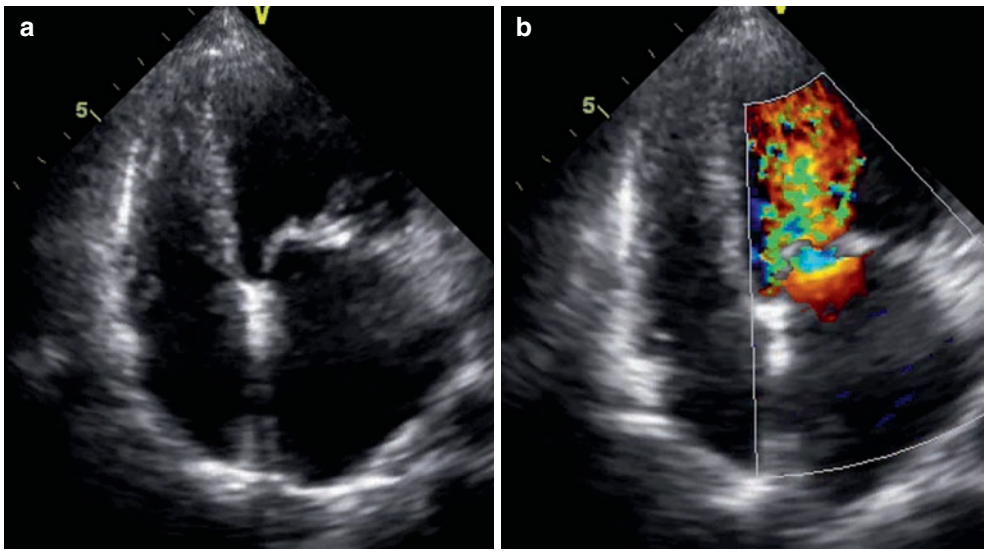

Fig. 7.15 Typical example of rheumatic mitral stenosis (apical views). **(a)** Apical 4-chamber view with diastolic doming of the anterior leaflet and calcified posterior leaflet. **(b)** Colour Doppler image (apical 4-chamber view) showing flow convergence upstream from the mitral valve orifice and turbulent high velocity flow downstream from the stenotic orifice

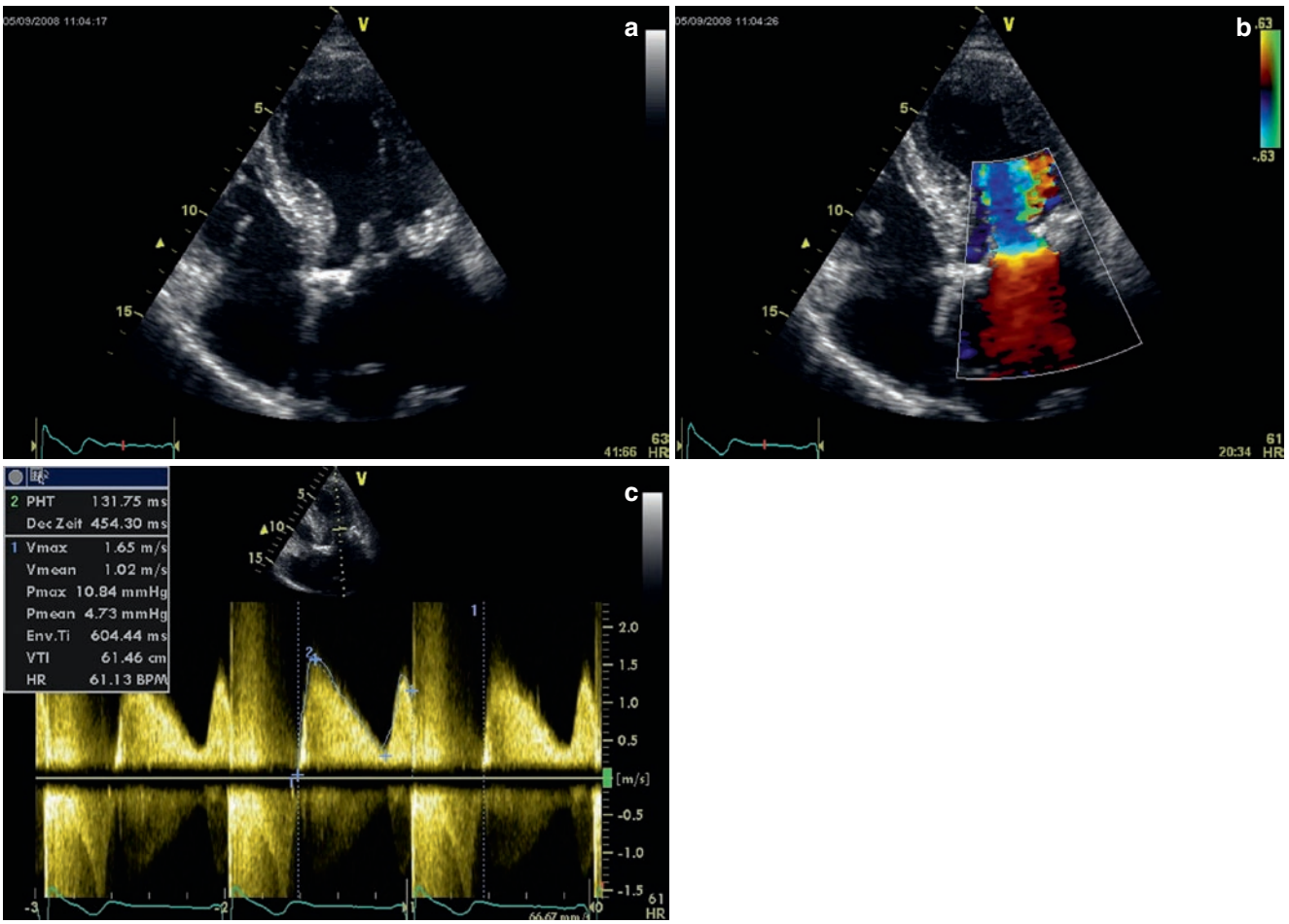

Fig. 7.16 Degenerative (calcific) mitral valve stenosis. **(a)** Apical 4-chamber view (diastole) showing the thickened and calcified base of the leaflets. **(b)** Colour Doppler image showing increased transvalvular velocity. **(c)** Mean gradient approximating 5 mmHg at a heart rate of 60 beats/min

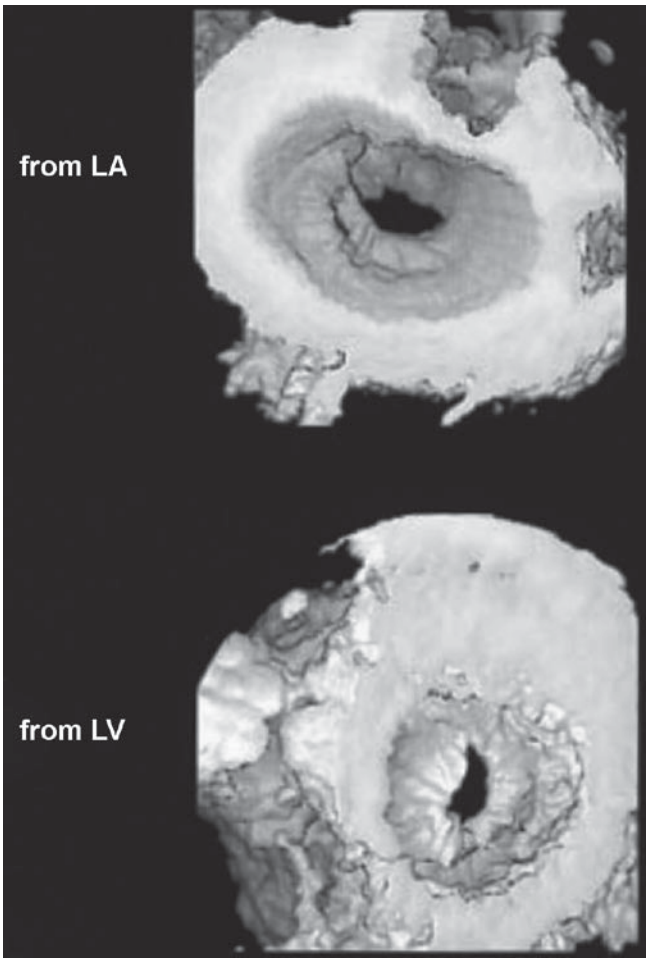

Fig. 7.17 3D reconstruction in a patient with mitral stenosis (atrial and ventricular aspects). Courtesy Dr. Thomas Binder, Vienna General Hospital, Vienna

particularly in highly rigid valves. Commissural fusion is assessed from the parasternal short-axis view (Fig. 7.14). Commissural fusion and mitral valve orifice can be even better visualized by 3D echocardiography (Fig. 7.17).

The morphology of the valve is of critical importance for the choice of intervention, particularly the suitability for balloon valvotomy. Scores combining information about mobility, thickening, and calcification of the valve and the subvalvular apparatus[19] (Table 7.2) are used to summarize the morphologic changes (Fig. 7.18), but reports should always include a comprehensive description of valve anatomy and not only a score number.

Stenosis Severity

Recommendations for classification of MS severity are given in Table 7.3.

Valve Area Planimetry

Planimetry of the mitral orifice has the advantage of being a direct measurement of MVA, not affected by flow, cardiac chamber compliance, or associated valvular lesions. Its correlation with anatomical valve area has been shown to be superior compared with other measurements, and is therefore considered the reference measurement of MVA[3–5].

Planimetry is performed in mid-diastole by direct tracing of the mitral orifice, including opened commissures, in a parasternal short-axis view. The measurement plane should be perpendicular to the mitral orifice and positioned at the leaflet tips (Fig. 7.14). Difficulties in defining the correct

Table 7.2. Assessment of mitral valve anatomy according to the Wilkins score[19]

Grade	Mobility	Thickening	Calcification	Subvalvular thickening
1	Highly mobile valve with only leaflet tips restricted	Leaflets near normal in thickness (4–5 mm)	A single area of increased echo brightness	Minimal thickening just below the mitral leaflets
2	Leaflet mid and base portions have normal mobility	Mid leaflets normal, considerable thickening of margins (5–8 mm)	Scattered areas of brightness confined to leaflet margins	Thickening of chordal structures extending to one third of the chordal length
3	Valve continues to move forward in diastole, mainly from the base	Thickening extending through the entire leaflet (5–8 mm)	Brightness extending into the mid portions of the leaflets	Thickening extended to distal third of the chords
4	No or minimal forward movement of the leaflets in diastole	Considerable thickening of all leaflet tissue (>8–10 mm)	Extensive brightness throughout much of the leaflet tissue	Extensive thickening and shortening of all chordal structures extending down to the papillary muscles

The total score is the sum of the four items and ranges between 4 and 16

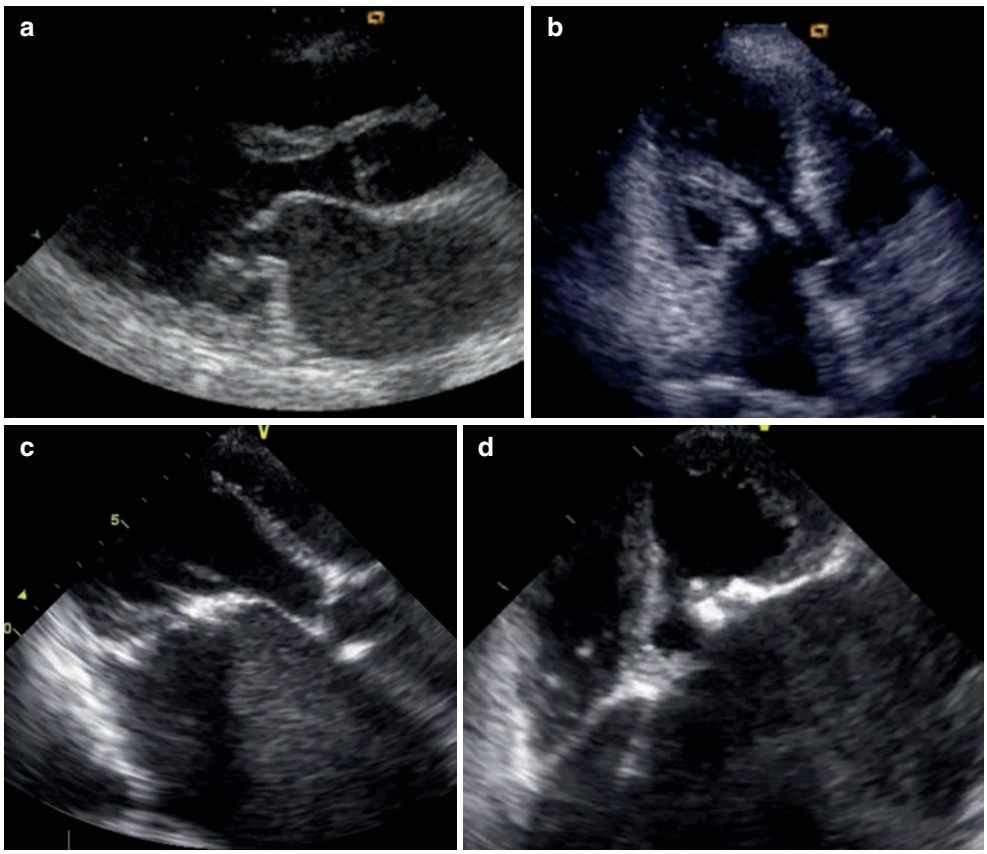

Fig. 7.18 Different morphologies of rheumatic mitral stenosis. **(a)** Ideal morphology for balloon mitral valvotomy (high mobility of the anterior leaflet with little thickening, no calcification, and no significant involvement of the subvalvular apparatus); parasternal long-axis view. **(b)** Reduced mobility of the severely thickened leaflets, severe involvement of the subvalvular apparatus but no calcification; apical long-axis view. **(c)** High mobility of the anterior leaflet. Basal half shows no thickening, but severe thickening and calcification of the residual leaflet; apical long-axis view. **(d)** Severely calcified mitral stenosis and giant left atrium; apical 4-chamber view

Table 7.3. Recommendations for the classification of mitral stenosis severity[3–5]

	Mild	Moderate	Severe
Specific findings			
Valve area (cm^2)	>1.5	1.0–1.5	<1.0
Supportive findings			
Mean pressure gradient (mm Hg)[a]	<5	5–10	>10
Systolic pulmonary artery pressure (mm Hg)	<30	30–50	>50

[a]At normal heart rate in sinus rhythm

image plane are a major cause of error. Real-time 3D echo and 3D-guided biplane imaging can be helpful in this regard, and have been shown to improve the accuracy and reproducibility of planimetry (Fig. 7.19).

The application of MVA planimetry is limited in patients with a poor acoustic window or with severe calcification of the leaflet tips. In such cases, excessive gain setting may cause under-estimation of MVA. Gain setting, therefore, should be carefully adapted to be just sufficient to visualize the contour of the mitral orifice.

Valve Area by Pressure Half-time

The pressure half-time ($T_{1/2}$) is defined as the time interval between the maximum transmitral gradient in early diastole and the time point where the gradient has declined to half of the maximum initial value. It is inversely related to the MVA, which can be calculated using the empirically derived formula[20]:

$$\text{MVA (cm}^2\text{)} = 220/T_{1/2}$$

The pressure half-time is obtained by tracing the deceleration slope of the E-wave on the Doppler spectral display of transmitral flow (Fig. 7.20). The deceleration slope is sometimes bimodal, and the dicline of the mitral flow velocity is more rapid in early diastole than during the following part of the E-wave. In these cases it is recommended to trace the deceleration slope in mid-diastole (Fig. 7.20).[20] In rare cases of patients with a concave shape of tracing, the pressure half-time measurement may not be feasible. In patients with atrial

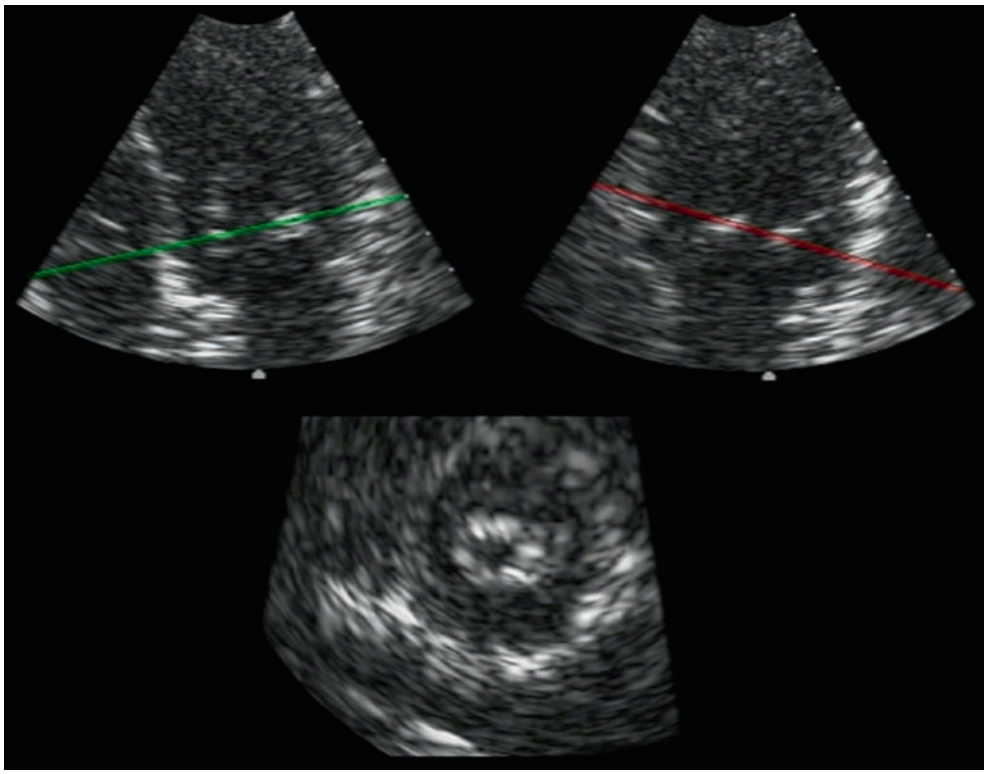

Fig. 7.19 3D echo data set allows optimizing the image plane for mitral valve area calculation without the requirement of an adequate parasternal view. Courtesy Dr. Thomas Binder, Vienna General Hospital, Vienna

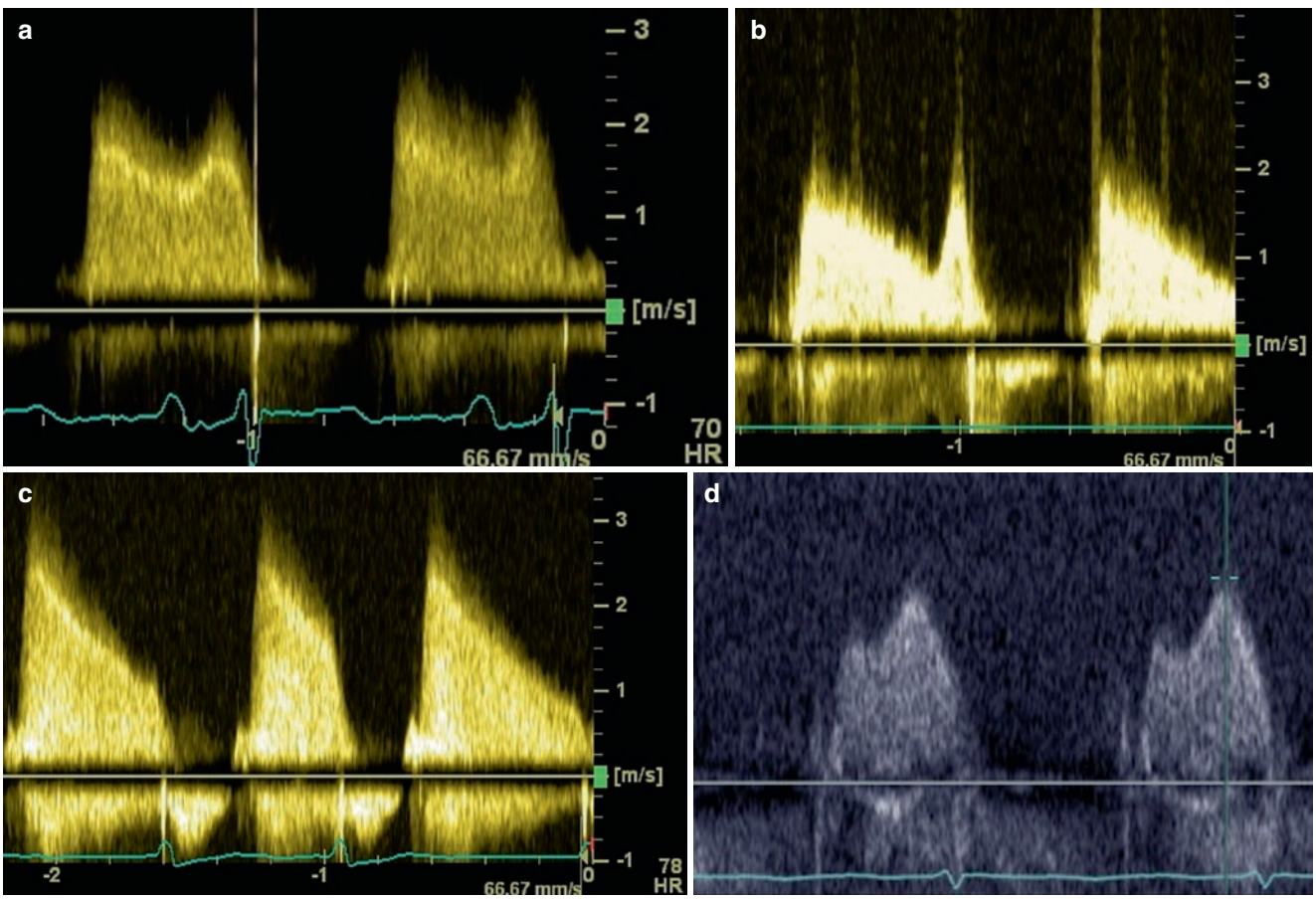

Fig. 7.20 CWD recordings of mitral stenosis (MS). **(a)** Severe MS in sinus rhythm. **(b)** Moderate MS in sinus rhythm. **(c)** MS in atrial fibrillation (no A-wave). In contrast to **(a)** and **(b)**, the slope is not linear but rather bimodal with the decline of mitral flow velocity being more rapid in early diastole than during the following part of the E-wave. In this case, it is recommended to trace the deceleration slope in mid-diastole. **(d)** The large A-wave indicates impaired LV relaxation. In this case, pressure half-time would overestimate MS severity and cannot be used for MVA calculation

fibrillation, tracing should be avoided in beats with short diastole. Ideally, an average of the different cardiac cycles should be chosen for measurement.

The pressure half-time method is easy to perform; however, it has important limitations. It not only depends on MVA but also on the initial transmitral pressure gradient, left atrial compliance, and LV diastolic function (relaxation and compliance).[21] Despite severe MS, misleadingly short $T_{1/2}$ can be observed in patients who have particularly low left atrial compliance. $T_{1/2}$ is also shortened in patients who have associated severe aortic regurgitation or restrictive LV filling. $T_{1/2}$ can, on the other hand, be prolonged in the case of impaired LV relaxation. In this situation, initial E-velocity will be relatively low and A-wave will be high, indicating that $T_{1/2}$ cannot be used for MVA estimation (Fig. 7.20). Impaired LV diastolic function is a likely explanation of the lower reliability of $T_{1/2}$ for MVA assessment in the elderly.

Transmitral Pressure Gradient

The estimation of the diastolic pressure gradient is a reliable measurement derived from the transmitral velocity flow curve using the simplified Bernoulli equation $\Delta P = 4v^2$.[22] Continuous-wave Doppler (CWD) should be used to ensure recording of maximal velocities (Fig. 7.20). In most cases, optimal alignment of the ultrasound beam and mitral inflow can be achieved from an apical window. Additional use of colour Doppler is helpful to identify eccentric jets and to guide the Doppler beam alignment. The mean gradient is the relevant haemodynamic finding, while the maximum gradient is of less interest as it is influenced by left atrial compliance and LV diastolic function.

Although the mean mitral gradient can be reliably assessed by Doppler, it is not an ideal marker of MS severity. It is not only determined by the MVA, but is highly dependent on the heart rate and transmitral flow rate (cardiac output, associated mitral regurgitation). Heart rate should therefore always be reported, and measurements preferably performed at normal heart rates. Despite these limitations, mean gradient offers important additional information, particularly in combined mitral valve disease and when other parameters provide conflicting or unreliable results.

Pulmonary Artery Pressure (PAP)

PAP, in general, increases with MS severity, but is not closely related to it. Elevated PAP that cannot by explained by other causes would be inconsistent with insignificant MS; however, PAP can be normal or only mildly elevated even in the presence of severe MS. Thus, PAP is only a supportive parameter for MS grading. Nevertheless, careful assessment of systolic PAP, using tricuspid regurgitant velocity, is of great importance as it provides prognostic information and influences management decisions (see below).

Alternative Methods of MS Quantification

There are alternative methods for quantification of MS that are less established and not recommended to be used in every patient, but may be reasonable in selected patients when additional information is needed.[5]

Continuity Equation

When the continuity equation is used in mitral stenosis, it is assumed that the filling volume of diastolic mitral flow is equal to the aortic stroke volume. MVA can then be calculated as follows:

$$\text{MVA (cm}^2) = \pi \cdot D^2/4 \cdot \text{VTI}_{\text{Aortic}}/\text{VTI}_{\text{Mitral}}$$

where D is the diameter of the LVOT.

Stroke volume can also be estimated from the pulmonary artery; however, this is rarely performed because of limited acoustic windows.

The usefulness of the continuity equation is hampered by the numerous measurements, increasing the impact of errors and its inapplicability in atrial fibrillation or associated significant mitral or aortic regurgitation.

Proximal Isovelocity Surface Area Method

The proximal isovelocity surface area method using the colour Doppler visualization of flow convergence proximal to the mitral orifice is another alternative to calculate the MVA as follows:

$$\text{MVA (cm}^2) = \pi \cdot r^2 \cdot V_{\text{aliasing}}/\text{peak } V_{\text{Mitral}} \cdot \alpha/180°$$

where r is the radius of the convergence hemisphere in cm, V_{aliasing} is the aliasing velocity in cm/s, peak V_{Mitral} is the peak CWD velocity of mitral inflow in cm/s, and α is the opening angle of mitral leaflets relative to flow direction.[24]

The method is technically demanding and requires multiple measurements; its accuracy is influenced by uncertainties in the measurement of the radius of the convergence hemisphere and the opening angle.

Mitral Valve Resistance

Mitral valve resistance is defined as the ratio of mean mitral gradient to transmitral diastolic flow rate, which is calculated by dividing SV by diastolic filling period. Mitral valve resistance has been argued to be less dependent on flow

conditions, which is not the case. It correlates well with PAP; however, it has not been shown to have an additional value for assessing MS severity when compared with valve area.[25]

Additional Findings

The echocardiographic assessment should also include the evaluation of additional valve disease, particularly tricuspid regurgitation, of the left atrium, including the search for thrombi (Fig. 7.21) and the right ventricle.

Role of MRI and CT

Planimetry of the MVA by MRI has been shown to be feasible in a small number of patients, but tends to overestimate echo as well as catheter-derived valve areas.[26] CT currently does not play a role in the assessment of MS.

Prognostic Information Provided by Imaging

The impact of echocardiographic findings on the prognosis of MS has been studied mainly after balloon mitral commissurotomy. Multi-variate analyses identified valve anatomy as a strong predictive factor of event-free survival.[27] Indices of the severity of MS or its haemodynamic consequences immediately after balloon commissurotomy are also predictors of event-free survival, irrespective of whether it is MVA, mean gradient, and left atrial or PAP.[27, 28] The degree of MR following balloon mitral commissurotomy and baseline patient characteristics, such as age, functional class, and cardiac rhythm are also strong predictors of long-term outcome after balloon mitral commissurotomy.[27, 28]

Numerous studies on the natural history and the results of surgical commissurotomy predate current echocardiographic practice, and thus do not aid in the assessment of the prognostic value of echocardiographic findings.

Interventions and Imaging

Echocardiography plays a major role in mitral balloon valvotomy, not only for patient selection (see morphology), but also for monitoring the procedure either by TTE or TOE and for evaluating the results. TOE is required to exclude left atrial thrombi prior to the procedure. Although not mandatory, echo may aid safe transseptal puncture and selection of the optimal puncture site. Complications such as pericardial effusion can quickly be recognized. Stepwise dilation of the valve with careful echocardiographic assessment of changes in the morphology, successful opening of commissures, leaflet tears (Fig. 7.22), and the degree of mitral regurgitation may improve the results.

Imaging in Clinical Decision-making

Echocardiography plays a key role in decision-making. It has become the gold standard for diagnosing and quantifying MS. Intervention is indicated in patients with MVA of $< 1.5\ cm^2$,who become symptomatic. Balloon valvotomy is preferred and its feasibility is again assessed by echo. It is considered in asymptomatic patients with favourable morphologic characteristics, high thromboembolic risk, and high risk of haemodynamic decompensation. Criteria for risk assessment are clinical (previous embolic event, recent or paroxysmal episodes of atrial fibrillation, need for major non-cardiac surgery, desire of pregnancy) and echocardiographic

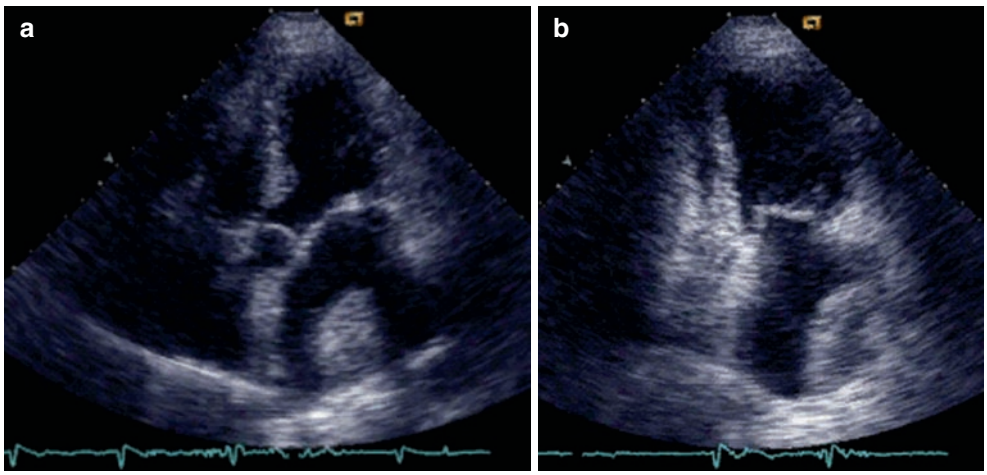

Fig. 7.21 4-chamber **(a)** and 2-chamber view **(b)** of a patient with mitral stenosis and a large left atrial thrombus

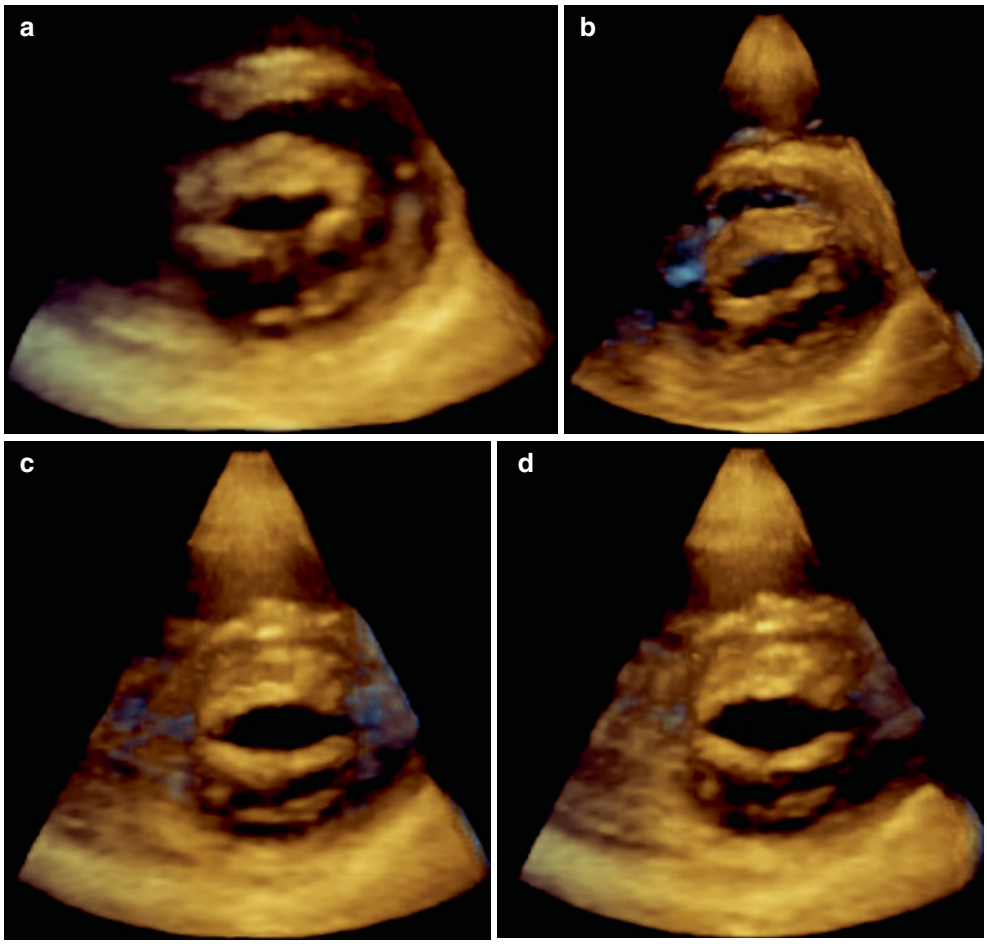

Fig. 7.22 Real-time 3D images of a patient with mitral stenosis undergoing balloon valvotomy. The baseline image is shown in panel **(a)**. Panels **(b–d)** show the gradual increase in commissural splitting after step-by-step dilation with increasing balloon size. Courtesy Dr. Eric Brochet, Bichat Hospital, Paris

(dense spontaneous echo contrast in the left atrium, systolic PAP > 50 mmHg at rest). For details, see ESC Guidelines on the management of valvular heart disease.[4]

Tricuspid Stenosis (TS)

Echocardiographic Assessment of Morphology and Severity with its Pitfalls and Limitations

Tricuspid stenosis (TS) is the least common stenotic valve lesion. In most cases, TS is of rheumatic origin and associated with some degree of regurgitation. In the presence of anatomic findings consistent with TS by 2D echo, a mean pressure gradient of ≥ 5 mmHg, T½ ≥ 190 ms, inflow time velocity integral > 60 cm, and a valve area by the continuity equation ≤ 1 cm^2 are consistent with significant stenosis. Supportive findings are a more than moderately enlarged right atrium and a dilated inferior vena cava.

Valve Morphology

Anatomical signs of TS are valve thickening and/or calcification, restricted mobility, diastolic doming, and right atrial enlargement (Fig. 7.23).

Tricuspid Stenosis Severity

Measurement of the valve area (TVA) is difficult in TS. It cannot be done by 2D echo, 3D echo has not yet been validated for this purpose. Other Doppler sonographic methods for calculating TVA also appear to be less accurate than in MS (see below).

Pressure Gradient

Mean pressure gradient can be measured easily by Doppler, but has its limitations for quantification of TS. The tricuspid inflow velocity is best recorded from either a low parasternal right ventricular inflow view or from the apical 4-chamber view. As tricuspid inflow velocities are affected by respiration,

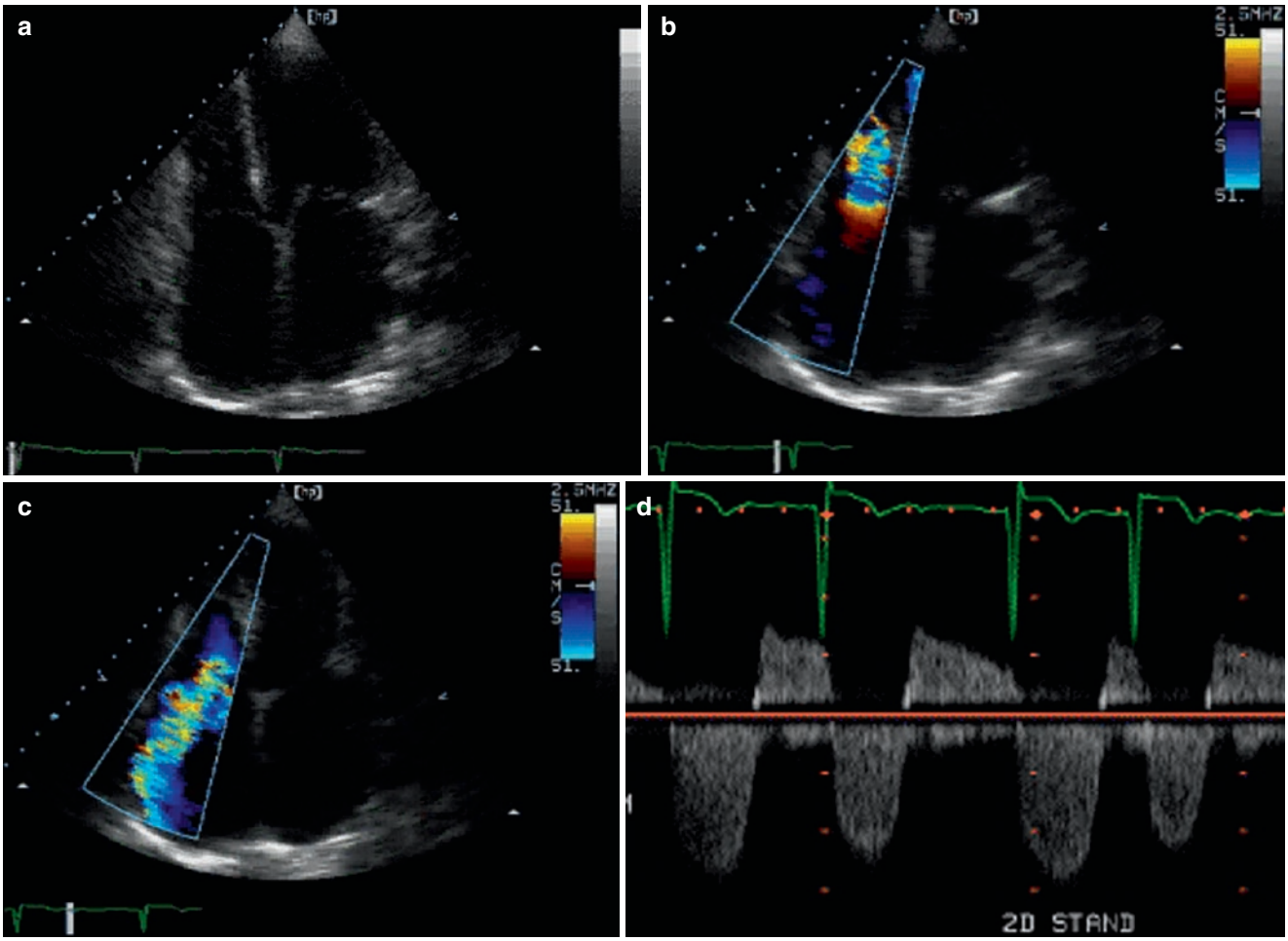

Fig. 7.23 Patient with severe combined rheumatic tricuspid valve disease. **(a)** Diastolic 2D image, 4-chamber view, showing doming of the tricuspid valve. **(b)** Diastolic colour Doppler image, 4-chamber view, indicating stenosis. **(c)** Systolic colour Doppler image, 4-chamber view, showing tricuspid regurgitation. **(d)** CWD recording

all measurements must be averaged throughout the respiratory cycle or recorded at end-expiratory apnea. In patients with atrial fibrillation, average measurements of five cardiac cycles should be taken at a mean heart rate of < 100 beats/min. In addition, mean gradients are highly dependent on heart rate and flow (cardiac output, tricuspid regurgitation).

Peak inflow velocity through a normal tricuspid valve rarely exceeds 0.7 m/s.

In general, the mean pressure gradient is lower in TS than in MS, usually ranging between 2 and 10 mmHg, and averaging around 5 mmHg.[5] Higher gradients may be seen with concomitant regurgitation[29] (Fig. 7.23).

Pressure Half-time

The pressure half-time (T1/2) method has been applied in a manner analogous to MS. Constants of 220 as well as 190 have been proposed for valve area estimation.[29] In validation studies, TS valve area determined by the $T_{1/2}$ method appeared less accurate than in MS. However, $T_{1/2}$ values > 190 ms suggest significant stenosis.[5]

Continuity Equation

The main limitation of the method is to obtain an accurate measurement of the inflow volume passing through the tricuspid valve. In the absence of significant tricuspid regurgitation, the stroke volume obtained from either the left or right ventricular outflow can be used; an estimated valve area ≤ 1cm^2 is considered indicative of severe TS. However, as severity of tricuspid regurgitation increases, the valve area is progressively under-estimated by this method.

Role of MRI and CT

Although MRI and CT should be feasible, these imaging modalities have so far gained no role in the assessment of TS.

Prognostic Information Provided by Imaging

No data are currently available regarding the prognostic value of imaging in TS.

Interventions and Imaging

Suitability of balloon valvotomy is assessed by echocardiography (morphology, less than moderate regurgitation), and the procedure can be monitored by echo.

Imaging in Decision-Making

Diagnosis and quantification of TS are, in general, provided by echo. Intervention is indicated in severe TS when patients are symptomatic despite medical therapy or at the time of left-sided surgery.[4]

Pulmonic Stenosis (PS)

Pulmonary stenosis is almost always congenital of origin. Stenosis below (proximal to) the pulmonary valve may result from both congenital and acquired causes. Stenosis of the pulmonary artery distal to the valve may occur in the main pulmonary trunk, or more distally in the branch vessels.

Echocardiographic Assessment of Morphology and Severity with its Pitfalls and Limitations

Valve Anatomy

Evaluation of anatomy is important in defining the location of stenosis. The valve itself may be dome-shaped (Fig. 7.24), dysplastic, or, in rare cases, calcified. A post-stenotic dilatation is common in dome-shaped valves.

Stenosis Severity

Pressure Gradient

Quantitation of pulmonary stenosis severity is primarily based on the transpulmonary pressure gradient, using the simplified Bernoulli equation, $\Delta P = 4v^2$.[5]

This estimation is reliable and correlates well with invasive catheter measurements.[30] It is particularly important that the CWD beam is positioned in parallel to the stenotic jet to avoid under-estimation of the gradient (Fig. 7.24). In adults, this is usually best performed from a parasternal short-axis view; however, in children and in some adults, the highest gradients may be found from a sub-costal window. A modified apical 5-chamber view may also be used. In most instances of valvular pulmonary stenosis, the modified Bernoulli equation works well and there is no need to account for the proximal velocity, as this is usually < 1 m/s. However, there are exceptions to this. In certain (congenital) settings, the presence of two stenoses in series may make it impossible to precisely ascertain the individual contribution of each. In addition, serial stenoses may cause significant pressure recovery resulting in a higher Doppler gradient compared with the net pressure drop across both stenoses.

Muscular infundibular obstruction is frequently characterized by a late peaking systolic jet that appears "dagger shaped," reflecting the dynamic nature of the obstruction; this pattern can be useful in separating the dynamic muscular obstruction from a fixed valvular obstruction, where the peak velocity is generated early in systole.

Severe stenosis is defined by a peak jet velocity of > 4 m/s (peak gradient > 64 mmHg), moderate stenosis is defined by a peak jet velocity of 3–4 m/s (peak gradient 36–64 mmHg), and mild stenosis is defined by a peak jet velocity of < 3 m/s (peak gradient < 36 mmHg).[5]

Other Indices of Severity

The continuity equation and the PISA method, although theoretically feasible, have not been validated with respect to pulmonary stenosis. Assessment of pulmonic valve area by planimetry is not possible, as the required imaging plane is generally not available.

A useful index of severity is the RV systolic pressure from the tricuspid regurgitant velocity and the addition of an estimate of right atrial pressure (Fig. 7.24). The pulmonary artery systolic pressure should equal RV systolic pressure minus pulmonary valve pressure gradient.

Role of MRI and CT

Although MRI and CT should be able to yield similar information when compared with AS, these imaging modalities have so far gained little role in the assessment of PS. MRI is, however, definitely helpful in patients with poor image quality and for detailed anatomic evaluation (subvalvular–valvular–supra-valvular stenosis–pulmonary arteries) (Fig. 7.25).

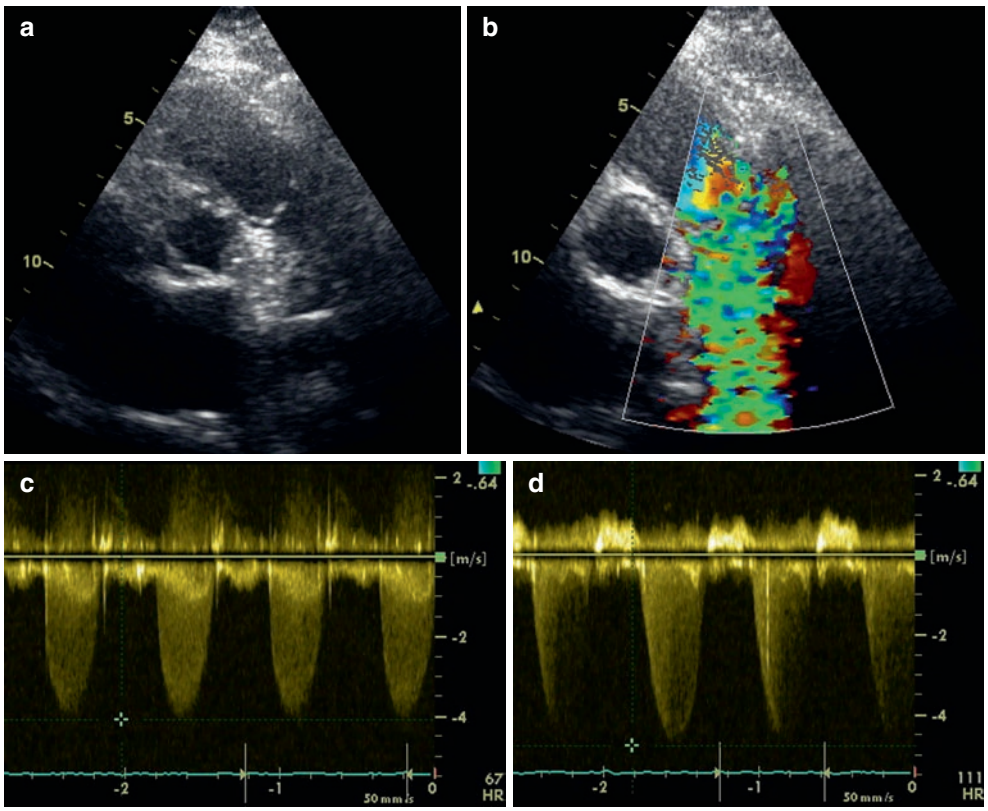

Fig. 7.24 Patient with severe pulmonic stenosis. **(a)** Parasternal short-axis view, 2D image showing doming of the pulmonic valve (*arrows*). **(b)** Parasternal short-axis view, colour Doppler image, showing flow acceleration (*arrow*) and the stenotic jet. **(c)** CWD recording of pulmonic stenosis. **(d)** CWD recording of the corresponding tricuspid regurgitation

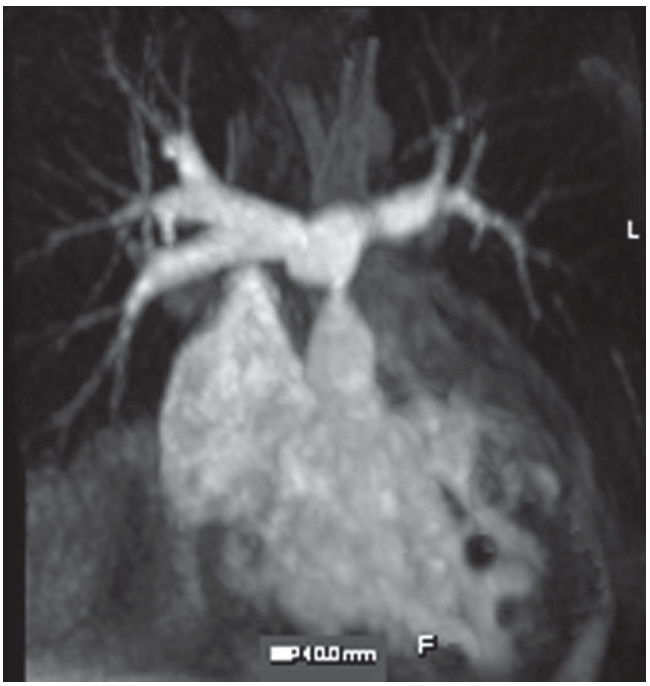

Fig. 7.25 Contrast-enhanced MR angiography of a patient with severe supra-valvular pulmonic stenosis (*arrow*) after surgery for complex congenital heart disease

Prognostic Information Provided by Imaging

No data are currently available regarding the prognostic value of imaging in PS.

Interventions and Imaging

Suitability of balloon valvotomy is assessed by echocardiography (morphology). Native PS intervention does not require imaging modalities besides fluoroscopy. However, imaging techniques such as MRI may become more important for re-intervention in homograft or conduit stenosis using percutaneous valve implantation.

Imaging in Decision-Making

Diagnosis and quantification of PS are, in general, provided by echo. Intervention is indicated in patients with peak gradients of > 60 mmHg.[3]

References

1. Roberts WC, Ko JM. Frequency by decades of unicuspid, bicuspid, and tricuspid aortic valves in adults having isolated aortic valve replacement for aortic stenosis, with or without associated aortic regurgitation. *Circulation*. 2005;111:920–925
2. Rosenhek R, Binder T, Porenta G, et al Predictors of outcome in severe, asymptomatic aortic stenosis. *N Engl J Med*. 2000;343:611–617
3. Bonow RO, Carabello BA, Chatterjee K, et al ACC/AHA 2006 guidelines for the management of patients with valvular heart disease: a report of the American College of Cardiology/American Heart Association Task Force on Practice Guidelines (writing committee to revise the 1998 guidelines for the management of patients with valvular heart disease) developed in collaboration with the Society of Cardiovascular Anesthesiologists endorsed by the Society for Cardiovascular Angiography and Interventions and the Society of Thoracic Surgeons. *J Am Coll Cardiol*. 2006;48:e1–148
4. Vahanian A, Baumgartner H, Bax J, et al Guidelines on the management of valvular heart disease: the task force on the management of valvular heart disease of the European Society of Cardiology. *Eur Heart J*. 2007;28:230–268
5. Baumgartner H, Hung J, Bermejo J, et al Echocardiographic assessment of valve stenosis: EAE/ASE recommendations for clinical practice. *Eur J Echocardiogr*. 2009;10:1–25
6. Currie PJ, Seward JB, Reeder GS, et al Continuous-wave Doppler echocardiographic assessment of severity of calcific aortic stenosis: a simultaneous Doppler-catheter correlative study in 100 adult patients. *Circulation*. 1985;71:1162–1169
7. Baumgartner H, Stefenelli T, Niederberger J, Schima H, Maurer G. "Overestimation" of catheter gradients by Doppler ultrasound in patients with aortic stenosis: a predictable manifestation of pressure recovery. *J Am Coll Cardiol*. 1999;33:1655–1661
8. Otto CM, Pearlman AS, Comess KA, Reamer RP, Janko CL, Huntsman LL. Determination of the stenotic aortic valve area in adults using Doppler echocardiography. *J Am Coll Cardiol*. 1986;7:509–517
9. Oh JK, Taliercio CP, Holmes DR Jr, et al Prediction of the severity of aortic stenosis by Doppler aortic valve area determination: prospective Doppler-catheterization correlation in 100 patients. *J Am Coll Cardiol*. 1988;11:1227–1234
10. Monin JL, Quere JP, Monchi M, et al Low-gradient aortic stenosis: operative risk stratification and predictors for long-term outcome: a multicenter study using dobutamine stress hemodynamics. *Circulation*. 2003;108:319–324
11. Schlosser T, Malyar N, Jochims M, et al Quantification of aortic valve stenosis in MRI-comparison of steady-state free precession and fast low-angle shot sequences. *Eur Radiol*. 2007;17:1284–1290
12. Lembcke A, Thiele H, Lachnitt A, et al Precision of forty slice spiral computed tomography for quantifying aortic valve stenosis: comparison with echocardiography and validation against cardiac catheterization. *Invest Radiol*. 2008;43:719–728
13. Pouleur AC, le Polain de Waroux JB, Pasquet A, Vanoverschelde JL, Gerber BL. Aortic valve area assessment: multidetector CT compared with cine MR imaging and transthoracic and transesophageal echocardiography. *Radiology*. 2007;244:745–754
14. Pouleur AC, le Polain de Waroux JB, Kefer J, et al Usefulness of 40-slice multidetector row computed tomography to detect coronary disease in patients prior to cardiac valve surgery. *Eur Radiol*. 2007;17:3199–207
15. Otto CM, Burwash IG, Legget ME, et al Prospective study of asymptomatic valvular aortic stenosis. Clinical, echocardiographic, and exercise predictors of outcome. *Circulation*. 1997;95:2262–2270
16. Rosenhek R, Klaar U, Schemper M, et al Mild and moderate aortic stenosis; natural history and risk stratification by echocardiography. *Eur Heart J*. 2004;25:199–205
17. Lancellotti P, Lebois F, Simon M, Tombeux C, Chauvel C, Pierard LA. Prognostic importance of quantitative exercise Doppler echocardiography in asymptomatic valvular aortic stenosis. *Circulation*. 2005;112:I377–382
18. Vahanian A, Alfieri O, Al-Attar N, et al Transcatheter valve implantation for patients with aortic stenosis: a position statement from the European Association of Cardio-Thoracic Surgery (EACTS) and the European Society of Cardiology (ESC), in collaboration with the European Association of Percutaneous Cardiovascular Interventions (EAPCI). *Eur Heart J*. 2008;29:1463–1470
19. Wilkins GT, et al Percutaneous balloon dilatation of the mitral valve: an analysis of echocardiographic variables related to outcome and the mechanism of dilatation. *Br Heart J*. 1988;60:299–308
20. Gonzalez MA, Child JS, Krivokapich J. Comparison of two-dimensional and Doppler echocardiography and intracardiac hemodynamics for quantification of mitral stenosis. *Am J Cardiol*. 1987;60:327–332
21. Thomas JD, Weyman AE. Doppler mitral pressure half-time: a clinical tool in search of theoretical justification. *J Am Coll Cardiol*. 1987;10:923–929
22. Nishimura RA, et al Accurate measurement of the transmitral gradient in patients with mitral stenosis: a simultaneous catheterization and Doppler echocardiographic study. *J Am Coll Cardiol*. 1994;24:152–158
23. Nakatani S, et al Value and limitations of Doppler echocardiography in the quantification of stenotic mitral valve area: comparison of the pressure half-time and the continuity equation methods. *Circulation*. 1988;77:78–85
24. Messika-Zeitoun D, et al Sequential assessment of mitral valve area during diastole using colour M-mode flow convergence analysis: new insights into mitral stenosis physiology. *Eur Heart J*. 2003;24:1244–1253
25. Izgi C, et al Mitral valve resistance as a determinant of resting and stress pulmonary artery pressure in patients with mitral stenosis: a dobutamine stress study. *J Am Soc Echocardiogr*. 2007;20:1160–1166
26. Djavidani B, et al Planimetry of mitral valve stenosis by magnetic resonance imaging. *J Am Coll Cardiol*. 2005;45:2048–2053.
27. Palacios IF, et al Which patients benefit from percutaneous mitral balloon valvuloplasty? Prevalvuloplasty and postvalvuloplasty variables that predict long-term outcome. *Circulation*. 2002;105:1465–1471
28. Iung B, et al Late results of percutaneous mitral commissurotomy in a series of 1024 patients. Analysis of late clinical deterioration: frequency, anatomic findings, and predictive factors. *Circulation*. 1999;99:3272–3278
29. Fawzy ME, et al Doppler echocardiography in the evaluation of tricuspid stenosis. *Eur Heart J*. 1989;10:985–990
30. Lima CO, et al Noninvasive prediction of transvalvular pressure gradient in patients with pulmonary stenosis by quantitative two-dimensional echocardiographic Doppler studies. *Circulation*. 1983;67:866–871

Chapter 8

VALVULAR REGURGITATION

Luc A. Pierard, Marie Moonen, and Patrizio Lancellotti

J. L. Zamorano et al. (eds.), *The ESC Textbook of Cardiovascular Imaging*
DOI: 10.1007/978-1-84882-421-8_8, © Springer-Verlag London Limited 2010

Introduction

Valvular regurgitation has long been recognized as an important cause of morbidity and mortality. Non-invasive cardiac imaging, mainly including echocardiographic examination, is the method of choice to detect and quantitate the severity of the regurgitation and allows accurate estimation of the underlying mechanisms. The extent of the lesion process and the severity of valvular regurgitation may identify patients in whom valve repair is highly likely. The quantified degree of the valvular regurgitation as well as its consequences on left ventricular (LV) function is of prognostic importance. The anatomic structure of the heart in relation with the valves can be perfectly examined by echocardiography and cardiac magnetic resonance imaging (MRI). Both techniques have significantly changed the management of patients with valvular regurgitation.

Aortic Regurgitation

Aortic regurgitation (AR) is a common valvular disease. Techniques for making the diagnosis include physical examination, contrast angiography, cardiac MRI, CT scanner, and echocardiography. A precise determination of the severity of the regurgitation and its repercussions on LV function is essential for clinical management and, in particular, for appropriate timing of surgical intervention. For many years, quantification of AR has relied on cardiac catheterization with contrast angiography. However, this technique is only semi-quantitative and imperfect. In addition, the invasive nature of this procedure makes it impossible for screening and follow-up examinations. Echocardiography has therefore become the most frequently used and validated non-invasive method for the assessment of AR. Recently, cardiac MRI has provided new insights into the evaluation of AR and offers interesting information for follow-up.

Role of Echo in Aortic Regurgitation

Echocardiography is the cornerstone examination of patients with AR. Echo helps for the diagnosis of AR, provides reliable evaluation of the aortic valve and the root anatomy, and allows identification of the mechanism of the regurgitation. The specific aetiology of the disease may be suggested in the presence of pathognomonic anatomic findings. Doppler and two-dimensional (2D) echocardiographic methods allow semi-quantitative and quantitative evaluation of the severity of the regurgitation and determine the haemodynamic repercussions. Echo permits detecting associated lesions of the aortic root or the other valves. In symptomatic patients, echocardiography is fundamental in confirming the severity of AR, and identifying patients who should be considered for elective surgical intervention. In asymptomatic patients with moderate or severe AR, echocardiography is essential for regular follow-up, by providing precise and reproducible measures of LV dimensions, volumes, and function. In most cases, transthoracic echocardiography (TTE) provides all informations needed. Trans-oesophageal echocardiography (TOE) is usually not necessary unless needed clinically. Real-time three-dimensional (3D) TTE has the potential to be complementary to 2D echocardiography in AR quantification by increasing the level of confidence, especially when clinical findings and 2D echocardiographic data are discordant. Tissue Doppler imaging and/or the speckle tracking method are promising for detecting LV dysfunction, by identifying early changes in LV systolic deformation in patients with asymptomatic severe AR.

The Diagnosis of Aortic Regurgitation

Two-dimensional and M-mode Echocardiography

Although the diagnosis of AR is provided by Doppler techniques, 2D and M-mode echocardiography are still useful in the evaluation of AR. In some circumstances, structural abnormalities are obvious (e.g. dilated aortic root, endocarditis, aortic dissection, prosthetic valve dysfunction, degenerative calcific aortic valve). The mechanism of AR is easily identified. It can be classified into three types, similar to those of mitral regurgitation (MR): Type 1: normal motion (leaflet perforation), Type II: increased motion (prolapse of one or more cusps), and Type III: restricted motion (rheumatic disease or the consequence of aortic root dilatation).[1] However, 2D TTE does not always show the lesion responsible for leaflet malcoaptation. In patients with chronic severe AR, the parasternal long-axis view reveals a dilated LV, pulsation of the aorta, and sometimes, incomplete coaptation of the aortic leaflets with persistent central hiatus in diastole. A high-frequency diastolic flutter of the anterior mitral valve leaflet may occur in 80% of cases when the regurgitant jet is eccentric. This fluttering can also appear on the mitral valve chordae or the inter-ventricular septum (Fig. 8.1). Its absence (e.g. in the case of mitral valve stenosis) cannot rule out the diagnosis of AR, and a pseudofluttering can be observed in atrial fibrillation and cardiac hyperkinesia. Other mitral abnormalities include reverse diastolic doming of the anterior mitral valve leaflet in parasternal long-axis or apical 4-chamber views and diastolic indentation of the anterior

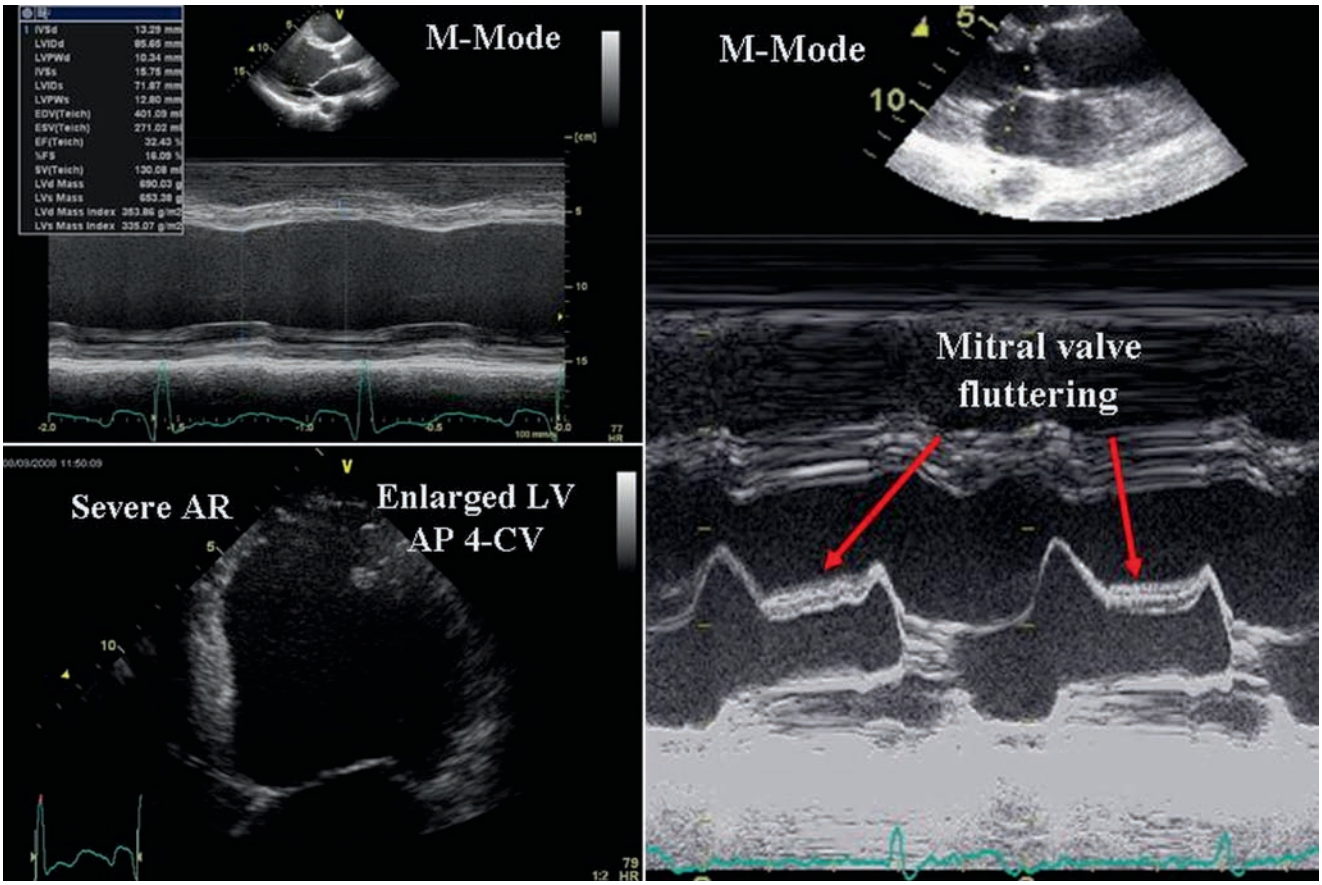

Fig. 8.1 M-mode and 2D echocardiograms of the left ventricle and mitral valve showing an enlarged LV with decreased function and the fluttering motion (*arrows*) of the anterior mitral leaflet caused by significant AR. *AP 4-CV*; apical 4-chamber view

mitral valve leaflet in parasternal short-axis view. When AR is severe and acute, LV pressure rises rapidly in diastole and often exceeds LA pressure during diastole, producing premature mitral valve closure, best assessed by M-mode. Rarely, a premature diastolic opening of the aortic valve may appear if LV pressure exceeds aortic pressure.

Doppler and Colour Flow Imaging

Echocardiographic evaluation of AR requires colour flow imaging, pulsed wave Doppler recordings of the descending thoracic aorta and the mitral inflow, and continuous wave (CW) Doppler recording of the regurgitant jet (Figs. 8.2–8.4, Videos 8.2–8.4).

Colour Doppler is both sensitive and specific in the qualitative diagnosis of AR, but its utility for quantitative evaluation of AR severity is limited. It allows real-time, colour-encoded flow mapping, and non-invasive visualization of regurgitant blood. Colour flow imaging of the AR is best performed from the parasternal long-axis and short-axis views by TTE and from the left ventricular outflow tract (LVOT) view by TOE. The presence of AR is detected as abnormal, holodiastolic, high velocity, and turbulent flow originating from the aortic valve and extending into the LVOT. Central jet is highly suggestive of rheumatic disease, while eccentric jet is associated with aortic valve prolapse or perforation. M-mode colour Doppler is useful for the evaluation of the jet chronology: regurgitant aortic jet is holodiastolic and rectangular. Physiologic mild AR is possible after the age of 50 years, and seems to be the consequence of aortic valve leaflet thickening and/or aortic root dilatation.

AR produces a holodiastolic turbulent flow with aliasing with pulsed Doppler imaging, when the sample volume is positioned under the aortic leaflets in the LVOT in the apical long-axis view. This technique is sensitive and specific in the diagnosis of AR.

CW Doppler echocardiography allows for the measurement of high-velocity flow. Apical long-axis view is most useful with CW Doppler. The hallmark characteristic of AR is the detection of a positive high-velocity, box-like, unidirectional flow, extending into the LVOT in diastole. The velocity is high in early diastole owing to the important pressure gradient between aorta and the LV in protodiastole. AR

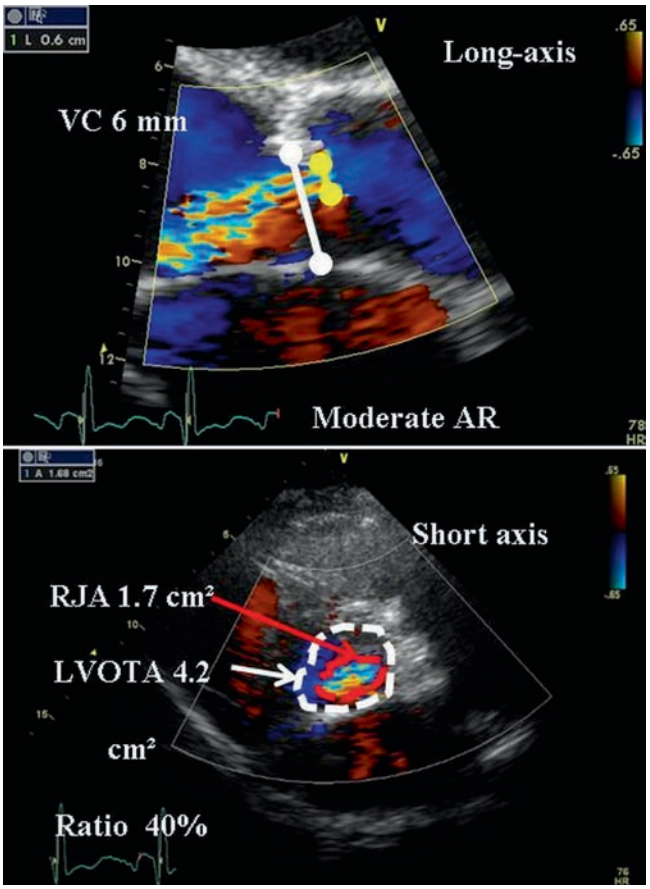

Fig. 8.2 Assessment of AR severity by using colour-flow imaging. *Top* Measurements of the left ventricular outflow dimension and regurgitant jet width (VC = vena contracta) in a patient with moderate AR. *Bottom* Regurgitant jet area (RJA) (*red arrow*) is measured from the parasternal short-axis view at the aortic valve level. The ratio of RJA to the left ventricular outflow area (LVOTA) (*white arrow*) can be calculated

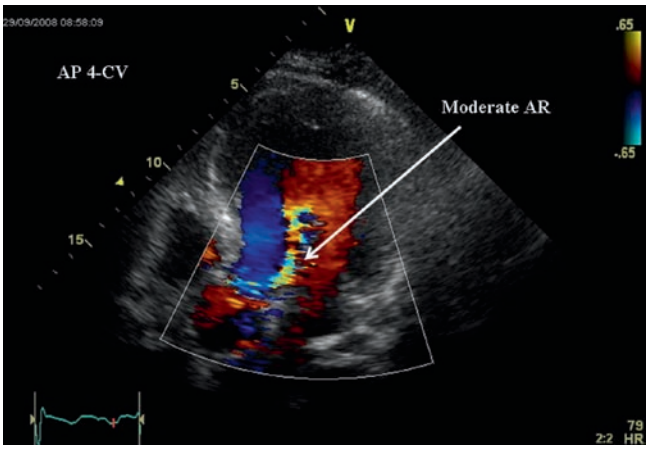

Fig. 8.3 An example of a patient with an eccentric moderate AR. Note the impingement of the jet on the anterior mitral valve. *AP 4-CV*; apical 4-chamber view

should not be confused with mitral stenosis. Their durations are different: AR flow begins just after aortic valve closure and before mitral valve opening, is present during the isovolumic relaxation phase, and usually ends after mitral valve closure. The morphology of AR flow is decrescendo throughout diastole. In patients with mitral stenosis, the duration of turbulent flow is shorter from opening to closure of the mitral valve. However, velocities are less important.

The Aetiology of Aortic Regurgitation

AR may be the consequence of several diseases (Table 8.1), and their relative contribution has changed over time. Identifying the aetiology is very important in patient management.

Degenerative AR is the most common aetiology in developed countries, accounting for approximately one-half of AR in the Euro Heart Survey on valvular heart diseases.[2] It is a heterogeneous entity that involves leaflet lesions, which are thin and subject to prolapse, or induces an aneurismal dilatation of the ascending aorta predominating at the sinuses of Valsalva, known as annulo-aortic ectasia. In the developing world, the most common cause of AR is rheumatic heart disease. Rheumatic fever is responsible for commissural fusion, thickening, and retraction of aortic leaflets usually inducing central regurgitation. Congenital abnormalities are also a frequent aetiology of AR. The aortic valve can be purely bicuspid, unicuspid, or rarely quadricuspid. Abnormal stress on the leaflets progressively modifies the valve structure and may cause AR, mainly through valve prolapse. An aneurysm that predominates above the sinus of Valsalva is often associated, and intrinsic pathology of the media appears to be responsible for aortic enlargement beyond that predicted by haemodynamic factors. Ventricular septal defect or subvalvular aortic stenosis may also induce AR and, in those cases, regurgitation is caused by jet lesions. Dilatation of the aortic root with secondary AR is encountered in Marfan syndrome and in rare degenerative diseases, such as Ehlers–Danlos disease or osteogenesis imperfecta, as well as in patients who do not have generalized tissue disease (annulo-aortic ectasia). Aortic aneurysm alone may cause AR, even when the leaflets are normal, because changes in the geometry of the aortic root create abnormal stress on the leaflet implantation. Aortitis, an inflammatory process, is a heterogeneous group representing less than 5% of the aetiologies. It may be encountered in inflammatory diseases, such as lupus erythematosus, rheumatoid arthritis, ankylosing spondylitis, Reiter syndrome, relapsing polychondritis, syphilis, Takayasu arteritis, or giant cell arteritis. Valvular abnormalities have been described in association with drugs. Long-term use of chloroquine may result in infiltrative cardiomyopathy that can be

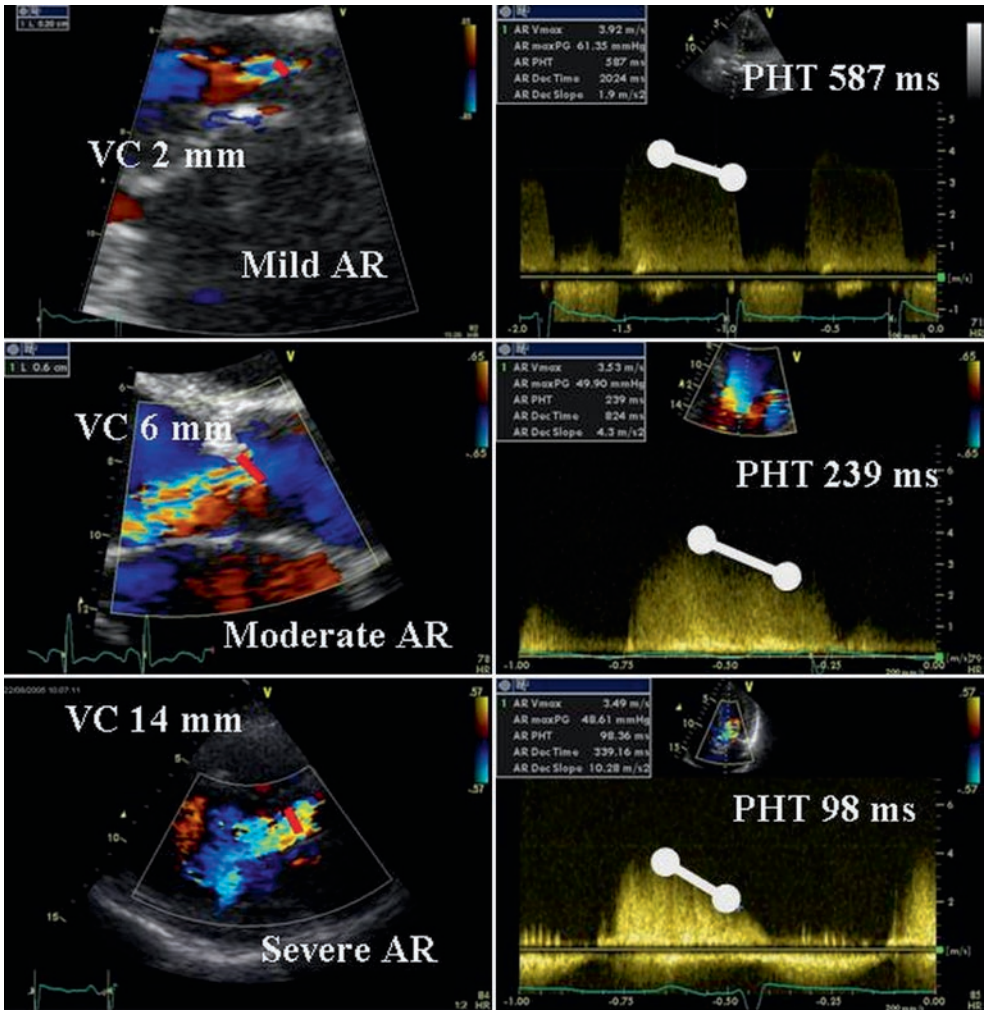

Fig. 8.4 Three examples of AR are provided, all taken from the parasternal long-axis view using colour Doppler (*left*) and from the apical 5-chamber view using continuous wave (CW) Doppler (*right*). The regurgitant jet width (VC = vena contracta) increases with the severity of AR. The pressure half-time (PHT) decreases with more severe AR

associated with valvular regurgitation. Some other drugs that commonly produce increasing serotonin activity were used in different indications, such as anorectic drugs (fenfluramine and dexfenfluramine), drugs used in the treatment of Parkinson disease (ergot-derived dopamine agonists, pergolide, and cabergoline),[3] or drugs used in the treatment of migraine (ergot alkaloid agents like ergotamine and methysergide). In carcinoid heart disease, AR develops more frequently in patients with patent foramen ovale and is associated with right heart valve involvement. The aortic valves are thickened with leaflet retraction. Endocarditis still represents approximately 10% of aetiology of AR. The regurgitation is related to leaflet tearing or perforation, or to a perivalvular abscess communicating with the aorta and the LV. Acute AR aetiologies include aortic dissection and traumatic rupture of the valve leaflets. Dissection of the ascending aorta can result in AR by dilatation of the sinuses with incomplete cooptation of the leaflets or extension of the dissection into the base of the leaflets. The remaining causes of AR include radiation-induced valve damage, prosthetic valve dysfunction, and acromegaly.

Quantification of the Regurgitation

Aortic Regurgitation Depth Mapping

Mapping the depth of the diastolic flow signal of AR into the LV cavity by systematic displacement of the sample volume has been used is one Doppler approach to grossly estimate the severity of regurgitation. Although the pulsed Doppler method is reproducible and correlates with angiography,[2] it is time-consuming, and became obsolete[4] when colour flow mapping was introduced (Table 8.2).

Regurgitant Jet Area

Colour flow imaging of the AR is best performed from the parasternal long-axis and short-axis views by TTE, and from the LVOT view by TOE, at 135°. The maximal length and jet area of the regurgitant jet are poorly correlated with the angiographic severity of AR because they depend not only on the size of the regurgitant orifice, but also on LV

Table 8.1. Major causes of aortic regurgitation (AR)

	Leaflets abnormalities	Aortic root or ascending aorta dilatation
Degenerative AR	+	+ Annulo-aortic ectasia
Rheumatic fever	+	–
Congenital AR	+ Bicuspid aortic valve Tricuspid aortic valve with commissural fusion Quadricuspid aortic valve Ventricular septal defect Subvalvular aortic stenosis	+ Aortic aneurysm that predominates above the sinus of Valsalva
Diseases of the aorta	–	+ Marfan syndrome Ehlers-Danlos disease Osteogenesis imperfecta Aortitis: lupus erythematosus, rheumatoid arthritis, ankylosing spondylitis, Reiter syndrome, relapsing polychondritis, syphilis, Takayasu arteritis or giant cell arteritis
Drugs	+ Chloroquine Fenfluramine and dexfenfluramine Ergot alkaloid agents ergotamine and methysergide Ergot-derived dopamine agonists, pergolide and cabergoline	–
Carcinoid syndrome	+	–
Endocarditis	+	±
Aortic dissection	+	+
Traumatic injuries	+	+
Radiation-induced cardiac disease	+	
Prosthetic valve dysfunction	+	–
Acromegaly	+	+

Table 8.2. Main used criteria of severe quantification of aortic regurgitation

2D and M-mode echocardiography	Left ventricular diastolic diameter ³75 mm
Colour-flow Doppler	Regurgitant jet height/LVOT height ratio ≥60% Regurgitant jet area/LVOT area ratio ≥60% Vena contracta width (VCW) > 6 mm Effective regurgitant orifice (ERO) >30 mm²
CW Doppler	pressure half-time <200 ms Slope of the decay >3 m/s²
Pulse wave Doppler	Holodiastolic flow reversal in the descending aorta

compliance, the pressure gradient across the defect, and the duration of this gradient.[5] The jet extent can be affected by changes in heart rate or LV filling conditions. The best colour flow index is the height (maximal antero-posterior diameter) of the regurgitant jet at the junction between LVOT and aortic annulus in the parasternal long-axis view. Its accuracy can be improved by dividing the jet height by the LVOT height.[5] The short-axis area of the regurgitant jet at the level of the high LVOT, relative to the short-axis area of the LVOT, is also a good predictor of AR severity. A regurgitant jet height/LVOT height ratio ≥60% or regurgitant jet area (RJA)/LVOT area ratio ≥60% indicate severe AR. However, colour Doppler imaging is significantly dependent on the operator and the machine, and even a small modification in

probe angulation can induce significant changes in the jet visualization and size. The morphology of the regurgitant orifice also affects the aortic regurgitant jet both in height and length.

Vena Contracta

Vena contracta is the smallest neck of the regurgitant jet at the level of the aortic valve, immediately after the flow convergence region, and is preferably measured in the parasternal long-axis view. Vena contracta is thus smaller than the height of the jet in the LVOT. A vena contracta width (VCW) >6 mm is specific for severe AR, whereas mild AR is identified by VCW < 3mm.[6]

Effective Regurgitant Orifice and Regurgitant Volume

Several experimental and clinical studies indicate that the effective regurgitant orifice (ERO) is less influenced by haemodynamic conditions than regurgitant volume (RVol) and fraction. ERO can be quantified by the proximal isovelocity surface area (PISA) method (Fig. 8.5, Video 8.5). A clearly visible, hemispheric PISA is required for calculation. Practically, the following steps are applied: expansion of the region of interest using the zoom or regional expansion selection, and maximizing the smallest angle between flow convergence and ultrasound beam. The frame rate is maximized to reduce the depth of the imaging sector, by using the narrowest colour sector to the frame rate, with upwards shift of the colour flow velocity scale baseline to reduce aliasing velocity, and measurement of the PISA radius as the distance between the regurgitant orifice and the first aliasing in early diastole. The regurgitant flow rate across the aortic valve is obtained from the flow rate of a proximal surface area with a known flow velocity corresponding to the aliasing velocity.[7]

$$\text{Flow rate} = 2\pi r^2 \times \text{Aliasing velocity}$$
$$\text{ERO} = \text{Flow rate}/\text{Peak AR velocity}$$
$$\text{ERO} = (6.28 \times r^2 \times \text{Aliasing velocity})/\text{Peak AR velocity}$$
$$\text{RVol per beat} = \text{ERO} \times \text{AR TVI}$$

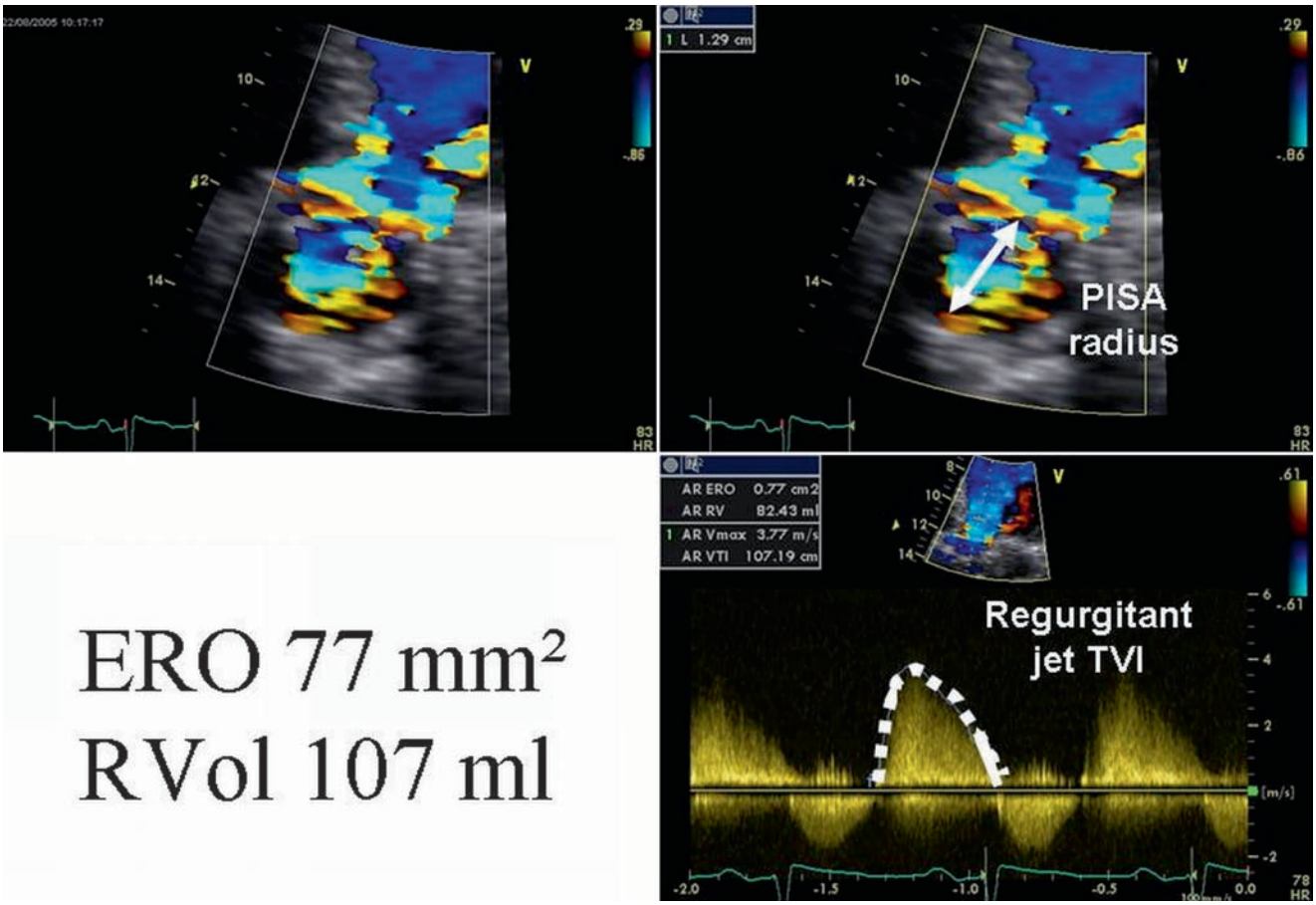

Fig. 8.5 Evaluation of aortic regurgitation severity by the PISA method. Colour flow imaging of the flow convergence zone is obtained from the apical 5-chamber view. The colour flow baseline is shifted *upward* and the convergence zone appears in *blue*. After measuring the PISA radius, the effective regurgitant orifice (ERO) is calculated by the ratio of flow rate to peak orifice velocity obtained by AR CW Doppler. The regurgitant volume (RVol) is calculated by using the aortic regurgitant jet time velocity integral (TVI)

ERO = effective regurgitant orifice, r = PISA radius, peak AR velocity = aortic regurgitant flow peak velocity in CW Doppler, RVol = regurgitant volume, AR TVI = time velocity integral of aortic regurgitant flow in CW Doppler.

An ERO > 30 mm² indicates a severe AR. The limitations of the flow convergence method include reduction of the PISA during diastole and under-estimation in the presence of an eccentric jet.

Diastolic Flow in the Descending Aorta

Pulsed Doppler recordings of flow in the descending aorta can also be helpful in the assessment of AR severity. Severe AR is associated with diastolic reversal of flow in the aorta[8] as well as systolic augmentation of flow within the central aorta (Fig. 8.6). From the supra-sternal imaging window, pulsed Doppler velocities of aortic flow are obtained by placing the sample volume just distal to the origin of the left subclavican artery, aligning it as much as possible along the major axis of the aorta. The Doppler filter has to be decreased to its lowest setting to allow detection of low velocities (<10 cm/sec). The Doppler end-diastolic velocity measured at the peak height of the R-wave has been shown to be the best descending aortic correlate of the regurgitant severity requiring only a single measurement. A flow velocity ≥18 cm/s corresponds to an AR with a regurgitant fraction (RF) ≥40% with a sensibility of 88% and a specificity of 92%.[9] Under-estimation occurs when heart rate is low (<50 bpm) and overestimation occurs if heart rate is >90 bpm. Diastolic flow reversal in the aorta is also related to aortic compliance. Therefore, abnormal diastolic flow patterns can be observed in case of abnormal compliance in the proximal aorta or in patients with patent ductus arteriosus. In severe acute AR, diastolic velocity decreases quickly with no end-diastolic velocity owing to equalization of aortic and LV diastolic pressures.

Aortic Regurgitation Velocity Decline

The rate of the decline of the AR velocity as determined with CW Doppler can be used to quantify AR. In severe AR, systemic diastolic pressure decreases quickly and the AR signal (representing the pressure difference between the aorta and the LV) has a shortened deceleration time, thus, a steep deceleration slope. This decline in velocity is quantified as the pressure half-time (PHT) or as the slope of the decay. PHT is the time required for the peak diastolic pressure gradient to decay by 50%. The half-time of the aortoventricular pressure difference obtained with Doppler correlates well with those obtained from pressure recordings at catheterization. This parameter is also influenced by systemic vascular resistance, aortic and LV compliance, and LV end-diastolic pressure. Despite these limitations, a <300 msec PHT indicates severe regurgitation.[10] The slope of the decay can also be used. A > 3 m/s² slope is in favour of severe AR. Adequate spectral envelope is mandatory to use these measurements.

Trans-oesophageal Echocardiography

TOE enables the anatomy of the aortic leaflets and the aortic root to be accurately assessed, and can help in identifying AR aetiology (e.g. aortic dissection, bicuspid aortic valve,

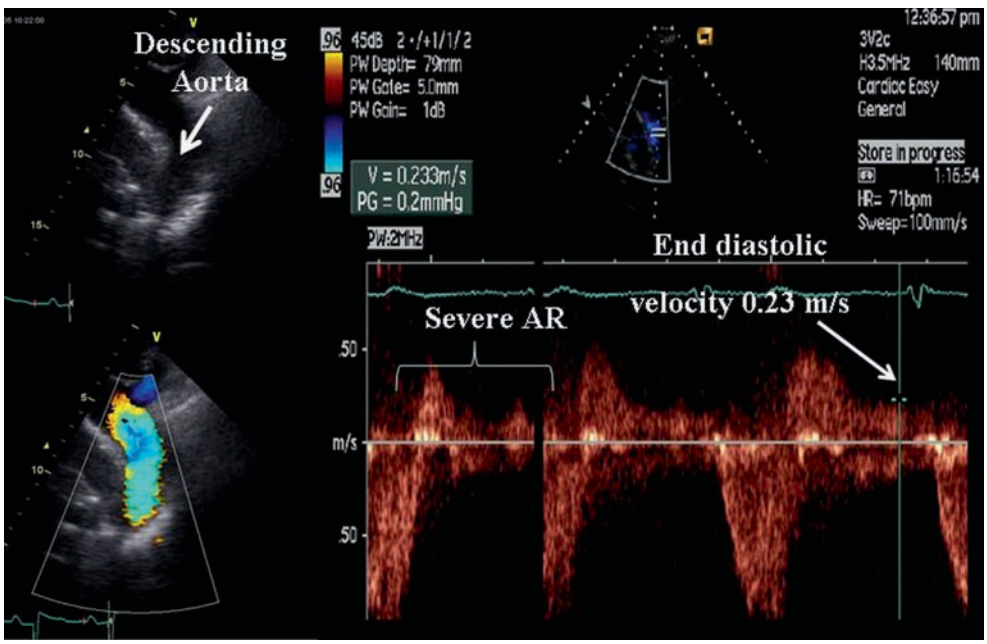

Fig. 8.6 A pulsed Doppler recording within the descending aorta from a patient with severe AR demonstrates flow reversal throughout diastole. An end diastolic flow velocity greater than 18 cm/s is indicative of severe AR

and aortic aneurysm). TOE is the reference examination in non-echogenic patients for AR quantification. Vena contracta imaging by TOE colour flow mapping in long-axis (135°) is an accurate marker of AR severity.[11] Multi-plane TOE allows, in the absence of important aortic annulus calcifications, planimetry of the regurgitant jet using colour Doppler (with an angle between 20 and 70°). Regurgitant jet width and area >6 mm and >7.5 mm², respectively, are in favour of a severe AR with an RF > 50%. TOE can also be performed to better define the anatomy of the valve and the ascending aorta when valve-sparing intervention is considered.

Three-Dimensional Transthoracic Echocardiography

Accurate quantification of the severity of AR using various 2D and Doppler echocardiographic techniques remains challenging. This is primarily because the 2D techniques try to describe and quantify a 3D structure. Recent studies demonstrate the feasibility and accuracy of 3D TTE in quantifying AR.[12,13] After completion of the standard 2D TTE, live and real-time 3D images can be obtained from parasternal and apical views. 3D TTE vena contracta area (VCA) has been validated and compared with AR assessment by aortography and surgery with a better correlation than 2D TTE measurements. Indeed, it obviates the need to suppose that vena contracta is circular or elliptical in shape, which is done when using conventional TTE. Systematic cropping of the acquired 3D TTE data set is used to measure VCA. The first step is obtaining the best AR jet in long-axis from a parasternal long-axis view or from an apical view (in case of poor parasternal window) by posterior-to-anterior cropping of the 3D TTE data set. The 3D TTE colour Doppler data set is then cropped from the aortic side to the level of the vena contracta, at or just below the aortic valve leaflets, in a plane that is exactly perpendicular to the AR jet viewed in long-axis. The image is tilted en face, and the cropped portion of the data set is added back to obtain the maximum area of vena contracta viewed in short-axis in systole. When patients present multiple AR jets, all individual VCAs are summed. The advantage of this 3D TTE AR evaluation is that the VCA can be multiplied by the velocity time integral to accurately estimate the instantaneous regurgitant volume.

Evaluation of Left Ventricular Function

LV size and function are two important parameters in decision-making as emphasized in the guidelines.[14] End-diastolic and end-systolic dimensions are measured according to the leading edge to leading edge method. End-diastolic and end-systolic volumes are obtained according to Simpson's biplane rule. LV function is assessed by LVEF. Emerging data have evaluated the role of new indices of LV function obtained with new ultrasonic modalities. However, they are not yet included in the guidelines. Indeed, asymptomatic patients with severe AR and LV dilatation may develop irreversible LV damage while awaiting surgery, and there is a need for early markers of LV dysfunction.

Exercise echocardiography has demonstrated its interest in a population of patients with asymptomatic or minimally symptomatic severe AR and preserved LVEF, in which decision-making is known to be easy. Stress echocardiography is used to evaluate post-exercise and resting LVEF. The difference between post-exercise and resting LVEF defines the contractile reserve (CR). In medically treated patients, CR predicts the preserved LVEF on follow-up, unlike patients without CR who more often have a decreased LVEF. In patients submitted to surgery, CR is also a good predictor of the resting post-operative LVEF: patients with a CR show post-operative increase in LVEF, unlike patients without CR who show the same or worse LVEF on post-operative follow-up.[15] In patients with asymptomatic severe AR and no clear indication of surgery, the presence of CR allows a watchful waiting approach. The absence of CR suggests latent LV dysfunction and makes surgery reasonable.[16] Other LV function indices newly studied in asymptomatic severe AR patients undergoing exercise echocardiography evaluate LV long-axis contraction using tissue Doppler and M-mode echocardiography. Annular mitral systolic excursion is obtained with the cross section of medial mitral annulus guided by M-mode and measured from the onset to peak systolic annular motion towards apex. Peak mitral systolic velocity corresponds to the maximal velocity (in cm/s) of mitral annulus in pulsed Doppler with the sample volume placed just apical to the medial or lateral mitral annulus. A resting velocity of 9.5 cm/s seems to be the best indicator of a poor exercise response.[8]

Strain (S) and strain rate (SR) imaging can also be useful for the evaluation of AR. Radial and longitudinal peak systolic SR are lower in patients with moderate or severe AR as compared with healthy subjects. Changes in regional LV deformation also correlate inversely with LV end-diastolic and end-systolic volumes. Deformation changes can be detected before reduction of LVEF, but the prognostic value of these findings is not yet validated.

Acute Aortic Regurgitation

Acute AR corresponds to the acute onset of a massive regurgitant volume filling a normal LV, and resulting in an acute increase in LV diastolic pressure and a fall in forward cardiac output. The most common causes of acute AR are endocarditis, aortic dissection, and trauma. Echocardiography is diagnostic in acute AR. The important increase in LV diastolic filling pressure produces an inversion of diastolic

atrio-ventricular pressure gradient leading to a premature mitral valve closure, observed with M-mode echocardiography. Diastolic MR can also be found with colour Doppler, pulsed Doppler, or CW Doppler techniques. In addition, a premature diastolic opening of the aortic valve may appear if LV pressure exceeds aortic pressure. A dense CW Doppler signal is found with a steep diastolic slope resulting in a PHT < 200 ms. LV inflow has a restrictive pattern with increased E-wave, decreased deceleration time (<150 ms), and E/A ratio >3. The VCW is often difficult to measure because of frequent eccentric jets. TOE can be more accurate than TTE in determining the cause of acute AR.

Role of Cardiac Magnetic Resonance Imaging in Aortic Regurgitation

Cardiovascular MRI can image the regurgitant jet in any plane, and thus can provide a 3D appreciation of regurgitant jet. MRI quantifies the regurgitant volume either in absolute value or as an RF. Furthermore, a planimetry of the anatomic regurgitant orifice is made possible. MRI can also supply information on LV function. As the available data are limited, cardiac MRI is not yet recommended for routine clinical practice in the current guidelines. MRI is only considered as an alternative technique when echocardiography is not feasible or of poor quality.

The MRI protocol in AR includes a sequence for assessing the configuration of the aortic valve and the ascending aorta, the quantification of LV ejection fraction, LV mass, and RVol in the ascending aorta. Three planes are commonly used in daily MRI evaluation of AR. All the planes result from a basal short-axis plane. The first plane runs through the mitral valve and aortic valve on the basal short-axis plane and allows visualization of the LV inflow and outflow tracts. It corresponds to a 3-chamber view. The second plane, corresponding to a 2-chamber view, is perpendicular to the regurgitant jet visualized in the 3-chamber view. The third plane is an oblique axial plane in the aortic root, just above the aortic valve, at the level of the coronary arteries, obtained from both 2- and 3-chamber views.[17]

Three MRI techniques are commonly used for AR evaluation:

1. Qualitative assessment of signal loss on cine gradient-echo imaging
2. Quantitative assessment by measurement of ventricular volumes
3. Quantitative assessment by plane-contrast velocity mapping

In cine gradient-echo imaging, turbulent flows induce a decrease in gradient echo signal intensity owing to signal loss. This decrease in signal intensity allows regurgitation flow identification and grading in a similar way as Doppler echocardiography or cineangiography. However, with the increasing use of balanced steady-state free precession (b-SSFP) cine imaging in cardiac MRI, qualitative assessment of signal loss has a reduced accuracy in regurgitation flow identification, in particular, when AR is mild. Therefore, this MRI technique only allows AR diagnosis. Care must be taken to ensure that the entire jet has been visualized. However, cine MRI b-SSFP allows visualization of the aortic valve area in an appropriate plane with excellent quality. Planimetry of the aortic valve area has been recently validated in aortic stenosis. The accuracy of planimetry of the ERO of AR has been recently studied in an analogous way as in aortic stenosis. The authors demonstrated the feasibility of this technique as well as its strong correlation with RVol and RF assessed by velocity mapping.

Quantitative evaluation of LV volumes is possible with b-SSFP imaging. This technique offers a good blood vs. endocardial contrasted images in a single breath-hold. LVEF is obtained using a set of short-axis cuts covering the length of the LV, in combination with Simpson's rule. Furthermore, the measurement of left and right ventricular volumes evaluation provides the opportunity to obtain the RVol by their subtraction.

For velocity mapping, phase information and not magnitude is displayed. The flow velocity component in any desired direction may be measured by appropriate gradient profile modifications, producing velocity-dependent phase shifts that can be displayed by phase mapping. The sequence allows fast repetition so that flow information may be acquired rapidly from many points in the cardiac cycle, and permits measurement of instantaneous blood flow in the heart chambers and great vessels. Stationary structures are mid-gray colour mapped, while increasing velocities in either direction are shown as increasing grades of black and white. Measurement of the spatial mean velocity for all pixels in an orifice of known area enables the calculation of the instantaneous flow volume. Flow volume per heart beat is the integral of instantaneous flow volume throughout the cardiac cycle in ml/beat. This method is the most accurate for quantifying AR.[18] The aortic regurgitant volume can be obtained as an absolute value by calculating the backflow through the aortic valve or the RF in an oblique axial plane above the valve.

$$\text{RF (\%)} = [\text{Aortic retrograde flow (ml/beat)}/\text{Aortic forward flow (ml/beat)}] \times 100$$

The good reproducibility of velocity cine MRI for quantitative assessment of RV and RF indicates the potential of this technique for follow-up and monitoring of response to therapy.[9]

Segment-based myocardial T1 mapping is an MRI technique not used in daily AR MRI evaluation, but allows the identification of myocardial fibrosis by comparing the T1

relaxation time of pixel within a parametric image. This technique has been applied in a first feasibility study with chronic AR patients to identify myocardial fibrosis as an early evidence of myocardial dysfunction. The results seem to be encouraging, but further data are needed before its larger utilization.

Imaging in Decision-Making

Echocardiography is actually the most recommended technique for AR evaluation. Decision-making is, therefore, based on it. However, this technique does not evaluate AR in a perfectly reliable manner in 100% of patients. Actually, physicians cope with these echocardiographic pitfalls and limitations by using an integrated combination of echo parameters in the quantification of AR. Emerging data stress the growing interest of MRI. The optimal timing for surgical intervention in chronic AR remains controversial. Clearly, surgery is indicated in patients with severe AR and significant symptoms attributable to their valvular disease, but emerging data seem to demonstrate the benefit of early surgery before the development of LV dysfunction.

Mitral Regurgitation

MR is increasingly prevalent in Europe, despite the reduced incidence of rheumatic disease. The development of surgical mitral valve repair introduced in the early 1970s by Carpentier, has dramatically changed the prognosis and management of patients presenting with severe MR. Imaging techniques and, in particular, Doppler echocardiography have a prominent role in the evaluation and follow-up of valvular heart diseases, particularly, MR. A close cooperation between echocardiographists and surgeons is of utmost importance. The assessment of MR by imaging should provide precise information on anatomical lesions, mechanisms of regurgitation, aetiology, quantified degree of regurgitation, and repairability of the valve. It is essential to distinguish between organic and functional MR, which radically differ in their pathophysiology, prognosis, and management.[19]

Anatomy and Function of the Mitral Valve

The different components of the mitral valve apparatus (annulus, leaflet, chordae, and papillary muscles) need to be assessed and described.

Mitral Annulus

Mitral annulus is oval and saddle-shaped. Its anterior portion is flat and rigid and cannot dilate. The posterior two-thirds may contribute to annular dilatation. The anterior-posterior diameter can be measured using real-time 3D echo or by conventional 2D echo in the parasternal long-axis view. The diameter is compared with the length of the anterior leaflet in diastole. Annular dilatation is present when the quotient annulus/anterior leaflet is >1.3 or when the diameter is >35 mm. The presence and extent of annular calcification is an important parameter to describe.

Valvular Leaflets

The following features should be analyzed:

- Thickness of the leaflet, eventually associated with redundant and excessive tissue. A myxomatous or dystrophic valve implies an increased thickness >5 mm, preferably measured with M-mode.
- Presence and extent of calcifications or vegetations.
- Observation of the anterior and posterior commissures.
- Length or area of leaflet coaptation throughout systole.

Chordae Tendinae and Papillary Muscles

The analysis of the subvalvular apparatus includes the measurement of the chordal length, the description of calcification, fusion, elongation, and rupture. The possible displacement of the papillary muscles needs to be quantified.

Valvular Segmentation

The posterior leaflet is inserted into the posterior two-thirds of the annulus, and consists of three scallops identified as P1, P2, and P3. The P1 scallop corresponds to the external, antero-lateral portion of the posterior valve, close to the anterior commissure and the left atrial appendage. The P2 scallop is medium and more developed. The P3 scallop is internal, close to the posterior commissure and the tricuspid annulus. The anterior leaflet is artificially divided into three portions A1, A2, and A3, corresponding to the posterior scallops P1, P2, and P3 (Fig. 8.7). This segmentation is particularly useful to precisely define the anatomical lesions and the prolapsing segments in patients with degenerative MR.

Anatomy of Functional Mitral Regurgitation

If organic severe MR can progress and induce heart failure, then functional MR is not a valvular disease but

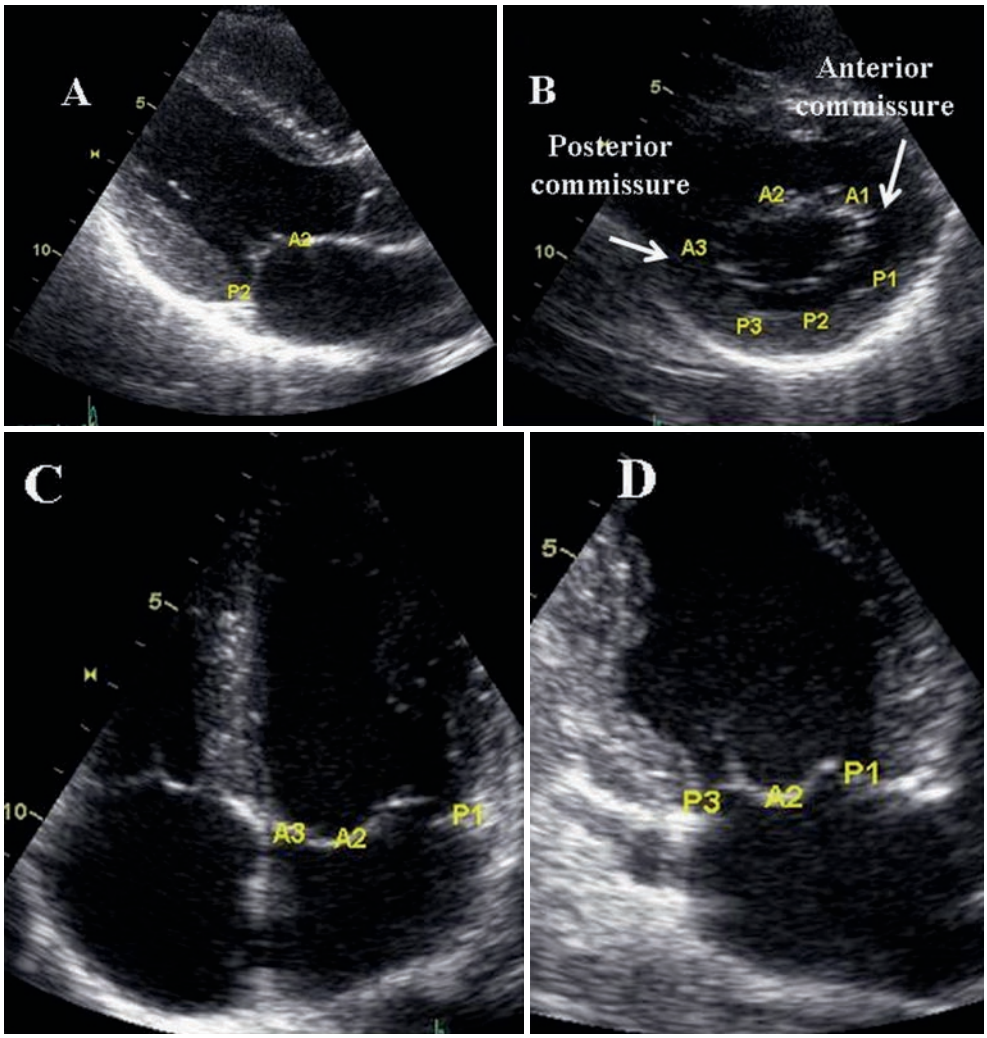

Fig. 8.7 Mitral valvular segmentation. **(a)** Parasternal long axis view. **(b)** Short-axis view, **(c)** Apical 4-chamber view. **(d)** Apical 2-chamber view. *Anterior leaflet*: A1-A2-A3, *posterior leaflet*: P1-P2-P3

mainly the consequence of LV re-modelling and dysfunction. The leaflets are typically normal, although their area can increase with time as an adaptive mechanism. The annulus is usually dilated and becomes more circular with lack of dynamic systolic contraction. The LV is dilated and more spherical. Several measurements can be obtained to quantify global and regional LV re-modelling and the severity of altered geometry of the mitral valve apparatus (Table 8.3).

The location and extent of regional and global LV dysfunction are easily assessed in the classical views (parasternal long-axis and short-axis and apical 2-, 3-, and 4-chamber views). Thin (diastolic thickness <5.5 mm) and hyperechogenic ventricular segments usually imply the presence of trans-mural infarction. Global LV re-modelling is quantified by the measurements of end-diastolic and end-systolic volumes, and ejection fraction by 2D echo using the Simpson's method or preferably by real-time 3D echocardiography. Furthermore, the sphericity index can be calculated.

Table 8.3. Echo-morphologic parameters in MR

Global left ventricular re-modelling
End-diastolic volume
End-systolic volume
Ejection fraction
Systolic and diastolic sphericity indexes
Regional and ventricular re-modelling
Posterior displacement of posterior/anterior papillary muscles
Lateral displacement of posterior/anterior papillary muscles
Separation between the papillary muscles
Distance papillary muscles/fibrosae
Alteration of mitral valve geometry
Tenting area
Distance point of coaptation—annulus
Diastolic and systolic annular area
Annular contraction
Posterior lateral angle

Regional re-modelling is quantified by the posterior and lateral displacements of one or both papillary muscles. The tenting area is measured in mid-systole as the area between the mitral annulus and the two leaflets. The apical displacement of the coaptation point represents the distance between the mitral annular plane and the point of coaptation. Annular area and contraction can also be estimated.

Lesions and Mechanisms

Functional Classification

The analysis of the mechanisms of MR is an essential component of the echocardiographic examination, in particular, when mitral valve repair is considered. The most frequently used classification of this dysfunction has been described by Carpentier, according to leaflet motion, independent of the etiology.[20]

Type I: The leaflet motion is normal. MR is determined by leaflet perforation (infective endocarditis) or more frequently by annular dilatation.

Type II: Increased and excessive leaflet mobility accompanied by displacement of the free edge of one or both leaflets beyond the mitral annular plane (mitral valve prolapse).

Type III: Reduced leaflet motion or mobility of one or both leaflets. Type III is subdivided into Type IIIA, implying restricted leaflet motion during both diastole and systole owing to shortening of the chordae and/or leaflet thickening such as in rheumatic disease; and Type IIIB, when leaflet motion is restricted only during systole.

The pathophysiology of MR is frequently complex, including more than one of these mechanisms. Acute or chronic ischaemic MR can correspond to these three mechanisms.

Type I: The dilation of the posterior part of the mitral annulus is frequent in chronic ischaemic MR, which can produce asymmetric distortion frequently predominant in the P3 region. Patients with ischaemic MR usually have larger annular diameters than those with organic MR. Annular areas are also larger in both diastole and systole, whereas systolic annular shortening is smaller in ischaemic MR.

Type II: This mechanism occurs in patients with acute myocardial infarction complicated by papillary muscle rupture. Partial rupture of the postero-medial papillary muscle is most frequently observed. TTE or TOE is frequently performed at the bedside in the intensive care unit. Imaging shows the complete version of the leaflet to which the ruptured portion of the papillary muscle is attached. The direction of the regurgitant jet with colour Doppler indicates the affected leaflet: the posterior leaflet when the jet is directed towards the inter-atrial septum vs. the anterior leaflet if the jet is directed towards the lateral wall of the left atrium. The severity of MR is frequently under-estimated and can be appreciated by the increased velocity of early LV filling and the characteristics of the CW recording showing a rapid reduction of velocity on the regurgitant flow during systole, reflecting the rapid reduction of the pressure gradient during systole between the left ventricle and the left atrium.

Type IIIB is the most frequent mechanism in chronic ischaemic MR. The restrictive motion occurs essentially during systole and is most frequent in patients with previous posterior infarction. In this setting, the traction on the anterior leaflet by secondary chordae can induce the so called "seagle sign." In patients with idiopathic cardiomyopathy or with both anterior and inferior infarctions, both leaflets exhibit a reduced systolic motion leading to incomplete coaptation.

Degenerative Organic Mitral Regurgitation

- Several terms are used that should be distinguished[21] (Figs. 8.8 and 8.9, Videos 8.8B, 8.8D, 8.9A, 8.9B, C, 8.9D). A billowing valve is observed in systolic displacement of one or both leaflets behind the annular plane, but a normal coaptation before the annular plane. MR is usually mild in this condition.
- A floppy valve is a morphologic abnormality with thickened leaflet owing to redundant tissue.
- Mitral valve prolapse implies that the coaptation line is behind the annular plane. With 2D echo, the diagnosis of prolapse should be made in the parasternal or eventually, the apical long-axis view, but not in the apical 4-chamber view because of the saddle-shaped annulus.
- Flail leaflet: This term is used when the free edge of a leaflet is completely reversed in the left atrium, usually as a consequence of ruptured chordae (degenerative MR or infective endocarditis).

Localization of Anatomic Lesions

The precise localization of the lesions is essential. The different portions of both leaflets should be described as well as the location of ruptured chordae. Real-time 3D transthoracic and, in particular, trans-oesophageal echocardiographic imaging provide comprehensive visualization of the different components of the mitral valve apparatus. However, the examination still relies frequently on 2D transthoracic or oesophageal images recorded in appropriate standardized views.

Short-Axis View

This view can be obtained by TTE or TOE, using the classical parasternal short-axis view and the transgastric view at 0°.

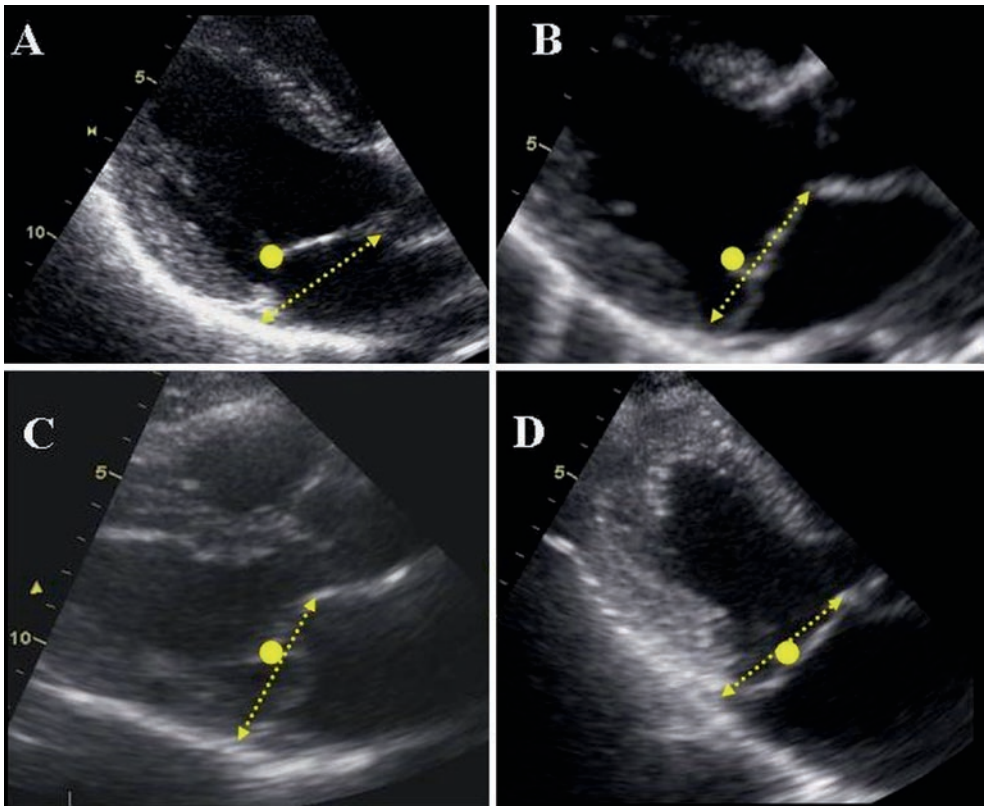

Fig. 8.8 **(a)** In normal mitral valve, the coaptation occurs beyond the mitral annular plane (*arrows*). **(b)** Billowing mitral valve is observed when a part of the mitral valve body protrudes into the left atrium. **(c, d)** Mitral valve prolapse is defined as abnormal systolic displacement of one (**(c)**, posterior prolapse) or both leaflets into the left atrium below the annular (**(d)**, bileaflet prolapse)

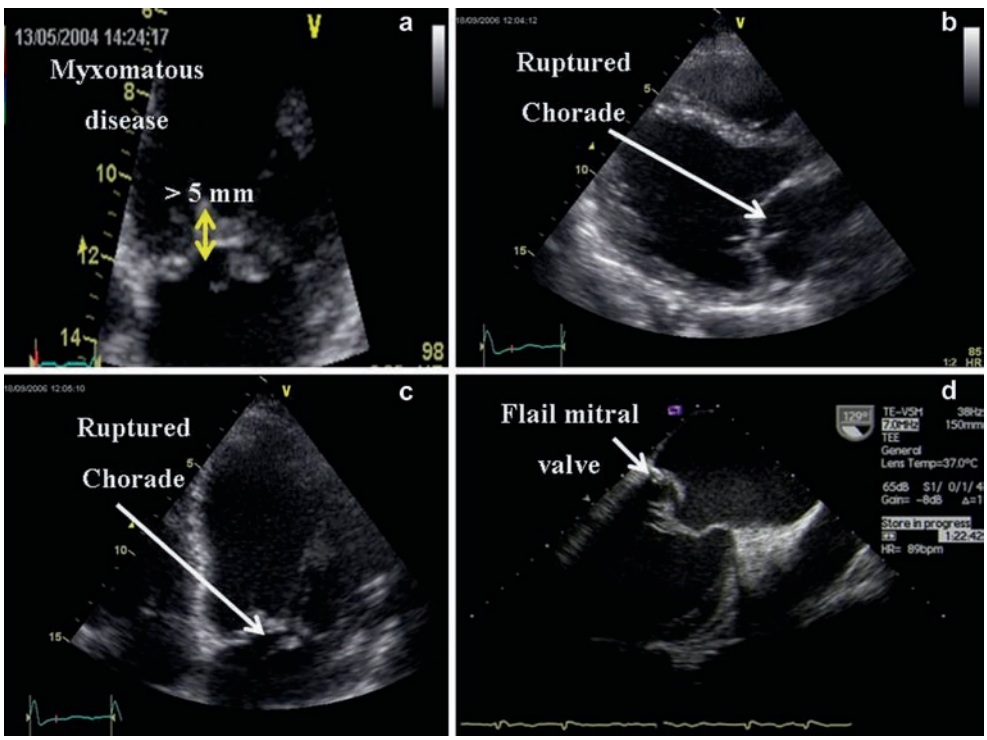

Fig. 8.9 Four examples of degenerative mitral valve disease. **(a)** Myxomatous vale. **(b, c)** Ruptured chordae. **(d)** Flail mitral valve

This view permits the assessment of the six leaflet segments and the two commissures in diastole. In systole, the localization of prolapsus is indicated by the origin of the regurgitant jet.

4-Chamber View

With TTE, a classical apical 4-chamber view is obtained and explores the anterior leaflet, segments A3 and A2, and the posterior leaflet in its external scallop P1. With TOE, different valvular segments that depend on the position of the probe in the oesophagus, which progresses up and down, are observed. This permits successive observation of A1 and P1 close to the antero-lateral commissure, A2 and P2, and finally, A3 and P3 close to the postero-medial commissure.

Longitudinal Views

The prasternal long-axis view with TTE and sagittal view at 120° with TOE show the medium portion of the leaflets (A2 and P2).

A bi-commissural view can be obtained in the apical 2-chamber view with TTE and a view at 40–60° with TOE showing the two commissural regions and from left to right, P3, A2, and P1.

A 2-chamber view in the transgastric position, orthogonal to the subvalvular apparatus, permits measuring the length of the chordae and the distances between the head of the papillary muscle and the mitral annulus.

Real-time 3D echo is particularly useful in the dialog between the echocardiographer and the surgeon. Multiple views are available which permit precise determination of the localization and the extent of the prolapse. The "en face" view, seen from the left atrium, is identical to the surgical view in the operating room.

Rheumatic Mitral Regurgitation

Rheumatic MR is characterized by variable thickening of the leaflets, especially at the level of their free edges. Fibrosis of the chordae is frequent, especially of those attached to the posterior valve, explaining the rigidity and reduced motion of the posterior leaflet in diastole.

In some patients, the posterior leaflet remains in a semi-open position throughout the cardiac cycle, and the motion of the anterior leaflet in systole produces a false aspect of prolapse. In this situation, the regurgitant jet in colour Doppler is directed to the posterior wall of the left atrium.

Commissural jets are possible in the presence of rigidity and calcification of one or both commissures.

Infective Endocarditis

The most recent diagnostic criteria of the Duke University include echocardiographic parameters. The presence of vegetations is the most characteristic feature.

MR of this condition can be related to different mechanisms such as valvular prolapse with ruptured chordae, abscess, false aneurysm, or valvular perforation. The precise documentation of the lesions is best obtained with TOE.

Ischaemic Mitral Regurgitation

Ischaemic MR relates to a balance between tethering force and closing force.[22] The tethering force relates to the extent of LV re-modelling and displacement of the papillary muscles, and can be quantitated using different morphologic parameters (Table 8.3) (Fig. 8.10, Videos 8.10A and B). The reduced closing forces relate to the extent of LV dysfunction. LV ejection fraction is not an accurate parameter for its assessment. More interesting parameters include the estimation on LV dP/dt through the measurement of the time interval on the CW recording of the regurgitant jet between 1m/s and 3m/s. The simplified Bernoulli equation can be applied as 36–4 mm Hg/Δt, thus 32 mm Hg/Δt. Closing forces can also be reduced in the presence of LV dyssynchrony, which can be assessed and quantitated by the different available methods.

Other Aetiologies

MR can be observed in other clinical settings. MR is frequent in patients with hypertrophic cardiomyopathy, especially if systolic anterior motion of the mitral valve occurs when dynamic obstruction develops in the LV outflow tract. In this condition, the aspiration of the mitral leaflet by a Venturi effect in the ejection flow produces a kind of tunnel between the leaflets predominating at end-systole. In patients with lupus erythomatosus, Libman Sacks endocarditis can occur, especially in patients with anti-phospholipid antibodies. The evolution of these lesions is quite variable from patient to patient and from time to time. Annular calcification is frequent in the elderly or in patients with renal failure, but MR is rarely severe in this condition. Finally, valvular heart disease can be associated with several drugs such as fenfluramine or Pergolide.

Quantification of Mitral Regurgitation

The assessment of the severity of MR is essential in the management of patients. Semi-quantitative methods have first

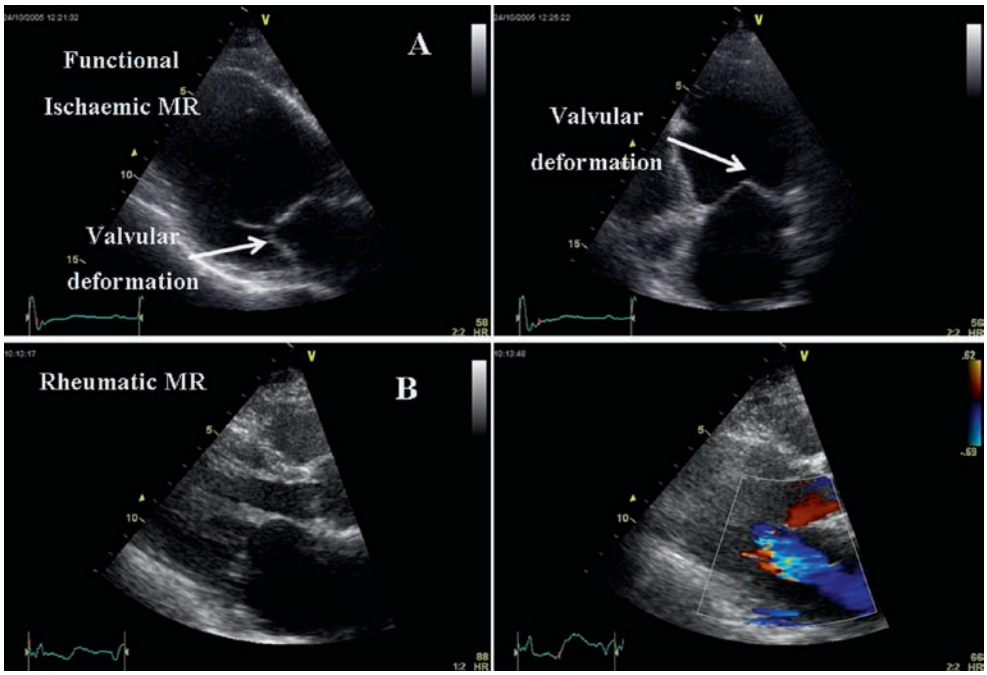

Fig. 8.10 **(a)** A patient with functional mitral regurgitation. Note the important mitral valvular deformation. **(b)** A patient with rheumatic mitral regurgitation

been introduced, but more quantitated methods have been validated which permit to obtain measurements of RVol, RF, and ERO, the latter being the most robust parameter.[23]

Semi-Quantitative Method

Colour Flow Mapping

The RJA is frequently measured by planimetry from the apical 4-chamber view (Fig. 8.11). The ratio of RJA to left atrial area is calculated. Although these measurements appear to be the easiest method, the jet area is influenced by numerous factors: mechanism of regurgitation, direction of the jet, loading conditions, and left atrial size. Other limitations and pressure gradients include technical factors, such as gain settings, pulse repetition frequency, and aliasing velocity.[24] Practically, gain should be optimized and aliasing velocity should be at least 50–60 cm/s. A jet area <4 cm² indicates mild MR, between 4 and 8 cm² moderate MR, and >8 cm² severe MR. The cut-off values of jet area to left atrial area are <20% for a mild, 20–40% for a moderate, and >40% for severe MR (Fig. 8.12).

Vena Contracta Width

The vena contracta is the narrowest portion of the MR jet, downstream from the orifice. It should be measured from two orthogonal planes; the zoom should be used to optimize visualization; the colour sector should be as narrow as possible; and the aliasing velocity can be adapted to identify the three components,

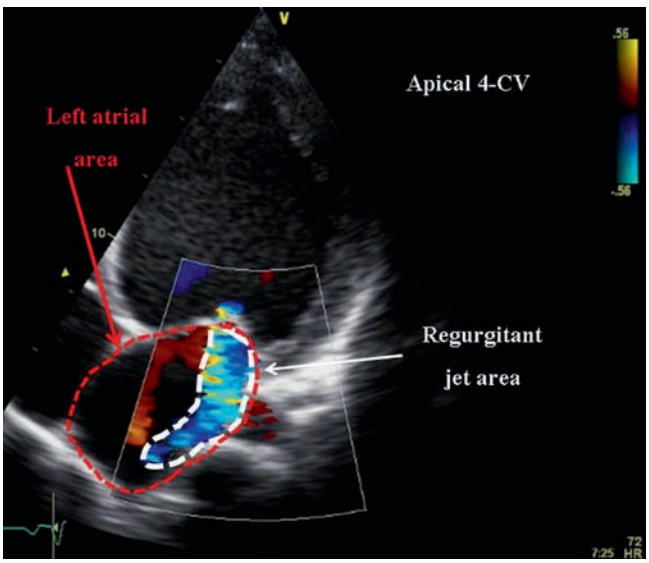

Fig. 8.11 Semi-quantitative assessment of MR severity using colour flow mapping of the regurgitant jet. The ratio of regurgitant jet to left atrial area can be calculated. *AP 4-CV*; apical 4-chamber view

namely, flow conversion, vena contracta, and regurgitant jet. A vena contracta <3 mm indicates mild MR, and VCW ≥7 mm defines severe MR[25] (Fig. 8.13, Video 8.13).

Anterograde Velocity of Mitral Flow

When MR is severe, mitral stroke volume is increased. A peak velocity >1.2 m/s suggests severe MR. The specificity is increased if the cut-off value is >1.5 m/s.

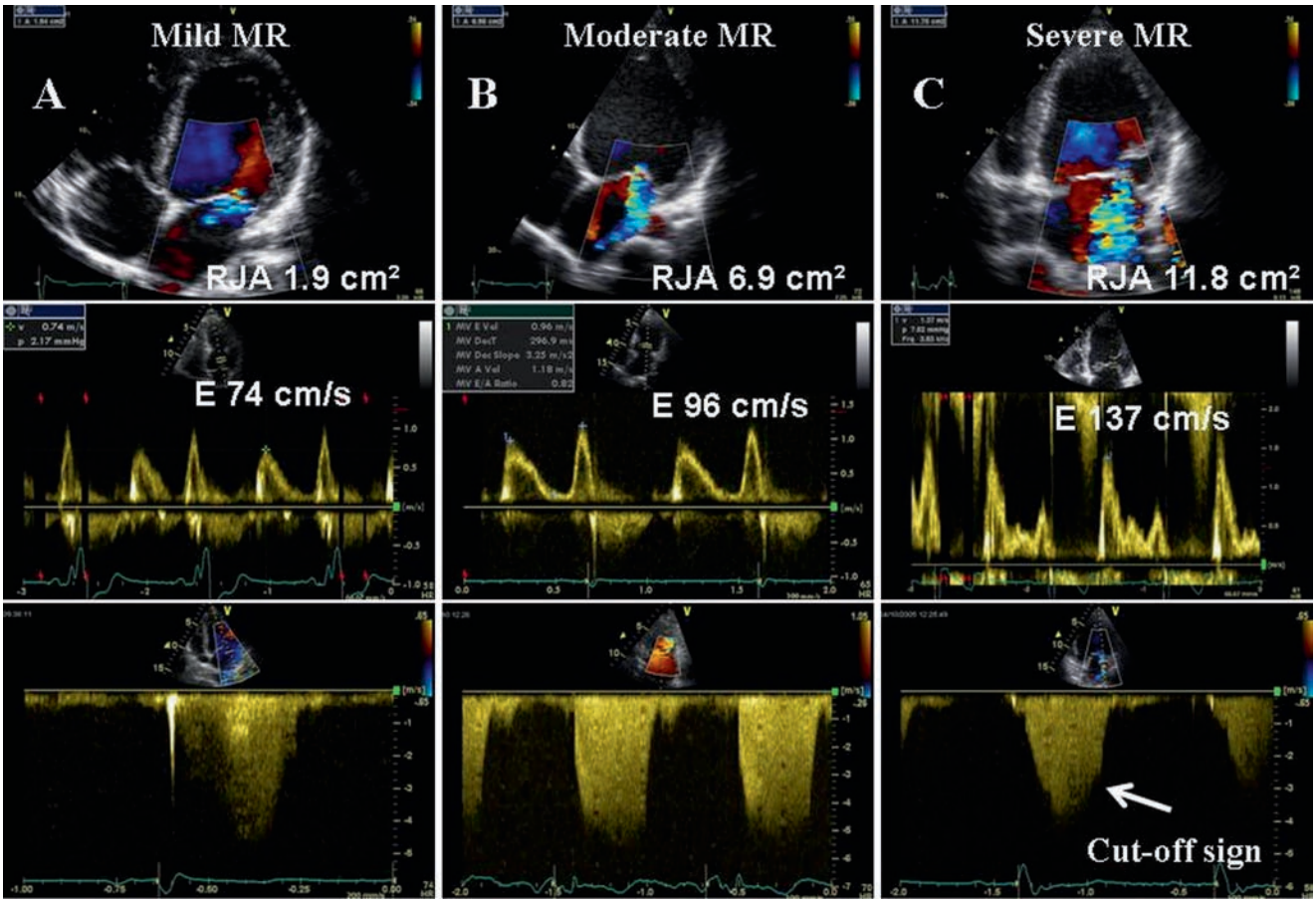

Fig. 8.12 Three examples of various degrees of MR, mild **(a)**, moderate **(b)**, and severe **(c)** are provided. The RJA as well as the mitral E-wave velocity increase with the severity of MR. In severe MR, the CW Doppler signal of the regurgitant jet is truncated, triangular, and intense. Notching of the CW envelope (cut-off sign) can occur in severe MR

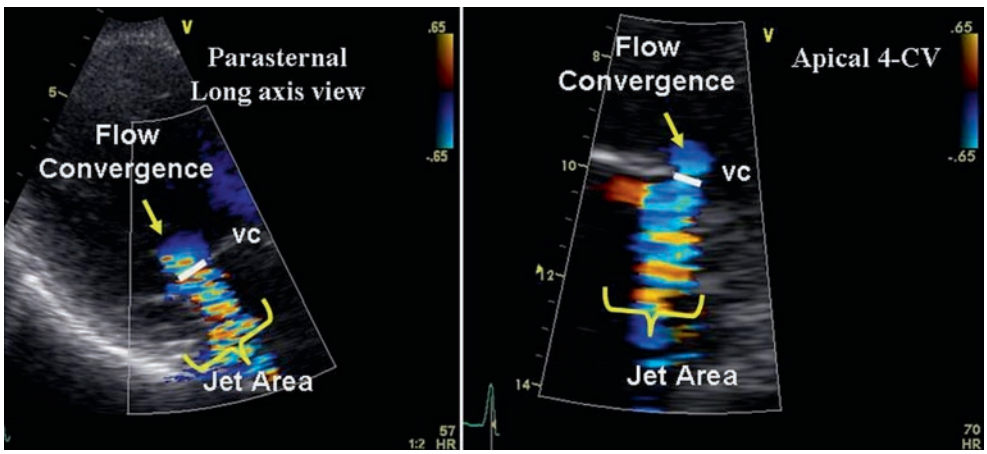

Fig. 8.13 Semi-quantitative assessment of MR severity using the vena contracta width (VCW). *AP 4-CV*; apical 4-chamber view

Quantitative Methods *(Figs. 8.14–8.17, Video 8.14, Video 8.16)*

Doppler Volumetric Method

Quantitative Doppler echocardiography is reliable, but not applicable in the presence of significant AR. The regurgitant volume is the difference between the mitral inflow stroke volume and the aortic stroke volume. The ERO is calculated as:

ERO = regurgitant volume/TVI of MR velocity by CW Doppler.[26]

The Flow-Convergence Method

The theoretic basis of the flow-convergence method has been described earlier.[27] The following steps should be followed: colour flow imaging of MR should be optimized with a small

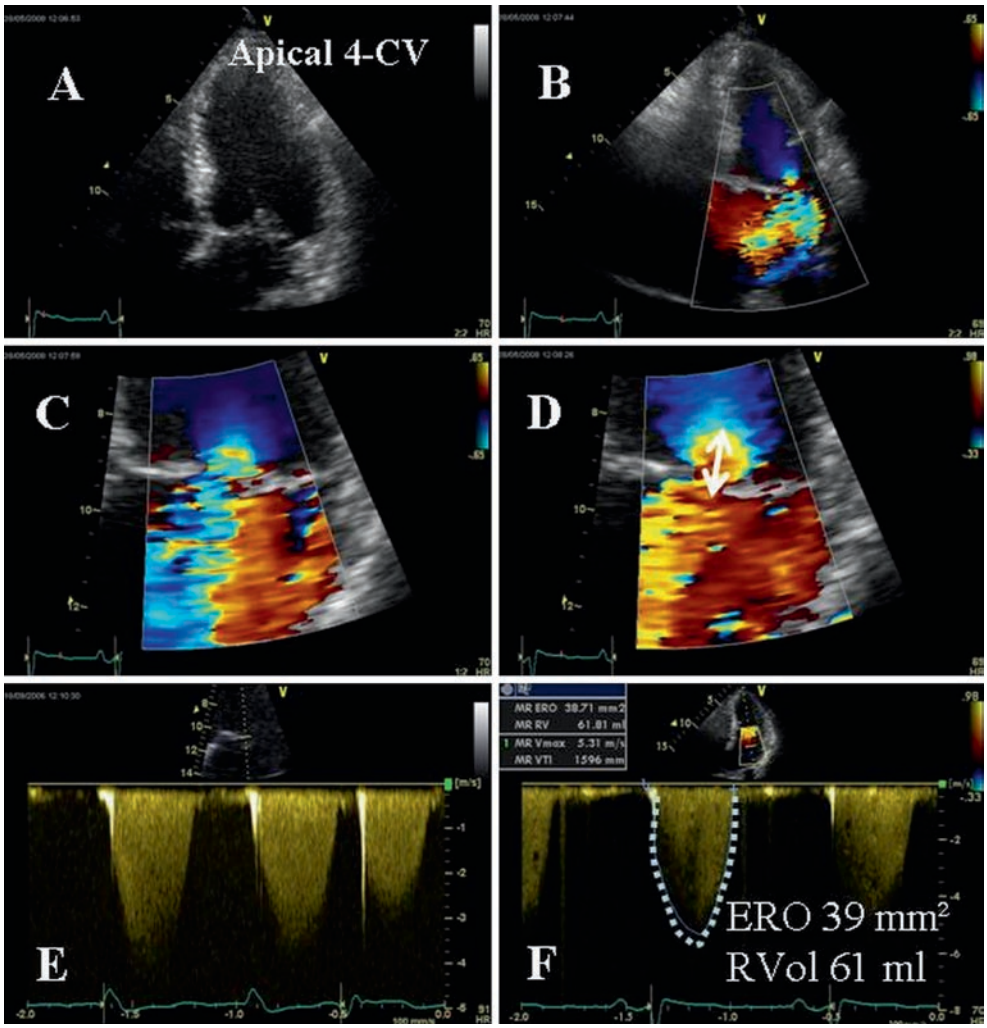

Fig. 8.14 Quantitative assessment of MR severity using the PISA method. Stepwise analysis of MR. **(a)** Apical 4-chamber view (AP 4-CV). **(b)** Colour flow display. **(c)** Zoom of the selected zone. **(d)** Downward shift of 0 baseline to obtain a hemispheric PISA. **(e)** CW Doppler of MR jet. **(f)** Calculation of the ERO and regurgitant volume (RVol)

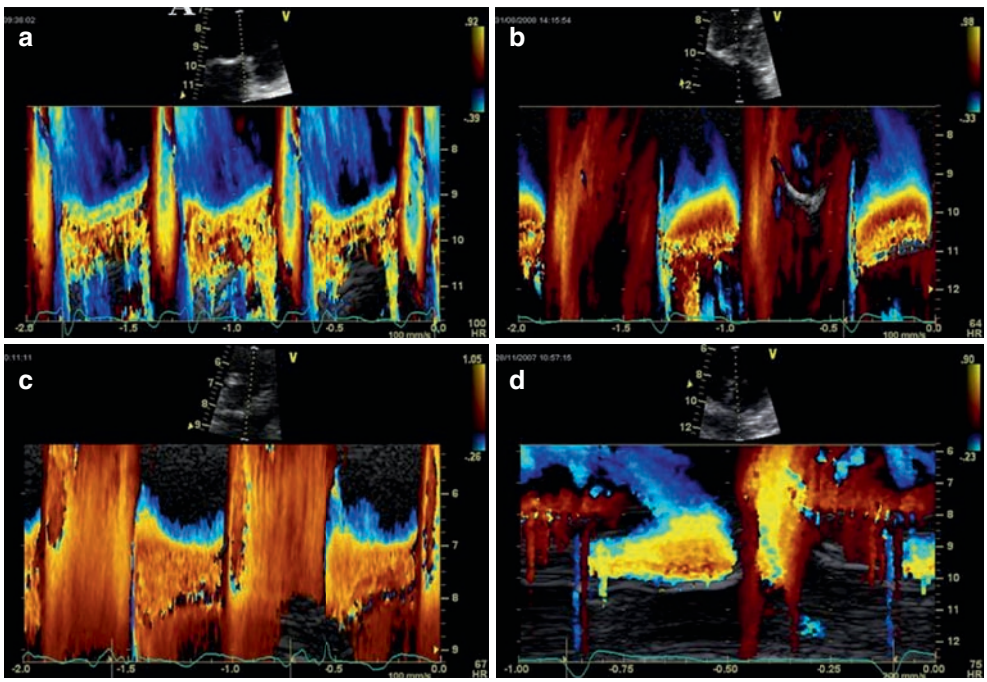

Fig. 8.15 Four examples of flow convergence zone changes using colour M-mode. **(a, b)** Functional MR. **(a)** Early and late peaks and mid-systolic decrease. **(c)** Rheumatic valve. **(d)** Mitral valve prolapse (late systolic enhancement)

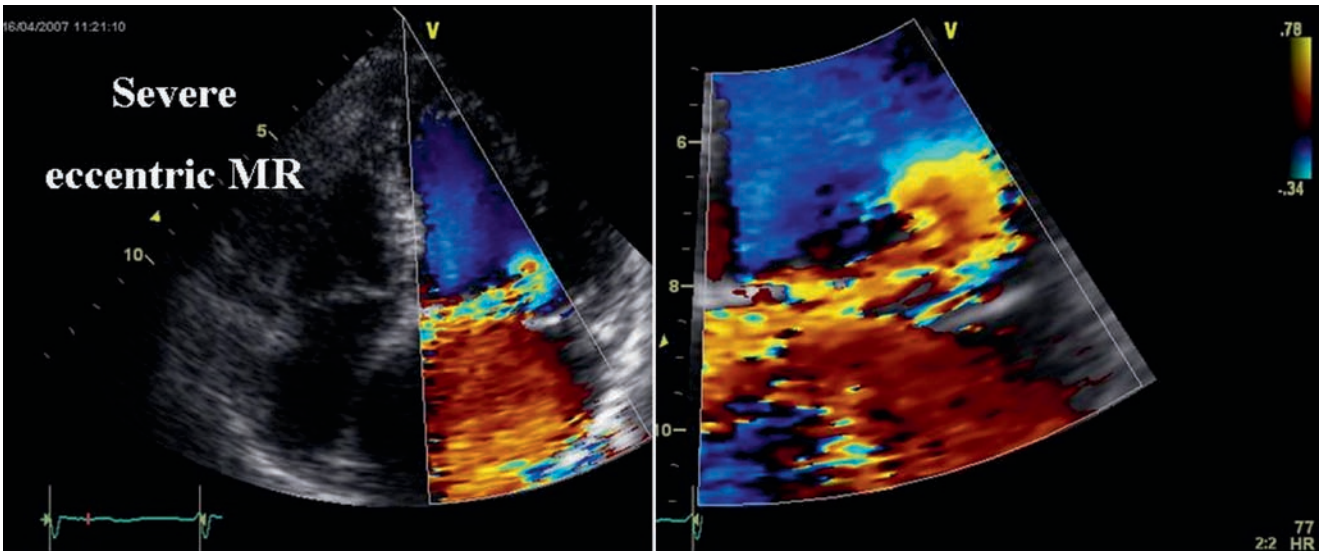

Fig. 8.16 Severe eccentric MR that can be perfectly assessed by using the PISA method

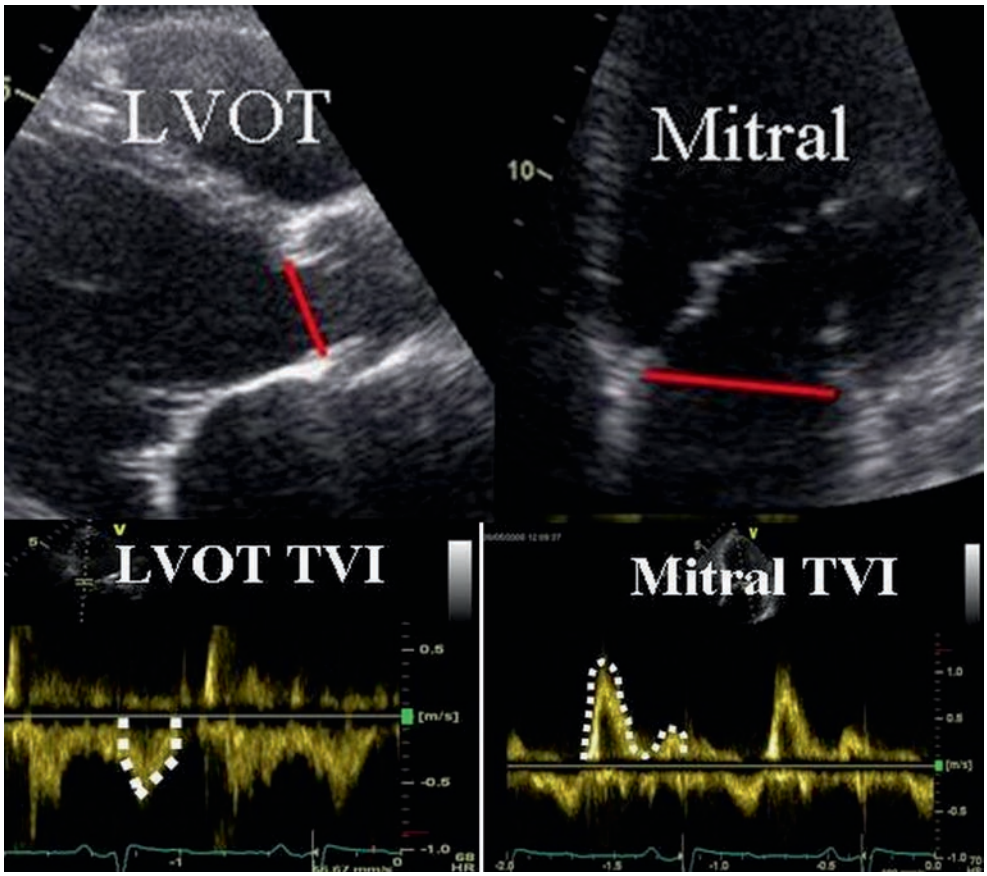

Fig. 8.17 The quantitative assessment of MR severity by the Doppler volumetric method requires the measurement of the left ventricular outflow tract diameter, the mitral annulus diameter, and of two pulse wave velocity profiles (outflow tract and mitral inflow velocities)

angle from the apical window. The image of MR is extended by using zoom or regional extension selection. Colour flow baseline needs to be shifted downwards to obtain hemispheric PISA, using the negative aliasing velocity between 15 and 40 cm/s. The radius of the PISA is measured at mid-systole using the first aliasing. RVol and ERO are obtained using the standard formula.

Flow rate at PISA = flow rate at regurgitant orifice.
ERO = $6.28r^2$ × aliasing velocity/MR velocity.
RVol = ERO × MR TVI.

The ratio of the aliasing velocity to the peak orifice velocity should be <10%. Several pitfalls of this method exist. The hemispheric assumption by 2D echo frequently underscores

the true severity of MR. Indeed, real-time 3D echo has shown that PISA is more frequently hemi-elliptic rather than truly hemispheric. However, the PISA method, which is less dependent on instrumentation and haemodynamic factors, can be used in the presence of eccentric jets. The aetiology of MR and the presence of associated valvular disease do not affect calculation.

Colour M-mode is important to assess the changes in the PISA radius during systole. The PISA radius is most frequently constant in patients with rheumatic MR. It frequently increases progressively with a maximum during the second half of systole in patients with mitral valve prolapse. In the presence of functional MR, there is a dynamic variation of regurgitant orifice area with early and late systolic peaks and a mid-systolic decrease. The phasic changes in transmitral pressure act to close the mitral leaflets more effectively when pressure reaches its peak in mid-systole. ERO is the most robust parameter. However, it is the amount of regurgitant flow and not orifice size that determines left atrial pressure.

Pulmonary Venous Flow

Reversed systolic flow in the pulmonary vein usually implies severe MR. However, this observation is not accurate if MR is directed into the sampled vein (Fig. 8.18).

Continuous Wave Doppler

The morphology of the CW Doppler also can be used in acute severe MR. There is a rapid decrease in velocity indicating a reduction in the pressure gradient between the LV and the left atrium, corresponding to a large V-wave observed with cardiac catheterization. A distinction between mild, moderate, and severe MR should integrate all these different parameters and measurements (Tables 8.4–8.6).

Consequences of Mitral Regurgitation

Several parameters and measurements are required to assess the haemodynamic repercussions of severe MR.

Left Ventricular Parameters

Although real-time 3D echo permits reliable measurement of LV volumes and ejection fraction, the most recent guidelines still refer to M-mode measurements.

End-systolic diameter is still an important measurement, although the European and American Guidelines differ in the cut-off value recommending mitral valve repair in severe chronic organic MR (45 mm in the European recommendations

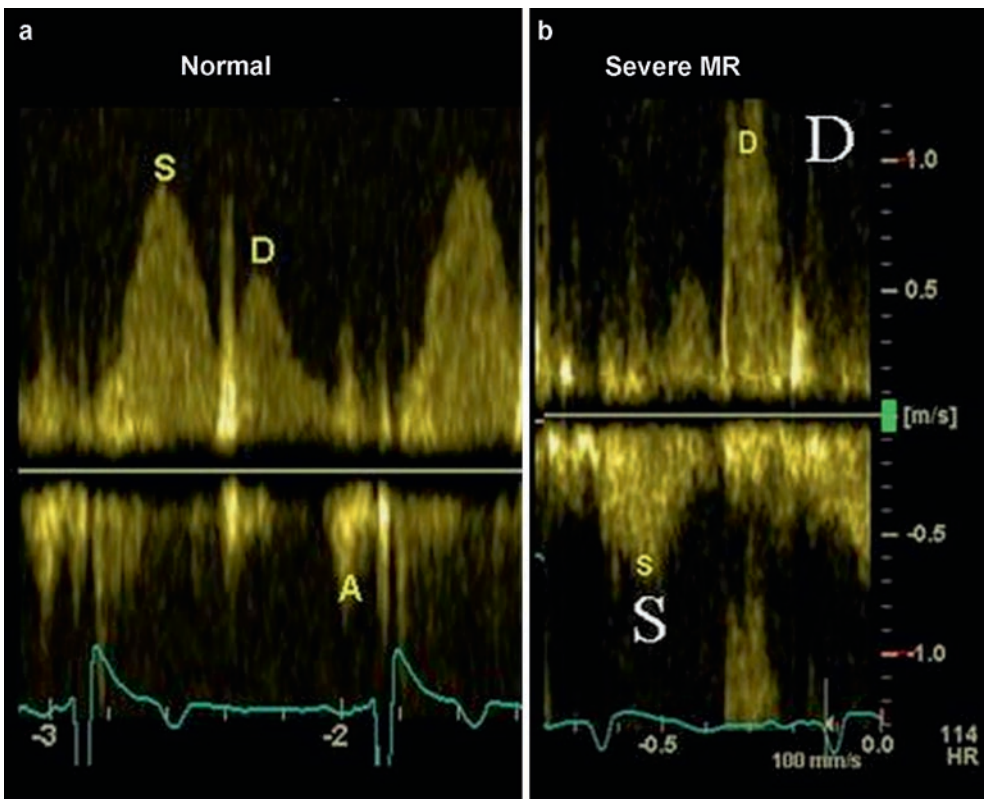

Fig. 8.18 **(a)** Normal pulmonary vein flow pattern. **(b)** Reversed systolic pulmonary flow in a patient with severe MR

Table 8.4. Qualitative assessment of MR: specific signs

Mild	Moderate	Severe
Small central jet <4 cm² or <20% of left atrial area	Intermediate signs	Vena contracta ≥0.7 cm with large central MR jet (area >40% of left atrial area) or with a wall-impinging jet of any size
Vena contracta <0.3 cm		Large flow convergence
		Systolic reversal in pulmonary vein
No or minimal flow convergence		Prominent flail/ruptured papillary muscle

Table 8.5. Qualitative assessment of MR: supportive signs

Mild	Moderate	Severe
Systolic dominant flow in pulmonary vein	Intermediate signs	Dense, triangular CW Doppler MR signal
A-wave dominant mitral inflow		E-wave dominant mitral inflow (E >1.2 cm/s)
Soft density, parabolic CW Doppler MR signal		Enlarged LA (≥28 cm/m²)
Normal left ventricular size		Enlarged LVD (≥82 mL/m²)

CW continuous wave Doppler

Table 8.6. Qualitative assessment of MR: Grading of severity

Mild	Mild	Moderate	Severe
Regurgitant volume (ml/beat)	<30	30–44/45–59	≥60
Regurgitant fraction (%)	<30	30–44/45–59	≥50
ERO (cm²)	<0.20	0.20–0.29/0.30–0.39	≥0.40

Ischaemic MR: ERO ≥ 0.20 cm² or R Vol ≥ 30 mL should be considered as severe

and 40 mm in the ACC/AHA Guidelines). The cut-off value for ejection fraction is similar (<60%).[14, 28] However, the variability of LV dimensions increases in a spherical LV; a 10% error in diameter lead to a 30% error in volume. LV shape is important to assess using the sphericity index.

Left Atrial and Pulmonary Pressures

Although the left atrial size is not included in the guidelines, it is an important parameter. Left atrial volume should be obtained by 3D echo or by 2D echo using the Simpson rule. The presence of tricuspid regurgitation (TR), even if it is mild, permits the estimation of systolic pulmonary arterial pressure. Recommendation for mitral valve surgery is a class IIa when pulmonary arterial systolic pressure is >50 mm Hg at rest.

Left Ventricular Function

LV ejection fraction is a load-dependent parameter and thus, is not reliable in a situation of volume overload and low impedance. Indeed, the LV ejection fraction represents the sum of the forward ejection fraction and the RF. New parameters are currently available for a better assessment of LV function. Global radial or preferably longitudinal strain has been shown to be useful to predict post-operative LV function in patients with asymptomatic severe MR.

Exercise-Echocardiography

Organic Mitral Regurgitation

According to the ACC/AHA 2006 Guidelines, exercise Doppler echocardiography is reasonable (class IIa, level of evidence C) in asymptomatic patients with severe MR to assess exercise tolerance and the effect of exercise on pulmonary artery pressure (significant if > 60 mm Hg) and MR severity. This is not included in the ESC Guidelines in 2007, probably because of lack of robust data. Several studies have used post-exercise echo and measured LV volumes and ejection fraction. It was found that the best predictors of post-operative LV dysfunction were exercise variables rather than similar parameters measured at rest.

Longitudinal strain at exercise and exercise-induced changes in this parameter appear to be interesting for this prediction. Confirmation is required to implement the cut-off values found in the future guidelines.[29]

Ischaemic Mitral Regurgitation

Ischaemic MR varies dynamically, depending on loading conditions and a balance of closing force and mitral valvular

deformation. Quantitation of functional MR during exercise is feasible using the PISA or the Doppler volumetric methods. The degree of MR at rest is unrelated to exercise-induced changes in ERO, which are related to those in local LV re-modelling and in mitral deformation. Dynamic MR is strongly related to exercise-induced changes in systolic tenting area and to intermittent changes in LV synchronicity. Large exercise-induced increases in ischaemic MR are associated with dyspnea or acute pulmonary oedema. Dynamic MR also predicts mortality and hospitalization for heart failure.[30–32]

Repairability

Symptomatic patients with severe organic MR should be submitted to mitral valve surgery, preferably mitral valve repair. In patients with asymptomatic severe MR, the reparability of the valve is utmost important in clinical decision-making. The probability of repair is highly dependent on the surgeon's skill and experience. The surgeon needs to know the mechanism and the anatomic classification. In the presence of valve prolapse, it is essential to determine which scallops are involved, whether the commissural MR is present, the extent of redundant leaflet tissue, and the extent of valvular and annular calcification.

Role of Echocardiography in the Follow-Up

Moderate MR requires clinical examination every year and an echocardiogram every 2 years. In patients with severe MR, clinical assessment is needed every 6 months and an echocardiogram every year. If the ejection fraction is 60–65% and/or if the end-systolic diameter is between 40 and 45 mm, the echocardiogram should be performed every 6 months.

Progression of severity of MR is frequent with important individual differences. The average yearly increase in RVol is 7.5 mL and in ERO is 5.9 mm^2. In addition, progression of lesions needs to be assessed such as an increase in annular size, the development of a flail leaflet, the evolution of LV end-systolic dimension, ejection fraction, left atrial area or volume, pulmonary systolic arterial pressure, exercise capacity, and occurrence of atrial arrhythmias.

The measurement of functional ischaemic MR is controversial. In addition to clinical evaluation, echo should provide important information, such as the severity of MR (ERO ≥ 20 mm^2), dynamic MR (increase in ERO > 13 mm^2 at exercise), extent of LV re-modelling and sphericity, of mitral valve deformation, presence and extent of LV dyssynchrony, and presence and extent of viable and ischaemic tissue.

Role of Magnetic Resonance Imaging

Evaluation of the patient with MR should include confirming the presence of regurgitation, quantifying it, and determining its influence on LV volumes and systolic function.[33] Echocardiography and, to a lesser extent, cardiac catheterization are most commonly used to evaluate MR. However, because MRI is a 3D volumetric technique, it can better quantify the severity of regurgitation, as well as quantify its effect on LV size and function. In patients with isolated MR, MRI can quantify the leak using two different methods. The regurgitant volume can be calculated as (1) the difference between the LV stroke volume and the aortic flow or (2) the difference between the LV and RV stroke volumes. Having two distinct volumetric methods of quantifying the regurgitant volume often increases the diagnostic confidence in the MRI results. Furthermore, because MRI does not rely on direct assessment of the regurgitant jet, quantifying eccentric or multiple regurgitant jets is not problematic because it can be carried out with echocardiography. Finally, the assessment of MR with MRI is completely non-invasive. It does not require intravenous contrast, and it does not use ionizing radiation. As with AR, MR may be acute or chronic. The main haemodynamic consequence of chronic MR is gradual LV dilatation and ultimately, LV failure. Thus, MRI is well placed to accurately quantify and monitor the severity of MR and the haemodynamic consequences on LV function. Hitherto, no large-scale clinical studies have assessed the use of MRI for defining the timing of surgical repair of MR. In ischaemic functional MR, MRI can also be used to identify and evaluate the extent of viable myocardium.

Tricuspid Regurgitation

TR is a commonly diagnosed pathology. As it is mostly asymptomatic and not easily audible on physical examination, it is frequently only diagnosed by echocardiography performed for another indication. Although a mild degree of TR is frequent and benign, moderate and severe TR is associated with poor prognosis.[34]

Tricuspid Valve Anatomy and Incidences

The tricuspid valve is composed of the annulus, three leaflets, papillary muscles, and chordae tendinae. It lies between the right atrium and the RV in a more apical position than the mitral valve. The tricuspid annulus, providing a firm support for the tricuspid leaflets insertion, is less fibrous than other annuluses and slightly larger than the mitral valve annulus.

Until recently, the shape of the tricuspid annulus had not been established. In a recent 3D study, the tricuspid annulus is found to have a less non-planar shape than the mitral annulus, having a wider non-planar angle closer to 170°. On projected view, it revealed a round or oval shape, whereas the mitral annulus demonstrated a fan-like shape, which may probably be due to less non-planarity of the tricuspid annulus compared with the mitral annulus. The tricuspid valve has three thin and membranous leaflets. The commissures appear more like indentations than true commissures. The three leaflets are the anterior, septal, and posterior leaflets, with the anterior and septal being larger than the posterior leaflet. The three papillary muscles are the anterior, posterior, and septal papillary muscles. The anterior and septal papillary muscles are the largest. The posterior papillary muscle is small and sometimes absent. Each leaflet has chordal attachments to one or more papillary muscles.

The three main transthoracic incidences allowing the tricuspid valve visualization are the left views, the apical 4-chamber view, and the sub-costal view. Parasternal long-axis view of the RV inflow is obtained by tilting the probe inferomedially and rotating it slightly clockwise from the parasternal long-axis view of the left ventricle. This incidence reveals the anterior tricuspid leaflet (near the aortic valve) and the posterior tricuspid leaflet. Parasternal short-axis view, at the level of the aortic valve, apical 4-chamber view, and subcostal position visualizes the septal and anterior tricuspid leaflets. However, it is not possible to visualize the three leaflets simultaneously by 2D echo. Real-time 3D TTE is now routinely available and allows simultaneous analysis of the three leaflets of the tricuspid valve within a reasonable time.[35]

TOE for the tricuspid valve is possible with the 4-chamber view at 0° in the basal oesophageal and esogastric junction planes. TOE is of interest for the diagnosis of endocarditis when suspected. It is particularly essential to diagnose venous catheters and pacemaker-lead infection because TTE is often non-diagnostic in these settings. TOE can also help accurate tricuspid valve chordae visualization when traumatic rupture is suspected with TTE.

Aetiology

A mild degree of TR is frequently reported in healthy subjects related to age. Percentages of 65–75 have been reported in prospective studies of healthy volunteers. On echocardiography, this "physiological" TR is associated with normal valve leaflets and no dilatation of the RV. It is localized in a small region adjacent to valve closure (< 1 cm) with a central thin jet, and often does not extend throughout systole. Peak systolic velocities are between 1.7 and 2.3 m/s.

Moderate and severe TR can be either secondary or functional, i.e. without tricuspid valve structural abnormality, or much less often primary or organic, owing to a tricuspid valve disease. In a study of 242 consecutive patients diagnosed for severe TR, primary tricuspid valve disease was evident in 10% and secondary functional TR in 90%: tricuspid annulus and RV dilatation (secondary to aging, atrial fibrillation, or other causes) were the most common mechanisms of TR in these patients. The principal causes of functional and organic TR are shown in Tables 8.7 and 8.8. Functional TR is thought to be caused by TV annulus dilatation and tethering of the tricuspid leaflet when right ventricular dilatation results in a decrease in the degree of leaflet overlap or coaptation at their tips.

Table 8.7. Causes of functional tricuspid regurgitation (TR)

Primary right ventricular and tricuspid annulus dilatation
Right ventricular myocardial infarction
Dilated cardiomyopathy of any cause
Right ventricular dysplasia
Post-transplant right ventricular myocardial disease
Pulmonary hypertension and secondary right ventricular and tricuspid annulus dilatation
Left-sided heart failure
Mitral valve stenosis or regurgitation
Primary pulmonary disease: Cor pulmonale, pulmonary embolism, pulmonary hypertension of any cause
Left to right shunt: atrial septal defect, ventricular septal defect, anomalous pulmonary venous return
Eisenmenger syndrome
Pulmonary artery or pulmonary valve stenosis
Hyperthyroidism
Right atrial dilatation and secondary tricuspid annulus dilatation
Atrial fibrillation

Table 8.8. Causes of organic TR

Ebstein anomaly
Infective endocarditis
Rheumatic fever
Trauma
Ischaemic heart disease responsible for papillary muscle dysfunction or rupture
Connective tissue disorder (e.g. Marfan Syndrome)
Myxomatous degeneration or prolapse (associated to mitral valve prolapse in 40% of cases)
Marantic endocarditis in systemic lupus erythematosus or rheumatic arthritis
Iatrogenic: Pacemaker implantation, endomyocardial biopsy
Drugs: Anorectic drugs (fenfluramine and phentermine), dopamine agonist (pergoline)

Echocardiographic Diagnostic of Tricuspid Regurgitation

Table 8.9 summarizes the different parameters that define a severe TR.

Table 8.9. Criteria of severe TR

Echocardiographic mode	Criteria of severe TR
2D Echocardiography	Inadequate cusp Systolic tricuspid annulus diameter >3.2 cm or a diastolic tricuspid annulus diameter >3.4 cm
Colour flow Doppler	Regurgitant jet area > 10 cm² VCW > 0.65 cm PISA radius of >0.9 cm ERO >40 mm² Regurgitant volume ≥45 mL Systolic flow reversal in the vena cava and hepatic vein
CW Doppler	Dense CW Doppler signal Late systolic concave configuration of the CW Doppler signal Increased tricuspid inflow velocity ≥ 1 m/s
Pulse wave Doppler	E-wave velocity of ≥65 cm/s

Two-Dimensional

2D allows the detection of the mechanism and the cause of regurgitation. The pathognomonic presence of an inadequate cusp coaptation is associated with severe TR. The presence and degree of TR can be assessed by precise inspection of RV size and function, right atrial size and function, tricuspid valve morphology, and vena cava. Good correlation exists between tricuspid annulus diameter and TR severity: a systolic tricuspid annulus diameter >3.2 cm or a diastolic tricuspid annulus diameter >3.4 cm are in favour of severe TR.[35]

Colour Flow Doppler Echocardiography

Colour flow Doppler echocardiography is the most frequently used technique for TR diagnosis and quantification. Apical 4-chamber view and parasternal short-axis view at the level of the aortic valve are the two incidences that permit TR colour flow analysis. Proper settings of the echomachine require the choice of an aliasing velocity of 50–60 cm/s and an optimized colour gain to eliminate random colour speckles (Figs. 8.19 and 8.20, Videos 8.19 and 8.20).

Colour Flow Mapping

Quantification of the severity of TR by mapping the extent of the regurgitant jet in the right atrium is quite obsolete and old

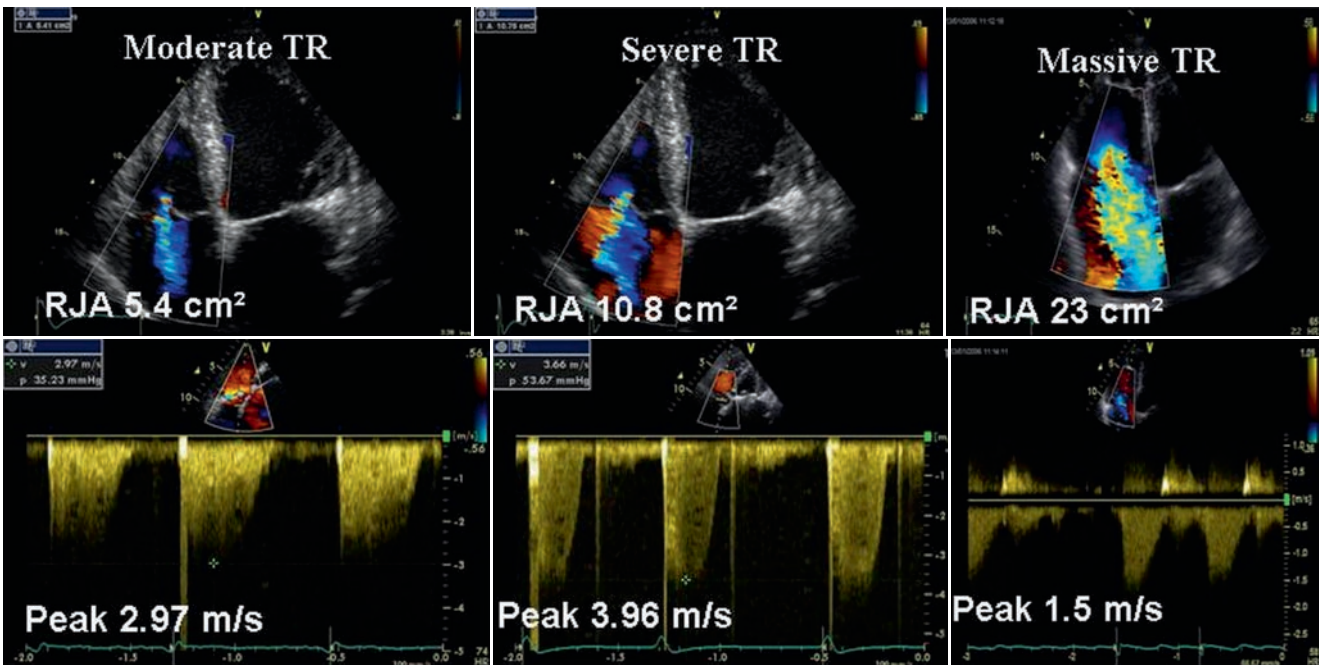

Fig. 8.19 Three examples of various degrees of TR, mild (left), moderate (middle), and severe (right) are provided. The RJA increases with the severity of TR. The peak velocity of TR (CW Doppler) allows the estimation of pulmonary pressure except in case of massive TR, as the Bernouilli equation is not applicable

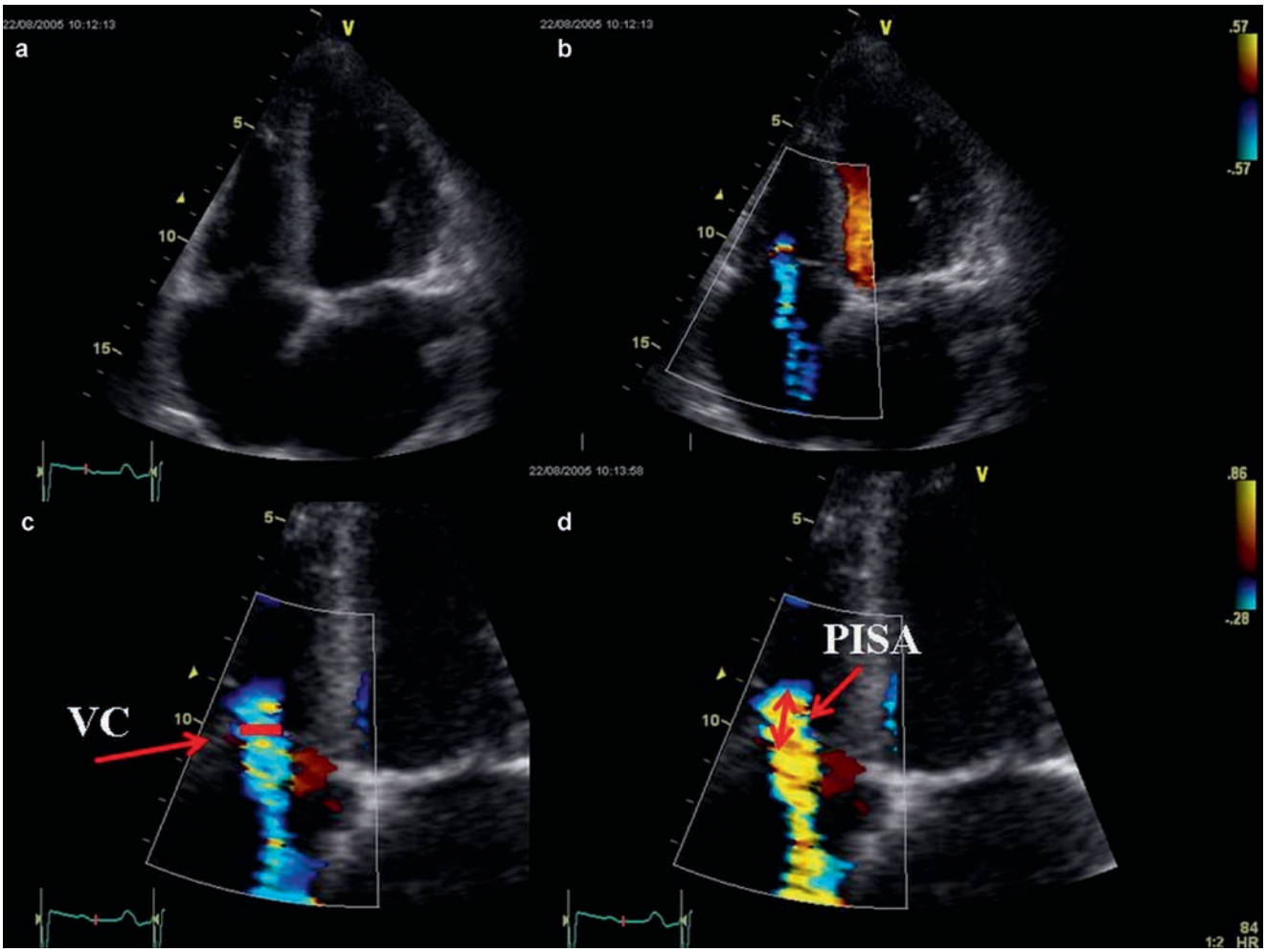

Fig. 8.20 Quantitative assessment of TR severity using the VCW and the PISA method. Stepwise analysis of TR. **(a)** Apical 4-chamber view (AP 4-CV). **(b)** Colour flow display. **(c)** Zoom of the selected zone to obtain the vena contracta and the three components of TR jet. **(d)** Downward shift of zero baseline to obtain an hemispheric PISA

fashion. The maximal jet regurgitant area (RJA) in apical 4-chamber view is, therefore, more frequently used to quantify the severity of regurgitation (Figure and Video).[36] A mild TR is associated with an RJA< 4 cm² and severe TR with RJA > 10 cm². Moderate TR is found within the interval. The size of the colour flow jet in the right atrium is correlated with the angiographic severity of the TR only when it is severe. The main limitations of this technique include technical factors such as gain settings and pulse repetition frequency, loading conditions, and right atrial size. A potential source of underestimation of the RJA is owing to the eccentric direction taken by the jet as it enters the right atrium owing to the Coanda effect.

Vena Contracta Width

A more accurate method of TR quantification is the assessment of the VCW. Vena contracta is the smallest neck of the regurgitant jet that occurs just at the level of the tricuspid valve, immediately after the flow convergence region in the apical 4-chamber view. Zooming allows better visualization of the neck of the regurgitant jet. The colour sector has to be as narrow as possible to maximize lateral and temporal resolution, and aliasing velocity should be detected between 46 and 96 cm/s. To increase the validity of the measure, it is recommended to record several measures in inspiration and expiration, and then to average them owing to the influence of the respiratory cycle on TR severity. A severe TR corresponds to a VCW of >0.65 cm (sensitivity of 89%, specificity of 93%).[37] Overlap exists between mild and moderate cases. The major limitation of this technique is associated with non-circular orifice and multiple jets.

Proximal Isovelocity Surface Area Method

Another method used for quantifying TR severity is the PISA method. Colour flow imaging displays the convergent PISA

signal as a hemispheric shell with surface velocity equal to the chosen aliasing velocity. Therefore, a clearly visible, round PISA is required for calculation. This is made possible by a zoom view of the region of interest in the apical 4-chamber or parasternal short-axis (at the level of the aortic valve) views. The proper settings include the reduction of the depth of the imaging sector and the use of the narrowest possible colour sector. The colour flow velocity scale baseline is shifted to reduce aliasing velocity (of about 28 cm/s). The PISA radius is obtained by measuring the distance between the regurgitant orifice and first aliasing. The regurgitant flow rate across the tricuspid valve is obtained from the flow rate of the PISA, by determining the flow velocity corresponding to the aliasing velocity. The ERO is obtained by dividing the flow rate through the regurgitant orifice by the peak velocity of the regurgitant jet with CW Doppler.

Flow rate = $2\pi r^2 \times$ aliasing velocity
ERO = Flow rate/peak TR velocity
ERO = $(6.28 \times r^2 \times$ aliasing velocity)/peak TR velocity
RVol per beat = ERO × TR TVI

ERO = effective regurgitant orifice, r = PISA radius, peak TR velocity = TR flow peak velocity in CW Doppler, RVol = Regurgitant volume, TR TVI = time velocity integral of TR flow in CW Doppler

With an aliasing velocity of 28 cm/s, a TR PISA radius of <0.5 cm is categorized as mild, a radius of 0.6–0.9 cm is moderate, and a radius of >0.9 cm is severe, and correspond to an ERO of >40 mm². PISA method limitations include reduced accuracy for eccentric jets, difficulty indentifying the regurgitant orifice, and inaccurate estimation of the convergence shape. The flow convergence method and the jet area method

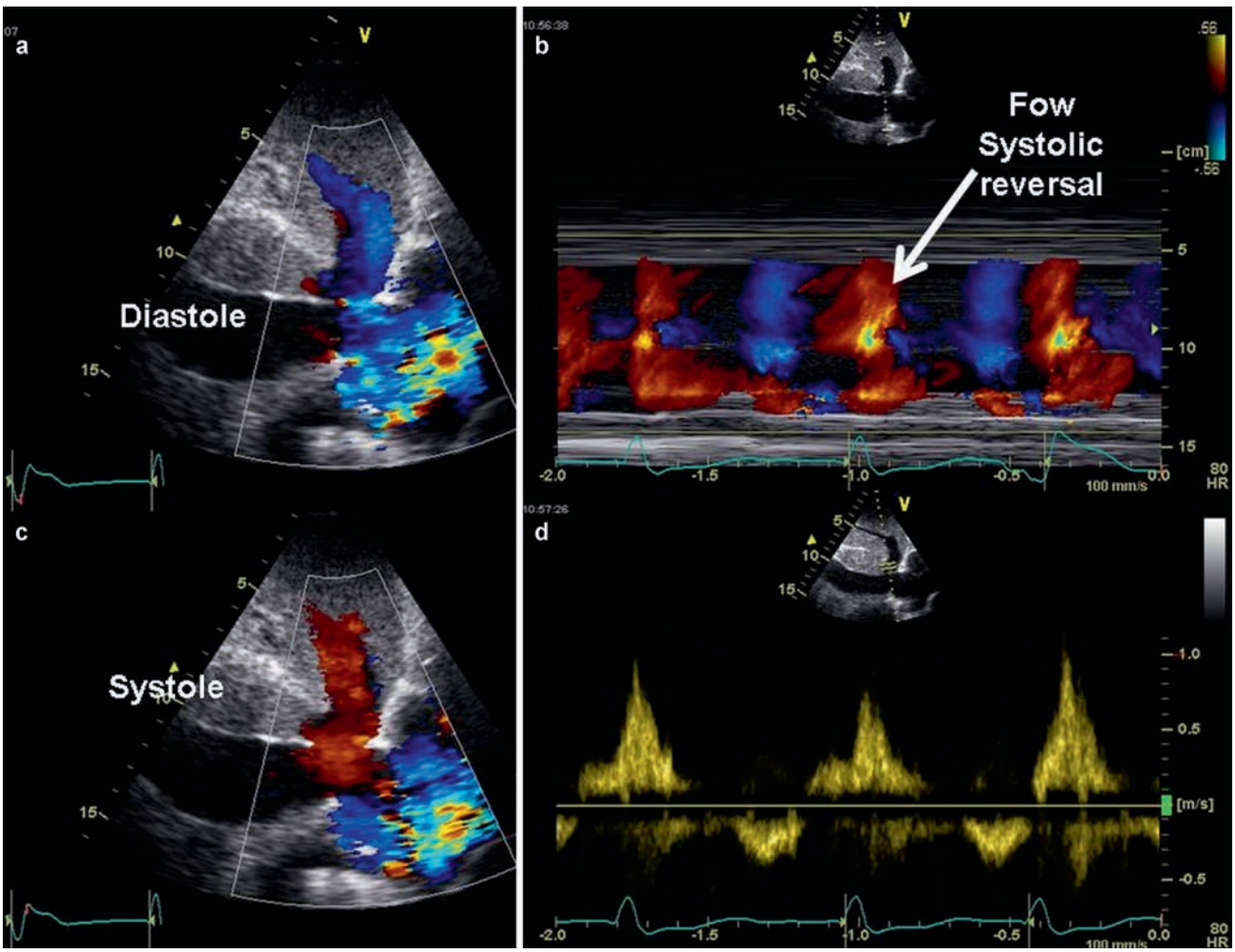

Fig. 8.21 Sub-costal echocardiogram recorded in a patient with severe TR. **(a–c)** The colour Doppler confirms retrograde flow into the vena cava and hepatic vein in systole consistent with TR (*red*). **(d)** A spectral Doppler recording from a hepatic vein, also confirming the systolic retrograde flow

are of similar value for the determination of the severity of TR. However, under-estimation of severe TR in 20–30% of the case represents serious limitation of both methods.

Inferior Vena Caval and Hepatic Vein Flow

In case of TR, colour flow Doppler demonstrates alterations in inferior vena caval and hepatic flow. Normally, blood flow is towards the right atrium throughout the cardiac cycle, except briefly after atrial contraction. In the presence of a significant TR, the dominant systolic wave may be blunted (moderate TR) or reversed (severe TR), with accentuation during inspiration (Fig. 8.21).

Continuous Wave Doppler

The shape, density, and peak velocity of the TR jet are the parameters analyzed using CW Doppler. The shape of the jet is used as a parameter to grade TR. Mild TR is usually associated with a symmetric and parabolic shape, moderate TR is associated with variable contour, and severe TR is associated with triangular early peaking jet. This V-wave appears to be one of the most useful and reliable sign of severe TR. The density of the TR CW Doppler signal indicates the magnitude of the RF. Mild TR has soft TR jets, whereas moderate and severe TR have dense TR jets. An increased tricuspid inflow velocity ≥ 1 m/s is associated with severe TR. A reliable peak velocity of the TR jet measure requires low angle between the incident ultrasound beam and the regurgitant jet. Modified Bernoulli equation allows estimation of the peak TR gradient. Right ventricular systolic pressure is estimated by summing the right atrial pressure and peak TR pressure gradient. It is equal to the pulmonary artery systolic pressure if there is no pulmonic valve stenosis. The presence of a severe pulmonary hypertension is not an indicator of severe TR.

Pulsed Wave Doppler

Peak E-wave and TVI of RV inflow are increased proportionately with TR severity. Increased peak tricuspid E-wave velocity is associated with severe TR, and thus, can be used as a simple measure of TR grade. A peak E-wave velocity of ≥65 cm/s had a sensitivity of 73% and specificity of 88% for the detection of severe TR. Pulsed wave Doppler is also used for inferior vena cava and hepatic vein flow analysis. Severe TR is associated with a systolic venous flow reversal.

References

1. Duran CM. Present status of reconstructive surgery for aortic valve disease. *J Card Surg*. 1993;8:443–452
2. Lung B, Baron G, Butchart EG, et al A prospective survey of patients with valvular heart disease in Europe: the euro heart survey on valvular heart disease. *Eur Heart J*. 2003;24:1231–1243
3. Zanettini R, Antonini A, Gatto G, et al Valvular heart disease and the use of dopamine agonists for Parkinson's disease. *N Engl J Med*. 2007;356:39–46
4. Ekery DL, Davidoff R. AR: quantitative methods by echocardiography. *Echocardiography*. 2000;17:293–302
5. Perry GJ, Helmcke F, Nanda NC, et al Evaluation of aortic insufficiency by Doppler color flow mapping. *J Am Coll Cardiol*. 1987;9:952–959
6. Tribouilloy CM, Enriquez-Sarano M, Bailey KR, et al Assessment of severity of AR using the width of the vena contracta: a clinical color Doppler imaging study. *Circulation*. 2000;102:558–564
7. Tribouilloy CM, Enriquez-Sarano M, Fett SL, et al Application of the proximal flow convergence method to calculate the effective regurgitant orifice area in AR. *J Am Coll Cardiol*. 1998;32:1032–1039
8. Vinereanu D, Ionescu AA, Fraser AG. Assessment of LV long-axis contraction can detect early myocardial dysfunction in asymptomatic patients with severe AR. *Heart*. 2001;85:30–36
9. Dulce MC, Mostbeck GH, O'Sullivan M, et al Severity of AR: interstudy reproducibility of measurements with velocity-encoded cine MR imaging. *Radiology*. 1992;185:235–240
10. Samstad SO, Hegrenaes L, Skjaerpe T, et al Half time of the diastolic aortoventricular pressure difference by continuous wave Doppler ultrasound: a measure of the severity of AR? *Br Heart J*. 1989;61:336–343
11. Willett DL, Hall SA, Jessen ME, et al Assessment of AR by transesophageal color Doppler imaging of the vena contracta: validation against an intraoperative aortic flow probe. *J Am Coll Cardiol*. 2001;37:1450–1455
12. Shiota T, Jones M, Tsujino H, et al Quantitative analysis of AR: real-time 3-dimensional and 2-dimensional color Doppler echocardiographic method - a clinical and a chronic animal study. *J Am Soc Echocardiogr*. 2002;15:966–971
13. Fang L, Hsiung MC, Miller AP, et al Assessment of AR by live three-dimensional transthoracic echocardiographic measurements of vena contracta area: usefulness and validation. *Echocardiography*. 2005;22:775–781
14. Vahanian A, Baumgartner H, Bax J, et al Guidelines on the management of valvular heart disease: The Task Force on the Management of Valvular Heart Disease of the European Society of Cardiology. *Eur Heart J*. 2007;28:230–268
15. Piérard LA, Lancellotti P. Stress testing in valve disease. *Heart*. 2007;93:766–772
16. Wahi S, Haluska B, Pasquet A, et al Exercise echocardiography predicts development of LV dysfunction in medically and surgically treated patients with asymptomatic severe AR. *Heart*. 2000;84:606–614
17. Chatzimavroudis GP, Walker PG, Oshinski JN, et al Slice location dependence of AR measurements with MR phase velocity mapping. *Magn Reson Med*. 1997;37:545–551
18. Søndergaard L, Lindvig K, Hildebrandt P, et al Quantification of AR by magnetic resonance velocity mapping. *Am Heart J*. 1993;125:1081–1890
19. Gillam LD. Is it time to update the definition of functional mitral regurgitation? Structural changes in the mitral leaflets with left ventricular dysfunction. *Circulation*. 2008;118:797–799

20. Carpentier A, Chauvaud S, Fabiani JN, et al Reconstructive surgery of mitral valve incompetence: ten-year appraisal. *J Thorac Cardiovasc Surg*. 1980;79:338–348
21. Waller B, Morrow A, Maron B, et al Etiology of clinically isolated, severe, chronic, pure mitral regurgitation: analysis of 97 patients over 30 years of age having mitral valve replacement. *Am Heart J*. 1982;104:276–288
22. He S, Fontaine AA, Schwammenthal E, et al An integrated mechanism for functional mitral regurgitation: leaflet restriction vs, coapting force - in vivo studies. *Circulation*. 1997;96:1826–1834
23. Zoghbi WA, Enriquez-Sarano M, Foster E, et al Recommendations for evaluation of the severity of native valvular regurgitation with two-dimensional and Doppler echocardiography. *J Am Soc Echo*. 2003;16:777–802
24. Chen CG, Thomas JD, Anconina J, et al Impact of impinging wall jet on color Doppler quantification of mitral regurgitation. *Circulation*. 1991;84:712–720
25. Grayburn P, Fehske W, Omran H, et al Multiplane transesophageal echocardiographic assessment of mitral regurgitation by Doppler color flow mapping of the vena contracta. *Am J Cardiol*. 1994;74: 912–917
26. Enriquez-Sarano M, Bailey KR, Seward JB, et al Quantitative Doppler assessment of valvular regurgitation. *Circulation*. 1993;87: 841–848
27. Recusani F, Bargiggia GS, Yoganathan AP, et al A new method for quantification of regurgitant flow rate using color Doppler flow imaging of the flow convergence region proximal to a discrete orifice: an in vitro study. *Circulation*. 1991;83:594–604
28. Bonow RO, Carabello BA, Chatterjee K, et al 2008 Focused update incorporated into the ACC/AHA 2006 guidelines for the management of patients with valvular heart disease: a report of the American College of Cardiology/American Heart Association Task Force on Practice Guidelines (writing committee to revise the 1998 guidelines for the management of patients with valvular heart disease): endorsed by the Society of Cardiovascular Anesthesiologists, Society for Cardiovascular Angiography and Interventions, and Society of Thoracic Surgeons. *Circulation*. 2008;118:e523–661
29. Lancellotti P, Cosyns B, Zacharakis D, et al Importance of left ventricular longitudinal function and functional reserve in patients with degenerative mitral regurgitation: assessment by 2-D speckle tracking. *J Am Soc Echocardiogr*. 2008;21:1331–1336
30. Piérard LA, Lancellotti P. The role of ischemic mitral regurgitation in the pathogenesis of acute pulmonary edema. *N Engl J Med*. 2004;35:1627–1634
31. Lancellotti P, Troisfontaines P, Toussaint AC, et al Prognostic importance of exercise-induced changes in mitral regurgitation in patients with chronic ischemic left ventricular dysfunction. *Circulation*. 2003;108:1713–1717
32. Lancellotti P, Gérard P, Piérard LA. Long-term outcome of patients with heart failure and dynamic functional mitral regurgitation. *Eur Heart J*. 2005;26:1528–1532
33. Hundley WG, Li HF, Willard JE. Magnetic resonance imaging assessment of the severity of mitral regurgitation. Comparison with invasive techniques. *Circulation*. 1995;92:1151–1158
34. Nath J, Foster E, Heidenreich PA. Impact of tricuspid regurgitation on long-term survival. *J Am Coll Cardiol*. 2004;43:405–409
35. Schnabel R, Khaw AV, von Bardeleben RS, et al Assessment of the tricuspid valve morphology by transthoracic real-time-3D-echocardiography. *Echocardiography*. 2005;22:15–23
36. Chopra HK, Nanda NC, Fan P, et al Can two-dimensional echocardiography and Doppler color flow mapping identify the need for tricuspid valve repair? *J Am Coll Cardiol*. 1989;14:1266–1274
37. Tribouilloy CM, Enriquez-Sarano M, Bailey KR, et al Quantification of tricuspid regurgitation by measuring the width of the vena contracta with Doppler color flow imaging: a clinical study. *J Am Coll Cardiol*. 2000;36:472–478

Chapter 9

HEART VALVE PROSTHESES

Luigi P. Badano and Rosa Sicari

CONTENTS

J. L. Zamorano et al. (eds.), *The ESC Textbook of Cardiovascular Imaging*
DOI: 10.1007/978-1-84882-421-8_9,

Introduction

Prosthetic heart valves may be mechanical or bioprosthetic. Mechanical valves, which are composed primarily of metal or carbon alloys, are classified according to their design as ball-caged, single-tilting-disc, or bileaflet-tilting-disc valves (Fig. 9.1). In ball-caged valves, the occluder is a sphere that is contained by a metal "cage" when the valve is in its open position, and fills the orifice when the valve is in its closed position. In single-tilting-disc valves, the occluder is a single circular disc that is constrained in its motion by a cage, a central strut, or a slanted slot in the valve ring; therefore, it opens at an angle less than 90° to the sewing ring plane. In bileaflet-tilting-disc valves, the two occluders are two semi-circular discs that open forming three orifices–a central one and two lateral ones.

Biological tissue-valve prostheses may be heterografts, which are composed of porcine, bovine, or equine tissue (valvular or pericardial), or homografts, which are preserved human aortic valves. Heterografts include stented and stentless bioprostheses (Fig. 9.2). In stented valves, the biological tissue of the valve is mounted on a rigid stent (plastic or metallic) and covered with a fabric. Conversely, stentless bioprostheses use the patient's native aortic root as the valve stent. The absence of a stent and sewing ring cuff make it possible to implant a larger valve for a given native annulus size, resulting in a greater effective orifice area (EOA).

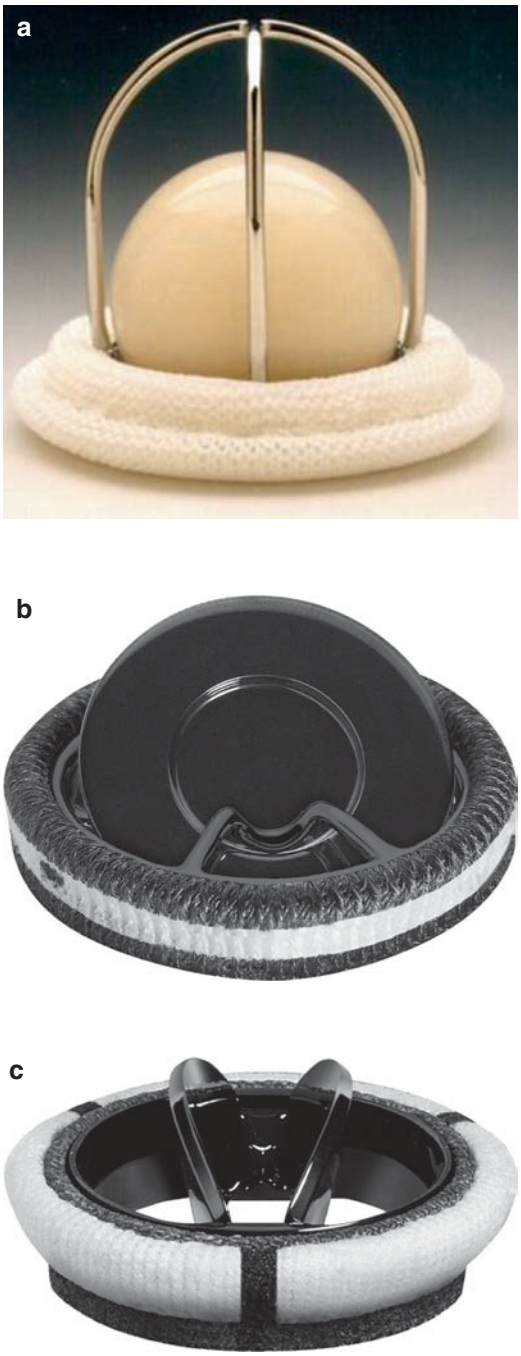

Fig. 9.1 Different types of mechanical valve prostheses. **(a)** Starr–Edwards ball-caged valve. **(b)** All carbon tilting-disc-valve, **(c)** Fit-line aortic bileaflet-tilting-disc valve. Courtesy of Edwards Lifesciences, Irvine, CA, and Sorin Biomedica Cardio S.p.A., Saluggia, IT

Heart Valve Prostheses Specifications and Functional Parameters

The size of mechanical and stented biological valve prostheses can be described using geometrical and functional parameters. Geometrical parameters are measurements obtained by the manufacturers and usually reported in product brochure. The sewing ring diameter (SRD) (measured in mm) is the largest diameter of the sewing cuff (Fig. 9.3). The internal orifice diameter (IOD, in mm) is the internal diameter of the stent. From the IOD, the geometric orifice area (GOA) of the prosthesis (the internal valve area theoretically available for the bloodstream to pass through) can be calculated using the geometric formula $\mu(IOD/2)^2$. The external diameter (ED, in mm) is the diameter of the stent plus fabric. From the ED, the mounting area of the prosthesis (the area that the prosthesis will occupy within the patient's native annulus) may be calculated using the geometric formula $\mu(ED/2)^2$. The latter is rarely reported in product brochures, but it is needed in order to calculate the ratio between the GOA and the mounting area. This ratio depends on the prosthesis design and gives an indication of the space subtracted from the native annulus "flow area" by the fixed structures (stent and cuff) of the prosthesis. This ratio also depends on the implant

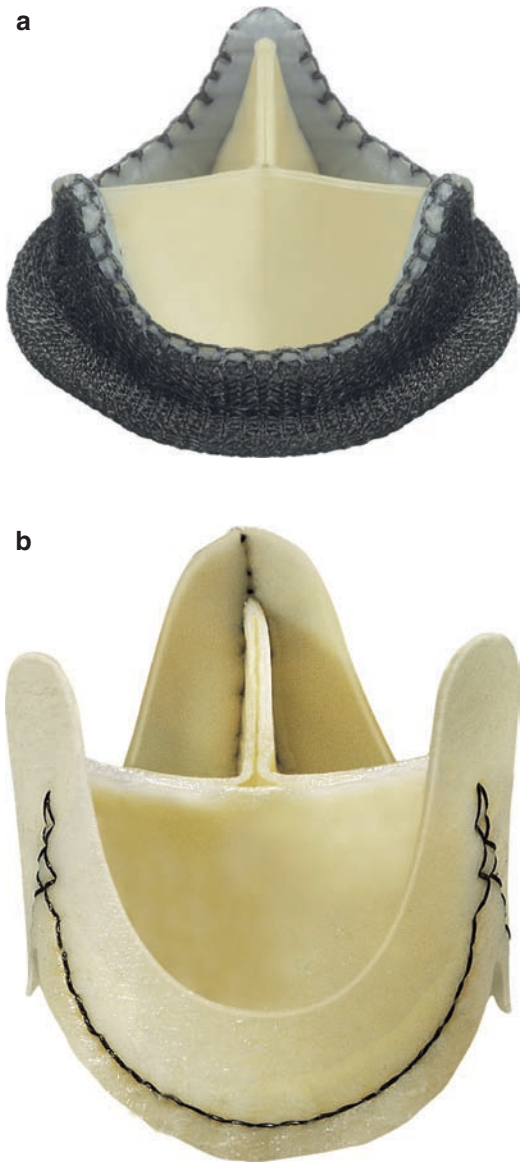

Fig. 9.2 Biological tissue valves. **(a)** Stented Soprano pericardial valve. **(b)** Stentless Solo pericardial valve. Courtesy of Sorin Biomedica Cardio S.p.A., Saluggia, IT

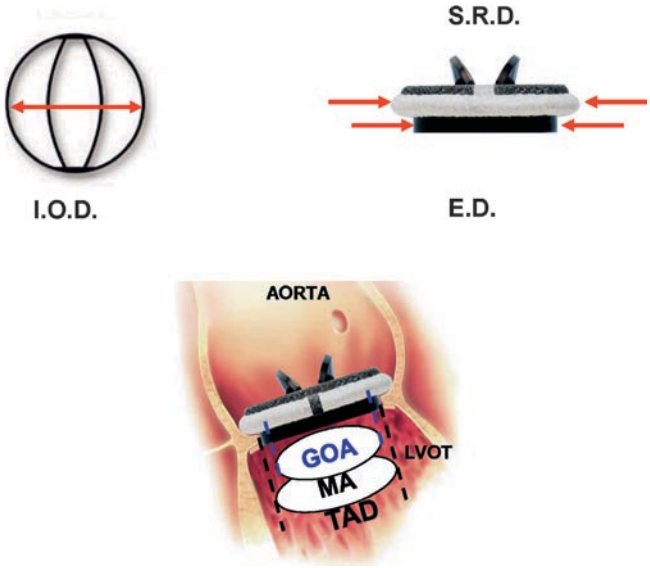

Fig. 9.3 Geometrical valve size specifications. The sewing ring diameter (SRD) is the maximum diameter of the sewing cuff. The ED is the diameter of the housing or housing plus fabric. From ED, the area that the prosthesis will occupy within the patient annulus (mounting area, MA) is calculated (see text for details). The IOD is the internal diameter of the housing. From IOD, the internal valve area theoretically available for bloodstream to pass through (geometric orifice area, GOA) is calculated (see text for details). LVOT, left ventricular outflow tract; TAD, native tissue annulus diameter

technique used. Generally, for a totally intra-annular prosthesis, this ratio is 40–70%,[1] and it increases to 80–85% for partially supra-annular prostheses, and reaches 100% (resulting in a maximization of blood flow) for totally supra-annular prostheses.

Functional parameters of prosthesis size include both in vitro and in vivo EOA. In vitro EOA can be measured under static hydrodynamic conditions at a variety of flow rates, or under dynamic conditions with variable pulsatile waveforms and flow rates. Estimates of static EOA for bioprostheses vary by as much as 100% as the steady flow rate increases. Dynamic pulsatile in vitro EOA data are non-standardized, unreproducible, and unavailable. Therefore, in vitro EOA is generally unsuitable for the assessment of the clinical effect of prosthesis size.[2] In vivo EOA is always smaller than the GOA and corresponds to the smallest area of the jet passing through the prosthesis as it exits the valve (vena contracta). Both the shape of the inlet and the size of the orifice affect the ratio between the geometric area and the EOA (coefficient of orifice contraction).[3]

For clinical purposes, the size of prostheses is reported as labelled prosthesis size (i.e. 19 mm, 21 mm, etc.). However, labelled size is often the approximation of an integer number (i.e. labelled size = Bicarbon 21 mm; actual size = 21.2 mm). Recently, the International Organization for Standardization (ISO) specification concerning the valve size labelling of heart valve prostheses (ISO/CD 5840) recommended that labelled prosthesis size should represent the tissue annulus diameter (TAD) of the patient into whom the valve is intended to be implanted.

Assessment of Prosthetic Valve Function

Several imaging techniques can be used to assess valve prosthesis function.

Echocardiography

Echocardiography remains the imaging technique of choice for the assessment of prostheses function. 2D transthoracic echocardiography can be used to assess sewing-ring stability and occluder motion (Fig. 9.4, Videos 9.4A–D). The mechanical valves have a specific pattern of echoes that can help to identify the type of prosthesis. A ball-caged valve will display a cage and the moving echo of the ball on the ventricular side. A single echo moving up and down on the ventricular side can be seen with a tilting-disc valve (Fig. 9.4, Videos 9.4A–D), and the two leaflets of the bileaflet valve can be visualized separately (Fig. 9.4, Videos 9.4A–D). The transthoracic echocardiography has a higher sensitivity for demonstrating the motion of the two leaflets of a bileaflet-tilting-disc valve in mitral position than for the aortic position. The heterograft bioprosthesis (porcine or pericardial) are trileaflet structures. The 2D and M-mode appearance of the leaflets of these valves is similar to those of the native aortic valve, which is a box-like opening in systole, if implanted in the aortic position (Fig. 9.5, Videos 9.5A and B), or in diastole, if implanted in the mitral position. However, similar to what happens with mechanical prosthesis, the sewing ring and the struts may limit the visualization of the leaflets. The stentless bioprosthetic aortic valves have an appearance similar to that of the native aortic valve, except for increased echogenicity in the aortic root (Fig. 9.5, Videos 9.5A and B). An aortic homograft appears similar to a native aortic valve except for an increased thickness in the left ventricular outflow tract (LVOT) and the ascending aorta.

However, mechanical valve prostheses and stented bioprostheses are often difficult to visualize (prosthesis in aortic position is more difficult than in mitral position) because of the presence of artificial components with far different acoustic properties that the surrounding cardiac tissue that creates reverberations, artefacts, and acoustic shadowing. The latter can be overcome with the use of the trans-oesophageal approach

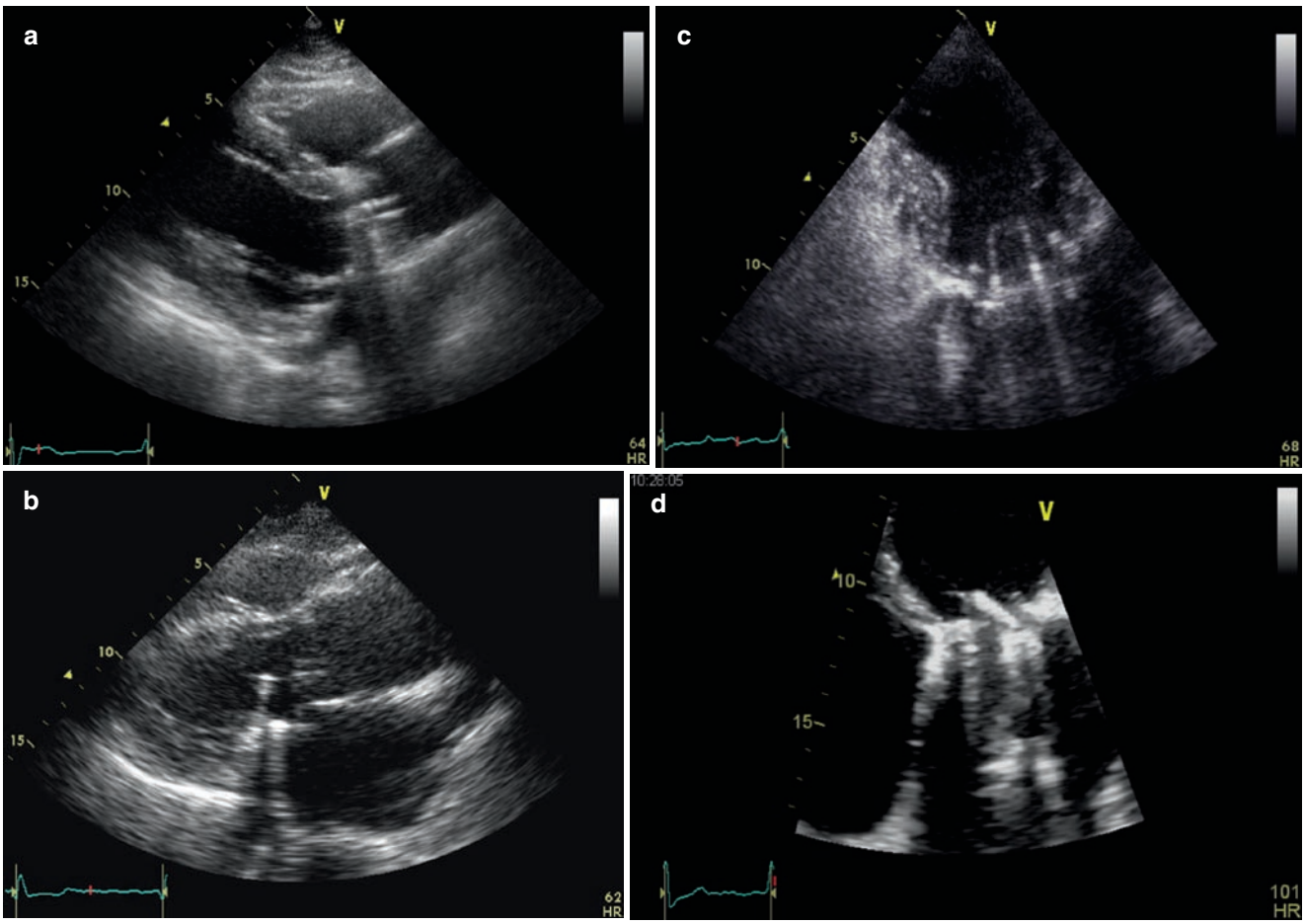

Fig. 9.4 2D echocardiographic characteristic features of mechanical heart valve. **(a)** Bileaflet-tilting-disc valve in aortic position visualized from parasternal approach. **(b)** Single-tilting-disc valve in mitral position visualized from parasternal approach. **(c)** Bileaflet-tilting-disc valve in mitral position visualized from apical approach. **(d)** Single-tilting-disc valve in mitral position visualized from apical approach

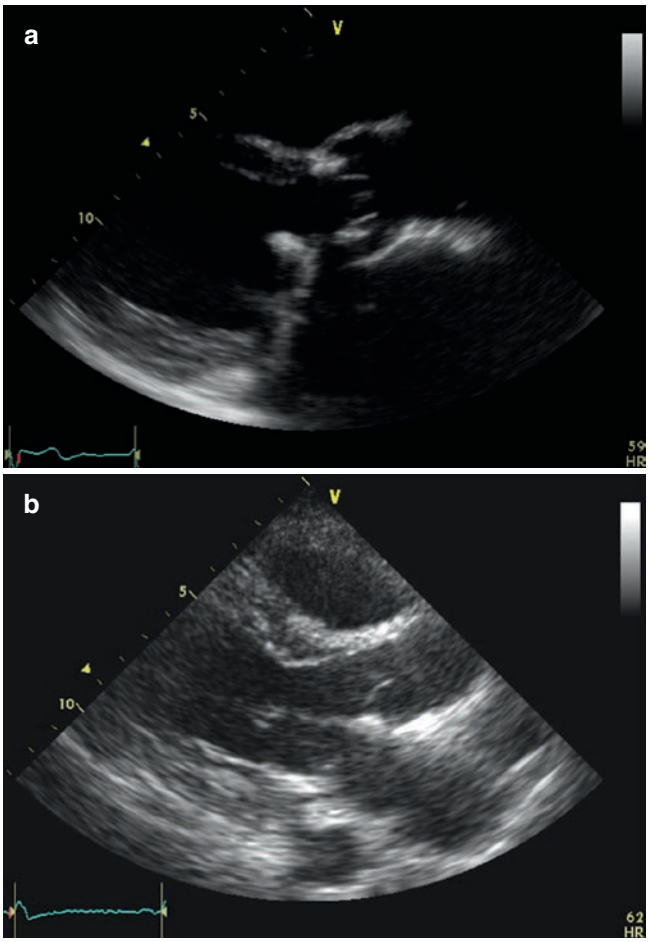

Fig. 9.5 Two dimensional echocardiographic characteristics of bioprostheses: stented bioprosthesis (Mosaic 23 mm) in aortic position visualized from parasternal approach **(a)** and stentless bioprosthesis (Freedom 21-mm) in aortic position visualized from parasternal approach **(b)**

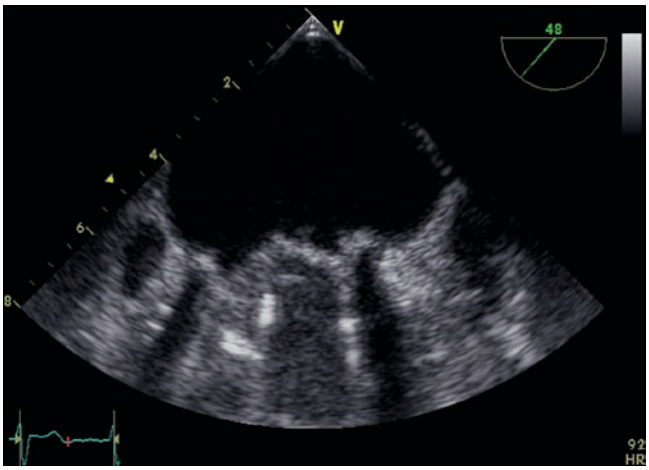

Fig. 9.6 Trans-oesophageal echocardiographic visualization of a normofunctioning bileaflet tilting-disc prosthesis in the mitral position.The metallic leaflet are very well visualized in systole, in the closing position. During systole there is an intense shadowing on the left ventricular side

and casting the shadowing in the opposite direction[4] (Fig. 9.6, Video 9.6). In addition, as all echo systems are calibrated to measure the distance on the velocity of ultrasound in the human body tissue, the presence of prosthetic material may alter the displayed size and location of the prosthesis and can distort the appearance of its components.

Transthoracic Doppler echocardiography, by providing a complete haemodynamic assessment, is pivotal in assessing a valve prosthesis function. The Bernoulli equation is used to calculate the peak and mean pressure gradients from the Doppler velocities. Although many assumptions are made in the derivation of the Bernoulli equation, an excellent correlation has been obtained. The continuity equation is used to calculate the effective aortic orifice area.

In general, the same principles used in native aortic valves are applicable to assess the function of the prosthetic valve using echocardiography. However, the fluidodynamic characteristics of the prosthetic valves are not exactly the same as those of the native valves, and proper formula should be used to calculate the reliable transprosthetic gradients and EOA. Although good agreement between Doppler-derived and catheter-derived pressure gradients for a variety of different valve prostheses has been reported (Table 9.1), some investigators have found significant overestimation of pressure gradients by Doppler in the prosthetic valves.[5,6] There are several reasons that may explain these apparent discrepancies between Doppler and catheter gradients. The presence of pressure recovery downstream from the prosthesis has been suggested as one potential cause.[5] Localized pressure gradients may be recorded by selectively sampling the velocity in the narrow "slitlike" central orifice of some bileaflet-tilting-disc prostheses,[5] but not in all.[7] However, the most important cause of transprosthetic gradient overestimation using Doppler echocardiography is a methodological one.

Routine echocardiographic assessment of gradients through stenotic native or prosthetic valves in the aortic position is usually performed using the "simplified" ($4V_2^2$) instead of the "modified" [$4(V_2^{2-}V_1^2)$] Bernoulli equation (the former does not take into account the velocity [V_1] in the LVOT). However, the simplified Bernoulli equation ignores the viscous friction and the energy required to overcome the initial forces caused by flow acceleration found in a pulsatile system, and is only reliable for flow that is[8]:

1. Through a restrictive orifice (negligible inertial component), and
2. With V_2 much greater than V_1.

Table 9.1. Studies that have validated transprosthetic gradients measured by Doppler echocardiography with cardiac catheterization data

Author/reference	Valve type/position	Type of study (patients)	*r*	SEE (mmHg)
Sagar[37]	Hancock, Bjork-Shiley/Mitral	In vivo (19)	0.93	2.5
	Hancock, Bjork-Shiley/Aortic	In vivo (11)	0.94	7.4
Wilkins[38]	Starr-Edwards, Bjork-Shiley, porcine/Mitral	In vivo (11)	0.96	
Burstow[39]	Not specified/ Aortic	In vivo (20)	0.94	3
	Not specified/Mitral	In vivo (20)	0.97	1.2
Baumgartner[40]	St Jude	In vitro	0.98	1.9
	Hancock	In vitro	0.98	1.4
Stewart[41]	Bioprostheses	In vitro	0.78–0.98	
Baumgartner[42]	St Jude	In vitro	0.98	2.0
	Medtronic-Hall	In vitro	0.99	0.5
	Starr-Edwards	In vitro	0.97	2.0
	Hancock	In vitro	0.99	1.5

As new normofunctioning prosthetic valves (especially stentless and stented supra-annular bioprostheses) do not have a restrictive orifice, and show very low V_2 values (usually < 2 m/s), the use of the simplified Bernoulli equation causes a significant overestimation of transprosthetic gradients also in patients with V_1 < 1 m/s. This overestimation may be negligible in stenotic native valves with a restrictive orifice and high V_2 values (+3 to +5%), but it is clinically significant in normofunctioning bioprosthetic stentless valves (+13 to +19%).[9]

In vivo EOA for prosthesis in aortic position is calculated from the continuity equation. The continuity equation assumes that flow coming into the narrowed orifice has a flat profile. The actual flow profile varies between prostheses, with mechanical tilting-disc prostheses having the greatest variance from a flat profile, and bioprosthetic valves showing a nearly flat profile of transprosthetic flow.[1]

Similar to stenotic native valves, the main source of error in calculating prosthesis EOA with the continuity equation is the measurement of the LVOT diameter. Due to the potential errors (inner-edge-to-inner-edge measurement, foreshortening of LVOT) and limitations (interference of prosthesis shadowing), it was suggested that the nominal size of the replacement heart valve should be substituted for the direct measurement of the outflow tract when applying the continuity equation.[10,11] The assumption is that, regardless of the manufacturer or model, all valves of a certain nominal size are interchangeable for a given patient tissue annulus diameter. However, this is not true. Studies attempting to assess the size of a valve by echocardiography show good agreement between LVOT diameter and valve size for stentless valves.[12] Conversely, as much as 2 mm difference was shown in one study on mechanical and stented biological valves.[13] Another study found a 95% confidence interval from −8.5 to +5.1 mm between LVOT measured by transthoracic echocardiography and nominal valve size.[14] Therefore, the ED of the prosthesis (if known), but not the labelled size, can be used as a surrogate for LVOT diameter. However, the ED of the prosthesis is rarely available; hence, the most convenient way is still to measure the LVOT diameter during the baseline echocardiographic assessment of a given valve, and then use this constant value during follow-up echocardiographic controls.

Although the Hatle's method has been proposed to calculate the EOA for prosthetic valves in mitral position, it should be theoretically applicable to such valves, as pressure half-time is a physiologic measure of obstruction and does not require assumptions about inlet geometry and flow rate.[15] However, there is now good evidence that the Hatle's method is not valid in normofunctioning prosthetic valves in mitral position.[7,16] In such valves with relatively large orifice areas, the pressure half-time is more dependent on other factors such as heart rate, transmitral pressure gradient at the onset of diastole, stroke volume, and left atrial and ventricular compliance, than on prosthetic orifice area.

A complete echocardiographic study should include estimation of the pressure peak and mean gradients, valve area, and mean transprosthetic flow rate. However, there are some peculiarities that should be taken into account to correctly interpret echocardiographic results.

First, all prostheses are not equal. Different types (i.e. mechanical bileaflet, mechanical tilting-disc, stented bioprosthesis, stentless bioprosthesis) show markedly different haemodynamics. For example, an EOA of 1.1 cm may be

normal in a 21 mm single-tilting-disc prosthesis,[16] but it will be a pathologic finding in a 21 mm stentless bioprosthesis (Table 9.2). Different models of the same type show markedly different haemodynamics, despite having the same labelled size and being made of the same tissue (i.e. bovine pericardium).[17] The 21 mm Hancock II-stented bioprosthesis shows a mean EOA (1.2 ± 0.7 cm^2)[18] that is significantly lower than or the Pericarbon (1.5 ± 0.4 cm^2).[19] Different sizes of the same valve model and type show different haemodynamics (Table 9.2).[17] Therefore, the important message to the echocardiographer is the need to know the model, type, and size of the implanted valve, in order to interpret echocardiographic haemodynamic data correctly.

Second, reference values reported in the literature about the haemodynamic performance of different valve prostheses represent a poor reference for the individual patient. This is particularly true for biological prostheses. Estimates of bioprosthesis in vivo EOA are particularly sensitive to cardiac output and blood pressure.[20] In addition, in vivo EOA of stentless bioprostheses has been observed to increase during the first year after implantation, as haemodynamic data change and perivalvular haematoma and oedema resolve. Transprosthetic gradients are particularly sensitive to transprosthetic flow rate and change significantly with the haemodynamic state of the patient. Therefore, the second important message to the echocardiographer is to obtain a baseline, full haemodynamic assessment of that prosthesis in a given patient together with his/her haemodynamic status (i.e. body surface area, cardiac rhythm, heart rate, blood pressure, haemoglobin level, and left ventricular function) to use as a reference for interpreting follow-up studies.

The timing of baseline assessment of valve prosthesis haemodynamics is crucial. Ideally, it should be performed as soon as possible after the operation, to make sure that the valve is actually normofunctioning (i.e. no tissue degeneration for biological valves or pannus formation for mechanical valves), but not too soon, in order to avoid misleading data. In patients undergoing aortic valve replacement, there is a relatively high output state immediately after the operation due to relative anaemia and sudden reduction of left ventricular afterload, which affects transprosthetic gradients. Moreover, perivalvular oedema and haematoma may reduce prosthetic EOA. Finally, left ventricular function will change significantly soon after aortic valve replacement due to regression of hypertrophy and adaptation to the changed pre- and afterload conditions. Therefore, the optimal timing of the baseline assessment of valve prosthesis haemodynamics should be placed between the third and the sixth month (not later than 1 year) after surgery. The predischarge study should be used to assess postoperative left ventricular function, exclude complications or early malfunction of the prosthesis, but not to assess normal function parameters of a certain valve in a given patient.

Follow-up examinations in asymptomatic patients without complications and with a "normal" initial echocardiogram can be performed at yearly intervals, and should consist of a detailed history and physical examination. Echocardiography should be performed whenever there is evidence of a new heart murmur, when there are doubts of prosthetic valve integrity or function, or when there are concerns about ventricular or other valve function. There is no support in the literature for the strategy of performing a Doppler echocardiogram annually in patients without complications.[21]

Stress Echocardiography in Valvular Prostheses

The application of stress echocardiography for valve prostheses assessment is still a moving target that needs to be addressed in prospective studies in order to demonstrate its potential and additive value in this subset of patients. Nonetheless, a dynamic assessment of prostheses (in particular, mitral and aortic) appears to be very promising. Evidence accumulated in the last 5 years has led to the incorporation of stress echocardiography in the guidelines of American Heart Association/American College of Cardiology,[22] European Society of Cardiology,[23] and in the latest recommendations of stress echocardiography use in valvular heart disease of American Society of Echocardiography[24] and European Association of Echocardiography.[25]

The main indication to stress echocardiography in patients with valve prosthesis is the presence of exertional symptoms in a patients with normal functional parameters of the prosthesis at echocardiography (both transthoracic and trans-oesophageal) and normal excursion of the occluder at cinefluoroscopy evaluating prosthetic valve dysfunction. In these patients, exercise stress echocardiography should be performed to evaluate the valve prosthesis haemodynamics at higher cardiac outputs. A disproportionate transvalvular gradient rise suggests the possibility of prosthesis dysfunction. In patients with normal prosthetic valve, only an absent-to-mild stenosis is expected at rest, with a mean gradient <5 mmHg for mitral and <25 mmHg for aortic prostheses. In patients with normal prosthetic valves and left ventricular function, only a mild-to-moderate increase in pressure gradients during high flow states is expected, usually <100% of baseline values. Conversely, individuals with stenotic prosthesis have severe increase (up to >100%) in the transprosthesis gradient, with absolute mean pressure gradient >10 mmHg for mitral[26] and >40 mmHg for aortic prosthesis[27, 28] (Figs. 9.7 and 9.8, Video 9.8). This can be an unsettling outcome, considering that the patient's daily activities may well evoke similar pressure gradients. Careful assessment by a controlled stress examination might guide recommendations for

Table 9.2. Published data about Doppler haemodynamic parameters of normofunctioning prosthetic valves in aortic position

Type	Doppler	Size (mm)									
	Parameter	19	20	21	22	23	24	25	26	27	29
Single-tilting-disc valves											
Starr-Edwards (n = 79)	GOA			1.41		1.67	1.79		1.94	2.16	2.57
	EOA			1.3		1.45	1.44		1.53	1.53	1.53
	Mean gr.			34 ± 6		29 ± 11	27 ± 9		23 ± 8	23 ± 1	
Bjork-Shiley[a] (n = 106)	GOA	1.5		2		2.5		3.1		3.8	4.6
	EOA	0.7 ± 0.2		1.1 ± 0.1		1.6 ± 0.3		2.0 ± 0.4		2.6 ± 0.4	
	Mean gr.	16 ± 4		13 ± 5		13 ± 3		11 ± 4		8 ± 4	
Medtronic-Hall (n = 108)	GOA										
	EOA			1.2 ± 0.5		1.1 ± 0.2		1.4 ± 0.4		1.9 ± 0.4	1.9 ± 0.5
	Mean gr.			14 ± 6		14 ± 5		10 ± 4		9 ± 6	
Omnicarbon (n = 49)	GOA	1.63		2.11	2.55		3.14		3.80	3.80	
	EOA			1.4 ± 0.1		1.5 ± 0.2		1.8 ± 0.4		1.9 ± 0.4	2.2 ± 0.2
	Mean gr.			21 ± 7		13 ± 3		11 ± 4		13 ± 3	9 ± 2
Allcarbon (n = 83)	GOA	1.5		2.0		2.5		3.1		3.8	4.5
	EOA	0.9 ± 0.1		1.1 ± 0.2		1.4 ± 0.2		2.1 ± 0.8		2.8 ± 0.6	4.1 ± 0.7
	Mean gr.	29 ± 8		22 ± 7		20 ± 6		15 ± 4		11 ± 4	8 ± 2
Bileaflet-tilting-disc valves											
St Jude medical (n = 67)	GOA	1.63		2.06		2.55		3.09		3.67	4.52
	EOA	1.0 ± 0.2		1.3 ± 0.2		1.3 ± 0.3		1.8 ± 0.4		2.4 ± 0.6	2.7 ± 0.3
	Mean gr.	17 ± 7		14 ± 5		16 ± 6		13 ± 6		11 ± 5	7 ± 1
St Jude medical Hp (n = 49)	EOA	1.7 ± 0.2		2.2 ± 0.3							
	Mean gr.	16 ± 4		10 ± 3							
(n = 96)	EOA	1.0 ± 0.4		1.5 ± 0.3		1.6 ± 0.3		2.0 ± 0.4		2.4 ± 0.5	2.6 ± 0.4
	Mean gr.	19 ± 6		12 ± 4		10 ± 4		8 ± 4		9 ± 3	6 ± 3
Carbomedics Top-Hat (n = 65)	GOA										
	EOA	1 ± 0.2		1.2 ± 0.3		1.4 ± 0.4					
	Mean gr.	20 ± 2		17 ± 6		13 ± 4		11			
Duromedics Tekna (n = 90)	GOA	1.53		2.02		2.36		2.94		3.58	
	Mean gr.			8 ± 5		7 ± 2		5 ± 2		6 ± 3	
Bicarbon (n = 166)	GOA	1.76		2.27		2.83		3.45		4.14	5
	EOA	1.0 ± 0.3		1.6 ± 0.3		2.1 ± 0.4		2.5 ± 0.6		3.6 ± 0.8	3.5 ± 0.3
	Mean gr.	13 ± 1		14 ± 5		11 ± 4		11 ± 3		7 ± 2	5 ± 1
ATS open pivot (n = 59)	EOA	1 ± 0.2		1.6 ± 0.4		1.8 ± 0.2		2.2 ± 0.4		2.5 ± 0.3	3.1 ± 0.3
	Mean gr.	26 ± 8		14 ± 4		12 ± 4		11 ± 4		9 ± 2	8 ± 2
On X (n = 60)	EOA	1.5 ± 0.2		1.7 ± 0.4		2 ± 0.6		2.4 ± 0.8		3.2 ± 0.6	
	Mean gr.	12 ± 3		10 ± 4		9 ± 3		9 ± 5		6 ± 3	
Jyros (n = 23)	EOA				1.5		1.5		1.7		
	Mean gr.				11		11		8		
Stented bioprostheses											
Hancock I (n = 64)	EOA										
	Mean gr.						12 ± 4	11 ± 2		10 ± 3	
Hancock II (n = 376)	EOA	1.2 ± 0.3					1.4 ± 0.2	1.5 ± 0.2		1.6 ± 0.2	1.6 ± 0.2
	Mean gr.	15 ± 4					17 ± 7	3		—	—
Bio medical°	EOA				1.3 ± 0.4			1.6 ± 0.6	2.1 ± 0.7	3.2	
	Mean gr.			9 ± 4				8 ± 2	7 ± 5	6	

Table 9.2. (continued)

Type	Doppler	Size (mm)									
	Parameter	19	20	21	22	23	24	25	26	27	29
Carpentier-Edwards porcine (n = 419)	EOA Mean gr.	0.9 ± 0.2 26 ± 8		1.5 ± 0.3 17 ± 6			1.7 ± 0.5 16 ± 6	1.9 ± 0.5 13 ± 4		2.3 ± 0.5 12 ± 6	2.8 ± 0.5 10 ± 3
Carpentier-Edwards pericardial (n = 75)	EOA Mean gr.	1.2 ± 0.1 24 ± 9		1.5 ± 0.4 20 ± 9			2.3 ± 0.5	1.8 ± 0.3	— 9 ± 2	— 6	
Carpentier-Edwards supra-annular (n = 23)	EOA Mean gr.	1.1 ± 0.1		1.1 ± 0.2 14 ± 5							
Medtronic intact (n = 243)	EOA Mean gr	24 ± 9		1.6 ± 0.4 19 ± 8			1.7 ± 0.4 19 ± 6	1.9 ± 0.3 16 ± 6		2.2 ± 0.2 15 ± 4	2.4 ± 0.5 16 ± 2
Medtronic mosaic (n = 279)	EOA Mean gr.			1.6 ± 0.7 12 ± 7			12 ± 7	2.1 ± 0.8	10 ± 5	2.1 ± 1.6 9	
Mitrofow (n = 21)	EOA Mean gr.	1.1 ± o.2 10 ± 3		15			8 ± 3		11 ± 7	7 ± 2	
Pericarbon more (n = 22)	EOA Mean gr.	1.2 ± 0.3 23 ± 9		1.5 ± 0.4 18 ± 8			16 ± 5	1.8 ± 0.5			
Soprano (n = 77)	EOA Mean gr.				7 ± 4	1.9 ± 0.5		7 ± 4	2.1 ± 0.5		
Ionescu-Shiley (n = 95)	EOA Mean gr.	1.2 ± 0.2 20 ± 9		15 ± 2			10 ± 3			9 ± 6	
Stentless bioprostheses											
Toronto SPV	EOA	1.3 ± 0.38		1.2 ± 0.7			1.2	1.6 ± 0.8	1.6 ± 0.4	2.0 ± 0.4	
(n = 554)	Mean gr.	8 ± 4	5	8 ± 4				7 ± 4	6 ± 4	5 ± 2	
Medtronic freestyle (n = 369)	EOA Mean gr.	13		1.6 ± 0.3 8 ± 3			7 ± 3	1.9 ± 0.5	2.0 ± 0.4 5 ± 2	2.5 ± 0.5 5 ± 2	
O'Brien Angell (n = 50)	EOA Mean gr.			1.2 ± 0.1 15 ± 8 9 ± 1			19 ± 13 8 ± 1	1.1 ± 0.3	1.6 ± 0.2 18 ± 13 9 ± 1	2.1 ± 1.2 12 ± 7 7 ± 1.4	
Cryolige O'Brien (n = 329)	EOA Mean gr.	1.3 ± 0.1 12 ± 5		1.6 ± 0.6 10 ± 2			9	2.2	2.3 8	2.7 7	
Edwards prima (n = 253)	EOA Mean gr.	1 ± 0.3 15 ± 7		1.3 ± 0.3 16 ± 11			1.5 ± 0.5 12 ± 5	1.7 ± 0.6 11 ± 9		2 ± 0.6 7 ± 4	2.5 ± 0.5 5 ± 5
Biocor (n = 331)	EOA Mean gr.			1.4 ± 0.5 18 ± 4			19 ± 7	1.6 ± 0.4	18 ± 7	1.9 ± 0.5 18 ± 2	
Biocor extended (n = 50)	EOA Mean gr.	1.3 ± 0.4 10 ± 4		1.6 ± 0.3 8 ± 3			8 ± 2	1.8 ± 0.3			
Homograft (n = 27)	EOA Mean gr.			2.1 ± 1.3 13 ± 1			10	3.6	2.4 ± 0.7 8 ± 2	2.6 ± 1 12 ± 1	

[a]Monostrut *GOA* geometric orifice area, provided by the manufacturer in cm^2, *EOA* effective orifice area (continuity equation) in cm^2, *Mean gr.* mean transprosthetic gradient in mm; *n* examined patients

prescribed activity levels. However, the actual prognostic benefit of the increase in mean gradient with stress is difficult to assess. Despite its utility in determining the function of the valves, most studies do not show a convincing correlation among valve size, resting and exercise gradients, and exercise capability.[28] There is also contradictory evidence linking high gradients with a higher risk of death and other complications.[29,30] When a normally functioning aortic prosthesis does

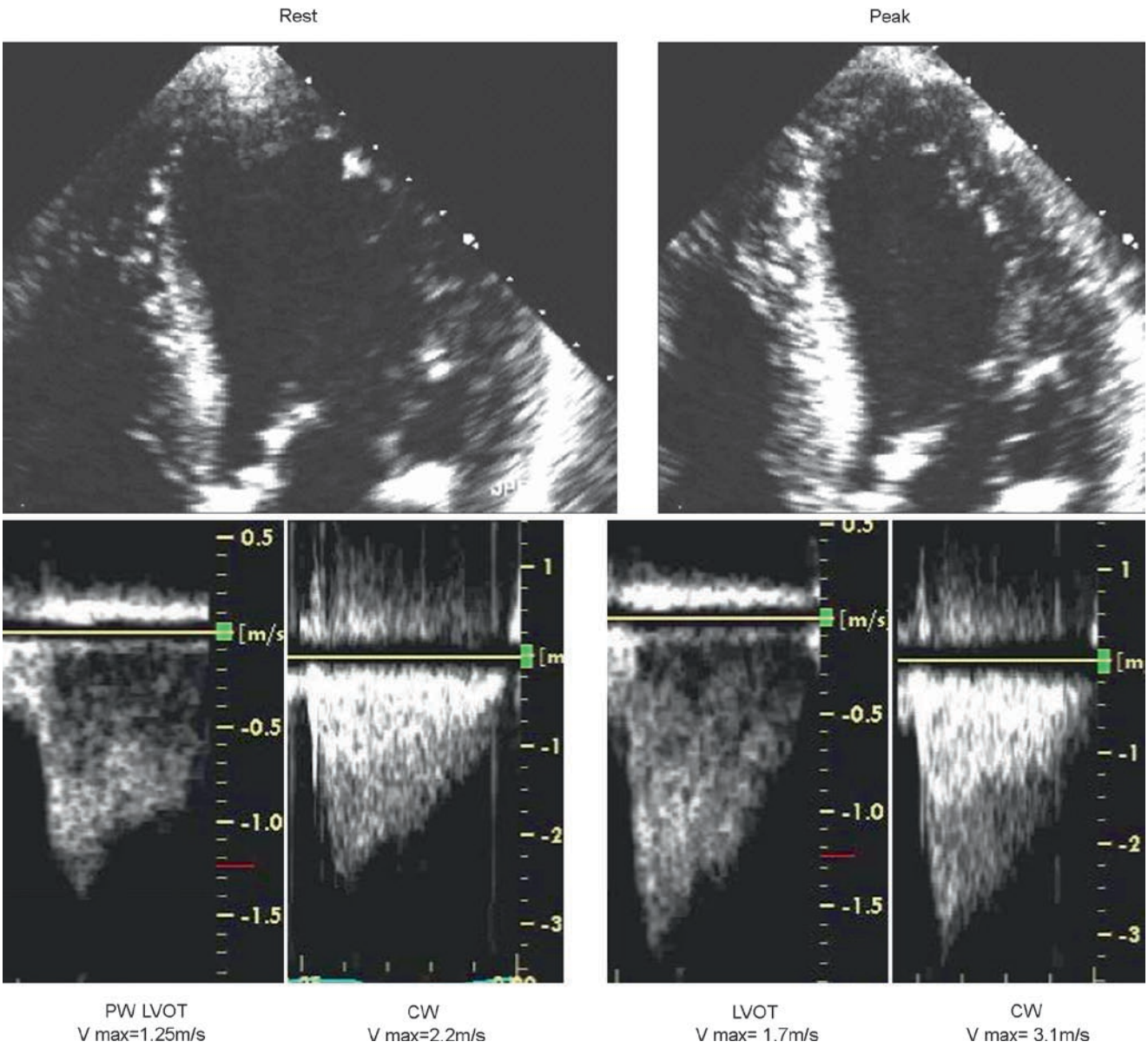

Fig. 9.7 Exercise echocardiography in a patient with aortic prosthetic valve

not provide an adequate outflow area in relation to the cardiac output based on patient size, it is known as valve prosthesis–patient mismatch.[31] Prothesis–patient mismatch was first described in 1978 by Rahimtoola as follows: "Mismatch can be considered to be present when the effective prosthetic valve area, after insertion into the patient, is less than that of a normal human valve."[31] Thus, prosthesis–patient mismatch is observed when the effective orifice of the inserted prosthetic valve is too small in relation to the body size. Its main haemodynamic consequence is to generate higher than expected gradients through normally functioning prosthetic valves. Prosthesis–patient mismatch is common (20–70% of aortic valve replacements) and has been shown to be associated with worse haemodynamic function, less regression of left ventricular hypertrophy, more cardiac events, and lower survival.[28] The presence of a mild (1.0–0.5 cm^2/m^2), moderate (0.85–0.6 cm^2/m^2), and especially severe (<0.6 cm^2/m^2) patient–prosthesis mismatch has a negative impact on survival, especially in the presence of a depressed left ventricular function[28] (Figs. 9.9–9.11). Patient–prosthesis mismatch is, by far, the most frequent cause of increased transprosthetic gradient. It is important to differentiate this condition from acquired prosthetic obstruction, which may result from leaflet calcification of bioprostheses and pannus overgrowth or thrombus formation on mechanical prostheses. In contrast to a normally functioning and well-matched prosthesis (including a bileaflet mechanical valve with a localized high gradient at rest), an obstructed valve prosthesis or patient–prosthesis mismatch is generally associated with a marked increase

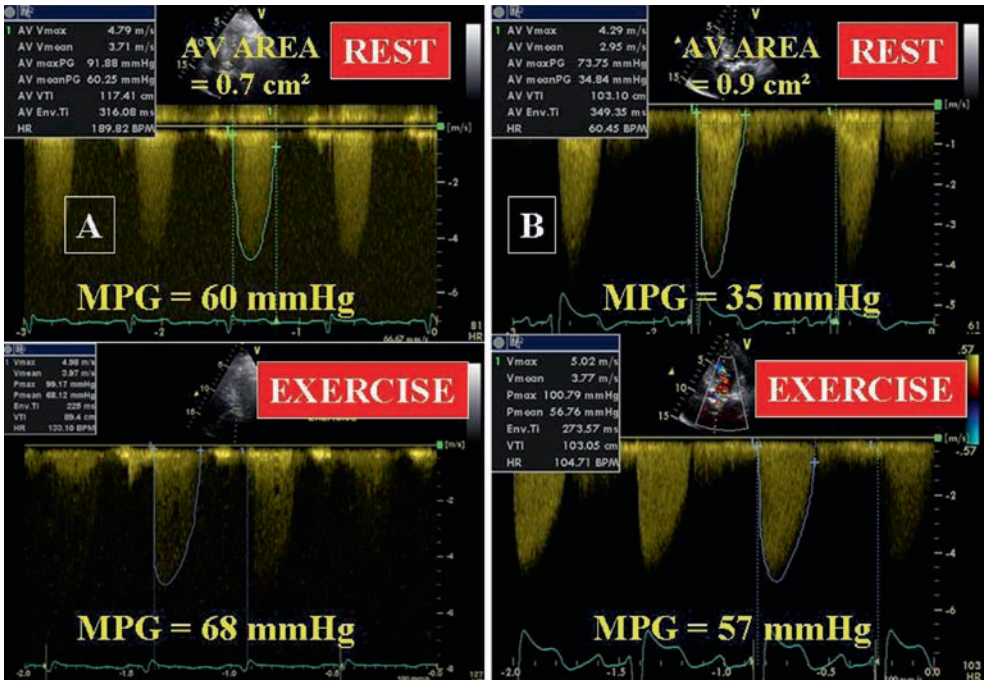

Fig. 9.8 Examples of exercise-induced changes in mean transaortic pressure gradient (MPG) in two asymptomatic patients with severe aortic stenosis. **(a)** Small increase in MPG with exercise. **(b)** Significant exercise-induced increase in MPG

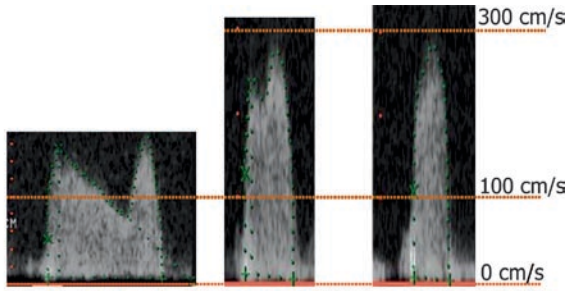

	Rest	30-W excercise	Peak Excercise
HR (b/min)	55	116	159
DFT (ms)	607	228	200
SV (ml)	66	59	57
Q_{mean} (ml/s)	109	259	284
ΔP (mmHg)	5	23	27
PAPs(mmHg)	40	62	69

Fig. 9.9 Exercise stress echocardiography in a symptomatic patient with mitral stenosis (mitral valve area: 1.2 cm^2) and relatively low resting mean transmitral pressure gradient (ΔP). With exercise, there is a marked increase in the transvalvular gradient and systolic pulmonary arterial pressure (PAPs). In this patient, the exercise-induced increase in mean transvalvular flow rate (Q_{mean}) was caused by the dramatic shortening in diastolic filling time (DFT). *HR* heart rate; *SV* stroke volume

in gradient with exercise, often associated with pulmonary arterial hypertension, development of symptoms, and impaired exercise capacity on exercise echocardiography. A disproportionate increase in transvalvular gradient (>20 mmHg for aortic prostheses or > 12 mmHg for mitral prostheses) generally indicates severe prosthesis dysfunction or patient–prosthesis mismatch (Fig. 9.11). High resting and stress gradients occur more often with biological rather than mechanical prostheses, stented rather than stentless bioprostheses, smaller (≤21 for aortic and ≤25 for mitral) rather than larger size prostheses, and mismatched rather than non-mismatched prostheses. In fact, the behaviour of the transprosthetic pressure gradient under exercise conditions is essentially determined by the indexed EOA (Fig. 9.11), which in turn may be influenced by the patient's body size, prosthesis model and size, mismatch between body size and prosthesis size, and pathologic obstruction of the prosthesis caused by leaflet calcification, pannus, or thrombus. It should be emphasized that exercise stress echocardiography does not distinguish between acquired prosthesis stenosis and patient–prosthesis mismatch, as in both cases, the EOA remains small and the gradient increases markedly with stress. In this situation, one should compare the EOA values obtained during stress echocardiography with the normal reference values of EOA for the model and size of the specific prosthesis that has been implanted in the patient. If the measured EOA is substantially lower than the normal reference EOA, one should suspect prosthesis dysfunction. If, on the other hand, the measured EOA is within the normal reference range and the indexed EOA is low, one should consider the presence of patient–prosthesis mismatch.

The additive value of exercise stress echocardiography in this subset of patients remains to be established, and current guidelines do not recommend its routine use.

Nonetheless, as it applies to asymptomatic aortic stenosis, semi-supine exercise stress echocardiography can provide potential useful information on symptom status, behaviour of velocities at peak exercise, and contractile function. Thus, further studies are needed in this challenging field.

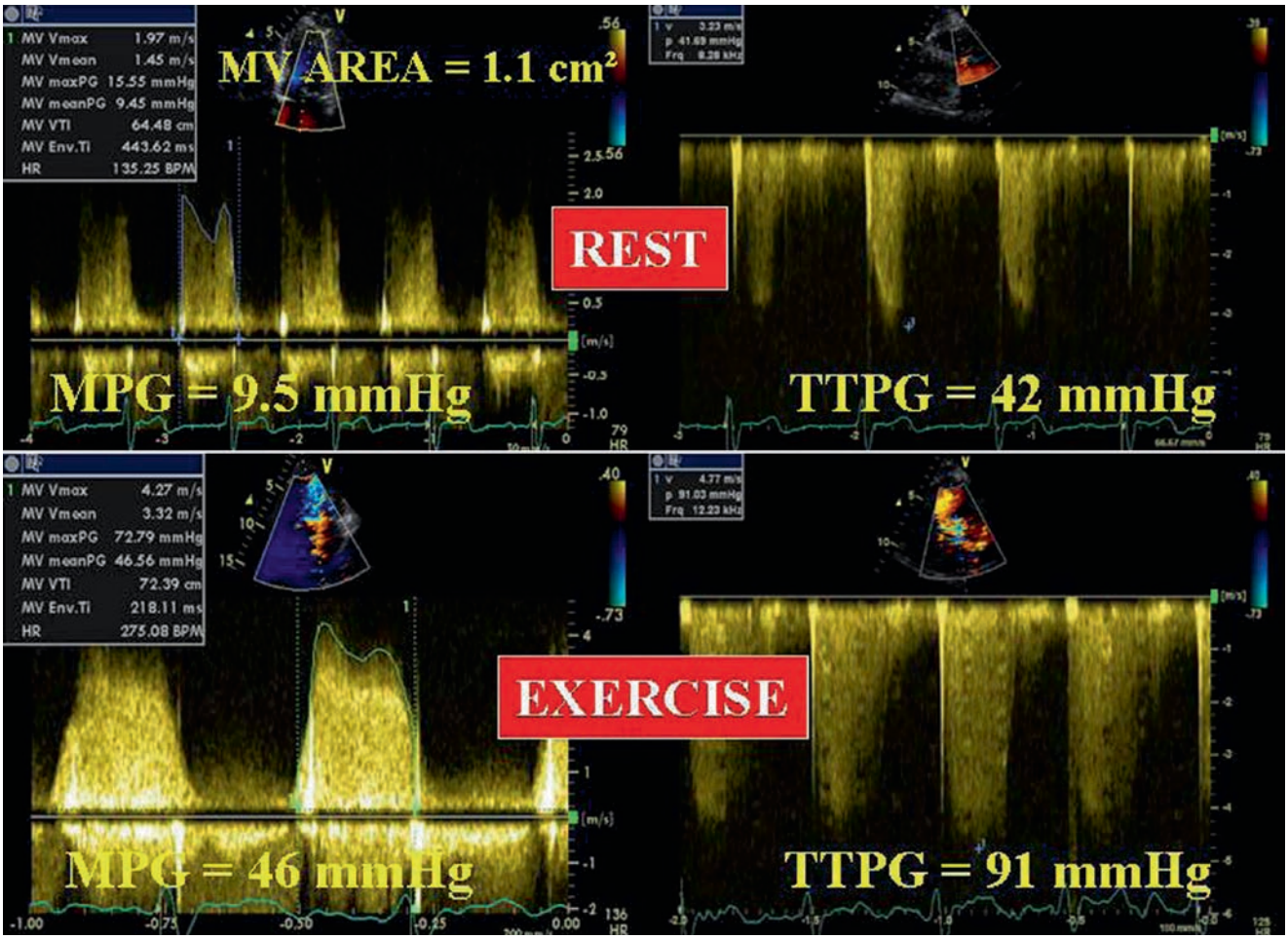

Fig. 9.10 Example of an asymptomatic patient with severe mitral valve stenosis, but with moderately elevated mean transmitral pressure gradient (MPG) at rest. During exercise, the MPG increases markedly as does the systolic transtricuspid pressure gradient (TTPG), indicative of pulmonary hypertension

Cinefluoroscopy

Cinefluoroscopy is a simple, rapid, inexpensive, and accurate technique to assess valve prosthesis function. The main indications for cinefluoroscopy are in patients with abnormally high aortic or mitral gradients or unusual regurgitant flow patterns observed with colour Doppler echocardiography.

The cinefluoroscopic exam usually begins by determining the valve's rotational orientation with a view perpendicular to the valve plane. By positioning the image intensifier in the right anterior oblique cranial position, the view is roughly perpendicular to either the aortic or mitral valve plane. Occasionally, a left anterior oblique caudal view is required to image the mitral valve. For example, in a normally functioning bileaflet-tilting-disc valve, two parallel lines appear and disappear intermittently. If only one (or neither) of the lines fails to appear or disappear, the valve leaflet motion may be restricted or one leaflet may have escaped. Then we should obtain a side view to assess the leaflet opening and closing angles (Fig. 9.12, Videos 9.12A and B). To obtain this view, the image intensifier is moved 90°longitudinally, usually caudally and transversely, to a position in line with the valve leaflet axis of rotation. Opening and closing angles are defined as the distance between the valve housing and the disc at its full opening and closing in single-disc valves, and as the distance between leaflets in the fully open and closed positions for bileaflet valves. Table 9.3 lists the approximate normal opening and closing angles of several heart valve prostheses. Deviation from the listed angles or differences between the open or closed angle of one leaflet relative to the other in bileaflet valves may indicate restricted leaflet motion. A slight asynchrony of leaflet motion is normal, especially in valves in mitral position.

Although it cannot visualize the leaflet of bioprostheses, it is very useful to assess the excursion of occluders in mechanical valves; a diminished motion of the disc or poppet suggests obstruction of the prosthesis from thrombus or ingrowth of tissue (Fig. 9.13, Video 9.13).[32] Conversely, excessive tilt or rocking of the sewing ring is consistent with partial dehiscence of the valve (Fig. 9.14, Video 9.14).

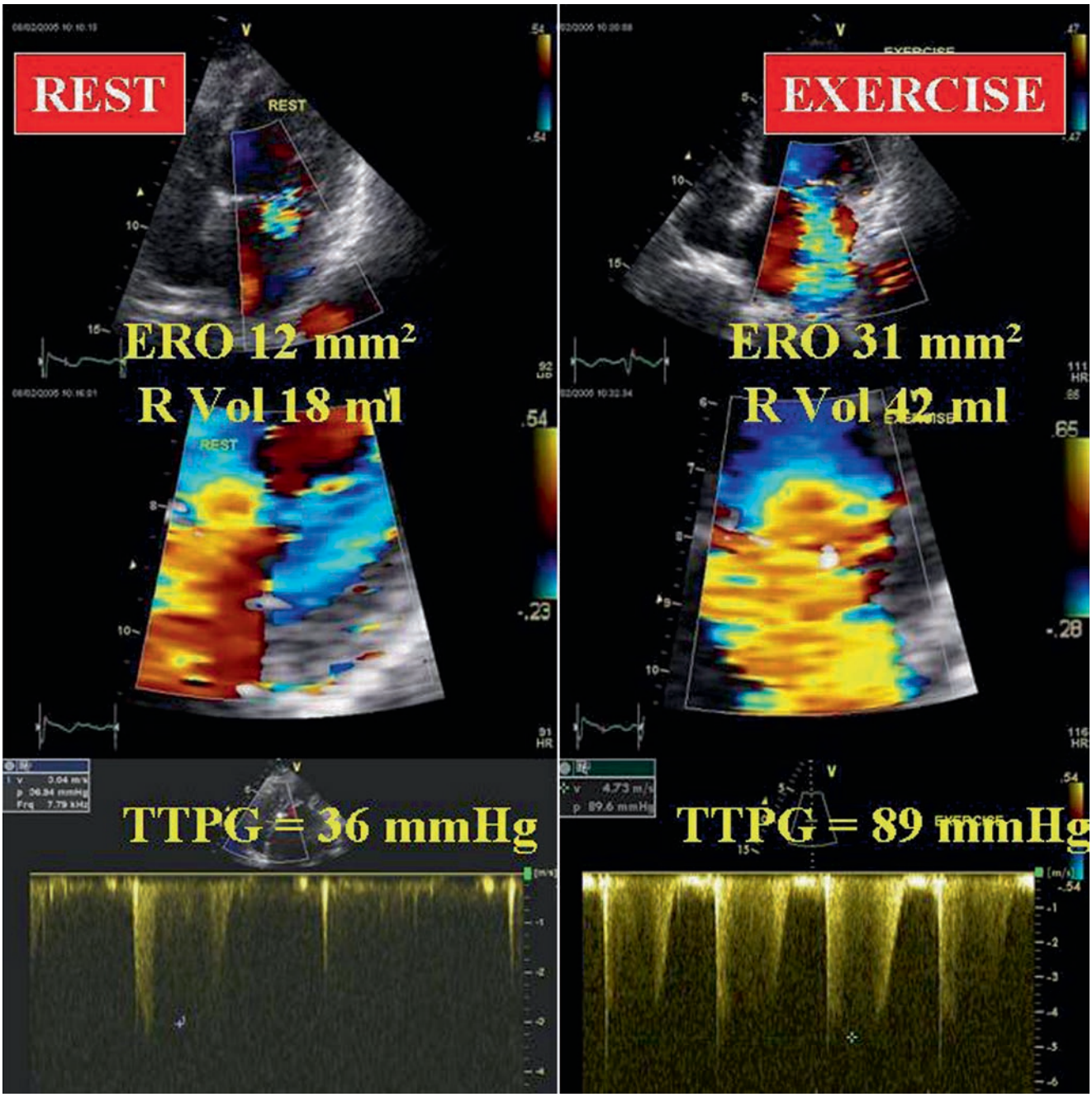

Fig. 9.11 Apical 4-chamber view showing colour flow Doppler and proximal flow convergence region at rest and during exercise in a patient with a large exercise-induced increase in mitral regurgitation and estimated pulmonary artery systolic pressure. *ERO* effective regurgitant orifice; *RVol* regurgitant volume; *TTPG* systolic transtricuspid pressure gradient

Cardiac Catheterization

As cardiac catheterization is an invasive technique, it is indicated only when the information obtained by non-invasive techniques is inconclusive. With cardiac catheterization, the transprosthetic pressure gradients and flow can be measured and EOA calculated. A catheter can be passed safely through the orifice of a bioprosthesis without adverse effects. However, the catheter may become entrapped in the orifice of a single-tilting-disc, sometimes requiring immediate surgical removal, or cause substantial valvular regurgitation if placed through the orifice of the ball-caged-valve.

Cardiac Magnetic Resonance

The low cost and wide availability of echocardiography make it the primary clinical tool for the assessment of valvular heart disease and prostheses. However, cardiac magnetic

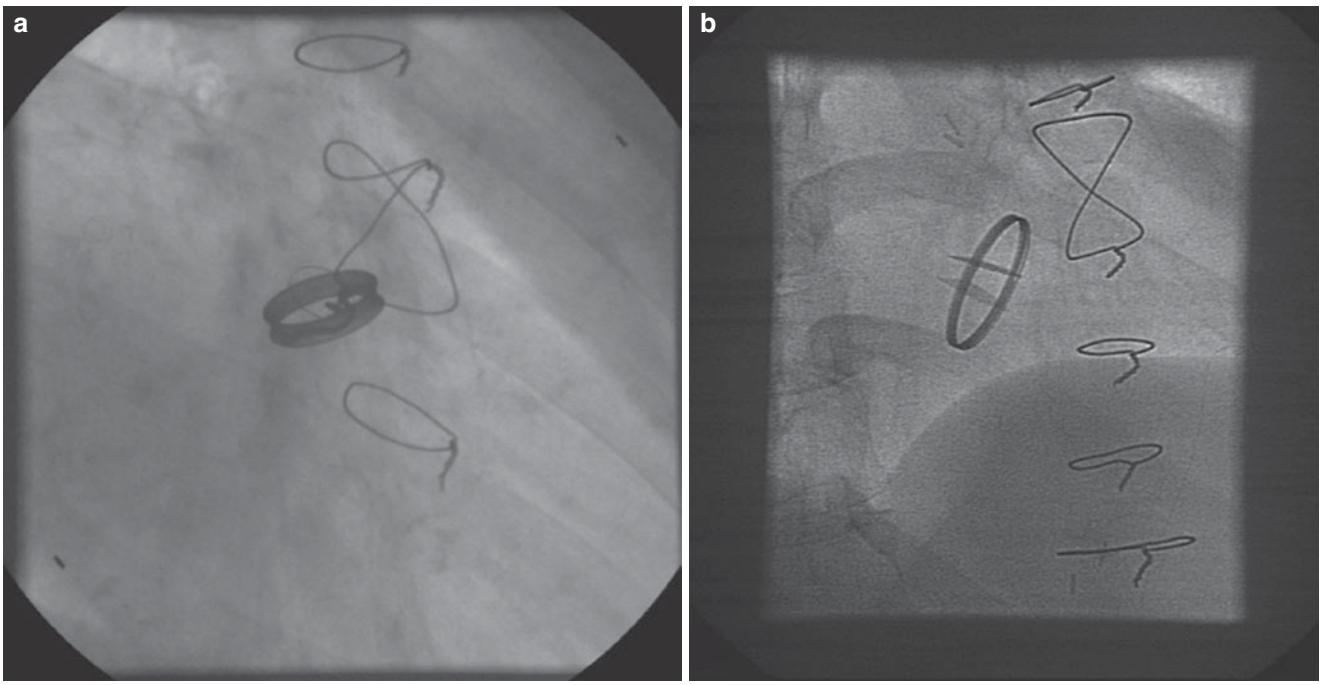

Fig. 9.12 Cinefluoroscopic side view of an Allcarbon single-tilting-disc **(a)** and a St. Jude Medical bileaflet-tilting-disc **(b)** valve in open position. The disc of the Allcarbon valve forms an angle of 60° with the housing plane. The two hemidiscs of the St. Jude Medical form a 10° angle. See text for details

Table 9.3. Cinefluoroscopic opening and closing angles of commonly used normofunctioning mechanical heart valves (see text for details on how to measure angles)

Heart valve prosthesis	Specification	Opening angle (°)	Closing angle (°)
Bileaflet-tilting-disc valves			
St Jude medical	19–25 mm	10	120
	27–33 mm	10	130
Carbomedics		12	118
Bicarbon		22	138
Edwards-Duromedics	Aortic	27	148
	Mitral	35	148
Jyros valve		22	111
Single-tilting-disc valves			
Bjork-Shiley		60	0
Medtronic-Hall	aortic	75	0
	mitral	70	0
Allcarbon		60	NA
Omniscience		80	12

NA not available

resonance (CMR) may play a complementary role when transthoracic acoustic windows are poor and a TOE approach is undesirable. Therefore, its role is marginal when compared with ultrasounds. In the assessment of valve prostheses, CMR has limited potential because of the focal artefacts and signal loss relative to the distortion of the magnetic field by the metal contained in the prostheses.[33] The artefacts are least pronounced on spin-echo images and more pronounced with

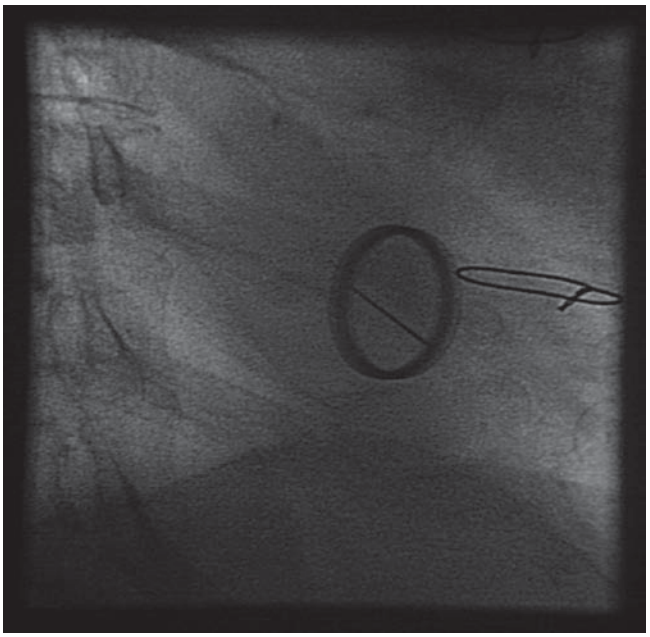

Fig. 9.13 Cinefluoroscopy of a thrombosed St. Jude Medical valve. The left-sided leaflet is stuck in closed position during the entire cardiac cycle indicative of valve obstruction by thrombus

gradient-echo cines. On the contrary, when the metal components are absent (as in biological valves), the CMR exam is similar to that performed on a native valve. However, incompatible prostheses to CMR are very rare. The major limitations of CMR for valve assessment are the sub-optimal spatial and temporal resolution and the need for a regular cardiac rhythm (Fig. 9.15).

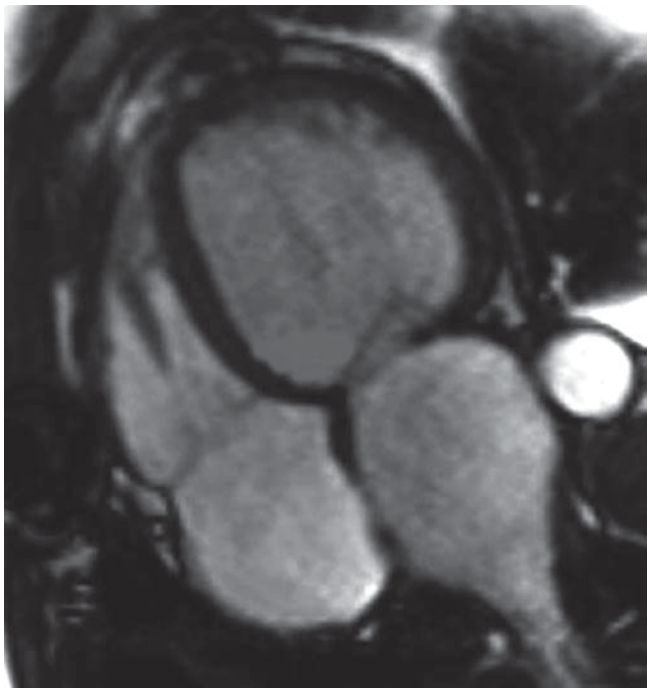

Fig. 9.15 Allcarbon single-tilting-disc prosthesis in mitral position. Horizontal long-axis steady-state free-precession cine magnetic resonance image

Cardiac Multi-detector Computerized Tomography

Cardiac multi-detector computerized tomography (MDCT) is an emerging technique in non-invasive cardiac imaging. Using data recorded during cardiac cycle, it is possible to

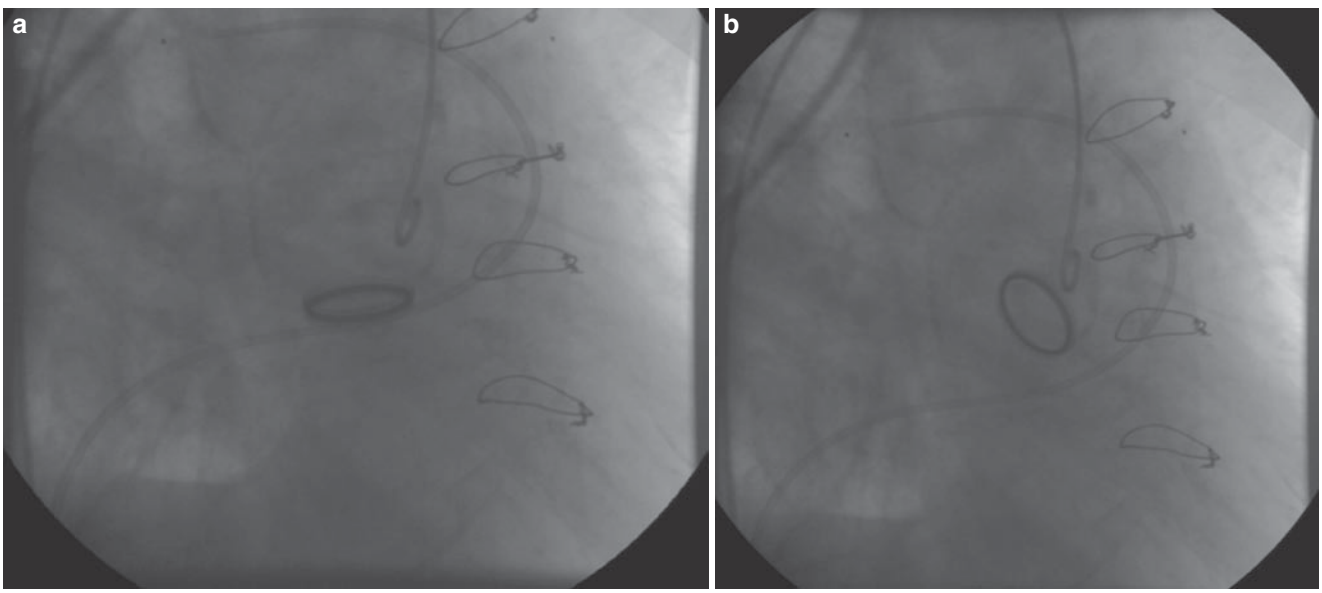

Fig. 9.14 Cineangiography in a patient with partial dehiscence of a mechanical prosthesis in the aortic position. An excessive motion of the prosthetic housing from diastole **(a)** to systole **(b)** can be readily noticed

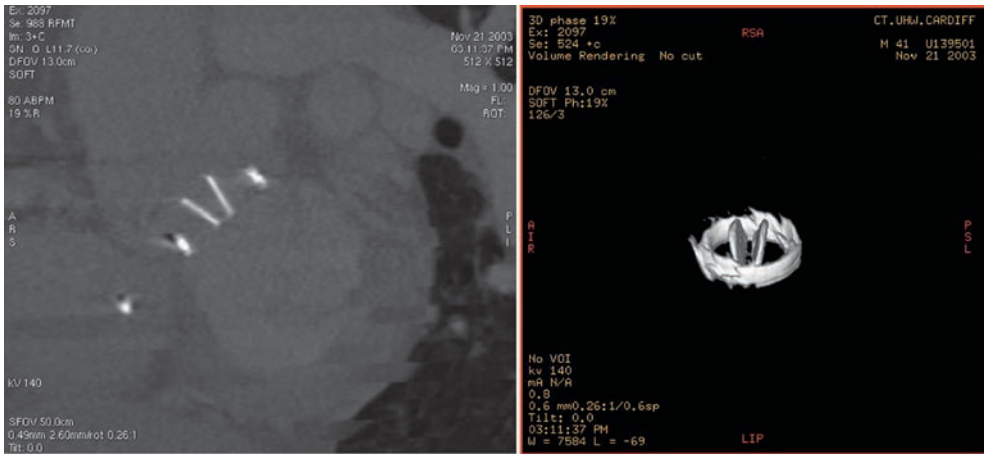

Fig. 9.16 St Jude Medical bileaflet valve in the mitral position. Sixty-four-section multi–detector row CT scans show the mechanical bileaflet valve during diastole (*left panel*). A reconstructed three-dimensional CT image using volumetric rendering method showing the same valve (*right panel*). Courtesy of Dr Andrew Wood, Consultant Radiologist, University Hospital of Wales

reconstruct multiple incremental data sets throughout the R–R interval. These data sets can be sequentially combined to provide functional imaging in a cine loop that allows evaluation of the valvular leaflet morphology and function (Fig. 9.16, Video 9.16). Even though its role is expanding in the evaluation of cardiac diseases, there is no clear indication for the use of MDCT for the assessment of valve diseases and prostheses. Moreover, concerns have been raised on the radiation burden of MDCT scanning. In fact, it has been estimated that about 0.4% of all cancers in the United States may be attributable to the radiation from MDCT studies. Therefore, the lack of a clear clinical benefit of CT for the assessment of prosthetic valve diseases should be weighed on the potential detrimental long-term risks.

Valve Prosthesis Normal Function and Dysfunction

Normal Anterograde Flow

From what has been written in the previous sections on heart valve prostheses specifications and functional parameters (see also Fig. 9.3), it is easy to understand why, when compared with native valves, all normofunctioning heart valve prostheses are inherently stenotic. Therefore, the anterograde velocities and pressure gradients across a normofunctioning heart valve prosthesis will be higher, and prosthetic EOA will be smaller than the corresponding parameters measured in a normal native heart valve in the same position.

The expected velocities, pressure gradients, and EOAs depend on the specific type, size, and position of the heart valve prosthesis and on the transprosthetic flow rate across that valve (Tables 9.2 and 9.4). The strong dependency of pressure gradients on transprosthetic flow rate explains the wide standard deviation of the reported values.

Different valve types also show different patterns of anterograde flow at colour Doppler examination (Fig. 9.17, Videos 9.17), which should be known because alterations of these patterns are early and sensitive markers of prosthetic valve obstruction, especially in single-tilting-disc valves (Fig. 9.18).

Normal Regurgitant Flow

Normally functioning mechanical valves have physiologic regurgitant jets with a low velocity and limited penetration into the proximal chamber, generally < 3 cm (Fig. 9.19, Videos 9.19A and B). The normal regurgitant volume can be up to 10% of the stroke volume and very prominent, especially at trans-oesophageal examination. The main reason for manufacturing these valves with a small amount of leakage is to prevent a sudden and irreversible occlusion. This physiologic regurgitation of mechanical valves is less likely to be detected in mitral position than in the aortic position, which is due to the shielding of the regurgitant jets by the prosthetic valve in the mitral position. Therefore, colour flow Doppler mapping is generally less sensitive than the continuous wave Doppler in detecting mechanical valve regurgitation in prosthesis in mitral position. Conversely, mitral valve "physiologic" regurgitation patterns are visualized particularly well with trans-oesophageal colour Doppler, because of its excellent image quality and spatial resolution.

The regurgitant flow (backflow) through a normally functioning valve prosthesis can be divided into "closure backflow" occurring with the closure of the valve and "leakage backflow" occurring after the closure of the valve. The wide opening excursion of the current mechanical valves may result in significant closure backflow, as back pressure swings

Table 9.4. Published data about Doppler haemodynamic parameters of normofunctioning prosthetic valves in mitral position

Type	Doppler	Size (mm)					
	parameters	23	25	27	29	31	33
Singl-tilting-disc prostheses							
Bjork-Shiley[a] (*n* = 237)	GOA	2.5	3.1	3.8	4.6	4.6	
	PHT	115	99 ± 27	89 ± 27	79 ± 17	70 ± 14	
	Mean gr.		6 ± 2	5 ± 2	3 ± 1	2 ± 2	
Medtronic-Hall (*n* = 47)	GOA	2.54	3.14	3.80	4.52		4.52
	PHT			78	69 ± 15	77 ± 17	
	Mean gr.		5 ± 3	4 ± 2	3 ± 1		3 ± 1
Omnicarbon (*n* = 140)	GOA	2.55	3.14	3.8	3.8	4.52	4.52
	PHT		102 ± 16	105 ± 33	120 ± 40	134 ± 31	
	Mean gr.	6 ± 2	5 ± 2	5 ± 2	4 ± 1	4 ± 2	4
Allcarbon (*n* = 73)	GOA		3.1	3.8	4.5	4.5	
	PHT		105 ± 29	89 ± 14	85 ± 23	88 ± 27	
	Mean gr.		5 ± 1	4 ± 1	4 ± 1	4 ± 1	
Bileaflet-tilting-disc prostheses							
St. Jude Medical (*n* = 40)	GOA	2.55	3.09	3.67	4.52	5.18	
	PHT	160	76 ± 4	72 ± 11	74 ± 15	71 ± 14	
	EOA[a]	1.03	1.4 ± 0.2	1.7 ± 0.2	1.8 ± 0.2	2.0 ± 0.3	
	Mean gr.	4	3 ± 1	5 ± 2	3 ± 1	4 ± 2	
Duromedics (*n* = 69)	GOA			3.58			
	PHT			87 ± 15	89 ± 25	86 ± 12	85
	Mean gr.			5 ± 3	3 ± 1	3 ± 1	2
Carbomedics (*n* = 75)	GOA	1.75	2.19	2.63	3.07	3.07	3.07
	PHT	104	81 ± 10	78 ± 19	67 ± 10	83 ± 26	79 ± 18
	EOA[a]	1.3	2.2 ± 0.5	2.1 ± 0.6	2.1 ± 0.5	1.9 ± 0.9	2.3 ± 0.7
	Mean gr.	7	4 ± 2	4 ± 2	3 ± 1	3 ± 1	3 ± 2
Bicarbon (*n* = 68)	GOA		3.45	4.14	5	5	5
	PHT		67 ± 1	84 ± 27	81 ± 18	81 ± 15	55
	Mean gr.		5 ± 3	4 ± 1	5 ± 2	4 ± 1	7
On X (*n* = 33)	PHT						
	Mean gr.		5 ± 2	5 ± 2	5 ± 2	5 ± 2	
Stented bioprostheses							
Medtronic-intact (*n* = 26)	GOA		1.34	1.51	1.65	1.86	
	EOA[a]		1.4 ± 0.1	1.5 ± 0.1	1.6 ± 0.1	1.8 ± 0.2	
	Mean gr.		8 ± 2	5 ± 2	4 ± 1	4 ± 1	
Hancock I (*n* = 46)	PHT				115 ± 20	95 ± 17	90 ± 12
	Mean gr.			5 ± 2	2 ± 1	5 ± 2	4 ± 2
Hancock II (*n* = 54)	PHT				105 ± 63	81 ± 23	
	Mean gr.			5 ± 2	3 ± 1	4 ± 1	
Hancock pericardial (*n* = 22)	PHT				105 ± 36	81 ± 23	
	Mean gr.				3 ± 1	4 ± 1	
Ionescu-Shiley (*n* = 45)	PHT				80 ± 30	79 ± 15	75 ± 19
	Mean gr				3 ± 1	3 ± 1	4 ± 1
Carpentier-Edwards (*n* = 12)	PHT			100	110 ± 15	90 ± 11	80
	Mean gr.			3.6	5 ± 2	4 ± 1	1
Mitroflow (*n* = 24)	PHT		90	90 ± 20	102 ± 21	91 ± 22	
	Mean gr.		7	3 ± 1	4 ± 2	4 ± 1	

[a]Monostrut *GOA* geometric orifice area provided by the manufacturer in cm^2; *EOA* effective orifice area (continuity equation) in cm^2; *Mean gr.* mean transprosthetic gradient in mm Hg; *n* examined patients

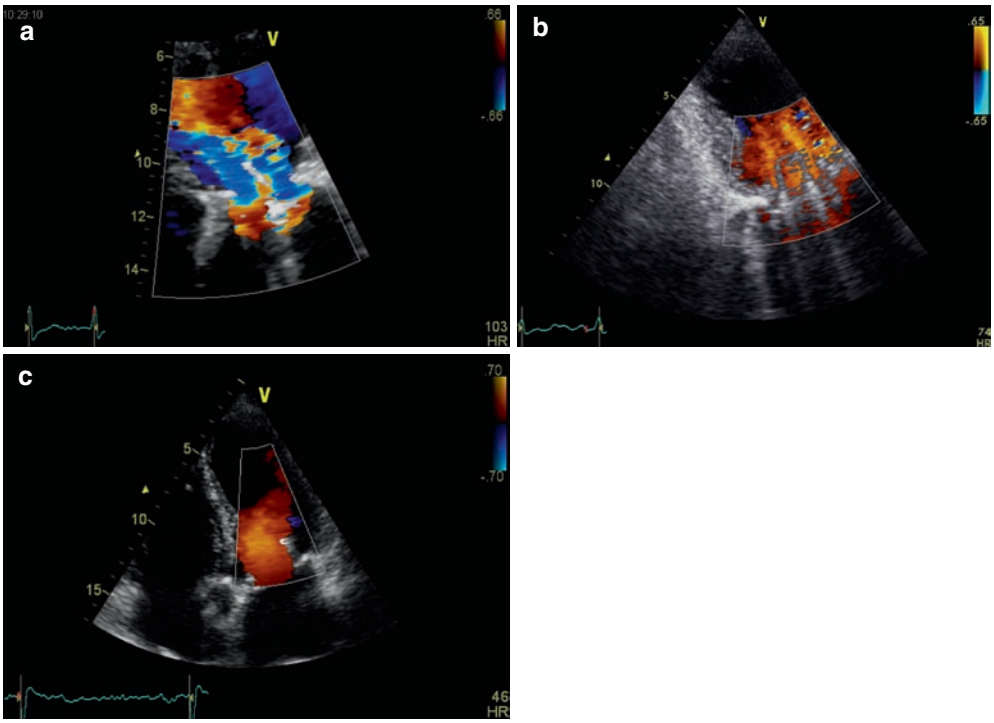

Fig. 9.17 **(a)** Normal colour Doppler echocardiography appearance of anterograde flow across different valve types in the mitral position: a single-tilting-disc valve with a major jet towards the lateral wall and a minor jet directed towards the centre of the cavity **(a)**; a bileaflet-tilting-disc valve in which flow passes through three well-separated orifices creating a near physiological flow pattern **(b)**; and a bioprosthetic valve in which there is a single, central flow very similar to that of native valves **(c)**

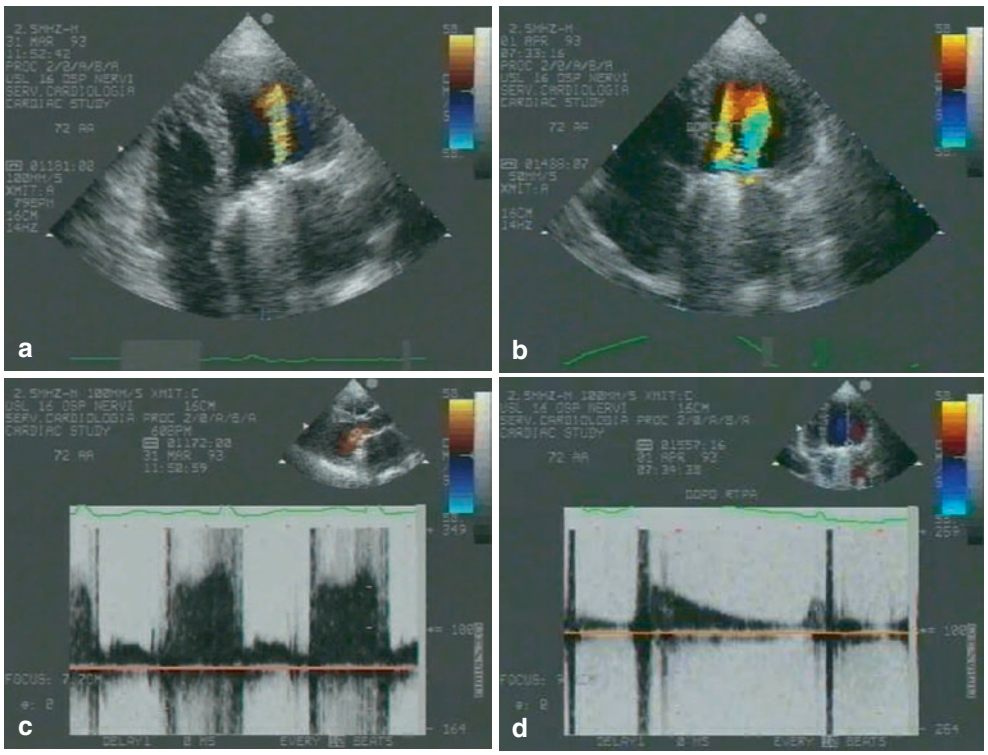

Fig. 9.18 Single-tilting-disc valve thrombosis. Colour Doppler echocardiography at presentation **(a)** shows the absence of the central minor jet and increase in the velocity at CW spectral Doppler of the lateral major jet **(c)**. After i.v. thrombolysis, the reappearance of the normal colour Doppler pattern of the anterograde flow **(b)** and a significant decrease in the anterograde flow velocity at CW spectral Doppler **(d)** were observed

the leaflets through the long closing arc. Accordingly, a small jet occurring during the first 40–50 ms of systole can be invariably observed at the trans-oesophageal examination in patient with tilting-disc mechanical valves. Bileaflet-tilting-disc valves show two converging regurgitant jets from the pivot points (designed to reduce the likelihood of prosthesis thrombosis) - one central jet and variable number of peripheral jets[7] (Fig. 9.20, Video 9.20). Bjork–Shiley valves have a large central regurgitant jet originating from the central disc hole and a variable number of peripheral jets. The central

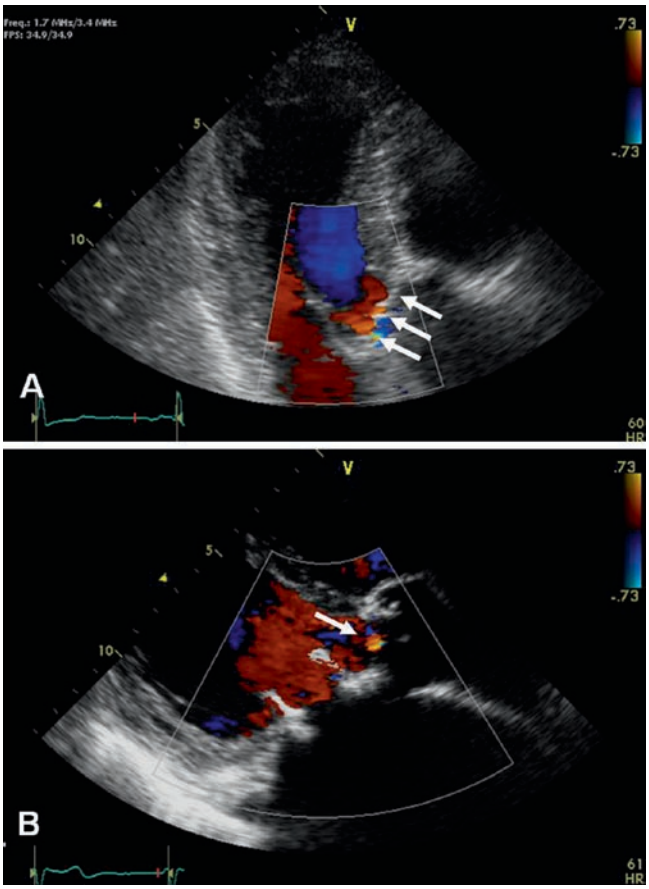

Fig. 9.19 Colour Doppler imaging during diastole showing the normal appearance of three "physiologic" regurgitant jets ("leakage backflow," *white arrows*) from a bileaflet valve **(a)** and a bioprosthesis (*white arrow,* **b**) in aortic position

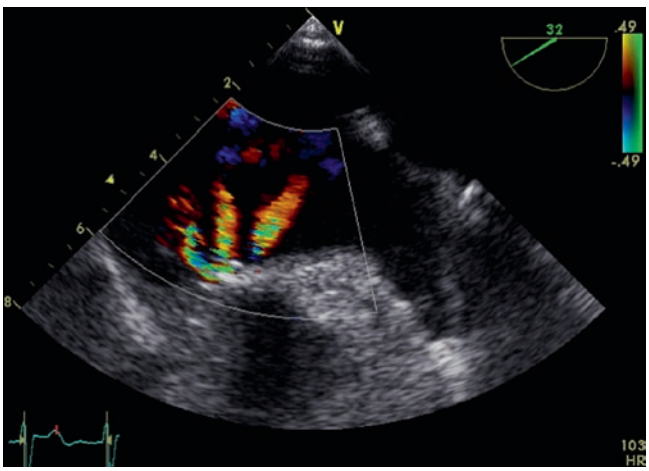

Fig. 9.20 Trans-oesophageal echocardiographic depiction of leakage backflow from a bileaflet-tilting-disc valve in mitral position. These three jets represent the "physiologic" leakage from pivotal points (*peripheral jets*) and central closure line (*central jets*) and should not be interpreted as pathologic prosthetic regurgitation

regurgitant jet makes most of the colour Doppler signal but actually accounts for 30% of the regurgitant volume, the rest of the 70% is from the less prominent peripheral jets. The Starr-Edwards ball-cage valves have very low regurgitant volumes, because the ball completely occludes the primary flow orifice.

The stented bioprosthetic valves usually show only one centrally directed regurgitant jet originating from the central part of the valve (Fig. 9.19, Videos 9.19A and B). The prevalence of physiologic regurgitation across stented bioprosthetic valves is 19–25% and 26–30% for mitral and aortic positions, respectively. The newer generation stentless valves are being used frequently because of their excellent haemodynamic profile. The prevalence of mild aortic regurgitation with these valves may be up to 17%, but the presence of significant amount of regurgitation is very low.

Prosthetic Valve Obstruction

Prosthetic heart valve obstruction may be caused by thrombus formation, fibrous tissue ingrowth (or pannus formation), or a combination of both, or by endocarditis. The aetiology may be difficult to determine and requires knowledge of the clinical presentation and findings on transthoracic and trans-oesophageal echocardiography. The possibility of prosthetic valve thrombosis or endocarditis should be ruled out in patients with embolization.

The incidence of prosthetic heart valve thrombosis has been reported to be 13% in the first year in any valve position, and even 20% for mechanical prostheses in the tricuspid position.[34] At any time, for prostheses in the mitral and/or aortic position, the overall incidence is 0.5–6% per patient-year, highest in the mitral position. The risk of thrombus, in spite of adequate oral anticoagulation, has been estimated to be between 1 and 4% per year.

Echocardiography is the initial diagnostic approach for patients with suspected prosthetic heart valve obstruction. The increase in the transprosthetic pressure gradients and a reduction in the effective area of the valve orifice, particularly in comparison with the previous data in that patient, may be diagnostic (Fig. 9.17c). In experienced hands, transthoracic echocardiography can also detect an altered anterograde flow pattern with colour Doppler suggestive of intrinsic prosthesis obstruction (Fig. 9.21, Video 9.21). Increased anterograde transprosthetic flow velocities due to prosthesis obstruction should be differentiated from those as a result of high cardiac output state or coexisting prosthesis regurgitation, which may increase the anterograde volume flow rate across the prosthesis resulting in a high velocity and high transprosthetic gradients. However, in case of increased anterograde volume flow rate, the valve area remains relatively normal.

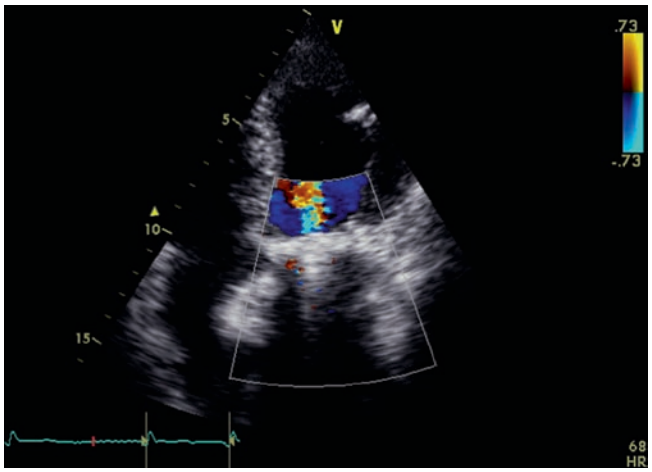

Fig. 9.21 Single-tilting-disc valve obstruction. Colour Doppler echocardiography shows only one anterograde jet

Trans-oesophageal echocardiography is the most accurate diagnostic technique to assess the alterations in the occlusive mechanism or the existence of thrombus on heart valve prostheses, especially for valves in the mitral position. Partial blockade of the prosthetic disc by thrombus can be easily detected by trans-oesophageal echocardiography, as it usually holds it in a semi-open position, leaving an eccentric communication open in systole and diastole. The colour Doppler further facilitates more precise localization of prosthetic obstruction, showing acceleration proximal to a stenosis and any associated degree of regurgitation caused by the lack of mobility of the occluder. In most cases, an echogenic mass is observed on the prosthetic valve surface at the site of the stenosis (Fig. 9.22, Videos 9.22A–C). Trans-oesophageal echocardiography may also be useful to differentiate thrombus from pannus, as the mechanism of prosthetic obstruction. In prosthetic thrombosis, the movement of the disc is always abnormal, whereas in 40% of patients with obstruction due to pannus, the mobility of the disc is normal. The visualization of an echogenic mass is almost diagnostic for thrombosis, but it can be detected in only 70% of obstructions caused by pannus. The echogenic characteristics of the mass are very important in differentiating thrombus from pannus. The thrombus tends to be mobile, have soft ultrasound density, and is attached to the valve occluder (Fig. 9.23, Video 9.23). The pannus is firmly fixed, have bright ultrasound density, and is attached to the valve apparatus. In addition, finding echo density around the sewing ring with bright reflective echoes and adequate anticoagulation heightens the suspicion of a pannus. A thrombotic mass is usually larger than pannus. In mitral prosthetic thrombosis, the mass frequently extends into the atrial endocardial surface, a feature rarely seen in obstruction caused by pannus.

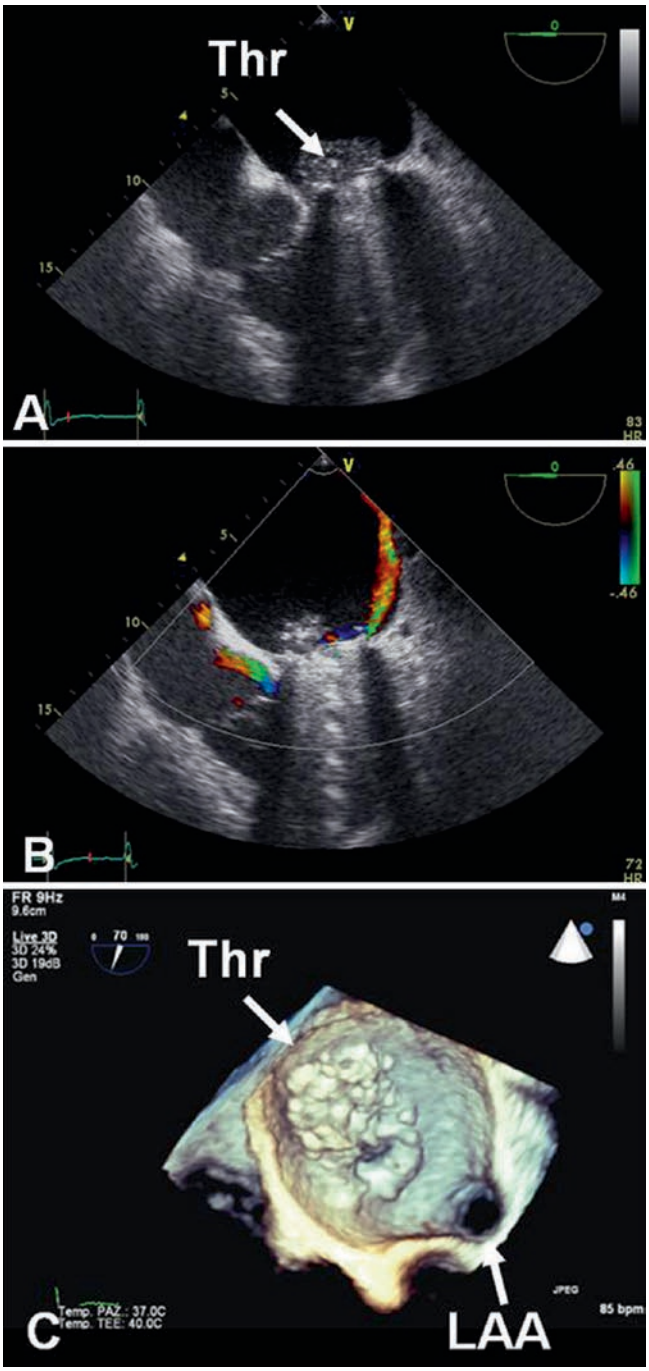

Fig. 9.22 Massive thrombosis on the atrial side of a bileaflet-tilting-disc valve in the mitral position (*white arrow*), **(a)** at trans-oesophageal. The presence of thrombus usually holds it in a semi-open position that creates an eccentric intra-prosthetic regurgitation **(b)**. Real-time 3D trans-oesophageal echocardiography offers a better assessment of the extension and dimensions of the Thr, thrombus, LAA, left atrial apendix**(c)**

Prosthetic Valve Regurgitation

Echocardiography is highly useful in detecting prosthetic valvular regurgitation, but with certain technical limitations,

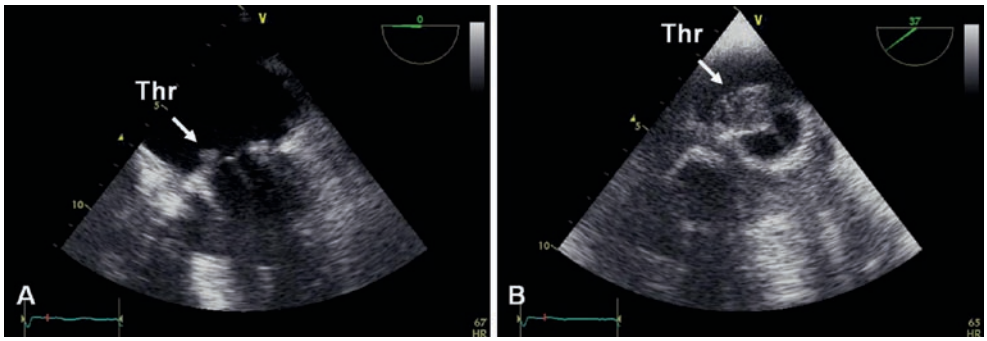

Fig. 9.23 Trans-oesophageal echocardiogram showing a thrombus (*white arrow*) visualized as a soft, small and highly mobile mass on the atrial side of a mitral bioprosthetic valve entering the valve orifice during diastole. Long axis view **(a)**; Short axis view **(b)**.

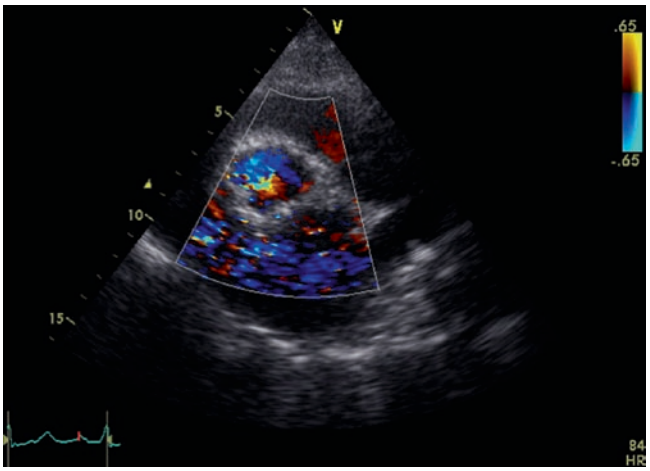

Fig. 9.24 Parasternal short-axis view by transthoracic approach showing a pathologic intra-prosthetic leakage of a bioprosthesis in the aortic position

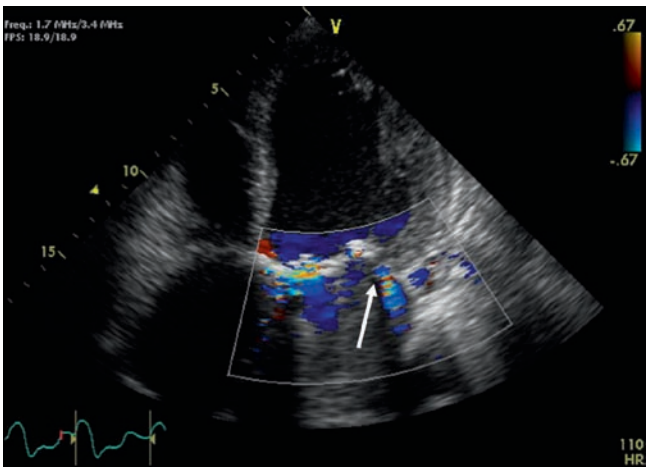

Fig. 9.25 Prosthetic mitral regurgitation jet (*white arrow*) detected by transthoracic echocardiography despite shadowing artefacts in the left atrium caused by the mechanical prosthesis

the most important of which are the problems of acoustic shadowing, reverberation, and beam-width artefacts that occur when the ultrasound beam should traverse a reflective prosthesis before entering the cardiac chamber receiving the regurgitant jet. This occurrence may lead to non-visualization or under-estimation of the severity of regurgitation, especially with mechanical valves. In addition, colour artefacts are common in patients with heart valve prostheses and may alter the detection of abnormal jets.

For prostheses in aortic position, both parasternal and apical approaches may be useful as the ultrasound beam reaches the LVOT without crossing the prosthesis (Fig. 9.24, Video 9.24). For prostheses in mitral position, the parasternal approach may be helpful if a view in which the atrial side of the prosthesis can be obtained without acoustic shadowing. Apical views are rarely useful because of acoustic shadowing of the prostheses, even if in some cases, a paraprosthetic regurgitant jet can be visualized from this approach (Fig. 9.25, Video 9.25). Therefore, the transthoracic approach has a low sensitivity for detection and quantitation of prosthetic regurgitation of mitral valve prostheses, and usually the trans-oesophageal approach is needed to visualize the left atrial size of the prosthesis. Sometimes, colour Doppler may visualize proximal flow acceleration on the ventricular side of the prostheses in mitral position as a clue for raising the suspect of significant paravalvular regurgitation.

When a heart valve prosthesis regurgitation is detected, the first important question to the echocardiographer is whether "physiologic" or pathologic prosthetic regurgitation is present. Differential characteristics of "physiologic" from pathologic prosthetic valve regurgitation are uniform colour pattern, rather than the mosaic flow disturbance, short extension into the receiving chamber (usually <2 cm), and the absence of supporting features like increased anterograde velocity, enlargement of cardiac chambers, and/or pulmonary hypertension.

The most likely cause of intra-prosthetic pathologic regurgitation in mechanical valves is the incomplete closure of occluders owing to pannus, ingrowth, thrombus formation, or vegetation growth (Fig. 9.26, Video 9.26). On the other

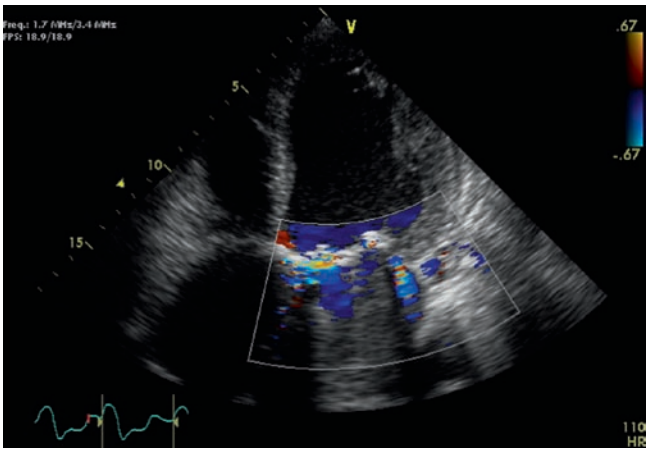

Fig. 9.26 Trans-oesophageal colour Doppler echocardiography showing an extensive intra-prosthetic leakage of a single-tilting-disc prosthesis caused by pannus ingrowth

hand, pathologic intra-prosthetic regurgitation of bioprostheses is usually due to structural valve deterioration (Fig. 9.27, Videos 9.27A and B).

Paraprosthetic regurgitation is always pathological. Small paraprosthetic regurgitation around the circumference of a prosthetic valve between the sewing ring and the annulus of the native valve is common. The regurgitant jet is usually eccentric and it extends in the receiving chamber. More than one regurgitant jets may be simultaneously present. During the first year after valve replacement, these regurgitations are mostly related to surgical factors, are not associated with increased subclinical haemolysis, and are generally benign. Sometimes, it may be difficult to distinguish intra- from paraprosthetic regurgitation using the transthoracic approach. In these cases, the trans-oesophageal approach is needed.

Structural Valve Deterioration

Structural deterioration is generally a problem only for the biological valves, and is usually non-existent for the current generation of mechanical valves. However, in 1986, the Bjork–Shiley convexo–concave single-tilting-disc valve was withdrawn from the market after reports of fracture of the valve-ring strut, resulting in dislodgment and embolization of the disc. Similarly, the TRI technologies' mechanical valve has been withdrawn from clinical use because of the high risk of structural failure after several cases of occluder escape.[35] Strut fracture usually results in the abrupt onset of dyspnea, loss of consciousness, or cardiovascular collapse owing to embolization of the disc and acute severe valvular regurgitation that can be demonstrated at echocardiography. Cinefluoroscopy may visualize the absence of the strut and the radiopaque disc marker within the housing of the valve. Cinefluoroscopy has also been used to identify patients implanted with the Bjork–Shiley convexo–concave single-tilting-disc valve, who have outlet–strut separation without complete strut fracture. The valve prosthesis should be prophylactically replaced in these patients.

Structural deterioration of a bioprosthetic valve usually is the result of a progressive tissue degeneration with fibrosis and calcification of valve leaflets resulting in increased resistance to open (stenosis) or failure to close properly (regurgitation). Regurgitation may also occur because of leaflet tear (Fig. 9.28, Videos 9.28A and B) or rupture of one or more of the valve cusps (Fig. 9.29, Videos 9.29A and B), and in these patients, the clinical presentation is that of an acute regurgitation.[36] The risk of structural valve deterioration increases over time. Typically, failure of bioprostheses occurs 10 years after implant.

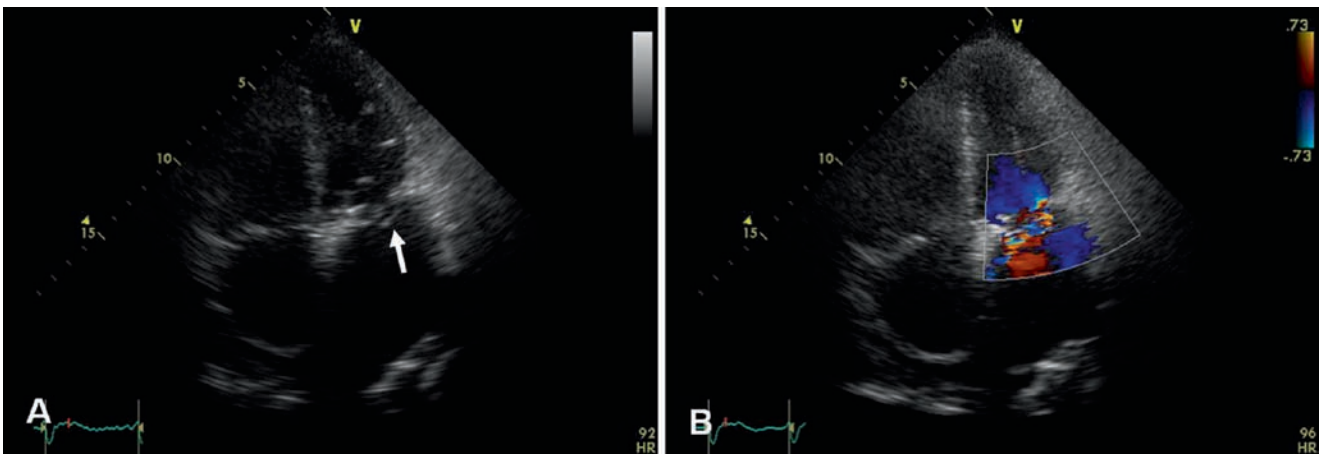

Fig. 9.27 Structural deterioration of a bioprosthetic valve in the mitral position causing fracture of one leaflet, which prolapses in the left atrium (*white arrow*), **(a)**. An eccentric and turbulent jet into the left atrium is visualized in **(b)**

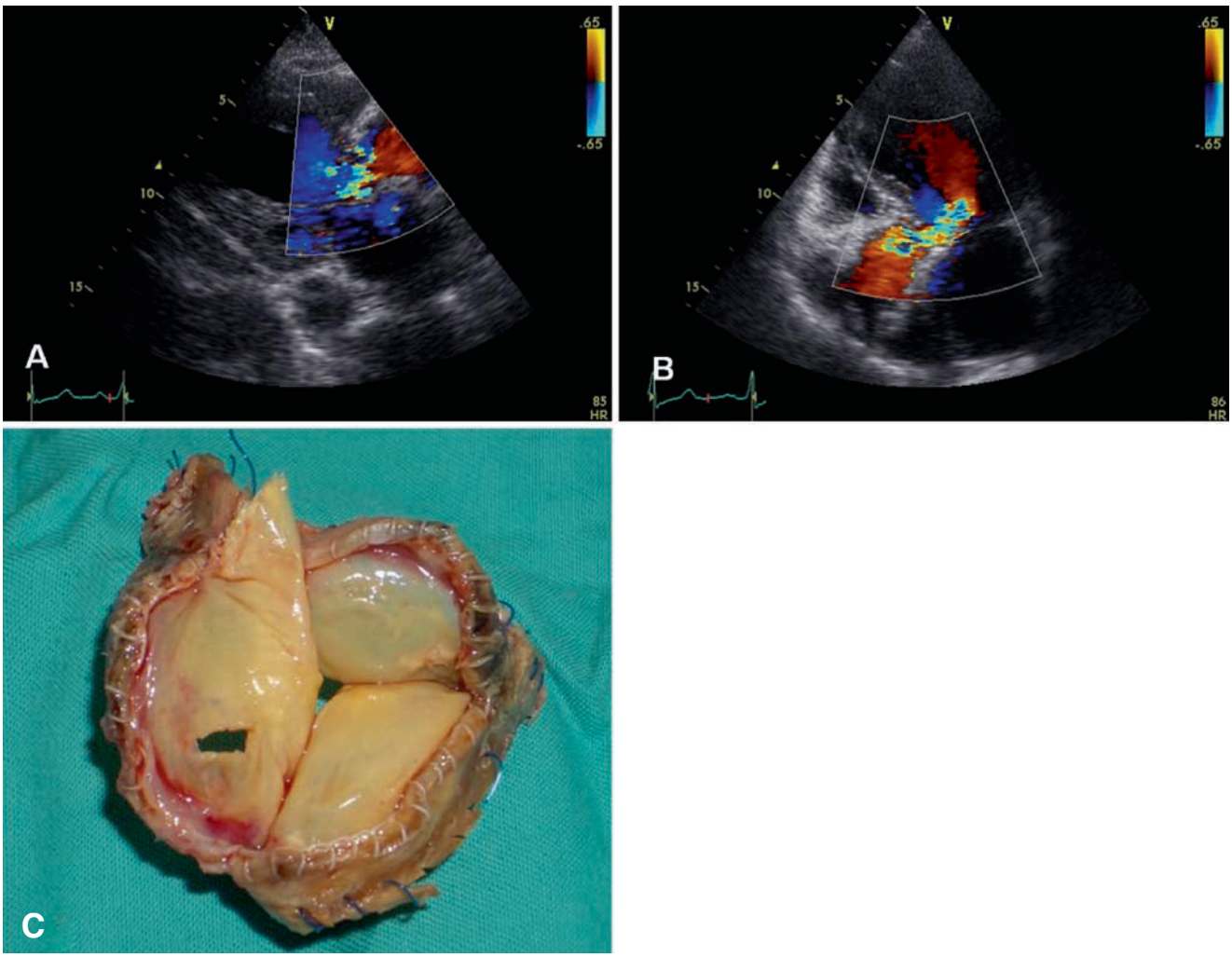

Fig. 9.28 Transthoracic colour Doppler echocardiography demonstrating severe regurgitation of a Cryolife O'Brien bioprosthesis from parasternal **(a)** and apical approach **(b)**. The explanted valve **(c)** showed a tear

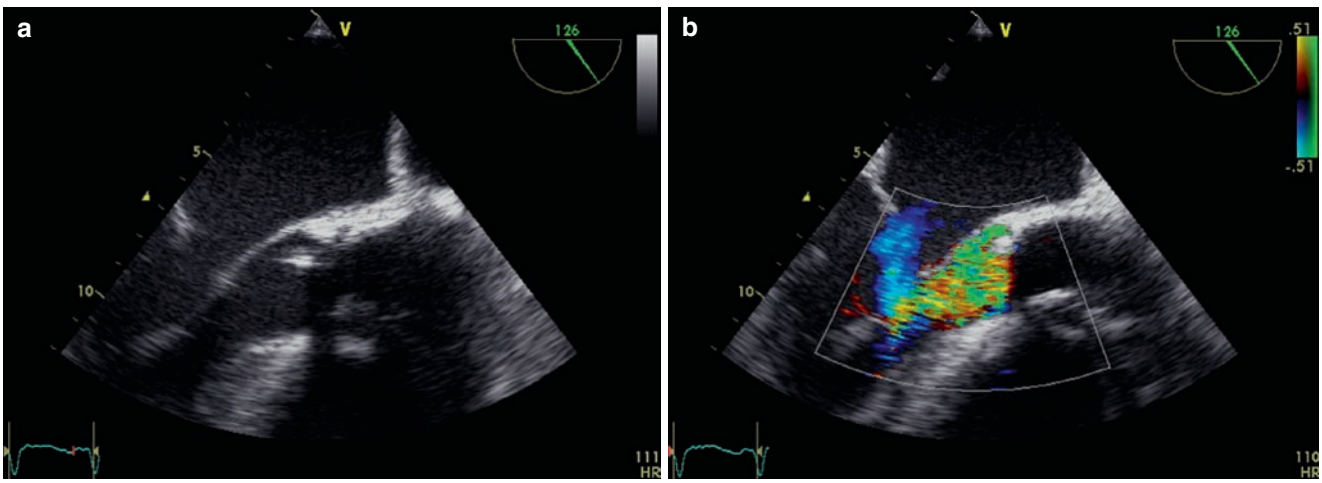

Fig. 9.29 Trans-oesophageal echocardiography showing degenerative calcification and rupture of a cusp, **(a)** determining severe regurgitation **(b)** of a bioprosthesis in the aortic position

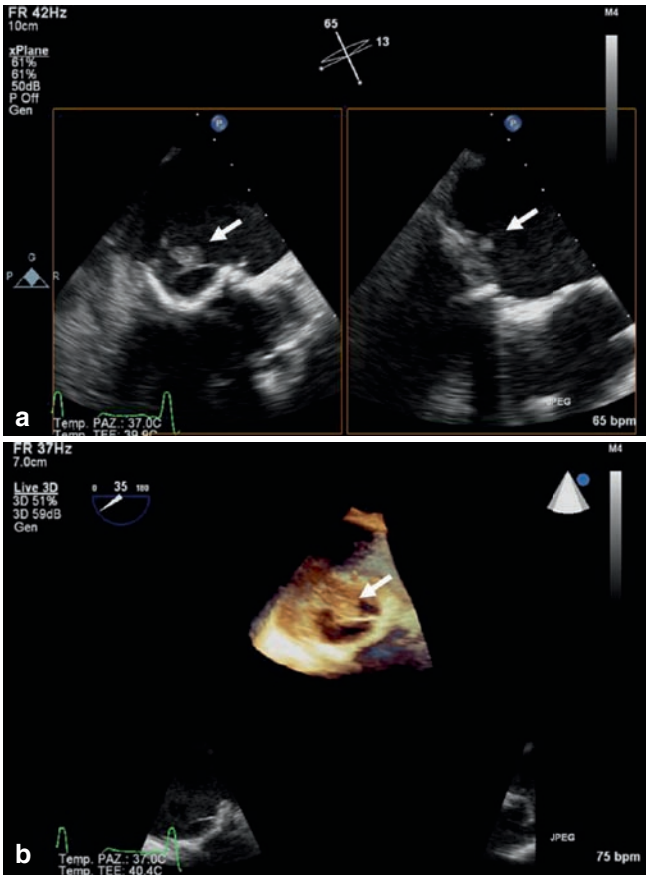

Fig. 9.30 Real-time 3D trans-oesophageal echocardiography showing a small vegetation attached to the leaflet of a bioprosthetic valve in the mitral position. Multi-plane visualization of the vegetation (*white arrows*), **(a)**. Rendering display of the vegetation allows better assessment of the size and shape of the vegetation (*white arrow*), **(b)**

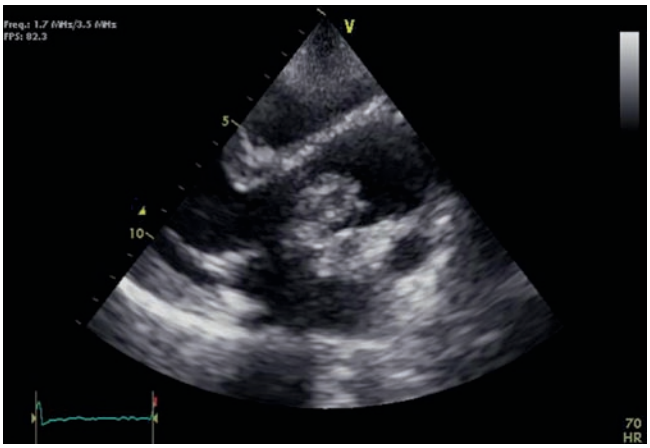

Fig. 9.31 Transthoracic echocardiography showing a large and highly mobile vegetation on the leaflet of a bioprosthesis in the aortic position

Prosthetic Valve Endocarditis and Related Complications

A prosthetic valve represents a foreign body within the circulatory system, which is a potential site of infection. The characteristic lesion of valve prosthesis endocarditis is vegetation, similar to native valves. When vegetations are small, they appear as irregular, immobile echogenic structures attached to the valve components (Fig. 9.30, Videos 9.30A and B). As they grow and become larger, they usually become sessile and move following the blood flow through the valve (Fig. 9.31, Video 9.31). Because of to the presence of the prosthetic material, the sensitivity of echocardiography (both transthoracic and trans-oesophageal) to detect vegetations on prosthetic valves is lower than that in native valves. Large vegetations can occasionally cause prosthesis obstruction (Fig. 9.32, Videos 9.32A and B). Taking into account the low sensitivity of the technique, a negative transthoracic study in a patient with moderate or high clinical suspicion of endocarditis did not exclude the diagnosis, and trans-oesophageal examination should be warranted in those cases. It has also been reported that vegetations longer than 10 mm are associated with an increased risk of embolization, and vegetation size is a useful information to determine the urgency of surgical intervention.

Prosthetic valve endocarditis may evolve with paravalvular abscess formation. In the mitral position, a paravalvular abscess appears as an echo-free space adjacent to the sewing ring. However, often, the only signs of abscess are indirect, such as an increased prosthesis mobility resulting from suture dehiscence and lack of annular support. Frequently, ring or myocardial abscesses are only detected at surgery, suggesting the low sensitivity of the technique for valves in this position. For prosthesis in aortic position, increased thickening of the aortic root, with or without echo-free space inside confirmed in two views, suggests the presence of a ring abscess (Fig. 9.33, Video 9.33). Sometimes, the diagnosis is difficult and the echo study should be repeated after a few days to look for an evolution of the finding (Fig. 9.34, Videos 9.34A and B). Fistolous communications with the right atrium, left atrium, or right ventricle can be detected with colour Doppler.

Haemolysis

Although subclinical intra-vascular haemolysis (as evidenced by decreased serum haptoglobin, reticulocytosis, and increased lactate dehydrogenase concentrations) can be documented in most patients with normofunctioning mechanical heart valve prostheses, severe haemolytic anaemia is uncommon and suggests paravalvular leakage due to partial dehiscence of the valve or infection or interaction of the jet with foreign bodies such as annular rings (Fig. 9.35, Video 9.35).

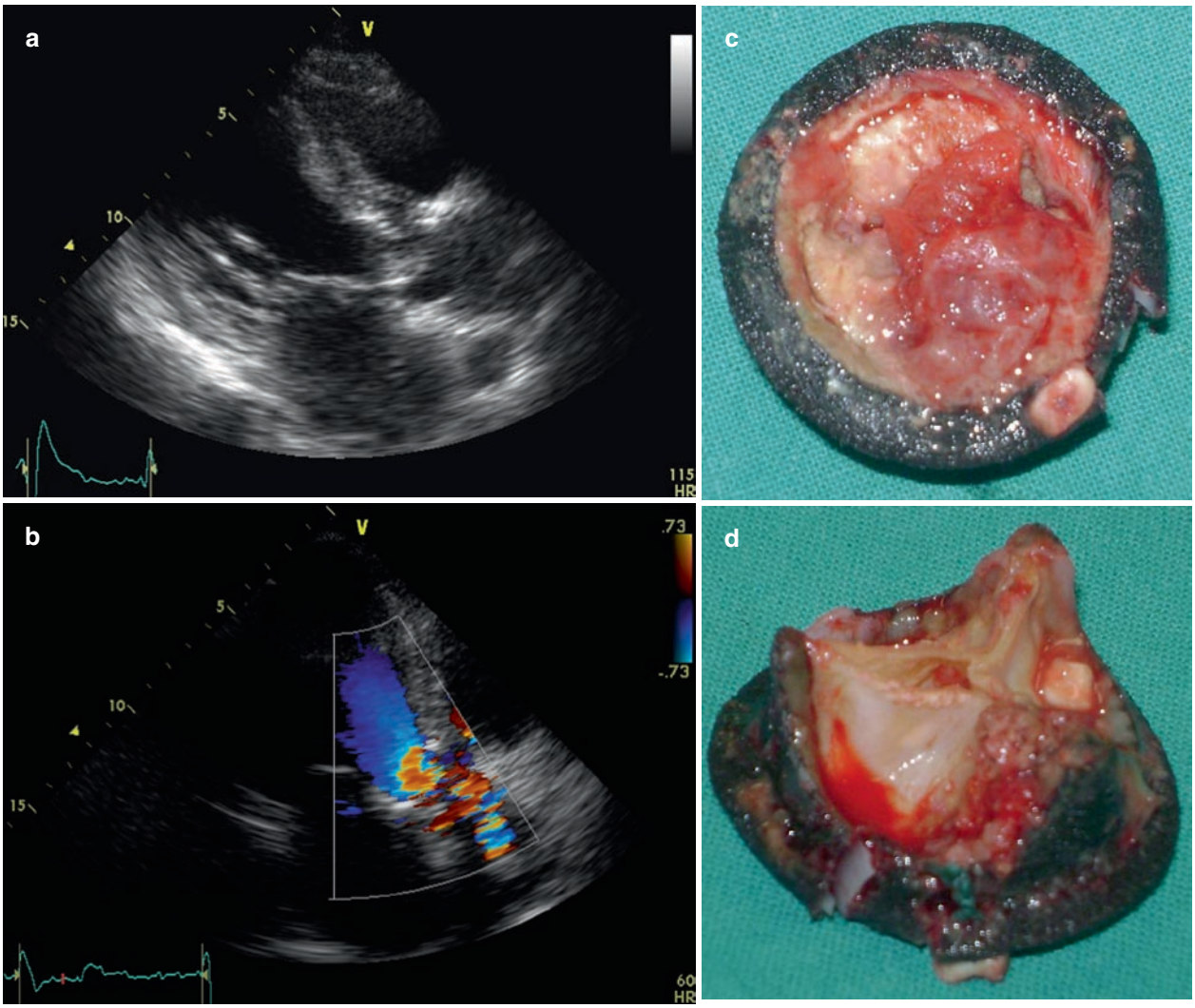

Fig. 9.32 Transthoracic echocardiography showing a large vegetation on the left ventricular side of a bioprosthesis in the aortic position. The vegetation enters the valve orifice during systole obstructing it **(a, b)**. At surgery, the extensive obstruction of the bioprosthesis was confirmed **(c, d)**

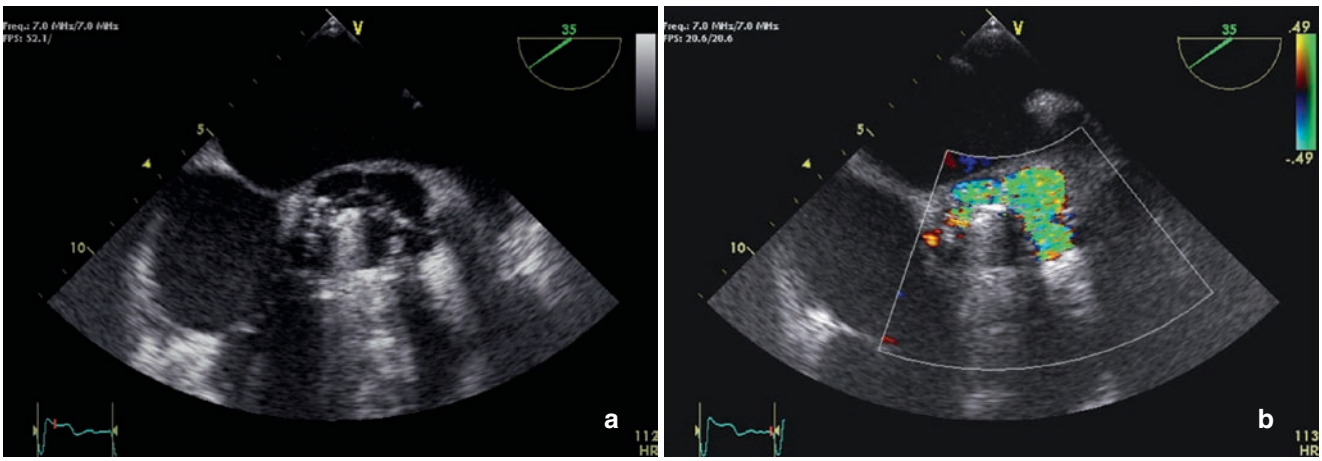

Fig. 9.33 Trans-oesophageal imaging of a short-axis view of the aortic root showing a prosthetic aortic valve endocarditis complicated by abscess and pseudoaneurysm formation. In the posterior part of the aortic root, an echolucent space can be visualized suggesting the degeneration of the abscess in pseudoaneurysm of the mitral–aortic intervalvular fibrosa **(a)**. By colour Doppler imaging, the blood flow is visualized exiting the pseudoaneurysm into the left ventricular outflow tract during diastole **(b)**

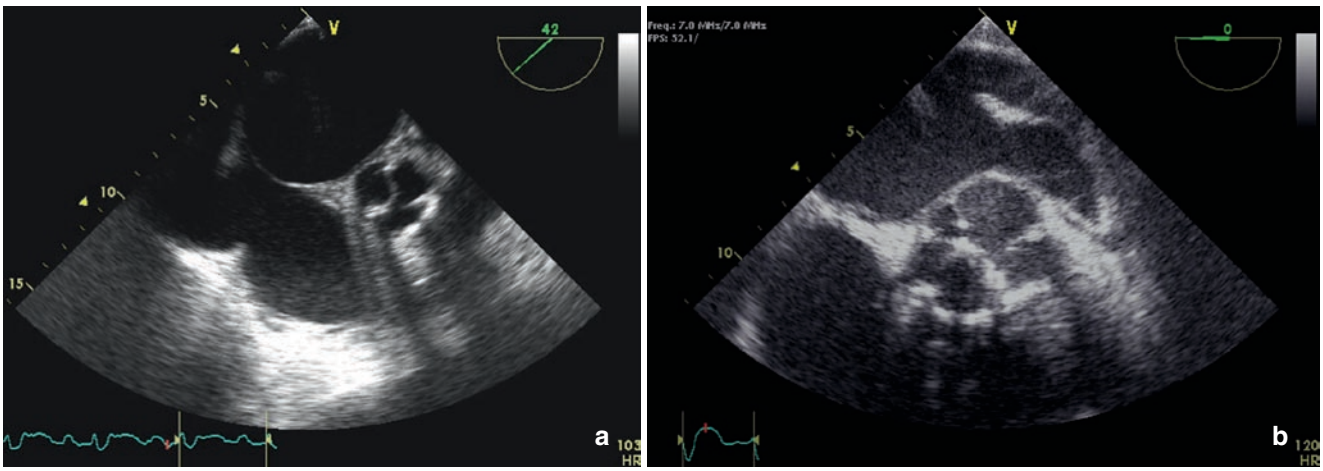

Fig. 9.34 At early stages, abscess appears as a thickening of the aortic wall, which is difficult to differentiate from haematoma **(a)**. However, a trans-oesophageal echocardiogram repeated 5 days later showed evolution of the echocardiographic images with vacuolization confirming the original suspicion of an abscess **(b)**

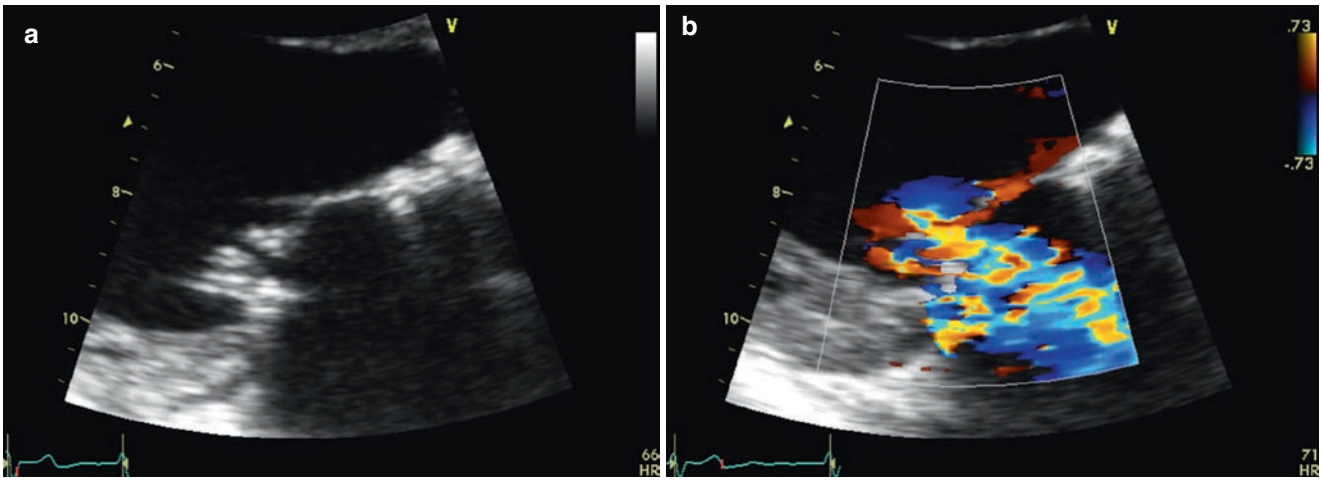

Fig. 9.35 Severe haemolysis in a female patient after mitral annuloplasty. Transthoracic echocardiography **(a, b)** showed a moderate regurgitant jet directed towards the annular ring, causing fragmentation of red cells and haemolysis

References

1. Yoganathan AP, He Z, Casey J. Fluid mechanics of heart valves. *Annu Rev Biomed Eng*. 2004;6:331–362
2. Gillinov AM, Blackstone EH, Rodriguez LL. Prosthesis-patient size: measurement and clinical implications. *J Thorac Cardiovasc Surg*. 2003;126:313–316
3. Flaschkampf FA, Weyman AE, Guerrero JL. Influence of orifice geometry and flow rate on effective valve area: an in vitro study. *J Am Coll Cardiol*. 1991;15:1173–1180
4. Van den Brink RBA. Evaluation of prosthetic heart valves by transesophageal echocardiography: problems, pitfalls, and timing of echocardiography. *Semin Cardiothorac Vasc Anesth*. 2006;10:89–100
5. Baumgartner H, Khan S, DeRobertis M, et al Discrepancies between Doppler and catheter gradients in aortic prosthetic valves in vitro: a manifestation of localized pressure gradients and pressure recovery. *Circulation*. 1990;82:1467–1475
6. Rothbart RM, Smucker ML, Gibson RS. Overestimation by Doppler echocardiography of pressure gradients across Starr–Edwards prosthetic valves in the aortic position. *Am J Cardiol*. 1988;61:475–476
7. Badano LP, Mocchegiani R, Bertoli D, et al Normal echocardiographic characteristics of the Sorin–Bicarbon bileaflet prosthetic heart valve in mitral and aortic position. *J Am Soc Echocardiogr*. 1997;10:632–643
8. Currie PJ, Seward JB, Reeder GS, et al Continuous wave Doppler echocardiographic assessment of severity of calcific aortic stenosis: a simultaneous Doppler–catheter correlative study in 100 adult patients. *Circulation*. 1985;71:1162–1169
9. Badano LP, Zamorano JL, Pavoni D, et al Clinical and hemodynamic implications of supra-annular implant of biological aortic valves. *J Cardiovasc Med*. 2006;7:524–532
10. McDonald ML, Daly RC, Schaff HV, et al Hemodynamic performance of small aortic valve bioprostheses: is there a difference? *Ann Thorac Surg*. 1997;63:362–366
11. Chafizadeh ER, Zoghbi WA. Doppler echocardiographic assessment of the St Jude Medical prosthetic valve in the aortic position using the continuity equation. *Circulation*. 1991;83:213–223
12. Walther T, Falk V, Autschbach R, et al Hemodynamic assessment of the stentless Toronto SPV bioprosthesis by echocardiography. *J Heart Valve Dis*. 1994;3:657–665
13. Caldwell RL, Girod DA, Hurwitz RA, Mahoney L, King H, Brown J. Pre-operative two-dimensional echocardiographic prediction of

prosthetic aortic and mitral valve size in children. *Am Heart J*. 1987;113:873–878
14. Harpaz D, Shah P, Bezante G, Heo M, Stewart S, Hicks GL. Transthoracic and transesophageal echocardiographic sizing of the aortic annulus to determine prosthesis size. *Am J Cardiol*. 1993;72: 1411–1417
15. Yoganathan AP, Cape EG, Sung H, Williams FP, Timoh A. Review of hydrodynamic principles for the cardiologist: application to the study of blood flow and jets by imaging techniques. *J Am Coll Cardiol*. 1988;12:1344–1353
16. Badano LP, Bertoli D, Astengo D, et al Doppler hemodynamic assessment of clinically and echocardiographically normal mitral and aortic Allcarbon valve prostheses: Valve Prosthesis Ligurian Cooperative Doppler study. *Eur Heart J*. 1993;14:1602–1609
17. Rosenheck R, Binder T, Maurer G. Normal values for Doppler echocardiographic assessment of heart valve prostheses. *J Am Soc Echocardiogr*. 2003;16:1116–1127
18. David TE, Armstrong S, Sun Z. Clinical and hemodynamic assessment of the Hancock II bioprosthesis. *Ann Thorac Surg*. 1992;54: 661–667
19. Badano LP, Pavoni D, Musumeci S, et al Stented bioprosthetic valve hemodynamics. How much is the supra-annular implant better than the intra-annular one? *J Heart Valve Dis*. 2006;15:238–246
20. Pibarot P, Dumesnil JG, Jobin J, Cartier P, Honos G, Durand LG. Hemodynamic and physical performance during maximal exercise in patients with an aortic bioprosthetic valve: comparison of stentless versus stented bioprostheses. *J Am Coll Cardiol*. 1999;34: 1609–1617
21. Seiler C. Management and follow-up of prosthetic heart valves. *Heart*. 2004;90:818–824
22. Bonow RO, Carabello BA, Chatterje K, et al Focused update incorporated into the ACC/AHA 2006 guidelines for the management of patients with valvular heart disease. *J Am Coll Cardiol*. 2008;52: e1–142
23. Vahanian A, Baumgartner H, Bax J, et al Task force on the management of valvular heart disease of the european society of cardiology; esc committee for practice guidelines. Guidelines on the management of valvular heart disease. *Eur Heart J*. 2007;28:230–268
24. Pellikka PA, Nagueh SF, Elhendy AA, Kuehl CA, Sawada SG. American Society of Echocardiography recommendations for performance, interpretation, and application of stress echocardiography. *J Am Soc Echocardiogr*. 2007;20:1021–1041
25. Sicari R, Nihoyannopoulos P, Evangelista A, et al Stress echocardiography expert consensus statement from the European Association of Echocardiography. *Eur J Echocardiogr*. 2008;9:415–437
26. Decena BF III, Tischler MD. Stress echocardiography in valvular heart disease. *Cardiol Clin*. 1999;17:555–572
27. Bacassis P, Hayot M, Frapier JM, et al Postoperative exercise tolerance after aortic valve replacement by small-size prosthesis. *J Am Coll Cardiol*. 2000;36:871–877
28. Pibarot P, Dumesnil JG. Prosthesis–patient mismatch: definition, clinical impact, and prevention. *Heart*. 2006;92:1022–1029
29. Medalion B, Blackstone E, Lytle B, White J, Arnold J, Cosgrove D. Aortic valve replacement: is valve size important? *J Thorac Cardiovasc Surg*. 2000;119:963–974
30. Rahimtoola SH. Is severe valve prosthesis–patient mismatch (VP–PM) associated with a higher mortality? *Eur J Cardiothorac Surg*. 2006;30:1
31. Rahimtoola SH. The problem of valve prosthesis–patient mismatch. *Circulation*. 1978;58:20–24
32. Muratori M, Montorsi P, Teruzzi G, et al Feasibility and diagnostic accuracy of quantitative assessment of mechanical prostheses leaflet motion by transthoracic and transesophageal echocardiography in suspected prosthetic valve dysfunction. *Am J Cardiol*. 2006;97: 94–100
33. Pennel DJ, Sechtem UP, Higgins CB, et al Society for Cardiovascular Magnetic Resonance; Working Group on Cardiovascular Magnetic Resonance of the European Society of Cardiology. Clinical indications for cardiovascular magnetic resonance (CMR): consensus panel report. *Eur Heart J*. 2004;25:1940–1965
34. Caceres-Loriga FM, Perez-Lopez H, Santos-Garcia J, Morlans-Hernandez K. Prosthetic heart valve thrombosis: pathogenesis, diagnosis and management. *Int J Cardiol*. 2006;110:1–6
35. Bottio T, Casarotto D, Thiene G, Caprili L, Angelini A, Gerosa G. Leaflet escape in a new bileaflet mechanical valve: TRI technologies. *Circulation*. 2003;107:2303–2306
36. Pavoni D, Badano LP, Ius F, et al Limited long-term durability of the Cryolife O'Brien stentless porcine xenograft valve. *Circulation*. 2007;116:I307–I313
37. Sagar KB, Wann LS, Paulsen WH, Romhilt DW. Doppler echocardiographic evaluation of Hancock and Bjork-Shiley prosthetic values. *J Am Coll Cardiol* 1986;7:681–687
38. Wilkins GT, Gillam LD, Kritzer GL, Levine RA, Palacios IF, Weyman AE. Validation of continuous-wave Doppler echocardiographic measurements of mitral and tricuspid prosthetic valve gradients: a simultaneous Doppler- catheter study. *Circulation* 1986; 74:786–795
39. Burstow DJ, Nishimura RA, Bailey KR, Reeder GS, Holmes DR Jr, Seward JB, Tajik AJ. Continuous wave Doppler echocardiographic measurement of prosthetic valve gradients. A simultaneous Doppler-catheter correlative study. *Circulation* 1989;80:504–514
40. Baumgartner H, Khan S, DeRobertis M, Czer L, Maurer G. Discrepancies between Doppler and catheter gradients in aortic prosthetic valves in vitro. A manifestation of localized gradients and pressure recovery. *Circulation* 1990;82:1467–1475
41. Stewart SF, Nast EP, Arabia FA, Talbot TL, Proschan M, Clark RE. Errors in pressure gradient measurement by continuous wave Doppler ultrasound: type, size and age effects in bioprosthetic aortic valves. *J Am Coll Cardiol* 1991;18:769–779
42. Baumgartner H, Khan S, DeRobertis M, Czer L, Maurer G. Effect of prosthetic aortic valve design on the Doppler-catheter gradient correlation: an in vitro study of normal St. Jude, Medtronic-Hall, Starr-Edwards and Hancock valves. *J Am Coll Cardiol* 1992;19: 324–332

Chapter 10

ENDOCARDITIS

Gilbert Habib and Franck Thuny

CONTENTS

J. L. Zamorano et al. (eds.), *The ESC Textbook of Cardiovascular Imaging*
DOI: 10.1007/978-1-84882-421-8_10, © Springer-Verlag London Limited 2010

Introduction

Imaging plays a key role in the assessment of infective endocarditis (IE). Echocardiography, particularly trans-oesophageal echocardiography (TOE), gives useful information concerning the diagnosis of IE, the assessment of the severity of the disease, the prediction of short-term and long-term prognosis, and the follow-up of patients under specific antibiotic therapy. Other imaging techniques, including magnetic resonance imaging (MRI), CT scan, and invasive angiography, are of limited value for the diagnosis of IE, but are useful for the diagnosis and management of its complications. Finally intra-operative echocardiography must be performed in IE to help surgeons in the intra-operative assessment and management of patients with IE.

IE is a life-threatening disease associated with a high mortality rate.[1,2] Despite major improvements in diagnostic and therapeutic procedures, both the diagnosis of IE and its management remain a challenge. Several complications may occur during the course of IE and are the cause of the persistent high morbidity and mortality of the disease.[3] Because of these very frequent and severe complications, about half the patients with IE are operated on during the active phase of the disease (early surgery).[4] Imaging, particularly echocardiography, plays a key role in both the diagnosis and the management of infective endocarditis. Echocardiography is also useful for the prognostic assessment of patients with IE for their follow-up under therapy and during surgery.[5]

Echocardiography for the Diagnosis of Infective Endocarditis

When to Perform Echocardiography in IE

IE is not a single disease but may present with several very different initial symptoms, including heart failure, cerebral embolism, pacemaker infection, or isolated fever. IE must be suspected in the presence of fever associated with regurgitant heart murmur, known cardiac disease, bacteraemia, new conduction disturbance, and embolic events of unknown origin.[6] In all these situations, echocardiography must be performed. Figure 10.1 is a proposed algorithm illustrating the respective indications of transthoracic (TTE) and trans-oesophageal (TOE) echocardiography. TTE must be performed first in all cases, because it is a non-invasive technique giving useful information both for the diagnosis and the assessment of severity of IE. TOE must also be performed in the majority of patients with suspected IE because of its better image quality and better sensitivity, except in case of good-quality negative TTE associated with a low level of clinical suspicion.

Anatomic Definitions: Echocardiographic Correlations (Table 10.1)

Anatomically, IE is characterized by a combination of vegetations and destructive lesions.

Vegetations are typically attached onto the low-pressure side of the valve structure, but may be located anywhere on the components of the valvular and subvalvular apparatus as well as on the mural endocardium of the cardiac chambers or the ascending aorta. When large and mobile, vegetations are prone to embolism and, less frequently, to valve or prosthetic obstruction.

Destructive lesions are very frequently associated with vegetations or may be observed alone. The consequences of this destructive process may include valve aneurysm, perforation or prolapse, and chordae, or, less frequently, papillary muscle rupture. The main consequences of these lesions are severe valve regurgitation and heart failure.

The third main anatomic feature of IE is *abscess formation.* Abscesses are more frequent in aortic and prosthetic valve IE and may be complicated by pseudo-aneurysm or fistulization.

These three anatomic features are frequently present together and must be meticulously described by the echocardiographic examination. Knowledge of these main anatomic and echocardiographic definitions is mandatory (Table 10.1).

Duke "Echocardiographic" Criteria

In 1994, Durack proposed a new classification of criteria for IE called Duke criteria.[7] This new classification was a big step in the diagnosis of IE because it included echocardiography as a major criterion for IE. The major echographic criteria for IE are vegetation, abscess, and new dehiscence of a prosthetic valve.

Vegetation

Echocardiography is the reference method for the diagnosis of vegetation. Typically, vegetation presents as an oscillating mass attached onto a valvular structure, with a motion independent to that of this valve (Figs. 10.2 and 10.3, Video 10.2). However, vegetation may also present as a non-oscillating mass and with an atypical location (Video 10.22). Vegetations are usually localized on the atrial side of the atrio-ventricular valves and on the ventricular side of the

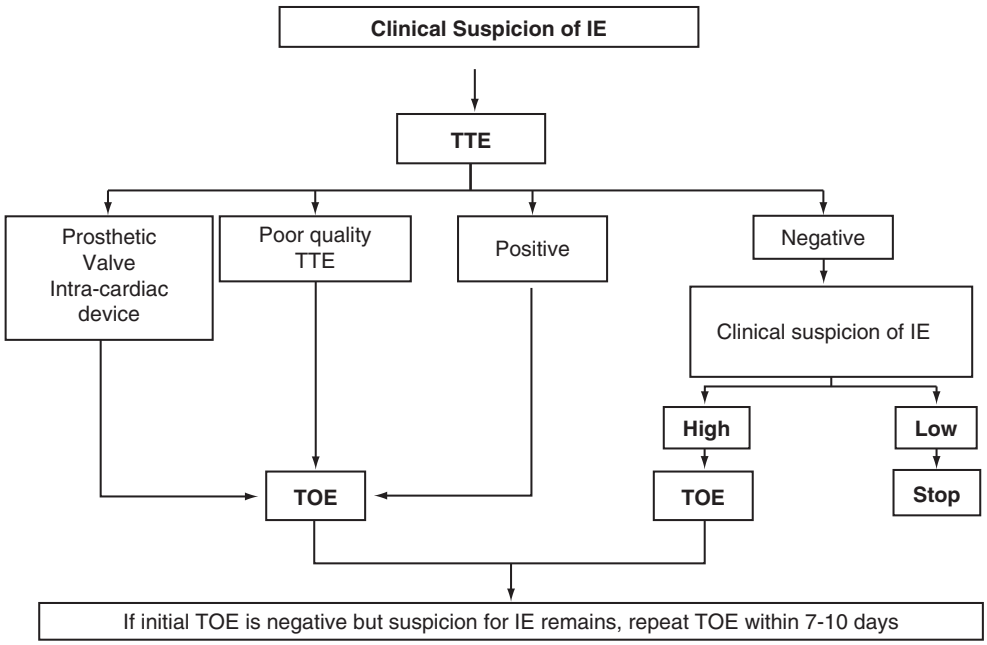

Fig. 10.1 Algorithm showing the role of echocardiography in the diagnosis and assessment of infective endocarditis. Adapted from Horstkotte et al.[6] *IE* infective endocarditis; *TTE* transthoracic echocardiography; *TOE* trans-oesophageal echocardiography

aortic and pulmonary valves. Less frequently, vegetations are localized on mural endocardium, papillary muscles, or ascending aorta. TTE has a sensitivity of about 75% for the diagnosis of vegetations. However, the sensitivity of TTE may be reduced in case of low echogenicity, very small vegetations, and in IE affecting intra-cardiac devices. TOE is mandatory in case of doubtful transthoracic examination, in prosthetic and pacemaker IE, and when an abscess is suspected. TOE enhances the sensitivity of TTE to about 85–90% for the diagnosis of vegetations. In addition, both TTE and TOE are useful to assess the size and mobility of the vegetation as well as its evolution under antibiotic therapy.[8]

Abscess Formation

The second major echocardiographic criterion for endocarditis is the presence of perivalvular abscesses. They are more frequently observed in aortic valve IE and prosthetic valve IE. Abscess typically presents as a perivalvular zone of reduced echo density, without colour flow detected inside. The diagnosis is easy in the presence of a clear free space in the aortic root (Figs. 10.4 and 10.5), but may be much more difficult at the early stage of the disease when only a thickening of the aortic root is evidenced (Figs. 10.6 and 10.7). The sensitivity of TTE is about 50%, and that of TOE is 90%. The additional value of TOE is much higher for the diagnosis

Table 10.1. Echocardiographic definitions.

	Surgery/necropsy	Echocardiography
Vegetation	Infected mass attached to an endocardial structure or on implanted intra-cardial material	Oscillating or non-oscillating intra-cardial mass on valve or other endocardial structures or on implanted intra-cardial material
Pseudo-aneurysm	Perivalvular cavity communicating with the cardiovascular lumen	Pulsatile perivalvular echo-free space with colour flow detected
Abscess	Perivalvular cavity with necrosis and purulent material not communicating with the cardiovascular lumen	Perivalvular zone of reduced echo density without colour flow
Perforation	Interruption of endocardial tissue continuity	Interruption of endocardial tissue continuity traversed by colour Doppler flow
Fistula	Communication between two neighbouring cavities through a perforation	Colour Doppler communication between two neighbouring cavities through a perforation
Valve aneurysm	Saccular outpouching of valvular tissue	Saccular bulging of valvular tissue (most usually affects the mitral valve)
New dehiscence of a prosthetic valve	Dehiscence of the prosthesis	New paravalvular regurgitation identified by TTE/TOE not present at a previous study

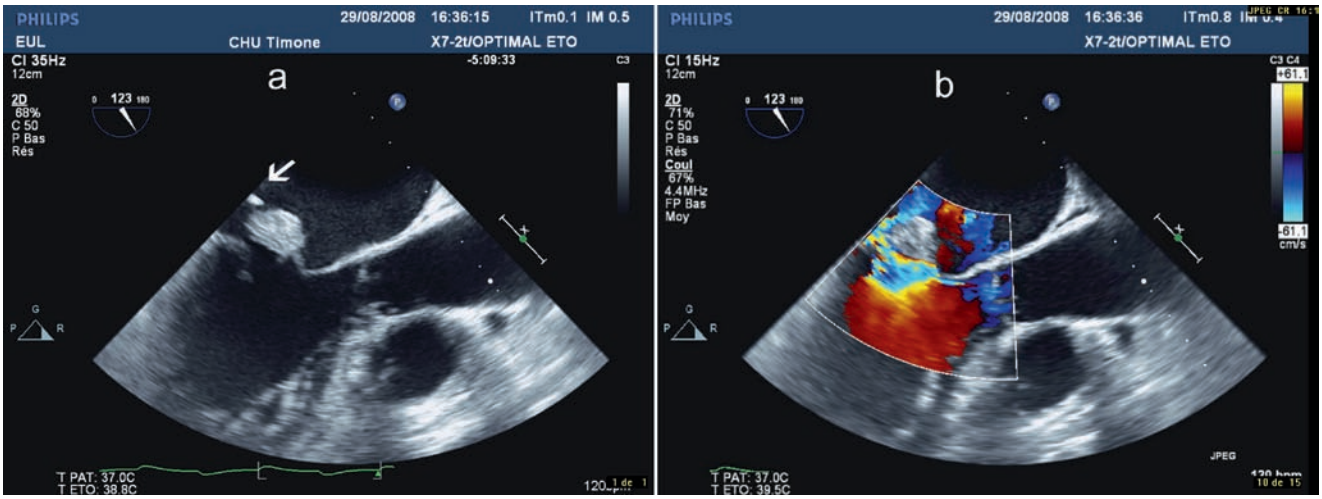

Fig. 10.2 TOE showing a large mitral vegetation on the anterior leaflet associated with a chordae rupture **(a)** and severe mitral regurgitation **(b)**

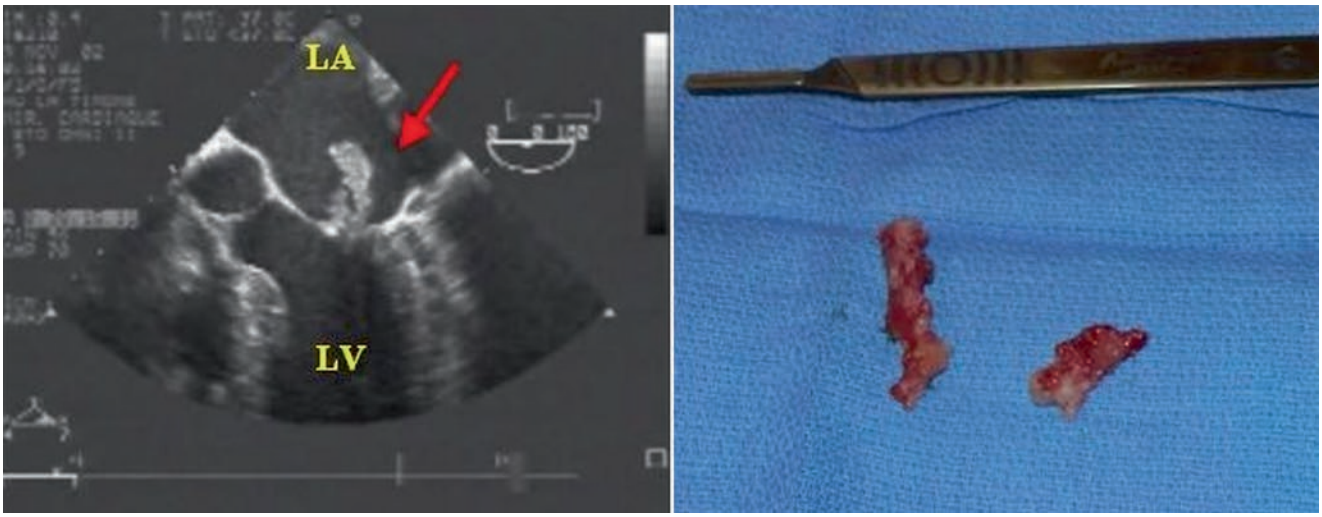

Fig. 10.3 Echo/anatomic correlations. TOE: Large vegetations on the two mitral leaflets (*arrow*). *LA* left atrium; *LV* left ventricle

of abscess than for the diagnosis of vegetation. For this reason, TOE must be systematically performed in aortic valve IE and as soon as an abscess is suspected.

Abscess formation is only one type of perivalvular involvement in IE. Considering echographic and anomic definitions (Table 10.1), three types of perivalvular lesions may be described.

- Abscess is a non-communicating zone of necrosis with purulent material. Echographic appearance is a non-circulating perivalvular zone of reduced echo density (Fig. 10.8).
- Pseudo-aneurysm is characterized anatomically by a perivavular cavity communicating with the cardiovascular lumen. The echographic hallmark of pseudo-aneurysm is the presence of a pulsatile perivalvular echo-free space with colour Doppler flow inside (Figs. 10.9 and 10.10). The echographic appearance of partial systolic collapse proves that the abscess communicates with the cardiovascular lumen.
- Fistula may be a complication of both abscesses and pseudo-aneurysm. They are defined anatomically by a communication between two neighbouring cavities and echographically by a colour Doppler communication between two adjacent cavities.

All these perivalvular lesions are more frequently observed in aortic endocarditis and then involve the mitral-aortic intervalvular fibrosa (Fig. 10.11, Video 10.11).[9]

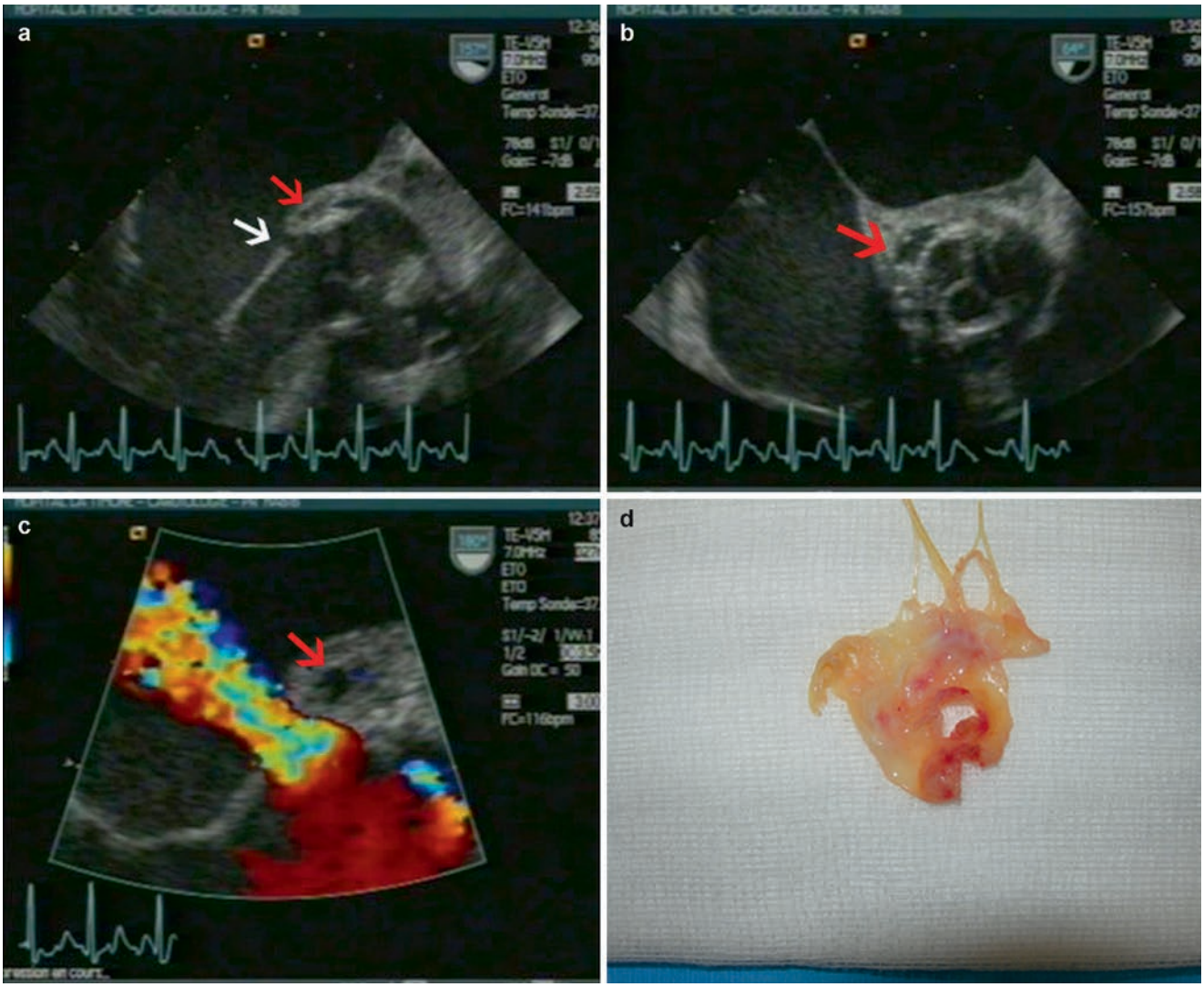

Fig. 10.4 TOE showing the periannular damages of an aortic bioprosthetic valve endocarditis. We can see the association of an annular abscess (**a-c**, *red arrow*) with a perforation of the basal area of the anterior mitral leaflet (**a**, *white arrow*, **c**, **d**) leading to mitral regurgitation

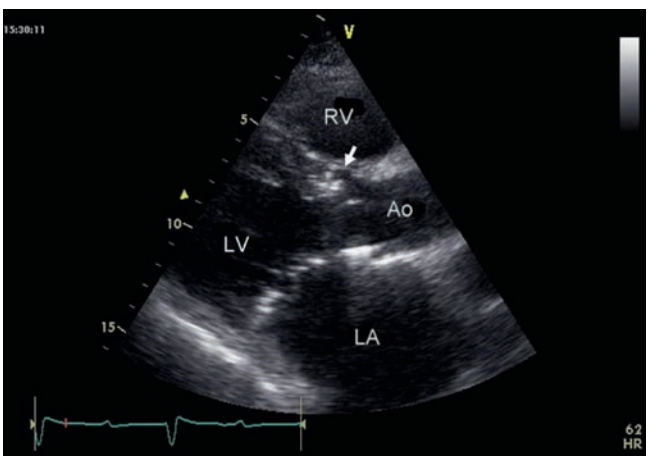

Fig. 10.5 TTE showing an anterior aortic annular abscess (*arrow*)

New Dehiscence of a Prosthetic Valve

It represents the third main diagnostic criterion for IE.[7] IE must be suspected in the presence of a new perivalvular regurgitation, even in the absence of vegetation or abscess. TOE has a better sensitivity than TTE for this diagnosis, especially in mitral prosthetic valve infective endocarditis (PVIE) (Fig. 10.12). Hence, systematic post-operative echocardiography must be performed after any valve replacement to serve as reference for better interpretation of future echocardiographic abnormalities.

Other Echocardiographic Findings in IE

Other echocardiographic features are not the main criteria for IE, but may be suggestive of the diagnosis. They

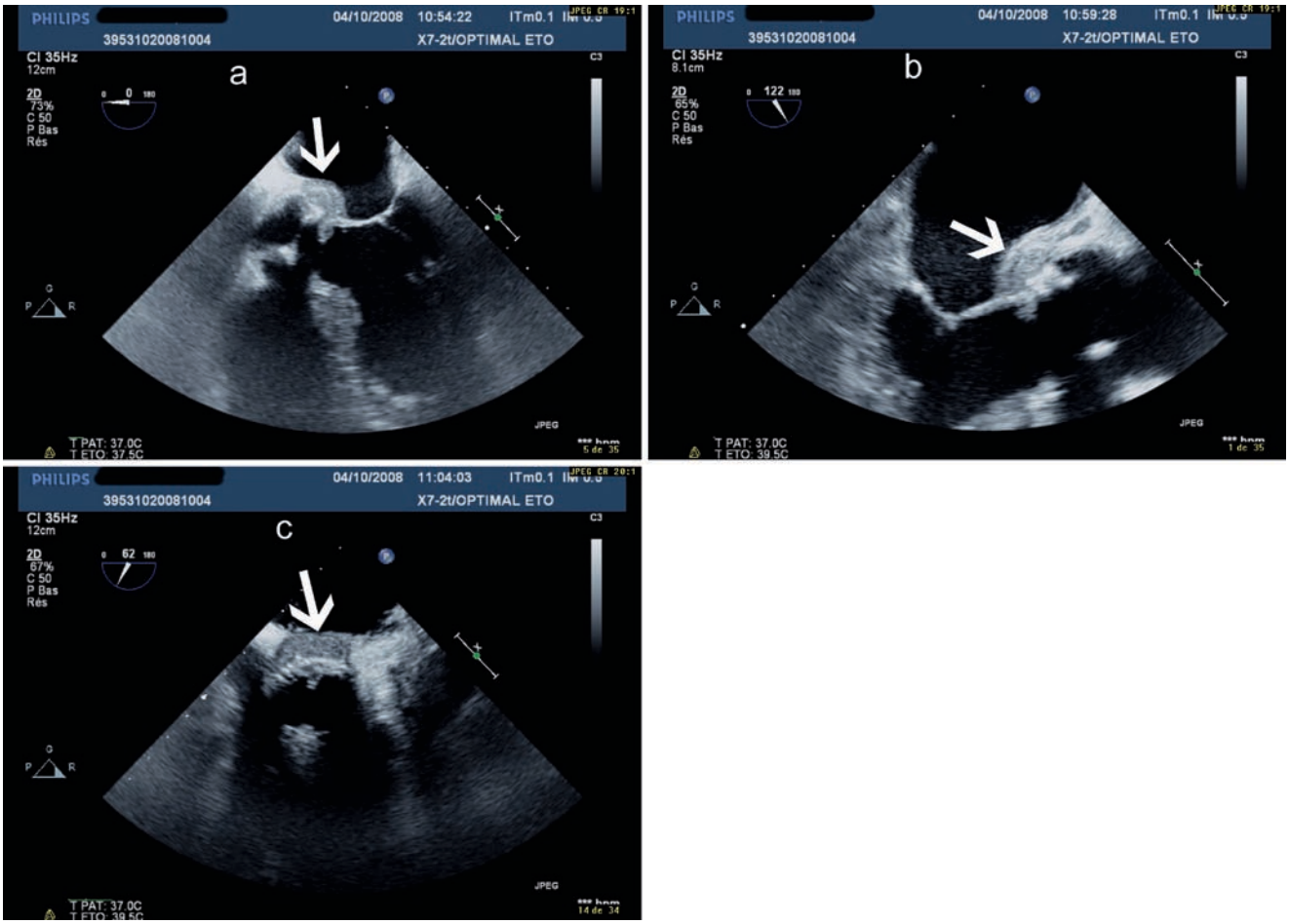

Fig. 10.6 a, b, c: three TOE views showing an echodense thickening around the annulus of a bioprosthetic valve corresponding to a perian-nular abscess (*arrow*)

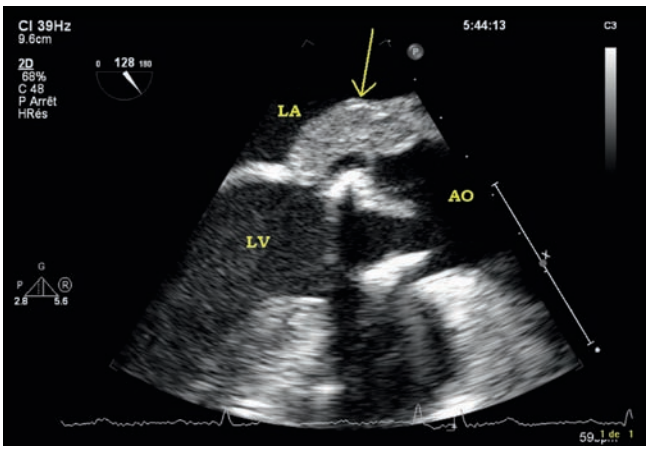

Fig. 10.7 Aortic bioprosthetic abscess presenting as a thickening of the posterior aortic root (*arrow*). *AO* aorta; *LV* left ventricle; *LA* left atrium

include valve destruction and prolapse, aneurysm, and/or perforation of a valve (Fig. 10.13). The most frequent is anterior mitral valve perforation, which is usually a complication of aortic valve IE. It may be observed either isolated or as a complication of a mitral valve aneurysm (Fig. 10.11). Perforation of the mitral valve may be the consequence of an infected aortic regurgitant jet and is best visualized by TOE.[10]

In addition, both TTE and TOE are useful for the assessment of the underlying valve disease and for the assessment of the consequences of IE, including:

- Left ventricular size and function
- Quantification of valve regurgitation/obstruction
- Right ventricular function, estimation of pulmonary pressures

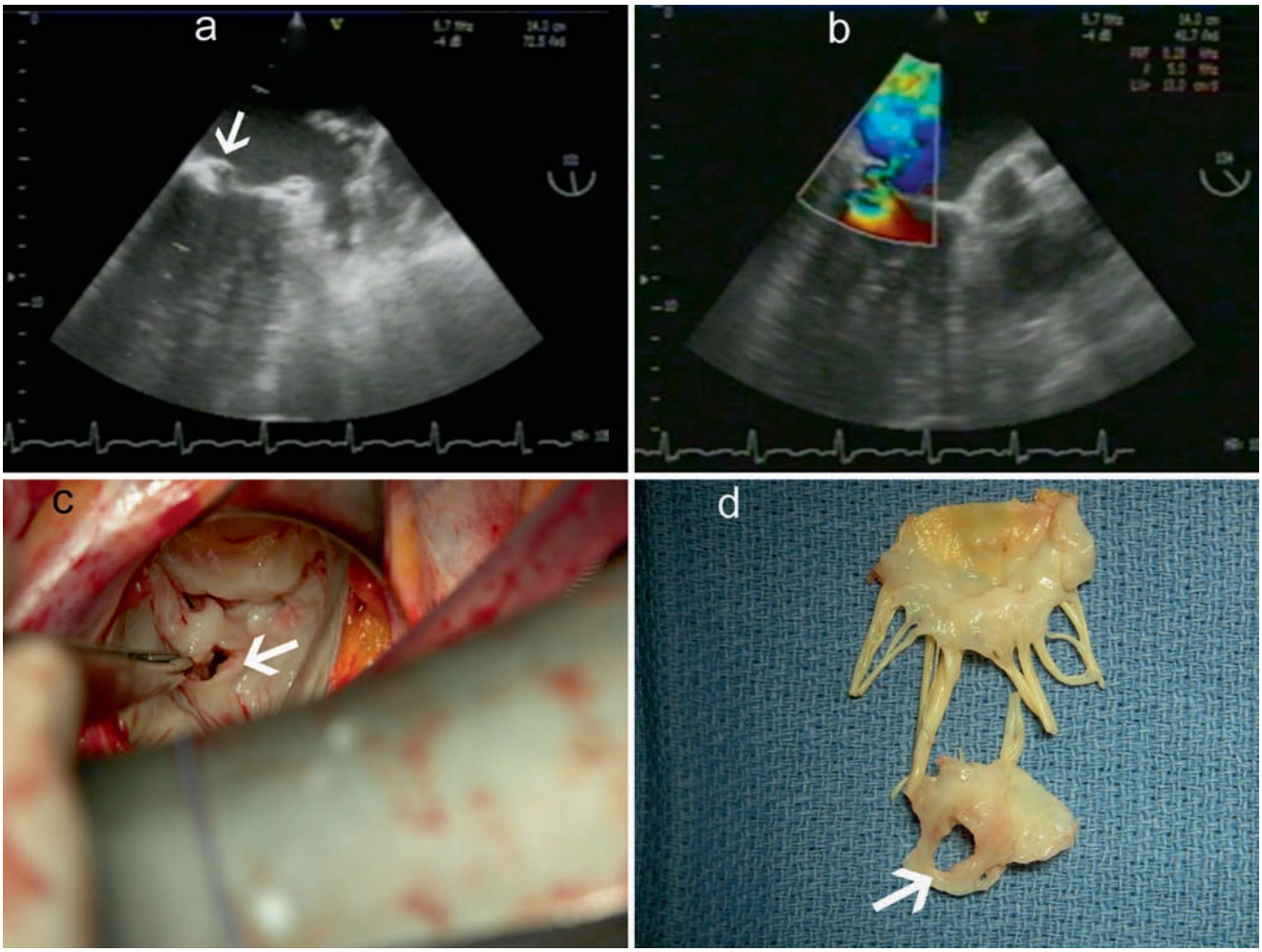

Fig. 10.8 TOE showing a mitral annular abscess (*arrows*, **a**) with perforation **(b). (c, d)** show the valvular and perivalvular damages observed during the operation

Limitations and Pitfalls of Echocardiography

In clinical practice, the echocardiographic diagnosis of IE remains difficult in three main situations:

- In case of normal or doubtful echocardiography
- In IE affecting intra-cardiac devices
- In patients with PVIE

In all these situations, echographic findings, positive or negative, must be interpreted with caution, taking into account the clinical presentation and the likelihood of IE.

Normal or Doubtful Echocardiography

A negative echocardiography may be observed in about 15% of IE. The most frequent explanations for negative echocardiography are very small or absent vegetations and difficulties in identifying vegetations in the presence of pre-existent severe lesions (mitral valve prolapse, degenerative lesions, and prosthetic valves). Similarly, diagnosis of IE may be more difficult in the case of non-oscillating vegetation and vegetations of atypical location (Video 10.22). In addition, the diagnosis may be difficult at the early stage of the disease, when vegetations are not yet present or too small to be identified. In one series,[11] among 93 patients with anatomically confirmed IE, vegetation was observed by TOE in only 81%. In another series,[12] among 105 patients with suspected IE, 65 had an initial negative TOE; in three cases, vegetation appeared on a repeat TOE. For this reason, repeat TTE/TOE examination must be performed 7–10 days after the first examination when the clinical level of suspicion is still high.

Conversely, false diagnosis of IE may occur in other situations; for example, it may be difficult to differentiate between vegetations and thrombi, cusp prolapse, cardiac tumours, myxomatous changes, Lambl's excrescences, strands, or non-infective vegetations (marantic endocarditis). Non-infective

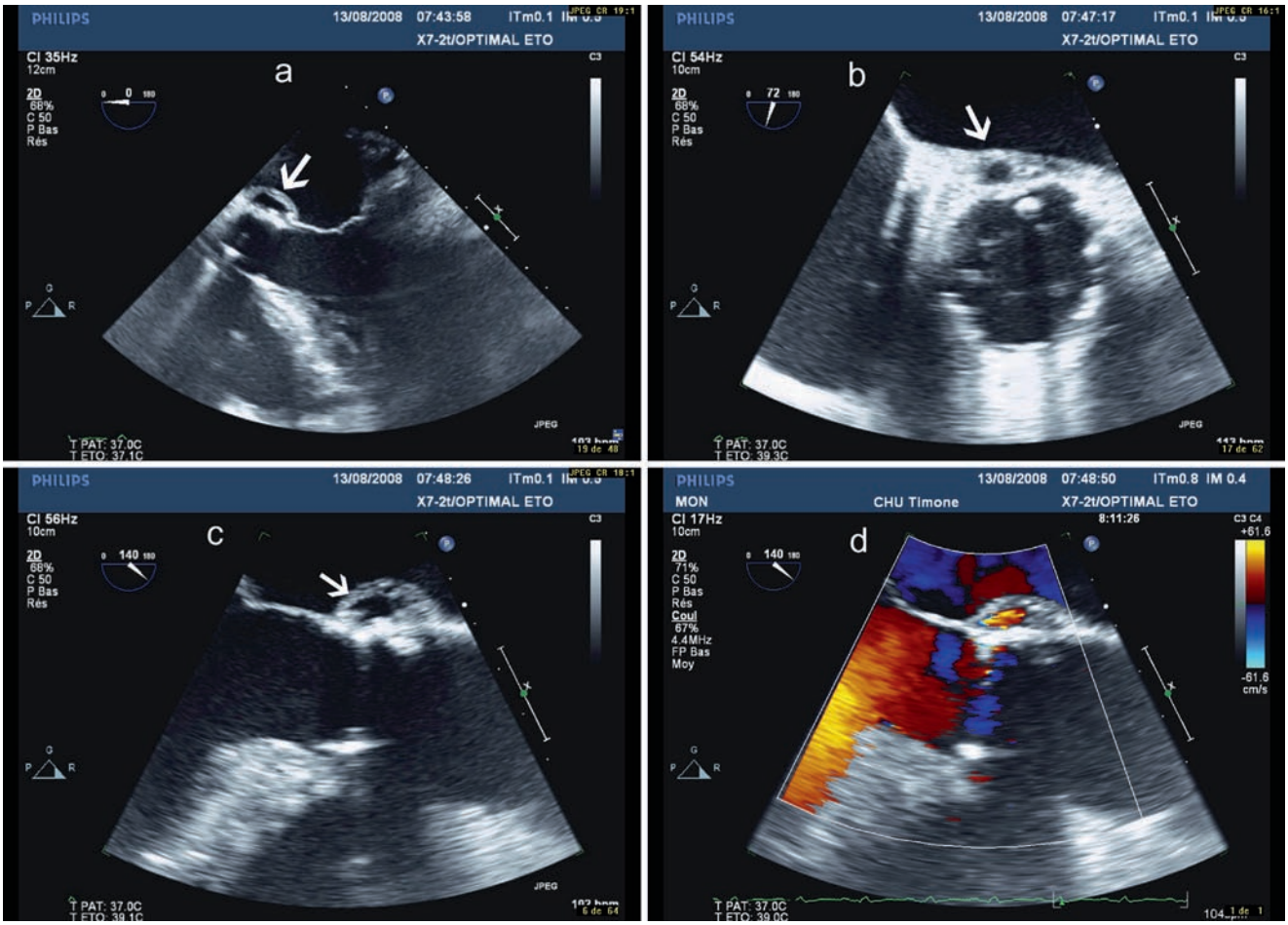

Fig. 10.9 TOE showing an aortic pseudo-aneurysm in a patient with a bioprosthetic valve. This periannular complication is diagnosed by demonstration of an echolucent cavity within the posterior area of the valvular annulus (**a, b, c,** *arrows*) and a flow detected by colour Doppler into this cavity **(d)**

vegetations are impossible to differentiate from infective vegetations. They can be suspected in the presence of small and multiple vegetations, changing from one examination to another, and without associated abscess or valve destruction.

Similarly, diagnosis of a perivalvular abscess may be difficult, even with the use of TOE, in the case of small abscess (Fig. 10.14), when echocardiography is performed very early in the course of the disease or in the immediate postoperative period after aortic root replacement or Bentall procedure. In these latter situations, a thickening of the aortic wall may be observed in the absence of IE, mimicking abscess formation. Recent publications[13] underlined the discrepancies between the results of TOE and anatomical findings, particularly in patients with abscess localized around calcification in the posterior mitral annulus. Finally, a normal echocardiogram does not completely rule out IE, even if TOE is performed and even in expert hands, and a repeat examination has to be performed in case of high level of clinical suspicion.

Cardiac Devices-Related Infective Endocarditis (CDRIE)

CDRIE, including permanent pacemaker and implantable cardioverter defibrillators, is a severe disease associated with high mortality.[14] CDRIE is defined by an infection extending to the electrode leads, cardiac valve leaflets, or endocardial surface. CDRIE is probably one of the most difficult forms of IE to diagnose.

Similar to other forms of IE, echocardiography plays a key role in CDRIE and is helpful both for the diagnosis of lead vegetation, diagnosis of tricuspid involvement, diagnosis of tricuspid regurgitation, sizing of vegetations, as well as follow-up after lead extraction. With regard to diagnosis, although TOE has superior sensitivity and specificity than TTE, both must be systematically performed in suspected CDRIE. Vegetations may be observed both on the electrode leads, cardiac valve leaflets, or endocardial surface (Video 10.23). Careful examination of the entire leads is mandatory,

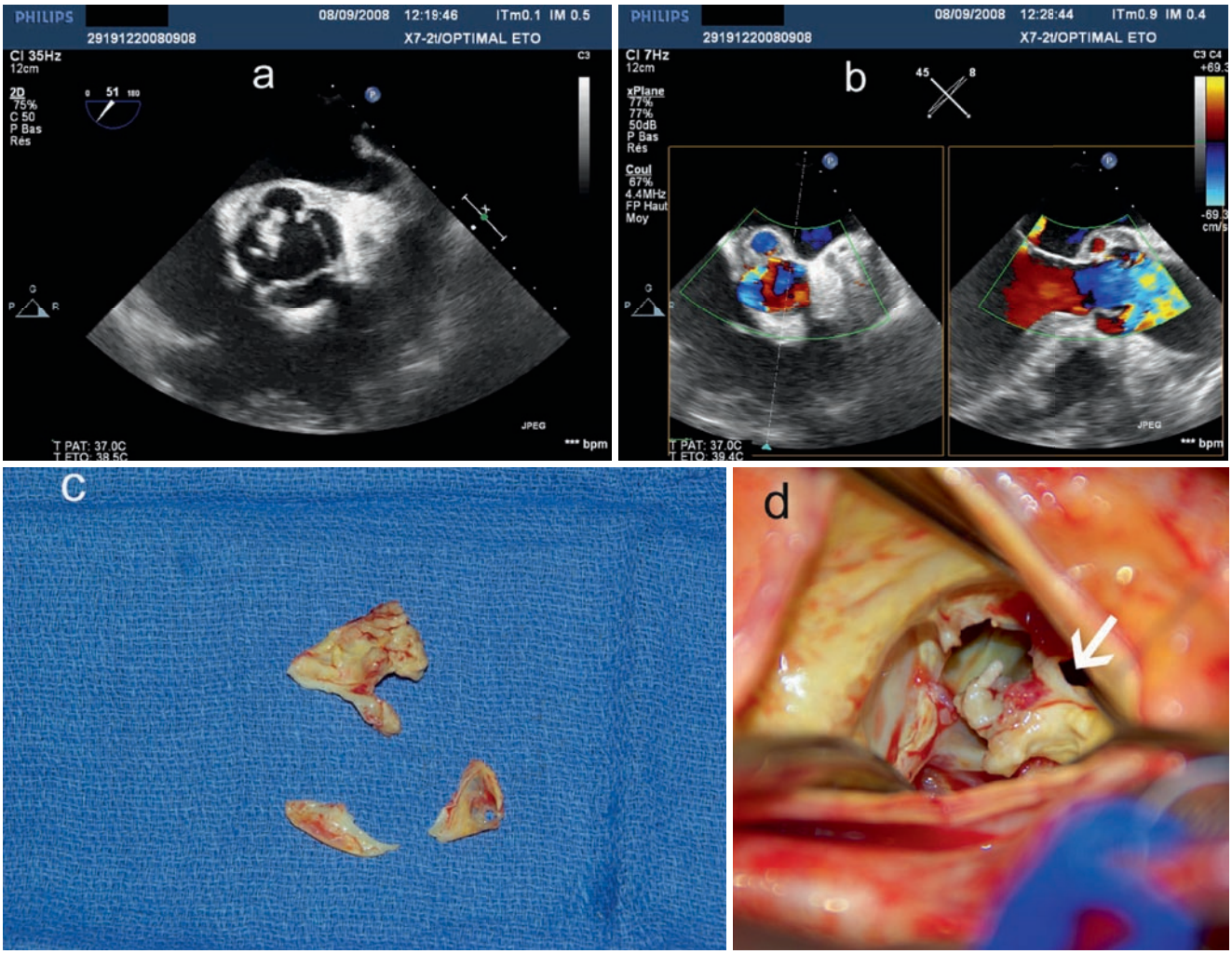

Fig. 10.10 TOE showing an aortic endocarditis with a destruction of the commissure between the non-coronary cusp and the left-anterior cusp **(a)**. Large vegetation is seen on the non-coronary cusp **(a)**. **(b)** shows two orthogonal views of the aortic root during the same time by using the 3D TOE probe. There is a pseudo-aneurysm into the posterior wall of the aortic root. **(c)** shows the aortic cups after surgical excision. **(d)** shows the gap of the pseudo-aneurysm in the aortic wall (*arrow*)

from the superior vena cava to the apex of the right ventricle. However, both TTE and TOE may be falsely negative in CDRIE, and a normal echographic examination does not rule out CDRIE. Atypical findings are frequent, including thickening and "sleeve-like" appearance of the pacemaker lead[14] and must be differentiated from normal findings.

The Duke criteria have been used for the diagnosis of infective endocarditis in cases of suspected CDRIE, but are difficult to apply in these patients, because of lower sensitivity, despite proposed modifications.[14]

Prosthetic Valve Infective Endocarditis (PVIE)

The anatomic involvement differs between PVIE affecting either mechanical or bioprosthetic valves.[15] In mechanical valves, the infection usually involves the junction between the sewing ring and the annulus, leading to perivalvular abscess, dehiscence, pseudo-aneurysms, and fistula. Although similar mechanisms may also be observed in bioprosthetic PVIE, infection is more frequently located on the leaflets in those patients, leading to cusp rupture, perforation, and vegetations. Echocardiography, particularly TOE, plays a key role in the diagnosis and evaluation of PVIE (Fig. 10.15, Video 10.15). TOE is mandatory in PVIE because of its better sensitivity and specificity for the detection of vegetations, abscesses, and perivalvular lesions. However, the value of both TTE and TOE is lower in PVIE when compared with NVE, because of both lower sensitivity and specificity and because the presence of intra-cardiac material may hinder the identification of both vegetations and abscesses. Consequently, a negative echocardiography is frequently observed in PVE,[16] and does not rule out the diagnosis of PVE. The Duke criteria

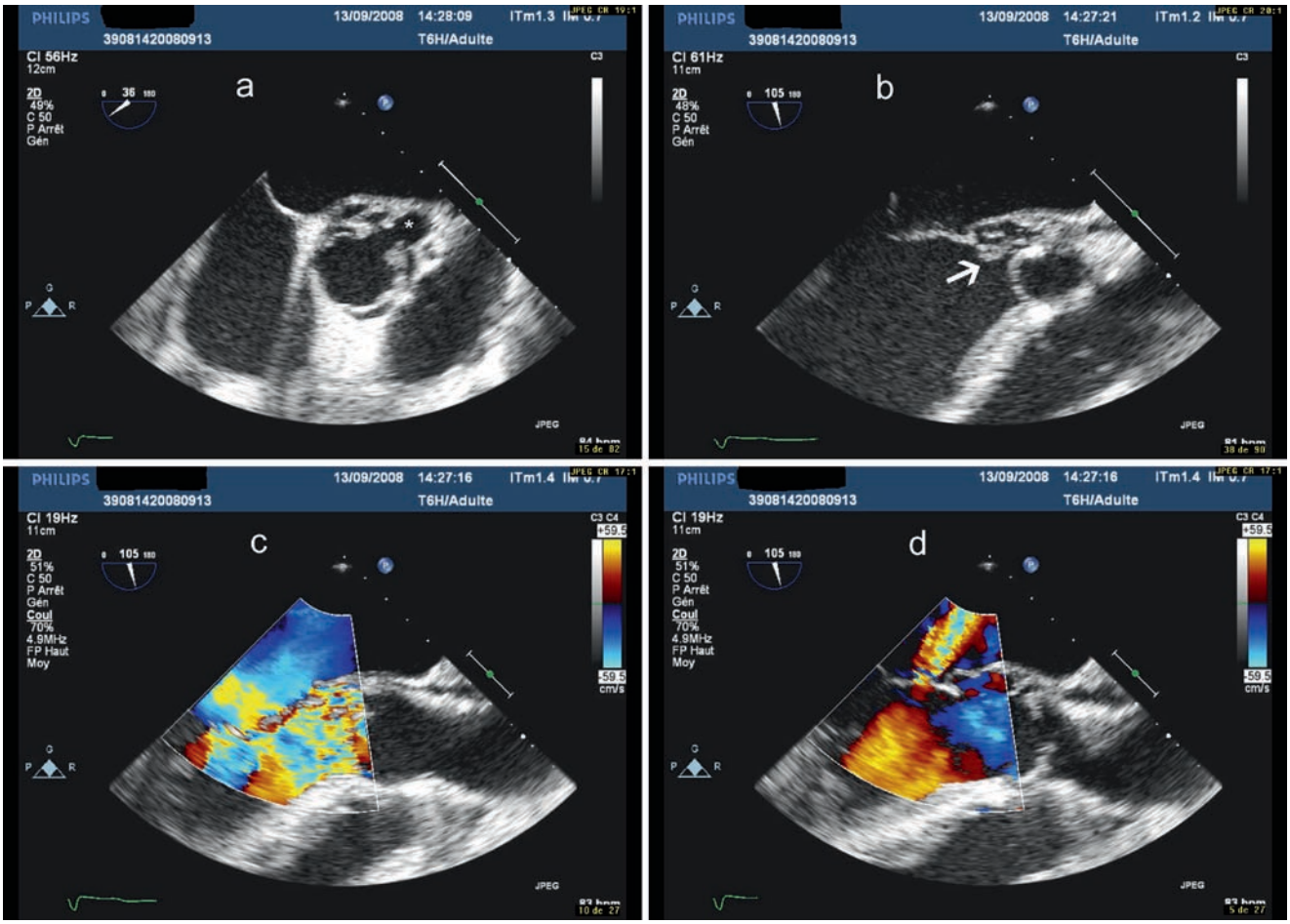

Fig. 10.11 TOE showing a mitral–aortic endocarditis with a pseudo-aneurysm of the mitral–aortic fibrous intervalvular area. Destruction of the posterior commissure of a bicuspid valve (**a**, *white star*). Large, mobile aortic vegetations prolapsing into the left ventricular outflow tract during diastole and contacting the ventricular aspect of the anterior mitral leaflet (**b**, *arrow*). These lesions lead to a severe aortic regurgitation (**c**) and a mitral perforation (**d**)

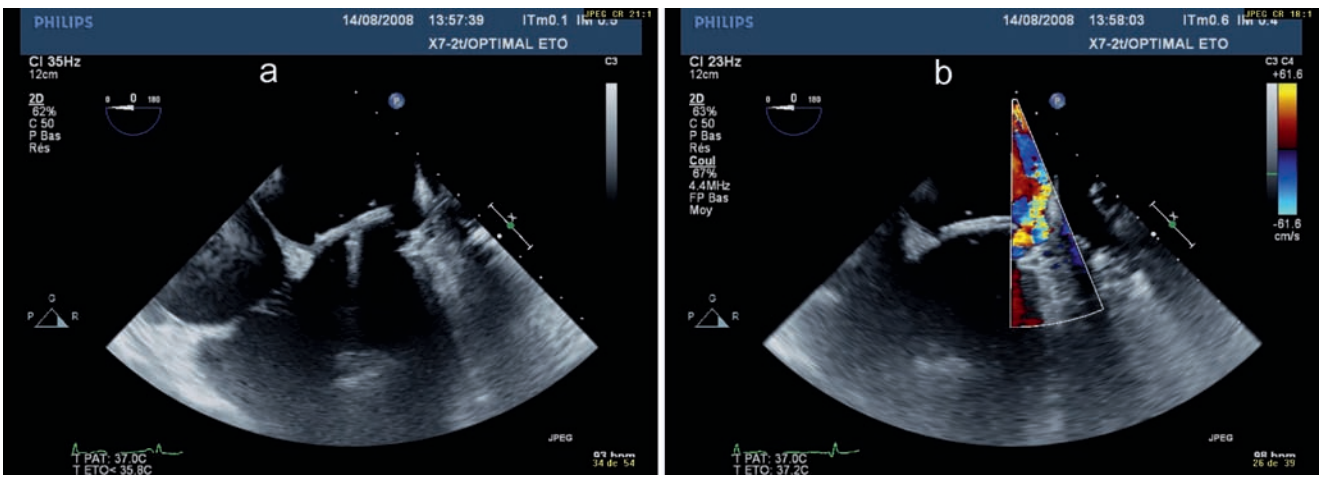

Fig. 10.12 TOE showing a large perivalvular desinsertion on the lateral part of the annulus of mechanical prosthetic valve leading to a severe mitral regurgitation in a patient with an early prosthetic valve endocarditis

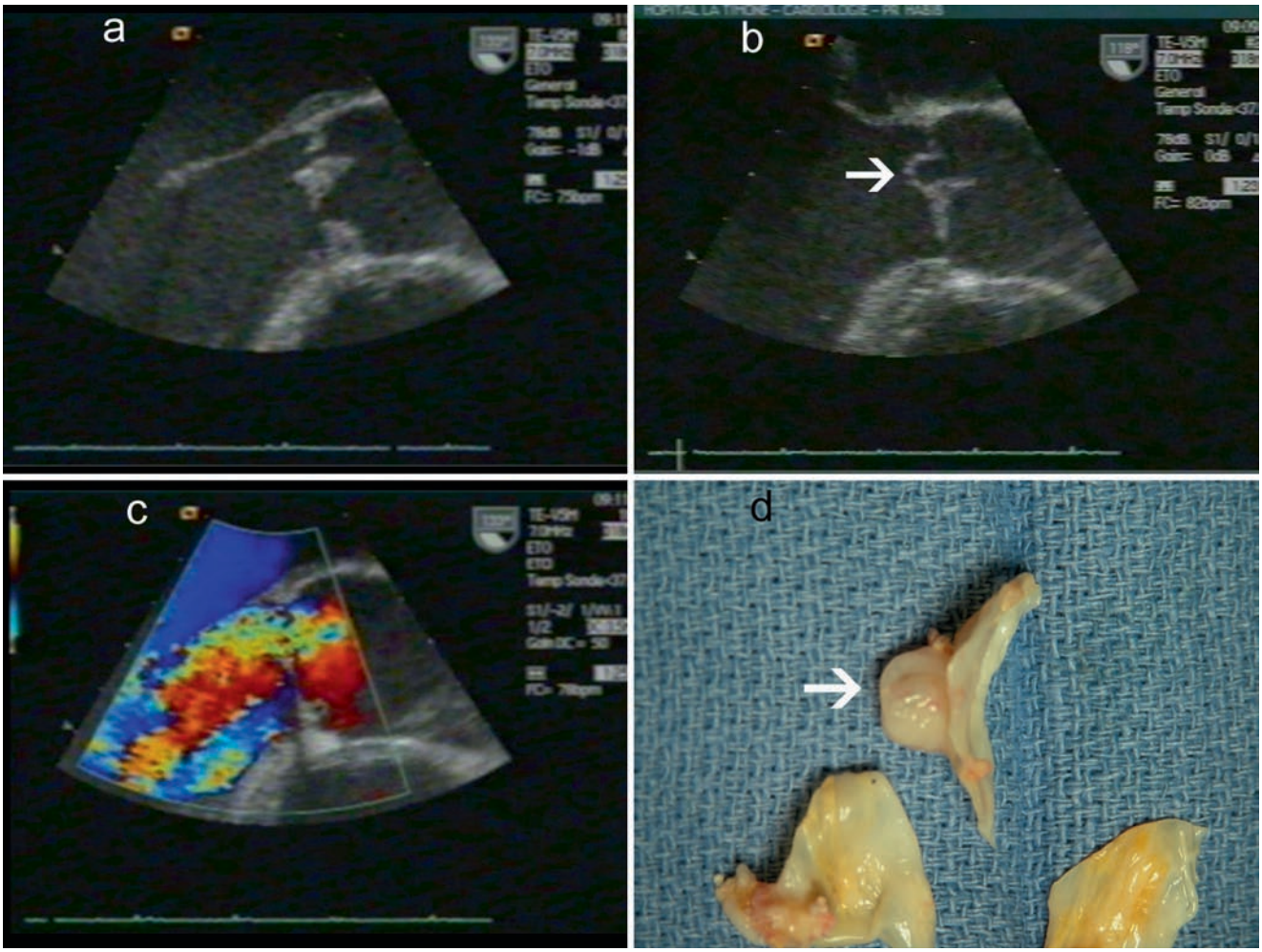

Fig. 10.13 TOE showing a native aortic valve endocarditis with a "valvular aneurysm" (*arrow*) associated with a perforation leading to an acute aortic regurgitation

cannot be applied in clinical practice in PVIE because of their lower sensitivity in this setting.[17]

Other Imaging Techniques

Other imaging modalities are of relatively limited value for the diagnosis of IE, but are sometimes useful for the assessment and follow-up of IE complications.

Intra-cardiac Echocardiography and 3D Echocardiography

They add little information to conventional echocardiography. Their use has been occasionally reported in case reports or short series. 3D echocardiography is not better than TTE or TOE for the diagnosis of vegetation, because of its lower spatial resolution, but may be useful for the diagnosis and assessment of abscesses, false aneurysms, and anterior mitral valve perforation (Fig. 10.16).

Cardiac CT Scan and Cardiac Magnetic Resonance Imaging (MRI)

Similarly, they are potentially useful for the assessment and follow-up of perivalvular complication, including abscesses and pseudo-aneurysm (Fig. 10.17). They may be used to assess perivalvular lesions when TOE is doubtful or not feasible. However, although multiple case reports of the use of MRI and cardiac CT scan in patients with IE have been published, no large studies have been performed.

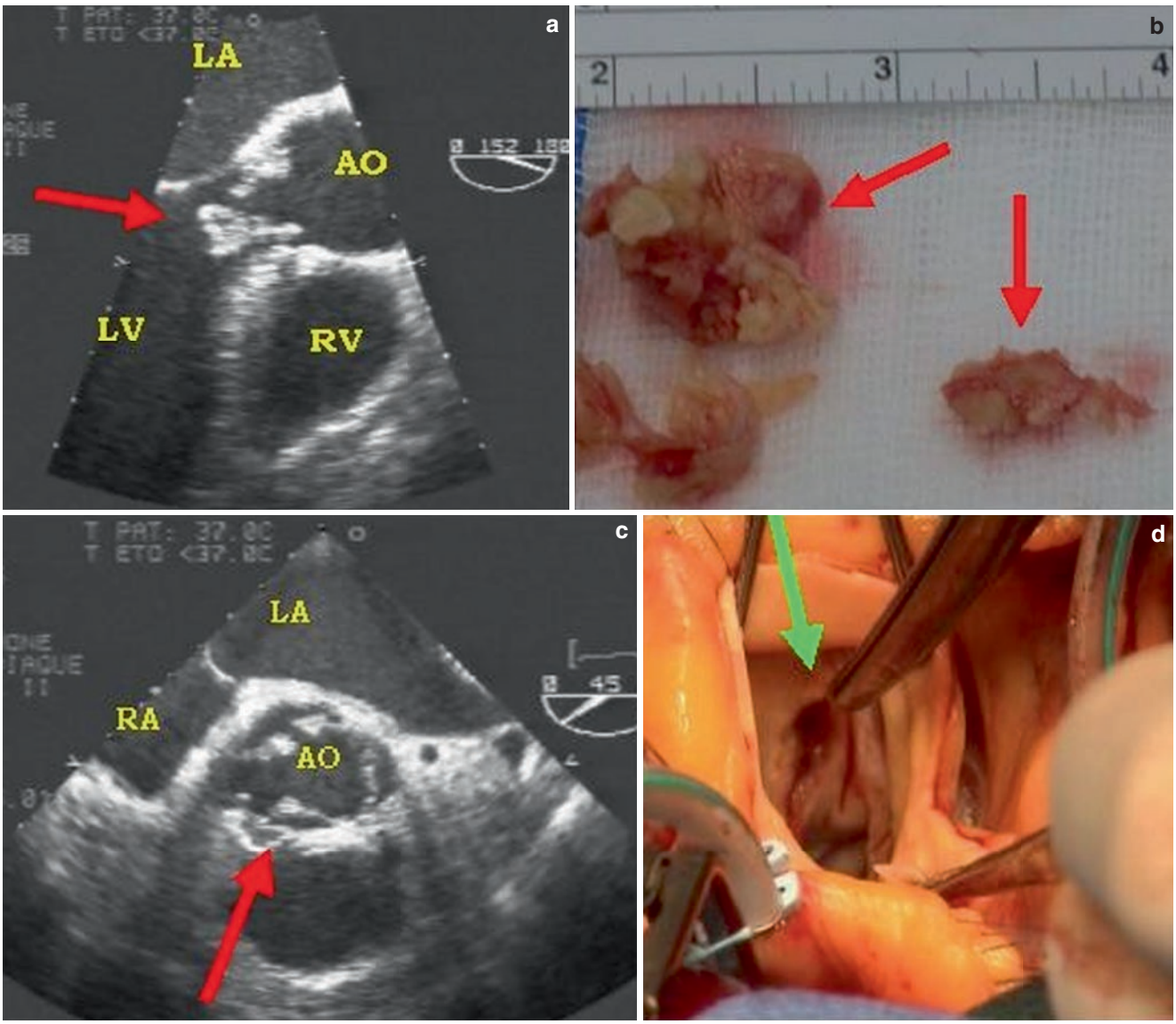

Fig. 10.14 Severe aortic endocarditis with large vegetation, valve destruction, and perivalvular abscess. **(a)** Large vegetation (17-mm long) on the aortic valve by TOE (*arrow*) with diastolic prolapse and severe valve destruction. **(b)** Anatomic confirmation of large vegetations on the aortic leaflets (*arrows*). **(c)** Small abscess formation near the right coronary sinus (*red arrow*) in the same patient. **(d)** Anatomic confirmation (*green arrow*). In this patient, the combination of severe regurgitation, perivalvular abscess, and large vegetation indicates very early surgery. *LV* left ventricle; *LA* left atrium; *Ao* aorta; *RV* right ventricle; *RA* right atrium

Cerebral and Abdominal CT Scan, MRI Angiography, and Invasive Vascular Angiography

Cerebral and abdominal CT scans are frequently used to diagnose embolic complications of IE. For example, splenic embolism is very frequent in IE. It may be silent and detected only by systematic abdominal CT scan (Fig. 10.18).

Cerebral CT scan/MRI are of utmost value for the diagnosis and management of cerebral complications of IE. MRI or conventional angiography may be used in case of suspected arterial mycotic aneurysm (Figs. 10.19 and 10.20).

Prognostic Value of Echocardiography

In addition to its role in diagnosing IE, echocardiography also has a major prognostic value in IE, for both prediction of death and embolic events.

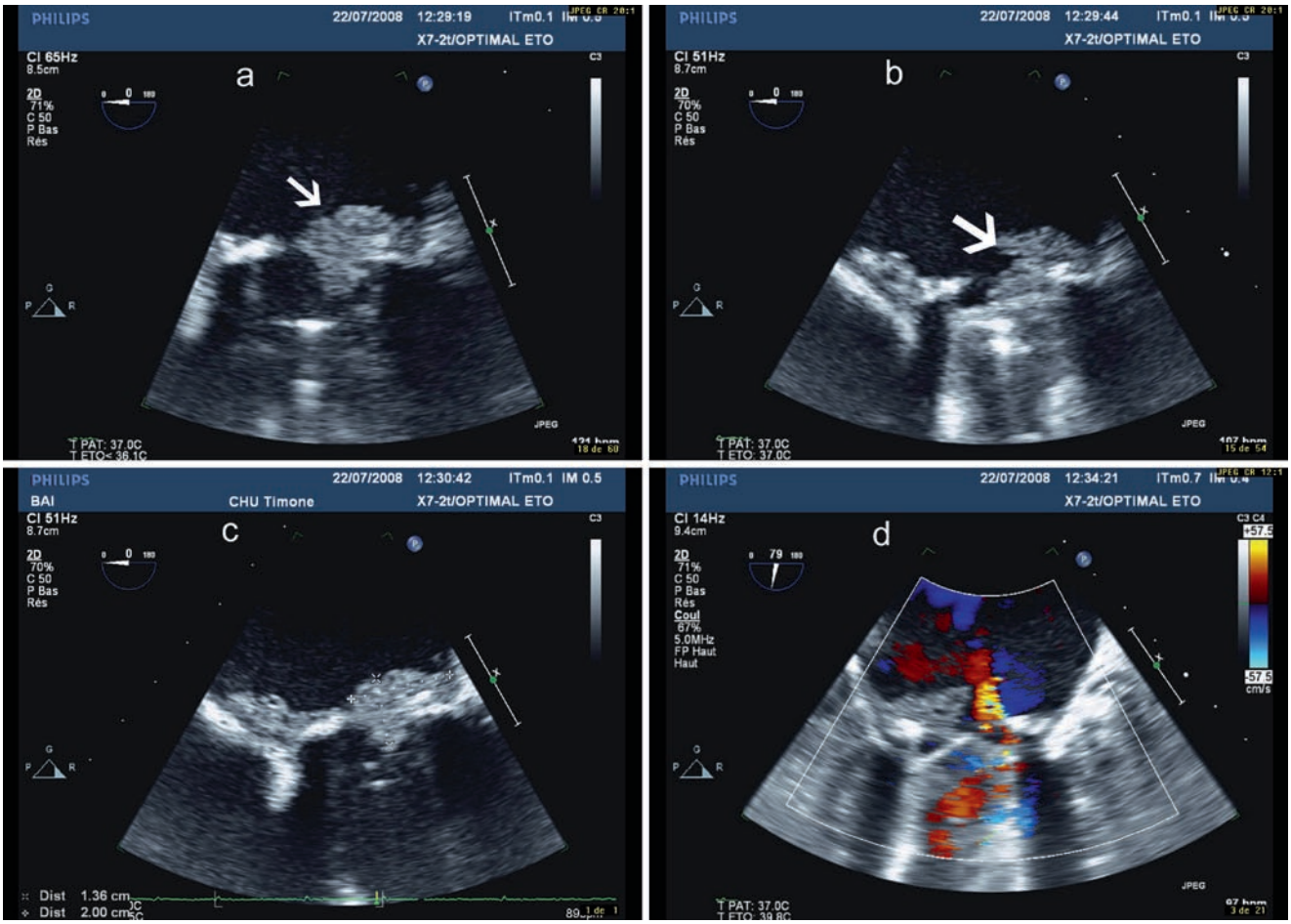

Fig. 10.15 TOE showing a large vegetation prolapsing into a mitral mechanical prosthetic valve (**a, b, c**, *arrows*). Disparition of two physiological regurgitations **(d)**

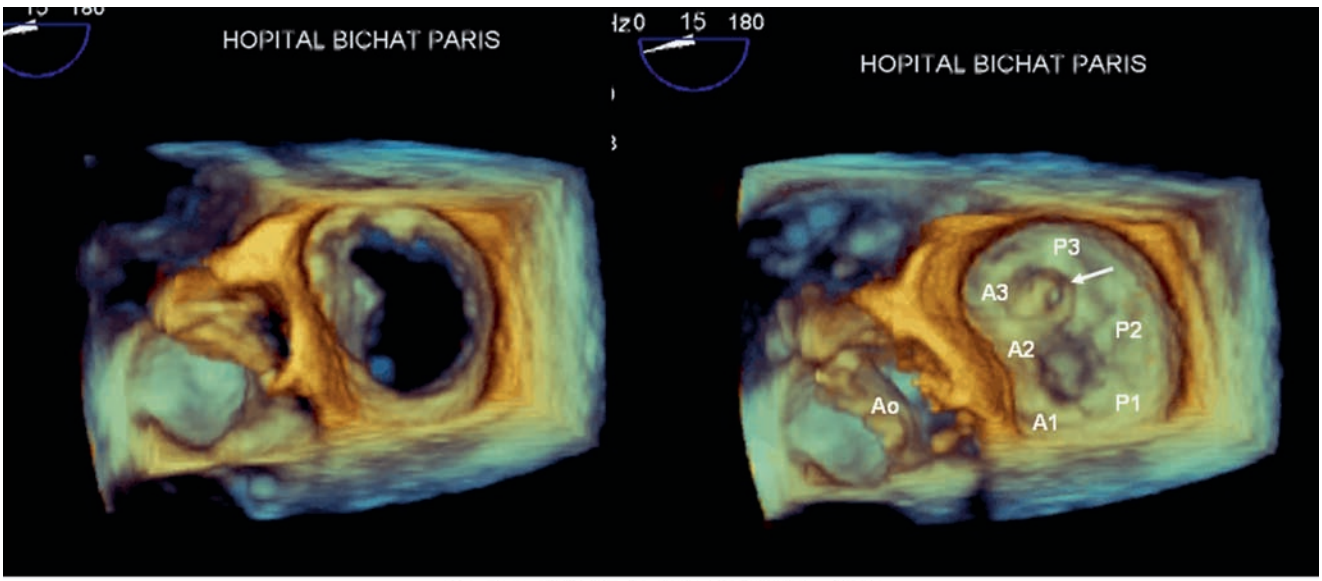

Courtesy of Dr Brochet, Hopital Bichat – Paris

Fig. 10.16 3D TOE: Aneurysm and perforation of the anterior mitral leaflet (*arrow*)

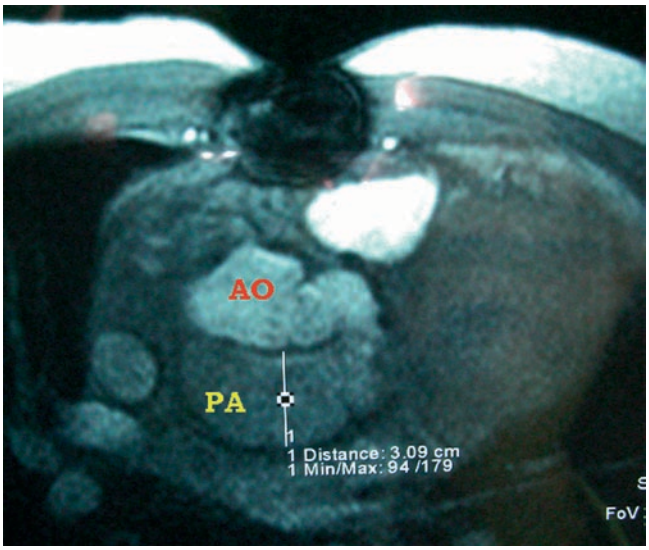

Fig. 10.17 CT scan: Pseudo-aneurysm of the ascending aorta. *PA* pseudo aneurysm; *AO* aorta

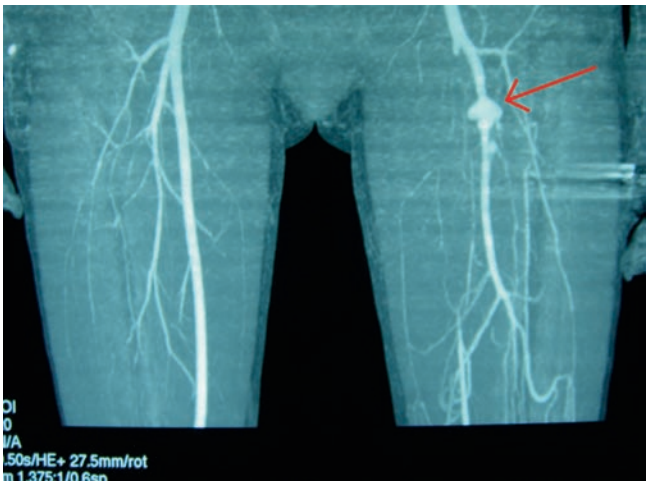

Fig. 10.19 Mycotic aneurysm of the left femoral artery (*arrow*) in a young intravenous drug abuser woman with staphylococcal endocarditis

Echocardiography Predicts Both In-Hospital Mortality and Long-Term Prognosis in IE

Mortality is still high in IE, although it has declined in the recent years. Several factors have been associated with an increased risk of death in IE, including patients' characteristics (diabetes, co-morbidity), presence or absence of complications (heart failure, stroke, renal failure), and type of micro-organism.[18] Echocardiography also plays a very important prognostic role in IE. Several echocardiographic features have been associated with worse prognosis, including periannular complications, severe valve regurgitation or obstruction, low LV ejection fraction, pulmonary hypertension, and premature mitral valve closure.

Premature mitral closure (Fig. 10.21) is an old but still useful M-mode sign observed in severe aortic regurgitation and indicates high left ventricular diastolic pressures and usually a need for early surgery. The presence of a vegetation, its size, and its multi-valvular location have been associated with a worse prognosis. In a recent series,[19] large vegetations (>15 mm length) were associated with a worse prognosis. Echocardiography appears predictive of both the risk of embolism and death in IE.

Risk of Embolism

Incidence of Embolic Events in IE

Embolic events are a frequent and life-threatening complication of IE, related to the migration of cardiac vegetations. Cerebral arteries and spleen are the most frequent sites of embolization in left-side IE, while pulmonary embolism is

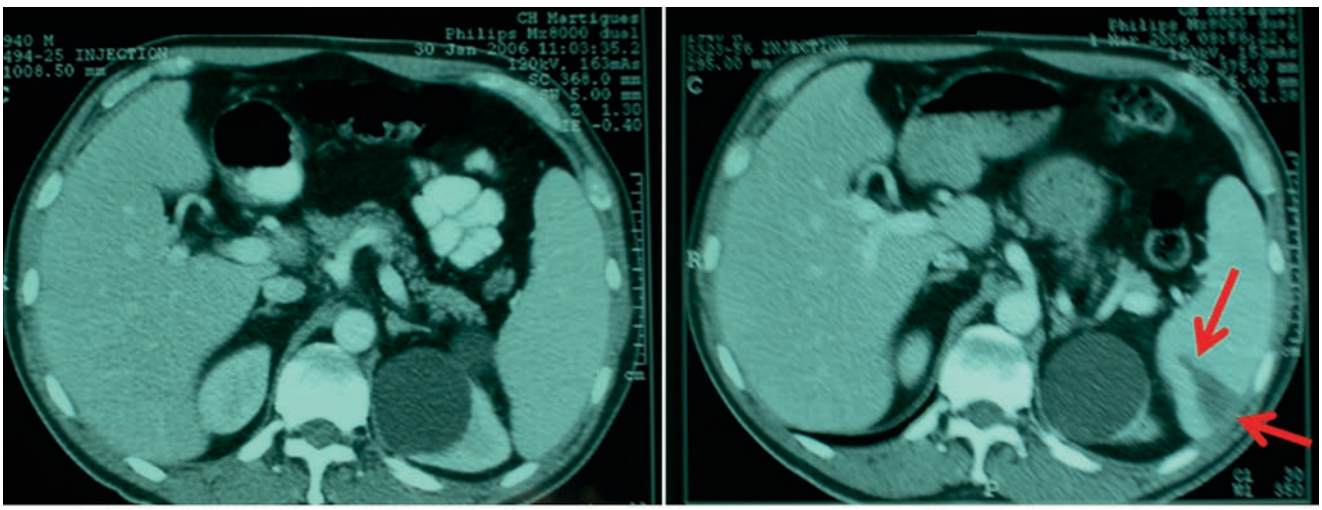

Fig. 10.18 Splenic embolism in a patient with infective endocarditis. *January 2006*: Normal systematic CT scan on admission. *March 2006*: New asymptomatic splenic embolism detected by repeat examination

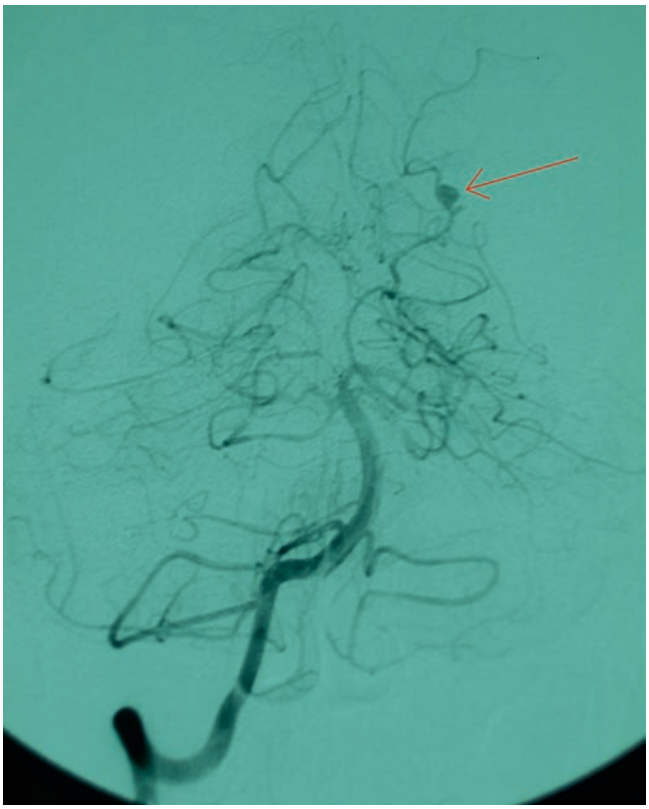

Fig. 10.20 Cerebral mycotic aneurysm (*arrow*) in a young woman with hypertrophic cardiomyopathy and staphylococcal endocarditis (same patient as Fig. 10.2)

frequent in right-side and pacemaker-lead IE. Stroke is a severe complication of cerebral embolism, which is the most frequent embolic complication and is associated with an increased morbidity and mortality.[1] Conversely, embolic events may be totally silent in about 20% of patients with IE, especially in case of splenic or cerebral embolisms, and must be diagnosed by systematic non-invasive imaging. Total embolic risk is very high in IE, with EE occurring in 20–50% of IE. However, the risk of new EE (i.e. occurring after initiation of antibiotic therapy) is only 6–21%.[1]

Predicting the Risk of Embolism

Echocardiography plays a key role in predicting embolic events, although this prediction remains difficult in the individual patient. Several factors have been associated with an increased risk of embolism, including the size and mobility of vegetations, the localization of the vegetation on the mitral valve, the increasing or decreasing size of the vegetation under antibiotic therapy, some micro-organisms (staphylococci, *Streptococcus bovis*, *Candida* spp.), previous embolism, multi-valvular endocarditis, and biological markers.[1] Among them, the size and mobility of the vegetations are the most potent independent predictors of new embolic event in patients with IE. For example, in one study,[20] a large number of patients (178) with strict criteria for IE were prospectively

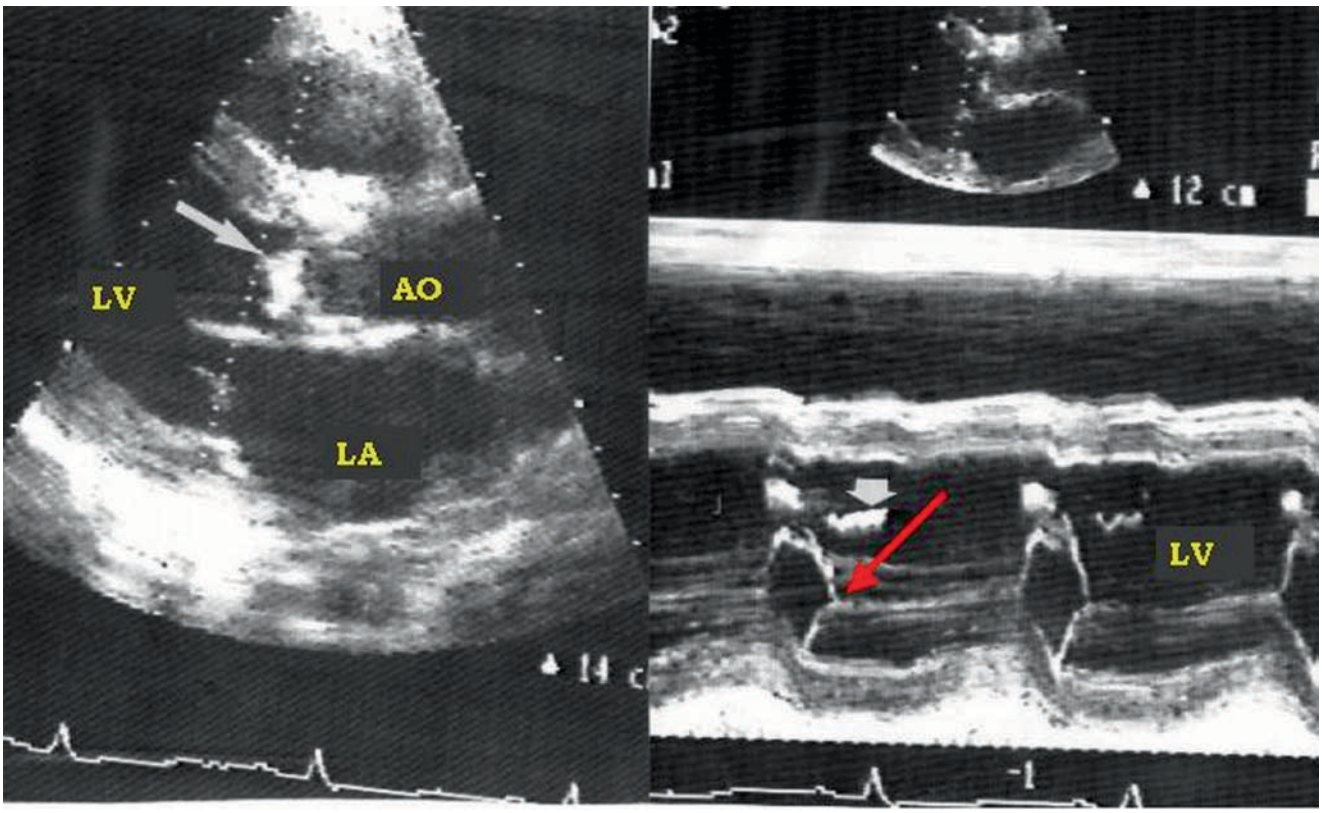

Fig. 10.21 Acute aortic endocarditis. TTE. *Left*: Long-axis 2D view showing a large vegetation (*white arrow*) attached to an aortic cusp. *Right*: M-mode recording showing a premature closure of the mitral valve (*red arrow*). *LV* left ventricle; *LA* left atrium; *Ao* aorta

included. A significant relationship was found between presence of vegetation and occurrence of embolism, between vegetation size and embolism, and between vegetation mobility and embolism. Embolic events were particularly frequent among patients with both severely mobile and very large vegetations (>15 mm). By multi-variate analysis, mobility and size of the vegetation were the only independent predictors of embolism. Several studies subsequently confirmed that patients with large vegetations are at higher risk of embolism and this risk is particularly high in patients with very large (>15 mm) and mobile vegetations, especially in staphylococcal mitral valve endocarditis. It must be emphasized that the risk of new embolism is highest during the first days following the initiation of antibiotic therapy and decreases after 2 weeks,[19, 21] although some degree of risk persists indefinitely in the presence of a vegetation. However, even in studies focussing on new embolic events, the size and mobility of vegetation are still associated with an increased risk of embolism.[19] Hence, the benefit of surgery to prevent embolization will be greatest during the first week of antibiotic therapy when the embolic rate is highest.

Follow-up

Echocardiography must be used for follow-up of patients with IE under antibiotic therapy, along with clinical follow-up. The number, type, and timing of repeat examinations depend on the clinical presentation, the type of micro-organism, and the initial echocardiographic findings. For example, only weekly TTE study may be sufficient to follow a non-complicated streptococcal native mitral valve IE. Conversely, early repeat TOE may be necessary in a patient with severe staphylococcal aortic IE, with suspected perivalvular involvement or large vegetation.

Few studies followed the outcome of vegetations under therapy. The results of such studies are difficult to interpret because the reduction in size of a vegetation may be either due to a healing of endocarditis or to the embolism of a part of the vegetation. Moreover, early surgical treatment may alter the course of the follow-up. In one study, failure to decrease vegetation size with antibiotic treatment was associated with an increased risk of embolism.[8] Conversely, Vilacosta[22] showed that most vegetation (83.8%) remains constant in size under therapy, and that this does not worsen prognosis. However, in this study, both increase in the vegetation size under antibiotic therapy (observed in 10.5% of patients with IE) and reduction in the vegetation size under therapy were associated with an increased embolic risk. Thus, increasing vegetation size under therapy must be considered as a risk factor for new embolic event, while unchanged or reduced vegetation size under therapy may be more difficult to interpret.[1]

Imaging and Decision-Making

Indications for surgery in IE may be subdivided into three categories—haemodynamic, infectious, and embolic indications.[6] Decision to operate is frequently difficult and must be discussed on an individual basis, using a multi-disciplinary approach including cardiologist, infectious disease specialist, and cardiac surgeon. Imaging plays a central role in this decision, along with the clinical presentation. More specifically, echocardiography plays a central role in helping clinician to choose the optimal timing of surgery.

Haemodynamic Indications

Presence of heart failure represents the main indication for surgery in IE. Recent European guidelines recommend early surgery to be performed in patients with acute regurgitation and Congestive Heart Failure (CHF), as well as in patients with obstructive vegetations.[6] Echocardiography is useful in both situations. In acute regurgitation, it allows detailed assessment of valve lesions, quantification of valve regurgitation, and evaluation of the haemodynamic tolerance of the regurgitation (cardiac output, pulmonary arterial pressures, left and right ventricular function). Some echocardiographic features suggest the need for urgent surgery including premature mitral valve closure (in aortic IE), massive regurgitation, and extensive destructive valvular lesions. The second haemodynamic indication is obstructive vegetation. In this situation, echocardiography is also useful for the assessment of mechanism and quantification of valve obstruction (Fig. 10.15). Patients with initial heart failure not treated by urgent/emergency surgery must be closely followed by repeat clinical and echocardiographic examinations to detect worsening cardiac lesions.

Infectious Indications

They represent the second most frequent indication for early surgery in Europe.[4] In the European guidelines, the infectious complications needing surgery include perivalvular extension, persistent fever, and some specific micro-organisms with poor response to antibiotic therapy.[6] Echocardiography plays a key role in the assessment of perivalvular lesions, including abscess, false aneurysm, fistula, and mitral valve aneurysm/perforation. Recent studies showed convincing evidence that aorto–cavitary fistulous tract formations are associated with bad prognosis[23] both in

native and prosthetic valve aortic endocarditis. Early surgery must be performed in these high-risk subgroups when possible. In some situations, emergency surgery may be necessary because of extensive perivalvular lesions associated with severe heart failure. Rarely, medical therapy alone may be attempted in patients with small non-staphylococcal abscesses (surface area <1 cm²) without severe valve regurgitation and without heart failure, in case of rapid and favourable response to antibiotic therapy. A careful clinical and echocardiographic follow-up is mandatory in this situation.

Embolic Indications

The last reason for early surgery is because a high embolic risk is suspected. Again, echocardiography presents with a major value for the assessment of this risk. However, prevention of emboli represents the most controversial indication in IE. In the Euro Heart Survey,[4] the size of the vegetation was one of the reasons for surgery in 54% of native valve IE and in 25% of PVIE, but the value of early surgery in this indication has never been proven. European guidelines recommend early surgery in patients with large (>10 mm length) vegetations before or during the first week of antibiotic treatment, or in case of recurrent emboli despite appropriate antibiotic therapy.[6] Thus, careful measurement of the maximal vegetation size is crucial in IE, because this parameter is clearly related to the risk of new embolic event. Today, it appears reasonable to propose early surgery to prevent embolic risk in the following situations:

- In cases of recurrent emboli despite appropriate antibiotic therapy
- In the presence of a large vegetation (>10 mm) following one or more clinical or even silent embolic events
- When the presence of the large vegetation (>10 mm) is associated with known other predictors of complicated course (heart failure, persistent infection under therapy, abscess, and prosthetic endocarditis). In these situations, the presence of a large vegetation indicates an earlier surgical decision.

The decision to operate early in cases of isolated large vegetation is more difficult and must be specific for the individual patient. Surgery may be considered in the presence of very large (>15 mm) and mobile vegetations, especially when a conservative surgery seems possible. Finally, the benefit of surgery may be weighed against the operative risk and considering the clinical status of the patient and the co-morbidities.

Intra-operative Echocardiography

Intra-operative echocardiography is mandatory in patients operated on for IE. It provides the surgeon a final anatomic evaluation of the valvular and perivalvular lesions, and is particularly useful to assess the immediate result of conservative surgery, as well as in cases of complex perivalvular repair.[24] Intra-operative TOE must be performed in homograft or autograft surgery, which is relatively frequently used in IE.

Conclusion

Imaging plays a key role in IE, both concerning its diagnosis, the diagnosis of its complications, its follow-up under therapy, and its prognostic assessment. Echocardiography is particularly useful for the initial assessment of embolic risk and in decision-making in IE. TOE plays a major role both before surgery and during surgery (intra-operative echocardiography).

References

1. Habib G. Embolic risk in subacute bacterial endocarditis. Role of transesophageal echocardiography. *Curr Cardiol Rep*. 2003;5:129–136
2. Hoen B, Alla F, Selton-Suty C, et al Changing profile of infective endocarditis: results of a 1-year survey in France. *JAMA*. 2002;288: 75–81
3. Hasbun R, Vikram HR, Barakat LA, Buenconsejo J, Quagliarello VJ. Complicated left-sided native valve endocarditis in adults: risk classification for mortality. *JAMA*. 2003;289(15):1933–1940
4. Tornos P, Iung B, Permanyer-Miralda G, et al Infective endocarditis in Europe: lessons from the Euro heart survey. *Heart*. 2005;91: 571–575
5. Habib G, Avierinos JF, Thuny F. Aortic valve endocarditis: is there an optimal surgical timing? *Curr Opin Cardiol*. 2007;22:77–83
6. Horstkotte D, Follath F, Gutschik E, et al Guidelines on prevention, diagnosis and treatment of infective endocarditis executive summary: the task force on infective endocarditis of the European society of cardiology. *Eur Heart J*. 2004;25:267–276
7. Durack DT, Lukes AS, Bright DK. New criteria for diagnosis of infective endocarditis: utilization of specific echocardiographic findings. Duke Endocarditis Service. *Am J Med*. 1994;96: 200–209
8. Rohmann S, Erbel R, Darius H, et al Prediction of rapid versus prolonged healing of infective endocarditis by monitoring vegetation size. *J Am Soc Echocardiogr*. 1991;4:465–474
9. Karalis DG, Bansal RC, Hauck AJ, et al Transesophageal echocardiographic recognition of subaortic complications in aortic valve endocarditis. Clinical and surgical implications. *Circulation*. 1992; 86:353–362
10. Vilacosta I, San Roman JA, Sarria C, et al Clinical, anatomic, and echocardiographic characteristics of aneurysms of the mitral valve. *Am J Cardiol*. 1999;84:110–113, A119

11. Habib G, Derumeaux G, Avierinos JF, et al Value and limitations of the Duke criteria for the diagnosis of infective endocarditis. *J Am Coll Cardiol*. 1999;33:2023–2029
12. Sochowski RA, Chan KL. Implication of negative results on a monoplane transesophageal echocardiographic study in patients with suspected infective endocarditis. *J Am Coll Cardiol*. 1993;21:216–221
13. Hill EE, Herijgers P, Claus P, Vanderschueren S, Peetermans WE, Herregods MC. Abscess in infective endocarditis: the value of transesophageal echocardiography and outcome: a 5-year study. *Am Heart J*. 2007;154:923–928
14. Klug D, Lacroix D, Savoye C, et al Systemic infection related to endocarditis on pacemaker leads: clinical presentation and management. *Circulation*. 1997;95:2098–2107
15. Piper C, Korfer R, Horstkotte D. Prosthetic valve endocarditis. *Heart*. 2001;85:590–593
16. Habib G, Thuny F, Avierinos JF. Prosthetic valve endocarditis: current approach and therapeutic options. *Prog Cardiovasc Dis*. 2008;50:274–281
17. Lamas CC, Eykyn SJ. Suggested modifications to the Duke criteria for the clinical diagnosis of native valve and prosthetic valve endocarditis: analysis of 118 pathologically proven cases. *Clin Infect Dis*. 1997;25:713–719
18. San Roman JA, Lopez J, Vilacosta I, et al Prognostic stratification of patients with left-sided endocarditis determined at admission. *Am J Med*. 2007;120:369, e361–367
19. Thuny F, Di Salvo G, Belliard O, et al Risk of embolism and death in infective endocarditis: prognostic value of echocardiography: a prospective multicenter study. *Circulation*. 2005;112:69–75
20. Di Salvo G, Habib G, Pergola V, et al Echocardiography predicts embolic events in infective endocarditis. *J Am Coll Cardiol*. 2001; 37:1069–1076
21. Steckelberg JM, Murphy JG, Ballard D, et al Emboli in infective endocarditis: the prognostic value of echocardiography. *Ann Intern Med*. 1991;114:635–640
22. Vilacosta I, Graupner C, San Roman JA, et al Risk of embolization after institution of antibiotic therapy for infective endocarditis. *J Am Coll Cardiol*. 2002;39:1489–1495
23. Anguera I, Miro JM, Vilacosta I, et al Aorto-cavitary fistulous tract formation in infective endocarditis: clinical and echocardiographic features of 76 cases and risk factors for mortality. *Eur Heart J*. 2005;26:288–297
24. Shapira Y, Weisenberg DE, Vaturi M, et al The impact of intraoperative transesophageal echocardiography in infective endocarditis. *Isr Med Assoc J*. 2007;9:299–302

Section 3

Coronary artery disease

Chapter 11

ECHOCARDIOGRAPHY AND DETECTION OF CORONARY ARTERY DISEASE

Don Poldermans, Willem-Jan Flu, and Thomas H. Marwick

CONTENTS

J. L. Zamorano et al. (eds.), *The ESC Textbook of Cardiovascular Imaging*
DOI: 10.1007/978-1-84882-421-8_11, © Springer-Verlag London Limited 2010

Introduction

Coronary artery stenosis causes an imbalance between myocardial oxygen supply and demand leading to myocardial ischaemia and infarction. Echocardiography is a well-established imaging technique in the detection and quantification of coronary artery disease. Regional and global wall motion abnormalities represent ischaemic and infarcted myocardial regions supplied by a stenotic coronary vessel. With the use of stress echocardiography (exercise, dobutamine, or dipyridamole), reversible ischaemia can be distinguished from irreversible myocardial infarction. Contrast enhancement exerts beneficial effects in identifying the endocardial border of the left ventricle cavity, allowing a more subtle assessment of myocardial perfusion and contractility. LV dysfunction is a major predictor of mortality after myocardial infarction and may manifest as LV enlargement and reduced ejection fraction. Echocardiography plays a pivotal role in the detection of CAD complications, including infarct expansion, mitral valve regurgitation, ventricular wall rupture, right ventricle infarction, and pericardial effusion. Technical developments such as tissue Doppler, strain rate imaging, and speckle tracking will further improve the quantitation of echocardiography.

Edler and Hertz introduced echocardiography in 1954 with the publication of their milestone paper "The use of ultrasonic reflectoscope for continuous recordings of the movements of heart valves."[1] Echocardiography has developed to be an established non-invasive imaging technique widely available for cardiovascular investigation. With the introduction of M-mode and 2D ultrasound, pivotal information about the anatomy of the heart could be obtained, including cardiac valves, ventricular wall, tumours, and masses. The introduction of Doppler ultrasound made it possible to perform flow-related measurements providing information about cardiac function such as diastolic and systolic ventricular function. Without directly visualizing (most of) the coronary arteries, echocardiography has proven to be an excellent diagnostic tool in the detection and quantification of coronary artery disease.

Coronary Artery Disease: Pathophysiology

The heart, an active metabolic organ, requires a high level of oxygen supply. Due to the high metabolic demand of the heart, the myocardium is susceptible to ischaemia and infarction. The progression of coronary atherosclerosis causes a gradual reduction in vascular cross-sectional area, which leads to coronary artery stenosis/occlusion and causes a critical flow reduction to the myocardium. An imbalance between myocardial oxygen supply and demand leads to ischaemia, followed by (1) metabolic changes, (2) regional wall contraction alterations, and, at a later stage, (3) ECG changes, (4) global left ventricle dysfunction, and (5) chest pain, described in the "classic ischaemic cascade."

Thus, when the ischaemic cascade is triggered, it causes myocardial dysfunction with ischaemia present as (1) wall motion abnormalities alone ("super silent" ischaemia), (2) wall motion abnormalities with ST segment alterations (silent ischaemia), and (3) wall motion abnormalities and symptoms of angina pectoris with or without ECG changes (symptomatic ischaemia).[2] Not all patients follow the reassuring paradigm proposed in the "classic ischaemic cascade." ECG changes in combination with chest pain may occur in patients without wall contraction alterations detectable with echocardiography, a process called the "alternative ischaemic cascade."[3] Explanations for this apparent paradox could be a reduction in coronary flow reserve, not detectible as regional or global wall contraction alterations, but as local perfusion defects,[4] as well as sub-endocardial ischaemia with preservation of overall segmental function due to the intact sub-epicardium.

Myocardial ischaemia generally occurs at the time of occlusion when decreased blood flow is associated with low adenosine triphosphate (ATP) production and contractile failure secondary to a decreased energy supply. Five myocardial outcomes are possible during or after a coronary occlusion: (1) normal structure and function, (2) myocardial ischaemia, (3) stunned myocardium, (4) myocardial hibernation, and (5) myocardial infarction. After a coronary occlusion, normal structure and function of the myocardium is maintained when myocardial perfusion is preserved due to the presence of collateral vessels.

The subendocardium is the most functionally active myocardial layer with the lowest perfusion reserve and, therefore, the greatest vulnerability to ischaemia and infarction.[5,6] Myocardial ischaemia starts in the endocardium and may lead to a non-transmural myocardial infarction (non-Q-wave MI). Because less severe ischaemia does not lead to irreversible damage, myocytes become damaged (but not necrotic) and maintain viability. The myocardium becomes stunned (reduction or absence of normal contractility) after a coronary occlusion has been relieved. Myocardial dysfunction due to stunning (1) can persist in the absence of irreversible damage and despite restoration of a normal coronary flow, (2) can last weeks to months after normal perfusion has been recovered, and (3) often lies adjacent to an infarcted necrotic myocardial segment.[7,8]

After prolonged coronary occlusion (4–6 h), myocardial necrosis progresses from endocardium to epicardium in a wavefront. If perfusion is reinstituted, an incomplete (non-trans-mural) infarction results, but if not, a complete

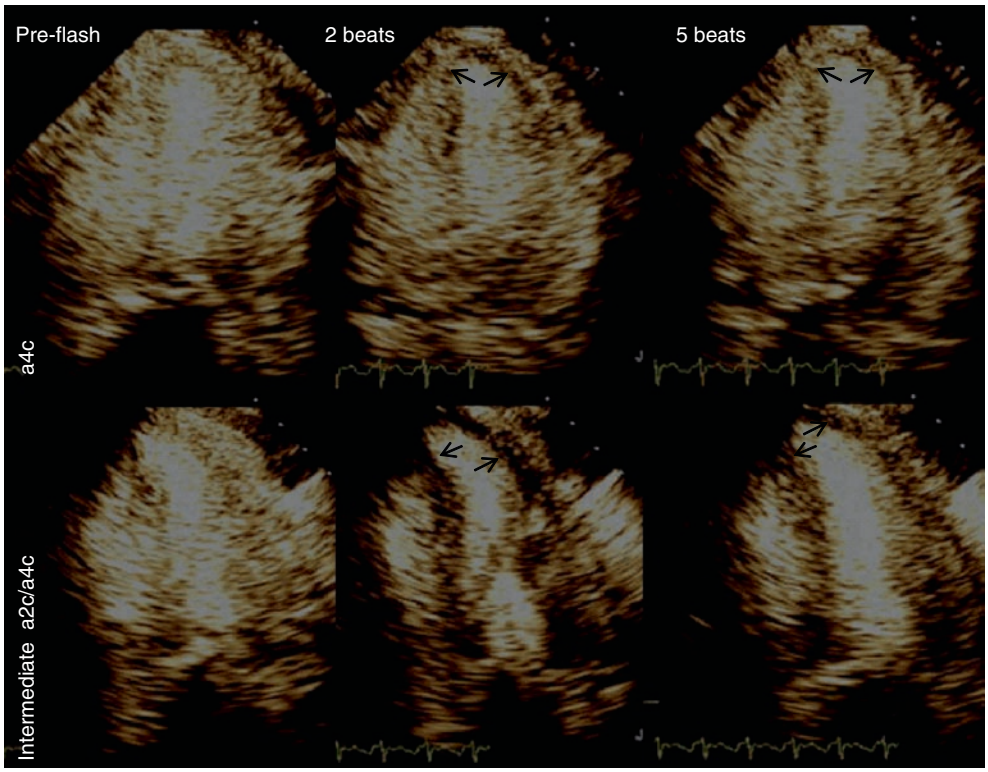

Fig. 11.1 End-systolic freeze-frames showing LAD territory (apical septum, lateral, inferior and anterior walls) sub-endocardial perfusion abnormalities, after opacification of the remaining muscle and persisting up to five beats post flash. The accompanying loops show no inducible wall motion abnormalities

(trans-mural, or "Q-wave") infarction will occur.[9, 10] In necrotic myocardium, the local capillary network becomes thrombosed and occluded, leading to irreversible damage of membrane integrity, glycolytic or mitochondrial function, and absence of contractile potential.

Changes in myocardial function and perfusion can be detected by echocardiography as global systolic and diastolic left ventricular dysfunction, regional wall motion and wall thickening abnormalities, and left ventricular perfusion defects[11] (Fig. 11.1, Video 11.1).

Echocardiography Detecting Coronary Artery Disease

Regional Wall Motion Assessment

Rest Echocardiography

In the early 1970s, M-mode recordings were used to assess wall motion of the left ventricle; however, 2D imaging has replaced M-mode echocardiography for evaluation of global and regional wall motion. With 2D echocardiography, ischaemic segmental wall motion abnormalities can be detected in patients with CAD. Visual assessment ("eyeball approach") categorizes wall motion as being normal or abnormal on the basis of degree of endocardial excursion (which is subject to tethering and translational motion), thickening, the timing of motion, and the shape of the LV. Timing is particularly important, and accurate wall motion assessment requires frame-by-frame review to overcome the limited temporal resolution of the human eye.[12] Wall motion abnormalities are characterized as hypokinetic, akinetic, or dyskinetic, and changes in LV shape are important and often neglected (Fig. 11.2, Vidoes 11.2a-c). Normally the endocardium thickens during systole; however, ischaemic myocardium shows different patterns of wall thickening or even thinning during systole as shown in Table 11.1, Fig. 11.3a, b, and Video 11.3a-c.

Although there is tremendous variability in the coronary artery blood supply to the myocardium, a model with 17 segments assigned to one of the three major coronary arteries is recommended for visual interpretation of regional left ventricular wall motion abnormalities (Fig. 11.4). Unfortunately, the true apical cap is rarely visualized by echo, so some investigators continue to use the 16-segment model.[13] Therefore, individual myocardial segments can be assigned to one of the three major coronary arteries with recognition that there is anatomic variability. Wall motion abnormalities at rest may represent scar tissue (caused by trans-mural infarction), hibernation, or myocardial stunning (viable myocardium with a reduction or absence of contractility). Ischaemic myocardial segments can have a normal or abnormal function at rest with

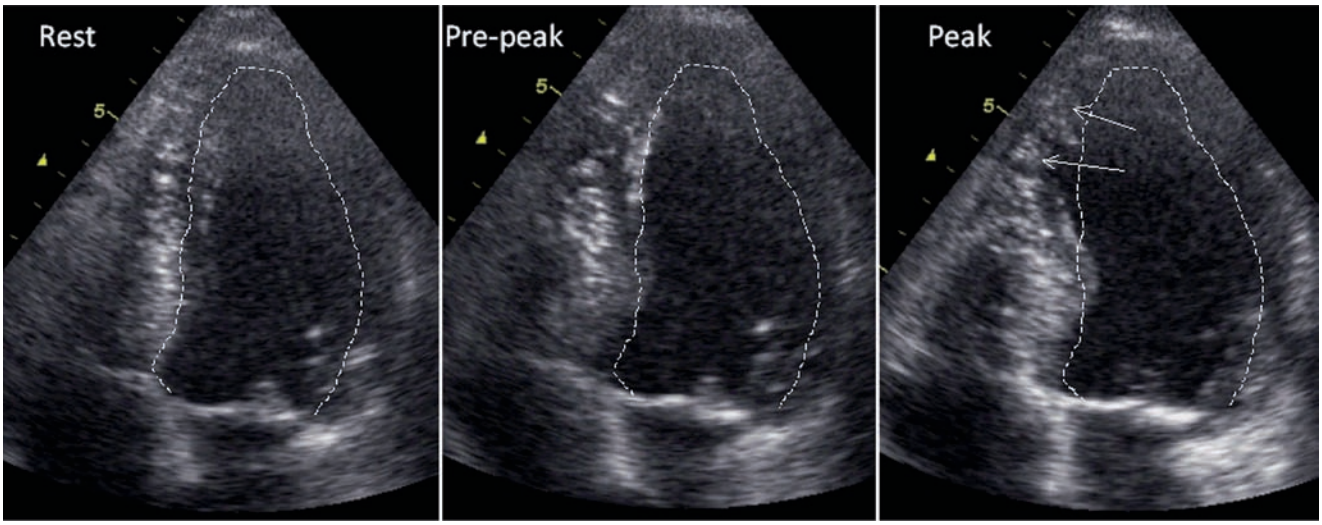

Fig. 11.2 Resting, low-dose, and peak-dose dobutamine images, showing LAD territory ischaemia involving the apical septum. The value of LV shape as a marker of ischaemia is emphasized by superimposition of the resting end-systolic contour on each image. The shape of the apex changes with ischaemia (*arrows*)

Table 11.1. Regional systolic wall function

Normal	1	Normal inward systolic motion	4–10 mm systolic thickening – double thickness
Mild hypokinesia	2	Mildly reduced inward systolic motion	Mildly reduced systolic thickening – delayed
Severe hypokinesia	2.5	Severely reduced inward systolic motion	Severely reduced systolic thickening – delayed
Akinesia	3	Absent inward systolic motion	Absent systolic thickening
Dyskinesia	4	Abnormal outward systolic motion	Systolic thinning
Aneurysmal	5	Abnormal shape at rest	Systolic thinning

development of wall motion abnormalities during exercise or stress. In general, wall motion and wall-thickening abnormalities show the highest specificity in the determination of CAD, representing the "classic ischaemic cascade." Myocardial perfusion is the most sensitive indicator for CAD, as it includes the "alternative ischaemic cascade." 2D echocardiography in combination with a contrast agent (further discussed in the section on contrast-enhanced echocardiography) provides a means of recognition of sub-endocardial hypo-perfusion with high spatial resolution. The combination of perfusion and wall motion affords a simple method to predict functional recovery of dysfunctional segments after revascularization by evaluating end-diastolic wall thickness and perfusion abnormalities, as shown in Table 11.2.[14]

Stress Echocardiography

During exercise or stress, the myocardial oxygen demand is increased and demand ischaemia occurs in patients with a coronary artery stenosis. Stress testing can detect reversible ischaemia, distinguish ischaemia and viability from scar, and identify regions supplied by a specific coronary vessel. When stress testing induces ischaemia, it permits wall motion analysis during stress with the use of treadmill and bicycle exercise or pharmacologically induced stress. Regardless of the technique used, resting images are recorded first and serve as a baseline for comparison[15] with stress images obtained during peak stress or immediately after exercise. The images are analyzed using a segmental model. Wall motion and wall thickness is scored in each myocardial segment on a 4-point scale, and test results are considered positive when wall motion or wall thickness deteriorates by one grade or more in any segment.[16] During stress testing, five different ventricular wall motion response patterns can be observed: (1) normokinesis or normal systolic wall motion, (2) hyperkinesis or increased inward systolic wall movement, (3) hypokinesis or reduced inward systolic wall movement, (4) akinesis or no systolic wall movement, and (5) dyskinesis or outward systolic wall movement. Necrotic myocardium can be akinetic or dyskinetic at rest. Akinetic and dyskinetic myocardium could be viable as well, and assessing

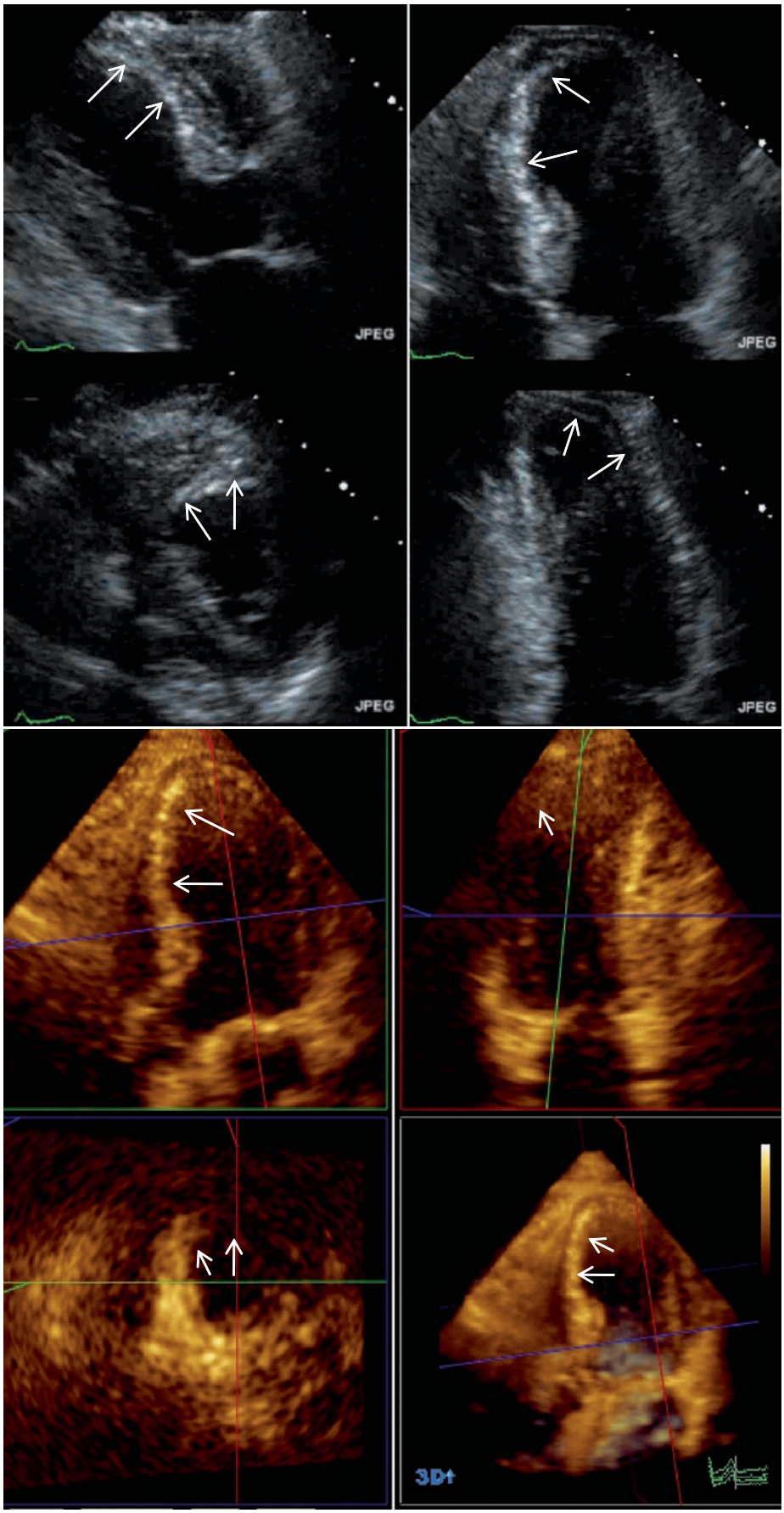

Fig. 11.3 (**a**) End-systolic freeze-frames showing LAD territory infarction without wall thinning (*arrows*) in 3D and 2D images (below). Accompanying loops show no inducible ischaemia

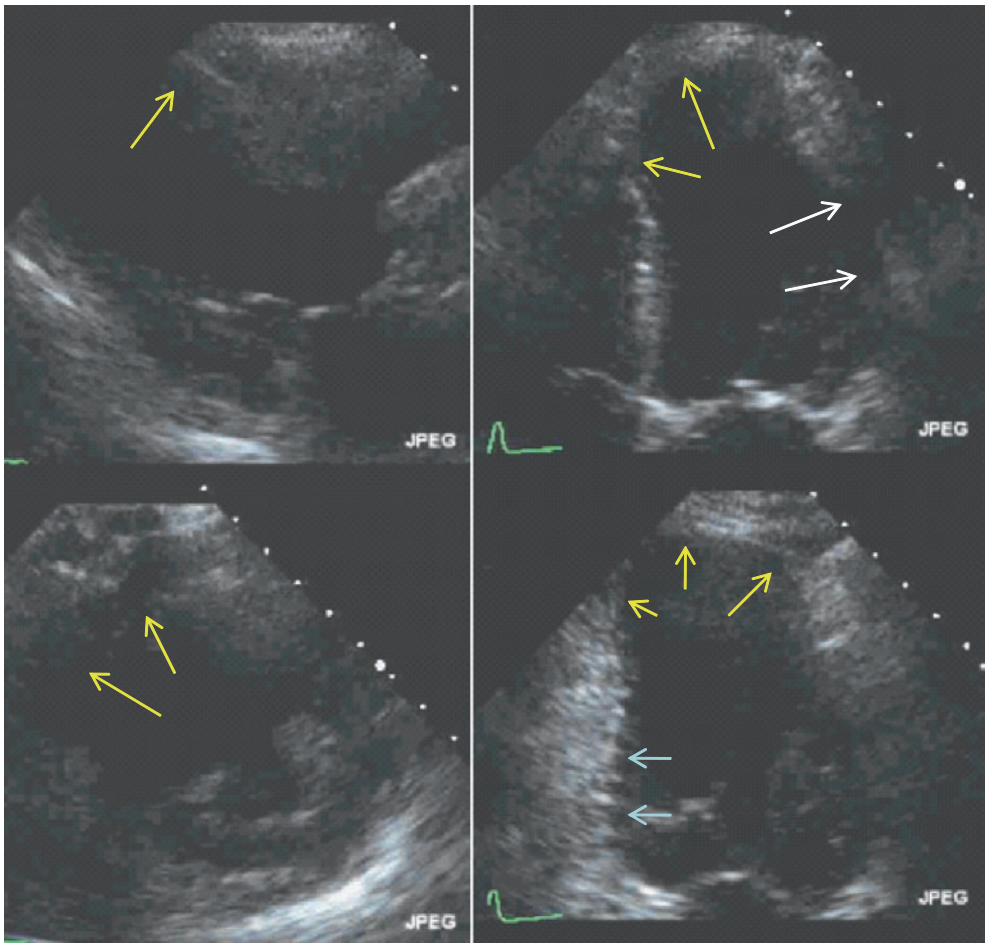

Fig. 11.3. (**b**) End-systolic freeze-frames of showing infarction in the LAD territory with wall thinning (*yellow arrows*), as well as LCX territory (*white arrows*) and RCA territory akinesis (*blue arrows*). Accompanying loops show no inducible ischaemia

the ventricular wall motion response to stress can make a distinction between viable and necrotic tissue. Although hypokinetic myocardium is sometimes labelled as viable, it may not necessarily show improvement after revascularization, for instance, when hypokinesis is caused by subendocardial scar. In the normal response to stress, normokinetic wall segments remain normokinetic during stress or become hyperkinetic. During an ischaemic response, wall segments become hypokinetic, akinetic, or dyskinetic during stress (Fig. 11.5, Video 11.5a-e). In a necrotic response, wall segments that are akinetic or dyskinetic at rest will remain akinetic or dyskinetic during stress. A viable response is seen when hypokinetic, akinetic, or dyskinetic segments show improved contractility during stress (Table 11.3). Hibernating myocardium is identified when improved contractility at low stress rate is followed by reduced contractility at high stress rate, i.e. the biphasic response.[17] Stunned myocardium shows sustained improvement of myocardial contraction at both low and high stress rates. Because hibernating myocardium improves after revascularization, separating hibernating from stunning myocardium is of great clinical importance. The three most common stressors used in stress echocardiography are (1) exercise, (2) dobutamine, and (3) dipyridamole.

Exercise Stress Testing

Exercise testing can be subdivided into treadmill and bicycle testing. Scanning during exercise can be performed but it is difficult. Therefore, images must be taken immediately after the exercise is performed, and echocardiographic examination must be completed within 1–2 min. When exercise is terminated, myocardial oxygen demand gradually declines with recovery of reversible wall motion abnormalities. New or increased wall motion abnormalities can persist up to 30 min post-exercise, demonstrating stunned myocardium depending on the severity and extent of the underlying CAD. Stunning is often induced by treadmill testing.[18] However, when wall motion recovers very rapidly and persists only for several minutes, treadmill testing can miss resolved wall motion abnormalities. This may lead to false negative results

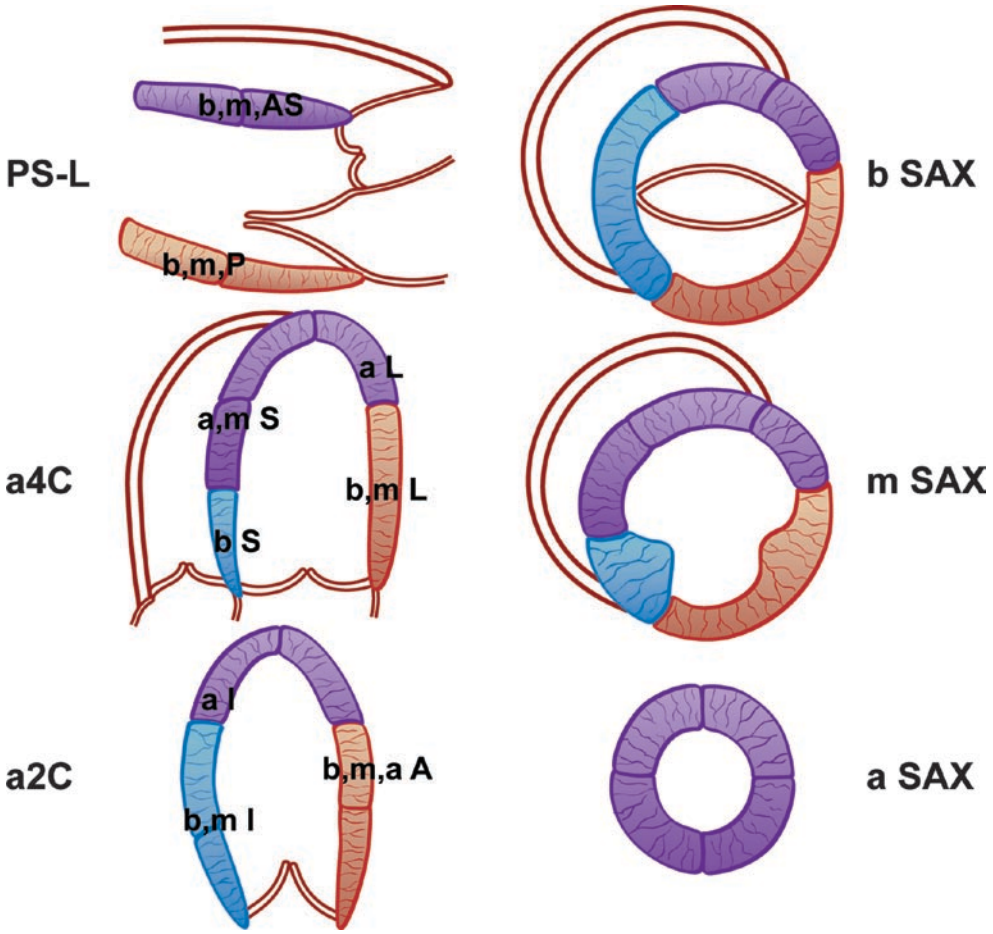

Fig. 11.4 Segmentation of the LV for visual assessment of regional function in standard views – parasternal long-axis [PS-L], short-axis [SAX], apical 4- and 2-chamber (a4C and a2C). The 16-segment model may be modified to a 17-segment model by addition of an apical cap. Territories are attributed to the coronary vessels as follows: LAD – septum [S], antero-septum [AS], anterior [A], and apical [a] (*green*), LCX – mid (m) and basal (b) posterior [P] and lateral [L] (*red*) and RCA – inferior [I], and basal septum [bS] (*blue*)

affecting the sensitivity of the test in detecting ischaemia. Bicycle exercise is performed in upright and supine position and permits echocardiographic examination during exercise. With the patient in the supine posture, it is possible to record images from multiple views during graded exercise. In the upright posture, imaging is generally limited to either apical or sub-costal views. The overall sensitivity of exercise echocardiography has been reported to range from 76 to 89%, and sensitivity is greater with more high-grade coronary disease.[19, 20] However, although angiographic comparison is respected as a common metric for the assessment of the accuracy of these tests, it should be remembered that the angiogram is imperfect because the severity of diffuse narrowing can be under-estimated and because this anatomic test ignores the contribution of vascular function to perfusion, even in the context of normal conduit vessels.

Table 11.2. Likelihood of functional recovery after PCI

EDTW > 11, Perfusion+	Highest likelihood of recovery
EDTW > 11, Perfusion−	High likelihood of recovery
EDTW < 11, Perfusion+	Intermediate likelihood of recovery
EDTW < 11, Perfusion−	Low likelihood of recovery

Pharmacological Stress Testing

Although exercise testing is more physiologic than pharmacologic stress, it is not feasible in many situations. Out of five patients referred for stress, one will not exercise and one will exercise submaximally.[21] For instance, patients with peripheral vascular disease are unable to exercise maximally, so with a pharmacologic stress, echocardiography serves as a good alternative in these patients. Pharmacologic stress testing is performed during the infusion of dobutamine or dipyridamole. These two stressors induce ischaemia through different haemodynamic mechanisms. Dobutamine stimulates adrenoreceptors, thereby increasing ventricular contractility and myocardial oxygen-demand during stress testing.[22] Dipyridamole exerts vasodilatory properties by stimulating adrenaline receptors – although steal phenomena are commonly cited, experimental evidence suggests that ischaemia is more likely caused by tachycardia and hypotension in the setting of reduced sub-endocardial flow reserve.[23] Although dipyridamole is often cited as the stressor of preference in the assessment of myocardial perfusion and dobutamine may be preferred to assess regional wall motion abnormalities, either can be used for each purpose. Dobutamine infusion increases myocardial oxygen demand through positive chronotropic

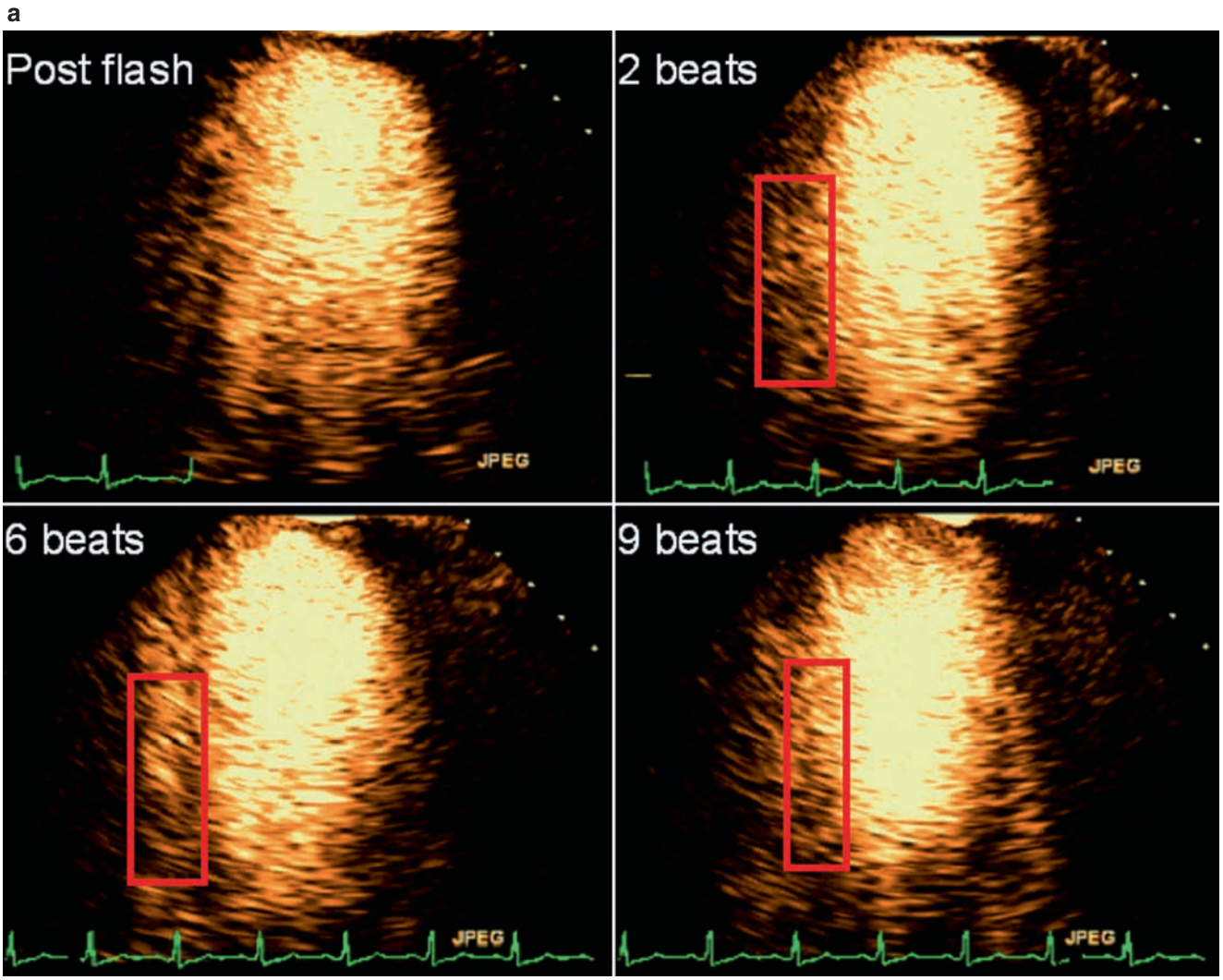

Fig. 11.5 The spectrum of ischaemic wall motion responses to stress. Probable angina in a 61-year-old man with multiple risk factors. Normal resting ECG. Exercise test showed no chest pain, 1 mm ST depression, submax heart rate (79%), seven MET ex capacity. Non-contrast and LV opacification images (see loops) show questionable inferoseptal hypokinesis. Use of destruction-replenishment imaging to examine myocardial perfusion shows (**a**) inferior and (**b**) apical perfusion defects

and inotropic effects and impairs myocardial oxygen supply by shortening diastole. These effects result in myocardial ischaemia and systolic dysfunction in myocardial regions supplied by critically stenotic arteries.

Performing these tests requires careful patient monitoring, access to antidotes to stress agents, and the presence of an experienced physician. A graded dobutamine infusion starting at 5 μg/kg/min and increasing at 5 min stage to 10, 20, 30, and 40 μg/kg/min is the standard for dobutamine stress echocardiography. To assess myocardial viability, a thorough resting evaluation is important (Fig. 11.6a, Video 11.6a) followed by multiple low-dose stages – in most cases, the study should progress to peak dose dobutamine to check for ischaemia (Fig. 11.6b, c, Video 11.6b, c). The recommended protocol for dipyridamole echocardiography includes continuous echocardiographic monitoring during a two-stage infusion. The first stage consists of 0.56 mg/kg dipyridamole over 4 min. Monitoring continues for 4 min, and if there is no clinical effect, an additional 0.28 mg/kg is infused over 2 min. Aminophylline (240 mg i.v.) should be available for use in case of an adverse event related to dipyridamole. Adenosine can be used in a similar manner and is typically infused at a maximum dose of 140 mg/min during imaging.[24] Patients undergoing pharmacological stress testing often take beta-blockers, which may limit heart rate response and influence the sensitivity of the test to detect CAD. In both dobutamine and dipyridamole echocardiography, atropine can be added after the second stage to increase heart rate and improve sensitivity.[25, 26] Atropine should be used at the minimum effective dose and administered in 0.25 mg increments every 60 s until the desired heart response is seen.

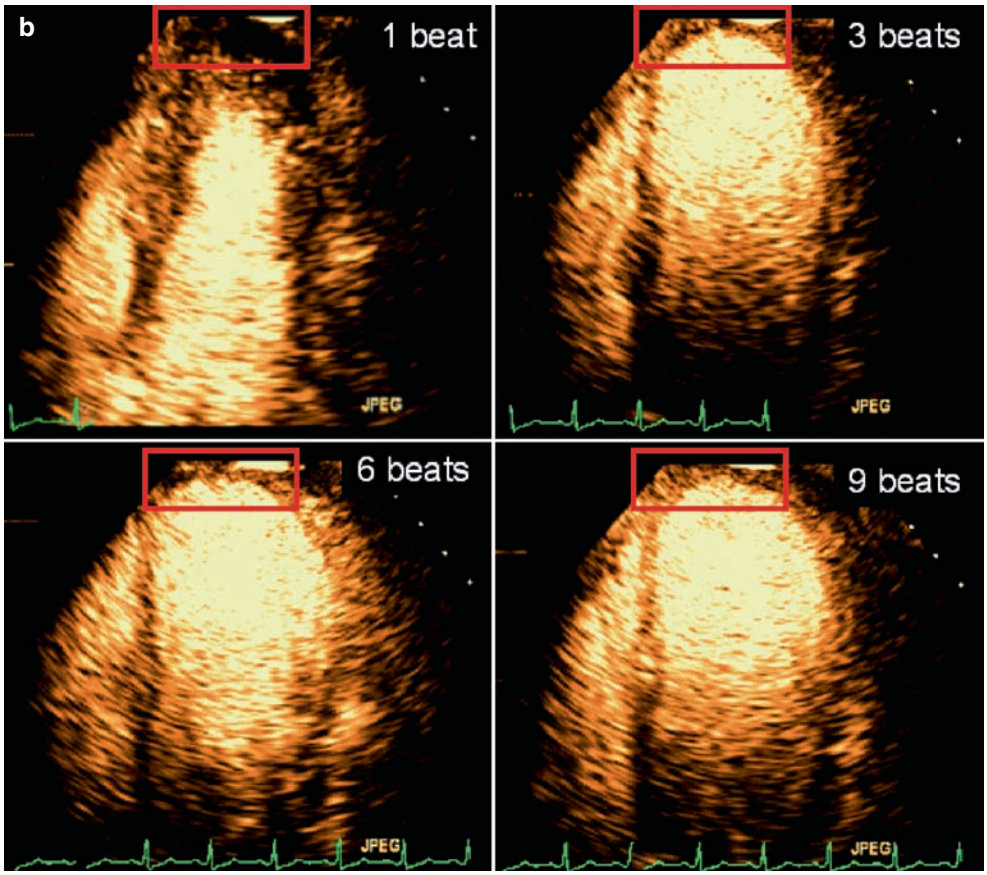

Fig. 11.5 (**b**)

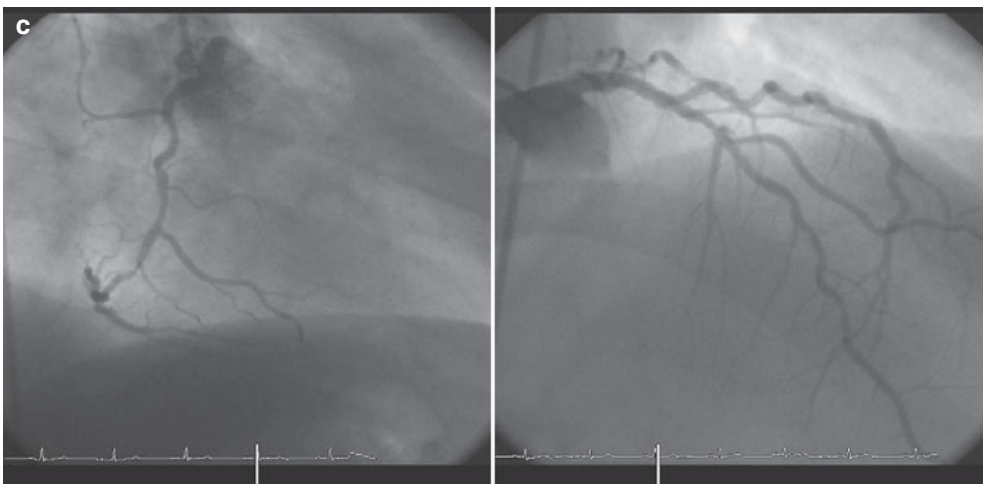

Fig. 11.5 (**c**) Coronary angiography showed significant 70% distal RCA and 60% mid LAD stenoses

Side Effects and Contraindications

There are few contraindications (e.g. severe aortic stenosis), and side effects (e.g. MI, death, arrhythmia) associated with physical exercise are uncommon. Pharmacological stress testing with dobutamine and dipyridamole is considered to be a safe test that is generally well tolerated. Major complications such as myocardial infarction, death, and bronchospasm occur in ~1:1,000. Potential side effects of pharmacological stress testing are transient arrhythmias and haemodynamic abnormalities, which resolve rapidly after cessation of the infusion. Dobutamine is contraindicated in patients with current ventricular or atrial arrhythmias and moderate to severe hypertension (defined as diastolic blood pressure above 110 mmHg). Stress echocardiography with dipyridamole is contraindicated in patients with high-grade heart block, bronchospasm, unstable carotid disease, and patients receiving theophylline treatment.[24] Minor, self-limiting side effects such as chest pain, nausea, and headache can occur infrequently during dipyridamole infusion.

Table 11.3. Wall motion response to stress

Rest	Stress	Diagnosis
Normal hypokinesia	Normal	Normal
	Hyperkinesia	Normal
	Hypokinesia	Non-transmural infarction
Normal hypokinesia	Hypokinesia	Ischaemia
	Akinesia	Ischaemia
	Dyskinesia	Ischaemia
Akinesia	Normal	Viable
	Hypokinesia	Viable
Akinesia	Akinesia	Necrosis
Dyskinesia	Dyskinesia	Necrosis

Comparison of Diagnostic and Prognostic Performance of Exercise and Pharmacological Stress Testing

The results from multiple meta-analyses comparing exercise, dobutamine, and dipyridamole stress testing are shown in Table 11.4. A recent meta-analysis conducted by Picano et al., analyzed five studies regarding the diagnostic accuracy of dobutamine vs. dipyridamole stress echocardiography. They noted dipyridamole and dobutamine to have similar (1) accuracy (87%, 95% confidence intervals, CI, 83–90, vs. 84%, CI, 80–88, $p = 0.48$), (2) sensitivity (85%, CI 80–89, vs. 86%, CI 78–91, $p = 0.81$), and (3) specificity (89%, CI 82–94 vs. 86%, CI 75–89, $p = 0.15$) for the detection of CAD.[27] These conclusions are in line with other meta-analysis, shown in Table 11.4, generally concluding that stress echocardiography shows a higher specificity than sensitivity.[19, 20, 27–29] A higher sensitivity than specificity is seen in a metaanalysis

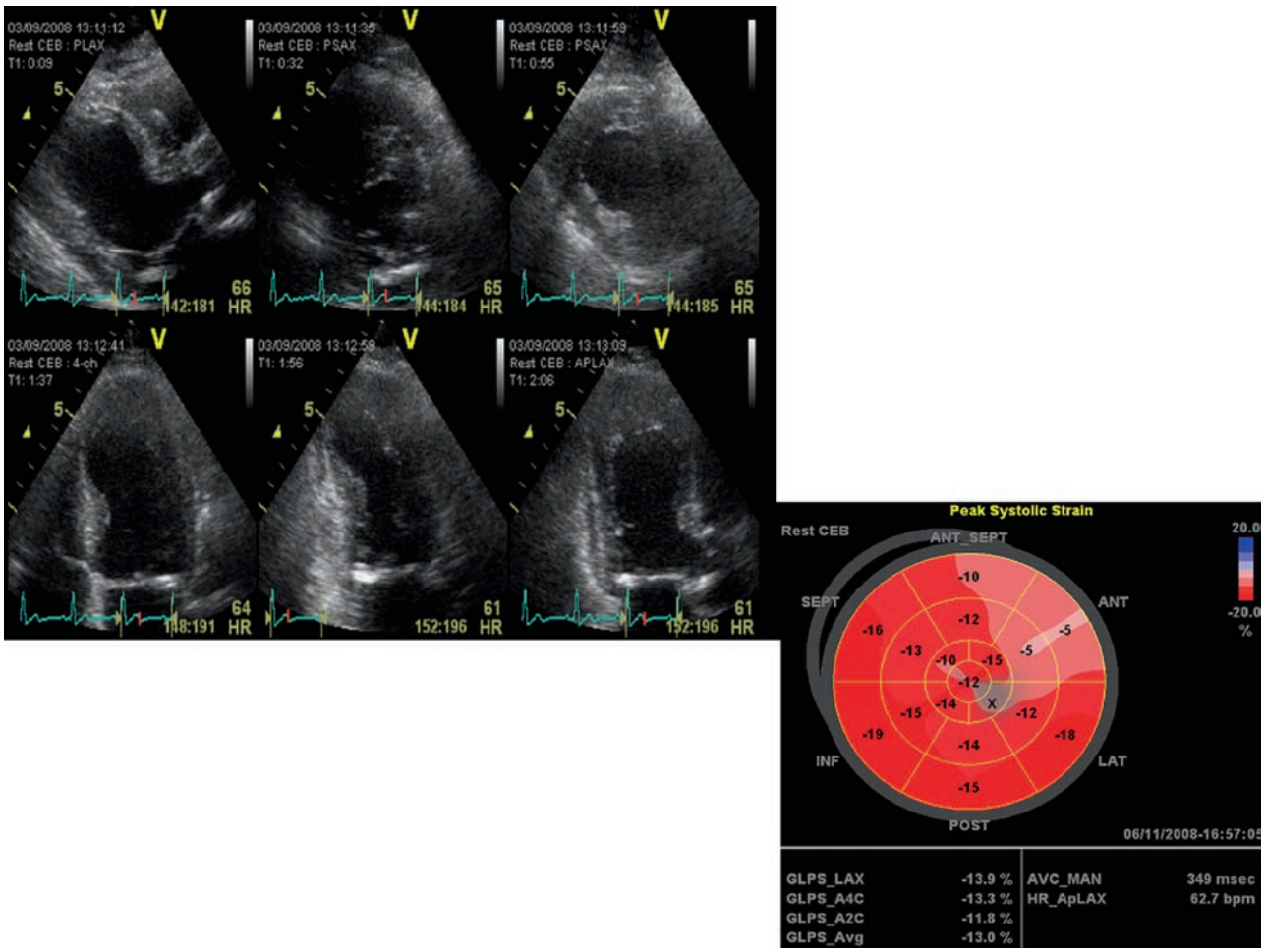

Fig. 11.6 (**a**) Resting echocardiogram (end-systolic images) showing LV enlargement and resting wall motion abnormalities with preserved wall thickness in the antero-septum, septum, and apex. The bull's eye display shows reduced longitudinal shortening in these areas (numbers correspond to regional strain; normal strain is approximately 18%)

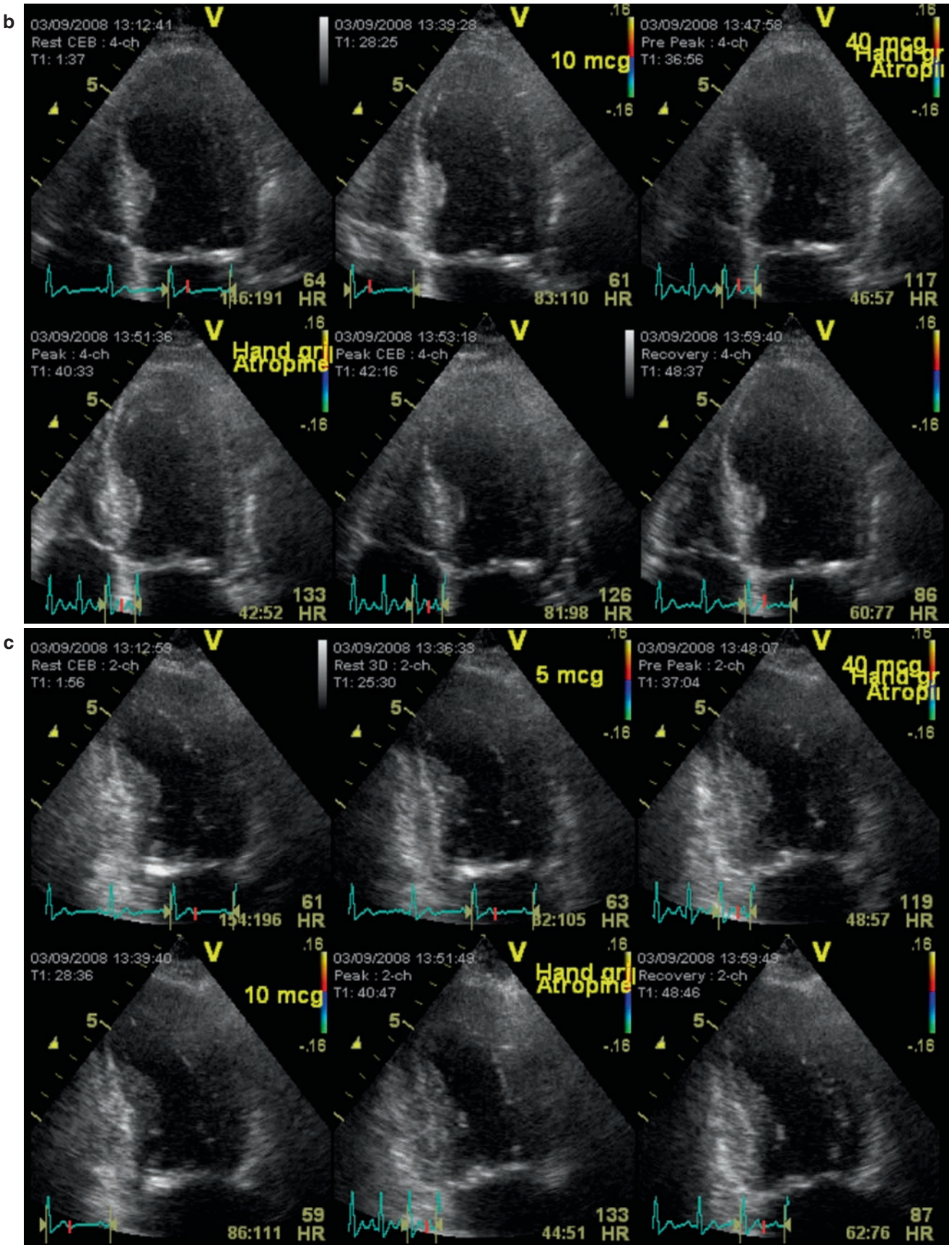

Fig. 11.6 (**b**) End-systolic images at rest, low dose, peak dose, and recovery in the apical 4-chamber view. The apical and mid-septal akinetic area does not change at low dose, and therefore suggests a non-viable area. The apical lateral wall improves at peak stress, indicating non-transmural infarction. (**c**) End-systolic images at rest, low dose, peak dose, and recovery in the apical 2-chamber view. The apical inferior akinetic area thickens at the 10 mcg dose, but does not deteriorate, denoting a non-transmural infarction. The antero-apical wall deteriorates at peak stress, indicating ischaemia

Table 11.4. Accuracy of stress echocardiography

Meta-analysis	Year	Number of studies	Number of patients	Outcome	Sensitivity (%)			Specificity (%)		
					Exe	Dob	Dip	Exe	Dob	Dip
A. Diagnostic performance of stress echocardiography										
Picano et al.	2008	5	299	CAD	–	85	86	–	92	87
Noguchi et al.	2005	164	–	CAD	83	80	71	84	85	92
Kim et al.	2001	60	5932	CAD	–	80	70	–	84	93
Picano et al.	2000	12	568	CAD	–	77	71	–	87	93
Kwok et al.[a]	1999	3	296	CAD	76	–	–	89	–	–
B. Viability assessment of stress echocardiography										
Schinkel et al.	2007	41	1421	Viability	–	80	–	–	78	–
Bax et al.[b]	2001	28	925	Viability	–	82	–	–	79	–
C. Prognostic Performance of Stress Echocardiography										
Kertai et al.[c]	2003	12	805	Post-operative CE[b]	–	85	74	–	70	86

Sensitivity and specificity relate to correct identification or exclusion of A. significant coronary stenoses (criteria vary from 50 to 70% in different trials), B. recovery of regional function after revascularization, C. peri-operative cardiac events
[a]In women
[b]Low-dose dobutamine
[c]Cardiac events

performed by Bax et al., in which low-dose dobutamine was administered in the assessment of myocardial viability, as shown in Table 11.4.[30] The prognostic performance of dobutamine stress echocardiography in the prediction of post-operative cardiac events is outlined in Table 11.4.[31]

Comparison: Stress Testing with Other Non-invasive Imaging Techniques

Stress echocardiography has the advantage of being a safe, widely available, non-invasive technique, feasible in almost all circumstances at low cost. Furthermore, pharmacological stress echocardiography is a reliable method for diagnosing CAD in patients with a cardiac pacemaker, whereas, for instance, exercise myocardial SPECT may show false positive results in pacemaker patients.[32] However, image quality is negatively affected by obstructive lung disease, chest deformation, and obesity. During peak stress, the image quality is negatively affected by an increased heart rate and breathing artefact. Furthermore, mechanical tethering, defined as decreased contractility of non-infarcted regions adjacent to infarcted regions, may lead to an overestimation of the extent of an infarcted region.[33, 34] Finally, the accuracy of stress echocardiography is dependent on operator experience.

A meta-analysis conducted by Beattie et al. analyzed the predictive value of pharmacological stress testing in predicting peri-operative cardiac events, compared with thallium myocardial perfusion scintigraphy (MPS). This report included 25 studies (3,373 patients) of mainly dobutamine and several dipyridamole stress echocardiography. The likelihood ratio of a peri-operative event with a positive stress echocardiogram was 4.09 (95% CI 3.21–6.56) compared with 1.83 (95% CI 1.59–2.10) in patients undergoing thallium MPS.[35] Table 11.5 shows various meta-analyses comparing sensitivity and specificity of pharmacological stress testing in detecting CAD (Table 11.5)[28, 31] and functional improvement after revascularization (Table 11.5).[30, 36] The cost differential between non-invasive tests for coronary disease is summarized in Fig. 11.7.

The following guidelines (Table 11.6) have been described in the 2008 ASC/AHA guidelines concerning the appropriateness criteria for stress echocardiography with or without contrast enhancement.[16] These criteria are also in agreement with ESC guidelines.

Contrast-Enhanced Echocardiography

Stress echocardiography is widely used for the detection of inducible ischaemia and regional wall motion abnormalities. Analyzing regional wall motion abnormalities relies on the identification of the endocardial border of the LV cavity. Image quality can be severely impaired in patients with obstructive

Table 11.5. Accuracy of various stress tests

	Number of studies	Number of patients	Outcome	Sensitivity	Specificity
Performance in detecting CAD and predicting cardiac events					
Kim et a.l[28]					
Dipyridamole stress echo	20	1,835	CAD	70	93
MPS, dipyridamole SPECT	21	1,464	CAD	89	65
Dobutamine stress echo	40	4,097	CAD	80	84
MPS, dobutamine SPECT	14	1,066	CAD	82	75
Kertai et al.[31]					
Dobutamine stress echo	8	1,877	Peri-operative CE	85	70
Dipyridamole stress echo	4	850	Peri-operative CE	74	86
MPS, Tl-201	23	3,119	Peri-operative CE	83	49
Exercise electrocardiography	7	685	Peri-operative CE	74	69
Performance in predicting functional improvement after revascularization					
Bax et al.[30]					
Dobutamine stress echo[a]	28	925	Functional recovery	82	79
MPS, Tl-201 (rest-redistribution)	22	557	Contractile function	86	59
MPS Tl-201 (re-injection)	11	301	Contractile function	88	50
MPS, Tc-99m labelled (nitrates)	13	308	Functional recovery	79	58
MPS, Tc-99m labelled (no nitrates)	7	180	Functional recovery	81	66
MPS, PET 18-FDG[b]	20	598	Contractile function	93	58
Schinkel et al.[36]					
Dobutamine stress echo	41	1,421	Regional wall function	82	80
MPS, Tl-201 (rest-redistribution)	28	776	Regional wall function	87	56
MPS, Tl-201 (re-injection)	343	12	Regional wall function	87	50
MPS, Tc-99m labelled	25	721	Regional wall function	83	65
MPS, PET 18-FDG[b]	24	756	Regional wall function	92	63
MRI	13	420	Regional wall function	84	63

[a]Low dose
[b]18-Fluorodeoxyglucose

lung disease, obesity, and chest wall deformities resulting in suboptimal acoustic windows. Furthermore, an increase in heart rate and breathing artefacts due to hyperventilation causes difficulties in identifying the endocardial border of the LV cavity and interpreting the stress images. Since the first report in 1968, contrast echocardiography has become an indispensable tool for cardiovascular imaging.[37] The development and usage of ultrasound contrast agents have shown to be beneficial in assessing the endocardial border of the LV cavity, and, therefore, exert a beneficial effect in analyzing myocardial contractility and perfusion. LV opacification has shown to improve (1) image quality, (2) percentage of wall segments visualized, and (3) confidence of interpretation of wall motion abnormalities both at rest and during peak stress.[38] The contrast agents used are suspensions of micro-bubbles, which have the same size as red blood cells and are filled with perfluorocarbon gas. Because of the availability of sensitive contrast imaging technologies, only small dosages of contrast (0.1–0.3 mL) are needed to obtain enhanced images. The accuracy of end-diastolic wall thickness measurements is improved as well, and can be used, in combination with perfusion abnormalities, to predict recovery of function after revascularization.[14]

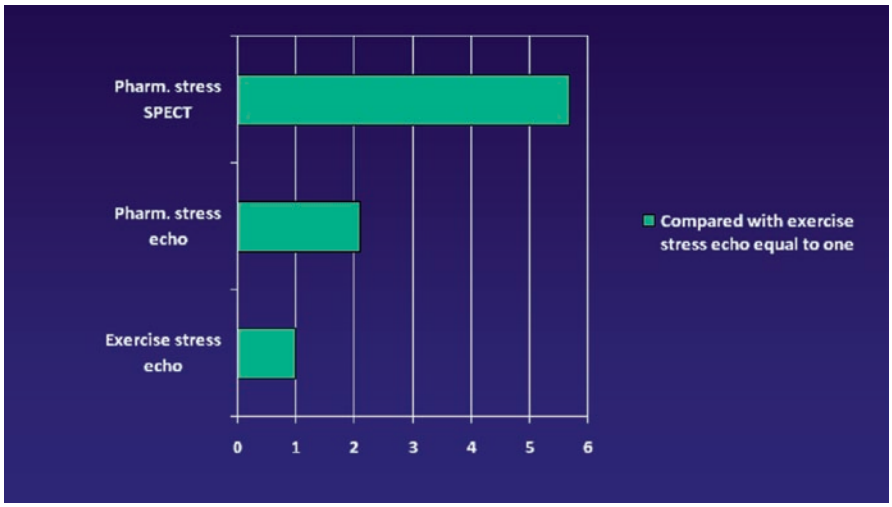

Fig. 11.7 Relative costs of stress testing procedures. *Pharm.* pharmacological; *SPECT* single photon emission computed tomography

Contrast-enhanced echocardiography allows visualization of subtle wall motion abnormalities that are difficult to detect with normal echocardiography. Furthermore, the observation of subtle wall motion abnormalities can be confirmed with the identification of perfusion abnormalities. Finally, contrast-enhanced echocardiography can visualize regional perfusion abnormalities before contractile abnormalities evolve, potentially identifying coronary artery disease at an earlier stage. Contrast perfusion imaging has proven to be a valuable tool for the detection of myocardial viability. Increased brightness is observed in normally perfused myocardial segments, due to contrast enhancement.[39,40] Myocardial viability can be expressed as contrast intensity and myocardial replenishment, assessed after 10–15 cardiac cycles after a destructive pulse. Fully replenished myocardium with homogeneous contrast intensity indicates the presence of myocardial viability[41,42] (Fig. 11.8, Video 11.8a-f). The use of contrast in association with exercise and pharmacologic stress echocardiography improves the visualization of wall motion when this is technically difficult, but is not recommended for all studies. The detection of perfusion abnormalities is an "off label" use of contrast that is feasible but technically challenging. The development of new contrast agents will be needed in order to move this to mainstream use (Table 11.7).

Global Wall Motion Assessment

Heart failure, a clinical syndrome in which the ability of the ventricles to fill with or eject blood is impaired, is a major predictor of mortality after myocardial infarction. Often, this is transient due to spontaneous recovery in the coronary care unit or after coronary revascularization, but may progress to chronic heart failure.[43] Coronary artery disease is the most common cause of myocardial disease, being the initial cause in 70% of patients with predominantly systolic HF.[44,45]

Resting echocardiography is pivotal in the recognition of systolic HF, which is associated with progressive chamber dilation and eccentric re-modelling.[46] Left ventricular ejection fraction (LVEF, the fraction of blood ejected out of the left ventricle during one heartbeat) has a number of limitations, including sensitivity to haemodynamic setting, but has the advantage of being a simple numerical parameter that has been linked to outcome and decision making. In patients with LV dysfunction without heart failure, regional wall motion scoring may be more sensitive than ejection fraction, which may be preserved by compensatory hyperkinesis. Subclinical LV dysfunction describes the situation of apparently normal function where sensitive indices such as strain are abnormal, or where LV contractile reserve is reduced. The latter reflects the response to stress, which usually involves a reduction of LV volumes and an increment of LVEF. Echocardiographic assessment of global systolic LV function is often performed subjectively, but this is increasingly considered suboptimal. This approach is dependent on the eye of an experienced observer and is misleading in situations of (1) irregular heart rhythm, (2) very large or small left ventricle size, and (3) extreme heart rates.[47,48] The most common method for the quantitation of LV volumes is the modified Simpson's rule, a technique that requires imaging in apical, 4-, or 2-chamber views. First the endocardial border has to be outlined in end-diastole and end-systole, and the LV cavity is divided into a series of discs of equal height along its long axis. When the central axis of the LV cavity is defined and the endocardial border is identified, the volume of each disc can be automatically defined. Each disc volume is calculated as disc area x height (height defined as the total length of the LV long axis divided by the number of discs). The surface area of each disc is

Table 11.6. Appropriateness criteria for stress echocardiography[16]

Evaluation of chest pain syndrome or anginal equivalent	
Low pretest probability of CAD ECG interpretable and able to exercise	Inappropriate
Low pretest probability of CAD ECG un-interpretable or unable to exercise	Appropriate
Intermediate pretest probability of CAD ECG interpretable and able to exercise	Appropriate
Intermediate pretest probability of CAD ECG un-interpretable or unable to exercise	Appropriate
High pretest probability of CAD Regardless of ECG interpretability and ability to exercise	Appropriate
Prior stress ECG is un-interpretable or equivocal	Appropriate
General patient populations	
Low CHD risk (Framingham risk criteria) Moderate CHD risk (Framingham risk criteria)	Inappropriate
High CHD risk (Framingham risk criteria)	Indeterminate
Acute chest pain	
Intermediate pretest probability of CAD ECG-no dynamic ST changes and serial cardiac enzymes negative	Appropriate
High pretest probability of CAD ECG-ST elevation	Inappropriate
New-onset/diagnosed heart failure with chest pain syndrome or anginal equivalent	
Intermediate pretest probability of CAD Normal LV systolic function	Appropriate
LV systolic function	Indeterminate
Ischaemic cardiomyopathy, assessment of viability/ischaemia	
Known CAD on catheterization In a patient eligible for revascularization	Appropriate

determined from the diameter of the ventricle at that point. The ventricular volume is calculated by summing the disc volumes, which are equally spaced along the LV long axis. Once the LV volumes have been measured, LV ejection fraction can be calculated as (LVESV-LVEDV) × 100/LVEDV.[49] In more than 15% of patients examined with ultrasound, poor ultrasonic windows preclude optimal visualization of the endocardial border,[50] despite the use of tissue harmonic imaging. In this situation, the use of LV opacification with contrast-enhanced echocardiography will improve endocardial border definition.[51, 52] Contrast-enhanced echocardiography has also been shown to improve the assessment of LV volumes and LVEF.[53, 54] The use of contrast may also facilitate 3D assessment, which appears to be the most reproducible and accurate (but not yet the most robust) echocardiographic means of LV volume assessment. The development of real-time 3D imaging has simplified and shortened the process of acquisition and calculation of 3D measurements, to the extent that this is not feasible for routine echocardiography (Fig. 11.9).

Detection of Coronary Artery Disease Complications

In-hospital mortality caused by acute myocardial infarction is mainly due to circulatory failure resulting from severe LV dysfunction or mechanical complications of myocardial infarction. These complications of acute MI can be visualized and diagnosed using 2D echocardiography. In the following paragraphs we will discuss mechanical complications caused by acute myocardial infarction, such as: (1) infarct expansion leading to LV aneurysm and possible thrombus formation, (2) mitral regurgitation, (3) ventricular wall rupture, (4) right ventricular infarction, and (5) pericardial effusion. These mechanical complications can occur in the setting of a well-preserved left ventricular function. Accurate diagnostics with the use of echocardiography will guide proper treatment in often life threatening situations.

Infarct Expansion

Infarct expansion represents acute thinning of the ventricular wall occurring 24–72 h after the occurrence of a trans-mural (Q-wave) MI. The expansion area consists of necrotic myocardial tissue with disruption of cells leading to a 50% reduction of wall thickness (i.e. 4–6 mm compared with the normal 10–11 mm) in the affected region.[55] Infarct expansion is an important precursor for the development of LV aneurysm.[56] A true ventricular aneurysm is characterized by disturbance of diastolic shape and thinning of the LV wall, usually due to trans-mural MI; >85% are localized in the apical and antero-septal walls.[57] Alteration of normal LV contraction and filling properties can result in congestive heart failure, and >50% of patients with true LV aneurysms develop mural thrombi.[58] In contrast, pseudo-aneurysms form when free wall rupture is contained by overlying adjacent pericardium (see below).[59] Ventricular thrombi are most commonly localized in the antero-apical segments and should be visualized in more than one echocardiographic view, preferably from different transducer positions. Thrombus protrusion and mobility can be identified with 2D echo and are

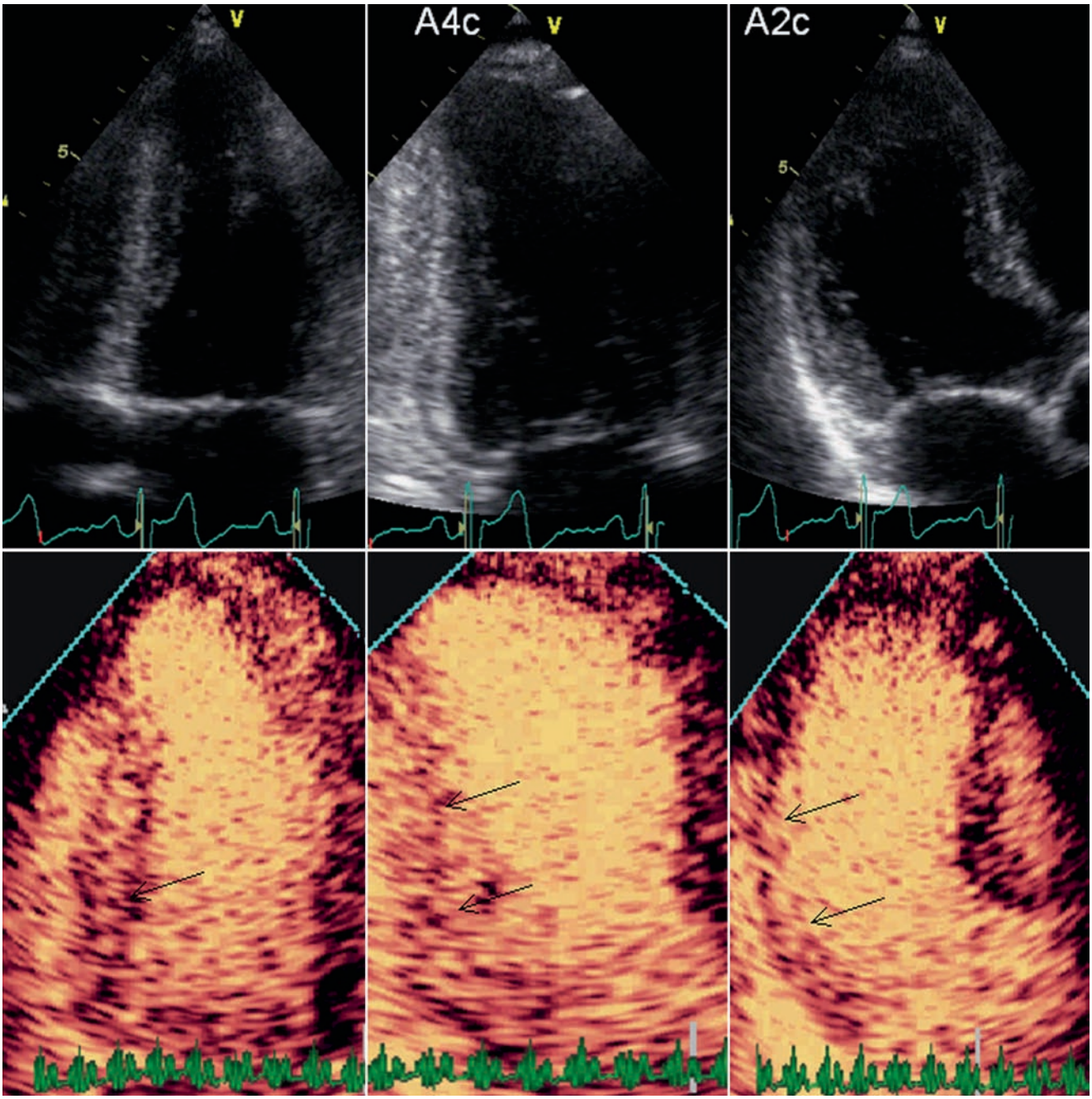

Fig. 11.8 Resting and myocardial contrast echocardiography in a 65-year-old man after late presentation MI. Despite regional wall motion abnormalities in the inferior wall, perfusion is preserved, (myocardial contrast marked by arrows) suggesting viability

Table 11.7. Contrast use[16]

Use of contrast with stress echo	
Routine use of contrast	Inappropriate
All segments visualized on non-contrast images	
Selective use of contrast	Appropriate
Two or more contiguous segments are not seen on non-contrast images	

associated with the risk of embolization.[60,61] The use of contrast-enhanced echocardiography can improve the diagnostic accuracy of 2D echocardiography in situations of suboptimal acoustic windows leading to poor image quality (Fig. 11.10).

Mitral Valve Regurgitation

Ischaemic mitral valve regurgitation (MR) most often occurs in the setting of an inferior infarction. The incidence of

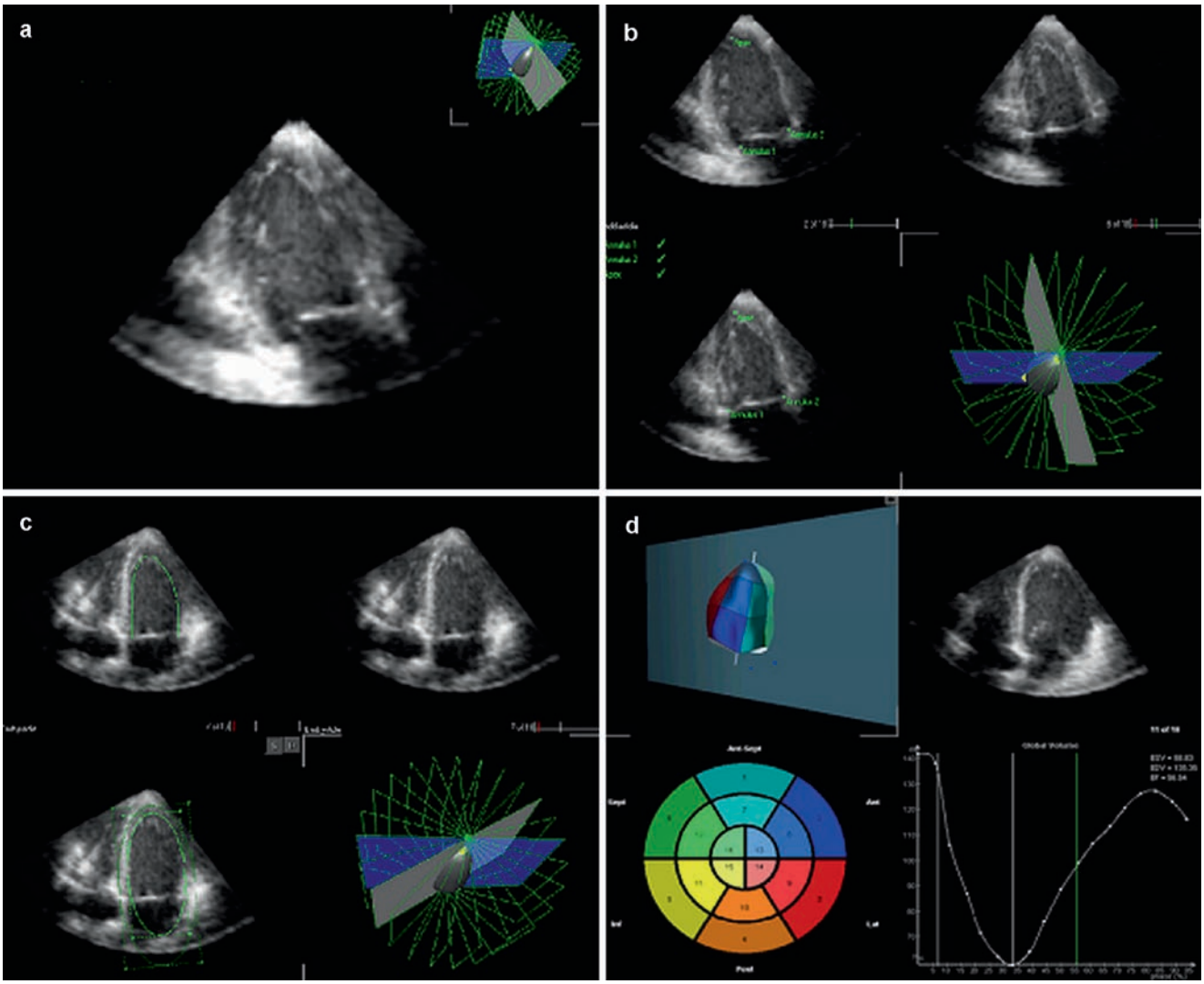

Fig. 11.9 Four steps for the use of 3D echo for LV volume and EF assessment in the post-infarct heart. **(a)** Defining landmarks at the base and apex of the left ventricle in end-diastole and end-systole. **(b)** Selection of imaging planes – we use 12 imaging planes, especially in irregularly shaped hearts. **(c)** Contours are defined automatically but commonly require revision. **(d)** Display of the volumes and the ejection fraction using a time volume curve

MR is 38% in patients with inferior MI compared with 10% of patients with an anterior MI.[62] Ischaemic MR occurs due to papillary muscle rupture, dysfunction, or displacement (Fig. 11.11, Video 11.11a, c). Functional MR may also arise from LV dilatation, sphericity, annular dilatation, or papillary muscle dyssynchrony. Papillary muscle displacement is mostly caused by chronic ischaemic heart disease, whereas papillary muscle rupture is associated with the acute phase of MI. Mild to moderate MR is common in the early phase after an acute MI and often decreases or resolves after reverse re-modelling. Severe acute MR caused by papillary muscle rupture is a rare but life-threatening situation that accounts for approximately 5% of acute MI deaths and (unlike other complications) is not necessarily associated with a large infarct. Predominantly, the postero-medial papillary muscle involved, because of its blood supply, is primarily derived from the posterior descending coronary artery.[63] Colour flow Doppler echocardiography is the standard diagnostic tool for detecting MR, but a high level of clinical suspicion may be needed, as the usual semi-quantitative measure of MR severity (based on jet size in relation to the LA)[64] can be misleading. This is because rapid increment in LA pressure due to severe MR may cause pressure equalization and limit flow. A marked systolic expansion of the left atrium and flail or incomplete closure of the mitral valve are important correlative findings. Incomplete closure caused by a posterior flail leaflet usually leads to an anterior directed eccentric jet.

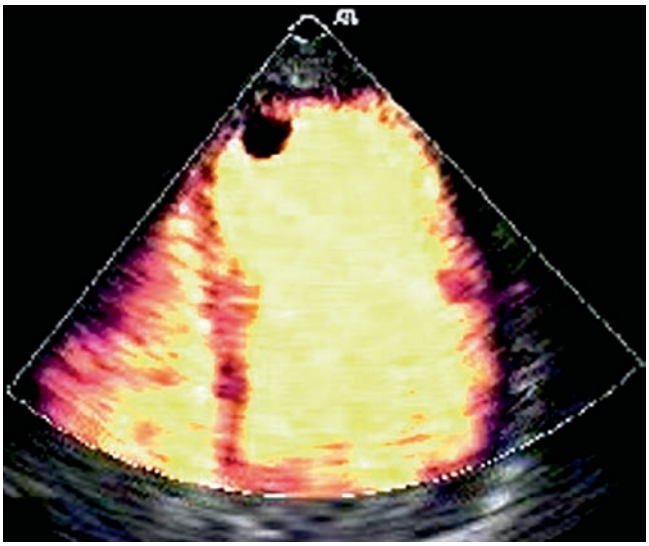

Fig. 11.10 Value of LV opacification in the detection of LV mural thrombus

Ventricular Wall Rupture

Unlike papillary muscle rupture, ventricular wall rupture is noted in anterior and inferior MI, in the same frequency and generally preceded by infarct expansion. Free wall rupture has been reported to complicate 4–24% of acute MI.[65–68] Septal wall rupture is associated with anterior MI, and the defect is most commonly found in the apical septum (Fig. 11.12, Video 11.12a-d, e) and contrasts with inferior MI where septal rupture occurs at the base of the heart. The characteristic echocardiographic findings are a distinct break in the septal contour and the detection of turbulent flow directed from the LV to the RV cavity. RV dilatation due to shunt should be considered in the differential diagnosis of RV infarction and dysfunction associated with inferior MI.[69] Contrast echocardiography is useful for the detection of cardiovascular shunts.[70] Risk factors for post-infarction left ventricular free wall rupture include (1) age > 60 years, (2) female gender, (3) pre-existing hypertension, (4) absence of left ventricular hypertrophy, (5) first myocardial infarction, and (6) mid-ventricular or lateral wall trans-mural infarctions.[71] The majority of ruptures occur within the first week after MI, and suspicious features on echocardiography include (1) thinning and delineation of the free wall, (2) pseudo-aneurysm, and (3) accumulation of pericardial fluid suggestive for pericardial effusion or cardiac tamponade. Although echocardiography is considered the diagnostic tool of choice, in most cases free wall rupture will lead to instant death (Fig. 11.13).

Right Ventricular Infarction

Right ventricular MI is strongly associated with inferior myocardial infarction caused by a proximal occlusion of the right coronary artery. RV dilation may cause tricuspid annulus dilation resulting in acute tricuspid insufficiency.[72] Wall motion abnormalities can be best visualized in sub-costal and parasternal short-axis views.

Pericardial Effusion

Pericardial effusion can be seen as an echo-free space surrounding the heart, which does not extend posterior to the

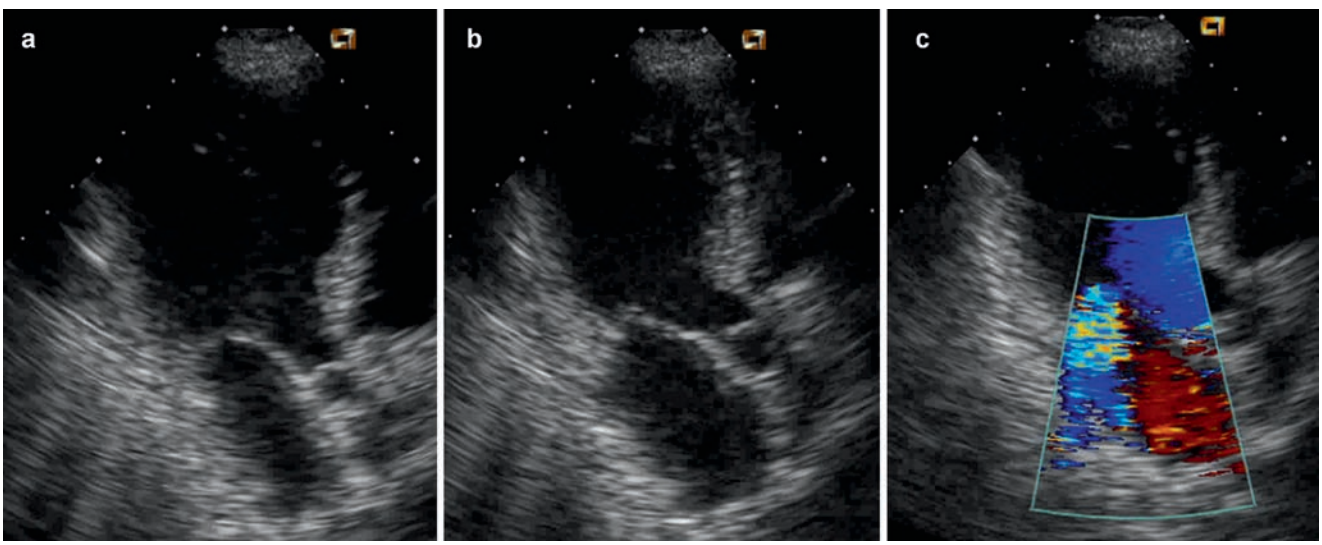

Fig. 11.11 Typical ischaemic MR due to papillary muscle displacement (note the same location of the posterior wall in end-diastole **(a)** and end-systole **(b)**. This causes tethering of the posterior mitral leaflet with posteriorly-directed MR **(c)**

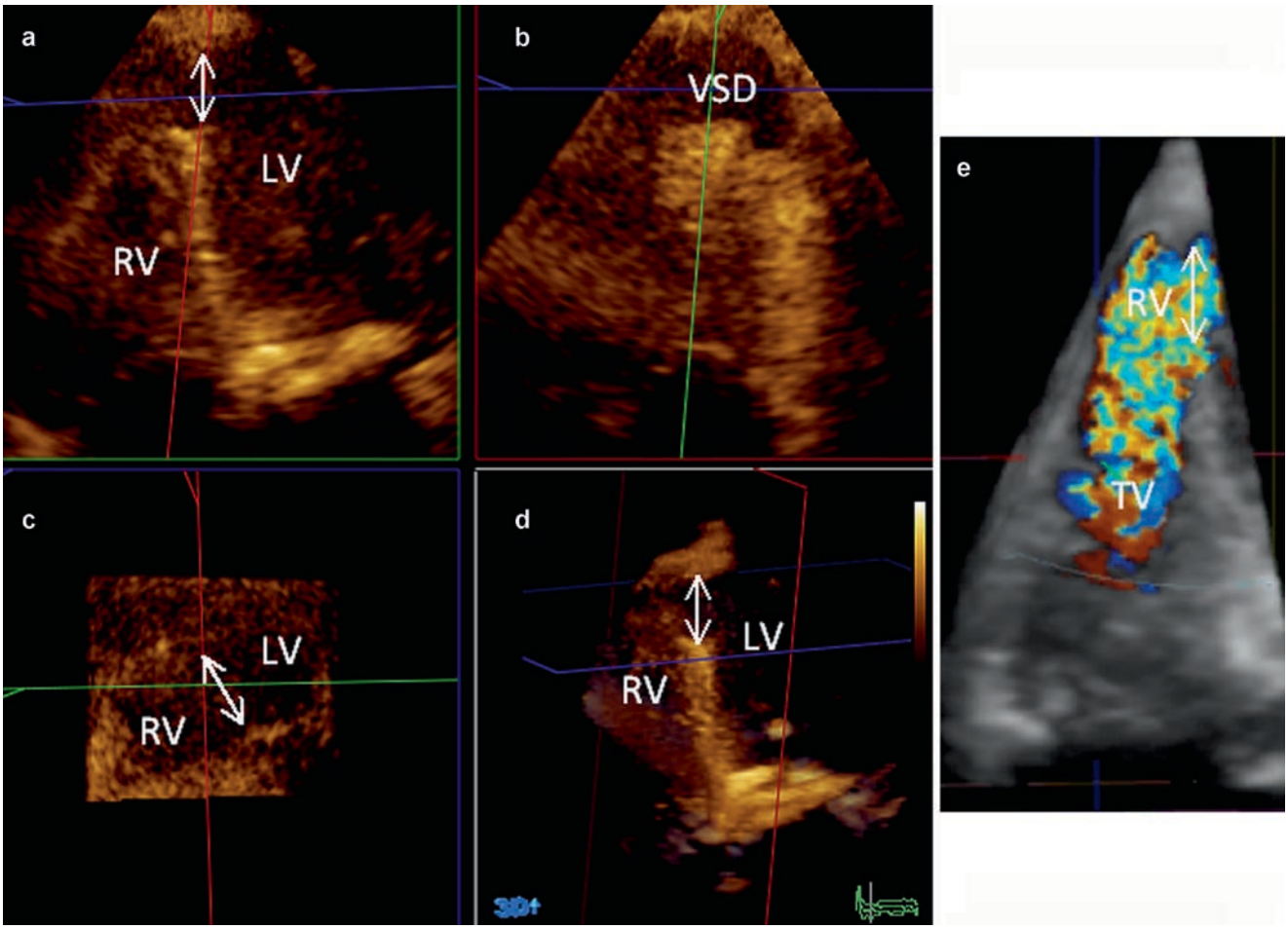

Fig. 11.12 Multiplanar reconstruction of an apical VSD showing defect diameter (*arrow*) in the 4-chamber view **(a)**, defect circumference in a modified 2-chamber view **(b)** where it is seen "en face," a short-axis cut through the defect **(c)**, and a 3D display **(d)**. The colour map **(e)** shows the left-right shunt. *TV* tricuspid valve

descending aorta (unlike pleural effusion). Inflammation might be an important cause for post-ischaemic pericardial effusion.[73] However, a large amount of pericardial fluid with a haemorrhagic appearance is suggestive for myocardial rupture.

Advantages, Limitations, and Future Perspective

Advantages and Limitations of Echocardiography

In comparison with other non-invasive cardiac imaging procedures, such as nuclear cardiology, cardiac computed tomography (cCT) and cMRI, 2D echocardiography has some limitations and advantages. As already noted, the impairment of image quality in patients with obstructive lung disease, obesity, and chest wall deformities can be minimized by the use of echocardiographic contrast agents, albeit at additional cost.[74] Increases in heart rate and hyperventilation may cause difficulties in the analysis of echocardiographic images. 2D echocardiography has the advantage of being (1) safe (i.e. no radiation or ionizing substances required), (2) widely available, (3) non-invasive, and (4) feasible in almost all circumstances at low cost (Fig. 11.14).[75] Cardiac MRI has the ability to provide information about cardiac anatomy, function and perfusion simultaneously and has a superior spatial resolution to 2D echocardiography. However, cardiac MRI has a lower temporal resolution (which is a problem for flow measurement, especially diastology), usually requires breath-holding sequences during data acquisition, and is relatively expensive and less available than echocardiography. According to the 2008 Appropriateness Criteria for Stress Echocardiography, the use of stress echocardiography and SPECT nuclear imaging show similar bodies of evidence to support their use

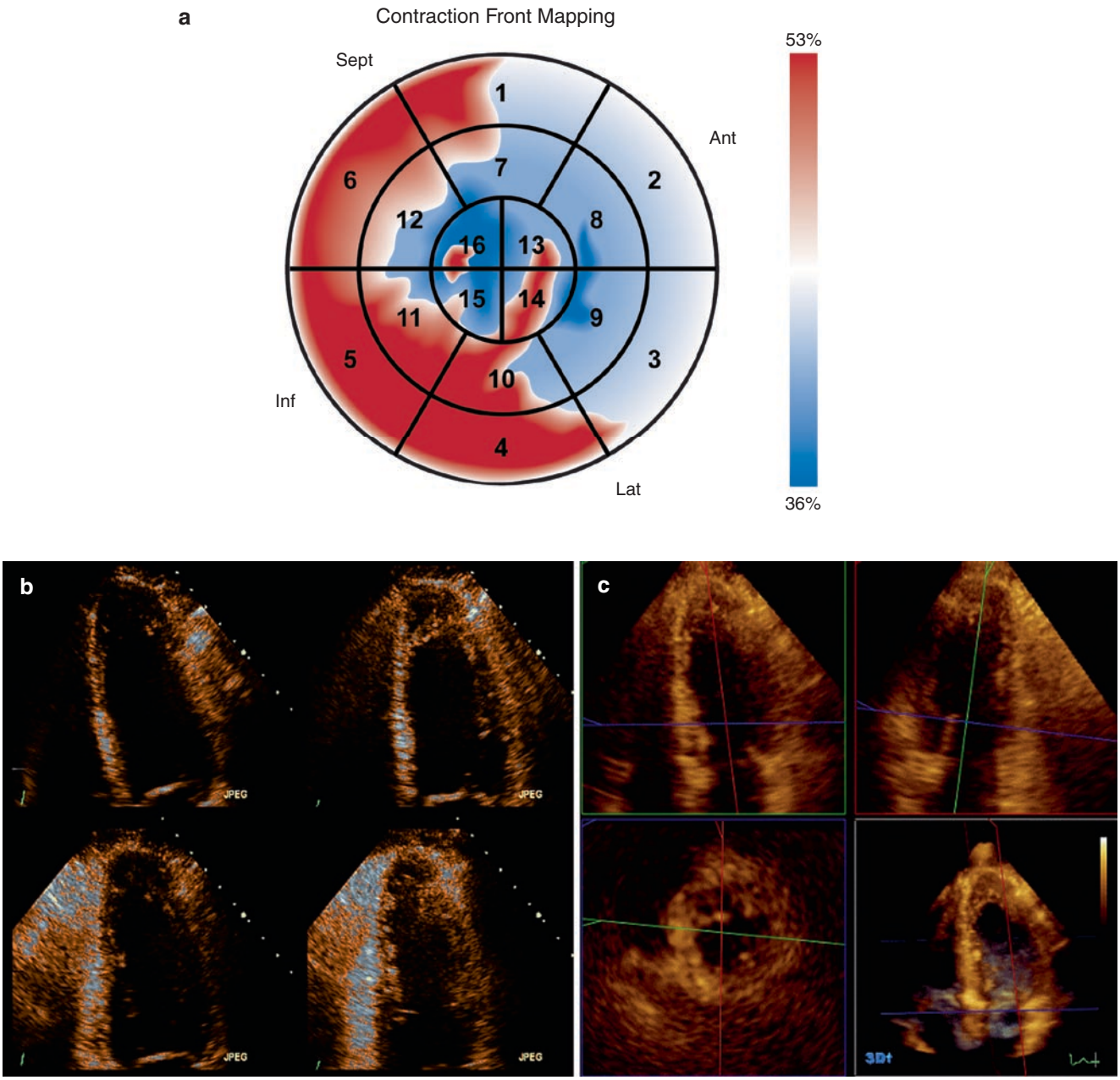

Fig. 11.13 Contained apical rupture following antero-apical infarction. The contraction front map display derived from the 3D dataset **(a)** shows akinesis of the antero-septal, anterior, and antero-lateral walls (*coloured blue*). The 2D images **(b)** show a contained rupture (*white arrow*) at the apex, confirmed on the 3D images **(c)**

for ischaemia detection.[16] Nuclear cardiology (e.g. PET and SPECT imaging) has the advantages of (1) higher sensitivity, (2) higher technical success rate, and (3) better accuracy when multiple resting left wall abnormalities are present, compared with echocardiography. The following advantages are in favour of echocardiography: (1) higher specificity, (2) higher versatility, and (3) greater convenience.[76] The ability to directly visualize the coronary arteries with coronary CT represents a major shift from the functional assessment of CAD to an anatomic evaluation. The ramifications of this on revascularization decisions and cost-effectiveness are unexplored. Apart from the requirements for breath-holding sequences and bradycardia (<65 beats/min), CT is less versatile in the assessment of wall motion abnormalities, ventricular function, valve abnormalities, and pericardial disease.

Future Developments of Echocardiography

There are unifying attractions in the application of new echocardiographic technologies to improve the quantitation of echocardiography. Ejection fraction is a widely used

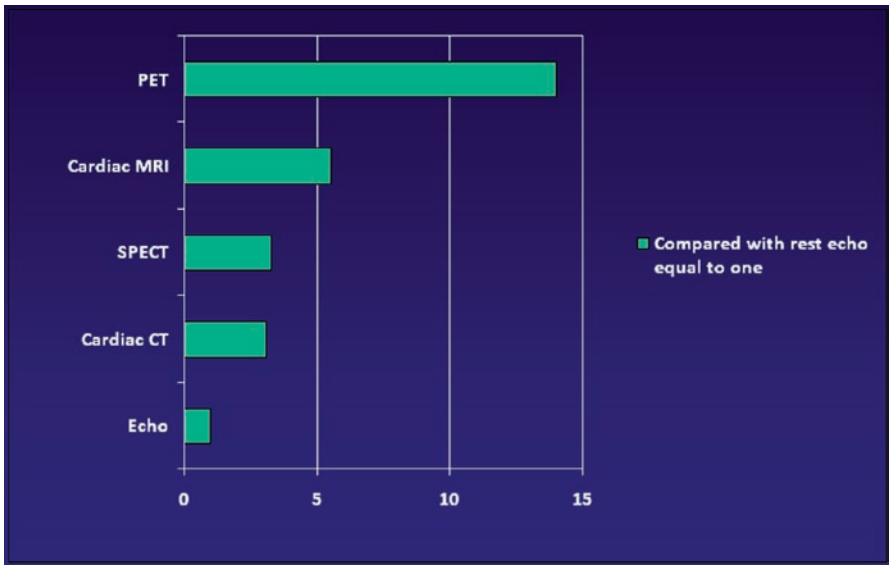

Fig. 11.14 Costs of cardiac imaging procedures relative to echo. *CT* computed tomography; *MRI* magnetic resonance imaging; *PET* positron emission tomography; *SPECT* single photon emission computed tomography

parameter in decision making, and the reliability of 2D-EF is tenuous when the implications of this measurement (e.g. implantable defibrillator insertion) are considered. The use of contrast has been shown to improve reliability of these measurements,[53] and 3D-EF may also be attractive. Likewise, although LV volumes are known to be a powerful prognosticator, the reliability of these measurements with 2D echocardiography is limited, and 3D imaging has been shown to produce analogous measures to MRI.[77] The interpretation of regional function (including stress echocardiography) is the most challenging aspect of echocardiography, as well as the most difficult to quantify. Recent developments in tissue Doppler, strain rate imaging and speckle tracking echocardiography may prove useful for this purpose. The contribution of tissue Doppler in ischaemic heart disease is limited by its lack of site specificity, which makes its measurements susceptible to translation and tethering problems.[78] In contrast, strain measurements are specific to location, and strain rate in particular has been used to facilitate the identification of viable myocardium.[79] The use of deformation analysis to facilitate the recognition of ischaemia is problematic – tissue-velocity based strain may be limited by signal noise, and the tracking process for speckle strain is challenging at high heart rates. Further technical developments will facilitate the clinical adoption of these techniques.

Conclusion

Echocardiography is central in the evaluation and management of the patient with ischaemic heart disease. Although the imaging choices for the evaluation of ischaemic heart disease have expanded over the last few years, echocardiography remains the initial test in most settings. The utility of echo will likely be increased by a number of new developments.

Video 11.1

Pre- and post-exercise apical views from a contrast stress echocardiogram showing both LV opacification and myocardial perfusion. There are no inducible wall motion abnormalities. After the destruction frames (marked by the flash), there is opacification of most of the myocardium. The apical parts of septum, lateral, inferior, and anterior walls (i.e. distal LAD territory) show sub-endocardial perfusion abnormalities that persist for up to five beats post-flash. These are best seen in the end-systolic freeze-frames in Fig. 11.1

Video 11.2

Apical 4-chamber views during resting (**a**), prepeak (**b**), and peak dose dobutamine (**c**). There is ischaemia involving the apical septum. The value of LV shape as a marker of ischaemia is emphasized by superimposition of the resting end-systolic contour on each image in Fig. 11.2

Video 11.3

Parasternal and apical 2D-echo (**a**) views, pre- and post-exercise (**b**), and resting 3D-echo (**c**) views showing LAD territory infarction without wall thinning. The post-exercise loops show no inducible ischaemia

Videos 11.5a-e

The spectrum of ischaemic wall motion responses to stress is shown in this 61-year-old man with multiple risk factors and probable angina. The resting ECG was normal, and the exercise test showed no chest pain, 1 mm ST depression, submax heart rate (79%), and an exercise capacity of seven METS. Video loops of images showed questionable inferoseptal hypokinesis, also apparent on LV opacification images. Destruction-replenishment imaging showed inferior and apical perfusion defects (best seen in the end-systolic freeze-frames in Fig. 11.5a, b). Coronary angiography (Fig. 11.5c) showed significant 70% distal RCA and 60% mid-LAD stenoses

Video 11.6

(**a**) Resting echocardiograms (GC baseline) in parasternal and apical views show LV enlargement and resting wall motion abnormalities with preserved wall thickness in the antero-septum, septum, and apex. The bullseye display (Fig. 11.6a) shows reduced longitudinal shortening in these areas (numbers correspond to regional strain (normal strain is approximately 18%). (**b**) Rest, low, peak dose, and recovery Video loops of the apical 4-chamber view. The apical and mid-septal akinetic area does not change at low dose and, therefore, suggests a non-viable area. The apical lateral wall improves at peak stress, indicating non-transmural infarction. (**c**) End-systolic images at rest, low, peak dose, and recovery in the apical 2-chamber view. The apical inferior akinetic area thickens at the 10 mcg dose, but does not deteriorate, denoting a non-transmural infarction. The antero-apical wall deteriorates at peak stress, indicating ischaemia

Video 11.8a-f

Resting apical 2-chamber (**a**), 4-chamber (**b**), and long-axis (**c**) echocardiograms, repeated with myocardial contrast using a destruction-replenishment protocol (MCE) (**d-f**) in a 65-year-old man after late presentation MI. Despite regional wall motion abnormalities in the inferior wall, perfusion is preserved, suggesting viability

Videos 11.11

Typical ischaemic MR due to papillary muscle displacement. Note the akinesis of the posterior wall in (**a**). This causes tethering of the posterior mitral leaflet with posteriorly-directed MR (**c**)

Videos 11.12

Multi-planar reconstruction of an apical VSD (**a-d**) showing defect diameter in the 4-chamber view (*upper left*), defect circumference in a modified 2-chamber view (*upper right*) where it is seen "en face," a short-axis cut through the defect (*lower left*) and a 3D display (*lower right*). The colour map (**e**) shows the left-right shunt. *TV* tricuspid valve

References

1. Edler I, Lindstrom K. The history of echocardiography. *Ultrasound Med Biol*. 2004;30(suppl 12):1565–1644
2. Nesto RW, Kowalchuk GJ. The ischemic cascade: temporal sequence of hemodynamic, electrocardiographic and symptomatic expressions of ischemia. *Am J Cardiol*. 1987;59(suppl 7):23C–30C
3. Picano E, Palinkas A, Amyot R. Diagnosis of myocardial ischemia in hypertensive patients. *J Hypertens*. 2001;19(suppl 7):1177–1183
4. Legrand V, Hodgson JM, Bates ER, et al Abnormal coronary flow reserve and abnormal radionuclide exercise test results in patients with normal coronary angiograms. *J Am Coll Cardiol*. 1985;6(suppl 6):1245–1253
5. Gallagher KP, Matsuzaki M, Koziol JA, et al Regional myocardial perfusion and wall thickening during ischemia in conscious dogs. *Am J Physiol*. 1984;247(5 pt 2):H727–H738
6. Grattan MT, Hanley FL, Stevens MB, et al Transmural coronary flow reserve patterns in dogs. *Am J Physiol*. 1986;250(2 pt 2): H276–H283
7. Braunwald E, Kloner RA. The stunned myocardium: prolonged, postischemic ventricular dysfunction. *Circulation*. 1982;66(suppl 6):1146–1149
8. Marwick TH. The viable myocardium: epidemiology, detection, and clinical implications. *Lancet*. 14 1998;351(suppl 9105):815–819
9. Bogaert J, Maes A, Van de Werf F, et al Functional recovery of subepicardial myocardial tissue in transmural myocardial infarction after successful reperfusion: an important contribution to the improvement of regional and global left ventricular function. *Circulation*. 1999;99(1):36–43
10. Reimer KA, Lowe JE, Rasmussen MM, et al The wavefront phenomenon of ischemic cell death. 1. Myocardial infarct size vs duration of coronary occlusion in dogs. *Circulation*. 1977;56(suppl 5):786–794
11. Hauser AM, Gangadharan V, Ramos RG, et al Sequence of mechanical, electrocardiographic and clinical effects of repeated coronary artery occlusion in human beings: echocardiographic observations

during coronary angioplasty. *J Am Coll Cardiol*. 1985;5(2 pt 1): 193–197
12. Kvitting JP, Wigstrom L, Strotmann JM, et al How accurate is visual assessment of synchronicity in myocardial motion? An In vitro study with computer-simulated regional delay in myocardial motion: clinical implications for rest and stress echocardiography studies. *J Am Soc Echocardiogr*. 1999;12(suppl 9):698–705
13. Cerqueira MD, Weissman NJ, Dilsizian V, et al Standardized myocardial segmentation and nomenclature for tomographic imaging of the heart: a statement for healthcare professionals from the Cardiac Imaging Committee of the Council on Clinical Cardiology of the American Heart Association. *Circulation*. 2002;105(suppl 4): 539–542
14. Biagini E, Galema TW, Schinkel AF, et al Myocardial wall thickness predicts recovery of contractile function after primary coronary intervention for acute myocardial infarction. *J Am Coll Cardiol*. 2004;43(suppl 8):1489–1493
15. Kraunz RF, Kennedy JW. Ultrasonic determination of left ventricular wall motion in normal man. Studies at rest and after exercise. *Am Heart J*. 1970;79(suppl 1):36–43
16. Douglas PS, Khandheria B, Stainback RF, et al ACCF/ASE/ACEP/AHA/ASNC/SCAI/SCCT/SCMR 2008 appropriateness criteria for stress echocardiography: a report of the American College of Cardiology Foundation Appropriateness Criteria Task Force, American Society of Echocardiography, American College of Emergency Physicians, American Heart Association, American Society of Nuclear Cardiology, Society for Cardiovascular Angiography and Interventions, Society of Cardiovascular Computed Tomography, and Society for Cardiovascular Magnetic Resonance: endorsed by the Heart Rhythm Society and the Society of Critical Care Medicine. *Circulation*. 2008;117(suppl 11):1478–1497
17. Cornel JH, Bax JJ, Elhendy A, et al Biphasic response to dobutamine predicts improvement of global left ventricular function after surgical revascularization in patients with stable coronary artery disease: implications of time course of recovery on diagnostic accuracy. *J Am Coll Cardiol*. 1998;31(suppl 5):1002–1010
18. Kloner RA, Allen J, Cox TA, et al Stunned left ventricular myocardium after exercise treadmill testing in coronary artery disease. *Am J Cardiol*. 1991;68(suppl 4):329–334
19. Noguchi Y, Nagata-Kobayashi S, Stahl JE, et al A meta-analytic comparison of echocardiographic stressors. *Int J Cardiovasc Imaging*. 2005;21(suppl 2–3):189–207
20. Kwok Y, Kim C, Grady D, et al Meta-analysis of exercise testing to detect coronary artery disease in women. *Am J Cardiol*. 1999;83 (suppl 5):660–666
21. Sicari R, Nihoyannopoulos P, Evangelista A, et al Stress echocardiography expert consensus statement: European Association of Echocardiography (EAE) (a registered branch of the ESC). *Eur J Echocardiogr*. 2008;9(suppl 4):415–437
22. Mazeika P, Nihoyannopoulos P, Joshi J, et al Evaluation of dipyridamole-Doppler echocardiography for detection of myocardial ischemia and coronary artery disease. *Am J Cardiol*. 1991;68 (suppl 5):478–484
23. Bin JP, Le E, Pelberg RA, et al Mechanism of inducible regional dysfunction during dipyridamole stress. *Circulation*. 2002;106(suppl 1):112–117
24. Armstrong WF, Pellikka PA, Ryan T, et al Stress echocardiography: recommendations for performance and interpretation of stress echocardiography. Stress Echocardiography Task Force of the Nomenclature and Standards Committee of the American Society of Echocardiography. *J Am Soc Echocardiogr*. 1998;11(suppl 1): 97–104
25. McNeill AJ, Fioretti PM, el-Said SM, et al Enhanced sensitivity for detection of coronary artery disease by addition of atropine to dobutamine stress echocardiography. *Am J Cardiol*. 1992;70(suppl 1): 41–46
26. Picano E, Pingitore A, Conti U, et al Enhanced sensitivity for detection of coronary artery disease by addition of atropine to dipyridamole echocardiography. *Eur Heart J*. 1993;14(suppl 9):1216–1222
27. Picano E, Molinaro S, Pasanisi E. The diagnostic accuracy of pharmacological stress echocardiography for the assessment of coronary artery disease: a meta-analysis. *Cardiovasc Ultrasound*. 2008;6:30
28. Kim C, Kwok YS, Heagerty P, et al Pharmacologic stress testing for coronary disease diagnosis: A meta-analysis. *Am Heart J*. 2001; 142(suppl 6):934–944
29. Picano E, Bedetti G, Varga A, et al The comparable diagnostic accuracies of dobutamine-stress and dipyridamole-stress echocardiographies: a meta-analysis. *Coron Artery Dis*. 2000;11(suppl 2):151–159
30. Bax JJ, Poldermans D, Elhendy A, et al Sensitivity, specificity, and predictive accuracies of various noninvasive techniques for detecting hibernating myocardium. *Curr Probl Cardiol*. 2001;26(suppl 2):147–186
31. Kertai MD, Boersma E, Bax JJ, et al A meta-analysis comparing the prognostic accuracy of six diagnostic tests for predicting perioperative cardiac risk in patients undergoing major vascular surgery. *Heart*. 2003;89(suppl 11):1327–1334
32. Ciaroni S, Bloch A, Albrecht L, et al Diagnosis of coronary artery disease in patients with permanent cardiac pacemaker by dobutamine stress echocardiography or exercise thallium–201 myocardial tomography. *Echocardiography*. 2000;17(suppl 7):675–679
33. Lieberman AN, Weiss JL, Jugdutt BI, et al Two-dimensional echocardiography and infarct size: relationship of regional wall motion and thickening to the extent of myocardial infarction in the dog. *Circulation*. 1981;63(suppl 4):739–746
34. Scherrer-Crosbie M, Liel-Cohen N, Otsuji Y, et al Myocardial perfusion and wall motion in infarction border zone: assessment by myocardial contrast echocardiography. *J Am Soc Echocardiogr*. 2000;13(suppl 5):353–357
35. Beattie WS, Abdelnaem E, Wijeysundera DN, et al A meta-analytic comparison of preoperative stress echocardiography and nuclear scintigraphy imaging. *Anesth Analg*. 2006;102(suppl 1):8–16
36. Schinkel AF, Bax JJ, Poldermans D, et al Hibernating myocardium: diagnosis and patient outcomes. *Curr Probl Cardiol*. 2007; 32(suppl 7):375–410
37. Gramiak R, Shah PM, Kramer DH. Ultrasound cardiography: contrast studies in anatomy and function. *Radiology*. 1969;92(suppl 5): 939–948
38. Garcia-Fernandez MA, Bermejo J, Perez-David E, et al New techniques for the assessment of regional left ventricular wall motion. *Echocardiography*. 2003;20(suppl 7):659–672
39. Linka AZ, Sklenar J, Wei K, et al Assessment of transmural distribution of myocardial perfusion with contrast echocardiography. *Circulation*. 1998;98(suppl 18):1912–1920
40. Olszewski R, Timperley J, Szmigielski C, et al The clinical applications of contrast echocardiography. *Eur J Echocardiogr*. 2007;8 (suppl 3):S13–S23
41. Hayat SA, Senior R. Contrast echocardiography for the assessment of myocardial viability. *Curr Opin Cardiol*. 2006;21(suppl 5):473–478
42. Janardhanan R, Moon JC, Pennell DJ, et al Myocardial contrast echocardiography accurately reflects transmurality of myocardial necrosis and predicts contractile reserve after acute myocardial infarction. *Am Heart J*. 2005;149(suppl 2):355–362
43. Dickstein K, Cohen-Solal A, Filippatos G, et al ESC Guidelines for the diagnosis and treatment of acute and chronic heart failure 2008: The Task Force for the Diagnosis and Treatment of Acute and Chronic Heart Failure 2008 of the European Society of Cardiology. Developed in collaboration with the Heart Failure Association of the ESC (HFA) and endorsed by the European Society of Intensive Care Medicine (ESICM). *Eur Heart J*. 2008;29:2388–442
44. Murdoch DR, Love MP, Robb SD, et al Importance of heart failure as a cause of death. Changing contribution to overall mortality and coronary heart disease mortality in Scotland 1979–1992. *Eur Heart J*. 1998;19(suppl 12):1829–1835

45. Fox KF, Cowie MR, Wood DA, et al Coronary artery disease as the cause of incident heart failure in the population. *Eur Heart J*. 2001;22(suppl 3):228–236
46. Ciampi Q, Villari B. Role of echocardiography in diagnosis and risk stratification in heart failure with left ventricular systolic dysfunction. *Cardiovasc Ultrasound*. 2007;5:34
47. Foster E, Cahalan MK. The search for intelligent quantitation in echocardiography: "eyeball," "trackball" and beyond. *J Am Coll Cardiol*. 1993;22(suppl 3):848–850
48. Marwick TH. Techniques for comprehensive two dimensional echocardiographic assessment of left ventricular systolic function. *Heart*. 2003;89(Suppl 3):iii2–iii8
49. Stamm RB, Carabello BA, Mayers DL, et al Two-dimensional echocardiographic measurement of left ventricular ejection fraction: prospective analysis of what constitutes an adequate determination. *Am Heart J*. 1982;104(suppl 1):136–144
50. Schiller NB, Shah PM, Crawford M, et al Recommendations for quantitation of the left ventricle by two-dimensional echocardiography. American Society of Echocardiography Committee on Standards, Subcommittee on Quantitation of Two-Dimensional Echocardiograms. *J Am Soc Echocardiogr*. 1989;2(suppl 5): 358–367
51. Cohen JL, Cheirif J, Segar DS, et al Improved left ventricular endocardial border delineation and opacification with OPTISON (FS069), a new echocardiographic contrast agent. Results of a phase III Multicenter Trial. *J Am Coll Cardiol*. 1998;32(suppl 3):746–752
52. Crouse LJ, Cheirif J, Hanly DE, et al Opacification and border delineation improvement in patients with suboptimal endocardial border definition in routine echocardiography: results of the Phase III Albunex Multicenter Trial. *J Am Coll Cardiol*. 1993;22(suppl 5):1494–1500
53. Hoffmann R, von Bardeleben S, ten Cate F, et al Assessment of systolic left ventricular function: a multi-centre comparison of cineventriculography, cardiac magnetic resonance imaging, unenhanced and contrast-enhanced echocardiography. *Eur Heart J*. 2005;26 (suppl 6):607–616
54. Malm S, Frigstad S, Sagberg E, et al Accurate and reproducible measurement of left ventricular volume and ejection fraction by contrast echocardiography: a comparison with magnetic resonance imaging. *J Am Coll Cardiol*. 2004;44(suppl 5):1030–1035
55. Hutchins GM, Bulkley BH. Infarct expansion versus extension: two different complications of acute myocardial infarction. *Am J Cardiol*. 1978;41(suppl 7):1127–1132
56. Meizlish JL, Berger HJ, Plankey M, et al Functional left ventricular aneurysm formation after acute anterior transmural myocardial infarction. Incidence, natural history, and prognostic implications. *N Engl J Med*. 1984;311(suppl 16):1001–1006
57. Friedman BM, Dunn MI. Postinfarction ventricular aneurysms. *Clin Cardiol*. 1995;18(suppl 9):505–511
58. Antunes MJ, Antunes PE. Left-ventricular aneurysms: from disease to repair. *Expert Rev Cardiovasc Ther*. 2005;3(suppl 2):285–294
59. Brown SL, Gropler RJ, Harris KM. Distinguishing left ventricular aneurysm from pseudoaneurysm. A review of the literature. *Chest*. 1997;111(suppl 5):1403–1409
60. Haugland JM, Asinger RW, Mikell FL, et al Embolic potential of left ventricular thrombi detected by two-dimensional echocardiography. *Circulation*. 1984;70(suppl 4):588–598
61. Keren A, Goldberg S, Gottlieb S, et al Natural history of left ventricular thrombi: their appearance and resolution in the posthospitalization period of acute myocardial infarction. *J Am Coll Cardiol*. 1990;15(suppl 4):790–800
62. Kumanohoso T, Otsuji Y, Yoshifuku S, et al Mechanism of higher incidence of ischemic mitral regurgitation in patients with inferior myocardial infarction: quantitative analysis of left ventricular and mitral valve geometry in 103 patients with prior myocardial infarction. *J Thorac Cardiovasc Surg*. 2003;125(suppl 1):135–143
63. Reeder GS. Identification and treatment of complications of myocardial infarction. *Mayo Clin Proc*. 1995;70(suppl 9):880–884
64. Helmcke F, Nanda NC, Hsiung MC, et al Color Doppler assessment of mitral regurgitation with orthogonal planes. *Circulation*. 1987;75 (suppl 1):175–183
65. Pollak H, Nobis H, Mlczoch J. Frequency of left ventricular free wall rupture complicating acute myocardial infarction since the advent of thrombolysis. *Am J Cardiol*. 1994;74(suppl 2):184–186
66. Raitt MH, Kraft CD, Gardner CJ, et al Subacute ventricular free wall rupture complicating myocardial infarction. *Am Heart J*. 1993; 126(suppl 4):946–955
67. Pollak H, Diez W, Spiel R, et al Early diagnosis of subacute free wall rupture complicating acute myocardial infarction. *Eur Heart J*. 1993;14(suppl 5):640–648
68. Veinot JP, Walley VM, Wolfsohn AL, et al Postinfarct cardiac free wall rupture: the relationship of rupture site to papillary muscle insertion. *Mod Pathol*. 1995;8(suppl 6):609–613
69. Anderson DR, Adams S, Bhat A, et al Post-infarction ventricular septal defect: the importance of site of infarction and cardiogenic shock on outcome. *Eur J Cardiothorac Surg*. 1989;3(suppl 6): 554–557
70. Soliman OI, Geleijnse ML, Meijboom FJ, et al The use of contrast echocardiography for the detection of cardiac shunts. *Eur J Echocardiogr*. 2007;8(suppl 3):S2–S12
71. Batts KP, Ackermann DM, Edwards WD. Postinfarction rupture of the left ventricular free wall: clinicopathologic correlates in 100 consecutive autopsy cases. *Hum Pathol*. 1990;21(suppl 5): 530–535
72. Hansing CE, Rowe GG. Tricuspid insufficiency. A study of hemodynamics and pathogenesis. *Circulation*. 1972;45(suppl 4):793–799
73. Abbate A, Bonanno E, Mauriello A, et al Widespread myocardial inflammation and infarct-related artery patency. *Circulation*. 2004;110(suppl 1):46–50
74. Mulvagh SL, Rakowski H, Vannan MA, et al American Society of Echocardiography Consensus Statement on the Clinical Applications of Ultrasonic Contrast Agents in Echocardiography. *J Am Soc Echocardiogr*. 2008;21(suppl 11):1179–1201; quiz 1281
75. Pennell DJ, Sechtem UP, Higgins CB, et al Clinical indications for cardiovascular magnetic resonance (CMR): Consensus Panel report. *Eur Heart J*. 2004;25(suppl 21):1940–1965
76. Picano E. Stress echocardiography. *Expert Rev Cardiovasc Ther*. 2004;2(suppl 1):77–88
77. Jenkins C, Bricknell K, Marwick TH. Use of real-time three-dimensional echocardiography to measure left atrial volume: comparison with other echocardiographic techniques. *J Am Soc Echocardiogr*. 2005;18(suppl 9):991–997
78. Marwick TH. Measurement of strain and strain rate by echocardiography: ready for prime time? *J Am Coll Cardiol*. 2006;47(suppl 7):1313–1327
79. Hanekom L, Jenkins C, Jeffries L, et al Incremental value of strain rate analysis as an adjunct to wall-motion scoring for assessment of myocardial viability by dobutamine echocardiography: a follow-up study after revascularization. *Circulation*. 2005;112(suppl 25): 3892–3900

Chapter 12

NUCLEAR CARDIOLOGY AND DETECTION OF CORONARY ARTERY DISEASE

James Elliott Stirrup and Stephen Richard Underwood

CONTENTS

J. L. Zamorano et al. (eds.), *The ESC Textbook of Cardiovascular Imaging*
DOI: 10.1007/978-1-84882-421-8_12, © Springer-Verlag London Limited 2010

Introduction

Experience with radionuclide assessment of myocardial perfusion has been gained over decades. Single-photon emission computed tomography (SPECT) myocardial perfusion scintigraphy (MPS) is extensively validated for the diagnosis of ischaemic heart disease, for the assessment of myocardial viability and function, and for the assessment of prognosis in this condition. Its use is, therefore, embedded in national and international guidelines. Positron emission tomography (PET) is also well validated for the assessment of myocardial viability, but it is also now used to detect inducible perfusion abnormalities and, hence, obstructive coronary artery disease (CAD). With the increasing number of imaging techniques available for the assessment of the heart, it is important to understand the principles, indications, and pitfalls of the available options. No single technique provides a complete assessment of the heart and many provide complementary rather than equivalent information. In this chapter, the value of cardiac radionuclide imaging in stable CAD and acute coronary syndromes (ACS) is discussed with a particular emphasis on MPS, the most commonly used technique in nuclear cardiology.

Spectrum of Coronary Artery Disease

CAD is characterized by the progressive development of atheromatous plaques within the intima of the coronary artery. Knowledge of the development and progression of atheroma helps to put the various cardiac imaging techniques into context. Techniques concerned mainly with coronary artery anatomy, such as invasive coronary angiography (ICA) or computed tomography coronary angiography (CTCA), are able to detect atheromatous plaques causing minor luminal narrowing and beyond. However, in isolation, they provide no assessment of the impact of these plaques on coronary function. The functional significance of a coronary artery stenosis is most often extrapolated from a visual estimation of its severity, but the extrapolation is prone to errors and direct measurements of myocardial perfusion or coronary flow reserve are preferable. Note that myocardial perfusion and coronary flow are not synonymous, the former incorporating collateral flow and arguably being the more important.

Ultimately, the choice of cardiac imaging test is determined by the clinical question to be answered. If the aim of imaging is to detect CAD of any type or severity, such as in a patient with a strong family history of premature CAD in whom the exclusion of CAD would be reassuring, then an anatomical test such as CTCA may be sufficient. However, the majority of patients present with symptoms of some kind, and here it is inducible ischaemia that must be excluded, and a test of coronary function is more appropriate.

The Ischaemic Cascade

Ischaemia is the result of myocardial oxygen demand exceeding supply. Inducible ischaemia is usually caused by impaired myocardial perfusion reserve, although excessive demand, such as in high-output heart failure or prolonged tachycardia, may have the same effect. Impaired myocardial perfusion leads to a cascade of downstream effects depending upon its severity (Fig. 12.1). With increasing impairment, metabolic abnormalities arise, such as a change from glucose to fatty acid metabolism. Thereafter, this leads to abnormalities of first diastolic and then systolic left ventricular function, and later to repolarization abnormalities that may be seen on the surface electrocardiogram (ECG) accompanied with symptoms of chest pain. Functional imaging tests interrogate different parts of this cascade, but MPS is likely to be the most sensitive because of its detection of the initial perfusion heterogeneity.

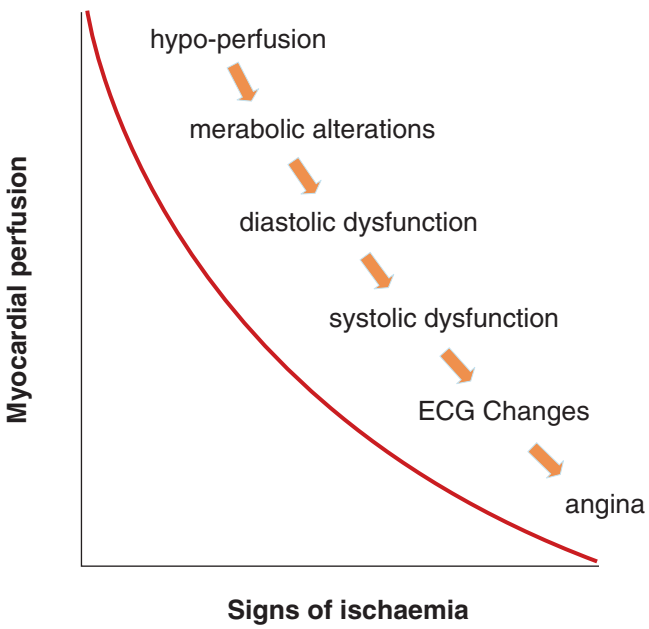

Fig. 12.1 The ischaemic cascade

Pretest Likelihood of Coronary Artery Disease and Imaging Strategy

When a patient presents with possible CAD, the choice of investigation, if any, should be informed by the presenting likelihood of CAD or, in other words, the prevalence of disease in a population of similar patients. It is helpful to consider the diagnostic process in Bayesian terms.[1] This converts the pretest likelihood of disease into the post-test likelihood, depending upon the diagnostic accuracy of a test (its sensitivity and specificity) and the outcome of the test (normal or abnormal). This is demonstrated in Fig. 12.2 where an abnormal stress electrocardiography (sECG) in a patient with a 50% pretest likelihood of CAD generates a post-test likelihood of only 75%, which is not high enough to be sufficiently confident of the diagnosis. If the same patient has an abnormal MPS as in the initial test, the post-test likelihood improves to 90%, which might be considered sufficient to classify the patient as having disease with clinically meaningful certainty.

Pretest likelihood of CAD may be estimated by a variety of predictive nomograms. Among them, the Diamond and Forrester predictive table integrates three clinical variables (quality of chest pain, gender, and age) to provide an estimate of the likelihood of angiographically significant coronary stenosis.[2] This approach can be refined by incorporating other predictors such as serum cholesterol, systolic blood pressure, and diabetes.[3] Those at intermediate pretest likelihood have the most to gain from further investigation, as a normal or abnormal test allows revision of pretest likelihood to either low or high post-test likelihood, respectively.

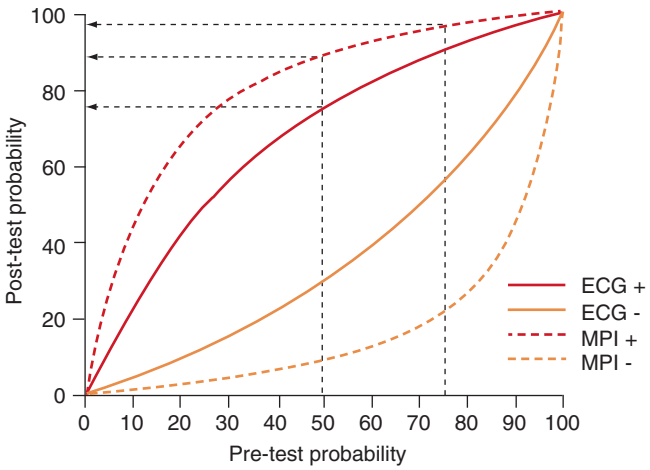

Fig. 12.2 Impact of pretest probability on post-test likelihood of disease. In a patient with a 50% pretest likelihood of coronary artery disease, positive stress electrocardiography renders the post-test likelihood around 75%. This is not sufficient to make the diagnosis with confidence. If the same patient goes on to have a positive myocardial perfusion scan (MPS), the probability is refined further to around 96%, which is sufficient to be confident of the diagnosis. If MPS had been performed as the initial test, pretest likelihood would have been revised from 50% to around 90% based on a positive result, after which further testing would not be required. *ECG*± stress electrocardiogram positive/negative; *MPI*± myocardial perfusion imaging positive/negative

Methods of Cardiac Stress

Dynamic Exercise

This is the preferred method of cardiac stress in many patients (Table 12.1) because it is the most physiological, and both symptoms and haemodynamic and ECG variables provide diagnostic and prognostic information.[4] However, exercise may be either difficult in those with limited mobility or contraindicated, such as in patients with severe left ventricular outflow tract obstruction or severe left main stem stenosis. Furthermore, certain conditions, such as left bundle branch block (LBBB) and permanent pacing, can be associated with stress-induced perfusion abnormalities in the absence of obstructive coronary disease.

Pharmacological Stress

Myocardial perfusion reserve can be assessed more directly by vasodilators such as adenosine and dipyridamole. Endogenous adenosine plays a central role in coronary autoregulation. When given exogenously, stimulation of adenosine A2 receptors leads to coronary arteriolar dilatation and increased myocardial perfusion up to three to five times the baseline. Dipyridamole has the same effect, albeit indirectly through an increase in endogenous adenosine owing to inhibition of local adenosine reuptake. Simultaneous stimulation of A1 receptors within the sinoatrial and atrio-ventricular nodes and in bronchial smooth muscle leads to heart block and bronchospasm, respectively, leading to problems with these agents in patients with nodal disease or obstructive airways disease. Such patients are more suited to dobutamine stress, an α-1, β-1, and β-2 adrenergic agonist that causes secondary coronary vasodilatation by increasing the myocardial demand in a similar way to dynamic exercise. At higher doses, dobutamine causes direct coronary vasodilatation and can therefore be used to study flow heterogeneity even if target heart rate is not achieved.

Table 12.1. Stress test protocols

	Exercise	Adenosine	Dipyridamole	Dobutamine
Action	Reflex coronary vasodilatation in response to increased myocardial work	Direct adenosine receptor stimulation	Endogenous adenosine reuptake inhibitor	Beta-adrenergic agonist
Half-life	–	10s	40 min	2 min
Side effects	Tachyarrhythmia	Bronchospasm	Bronchospasm	Tachyarrhythmia
	Hypotension	Heart block	Heart block	Hypotension
Limitations	Limited mobility	Severe asthma	Severe asthma	History of ventricular tachyarrhythmia
	Severe three-vessel disease	Second- or third-degree heart block without PPM	Second- or third-degree heart block without PPM	Severe three-vessel disease
	Severe LVOTO			Severe LVOTO
Protocol	Dynamic exercise with 1–2 min increments up to maximum achievable	140 mcg/kg/min	140 mcg/kg/min	5–40 mcg/kg/min
Duration of test	Terminate test and inject tracer once 85% target heart rate achieved or at peak exercise	6 min	4 min	Terminate infusion and inject tracer once 85% target heart rate achieved or after 3 min at 40 mcg/kg/min
Radionuclide injection time		2–3 min after start of infusion	7–9 min after start of infusion	

PPM permanent pacemaker; *LVOTO* left ventricular outflow tract obstruction

Stable Coronary Artery Disease

Diagnosis

Stable CAD is characterized by predictable central chest pain provoked by exertion, and relieved by rest. Stable but progressive atherosclerosis causes reduction in coronary flow reserve, resulting in reduced myocardial perfusion and, ultimately, ischaemia during states of increased myocardial demand.

sECG is commonly used to investigate chest pain because it is widely available, easy to administer, and involves no ionizing radiation. sECG allows a more physiological evaluation of symptoms, exercise tolerance, haemodynamic response, and ECG changes during exercise stress, which is usually equal to or greater than the normal level of exertion for the patient. However, in meta-analysis, its sensitivity and specificity for detecting angiographically defined coronary stenosis is only around 68 and 77%, respectively (Fig. 12.3).[5] Its positive predictive value[6] is particularly poor in women[5] leading to normal coronary angiography rates as high as 56% in women referred on the basis of the sECG alone.[7] Furthermore, sECG has limited value when exercise capacity is poor or in the presence of an abnormal resting ECG that precludes ST-segment assessment. These limitations have led to the suggestion that sECG fails to prevent downstream testing and may even lead to an increase in ICA.[8]

MPS is ideally suited for the diagnosis of stable CAD because of its ability to detect impaired myocardial perfusion reserve even before abnormalities of regional function and the surface ECG arise. Although differences exist in their physical and biological properties, the three commercially available MPS radiopharmaceuticals all have comparable accuracy for the detection of CAD.[9] Normal myocardial perfusion after stress (Fig. 12.4, Videos 12.4a, b) indicates the absence of functionally significant CAD and predicts a low likelihood (<1%) of future cardiac events.[10] It should be noted though that normal stress perfusion does not indicate absence of CAD, as coronary atherosclerosis need not necessarily cause stenosis of sufficient severity to cause impairment of perfusion reserve (Fig. 12.5). However, such disease is unlikely to be the cause of stable symptoms. Although normal perfusion carries a good prognosis, the prognostic importance of subclinical disease is still a matter of debate, especially in the light of data derived from techniques such as coronary calcium scoring (CCS).

MPS has a 15% greater median sensitivity for the detection of significant CAD defined angiographically compared with sECG.[11] On recent meta-analysis, sensitivity and specificity were 85–90 and 70–75% (Fig. 12.3), respectively.[12] It should be reiterated that ICA is an anatomical rather than a functional technique and that "significant" stenosis on ICA may be associated with normal perfusion reserve. Perfect agreement is therefore neither expected nor required. In addition, the specificity of MPS is under-estimated in many

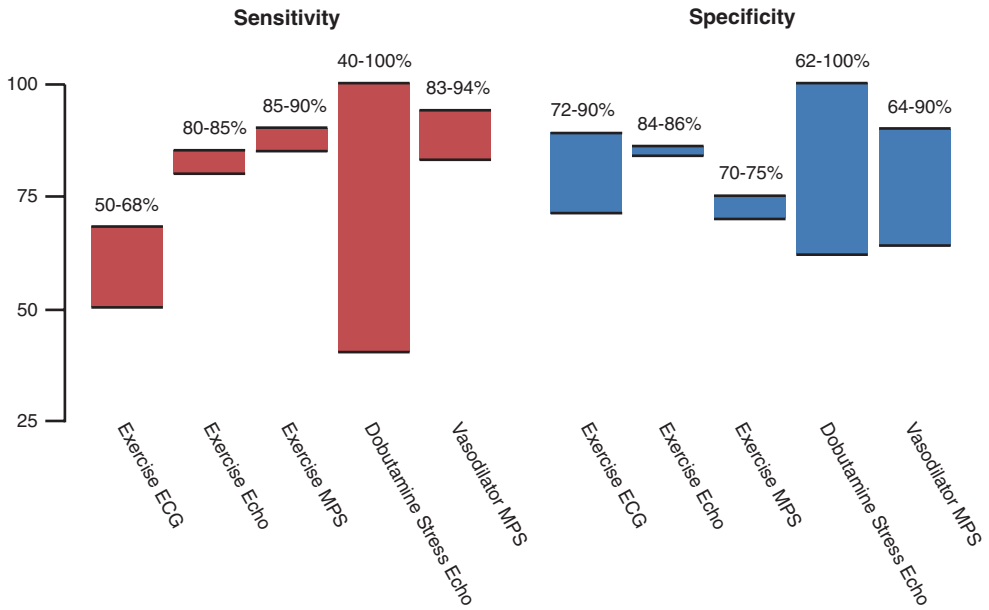

Fig. 12.3 Range of mean sensitivities and specificities of exercise ECG and MPS for the diagnosis of stable coronary artery disease. Adapted from Fox et al.[5] with permission. *ECG* electrocardiogram; *MPS* myocardial perfusion scintigraphy; *Echo* echocardiography

studies because of post-test referral bias and normalcy, the number of patients at low likelihood of coronary disease with normal MPS, is a better measure of the performance of the test in excluding disease. Despite the various tracers and stress techniques available, MPS may be considered reasonably to be a single test with a sensitivity and normalcy as high as 90 and 89%, respectively, for the detection of functionally significant CAD.[12] The technique has slightly greater sensitivity but similar specificity to stress echo[13] and MRI.[14] However, MPS is less operator-dependent than echocardiography, and is more widely available than MRI.

The accuracy of MPS may be improved using ECG gating[15] and attenuation correction.[16] ECG gating allows quantitation of global and regional ventricular function, which, apart from providing important prognostic information, aids in the distinction of artefacts from true perfusion defects, thus improving specificity and normalcy. Fixed defects in the anterior and inferior walls, commonly owing to breast and diaphragmatic attenuation artefacts in women and men, respectively, may be mistaken for myocardial infarction (MI), but for the fact that myocardial motion and thickening in these areas are normal on gated images. Similarly, attenuation correction improves the recognition of attenuation artefacts and, hence, diagnostic accuracy (Fig. 12.6, Videos 12.6a, c).

The extent and depth of inducible perfusion abnormalities can provide diagnostic information and guide subsequent management (Figs. 12.7–12.9, Videos 12.8C1, C2, and 12.9c). Ultimately, the clinician must decide whether to offer revascularization in addition to optimal medical management, and debate concerning the appropriateness of each in the management of CAD is still continuing. The COURAGE trial suggest that in stable CAD with objective evidence of myocardial ischaemia, percutaneous coronary intervention (PCI) does not reduce the risk of death, MI, or other major cardiovascular events when added to optimal medical therapy, although it is initially better at abolishing symptoms.[17] Although subanalysis suggests that the addition of PCI leads to greater reduction in ischaemia on MPS,[18] the prognostic importance of this is relatively short-lived. Nonetheless, assessments of myocardial perfusion remain central to the management of stable CAD.

Prognosis

The likelihood of future cardiac events such as MI or death can be an important factor in determining treatment. This likelihood can be estimated from a number of factors, such as extent of CAD, total ischaemic burden, left ventricular function, angina threshold, presence of diabetes or other arterial disease, and uncontrolled CAD risk factors. However, MPS has incremental prognostic value even when clinical history, sECG, and ICA are available.[19]

MPS in risk stratification and patient management has been validated extensively. Normal MPS is associated with a 0.7% annual risk of MI and cardiac death, which is similar to the general population.[20] This has important clinical implications because a normal study generally renders further invasive investigation or treatment unnecessary. These figures, however, relate to populations of patients, and test findings should always be interpreted in the context of the individual patient. For instance, a patient with normal myocardial perfusion but significant ST-segment depression during adenosine stress is at increased risk of non-fatal MI.[21] Specific groups, such as the elderly and those with diabetes or known CAD, have a somewhat higher annual event rate (1.4–1.8% per year) despite normal MPS.[22] The "warranty period" of normal MPS in this

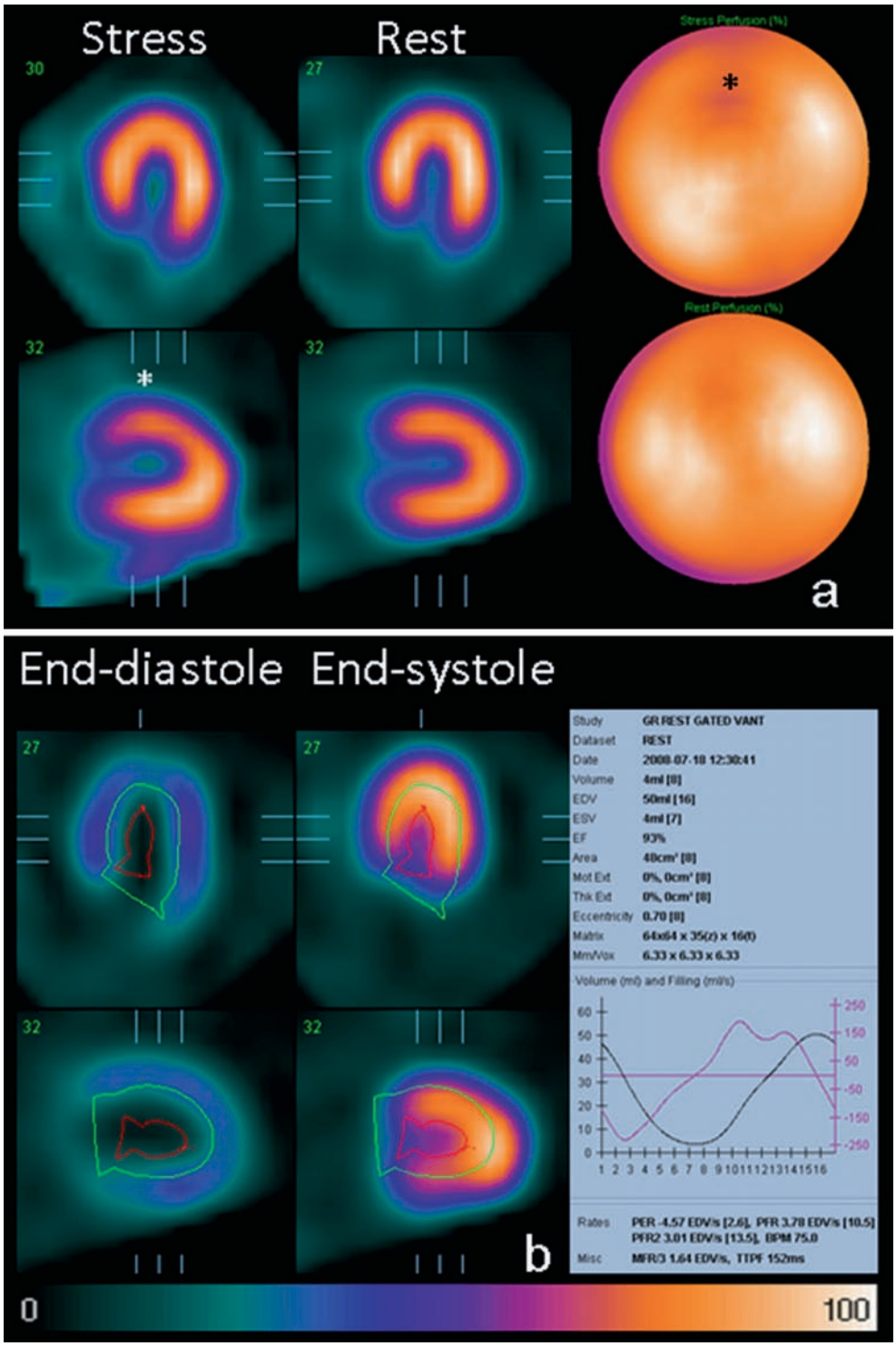

Fig. 12.4 Normal myocardial perfusion scintigraphy. A 70-year-old lady with diabetes, hyperlipidemia, and hypertension presents to a rapid access chest pain clinic with atypical chest pain. Stress electrocardiography was equivocal and subsequent invasive coronary angiography showed 30% distal LAD and 50% mid RCA stenoses. Stress/rest MPS **(a)** shows minor reduction in counts in the basal anterior wall (*asterisks*) consistent with breast attenuation artefact. [Electronic version: Evaluation of raw data (video) demonstrates breast shadows]. There is otherwise homogenous myocardial tracer uptake throughout the myocardium during both stress and rest. ECG gating of the resting tomograms **(b)** shows normal global and regional left ventricular function

setting is around 2 years, after which repeat scanning may be necessary to redefine prognosis.

An abnormal scan confers a sevenfold increase in annual cardiac events compared with a normal study.[23] The likelihood of a cardiac event increases with the extent and severity of the inducible perfusion abnormalities (Figs. 12.10 and 12.11). Those with only mild inducible ischaemia have an annual event rate of around 3% rising to 7% in those with severe ischaemia (Fig. 12.12).[10] The presence of corollary markers of severe three-vessel disease, such as transient left ventricular dilatation[25] or increased lung uptake of thallium-201,[26] increases the event rate still further. Whilst perfusion data are most useful in predicting risk of future ischaemic events, concomitant analysis of left ventricular

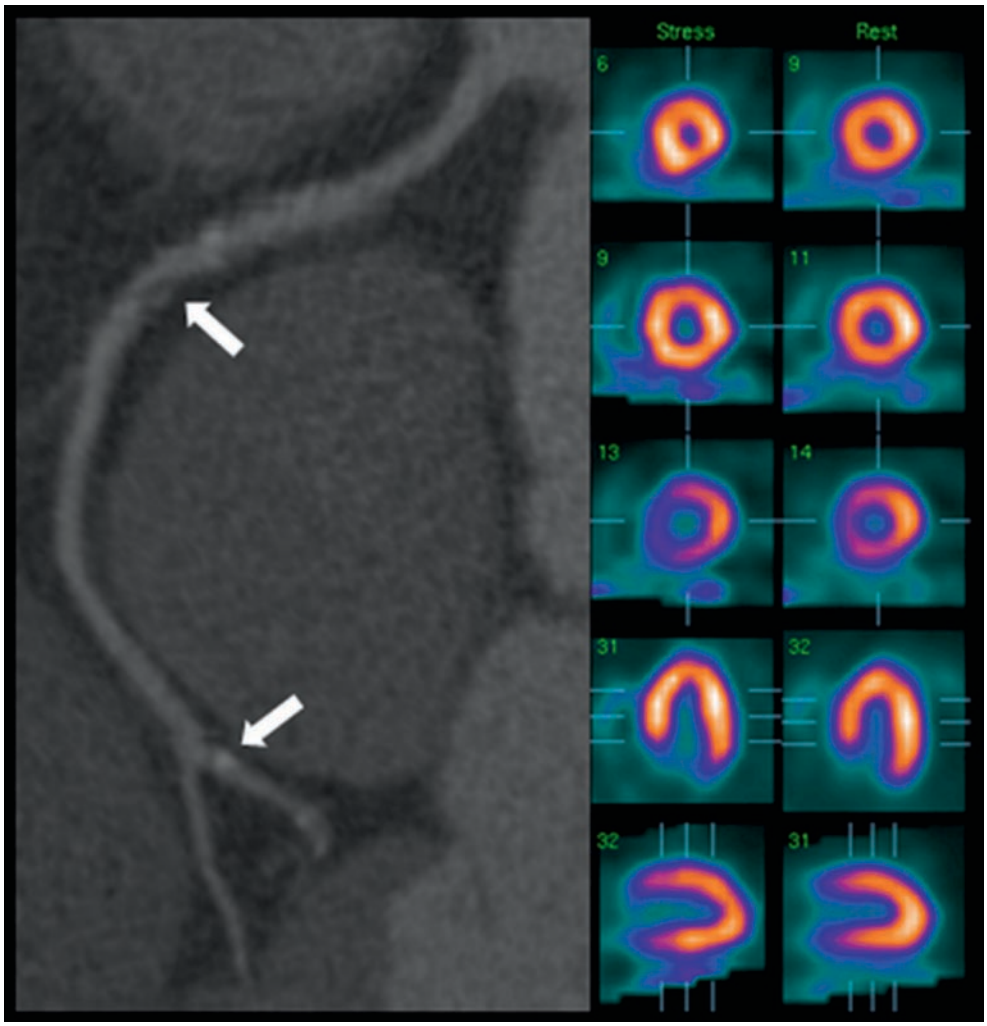

Fig. 12.5 Atheromatous plaques identified in the right coronary artery on computed tomography coronary angiography (*arrows*). These plaques are not of sufficient severity to cause abnormalities on myocardial perfusion scintigraphy

function provides an independent estimate of the risk of cardiac death (Fig. 12.11).[28]

MPS is not generally recommended to assess prognosis in asymptomatic individuals except in certain settings. CCS using X-ray computed tomography identifies subclinical atherosclerosis and predicts the likelihood of future coronary events.[27] Higher calcium scores are associated with increased likelihood of cardiac events even within individual Framingham risk groups.[28] This allows further risk stratification and definition of the appropriateness and intensity of medical treatment or the need for stress testing. Current guidelines suggest that those with CCS ≥ 400 should undergo MPS, as the likelihood of at least one significant coronary artery stenosis is high.[29] Those with diabetes or metabolic syndrome may require a lower threshold (100–400), as reversible perfusion defects may be seen in almost half of those with CCS > 100.[30] CCS and MPS are synergistic in predicting short-term coronary events,[31] suggesting that CCS should be used routinely in asymptomatic diabetic adults to more accurately stratify risk. However, those at high Framingham risk may derive greater benefit from direct referral for MPS to more accurately quantify ischaemic burden.[34]

Cost-Effectiveness

By quantifying the presence, extent, and severity of inducible ischaemia, MPS is ideally placed to stratify patients to either conservative or invasive management strategies. Further, those with minor inducible ischaemia may be managed conservatively, suggesting that even an abnormal MPS need not lead to further investigation or invasive treatment. An investigation strategy involving MPS, therefore, ought to be more cost-effective than the one based on either sECG alone or direct referral for ICA. This supposition is supported by assessments of cost-effectiveness in both Europe and the US. MPS is cost-effective in patients presenting with stable chest pain both at intermediate and high pretest likelihood of

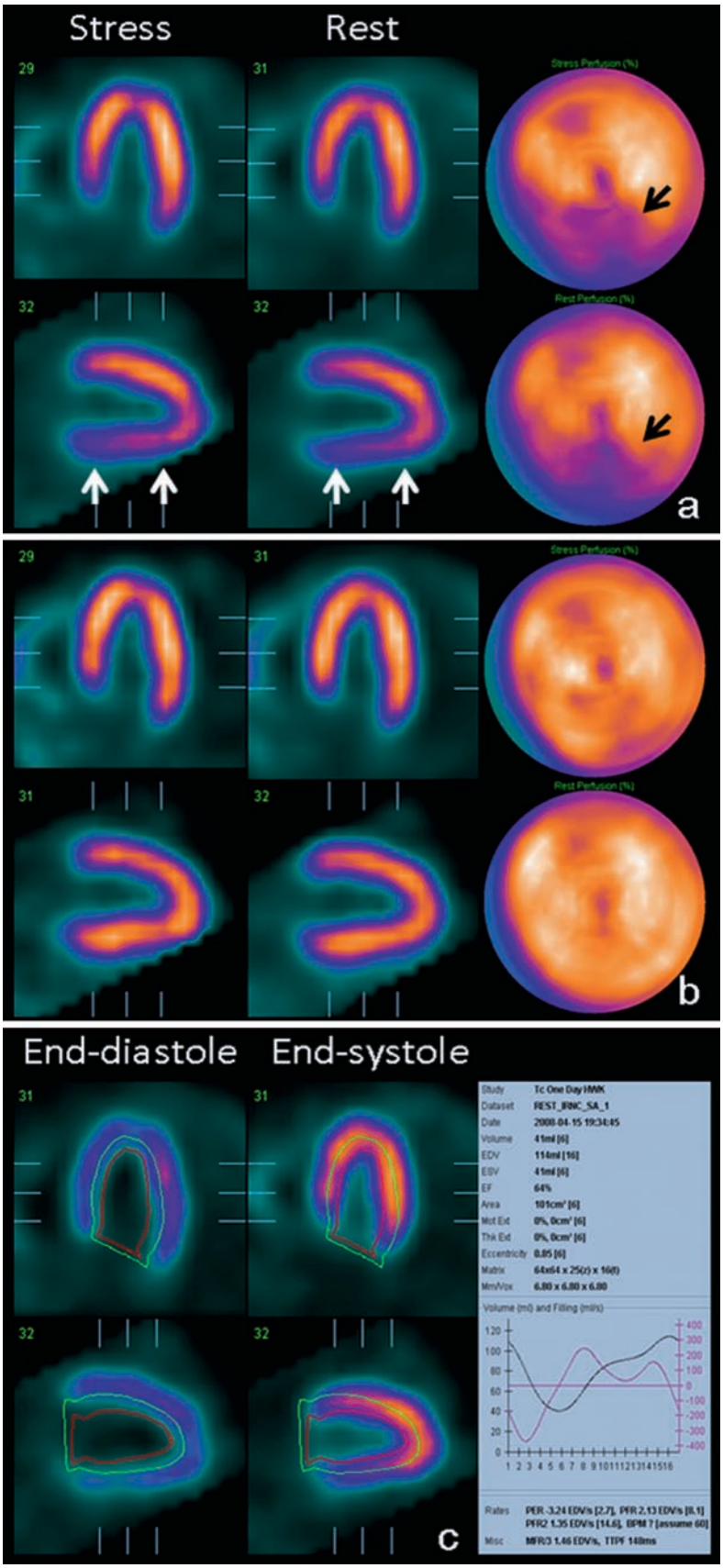

Fig. 12.6 Diaphragmatic attenuation artefact. A 73-year-old man with hypertension and hyperlipidemia presents with central chest pain unrelated to exertion and occasional palpitation. Uncorrected images **(a)** show mild reduction of counts in the whole inferior wall that is present in both stress and resting images (*arrows*). [Electronic version: Evaluation of raw data (video) shows the presence of the diaphragm in the lateral projections]. X-ray computed tomography attenuation correction **(b)** of the images recovers counts in the inferior wall to normal. Additionally, ECG-gating of the uncorrected images **(c)** demonstrates normal wall motion and thickening inferiorly, despite the reduced counts. In this case, the clinical history, attenuation-corrected images and ECG-gating all point to diaphragmatic attenuation rather than to partial thickness myocardial damage as a cause for the reduction in counts inferiorly

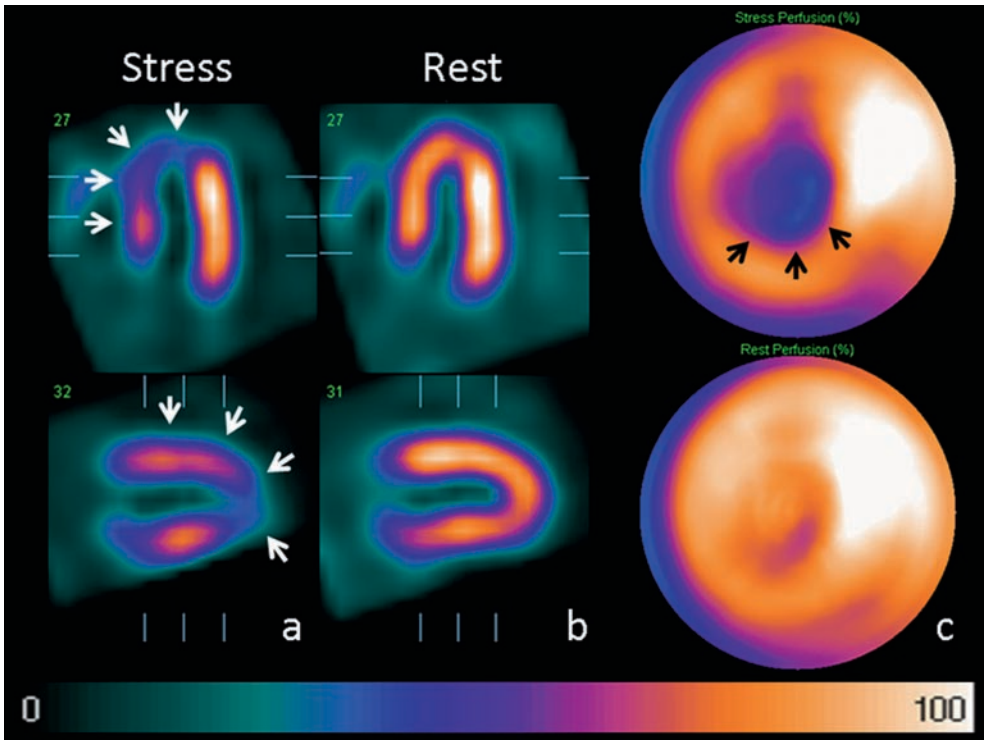

Fig. 12.7 Pure inducible ischaemia on stress **(a)** and rest **(b)** imaging and polar plots **(c)**. A 62-year-old man with a family history of premature coronary artery disease and hyperlipidemia presents to a chest pain clinic with typical angina. sECG demonstrated no ECG changes, although the patient did get chest pain during stage 4 of the Bruce protocol. On MPS, reduction of tracer uptake was observed on stress imaging (*arrows*), severe at the apex and mild in the anterior wall, which returned to normal at rest

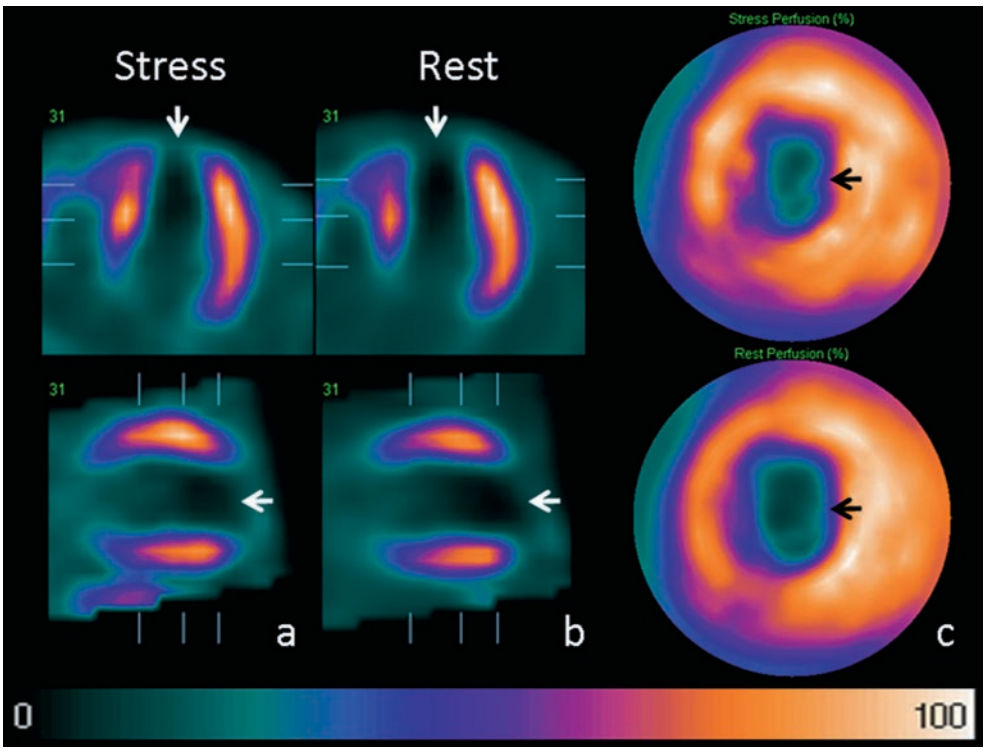

Fig. 12.8 Pure myocardial infarction (MI) on stress **(a)** and rest **(b)** imaging and polar plots **(c)**. A 64-year-old man with previous MI and two-vessel coronary artery bypass grafting is referred for pre-operative assessment prior to umbilical hernia surgery. Although suffering from occasional atypical chest pain, stable exertional breatlessness was the patient's main symptom. [Electronic version: Evaluation of raw data (Video c1) shows a dilated left ventricle with absent uptake at the apex]. There is absence of uptake at the apex on stress images, which remains unchanged on rest imaging (*arrows*), indicating MI without superimposed ischaemia. [Electronic version: ECG gating of the resting tomograms (Video c2) confirms the dilated left ventricle. There is absent motion and thickening in the apex and apical anterior wall and moderate reduction in the adjacent apical parts of the antero-septum and inferior wall. There is further reduced motion but preserved thickening in the remainder of the septum consistent with LBBB.] The absence of inducible ischaemia indicates that the risk of peri-operative coronary events is not high

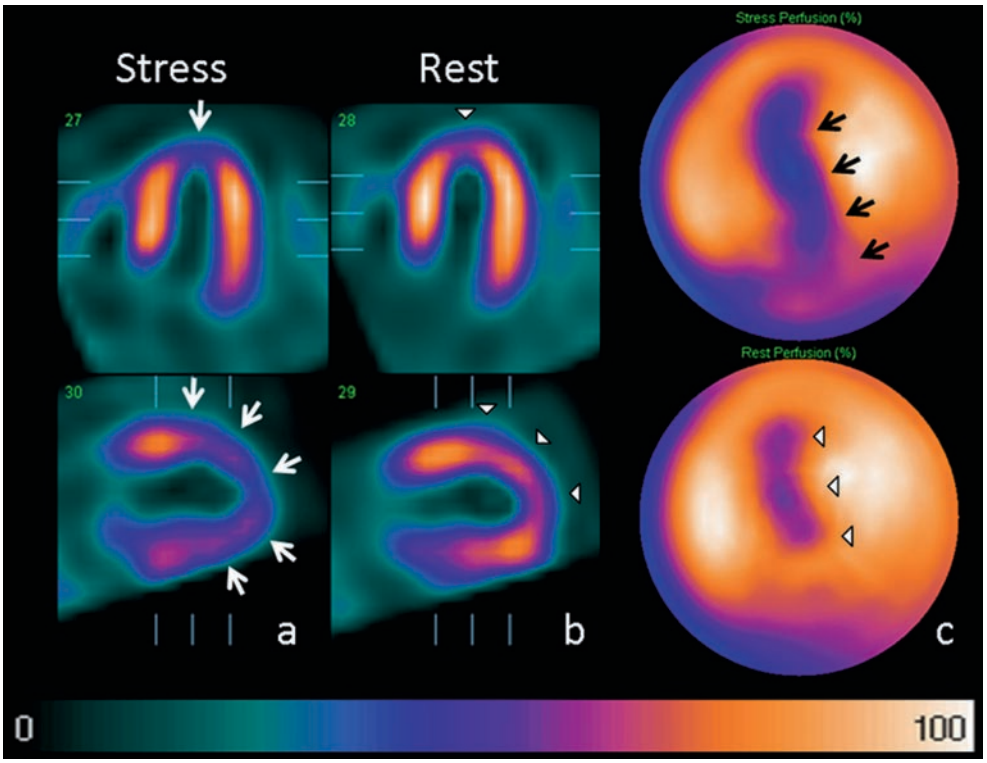

Fig. 12.9 Mixed inducible ischaemia and partial thickness myocardial infarction (MI) on stress **(a)** and rest **(b)** imaging and polar plots **(c)**. A 45-year-old man with known previous MI, right coronary artery stenting but untreated mid-left anterior descending artery occlusion presents to clinic with diminished exercise tolerance but no chest pain. There is moderate reduction of tracer uptake in the apex and apical anterior and inferior walls (*arrows*) on stress imaging. Images acquired at rest show improvement in these areas, but the anterior wall and apex do not return to normal, indicating partial thickness myocardial damage (*arrowheads*). [Electronic version: ECG gating of the resting tomograms (video) shows mild reduction of wall motion and thickening in the apical anterior wall but normal regional function elsewhere]

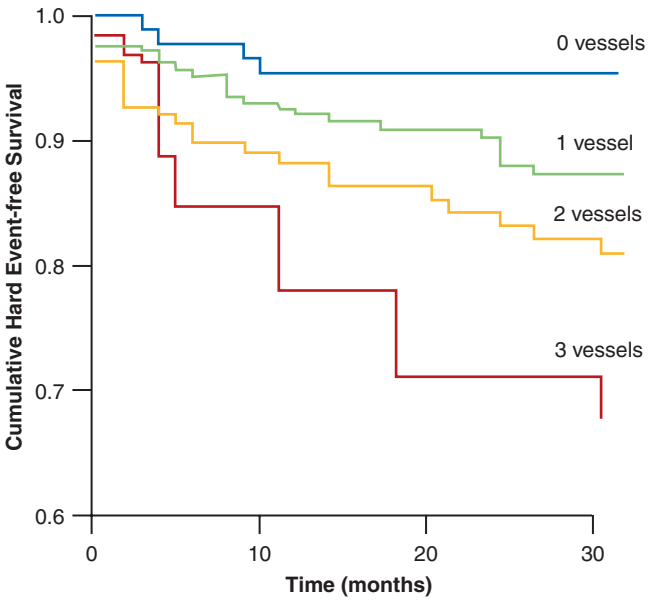

Fig. 12.10 Cumulative hard event-free survival in patients with known or suspected CAD according to the number of ischaemic vascular territories on ^{99m}Tc MPS. Adapted from Petix et al.[23] with permission

CAD and with or without known CAD.[32, 33] In the European setting, strategies involving MPS are cheaper, have greater prognostic power at diagnosis, and lead to lower normal ICA rates when compared with strategies without MPS (Fig. 12.13).[38] Where sECG is used as the initial test, MPS remains cost-effective for the further investigation of patients who remain at intermediate or greater likelihood of CAD.[39, 35] An MPS-led strategy reduces costs by 30–40% when compared with an aggressive interventional strategy, presumably because of reduced use of downstream resources in those with normal scintigraphy.[36] This is particularly true in women, where stratification of patients to ICA based on MPS results leads to significant cost savings, regardless of the pretest likelihood of the disease.[37] In the UK setting, MPS performed after sECG results in a 20–25% reduction in unnecessary ICA and has equal diagnostic accuracy and cost for the identification of those requiring revascularization when compared with direct referral for ICA.[38] For pre-operative assessment of patients with chronic stable angina, MPS allows more cost-effective stratification to either ICA and revascularization or medical therapy, when compared with other commonly used strategies.[12]

Positron Emission Tomography

Although used mainly to assess myocardial viability, PET may be used to assess stress and resting myocardial perfusion, and is generally considered the non-invasive gold standard for this indication. Although cyclotron-produced radiotracers such as ^{13}N-ammonia or ^{15}O-water are regularly used, recent efforts have focussed on the use of rubidium-82. This tracer is produced by a generator, compares favourably

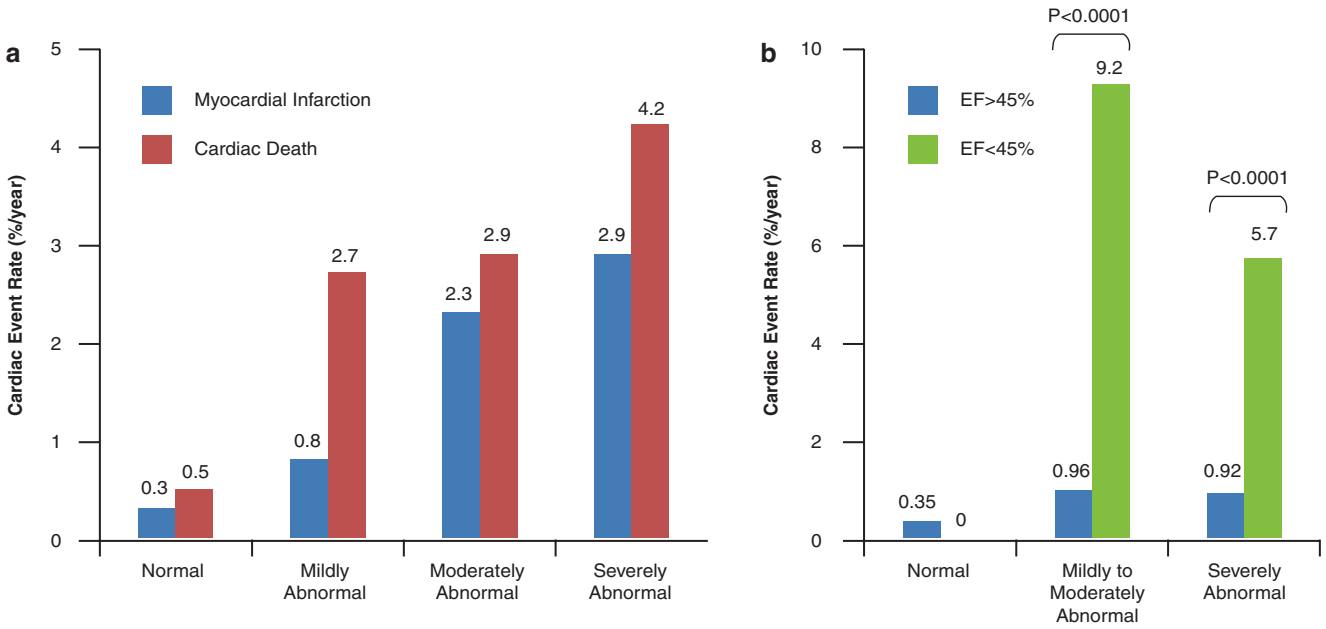

Fig. 12.11 **(a)** Rates of myocardial infarction and cardiac death according to severity of myocardial perfusion abnormalities. Adapted from Hachamovitch et al.[10] with permission. **(b)** Cardiac death rates in patients with differing severities of myocardial perfusion abnormalities, separated according to left ventricular ejection fraction (LVEF). Those with EF < 45% are at a markedly higher risk of death compared with those with normal left ventricular function. Adapted from Sharir et al.[24] with permission

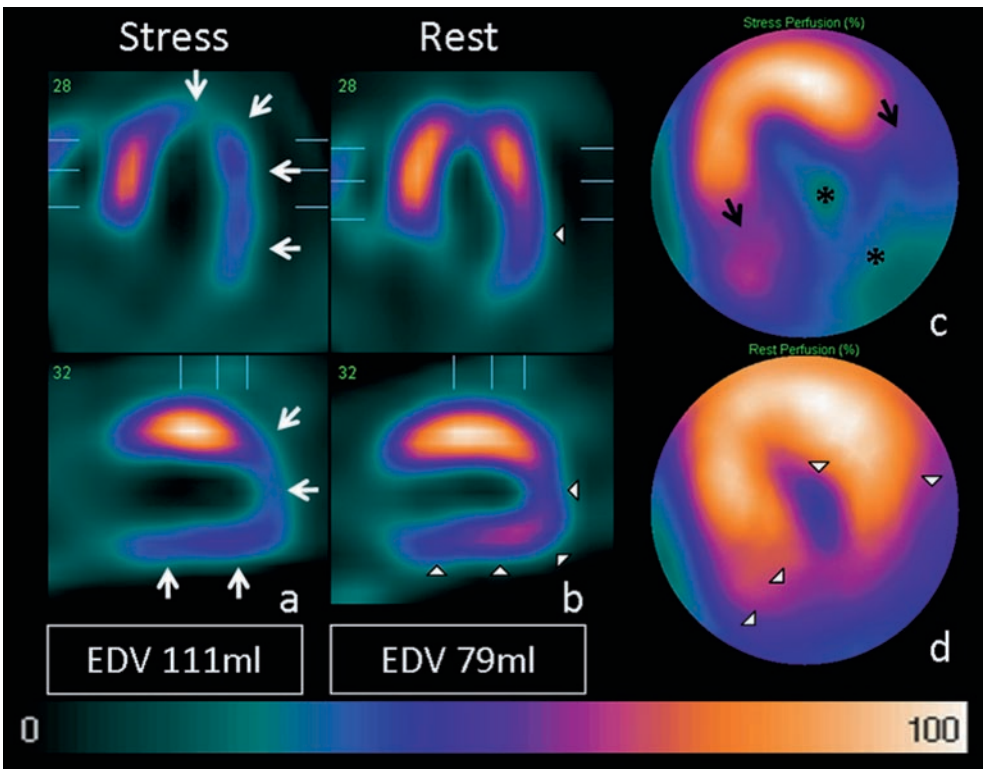

Fig. 12.12 Prognosis defined by extent and severity of inducible myocardial ischaemia. Stress imaging **(a, c)** demonstrates severe reduction of counts in the apex and apical antero-septum, the whole lateral wall and adjacent inferolateral segments, and, finally, moderate reduction of counts inferiorly and inferoseptally (*arrows*). Counts are poorest at the apex and inferolaterally (*asterisks*). Images at rest **(b, d)** show marked improvement in all areas, although the apex, inferior, and basal lateral and inferolateral walls do not return to normal, indicating partial thickness myocardial damage (*arrowheads*). Of note, the end-diastolic volume after stress is significantly larger than at rest (111 vs. 79 mL; TID ratio 1.41). This transient left ventricular cavitary dilatation is a marker of significant three-vessel coronary artery disease. The total amount of ischaemia demonstrated in this study is extensive and severe and suggests that the likelihood of future cardiac events is high. *EDV* end-diastolic volume

Fig. 12.13 Mean cost of diagnosis of coronary artery disease from the Economics of Myocardial Perfusion Imaging in Europe (EMPIRE) study. Four diagnostic strategies were employed: 1–Stress electrocardiography (sECG) followed by invasive coronary angiography (ICA), 2 - sECG followed by myocardial perfusion scintigraphy (MPS), followed by ICA, 3–MPS followed by ICA, 4–Direct referral to ICA. The most cost-effective strategy involved referral of patients with positive or equivocal sECG to MPS with subsequent ICA only in those with evidence of inducible ischaemia. The mean cost of diagnosis was significantly lower in centres that were regular users of MPS (Scint) compared with those that referred infrequently (Non-scint). Reproduced from Underwood et al.[34] with permission

with other PET tracers for measurements of myocardial perfusion and perfusion reserve,[39] and is an attractive option for hospitals without easy access to a cyclotron. PET offers higher resolution images and provides quantification of perfusion in absolute terms (ml/g/min). The latter is partly due to the use of computed tomography (CT) to provide high-quality attenuation maps employed to correct the PET images. PET may have better sensitivity and specificity than SPECT MPS for the detection of CAD, particularly where there is severe disease in all three coronary arteries.[40] Despite demonstration of cost-effectiveness in high-throughput centres,[41] the clinical utility of PET is constrained by high upfront cost and low availability compared with conventional gamma cameras.

Current Guidelines

Myocardial perfusion imaging is heavily embedded in both European and US guidelines for the management of stable CAD (Table 12.2).[29, 42] MPS and stress echocardiography are considered as equivalent tests for the assessment of myocardial perfusion with regional availability and expertise defining ultimate choice. sECG remains the initial stress test of choice because of wide availability, ease of administration, and prognostic value of exercise variables. Stress MPS should be the initial investigation in patients who are unlikely to exercise adequately or where resting ECG abnormalities such as LBBB, preexcitation, left ventricular hypertrophy, or drug effects are likely to render the sECG uninterpretable (Class I indications). For symptomatic female patients, the high false positive rate of sECG argues in favour of MPS as a first line test, a strategy with a Class IIa indication in

Table 12.2. ESC guidelines for the use of exercise stress with imaging techniques in the initial diagnostic assessment of stable angina.[5] Vasodilator stress should be used according to the same indications if the patient is unable to exercise adequately

Indication	Class	Level of evidence
Patients with resting ECG abnormalities, LBBB, >1 mm ST segment depression, paced rhythm or WPW which prevent accurate interpretation of sECG	Class I	B
Patients with a non-conclusive sECG but reasonable exercise tolerance who do not have a high pretest likelihood of CAD but in whom the diagnoses is still in doubt		B
Patients with prior revascularization in whom the localization of ischaemia is important	Class IIa	B
As an alternative to sECG in patients where cost, facilities, and personnel resources allow		B
As an alternative to sECG in patients with a low pretest probability of disease, such as women with atypical chest pain		B
To assess the functional severity of intermediate lesion on ICA		C
To plan revascularization strategies in patients who have already undergone ICA		B

(s)ECG (stress) electrocardiogram; *LBBB* left bundle branch block; *CAD* coronary artery disease; *ICA* invasive coronary angiography

current ESC guidelines. As a secondary test, MPS should be performed either when the sECG is equivocal or further information on myocardial perfusion or function is required to assist management decisions. In those with established but stable CAD, MPS is recommended for those in whom symptoms develop (or persist) after revascularization. PET has a Class IIa indication as a first-line test for the diagnosis of CAD, but is favoured as a secondary test in those in whom SPECT is equivocal (Class I).

Future Directions

CT coronary angiography (CTCA) has been proposed as an alternative technique for the detection of CAD. In patients with low to intermediate likelihood of CAD, CTCA has an excellent negative predictive value (>97%),[43] but is limited by a poorer positive predictive value. There is growing interest in hybrid imaging using scanners combining PET or SPECT with multi-detector X-ray CT, but the exact role and clinical utility of these techniques are still under investigation. While it is attractive to combine anatomical and functional assessment of the coronary arteries into a single test, the necessity of this approach in all patient is doubtful. Radiation exposure is a major issue, as is the cost-effectiveness of combining two imaging modalities into a single imaging unit where one half of the unit may not be required.

Acute Coronary Syndromes

Diagnosis

The ACS comprises a spectrum from unstable angina, through non-ST-elevation MI to ST-elevation MI. The hallmark of ACS is atherosclerotic plaque rupture and intracoronary thrombosis. In those with ST-elevation and chest pain, either immediate PCI or, if this is unavailable, thrombolysis is warranted. Patients without ST-elevation but with high-risk features may also require PCI. Patients who present with non-specific symptoms and equivocal electrocardiographic changes are a diagnostic challenge, with many subsequently found to have non-cardiac chest pain after substantial and ultimately unnecessary use of resources. Conversely, in some patients the diagnosis of MI may be missed with consequent increase in morbidity and mortality.

MPS has the same sensitivity for the detection of acute MI as serial troponin analysis.[44] However, while cardiac biomarkers require 6–12 h to become abnormal, myocardial injury may be detected on resting MPS within 2 h of chest pain onset, making it a more sensitive test at the time of presentation.[45] MPS is especially useful in patients with an intermediate likelihood of CAD and chest pain in the absence of diagnostic ECG changes.[51] Abnormal resting MPS in this setting has a high sensitivity for acute infarction,[52] particularly if it is associated with regional wall-motion abnormalities on gated imaging. Furthermore, as the technique provides information on both viability and regional myocardial blood flow at the time of injection, administration of tracer before and after thrombolysis or revascularization helps to define the extent of jeopardized myocardium and myocardial salvage. MPS is also useful after primary PCI to evaluate the functional significance and need for treatment of intermediate non-culprit coronary artery stenoses. Normal resting MPS excludes acute infarction and suggests that either sECG or stress MPS should be the next diagnostic step. If tracer injection occurs during chest pain, normal MPS rules out an ACS and allows the patient to be discharged. MPS is therefore especially useful in the stratification of patients with symptoms suggestive of ACS, but without ECG changes to either admission or discharge.[46]

Prognosis

Patients with ACS are often referred directly for ICA. However, patients with preserved LV function and without high-risk indicators may do at least equally well with a conservative approach. In the stable post-infarction period, intensive medical therapy alone is equally good at suppressing ischaemia when compared with coronary revascularization, and is associated with a similar incidence of death and non-fatal MI at 1 year.[47] This suggests that, in the absence of medical instability, intensive medical therapy should be the primary treatment strategy. Cardiac catheterization can therefore be reserved for those with high-risk features or those who remain symptomatic despite optimal medical treatment.

The role of MPS early after infarction is reflected in both European and American guidelines.[20, 29, 48] The technique is helpful in those with atypical presentation and positive troponins because an abnormal scan in this setting is associated with a sevenfold increase in risk of cardiac events at 6 months.[49] In patients without post-infarction angina, complex arrhythmias, or congestive heart failure, early MPS using pharmacological stress is the test of choice for prognostic assessment. It is better than sECG for risk stratification and can be performed safely 2–4 days after infarction.[50] In addition to quantifying myocardial ischaemia, MPS allows measurement of left ventricular ejection fraction (LVEF), an important prognostic predictor of cardiac death after MI.[51] Early MPS allows the prompt discharge of lower-risk patients and appropriate referral of those at higher risk, such as those

with LVEF <35% or inducible ischaemia in >50% of the remaining viable myocardium, for ICA.[59]

Cost-Effectiveness

MPS in the assessment of acute chest pain is cost-effective. Although the costs of initial MPS are greater than strategies that involve assessment of the ECG, biomarkers, and potentially echocardiography, the downstream reduction in unnecessary treatment, hospital admission, and ICA leads to an overall reduction in cost. The use of normal resting MPS alone to exclude MI in patients with non-diagnostic ECG changes cost-effectively reduces unnecessary admissions irrespective of gender, age, or risk factors for CAD.[52] When compared prospectively with usual care, acute resting MPS has no impact on the clinical decision-making in those with definitive acute cardiac ischaemia, but reduces unnecessary admissions by up to 20% in those without.[61] This holds true even in patients with diabetes,[53] a sub-population considered to have CAD-equivalent status. Importantly, discharge of these patients is safe.[54,55] When resting MPS is performed explicitly during an episode of chest pain, MPS allows more appropriate stratification to admission or discharge and, ultimately, reduces total admissions.[56] When used routinely in conjunction with early exercise testing in the emergency department, median costs are $1,843 (€1,400) lower and length of admission is shorter when an MPS strategy is used.[57] Studies of cost-effectiveness of MPS in the acute setting largely originate from the U.S., and it can be difficult to extrapolate such findings to Europe. Furthermore, the wider use of acute resting MPS in Europe is limited by local availability and experience. Nonetheless, the evidence suggests that acute resting MPS offers a safe, rapid, and cost-effective strategy for the exclusion of CAD as a cause for acute chest pain when ECG is non-diagnostic.

Guidelines

The use of resting MPS as an initial test in stabilized patients with ACS is supported in European guidelines (Table 12.3) for ACS, but it is not explicitly recommended.[58] However, an ESC Task Force for the management of chest pain recommended MPS in patients with acute chest pain and equivocal clinical history, ECG, or cardiac biomarkers, where a low-risk study might prevent admission and unnecessary treatment.[59] Resting MPS has a Class Ia indication in American Heart Association guidelines and Class IIb in those of the ESC for the assessment of prognosis in patients with suspected ACS, non-diagnostic ECG, and negative initial cardiac biomarkers.[20] For the explicit diagnosis of CAD in the same cohort, MPS has class Ib and IIb indications in the ACC and ESC guidelines, respectively.

Both European and U.S. guidelines acknowledge the role of MPS for risk stratification after acute MI.[20, 48, 58] In those admitted with NSTEMI, MPS is recommended to evaluate the presence, severity, and extent of inducible ischaemia either in patients with equivocal sECG or those who are unable to exercise, or in women. The likelihood of future cardiac events is closely linked to the degree of MPS abnormality and, hence, has important implications for management. After STEMI, MPS is recommended for the definition of infarct size and residual ischaemia to guide management and assess prognosis. Those with high-risk features on MPS are candidates for revascularization, while those at low risk can be managed conservatively. MPS is also the initial test of choice to assess the functional significance of intermediate non-culprit coronary artery stenoses in patients who have already undergone ICA.

Future Directions

In the future, diagnosis of patients with acute chest pain may be undertaken through assessment of myocardial metabolism. Under normal conditions, myocytes use fatty acids as the primary source of energy; during ischaemia, fatty-acid reserves are quickly exhausted and cellular metabolism switches to glucose. After resolution of ischaemia, there is a delay in the return of metabolism to normalcy (up to 24 h) with the continuation of glucose metabolism in preference to fatty acids. This is known as ischaemic memory; abnormal uptake of fatty acids during this time is a phenomenon that can be exploited by appropriately labelled radiotracers, the most common of which is iodine-123 β-methyl-*p*-iodophenyl-pentadecanoic acid (BMIPP). Several studies have shown encouraging results and this could become an attractive option for the assessment of patients whose ischaemic insult may have occurred hours before presentation.

Conclusion

MPS has proven value for the diagnosis and prognosis of both stable CAD and ACS, and is additionally safe and cost-effective in a wide variety of clinical settings. Experience with the technique has been gained over decades, and there is a large body of evidence to support the integration of MPS into diagnostic strategies for the investigation of CAD. The technique is, therefore, recommended in national European and American guidelines. Although less widely available and relatively more expensive, PET may be used to detect obstructive coronary disease, and allows absolute

Table 12.3. Summary of European and US guidelines for the use of myocardial perfusion scintigraphy in acute coronary syndromes

Technique	Condition	Indication	Class	Level of evidence	Issuing body
Rest MPS	Diagnosis of CAD during acute chest pain	Intermediate pretest probability of CAD, absence of ST elevation on ECG, and negative initial cardiac enzymes	IIb	B	ESC
	Detection of acute myocardial infarction	Intermediate pretest probability of CAD, absence of ST elevation on ECG, and negative initial cardiac enzymes	IIb	B	ESC
	Unstable angina/ NSTEMI	Identification of the severity/extent of CAD in patients with ongoing suspected ischaemia symptoms but non-diagnostic ECG	IIa	B	ACC/AHA
Stress/rest MPS	After acute STEMI	Detection of inducible ischaemia and myocardium at risk after thrombolytic therapy without ICA	I	B	ESC ACC/AHA
		Assessment of infarct size and residual viable myocardium	I	B	ESC ACC/AHA
		Assessment of resting LV function	I	B	ACC/AHA
	Unstable angina/ NSTEMI	Identification of the severity/extent inducible ischaemia in patients without intermediate to high-risk features (risk stratification)	I	C	ESC ACC/AHA
		Identification of the severity/extent of inducible ischaemia in patients in whom the diagnosis is uncertain	I	A	ESC ACC/AHA
		Identification of haemodynamic significance of coronary stenosis after ICA	I	B	ACC/AHA
		Measurement of baseline LV function.	I	B	ACC/AHA
		Assessment of inducible ischaemia 4–7 weeks after discharge if not performed prior to discharge	IIa	C	ESC

Adapted from refs[19, 20, 29, 48, 58, 59]
MPS myocardial perfusion scintigraphy; *CAD* coronary artery disease; *ECG* electrocardiogram; *ICA* invasive coronary angiography; *(N)STEMI* (non-)ST elevation myocardial infarction; *LV* left ventricular

quantification of myocardial perfusion. As with any test, appropriate referral depends upon local availability, pretest likelihood of CAD, the suitability of the patient to different forms of cardiac stress, and an understanding of the answers that MPS can provide. When used appropriately, MPS continues to be a powerful tool for the investigation of CAD.

References

1. Goodman SN. Toward evidence–based medical statistics. 2: The Bayes factor. *Ann Intern Med*. 1999;130:1005–1013
2. Diamond GA, Forrester JS. Analysis of probability as an aid in the clinical diagnosis of coronary-artery disease. *N Engl J Med*. 1979;300:1350–1358
3. Wilson PW, D'Agostino RB, Levy D, Belanger AM, Silbershatz H, Kannel WB. Prediction of coronary heart disease using risk factor categories. *Circulation*. 1998;97:1837–1847
4. Mark DB, Shaw L, Harrell FE Jr, et al Prognostic value of a treadmill exercise score in outpatients with suspected coronary artery disease. *N Engl J Med*. 1991;325:849–853
5. Fox K, Garcia MA, Ardissino D, et al Guidelines on the management of stable angina pectoris: executive summary: the Task Force on the Management of Stable Angina Pectoris of the European Society of Cardiology. *Eur Heart J*. 2006;27:1341–1381
6. Gershlick AH, de BM, Chambers J, et al Role of non-invasive imaging in the management of coronary artery disease: an assessment of likely change over the next 10 years. A report from the British Cardiovascular Society Working Group. *Heart*. 2007;93:423–431
7. Wong Y, Rodwell A, Dawkins S, Livesey SA, Simpson IA. Sex differences in investigation results and treatment in subjects referred for investigation of chest pain. *Heart*. 2001;85:149–152

8. Marwick TH, Shaw L, Case C, Vasey C, Thomas JD. Clinical and economic impact of exercise electrocardiography and exercise echocardiography in clinical practice. *Eur Heart J*. 2003;24: 1153–1163
9. Kapur A, Latus KA, Davies G, et al A comparison of three radionuclide myocardial perfusion tracers in clinical practice: the ROBUST study. *Eur J Nucl Med Mol Imaging*. 2002;29:1608–1616
10. Hachamovitch R, Berman DS, Shaw LJ, et al Incremental prognostic value of myocardial perfusion single photon emission computed tomography for the prediction of cardiac death: differential stratification for risk of cardiac death and myocardial infarction. *Circulation*. 1998;97:535–543
11. Mowatt G, Vale L, Brazzelli M, et al Systematic review of the effectiveness and cost–effectiveness, and economic evaluation, of myocardial perfusion scintigraphy for the diagnosis and management of angina and myocardial infarction. *Health Technol Assess*. 2004;8: iii–iv; 1–207
12. Underwood SR, Anagnostopoulos C, Cerqueira M, et al Myocardial perfusion scintigraphy: the evidence. *Eur J Nucl Med Mol Imaging*. 2004;31:261–291
13. Schuijf JD, Poldermans D, Shaw LJ, et al Diagnostic and prognostic value of non-invasive imaging in known or suspected coronary artery disease. *Eur J Nucl Med Mol Imaging*. 2006;33:93–104
14. Paetsch I, Jahnke C, Wahl A, et al Comparison of dobutamine stress magnetic resonance, adenosine stress magnetic resonance, and adenosine stress magnetic resonance perfusion. *Circulation*. 2004;110: 835–842
15. Smanio PE, Watson DD, Segalla DL, Vinson EL, Smith WH, Beller GA. Value of gating of technetium–99m sestamibi single–photon emission computed tomographic imaging. *J Am Coll Cardiol*. 1997;30: 1687–1692
16. Garcia EV. SPECT attenuation correction: an essential tool to realize nuclear cardiology's manifest destiny. *J Nucl Cardiol*. 2007;14: 16–24
17. Boden WE, O'Rourke RA, Teo KK, et al Optimal medical therapy with or without PCI for stable coronary disease. *N Engl J Med*. 2007;356:1503–1516
18. Shaw LJ, Berman DS, Maron DJ, et al Optimal medical therapy with or without percutaneous coronary intervention to reduce ischemic burden: results from the Clinical Outcomes Utilizing Revascularization and Aggressive Drug Evaluation (COURAGE) trial nuclear substudy. *Circulation*. 2008;117:1283–1291
19. Marcassa C, Bax JJ, Bengel F, et al Clinical value, cost–effectiveness, and safety of myocardial perfusion scintigraphy: a position statement. *Eur Heart J*. 2008;29:557–563
20. Klocke FJ, Baird MG, Lorell BH, et al ACC/AHA/ASNC guidelines for the clinical use of cardiac radionuclide imaging – executive summary: a report of the American College of Cardiology/American Heart Association Task Force on Practice Guidelines (ACC/AHA/ASNC Committee to Revise the 1995 Guidelines for the Clinical Use of Cardiac Radionuclide Imaging). *Circulation*. 2003;108: 1404–1418
21. Abbott BG, Afshar M, Berger AK, Wackers FJ. Prognostic significance of ischemic electrocardiographic changes during adenosine infusion in patients with normal myocardial perfusion imaging. *J Nucl Cardiol*. 2003;10:9–16
22. Hachamovitch R, Hayes S, Friedman JD, et al Determinants of risk and its temporal variation in patients with normal stress myocardial perfusion scans: what is the warranty period of a normal scan? *J Am Coll Cardiol*. 2003;41:1329–1340
23. Petix NR, Sestini S, Coppola A, et al Prognostic value of combined perfusion and function by stress technetium-99m sestamibi gated SPECT myocardial perfusion imaging in patients with suspected or known coronary artery disease. *Am J Cardiol*. 2005;95:1351–1357
24. Sharir T, Germano G, Kavanagh PB, et al Incremental prognostic value of post-stress left ventricular ejection fraction and volume by gated myocardial perfusion single photon emission computed tomography. *Circulation*. 1999;100:1035–1042
25. Abidov A, Bax JJ, Hayes SW, et al Transient ischemic dilation ratio of the left ventricle is a significant predictor of future cardiac events in patients with otherwise normal myocardial perfusion SPECT. *J Am Coll Cardiol*. 2003;42:1818–1825
26. Gill JB, Ruddy TD, Newell JB, Finkelstein DM, Strauss HW, Boucher CA. Prognostic importance of thallium uptake by the lungs during exercise in coronary artery disease. *N Engl J Med*. 1987;317:1486–1489
27. Shaw LJ, Raggi P, Schisterman E, Berman DS, Callister TQ. Prognostic value of cardiac risk factors and coronary artery calcium screening for all–cause mortality. *Radiology*. 2003;228:826–833
28. Greenland P, LaBree L, Azen SP, Doherty TM, Detrano RC. Coronary artery calcium score combined with Framingham score for risk prediction in asymptomatic individuals. *JAMA*. 2004; 291:210–215
29. Brindis RG, Douglas PS, Hendel RC, et al ACCF/ASNC appropriateness criteria for single–photon emission computed tomography myocardial perfusion imaging (SPECT MPI): a report of the American College of Cardiology Foundation Quality Strategic Directions Committee Appropriateness Criteria Working Group and the American Society of Nuclear Cardiology endorsed by the American Heart Association. *J Am Coll Cardiol*. 2005;46: 1587–1605
30. Anand DV, Lim E, Lahiri A, Bax JJ. The role of non-invasive imaging in the risk stratification of asymptomatic diabetic subjects. *Eur Heart J*. 2006;27:905–912
31. Anand DV, Lim E, Hopkins D, et al Risk stratification in uncomplicated type 2 diabetes: prospective evaluation of the combined use of coronary artery calcium imaging and selective myocardial perfusion scintigraphy. *Eur Heart J*. 2006;27:713–721
32. Hachamovitch R, Hayes SW, Friedman JD, Cohen I, Berman DS. Stress myocardial perfusion single-photon emission computed tomography is clinically effective and cost effective in risk stratification of patients with a high likelihood of coronary artery disease (CAD) but no known CAD. *J Am Coll Cardiol*. 2004;43:200–208
33. Berman DS, Hachamovitch R, Kiat H, et al Incremental value of prognostic testing in patients with known or suspected ischemic heart disease: a basis for optimal utilization of exercise technetium–99m sestamibi myocardial perfusion single-photon emission computed tomography. *J Am Coll Cardiol*. 1995;26:639–647
34. Underwood SR, Godman B, Salyani S, Ogle JR, Ell PJ. Economics of myocardial perfusion imaging in Europe – the EMPIRE Study. *Eur Heart J*. 1999;20:157–166
35. Hachamovitch R, Berman DS, Kiat H, Cohen I, Friedman JD, Shaw LJ. Value of stress myocardial perfusion single photon emission computed tomography in patients with normal resting electrocardiograms: an evaluation of incremental prognostic value and cost–effectiveness. *Circulation*. 2002;105:823–829
36. Shaw LJ, Hachamovitch R, Berman DS, et al The economic consequences of available diagnostic and prognostic strategies for the evaluation of stable angina patients: an observational assessment of the value of precatheterization ischemia. Economics of Noninvasive Diagnosis (END) Multicenter Study Group. *J Am Coll Cardiol*. 1999;33:661–669
37. Shaw LJ, Heller GV, Travin MI, et al Cost analysis of diagnostic testing for coronary artery disease in women with stable chest pain. Economics of Noninvasive Diagnosis (END) Study Group. *J Nucl Cardiol*. 1999;6:559–569
38. Sharples L, Hughes V, Crean A, et al Cost-effectiveness of functional cardiac testing in the diagnosis and management of coronary artery disease: a randomised controlled trial. The CECaT trial. *Health Technol Assess*. 2007 Dec; 11(49):iii-iv, ix-115
39. Lortie M, Beanlands RS, Yoshinaga K, Klein R, Dasilva JN, Dekemp RA. Quantification of myocardial blood flow with 82Rb

dynamic PET imaging. *Eur J Nucl Med Mol Imaging*. 2007;34: 1765–1774
40. Nandalur KR, Dwamena BA, Choudhri AF, Nandalur SR, Reddy P, Carlos RC. Diagnostic performance of positron emission tomography in the detection of coronary artery disease: a meta–analysis. *Acad Radiol*. 2008;15:444–451
41. Merhige ME, Breen WJ, Shelton V, Houston T, D'Arcy BJ, Perna AF. Impact of myocardial perfusion imaging with PET and (82)Rb on downstream invasive procedure utilization, costs, and outcomes in coronary disease management. *J Nucl Med*. 2007;48:1069–1076
42. Gibbons RJ, Abrams J, Chatterjee K, et al ACC/AHA 2002 guideline update for the management of patients with chronic stable angina – summary article: a report of the American College of Cardiology/American Heart Association Task Force on Practice Guidelines (Committee on the Management of Patients With Chronic Stable Angina). *Circulation*. 2003;107:149–158
43. Hamon M, Biondi-Zoccai GG, Malagutti P, et al Diagnostic performance of multislice spiral computed tomography of coronary arteries as compared with conventional invasive coronary angiography: a meta-analysis. *J Am Coll Cardiol*. 2006;48:1896–1910
44. Kontos MC, Jesse RL, Anderson FP, Schmidt KL, Ornato JP, Tatum JL. Comparison of myocardial perfusion imaging and cardiac troponin I in patients admitted to the emergency department with chest pain. *Circulation*. 1999;99:2073–2078
45. Duca MD, Giri S, Wu AH, et al Comparison of acute rest myocardial perfusion imaging and serum markers of myocardial injury in patients with chest pain syndromes. *J Nucl Cardiol*. 1999;6:570–576
46. Udelson JE, Beshansky JR, Ballin DS, et al Myocardial perfusion imaging for evaluation and triage of patients with suspected acute cardiac ischemia: a randomized controlled trial. *JAMA*. 2002;288:2693–2700
47. Mahmarian JJ, Dakik HA, Filipchuk NG, et al An initial strategy of intensive medical therapy is comparable to that of coronary revascularization for suppression of scintigraphic ischemia in high–risk but stable survivors of acute myocardial infarction. *J Am Coll Cardiol*. 2006;48:2458–2467
48. Van de WF, Ardissino D, Betriu A, et al Management of acute myocardial infarction in patients presenting with ST-segment elevation. The Task Force on the Management of Acute Myocardial Infarction of the European Society of Cardiology. *Eur Heart J*. 2003;24:28–66
49. Dorbala S, Giugliano RP, Logsetty G, et al Prognostic value of SPECT myocardial perfusion imaging in patients with elevated cardiac troponin I levels and atypical clinical presentation. *J Nucl Cardiol*. 2007;14:53–58
50. Brown KA, Heller GV, Landin RS, et al Early dipyridamole (99m) Tc–sestamibi single photon emission computed tomographic imaging 2–4 days after acute myocardial infarction predicts in–hospital and postdischarge cardiac events: comparison with submaximal exercise imaging. *Circulation*. 1999;100:2060–2066
51. Kroll D, Farah W, McKendall GR, Reinert SE, Johnson LL. Prognostic value of stress-gated Tc-99m sestamibi SPECT after acute myocardial infarction. *Am J Cardiol*. 2001;87:381–386
52. Heller GV, Stowers SA, Hendel RC, et al Clinical value of acute rest technetium-99m tetrofosmin tomographic myocardial perfusion imaging in patients with acute chest pain and nondiagnostic electrocardiograms. *J Am Coll Cardiol*. 1998;31:1011–1017
53. Kapetanopoulos A, Heller GV, Selker HP, et al Acute resting myocardial perfusion imaging in patients with diabetes mellitus: results from the Emergency Room Assessment of Sestamibi for Evaluation of Chest Pain (ERASE Chest Pain) trial. *J Nucl Cardiol*. 2004; 11:570–577
54. Stewart RE, Dickinson CZ, Weissman IA, O'Neill WW, Dworkin HJ, Juni JE. Clinical outcome of patients evaluated with emergency centre myocardial perfusion SPET for unexplained chest pain. *Nucl Med Commun*. 1996;17:459–462
55. Weissman IA, Dickinson CZ, Dworkin HJ, O'Neill WW, Juni JE. Cost-effectiveness of myocardial perfusion imaging with SPECT in the emergency department evaluation of patients with unexplained chest pain. *Radiology*. 1996;199:353–357
56. Knott JC, Baldey AC, Grigg LE, Cameron PA, Lichtenstein M, Better N. Impact of acute chest pain Tc–99m sestamibi myocardial perfusion imaging on clinical management. *J Nucl Cardiol*. 2002; 9:257–262
57. Stowers SA, Eisenstein EL, Th Wackers FJ, et al An economic analysis of an aggressive sestamibi myocardial perfusion imaging on clinical managementtesting in emergency department patients who present with chest pain but nondiagnostic electrocardiograms: results from a randomized trial. *Ann Emerg Med*. 2000;35:17–25
58. Bassand JP, Hamm CW, Ardissino D, et al Guidelines for the diagnosis and treatment of non-ST-segment elevation acute coronary syndromes. *Eur Heart J*. 2007;28:1598–1660
59. Erhardt L, Herlitz J, Bossaert L, et al Task force on the management of chest pain. *Eur Heart J*. 2002;23:1153–1176

Chapter 13

CARDIAC CT AND DETECTION OF CORONARY ARTERY DISEASE

Stephan Achenbach and Pim J. de Feyter

CONTENTS

J. L. Zamorano et al. (eds.), *The ESC Textbook of Cardiovascular Imaging*
DOI: 10.1007/978-1-84882-421-8_13, © Springer-Verlag London Limited 2010

Introduction

Cardiac CT allows non-invasive imaging of the coronary arteries. Under certain circumstances, it can, therefore, play an important role for diagnosing coronary artery disease. Particularly in patients with a relatively low pre-test likelihood of the disease, coronary CT angiography has been shown to allow for the detection of coronary stenoses with high sensitivity and is considered a useful technique to rule out coronary artery disease in selected clinical settings. Coronary artery imaging in patients with advanced disease or after coronary revascularization is more difficult and currently not considered a clinical indication for CT. In addition to detecting luminal stenosis, CT has the potential to visualize and characterize non-stenotic coronary atherosclerotic plaque. Based on a large amount of prognostic data, coronary calcium can be used for refined risk stratification concerning future cardiovascular events. Imaging of non-calcified plaque is currently considered experimental, and should not be used for clinical decision-making. Future improvements in image quality are expected to expand the clinical role of cardiac CT in the assessment of coronary artery disease.

The high temporal and spatial resolution of cardiac CT allows non-invasive visualization of the coronary arteries in selected patients and, therefore, makes the method very interesting for the non-invasive workup of patients with suspected coronary artery stenoses. However, spatial and temporal resolutions of CT imaging, even with the latest scanner generations, are not similar to invasive coronary angiography. Diagnostic accuracy is impaired when image quality is reduced, and image quality, in turn, is influenced by many factors such as the patient's heart rate, body weight, ability to cooperate, and extent of coronary calcification. Therefore, the clinical utility of coronary CT angiography significantly depends on the specific clinical situation, and thorough consideration of the advantages and disadvantages of CT angiography is necessary when deliberating the use of CT imaging in the workup of patients with known or suspected coronary artery disease.

In addition to the visualization of coronary artery stenoses, CT also allows the detection of coronary atherosclerotic plaque. In non-enhanced scans, coronary calcification is readily detectable, and in contrast-enhanced coronary CT angiography data sets of high-quality, coronary atherosclerotic plaques, including calcified and non-calcified components, can be visualized. There is tremendous interest in using this information for risk stratification concerning the occurrence of future coronary artery disease events.

This chapter will outline the potential applications of CT imaging for coronary artery visualization, detection of coronary artery stenoses, and risk stratification.

Coronary CT Angiography: Stenosis Detection

Imaging Protocols

For the assessment of symptomatic patients with chest pain, cardiac CT allows direct visualization of the coronary artery lumen ("coronary CT angiography"). As the small dimensions and the rapid motion of the coronary vessels pose tremendous challenges for non-invasive imaging, high-end CT equipment and adequate imaging protocols must be used. Currently, 64-slice CT is considered the "state of the art" for coronary artery imaging, and newer technology, such as Dual Source CT and scanners with 256 or 320 detectors, may provide further improved image quality.

Prerequisites for CT imaging of the coronary arteries include the ability to understand and follow breath-hold commands, because even slight respiratory motion during data acquisition will cause substantial artefact. Of further importance is a regular and, preferably, low heart rate (optimally below 60/min, even though this is not as strictly required for Dual Source CT).[1, 2] Patients usually receive premedication with short-acting beta-blockers to lower heart rate, and nitrates are given to achieve coronary dilatation, which noticeably improves image quality. Iodine-based contrast agent is injected intravenously to achieve vascular enhancement during the scan. Typically, 50–100 mL of contrast agent is used. Data acquisition can follow various principles (see details in Chap. 5). *Retrospectively gated* scans are acquired in spiral mode and usually provide for higher image quality, more flexibility to choose the cardiac phase during which images are reconstructed, as well as the ability to reconstruct "functional" data sets throughout the cardiac cycle to assess wall motion. *Prospectively triggered* scans are associated with substantially lower radiation exposure and, especially in patients with truly low heart rates, are often adequate to assess the coronary lumen. Less flexibility to reconstruct data at different time instants in the cardiac cycle as well as greater susceptibility to artefacts caused by arrhythmia sometimes impair image quality so that there is a trade-off for the advantage of lower dose. Currently, the preferred strategy for coronary CT angiography has not been defined; however, in young patients in whom radiation dose may be of major concern, prospectively triggered scans should be strongly considered (also see Chap. 1e).

Typical data sets for coronary artery visualization by CT consist of approximately 200–300 transaxial slices with a thickness of 0.5–0.75 mm (see Fig. 13.1). Data interpretation is usually based on interactive manipulation of these data sets using post-processing workstations. Useful post-processing tools include maximum intensity projections and multi-planar

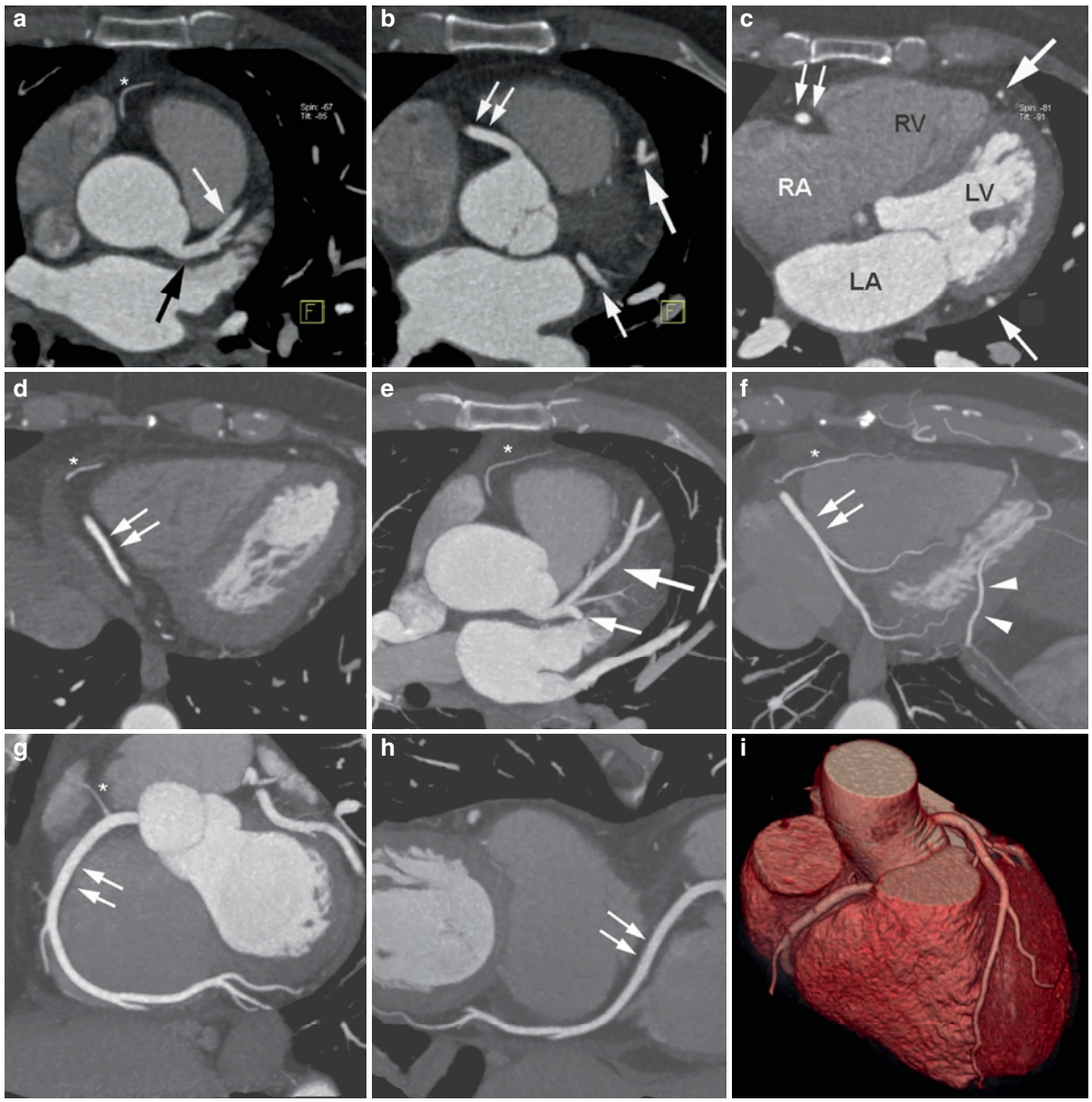

Fig. 13.1 Visualization of the coronary arteries in contrast-enhanced coronary CT angiography (Dual Source CT). Spiral data acquisition with ECG-correlated tube current modulation and 100 kV tube current was used to reduce radiation exposure (here: 4.7 mSv). **(a)** Transaxial slice at the level of the left main coronary artery. The left main divides into the left anterior descending coronary artery (*large arrow*) and left circumflex coronary artery (*small arrow*). In addition, a very small intermediate branch is present. The *asterisk* indicates a conus branch of the right coronary artery. **(b)** Transaxial slice at the level of the ostium of the right coronary artery (*double arrows*). In addition, cross sections of the left anterior descending coronary artery (at a bifurcation with a diagonal branch, *large arrow*) and of the left circumflex coronary artery (*small arrow*) can be seen. **(c)** Transaxial slice at a mid-ventricular level. Cross sections of the left anterior descending coronary artery (*large arrow*), obtuse marginal branch (*small arrow*, this branch is larger than the distal left circumflex), and right coronary artery (*double arrows*) can be seen. *RA* right atrium; *RV* right ventricle; *LA* left atrium; *LV* left ventricle. **(d)** Transaxial slice at the level of the distal right coronary artery (*double arrows*). The *asterisk* indicates a small right ventricular branch. **(e)** "Maximum intensity projection" in transaxial orientation, showing the left main and the proximal to mid-left anterior descending coronary artery. This image represents a 10 mm thick slice, and therefore visualized longer segments of the coronary arteries. (*Large arrow*: Left anterior descending coronary artery; *small arrow*: Left circumflex coronary artery, *asterisk*: conus branch) **(f)** "Maximum intensity projection" in transaxial orientation, showing the distal right coronary artery (*double arrows*). The division of the right coronary artery into the posterior descending coronary artery and right postero-lateral branch is visible. The *asterisk* indicates a right ventricular branch. The *arrowheads* point at a vessel that is situated below the diaphragm. Because of the projectional nature of "maximum intensity projections," the exact position cannot be discerned in this image. **(g)** Oblique "maximum intensity projection," which shows almost the entire course of the right coronary artery (*double arrows*) in a single image. The *asterisk* indicates the conus branch. **(h)** "Curved multi-planar reconstruction" of the right coronary artery (*double arrows*). These reconstructions allow visualization of the entire vessel course in a single image. **(i)** 3D rendering of the heart and coronary arteries. While visually appealing, 3D reconstructions are not helpful for the identification of stenoses

reconstructions. 3D renderings allow fairly impressive visualization of the heart and coronary arteries, but they are not accurate for stenosis detection and play no role in data interpretation.[3] It is of importance that the reading physician must interactively manipulate the data set and integrate all information obtained by using the various post-processing techniques. Mere assessment of single images prerendered by a technician or automated software is not adequate.

Accuracy

Clinical applications of coronary CT angiography will critically depend on its accuracy for detection of significant coronary artery stenoses (see Figs. 13.2–13.4). Numerous recent studies have assessed the accuracy of coronary CT angiography for stenosis detection in comparison with invasive, catheter-based coronary angiography. Using 40-slice CT,[4–7] 64-slice CT,[8–17] or Dual Source CT,[2, 18–23] the sensitivity for the detection of coronary artery stenoses has ranged from 86 to 100% and specificity has been reported between 91 and 98%. Accuracy values are not uniform across all patients. Several trials have demonstrated that high heart rates and extensive calcification negatively influence accuracy.[24–27] Usually, degraded image will lead to false-positive rather than false-negative findings,[24] and specificity and positive predictive value will, therefore, be worst affected (see Fig. 13.5).

Most published trials on the accuracy of coronary CTA for stenosis detection were rather small and performed in single centres. To overcome the limitation of small study cohorts, several available meta-analyses analyzed the accuracy data for coronary CT angiography with various generations of CT technology.[27–31] Table 13.1 lists the results of several meta-analyses that again rather uniformly show a high sensitivity, specificity, and negative predictive value, while the positive predictive value, as a consequence of the often low prevalence of disease, is often lower, especially on the per-segment level.

It has been criticized that most of the data on the accuracy of coronary CT angiography originate from single-centre trials that were performed at experienced institutions. So far, only two multi-centre trials, both using 64-slice technology, have been published. One trial, which included 230 patients studied at 16 different sites, reported a sensitivity of 95% and specificity of 83% for the identification of patients with at least one coronary artery stenosis.[26] The negative predictive value was high (99%), but positive predictive value was lower (64%). This is partly attributable to a low prevalence of disease in the patient cohort; only 25% of subjects had one or more stenoses of at least 50% luminal narrowing. Another multi-centre trial investigated a patient group with a substantially higher pre-test likelihood of the disease (prevalence of stenoses >50:56%) and a large fraction of patients with prior infarcts (20%) or previous coronary revascularization (10%).[32] In this trial, accuracy was lower. Sensitivity was 85%, specificity was 90%, negative predictive value was 83%, and positive predictive value was 91%.

Another study provided further evidence that the accuracy of coronary CT angiography depends on the pre-test likelihood of the disease.[33] In an analysis of 254 patients referred to invasive angiography and also studied by CT, it was demonstrated that coronary CT angiography performs best in patients with a low to intermediate clinical likelihood of coronary artery stenoses (negative predictive value: 100% in both groups), while accuracy was substantially lower in high-risk patients, most likely owing to the more challenging conditions for imaging (see Table 13.2).[33]

Over all, the good diagnostic performance of coronary CT angiography in patients who are not at high likelihood of having coronary artery stenoses, and especially the very high negative predictive value found for such patients indicate that coronary CTA may be a clinically useful tool in symptomatic patients who have a lower or intermediate likelihood of coronary disease, but require further workup to rule out significant coronary stenoses. A negative coronary CT angiography scan, if of high quality, will obviate the need for further testing. Indeed, several recent observational trials clearly demonstrated that when coronary CT angiography was negative in symptomatic patients, they had a very favourable clinical outcome even without further additional testing.[34–36] In one of these studies, 421 consecutive patients with chest pain and a positive SPECT myocardial perfusion scan indicating an intermediate degree of ischaemia were subjected to 64-slice coronary CT angiography. In 343 patients, CT ruled out the need for invasive coronary angiography and medical treatment was recommended. Over the course of the following 15 months, no infarct occurred, only six clinically driven coronary angiograms were performed, and only one revascularization occurred.[34] Similarly, Min et al. identified 1,647 individuals in whom coronary CT angiography was performed without previously known coronary artery disease.[37] They showed that the rate of downstream catheterization was substantially lower if CT was performed than in patients in whom stress myocardial perfusion imaging had been performed (1.7 vs. 9.6%), the rate of revascularization was 0.2 vs. 0.8%, but outcomes were not worse for CT angiography as the initial test, with a lower rate of hospitalization for CAD (0.7 vs. 1.1%) and a lower rate of angina (4.3 vs. 6.4%). Thus, emerging data are available that indicate that it is indeed safe to forego further testing in chest pain patients if coronary CT angiography demonstrates the absence of coronary artery stenoses.

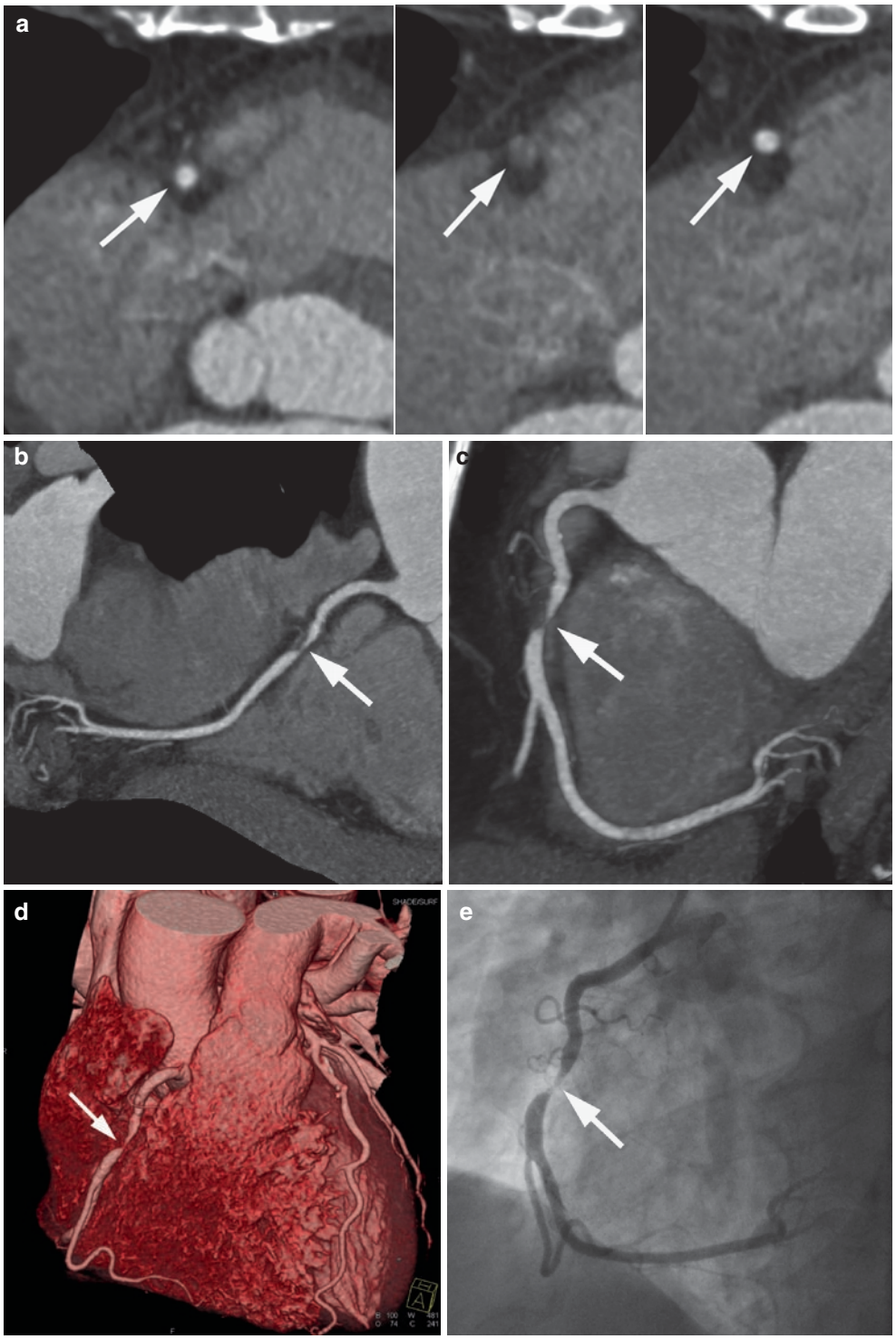

Fig. 13.2 Detection of a coronary artery stenosis in contrast-enhanced coronary CT angiography. **(a)** Cross-sectional images of the right coronary artery at three consecutive levels are shown (*arrows*). While the topmost image (*left*) shows a contrast-enhanced lumen, the next slice (*middle*) shows the vessel cross section, but it is not enhanced by contrast. A few mm further distal (*right*), the lumen is again contrast-enhanced. **(b)** Maximum intensity projection in an oblique plane that shows a long segment of the right coronary artery. The stenosis is clearly visible (*arrow*). **(c)** Curved multi-planar reconstruction, which displays the right coronary artery along its centreline. Again, the short, concentric stenosis is clearly visible (*arrow*). **(d)** 3D reconstruction, also showing the stenosis of the right coronary artery (*arrow*). **(e)** Corresponding invasive coronary angiogram (*arrow* = stenosis)

Specific Clinical Situations

Besides patients with stable chest pain, other clinical presentations and situations are also often needed to rule out coronary artery stenosis, even though the pre-test likelihood may not be high. Several studies have specifically addressed the accuracy of coronary CTA in such settings. For example, Andreini et al. studied 61 patients with heart failure of unknown aetiology and reported a sensitivity of 99% and specificity of 96% to identify patients with coronary artery stenoses using a 16-slice CT scanner.[38] In a similar small study, Manghat et al. found 100% accuracy for the

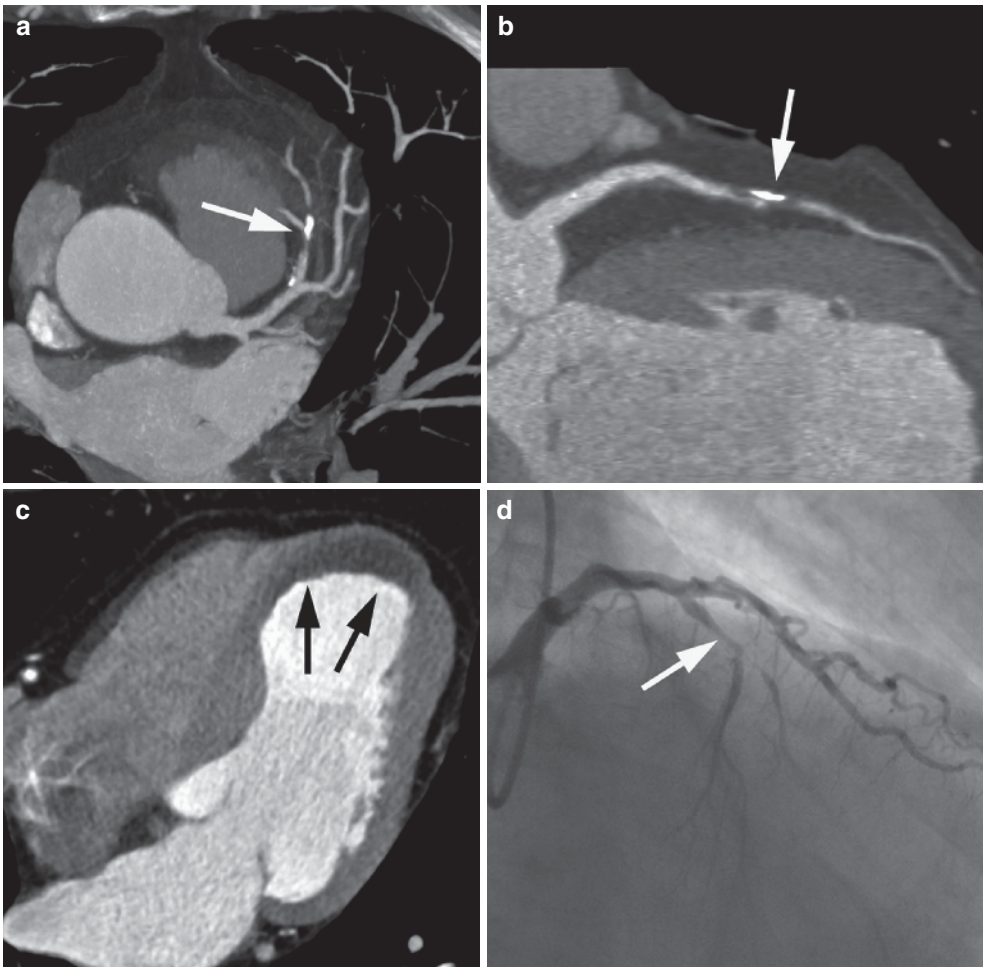

Fig. 13.3 Detection of a subtotal stenosis of the left anterior descending coronary artery. The vessel lumen is relatively small and there is some calcification. **(a)** Maximum intensity projection in a transaxial plane. The interruption of the contrast-enhanced lumen of the left anterior descending coronary artery is clearly seen (*arrow*). There is some calcium in the lesion. **(b)** Curved multi-planar reconstruction. The vessel is relatively small. The *arrow* points at the high grade stenosis. **(c)** A cross section of the left ventricle shows thinning of the apical wall and a mural thrombus (*arrows*). Such morphologic information, along with detailed information on left ventricular function, can easily be obtained from coronary CT angiography data sets. **(d)** Invasive angiogram, which shows the subtotal lesion of the mid left anterior descending coronary artery (*arrow*), with very poor flow into the distal vessel segments

identification of patients with coronary stenoses among 18 patients presenting with cardiomyopathy.[39] Gosthine et al. evaluated the accuracy of 64-slice coronary CT angiography in 66 patients with left bundle branch block and reported a sensitivity of 97%, specificity of 95%, as well as a negative predictive value of 97% for the detection of patients who had significant coronary artery stenoses.[25]

Two studies addressed the use of coronary CT angiography to rule out coronary stenoses in patients who require non-coronary cardiac surgery. Notably, in a larger study, which comprised 105 consecutive patients with aortic valve stenosis who required surgery, 35 patients could not be scanned by CT because of atrial fibrillation, renal failure, or other reasons. In the remaining 70 patients, the authors found a sensitivity of 100% (18 of 18 stenoses detected) and specificity of 92% for the detection of coronary artery stenoses.[40] Thus, CT angiography is not an option for all of these patients, but if feasible, performs well (see Fig. 13.6). In the second trial of 50 patients requiring aortic valve replacement for severe regurgitation, 100% sensitivity and 95% specificity for the identification of subjects who had significant coronary stenoses was reported.[41]

Another situation in which the use of a non-invasive imaging technology to rapidly and reliably rule out coronary stenoses could be of tremendous clinical value is the setting of acute chest pain. In particular, if the ECG is normal and myocardial enzymes are not elevated, the likelihood of coronary disease is low, but the possibility of myocardial infarction requires a rapid and definite diagnosis. In initial trials, CT angiography has been shown to be both accurate and safe to stratify patients with acute chest pain and absence of ECG changes, as well as myocardial enzyme elevation[13, 42–45] (see Fig. 13.7). One study demonstrated a cost advantage of incorporating CT angiography in the workup of low-likelihood acute chest pain patients when compared with the standard of care.[44]

Imaging of Patients with Bypass Grafts and Stents

Coronary CT angiography has substantial limitations in patients with previous coronary revascularization. In patients

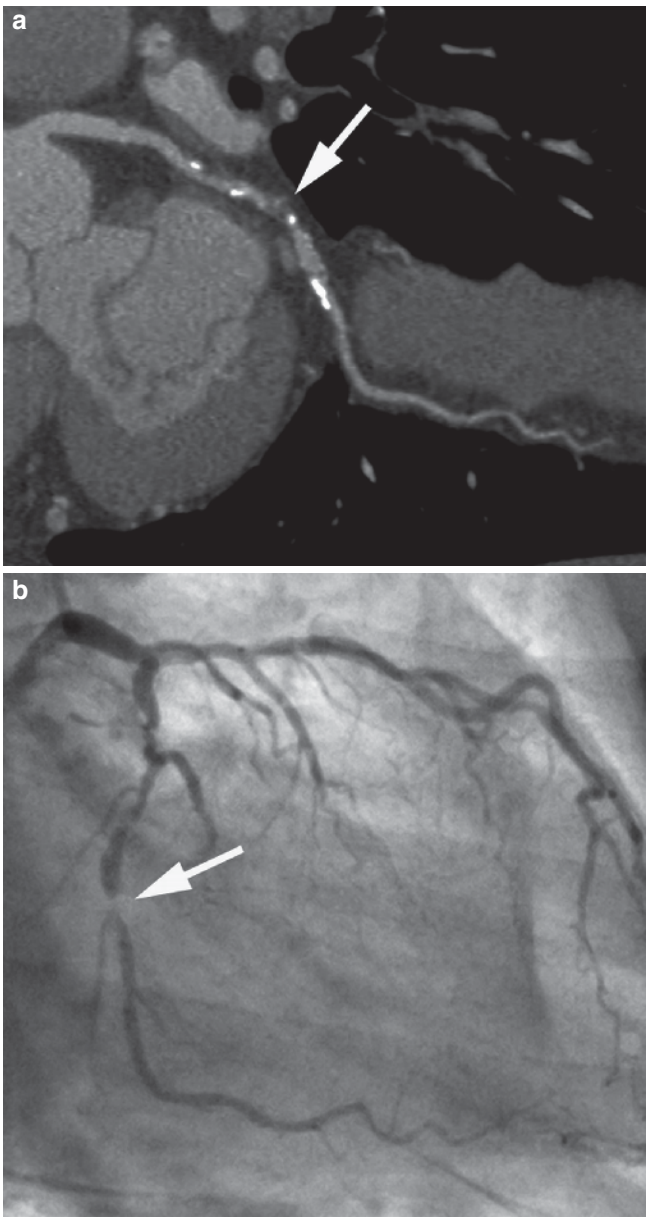

Fig. 13.4 Visualization of the left circumflex coronary artery in a patient with diffuse, severe disease. Data sets of patients with severe atherosclerosis can be substantially more difficult to interpret when compared with patients who have less burden of disease. **(a)** Curved multi-planar reconstruction of the left main and left circumflex coronary artery (*arrow*), which shows multiple calcified plaques and several high grade luminal stenoses. **(b)** Corresponding invasive coronary angiogram (arrows = left circumflex artery)

after bypass surgery, accuracy for the detection of bypass graft stenosis and occlusion is extremely high (see Fig. 13.8).[46–51] However, assessing the native coronary arteries can be extremely difficult because of their often small diameter and severe calcification (see Fig. 13.9). Consequently, accuracy for detecting and ruling out stenoses in non-grafted and run-off vessels is substantially lower.[47, 49] A recent study performed by 64-slice CT found a sensitivity and specificity of only 86 and 76%, respectively, for the detection of stenoses in the native coronary arteries after patients with bypass surgery.[49]

Similarly, assessment of coronary artery stents is often unreliable (see Fig. 13.10). The dense metal of the stents can cause artefacts that impair the evaluability. The ability to assess stents concerning in-stent restenosis depends on many factors, which include stent type and diameter[52] as well as the overall quality of the data set.[53–57] Some recently published studies suggest that the analysis of large stents (e.g. stents implanted in the left main coronary artery[53)] may be possible by CT (see Fig. 13.11). In some studies, sensitivities of up to 95% for the detection of in-stent restenosis have been reported.[55–57] However, the overall number of included stents was small, and patients were heavily selected so that the results cannot be generalized. Also, the positive predictive values were low (54–94%). A recent meta-analysis reported that 20% of stents were unevaluable by CT, and the sensitivity for stenosis detection was only 82% in evaluable stents.[58] Imaging of patients with previously implanted stents should therefore not be routinely considered for coronary CT angiography.

Coronary CTA and Ischaemia

Coronary CTA, like invasive angiography, is a purely morphologic imaging modality and cannot demonstrate the functional relevance of stenoses (ischaemia). Particularly, in the case of lesions with borderline degree of stenosis, this may be a limitation. Not surprisingly, coronary CTA is a better predictor of angiographic findings than testing for ischaemia.[59–61] For example, an analysis of 114 patients with intermediate likelihood of coronary disease demonstrated that only 19 of 33 patients in whom stenoses were demonstrated by coronary CTA had ischaemia in SPECT myocardial perfusion imaging. On the other hand, 28 of the 33 patients had obstructive coronary lesions in invasive coronary angiography. However, all 25 patients who received invasive angiography, even though coronary CTA had ruled out the presence of obstructive stenoses, had, in fact, a "negative" coronary angiogram.[59] Similarly, a comparison of SPECT and CT in 38 patients revealed that ruling out coronary artery stenoses by CTA had a negative predictive value of 94%, but detecting stenoses by CT only had a positive predictive value of 32% to predict ischaemia in myocardial perfusion imaging.[61]

These results underscore that a "negative" coronary CTA result is a reliable predictor to rule out the presence of coronary artery stenoses and the need for revascularization, and that it may therefore be used as a "gatekeeper" to avoid invasive angiograms. On the other hand, coronary CTA – like invasive angiography – should not be performed in an unselected patient

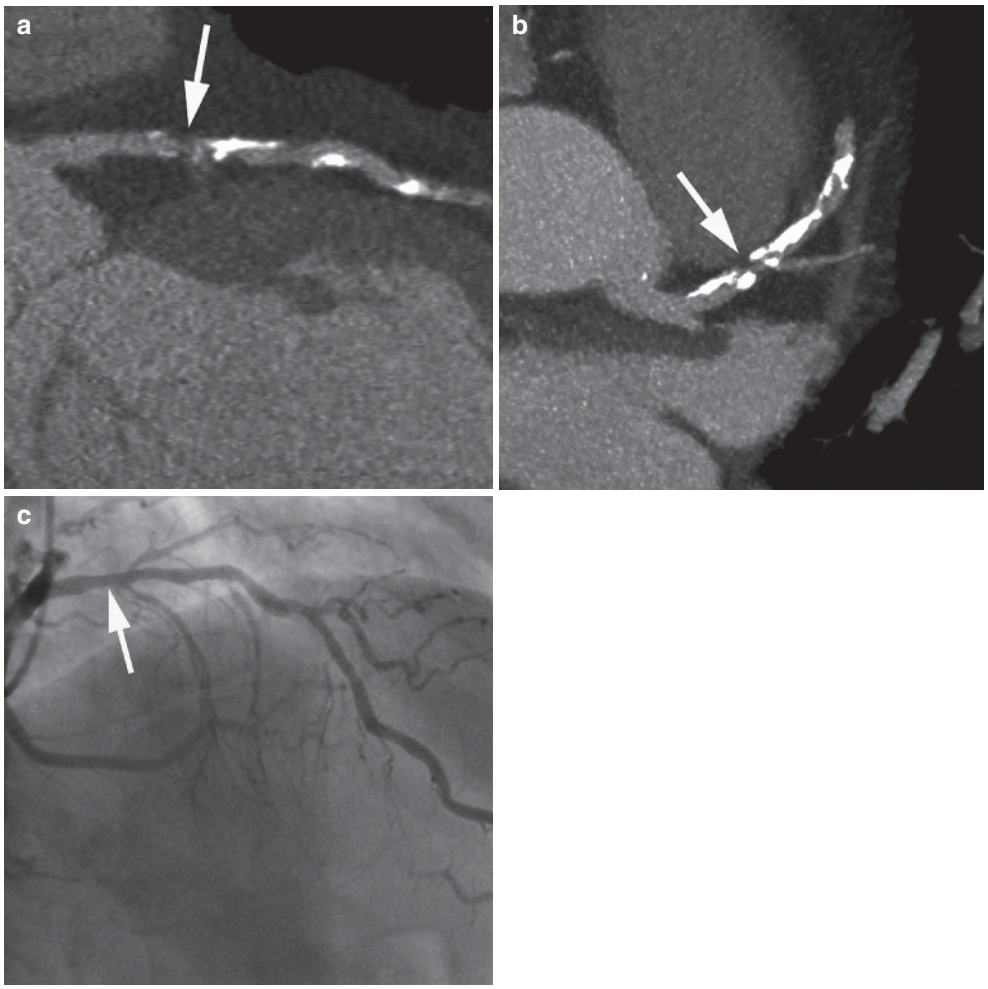

Fig. 13.5 Severe calcifications can impair evaluability of coronary CT angiography data sets. Much more than causing false-negative findings, they tend to cause false-positive CT angiography results, such as in the case shown here. **(a)** Curved multi-planar reconstruction showing the left main and proximal left anterior descending coronary artery. A high-grade stenosis seems to be present (*arrow*). Substantial calcifications can be seen. **(b)** In a maximum intensity projection (axial orientation), the true extent of calcification is appreciated. Again, there seems to be a high-grade luminal stenosis just before the origin of the diagonal branch (*arrow*). **(c)** Invasive angiography of the left anterior descending coronary artery shows severe atherosclerosis, but no high-grade stenosis (*arrow*)

population and not for "screening" purposes. A positive CT scan by itself does not strongly predict the need for revascularization.[62]

Coronary CT Angiography for Stenosis Detection: Guidelines and Recommendations

Obviously, the possibility to perform non-invasive coronary angiography with CT is immensely attractive, and there may be a tendency towards overuse, and potentially towards using this imaging method in patient groups who ultimately will not benefit from the test. There is the potential danger of creating a "new layer" of testing that may be added to the currently available tools, without replacing other testing procedures or, in the worst case, even leading to additional, unnecessary downstream testing. Also, the accuracy and clinical utility of coronary CT angiography do depend on the expertise of the investigator – at the current early stage of this technology, potentially more so than in the other, more established diagnostic imaging modalities that are used in cardiology. Finally, while there is rapidly accumulating evidence on accuracy, there are no data that link the use of CT angiography to improved outcomes. Consequently, official bodies and professional organizations have been reluctant to issue guidelines that would support the use of CT imaging in the workup of coronary artery disease.

In a "Scientific Statement" on non-invasive coronary artery imaging issued by the American Heart Association,[63] the following comments are made regarding coronary CT angiography for the detection of coronary artery stenoses.

- Neither coronary CT angiography nor coronary MR angiography should be used to screen for coronary artery disease in patients who have no signs or symptoms suggestive of coronary artery disease (Class III, level of evidence C).
- The potential benefit of non-invasive coronary angiography is likely to be greatest and is reasonable for symptomatic patients who are at intermediate risk for coronary artery disease after initial risk stratification, including patients with equivocal stress-test results (Class II, level of evidence B). Diagnostic accuracy favours coronary CT

Table 13.1. Results of meta-analyses that have evaluated the accuracy of coronary CT angiography for stenosis detection in comparison to invasive coronary angiography

	Studies/patients		Sensitivity (%)	Specificity (%)	NPV (%)	PPV (%)
Per-segment analysis						
Vanhoenaker et al.[27]						
16-slice CT	26	704	83	96	–	–
64-slice CT	6	363	93	96	–	–
Hamon et al.[28]						
16-slice CT	16	1292	77	91	96	60
64-slice CT	12	695	88	96	98	79
Abdulla et al.[29]						
64-slice CT	19	1251	86	96	97	83
Gopalakrishnan et al.[30]						
16-slice CT	29	2214	84	94	97	72
40- to 64-slice CT	10	596	91	96	98	78
Mowatt[31]						
64-slice CT	28	1286	90	97	99	76
Per-patient analysis						
Vanhoenaker et al.[27]						
16-slice CT	26	704	97	81	–	–
64-slice CT	6	363	99	93	–	–
Hamon et al.[28]						
16-slice CT	16	1292	95	69	92	79
64-slice CT	12	695	97	90	96	93
Abdulla et al.[29]						
64-slice CT	13	875	98	91	94	97
Gopalakrishnan et al.[30]						
16-slice CT	29	2214	91	77	89	77
40- to 64-slice CT	10	596	96	91	96	93
Mowatt[31]						
64-slice CT	28	1286	99	89	100	93

Table 13.2. Diagnostic performance of 64-slice CT depending on the clinical pre-test likelihood of coronary artery disease in 254 patients[33]

Pre-test probability*	N	Sensitivity (%)	Specificity (%)	Positive predictive value (%)	Negative predictive value (%)
Predictive value					
High	105	98	74	93	89
Intermediate	83	100	84	80	100
Low	66	100	93	75	100

*Estimated with the Duke Clinical Risk Score

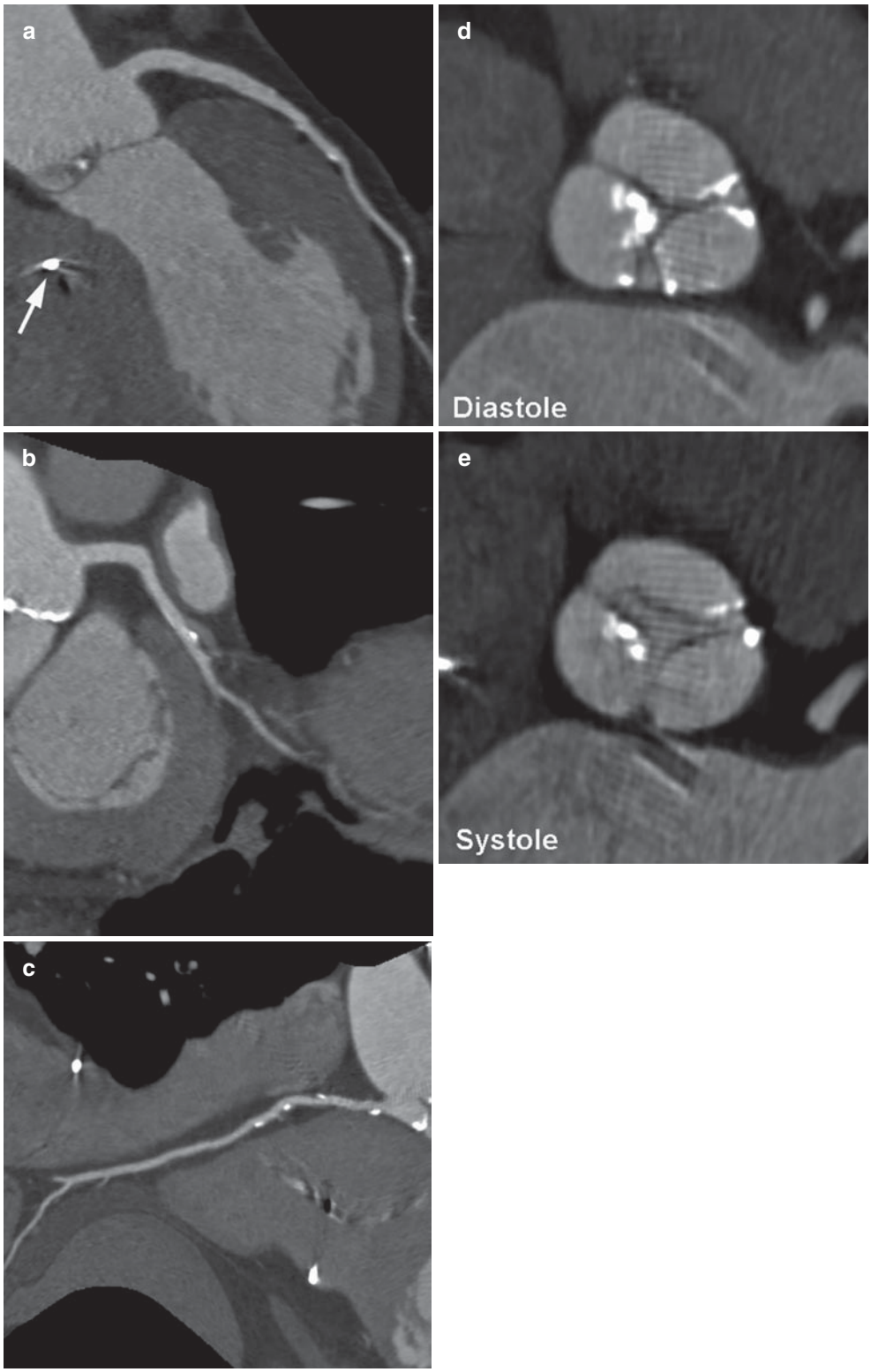

Fig. 13.6 Use of coronary CT angiography to rule out coronary artery stenoses in a patient with aortic valve stenosis. **(a)** Curved multi-planar reconstruction of the left main and left anterior descending coronary artery. Stenoses can be ruled out. *Arrow* = cross section of a pacemaker electrode, which causes some artefact. **(b)** Curved multi-planar reconstruction of the small left circumflex coronary artery. Again, stenoses can be ruled out. **(c)** Curved multi-planar reconstruction of the right coronary artery. Some small atherosclerotic plaques are present in the proximal segment, but significant luminal narrowing can be ruled out. **(d)** Visualization of the aortic valve in diastole. The tricuspid valve is calcified. Some artefacts are present, which are caused by the pacemaker lead (outside the field of view). **(e)** Visualization of the aortic valve in systole. Opening is impaired (orifice area: 0.8 cm^2)

angiography over MR angiography for these patients (Class I, level of evidence B).

A report by a Writing Group deployed by the Working Group Nuclear Cardiology and Cardiac CT of the European Society of Cardiology and the European Council of Nuclear Cardiology on "Cardiac computed tomography: indications, applications, limitations, and training requirements" states the following concerning coronary CT angiography.[64]

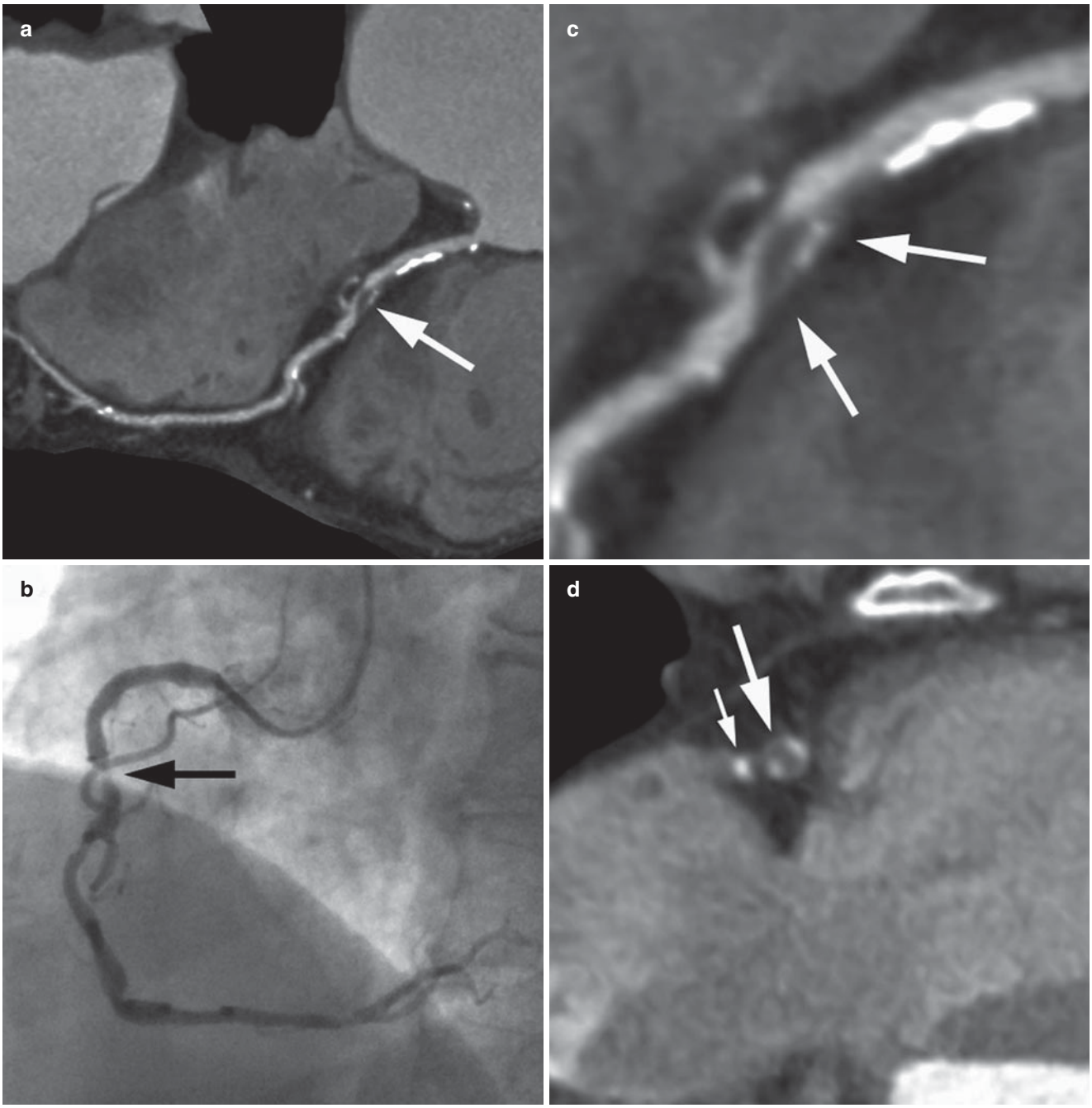

Fig. 13.7 Coronary CT angiography in a patient with acute chest pain. **(a)** Curved multi-planar reconstruction of the right coronary artery. Besides some calcification, a luminal stenosis of the proximal right coronary artery is visible (*arrow*). **(b)** Corresponding invasive coronary angiography (*arrow* = stenosis). **(c)** In CT angiography, the lesion of the right coronary artery shows some characteristics that are often observed in acute coronary syndromes. A typical finding is positive re-modelling as seen in this enlarged view (*arrows*). **(d)** Another typical finding – but not observed in all cases – is ring-like enhancement (around a central thrombus, *large arrow*). The *small arrow* points at the cross section of a side branch

Detection of Coronary Artery Stenoses

- In summary, the clinical application of coronary CT angiography to detect or rule out coronary artery stenoses seems most beneficial and, according to current data, can be recommended in patients with intermediate risk of CAD in whom the clinical presentation – stable or with acute symptoms – mandates the evaluation of possible underlying CAD.
- The use of coronary CT angiography should be restricted to patients in whom diagnostic image quality can be expected (e.g. absence of arrhythmias), and scans need to be expertly performed and interpreted.

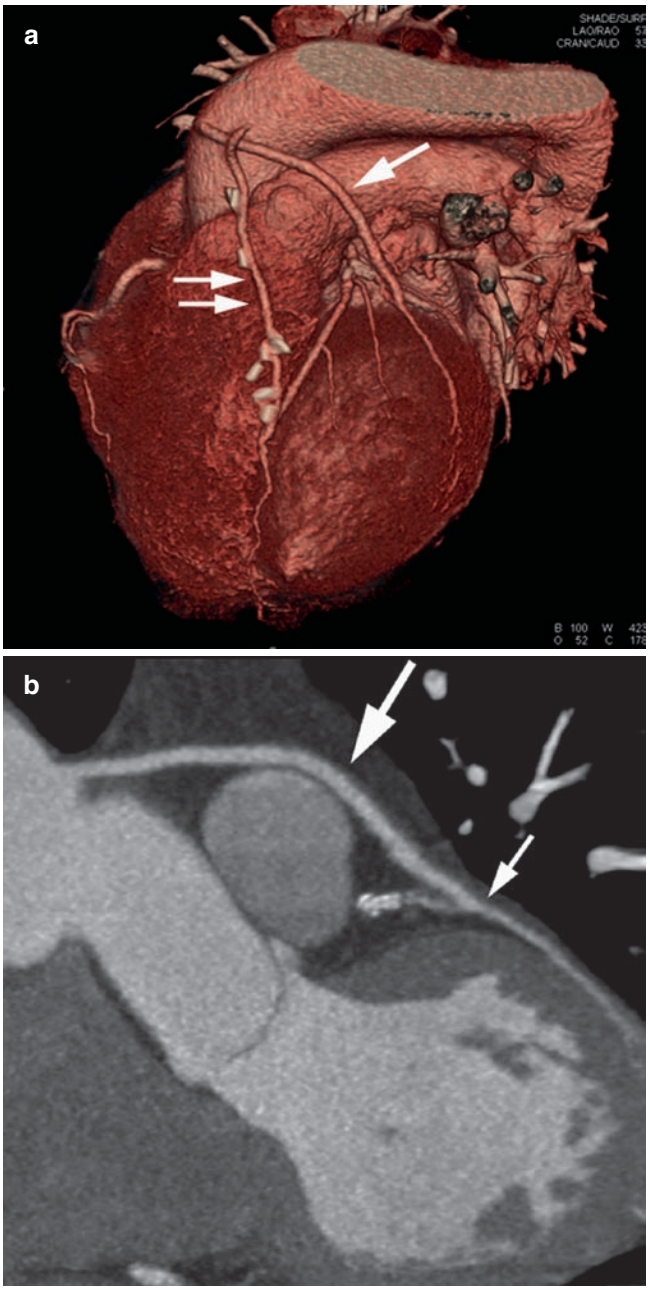

Fig. 13.8 CT visualization of bypass grafts. **(a)** 3D reconstruction in a patient with an internal mammary artery graft to the left anterior descending coronary artery (*double arrows*) and a vein graft from the aorta to a diagonal branch (*large arrow*). **(b)** Curved multi-planar reconstruction of the bypass graft to the diagonal branch which shows the body of the bypass graft (*large arrow*), the coronary anastomosis (*small arrow*), and the distal lumen of the diagonal branch

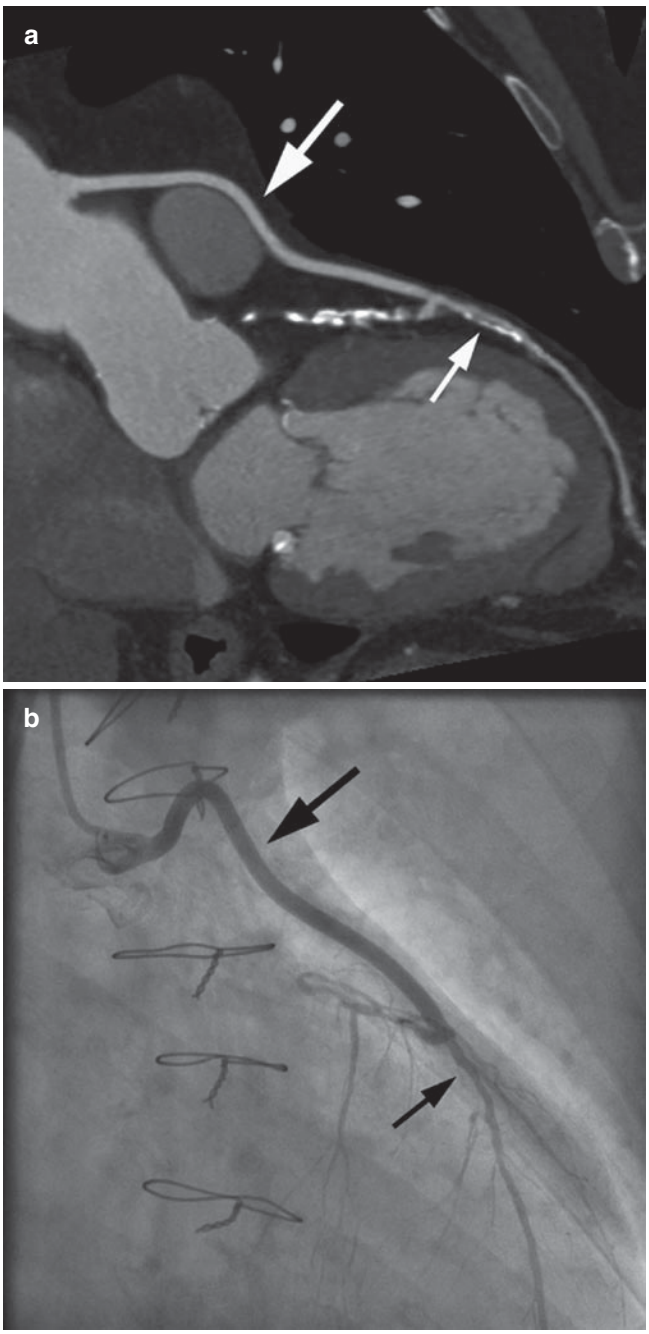

Fig. 13.9 Native coronary arteries in patients after bypass surgery are often severely calcified, which makes their evaluation by CT angiography difficult. **(a)** Curved mulitplanar reconstruction of a bypass graft to the left anterior descending coronary artery (*large arrow*). The bypass lumen is clearly visualized. However, there is substantial calcification of the distal left anterior descending coronary artery. Along with the small vessel lumen, this can cause problems with interpretation (*small arrow*). **(b)** Invasive coronary angiogram of the same patient, showing the bypass graft to the left anterior descending coronary artery and the distal vessel. No stenosis is present

Coronary Stent Imaging

- Although in single, carefully selected cases (e.g. large diameter stents in a proximal vessel segment, low and stable heart rate, and absence of excessive image noise) coronary CT angiography may be a possibility to rule out in-stent restenosis, routine application of CT to assess patients with coronary stents is currently not recommended.

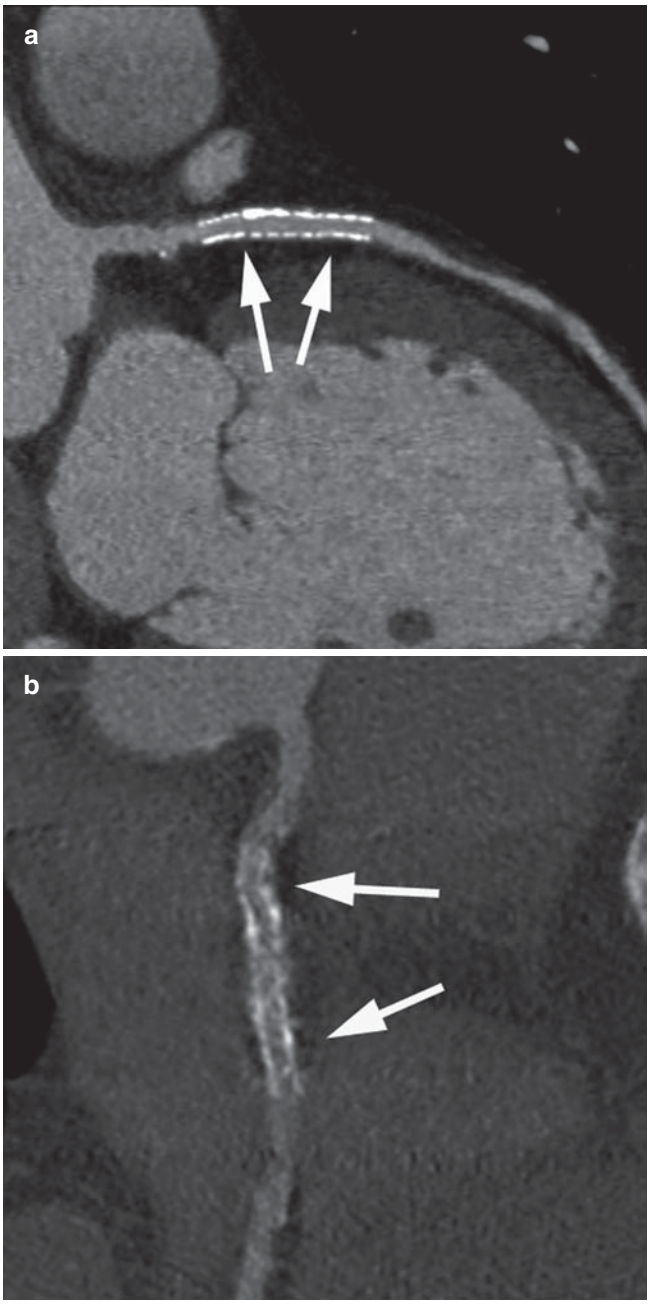

Fig. 13.10 Imaging of coronary artery stents by CT angiography. **(a)** Visualization of a stent implanted in the proximal left anterior descending coronary artery. No artefacts are present and the in-stent lumen can be assessed very clearly (*arrows*). **(b)** In this case, motion artefacts are present, which make it impossible to assess the lumen of two stents implanted in the proximal right coronary artery

- Visualization of the stent lumen is often affected by artefacts, and especially, the positive predictive value is low.

Coronary Artery Bypass Grafts

- Although the clinical application of CT angiography may be useful in very selected patients in whom only bypass graft assessment is necessary (e.g. failed visualization of a graft in invasive angiography), the inability to reliably visualize the native coronary arteries in patients post-CABG poses severe restrictions to the general use of CT angiography in post-bypass patients.

A group of U.S.-based professional societies (both cardiology and radiology) jointly issued a statement of Appropriateness Criteria for cardiac CT and MR imaging in the year 2006. The document lists several situations in which coronary CT angiography is considered to be of clinical value.[65] Such situations include the use of CT coronary angiography to rule out coronary artery stenoses in patients who are symptomatic, but who have a non-interpretable or equivocal stress test, who are unable to exercise, or who have a non-interpretable ECG. Furthermore, the document considers the use of coronary CT angiography appropriate for patients with new onset heart failure, and for patients who present with acute chest pain and an intermediate pre-test likelihood of coronary artery disease, but who have a normal ECG and absence of enzyme elevation (see Table 13.3).[65] Finally, the use of CT angiography is considered "appropriate" to evaluate patients with anomalous coronary arteries.[65]

Imaging of Coronary Atherosclerotic Plaque

Coronary Calcification

Using cardiac CT, calcium deposits in the coronary arteries can be detected and quantified in low-radiation, non-enhanced image acquisition protocols (see Fig. 13.12). Tissue within the vessel wall with a CT number of 130 HU or more is defined as "calcified." The so-called Agatston Score, which takes into account the area and the CT density of calcified lesions, is most frequently used to quantify the amount of coronary calcium in CT, and large population reference databases are available.[66]

Coronary calcifications, with the possible exception of patients with renal failure,[67] are always due to coronary atherosclerotic plaque. In fact, the amount of calcium roughly correlates with the overall plaque volume.[68] On the other hand, not every atherosclerotic coronary plaque is calcified, and calcification is neither a sign of stability nor of instability of an individual plaque.[69]

In several trials, the absence of coronary calcium has proven highly predictive to rule out the presence of significant coronary artery stenoses.[70, 71] Clinical experience, however, teaches that especially younger patients with more recent onset of symptoms may have significant coronary artery stenoses in the complete absence of calcification. Therefore, the lack of calcium in clinical practice does not reliably eliminate the

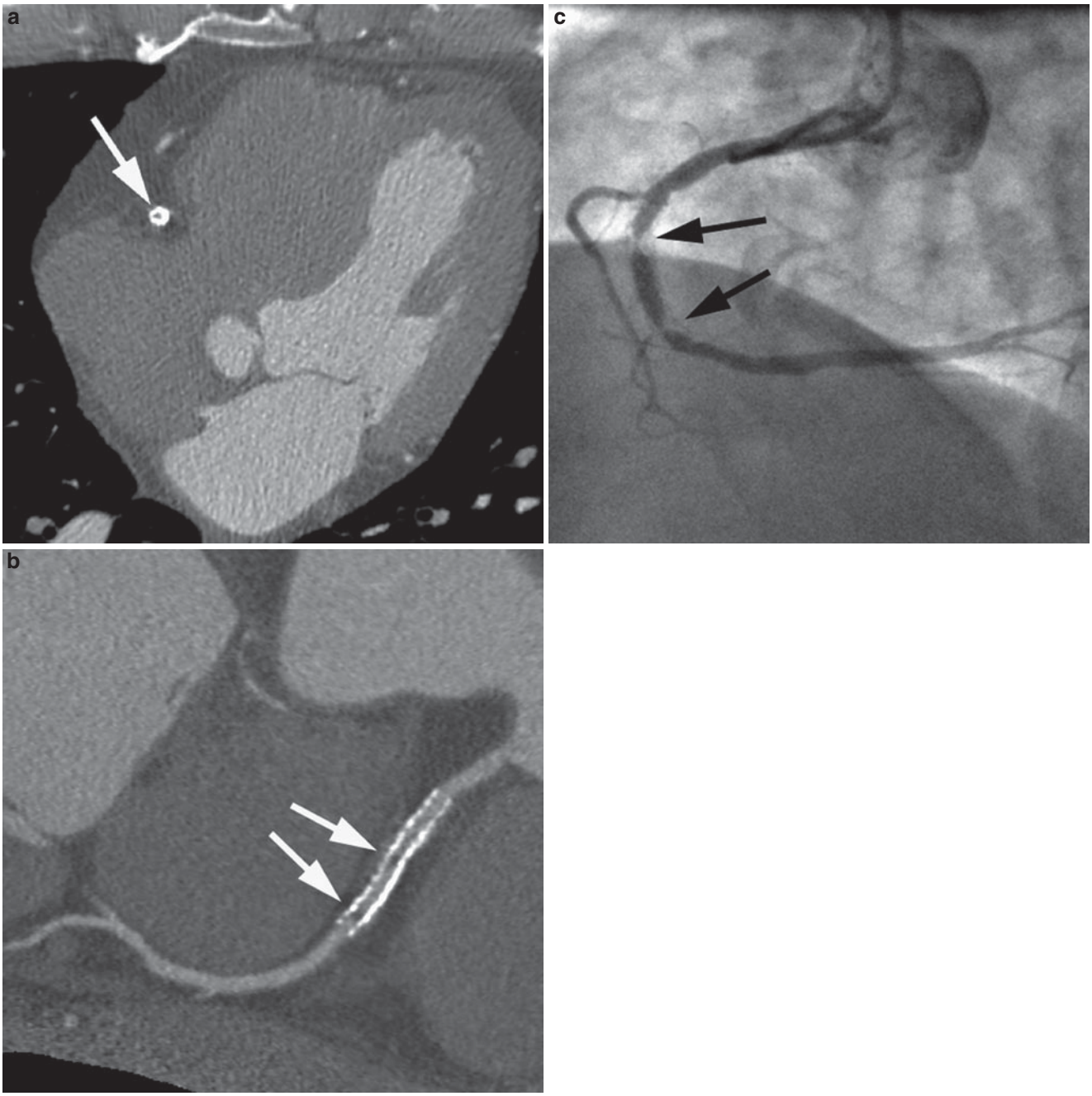

Fig. 13.11 Visualization of focal in-stent stenosis. **(a)** Transaxial image showing a stent in the right coronary artery (*arrow*). **(b)** For the assessment of stents, if image quality is sufficient, longitudinal reconstructions of the stent lumen are best suited. Here, a curved multiplanar reconstruction shows two focal in-stent stenoses (*arrow*). **(c)** Corresponding invasive coronary angiogram

possibility of coronary artery stenoses. On the other hand, it is also very important to note that even substantial amounts of coronary calcium are not necessarily associated with the presence of haemodynamically relevant luminal narrowing. Even very high calcium scores can be found in the absence of coronary stenoses. Therefore, the detection of coronary calcium, even in large amounts, should not prompt invasive coronary angiography in otherwise asymptomatic individuals.

Numerous prospective trials have demonstrated that the presence of coronary calcium in asymptomatic individuals is a prognostic parameter with strong predictive power for future hard cardiac events.[72–83] While the predictive power of coronary calcium is undisputed, the effect of performing "calcium screening" on downstream coronary artery disease events has not been prospectively investigated. It is expert consensus that calcium assessment to risk stratification will

Table 13.3. "Appropriate" indications for CT coronary angiography according to an Expert Consensus Document [65]

Detection of CAD with prior test results - evaluation of chest pain syndrome
Uninterpretable or equivocal stress test result (exercise, perfusion, or stress echo)
Detection of CAD: symptomatic - evaluation of chest pain syndrome
Intermediate pre-test probability of CAD, ECG uninterpretable or unable to exercise
Detection of CAD: symptomatic - acute chest pain
Intermediate pre-test probability of CAD, no ECG changes, and serial enzymes negative
Evaluation of coronary arteries in patients with new onset heart failure to assess aetiology
Detection of CAD: symptomatic
Evaluation of suspected coronary anomalies

most likely be clinically useful in individuals who seem to be at intermediate risk for coronary events (1.0–2.0% annual risk) based on traditional risk factor analysis.[70,71] Unselected "screening" or patient self-referral is uniformly not recommended, and clinical utility of calcium scoring in individuals with very low (<1.0% annual risk) or very high risk (>2.0% annual risk) has not been clarified.

Follow-up studies have shown that the degree of progression of coronary calcium is approximately 20–40% per year. Only preliminary studies are available that have linked the progression of coronary calcium to cardiac event rates.[84] Results concerning the influence of lipid-lowering therapy on the progression of coronary calcium have not been homogeneous.[85–89] In addition, the variability of coronary calcification measurements is high. Therefore, there is broad consensus that repeated coronary calcium score measurements for the purpose of assessing calcium progression are not useful and cannot be recommended.[70,71]

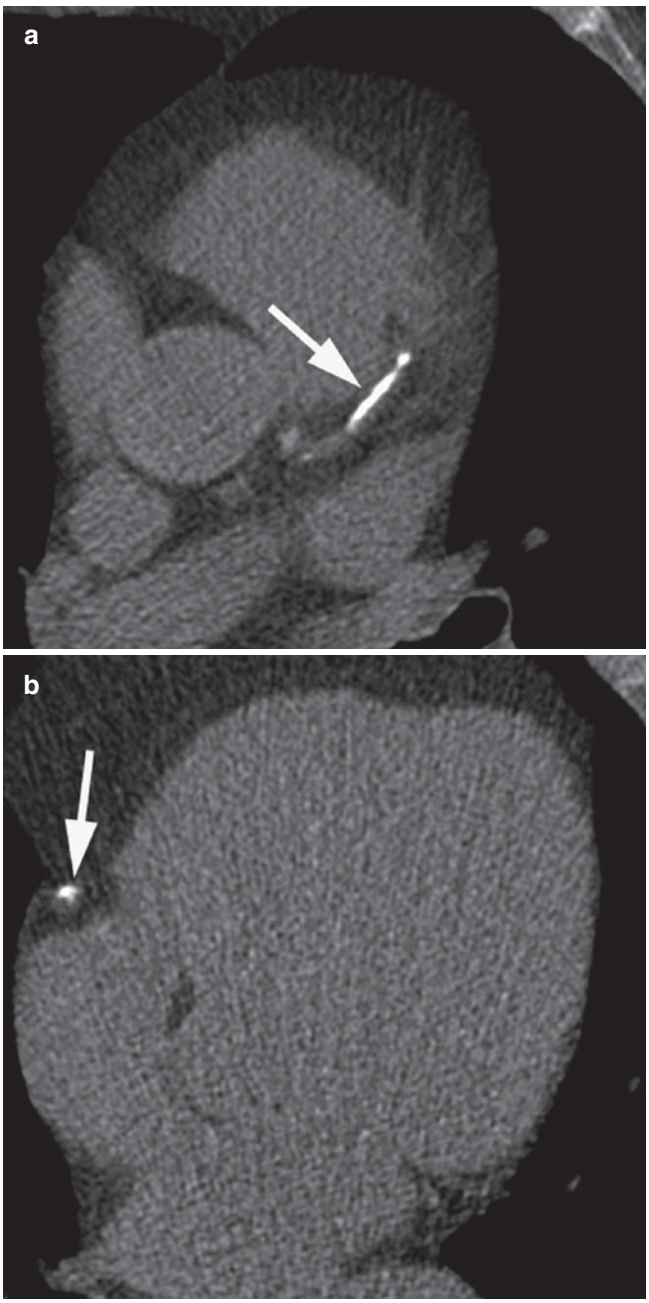

Fig. 13.12 Detection of coronary calcification by CT. **(a)** CT scans to detect coronary calcification are performed without contrast enhancement and with lower spatial resolution when compared with coronary CT angiography. Here, a calcification of the proximal left anterior descending coronary artery is visible (*arrow*). **(b)** Calcification of the right coronary artery (same patient as in **(a)**)

Plaque in Coronary CT Angiography

In data sets that are free of artefact and provide high image quality, coronary CT angiography allows to visualize non-stenotic, non-calcified coronary atherosclerotic plaque (see Figs. 13.13 and 13.14). Obviously, the detection and characterization not only of calcified, but also of non-calcified plaque components is perceived as an extremely promising tool for improved risk stratification. However, the ability of CT to provide such information is limited. In comparison with IVUS, the accuracy for detecting non-calcified plaque has been found to be approximately 80–90%.[90–92] To a certain extent, coronary CT angiography allows plaque characterization: On an average, CT attenuation within "fibrous" plaques is higher than within "lipid-rich" plaques (mean attenuation values of 91–116 HU vs. 47–71 HU).[93–96] However, the variability of density measurements within plaque types is large,[96] and density measurements within plaque are heavily influenced by contrast attenuation in the adjacent lumen.[97] Therefore, accurate classification of plaque composition by coronary CTA is not

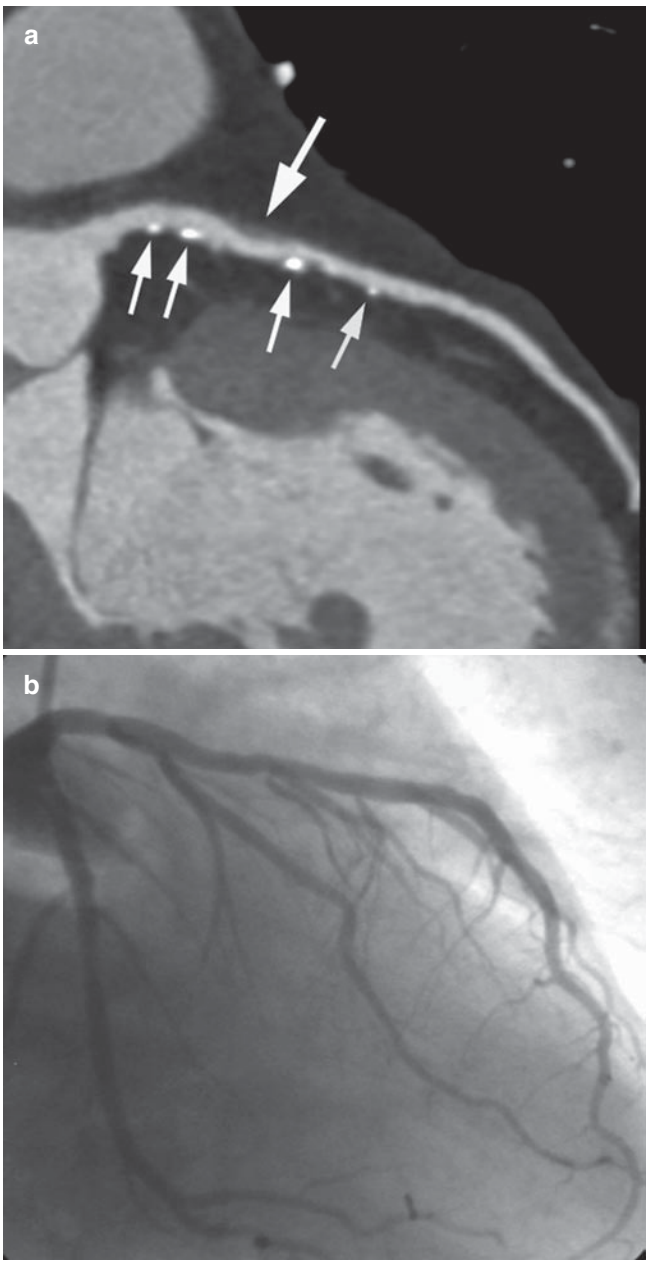

Fig. 13.13 Detection of non-calcified plaque by contrast-enhanced CT angiography. **(a)** In this curved multi-planar reconstruction of the left main and left anterior descending coronary artery, several small coronary calcifications can be detected (*small arrows*) and, in addition, a larger non-calcified plaque is present. These atherosclerotic lesions do not cause a significant coronary artery stenosis. **(b)** Corresponding invasive coronary angiogram

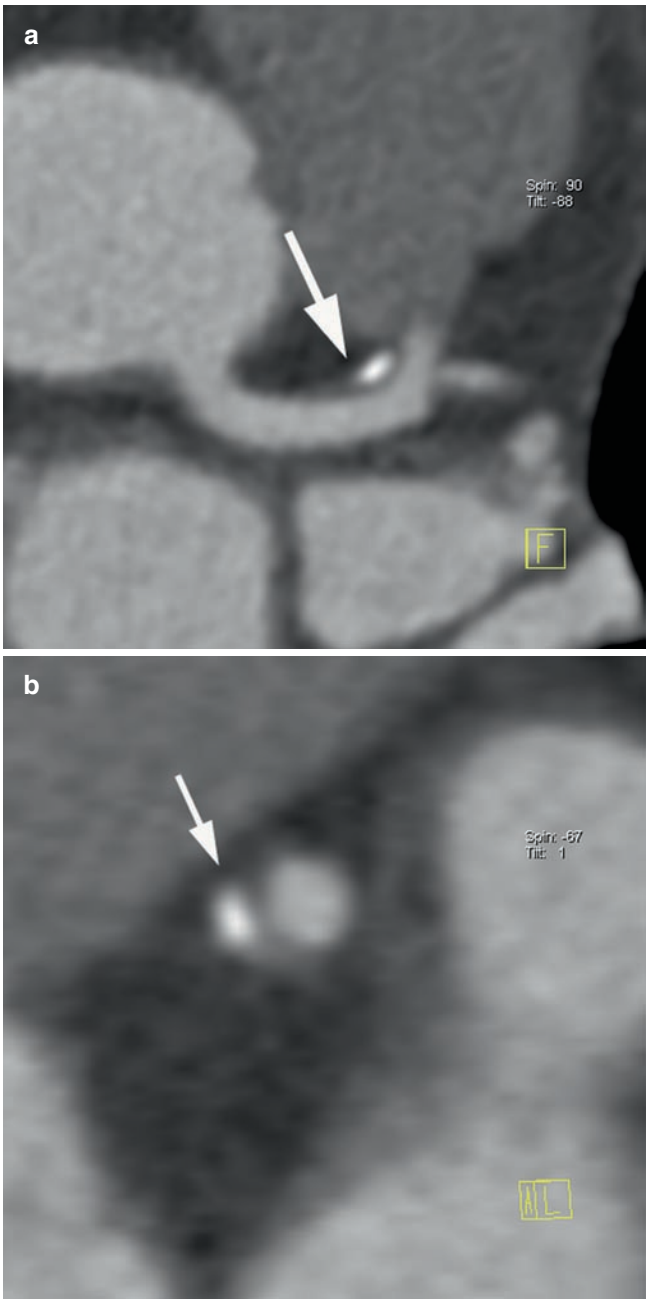

Fig. 13.14 Visualization of partly calcified plaque by coronary CT angiography. **(a)** A transaxial image shows a partly calcified, partly non-calcified plaque at the distal left main and very proximal left anterior descending coronary artery. **(b)** Cross-sectional view of the same lesion. Contrast-enhanced lumen and an eccentric plaque with non-calcified and calcified components (*arrow*) can be appreciated

currently possible. On the other hand, some parameters that are more readily available from CT might contribute to the detection of "vulnerable" plaques. They include plaque volume and the degree of re-modelling (see Fig. 13.15).[98–100]

The clinical utility of these observations is uncertain. Very few prospective studies have analyzed the predictive power of plaque seen in coronary CT angiography. In a single-centre cohort study of 1.127 *symptomatic* patients with chest pain who were studied by coronary CT angiography and followed for 15 months, the authors demonstrated that the presence of any stenosis of ≥70% diameter reduction, the presence of stenoses in the left main coronary artery, as well as the presence of plaque, whether obstructive or non-obstructive, in five or more coronary artery segments

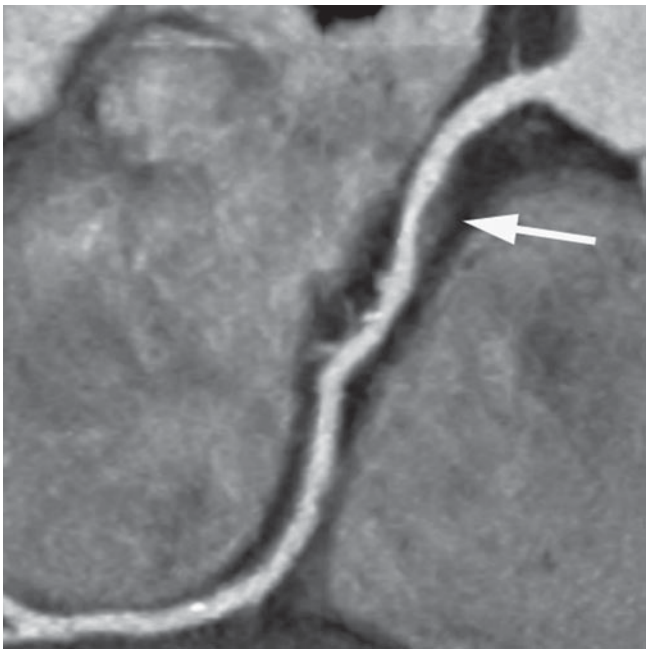

Fig. 13.15 Pronounced positive re-modelling of a non-calcified plaque in the proximal right coronary artery (*arrow*)

was significantly predictive of all-cause mortality.[101] Importantly, very small amounts of plaque were not predictive of mortality in this study (which had a relatively short follow-up period). Because of the lower overall event rates, predicting acute coronary syndromes in *asymptomatic* individuals is more difficult. In fact, a trial of 1,000 middle-aged asymptomatic Korean individuals (among whom 22% had detectable plaque in CT) was not able to identify any prognostic value of coronary CT angiography during a 17-month follow-up period.[102]

Because of the difficulty in reliably detecting non-calcified plaque, because of the high prevalence of plaques and low consecutive event rates, and because of the lack of ultimate proof that non-calcified plaque allows for risk stratification concerning future cardiovascular events in asymptomatic individuals, let alone better risk stratification than coronary calcium measurement, it is currently not recommended to perform coronary CT angiography in asymptomatic individuals.

Limitations and Outlook

In spite of the impressive image quality, which continues to improve, coronary CT angiography will not be a general replacement for invasive, catheter-based diagnostic coronary angiography in the foreseeable future. Spatial resolution and temporal resolution are substantially lower than those obtained by invasive angiography. In addition, arrhythmias – most prominently atrial fibrillation – high heart rates, and inability to perform a sufficiently long breath-hold may preclude CT angiography in a significant number of patients who require a workup for coronary artery disease. Similarly, in patients with diffuse, severe disease, with substantial coronary calcification or with small coronary arteries (as often encountered, for example, in patients with diabetes), the spatial resolution of CT may not be high enough to allow reliable interpretation of the coronary system. For challenging cases like these, invasive angiography will remain the best diagnostic option.

However, in many other situations, coronary CT angiography, if expertly performed, constitutes a reasonable tool to rule out coronary artery stenoses and avoid further testing. Care needs to be taken to identify these situations and to avoid the use of coronary CT angiography when it is not likely to lead to changes in patient management or to replace other testing procedures. Accumulating evidence will help to better understand the clinical settings in which CT angiography is most useful. In addition, CT technology continues to evolve at an impressive pace, and improvements in image quality are likely to translate into broader applications of coronary CT angiography in the future.

References

1. Achenbach S, Cardiac CT. State of the art for the detection of coronary arterial stenosis. *J Cardiovasc Comput Tomogr*. 2007;1:3–20
2. Achenbach S, Ropers U, Kuettner A, et al Randomized comparison of 64-slice single- and dual-source computed tomography for the detection of coronary artery disease. *J Am Coll Cardiol Imaging*. 2008;1:177–186
3. Ferencik M, Ropers D, Abbara S, et al Diagnostic accuracy of image postprocessing methods for the detection of coronary artery stenoses by using multidetector CT. *Radiology*. 2007;243:696–702
4. Lim MCL, Wong TW, Yaneza LO, De Larrazabal C, Lau JK, Boey HK. Non-invasive detection of significant coronary artery disease with multi-section computed tomography angiography in patients with suspected coronary artery disease. *Clin Radiol*. 2006;61: 174–180
5. Halon DA, Gaspar T, Adawi S, et al Uses and limitations of 40 slice multi-detector row spiral computed tomography for diagnosing coronary lesions in unselected patients referred for routine invasive coronary angiography. *Cardiology*. 2007;108:200–209
6. Watkins MW, Hesse B, Green CE, et al Detection of coronary artery stenosis using 40–channel computed tomography with multisegment reconstruction. *Am J Cardiol*. 2007;99:175–181
7. Grosse C, Globits S, Hergan K. Forty-slice spiral computed tomography of the coronary arteries: assessment of image quality and diagnostic accuracy in a non-selected patient population. *Acta Radiol*. 2007;48:36–44
8. Ropers D, Rixe J, Anders K, et al Usefulness of multidetector row computed tomography with 64 x 0.6 mm collimation and 330-ms rotation for the noninvasive detection of significant coronary artery stenoses. *Am J Cardiol*. 2006;97:343–348
9. Fine JJ, Hopkins CB, Ruff N, Newton FC. Comparison of accuracy of 64-slice cardiovascular computed tomography with coronary

angiography in patients with suspected coronary artery disease. *Am J Cadiol*. 2006;97:173–174
10. Nikolaou K, Knez A, Rist C, et al Accuracy of 64-MDCT in the diagnosis of ischemic heart disease. *AJR*. 2006;187:111–117
11. Schlosser T, Mohrs OK, Magedanz A, et al Noninvasive coronary angiography using 64-detector-row computed tomography in patients with a low to moderate pretest probability of significant coronary artery disease. *Acta Radiol*. 2007;48:300–307
12. Mühlenbruch G, Seyfarth T, Soo CS, Pregalathan N, Mahnken AH. Diagnostic value of 64-slice multi-detector row cardiac CTA in symptomatic patients. *Eur Radiol*. 2007;17:603–609
13. Meijboom WB, Mollet NR, Van Mieghem CA, et al 64-slice computed tomography coronary engiography in patients with non-ST elevation acute coronary syndrome. *Heart*. 2007;93:1386–1392
14. Herzog C, Zwerner PL, Doll JR, et al Significant coronary artery stenosis: comparison on per-patient and per-vessel or per-segment basis at 64-section CT angiography. *Radiology*. 2007;244: 112–120
15. Ehara M, Surmely JF, Kawai M, et al Diagnostic accuracy of 64–slice computed tomography for detecting angiographically significant coronary artery stenosis in an unselected consecutive patient population. *Circ J*. 2007;70:564–571
16. Hausleiter J, Meyer T, Hadamitzky M, et al Non-invasive coronary computed tomographic angiography for patients with suspected coronary artery disease: the Coronary Angiography by Computed Tomography with the Use of a Submillimeter Resolution (CACTUS) trial. *Eur Heart J*. 2007;28:3034–3041
17. Shabestari AA, Abdi S, Akhlaghpoor S, et al Diagnostic performance of 64-channel multislice computed tomograohy in assessment of significant coronary artery disease in symptomatic subjects. *Am J Cardiol*. 2007;99:1656–1661
18. Scheffel H, Alkadhi H, Plass A, et al Accuracy of dual-source CT coronary angiography: first experience in a high pre-test probability population without heart rate control. *Eur Radiol*. 2006;16: 2739–2747
19. Heuschmid M, Burgstahler C, Reimann A, et al Usefulness of non-invasive cardiac imaging using dual-source computed tomography in an unselected population with high prevalence of coronary artery disease. *Am J Cardiol*. 2007;100:587–592
20. Ropers U, Ropers D, Pflederer T, et al Influence of heart rate on the diagnostic accuracy of dual-source tomography computed angiography. *J Am Coll Cardiol*. 2007;50:2393–2398
21. Leber AW, Johnson T, Becker A, et al Diagnostic accuracy of dual-source multi-slice CT-coronary angiography in patients with an intermediate pretest likelihood for coronary artery disease. *Eur Heart J*. 2007;28:2354–2360
22. Weustink AC, Meijboom WB, Mollet NR, et al Reliable high-speed coronary computed tomography in symptomatic patients. *J Am Coll Cardiol*. 2007;50:786–794
23. Alkadhi H, Scheffel H, Desbiolles L, et al Dual-source computed tomography coronary angiography: influence of obesity, calcium load, and heart rate on diagnostic accuracy. *Eur Heart J*. 2008;29: 766–776
24. Hoffmann U, Moselewski F, Cury RC, et al Predictive value of 16–slice multidetector spiral computed tomography to detect significant obstructive coronary artery disease in patients at high risk for coronary artery disease: patient-versus segment-based analysis. *Circulation*. 2004;110:2638–2643
25. Gosthine S, Caussin C, Daoud B, et al Non-invasive detection of coronary artery disease in patients with left bundle branch block using 64-slice computed tomography. *J Am Coll Cardiol*. 2006;48: 1929–1934
26. Budoff MJ, Dowe D, Jollis JG, et al Diagnostic performance of 64-multidetector row coronary computed tomographic angiography for evaluation of coronary artery stenosis in individuals without known coronary artery disease: results from the prospective multicenter ACCURACY (Assessment by Coronary Computed Tomographic Angiography of Individuals Undergoing Invasive Coronary Angiography) trial. *J Am Coll Cardiol*. 2008;52: 1724–1732
27. Vanhoenacker PK, Heijenbrok–Kal MH, Van Heste R, et al Diagnostic performance of multidetector CT angiography for assessment of coronary artery disease: meta-analysis. *Radiology*. 2007;244:419–428
28. Hamon M, Lepage O, Malagutti P, et al Coronary arteries: diagnostic performance of 16- versus 64-section spiral CT compared with invasive coronary angiography - meta–analysis. *Radiology*. 2007;245:720–731
29. Abdulla J, Abildstrom SZ, Gotzsche O, Kober L, Torp-Pedersen C. 64-multislice detector computed tomography coronary angiography as a potential alternative to conventional coronary angiography: a systematic review. *Eur Heart J*. 2007;28:3042–3050
30. Gopalakrishnen P, Wolson GT, Tak K. Accuracy of multislice computed tomography coronary angiography: a pooled estimate. *Cardiol Rev*. 2008;16:189–196
31. Mowatt G, Cook JA, Hillis GS, et al 64-Slice computed tomography angiography in the diagnosis and assessment of coronary artery disease: systematic review and meta–analysis. *Heart*. 2008;94: 1386–1393
32. Miller JM, Rochitte CE, Dewey M, et al Diagnostic performance of coronary angiography by 64-row CT. *N Engl J Med*. 2008;359: 2324–2336
33. Meijboom WB, van Mieghem CA, Mollet NR, et al 64-Slice computed tomography coronary angiography in patients with high, intermediate, or low pretest probability of significant coronary artery disease. *J Am Coll Cardiol*. 2007;50:1469–1475
34. Danciu SC, Herrera CJ, Stecy PJ, Carell E, Saltiel F, Hines JL. Usefulness of multislice computed tomographic coronary angiography to identify patients with abnormal myocardial perfusion stress in whom diagnostic catheterization may be safely avoided. *Am J Cardiol*. 2007;100:1605–1608
35. Gilard M, Le Gal, G, Cornily JC, et al Midterm prognosis of patients with suspected coronary artery disease and normal multislice computed tomography findings. A prospective management outcome study. *Arch Intern Med*. 2007;165:1686–1689
36. Lesser JR, Flygenring B, Knickelbine T, et al Clinical utility of coronary CT angiography: coronary stenosis detection and prognosis in ambulatory patients. *Cath Cardiovasc Interv*. 2007;69:64–72
37. Min JK, Kang N, Shaw LJ, et al Costs and clinical outcomes after coronary multidetector CT angiography in patients without known coronary artery disease: comparison to myocardial perfusion SPECT. *Radiology*. 2008;249:62–70
38. Andreini D, Pontone G, Pepi M, et al Diagnostic accuracy of multidetector computed tomography coronary angiography in patients with dilated cardiomyopathy. *J Am Coll Cardiol*. 2007;49: 2044–2450
39. Manghat NE, Morgan-Hughes GJ, Shaw SR, et al Multi-detector row CT coronary angiography in patients with cardiomyopathy - initial single-centre experience. *Clin Radiol*. 2007;62:632–638
40. Meijboom WB, Mollet NR, Van Mieghem CA, et al Pre-operative computed tomography coronary angiography to detect significant coronary artery disease in patients referred for cardiac valve surgery. *J Am Coll Cardiol*. 2006;48:1658–1665
41. Scheffel H, Leschka S, Plass A, et al Accuracy of 64-slice computed tomography for the preoperative detection of coronary artery disease in patients with chronic aortic regurgitation. *Am J Cardiol*. 2007;100:701–706
42. Hoffmann U, Nagurney JT, Moselewski F, et al Coronary multidetector computed tomography in the assessment of patients with acute chest pain. *Circulation*. 2006;114:2251–2260
43. Gallagher MJ, Ross MA, Raff GL, Goldstein JA, O'Neill WW, O'Neil B. The diagnostic accuracy of 64-slice computed tomography coronary angiography compared with stress nuclear imaging in

emergency department low-risk chest pain patients. *Ann Emerg Med*. 2007;49:125–136
44. Goldstein JA, Gallagher MJ, O'Neill WW, Ross MA, O'Neil BJ, Raff GL. A randomized controlled trial of multi-slice coronary computed tomography for evaluation of acute chest pain. *J Am Coll Cardiol*. 2007;49:863–871
45. Coles DR, Wilde P, Oberhoff M, Rogers CA, Karsch KR, Baumbach A. Multislice computed tomography coronary angiography in patients admitted with a suspected acute coronary syndrome. *Int J Cardiovasc Imaging*. 2007;23:603–614
46. Chiurlia E, Menozzi M, Ratti C, Romagnoli R, Modena MG. Follow-up of coronary artery bypass graft patency by multislice computed tomography. *Am J Cardiol*. 2005;95:1094–1097
47. Salm LP, Bax JJ, Jukema JW, et al Comprehensive assessment of patients after coronary artery bypass grafting by 16-detector-row computed tomography. *Am Heart J*. 2005;150:775–781
48. Anders K, Baum U, Schmid M, et al Coronary artery bypass graft (CABG) patency: assessment with high-resolution submillimeter 16–slice multidetector-row computed tomography (MDCT) versus coronary angiography. *Eur J Radiol*. 2006;57:336–344
49. Ropers D, Pohle FK, Kuettner A, et al Diagnostic accuracy of noninvasive coronary angiography in patients after bypass surgery using 64-slice spiral computed tomography with 330-ms gantry rotation. *Circulation*. 2006;114:2334–2341
50. Meyer TS, Martinoff S, Hadamitzky M, et al Improved noninvasive assessment of coronary artery bypass grafts with 64-slice computed tomographic angiography in an unselected patient population. *J Am Coll Cardiol*. 2007;49:946–950
51. Feuchtner GM, Schachner T, Bonatti J, et al Diagnostic performance of 64-slice computed tomography in evaluation of coronary artery bypass grafts. *AJR Am J Roentgenol*. 2007;189(3):574–580
52. Maintz D, Seifarth H, Raupach R, et al 64-slice multidetector coronary CT angiography: in vitro evaluation of 68 different stents. *Eur Radiol*. 2006;16:818–826
53. Van Mieghem CA, Cademartiri F, Mollet NR, et al Multislice spiral computed tomography for the evaluation of stent patency after left main coronary artery stenting: a comparison with conventional coronary angiography and intravascular ultrasound. *Circulation*. 2006;114:645–653
54. Rixe J, Achenbach S, Ropers D, et al Assessment of coronary artery stent restenosis by 64–slice multi-detector computed tomography. *Eur Heart J*. 2006;27:2567–2572
55. Oncel D, Oncel G, Karaca M. Coronary stent patency and in-stent restenosis: determination with 64-section multidetector CT coronary angiography - initial experience. *Radiology*. 2007;242:403–409
56. Ehara M, Kawai M, Surmely JF, et al Diagnostic accuracy of coronary in-stent restenosis using 64-slice computed tomography. *J Am Coll Cardiol*. 2007;49:951–959
57. Cademartiri F, Schuijf JD, Pugliese F, et al Usefulness of 64-slice multislice computed tomography coronary angiography to assess in–stent restenosis. *J Am Coll Cardiol*. 2007;49:2204–2210
58. Vanhoenacker PK, Decramer I, Bladt O, et al Multidetector computed tomography angiography for assessment of in-stent restenosis: meta–analysis of diagnostic performance. *BMC Med Imaging*. 2008;8:14
59. Schuijf JD, Wijns W, Jukema JW, et al Relationship between noninvasive coronary angiography with multi-slice computed tomography and myocardial perfusion imaging. *J Am Coll Cardiol*. 2006; 48:2508–2514
60. Hacker M, Jakobs T, Hack N, et al Combined use of 64-slice computed tomography angiography and gated myocardial perfusion SPECT for the detection of functionally relevant coronary artery stenoses. First results in a clinical setting concerning patients with stable angina. *Nuklearmedizin*. 2007;46:29–35
61. Hacker M, Jakobs T, Hack N, et al Sixty-four slice spiral CT angiography does not predict the functional relevance of coronary artery stenoses in patients with stable angina. *Eur J Nucl Med Mol Imaging*. 2007;34:4–10
62. Berman DS, Hachamovitch R, Shaw LJ, et al Roles of nuclear cardiology, cardiac computed tomography, and cardiac magnetic resonance: Noninvasive risk stratification and a conceptual framework for the selection of noninvasive imaging tests in patients with known or suspected coronary artery disease. *J Nucl Med*. 2006;47: 1107–1118
63. Bluemke DA, Achenbach S, Budoff M, et al Noninvasive coronary artery imaging: magnetic resonance angiography and multidetector computed tomography angiography: a scientific statement from the American Heart Association Committee on Cardiovascular Imaging and Intervention of the Council on Cardiovascular Radiology and Intervention, and the Councils on Clinical Cardiology and Cardiovascular Disease in the Young. *Circulation*. 2008;118: 586–606
64. Schroeder S, Achenbach S, Bengel F, et al Cardiac computed tomography: indications, applications, limitations, and training requirements: Report of a Writing Group deployed by the Working Group Nuclear Cardiology and Cardiac CT of the European Society of Cardiology and the European Council of Nuclear Cardiology. *Eur Heart J*. 2008;29:531–556
65. Hendel RC, Patel MR, Kramer CM, et al ACCF/ACR/SCCT/ SCMR/ASNC/NASCI/SCAI/SIR 2006 appropriateness criteria for cardiac computed tomography and cardiac magnetic resonance imaging: a report of the American College of Cardiology Foundation Quality Strategic Directions Committee Appropriateness Criteria Working Group, American College of Radiology, Society of Cardiovascular Computed Tomography, Society for Cardiovascular Magnetic Resonance, American Society of Nuclear Cardiology, North American Society for Cardiac Imaging, Society for Cardiovascular Angiography and Interventions, and Society of Interventional Radiology. *J Am Coll Cardiol*. 2006;48:1475–1497
66. McClelland RL, Chung H, Detrano R, Post W, Kronmal RA. Distribution of coronary artery calcium by race, gender, and age: results from the Multi-Ethnic Study of Atherosclerosis (MESA). *Circulation*. 2006;113:30–37
67. Amann K, Tyralla K, Gross ML, Eifert T, Adamczak M, Ritz E. Special characteristics of atherosclerosis in chronic renal failure. Clin Nephrol. 2003;60(suppl 1):S13–S21
68. Rumberger JA, Simons DB, Fitzpatrick LA, Sheedy PF, Schwartz RS. Coronary artery calcium area by electron-beam computed tomography and coronary atherosclerotic plaque area. A histopathologic correlative study. *Circulation*. 1995;92:2157–2162
69. Schmermund A, Erbel R. Unstable coronary plaque and its relation to coronary calcium. *Circulation*. 2001;104:1682–1687
70. Greenland P, Bonow RO, Brundage BH, et al ACCF/AHA 2007 clinical expert consensus document on coronary artery calcium scoring by computed tomography in global cardiovascular risk assessment and in evaluation of patients with chest pain: a report of the American College of Cardiology Foundation Clinical Expert Consensus Task Force (ACCF/AHA Writing Committee to Update the 2000 Expert Consensus Document on Electron Beam Computed Tomography). *Circulation*. 2007;115:402–426
71. Budoff MJ, Achenbach S, Blumenthal RS, et al Assessment of coronary artery disease by cardiac computed tomography: a scientific statement from the American Heart Association Committee on Cardiovascular Imaging and Intervention, Council on Cardiovascular Radiology and Intervention, and Committee on Cardiac Imaging, Council on Clinical Cardiology. *Circulation*. 2006;114:1761–1791
72. Raggi P, Callister TQ, Cooil B, et al: Identification of patients at increased risk of first unheralded acute myocardial infarction by electron–beam computed tomography. *Circulation*. 2000;101: 850–855
73. Arad Y, Spadaro LA, Goodman K, et al Prediction of coronary events with electron beam computed tomography. *J Am Coll Cardiol*. 2000;36:1253–1258

74. Park R, Detrano R, Xiang M, et al: Combined use of computed tomography coronary calcium scores and C-reactive protein levels in predicting cardiovascular events in nondiabetic individuals. *Circulation*. 2002;106:2073–2075
75. Vliegenthart R, Oudkerk M, Song B, et al Coronary calcification detected by electron-beam computed tomography and myocardial infarction. The Rotterdam Coronary Calcification Study. *Eur Heart J*. 2002;23:1596
76. Wong ND, Hsu JC, Detrano RC, et al Coronary artery calcium evaluation by electron beam computed tomography and its relation to new cardiovascular events. *Am J Cardiol*. 2000;86:495
77. Kondos GT, Hoff JA, Sevrukov A, et al Electron-beam tomography coronary artery calcium and coronary events: a 37-month follow-up of 5635 initially asymptomatic low- to intermediate-risk adults. *Circulation*. 2003;107:2571–2574
78. Taylor AJ, Bindeman J, Feuerstein I, et al Coronary calcium independently predicts incident premature coronary heart disease over measured cardiovascular risk factors: mean three-year outcomes in the Prospective Army Coronary Calcium (PACC) project. *J Am Coll Cardiol*. 2005;46:807–814
79. Greenland P, LaBree L, Azen SP, et al Coronary artery calcium score combined with Framingham score for risk prediction in asymptomatic individuals. *JAMA*. 2004;291:210–215
80. Arad Y, Goodman KJ, Roth M, et al Coronary calcification, coronary disease risk factors, C-reactive protein, and atherosclerotic cardiovascular disease events: the St. Francis Heart Study. *J Am Coll Cardiol*. 2005;46:158–165
81. O'Malley PG, Taylor AJ, Jackson JL, et al Prognostic value of coronary electron–beam computed tomography for coronary heart disease events in asymptomatic patients. *Am J Cardiol*. 2000;85:945
82. Becker A, Leber A, Becker C, Knez A. Predictive value of coronary calcifications for future cardiac events in asymptomatic individuals *Am Heart J*. 2008;155:154–160
83. Detrano R, Guerci AD, Carr JJ, et al Coronary calcium as a predictor of coronary events in four racial or ethnic groups. *N Engl J Med*. 2008;358:1336–1345
84. Raggi P, Callister TQ, Shaw LJ. Progression of coronary artery calcium and risk of first myocardial infarction in patients receiving cholesterol–lowering therapy. *Arterioscler Thromb Vasc Biol*. 2004;24:1272–1277
85. Callister TQ, Raggi P, Cooil B, et al Effect of HmG-CoA reductase inhibitors on coronary artery disease as assessed by electron–beam computed tomography. *N Engl J Med*. 1998;339:1972–1977
86. Achenbach S, Ropers D, Pohle K, et al Influence of lipid-lowering therapy on the progression of coronary artery calcification: a prospective evaluation. *Circulation*. 2002;106:1077–1081
87. Budoff MJ, Lane KL, Bakhsheshi H, et al Rates of progression of coronary calcium by electron beam tomography. *Am J Cardiol*. 2000;86:8–12
88. Schmermund A, Achenbach S, Budde T, et al Effect of intensive versus standard lipid-lowering treatment with atorvastatin on the progression of calcified coronary atherosclerosis over 12 months: a multicenter, randomized, double-blind trial. *Circulation*. 2000; 113:427–437
89. Arad Y, Spadaro LA, Roth M, et al Treatment of asymptomatic adults with elevated coronary calcium scores with atorvastatin, vitamin C, and vitamin E: the St. Francis Heart Study randomized clinical trial. *J Am Coll Cardiol*. 2005;46:166–172
90. Achenbach S, Moselewski F, Ropers D, et al Detection of calcified and coronary atherosclerotic plaque by contrast-enhanced, submillimeter multidetector spiral computed tomography: a segment-based comparison with intravascular ultrasound. *Circulation*. 2004;109:14–17
91. Leber AW, Knez A, Becker A, et al Accuracy of multidetector spiral computed tomography in identifying and differentiating the composition of coronary atherosclerotic plaques: a comparative study with intracoronary ultrasound. *J Am Coll Cardiol*. 2004;43: 1241–1247
92. Leber AW, Becker A, Knez A, et al Accuracy of 64-slice computed tomography to classify and quantify plaque volumes in the proximal coronary system: a comparative study using intravascular ultrasound. *J Am Coll Cardiol*. 2006;47:672–627
93. Schroeder S, Kopp AF, Baumbach A, et al Noninvasive detection and evaluation of atherosclerotic coronary plaques with multislice computed tomography. *J Am Coll Cardiol*. 2001;37:1430–1435
94. Caussin C, Ohanessian A, Ghostine S, et al Characterization of vulnerable nonstenotic plaque with 16-slice computed tomography compared with intravascular ultrasound. *Am J Cardiol*. 2004;94:99–100
95. Carrascosa PM, Capunay CM, Garcia-Merletti P, Carrascosa J, Garcia MF. Characterization of coronary atherosclerotic plaques by multidetector computed tomography. *Am J Cardiol*. 2006;97: 598–602
96. Pohle K, Achenbach S, MacNeill B, et al Characterization of noncalcified coronary atherosclerotic plaque by multi-detector row CT: comparison to IVUS. *Atherosclerosis*. 2007;190:174–180
97. Cademartiri F, Mollet NR, Runza G, et al Influence of intracoronary attenuation on coronary plaque measurements using multislice computed tomography: observations in an ex vivo model of coronary computed tomography angiography. *Eur Radiol*. 2005; 15:1426–1431
98. Achenbach S, Ropers D, Hoffmann U, et al Assessment of coronary remodeling in stenotic and nonstenotic coronary atherosclerotic lesions by multidetector spiral computed tomography. *J Am Coll Cardiol*. 2004;43:842–847
99. Moselewski F, Ropers D, Pohle K, et al Comparison of measurement of cross-sectional coronary atherosclerotic plaque and vessel areas by 16-slice multidetector computed tomography versus intravascular ultrasound. *Am J Cardiol*. 2004;94:1294–1297
100. Bruining N, Roelandt JR, Palumbo A, et al Reproducible coronary plaque quantification by multislice computed tomography. *Catheter Cardiovasc Interv*. 2007;69:857–865
101. Min JK, Shaw LJ, Devereix RB, et al Prognostic value of multidetector coronary computed tomographic angiography for prediction of all-cause mortality. *J Am Coll Cardiol*. 2007;50: 1161–1170
102. Choi EK, Choi SI, Rivera JJ, et al Coronary computed tomography angiography as a screening tool for the detection of occult coronary artery disease in asymptomatic individuals. *J Am Coll Cardiol*. 2008;52:357–365

Chapter 14

CMR AND DETECTION OF CORONARY ARTERY DISEASE

Eike Nagel and Juerg Schwitter

CONTENTS

J. L. Zamorano et al. (eds.), *The ESC Textbook of Cardiovascular Imaging*
DOI: 10.1007/978-1-84882-421-8_14, © Springer-Verlag London Limited 2010

Introduction

Dobutamine-cardiovascular magnetic resonance (dobutamine-CMR) and perfusion-CMR are readily available to assess patients with suspected coronary artery disease or to determine the haemodynamic relevance of patients with intermediate coronary artery stenoses. Both tests have good diagnostic accuracy (with dobutamine-CMR being more specific and perfusion-CMR being more sensitive) and provide prognostically relevant information. Patients with normal MR stress studies show an excellent prognosis (0.7% event rate per year for the first 2 years) and in most patients with negative studies, no further examinations need to be performed. In combination with scar imaging and the assessment of LV and RV function and mass, a rapid and complete work-up of a large group of patients can be offered.

CMR imaging has moved from niche applications to the centre of cardiovascular decision-making, especially for complex patients, and standardized procedures are available. The evidence on a large variety of indications, including the diagnosis and assessment of ischaemic heart disease, has accumulated rapidly over the last years. This chapter will focus on the diagnosis of ischaemia. CMR imaging offers several options for understanding patients with known or suspected coronary artery disease (CAD); it has been shown to yield prognostic value, and it may also be used to visualize and characterize coronary plaque in the future.

Detection of Ischaemia and Coronary Artery Stenoses

With CMR, three different options are available to assess patients for the presence of significant coronary artery lesions. The first option is the direct assessment of ischaemia, i.e. the assessment of dobutamine-induced wall motion abnormalities during dobutamine-CMR. The second option relies on the assessment of myocardial perfusion during vasodilator-induced hyperaemia by perfusion-CMR, and the third option is based on the visualization of the coronary arteries—magnetic resonance coronary angiography (MRCA).

The first two options provide physiological information on the haemodynamic consequences of stenoses, whereas the last option provides identical information to the interventionalists as they are used to invasive angiography (location and degree of coronary artery stenosis). The main indications for the use of MR in suspected CAD are patients with intermediate pre-test likelihood of CAD who are unable to exercise and who have interpretable ECGs, and patients with intermediate stenoses by luminography (CT or catheterization).[1] In these patients, dobutamine-CMR or perfusion-CMR are recommended and regarded as interchangeable, even though specific differences may exist (discussed below). The direct visualization of the coronary arteries with MRI is only recommended for coronary artery anomalies[1] (e.g. abnormal proximal course), is more a domain of CT, and will not be discussed in this chapter. Even though ischaemia imaging might be less intuitive than stenosis visualization, the assessment of haemodynamics rather than stenosis degree has several advantages. Most importantly, the severity of a luminal narrowing is only weakly related to the amount of blood flow reduction. Also, the evidence is excellent demonstrating the strong predictive value of ischaemia for future cardiac events.[2] Accordingly, confirmed ischaemia is a Class 1A indication for revascularization.[3] Nevertheless, such testing appears strongly underused, as only 45% of patients had ischaemia detection before interventions in the United States.[4] The COURAGE trial results are in good accordance with this finding, and further underline the need for adequate ischaemia testing to optimize outcome.[5]

Both DSMR and myocardial perfusion imaging are based on the fundamental concept that a decrease in myocardial perfusion represents the first of several events in the progression of myocardial ischaemia, which is known as the ischaemic cascade. Wall motion abnormalities follow perfusion defects a little later in the ischaemic cascade, but occur much earlier than ECG changes in anginal pain. However, wall motion abnormalities only occur with the induction of myocardial ischaemia, whereas perfusion defects show a maldistribution of blood flow. Consequently, wall motion abnormalities are less sensitive, but more specific for the detection of coronary artery stenoses.[6] A major advantage for wall motion imaging with CMR is that it is technically much less challenging than perfusion-CMR. In addition, it may be superior in more complex patients, such as post bypass surgery, after myocardial infarction, and those with reduced coronary flow reserve owing to micro-vascular disease.

Dobutamine-CMR

State-of-the-art scanners allow for rapid switching of the magnetic field resulting in very short measurement times. This allows us to perform high-resolution cine imaging of the heart at rest and under stress conditions up to heart rates of 200 beats per minute. Today's standard sequences (steady state free precession, SSFP) provide an excellent visualization of the endocardial border owing to a high contrast between blood and myocardium without the need for contrast medium (CM) injection. Image quality is independent of limiting acquisition windows.

Stress Agents

The limited space within the scanner necessitates the application of pharmacological stress agents (usually dobutamine) for the detection of inducible wall motion abnormalities. Pharmacological stress is a well-documented alternative stress method to ergometry, and is superior in patients who are not able to exert themselves adequately. Even though vasodilator (adenosine/dipyridamole) stress has been suggested for the induction of ischaemic wall motion abnormalities and is considered interchangeable with dobutamine stress, a significantly lower diagnostic accuracy for the detection of epicardial coronary stenoses, both with CMR and echocardiography, has been reported for vasodilator vs. dobutamine stress.[6]

Dobutamine-CMR Protocol

The pharmacological stress protocol for CMR follows the standard high-dose dobutamine/atropine regimen as used in stress echocardiography (Fig. 14.1). The myocardium is divided into 17 segments. At rest, each of these segments is visualized in two standard views (apical, mid, and basal short-axis view; 4-chamber, 2-chamber, and 3-chamber view). Dobutamine is infused intravenously at 3-minute intervals at doses of 10, 20, 30, and 40 µg/kg/min, and imaging is repeated in all views at each stress level. If target heart rate (age-predicted submaximal heart rate ([220 − age] × 0.85) is not reached at the maximal dobutamine dose, a maximal dose of 2 mg atropine is applied in 0.25 mg fractions. Termination criteria are identical to those of dobutamine stress echocardiography.[7]

Safety of Dobutamine-CMR

A report on the safety of high-dose dobutamine-CMR in 1,000 consecutive patients showed a safety profile similar to dobutamine stress echocardiography: one patient suffered sustained ventricular tachycardia with successful conversion, and no cases of death or myocardial infarction occurred. The patients included in this study reflect the clinical practice with an intermediate pre-test likelihood and >50% positive findings.[8]

Imaging Technique

MR cine imaging is usually performed with the patient in the supine position (Fig. 14.2). Surface coils with several elements (usually four to eight) are placed on the thorax for signal detection. SSFP sequences in combination with parallel image acquisition and retrospective ECG gating are routinely used. During an expiratory breath-hold of 4–6 s, a cine loop of >25 phases/cardiac cycle can be acquired up to heart rates of 200 beats per minute. The in-plane spatial resolution of MR cine scans is usually between 1.5–2 mm × 1.5–2 mm with a slice thickness of 8 mm.

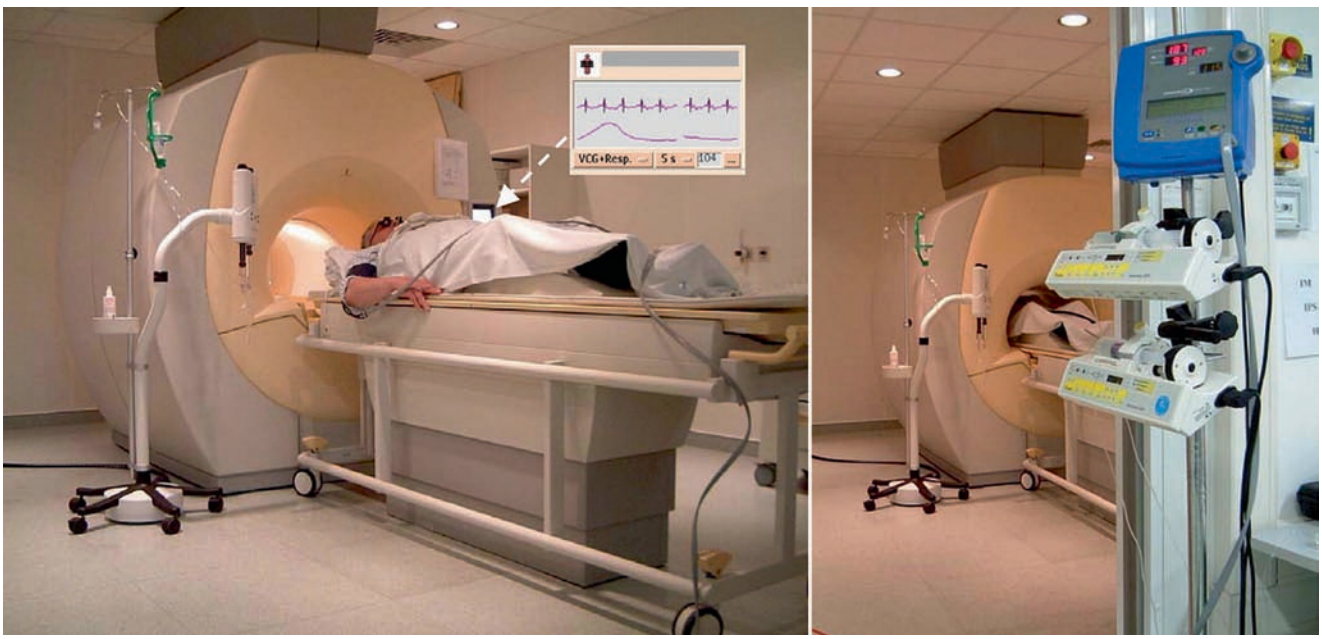

Fig. 14.1 Time sequence of high-dose dobutamine-atropine stress cardiovascular magnetic resonance. Reproduced from Wahl et al.[8]

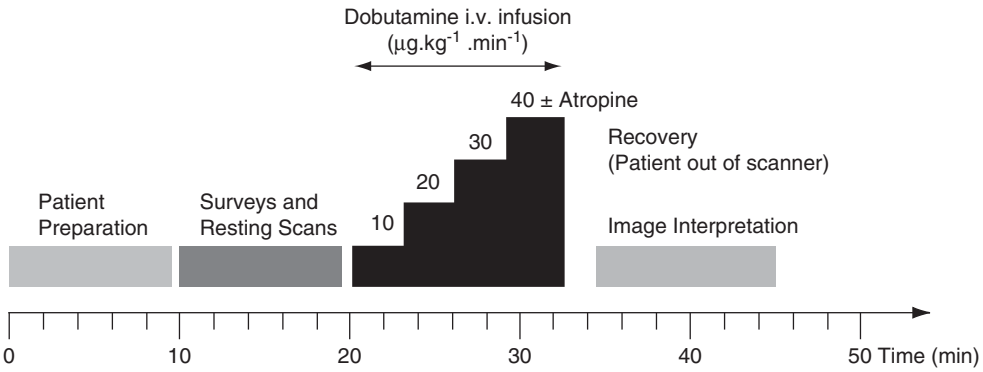

Fig. 14.2 *Left panel.* Overview of the 1.5 T clinical whole body MR tomograph (ACS NT, Philips, Best, The Netherlands) used for the study. The inset shows vector-ECG and respiratory monitoring, which is displayed both at the scanner (*arrow*) and on the operator's console. *Right panel.* Infusion pumps and blood-pressure monitoring system. Reproduced from Wahl et al.[8]

Image Display

During the pharmacological stress procedure, the examiner evaluates the MR cine images for the presence of new or worsening wall motion abnormalities. Cine images are displayed within 1 s after data acquisition and can be simultaneously transferred to an independent viewing station.

Diagnostic Criteria

Standard assessment of wall motion and wall motion abnormalities is performed visually for all 17 segments using a synchronized display of different dobutamine dose levels simultaneously (Figs. 14.3 and 14.4). First, the image quality is graded as good, acceptable or bad, and the

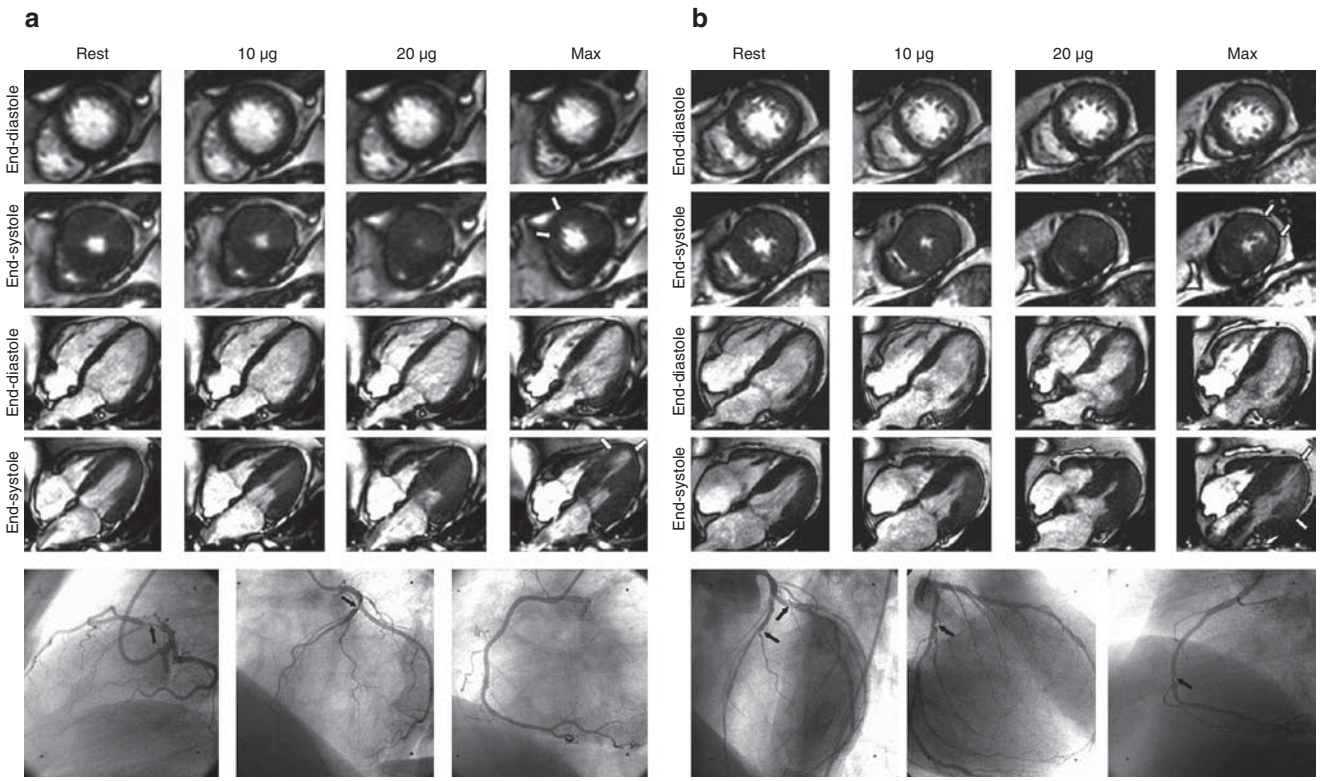

Fig. 14.3 **(a)** Cine images of the DSMR examination (apical short axis and 4-chamber view) in a patient with single-vessel disease of the LAD. The four readers showed perfect agreement regarding newly developed wall motion abnormalities in the anterior and anteroseptal segment and the apex (segment 17). **(b)** Cine images of the DSMR examination (apical short axis and 4-chamber view) in a patient with triple-vessel disease (significant stenoses of the first diagonal branch, proximal left circumflex, and distal RCA). The four readers detected newly developed wall motion abnormalities in the lateral wall (apical and equatorial segments). The development of a mitral regurgitation jet owing to ischaemic papillary muscle dysfunction is depicted as well. Reproduced from Paetsch et al.[12]

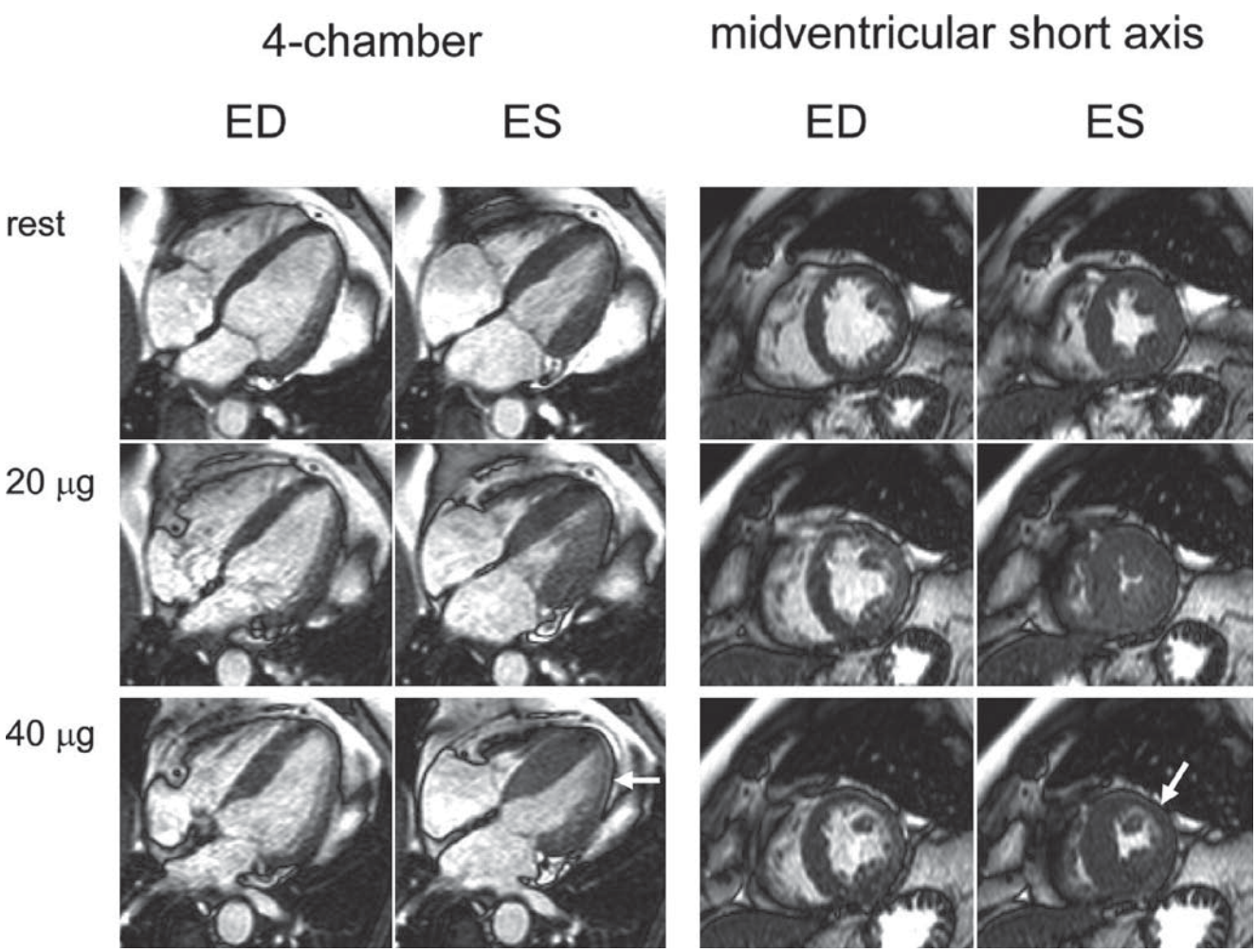

Fig. 14.4 4-chamber and mid-ventricular short-axis views at rest, and at intermediate- and peak-dose dobutamine stress (steady state free precession technique). Both end-diastolic (ED) and end-systolic (ES) frames are shown. Note the development of mid-lateral akinesia (*arrows*) at peak dobutamine stress. In this patient, invasive coronary angiography demonstrated a left circumflex coronary artery stenosis. Reproduced from Wahl et al.[8]

number of diagnostic segments is reported. Segmental wall motion is classified as normokinetic, hypokinetic, akinetic, or dyskinetic and assigned 1–4 points. The sum of the points is divided by the number of analyzed segments and yields a wall motion score. Normal contraction results in a wall motion score of 1, a higher score is indicative of wall motion abnormalities. During dobutamine stress with increasing doses, a decrease or no change in wall motion or systolic wall thickening are regarded as pathological findings.

Diagnostic Performance (Table 14.1)

In single-centre trials, dobutamine-CMR has been shown to be superior to dobutamine stress echocardiography for the detection of inducible wall motion abnormalities in patients with suspected CAD,[9] in patients with wall motion abnormalities at rest,[10] and in patients not well suited for second harmonic echocardiography.[11] The superiority of dobutamine-CMR has been attributed primarily to the consistently high endocardial border visualization inherent to the MR cine sequences, which is independent of limited acquisition windows, thereby allowing for the detection of subtle wall motion abnormalities. Thus, the gain in diagnostic accuracy is particularly high in those patients with inadequate acoustic windows or limited echocardiographic image quality despite the use of second harmonic imaging. The consistently high endocardial border visualization also leads to a high inter-observer reproducibility, as recently shown in a multi-centre read.[12] In a recent review, a meta-analysis of dobutamine-CMR for identifying coronary atherosclerosis resulted in a sensitivity of 87% with a specificity of 83%.[13]

Table 14.1. Diagnostic accuracy of stress wall motion studies

Author	Year	Journal	#	Characteristics	Sens	Spec	Comment
Dobutamine stress							
Pennell et al.[51]	1992	*AJC*	25	Suspected CAD	91	100	Non-breath-hold
van Rugge et al.[52]	1993	*JACC*	45	Suspected CAD	81	100	Non-breath-hold
Baer et al.[53]	1994	*Radiology*	35	Known CAD	84	–	Non-breath-hold
van Rugge et al.[54]	1994	*Circulation*	39	Suspected CAD	91	83	Non-breath-hold
Hundley et al.[11]	1999	*Circulation*	41	Suspected CAD	83	83	Poor acoustic windows on TTE
Nagel et al.[9]	1999	*Circulation*	172	Suspected CAD	86	86	Superior to dobutamine stress echo
Schalla et al.[55]	2002	*Radiology*	220	Suspected CAD	81	83	Real time imaging technique
Paetsch et al.[6]	2004	*Circulation*	79	Suspected or known CAD	89	81	Superior to perfusion imaging
Wahl[10]	2004	Radiology	160	Wall motion abnormalities	89	84	Patients with WMA at rest
Jahnke et al.[56]	2006	*Radiology*	40	Suspected or known CAD	89	75	4D single breath-hold technique
Paetsch et al.[12]	2006	*EHJ*	150	Suspected CAD	78	88	Multi-centre read
Vasodilator stress (adenosine or dipyridamole)							
Pennell et al.[57]	1990	*British Heart Journal*	40	Suspected CAD	62	100	Non-breath-hold
Baer et al.[58]	1992	*AJC*	23	Known CAD	78	–	Non-breath-hold
Zhao et al.[59]	1997	*Magn Res Imaging*	16	Known CAD	80*	75*	*Analysis by coronary territory
Paetsch et al.[6]	2004	*Circulation*	79	Suspected or known CAD	40	96	Inferior to dobutamine stress
Treadmill exercise stress							
Rerkpattanapipat et al.[60]	2003	*AJC*	27	Suspected CAD	79	85	Treadmill exercise stress

Functional Assessment of Viable Myocardium

In addition to the assessment of ischaemia, dobutamine-CMR offers the possibility of detecting viable myocardium after myocardial infarction. This information can be extracted from every dobutamine stress test and is based on the contractile response to low-dose dobutamine stimulation. Low-dose dobutamine stimulates recruitment of hibernating myocardium at a dose of 10–20 µg/kg/min. Thus, in areas with viable myocardium, typically a "biphasic response" can be observed with a wall motion abnormality at rest, improvement at low dose, and deterioration at high-dose dobutamine. When low-dose dobutamine stimulation was compared with scar imaging, it was found that low-dose dobutamine is superior to scar imaging in predicting recovery of function after revascularization.[14] This observation was most pronounced in segments with non-trans-mural scaring. As an explanation, it was suggested that even though scar imaging depicts the area of myocardial fibrosis, it does not assess the functional state of the surrounding (potentially viable) myocardium, and thus, its capability for the prediction of functional recovery of non-trans-murally scarred myocardium is limited. For a detailed discussion of viability imaging, readers can refer to.[15]

Prognostic Value of Dobutamine-CMR

Several single-centre studies have been presented on the prognostic value of dobutamine-CMR. Hundley et al.[16] found that

the presence of inducible wall motion abnormalities during dobutamine-CMR identifies patients at risk of myocardial infarction and cardiac death, independent of the presence of traditional risk factors for CAD. A low cardiac event rate was demonstrated in case of a negative dobutamine-CMR testing (2% over 2 years for patients with LVEF >40% and 0% over 2 years for patients with LVEF ≥60%). Recently, Jahnke et al.[17] reported a follow-up of 513 patients with known or suspected CAD for a median duration of 2.3 years. A normal dobutamine-CMR resulted in a cumulative event rate (death or myocardial infarction) of 1.2, 2.6, and 3.3% in the first 3 years, whereas patients with an abnormal dobutamine-CMR had a significantly higher event rate (7.3, 10.3, and 18.8% in the first 3 years).

Limitations

Dobutamine-CMR has several limitations, most of which are similar to dobutamine stress echocardiography.

1. Since the test is stopped, whenever a diagnostic wall motion abnormality occurs, the haemodynamically leading stenosis is detected. Potentially, other stenoses that cause significant ischaemia, but to a lesser extent, might be overlooked.
2. No quantification is performed and previous attempts to quantify regional wall motion have not been successful. One might draw conclusions on the severity of a stenosis from the stress level at which the wall motion abnormality occurs, however, since the haemodynamic response to the same dose of dobutamine is very different between different patients and even between two examinations of the same patient, this only provides a rough estimate.
3. Up to now, no multi-centre studies on dobutamine-CMR have been performed. This might be less important for dobutamine-CMR than for other techniques, e.g. perfusion-CMR, as the data acquisition is highly standardized and robust, and the variability of data interpretation has been assessed in a multi-centre read with good inter-observer variability. However, a multi-centre trial would enhance the evidence for this technique.

Conclusions

Dobutamine-CMR can be regarded the imaging method of choice in patients with moderate or worse echocardiographic image quality. It provides prognostically relevant information and can be used for pre-operative assessment of patients scheduled for non-cardiac surgery. In addition, functional assessment of viable myocardium with low-dose dobutamine-CMR is superior to myocardial scar imaging if scar trans-murality is <75%. This information is readily at hand in all patients with resting wall motion abnormalities referred for ischaemia testing with dobutamine-CMR.

CMR and Detection of Coronary Artery Disease: Perfusion-CMR

While dobutamine-CMR directly visualizes the functional consequences of ischaemia, i.e. impaired systolic thickening, perfusion-CMR utilizes a CM injection to probe myocardial perfusion. Consequently, for dobutamine-CMR, a direct proportional relation exists between ischaemia and function, i.e. a reduced function is directly indicative for the presence of ischaemia, and its measurement is only minimally dependent on the MR-acquisition technique. This is different for perfusion-CMR. Here, the relationship between perfusion and signal response in the myocardium is not linear; it might even be inverse and it depend on a variety of factors involving the type of the MR pulse sequence, the type and dose of CM, and other factors. Therefore, validation studies in the field of perfusion-CMR are of paramount importance. For example, one should keep in mind that a T_1-weighted MR perfusion pulse sequence combined with a rather low dose of a Gd-based CM will induce a signal increase during first-pass conditions, while in the same heart, a T_2-weighted perfusion sequence combined with a higher dose of the same Gd-based CM will induce a signal drop during first-pass conditions.[18] Many of these issues have been addressed in past studies, and the following discussion will only focus on the T_1-weighted approach in combination with Gd-based CM.

This chapter will not explicitly address other perfusion techniques like BOLD (*b*lood–*o*xygen *l*evel *d*ependent imaging)[19] or arterial spin labelling, which aim at perfusion measurements with endogenous CM. These techniques typically provide a rather flat relationship between myocardial signal and perfusion, and therefore appear limited at least with current approaches.

The "classical" T_1-weighted first-pass perfusion approach utilizing Gd-based conventional CM has now been validated in a large number of single-centre[6, 20–25, 48] and multi-centre studies[4, 26–28] against quantitative coronary angiography for its diagnostic performance in detecting coronary stenoses. The large multi-centre trials under the guidance of regulatory authorities[26–28] yielded evidence for a reliable and robust test for ischaemia detection and based on these studies, some Gd-chelates are officially approved for CMR use in many European countries. In centres with adequate expertise in perfusion-CMR, this technique is now an integral part of the work-up of patients with known or suspected

CAD. In patients with impaired LV function and suspicion of the presence of hibernating myocardium, the perfusion-CMR study is typically combined with a viability assessment. This viability assessment can be achieved by either low-dose dobutamine-CMR or the late gadolinium enhancement (LGE) CMR technique, with the first one demonstrating the functional reserve of hibernating myocardium upon inotropic stimulation and the second one directly differentiating scar tissue from viable myocardium, based on different CM distribution characteristics in the tissue.[29–31]

Perfusion-CMR: How It Is Used in the Detection/Monitoring of CAD

Principle of Perfusion-CMR and CMR Protocols

The perfusion-CMR approach in principle monitors the signal evolution in the myocardium during the first-pass of an MR-CM. To achieve this, a conventional Gd-based CM is injected into a brachial vein (injection rate about 5 mL/s) and simultaneously, the MR acquisition is started to acquire the perfusion data. At that point in time, the patient is instructed to hold his breath to eliminate motion artefacts in the data. To detect relevant hypo-perfusion, CM first-pass is assessed during hyperaemia (induced, e.g. by a standard dose of adenosine of 0.14 mg/kg/min over 3 min). A typical example is given in Fig. 14.5. As the first-pass situation during hyperaemic condition is as short as a few seconds, perfusion data acquisition is one of the most demanding tasks even for high-end state-of-the-art MR scanners. To obtain meaningful first-pass information, the LV myocardium must be covered with several short-axis slices every one to two heart beats, its spatial resolution must be adequate to differentiate trans-mural perfusion differences in the LV wall, and its sensitivity to the CM must yield a several-fold increase in signal vs. baseline during first-pass.[20] Accordingly, a huge variety of technical approaches was proposed for this goal.[32] Currently, the most precise and reliable results are obtained with a 90°-magnetization preparation applied for each slice, and read-out typically involves a type of hybrid-echoplanar pulse sequence. To further improve spatial and/or temporal resolution, this technique can be combined with parallel imaging strategies, and most recently, with temporo-spatial acceleration strategies[25,33] allowing to acquire perfusion information in the 1-mm range.[25] It should be kept in mind that the nominal spatial resolution of the MR pulse sequence is preserved because motion of the heart is eliminated during acquisition by ECG-triggering (eliminates cardiac contraction) and by breath-holding (eliminates respiratory motion).

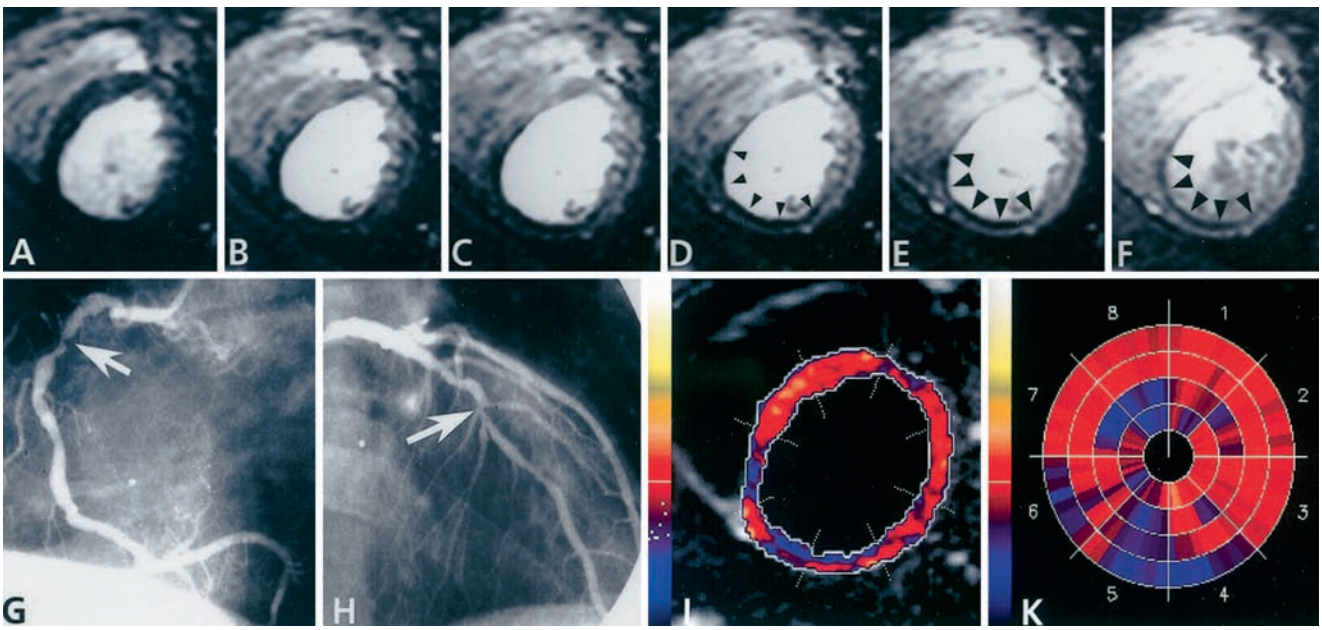

Fig. 14.5 In this patient with a stenosis in the right coronary artery (*arrow* in **g**), the transit of CM through the left ventricular myocardium during hyperaemia (time resolution, four slices every 1.2 s) demonstrates delayed wash-in in the subendocardium of sectors 4 through 6 (*arrowheads* in **d-f**). In the corresponding pixelwise parametric slope map **(i)**, the perfusion deficit is demonstrated in blue (colour-coding as in Fig. 14.1G). In **(k)**, a polar map represents perfusion in the subendocardium (with the apex located in the centre of the map and the anterior, lateral, inferior, and septal wall represented by sectors 1, 3, 5, and 6–8, respectively). The sub-endocardial perfusion deficit in the territory of the right coronary artery extends from base to apex, whereas the perfusion deficit in the anterior and septal wall (sectors 1, 7, and 8) extends from the mid-ventricular level to the apex (slices 3 and 4), in concordance with the stenosis in the mid-portion of the left anterior descending coronary artery (*arrow* in **h**). Reproduced from Schwitter et al.[48] with kind permission from the American Heart Association

While induction of hyperaemia by adenosine is straightforward and duplicates the approach already established for single-photon emission computed tomography (SPECT), the determination of the optimum CM dose is more challenging. The dose should be as high as possible with the aim to increase signal during first-pass. A higher dose (at the same injection speed) will also allow for a higher number of heart beats to be sampled during the first-pass, and thus, will provide more data points on a given signal-intensity—time curve. At higher CM doses, it is of particular importance to assure that the pulse sequence used is not susceptible for magnetic field inhomogeneities that can be induced by the high CM concentrations in the LV cavity during first-pass. Multi-centre data demonstrated an absence of susceptibility artefacts at the LV subendocardium up to a dose of 0.15 mmol/kg for a given MR pulse sequence.[27] Currently, doses of 0.075–0.10 mmol/kg are recommended.

Two types of protocols are mainly pursued when perfusion-CMR is performed. With both the protocols, detection of CAD is achieved by a stress-only protocol. In the case where a perfusion abnormality is present during hyperaemia, an LGE study is added to differentiate whether the perfusion deficit is located in viable myocardium or not. If the perfusion deficit resides in viable myocardium, this myocardial tissue would most likely experience ischaemia during physical stress. If such areas represent a substantial amount of myocardium, the corresponding coronary artery should undergo revascularization.[3] On the other hand, if the perfusion deficit resides in scar tissue, i.e. the LGE study is depicting this myocardial tissue with a high signal, such hypo-perfused, but scarred tissue is not expected to benefit from revascularization (see example in Fig. 14.6). This stress-only perfusion-CMR/LGE protocol corresponds to the principle of the

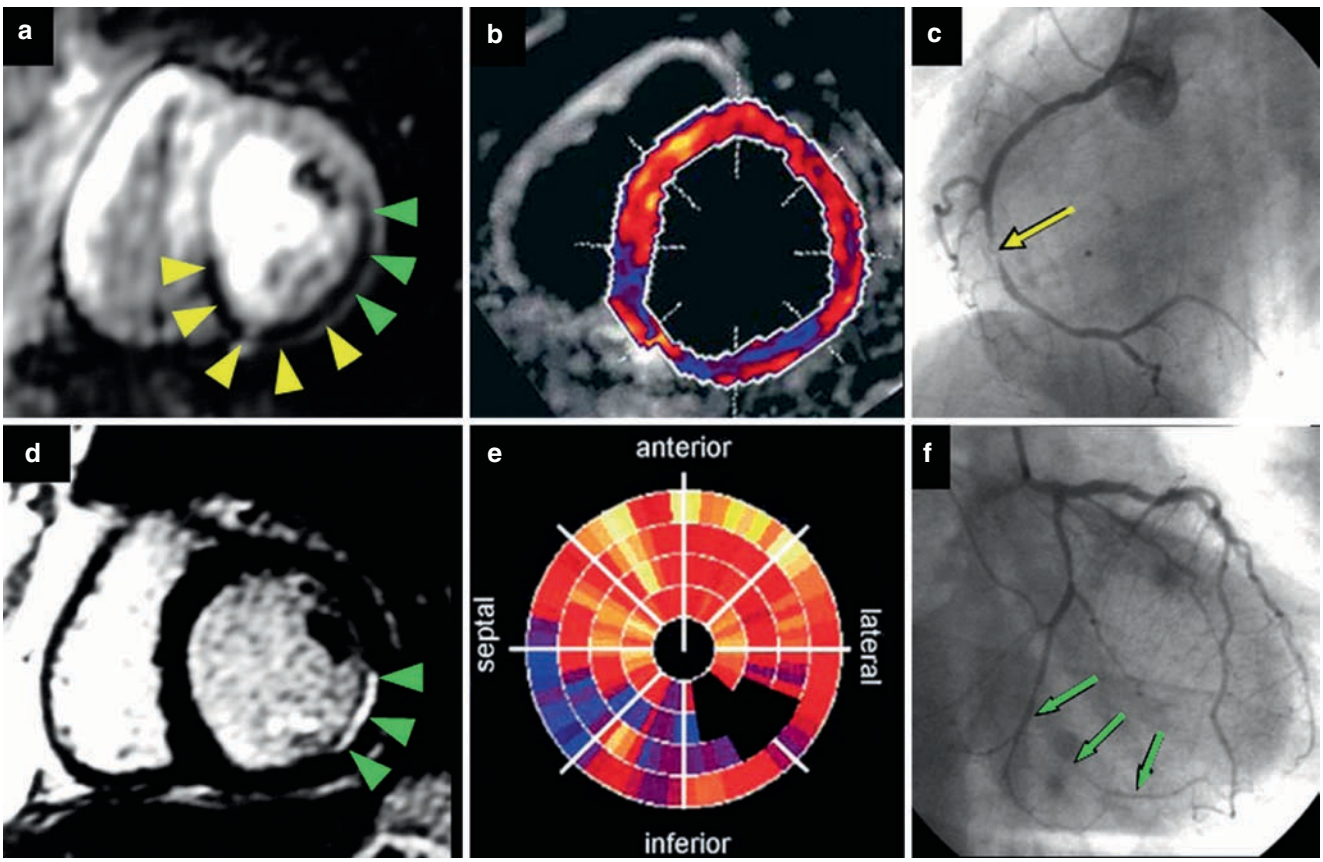

Fig. 14.6 In a 48-year-old woman with atypical chest pain and dyspnea during exercise, a first-pass perfusion MR study **(a)** reveals a perfusion deficit in the sub-endocardial layer of the inferior wall extending into the basal portion of the septum and the lateral wall. A parametric map **(b)** demonstrates contrast medium wash-in kinetics for the slice shown in **(a)**. On this parametric map, linear upslope data above/below the threshold (mean of controls – 1.75 SD) are encoded in shades of red and blue, respectively. The sub-endocardial zone of hypo-perfusion is also detected by the computer algorithm. Subsequent conventional X-ray coronary angiography confirmed stenosis of the right coronary artery **(c)**. In the same patient, delayed enhancement MR imaging **(d)** revealed a small sub-endocardial infarction in the lateral wall (bright zone), while viable myocardium appears dark. A polar map representation of perfusion is shown in **(e)** (with colour-encoding as given in **b**). In addition, the zone of infarction is depicted as black area in the lateral wall. Note that polar map representation of perfusion and viability/scar is given for the sub-endocardial layer (inner half of myocardial wall). In addition to the stenosis in the right coronary artery **(c)**, conventional X-ray coronary angiography demonstrates an occluded branch of the circumflex coronary artery (*arrows*) with retrograde filling **(f)**. Reproduced from Fuster et al.[50] with kind permission from the International Society on Thrombosis and Haemostasis

scintigraphic approach, with the scintigraphy demonstrating ischaemic territories with the stress study and the rest injection study visualizing scar tissue through re-distribution of the radio-tracer. A more detailed description of these concepts is available elsewhere.[32] Alternatively, perfusion-CMR can involve a stress-rest protocol. This strategy follows the concept applied in PET imaging, where myocardial territories with (severely) reduced coronary flow reserve (CFR) are assigned to coronary vessels with haemodynamically significant stenoses.[34] CFR is calculated as $flow_{hyperaemia}/flow_{rest}$, which requires perfusion quantification and correction of determinants of oxygen demand at rest[35] that renders this approach less attractive for perfusion-CMR.[36] The stress-rest CMR protocol is then completed by an LGE study for assessment of viability, whereas the corresponding PET approach is completed typically by a metabolic PET study utilizing ^{19}F-fluorodeoxy-glucose.[37, 32] These various perfusion-CMR strategies (involving various pulse sequences, CM doses, protocols) have consequences with respect to the reading and analysis/post-processing of the data.

Reading and Perfusion Data Analysis

The acquisition of adequate perfusion data requires a high-end scanner, operator skills, and patient cooperation with respect to both the cessation of medication and caffeine intake as well as breath-holding during first-pass. Consequently, before perfusion data can be read or analyzed, a check for adequate image quality is crucial. It is certainly advantageous that the CMR data allow, in most cases, to decide whether artefacts are present or not. Or, in other words, artefacts such as motion during first-pass, extra-systoles, or ECG mistriggering during first-pass, ghosting, and wrap-around artefacts can be readily identified as such. The presence of a susceptibility artefact (signal drop in the subendocardium during high CM concentration in the LV cavity) is a pulse sequence/CM feature, and thus, is not expected to differ substantially among patients. This type of artefact should, therefore, be eliminated by adequate tailoring of the pulse sequence, shimming of the magnet, and administration of a correct CM dose.

In a recent multi-centre study, a blinded read identified 15% of data as inadequate in quality.[27] In the remaining 85% of data, semi-automatic analysis with comparison vs. a normal database, yielded an excellent area under the ROC curve (AUC) of 0.91 for the detection of CAD (>50% diameter stenoses) corresponding to a sensitivity and specificity of 91 and 78%, respectively.[27] The influence of data quality on diagnostic performance is illustrated in Fig. 14.7.

Figure 14.8 shows the various levels for data analysis, and it also addresses the issue of observer interference with the data. Clearly, a fully automatic analysis yielding a 100% reproducibility per definition would be desirable. As such, analysis tools would work reliably only in data sets of

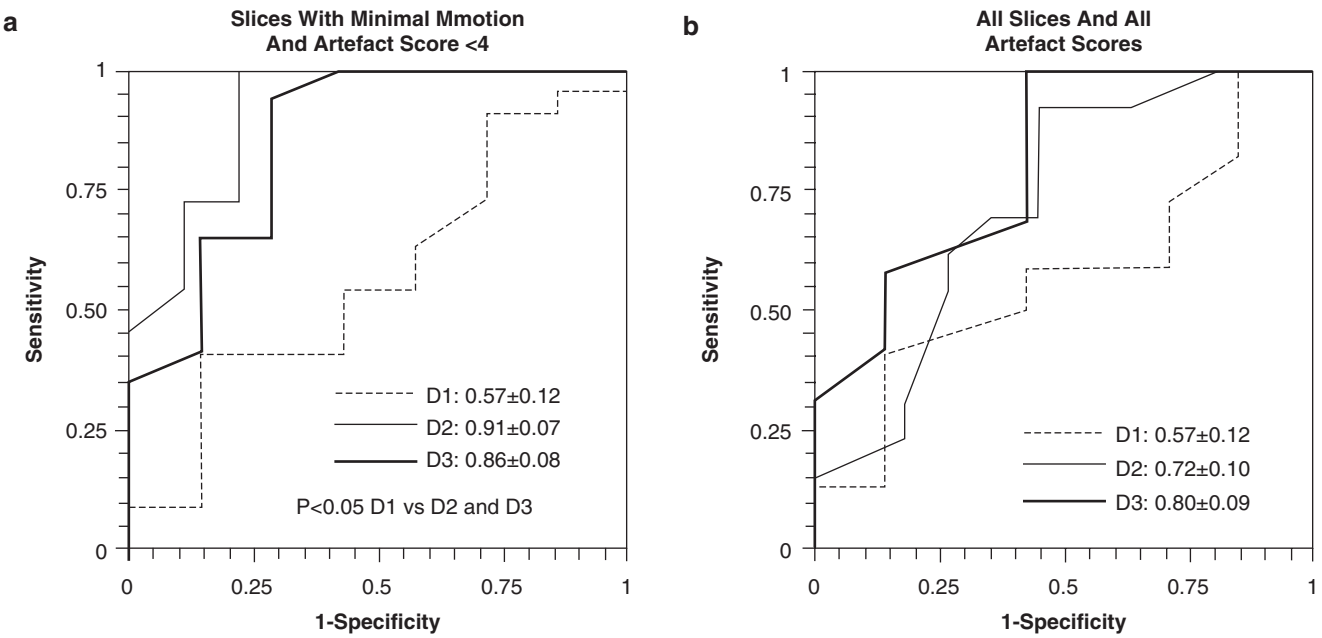

Fig. 14.7 ROC curves of MR upslope data are shown for the detection of coronary artery disease (≥50% diameter stenosis in ≥1 vessel by quantitative coronary angiography). MR upslope data from the subendocardial layer are highly reliable for the detection of disease when analysis is restricted to the three slices with minimal motion and the patients with adequate image quality. Numbers within the plots represent area under the ROC curve ± standard error for doses 1, 2, and 3 (=D1, D2, D3, respectively). AUC of dose 2 for the entire data (all slices, all quality scores, **(b)** was worst ($p < 0.05$ vs. *dose 2* in **a**). A dose of 0.05 mmol/kg (=D1) performed inadequately in all analyses. Reproduced from Giang et al.[27] with kind permission from the European Society of Cardiology

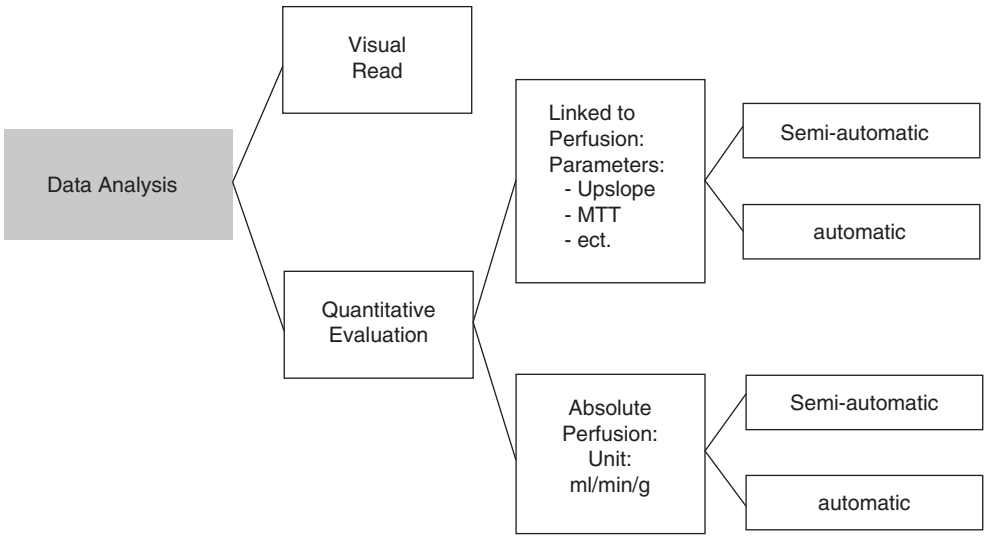

Fig. 14.8 Schematic for perfusion data analysis. *MTT* mean transit time

excellent quality; further improvement and standardizations for perfusion-CMR techniques are needed to allow for a semi-automatic or even fully automatic analysis of such data on a broad basis in clinical practice.

Diagnostic Performance

In the 1990s, the concept of first-pass perfusion MRI was successfully proven in animal studies.[38-40] Soon thereafter, first single-centre studies on humans confirmed the feasibility of this approach in a clinical setting. Inversion recovery preparation and single-slice strategies are nowadays replaced by saturation recovery preparation with identical delay times in multi-slice approaches (see Table 14.2 and Fig. 14.9). Also, higher CM doses in the range from 0.1 to 0.15 mmol/kg performed best.[27] With this setting, detection of CAD (defined anatomically by QCA) is typically achieved with sensitivities and specificities ranging from 75 to 90% as shown in Table 14.2. As a publication bias may influence this evidence, large multi-centre, multi-vendor trials are highly valuable for performance assessment, particularly, when these trials are monitored by official regulatory bodies.[26–28] The MR-IMPACT is the largest trial currently available and yielded a high AUC of 0.86, although 18 centres participated in this study involving all major MR machine types.[28] In this MR-IMPACT, which closely matches the real clinical situation, a sensitivity and specificity of 85% (95% CI: 69–93%) and 67% (95% CI: 35–89%) was achieved, respectively. Also, the perfusion-CMR proved robust with only 2.2% exclusion rate, and it was safe. The most severe adverse event in the 241 patients of this trial was angina over several minutes, most likely induced by the adenosine infusion; however, no death and no serious adverse events occurred.[28]

This diagnostic performance of perfusion-CMR is comparable with other imaging modalities such as stress echocardiography or SPECT.[41] Perfusion-CMR was compared with SPECT in the MR-IMPACT.[28] There was a significant superiority of perfusion-CMR to SPECT. However, no significance was found if perfusion-CMR was compared with gated-SPECT only (Fig. 14.10).[28] This data was confirmed in MR-IMPACT II,[42] which was performed in 33 centres. A sub-analysis of the MR-IMPACT II data also confirmed the superiority of perfusion-CMR over SPECT for both men and women.[42] The performance of perfusion-CMR in women is of particular importance, as women are more susceptible for radiation-induced cancer than men.[43–45]

A normal perfusion-CMR test also predicts a low event rate. This event rate, defined as cardiac death or non-fatal MI, was as low as 0.7% in the first year after a normal perfusion test and was 0.8%/year for a 3-year period after a normal test.[17] Thus, perfusion-CMR appears to be an excellent test to exclude prognostically relevant CAD, although evidence is not as large as for the scintigraphic techniques. Also, in the acute setting, perfusion-CMR confers prognostic information. A negative perfusion-CMR showed a 100% sensitivity, and a positive perfusion-CMR demonstrated a 91% specificity to predict future adverse cardiac events (MI, death, CAD on invasive coronary angiography, pathological SPECT during a 1-year follow-up).[46]

On considering the high diagnostic accuracy for the detection of CAD and also taking into account the data demonstrating the prognostic yield of perfusion-CMR, this new CMR application can be recommended as a valuable tool in the work-up of suspected or known CAD, at least in sites with adequate experience in this method. It is expected that for perfusion-CMR, similar indications will be established in future guidelines as for SPECT imaging.

Table 14.2. Performance of perfusion-CMR (1.5 T systems without inclusion of viability imaging)

	n	Protocol	CM (dose)	Acquisition	Analysis	Reference	AUC	Sens	Spe
Single centre studies									
Bertschinger et al.[20]	24	Stress-only	Gd-DTPA-BMA	Hybrid EP	Upslope	QCA	0.76	82%	73%
		Dip	0.1 mmol/kg	Same SR/slice	Trans stress	≥50% Stenosis			
Schwitter et al.[48]	57	Stress-only	Gd-DTPA-BMA	Hybrid EP	Upslope	QCA	0.91	87%	85%
		Dip	0.1 mmol/kg	Same SR/slice	Subendo stress	≥50% Stenosis			
Schwitter et al.[48]	43	Stress-only	Gd-DTPA-BMA	Hybrid EP	Upslope	$^{13}NH_3$-PET	0.93	91%	94%
		Dip	0.1 mmol/kg	Same SR/slice	Subendo stress	CFR < 1.7			
Nagel et al.[21]	84	Stress-rest	Gd-DTPA	Hybrid EP	Upslope	QCA	0.93	88%	90%
		Adeno	0.025 mmol/kg	Variable SR/slice	MPRI	≥75% Area stenosis			
Paetsch et al.[6]	79	Stress-rest	Gd-BOPTA	Hybrid EP	Visual	QCA	–	91%	62%
		Adeno	0.05 mmol/kg	Same SR/slice	Stress + rest	≥50% Stenosis			
Ishida et al.[22]	104	Stress-rest	Gd-DTPA	Hybrid EP	Visual	QCA	0.90	90%	85%
		Dip + handgrip	0.075 mmol/kg	Same SR/slice	Stress + rest	≥70% Stenosis			
Plein et al.[23]	92	Rest-stress	Gd-DTPA	Sense fast-GRE	Upslope	Visual	0.91	88%	82%
		Adeno	0.05 mmol/kg	Variable SR/slice	Subendo, MPRI	≥70% Stenosis			
Klem et al.[24]	92	Stress-rest	Gado-versetamid	Hybrid EP or	Visual	QCA	0.84	84%	58%
		Adeno	0.065 mmol/kg	Sense fast-GRE	Stress + rest	≥50% Stenosis			
				Same SR/slice		≥70% for left main			
Plein et al.[25]	54	Stress-only	Gadobutrol	Hybrid EP	Visual	QCA	0.85	–	–
		Adeno	0.1 mmol/kg	k-t-Sense	Stress	≥50% Stenosis			
Plein et al.[23]	35	Stress-only	Gadobutrol	Hybrid EP	Visual	QCA	0.80	–	–
		Adeno	0.1 mmol/kg	k-t-Sense	Stress	≥50% Stenosis			

Multi-centre trials									
Wolff et al.[26]	99	Stress-rest	Gd-DTPA-BMA	Hybrid EP	Visual	QCA	0.83	–	–
Monitored	3 centres	Adeno	0.15 mmol/kg	Same SR/slice	Stress + Rest	≥50% Stenosis			
	Single vendor								
Giang et al.[27]	99	Stress-only	Gd-DTPA-BMA	Hybrid EP	Upslope	QCA	0.91	91%	78%
Monitored	3 centres	Adeno	0.1 mmol/kg	Same SR/slice	Subendo stress	≥50% Stenosis			
	Single vendor								
Kitagawa et al.[4]	50	Stress-rest	Gd-DTPA	Hybrid EP	Visual	QCA	0.88	86%	75%
	3 centres	ATP	0.05 mmol/kg	Same SR/slice	Stress + Rest	≥50% Stenosis			
	Single vendor								
Schwitter et al.[28]	228	Stress-only	Gd-DTPA-BMA	Hybrid EP	Visual	QCA	0.86	85%	67%
"MR-IMPACT"	18 centres	Adeno	0.1 mmol/kg	or fast-GRE	Stress only	≥50% Stenosis			
Monitored	Multi-vendor			Same SR/slice					

Monitored: Trials were monitored by regulatory bodies (Food and Drug Administration (FDA) and European Medicines Agency (EMEA)).
Dip dipyridamole: 0.56 mg/kg for 4 min; *Adeno* adenosine: 0.14 mg/kg/min for 3 min; *ATP* 0.14 mg/kg/min for 3 min; *SR* saturation recovery preparation of magnetization; *hybrid EP* hybrid echo-planar acquisition; *fast-GRE* fast gradient-echo acquisition; *QCA* quantitative coronary angiography; *trans* full wall thickness considered in analysis; *subendo* inner half of wall thickness considered for analysis; *MPRI* myocardial perfusion reserve index; *AUC* area under the receiver-operator characteristics curve.

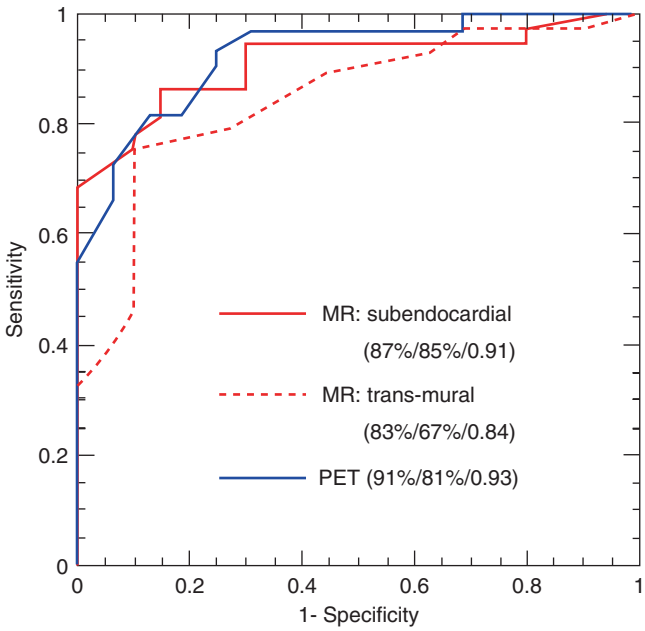

Fig. 14.9 ROC curves of MR upslope data are shown for the detection of coronary artery disease defined anatomically by quantitative coronary angiography (≥1 artery with ≥50% diameter stenosis; $n = 57$). MR upslope data, particularly from the sub-endocardial layer, are highly reliable in the detection of haemodynamically significant disease. In the detection of ≥50% diameter stenoses, the diagnostic performance of MR and PET are comparable. Numbers in parentheses represent sensitivity, specificity, and area under the ROC curve, respectively. Reproduced from Schwitter et al.[48] with kind permission from the American Heart Association

There is an increasing utilization of perfusion-CMR not only to detect obstructive coronary lesions. This technique has also been applied successfully to explore syndrome X,[47] as it discriminates more subtle sub-endocardial from transmural perfusion deficits.[47, 48]

Current Problems of the Technique and Future Developments

Perfusion-CMR is still a demanding technique, and, with an increasing request for such studies, the need for well-trained cardiac imagers will increase, and with it the need for ongoing standardization of this CMR application. Generally accepted protocols are now available and will be updated as the technique progresses.[61] Another limitation of CMR today is its restricted availability. Fortunately, common efforts are planned involving cardiac imagers from various fields, i.e. radiology, cardiology, and nuclear medicine, to address these issues. Along with this exists a heterogeneous and sometimes inadequate situation in Europe with regard to reimbursement of CMR studies. While CMR faces such "political" obstacles, there are also contraindications for CMR, as given in Table 14.3. With regard to pacemakers, the first MR-compatible pacemaker obtained approval from the European Medicines Agency (EMEA) for marketing in December 2008. Certainly, an increasing number of MR-compatible electronic devices will be available in the near future.

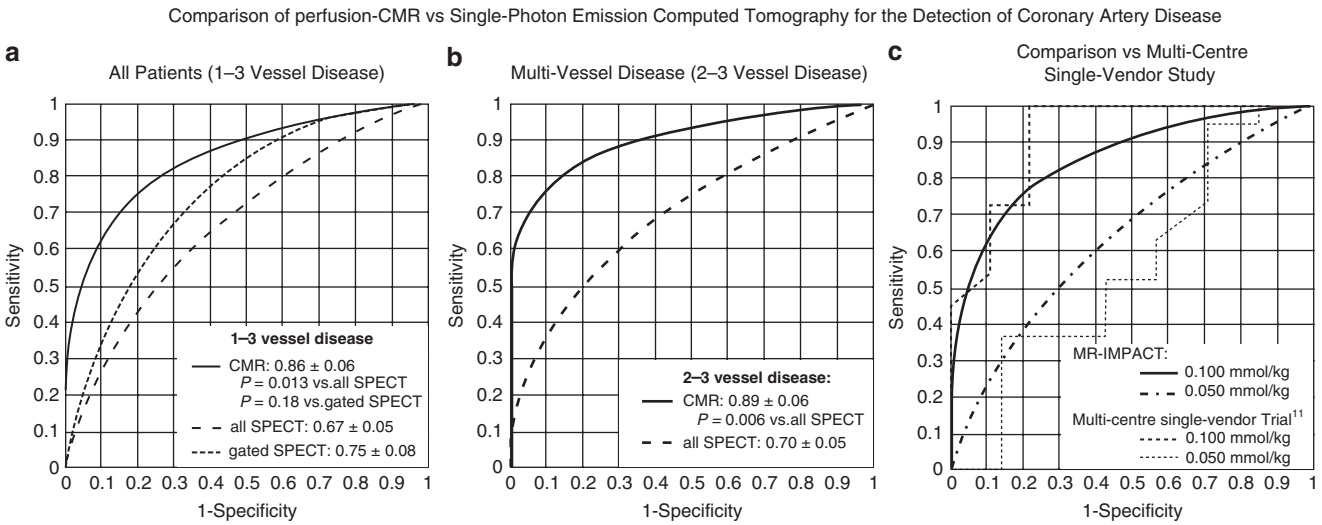

Fig. 14.10 MR-IMPACT: The area under the ROC curve for CMR is larger than for single-photon emission computed tomography (0.86 + 0.06 vs. 0.67 + 0.5 entire SPECT population, $p = 0.013$) for the detection of coronary artery disease. The difference between perfusion-CMR and gated-SPECT did not reach statistical significance. For multi-vessel disease in **(b)**, performance of perfusion-CMR is superior vs. the entire multi-vessel disease SPECT population (area under the ROC curve: 0.89 + 0.06 vs. 0.70 + 0.5, $p = 0.006$). The performance of perfusion-CMR in this trial is in good agreement with an earlier smaller multi-centre single-vendor trial as shown in **(c)**, assessing the doses of 0.10 and 0.05 mmol/kg (*thin dotted lines*).[29] Numbers indicate mean + SE of the area under the receiver operating characteristic curve. Reproduced from Schwitter et al.[28] with kind permission from the European Society of Cardiology

Table 14.3. Contraindications for CMR

Absolute Contraindications
Active devices such as pacemakers, ICDs, insulin pumps, and other electronic devices
Metallic foreign bodies in the eyes perform orbita X-ray in unclear cases
Relative Contraindication
Claustrophobia
MR-Conditional
Most of currently implanted stents, heart valves, sternum suture wires, cardiac closure and occluder devices, filters, embolization coils (at least up to 1.5 T)
Contraindications for Dobutamine-CMR
Severe arterial hypertension (> 220/120 mmHg)
Unstable angina pectoris
Acute myocardial infarction
Severe aortic stenosis (AVA < 1 cm^2)
Hypertrophic obstructive CMP
Acute perimyocarditis or endocarditis
Glaucoma
Contraindications for Perfusion-CMR
Contraindications for adenosine or dipyridamole infusion
AV-Block 2/3, trifascicular block, chronic obstructive pulmonary disease
Allergy against vasodilator
Allergy against contrast medium
Contraindication for gadolinium-chelate contrast media[a]
Severe renal impairment (GFR < 30 mL/min/1.73 m^2)
Relative contraindication: (GFR 30–60 mL/min/1.73 m^2)

Adapted with permission from Schwitter[61]

[a]Gd-chelates (primarily linear compounds) can cause nephrogenic systemic fibrosis (NSF) in patients with severe renal impairment. Approximately 270 cases of NSF were reported until June 2007 out of a total of approximately 110 Mio., administrations. For more information, see Schwitter[61]

Technically, there is still a trend towards higher-resolution perfusion-CMR.[25] Most likely, this will not substantially improve diagnostic performance, but it may be beneficial for (semi)automatic analysis of perfusion data, which would consequently improve post-processing reproducibility. An increase in field strength by moving from 1.5 to 3 T is accompanied by a better signal-to-noise ratio, which could be particularly useful for fast imaging as needed for perfusion-CMR. However, the techniques at 1.5 T are already very mature, and it seems difficult to outperform even at 3 T, as demonstrated in a recent study where the AUC for 3 and 1.5 T were not different for the detection of CAD (see Fig. 14.12).[25]

A new era in MR imaging is likely to be based on novel hyperpolarized CM. Hyperpolarization of ^{13}C-carbon is able to increase the magnetization by a factor of up to 10,000.[49] These CM will allow for better perfusion imaging, but most importantly, for real-time metabolic imaging as demonstrated in animal models.[32]

Conclusion

Perfusion-CMR has emerged as a novel and reliable technique for the assessment of CAD. It detects and excludes CAD with a high diagnostic performance, which as been confirmed in large multi-centre, multi-vendor trials (MR-IMPACT I and II). These trials also showed superiority of perfusion-CMR over SPECT. The evidence is now robust to recommend perfusion-CMR for the work-up of patients with suspected or known CAD, at least in centres with adequate experience. As perfusion-CMR lacks radiation exposure of patients, repetitive examinations can be ordered, even in women of lower age. Contraindications for perfusion-CMR are those of MR in general, in addition to the contraindications for CM and adenosine infusion. In patients with impaired resting LV function, a full work-up typically includes a viability test (LGE technique or low-dose dobutamine-CMR) that is added to ischaemia testing achieved by either perfusion-CMR or dobutamine-CMR.

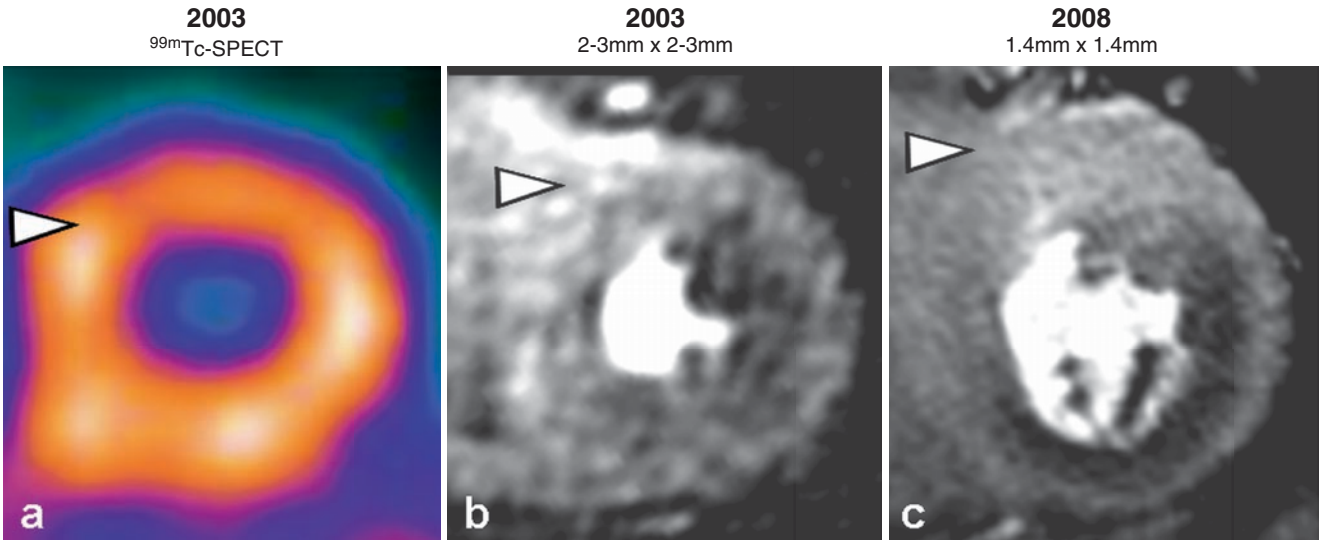

Fig. 14.11 This figure illustrates the impact of spatial resolution of perfusion data. A SPECT acquisition to the left **(a)** shows no clear perfusion deficit in this patient with a proven stenosis of >50% in the distal circumflex coronary artery. In the same patient, a perfusion-CMR study with higher spatial resolution **(b)** can resolve signal from the hypo-perfused lateral wall and the anterior papillary muscle. The nominal resolution of perfusion-CMR is preserved owing to the elimination of cardiac and respiratory motion during acquisition (ECG-triggering and breath-holding). Newer perfusion-CMR techniques exploiting temporo-spatial correlations of data allow for high-resolution imaging at 1.5T **(c)**. This allows for excellent discrimination of intra-mural perfusion differences (patient in c is not the same as in **a** and **b**). The *arrowhead* marks the anterior insertion of the right ventricular wall into the interventricular septum. Reproduced from Plein et al.[25] and Schwitter et al.[28] with kind permission from the European Society of Cardiology and the American Society of Radiology, respectively

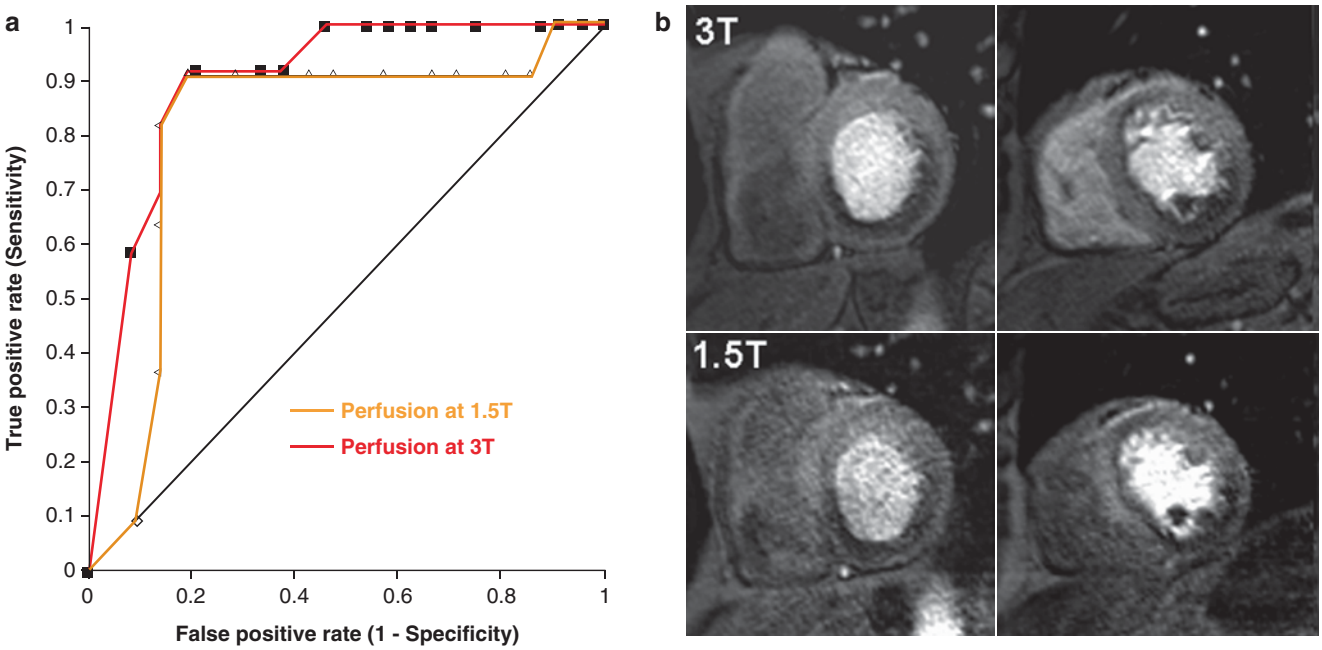

Fig. 14.12 A comparison of perfusion-CMR at 1.5 vs. 3 T yielded excellent results for both tests for the detection of coronary artery disease. With current techniques, the perfusion data at 1.5 T are of high quality, and the 3 T approach yielded similar results (area under the ROC curve not different, **a**). In **(b)**, an example is shown in a patient with perfusion deficits inferior and lateral, and a small deficit anterior. The coronary angiography confirmed a high-grade stenosis in the LCX, occluded RCA, and several minor lesions in the LAD. Reproduced from Plein et al.[25] with kind permission from Radiology

References

1. Hendel RC, Patel MR, Kramer CM, et al ACCF/ACR/SCCT/SCMR/ASNC/NASCI/SCAI/SIR 2006 appropriateness criteria for cardiac computed tomography and cardiac magnetic resonance imaging: a report of the American College of Cardiology Foundation Quality Strategic Directions Committee Appropriateness Criteria Working Group, American College of Radiology, Society of Cardiovascular Computed Tomography, Society for Cardiovascular Magnetic Resonance, American Society of Nuclear Cardiology, North American Society for Cardiac Imaging, Society for Cardiovascular Angiography and Interventions, and Society of Interventional Radiology. *J Am Coll Cardiol.* 2006;48(7):1475–1497
2. Iskander S, Iskandrian AE. Risk assessment using single–photon emission computed tomographic technetium–99m sestamibi imaging. *J Am Coll Cardiol.* 1998;32(1):57–62
3. Silber S, Albertsson P, Aviles F, et al Guidelines for percutaneous coronary interventions. *Eur Heart J.* 2005;26:804–847
4. Kitagawa K, Sakuma H, Nagata M, et al Diagnostic accuracy of stress myocardial perfusion MRI and late gadolinium–enhanced MRI for detecting flow–limiting coronary artery disease: A multicenter study. *Eur Radiol.* 2008;18:2808–2816
5. Boden WE, O'Rourke RA, Teo KK, et al Optimal medical therapy with or without PCI for stable coronary disease. *N Engl J Med.* 2007;356(15):1503–1516
6. Paetsch I, Jahnke C, Wahl A, et al Comparison of dobutamine stress magnetic resonance, adenosine stress magnetic resonance, and adenosine stress magnetic resonance perfusion. *Circulation.* 2004;110(7):835–842
7. Nagel E, Lorenz C, Baer F, et al Stress cardiovascular magnetic resonance: consensus panel report. *J Cardiovasc Magn Reson.* 2001;3(3):267–281
8. Wahl A, Paetsch I, Gollesch A, et al Safety and feasibility of high–dose dobutamine–atropine stress cardiovascular magnetic resonance for diagnosis of myocardial ischaemia: experience in 1000 consecutive cases. *Eur Heart J.* 2004;25(14):1230–1236
9. Nagel E, Lehmkuhl HB, Bocksch W, et al Noninvasive diagnosis of ischemia–induced wall motion abnormalities with the use of high–dose dobutamine stress MRI: comparison with dobutamine stress echocardiography. *Circulation.* 1999;99(6):763–770
10. Wahl A, Paetsch I, Roethemeyer S, et al High–dose dobutamine–atropine stress cardiovascular MR imaging after coronary revascularization in patients with wall motion abnormalities at rest. *Radiology.* 2004;233(1):210–216
11. Hundley WG, Hamilton CA, Thomas MS, et al Utility of fast cine magnetic resonance imaging and display for the detection of myocardial ischemia in patients not well suited for second harmonic stress echocardiography. *Circulation.* 1999;100(16):1697–1702
12. Paetsch I, Jahnke C, Ferrari VA, et al Determination of interobserver variability for identifying inducible left ventricular wall motion abnormalities during dobutamine stress magnetic resonance imaging. *Eur Heart J.* 2006;27(12):1459–1464
13. Mandapaka S, Hundley WG. Dobutamine cardiovascular magnetic resonance: a review. *J Magn Reson Imaging.* 2006;24(3):499–512
14. Wellnhofer E, Olariu A, Klein C, et al Magnetic resonance low–dose dobutamine test is superior to SCAR quantification for the prediction of functional recovery. *Circulation.* 2004;109(18):2172–2174
15. Bucciarelli–Ducci C, Wu E, Lee DC, et al Contrast–enhanced cardiac magnetic resonance in the evaluation of myocardial infarction and myocardial viability in patients with ischemic heart disease. *Curr Probl Cardiol.* 2006;31(2):128–168
16. Hundley WG, Morgan TM, Neagle CM, et al Magnetic resonance imaging determination of cardiac prognosis. *Circulation.* 2002;106(18):2328–2333
17. Jahnke C, Nagel E, Gebker R, et al Prognostic value of cardiac magnetic resonance stress tests. Adenosine stress perfusion and dobutamine stress wall motion imaging. *Circulation*. 2007;115(13):1769–1776
18. Saeed M, Wendland M, Yu K, et al Dual effects of gadodiamide injection in depiction of the region of myocardial ischemia. *J Magn Reson Imaging.* 1993;3(1):21–29
19. Fieno DS, Shea SM, Li Y, et al Myocardial perfusion imaging based on the blood oxygen level–dependent effect using T2–prepared steady–state free–precession Magnetic Resonance imaging. *Circulation.* 2004;110:1284–1290
20. Bertschinger KM, Nanz D, Buechi M, et al Magnetic resonance myocardial first–pass perfusion imaging: parameter optimization for signal response and cardiac coverage. *J Magn Reson Imaging.* 2001;14(5):556–562
21. Nagel E, Klein C, Paetsch I, et al Magnetic resonance perfusion measurements for the noninvasive detection of coronary artery disease. *Circulation.* 2003;108(4):432–437
22. Ishida N, Sakuma H, Motoyasu M, et al Noninfarcted myocardium: correlation between dynamic first–pass contrast–enhanced myocardial MR imaging and quantitative coronary angiography. *Radiology.* 2003;229(1):209–216
23. Plein S, Kozerke S, Suerder D, et al High spatial resolution myocardial perfusion cardiac magnetic resonance for the detection of coronary artery disease. *Eur Heart J.* 2008 July 18. [Epub ahead of print] PubMed PMID: 18641047; PubMed Central PMCID: PMC2519247
24. Klem I, Heitner JF, Shah DJ, et al Improved detection of coronary artery disease by stress perfusion cardiovascular magnetic resonance with the use of delayed enhancement infarction imaging. *J Am Coll Cardiol.* 2006;47(8):1630–1638
25. Plein S, Schwitter J, Suerder D, et al k–t SENSE–accelerated myocardial perfusion MR imaging at 3.0 Tesla – comparison with 1.5 Tesla. *Radiology.* 2008;249(2):493–500
26. Wolff SD, Schwitter J, Coulden R, et al Myocardial first–pass perfusion magnetic resonance imaging: a multicenter dose–ranging study. *Circulation.* 2004;110(6):732–737
27. Giang TH, Nanz D, Coulden R, et al Detection of coronary artery disease by magnetic resonance myocardial perfusion imaging with various contrast medium doses: first European multi–centre experience. *Eur Heart J.* 2004;25(18):1657–1665
28. Schwitter J, Wacker C, van Rossum A, et al MR–IMPACT: comparison of perfusion–cardiac magnetic resonance with single–photon emission computed tomography for the detection of coronary artery disease in a multicentre, multivendor, randomized trial. *Eur Heart J.* 2008;29:480–489
29. Schwitter J, Saeed M, Wendland MF, et al Influence of severity of myocardial injury on distribution of macromolecules: extravascular versus intravascular gadolinium–based magnetic resonance contrast agents. *J Am Coll Cardiol.* 1997;30(4):1086–1094
30. Kim RJ, Wu E, Rafael A, et al The use of contrast–enhanced magnetic resonance imaging to identify reversible myocardial dysfunction. *N Engl J Med.* 2000;343(20):1445–1453
31. Klein C, Nekolla SG, Bengel FM, et al Assessment of myocardial viability with contrast–enhanced magnetic resonance imaging: comparison with positron emission tomography. *Circulation.* 2002;105(2):162–167
32. Schwitter J. Myocardial perfusion imaging by cardiac magnetic resonance. *J Nuc Cardiol.* 2006;13(6):841–854
33. Kellman P, Derbyshire JA, Agyeman KO, McVeigh ER, Arai AE. Extended coverage of first–pass perfusion imaging using slice–interleaved TSENSE. *Magn Reson Med.* 2004;51:200–204

34. Schwaiger M. Myocardial perfusion imaging with PET. *J Nucl Med.* 1994;35(4):693–698
35. Schwitter J, DeMarco T, Kneifel S, et al Magnetic resonance–based assessment of global coronary flow and flow reserve and its relation to left ventricular functional parameters: a comparison with positron emission tomography. *Circulation.* 2000;101(23):2696–2702
36. Schwitter J. Myocardial perfusion in ischemic heart disease. In: Higgins CB, de Roos, A., ed. *MRI and CT of the Cardiovascular Systeme*. 2nd ed: Lippincott Williams & Wilkins; 2005
37. Knuesel PR, Nanz D, Wyss C, et al Characterization of dysfunctional myocardium by positron emission tomography and magnetic resonance: relation to functional outcome after revascularization. *Circulation.* 2003;108(9):1095–1100
38. Saeed M, Wendland MF, Sakuma H, et al Coronary artery stenosis: detection with contrast–enhanced MR imaging in dogs. *Radiology.* 1995;196(1):79–84
39. Wilke N, Simm C, Zhang J, et al Contrast–enhanced first pass myocardial perfusion imaging: correlation between myocardial blood flow in dogs at rest and during hyperemia. *Magn Reson Med.* 1993;29(4):485–497
40. Schwitter J, Saeed M, Wendland MF, et al Assessment of myocardial function and perfusion in a canine model of non–occlusive coronary artery stenosis using fast magnetic resonance imaging. *J Magn Reson Imaging.* 1999;9(1):101–110
41. Beller GA, Zaret BL. Contributions of nuclear cardiology to diagnosis and prognosis of patients wiht coronary artery disease. *Circulation.* 2000;101:1465–1478
42. Simor T, Wacker C, Wilke N, et al Detection of coronary artery disease in women by perfusion–CMR: comparison vs SPECT in a large multicenter multivendor trial (MR–IMPACT II). *Eur Heart J.* 2008; Annual Scientific Meeting, Munich, Germany. Abstract
43. Cardis E, Vrijheid M, Blettner M, et al Risk of cancer after low doses of ionising radiation: retrospective cohort study in 15 countries. *Br Med J.* 2005;331:77–82
44. National Research Council. www.nap.edu/catalog/11340.html
45. Einstein AJ, Henzkova MJ, Rajagopalan S. Estimating risk of cancer associated with radiation exposure from 64–slice computed tomography coronary angiography. *JAMA.* 2007;298:317–323
46. Ingkanisorn WP, Kwong RY, Bohme NS, et al Prognosis of negative adenosine stress magnetic resonance in patients presenting to an emergency department with chest pain. *J Am Coll Cardiol.* 2006;47(7):1427–1432
47. Panting JR, Gatehouse PD, Yang GZ, et al Abnormal subendocardial perfusion in cardiac syndrome X detected by cardiovascular magnetic resonance imaging. *N Engl J Med.* 2002;346(25): 1948–1953
48. Schwitter J, Nanz D, Kneifel S, et al Assessment of myocardial perfusion in coronary artery disease by magnetic resonance: a comparison with positron emission tomography and coronary angiography. *Circulation.* 2001;103(18):2230–2235
49. Ardenkjaer–Larsen JH, Fridlund B, Gram A, et al Increase in signal–to–noise ratio of > 10,000 times in liquid–state NMR. *Proc Nat Acad Sciences USA.* 2003;100(18):10158–10163
50. Fuster V, Corti R, Fayad ZA, Schwitter J, Badimon JJ. Integration of vascular biology and magnetic resonance imaging in the understanding of atherothrombosis and acute coronary syndromes. *J Thromb Haemost.* 2003;1(7):1410–1421
51. Pennell DJ, Underwood SR, Manzara CC, et al Magnetic resonance imaging during dobutamine stress in coronary artery disease. *Am J Cardiol.* 1992;70(1):34–40
52. van Rugge FP, van der Wall EE, de Roos A, Bruschke AV. Dobutamine stress magnetic resonance imaging for detection of coronary artery disease. *J Am Coll Cardiol.* 1993;22(2):431–439
53. Baer FM, Voth E, Theissen P, Schneider CA, Schicha H, Sechtem U. Coronary artery disease: findings with GRE MR imaging and Tc–99m–methoxyisobutyl–isonitrile SPECT during simultaneous dobutamine stress. *Radiology.* 1994;193(1):203–209
54. van Rugge FP, van der Wall EE, Spanjersberg SJ, et al Magnetic resonance imaging during dobutamine stress for detection and localization of coronary artery disease. Quantitative wall motion analysis using a modification of the centerline method. *Circulation.* 1994;90(1):12–138
55. Schalla S, Klein C, Paetsch I, et al Real–time MR image acquisition during high–dose dobutamine hydrochloride stress for detecting left ventricular wall–motion abnormalities in patients with coronary arterial disease. *Radiology.* 2002;224(3):845–851
56. Jahnke C, Paetsch I, Gebker R, Bornstedt A, Fleck E, Nagel E. Accelerated 4D dobutamine stress MR imaging with k–t BLAST: feasibility and diagnostic performance. *Radiology.* 2006;241(3): 718–728
57. Pennell DJ, Underwood SR, Ell PJ, Swanton RH, Walker JM, Longmore DB. Dipyridamole magnetic resonance imaging: a comparison with thallium–201 emission tomography. *Br Heart J.* 1990;64(6):362–369
58. Baer FM, Smolarz K, Jungehulsing M, et al Feasibility of high–dose dipyridamole–magnetic resonance imaging for detection of coronary artery disease and comparison with coronary angiography. *Am J Cardiol.* 1992;69(1):51–56
59. Zhao S, Croisille P, Janier M, et al Comparison between qualitative and quantitative wall motion analyses using dipyridamole stress breath–hold cine magnetic resonance imaging in patients with severe coronary artery stenosis. *Magn Reson Imaging.* 1997;15(8): 891–898
60. Rerkpattanapipat P, Gandhi SK, Darty SN, et al Feasibility to detect severe coronary artery stenoses with upright treadmill exercise magnetic resonance imaging. *Am J Cardiol.* 2003;92(5):603–606
61. Schwitter J (ed). *CMR Update*. 1st ed. Zurich; 2008. www.herz-mri.ch

Section 4

Heart Failure

Section 4

Heart Failure

Chapter 15

EVALUATION OF SYSTOLIC AND DIASTOLIC LV FUNCTION

Paolo Colonna and Rainer Hoffmann

CONTENTS

J. L. Zamorano et al. (eds.), *The ESC Textbook of Cardiovascular Imaging*
DOI: 10.1007/978-1-84882-421-8_15, © Springer-Verlag London Limited 2010

Evaluation of Left Ventricular Function in the Diagnosis of Heart Failure

Parameters of Systolic Function

The severity of left ventricular (LV) systolic dysfunction is a strong predictor of the clinical outcome for a wide range of cardiovascular diseases. Assessment of LV function is probably the most frequently requested indication to perform echocardiography and is an integral part of magnetic resonance imaging (MRI) and radionuclide studies. Visual estimates of global and regional function are supplemented by quantitative analysis of function. LV function is evaluated best from multiple tomographic planes, typically including parasternal long-axis, parasternal short-axis, apical 4-chamber, apical 2-chamber, and apical long-axis views. Systolic function relates to the function during the interval of the cardiac cycle lasting from mitral valve closure to aortic valve closure. LV diameters as well as ejection fraction and related volumes are the parameters normally determined to give a description of global LV function.

LV Dimensions and Volumes

The normal shape of the left ventricle is symmetric with two short axes of relatively similar length and a long axis from base to apex. Analysis of LV dimensions should consider gender and body surface area of the patient.[1] Table 15.1 shows the normal values for LV dimensions as well as the volumes and function.[1]

Global Systolic Function

The classic parameter of global systolic function is the ejection fraction, calculated from the end diastolic (LVEDV) and end systolic (LVESV) volumes of the left ventricle (EF = [LVEDV−LVESV]/LVEDV). The volumes provide clues to increased LV preload (increased end-diastolic volume) as well as increased afterload or impaired myocardial contractility (increased end-systolic volume). Using 2D echocardiography, the volumes should be determined using the modified Simpson's rule, applied monoplane on the apical 4-chamber view or biplane on the apical 4- and 2-chamber view. Typical difficulties in the analysis of these parameters using 2D echocardiography relate to a foreshortening of the apical views as the true apex is not visualized. This results in the under-estimation of systolic and diastolic volumes, while the analysis of ejection fraction is less affected. 3D echocardiography has been shown to result in significantly less under-estimation of LV volumes and high accuracy in the analysis of ejection fraction compared with the measurements obtained by MRI.[2] Another difficulty of current 2D echocardiographic techniques is the potential impairment of endocardial contours definition, in particular, using apical views resulting in inaccuracies with regard to definition of LV volumes. Administration of contrast agents may improve the accuracy in the analysis of volumes and ejection fraction.[3]

Doppler echocardiography allows evaluation of global LV systolic function based on the calculation of stroke volume and cardiac output. Using Doppler and 2D echo data, stroke volume is calculated as cross-sectional area of flow times the velocity-time integral of flow through that area: SV = CSA × VTI. However, the method is limited by potential inaccuracies related to the multiple required measurements.

Regional Systolic Function

Regional function abnormalities occur most frequently owing to coronary artery disease causing myocardial infarction, acute ischaemia, myocardial stunning, or hibernation. Dilative cardiomyopathy and myocarditis are less frequent causes. Regional LV function is normally evaluated considering a 16-segment model of the left ventricle (Fig. 15.1) as recommended by the American Society of Echocardiography, although a 17-segment model adding an apical segment has been suggested by the American Heart Association to homogenize with the myocardial scintigraphic perfusion analysis. Regional systolic function is characterized by wall thickening and endocardial inward motion. In clinical practice, regional function is evaluated visually using a qualitative score ranging from:

Table 15.1. Normal values of the left ventricle

	Women	Men
LV diastolic diameter (cm)	3.9–5.3	4.2–5.9
LV diastolic diameter/ BSA (cm/m^2)	2.4–3.2	2.2–3.1
LV diastolic volume (mL)	56–104	67–155
LV diastolic volume/ BSA (mL/m^2)	35–75	35–75
LV systolic volume (mL)	19–49	22–58
LV systolic volume/ BSA (mL/m^2)	12–30	12–30
Ejection fraction (%)	>55	>55

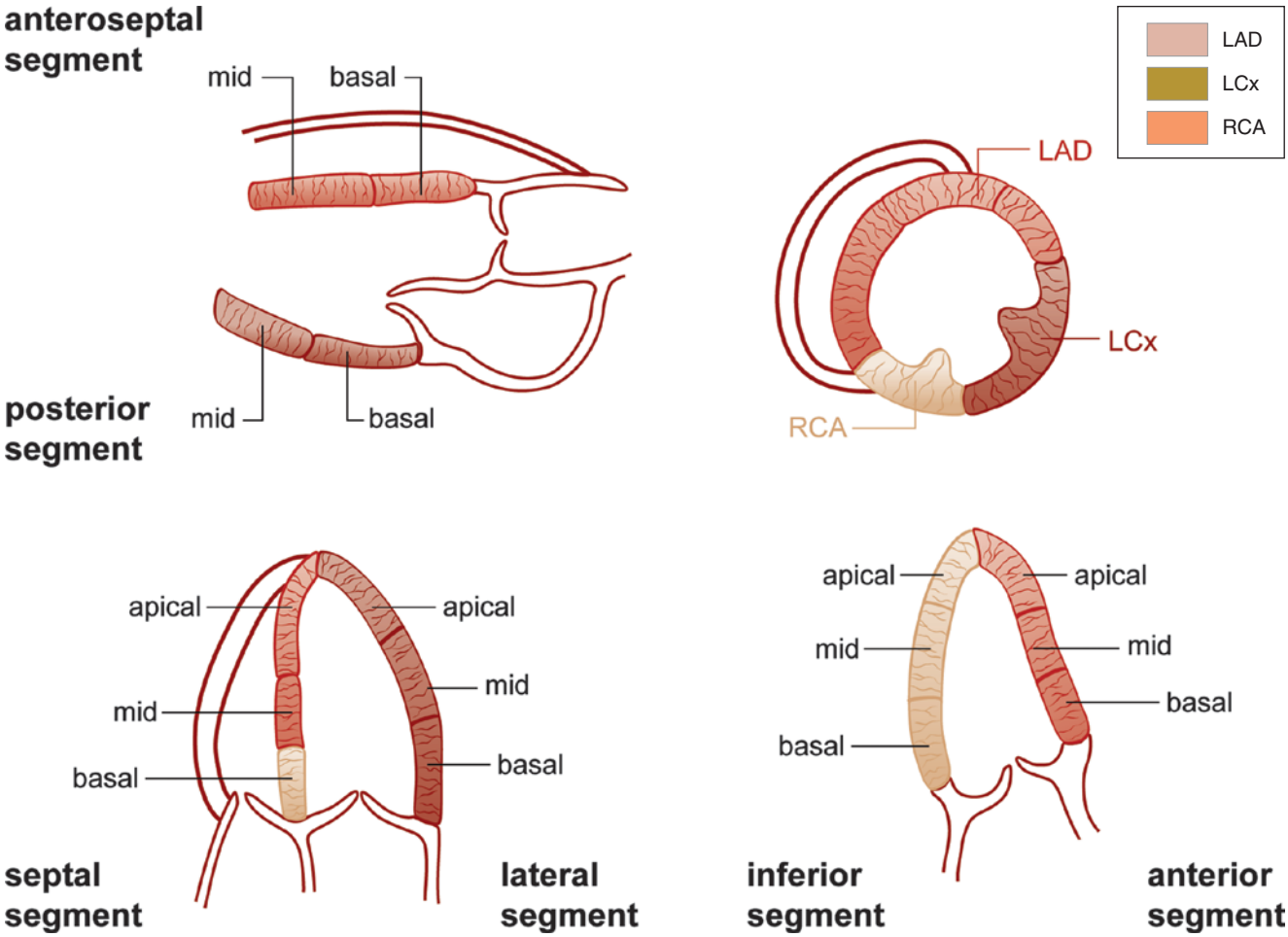

Fig. 15.1 16-segment model of the left ventricle according to the American Society of Echocardiography. The perfusion areas of the LAD (left anterior descending artery) and the joint territory of the RCA (right coronary artery) and LCX (left circumflex artery) are indicated

- Normokinesia: Normal inward motion and normal thickening
- Hypokinesia: Reduced but not absent inward motion and thickening
- Akinesia: Absent inward motion and thickening
- Dyskinesia: Systolic outward motion of the ventricular wall

Visual qualitative analysis of regional function on native 2D echocardiography has been found to be observer-dependent with only moderate to fair inter-observer agreement. A special difficulty relates to segments with poor visibility in which there is pronounced insecurity of the observers on the correct analysis of function. Application of left heart contrast agents enhances the visibility of endocardial systolic motion, and thereby improves accuracy of function analysis as well as agreement between different observers on regional function analysis[4] (Fig. 15.2). Owing to its superb image quality, MRI is known to allow high-quality assessment of LV function in almost all patients.

Several approaches for the quantification of regional systolic function have been suggested. Myocardial deformation imaging is based either on tissue Doppler velocity analysis or on speckle tracking within 2D echocardiograms, which are currently the preferred modalities for quantification[5, 6] (Fig. 15.3). However, derived strain and strain rate data may be affected by artefacts and noise, particularly in cases of impaired image quality.

Other Derived Indexes of Systolic Function

In addition to conventional parameters to describe global LV function, several other indexes have been suggested recently.

- The longitudinal shortening of the left ventricle significantly contributes to the ejection. A high correlation between the long-axis amplitude of the mitral annulus motion determined in apical views and the ejection fraction could be proven.
- Myocardial deformation imaging has been used to define a parameter of global LV function called global strain. This parameter obtained by speckle tracking analysis within 2D echocardiograms describes the degree of myocardial

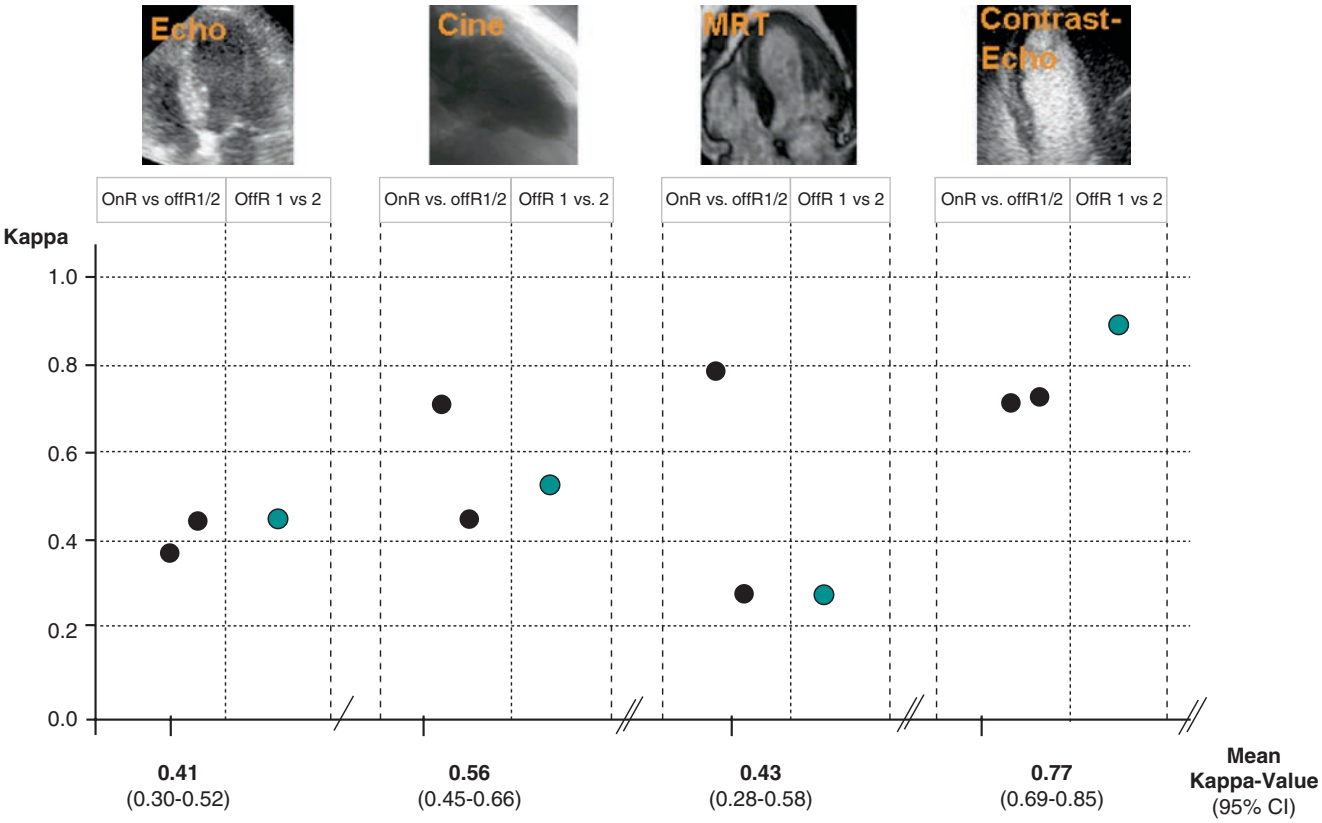

Fig. 15.2 Inter-observer agreement between three readers on cineventriculography, magnetic resonance imaging, echocardiography without and with contrast enhancement

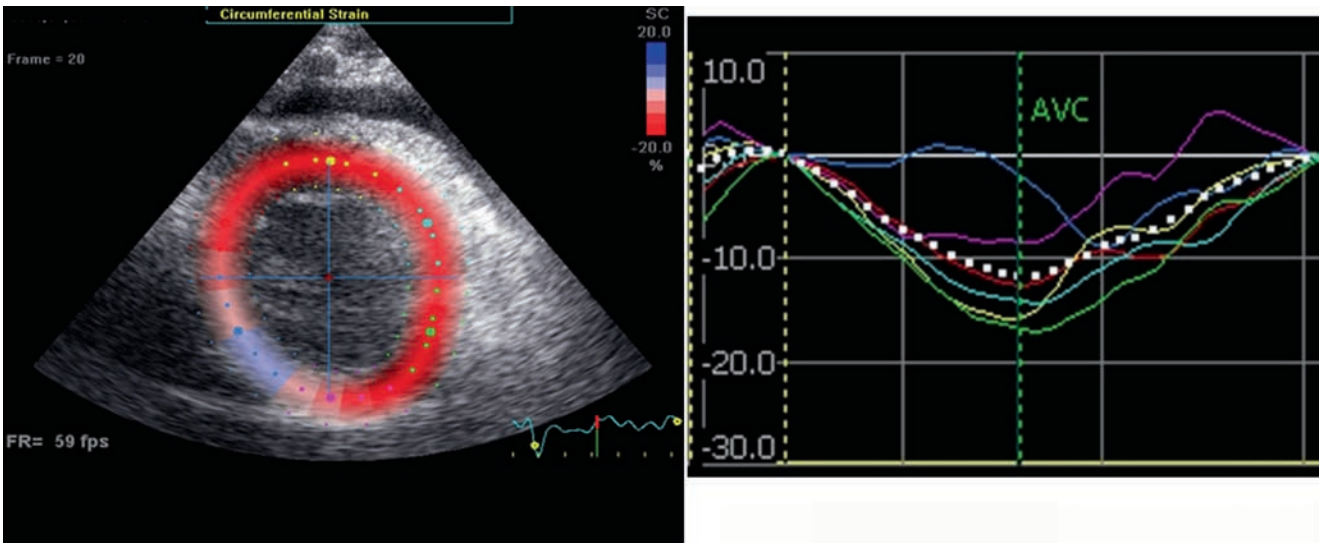

Fig. 15.3 Speckle tracking image showing circumferential strain of a patient with akinesia of the posterior wall

systolic shortening within all the segments of an apical view. This parameter has been found to have a high correlation with the LV ejection fraction (Fig. 15.3).

- Based on the analysis of a mitral insufficiency, early systolic pressure increase (dP/dt) can be calculated. Although this analysis is not based on the real LV pressure but a pressure difference between left ventricle and atrium, it provides a global parameter of LV contractility (normal >1,000 mmHg/s). To determine this parameter, the time interval between a regurgitant velocity of 1 m/s (equivalent

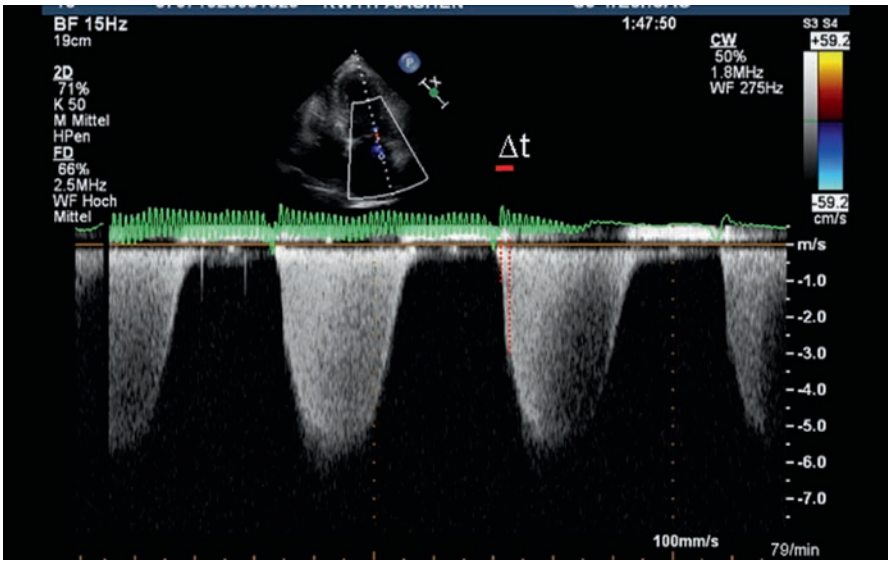

Fig. 15.4 Calculation of left ventricular pressure rise d*P*/d*t* from the mitral regurgitant jet

pLV- pLA t1= 4 mm Hg

pLV- pLA t2= 36 mm Hg

Δt = 60 msec

dp/dt = 36–4 mmHg/ 60ms

dp/dt = 533 mmHg/sec

to a ventriculoatrial pressure difference of 4 mmHg) and 3 m/s (equivalent to a ventriculoatrial pressure difference of 36 mmHg) is defined (Fig. 15.4).

- The myocardial performance index (MPI or Tei-index) provides a parameter of systolic and diastolic function.[7] It is based on the analysis of the Doppler mitral inflow and the aortic outflow signal to determine the time interval between the end of mitral inflow from a first cardiac cycle and the start of mitral inflow from the next cardiac cycle (A), as well as the duration of the ejection period (B). The MPI is calculated as A-B/B (Fig. 15.5). Myocardial diseases prolong the isovolumetric contraction and relaxation time. Thus, the value of MPI which is normally <0.49 increases.

Parameters of Diastolic Function

In a substantial number of patients with cardiac heart failure (CHF), a preserved systolic function is observed; therefore, it is also extremely important to evaluate the diastolic function. Diastolic dysfunction, estimated to be present in 15–45% of the patients with CHF, has been recently defined as heart failure with preserved ejection fraction (HFPEF) instead of diastolic heart failure.[8] In fact, for a precise definition of diastolic dysfunction, ascribing which part of the alteration is owing to the active and passive part of the diastole, a complex invasive pressure/volume relationship curve with cardiac catheterization should be performed. However non-invasive imaging techniques, and especially Doppler echocardiography, are able to observe several diastolic surrogates that give insight into

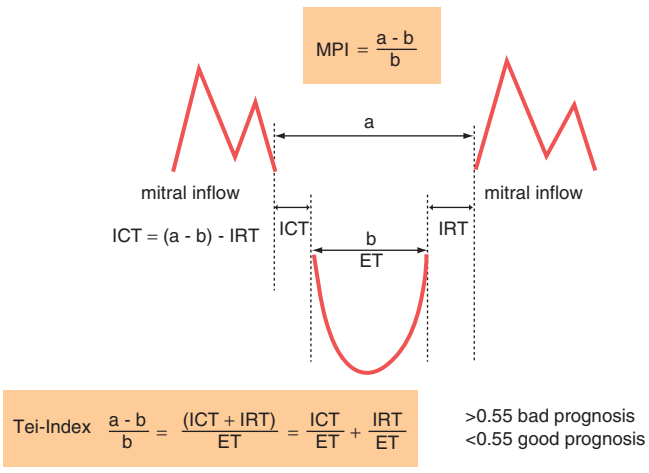

Fig. 15.5 Schematic illustration demonstrating the "myocardial performance index" from mitral inflow and left ventricular outflow profile

Table 15.2. Causes of heart failure with preserved left ventricular ejection fraction (HFPEF)

Diastolic heart failure owing to:	Primary cardiomyopathies (dilative, hypertrophic, restrictive, or non-compaction)
	Hypertension
	Infiltrative cardiomyopathy
Right heart failure owing to:	Severe pulmonary hypertension
	Right ventricular infarct
	Arrhythmogenic right ventricular dysplasia
Severe valvular stenosis and/or regurgitation	–
Cardiac tamponade	–
Constrictive pericarditis	–
Pulmonary vein stenosis	–
Congenital heart diseases	–

the diastolic function and identify a common clinical pathway (Table 15.2).

Normal Transmitral Inflow Velocities

In patients with stable sinus rhythm without significant mitral dysfunction, the spectrum of transmitral inflow velocities along the cardiac cycle and the calculation of time intervals allows for the estimation of the pressure gradients between left atrium and left ventricle, and thus, the dynamics of the LV filling and diastolic properties.[9]

The correct measurement of the transmitral inflow velocities is obtained by placing the sampling cursor parallel to the blood transmitral inflow (mostly in apical 4-chamber view), guided with the transmitral colour Doppler (Fig. 15.6). In patients with a marked LV dilation, it is useful to employ a 4-chamber view, with slightly modified positioning of the transducer laterally to the cardiac apex, to obtain a better alignment with the transmitral blood inflow (Fig. 15.7).

The sample volume has to be placed at the tip of the mitral leaflets during their opening to obtain the best spectrum and the highest E-wave and A-wave velocities (Fig. 15.8).

After optimization of the transmitral velocity spectrum, it is possible to divide the diastole into its four phases: (a) Isovolumic relaxation, when the LV relaxation begins and the intra-ventricular pressure declines after aortic valve closure (A2); (b) the rapid LV filling phase, after the mitral valve opening, owing to the left atrial pressure exceeding the LV pressure, with the early transmitral inflow (E-wave) observed at Doppler echocardiography; (c) the diastasis period, characterized by the equalization of atrial and ventricular diastolic pressure; and (d) the atrial contraction, with

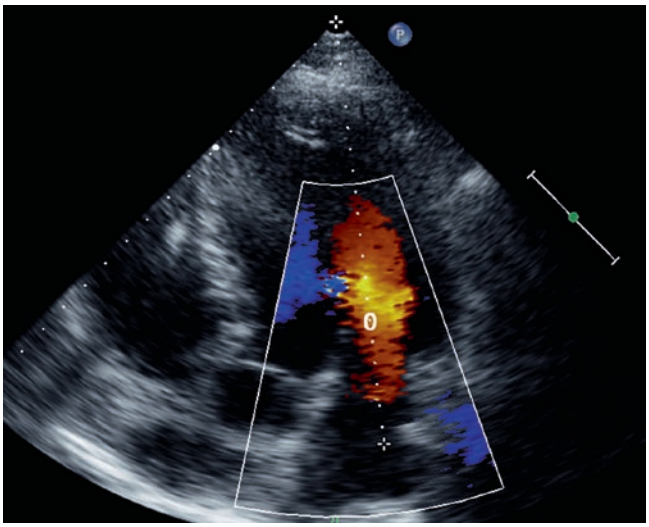

Fig. 15.6 Placement of the sampling cursor parallel to the blood transmitral inflow (in apical 4-chamber view), guided by the transmitral colour Doppler imaging

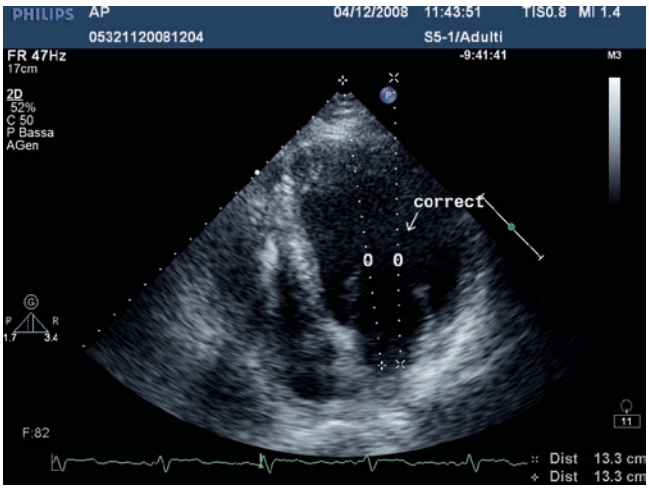

Fig. 15.7 A 4-chamber view with the correct positioning of the transducer, slightly lateral to the cardiac apex owing to LV dilation, for the best alignment with the transmitral blood inflow

the second increase in the LV filling (A-wave), owing to the new raise in the atrial pressure (Fig. 15.9).

Thus, the transmitral velocity spectrum can be used to calculate the E-wave velocity, A-wave velocity, deceleration time of E-wave, and isovolumic relaxation time (between the end of the LV ejection and the beginning of E-wave).

Abnormal Patterns of Transmitral Inflow Velocities

The first stage of diastolic dysfunction corresponds to the abnormal relaxation patterns (diastolic dysfunction stage I), with a delayed beginning of LV early filling (prolonged IVRT) and a reduced and prolonged early velocity (small E-wave with long deceleration time). Owing to this reduced early LV filling, the heart compensates with an increase in

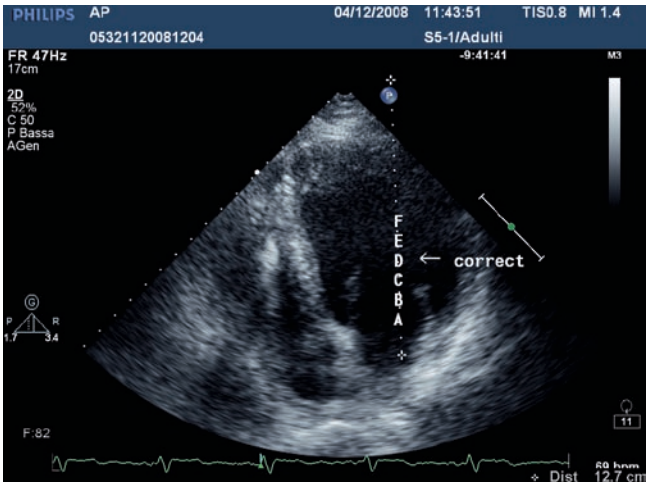

Fig. 15.8 Schematic diagram illustrating the positioning of the sample volume along the Doppler cursor. The correct positioning (*letter D*) is at the tip of the mitral leaflets during their opening, obtaining the best spectrum, and the highest E-wave and A-wave velocities

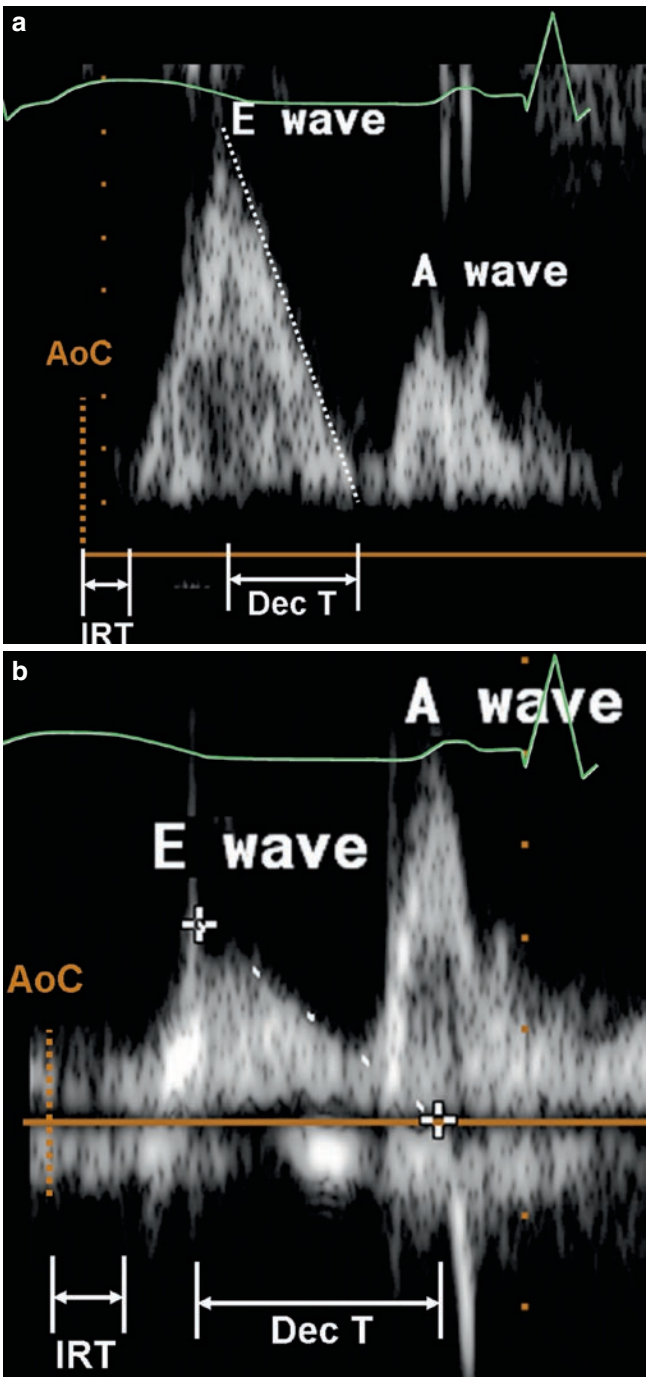

Fig. 15.9 Schematic illustration showing the deceleration time (Dec *T*) and isovolumic relaxation time (IRT) in the transmitral Doppler envelope from a subject with "normal diastolic pattern" (E/A > 1, Dec *T* = 185 ms and IRT = 85 ms) **(a)** and from a patient with "abnormal relaxation pattern" **(b)** (E/A < 1, Dec *T* = 277 ms and IRT = 120 ms). Range of values in different diastolic patterns are supplied in (**c**)

atrial contraction, causing an increased A-wave velocity (the E/A ratio is reduced with values <1).

With further disease progression, there is a reduction in LV compliance and the LV filling pressure begins to increase; at the transmitral flow, there is an increased early filling (there is normalization of the E/A with values >1) and the pseudonormalization pattern can be observed (diastolic dysfunction stage II). With this pattern, the study of pulmonary venous flow and mitral annular velocities is particularly useful for the diagnosis of pseudonormalization.

When the LV compliance is severely depressed and the LV filling pressure increases markedly, the diastolic restrictive pattern can be observed (diastolic dysfunction stage III). There is a high-velocity E-wave owing to the vigorous early filling (the E/A ratio is > > >1), with a brief IVRT, a steep (shortened) deceleration time, and very little additional LV filling during mid-diastole and atrial contraction.

If, additionally, in this restrictive pattern, the E/A ratio is fixed and cannot be reversed to a value <1 with the Valsalva manoeuvre, then the patient is considered to be in diastolic dysfunction stage IV with the highest LV filling pressure and the worst prognosis.

Pulmonary Venous Flow

The flow in the pulmonary and hepatic veins is used to complement the study of diastolic filling of the respective ventricles. The pulmonary venous flow, contrary to the hepatic one, does not change with respiration phases, unless in cases of cardiac tamponade, constrictive pericarditis, obstructive lung disease, and right ventricular infarction. It is recorded in 4-chamber apical view by placing the PW Doppler sample volume usually 1–2 cm into the lumen of the right upper pulmonary vein (refer to Table 15.3).

Normal pulmonary venous flow shows a systolic wave (s) higher than the diastolic (d) wave and a small amount of atrial reversal flow (AR) (Fig. 15.10). During relaxation abnormalities, the s-wave and the atrial reversal increase. During restrictive filling, the s-wave is limited by the high atrial pressure and the flow is predominantly diastolic;

Table 15.3. Imaging tips in the study of diastolic function with Doppler measurements

General suggestions	Use a colour flow guided imaging to align the Doppler cursor along flow propagation
	For the setting (to maximize axial and lateral flow resolution), use the lowest Doppler frequency (e.g. 2 MHz)
	The lowest Doppler filter
	A low Doppler gain
	The smallest sample volume (sized at 1 mm)
	The optimized velocity scale (maximized)
	For time intervals and deceleration time measurement, use higher sweep speeds (100 cm/s)
	For respiratory variations in flow patterns assessment, use shorter sweep speeds
For the study of mitral inflow velocity	Place PW sample volume at MV leaflet tip
	In patients with marked ventricular dilation position, the transducer laterally to the cardiac apex (for the best alignment with the blood inflow)
For the study of pulmonary venous flow velocity	Optimize the visualization of the roof of the left atrium in apical 4-chamber view
	Use a larger sample volume for pulsed Doppler (3–5 mm)
	Place the pulsed Doppler sample volume 1–2 cm into the lumen of the right upper pulmonary vein
For the study of Mitral annulus E' velocity	Use lateral and septal mitral annular E' velocities
	Use the cursor for Doppler interrogation aligned along the line of annular motion
	Place the pulsed Doppler sample volume (3–5 mm) where the spectrum of annular motion is clear

moreover, the atrial reversal wave has a higher velocity and a longer duration than in the normal subjects. A high and long atrial reversal wave is the most important point to differentiate abnormal diastolic patterns (including pseudonormalization) from the normal one.

Doppler Tissue Imaging of Mitral Annulus and Other Derived Indices of Diastolic Dysfunction

Several other derived indices can be useful in the detection of diastolic dysfunction, and besides, the execution of the Valsalva manoeuvre can be used to differentiate the "pseudonormal" from "normal" pattern in patients with an E/A wave ratio >1.

Using Doppler tissue imaging, the pulsed wave sample volume is placed in the medial or lateral mitral annulus to assess its systolic motion (S'-wave), early (E'-wave), and late/atrial (A'-wave) diastolic motion (refer to Table 15.3). The E'-wave velocity is relatively load-independent and correlates with the invasive measures of myocardial relaxation; a value of <8.5 cm/s is considered to be a rather accurate sign to detect "pseudonormal" pattern in patients with an E/A wave ratio of >1. When the E'-wave velocity is analyzed in conjunction with the E-wave of transmitral flow, the ratio between the transmitral flow E-wave velocity and mitral annulus early velocity E' (E/E' ratio) should be calculated. The E/E' ratio is an indicator of LV end diastolic pressure[10]: when its value is >15, it accurately identifies patients with advanced diastolic dysfunction (pseudonormal or restrictive pattern); when its value is <8, there is no diastolic dysfunction; and in the grey zone with an E/E' ratio between 8 and 15, other echocardiographic techniques should be used to determine the diastolic dysfunction[11] (Fig. 15.11).

Comparison of Strengths and Weaknesses of Different Modalities and Techniques

When a clinician has to choose the best imaging technique to evaluate the left and right ventricular function, he/she has to take into account the accuracy of different imaging techniques in calculating the exact function, the eventual presence of contraindications, and to balance the advantages and limitations in that particular subset of patients. The availability of a particular imaging technique is often the first reason for the selection, especially in patients with limited mobility, while the absence of ionizing radiations is important in young patients and in those who need frequent reevaluations of ventricular function. The knowledge of all the characteristics, advantages, and limitations of different imaging techniques, summarized in Table 15.4, must guide the wise clinician to the right patient diagnostic management.

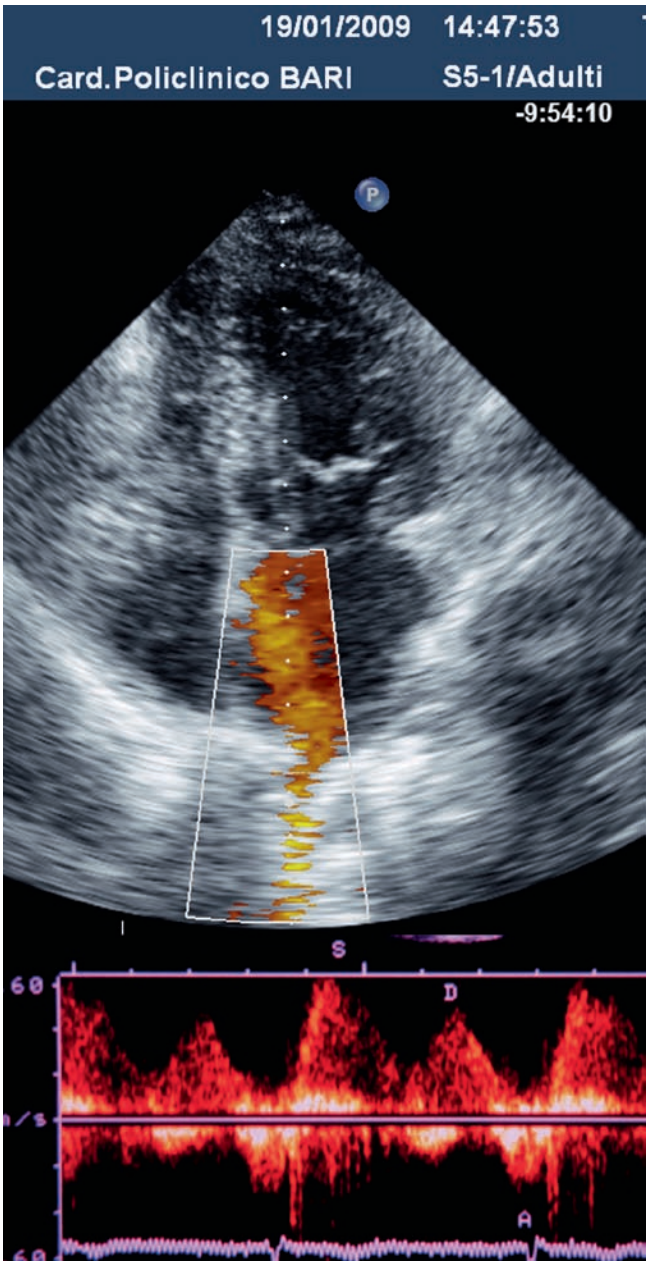

Fig. 15.10 Normal pulmonary venous calculated by positioning the PW Doppler sample of volume of 1.5 cm into the lumen of the right upper pulmonary vein (*upper panel*) with a pulmonary venous flow systolic wave (s) higher than the diastolic one (d), and a small amount of atrial reversal flow (A)

Echocardiography

Owing to its portability and immediate availability, Doppler echocardiography is considered as the technique of first choice (and very often, the single one utilized) to assess the regional and global LV function. Its features are also fundamental in all the uses in the emergency department and in the intensive care unit for the ancillary anatomic information. This widespread use as initial imaging diagnostic test is indeed owing to its capability of thoroughly detecting pathologies like ischaemic or non-ischaemic cardiomyopathies, valvular, pericardial, and other cardiac and extracardiac diseases. In a limited number of patients with unsatisfactory acoustic windows, the adoption of the tissue harmonic imaging, sometimes in conjunction with intravenous echo-contrast administration, can improve the wall motion and volumes analysis. The echocardiography has the highest temporal resolution among imaging techniques, and the spatial resolution is second only to last-generation MRI.

Analysis of regional wall motion is mainly based on subjective visual assessment. This qualitative analysis is limited by significant inter-observer variability. Administration of left heart contrast agents is able to improve endocardial border definition, and thereby can increase the observer's ability to define regional LV function. Using contrast-enhanced echocardiography, high inter-observer agreement and accuracy in the definition of regional wall motion could be demonstrated, which is comparable with MRI.

It is quick and useful for the estimation of RV function, although the 3D reconstruction of right ventricular volumes is still investigational. Conversely, the measurement of LV thickness and the calculation of LV mass are very precise with many confirmations in the medical literature. As extensively described, this technique has the greatest number of parameters to estimate the diastolic function.

The calculation of the ejection fraction and volumes is very accurate, especially when using echo-contrast and 3D echocardiography, although it is highly operator-dependent and the automatic analysis of these parameters is still suboptimal.

The patient's safety of echocardiography is at the highest level among different imaging techniques, because there is no use of ionizing radiation or nephrotoxic contrast material, and hence, it can be used for frequent follow-up examinations. In the end, with important practical implications, echocardiography is the most useful single technique in the cardiac imaging scenario when analyzing the cost/effectiveness ratio.

Cardiac Magnetic Resonance Imaging

Cardiac MRI has recently become the clinical gold standard for the quantitation of left and right ventricular volumes and mass, owing to its 3D nature.

The analysis of the regional function of left and right ventricle is very precise owing to the highest spatial resolution, the information on wall thickening, and the operator-independent imaging acquisition. However, the evaluation of the data obtained with MRI is found to be operator-dependent and does not reveal the best reproducibility, perhaps owing to the moving scanning plane (as stated in the previous paragraph).

MRI can supply information only partially achievable with novel echocardiographic techniques, such as the

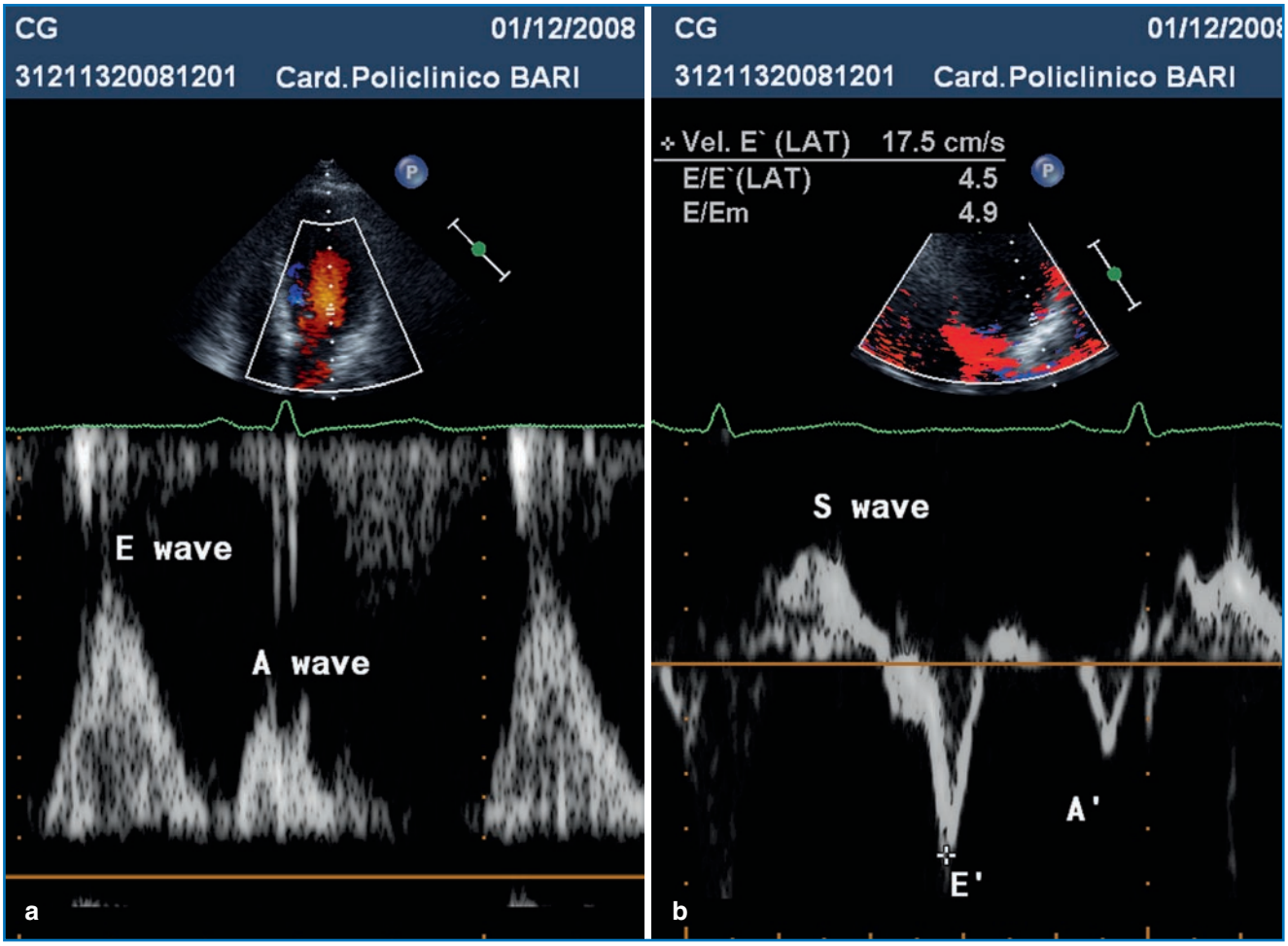

Fig. 15.11 Example from a normal subject showing a normal transmitral Doppler tracing **(a)** and a normal Doppler tissue imaging (PW sample volume placed in the lateral mitral annulus, **(b)** with a high early diastolic motion (E′-wave = 17.5 cm/s) realizing a E/E′ ratio of 4.5 (indicator of a normal LV end diastolic pressure). In the patient with diastolic dysfunction, the transmitral Doppler tracing shows an "abnormal relaxation pattern" **(c)** and an abnormal Doppler tissue imaging **(d)** with a low early diastolic motion at the PW sample volume of the lateral mitral annulus (E′-wave = 3.56 cm/s)

myocardial perfusion (obtained with gadolinium contrast) and the differential analysis of sub-endocardial, midwall, and sub-epicardial function (obtained with the tagging MRI). With high-speed MRI, it is possible to obtain the anatomical information and myocardial perfusion at the same time.

Similar to echocardiography, but with an increased spatial resolution, the MRI supplies ancillary anatomic information on ventricles and other cardiac and paracardiac structures that can be fundamental for a complete clinical diagnosis. It can also be very useful in the diagnosis of complex congenital heart disease and to visualize the coronary arteries, especially in their proximal part. Concerning the study of diastolic function, owing to the rotational and translational motion of the ventricle obtained with MRI tagging, the untwisting motion can be calculated in its time and direction and is a precise estimation of the diastolic properties of the LV.

Another important advantage of this technique is its clinical safety owing to the absence of ionizing radiation and the use of gadolinium contrast agent, with limited toxicity. However, several disadvantages of this technique still limit its utilization in clinical practice. The cost of a single MRI exam is still high, while the availability is limited (especially for cardiac-dedicated machine) and with no portability of the equipment. Patients with metallic prosthesis, pacemakers, implanted defibrillators, and other devices have to be excluded from the resonance analysis. Finally, there is a small percentage of subjects suffering from claustrophobia (especially during the pharmacologic stress test), which increases when analyzing elderly and severely ill patients.

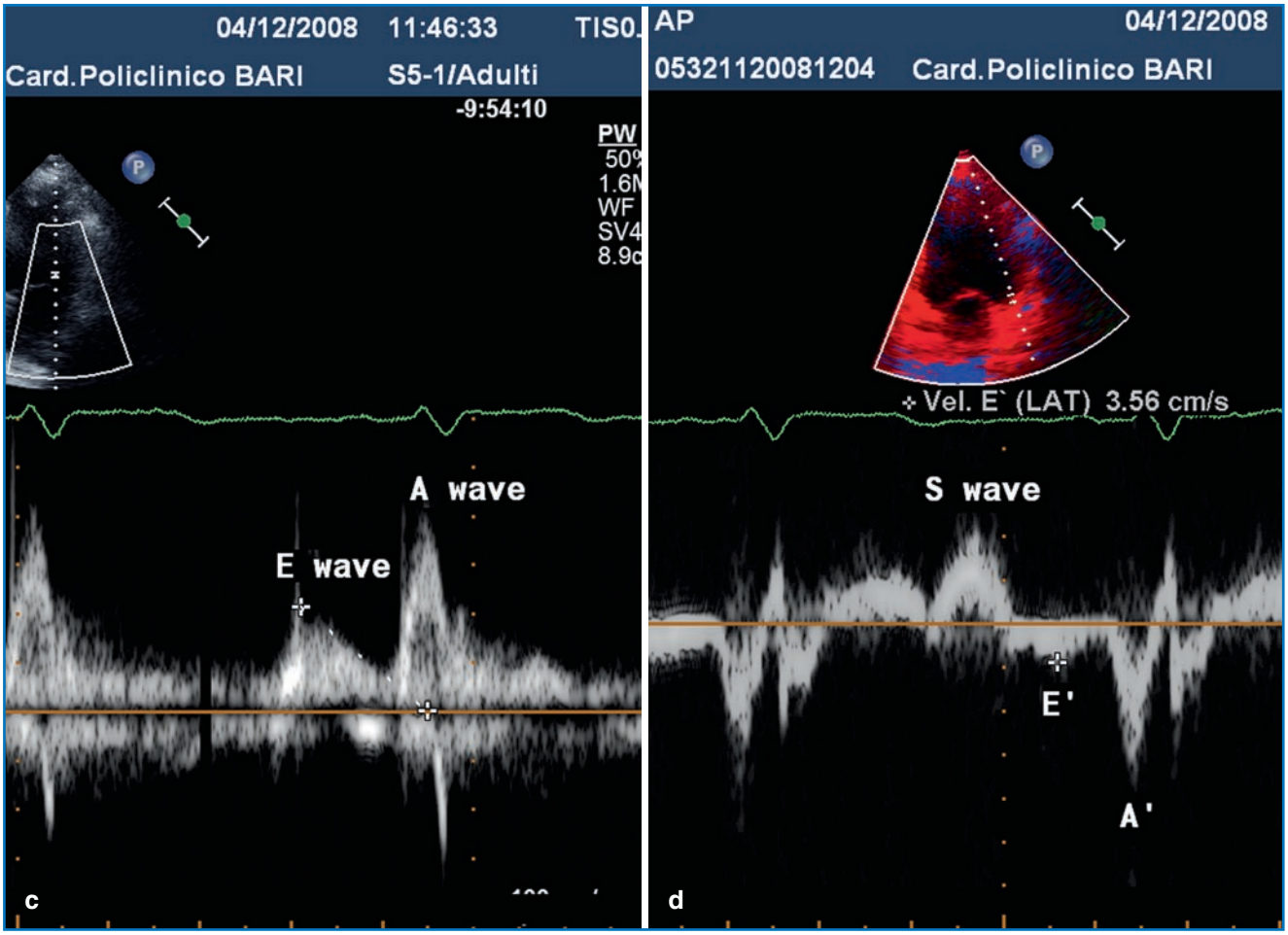

Fig. 15.11 (continued)

Nuclear Techniques

Two nuclear techniques can be used to evaluate left and right ventricular global and regional function: the radionuclide angiography (RNA), also known as radionuclide ventriculography, and the ECG-gated SPECT (single-photon emission computed tomography), for the simultaneous analysis of LV function and perfusion.

The RNA can be performed by first-pass or by equilibrium-gated modalities (often referred to as MUGA scanning), obtaining similar results, but using different tracings and data acquisitions.

The first-pass RNA has the advantages of great rapidity (the analysis is performed in 2–7 cardiac beats for right and left ventricle), a high signal-to-noise ratio, and a clear separation of left and right ventricle (with very rapid and clear definition of the right ventricular function).

The equilibrium-gated RNA, which is performed more commonly in clinical practice, has the advantage of identifying rapid changes during different conditions (stress-induced abnormalities) of multiple projections and high count density.

Both the RNA techniques determine the changes in the radionuclide counts in the left and right ventricles over the cardiac cycle generating time-intensity curves. Ventricular volumes can then be obtained with the comparison of the abovementioned counts with the counts in a blood sample of known volume. Thus, both the quantitative ejection fraction and volumes obtained in this way are not affected by any assumption of ventricular geometry. This point takes to the great advantage of RNA technique of high accuracy and reproducibility in the calculation of volumes and ejection fraction, used in several studies for accurate long-term follow-up calculations (e.g. in chemotherapy toxicity, ventricular re-modelling post-infarction, valvulopathy). Moreover, with RNA, it is also possible to obtain the LV time-activity curve, representative of the volume changes along the cardiac cycle. The computation of this curve derives several parameters of diastolic filling, which are well-related to Doppler echocardiographic diastolic measurements.

The major limitation of this technique is the lack of information on regional systolic thickening to supplement the

Table 15.4. Characteristics, advantages, and limitations of different imaging techniques to manage the diagnosis at best

	Echocardiography	Cardiac magnetic resonance	Nuclear radionuclide angiography (RNA)	Nuclear ECG-gated SPECT imaging
Operator skill (acquisition or evaluation)	Important in acquisition and evaluation	Important in evaluation	Mostly independent	Important in evaluation
Reproducibility	Dependent on acoustic window; excellent with contrast	Excellent in global function, good in regional	High	High
Spatial and temporal resolution	High	Highest spatial resolution	Intermediate	Limited with extensive perfusion defects
Perfusion	Investigational with contrast	Optimal resolution (also viability)	–	Largest data (also viability)
Regional systolic thickening	Largest data in literature	Includes different layers analysis (tagging)	–	Possible
Function during stress	Optimal	Optimal (expensive)	Feasible	Feasible
Diastolic dysfunction	Optimal	Untwisting study (tagging)	Quantitative LV filling	–
Three-dimensional analysis	Novel technique	Optimal	No	–
Ancillary structural info	Excellent	Excellent	Limited	No
LV hypertrophy and mass	Very good	Excellent	No	No
RV function assessment	Good (estimate)	Optimal	Accurate (direct)	No
Safety (ionizing radiation/contrast media)	Safe	Contrast (limited toxicity)	Ionizing radiation	Ionizing radiation
Portability and availability	Optimal	Limited	Limited	Limited
Cost	Lowest	High	Low	Low
Peculiar characteristics	Most useful and convenient as first /unique technique	Proximal coronary arteries visualization	Large literature data for function follow up	Simultaneous info on perfusion and function
Other limitations		Claustrophobia No metallic objects		

regional wall motion, and the lack of anatomic information supplementary to those on volumes and function.

The second nuclear method to evaluate ventricular function is the ECG-gated SPECT imaging, a recent and important evolution incorporated in the SPECT myocardial perfusion imaging, which enables the simultaneous analysis of LV function and perfusion. With this technique, every R-R interval at ECG is divided into several "frames" (generally eight), and owing to the synchronized gate openings of the detector, the myocardial wall is studied and reconstructed in each of these frames. A computed analysis rejects the ECG cycles above or below the limit of ±15% of the mean cycle length (such as in premature beats and atrial fibrillation). After a complex reconstruction, obtained with the gating of many cardiac cycles, the machine represents the LV wall in each frame, and it is possible to analyze the global and regional wall motion, calculating the end systolic and end diastolic volumes and ejection fraction.

This method has been studied mostly to supplement the myocardial perfusion study with regional and global wall motion, significantly improving both the sensitivity and specificity of this technique in determining stress-induced abnormalities (summation of perfusion and wall motion regional defects). Therefore, the major advantages of this technique are those related to the perfusion imaging, such as the study of myocardial infarction necrosis area, the amount of viable myocardium, and the presence of stress induced perfusion defects. A limitation of this technique is the imperfect spatial resolution in the presence of severe perfusion abnormalities, which interfere with the detection of the blood-endocardial edge of a part of the ventricular contour.

Both the nuclear techniques have the advantage of being mostly operator-independent. However, they share the disadvantages of the lack of portability of the machine and the patient's exposure to ionizing radiation.

Imaging to Guide the Treatment

As congestive heart failure is affected by high morbidity and mortality, it is very important to find information supplementary to those obtained in the clinical scenario to guide therapeutic management. Cardiac imaging has a great role in the diagnosis of systolic and diastolic dysfunction, both in patients with overt heart failure and with asymptomatic LV dysfunction.

First, in overt heart failure management, an individualized echocardiography-guided strategy that monitors the haemodynamic profile is able to evaluate the therapeutic effects much better than a conventional clinically oriented strategy. When echocardiography is used to guide pharmacologic therapy protocols in patients with heart failure and LV systolic dysfunction, mortality and hospitalization is reduced. In these patients, a larger amount of high-dose loop diuretics and vasodilators were used and a reduction in the pulmonary artery systolic pressure and systemic vascular resistance index was observed at echocardiography.

Second, besides the overt heart failure, cardiac imaging (mostly echocardiography) is able to identify a substantial number of subjects with asymptomatic LV dysfunction in the community, mostly owing to hypertensive cardiomyopathy and silent coronary artery disease.[12,13] This syndrome has recently been classified by the AHA/ACC as stage B in the continuum of heart failure.[14] It acts progressively, often beginning with asymptomatic LV dysfunction and culminates in the overt CHF with symptoms and signs from fluid overload and poor end organ perfusion. Patients can remain in this asymptomatic stage because of the compensatory mechanisms involving the autonomic nervous system, neurohormones, and re-modelling of cardiac structures and functions. At this point, the early identification of the subgroup of patients who can deteriorate despite these adaptations is essential to establish the appropriate therapy. In fact, in patients with asymptomatic LV dysfunction, a reduction in the progression rate to symptomatic heart failure with ACE inhibitors and beta-blocker therapy has been demonstrated in large-scale clinical trials.[15]

As a third goal, cardiac imaging can also guide therapeutic changes in patients with clinical syndrome of congestive heart failure and preserved systolic function, implying that abnormal LV diastolic function is the mechanism responsible for producing congestive symptoms. In fact, as the approach to treatment may differ depending on whether systolic or diastolic dysfunction is predominant, the recent guidelines recommend performing a cardiac imaging test (preferring echocardiography as a screening test) in all patients with suspected congestive heart failure.[15,16] In these patients,cardiac imaging is essential in the diagnosis of heart failure with preserved EF and its aetiology (ischaemia, re-modelling, dyssynchrony, etc.). In fact, as patients with heart failure, both with reduced- and preserved-EF, have a mixture of systolic and diastolic abnormalities, the aetiological diagnosis and the knowledge of the mechanisms involved are very useful. However, in the subset of patients with preserved-EF heart failure, the presence of diastolic dysfunction of moderate to severe grade at echocardiography is an independent factor for increased death rate and hospital admission and can guide the use of diuretics, ACE, and angiotensin inhibitors. On the other side, cardiac imaging is very useful to evaluate systolic and diastolic changes after therapy to evaluate its efficacy and to estimate overall prognosis.

Imaging to Guide the Follow-Up

Multiple pharmacologic and device-based treatment modalities have become available for the treatment of patients with systolic LV dysfunction. Sequential studies are required to define the impact of specific new treatment modalities and to determine the spontaneous development of a disease process as well as the efficacy of a selected treatment on left ventricular function in individual patients. High reproducibility in the analysis of LV volumes and function is required for a reliable analysis of changes induced by treatment. The quality of repeated analysis of LV function is assessed either as intra- and inter-observer variability, which relates to the repeated measurement of a single dataset, or as test-retest reproducibility, which involves repetition of the entire acquisition and analysis.[17] As previously mentioned, the different imaging techniques show different potential in reproducibility as well as in safety and costs.

LV systolic and diastolic volume as well as ejection fraction are the conventional quantitative parameters to determine LV function during follow-up studies. Newer parameters such as left atrial size and tissue Doppler imaging parameters have also been described for serial clinical testing of LV function. Subjective visual assessment of LV ejection fraction is effective for single assessments, but insufficiently reliable for sequential analysis. Conventional echocardiographic parameters based on 2D echocardiography have also been shown to have limited test-retest reproducibility. Major limiting factors are poor image quality, geometric issues related to volume calculations, and the performance of off-axis cuts. In a study on 50 patients, test-retest correlation of LV ejection fraction was found to be only moderate ($r = 0.66$) using quantitative

analysis based on 2D echocardiography.[18] In contrast, 3D echocardiography has been proven to have high test-retest correlation ($r = 0.92$). Intra- and inter-observer variability of real-time 3D echocardiography derived LV volumes and ejection fraction have also been shown to be only in the range of 5.1–7.6%. Thus, using 3D echocardiography intra- and inter-observer variability in the analysis of LV function can be similar to that obtained with MRI [17–19]. In a study on 346 patients, newer measurements of LV function such as tissue Em, LA area, and E/Em ratio have been evaluated with respect to variability. High variability in all of these measurements was reported, which was not better than the one observed for ejection fraction. Thus, these parameters are not recommended for sequential LV assessment. Considering the high intra- and inter-observer agreement as well as the low test-retest variation for 3D echocardiographic analysis of LV function parameters, 3D echocardiography should be used as the modality of choice if accurate echocardiographic analysis of LV function during follow-up studies is required.

Role of Imaging in Specific Groups of Patients

Evaluation of LV Function in the Heart for Transplantation

Several important points have to be investigated by cardiac imaging in patients prior to and after cardiac transplantation. First, how to select a well-functioning heart is of general interest, because every hospital can host a potential donor. In addition to clinical and general examination, it is very important to define global and regional systolic function. In fact, regional wall motion abnormalities can be observed in up to 50% of potential donors. Generally, a septal or localized hypokinesia, or global mild hypokinesia is observed; however, sometimes, there can be real akinesia or dyskinesia. Among the aetiological hypothesis formulated in addition to the classical coronary artery disease, there are the myocardial contusion and the cerebral haemorrhage with a high level of cathecolamine. Very often, hypokinesia disappears after the transplantation, confirming that pretransplantation hypokinesia is functional. However, in cases of donor age of >45 years or in presence of clear wall motion abnormalities, it is much safer to study the donor's heart with coronary arteriography.

After transplantation, the transplanted heart shows LV wall thickness and mass increase in comparison with normal subjects, while it shows normal regional and global systolic function, except for a possible post-surgical "paradoxical motion" of the inter-ventricular septum. Concerning the evaluation of patients for acute rejection (in the first year after transplantation), the diagnosis is performed with the invasive catheter myocardial biopsy, because the appearance of LV systolic dysfunction is present only in the advanced stage of acute severe rejection. On the other hand, diastolic abnormalities are often present, but with a limited sensitivity and specificity for the diagnosis of acute rejection.

The most important post-transplantation diagnosis is cardiac allograft vasculopathy, the main factor limiting long-term survival, which is angiographically documented in 40–50% of patients surviving 5 years after transplantation. Very often, because of the absence of warning anginal symptoms owing to heart denervation, the clinical manifestations of allograft vasculopathy are ventricular arrhythmias, silent myocardial infarction, or sudden death. Conversely, as the performance of a yearly based coronary arteriography is invasive and yields a low sensitivity because of the diffuse concentric nature of the disease, several non-invasive techniques have been suggested.

Dobutamine stress echocardiography shows a good sensitivity (about 80%) when compared with coronary angiography, a specificity of up to 88% compared with intra-vascular ultrasound as "gold standard", and a good predictive value for clinical outcome. Similarly, a combination of resting echocardiography and quantitative stress 99mTc sestamibi SPECT has a high negative predictive value and can be used for non-invasive monitoring, reserving coronary angiography for patients with resting wall motion abnormalities or perfusion defects. Echocardiographic new techniques, like perfusion defects at contrast echocardiography or reduced coronary flow reserve at trans-thoracic echo-Doppler, appear as reliable markers for coronary stenosis allograft vasculopathy and related to major cardiac events.

Also, the use of multi-detector CT is highly sensitive (over 80%) and specific (over 90%) for angiographic stenosis detection, with CT eventually being superior to identify non-obstructive vessel wall disease. However, bad image quality owing to high heart rate of patients even when treated with beta-blockers, distal pruning of small coronary arteries, risk for worsening of renal insufficiency owing to contrast, and high radiation exposure are among the several limitations. Initial data with gadolinium contrast-enhanced magnetic resonance or with ^{31}P chemical shift imaging of high-energy phosphates appear promising for a non-invasive detection of allograft vasculopathy without any radiation exposure.

Use of LV Assist Devices

Cardiac imaging to study the LV function is of paramount importance for both short- and long-term ventricular assist devices in all the different phases of the device utilization (pre-, intra-, and post-operative) [20].

In the period preceding the device insertion, it is essential to evaluate the heart and large vessels to exclude significant aortic regurgitation, tricuspid regurgitation, mitral stenosis, patent foramen ovale, atherosclerotic aortic disease, or other cardiac abnormality that could lead to right-to-left shunt after left VAD placement. The study of systolic and diastolic LV function is fundamental to indicate the assist device implantation; the right ventricular function needs to be assessed to identify patients at risk for severe right ventricular failure (requiring right mechanical support) and those needing LV support alone. Severe LV dysfunction requires an accurate search for thrombi, owing to the high risk of apical thrombus formation, especially if located near the inflow cannula insertion site. All these data can be obtained with echocardiography or by adding cardiac MRI/CT, when a more complete detection of cardiovascular anatomy and function is required.

During device implantation, at the beginning of circulatory support, the trans-oesophageal echocardiography has an essential role to guide cannula positioning and to evaluate the device functioning immediately after implantation. The examination of the device aims to confirm heart de-airing, cannula alignment, and patency and competency of device valves using 2D, colour, continuous, and pulsed-wave Doppler modalities.

When the LV is unloaded with a reduction in its size to approximately normal, echocardiography has to show a neutral inter-ventricular septum position (indicating an adequate LV filling and right ventricular function), a good LV unloading with adequate LV filling, and (especially in case of continuous flow pumps) absence of echo contrast enhancement or intra-cardiac clot formation. When there is a device malfunctioning (insufficient device ejection or cannula obstruction), then LV is not decompressed after the implantation, and a rightward septum shift can be seen. Conversely, in case of excessive decompression owing to high pump speed or right ventricular dysfunction, a leftward septal shift can be observed.

After the insertion of assistance device, the cardiac imaging is necessary for the reassessment of the heart and large vessels, investigating the same parameters studied in the pre- and intra-operative phases.

As the assistance device favours LV unloading, LV function is not accurately assessed during the device function. When a correct evaluation of LV function is necessary, usually to plan the device explantation, it is necessary to analyze several echocardiographic indices during temporary interruption of the ventricular assistance. The LV indices studied in this particular setting go from the classical ejection fraction, fractional shortening, or end diastolic LV diameter to novel complex Doppler indices (pre-ejection period divided by ejection time, heart rate corrected ejection time divided by the LA pressure, and the end systolic elastance). The only dependable index of ventricular function during the device function is the fractional shortening of the LV obtained when the systole coincides with device filling. This is the "pump-on" reliable information on intrinsic LV performance, and can be used as a guide to LV recovery.

Acute Dyspnea in the Emergency Room

Patients with acute respiratory distress represent a major part of patients presenting to emergency rooms. Echocardiography provides the ideal imaging modality for immediate bedside assessment of cardiac pathologies resulting in acute dyspnea. The major differential diagnoses are given in Table 15.5. Acute coronary syndromes resulting in impairment of regional and global LV function are the most frequent causes of acute respiratory distress. Potential complications of myocardial infarction, such as papillary muscle dysfunction or

Table 15.5. Major differential diagnosis among patients with acute dyspnea in the emergency room

	LV	RV	Doppler
Acute coronary syndrome	Regional WMA, impaired global LV function	Enlarged in right ventricular infarction	Diastolic dysfunction, functional MR
Congestive heart failure, myocarditis,	Impaired global LV function		Functional MR, diastolic dysfunction
Valvular dysfunction			Valvular regurgitation, dysfunction of valvular prosthesis
Pulmonary embolism		Enlarged	Increased right ventricular pressure
Pericardial effusion			Respiratory changes in LV and RV inflow

LV left ventricle; *MR* mitral regurgitation; *RV* right ventricle; *WMA* wall motion abnormality

disruption resulting in acute mitral regurgitation and ventricular septal defect, are important causes of acute aggravation of dyspnea. Congestive heart failure owing to a variety of myocardial diseases resulting in systolic and diastolic dysfunction can be defined by 2D echocardiography, Doppler analysis of the LV inflow signal, and tissue Doppler imaging. Acute mitral or aortic regurgitation resulting in significant haemodynamic and respiratory distress may be due to endocarditis, papillary muscle disruption, or degenerative causes of leaflet disruption. In patients with valvular prosthesis, thrombotic dysfunction resulting in valvular stenosis or central regurgitation, degenerative distorsion of bioprosthetic valvular leaflets, as well as significant paravalvular leakage owing to partial distachment of the valvular prosthesis are major causes of acute valvular dysfunction. Enlargement of the right ventricle and increased right ventricular pressures are important signs of pulmonary embolism and are associated with impaired prognosis even in haemodynamically stable patients.

References

1. Lang R, Bierig M, Devereux R, et al Recommendations for chamber quantification. A report from the American Society of Echocardiography's Nomenclature and Standards Committee, the Task Force on Chamber Quantification, and the European Association of Echocardiography. *Eur J Echocardiogr.* 2006;7: 79–108
2. Kühl HP, Schreckenberg M, Rulands D, et al High–resolution transthoracic real–time three–dimensional echocardiography: quantification of cardiac volumes and function using semi–automatic border detection and comparison with cardiac magnetic resonance imaging. *J Am Coll Cardiol.* 2004;43:2083–2090
3. Hoffmann R, von Bardeleben S, ten Cate F, et al Assessment of systolic left ventricular function: a multi–centre comparison of cineventriculography, cardiac magnetic resonance imaging, unenhanced and contrast–enhanced echocardiography. *Eur Heart J.* 2005;26:607–616
4. Hoffmann R, von Bardeleben S, Kasprzak JD, et al Analysis of regional left ventricular function by cineventriculography, cardiac magnetic resonance imaging, and unenhanced and contrast–enhanced echocardiography: a multicenter comparison of methods. *J Am Coll Cardiol.* 2006;47:121–128
5. Urheim S, Edvardsen T, Torp H, Angelsen B, Smiseth OA. Myocardial strain by Doppler echocardiography: validation of a new method to quantify regional myocardial function. *Circulation.* 2000;102:1158–1164
6. Amundsen BH, Helle–Valle T, Edvardsen T, et al Noninvasive myocardial strain measurement by speckle tracking echocardiography: validation against sonomicrometry and tagged magnetic resonance imaging. *J Am Coll Cardiol.* 2006;47:789–793
7. Tei C, Ling LH, Hodge DO, et al New index of combined systolic and diastolic myocardial performance: a simple and reproducible measure of cardiac function – a study in normal and dilated cardiomyopathy. *J Cardiol.* 1995;26:357–366
8. Paulus WJ, Tschöpe C, Sanderson JE. How to diagnose diastolic heart failure: a consensus statement on the diagnosis of heart failure with normal left ventricular ejection fraction by the Heart Failure and Echocardiography Associations of the European Society of Cardiology. *Eur Heart J.* 2007;28:2539–2550
9. Oh JK, Appleton CP, Hatle LK, Nishimura RA, Seward JB, Tajik AJ. The noninvasive assessment of left ventricular diastolic function with two–dimensional and Doppler echocardiography. *J Am Soc Echocardiogr.* 1997;10:246–270
10. Nagueh SF, Mikati I, Kopelen HA, Middleton KJ, Quinones MA, Zoghbi WA. Doppler estimation of left ventricular filling pressure in sinus tachycardia. A new application of tissue Doppler imaging. *Circulation.* 1998;98:1644–1650
11. Ommen SR, Nishimura RA, Appleton CP, et al Clinical utility of Doppler echocardiography and tissue Doppler imaging in the estimation of left ventricular filling pressures: a comparative simultaneous Doppler–catheterization study. *Circulation.* 2000;102: 1788–1794
12. Wang TJ, Evans JC, Benjamin EJ, et al Natural history of asymptomatic left ventricular systolic dysfunction in the community. *Circulation.* 2003;108:977–982
13. Colonna P, Pinto FJ, Sorino M, Bovenzi F, D'Agostino C, de Luca I. The emerging role of echocardiography in the screening of patients at risk of heart failure. *Am J Cardiol.* 2005;96:42L–51L
14. Hunt SA, Abraham WT, Chin MH, et al ACC/AHA 2005 guideline update for the diagnosis and management of chronic heart failure in the adult: a report of the American College of Cardiology/American Heart Association Task Force on Practice Guidelines. *Circulation.* 2005;112:el54–e235
15. Dickstein K, Cohen–Solal A, Filippatos G, et al ESC Guidelines for the diagnosis and treatment of acute and chronic heart failure 2008. *Eur Heart J.* 2008;29:2388–2442
16. Senni M, Rodeheffer RJ, Tribouilloy CM, et al Use of echocardiography in the management of congestive heart failure in the community. *J Am Coll Cardiol.* 1999;33:164–170
17. Soliman O II, Kirschbaum SW, van Dalen BM, et al Accuracy and reproducibility of quantitation of left ventricular function by real–time three–dimensional echocardiography versus cardiac magnetic resonance. *Am J Cardiol.* 2008;102:778–783
18. Jenkins C, Bricknell K, Hanekom L, Marwick TH. Reproducibility and accuracy of echocardiographic measurements of left ventricular parameters using real–time three–dimensional echocardiography. *J Am Coll Cardiol.* 2004;44:878–886
19. Chuang ML, Hibberd MG, Salton CJ, et al Importance of imaging method over imaging modality in noninvasive determination of left ventricular volumes and ejection fraction: Assessment by two– and three– dimensional echocardiography and magnetic resonance imaging. *J Am Coll Cardiol.* 2000;35:477–484
20. Chumnanvej S, Wood MJ, MacGillivray TE, Melo MF. Perioperative echocardiographic examination for ventricular assist device implantation. *Anesth Analg.* 2007;105(3):583–601

Chapter 16

ECHOCARDIOGRAPHY TO ASSESS VIABILITY

Roxy Senior, Nuno Cortez Dias, and Fausto Jose Pinto

CONTENTS

J. L. Zamorano et al. (eds.), *The ESC Textbook of Cardiovascular Imaging*
DOI: 10.1007/978-1-84882-421-8_16, © Springer-Verlag London Limited 2010

Introduction

The prevalence of heart failure (HF) is increasing worldwide mainly as the result of coronary artery disease (CAD), responsible for almost two-thirds of cases of left ventricular (LV) dysfunction. Established treatment options for ischaemic HF include medical therapy, revascularization, and cardiac transplantation. Cardiac resynchronization therapy (CRT) has been recently introduced as a treatment modality of HF, but other treatment strategies remain investigational.[1] Despite significant therapeutic advances, outcome of medical therapy in severe HF is poor.[2, 3] In specific subsets of patients, the potential benefits of revascularization must be weighed against the potential high peri-procedural risks.

Dysfunctional Myocardium in Coronary Artery Disease

Systolic LV dysfunction owing to CAD is the complex result of necrosis and scarring, as well as of functional and morphological adaptive abnormalities of the viable myocardium. Preservation of myocardial viability refers to the tissue capacity for survival. Although viable myocardium encompasses normally contracting and hypocontractile tissue, the term "viability" has been used interchangeably with "contractile recovery". Hence, in the setting of chronic LV dysfunction, this definition usually refers to the downregulation of contractile function in surviving myocardium in response to periodic or sustained reduction in coronary blood flow, which may be potentially reversed if normal blood flow is restored.

Viable myocardium exists as a spectrum, from complete trans-mural infarction with no viability, to trans-mural hibernation or stunning with the potential of full recovery. Moreover, patients can have various mixtures of stunned, hibernating, ischaemic and fibrotic myocardium, in a variety of arrangements. As approximately 40% of myocardial segments with resting wall motion abnormalities after acute myocardial infarction (AMI) have viable tissue that may recover contractile function if revascularised, detection of viable myocardium is clinically relevant.

Myocardial stunning describes the post-ischaemic metabolic and contractile compromise in viable myocardium after a transient coronary occlusion (i.e. post-successful reperfusion in AMI). In stunned myocardium, blood flow may be restored but contraction may not return to baseline. Pathogenesis likely involves oxygen-free radicals, calcium overload and structural changes in the collagen fibres of myocyte to myocyte struts. Dysfunction might persist from hours to weeks, but generally improves with time. An exception is repetitive stunning, defined as repeated episodes of ischaemia producing prolonged post-ischaemic contractile dysfunction,[4] which is similar to hibernation in that revascularization has the potential to improve contractile function.

Myocardial hibernation is a chronic state of contractile dysfunction at rest in non-infarcted myocardium as the result of persistently reduced blood flow, which has the potential to improve function after restoration of myocardial blood supply. Observations suggest that hibernation may be a temporal progression of chronic repetitive stunning, with an initial state of near-normal blood flow but reduced flow reserve, finally leading to decreased resting flow. The term jeopardised myocardium has been proposed to include the entire spectrum from repetitive stunning to hibernation. The deprived hibernating myocytes spend energy to preserve cellular integrity at the expense of contractile function. Biopsy studies demonstrated that hibernating myocardium develops histological changes of cellular dedifferentiation and an embryonic phenotype, including expression of foetal isoforms of structural proteins, disorganization of the cytoskeleton, depletion of myofilaments, loss of sarcoplasmic reticulum and T tubules, finally leading to progressive apoptosis and interstitial fibrosis.[4] The improvement of myocardial oxygen supply/demand relationship with revascularization (and to a lesser extent with medical therapy) leads to functional recovery of the hibernating myocardium. However, the ability to recover systolic function after revascularization depends on the severity of structural abnormalities, i.e. the correction of cellular changes and the amount of tissue fibrosis.[5] These observations and evidence that apoptosis is important in hibernation underscore the importance of early revascularization in this dynamic transition from reversible to irreversible contractile dysfunction.[4, 6]

Theoretically, hibernation and stunning are different pathophysiologic states, but practically, they are often indistinct, appear to co-exist in varying degrees in the same patient or myocardial region and represent a continuum of the same process.[7] However, the timing of functional recovery after revascularization appears to differ between stunned and hibernating myocardium. Stunned myocardium recovery appears to be early after revascularization and more complete, while recovery of hibernating myocardium is late and often incomplete.[6]

Revascularization in Ischaemic Cardiomyopathy

Randomised controlled trials of coronary revascularization in patients with HF and LV systolic dysfunction are lacking but studies are ongoing. Decisions are largely based on surgical studies performed 20 years ago. In Coronary Artery Surgery Study registry (420 medical patients and 231 surgical patients)[8] and Duke University Cardiovascular Database

(409 medical patients and 301 surgical patients),[9] CABG provided a significant long-term survival advantage over medical therapy, but surgical survival benefits were seen in patients with the most severe LV systolic dysfunction, extensive CAD and severe angina. Although these and other smaller studies, overall, favoured surgery over medical therapy, important limitations include the selection bias for revascularization, inadequate medical therapy in both medical and surgical groups, outdated surgical techniques,[10] small number of patients (particularly with predominant HF symptoms) and lack of pre-operative viability assessment.[11]

Peri-operative mortality for CABG in LV systolic dysfunction vary, from approximately 5%–30% depending on age, severity of LV, systolic dysfunction and co-morbidities,[12] Furthermore, in patients undergoing Percutaneous Intervention before stents, 18.2% of patients with LVEF between 25 and 35% experienced non-fatal myocardial infarction and acute closure.[13]

Limitations in study design and higher peri-procedural risk have created uncertainty about the optimal treatment strategy. This has provided the rationale for non-invasive viability testing, which has potential value in moderate-to-severe ischaemic cardiomyopathy, identifying patients whose symptoms and natural history may potentially improve with revascularization.

Assessment of Myocardial Viability

The main goal of myocardial viability assessment is to detect dysfunctional myocardium, which would improve function if normal blood supply were restored. Several observational studies demonstrated that patients with ischaemic LV dysfunction with extensive areas of viable myocardium have lower peri-operative mortality, greater regional and global LV function recovery, fewer HF symptoms and improved survival after revascularization (fivefold lower annual mortality rate when compared with medical treatment alone). After revascularization, the annual mortality rate in patients with viable myocardium was half as high as in patients without viable myocardium. Conversely, in those patients without significant myocardial viability, there was a trend towards a higher mortality following revascularization. Hence, it seems that survival benefit is obtained when the need for revascularization is guided by pre-operative assessment of myocardial viability.

A number of non-invasive imaging procedures have been developed to evaluate myocardial viability and to identify markers of functional recovery, including dobutamine stress echocardiography (DSE), myocardial contrast echocardiography (MCE), single-photon emission computed tomography (SPECT), positron emission tomography (PET) and cardiovascular magnetic resonance (CMR) imaging.

The currently available imaging techniques assess distinct characteristics of viable and dysfunctional myocardium, having different limitations and diagnostic accuracy. Comparison of the clinical utility of each in the assessment of myocardial viability is currently limited by the lack of randomised prospective trials. Besides, there is uncertainty about the best criterion to determine the clinical benefit of the assessment of myocardial viability, by which they should be compared. Several studies evaluated their accuracy for the prediction of segmental improvement, but of greater clinical relevance is the global LV functional recovery after revascularization. Theoretically, the best method should be the one with the optimal sensitivity (Sn) and specificity (Sp) for detection of viability. However, as the amount of hibernating myocardium is the critical determinant of global functional recovery, even methods of moderately high Sn may eventually identify those patients with great benefit. The precise extent of viability necessary to predict benefit from revascularization is unclear and may vary in different clinical circumstances. Most studies suggested that a substantial amount of viable myocardium (at least 20–30% of LV mass) is required for the improvement of LVEF. Hence, both identification and quantification of the extent of viable myocardium are required for a careful selection of patients who have a higher likelihood of benefit from revascularization. However, several authors showed that survival rates after coronary artery bypass surgery were similar whether or not function improved after intervention, suggesting that relevant clinical benefits may occur even without LVEF recovery. Preservation of small viable areas may improve clinical outcome by reducing the risk of subsequent ischaemic events, improving LV re-modelling processes, preventing additional LV dilatation, promoting electrical stability and eventually improving symptoms and functional capacity. Hence, large-scale prospective head-to-head comparisons of the available imaging modalities are needed to determine their independent value for the detection of viable myocardium and to evaluate their accuracy in predicting the patient's response to therapy, regarding LV function recovery, symptoms and survival.

As the use of a single viability test may not be optimal, the value of sequential multi-modality imaging should also be evaluated. Multi-modality imaging approach may theoretically enhance the prediction of functional recovery after revascularization in selected patients with ischaemic LV dysfunction.

Rest Echocardiography

Resting echocardiographic examination is the single most useful test in the assessment of HF, because structural abnormality, systolic dysfunction, diastolic dysfunction or

a combination of these abnormalities need to be obtained for the diagnosis of HF. Moreover, resting echocardiography provides valuable information that may guide the choice of imaging technique to use and assist in its interpretation. If there is adequate image quality, allowing full visualization of endocardial border and wall thickening in all myocardial segments, DSE may be the test of choice. If the acoustic window is insufficient to provide a high degree of diagnostic certainty, despite contrast enhancement, another imaging approach should be used. Moreover, the wall motion score and LVEF at rest differently affect the accuracy of the several imaging methods used to assess viability. Severe dysfunction at rest reduces the predictive accuracy of stress tests (either DSE or dobutamine-CMR), and in such patients delayed-enhancement CMR may be preferable.

The assessment of LV end-diastolic wall thickness can be used to obtain a first evaluation of myocardial viability: thinned (<6 mm) and dense myocardial segments typically reflect scar tissue and have particularly low probability of improvement in function, while dysfunctional segments with preserved wall thickness (≥6 mm) may be viable. The involvement of >4 ventricular wall segments by scarring is associated with low probability of global functional recovery after revascularization. Furthermore, the degree of LV remodelling and dilatation may be an additional guide to predict functional recovery post-revascularization. The likelihood of significant recovery of global LV function is inversely related to the ventricular volume. End-diastolic volume of >220 mL is unlikely to show significant functional recovery, as the likelihood of significant scar tissue is high in the severely re-modelled LV.

Until recently, resting echocardiography was considered of limited utility in discriminating viable from non-viable myocardium. However, myocardial velocity assessment with tissue Doppler imaging (TDI) and speckle tracking-derived parameters may unmask viable myocardium.

TDI allows accurate assessment of regional myocardial function during all the phases of the cardiac cycle. Experimental and clinical studies showed that TDI-derived analysis of ejection systolic velocities, strain and strain rate allow accurate definition of trans-murality of myocardial infarction. TDI-based longitudinal strain and strain rate are reduced in segments with sub-endocardial scarring, although the relationship is non-linear as the sub-endocardium governs the trans-mural contraction and longitudinal function. However, angle dependency (incapacity to assess shortening or thickening whenever the principal vector of contraction is not aligned with the ultrasound beam) significantly impairs their accuracy. Other TDI-derived parameters may be useful to assess the myocardial viability, particularly, the detection of myocardial positive pre-ejection velocity occurring during isovolumic contraction. Penicka et al.[14] demonstrated high accuracy of TDI-derived myocardial positive pre-ejection velocity qualitatively assessed by pulsed TDI to predict recovery of contractile function in patients with chronic CAD, wall motion abnormalities and global systolic dysfunction submitted to revascularization. The presence of positive pre-ejection velocity predicted improvement of regional function after revascularization (Sn: 93%; Sp: 77%) and the presence of positive pre-ejection velocity in ≥5 dysfunctional segments had a high accuracy to predict moderate (Sn: 92%; Sp: 79%) and marked (Sn: 93%; Sp: 60%) recovery of global systolic function. Moreover, in another group of similar but non-revascularized patients, Penicka et al. showed a good agreement between positive pre-ejection velocity and detection of viable myocardium at DES, FDG-PET and DE-CMR. However, the incremental value of positive pre-ejection velocity over reference techniques in the evaluation of myocardial viability was not assessed.

Speckle tracking is a new technique that tracks frame-to-frame movement of natural acoustic markers or speckles identified on standard 2D ultrasound tissue images. Local 2D tissue velocities are derived from spatial and temporal data of each speckle. Myocardial strain can be assessed from temporal differences in the mutual distance of neighbouring speckles, allowing the evaluation of circumferential, radial and longitudinal strain. Recently, Becker et al. showed that myocardial deformation imaging in rest, based on speckle tracking, allows the assessment of trans-murality, as radial and circumferential strain impairment is proportional to the transmural scarring extent. Moreover, they also found that peak systolic radial strain identifies reversible myocardial dysfunction and predicts regional and global functional recovery at 9 ± 2 months follow-up. Segments with functional recovery had significantly higher baseline peak systolic radial and circumferential strain values and a peak systolic strain of >17.2% predicted segmental functional recovery (Sn: 70.2%; Sp: 85.1%). Besides, a positive correlation was found between the number of segments with a peak systolic strain of >17.2% and LVEF improvement after surgical or percutaneous coronary revascularization. Moreover, the predictive value was similar to that achieved by contrast-enhanced CMR[15] (Fig. 16.1).

Myocardial Contrast Echocardiography

MCE is a technique that uses micro-bubbles during echocardiography. These micro-bubbles remain exclusively within the intra-vascular space and their presence within

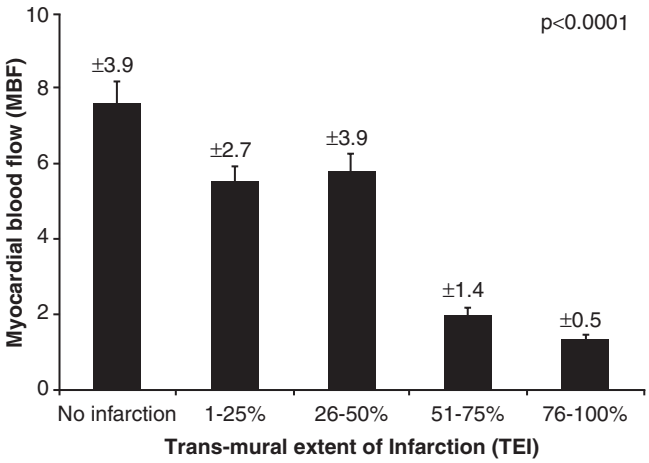

Fig. 16.1 Short-axis radial strain images in a patient with previous history of postero-lateral acute myocardial infarction, showing a low peak systolic radial strain of the posterior, inferior and lateral segments

any myocardial territory denotes the status of micro-vascular perfusion within that region. The volume of blood present in the entire coronary circulation (arteries, arterioles, capillaries, venules and veins) is approximately 12 mL/100 g of cardiac muscle; approximately one-third of this is present within the myocardium itself and is termed "myocardial blood volume".[12] The predominant (90%) component of the myocardial blood volume resides within the capillaries. Myocardial contrast intensity reflects the concentration of the micro-bubbles within the myocardium. When a steady state of micro-bubble concentration has been achieved in the myocardium, during a continuous infusion of contrast, the observed signal intensity denotes the capillary blood volume.[16, 18] Any alteration in signal intensity in this situation thus occurs principally as a result of a change in the capillary blood volume. Furthermore, it has been shown that after the destruction of micro-bubbles in the myocardium with high-energy ultrasound, myocardial contrast replenishment, both during low and high power, reflects myocardial blood velocity.[18] The product of these two components denotes myocardial blood flow at the tissue level.[18, 19] MCE can thus detect capillary blood volume and by virtue of its temporal resolution, can also assess myocardial blood flow.

Myocardial Contrast Echocardiography for the Detection of Myocardial Viability

Assessment of myocardial viability is based on the assumption that myocardial viability necessitates a preserved micro-vasculature, which can be assessed by MCE. With its excellent spatial resolution (<1 mm axially), MCE can accurately depict the presence of micro-vascular integrity. Kloner et al. showed that with myocardial infarction, myocyte loss was associated with a loss of micro-vasculature.[20] Thus, absence of myocardial contrast enhancement on MCE should define regions that lack myocardial viability. In patients with ischaemic cardiomyopathy undergoing coronary artery bypass grafting, Shimoni et al.[21] in an important study, demonstrated an excellent correlation between contrast signal intensity and capillary density obtained from myocardial biopsies of the same region. Moreover, contrast signal intensity was inversely related to the extent of fibrosis. Peak contrast signal intensity after micro-bubble destruction denotes capillary volume, which in turn is a measure of myocardial viability. Peak contrast intensity obtained in this manner has also been shown to correlate with the extent and severity of myocardial necrosis, as assessed by gadolinium-enhanced CMR imaging 7 days after AMI, in a study by Janardhanan et al.[22] (Figs. 16.2 and 16.3). Both studies evaluated the usefulness of peak contrast intensity as a measure of myocardial viability. Once the contrast agent has reached a steady state, during continuous intravenous infusion, high-energy impulses are used to achieve micro-bubble destruction within the myocardium. The replenishment of contrast can then be visualised using either high-power (mechanical index 0.9–1.0) or low-power (mechanical index 0.1–0.2) techniques. Myocardial replenishment is then observed over 10–15 cardiac cycles; fully replenished myocardium, which is of homogeneous contrast intensity, indicates the presence of myocardial viability. Normal contrast intensity by qualitative MCE has been shown to have a predictive value of almost 90% for the presence of contractile reserve, whereas the absence of contrast enhancement predicts a lack of contractile reserve in approximately 90% of cases.[22]

The concept underlying this is that in a low-flow state, such as the one that occurs after AMI, myocardial blood flow in the infarcted muscle is reduced either because of severe flow limiting stenosis, capillary plugging or an occluded infarct-related artery (IRA), with the myocardium being supplied by collateral blood flow. Using an experimental model, Coggins et al., in a novel study, showed that after occlusion, infarct size was best determined when contrast replenishment is observed 15 s after a destructive impulse.[23] In other words, collateral blood flow, which is usually low, maintains myocardial viability despite an occluded IRA. This was also shown in a human study in which Swinburn et al.[24] studied 96 patients after AMI. MCE was performed 3–5 days after AMI; the authors found that the absence of homogenous contrast replenishment within 10 s of myocardial micro-bubble destruction resulted in the non-recovery of these segments in 84% of cases (Fig. 16.4).

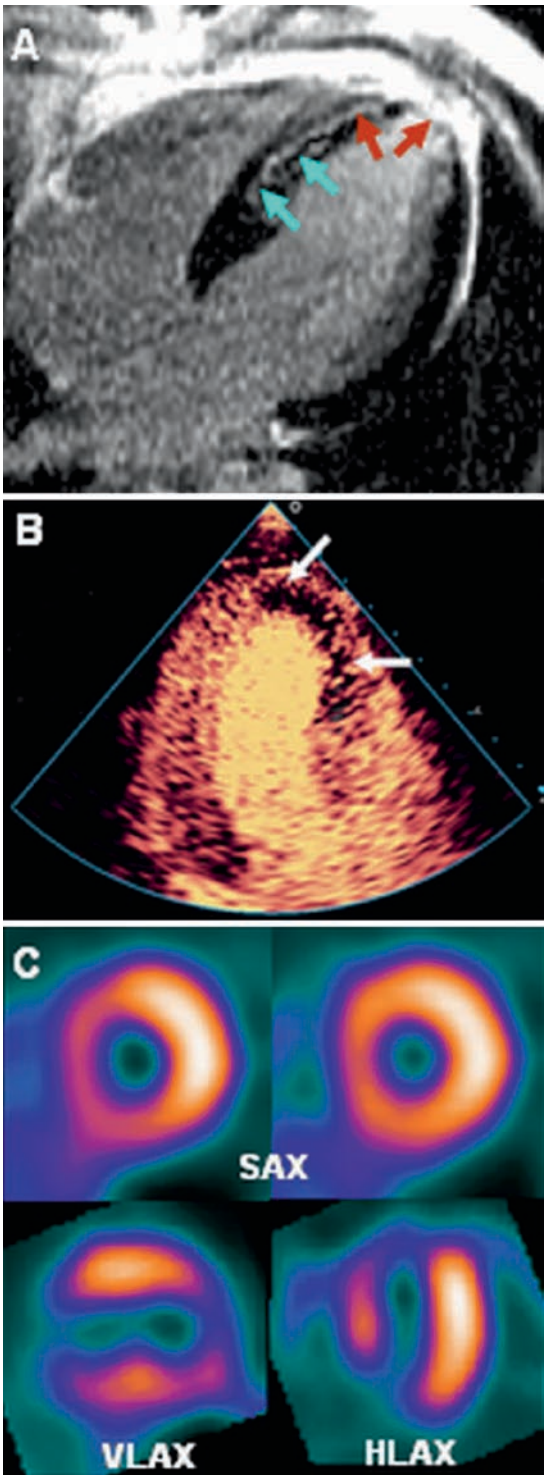

Fig. 16.2 Quantitative myocardial contrast echocardiography in relation to trans-mural extent of infarction (TEI) in dysynergic segments. **(a)** Peak contrast intensity. **(b)** Micro-bubble velocity. **(c)** Myocardial blood flow[21]

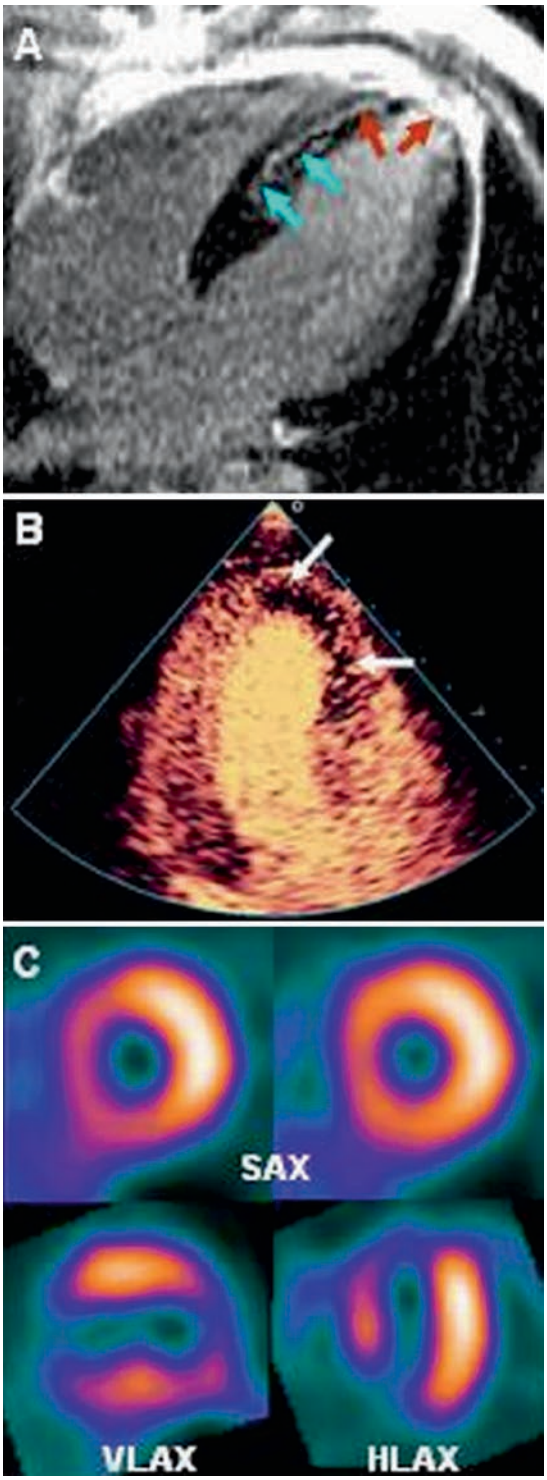

Fig. 16.3 Images from a 62-year-old patient who presented with an anterior myocardial infarction. **(a)** CMR demonstrates a full thickness apical infarct (*red arrows*), which extends to the mid-septum with greater than 50% myocardial wall involvement again implying low likelihood of viability. **(b)** The MCE apical 3-chamber view demonstrates not only an absence of contrast uptake at the apex but also severely reduced opacification extending to the mid-septum. **(c)** Although the SPECT images clearly demonstrate an apical full-thickness infarct, they only show a mild reduction in tracer uptake in the septum as demonstrated in the mid-apical short-axis view implying ≤50% TEI with significant viability in the infarct related territory

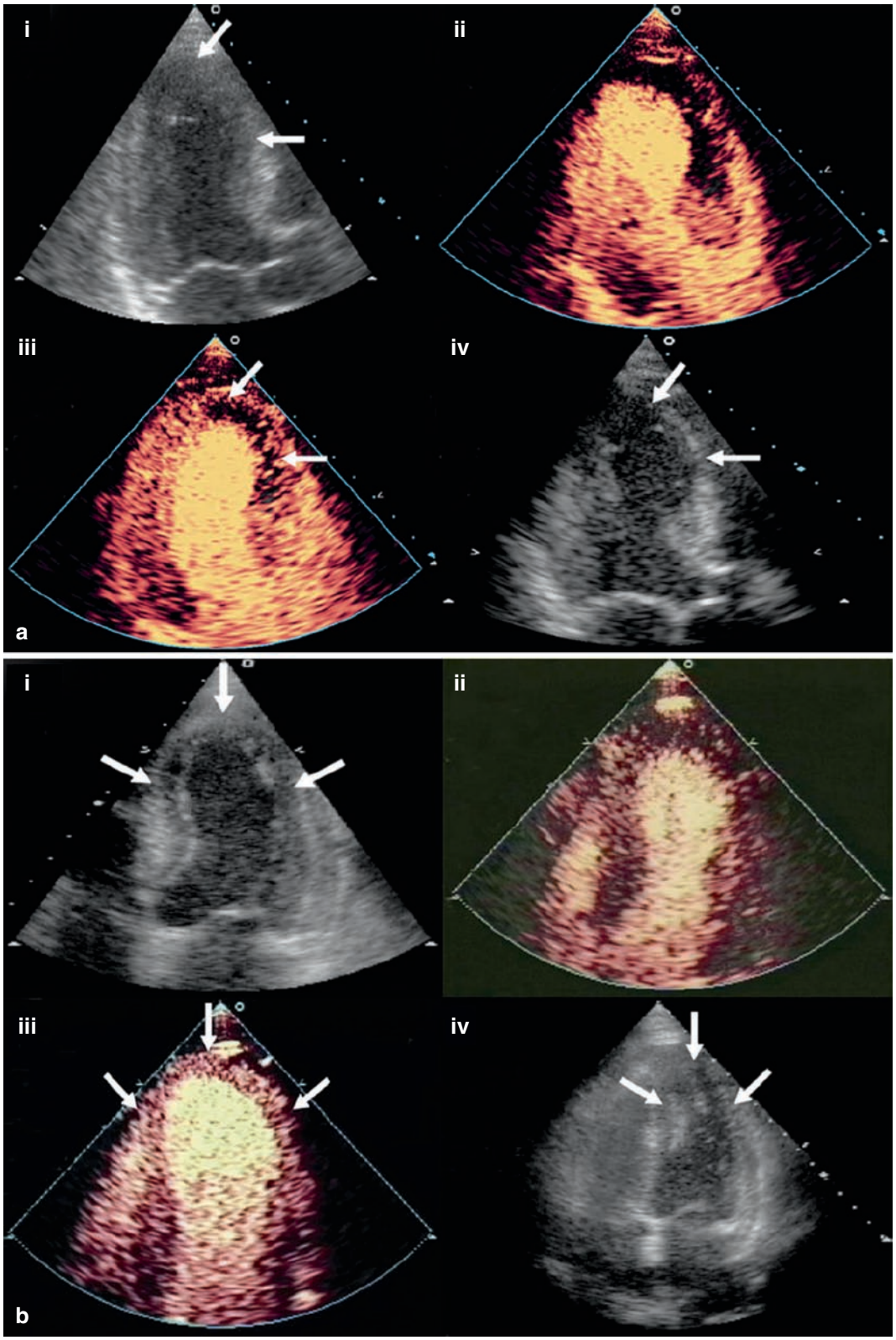

Fig. 16.4 **(a)** End-systolic frames of the apical 3-chamber view showing: (i) Akinetic mid-anterior septum and apex (*arrows*); (ii) complete destruction of myocardial contrast immediately after a high mechanical index pulse on MCE; (iii) lack of contrast opacification of the dysynergic segments, even at 15 cycles (*arrows*); (iv) lack of functional recovery at 12 weeks despite revascularization (*arrows*). **(b)** End-systolic frames of the apical 4-chamber view showing: (i) Akinetic mid-septum, apex and mid-lateral segments (*arrows*); (ii) complete destruction of myocardial contrast immediately after a high mechanical index pulse on MCE; (iii) homogenous contrast opacification of the dysynergic segments by 15 cardiac cycles (*arrows*); (iv) Functional recovery at 12 weeks after revascularization (*arrows*). Adapted from Janardhanan et al.[46]

Detection of Myocardial Viability After Acute Myocardial Infarction

A number of studies have demonstrated the important role that MCE plays in assessing the viability and predicting the recovery of regional and global systolic function post-AMI. It was noted that patients with a patent IRA and good contrast opacification demonstrated an improvement in contractile function compared with those with a poor or absent contrast opacification 1 month after AMI. Such studies have established the importance of an intact micro-vasculature after AMI, as assessed by MCE, to predict the myocardial viability. In post-AMI patients treated with thrombolysis, Jeetley et al.[25] (in the first study to show that real-time intravenous MCE can predict LV re-modelling after AMI and thrombolysis) first demonstrated that the extent and severity of contrast perfusion defects predicted adverse LV re-modelling. Furthermore, in that study, among all the clinical, biochemical, electrocardiogram and MCE markers that affect LV re-modelling, the contrast perfusion score index (PSI) was the only independent predictor of LV re-modelling. Low-dose dobutamine echocardiography (DSE) is widely used to assess myocardial viability. Huang et al.[26] recently published a comparison between MCE and low-dose DSE for the prediction of LV functional recovery in patients after AMI. The 92 patients were divided into three groups (post-operative cardiac ischaemia, 34; thrombolysis, 30 and conservative, 28). They found that there was good concordance between MCE and low-dose DSE in predicting functional recovery (kappa = 0.3, $p < 0.001$) and that the MCE PSI had a strong correlation with LV functional recovery ($r = -0.75$, $p < 0.1$). Senior and Swinburn[20] specifically addressed the incremental value of MCE in patients undergoing low-dose DSE for the assessment of myocardial viability after AMI. The study clearly established the incremental value of MCE in predicting myocardial viability in myocardial segment deemed non-viable by DSE. The authors demonstrated that the presence of contrast enhancement even in segments that lacked contractile response during dobutamine resulted in an improvement in regional function compared with those with no contrast enhancement. This is probably because after thrombolysis, a significant number of patients demonstrate residual IRA stenosis, which prevents the occurrence of contractile response in viable segments. As MCE is performed at rest, the uptake of contrast is unaffected in these patients.

Hickman et al.[27] compared MCE with SPECT for evaluating myocardial viability in post-AMI patients treated with thrombolysis. In this study of 56 patients, they found that 90% of segments showing homogenous contrast opacification on MCE demonstrated viability, whereas only 45% demonstrating normal radionuclide tracer uptake showed viability. Conversely, 85% of segments without contrast opacification on MCE did not show recovery of function; however, 25% of patients subsequently demonstrated recovery of function despite a severe reduction in tracer uptake on SPECT. This is probably because SPECT has a lower spatial and temporal resolution compared with MCE (Fig. 16.3).

Several MCE studies have demonstrated high Sn (75–90%), but poorer Sp (50–60%) in identifying the recovery of contractile function after AMI. The majority of the studies consisted of patients studied early after reperfusion and only assessed during rest. The combination of reactive hyperaemia, dynamic changes in the micro-circulation early after AMI and the fact that myocardial infarction involving more than 20% of the subendocardium can render the myocardium akinetic despite significant epicardial and mid-myocardial viability[28] tends to make MCE less specific for the detection of myocardial viability if viability is defined in terms of the recovery of systolic function. Technical factors such as the inability to distinguish micro-bubble signature from the underlying tissue can also contribute to the low Sp of MCE. Recent studies have, however, shown that assessing patients 3–5 days after AMI and an assessment of contractile reserve using background subtraction techniques, either on-line (low-power or high-power imaging) or off-line, considerably improved the Sp (75–80%) and positive predictive value (75–80%) of MCE.[29,30] The study by Main et al.[30] is an important paper that demonstrates the impact of technological advances in imaging techniques on the accuracy of MCE in identifying stunning and in the prediction of recovery of function after myocardial infarction. Balcells et al.[31], whose study elegantly demonstrated the optimal timing of performing MCE for the accurate prediction of myocardial viability, assessed the grades of perfusion 3–5 days after PCI and correlated them with contractile reserve assessed 1 month later. Almost all segments with good perfusion demonstrated contractile reserve; conversely, almost all segments with no perfusion failed to show contractile reserve. The authors also observed a threshold myocardial perfusion beyond which there was a strong correlation between perfusion and contractile reserve. The key to improved accuracy for determining viability in a reperfused territory after AMI is to perform MCE at least 24 h after reperfusion. The Sn and Sp of MCE for predicting myocardial viability are 83 and 75%, respectively.

Recent data indicated that the extent and severity of contrast perfusion defect after AMI predicted the mortality and combined mortality re-infarction, independent of clinical factors, ECG parameters, cardiac biomarkers and resting LVEF[32] (Fig. 16.5).

Detection of Myocardial Viability in Chronic Coronary Artery Disease

MCE using direct intra-coronary injections of micro-bubbles has also been compared with SPECT and DSE for predicting

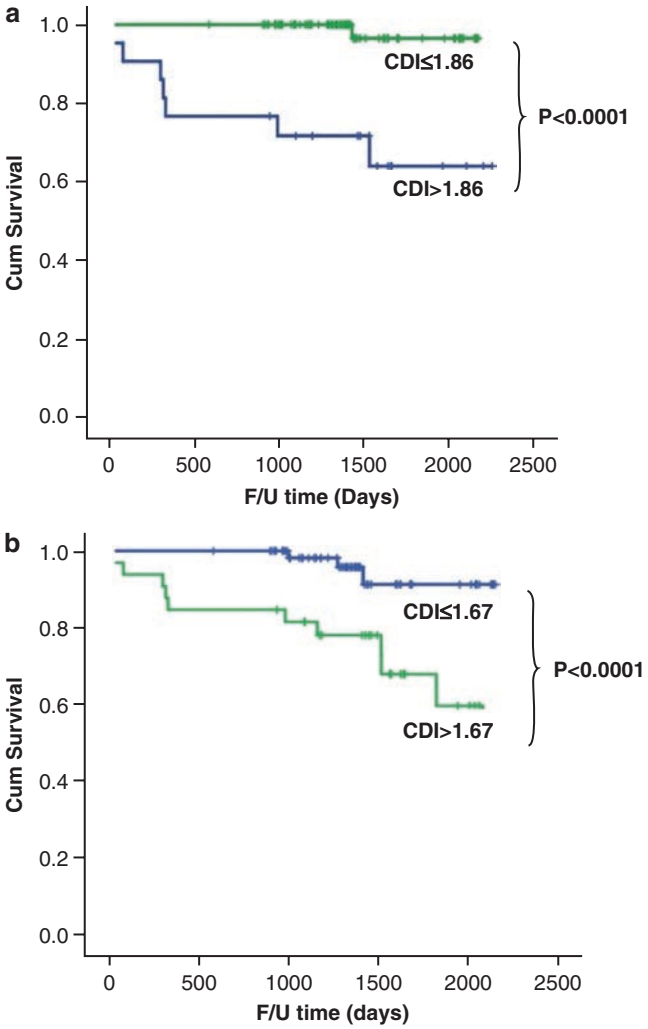

Fig. 16.5 **(a)** Kaplan–Meier survival curve (unadjusted) using a cut-off of CDI of 1.86 for the prediction of cardiac death. **(b)** Kaplan–Meier survival curve using a cut-off of CDI of 1.67 for the prediction of cardiac death or non–fatal AMI

the recovery of resting function after revascularization.[33] Similar to thallium uptake, the normalised peak contrast intensity of dysfunctional segments that recovered function was significantly higher than the segments that did not improve after revascularization. Both perfusion modalities were found to have comparable Sn, but a lower Sp compared with DSE. Other studies have confirmed the excellent Sn of MCE and also found a lower Sp for predicting the recovery of function after revascularization.[34, 35] It has been noted that a combined assessment of perfusion and contractile reserve provides the most optimum Sn and Sp.[35]

Intravenous MCE was recently assessed for the detection of myocardial viability by Shimoni et al.[36] in the first human study, using quantitative MCE for the detection of myocardial hibernation. The authors studied 20 patients with CAD and LV systolic dysfunction; the patients underwent MCE, DSE and rest-distribution thallium-201 scintigraphy 1–5 days before bypass surgery. They found that the Sn of quantitative resting intravenous MCE for predicting the recovery of function was 90% and was similar to thallium-201 scintigraphy (92%) and superior to DSE (80%); the Sp was higher than for thallium-201 and also for DSE (63, 45 and 54%, respectively; $p < 0.05$). A recent paper by Hummel et al.[37] demonstrated the application of viability assessment by MCE in patients with ischaemic cardiomyopathy undergoing CRT. The authors found an MCE-based assessment of viability, a PSI based on a visual assessment of contrast opacification correlated with an acute improvement in the LVEF ($p = 0.003$), stroke volume ($p = 0.02$) and end systolic volume ($p = 0.05$). In a multi-variate model, PSI provided incremental predictive value to the degree of dyssynchrony, measured by TDI, for predicting an improvement in the LVEF. At 6 months, PSI remained positively correlated with an improvement in ventricular performance and with a reduction in LV end-diastolic volume. Furthermore, patients with a higher PSI subsequently tended to have a lower New York Heart Association class, a better 6 min walking distance, an improved quality-of-life score and fewer hospital admissions for HF after CRT. In summary, MCE is reliable for the detection of myocardial viability after AMI and chronic HF. However, more outcome data is required to establish this technique as a robust marker of myocardial viability.

Stress Echocardiography

Stress echocardiography is based on evaluation of contractile reserve, a characteristic feature of viable myocardium, which may be elicited by catecholamine stimulation. The underlying principle is that adrenoreceptor stimulation by dobutamine will augment function before ischaemia is engendered by increased myocardial work and metabolic demands. Typically, inotropic response primarily occurs at low doses and tachycardia potentially eliciting ischaemia usually only develops at higher doses.

Standard DSE exam involves various stages of either low- or high-dose protocols, with increments from 5 to 40 μg/kg/min, with each stage lasting 3 min. Some advocate using an even lower starting dose of 2.5 μg/kg/min, because in patients with critical coronary stenosis, myocardial ischaemia may be elicited with doses as low as 5 μg/kg/min. Infusions of low-dose dobutamine (5–10 μg/kg/min) increase contractility in dysfunctional but viable myocardium usually without significant tachycardia. A combination of low and high (≥20 μg/kg/min) doses has been shown to provide the greatest diagnostic information and accuracy for the prediction of functional recovery after revascularization. This is ascribed to the ability of high-dose dobutamine infusion to recognise ischaemia with

higher accuracy. Echocardiographic second harmonic images are acquired at each stage to determine new wall motion abnormalities, worsening of pre-existing wall motion abnormalities or enhanced wall motion. Clear endocardial definition is crucial for optimal regional function evaluation, which is performed using a 5-point wall motion scoring system (1 = normokinesis, 2 = mild hypokinesis, 3 = moderate or severe hypokinesis, 4 = akinesis and 5 = dyskenesis) for the 16- or 17-segment model of the LV. As with conventional echocardiography, patient-dependent factors such as obesity and lung disease may lead to poor acoustic windows and reduce diagnostic accuracy. In those patients, contrast-enhanced endocardial border detection may be additionally used during the DSE to improve endocardial border detection. Moreover, evaluation of wall motion abnormalities may be challenging in patients with previous myocardial infarction, in whom passive tethering motion is a confounding variable. Finally, signal dropout can cause suboptimal images, leading to misdiagnosis in some patients.

During dobutamine infusion, there are four possible responses of regions with abnormal resting function: (1) biphasic response – at low levels of dobutamine stimulation, systolic wall thickening increases and starts earlier, improving contractile function, but at higher levels, the increase in myocardial demand cannot be matched by further increases in blood flow, leading to ischaemia and systolic function deterioration; (2) sustained functional improvement at low doses that persisted or further improved until peak dose; (3) worsening of resting wall motion during dobutamine infusion without any improvement and (4) no change in function. The stress echocardiographic sign of myocardial viability is a stress-induced improvement of contractile function during low levels of stress in a region that is abnormal at rest. However, the pattern of response is predictive of post-revascularization functional improvement. A biphasic response, indicating that the tissue is not only viable but also supplied by a stenosed artery, has greatest predictive accuracy for recovery – in a recent study, 72% of segments with biphasic response recovered function. A uniphasic response with sustained improvement has limited Sp to predict functional recovery, as augmentation alone may occur not only with non-jeopardised myocardium (stunned), but also in areas of non-trans-mural infarction without hibernating myocardium (sub-endocardial scar) or in re-modelled myocardium. Finally, about 20–25% of viable segments do not improve functionally during inotropic stimulation, as they have an almost exhausted blood flow reserve and extensive structural abnormalities. However, those viable segments without improvement with dobutamine stimulation usually do not recover contractile function after revascularization.

Laboratory experiences revealed that the DSE using visual wall motion assessment demonstrated a mean Sn of 85% and Sp of 79% in regional functional recovery prediction.[38] Identification of contractile reserve by DSE is highly specific, but may lack Sn, as some myocardial segments without inotropic reserve may demonstrate recovery of function following revascularization. Moreover, owing to the subjectivity of visual wall motion interpretation, DSE is an experience-dependent technique with high degree of inter- and intra-observer variability. However, in clinical setting, the diagnostic accuracy of DSE is generally adequate for the prediction of regional recovery after revascularization.

In addition, various studies demonstrated that LVEF improved only in patients with substantial viability on DSE. A linear relation was present between the number of viable segments and the likelihood of recovery of overall LV function after revascularization and the identification of ≥4 viable segments accurately predicted LVEF improvement (e.g. ≥5%) after revascularization (Sn: 86%; Sp: 90%), improvement in HF symptoms and reduction in event rate.[38]

Alternative protocols for echocardiographic assessment of myocardial viability include dipyridamole, low level exercise and more recently, levosimendan. Exercise induces catecholamine stimulation, but the early development of tachycardia may provoke ischaemia and mask the inotropic response. Dipyridamole stress has been used for myocardial viability assessment, mainly in Europe, but the pathophysiology of dipyridamole response is less clear. Dipyridamole induces endogenous adenosine accumulation. It has been proposed that the stimulation of adenosine receptors, which induces regional vasodilatation, may cause an increase in tissue turgor and produce a reflex increase in the regional function. Exercise, dobutamine and dipyridamole show similar diagnostic accuracy in the induction of ischaemia. However, DSE is the most extensively studied and the most widely used test for the assessment of myocardial viability.

Recently, Cianfrocca et al.[39] compared the accuracy of levosimendan stress echocardiography with conventional DSE. Levosimendan enhances cardiac contractility via Ca^{2+} sensitization without increasing myocardial oxygen consumption and induces vasodilatation through the activation of adenosine triphosphate-sensitive potassium channels. They found that levosimendan was more reliable than dobutamine in predicting reversible dysfunction, having higher Sn (75 vs. 59%; $p = 0.026$) and similar Sp (80%). Of note, a further improvement in the prediction of functional recovery was found when wall motion response during levosimendan stress echocardiography was complemented by the measurement of peak systolic strain rate based on TDI (Sn: 93%).

Similarly, Karagiannis et al.[40] proved the additional value of evaluating the recovery phase of DSE after acute β-blocker administration, identifying some additional ischaemic segments otherwise classified as normal. Dobutamine stimulates β1, β2 and α1-adrenergic receptors. Acute β-blockade at the peak dose of DSE leaves unopposed α1-adrenergic vasoconstriction, reducing the coronary flow reserve, which can paradoxically enhance the ischaemic response in the recovery

phase. This method applied to DSE increased Sn for viability estimation from 72 to 85% ($p < 0.001$), while Sp remained unchanged (78%). However, some concerns remain regarding the potential risk of myocardial infarction and arrhythmias induced by acute β-blockade, which should be further addressed in larger trials.

The state-of-the art diagnosis of ischaemia and myocardial viability in DSE remains the qualitative analysis of regional wall motion. The major potential drawback for the use of this index is semi-quantitative assessment of wall motion, which is limited by subjectivity and technical challenges. Inter- and intra-observer wall motion score variability is even greater in those patients with previous myocardial infarction owing to pre-existing wall motion abnormalities and intra-ventricular conduction defects. In the last years, quantitative parameters have been studied to provide objective and reproducible information on global and regional wall function during stress. The most important methods aimed to improve DSE diagnostic accuracy and to reduce its operator dependency are: (1) automatic contour techniques including acoustic quantification and colour kinesis and (2) tissue Doppler myocardial velocity derived parameters. In this context, myocardial tissue velocity, strain and strain rate evaluated by TDI have emerged as promising echocardiographic tools for the quantitative assessment of regional ventricular function. The ventricular systole is a complex three-dimensional deformation process, in which the apex stays relatively stationary, while the base of the heart is moving downward making a global twist and resulting in longitudinal and circumferential shortening as well as radial thickening. TDI measures low-frequency, high-amplitude signals of myocardial tissue motion allowing for the assessment of myocardial velocities. However, myocardial velocity profiles are unable to discriminate passive motion from active deformation. During the pre-ejection period, the LV does not change in shape and the tethering effect is thus minimised. Aggeli et al.[41] showed that pre-ejection longitudinal tissue velocity change and peak systolic longitudinal velocity change assessed by pulsed-wave TDI during low-dose dobutamine are reliable parameters of myocardial viability, as their increase during the stress test strongly predicts recovery after revascularization. However, evaluation of myocardial velocities by pulsed-wave TDI during DSE is a very time-consuming technique without proven incremental value and is impracticable in everyday practice.

The post-processing of colour-coded tissue Doppler data allows quantification of myocardial deformation by measuring strain and strain rate. These new TDI-derived techniques assess velocity gradients between different points in space, allowing the evaluation of active contraction of a given segment, independent of local tethering of the neighbouring regions. Strain and strain rate reflect the percentage of deformation and intrinsic rate of deformation of the analyzed myocardial segment, respectively. These parameters are less dependent on image quality and less subjective than the visual assessment of endocardial border motion. During DSE, circumferential strain and strain rate are significantly lower in segments with myocardial infarction, compared with both sub-endocardial infarcts and normal myocardium, thus assessing the degree of trans-murality. Hanekom et al.[42] demonstrated that the assessment of strain rate imaging as an adjunct to routine visual wall motion scoring during conventional DSE provides incremental value to predict regional and global functional recovery following revascularization, increasing Sn from 73 to 83% compared with visual assessment alone, without affecting the Sp. A strain rate increment of 0.25/s during DSE was the optimal cut-off for functional recovery prediction (Sn 80%; Sp 75%). Further experimental and clinical studies have validated strain-rate imaging for the assessment of myocardial viability and suggested that strain rate is a better quantitative parameter for the prediction of functional recovery compared with strain.[39] However, SRI is limited by signal noise, low reproducibility and angle dependence, as the TDI evaluation of apical myocardial segments is unreliable.

Cianfrocca et al.[39] compared the accuracy of two different pharmacological stress protocols, full-dose dobutamine and levosimendan, with and without the combination of strain rate analysis to the conventional subjective wall motion evaluation. As previously discussed, levosimendan stress protocol was more reliable than dobutamine in predicting reversible dysfunction. Moreover, the peak strain rate assessment was better than wall motion analysis in detecting inotropic recruitment during pharmacological stress testing, with either dobutamine or levosimendan. Besides, an increment in peak strain rate > -0.29/s after levosimendan had the highest Sp (93%) for predicting segmental function recovery after revascularization.

Although myocardial deformation imaging based on speckle tracking has been validated in various circumstances, there are few studies supporting its use in stress echocardiography. Since 2D strain analysis allows accurate assessment of regional myocardial function, it may theoretically improve DSE accuracy in the assessment of myocardial viability, through quantification of the regional function during stress in viable segments (Fig. 16.6). Recently, Hane Kom et al. [48] compared TDI strain rate and 2D strain in patients undergoing DSE and coronary angiography, and they found that both techniques are feasible and accurate, particularly in the assessment of ischaemia in left anterior descending territory. However, neither 2D strain nor TDI strain rate provided incremental accuracy to wall motion conventional analysis.

Recent advances in this technology raised the prospect that SRI may become a routinely employed modality for quantitative assessment of viability during DSE. However, it should be underscored that strain rate analysis is time-consuming, requiring 15–25 min of additional analysis.

Finally, technological advances in transducer and computer technology led to introduction of real-time 3D echocardiography

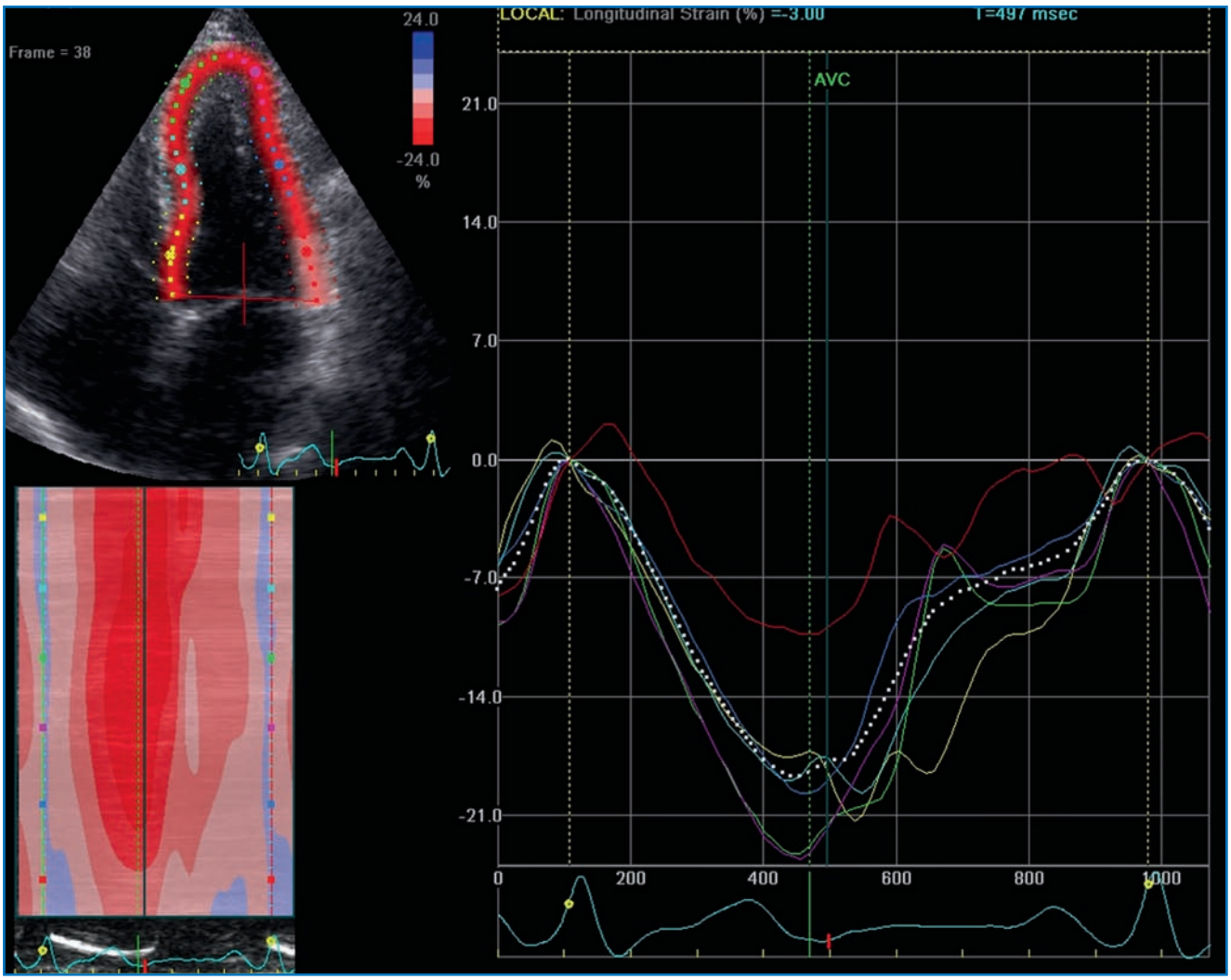

Fig. 16.6 Example of strain curves at rest **(a)** and with low dose dobutamine **(b)** in a patient with previous lateral acute myocardial infarction, showing improvement in the basal lateral segment demonstrating the presence of a viable segment

during stress, but no data currently show the additional value of this technique over conventional DSE.

Comparison with Other Modalities

Single-Photon Emission Computed Tomography

Among the radionuclide imaging techniques available to assess myocardial viability, the most commonly used is SPECT, either using thallium-201 or Tc-99m sestamibi. There are several SPECT protocols to evaluate myocardial viability, in stress and/or rest, which include imaging from 8 to 72 h after stress injection, re-injection of tracer at rest on the same day as the stress injection, a resting injection on a separate day or adjuncts such as nitrates.

Thallium-201 is a potassium analogue that is actively transported through the intact cell membrane of the myocyte. Thus, the initial uptake of thallium is determined by myocardial perfusion (either during stress or at rest) and is unaffected by hypoxia, hibernation or stunning, unless myocardial infarction is present. Conversely, delayed retention in the redistribution phase is dependent on cell membrane integrity, which is flow-independent. Thus, areas without thallium uptake in early rest image that fill-in in the redistribution phase represent hibernating myocardium, whereas fixed defect areas represent scars. Several protocols have been proposed with thallium-201 being the most frequently used rest-redistribution and stress-redistribution re-injection. The former assesses only myocardial viability and the latter assesses myocardial ischaemia and viability

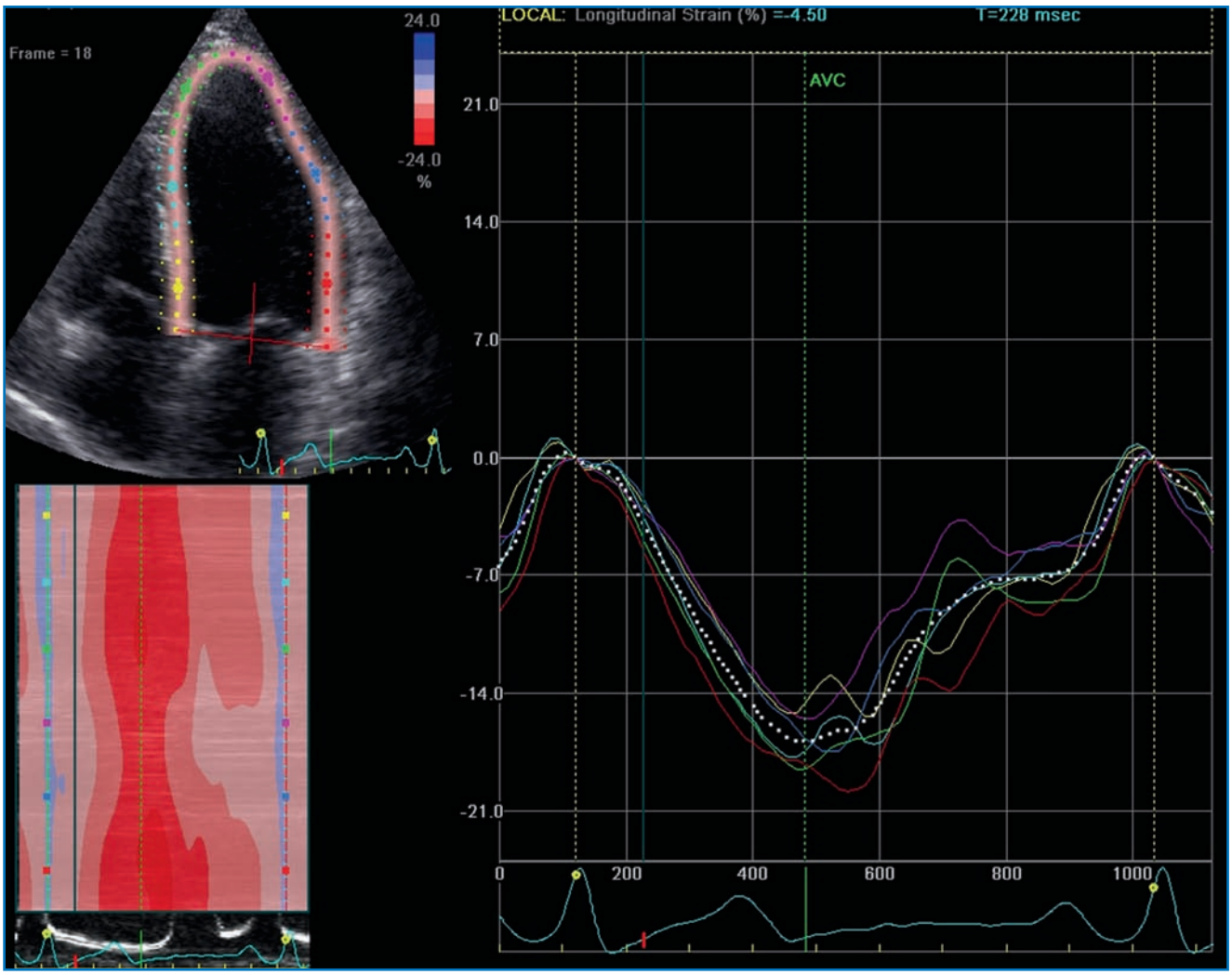

Fig. 16.6 (continued)

and is the recommended STECT imaging modality. Both protocols have high Sn for predicting regional function recovery after revascularization (86%), but have a relatively low Sp (50%).[38]

Myocardial uptake and retention of technetium-99m sestamibi/tetrofosmin is dependent on regional perfusion and requires mitochondrial membrane integrity, thus reflecting myocardial viability. Technetium-STECT also has high Sn (79%) but a relatively low Sp (58%) for the prediction of post-revascularization improvement of regional ventricular function.[38]

Nitrates administration increases antegrade and collateral blood flow to areas of reduced resting perfusion and therefore improves tracer delivery, either thallium or sestamibi, to viable regions of the myocardium. Thus, nitrate-enhanced rest perfusion imaging and gated-SPECT has higher accuracy for the detection of myocardial viability.

SPECT, either with thallium or technetium tracers, is more sensitive for detecting recoverable myocardium than DSE. Baumgartner et al.[43] effectively showed that the minimum critical mass of viable myocardium needed for the detection by DSE is higher than that required by thallium-SPECT or fluorodeoxyglucose-PET. By histological examination of 12 hearts of patients with CAD and severely reduced ventricular function referred for cardiac transplantation and previously submitted to the various imaging procedures, it was found that segments with <25% viable myocytes showed echocardiographic evidence of viability in only 19% of cases, compared with 33% for fluorodeoxyglucose-PET and 38% for thallium-SPECT. However, DSE is more specific for predicting functional improvement after revascularization, as the little amounts of viable tissue additionally recognised by nuclear modalities are frequently unable to contribute to regional function recovery.

Finally, the integrated biological risk-benefit balance of the examination method should be taken into account whenever SPECT is considered. Current protection standards and practices are based on the premise that ionising radiation can

result in serious detrimental health effects. These include long-term development of cancer and genetic damage. At a patient level, the effective dose of a single nuclear stress imaging ranges from 10 to 27 mSv, which is equivalent to the exposure to 500 chest X-rays (sestamibi-SPECT) or 1,200 chest X-rays (thallium-SPECT). As in practical terms SPECT and DSE accuracies are relatively similar, DSE should be preferred because of lower cost, wider availability, absence of environmental impact and lack of biological effects justified by its radiation-free nature.

Positron Emission Tomography

PET allows the evaluation of myocardial viability by qualitative and quantitative assessment of myocardial function, perfusion and metabolism. The assessment of function identifies regions with contractile dysfunction, which may potentially be viable myocardium. For the assessment of perfusion, several tracers are available, including N-13 ammonia, O-15 labelled water and rubidium-82. For the assessment of metabolism, F-18-fluorodeoxyglucose (FDG) is the most extensively used tracer owing to the central role of glucose metabolism in myocardial ischaemic areas, particularly if given under conditions that encourage glucose metabolism, such as oral glucose load, nicotinic acid or insulin and glucose infusion. The viable tissue is metabolically active, having preserved or increased glucose consumption, whereas scarred tissue is metabolically inactive. FDG and ammonia studies have been combined to achieve the maximum accuracy for the detection of viability. Normal tissue shows normal function, perfusion and metabolism. Stunned myocardium shows diminished function but relatively normal perfusion and metabolism. Hibernating myocardium can be identified by reduced perfusion with preserved or increased metabolism (metabolism-perfusion mismatch). Conversely, scar tissue has reduced function, perfusion and metabolism (metabolism-perfusion match).

Several non-randomized retrospective studies showed that FDG-PET predicts recovery of regional function after revascularization with high Sn (71–100%) but a relatively low Sp (33–91%).[38] PET systems generally have better Sn and spatial resolution than SPECT systems and provide more accurate attenuation correction. When compared with DSE, FDG-PET has higher Sn, identifying the uptake of the tracer in 30–50% of presumably non-viable segments. However, the identification of islets of viable myocytes in segments without contractile reserve does not necessarily results in regional recovery. That explains why Sp of FDG-PET is lower than the achieved by DSE. Furthermore, as PET demands significant exposure to radiation without relevant additional benefit, alternative imaging methods without biological adverse effects should be preferred.

Cardiovascular Magnetic Resonance Imaging

CMR is a rapidly emerging non-invasive imaging technique providing information on cardiac anatomy, function and perfusion with great spatial resolution in any desired plane and without radiation. CMR consists of several techniques that can be performed separately or in various combinations during a patient examination. The two most important CMR techniques to assess myocardial viability are the delayed enhancement CMR (DE-CMR) and the dobutamine CMR.

DE-CMR is a newly established technique to detect areas of acute or chronic infarct, which is presented as bright regions in inversion recovery images acquired 5–20 min after the intravenous administration of an extracellular gadolinium-based contrast agent. In the setting of AMI, the contrast agent passively diffuses into the intracellular space owing to the loss of membrane integrity of the necrotic cells, resulting in an increased tissue level contrast concentration and, therefore, in hyper-enhancement of the affected areas. In chronic infarcts, the increased interstitial space between collagen fibres and the delayed washout owing to reduced capillary density accounts for contrast enhancement in the scar tissue. Hence, in chronic CAD, hyper-enhanced areas correspond to fibrotic tissue within the myocardial wall. Conversely, viable myocardium, either stunned or hibernating, has normal distribution volume of the contrast medium, and therefore retention of contrast does not occur. Owing to its superior special resolution, DE-CMR has the unique ability to assess small volumes of irreversibly injured myocardium, as low as 2 g and to measure the trans-mural extent of myocardial infarction.

DE-CMR has been extensively validated in animal models of ischaemic injury as well as in a variety of patient cohorts. Clinical studies demonstrated that DE-CMR is effective in identifying the presence, location and trans-mural extent of myocardial scarring and found a strong correlation between DE-CMR, thallium-SPECT and FDG-PET. Moreover, the extent of contrast enhancement on a segmental basis is useful for the prediction of improvement in contractile function after revascularization in CAD patients. Regional wall motion improvement can be expected in dysfunctional segments with a hyper-enhancing portion of up to 50% of the wall thickness, with the chance of functional improvement lower in those segments with higher trans-mural extension of hyper-enhancement. Besides, unlike stress tests (either DSE or dobutamine CMR), which appear to have reduced accuracy if more severe dysfunction is present, DE-CMR seems to have greater accuracy in segments with the most severe dysfunction. Although there are no head-to-head comparisons of DSE and DE-CMR in the assessment of myocardial viability, historical studies suggest that DE-CMR may have higher Sn (≈90%) but lower Sp (≈50%), which is mainly because of the variable functional recovery in myocardial segments with 25–75% hyper-enhancement. Theoretically, in those patients with intermediate levels

of hyper-enhancement, the predictive value of DE-CMR is likely to increase by the combination of low-dose dobutamine, but no comparative studies have been performed yet.

Dobutamine-CMR assesses contractile reserve during low dose dobutamine stress testing. Similar to echocardiography, CMR allows the visualization of regional wall motion and systolic wall thickening, but is characterised by superior endocardial border definition. Regional function is qualitatively assessed as normal, hypokinetic, akinetic or dyskinetic. The improvement of contractile function during low-dose dobutamine stress is indicative of myocardial viability. The majority of studies suggest that dobutamine-CMR has a relatively modest Sn but high Sp for the prediction of regional recovery after revascularization, ranging from 50 to 90% and 73 to 94%, respectively.

The diagnostic performance of dobutamine-CMR is comparable to DSE and is superior in patients with poor acoustic windows. Moreover, DE-CMR appears to have a greater accuracy than dobutamine-CMR, even in segments with severe dysfunction, does not require pharmacological test, is technically easier as well as less observer dependent for interpretation. Thus, DE-CMR will probably become the routine procedure for CMR assessment of myocardial viability. However, in those patients with multiple segments having intermediate trans-murality (25–75%), complementary use of DE-CMR and dobutamine-CMR may be the optimal CMR strategy for predicting post-revascularization functional recovery.

When compared with DSE, CMR (either DE-CMR or dobutamine-CMR) disadvantages include higher costs, lower availability, need for breath-holding sequences during acquisition, lower temporal resolution, poor images with irregular rhythms and is unemployable in patients with implanted metallic devices. However, owing to the absence of ionising radiation, CMR is an excellent option when stress echocardiography is inconclusive or not feasible.

Multi-Slice Computed Tomography

Advances in multi-detector computed tomography, particularly with the introduction of ECG-gated multi-slice spiral computed tomography (MSCT) have radically changed the role of computed tomography in cardiac imaging. MSCT assessment of myocardial morphology, myocardial perfusion imaging and delayed myocardial contrast enhancement were introduced, with the latter evolving as the key concept of MSCT viability imaging.

On delayed enhanced MSCT, myocardial infarction shows increased attenuation values when compared with healthy myocardium, which is explained by a combination of delayed wash-in and wash-out contrast kinetics and an increased volume of distribution of the contrast in the expanded interstitial compartment of the fibrous scar.

Several studies in animals as well as in patients proved the reliability of enhanced MSCT to detect and characterise scar tissue. The majority of these clinical studies evaluated the accuracy of MSCT in detecting viable segments as identified by DSE, SPECT or CMR, in patients with previous myocardial infarction (1–6 months). Chiou et al.[44] recently showed that increasing segmental extent of MSCT late-enhancement is associated with an increase in segments classified as non-viable by both SPECT and DSE, and that the concordance between MSCT and DSE reached 91.1% when the segmental extent was >75%.

Cardiac MSCT is a promising non-invasive imaging technique that offers a better spatial resolution than CMR. However, it is coupled with a relevant radiation exposure, which seriously limits its clinical application. Moreover, MSCT usefulness for predicting contractile function recovery after revascularization in patients with chronic CAD was never evaluated.

Future Perspectives

Molecular imaging is a very new and promising area of research. It aims to develop techniques applicable to echocardiography, computed tomography or magnetic resonance, enabling the assessment of physiological and metabolic processes with these diagnostic modalities. In a simplistic view, molecular imaging will enable the study of physiological processes that are currently assessed only by PET/SPECT, without the drawbacks of the nuclear techniques and with higher spatial resolution. For example, ligands or antibodies can be attached to the surface of contrast echocardiography micro-bubbles, resulting in their binding to specific epitopes up-regulated on the endothelial surface.

Molecular imaging is still predominantly in the preclinical research phase. Recent studies in animal models have presented particularly promising results for ultrasound detection of arteriogenesis (desintegrins conjugated with micro-bubbles), severity and extent of post-ischaemic inflammation (phosphatidylserine incorporated into micro-bubbles) or remote ischaemic areas (P-selectins attached to micro-bubbles).[45]

Integrated Imaging in Clinical Practice

DSE, SPECT, DE-CMR, dobutamine-CMR and MCE have been proven to be useful for detecting myocardial viability and predicting overall LV function recovery, HF symptoms reduction and clinical outcome improvement in retrospective non-randomised studies. The absence of randomised clinical trials for head-to-head comparison of those imaging modalities limits the choice of the optimal diagnostic strategy and

one should exercise some care in their application to patient management. Nonetheless, considering the diagnostic accuracy, availability and risk of adverse effects, a pragmatic approach may be proposed (Table 16.1 and Fig. 16.7).

The assessment of myocardial viability should start with a resting echocardiographic study, evaluating the acoustic window, endocardial borders and wall thickening in all segments, severity of wall motion abnormalities and LVEF. In those patients with adequate acoustic window and without severe LV dysfunction at rest, myocardial viability may be evaluated by DSE.

Severe LV dysfunction at rest reduces the predictive accuracy of DSE. Poor image quality despite contrast enhancement of a non-stress diagnostic modality is preferable in such patients. For detecting viable myocardium in such patients, SPECT, PET, CMR and MCE may be useful. DE-CMR may be a preferred alternative owing to its radiation-free nature and good diagnostic accuracy. In those patients with multiple segments having intermediate trans-mural hyper-enhancement (25–75%), complementary use of DE-CMR and dobutamine-CMR may be relevant. MCE may also be a reasonable alternative, but larger outcome data are required. SPECT is a well-established modality, readily available and with proven usefulness. However, it entails significant exposure to radiation, which can result in detrimental health effects. Thus, it is likely that the growth of MRI and MCE in the coming years may make them the preferred diagnostic modality for patients who cannot be adequately assessed by DSE. The choice of diagnostic modality should to a great extent depend on the expertise of the medical centre.

Table 16.1. Criteria indicating low probability of improvement with revascularization in patients with global LV dysfunction and multi-vessel disease

≥4 Major criteria
Three major plus 1 minor
Two major plus 2 minor
Major criteria
LV wall thickness ≤5 to 6 mm
No response to low-dose DSE
SPECT negative for viability
>50% of wall thickness hyper-enhancement in DE-CMR
PET negative for hibernating myocardium
No myocardial enhancement on MCE
Minor criteria
LVEF ≤20%
LV volumes: 1 or more of the following
By angiography: LVEDVI ≥200 mL/m^2 and/or LVESVI ≥120 mL/m^2
By echocardiography: LVEDVI ≥170 mL/m^2 and/or LVESVI ≥90 mL/m^2
Echocardiographic dimension: LVEDDI ≥5.5 cm^2/m^2

Adapted from Rahimtoola et al.[47]
LVEDVI left ventricle end-diastolic volume/index; *LVEDDI* left ventricle end-diastolic dimension/index; *LVESI* left ventricle end-systolic volume/index

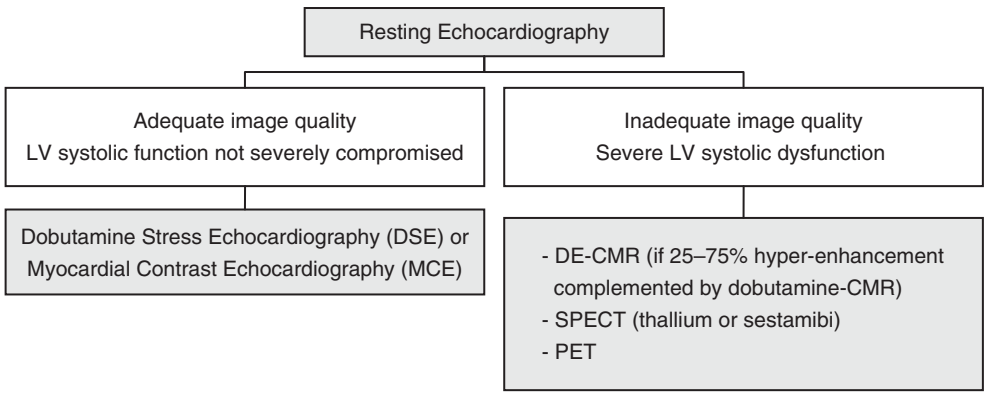

Fig. 16.7 Algorithm for the assessment of myocardial viability

References

1. Melo LG, Pachori AS, Kong D, et al Molecular and cell–based therapies for protection, rescue, and repair of ischemic myocardium: reasons for cautious optimism. *Circulation*. 2004;109(20): 2386–2393
2. Bax JJ, van der Wall EE, Harbinson M. Radionuclide techniques for the assessment of myocardial viability and hibernation. *Heart*. 2004;90(suppl 5):v26–v33
3. Cleland JG, Pennell DJ, Ray SG, et al Myocardial viability as a determinant of the ejection fraction response to carvedilol in patients with heart failure (CHRISTMAS trial): randomised controlled trial. *Lancet*. 2003;362(9377):14–21
4. Dispersyn GD, Borgers M, Flameng W. Apoptosis in chronic hibernating myocardium: sleeping to death? *Cardiovasc Res*. 2000;45(3): 696–703
5. Bax JJ, Visser FC, Poldermans D, et al Time course of functional recovery of stunned and hibernating segments after surgical revascularization. *Circulation*. 2001;104(12 suppl 1):I314–I318
6. Beanlands RS, Hendry PJ, Masters RG, deKemp RA, Woodend K, Ruddy TD. Delay in revascularization is associated with increased mortality rate in patients with severe left ventricular dysfunction and viable myocardium on fluorine 18–fluorodeoxyglucose positron emission tomography imaging. *Circulation*. 1998;98(19 suppl): II51–II56
7. Senior R, Lahiri A. Dobutamine echocardiography predicts functional outcome after revascularization in patients with dysfunctional myocardium irrespective of the perfusion pattern on resting thallium–201 imaging. *Heart*. 1999;82(6):668–673
8. Alderman EL, Fisher LD, Litwin P, et al Results of coronary artery surgery in patients with poor left ventricular function (CASS). *Circulation*. 1983;68(4):785–795
9. Bounous EP, Mark DB, Pollock BG, et al Surgical survival benefits for coronary disease patients with left ventricular dysfunction. *Circulation*. 1988;78(3 pt 2):I151–I157
10. Krishnamani R, El Zaru M, DeNofrio D. Contemporary medical, surgical, and device therapies for end–stage heart failure. *Curr Treat Options Cardiovasc Med*. 2003;5(suppl 6):487–499
11. Baker DW, Jones R, Hodges J, Massie BM, Konstam MA, Rose EA. Management of heart failure. III. The role of revascularization in the treatment of patients with moderate or severe left ventricular systolic dysfunction. *JAMA*. 1994;272(19):1528–1534
12. Kaul S, Jayaweera AR. Coronary and myocardial blood volumes: noninvasive tools to assess the coronary microcirculation? *Circulation*. 1997;96(3):719–724
13. Holmes DR Jr, Detre KM, Williams DO, et al Long–term outcome of patients with depressed left ventricular function undergoing percutaneous transluminal coronary angioplasty. The NHLBI PTCA Registry. *Circulation*. 1993;87(1):21–29
14. Penicka M, Tousek P, De Bruyne B, et al Myocardial positive pre–ejection velocity accurately detects presence of viable myocardium, predicts recovery of left ventricular function and bears a prognostic value after surgical revascularization. *Eur Heart J*. 2007;28(11): 1366–1373
15. Becker M, Lenzen A, Ocklenburg C, et al Myocardial deformation imaging based on ultrasonic pixel tracking to identify reversible myocardial dysfunction. *J Am Coll Cardiol*. 2008;51(15): 1473–1481
16. Wei K, Jayaweera AR, Firoozan S, Linka A, Skyba DM, Kaul S. Basis for detection of stenosis using venous administration of microbubbles during myocardial contrast echocardiography: bolus or continuous infusion? *J Am Coll Cardiol*. 1998;32(1):252–260
17. Linka AZ, Sklenar J, Wei K, Jayaweera AR, Skyba DM, Kaul S. Assessment of transmural distribution of myocardial perfusion with contrast echocardiography. *Circulation*. 1998;98(18):1912–1920
18. Wei K, Jayaweera AR, Firoozan S, Linka A, Skyba DM, Kaul S. Quantification of myocardial blood flow with ultrasound–induced destruction of microbubbles administered as a constant venous infusion. *Circulation*. 1998;97(5):473–483
19. Cobb FR, Bache RJ, Rivas F, Greenfield JC Jr. Local effects of acute cellular injury on regional myocardial blood flow. *J Clin Invest*. 1976;57(5):1359–1368
20. Senior R, Swinburn JM. Incremental value of myocardial contrast echocardiography for the prediction of recovery of function in dobutamine nonresponsive myocardium early after acute myocardial infarction. *Am J Cardiol*. 2003;91:397–402
21. Shimoni S, Frangogiannis NG, Aggeli CJ, et al Microvascular structural correlates of myocardial contrast echocardiography in patients with coronary artery disease and left ventricular dysfunction: implications for the assessment of myocardial hibernation. *Circulation*. 2002;106:950–956
22. Janardhanan R, Moon JC, Pennell DJ, Senior R. Myocardial contrast echocardiography accurately reflects transmurality of myocardial necrosis and predicts contractile reserve after acute myocardial infarction. *Am Heart J*. 2005;149(2):355–362
23. Coggins MP, Sklenar J, Le DE, et al Noninvasive prediction of ultimate infarct size at the time of acute coronary occlusion based on the extent and magnitude of collateral–derived myocardial blood flow. *Circulation*. 2001;104:2471–2477
24. Swinburn JM, Lahiri A, Senior R. Intravenous myocardial contrast echocardiography predicts recovery of dysynergic myocardium early after acute myocardial infarction. *J Am Coll Cardiol*. 2001;38: 19–25
25. Jeetley P, Swinburn J, Hickman M, et al Myocardial contrast echocardiography predicts left ventricular remodelling after acute myocardial infarction. *J Am Soc Echocardiogr*. 2004;17: 1030–1036
26. Huang WC, Chiou KR, Liu CP, et al Comparison of real–time contrast echocardiography and low–dose dobutamine stress echocardiography in predicting the left ventricular functional recovery in patients after acute myocardial infarction under different therapeutic intervention. *Int J Cardiol*. 2005;104:81–91
27. Hickman M, Janardhanan R, Dwivedi G, et al Clinical significance of perfusion techniques utilising different physiological mechanisms to detect myocardial viability: a comparative study with myocardial contrast echocardiography and single photon emission computed tomography. *Int J Cardiol*. 2007;114:139–140
28. Myers JH, Stirling MC, Choy M, et al Direct measurement of inner and outer wall thickening dynamics with epicardial echocardiography. *Circulation*. 1986;74:164–172
29. Swinburn JM, Senior R. Real time contrast echocardiography – a new bedside technique to predict contractile reserve early after acute myocardial infarction. *Eur J Echocardiogr*. 2002;3:95–99
30. Main ML, Magalski A, Chee NK, et al Full–motion pulse inversion power Doppler contrast echocardiography differentiates stunning from necrosis and predicts recovery of left ventricular function after acute myocardial infarction. *J Am Coll Cardiol*. 2001;38:1390–1394
31. Balcells E, Powers ER, Lepper W, et al Detection of myocardial viability by contrast echocardiography in acute infarction predicts recovery of resting function and contractile reserve. *J Am Coll Cardiol*. 2003;41:827–833
32. Dwivedi G, Janardhananan R, Hayat SA, Swinburn JM, Senior R. Prognostic value of myocardial viability detected by myocardial contrast echocardiography early after acute myocardial infarction. *J Am Coll Cardiol*. 2007;50(4):327–334
33. Nagueh SF, Vaduganathan P, Ali N, et al Identification of hibernating myocardium: comparative accuracy of myocardial contrast echocardiography, rest–redistribution thallium–201 tomography and dobutamine echocardiography. *J Am Coll Cardiol*. 1997;29: 985–993
34. deFilippi CR, Willett DL, Irani WN, et al Comparison of myocardial contrast echocardiography and low–dose dobutamine stress

echocardiography in predicting recovery of left ventricular function after coronary revascularization in chronic ischemic heart disease. *Circulation*. 1995;92:2863–2868
35. Meza MF, Ramee S, Collins T, et al Knowledge of perfusion and contractile reserve improves the predictive value of recovery of regional myocardial function post revascularization: a study using the combination of myocardial contrast echocardiography and dobutamine echocardiography. *Circulation*. 1997;96:3459–3465
36. Shimoni S, Frangogiannis NG, Aggeli CJ, et al Identification of hibernating myocardium with quantitative intravenous myocardial contrast echocardiography: comparison with dobutamine echocardiography and thallium–201 scintigraphy. *Circulation*. 2003;107: 538–544
37. Hummel JP, Lindner JR, Belcik JT, et al Extent of myocardial viability predicts response to biventricular pacing in ischemic cardiomyopathy. *Heart Rhythm*. 2005;2:1211–1217
38. Rizzello V, Poldermans D, Bax JJ. Assessment of myocardial viability in chronic ischemic heart disease: current status. *Q J Nucl Med Mol Imaging*. 2005;49(1):81–96
39. Cianfrocca C, Pelliccia F, Pasceri V, et al Strain rate analysis and levosimendan improve detection of myocardial viability by dobutamine echocardiography in patients with post–infarction left ventricular dysfunction: a pilot study. *J Am Soc Echocardiogr*. 2008; 21(9):1068–1074
40. Karagiannis SE, Feringa HH, Bax JJ, et al Myocardial viability estimation during the recovery phase of stress echocardiography after acute beta–blocker administration. *Eur J Heart Fail*. 2007;9(4): 403–408
41. Aggeli C, Giannopoulos G, Roussakis G, et al Pre–ejection tissue–Doppler velocity changes during low dose dobutamine stress predict segmental myocardial viability. *Hellenic J Cardiol*. 2007;48(1): 23–29
42. Hanekom L, Jenkins C, Jeffries L, et al Incremental value of strain rate analysis as an adjunct to wall–motion scoring for assessment of myocardial viability by dobutamine echocardiography: a follow–up study after revascularization. *Circulation*. 2005;112(25):3892–3900
43. Baumgartner H, Porenta G, Lau YK, et al Assessment of myocardial viability by dobutamine echocardiography, positron emission tomography and thallium–201 SPECT: correlation with histopathology in explanted hearts. *J Am Coll Cardiol*. 1998;32(6): 1701–1708
44. Chiou KR, Liu CP, Peng NJ, et al Identification and viability assessment of infarcted myocardium with late enhancement multidetector computed tomography: comparison with thallium single photon emission computed tomography and echocardiography. *Am Heart J*. 2008;155(4):738–745
45. Villanueva FS, Lu E, Bowry S, et al Myocardial ischemic memory imaging with molecular echocardiography. *Circulation*. 2007; 115(3):345–352
46. Janardhanan R, et al Am J Cardiol 2003;92:493–497
47. Rahimtoola SH, Dilsizian V, Kramer CM, Marwick TH, Vanoverschelde J–L J. Chronic ischemic left ventricular dysfunction: from pathophysiology to imaging and its integration into clinical practice. *JACC Cardiovasc Imaging*. 2008;1(4):536–555
48. Hanekom L, Cho gy, Leano R, et al Comparison of twodimensional speckle and tissue Doppler strain measurement during dobutamine stress echocardiography: an angiographic correlation. *Eur Heart J* 2007;28:1765–72

Chapter 17

NUCLEAR IMAGING AND MULTI-DETECTOR COMPUTED TOMOGRAPHY TO ASSESS VIABILITY

Pasquale Perrone-Filardi and Bernhard Lothar Gerber

CONTENTS

J. L. Zamorano et al. (eds.), *The ESC Textbook of Cardiovascular Imaging*
DOI: 10.1007/978-1-84882-421-8_17, © Springer-Verlag London Limited 2010

Introduction

Evaluation of myocardial viability by cardiac imaging plays a critical role in the decision-making therapeutic strategies for patients with ischaemic left ventricular (LV) dysfunction. Application of cardiac imaging for viability assessment follows distinct pathophysiological approaches, namely regional assessment of perfusion by either single-photon emission computed tomography (SPECT) or positron emission tomography (PET), regional assessment of perfusion and metabolism by PET, verification of residual contractile reserve in dysfunctional myocardium using dobutamine stimulation, or direct visualization of necrotic myocardium by magnetic resonance imaging (MRI) or multi-detector computed tomography (MDCT). Identification of viability bears relevant implications because it has been repeatedly reported that in patients with viability remaining in medical therapy, mortality is substantially higher than in those with viability undergoing revascularization.

For predicting the recovery of regional or global LV systolic function at rest, nuclear techniques (PET and SPECT) demonstrate very high sensitivity but reduced specificity, which in clinical terms translates into overestimation of potential for recovery of systolic function, whereas an opposite behaviour is reported by techniques assessing contractile reserve. MDCT, like MRI, directly evaluates the presence of necrotic tissue using late enhancement (LE) after injection of a contrast agent. Although no sufficient clinical experience has yet been reported, MDCT has the potential for a comprehensive anatomic and tissue characterization within a single test.

The concept of *myocardial viability* was established in the early 1970s when several clinical studies reported the observation that areas of dysfunctional myocardium at rest partially or completely recovered contraction following coronary revascularization. These observations led to the innovative conclusion that lack of contraction of the myocardium does not necessarily indicate irreversible myocyte damage due to myocardial necrosis, but may be a reversible phenomenon exhibiting recovery of function upon revascularization.[1] This new pathophysiological condition was conceptualized later by Rahimtoola, and termed *hibernating myocardium*.[2] Almost in parallel with the recognition of hibernation, the identification of *stunned myocardium*, a distinct pathophysiological phenomenon leading to transient and spontaneously reversible regional contractile dysfunction immediately following an acute ischaemic insult, was gaining growing clinical relevance as it was repeatedly demonstrated in several clinical conditions spanning from chronic stable coronary artery disease to acute coronary syndromes.[3] Thus, three distinct pathophysiological conditions listed in Table 17.1 may be responsible for LV dysfunction in patients with ischaemic cardiomyopathy. For clinical purposes, the concept of *viable myocardium* refers to the potential recovery of regional myocardial contractile function at rest independently on its pathophysiological substrate. Although useful and simple for clinicians, the introduction of such a broad clinical definition of viability reflects the difficulty of characterizing the substrate of regional contractile dysfunction in humans, which is very rarely sustained by a unique condition, but is more often the sum of admixture of viable dysfunctional (either stunning or hibernating) necrotic and normal myocardium. The original concept of hibernation has also been challenged in several aspects since the evidence of reduced blood flow yielded conflicting results in human studies.[4] Moreover, the possibility that the phenomenon could also be due to repetitive episodes of stunning because of reduced coronary flow reserve has been postulated.[5] In addition, the postulate of preserved albeit transient contractile reserve, despite reduced blood flow, has also been questioned because it was demonstrated that contractile reserve is abolished in metabolically viable myocardium where coronary reserve is severely reduced or absent,[6] which explains the reduced sensitivity for predicting functional recovery of techniques that evaluate contractile reserve in dysfunctional myocardium supplied by occluded coronary vessels.[7] Finally, more recent histopathologic studies have demonstrated progressive ultrastructural changes in hibernating myocardium characterized by an embryonic phenotype and apoptotic damage,[8] challenging the concept of a long-term smart adaptation to chronic hypo-perfusion and emphasizing the need for prompt revascularization to prevent irreversible impairment of the contractile machinery and obtain recovery of function.[9] Experimental data further challenged the benign conception of hibernation demonstrating a propensity for fatal arrhythmias in animals with hibernation, despite lack of necrosis. This provides a potential explanation for the negative prognosis of patients with evidence of viable myocardium undergoing medical therapy.[10]

Table 17.1. Pathophysiology of left ventricular regional contractile dysfunction

Condition	Resting perfusion	Metabolic activity	Contractile reserve	Recovery
Stunning	Normal	Enhanced	++	++
Hibernation	Reduced	Enhanced	±	±
Scar	Reduced	Absent	–	–

Clinical Outcomes and the "Gold Standard" of Viability

From histopathologic and pathophysiological viewpoints, myocardial viability is the *absence of myocardial necrosis*; however, from a clinical point of view and when assessing

the value of tests for identification of myocardial viability, several targets for assessing myocardial viability may be considered. Traditionally, the concept of viability refers to the identification of *reversible regional dysfunction* at rest, and all techniques so far evaluated for the identification of viable myocardium in humans have been tested against this end point. However, although it is intuitive that an increase of LV *ejection fraction (EF)* is a favourable effect in patients with depressed LV function, lack of EF increase may not necessarily indicate absence of favourable prognostic effects of revascularization.[11] In fact, EF at rest is not the only determinant of prognosis in patients with ischaemic LV dysfunction. *Re-modelling*, especially an increase in end-systolic volume, has been demonstrated to be a powerful predictor of mortality in patients with LV dysfunction, independent of EF.[12] Reduction of LV volumes may occur after revascularization without changes in EF, but this end point has never been adopted to test accuracy of techniques assessing viability. Yet, it has been demonstrated that the extent of viable myocardium directly correlates with the degree of LV re-modelling and predicts inverse re-modelling, i.e. reduction of end-systolic and end-diastolic LV volumes, after revascularization.[13] Actually, in patients with severe LV dysfunction undergoing resynchronization therapy, it has been reported that 6 months reduction of LV end-systolic volumes predicts short-term survival improvement, suggesting that changes in LV volumes may represent a valuable surrogate end point to predict the effects of therapies on prognosis. Interestingly, similar data are not available for EF at rest. Apart from reduction in ventricular volumes, there are several additional favourable effects that may be determined by revascularization without affecting EF (Table 17.2).

From the patient's point of view, the most important parameter to consider might be *improvement of heart failure symptoms*. This parameter can be assessed either subjectively (NYHA class) or objectively (maximal VO_2 or 6 min walking test), yet it has very infrequently been assessed. A final important end point is *improvement of survival*. In fact, there are actual data that suggest that areas of viable myocardium, although not large enough to impact global LV function, may represent territories of electrical instability potentially accounting for the development of malignant arrhythmias, as recently reported using MRI.[13] Therefore, it

Table 17.2. Favourable effects of revascularization of viable myocardium

Recovery of resting ejection fraction
Recovery of diastolic function
Prevention of inducible ischaemia
Prevention/stabilization of adverse re-modelling
Prevention of ventricular arrhythmias

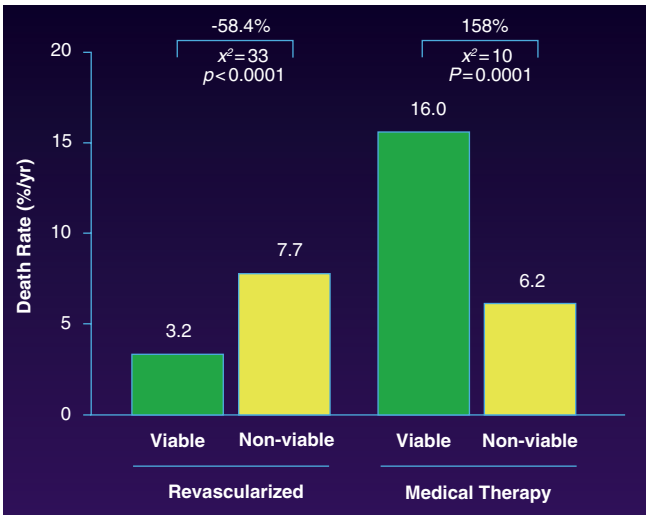

Fig. 17.1 Death rates for patients with ischaemic LV dysfunction undergoing medial therapy or revascularization, sub-grouped according to the presence of viable or non-viable myocardium. Revascularization of patients with viability is associated with a 79% yearly difference in mortality. Reproduced from Allman et al.[14] with permission

has been repeatedly reported that the presence of viable myocardium represents an independent unfavourable determinant of survival in patients with ischaemic LV dysfunction. Although only single-centre non-randomized studies are available, pooling of data clearly indicates that patients with evidence of viable myocardium treated with medical therapy have a substantially worse survival when compared to those with viable myocardium undergoing revascularization (Figs. 17.1 and 17.2).[14] As revascularization of viable myocardium was shown to favourably affect the different outcomes previously discussed, demonstration of viability in patients with ischaemic LV dysfunction is currently considered among the indications for revascularization. An important point that is still not completely understood is the minimal amount of viable myocardium that should prompt revascularization. Indeed, clinicians are often challenged by patients with evidence of small areas of viable myocardium, of which the clinical relevance is doubtful. Information from small studies indicates that a substantial improvement of EF at rest following revascularization may ensue when at least four (in a model dividing the myocardium in 17 segments) (Fig. 17.3) severely dysfunctional segments demonstrate preserved contractile reserve during dobutamine administration.[16] Retrospective data from patients with LV dysfunction undergoing medical therapy, in whom viability was evaluated by PET, indicate that mortality deeply rises when the amount of viable myocardium exceeds 15% of LV surface.[17]

However, despite consistency of several retrospective studies, the true impact of imaging assessment of viability on mortality and morbidity in patients with LV dysfunction suffers from the lack of large randomized trials. In fact, the only

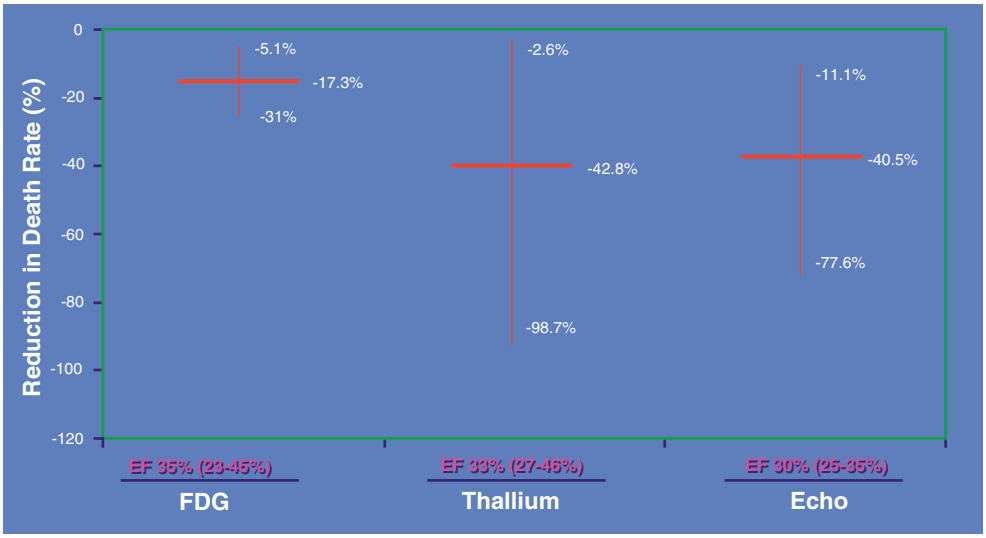

Fig. 17.2 Decrease in mortality in patients with ischaemic LV dysfunction undergoing revascularization and with evidence of viability evaluated by PET FDG, TI SPECT, or dobutamine echocardiography. Data shown as mean value with 95% confidence limits. No measurable difference in test performance was observed. Reproduced from Allman et al.[14] with permission

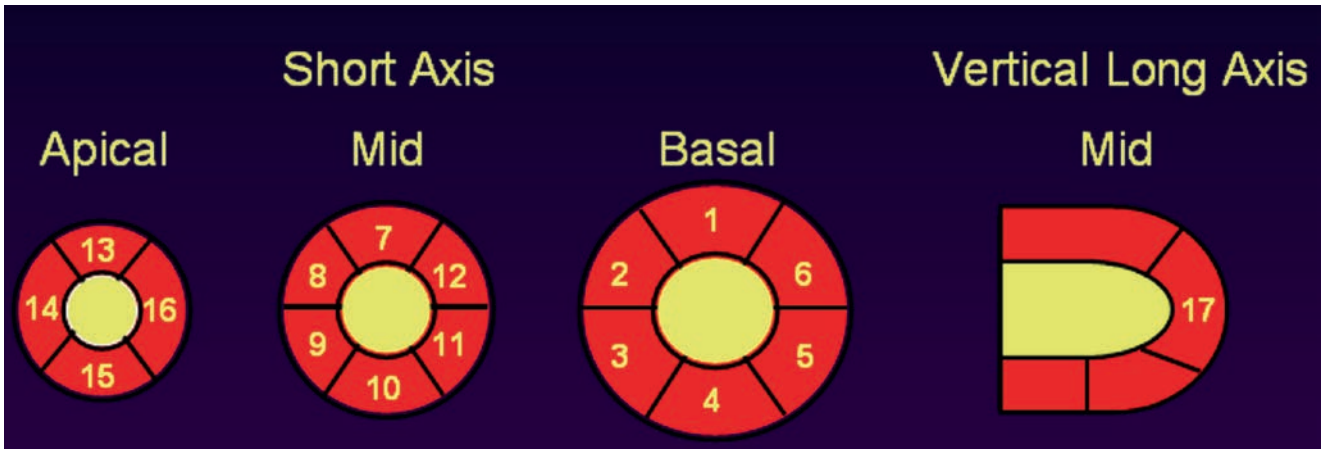

Fig. 17.3 Segmentation of the left ventricle for cardiac imaging analysis recommended by the principal cardiac and nuclear medicine associations. The left ventricle is divided in 17 myocardial segments derived from three short axis planes (basal, mid-ventricular and apical) with an additional apical segment from either long-horizontal or long-vertical axis. Reproduced from Cerqueira et al.[15] with permission

available study that randomized patients with LV ischaemic dysfunction to a PET assisted therapeutic management vs. a non-imaging assisted management reported no significant differences in outcomes.[18]

Imaging Techniques to Assess Viability

Table 17.3 summarizes currently available imaging techniques to evaluate non-invasively myocardial viability in patients with ischaemic cardiomyopathy. As it appears from the grouping of different modalities, there are three distinct pathophysiological approaches to distinguish viable from

Table 17.3. Current non-invasive techniques for assessing myocardial viability

Assessment of perfusion and metabolism
Positron emission tomography
Single-photon emission computed tomography
Contrast echocardiography
Assessment of systolic function and contractile reserve
Dobutamine echocardiography
Dobutamine magnetic resonance imaging
Dobutamine gated single-photon emission computer tomography
Doppler tissue imaging
Imaging of necrotic myocardium
Magnetic resonance delayed enhancement imaging
Multi-slice computed tomography delayed enhancement imaging

non-viable dysfunctional myocardium. One is represented by the demonstration of membrane cell and mitochondrial integrity within areas of dysfunction. Nuclear techniques, including PET and SPECT, are used for this purpose because uptake of perfusion and metabolic nuclear tracers indicates presence of viable myocytes. The second approach relies on the documentation of contractile reserve within areas of dysfunction, and is based on the imaging of dysfunctional myocardium using echocardiography or MRI during stimulation with dobutamine, an inotropic synthetic agent. The third approach is more recent and relies on the direct documentation of necrotic myocardium by MRI, and, more recently, by MDCT. As it is evident from Table 17.3, it has to be noted that, due to recent technical progresses, each imaging technique has the potential to assess more than one aspect of viability, on a regional as well as global basis, during the same study. In addition, comparison among different techniques has been made more reliable by the recommended use of a standard segmentation of the left ventricle (Fig. 17.3).

PET and SPECT represent the most used nuclear techniques for viability assessment, both relying on the documentation of cell integrity using a combination of metabolic and perfusion tracers or of perfusion tracers, respectively. Commonly used perfusion and metabolic tracers are listed in Table 17.4, and the mechanism of action of principal metabolic PET tracers is reported in Fig. 17.4.

Table 17.4. Perfusion and metabolic radionuclide tracers employed for clinical use

SPECT perfusion tracers
201-thallium
99m-technetiun sestamibi
99m-technetium tetrofosmine
PET perfusion tracers
^{15}O-water
^{13}N-ammonia
^{82}Rb-rubidium
PET metabolic tracers
^{18}F-fuorodeoxyglucose (glucose metabolism)
^{11}C-acetate (oxygen metabolism)
^{11}C-palmitate (fatty acids metabolism)

PET

PET has been a valuable technique for clinical detection of myocardial viability. By allowing to quantitatively measure physiological parameters such as absolute myocardial perfusion (using ^{13}N-ammonia and ^{15}O-water) and oxidative (using ^{11}C-acetate) and glucose metabolism (using ^{18}Fluorodeoxyglucose) (FDG) in dysfunctional myocardium, the technique has also provided important insight into the pathophysiology of dysfunctional hibernating myocardium.[19]

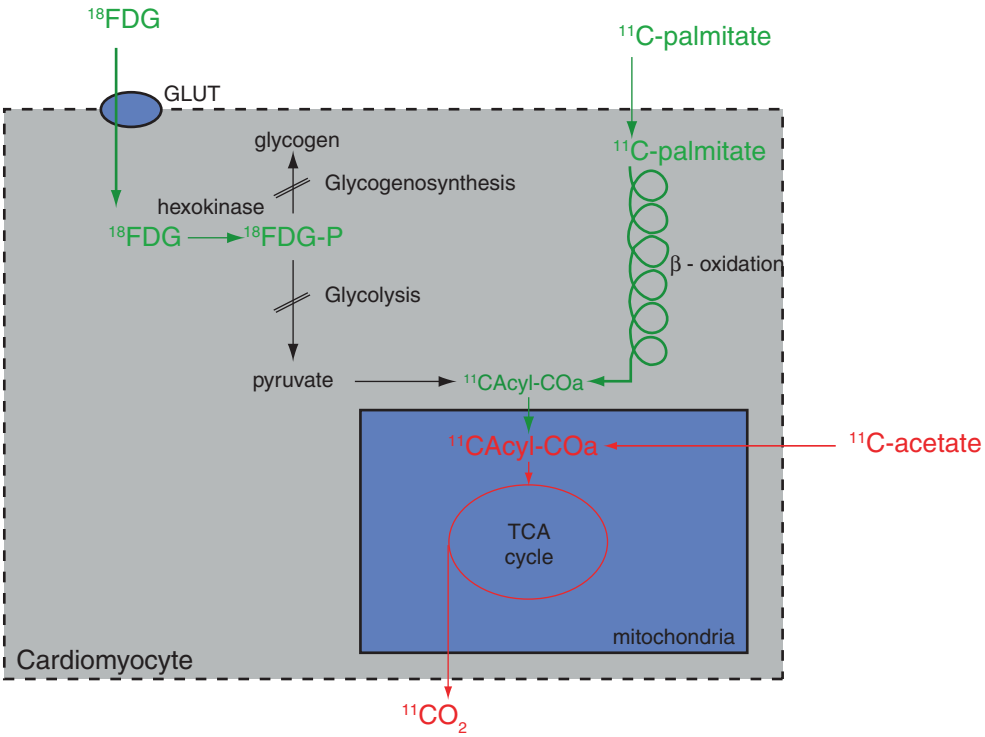

Fig. 17.4 Mechanism of action of different metabolic PET tracers

Insights into the Pathophysiology of Hibernating Myocardium and Principles of Detection of Viability by PET Imaging

Quantitative measurements of myocardial blood flow, using ^{13}N-ammonia and ^{15}O-water PET, challenged the initial hypothesis that hibernating myocardium might result from a chronic state of resting myocardial hypo-perfusion due to (sub)occlusion of an epicardial coronary artery. In fact, both in patients with a pure state of collateral dependent dysfunctional hibernating myocardium without necrosis and with infarcted dysfunctional myocardium recovering function after revascularization, measurements of absolute resting myocardial perfusion using PET were found to be normal or near normal.[4] This suggested that in order to avoid irreversible myocardial necrosis, resting perfusion in hibernating myocardium must be maintained close to normal. Measurements of maximal absolute myocardial blood flow reserve in dysfunctional myocardium using PET demonstrated reduced flow reserve, indicating a potential role for repeated stress-induced ischaemia and post-ischaemic stunning in the genesis of chronic myocardial hibernation.[5] Recently developed animal models mimicking human hibernation have shed a new light on both the mechanisms and the temporal progression of reversible ischaemic dysfunction. These studies suggest that development of chronic myocardial hibernation is a progressive phenomenon. During the first weeks after the onset of dysfunction, endocardial blood flow must remain normal or only marginally decreased, otherwise myocardial necrosis will occur. At that point of time, repetitive episodes of myocardial stunning were suggested as being the most likely mechanism for inducing dysfunction, a hypothesis that is further supported by the strong relationship existing between the reduction in sub-endocardial flow reserve and the severity of dysfunction. With time, and presumably also due to progression in the physiological significance of the underlying coronary stenosis, some of the dysfunctional segments that appeared "chronically stunned" on early examination eventually develop morphological abnormalities, such as reduction of myocardial contractile proteins. It is currently believed that these alterations, which occur in the transition from repeated stunning to chronic hibernations, reduce metabolic demand of oxygen and myocardial perfusion.[20] It is noteworthy that the transition from chronic stunning to chronic hibernation only occurs for threshold reductions in myocardial flow reserve. The critical nature of coronary flow reserve reduction required to produce hibernating myocardium likely explains why not all studies have demonstrated a progression to hibernating myocardium distal to a chronic stenosis.

Studies of myocardial glucose metabolism using FDG PET have also been important for our understanding of myocardial hibernation. The normal myocardium can use a variety of substrates for metabolism depending on dietary conditions. Under fasting conditions, when plasma insulin and glucose levels are low, free fatty acids are the preferred substrates of the myocardium. In the fed state when plasma glucose and insulin levels are high, glucose becomes the preferred substrate of the myocardium. Dysfunctional hibernating myocardium was found to have higher uptake rates of FDG than normal myocardium, especially under fasting conditions. Initially this was interpreted as indicating a shift from normal metabolism to anaerobic glycolysis in hibernating myocardium surviving under conditions of chronic low flow ischaemia. This view was, however, challenged by studies demonstrating maintained overall oxidative metabolism using ^{11}C-acetate in human hibernating myocardium, as well as by biopsies of human hibernating myocardium demonstrating increased rather than decreased glycogen storage. Experimental studies in animals demonstrated that the repeated aggression of ischaemia and reperfusion in the hibernating myocardium induces a series of changes in gene and protein expression. Among these are changes in membrane glucose transporters, with a shift from Glut 4 (insulin dependent) to Glut 1 (insulin non-dependent) transport molecules. It is believed that this increase of Glut 1 transporters allows higher inflow of FDG under low insulin (fasting) conditions into the hibernating myocardium compared to the normal myocardium, explaining the higher uptake of FDG in dysfunctional hibernating myocardium under fasting conditions.[19]

Clinical Assessment of Myocardial Viability Using PET

The typical assessment of myocardial viability using PET relies on a combination of semi-quantitative assessment of myocardial perfusion using an extractable perfusion tracer (either ^{13}N-ammonia or ^{82}Rubidium) and glucose extraction using FDG (Fig. 17.5). Diagnosis of myocardial viability is based on the comparison of relative ^{13}N-ammonia and FDG uptake in the dysfunctional area relative to the remote normally

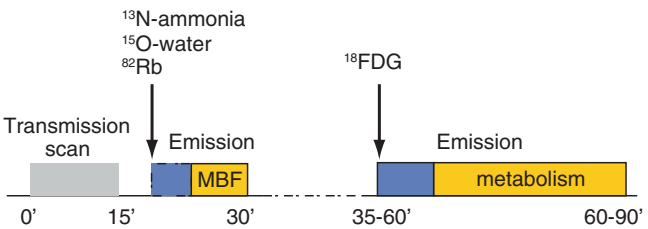

Fig. 17.5 Typical study protocol for ^{13}N-ammonia FDG PET viability study. First, a transmission scan is performed to allow correction of emission studies for attenuation. Myocardial perfusion is assessed using ^{13}N-ammonia (or ^{15}O-water or ^{82}Rb, as an alternative). After decrease of radioactivity, glucose metabolism is assessed after injection of FDG. To allow better image quality, FDG imaging is best performed either during euglycemic glucose clamp or after oral administration of nicotinic acid

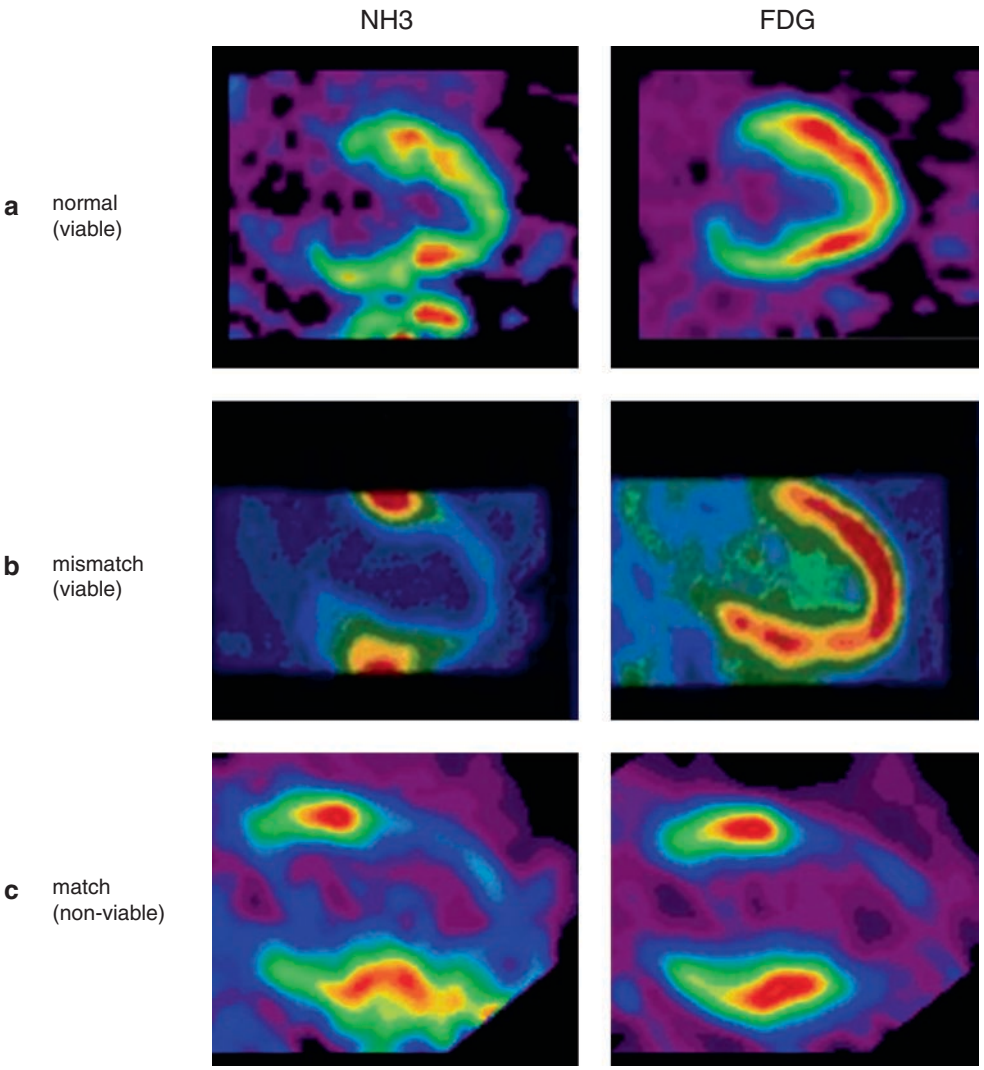

Fig. 17.6 Different ^{13}N-ammonia FDG PET patterns associated to dysfunctional myocardium. **(a)** Normal perfusion and metabolism. **(b)** Perfusion metabolism mismatch pattern, i.e. reduced ^{13}N-ammonia uptake and increased/maintained FDG uptake. **(c)** Perfusion metabolism match pattern, i.e. reduced ^{13}N-ammonia uptake and proportionally reduced FDG uptake

contracting myocardium. The following three different ^{13}N-ammonia FDG patterns have been described in dysfunctional myocardium and are related to the recovery of myocardial function (Fig. 17.6):

1. Normal perfusion and FDG uptake. As discussed previously, the preservation of perfusion and glucose metabolism in dysfunctional myocardium is indicative of maintained myocyte viability.
2. Reduced perfusion with concomitant reduced or absence of FDG uptake (perfusion-metabolism match) pattern. Such severe reduction of perfusion and metabolism is incompatible with myocardial survival, and is thus indicative of myocellular death and absence of viability.
3. Reduced perfusion with increased FDG uptake (perfusion-metabolism mismatch pattern). This pattern is observed mainly if studies are performed under fasting condition or during glucose load. Under such conditions, with low plasma insulin, glucose uptake in normal myocardium is reduced. As previously discussed, the increased FDG uptake translates into a maintained metabolic viability and higher expression of Glut 1 transporters, allowing preferential use of glucose rather than free fatty acids as metabolic substrate in dysfunctional stunned and hibernating myocardium.

Initially, PET studies were performed either after overnight fasting conditions or after an oral glucose load. This approach resulted, however, in poor image quality in diabetic patients and in patients with insulin resistance. Therefore, it is currently proposed to perform studies during hyper-insulinemic euglycemic glucose clamp or after administration of nicotinic acid, which blocks lipid utilization by the heart. This approach improves image quality, but somewhat reduces the incidence and magnitude of mismatch pattern vs. normal FDG uptake in dysfunctional segments by the fact that normal myocardium also presents high FDG uptake during insulin stimulation.

Clinical Value of ^{13}N-Ammonia FDG PET

Several studies have evaluated the diagnostic accuracy of ^{13}N-ammonia FDG PET for predicting recovery of regional dysfunction after revascularization. According to one meta-analysis,[21] combined information on perfusion and FDG uptake had a mean sensitivity of 88% and mean specificity of 74%, respectively (Table 17.5, Fig. 17.7). Recovery of global EF after revascularization is clinically more relevant than recovery of regional function, but has been addressed in fewer studies. In a multi-centre study involving six European countries,[23] sensitivity of PET during glucose clamp to predict significant (>5%) increase of EF was high (79%), but specificity was low (55%). Bax et al.[24] suggested that critical amount of at least four dysfunctional segments with viability needs to be present to obtain a significant improvement of LV EF (>5%) after revascularization. Other studies indicated a direct relationship between the number of dysfunctional viable segments by PET and the magnitude of recovery of EF after revascularization.[25]

Table 17.5. Accuracy of nuclear techniques to predict recovery of regional contractile function in patients with left ventricular dysfunction. NPA: negative predictive value; PPA: positive predictive value

Technique	Sensitivity (%)	Specificity (%)	PPA (%)	NPA (%)
Positron emission tomography				
Mismatch	93	58	71	86
Thallium-201				
Re-injection	86	50	57	83
Rest-redistribution	88	59	69	80
99-Tecnetium sestamibi	81	66	71	77
Dobutamine echocardiography	81	80	77	85

Several studies have examined the value of detection of viability by ^{13}N-ammonia FDG PET for predicting prognosis in patients with poor LV function in relation to medical or surgical treatment. Pooled analysis of these studies[14] demonstrated improved survival for patients with dysfunctional viable myocardium undergoing revascularization rather than medical treatment (Fig. 17.2). The major limitation of these studies was, however, their observational retrospective non-randomized design. So far there is only one study[18] that, in a randomized design, assessed whether PET-assisted management of patients with LV dysfunction may affect outcome. Unfortunately, this study did not demonstrate a significant reduction in cardiac events in patients with LV dysfunction and suspected coronary disease for FDG PET-assisted management vs. standard evaluation. This was probably related to the fact that revascularization management was not always dictated by PET findings. However, in the subgroup of patients managed according to

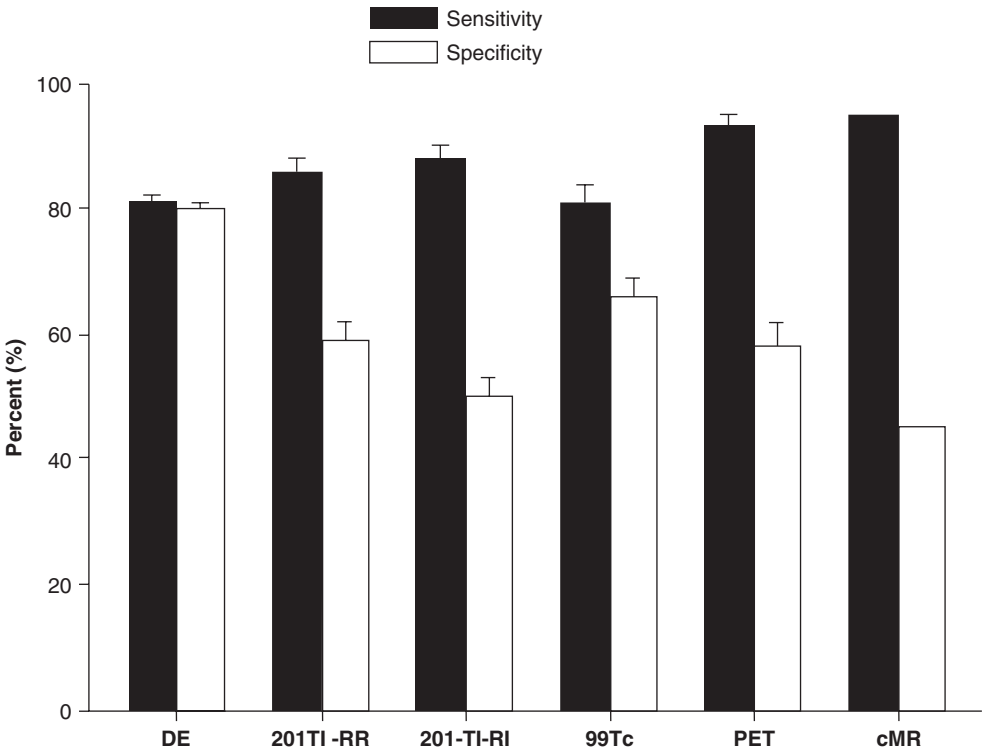

Fig. 17.7 Diagnostic accuracy of nuclear imaging techniques compared to dobutamine echocardiography and MRI. Modified from Bax et al.[22] DE: dobutamine echocardiography; ^{201}Tl-RR: ^{201}Thallium rest-redistribution; 201Tl-RI: ^{201}Thallium re-injection; 99Tc:^{99}mTecnetium; PET: proton emission tomography; cMR: contrast magnetic resonance

PET findings, significant benefits were observed. Ongoing trials will allow the assessment of the value of viability testing in the survival of patients randomized to revascularization vs. medical treatment.

PET Strengths and Weaknesses

As opposed to other techniques, PET has significant strengths. Its major advantage is the ability to correct for attenuation of photons and to quantify perfusion and metabolism in absolute terms, making it an ideal tool for studying the pathophysiology of dysfunctional myocardium. Also, as opposed to traditional nuclear imaging techniques, PET has higher image quality and higher spatial resolution not hampered by attenuation effects. Therefore, it has higher diagnostic accuracy than traditional nuclear imaging techniques. The major limitation of PET is its high cost related to isotope production and the length of acquisition. In addition, kinetic modelling to quantify perfusion in absolute terms is very time-consuming and difficult to perform, and therefore has not been used routinely in clinical practice.

SPECT

^{201}*Thallium (Tl) Imaging*

Tl is a potassium analogue that was first used for the evaluation of viability with SPECT. It is actively transported by the Na^+/K^+ ATPase pump through an intact cell membrane of the myocardial cells. Its initial uptake is mostly dependent on perfusion level, whereas late accumulation is dependent on cell integrity. At variance with more recently ^{99m}technetium (Tc) tracers, uptake of Tl is not irreversible, but is influenced by gradients concentration across the cell membrane. The consequence of this characteristic that greatly influences imaging protocols and interpretation is that collected images always represent the uptake at the time of image acquisition and not at the time of injection, as is the case for Tc agents. Therefore, areas of dysfunctional hypo-perfused yet viable myocardium where uptake of Tl is initially reduced compared to normally perfused myocardium may show enhanced uptake at later imaging (usually at least 3–4 h following initial administration) due to slow accumulation of Tl with partial or complete disappearance of the initial perfusion defect. This phenomenon, pertaining only to Tl, is termed *redistribution* and represents the basis for viability evaluation using this tracer. The two most used protocols to evaluate viability are represented by *stress-redistribution-reinjection* and *rest-redistribution* imaging.

Stress-Redistribution-Reinjection

With this protocol, images are acquired immediately after pharmacologic or physical stress and again after 3–4 h. If in this last set of images persistent fixed and severe defects are observed, a second dose of Tl is administered and a third set of images acquired immediately thereafter. This approach was developed from the observation that fixed defects at 3–4 h redistribution may not necessarily represent necrotic myocardium, as they frequently show preserved metabolic activity by PET or residual contraction with potential for recovery of function following revascularization[26] (Fig. 17.8). The identification of viability using this protocol is based on the demonstration of significant redistribution (usually an increase of at least 10% from initial uptake) or on the presence of at least >50% of maximal tracer uptake in a dysfunctional segment.

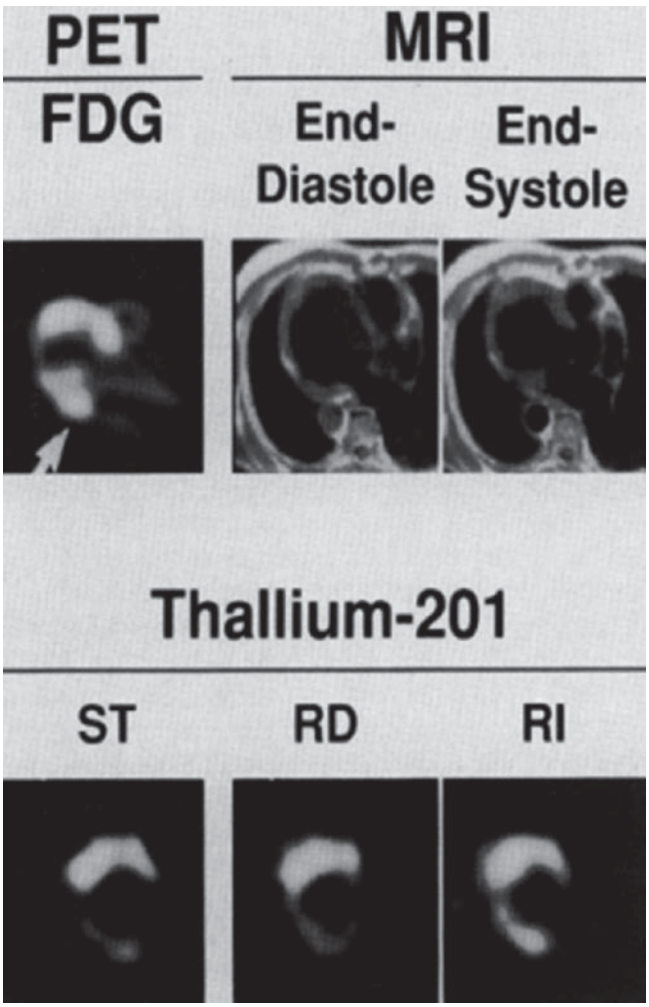

Fig. 17.8 Abnormal myocardial region (*arrow*) with reduced FDG activity by PET, normal end-diastolic wall thickness, and presence of systolic thickening by MRI. SPECT images demonstrate a corresponding fixed defect on stress and redistribution images that improves after re-injection. *ST* stress; *RD* redistribution; *RI* re-injection. Reproduced from Perrone-Filardi et al.[27] with permission

Data from 11 studies enrolling 301 patients using this protocol reported high sensitivity (weighted mean 86%, range 33–100%), but reduced specificity (weighted mean 50%, range 16–80%)[22] (Table 17.5, Fig. 17.7), indicating an overestimation of functional recovery in a substantial number of dysfunctional segments. Similarly, high sensitivity but suboptimal specificity has been reported when improvement of global EF was considered.[22] However, the advantage of this approach is that it also takes into account the presence of inducible ischaemia that is an additional determinant of prognosis representing a clinically relevant aspect for therapeutic management. As for PET, the prognostic independent role of this imaging approach has been reported in clinical studies[14] (Fig. 17.2).

Rest-Redistribution

Using this approach, Tl is injected at rest and images are acquired immediately thereafter and following 3–4 h of redistribution. Therefore, inducible ischaemia is not evaluated. Viability is defined when a dysfunctional segment shows significant redistribution (>10% increase in Tl uptake) or a relative uptake >50% of maximal activity. With these criteria, mean sensitivity for prediction of regional functional recovery averaged 88% (range 44–100%) and mean specificity was 59% (range 22–92%) in a pooled analysis of 22 studies reporting 557 patients[22] (Table 17.5, Fig. 17.7). Acquiring a third late set of images 24 h after injection to allow a prolonged redistribution time and fill-in of severely hypoperfused myocardium did not prove to be useful for predicting recovery of regional function.[27] The value of this protocol imaging to predict changes in global EF has been investigated in few clinical studies reporting high sensitivity but suboptimal specificity. The prognostic value of resting Tl imaging was tested in small clinical studies in which both the amount of viable myocardium and that of necrotic myocardium were identified to influence mortality and morbidity in patients with ischaemic LV dysfunction.[14]

Tc-Labelled Agents

Two compounds, i.e. Tc-sestamibi and Tc-tetrafosmine, are currently used for clinical purposes, although only the former has been adequately tested for viability evaluation. At variance with Tl, Tc agents are trapped almost irreversibly in mitochondria after intravenous injection and flow-dependent distribution to myocardial cells, and they do not undergo a clinically significant redistribution process. Therefore, the images reflect the uptake of the tracer at the time of injection and not at the time of acquisition, as it is for Tl. When only viability needs to be evaluated, a single set of images is sufficient, usually obtained after sublingual nitrate administration to maximally enhance uptake in hypo-perfused myocardium. However, for a more comprehensive evaluation of viability and ischaemia, two sets of images, and therefore two separate injections of the tracer, are needed, one during maximal physical or pharmacologic stress and a second one at rest or after nitrate administration. The criterion for defining viability is represented by a relative uptake >50% of maximal tracer activity in a dysfunctional segment. Pooled analysis of 13 studies using this approach and enrolling 308 patients reported average sensitivity of 79% (range 62–100%) and average specificity of 58% (range 30–86%), similar to other nuclear techniques using Tl[22] (Table 17.5, Fig. 17.7). Seven studies (reporting 180 patients) in which tracer uptake was maximized with nitrate administration reported a sensitivity of 86% and increased specificity of 83% to predict regional functional improvement.[21]

[22]An additional relevant advantage derived from favourable physical properties of these agents is represented by the opportunity to acquire ECG-gated images that allow the evaluation of regional and global function, particularly regional wall thickening, end-systolic and end-diastolic volumes, and LV EF. Thus, gated Tc SPECT is also suitable for dobutamine studies assessing, at the same time, global and regional contractile reserve and perfusion reserve. The accuracy of this approach to predict recovery of global LV function has been evaluated only in a small, single-centre study reporting a promising 79% sensitivity and 78% specificity.[22] As for Tc-tetrofosmine, which was less investigated than Tc-sestamibi, available studies reported a good agreement between the two tracers with similar accuracy for prediction of functional recovery after revascularization.[22]

MDCT

Principles of Detection of Myocardial Viability by MDCT

The ability of contrast enhanced computed tomography (CT) to detect myocardial infarction, and thus myocardial viability, was demonstrated in experimental animal models more than 30 years ago. However, the poor image quality of single slice CT without cardiac gating resulted in numerous artefacts and prohibited clinical use for in vivo cardiac imaging at that time. The technique was only recently matured to clinical use in humans with the advent of fast spiral MDCT imaging systems, which allow fast ECG gated cardiac imaging without motion artefacts. The principles underlying detection of myocardial viability by MDCT resemble very closely those of MRI. As a matter of fact, although iodinated contrast agents employed for MDCT imaging have completely different molecular structure than Gadolinium-based

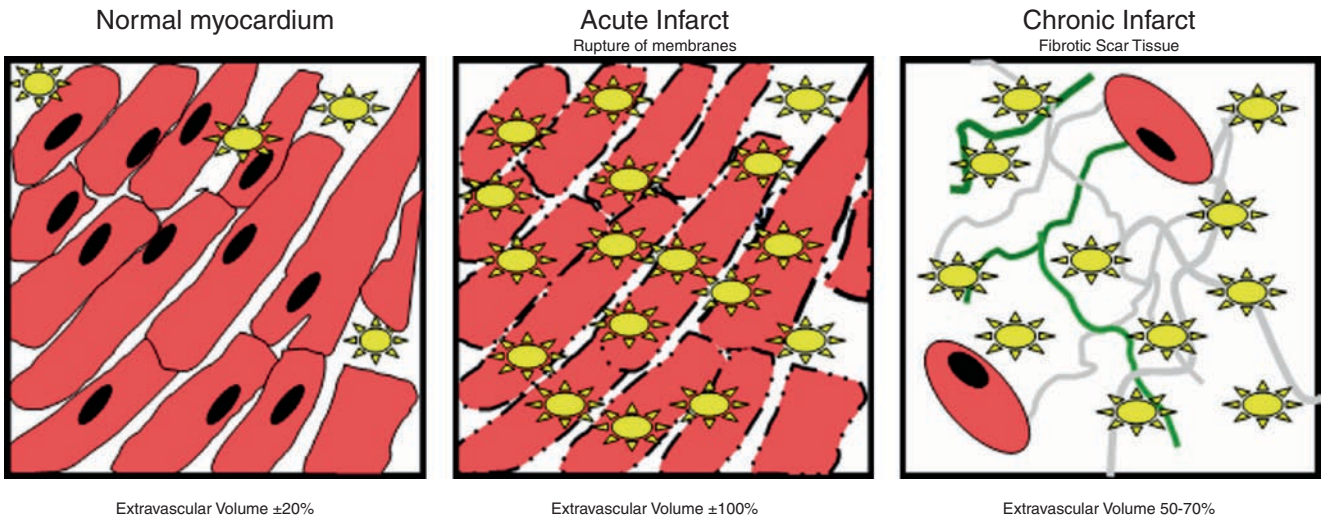

Fig. 17.9 Principles underlying MDCT contrast enhancement on late imaging. Iodinated contrast agents (*star*) have extra-vascular distribution volume. At equilibrium, in normal myocardium, the distribution volume is relatively small (approximately 20% of total cardiac volume). In acute myocardial infarct, due to rupture of cell membranes, distribution volume increases to almost the entire myocardial volume. In chronic infarcts, muscle is replaced by fibrous scar tissue. This tissue has large amounts of extra-vascular proteins, such as collagen and elastin, and low concentrations of cells. Therefore, the distribution volume of the iodinated contrast agent is also increased

contrast agents employed for MRI, they have surprisingly similar molecular weight and extra-vascular distribution volume. Therefore, they present similar kinetics in acutely and chronically infarcted myocardium as Gadolinium-based contrast agents[28] and, like contrast-enhanced MRI, MDCT can characterize infarcted myocardium with different contrast enhancement patterns depending on the time when imaging is performed with respect to contrast injection. On images performed immediately after contrast injection, acute infarcts can be revealed by the areas of reduced contrast enhancement situated in the core of the infarcted area. As for Gadolinium-DTPA enhancement, these areas correspond to the acutely infarcted regions with micro-vascular obstruction and no reflow. They represent, therefore, only a part of the total infarcted area. In addition, with later infarct detersion, these areas of no reflow disappear when infarcts become chronic.

On images performed at later time (5–10 min) after contrast injection, MDCT can, similar to Gadolinium-based contrast agents, demonstrate areas of increased contrast, i.e. hyper-enhancement. Late enhancement occurs both in acute and chronic infarcts, and is explained by the increased volume of distribution of the extra-vascular space, where contrast agent localizes, in the infarcted area compared to normal myocardium. In acute infarcts, such increase in extra-vascular volume results from disruption of cell membranes allowing access to the contrast agent. (Fig. 17.9) In chronic infarcts, it can be explained by replacement of myocytes by fibrous tissue with low cell content and high extra-vascular protein (collagen and elastin) concentrations.

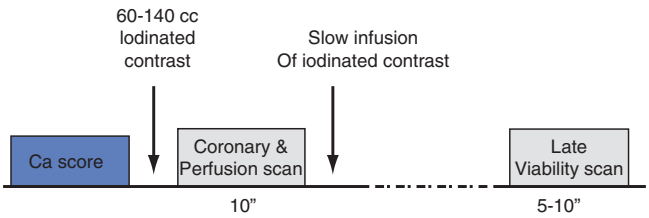

Fig. 17.10 Typical study protocol for assessment of myocardial viability by MDCT

Therefore, a typical imaging protocol for assessment of myocardial viability by MDCT requires imaging at two time points (Fig. 17.10). Early images are typically obtained at the time of coronary imaging immediately after contrast injection. A second acquisition is performed 5–10 min later to reveal late hyper-enhancement. Late hyper-enhancement of MDCT requires typically a higher dose of contrast than that given for coronary imaging alone (total dose 120–140 mL). This dose can either be given as bolus injection or during a slow infusion. According to experimental studies that evaluated the time course of MDCT enhancement in infarcts, late hyper-enhancement appears to be feasible at any time point between 4 and 24 min after contrast injection, but the optimal time varies between studies and appears to depend on the contrast agent. Late imaging is typically performed with lower tube voltage (80–90 kV) to reduce radiation dose exposure and increase contrast to noise of images.

Clinical Results Using MDCT

Several studies have compared infarct imaging by MDCT to histology and to Gadolinium-enhanced MRI, both in experimental animal models and in humans. In animals, the location and size of early defects by MDCT were found to correlate closely to histological measurements of no reflow area, while size of LE was found to correlate closely to areas of myocardial necrosis at histology. In addition, in humans the location and extent of contrast enhancement patterns by MDCT corresponded closely to those detected by contrast-enhanced MRI patterns (Fig. 17.11). While the quality of early images of MDCT was found to be about comparable to that of MRI, late images by MDCT were found to be of lower quality than late contrast-enhanced MRI images. This is mainly related to the ability to null signal of normal myocardium. Since the technique is relatively new, only few clinical studies evaluated the ability of late MDCT imaging to predict recovery of function in acute myocardial infarction.[29] So far, no study has been performed in the setting of chronic contractile dysfunction. Similar to MRI, non-ischaemic cardiomyopathies show either no LE or LE with atypical mid-ventricular or epicardial patterns. Therefore, it was suggested that combination of coronary and LE MDCT imaging might be useful to characterize aetiology of heart failure.[30]

MDCT Strengths and Weaknesses

MDCT has some unique advantages over other viability techniques as follows: (1) the technique is more available and less technically demanding than PET and MRI; (2) viability assessment by MDCT is substantially faster (10 min) than by LE MRI (30 min), or by SPECT and PET (1–2 h); (3) MDCT has the ability to combine assessment of myocardial viability with non-invasive coronary (and functional) imaging in a single test (Fig. 17.12); (4) finally, LE MDCT images can be acquired if contrast is injected for other purposes, for instance, to perform angioplasty procedure for acute myocardial infarction. Thus, viability imaging by MDCT can be performed immediately after the revascularization procedure without additional contrast injection.

MDCT viability imaging has, however, some significant limitations. The single most important limitation is that image quality for LE imaging is currently qualitatively

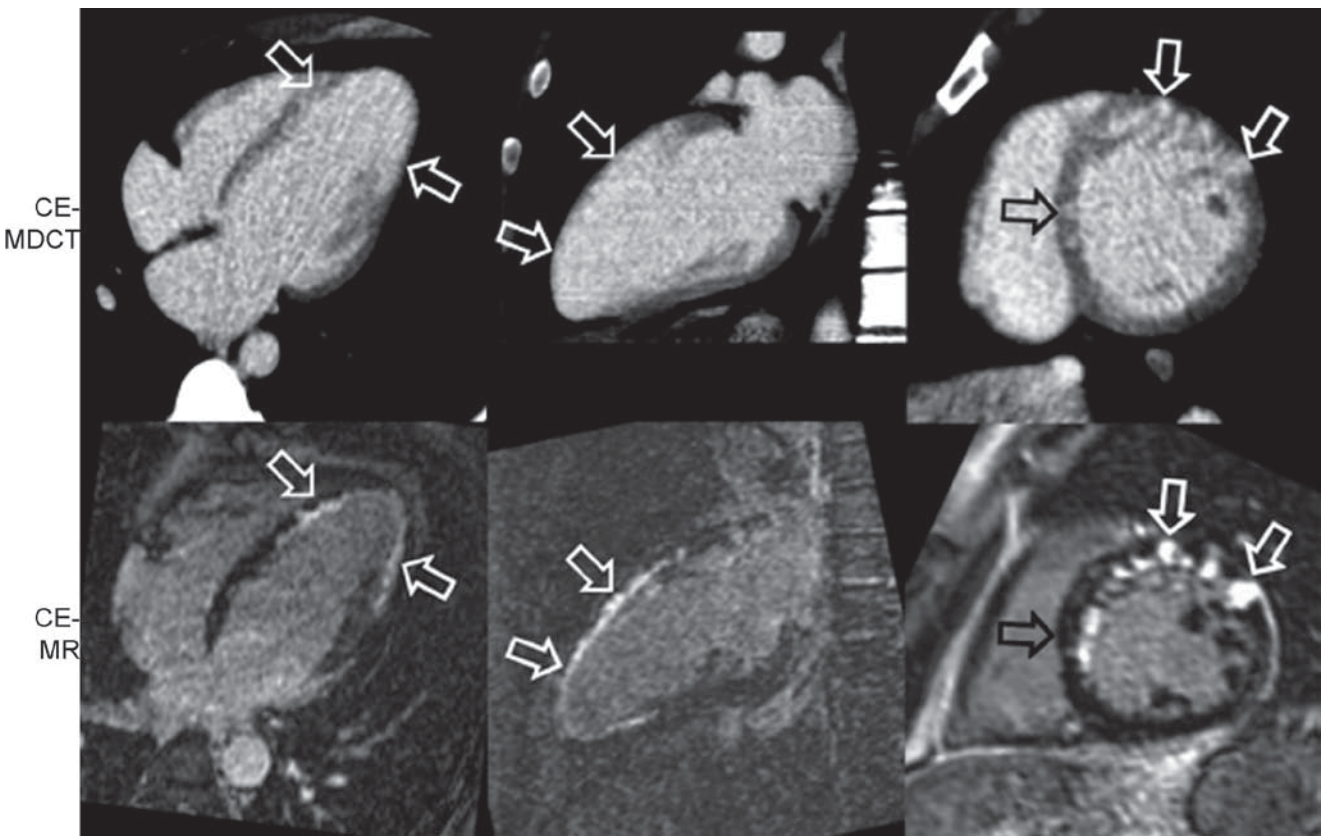

Fig. 17.11 Examples of late MDCT and corresponding CE MRI images in a patient with acute myocardial infarction 25 days earlier. *CE* contrast enhanced. Reproduced from Gerber et al.[28] with permission

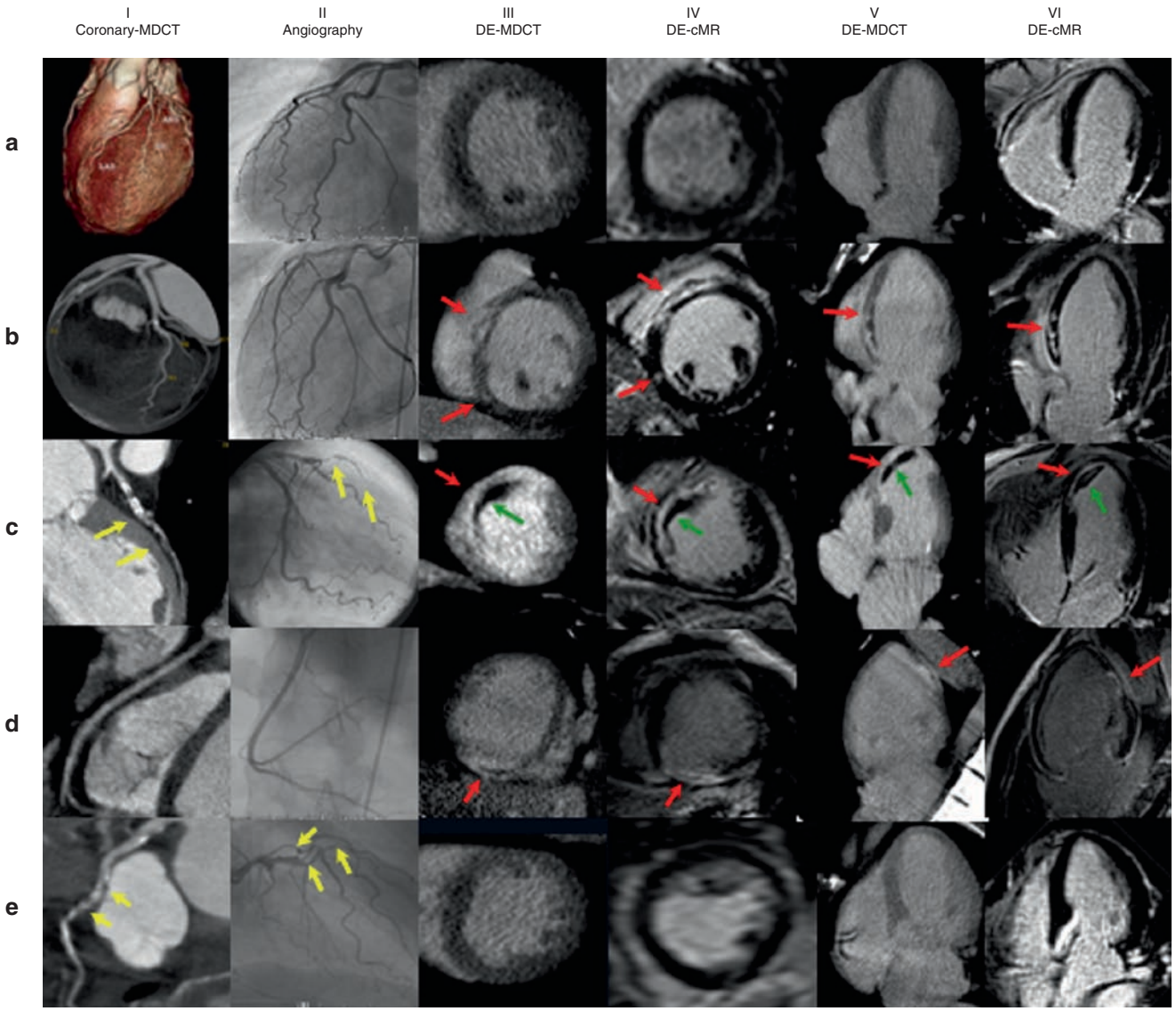

Fig. 17.12 Example of combined coronary (*I*) and late MDCT (*III* and *V*) to differentiate aetiology of heart failure in five representative patients and their correlations to coronary anatomy (*II*) and LE-MRI (*IV* and *VI*). **(a)** No coronary artery disease and absence of LE. **(b)** No coronary artery disease and mid-ventricular LE. **(c)** Occlusion of the proximal left descending coronary artery (*yellow arrow*) with trans-mural LE in the apex, septum, and antero-septal region (*red arrows*) and mural thrombus (*green arrows*). **(d)** Absence of coronary artery disease with trans-mural inferior necrosis. **(e)** Proximal and mid-left descending coronary artery and first diagonal stenosis (*yellow arrows*) without LE. Reproduced with permission from le Polain de Waroux et al.[30] *LE* late enhancement

inferior to that of MRI. An additional major limitation is that LE MDCT imaging causes extra (3–4 mSv) dose exposure in addition to the already high radiation burden (12–15 mSv) related to non-invasive coronary imaging. Currently, there is a concern that MDCT-induced radiation exposure may increase lifelong risk of cancer.[31] Although this concern may certainly be appropriate in asymptomatic young patients undergoing MDCT for screening purposes, the risk of radiation-induced cancer is probably negligible when balanced to disease-related prognosis in patients with low EF (up to 50% mortality at 5 years) requiring viability testing. Furthermore, the radiation dose exposure of MDCT is comparable to that of nuclear imaging techniques (SPECT and PET) used for viability imaging. Radiation dose can be reduced by lowering X-ray power during less important portions of the cardiac cycle (e.g. systole), an approach termed *tube current modulation* or *dose modulation*. In addition, the advent of even faster MDCT scanners with 128–356 detector rows will allow prospective gating acquisitions, which will reduce radiation exposure by about 3–4 times (to <5 mSv). A final limitation of MDCT is related to the potential toxicity of iodinated contrast agents, which may aggravate renal

function, especially in diabetic patients and in patients with pre-existing renal function impairment.

PET–CT/SPECT–CT Fusion and Hybrid Imaging

In recent years it has been attempted to combine nuclear and CT imaging. Such image fusion can be obtained by registering the two image techniques from separate acquisitions, although with the risk of some image misalignment. Therefore, hybrid imaging scanners that allow simultaneously acquiring SPECT or PET and CT images in a single exam have been introduced. While these techniques were primarily developed for oncology imaging, encouraging approaches for cardiac imaging have also been proposed. As a matter of fact, combining CT with SPECT imaging allows for a reliable CT-based attenuation correction of SPECT imaging, thereby minimizing attenuation artefacts. Whether this might allow for increased specificity of SPECT for viability detection has not yet been evaluated. Hybrid imaging also allows registering information of coronary anatomy and regional contractile function obtained from CT with myocardial perfusion or metabolism by SPECT or PET (Fig. 17.13). For the purpose of myocardial viability assessment, this might allow better definition of the localization and size of the dysfunctional area with respect to the location of coronary obstruction. Because of their recent introduction, the value of these techniques for assessment of myocardial viability as compared to conventional SPECT or PET imaging has not yet extensively been studied. The major limitation of PET and SPECT CT hybrid imaging is that CT adds significant additional radiation dose (15 mSV) to that of nuclear imaging. Indeed, for hybrid SPECT CT acquisitions, total dose exposures up to 43 mSV have been reported. An additional limitation of most current hybrid PET and SPECT CT systems is that the integrated CT component is not as technically advanced and the quality of non-invasive coronary imaging is not as high as the one obtained with the most recent stand alone MDCT systems.

Which Is the Optimal Test for Assessment of Myocardial Viability? Comparison Among Techniques

Several studies have compared the diagnostic accuracy of SPECT and PET for detection of myocardial viability vs. other imaging techniques. Results have been summarized in a metanalysis.[21] No significant difference between Tl and Tc SPECT tracers was reported, yet Tc tracers allow better image quality than Tl with reduced radiation exposure. PET appears to have higher sensitivity for detection of myocardial viability than SPECT, but similar suboptimal specificity. Pooled analyses suggest, furthermore, that nuclear imaging techniques (SPECT and PET) have higher sensitivity and negative predictive values, but lower specificity and positive predictive value than dobutamine echocardiography. More

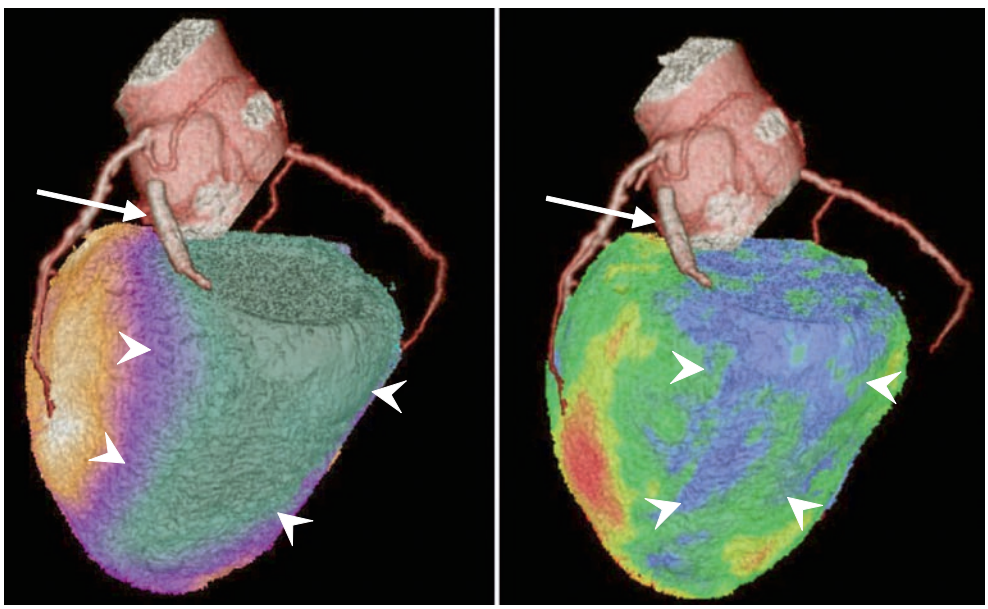

Fig. 17.13 Example of 3D volume-rendered fusion image generated from MDCT and SPECT with Tc-tetrofosmin at rest. **(a)** *Arrow* denotes an occluded stent in the proximal circumflex artery, and *arrowheads* demarcate the associated myocardial scar. **(b)** Fusion image of the same patient generated from MDCT angiography and PET with FDG. *Arrowheads* indicate a lack of viability in the postero-lateral region, associated with occlusion of the circumflex stent (*arrow*). Reproduced with permission from Gaemperli et al.[32]

recently, LE MRI was found to have similar good diagnostic performance as PET and SPECT. The major advantage of MRI is higher spatial resolution, allowing differentiation of sub-endocardial vs. trans-mural scar. Furthermore, MRI benefits from greater availability, less cost, and faster imaging than PET, without radiation exposure. Therefore, MRI has challenged PET as the gold standard for assessment of myocardial viability in clinical practice. However, in clinical practice, PET and MRI appear to perform similarly well for detection of myocardial viability.

As opposed to prediction of functional outcome, for predicting improvement of survival, all imaging techniques, i.e. dobutamine echo, MRI, SPECT, and PET, appear to have similar high value (Fig. 17.2).[14] However, only head-to-head comparisons of SPECT and dobutamine echocardiography, but not of other techniques, were reported for this purpose. Also, none of the studies were performed in a prospective randomized design. Obviously, the decision about which test to choose for assessment of myocardial viability in an individual patient will depend on several factors. The decision must be individually targeted to the patient and will not only depend on diagnostic performance of the test, but also on patients' preferences, potential contraindications, availability, and local experience with different techniques, as well as with concomitant medical therapy and coronary anatomy.[7]

Conclusions

Both SPECT and PET are established and well-validated techniques for assessment of myocardial viability. PET offers higher image quality and diagnostic accuracy than SPECT, but is more costly and less available. MDCT viability imaging has recently been introduced and could be an interesting alternative to MRI or nuclear imaging. Hybrid SPECT/CT and PET/CT imaging offers new opportunities of integrating coronary anatomy and function with myocardial perfusion and metabolism in a single exam, and might improve the ability of nuclear imaging techniques to characterize the areas of dysfunction in chronic coronary artery disease. However, it is still too early to predict whether these appealing technical advances in cardiac imaging will translate into more accurate decision-making process for individual patients At this time, no optimal imaging technique exists that can accurately describe the very complex pathophysiological substrate that often determines LV dysfunction and the potential for its reversibility. As a consequence, decision about revascularization of patients with ischaemic LV dysfunction remains challenging in most cases, requiring integration of different imaging modalities with clinical and anatomic information.

References

1. Chesebro JH, Ritman EL, Frye RL, et al Regional myocardial wall thickening response to nitroglycerin. A predictor of myocardial response to aortocoronary bypass surgery. *Circulation*. 1978;57: 952–957
2. Rahimtoola SH The hibernating myocardium. *Am Heart J*. 1989; 117:211–212
3. Heyndrickx GR, Millard RW, McRitchie RJ, et al Regional myocardial functional and electrophysiological alterations after brief coronary artery occlusion in conscious dogs. *J Clin Invest*. 1975;56: 978–985
4. Marinho NV, Keogh BE, Costa DC, Lammerstma AA. Pathophysiology of chronic left ventricular dysfunction. New insights from the measurement of absolute myocardial blood flow and glucose utilization. *Circulation*. 1996;93:737–744
5. Shen YT, Vatner SF. Mechanism of impaired myocardial function during progressive coronary stenosis in conscious pigs. Hibernation versus stunning? *Circ Res*. 1995;76:479–488
6. Lee HH, Dávila-Román VG, Ludbrook PA, et al Dependency of contractile reserve on myocardial blood flow: implications for the assessment of myocardial viability with dobutamine stress echocardiography. *Circulation*. 1997;96:2884–2891
7. Piscione F, Perrone-Filardi P, De Luca G, et al Low dose dobutamine echocardiography for predicting functional recovery after coronary revascularization. *Heart*. 2001;86:679–686
8. Elsässer A, Schlepper M, Klövekorn WP, et al Hibernating myocardium: an incomplete adaptation to ischemia. *Circulation*. 1997;96: 2920–2931
9. Tarakji KG, Brunken R, McCarthy PM, et al Myocardial viability testing and the effect of early intervention in patients with advanced left ventricular systolic dysfunction. *Circulation*. 2006;113:230–237
10. Canty JM Jr, Suzuki G, Banas MD, et al Hibernating myocardium: chronically adapted to ischemia but vulnerable to sudden death. *Circ Res*. 2004;94:1142–1149
11. Samady H, Elefteriades JA, Abbott BG, et al Failure to improve left ventricular function after coronary revascularization for ischemic cardiomyopathy is not associated with worse outcome. *Circulation*. 1999;100:1298–1304
12. White HD, Norris RM, Brown MA, et al Left ventricular end-systolic volume as the major determinant of survival after recovery from myocardial infarction. *Circulation*. 1987;76:44–51
13. Carluccio E, Biagioli P, Alunni GG, et al Patients with hibernating myocardium show altered left ventricular volumes and shape, which revert after revascularization: evidence that dyssynergy might directly induce cardiac remodeling. *J Am Coll Cardiol*. 2006;47:969–977
14. Allman KC, Shaw LJ, Hachamovitch R, et al Myocardial viability testing and impact of revascularization on prognosis in patients with coronary artery disease and left ventricular dysfunction: a meta-analysis. *J Am Coll Cardiol*. 202;39:1151–1158
15. Cerqueira MD, Weissman NJ, Dilsizian V, et al Standardized myocardial segmentation and nomenclature for tomographic imaging of the heart: a statement for healthcare professionals from the Cardiac Imaging Committee of the Council on Clinical Cardiology of the American Heart Association. American Heart Association Writing Group on Myocardial Segmentation and Registration for Cardiac Imaging. *Circulation*. 2002;105:539–542
16. Bax JJ, Poldermans D, Elhendy A, et al Improvement of left ventricular ejection fraction, heart failure symptoms and prognosis after revascularization in patients with chronic coronary artery disease and viable myocardium detected by dobutamine stress echocardiography. *J Am Coll Cardiol*. 1999;34:163–169
17. Desideri A, Cortigiani L, Christen AI, et al The extent of perfusion-F18-fluorodeoxyglucose positron emission tomography mismatch determines mortality in medically treated patients with chronic

ischemic left ventricular dysfunction. *J Am Coll Cardiol*. 2005;46: 1264–1269
18. Beanlands RS, Nichol G, Huszti E, et al F-18-fluorodeoxyglucose positron emission tomography imaging-assisted management of patients with severe left ventricular dysfunction and suspected coronary disease: a randomized, controlled trial (PARR-2). *J Am Coll Cardiol*. 2007;50:2002–2012
19. Canty JM Jr, Fallavollita JA. Hibernating myocardium. *J Nucl Cardiol*. 2005;12:104–119
20. Gerber BL, Vanoverschelde JL, Bol A, et al Myocardial blood flow, glucose uptake, and recruitment of inotropic reserve in chronic left ventricular ischemic dysfunction. Implications for the pathophysiology of chronic myocardial hibernation. *Circulation*. 1996;94:651–659
21. Vanoverschelde JL, Wijns W, Borgers M, et al Chronic myocardial hibernation in humans. From bedside to bench. *Circulation*. 1997;95: 1961–1971
22. Bax JJ, Poldermans D, Elhendy A, et al Sensitivity, specificity, and predictive accuracies of various noninvasive techniques for detecting hibernating myocardium. *Curr Probl Cardiol*. 2001;26:147–186
23. Gerber BL, Ordoubadi FF, Wijns W, et al Positron emission tomography using(18)F-fluorodeoxyglucose and euglycaemic hyperinsulinaemic glucose clamp: optimal criteria for the prediction of recovery of post-ischaemic left ventricular dysfunction. Results from the European Community Concerted Action Multicenter study on use of(18)F-fluoro-deoxyglucose Positron Emission Tomography for the Detection of Myocardial Viability. *Eur Heart J*. 2001;18:1691–1701
24. Bax JJ, Visser FC, Poldermans D, et al Relationship between preoperative viability and postoperative improvement in LVEF and heart failure symptoms. *J Nucl Med*. 2001;42:79–86
25. Beanlands RS, Ruddy TD, deKemp RA, et al 2 Positron emission tomography and recovery following revascularization (PARR-1): the importance of scar and the development of a prediction rule for the degree of recovery of left ventricular function. *J Am Coll Cardiol*. 2001;40:1735–1743
26. Perrone-Filardi P, Bacharach SL, Dilsizian V, Maurea S, Frank JA, Bonow RO. Regional left ventricular wall thickening. Relation to regional uptake of 18fluorodeoxyglucose and 201Tl in patients with chronic coronary artery disease and left ventricular dysfunction. *Circulation*. 1992;86:1125–1137
27. Perrone-Filardi P, Pace L, Prastaro M, et al Assessment of myocardial viability in patients with chronic coronary artery disease. Rest-4-hour-24-hour 201Tl tomography versus dobutamine echocardiography. *Circulation*. 1996;94:2712–2719
28. Gerber BL, Belge B, Legros GJ, et al Characterization of acute and chronic myocardial infarcts by multidetector computed tomography: comparison with contrast-enhanced magnetic resonance. *Circulation*. 2006;113:823–833
29. Habis M, Capderou A, Ghostine S, et al Acute myocardial infarction early viability assessment by 64-slice computed tomography immediately after coronary angiography: comparison with low-dose dobutamine echocardiography. *J Am Coll Cardiol*. 2007;49: 1178–1185
30. le Polain de Waroux JB, Pouleur AC, Goffinet C, et al Combined coronary and late-enhanced multidetector-computed tomography for delineation of the etiology of left ventricular dysfunction: comparison with coronary angiography and contrast-enhanced cardiac magnetic resonance imaging. *Eur Heart J*. 2008;29:2544–2551
31. Einstein AJ, Henzlova MJ, Rajagopalan S. Estimating risk of cancer associated with radiation exposure from 64-slice computed tomography coronary angiography. *JAMA*. 2007;298:317–323
32. Gaemperli O, Kaufmann PA. Hybrid cardiac imaging: more than the sum of its parts? *J Nucl Cardiol*. 2008;15:123–126

Chapter 18

HEART FAILURE: CMR TO ASSESS VIABILITY

John-Paul Carpenter, Sanjay Prasad, and Dudley Pennell

CONTENTS

J. L. Zamorano et al. (eds.), *The ESC Textbook of Cardiovascular Imaging*
DOI: 10.1007/978-1-84882-421-8_18, © Springer-Verlag London Limited 2010

Introduction

This chapter will discuss how cardiovascular magnetic resonance (CMR) can assess myocardial viability in patients with chronic heart failure, and help to identify those who will derive improvement in left ventricular (LV) function and (potentially) prognosis from revascularization. We will discuss the following CMR parameters as markers of viability:

- End-diastolic wall thickness
- Dobutamine stress ventriculography
- Late gadolinium enhancement and trans-murality of infarction
- New techniques (including MR spectroscopy and myocardial tagging)

Heart Failure and Coronary Disease

Coronary artery disease is the greatest underlying cause of myocardial dysfunction, accounting for at least 70% of all cases of heart failure.[1] Following myocardial infarction, remodelling occurs owing to abnormal loading conditions, not just in the infarcted segments, but also in the surrounding areas of myocardium. This leads to dilatation of the ventricle with an alteration in shape to a more spherical, less efficient pump with an adverse effect on contractile function (Fig. 18.1). Revascularization can improve function and outcome, but it is important to be able to distinguish viable and hibernating myocardium from non-viable scar to target patients appropriately for intervention, for a positive risk benefit ratio.

Viability and Hibernation

Before considering revascularization of a coronary artery territory subtended by a diseased or occluded epicardial coronary artery, it is essential to know if the underlying myocardial tissue is viable. Viable and hibernating myocardium can be characterized as dysfunctional myocardium with limited or no scarring, which has evidence of preserved but down-regulated metabolic activity in the presence of impaired coronary blood supply during stress, and also the potential for functional recovery following successful revascularization. The concept of hibernation was initially proposed by Rahimtoola.[3] There has been much debate about whether hibernating myocardium has normal resting blood flow and oxygen consumption. Current data indicate that myocardial perfusion is significantly impaired during stress when compared with normally perfused myocardium (reduced or abolished coronary flow reserve), but that resting myocardial perfusion is normal or near normal. Resting perfusion to hibernating areas may be mildly reduced as a direct consequence of reduced demand, because non-contractile myocardium has a lower oxygen (and therefore perfusion) requirement. However, there is no clinical evidence of a major reduction in perfusion to the level that is required in animal models to produce akinesia. Hibernation is distinct from myocardial stunning, which is transient, post-ischaemic myocardial dysfunction; however, the physiological induction of hibernation may result from repeated episodes of stunning owing to reduced myocardial perfusion

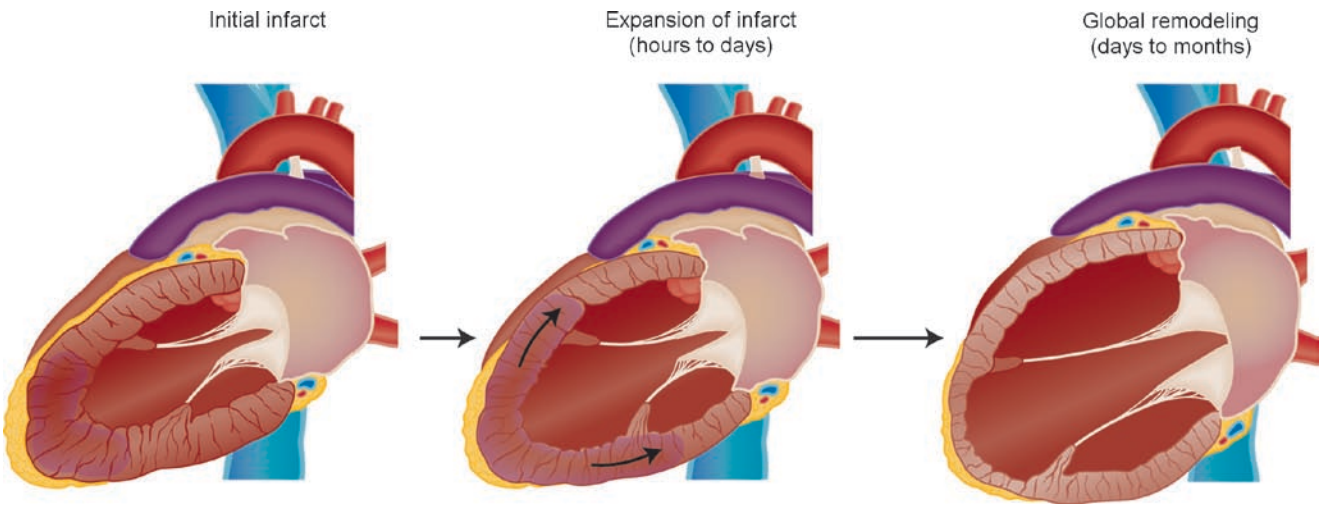

Fig. 18.1 Ventricular re-modelling after acute infarction. At the time of an acute myocardial infarction, there is no clinically significant change in overall ventricular geometry. Within hours to days, the area of myocardium affected by the infarction begins to expand and become thinner. Within days to months, global re-modelling can occur, resulting in wall thinning, overall ventricular dilatation, decreased systolic function, mitral valve dysfunction, and the formation of an aneurysm. Reproduced from Jessup and Brozena[2]

reserve. Hibernation can only be confirmed retrospectively once revascularization has been successful and objective evidence of contractile improvement is seen.

The current options available for clinical viability testing include[^{14}F] fluorodeoxyglucose positron emission tomography (FDG-PET), single photon emission computed tomography (SPECT) with an injectable myocardial perfusion tracer, dobutamine stress ventriculography imaged by echocardiography (DSE), or cardiovascular magnetic resonance (CMR). Although the "gold standard" for the presence of viability has been considered to be evidence of preserved metabolic activity using FDG-PET, the development of CMR techniques may challenge this. FDG-PET has a positive predictive accuracy of 82% and a negative predictive accuracy of 83% for recovery of regional function after revascularization, but CMR is the only technique with high resolution which can determine the trans-murality of infarction and detect small sub-endocardial infarcts that are missed by SPECT (Figs. 18.2 and 18.3).

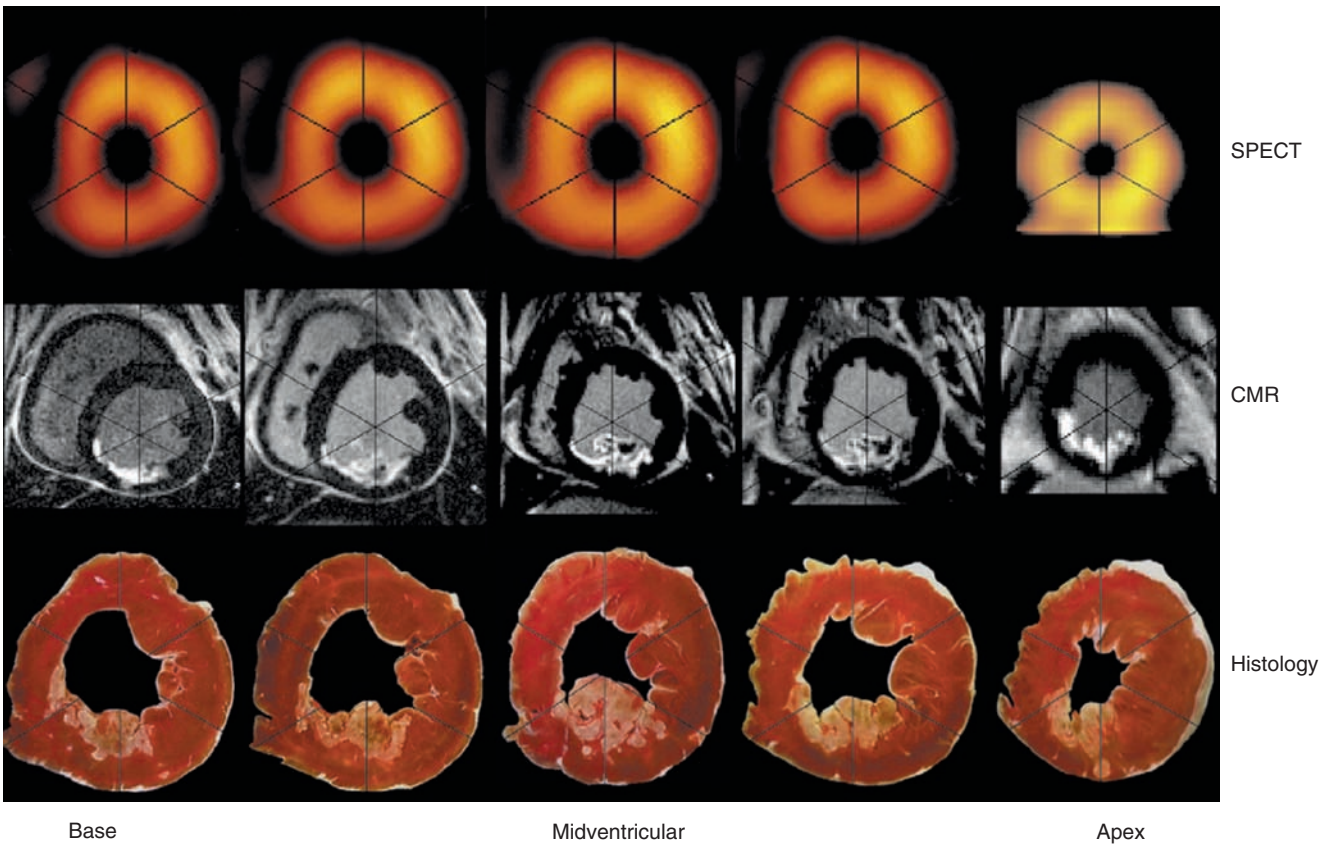

Fig. 18.2 Comparison of SPECT images in a canine model of infarction (*top row*), late gadolinium enhancement CMR images (*middle row*), and histological slides stained for infarction using TTC (*bottom row*). Sub-endocardial infarcts that are detected by CMR and confirmed by tissue staining are missed by SPECT owing to its inferior resolution. Reproduced from Wagner et al.[5]

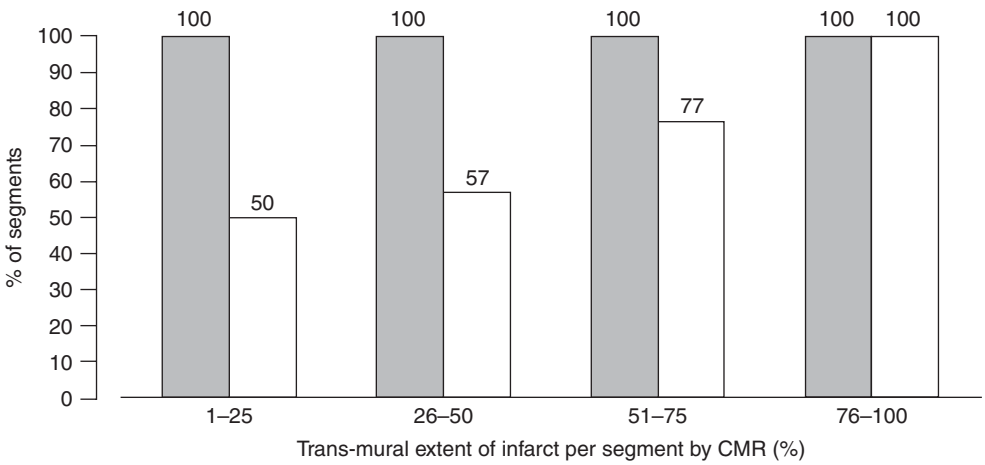

Fig. 18.3 Patient data. Comparison of infarcts detected by SPECT (*open bars*) against those detected by CMR late gadolinium enhancement (*shaded bars*). For segments in which the trans-mural extent of infarction is less than 75% by CMR, the number of segments not detected by SPECT increases as the trans-mural extent of infarction decreases. Reproduced from Wagner et al.[5]

Improvement in LV Function and Prognosis Following Revascularization

Recovery of contractile function in patients with LV dysfunction owing to chronic ischaemic heart disease occurs in some, but not all, patients who undergo revascularization. The recovery in function is not immediate but follows a progressive course over the weeks and months following the procedure. Recovery appears to be faster in stunned myocardium rather than hibernating myocardium, which can take longer (up to 14 months) to recover function.[6] It is frequently observed that those with the most severely impaired ventricular function gain important functional recovery, and, therefore, these patients may especially benefit from revascularization (Fig. 18.4).

A meta-analysis of 24 studies looking at the impact of revascularization on prognosis in patients with coronary artery disease and LV dysfunction showed a strong association between myocardial viability on non-invasive testing and improved survival; however, these were not randomized trials, and none of the studies included CMR assessment.[8] In patients with evidence of viability, there was a 76% reduction in annual mortality in those who underwent revascularization when compared with medical therapy. There was also a direct relationship between the severity of LV dysfunction and the magnitude of benefit from revascularization. In contrast, absence of viability was associated with no significant difference in the outcomes (Fig. 18.5).

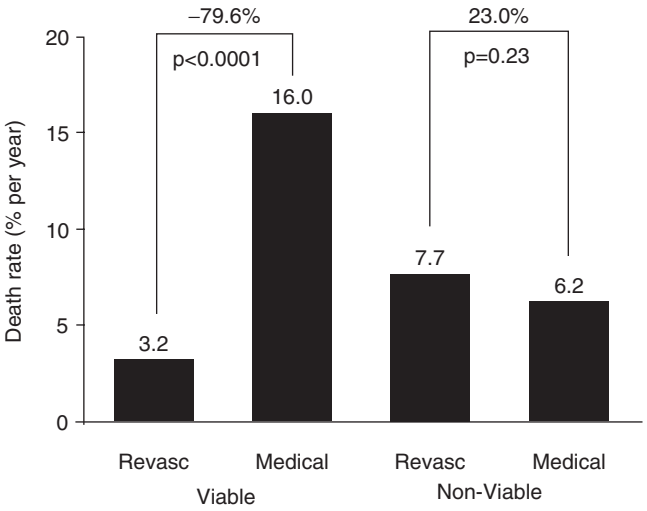

Fig. 18.5 Death rates for patients with and without evidence of myocardial viability treated by revascularization or medical therapy. There is a 79.6% relative reduction in mortality for patients with viability treated by revascularization. In patients without evidence of viability, there was no significant difference in mortality. Reproduced from Allman et al.[8]

CMR Assessment of Ventricular Function, Regional Wall Motion, and Valves

Baseline steady state free precession (SSFP) cine images of the left ventricle provide the current "gold standard" for the measurement of volumes and function, and these allow an excellent appreciation of regional function and systolic thickening. Regional function at rest can, however, be misleading for the assessment of infarction. Contraction may appear normal even in infarcted myocardium with approximately 50% trans-mural extent of infarction.[9] This may either represent true contraction or artefact because of tethering to normally functioning neighbouring segments or through-plane motion giving the appearance of wall thickening. These effects can result in an under-estimation of infarct size and, therefore, wall motion at rest cannot be relied upon in isolation to exclude myocardial infarction.

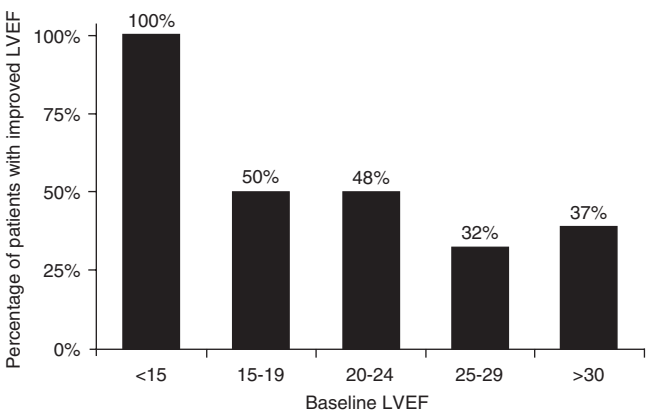

Fig. 18.4 Improvement in global LV ejection fraction (EF) by ≥5% after revascularization was observed more frequently in patients with the lowest baseline LVEF. Reproduced from Schinkel et al.[7]

CMR assessment of LV function can also provide information regarding the risks associated with surgery. Patients with very poor systolic function are known to be at higher peri-operative risk of death, and those with severe LV dilatation (end-systolic volume ≥140 mL) are less likely to show improvement in LV ejection fraction despite evidence of viability.[10] The detection of LV aneurysms, which may require reconstructive surgery (Fig. 18.6, Video 18.6), and of the presence of mitral regurgitation (owing to annular dilatation), which may require mitral annuloplasty, also helps to guide surgical management. Additional findings (such as ventricular thrombus) may also be identified (Fig. 18.7, Video 18.7).

Wall Thickness

In view of the thinning that occurs in chronic myocardial infarction, end-diastolic wall thickness has been used as a surrogate marker for the assessment of myocardial viability,

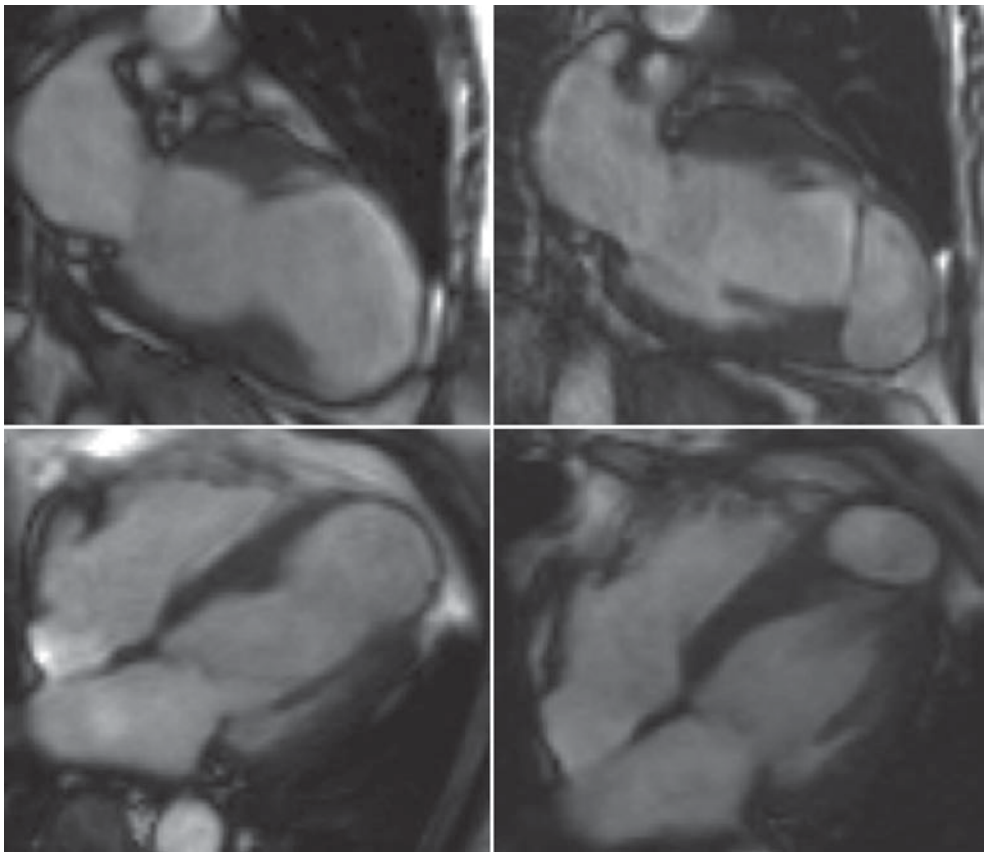

Fig. 18.6 The Dor procedure can be used to reconstruct the ventricular geometry. Pre-operatively, there was a large antero-apical aneurysm following anterior myocardial infarction (*left upper and lower panels*). At operation, a purse string suture was inserted between the muscular and fibrotic zones of the infarct and the resulting oval defect was closed with a patch of collagen-impregnated Dacron. The residual LV wall was closed over this patch. The aneurysmal part of the ventricle is therefore excluded and will eventually thrombose (*right upper and lower panels*). Video 18.1 shows the improvement in ejection fraction

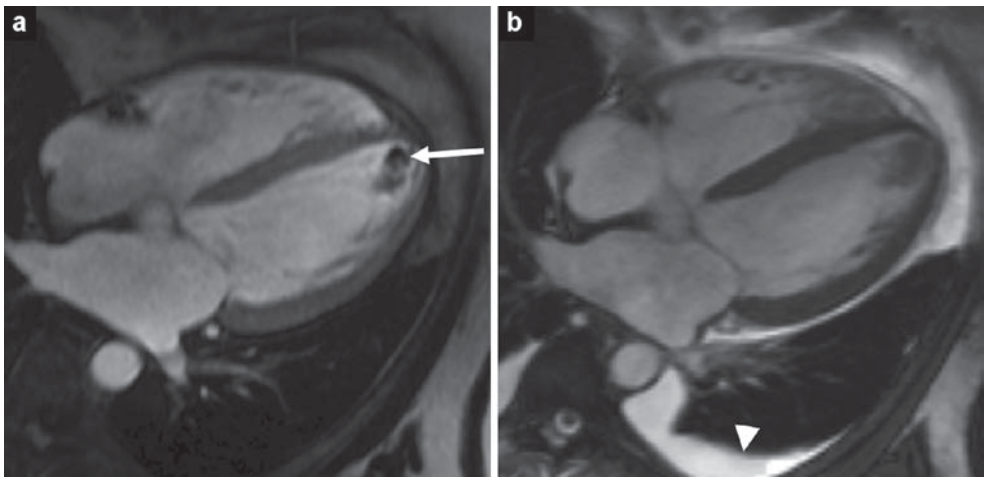

Fig. 18.7 Apical LV thrombus. **(a)** Thrombus appears as a dark filling defect in the early phase after gadolinium injection (*white arrow*). **(b)** Still image from SSFP cine (see Video 18.2). There is also a pleural effusion (*arrowhead*)

and it is known to be an important parameter that can predict recovery of myocardial function. Echocardiographic studies have suggested that dysfunctional myocardial segments with end-diastolic wall thickness of less than 6 mm are significantly scarred and show little improvement with revascularization. The re-modelling, which occurs in the first weeks following myocardial infarction, leads to wall thinning in regions with significant degree of trans-murality of infarction and scar with compensatory hypertrophy of other areas of the ventricle. Changes in the longitudinal and circumferential extent of infarction are variable but may result in expansion of the infarcted territory. Even with better treatment of acute myocardial infarction, the use of ACE inhibitors, statins, and beta-blocker therapy, re-modelling is still frequently seen, albeit to a lesser extent than before.

Early CMR trials examined end-diastolic wall thickness to assess whether this was related to the presence of viability in thinned, akinetic areas of myocardium. Baer et al.

compared CMR with both FDG-PET and SPECT.[11, 12] A value of <5.5 mm end-diastolic wall thickness was taken as the cut-off for identifying non-viable myocardium based on the normal range of wall thickness in healthy volunteers (5.5 mm = mean normal wall thickness − 2.5 standard deviations). This correlated well with technetium SPECT perfusion defects and autopsy specimens of hearts with full-thickness infarcts, which showed that regions with transmural scar measured <6 mm. When compared with FDG-PET, regions were graded as viable if [^{14}F] fluorodeoxyglucose uptake was ≥50% of the maximum uptake in a viable region of myocardial infarction with normal wall motion. Using these criteria, there was an 83% agreement between the CMR measurement of wall thickness and viability on FDG-PET. End-diastolic wall thickness of >5.5 cm was found to have 72% sensitivity, 89% specificity, and 91% positive predictive value for residual metabolic activity.

In a prospective study using CMR before and after bypass surgery, segments that remained akinetic after revascularization had a significantly lower end-diastolic wall thickness than those that showed an improved systolic wall thickening (6.0 ± 3.1 mm vs. 9.8 ± 2.6 mm, $p < 0.001$). The presence of end-diastolic wall thickness of <5.5 mm meant that the corresponding myocardial segment was highly unlikely to show functional improvement at follow-up (with a negative predictive value of 90.4%). Baer et al. concluded that the presence of significantly reduced end-diastolic wall thickness reliably indicated irreversible myocardial damage, and that dobutamine stress CMR could be restricted to those who had preserved LV end-diastolic wall thickness.[13] It was felt that if the myocardium was thin, this essentially excluded the presence of a clinically relevant residual amount of viable myocardium. It was noted, however, that preserved LV end-diastolic wall thickness was not sufficient on its own to predict the functional improvement of dysfunctional segments, as metabolic activity was present in some akinetic regions with reduced end-diastolic wall thickness.[14]

Reliance on LV end-diastolic wall thickness alone as a measure of viability is, therefore, suboptimal, and it has since been demonstrated that improvement in function can occur even in the presence of severe wall thinning, which itself can thicken after revascularization in a poorly understood process or reverse re-modelling (see Fig. 18.17). The poor predictive value with respect to functional recovery may result because wall thickness cannot assess the degree of trans-murality of infarction, which corresponds to the degree of scarring. A more recent study combining end-diastolic wall thickness with measurement of late gadolinium enhancement has confirmed that while wall thickness is an independent predictor of functional recovery, combination with other techniques of viability assessment adds incremental value (Fig. 18.8).[16] The development of the late-enhancement technique has shown that areas <5-mm thick (which would have previously been considered dead) do have the potential for functional recovery, especially if there is no evidence of late enhancement.

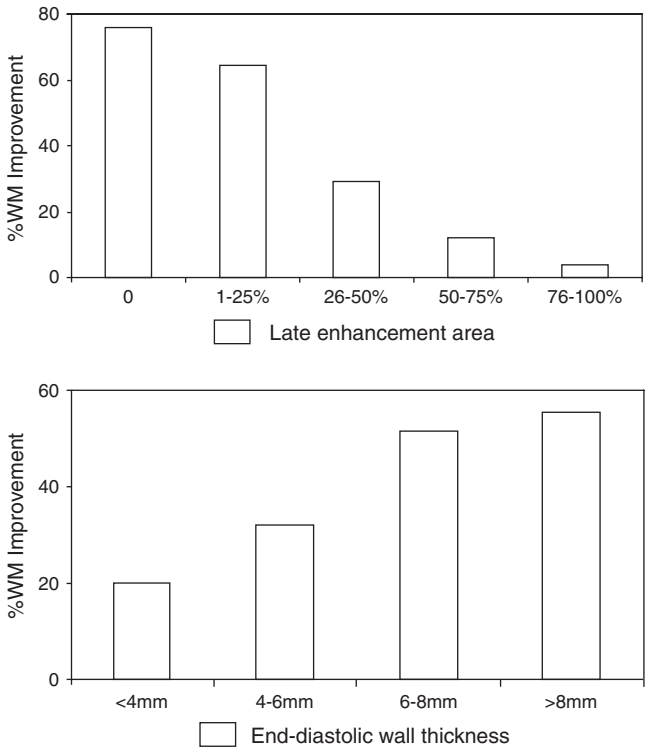

Fig. 18.8 The relationship between CMR markers of viability and recovery of LV function after coronary artery bypass surgery. The degree of recovery declines with increasing trans-murality of late gadolinium enhancement [LGE] (*upper panel*) and decreasing end-diastolic wall thickness (*lower panel*). Reproduced from Krittayaphong et al.[16]

Dobutamine Stress CMR

The evaluation of contractile reserve is another option for the assessment of viability (Fig. 18.9, Videos 18.9E-H). SSFP cine sequences generate excellent blood pool-myocardial definition and this can be exploited for the assessment of wall thickening in response to low-dose dobutamine stress (with doses of 5–10 μg/kg/min). Segmental analysis is used to assess contractile reserve, which simulates the effect of revascularization. During low-dose dobutamine infusion, systolic wall thickening increases in viable myocardium but not in irreversibly scarred areas. If contractile reserve can be elicited, the myocardium is more likely to improve after revascularization. With high-dose dobutamine infusion (20–40 μg/kg/min), additional information using CMR can be obtained regarding the presence of ischaemia and prognosis.[17] High-dose dobutamine CMR is accurate for the detection of inducible wall motion abnormalities that occur with ischaemia.

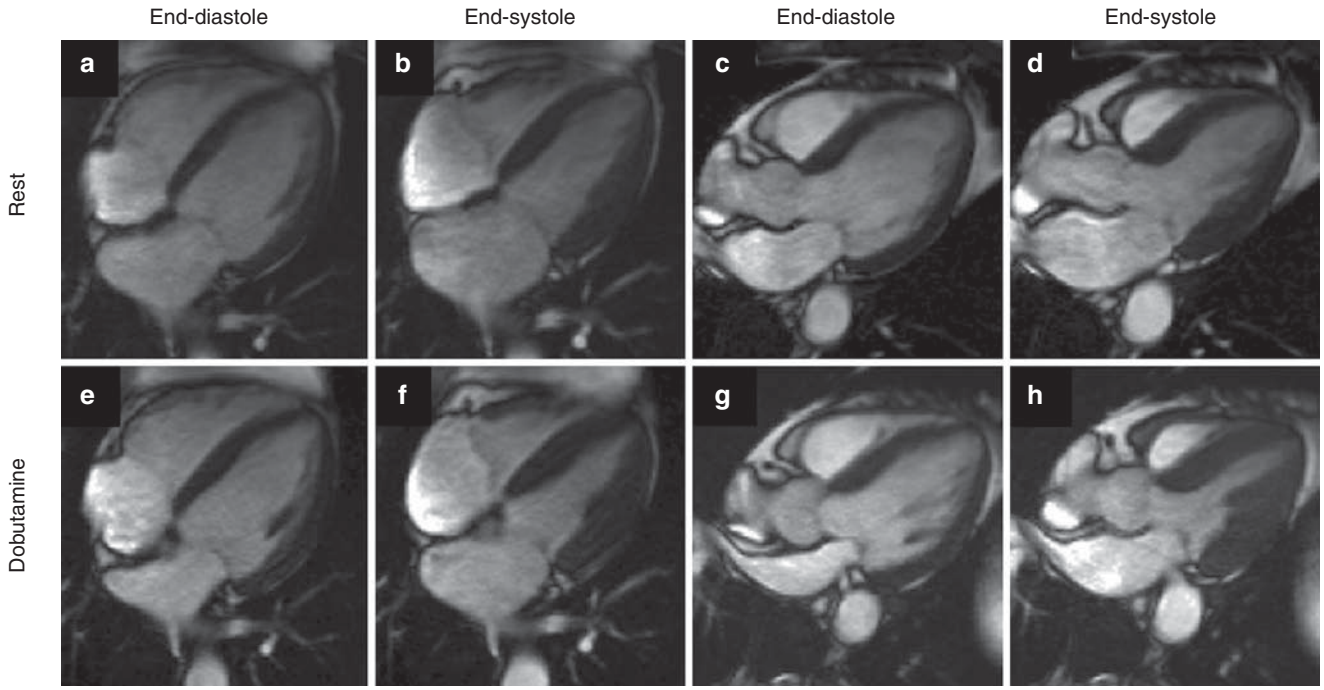

Fig. 18.9 Response to low-dose dobutamine stress. The top row of images shows a four-chamber view **(a, b)** and LV outflow tract view **(c, d)** at end-diastole and end-systole with resting antero-septal wall hypokinesia and reduced wall thickening. With low-dose dobutamine infusion (10 mcg/kg/min), there is evidence of contractile reserve with improvement in regional function and increased wall thickening **(e–h)**

The use of dobutamine stress CMR to assess patients with coronary artery disease was first described in 1992.[18] Baer et al. subsequently demonstrated that an inotropic response to dobutamine was present in ischaemic, viable, but akinetic myocardium when compared with FDG-PET, and that this response was a better predictor of viability than end-diastolic wall thickness. When combined with wall-thickness measurements, response to dobutamine predicted viability with a sensitivity of 88%, specificity of 87%, and positive predictive accuracy of 92%.[11] Dobutamine-induced systolic wall thickening also proved to be a better predictor of LV functional recovery than end-diastolic wall thickness.[13] They further investigated this dobutamine-induced contraction reserve in 103 patients with previous myocardial infarction before and after successful revascularization using trans-oesophageal echo and CMR. Patients had a mean LV ejection fraction of 38.7 ± 12.5% and, while there was no statistical difference between the two techniques, dobutamine CMR gave a positive predictive accuracy of 92% and negative predictive accuracy of 85%, predicting an overall increase of 13 ± 7% in predominantly viable regions when compared with only 2 ± 7% in regions graded as scar.[19] Sandstede et al. also tested the diagnostic value of dobutamine CMR for predicting the recovery of regional myocardial contractility after revascularization. On a per-segment analysis, they reported 61% sensitivity, 90% specificity, and 87% positive predictive value for the recovery of function, but if a patient-based analysis was performed, this was improved to 76% sensitivity with 100% specificity and positive predictive value.[20] Despite these encouraging results, the inotropic response to dobutamine depends on the presence of viable myocardium that has not undergone severe ultrastructural change with myofibrillar degeneration, which would prevent contractile improvement with inotropic stimulation. The technique is more sensitive for lesser grades of trans-mural infarction (Fig. 18.10).[21]

Developments in Quantification of Wall-Motion Assessment

Tagging, coupled with 3D strain analysis, allows quantitative assessment of regional myocardial contractility, and, although still a research tool, it has promise in the detection of viability using dobutamine stress. Sensitivity of detection of viability may be improved with the use of tagging, because true myocardial contraction is assessed rather than wall motion, with its inherent limitations. Specialized post-processing analysis software is available, and advanced techniques have made tagging much more approachable for clinical use (Fig. 18.11). These include harmonic phase

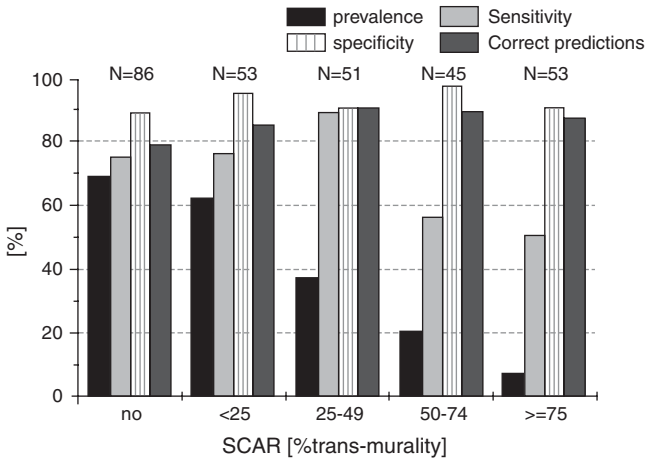

Fig. 18.10 Dobutamine stress CMR and trans-murality of scar. Prevalence of functional recovery, sensitivity, specificity, and correct predictions by dobutamine CMR are grouped with respect to degree of trans-murality. There is high specificity irrespective of the extent of scar, but sensitivity of dobutamine CMR declines with more than 50% scar. Reproduced from Wellnhofer et al.[21]

(HARP) tagging and DENSE (Displacement Encoding with Stimulated Echoes) imaging.

Late Gadolinium Enhancement

An alternative approach to the assessment of contractile reserve is the delineation of infarcted from normal myocardium. Accurate delineation of infarcted myocardium can now be achieved using gadolinium chelates, which are routinely used as CMR contrast agents. These contrast agents are given as a bolus injection via a peripheral vein and are distributed in the extracellular space, altering the relaxation properties of the tissues by predominantly shortening the T_1 recovery time. Gadolinium chelates do not enter cells with an intact cell membrane, but in areas of non-viable tissue, they exhibit delayed wash-in/wash-out kinetics and an increased volume of distribution. In normal myocardium, wash-in and wash-out rates are rapid. This means that late after injection, once gadolinium has mainly washed out of viable myocardium, the concentration remains increased in both acutely infarcted and chronically infarcted regions.[23]

In acute infarction, the disruption of myocyte sarcomere integrity and cell membrane rupture allows gadolinium to enter the previous intracellular space. In chronic infarct tissue, replacement fibrosis causes an increase in the interstitial space, and, hence, in the volume of distribution of gadolinium. Therefore, depending on the dose of gadolinium given, approximately 5–15 min after initial injection, a time window exists where the concentration of gadolinium in infarcted tissue is higher than the surrounding normal viable myocardium (Fig. 18.12).

The higher gadolinium concentration results in higher signal on T_1-weighted MR sequences, and this can be highlighted to the maximum by imaging the gadolinium distribution using an inversion recovery technique. This sequence relies on allowing the T_1 recovery of normal myocardium to pass through the point of zero signal (a technique known as nulling of the normal myocardium), which creates intense signal contrast between normal and infarcted myocardium (Fig. 18.13). This created the aphorism "bright is dead," although this is now known to be an oversimplification in other conditions such as cardiomyopathy. This single breath-hold technique produces strongly T_1-weighted images and allows good differentiation between injured and normal regions of myocardium with up to 500% difference in signal intensity and high resolution, such that trans-mural depiction of viability is now possible.[4] Images have an in-plane resolution of 1.5–2 mm, which approximates to 1 g of tissue. This late gadolinium enhancement technique has been shown to

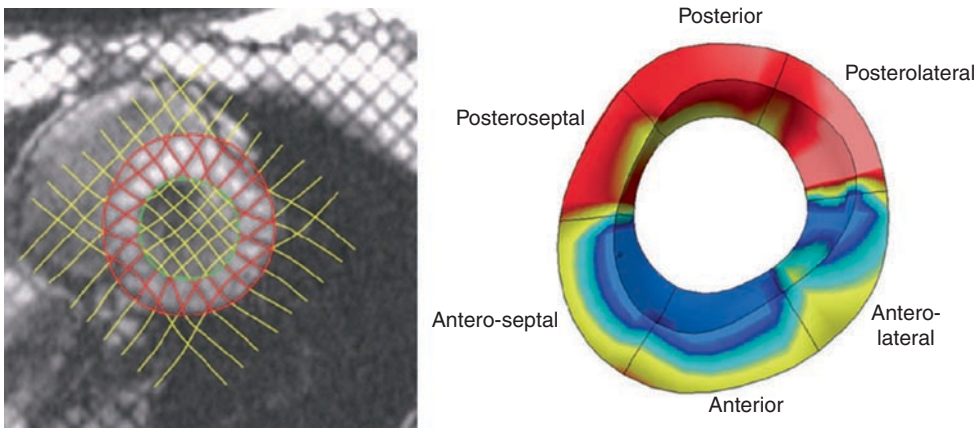

Fig. 18.11 Regional strain analysis using myocardial tagging. **(a)** Short-axis image at end-systole demonstrating myocardial borders and computer-assisted tag line representation. **(b)** Colour contour map of calculated circumferential strain. Areas in red indicate reduced contraction in this example from a patient with a large infero-posterior infarct. Reproduced from Bree et al.[22]

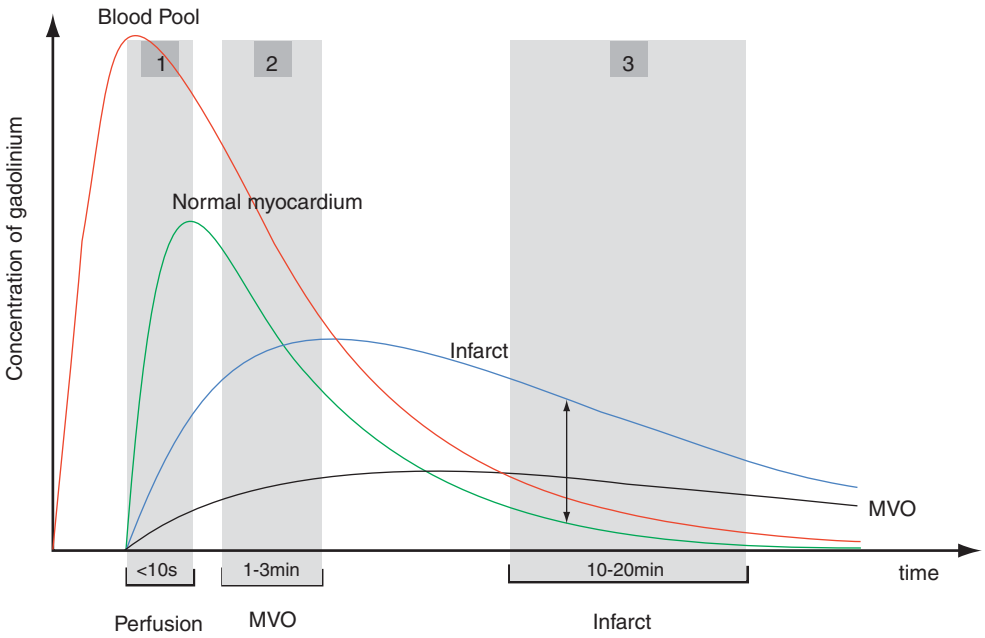

Fig. 18.12 Representation of the kinetics of gadolinium concentration following a bolus intravenous injection. The wash-in and wash-out is slower in infarcted tissue (*blue line*) than normal myocardium (*green line*), and results in a concentration difference (*arrowed line*), which is exploited for late enhancement imaging. Perfusion images are acquired during the first-pass phase (*1*). Early phase images allow the detection of micro-vascular obstruction (MVO) or ventricular thrombus (*2*). Delayed enhancement images are obtained in the late phase (*3*)

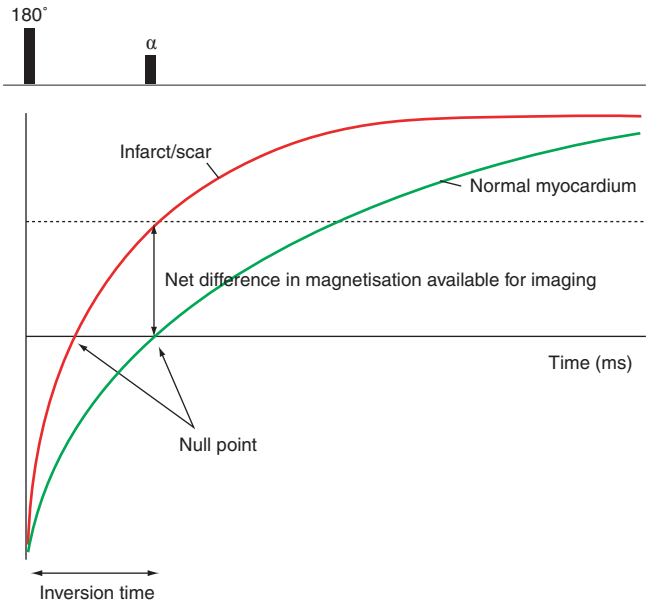

Fig. 18.13 Inversion recovery. The T_1 relaxation curves for normal myocardium (*green*) and infarct (*red*) are shown. The longitudinal relaxation time, T_1, is shortened by gadolinium chelates. Owing to a higher concentration of gadolinium in infarct tissue, the T_1 will be shorter than normal myocardium. A 180º prepulse will result in a T_1-weighted image, which will accentuate the contrast between normal myocardium (*dark*) and scar (*bright*). Contrast will be greatest if images are acquired at the correct inversion time when normal myocardium is passing through the null point

correlate very accurately with the area of infarction. Quantitative analysis software can be used to estimate the volume of infarcted tissue (Fig. 18.14).

The Use of Late Gadolinium Enhancement to Identify Infarcted Myocardium

As proof of concept, Kim et al. described the ligation of the left anterior descending or circumflex artery in a canine model causing acute myocardial infarction.[23] The area of late enhancement revealed a high correlation with the infarct distribution when the ex vivo hearts were stained with 2,3,5-triphenyltetrazolium chloride (TTC). The TTC stain forms a red precipitate in areas of viable myocardium, but necrotic areas fail to stain. In areas of myocardium subtended by coronary arteries where only transient ischaemia was induced, there was no evidence of infarction by either CMR or tissue staining. The accuracy of the late-enhancement technique to delineate infarct from viable tissue has been confirmed: the spatial extent of enhancement is near identical to the spatial extent of infarction at every stage of healing. The injection of fluorescent micro-particles into the left atrium during coronary artery occlusion confirms that the ischaemic area at risk can be reliably distinguished from the infarct zone as detected by late enhancement (Fig. 18.15). Further support that regional elevation in gadolinium chelate concentration is exclusively associated with areas of irreversible ischaemic injury has been provided in animal experiments using TTC histology combined with electron probe X-ray micro-analysis (EXPMA) to simultaneously determine the concentrations of gadolinium, sodium, phosphorous, sulphur, chlorine, potassium, and calcium. These areas of enhancement, representing sub-endocardial or trans-mural infarction, have significantly

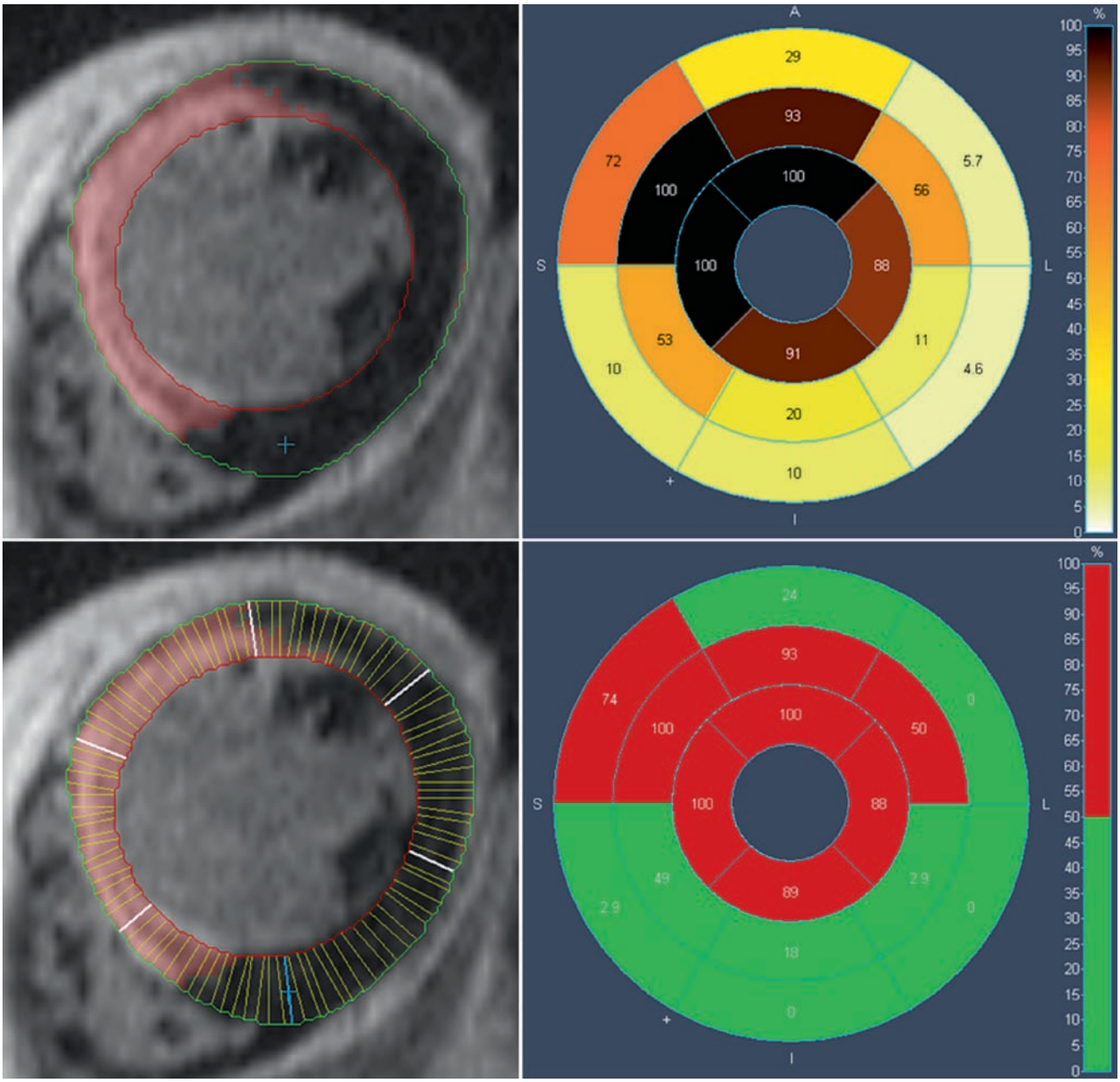

Fig. 18.14 Quantitative analysis of infarct volume. This example shows an antero-septal myocardial infarction. *Top left:* Thresholding delineates enhanced areas of scar (*pink shading*). *Top right:* 16-segment model bull's eye plot depicting trans-murality of scar in each segment [no scar = 0% (*white*), trans-mural scar = 100% (*black*)]. *Bottom left:* Radial chords superimposed on the image allow measurement of degree of trans-murality of infarct. *Bottom right:* Bull's eye viability plot. The threshold for viability is set at 50%. Any areas over 50% trans-mural scar are graded as non-viable (*red*). LV mass = 259 g, Calculated scar tissue volume = 115 mL (46%). Analysis performed with QMassMR. (Medis Medical Imaging Systems B.V, Leiden, The Netherlands)

altered electro-mechanical properties when assessed using endocardial voltage mapping. Klein et al. investigated 31 patients with poor LV systolic function secondary to ischaemic heart disease using late gadolinium enhancement CMR and FDG-PET. There was close agreement (r = 0.91, $p < 0.0001$) between the techniques, but importantly, 11% of the segments that were defined as viable according to PET criteria had evidence of late enhancement on CMR. This is likely to be the result of the superior resolution of CMR.[25]

Use of Late Gadolinium Enhancement to Assess Recovery After Revascularization

When correlated with coronary angiographic data, nearly all patients with confirmed myocardial infarction have the hallmark finding of sub-endocardial or trans-mural enhancement in the relevant corresponding coronary artery territory. In

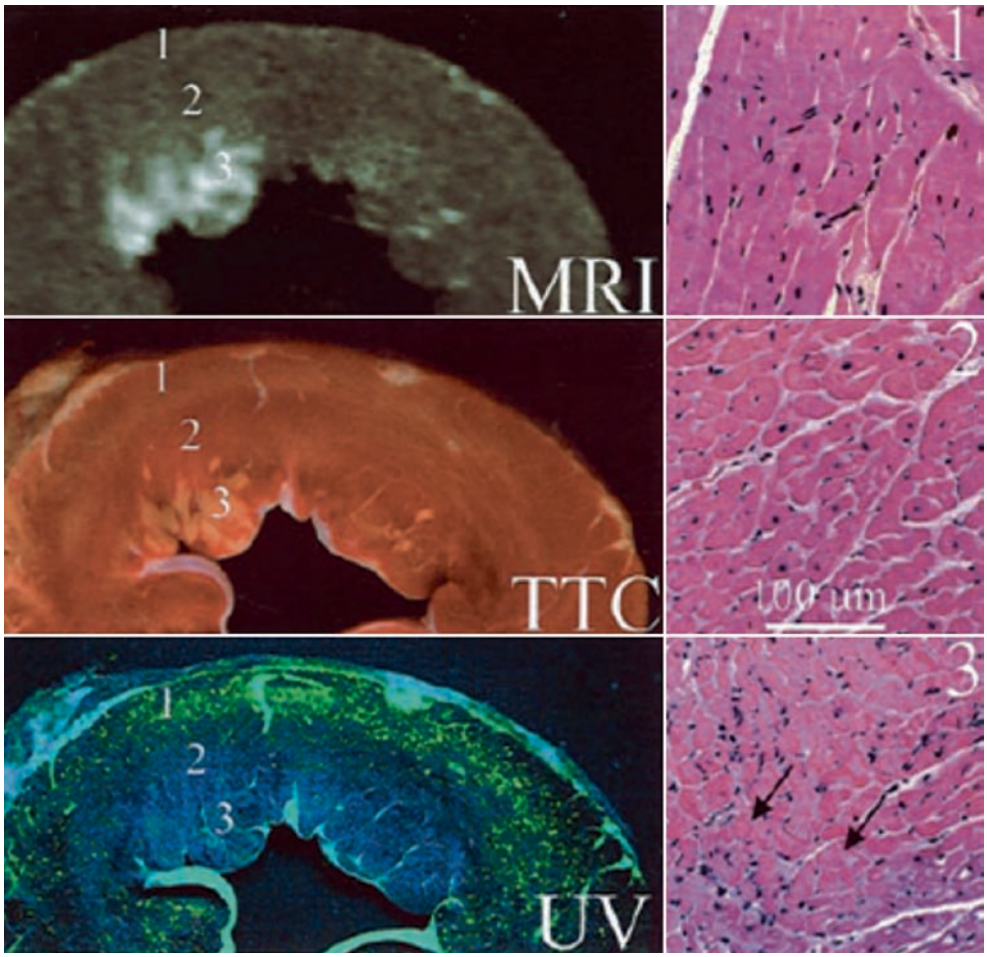

Fig. 18.15 Comparison of late enhancement (*left upper panel*), TTC staining (*left middle panel*), and the myocardium at risk (*region without green fluorescent micro-particles, left lower panel*) in a dog with a 1-day-old reperfused infarction. Light microscopy views of region 1 (not at risk, not infarcted), region 2 (at risk but not infarcted), and region 3 (infarcted) are shown on the *right panels. Arrows* point to contraction bands. This shows that the area of delayed enhancement correlates exactly with the area of infarction. Reproduced from Fieno et al.[24]

patients with heart failure owing to ischaemic heart disease, there is almost invariable evidence of sub-endocardial or trans-mural enhancement; however, in cases of dilated cardiomyopathy, there is usually either no enhancement or a diffuse mid-wall pattern of enhancement that does not follow coronary artery territory. Accordingly, 13% of patients with presumed idiopathic dilated cardiomyopathy demonstrate a pattern of enhancement that identifies ischaemic heart disease as the underlying cause for LV dysfunction.[26] The pattern of enhancement is therefore extremely useful in determining the underlying aetiology of LV impairment, differentiating those with coronary artery disease from cardiomyopathy in which revascularization would not result in an improvement in LV function.

In animal models and human studies, myocardial salvage with recovery in function following acute infarction has been shown to be inversely related to the degree of trans-murality of enhancement. In a canine model of acute infarction, myocardial segments with < 25% enhancement at day 3 post-MI showed 87% spontaneous recovery by 1 month, but if there was complete trans-mural enhancement, no recovery was seen.[27] In patients undergoing successful reperfusion therapy for acute MI, either with primary percutaneous coronary intervention or thrombolysis, the degree of improvement was again inversely related to the trans-murality of enhancement. The best predictor of improvement in segmental function at 2–3 months following acute infarction has been found to be late enhancement of <25% of the LV wall thickness.[28] Patients who undergo primary percutaneous coronary intervention to treat acute MI also have greater predicted recovery of myocardial contraction with lesser degrees of enhancement.

In chronic heart failure, the likelihood of functional improvement with revascularization had been previously described in histological studies looking at degree of fibrosis in needle biopsy specimens taken at the time of surgery. Viable areas of myocardium showed a lower degree of fibrosis, which in turn was an independent predictor of functional recovery. Having identified that the extent of late gadolinium enhancement exactly mirrors the infarcted tissue, researchers further investigated whether this technique could predict recovery of function following revascularization. In a landmark study, Kim et al. prospectively studied patients with established myocardial dysfunction and chronic coronary artery disease to assess the likelihood of recovery of akinetic or dysfunctional myocardial segments following revascularization. This study demonstrated that, in the context of chronic infarction, the

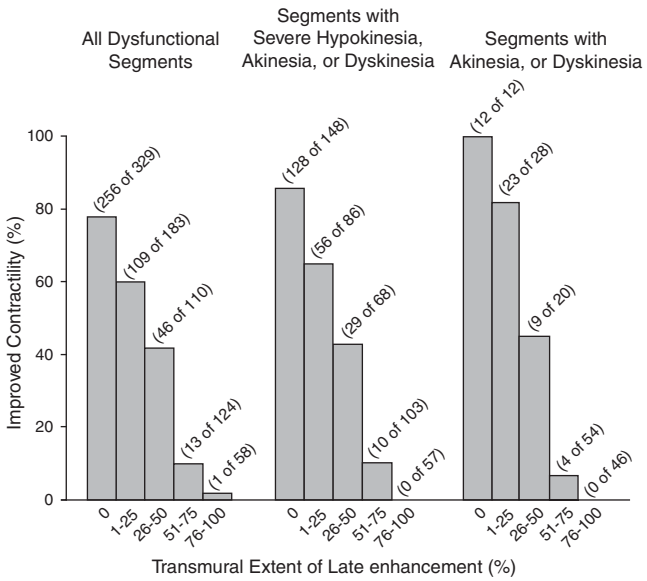

Fig. 18.16 Relationship between the trans-mural extent of late enhancement before revascularization and the likelihood of increased contractility after revascularization. Data are shown for all dysfunctional segments and separately for the segments with at least severe hypokinesia and segments with akinesia or dyskinesia. There was an inverse relation between the trans-mural extent of late enhancement and the likelihood of improvement in contractility. Reproduced from Kim et al.[29]

likelihood of functional recovery with successful surgical or percutaneous revascularization declined with increasing trans-murality of enhancement, such that patients with 50% or less trans-mural gadolinium enhancement showed a good degree of recovery, whereas those with 75% showed far less recovery and those with 100% virtually showed no response (Fig. 18.16).[29] Similar studies have since replicated these findings. It is clear that improvement in myocardial function is highly likely if there is < 25% trans-murality of enhancement and very unlikely if there is > 75% enhancement. Between these two extremes, there is a grey zone with variable recovery, but even up to 75% enhancement, there is evidence of some improvement in function with revascularization, and some groups therefore recommend dobutamine CMR for this cohort. The absence of late gadolinium enhancement (even in thinned myocardial wall segments that were previously felt to be scarred and unlikely to respond) is strongly associated with improvement in contractility and functional recovery after revascularization (Fig. 18.17).

Interestingly, the response to beta-blockade in patients with impaired LV function as a result of coronary artery disease can also be predicted by the extent of gadolinium enhancement. Improvement in contractile function with carvedilol or metoprolol is inversely related to the trans-murality of enhancement.[30] Infarct size, measured by CMR, may also be of prognostic significance following myocardial infarction; those with large amounts of scar being more likely to have inducible monomorphic ventricular tachycardia and hence, a higher theoretical risk of sudden arrhythmic death.[31] Kwong et al. looked at late gadolinium enhancement in elderly patients with suspected coronary disease, but no known myocardial infarction and found that the degree of late enhancement predicted worse event-free survival.[32]

Another way of viewing the relationship of infarction to functional recovery is to assess the thickness of the residual epicardial rim of viable tissue overlying the infarction. Kneusel et al. compared CMR with FDG-PET and showed that viable myocardial segments on CMR correlated well with FDG uptake. The segments with a viable rim of > 4.5 mm were found to have FDG uptake of ≥50% (a positive predictor of recovery). These thick, metabolically active segments had a high likelihood of recovery (85%) following revascularization, whereas segments that had a thin viable rim of tissue (albeit metabolically active) were less likely to recover (36%). In contrast, only 13% of thin non-viable segments improved (Fig. 18.18, Video 18.18).[33]

When using direct measurements of infarction, it is important to note that the results apply mainly to chronic infarction, that is months after the acute event. The relative thickness of the infarction and the epicardial rim varies with time after acute myocardial infarction owing to infarct resorption and hypertrophy of the epicardium. Even without revascularization, the thickness of the viable epicardial rim is a predictor of improvement in myocardial contractility between the acute convalescent phase (within the first week) and the chronic state following a myocardial infarct a few months later.

Micro-vascular Obstruction

The presence of micro-vascular obstruction (demonstrated by a region of dense signal void at the endocardial surface of the ventricle surrounded by gadolinium-enhanced myocardial tissue) signifies a poorer likelihood of recovery of ventricular function following an acute myocardial infarction.

Practical Aspects of Late Gadolinium Enhancement Imaging

Timing of Image Acquisition

One of the pitfalls to be aware of is the problem of imaging too early after gadolinium injection. It has been confirmed that imaging at 5–30 min after injection gives the best diagnostic correlation between the presence of trans-mural enhancement and non-viable myocardium, which is unlikely

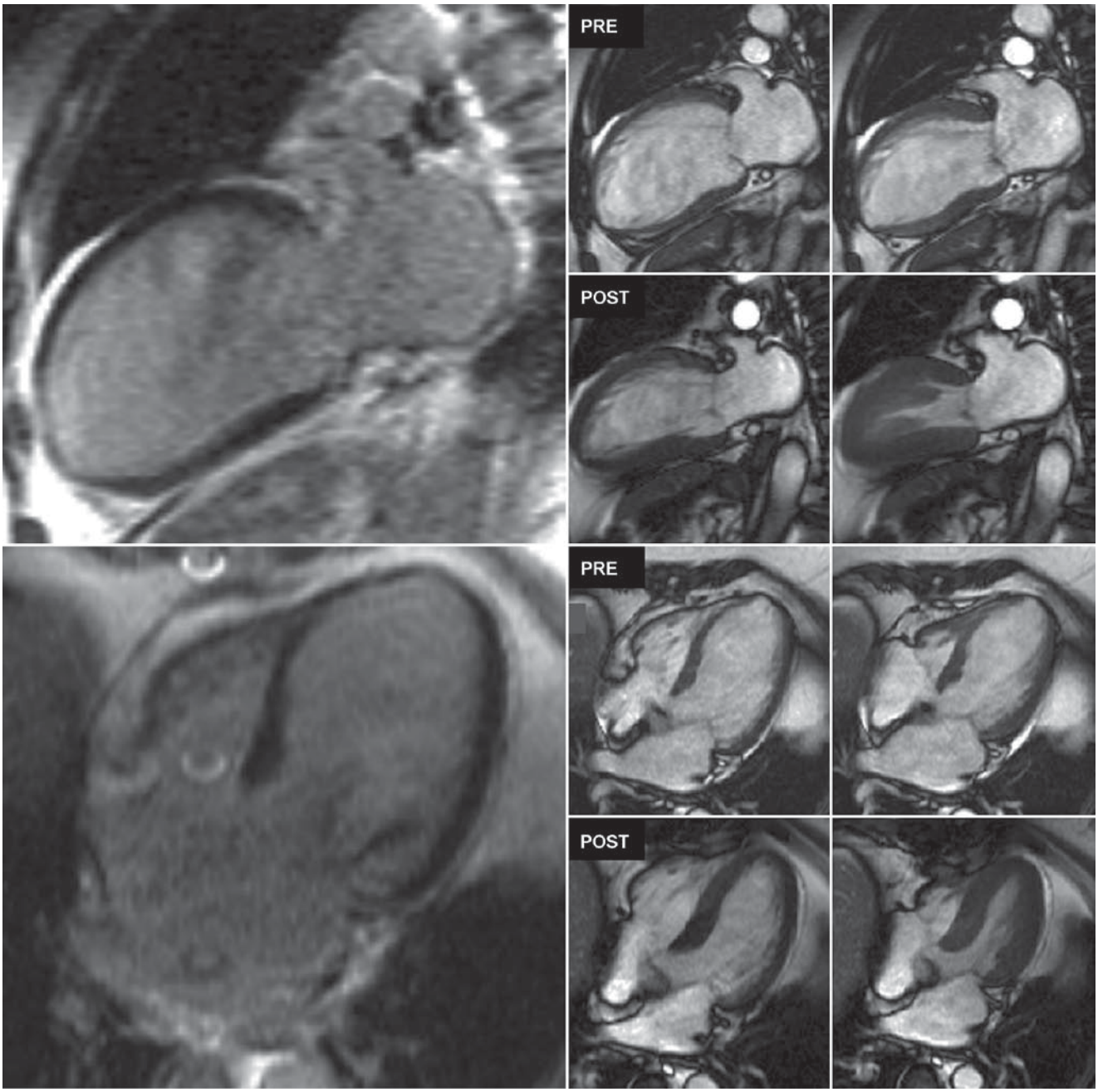

Fig. 18.17 Marked recovery of function following revascularization in an 81-year-old lady with severe left main stem disease and an occluded right coronary artery. The *upper left panel* shows the vertical long-axis late gadolinium enhancement image next to the systolic and diastolic frames before (pre) and after (post) revascularization. The *lower left panel* shows the four-chamber late gadolinium enhancement image next to diastolic and systolic frames before and after revascularization. On these late gadolinium images, there was very little enhancement and despite the severely dilated, thinned ventricle, there was remarkable recovery following successful revascularization. Reproduced from John et al.

to show functional improvement.[34] If images are acquired too early with very short inversion times, the intermediate wash-in kinetics in viable peri-infarct border zones will give rise to enhancement, and delayed contrast kinetics in the core of an infarct may mean that this area is relatively hypointense. As a result, infarct size may be wrongly estimated.

Optimizing Inversion Time

The optimal inversion time (TI) must be chosen to allow the best contrast enhancement of the infarcted region with nulling of normal viable ventricular myocardium.[4] As the concentration of gadolinium in normal myocardium constantly changes

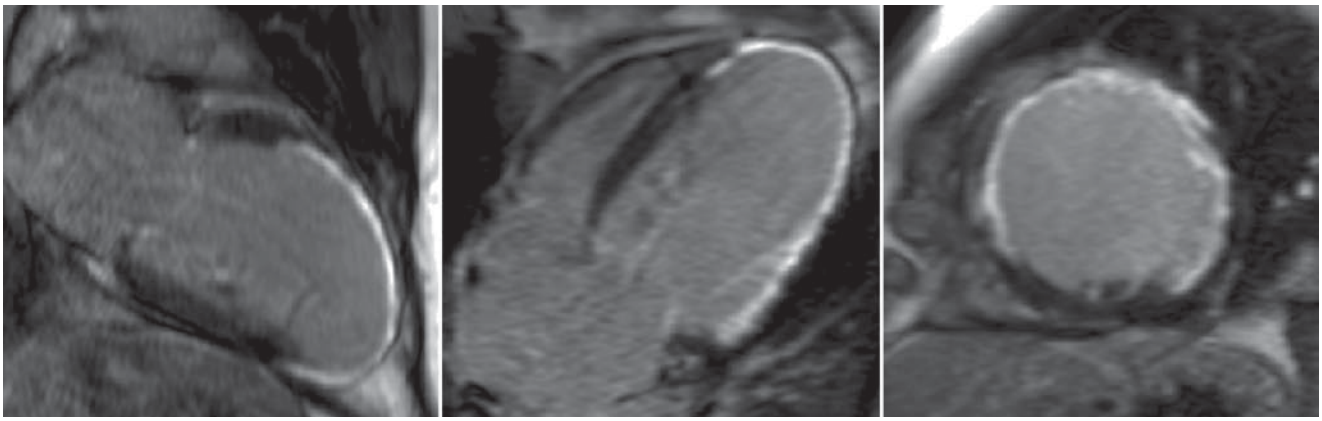

Fig. 18.18 Extensive myocardial infarction involving the anteroseptal wall, anterior wall, lateral wall, and apex. There is at least 75% trans-murality. The corresponding video clip shows extensive wall motion abnormality with dyskinetic anterior wall and akinetic septum. The likelihood of recovery of function in this situation is low

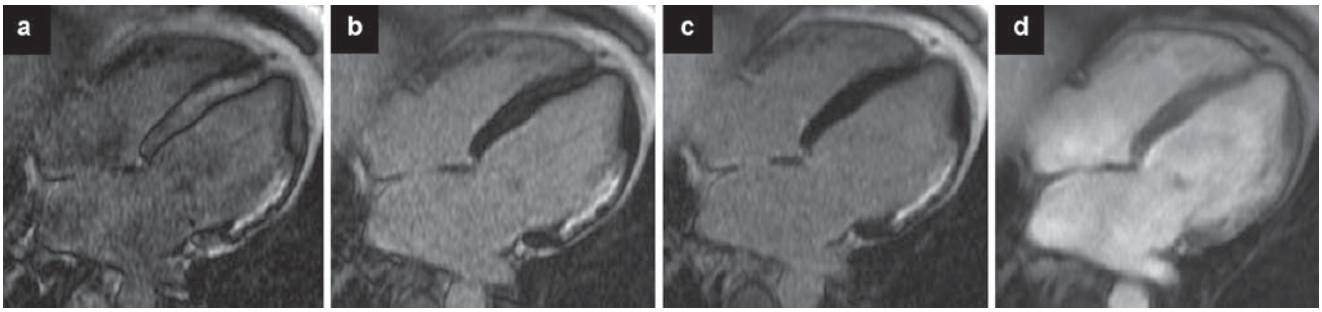

Fig. 18.19 The effect of inversion time on nulling of normal myocardium. **(a)** With the inversion time set too low, there is high signal both from normal myocardium and the lateral wall infarct. **(b)** Inversion time is still too low. **(c)** Correctly adjusted inversion time gives good differentiation between normal and enhanced myocardium. **(d)** When the inversion time is too high, there is once again high signal in both infarct tissue and normal myocardium

owing to the dynamic nature of wash-in/wash-out kinetics, the T_1 will lengthen with time, and therefore, the TI needs to be progressively lengthened throughout the scan to ensure that normal viable myocardium is nulled. If the TI is too short or too long, normal myocardium will appear grey rather than black, which can lead to poor discrimination of infarcted tissue from normal myocardium (Fig. 18.19). Many centres use a TI scout sequence that acquires a preliminary set of images with a range of inversion times, allowing the best value to be chosen. With experience, it is usually possible to predict the inversion time needed (bearing in mind that inversion times will vary with different gadolinium chelates). A typical range of values starting from 260 ms up to about 400 ms may be needed.

A newer pulse sequence that is less dependent on choosing the correct inversion time has been developed (Fig. 18.20). This phase-sensitive inversion recovery (PSIR) sequence consistently achieves good contrast and decreases background noise leading to an improved contrast-to-noise ratio between areas of high signal intensity (such as infarct tissue) and low signal intensity (such as normal myocardium which is nulled).[35]

Comparison with Cine Images

When interpreting late gadolinium enhancement images, it is often very useful to compare with a cine at the same slice position. The nature of balanced SSFP cine sequences gives very good blood/myocardial contrast, which allows the measurement of the thickness of corresponding wall segments as well as assessing regional function, including wall thickening (Fig. 18.21, Video 18.21). This is important when assessing hibernation, which by definition only occurs in segments that have resting contractile dysfunction.

Artefact or True Enhancement?

Artefacts can also be a problem when deciding whether there is evidence of enhancement or not. These artefacts occur in the phase-encode direction and may be owing to high signal from the chest wall, fat, or cerebrospinal fluid. Saturation bands applied over areas of high signal will help, but if artefacts are

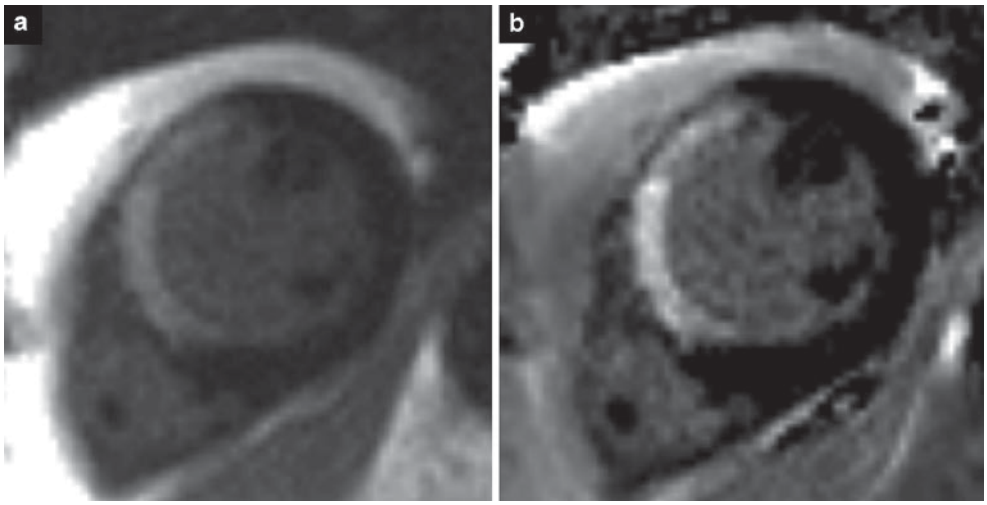

Fig. 18.20 The phase-sensitive inversion-recovery sequence generates two sets of images, the magnitude image **(a)** and the phase image **(b)**, both of which need to be correctly windowed to visualize areas of enhancement such as this trans-mural antero-septal infarct

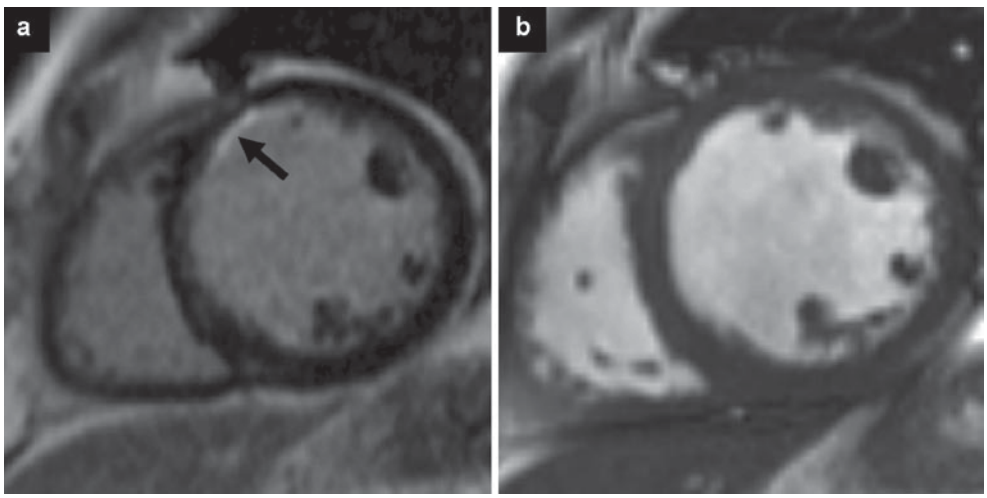

Fig. 18.21 Sub-endocardial infarction. **(a)** The inversion-recovery T_1-weighted image following gadolinium shows a limited area of sub-endocardial enhancement. **(b)** Comparison with the identical slice SSFP cine allows accurate measurement of the extent of trans-murality (graded as 25–50% enhancement) in the severely hypokinetic antero-septal wall

projected onto the myocardium, it can be difficult to see if there is true enhancement. Acquiring images in two orthogonal phase-swapped sets will mean that any artefact seen will be in a different position in each series (Fig. 18.22).

Assessment of Viability Using Magnetic Resonance Spectroscopy

Myocardial cells require adenosine triphosphate (ATP) and phosphocreatine (PCr) for their energy supply. Alterations in cardiac high-energy phosphate metabolism are present in patients with coronary artery disease and heart failure, and this can be directly observed using magnetic resonance spectroscopy (MRS). Phosphorous [^{36}P] MRS can directly measure ATP and PCr to allow assessment of the energetic state of the heart. Neubauer et al. demonstrated that PCr/ATP ratio correlated well with the severity of heart failure in the context of LAD stenosis and chronic myocardial infarction.[37] Although it has a potential use in the assessment of viability, MRS remains challenging owing to the inherently low signal-to-noise ratio as well as cardiac and respiratory motion. It requires a different radiofrequency (RF) coil from that used for conventional proton imaging, presents technical difficulties, and scan times are long. As a result, this technique has not found clinical use but may become more useful with higher field strength systems at 3 T.

Magnetic Resonance Protocols for the Investigation of Myocardial Viability

A combination of CMR techniques can be used to assess viability to give the optimal prediction for recovery of function (Table 18.1). All patients should undergo a standard

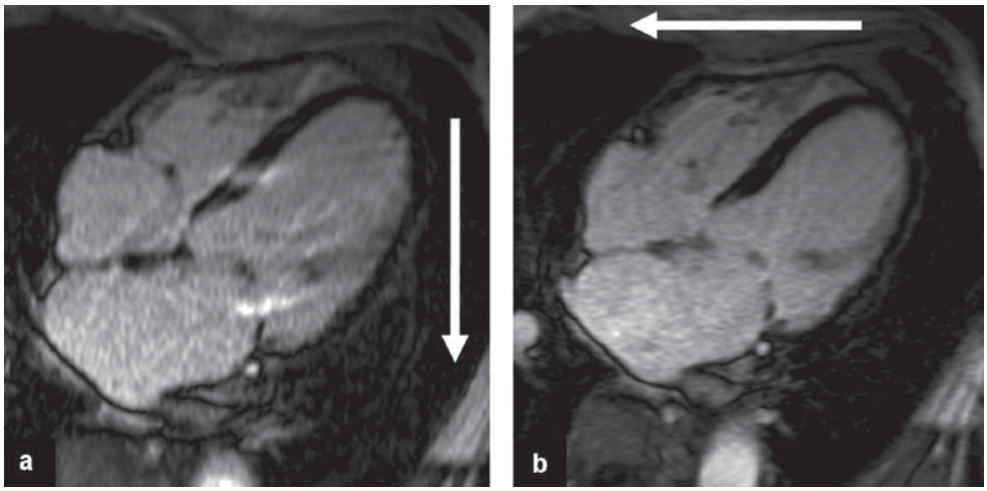

Fig. 18.22 Differentiating artefacts from true enhancement. **(a)** Artefact from the anterior chest wall is superimposed on the septum in the four-chamber view. **(b)** If the phase-encode direction is changed, the area of high signal in the septum is no longer visible and it becomes clear that this was an artefact. The *white arrow* shows the phase-encode direction

Table 18.1. Sensitivity and specificity of different CMR techniques (based on weighted mean values from pooled CMR trials)

	Number of patients	Sensitivity (%)	95% CI	99% CI	Specificity (%)	95% CI	99% CI
End-diastolic wall thickness	100	95	91–99	90–100	41	31–50	28–53
Dobutamine stress	259	73	68–78	66–80	83	78–87	77–89
Late gadolinium enhancement	132	95	91–99	90–100	45	37–54	34–56

Reproduced from Kaandorp TAM, et al.[38]

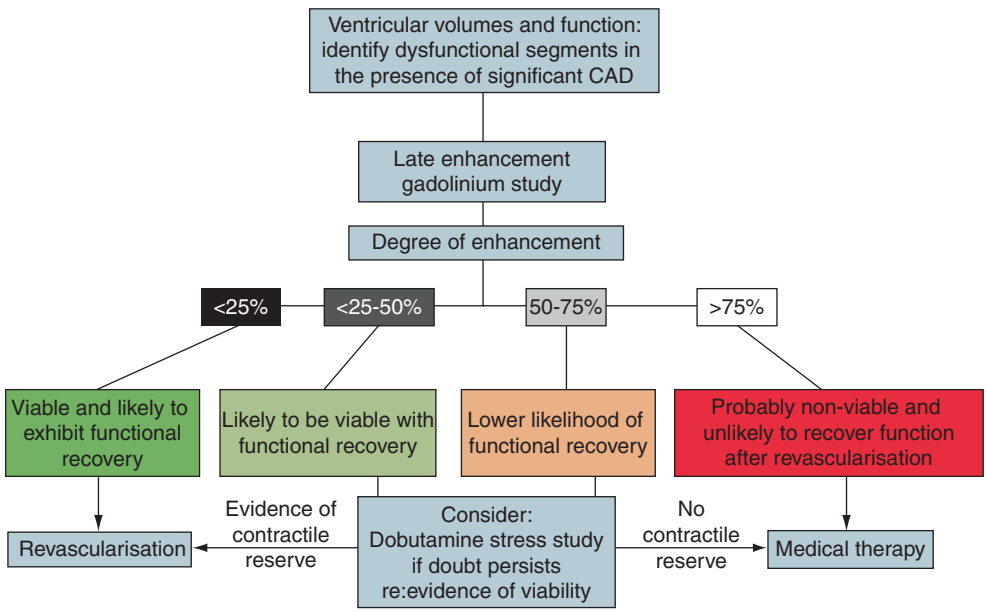

Fig. 18.23 Suggested protocol for the use of CMR to assess viability in ischaemic LV dysfunction. *CAD* coronary artery disease; *PCI* percutaneous coronary intervention

protocol including cine imaging for volumes and function, and unless there are contraindications, late gadolinium enhancement should be performed. Selected patients may then require dobutamine stress CMR for further evaluation (Fig. 18.23). This could be applied to those in whom the late enhancement CMR is not conclusive. Some groups recommend that this is used for patients with predominantly 25–50% trans-mural infarction.

Failure of Recovery Following Revascularization and Peri-procedural Infarcts

Despite the best available evidence of viability, some myocardial segments do not recover function when revascularized. The reasons for this are not always clear, but possible factors include myocardial damage at the time of surgery or incomplete revascularization. The presence of extensive ventricular re-modelling, especially in those with dilated ventricles and end-systolic volume of ≥140 mL, may also be a factor.[10] Approximately 38% of patients who have coronary artery bypass surgery and 28% of those undergoing percutaneous coronary intervention have evidence of new areas of gadolinium enhancement secondary to peri-procedural myocardial necrosis. Areas of new enhancement following PCI or surgery will worsen the outcome and this may also be the cause of non-recovery in functional status after revascularization.[36] The presence of new areas of late enhancement following the procedure is a negative predictor for improvement in global LV ejection fraction and volumes. This highlights the need for myocardial protection and optimal technique during these procedures. Further data on clinical rather than functional outcome is awaited.

Conclusion

In conclusion, CMR is a valuable tool in the assessment of myocardial viability in heart failure. It is becoming more widely available and has several major areas of strength. There is excellent spatial resolution and it is highly reproducible for the measurement of LV volumes and function, allowing serial evaluation of ventricular re-modelling together with the assessment of regional function. The transmural extent of infarction can be assessed, quantification of the total infarct burden can be performed, and the presence of micro-vascular obstruction can be identified. Dobutamine stress also allows for the assessment of contractile reserve.

References

1. Fox KF, Cowie MR, Wood DA, et al Coronary artery disease as the cause of incident heart failure in the population. *Eur Heart J*. 2001; 22:228–236
2. Jessup M, Brozena S. Heart failure. *N Engl J Med*. 2003;348: 2007–2018
3. Rahimtoola SH. The hibernating myocardium. *Am Heart J*. 1989; 117(1):211–221
4. Simonetti OP, Kim RJ, Fieno DS, et al An improved MR imaging technique for the visualization of myocardial infarction. *Radiology*. 2001;218:215–223
5. Wagner A, Mahrholdt H, Holly TA, et al Contrast enhanced MRI and routine single photon emission computed tomography (SPECT) perfusion imaging for detection of subendocardial myocardial infarcts: an imaging study. *Lancet*. 2003;361:374–379
6. Bax JJ, Visser FC, Poldermans D, et al Time course of functional recovery of stunned and hibernating segments after surgical revascularization. *Circulation*. 2001;104(suppl I):I-314-I-318
7. Schinkel AF, Poldermans D, Vanoverschelde JL, et al Incidence of recovery of contractile function following revascularization in patients with ischemic left ventricular dysfunction. *Am J Cardiol*. 2004;93:14–7
8. Allman KC, Shaw LJ, Hachamovitch R, et al Myocardial viability testing and impact of revascularization on prognosis in patients with coronary artery disease and left ventricular dysfunction: a meta-analysis. *J Am Coll Cardiol*. 2002;39:1151–1158
9. Marholdt H, Wagner A, Parker M, et al Relationship of contractile function to transmural extent of infarction in patients with chronic coronary artery disease. *J Am Coll Cardiol*. 2003;42:505–512
10. Schinkel AF, Poldermans D, Rizzello V, et al Why do patients with ischemic cardiomyopathy and a substantial amount of viable myocardium not always recover in function after revascularization? *J Thorac Cardiovasc Surg*. 2004;127:385–390
11. Baer FM, Voth E, Schneider CA, et al Comparison of low-dose dobutamine-gradient-echo magnetic resonance imaging and positron emission tomography with [^{18}F] fluorodeoxyglucose in patients with chronic coronary artery disease. *Circulation*. 1995;91:1006–1015
12. Baer FM, Smolarz K, Jungehulsing M, et al Chronic myocardial infarction: assessment of morphology, function, and perfusion by gradient echo magnetic resonance imaging and ^{99m}Tc-methoxy-isobutyl-isonitrile SPECT. *Am Heart J*. 1992;123:636–645
13. Baer FM, Theissen P, Schneider CA, et al Dobutamine magnetic resonance imaging predicts contractile recovery of chronically dysfunctional myocardium after successful revascularization. *J Am Coll Cardiol*. 1998;31:1040–1048
14. Perrone-Filardi P, Bacharach SL, Dilsizian V, et al Metabolic evidence of viable myocardium in regions with reduced wall thickness and absent wall thickening in patients with chronic ischemic left ventricular dysfunction. *J Am Coll Cardiol*. 1992;20:161–168
15. John AS, Dreyfus GD, Pennell DJ Images in cardiovascular medicine. Reversible wall thinning in hibernation predicted by cardiovascular magnetic resonance. *Circulation*. 2005;111:e24–5
16. Krittayaphong R, Laksanabunsong P, Maneesai A, et al Comparison of cardiovascular magnetic resonance of late gadolinium enhancement and diastolic wall thickness to predict recovery of left ventricular function after coronary artery bypass. *J Cardiovasc Magn Reson*. 2008;10:41
17. Jahnke C, Nagel E, Gebker R, et al Prognostic value of cardiac magnetic resonance stress tests. Adenosine stress perfusion and dobutamine stress wall motion imaging. *Circulation*. 2007;115: 1769–1776
18. Pennell DJ, Unerwood SR, Manzara CC, et al Magnetic resonance imaging during dobutamine stress in coronary artery disease. *Am J Cardiol*. 1992;70:34–40
19. Baer FM, Theissen P, Crnac J, et al Head to head comparison of dobutamine-transoesophageal echocardiography and dobutamine-magnetic resonance imaging for the prediction of left ventricular functional recovery in patients with chronic coronary artery disease. *Eur Heart J*. 2000;21:981–991
20. Sandstede JJW, Bertsch G, Beer M, et al Detection of myocardial viability by low-dose dobutamine cine MR imaging. *Magn Reson Imaging*. 1999;17:1437–1443

21. Wellnhofer E, Olariu A, Klein C, et al Magnetic resonance low-dose dobutamine test is superior to scar quantification for the prediction of functional recovery. *Circulation*. 2004;109:2172–2174
22. Bree D, Wollmuth JR, Cupps BP, et al Low-dose dobutamine tissue-tagged magnetic resonance imaging with 3-dimensional strain analysis allows assessment of myocardial viability in patients with ischemic cardiomyopathy. *Circulation*. 2006;114:I-33–I-36
23. Kim RJ, Fieno DS, Parrish TB, et al Relationship of MRI delayed contrast enhancement to irreversible injury, infarct age, and contractile function. *Circulation*. 1999;100:1992–2002
24. Fieno D, Kim R, Chen E, et al Contrast enhanced magnetic resonance imaging of myocardium at risk: distinction between reversible and irreversible injury throughout infarct healing. *J Am Coll Cardiol*. 2000:36;1985–1991
25. Klein C, Nekolla SG, Bengel FM, et al Assessment of myocardial viability with contrast-enhanced magnetic resonance imaging: comparison with positron emission tomography. *Circulation*. 2002;105:162–167
26. McCrohon JA, Moon JCC, Prasad SK, et al Differentiation of heart failure related to dilated cardiomyopathy and coronary artery disease using gadolinium-enhanced cardiovascular magnetic resonance. *Circulation*. 2003;108:54–49
27. Hillenbrand HB, Kim RJ, Parker MA, et al Early assessment of myocardial salvage by contrast-enhanced magnetic resonance imaging. *Circulation*. 2000;102:1678–1683
28. Choi KM, Kim RJ, Gubernikoff G, et al Transmural extent of myocardial infarction predicts long-term improvement in contractile function. *Circulation*. 2001;104:1101–1107
29. Kim RJ, Wu E, Rafael A, et al The use of contrast-enhanced magnetic resonance imaging to identify reversible myocardial dysfunction. *N Engl J Med*. 2000;343:1445–1453
30. Bello D, Shah DJ, Farah GM, et al Gadolinium cardiovascular magnetic resonance predicts reversible myocardial dysfunction and remodeling in patients with heart failure undergoing beta-blocker therapy. *Circulation*. 2003;108:1945–1953
31. Bello D, Fieno DS, Kim RJ, et al Infarct morphology identifies patients with substrate for sustained ventricular tachycardia. *J Am Coll Cardiol*. 2005;45:1104–1108
32. Kwong RY, Chan AK, Brown KA, et al Impact of unrecognized myocardial scar detected by cardiac magnetic resonance imaging on event-free survival in patients presenting with signs or symptoms of coronary artery disease. *Circulation*. 2006;113:2733–2743
33. Kneusel PR, Nanz D, Wyss C, et al Characterization of dysfunctional myocardium by positron emission tomography and magnetic resonance: relation to functional outcome after revascularization. *Circulation*. 2003;108:1095–1100
34. Wagner A, Marholdt H, Thomson L, et al Effects of time, dose, and inversion time for acute myocardial infarct size measurements based on magnetic resonance imaging-delayed contrast enhancement. *J Am Coll Cardiol*. 2006;47:2027–2033
35. Kellmann P, Arai AE, McVeigh ER, et al Phase-sensitive inversion recovery for detecting myocardial infarction using gadolinium-delayed hyperenhancement. *Magn Reson Med*. 2002;47:372–383
36. Bondarenko O, Beek AM, Nijveldt R, et al Functional outcome after revascularization in patients with chronic ischemic heart disease: a quantitative late gadolinium enhancement CMR study evaluating transmural scar extent, wall thickness and periprocedural necrosis. *J Cardiovasc Magn Reson*. 2007;9:815–821
37. Neubauer S, Krahe T, Schindler R, et al 31P magnetic-resonance spectroscopy in dilated cardiomyopathy and coronary artery disease. Altered cardiac high-energy phosphate metabolism in heart failure. *Circulation*. 1992;86:1810–1818
38. Kaandorp TAM, Lamb HJ, van der Wall EE, et al Cardiovascular MR to access myocardial viability in chronic ischaemic LV dysfunction. *Heart*. 2005;91:1359–1365

Chapter 19

IMAGING CARDIAC INNERVATION

Albert Flotats and Ignasi Carrió

CONTENTS

J. L. Zamorano et al. (eds.), *The ESC Textbook of Cardiovascular Imaging*
DOI: 10.1007/978-1-84882-421-8_19, © Springer-Verlag London Limited 2010

Introduction

Increasing data support the use of cardiac innervation imaging to risk-stratify patients with heart failure. Cardiac sympathetic imaging can help to improve the understanding of the pathophysiology of heart failure and how sympathetic hyperactivity exerts its deleterious actions, which may result in better therapy and outcome for patients with heart failure. Assessment of cardiac sympathetic activity would also contribute to more appropriate use of ICD, and may help predict and prevent further lethal cardiac episodes.

The heart, like most internal organs, is innervated by the autonomic nervous system (ANS) in a highly integrated circuitry at multiple levels. The ANS provides innervation through fibers originating from the autonomic ganglia located outside the central nervous system (CNS) in response to the preganglionic cholinergic stimulation from the CNS. The ANS has great influence on cardiovascular physiology by controlling the cardiac performance (contractility, conduction, and heart rate) to respond quickly and effectively to the changing demands on cardiovascular performance.

The ANS is divided into two efferent components, the sympathetic system (adrenergic or cervicothoracic, SNS) and the parasympathetic system (cholinergic or craniosacral, PNS). The main differences between the SNS and PNS are summarized in Table 19.1.

The SNS is dominant in the heart, principally in the ventricles, where the PNS is scarce. Sympathetic fibers travel along the vascular structures, penetrating into the myocardium from the epicardium towards the endocardium. There is a gradient distribution of nerve terminals from the base to the apex of the left ventricle (LV). Parasympathetic fibers are distributed throughout the atrial and ventricular walls, with a gradient from the former to the latter, where they predominate in the inferior wall.

Neurotransmitters are synthesized, stored, and metabolized within the nerve terminal. Upon neurostimulation, neurotransmitters are released by exocytosis within the synaptic cleft. Only a small portion of the released neurotransmitter is actually available to interact with the post-synaptic receptors in the myocardial cell, leading to the cellular response.

Most of the released norepinephrine (NE), the neurotransmitter of the SNS, undergoes re-uptake in the presynaptic neurons by the NE transporter (NET), a saturable and sodium energy and temperature-dependent transport protein, which is cocaine- and desipramine-sensitive, with high affinity to catecholamines and catecholamine analogs, in a process known as uptake-1. In addition, there is NE uptake by a second, corticosterone- and clonidine-sensitive, low-affinity, high-capacity, extra-neuronal transport system, known as uptake-2. Uptake-1 predominates at low concentrations of catecholamines, whereas uptake-2 predominates at higher concentrations, but its contribution in humans is low.

Once NE is again inside the nerve terminal, it is either metabolized by monoamine oxidase (MAO) or stored in the vesicles by the vesicular monoamine transporter (VMAT), a proton-dependent transport protein localized in the vesicle membrane. Neuronal uptake-1 regulates the concentration of

Table 19.1. Main differences between sympathetic and para-sympathetic nervous systems

	Sympathetic nervous system	Para-sympathetic nervous system
Principal neurotransmitter released by post-ganglionic fibers	Norepinephrine	Acetylcholine
Location of the ganglia	Near the spinal cord, either paravertebral (22 pairs) or prevertebral (unpaired)	Near or within the end innervated organs
Degree of divergence and convergence of pre-ganglionic input to post-ganglionic neurons	Considerable	Very little
Post-synaptic receptors	Adrenoreceptors (predomination of β1 in heart)	Muscarinic
Second messenger mechanism of cellular response	Interaction with guanosine triphosphate-associated stimulatory proteins (Gs proteins), leading to stimulation of adenyl cyclase or phospholipase C, resulting in increases in cAMP and calcium levels, which in turn result in activation of different protein kinases. The resultant protein phosphorylation modifies the activity of enzymes and the function of other cellular proteins.	Interaction with G inhibitory proteins (Gi proteins), leading to inhibition of adenylate cyclase or phospholipase C, resulting in decreases in cAMP and calcium levels, which in turn result in inactivation of different protein kinases, with no protein phosphorylation and no modification of the activity of enzymes and other cellular proteins.
Functional role	Stimulatory	Inhibitory

the adrenergic neurotransmitters in the synaptic cleft, playing important physiologic and pathophysiologic roles in modifying the signal transduction and extra-neuronal catecholamine concentration. It is of paramount importance in protecting the heart from the deleterious effects of elevated levels of circulating catecholamines.

On the other hand, most of the released acetylcholine (ACh), the neurotransmitter of the PNS, is degraded by acetylcholinesterase.

Cardiac neurotransmission imaging can be performed by positron emission tomography (PET) and single photon emission computed tomography (SPECT), because these are the only imaging techniques with sufficient sensitivity to assess processes that take place at picomolar concentrations in the human heart.[1–3]

Radiopharmaceuticals for Cardiac Neurotransmission Assessment

Tracers for radionuclide imaging of cardiac neurotransmission have been developed by radiolabelling of true neurotransmitters or their structural analogs (false neurotransmitters). Radiolabelled true neurotransmitters follow the entire metabolic pathways, whereas radiolabelled analogues often are resistant to specific steps of metabolism. Binding characteristics, selectivity, and binding reversibility determine the suitability of a given agent. Furthermore, radiochemical purity and specific activity required to minimize occupation of binding sites by non-labelled molecules, as well as the pharmacologic effects in patients, have to be defined in the process of validation of neurotransmission by radiopharmaceuticals for in vivo imaging.

Of the many radiopharmaceuticals that have been designed and tested to assess cardiac neurotransmission, the most commonly used are, at a pre-synaptic level, ^{18}F-fluorodopamine, to assess NE synthesis; and ^{11}C-hydroxyephedrine (^{11}C-HED), ^{11}C-ephedrine, and ^{123}I-metaiodobenzylguanidine (^{123}I-MIBG), to assess pre-synaptic re-uptake and storage. At a post-synaptic level, β-blockers such as ^{11}C-CGP12177 and ^{11}C-CGP12388 are available to assess β-adrenoceptor expression and density. All except ^{123}I-MIBG are PET tracers.[1, 3]

Tracers of Sympathetic Pre-synaptic Neuronal Function

Before the administration of these tracers, it is necessary to withdraw drugs known to interfere with the neuronal uptake-1, amine vesicular uptake and storage, and cellular calcium handling (tricyclic anti-depressants, cocaine, labetalol, reserpine, tetrabenacine, NE, serotonin, guanethidine, sympathicomimetic amines, and calcium antagonists), taking into account their respective blood half-lives.

^{18}F-6-Fluorodopamine

^{18}F-6-Fluorodopamine is taken up mainly via the pre-synaptic uptake-1 in the sympathetic nerve terminals, and transported into axoplasmic vesicles where it is converted into ^{18}F-fluoroNE and stored. During sympathetic stimulation, ^{18}F-fluoroNE is released from the sympathetic nerve terminals similar to ^{3}H-NE. Because of the half-life of 110 min for ^{18}F, tracer clearance from the heart can be surveyed over a longer period of time than with ^{11}C-labelled tracers (half-life of 20 min). ^{18}F-6-Fluorodopamine has been proposed as a tracer of cardiac sympathetic innervation and function because it permits measurement of tracer uptake and clearance, but its application remains limited because of complex synthesis at often low specific activity, as well as difficulties in modelling of its complex metabolic fate.[1, 3, 4]

^{11}C-HED

^{11}C-HED, the most frequently used PET tracer for the mapping of sympathetic neurons, is a false neurotransmitter that has the same neuronal uptake mechanism as NE (neuronal uptake-1), but is resistant to enzymatic metabolism. Additionally, the storage and release properties of ^{11}C-HED seem to differ from those of NE. Non-specific myocardial uptake of ^{11}C-HED is low. Although some vesicular storage seems to occur, binding inside the vesicles is reduced because of a higher lipophilicity of ^{11}C-HED when compared with NE. ^{11}C-HED is believed to undergo continuous release and re-uptake by the sympathetic neurons.[1, 3, 4]

^{11}C-Epinephrine

^{11}C-epinephrine may be a more physiologic tracer for the evaluation of pre-synaptic sympathetic nerve function regarding the uptake mechanism, vesicular storage, and metabolism. ^{11}C-epinephrine is rapidly transported into the pre-synaptic nerve terminal through uptake-1 and is stored in the vesicles similar to NE. Although ^{11}C-epinephrine is vulnerable to MAO degradation, efficient vesicular intra-neuronal storage causes very slow clearance of radioactivity from the heart. ^{11}C-epinephrine shows high myocardial retention and may be more sensitive to neuronal abnormalities as a result of more physiologic behaviour.[1, 3, 4]

^{123}I-MIBG

MIBG is an iodinated aromatic analogue of the hypotensive false neurotransmitter guanethidine, which, in its turn, is an artefacts of NE. MIBG and NE have similar molecular structures, and both utilize the same uptake, storage, and release mechanisms in the sympathetic nerve endings; however, MIBG is neither metabolized nor interacts with the post-synaptic receptors. Therefore, the labelling of MIBG with ^{123}I enables in vivo scintigraphic visualization of the sympathetic post-ganglionic presynaptic fibers, thus allowing the assessment of both anatomic integrity and function of the nerve terminals.[1, 2]

Tracers of Post-synaptic Adrenergic Receptors

The synthesis of receptor ligands for cardiac imaging is challenging because it requires ligands capable of being radiolabelled easily and reproducibly, with high selectivity and affinity, low lipophilicity (to avoid binding to inactive internalized receptors), high metabolic stability, low toxicity, and high-specific and low-non-specific binding. ^{11}C-[4-(3-*t*-butylamino-2-hydroxypropoxy)-benzimidazol-1](^{11}C-CGP12177) is a non-selective, hydrophilic β-receptor antagonist of difficult synthesis and the only adrenoreceptor tracer used in clinical studies. Recently, ^{11}C-CGP12388, another non-selective β-adrenoceptor antagonist of easier synthesis, has shown promise in isolated perfused rat hearts and also in human beings, but the strength of its application will need to be demonstrated in further clinical studies.[3]

A number of other subtype-specific or non-specific tracers for adrenergic receptors have been developed, but most of them have shown inappropriateness for clinical imaging mainly because of high-non-specific binding or lipophilicity.[3]

Tracers of Parasympathetic Innervation

Few tracers of the PNS are available. Imaging of presynaptic neurons is problematic because the density of cholinergic neurons within the ventricular myocardium is low, the mechanisms of parasympathetic neurotransmitter uptake and storage are highly specific for ACh, and cholinergic substances are rapidly degraded. ^{18}F-fluoroethoxybenzovesamicol, a tracer derived from vesamicol (which specifically binds to the receptors on parasympathetic neuronal vesicles and inhibits storage of ACh) has shown low-specific binding, consistent with low parasympathetic neuronal density, and high-non-specific binding and wash-out in isolated perfused rat hearts. Considerable flow dependency of uptake has further limited its usefulness.[3]

Post-synaptic parasympathetic muscarinic receptors were the first myocardial receptors targeted with PET. ^{11}C-methylquinuclidinyl benzilate (^{11}C-MQNB) is a highly specific hydrophilic antagonist of muscarinic receptors, with no metabolization, but with few studies performed in human beings.[3]

Imaging Techniques

Planar and SPECT Imaging with ^{123}I-MIBG

Usually, ^{123}I-MIBG (185–370 MBq) is IV administered 30 min after thyroid blockade by oral administration of 500 mg potassium perchlorate, though this could be avoided considering that ^{123}I is a gamma emitter with a short half-life (13 h). Planar and SPECT images of the thorax are acquired 15 min (early image) and 4 h (late image) after injection, using a low-energy high-resolution parallel hole collimator. A 20% window is usually used, centred over the 159 keV ^{123}I photopeak. Planar images are acquired for 10 min in the anterior and 45° left anterior oblique views and stored in 128 × 128 or 256 × 256 matrixes. SPECT images are acquired by a single pass of 60 steps at 30 s per step (64 × 64 matrix), starting at 45° right anterior oblique projection and proceeding anticlockwise to the 45° left posterior oblique projection. The data are reconstructed in short axis, horizontal long axis, and vertical long axis tomograms, and scatter or attenuation correction may be applied.

^{123}I-MIBG uptake is semi-quantified by calculating a heart-to-mediastinum ratio (HMR), after drawing ROIs over the heart (including or not including the cavity) and the upper mediastinum (avoiding the thyroid gland) in the planar anterior view. The average count per pixel in the myocardium is divided by the average count per pixel in the mediastinum. The myocardial wash-out rate (WR), from initial to late images, is also calculated and expressed in percentage as the rate of decrease in the myocardial counts over time between early and late imaging (normalized to mediastinal activity) (Fig. 19.1). The late HMR reflects the relative distribution of the sympathetic nerve terminals, offering the global information about neuronal function resulting from uptake, storage, and release. The WR reflects the neuronal integrity or sympathetic tone, mainly representing the uptake-1. More studies are needed to establish the differences in early HMR, late HMR, and WR. Intra-observer and inter-observer variability of these calculations are <5%. Normal values for late HMR and WR are ≥2.5 ± 0.3 and ≤20% ± 10, respectively, but vary related to age (inversely to the late HMR; directly to the WR).

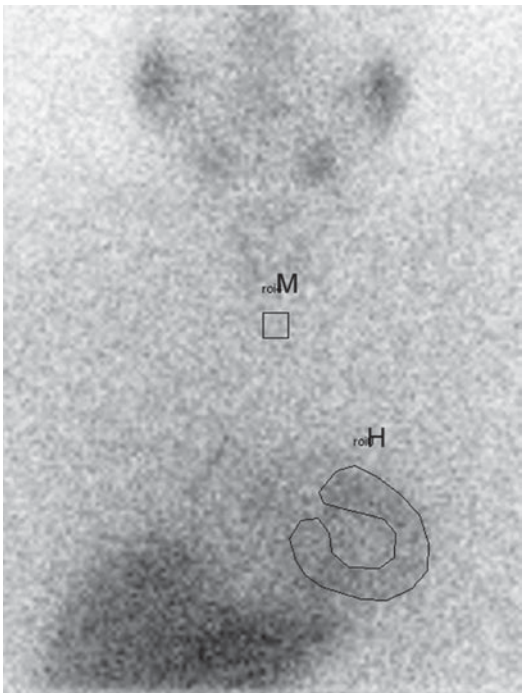

$$\bullet \text{HMR} = \frac{\{H\}}{\{M\}}$$

$$\bullet \text{WR} = \frac{\{H\}_e - (\{H\}_l \times 1.21^*)}{\{H\}_e} \times 100$$

$$\bullet \text{WR}_{\text{BKG corrected}} = \frac{(\{H\}_e - \{M\}_e) - ((\{H\}_l - \{M\}_l) \times 1.21^*)}{(\{H\}_e - \{M\}_e)} \times 100$$

{}= mean counts per pixel
*=^{123}I decay correction for 3 hr and 45 min (1÷0.8213)

Fig. 19.1 Semi-quantification of ^{123}I-MIBG activity on the planar anterior view. Heart-to-mediastinum ratio (HMR) and myocardial wash-out rate (WR) are calculated after drawing an ROI over the heart (H) and the upper mediastinum (M) in the early and late images

Moreover, these parameters fluctuate significantly owing to the lack of validation and standardization of acquisition parameters such as acquisition duration and type of collimation used (in relation to the additional photo peak of ^{123}I at 529 keV, capable of septal penetration when using the common low-energy collimators). Improved standardization of cardiac ^{123}I-MIBG imaging parameters would contribute to increased clinical applicability of this procedure.

SPECT images can be scored using a point scale for visual evaluation of ^{123}I-MIBG concentration in the given cardiac segments, comparable with the myocardial perfusion imaging scoring approach. Careful interpretation should be performed, with the knowledge of normal variants and potential artefacts. Normal cardiac ^{123}I-MIBG distribution includes a relatively low uptake in the inferior wall, which is more pronounced in the elderly. In addition, there may be substantial ^{123}I-MIBG uptake in the liver, which overlaps the inferior LV wall. Moreover, scattering from the lung field to the lateral LV wall may also occur. Polar maps can be generated from SPECT data and can be compared with those of normal individuals. Scores of the extension and severity of ^{123}I-MIBG eventual defects and calculation of the mean global and regional WR of the LV are feasible. However, it has to be taken into account that in some pathophysiologic conditions, cardiac ^{123}I-MIBG uptake may be severely reduced, hampering the acquisition and processing of the tomographic slices.[2]

PET Imaging

PET imaging protocols vary according to the radiotracer characteristics and the available instrumentation. Typically, PET imaging of cardiac neurotransmission uses dynamic imaging and is technically more demanding than SPECT imaging with ^{123}I-MIBG.

The obtained volumetric datasets are realigned according to standardized axes. Physiologic parameters such as quantification of neurotransmitter synthesis and transport can be assessed by applying tracer kinetic modelling to quantitative datasets. Typically, pre-synaptic NE re-uptake function is assessed by the calculation of the distribution volume of tracers using compartment models and non-linear regression analysis, to calculate influx and efflux rate constants. Myocardial adrenoceptor density (Bmax) can be measured by the injection of different amounts of radioactivity and cold substance, assessment of input function and estimation of metabolites, and graphic analysis.

Region-of-interest analysis of the activity concentration inside the LV cavity yields the time-activity curve of arterial blood, and allows assessment of the arterial input function.

Continuous thoracic PET scanning is performed for up to 3 h after ^{18}F-fluorodopamine infusion. The total scanning time is divided into intervals of 5–30 min, and the tomographic results of each interval are assessed. Scan sequences may consist of 5 frames × 1 min, 5 frames × 5 min, 4 frames × 15 min, and 3 frames × 30 min. Cardiac ^{18}F-fluorodopamine images can be analyzed by drawing regions of interest within the ventricular wall using a composite of the images for each plane. In computing time-activity curves, the logs of the concentrations of radioactivity, adjusted for the dose per kilogram of body weight, in the LV and arterial blood, can be expressed as a function of time after injection of the radiotracer. The specific activity of ^{18}F-fluorodopamine at the time of injection and the assayed plasma concentrations of ^{18}F-fluorodopamine can be used to estimate the proportions of the total plasma radioactivity that are owing to ^{18}F-fluorodopamine and its metabolites. Exponential curve fitting may be used to describe the relationships between time and radioactivity concentrations in myocardium, blood, and plasma. The differences between

the estimated and empiric values can be assessed graphically. The reported mean concentration of ^{18}F-fluorodopamine in the LV peaks at 5–8 min after infusion, and has been found to be 10.2 ± 67 nCi × kg/mL × mCi in healthy volunteers.

PET scanning of ^{11}C-HED and ^{11}C-epinephrine usually lasts for 60 min. Scan sequences may consist of 15 frames: 6 × 30 s, 2 × 60 s, 2 × 150 s, 2 × 300 s, 2 × 600 s, and 1 × 1,200 s. After correction for the contribution of ^{11}C-labelled metabolites, the calculated fraction of the intact tracers can be plotted as a function of time. The corrected blood time-activity curve is used as the arterial input function for the calculation of myocardial retention of tracers in absolute terms. The retention fraction (L/min) can be calculated for each region by dividing the tissue ^{11}C concentration at 60 min by the integral of the radiotracer concentration in the arterial blood from the time of injection to the end of the last scan: retention = $Ct(T_1{:}T_2)/\int^{T2}C_b(t)dt$, where $Ct(T_1{:}T_2)$ is the tissue activity in the image frame between T_1 and T_2 (MBq/mL tissue), and C_b is the blood activity (MBq/mL blood) integrated from time = 0 to time = T_2. Cardiac images can be analyzed by volumetric sampling procedures to generate time-activity curves and polar maps, to assess the homogeneity of myocardial tracer distribution. Volume distribution for ^{11}C-HED in healthy volunteers has been reported to be 71 ± 19 mL/g of tissue. Myocardial retention fractions of ^{11}C-HED and ^{11}C-epinephrine in healthy volunteers at 5 min after injection have been reported to be 0.24 ± 0.02 and 0.29 ± 0.02, respectively. In contrast to SPECT imaging with ^{123}I-MIBG, where lower uptake in the inferior LV wall has been observed, distribution of ^{11}C-HED throughout the LV myocardium in healthy normal individuals is regionally homogeneous with high uptake in all myocardial segment.

With ^{11}C-CGP, continuous thoracic scanning, recording data in the list mode is typically performed for 1 h after infusion. To quantitatively assess the concentration of the receptor sites, mathematic models need to be used. The model parameters, including the receptor concentration and the kinetic rate constants, can be derived from experimental data using a kinetic or graphical method. The kinetic method is based on a fitting procedure and needs to measure the input function, which is hampered by the presence of metabolites. Furthermore, the kinetic method needs to maintain a balance between the respective complexities of the model structure and the experimental protocol, and is more complex than the graphical method, which circumvents issues related to metabolites. The graphical method requires a dual-injection protocol with doses of high- and low-specific activity, and does not require measurement of the input function. With this approach, values of Bmax have been reported to be 10 ± 3 pmol/g of tissue in healthy volunteers, with a dissociation constant of 0.014 ± 0.002/min.

LV muscarinic receptors can be quantified after PET imaging with a mathematic model that allows for the quantification of receptor concentration, association, and dissociation constants. The model is based on a multi-injection protocol of labelled and unlabelled MQNB. The input function can be derived from a region of interest drawn within the LV cavity. Time-activity curves can be generated for different LV regions after correction for decay and expressed as pmol/mL after dividing by specific radioactivity at time 0. After compartmental modelling, the Bmax values reported in healthy volunteers were 25 ± 7.7 pmol/L, with a dissociation constant of 2.2 ± 1 pmol/mL without significant differences in the septal, anterior, and lateral regions of the LV.[1]

Radionuclide Imaging of Sympathetic Cardiac Innervation in Heart Failure

Pathophysiology

HF is a complex clinical syndrome characterized by dyspnoea, fatigue, and fluid retention, which results from any structural or functional cardiac disorder that impairs the ability of the LV to fill with or eject blood. It is a common, costly, disabling, and potentially fatal disorder. The prevalence and incidence of HF are increasing rapidly in the Western world because of the aging population and an ever-increasing number of survivals to acute coronary syndromes (CAD is the most prevalent underlying aetiology, affecting about 70% of cases), despite the advances in different pharmacological and non-pharmacological therapies.

The development of HF initiates with some injury to, or stress on, the myocardium, which usually produces progressive changes in the geometry and structure of the LV, with pathologic hypertrophic growth. This pathologic re-modelling involves a shift towards glycolytic metabolism, disorganization of the sarcomere, alterations in calcium handling, changes in contractility, loss of myocytes with fibrotic replacement, LV dilatation, systolic or diastolic dysfunction, and electrical re-modelling (i.e. alterations in the expression or function of ion-transporting proteins, or both), with propensity to malignant ventricular arrhythmia.

Patients with HF have elevated circulating or tissue levels of NE, angiotensin II, aldosterone, endothelin, vasopressin, and cytokines. Initially, after the onset of HF, enhanced SNS activity is responsible for the increase in heart rate, contractility, venous return, and systemic arterial constriction, thus supporting the cardiovascular system to preserve organ perfusion. However, chronic activation of endogenous neurohormonal systems has deleterious effects on the cardiovascular system. Activation of the renin-angiotensin system not only increases haemodynamic stresses and energetic requirements

of the LV by causing sodium retention and peripheral vasoconstriction, but may also exert direct noxious effects on cardiomyocytes (apoptosis and regression to a fetal phenotype) and changes in the nature of the extracellular matrix (stimulation of myocardial fibrosis), which can further alter the architecture and impair the performance of the failing heart.

The hyperadrenergic state in HF results in the down-regulation and uncoupling of cardiac β-adrenergic receptors, which contributes to progressive impairment of LV systolic function, by altering the post-synaptic signal transduction.[5]

Detrimental effects of prolonged sympathetic hyperactivity in chronic HF are confirmed by the beneficial effects of treatment with angiotensin converting enzyme inhibitors (ACEIs) and β-adrenoceptor antagonists. Accordingly, reduction in the sympathetic nervous activity is an important target for drug treatment of HF. Furthermore, in HF, the increased sympathetic tone is directly linked to disease progression, prognosis, and risk of sudden cardiac death (SCD). Therefore, non-invasive strategies to determine the state of cardiac autonomic regulation are of significant interest.

In HF patients, global sympathetic denervation has been demonstrated with ^{11}C-HED PET. The reduction in cardiac ^{11}C-HED uptake is associated with reduced LV function, indicating a link between altered innervation and LV function.[3] In vivo studies using ^{11}C-CGP12177 PET confirmed the down-regulation of β-receptors that have been observed to be associated with decreased contractile responsiveness to dobutamine, indicating the relationship between changes in the receptor number and its biological function.[6] Muscarinic receptor density, measured by PET and ^{11}C-MQNB, was found to be up-regulated as a potential adaptive mechanism.[7]

Consistent with PET studies with ^{11}C-HED, planar and/or SPECT studies with ^{123}I-MIBG show reduced ^{123}I-MIBG activity in the myocardium (low HMR and high WR) in patients with HF (Fig. 19.2). Reduced tracer uptake is more extensive in patients with HF than in patients with ischaemic heart disease in whom reduced uptake is mainly localized in ischaemic or infarcted myocardial segments as a result of direct neuronal ischaemic damage. In patients with HF, reduced tracer uptake can result from either a reduced uptake-1 of ^{11}C-HED/^{123}I-MIBG/catecholamines and/or an increased release of ^{11}C-HED/^{123}I-MIBG/catecholamines into the synaptic cleft. All mechanisms would lead to an enhanced catecholamine concentration in the synaptic cleft

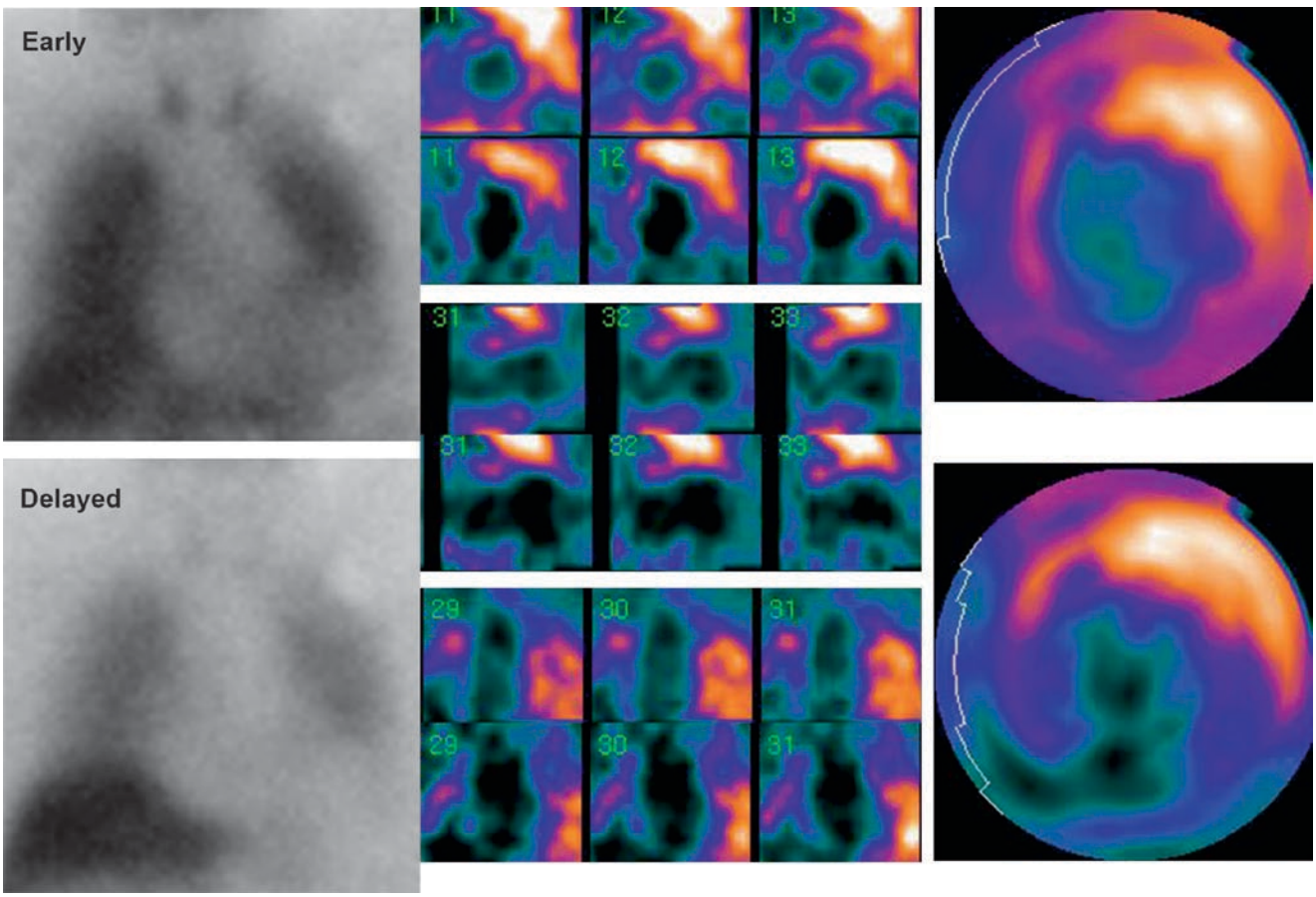

Fig. 19.2 ^{123}I-MIBG planar and SPECT studies of a patient with ischaemic dilated heart disease and LVEF of 20%. Heart-to-mediastinum ratios: early 1.25, late 1.15; wash-out rate 30%. SPECT images correspond to early and late standardized axes slices with respective polar maps

with subsequent downregulation of the post-synaptic β-adrenoceptor density. This pathophysiological condition may predispose to abnormal conduction and dispersion of refractoriness, which may trigger and maintain ventricular arrhythmias. In particular, the association of decreased ^{123}I-MIBG activity with normal myocardial perfusion is common in many different arrhythmogenic cardiac diseases, and suggests that ^{123}I-MIBG imaging, together with myocardial perfusion, may also serve as an indicator of increased individual risk of future arrhythmic events.[8]

Assessment of Prognosis

In HF, the prognostic value of ^{123}I-MIBG imaging is supported by numerous studies. Merlet et al.[9] evaluated 90 patients with ischaemic and non-ischaemic HF; these patients underwent ^{123}I-MIBG imaging in addition to routine care, including echocardiography and radionuclide LVEF assessment. During a follow-up period of a maximum of 27 months, ten patients underwent cardiac transplantation and 22 died. Among all clinical and imaging variables, cardiac ^{123}I-MIBG activity, using a threshold value to identify reduced ^{123}I-MIBG uptake, was the only predictor of event-free survival. The same group[10] subsequently evaluated 112 patients with HF and dilated cardiomyopathy (NYHA class II-IV, LVEF <40%, LV end-diastolic diameter 70 ± 8 mm, and pulmonary capillary wedge pressure 19 ± 8 mmHg). Among all the variables, only cardiac ^{123}I-MIBG activity and the LVEF were predictive for long-term survival. Cohen-Solal et al.[11] evaluated 93 HF patients with ^{123}I-MIBG imaging and demonstrated that the reduction in cardiac ^{123}I-MIBG uptake was related to LVEF, cardiac index, pulmonary wedge pressure, and peak oxygen uptake. Reduced ^{123}I-MIBG uptake and peak oxygen uptake were predictive of death or cardiac transplantation over subsequent follow-up. Nakata et al.[12] evaluated 414 patients with ^{123}I-MIBG imaging, with 173 having symptomatic HF. Over a mean follow-up of 22 months, 37 cardiac deaths occurred. Five main predictors of death were identified including cardiac ^{123}I-MIBG activity, LVEF, NYHA class III or IV, age >60 year, and a history of myocardial infarction. Wakabayashi et al.[13] compared the prognostic value of cardiac ^{123}I-MIBG imaging in patients with ischaemic (n = 76) and non-ischaemic cardiomyopathy (n = 56). Over a maximum period of 55 months, 69 cardiac deaths occurred. Both in the patients with ischaemic and non-ischaemic cardiomyopathy, cardiac ^{123}I-MIBG activity was the strongest predictor of survival.

Not only does the assessment of cardiac ^{123}I-MIBG uptake brings prognostic information, the evaluation of the early and late uptake after injection and calculated WR from the myocardium may also be helpful. Ogita et al.[14] evaluated 79 HF patients with LVEF <40% with ^{123}I-MIBG imaging, and found that the ^{123}I-MIBG WR from the myocardium was a strong predictor of survival. Yamada et al.[15] also observed that the ^{123}I-MIBG WR was the strongest predictor of survival in 65 HF patients with LVEF <40%, followed by a mean period of 34 months. Anastasiou-Nana et al.[16] evaluated 52 HF patients with LVEF <40%, and observed that the early ^{123}I-MIBG HMR was the best predictor for long-term (2 years) outcome. Wakabayashi et al.[21] demonstrated in 132 patients that the late ^{123}I-MIBG HMR provided superior prognostic information over the early HMR and the subsequent ^{123}I-MIBG WR. Kioka et al.[17] recently reported the prognostic value of ^{123}I-MIBG imaging for predicting SCD in 97 patients with chronic HF. In patients with abnormal WR (≥27%), SCD was significantly more frequently observed than in the group with normal WR. Moreover, multi-variate analysis showed that WR was the only independent predictor of SCD. A recent meta-analysis performed by Verbene et al.[18] on 18 studies with a total of 1,755 patients has shown that patients with HF and decreased cardiac ^{123}I-MIBG uptake or increased WR have a worse prognosis when compared with patients with normal ^{123}I-MIBG parameters.

Larger studies have been providing standardization of cardiac ^{123}I-MIBG data acquisition and analysis. Agostini et al.[19] recently reported the results of a recent retrospective study on 290 HF patients (121 ischaemic and 169 non-ischaemic cardiomyopathy, NYHA class II-IV, 262 patients with LVEF <50%, obtained in six European centres) who underwent cardiac ^{123}I-MIBG imaging, and were analyzed in a core laboratory. Blind review and prospective quantitative re-analysis of the late HMR with follow-up data for 2 years permitted the identification of potential late HMR threshold values for defining groups with high and very low likelihood of major cardiac events. A total of 67 patients (23% of the population) experienced an event, including 18 cardiac deaths, 44 cardiac transplantations, and 5 potentially lethal ventricular arrhythmias. The mean HMR was significantly different between patients with and without events (1.51 vs. 1.97). Based on receiver operating characteristic (ROC) curve analysis, a threshold value for MHR of 1.75 yielded a sensitivity of 84% with a specificity of 60% to predict events. Based on this threshold value, the 2-year event-free survival was 62% for late HMR <1.75, vs. 95% for late HMR ≥1.75 ($p < 0.001$). Logistic regression showed late HMR and LVEF as the only significant predictors of major cardiac events. When the late HMR were divided into quartiles, the 2-year event-free survival rates in the lowest quartile (1.45) and the highest quartile (2.17) were 52% and 98%, respectively. These data further support the use of cardiac ^{123}I-MIBG imaging for prognostic purposes in HF patients.

Similar to ^{123}I-MIBG imaging, a prognostic value has been suggested for quantitative ^{11}C-HED PET imaging in HF.

Pietila et al.[20] found that reduced global ^{11}C-HED retention was an independent predictor of adverse outcome in 46 NYHA class II-III HF patients. Over a mean follow-up period of 55 months, 11 cardiac deaths occurred and two patients underwent heart transplantation. Multi-variate analysis demonstrated that peak oxygen uptake, LV end-diastolic volume, and ^{11}C-HED retention were the only predictors of outcome.

Assessment of Treatment

Cardiac innervation imaging can be used to monitor therapeutic effects of medical treatment in patients with HF. Recently, Kasama et al.[21], taking into account that ^{123}I-MIBG imaging improves by the current medical treatment for HF, analyzed the usefulness of serial ^{123}I-MIBG studies for prognostication in 208 patients with stabilized mild-to-moderate HF and LVEF <45%, of both ischaemic and non-ischaemic origin. ^{123}I-MIBG and echocardiographic studies were performed once patients were stabilized and after 6 months of treatment, which included ACEIs, angiotensin receptor blockers, β-blockers, loop diuretics, and spironolactone. Treatment did no change during the follow-up period of 4.5 years. Fifty-six patients experienced fatal cardiac events (13 died from SCD). Clinical characteristics were similar in both non-cardiac death and cardiac death group, and only the use of β-blockers was significantly higher in the non-cardiac death group. The variation in the WR between the sequential ^{123}I-MIBG (Δ-WR) was the only independent predictor of cardiac death. The Δ-WR was significantly lower in the non-cardiac death group (< - 5%) than that in the cardiac death group (≥ - 5%). Moreover, this parameter was also useful for predicting SCD in patients with HF, indicating that serial ^{123}I-MIBG imaging is useful for predicting cardiac death and SCD in stabilized patients with HF.

In addition, the merits of ^{123}I-MIBG in predicting the efficacy of β-blockers and ACEIs have been studied by Nakata et al.[22], who compared 88 HF patients treated with β-blockers and ACEIs, with 79 HF patients treated conventionally without β-blockers and ACEIs during a follow-up of 43 months, with cardiac death as the primary endpoint. Forty-two cardiac deaths occurred. The prevalence of cardiac death was significantly lower in patients treated with β-blockers and/or ACEIs when compared with the control group (15% vs. 37%, p= 0.002). After the patients were divided into two groups by applying a threshold value of 1.53 for the late HMR (which was the median of the late HMR in patients with cardiac death), it was shown that treatment with β-blockers and/or ACEIs reduced the risk of death from 36% to 12% if the HMR was ≥1.53 (p< 0.05). If the HMR was <1.53, the risk of death was decreased from 53% to 37% (p <0.05). Survival in the patients treated with β-blockers and/or ACEIs remained dependent on the severity of impairment of cardiac ^{123}I-MIBG activity.

In recent years, cardiac resynchronization therapy (CRT) has become an option for patients with drug-refractory end-stage HF. Recently, it has been shown that CRT has a beneficial effect on cardiac sympathetic innervation as reflected by improved ^{123}I-MIBG uptake, which supports the value of ^{123}I-MIBG imaging in the assessment of the efficacy of CRT in patients with HF.[23]

ICD: Selection of Candidates

The efficacy of the ICD in reducing SCD incidence is supported by evidence from randomized trials of both primary and secondary prevention. Absolute mortality reduction achieved after ICD implantation was 5.6% in MADIT 2 at 5 years, and 7.2% in SCD-HeFT. However, ICD implantation is costly (the number of ICDs that need to be implanted to save one life is 18) and, in addition, can have negative effects on the quality of life. More recently, two different trials, the Coronary Artery Bypass Graft (CABG) Patch trial and Defibrillator in Acute Myocardial Infarction Trial (DINAMIT) trial, have produced neutral results and have generated interesting questions regarding the mechanisms of SCD and the role of the ICD in the primary prevention of SCD. The degree of impairment of LVEF is used as the main indication for the implantation of ICDs in patients post-myocardial infarction. However, LVEF is not an ideal risk-stratification test on which to base the prophylactic ICD therapy. Multiple factors interact with LVEF to influence the mortality of patients with similar degrees of LV dysfunction. Thus, attention has been focussed on the methods to identify patients at high and low risk of ventricular tachyarrhythmia to determine the benefit of ICD prophylaxis. New data are emerging to indicate the potential of cardiac sympathetic imaging for the selection of patients who are at greater risk for SCD and who could benefit most from ICD use. Bax et al.[24] have recently assessed the relationship between the abnormalities of ventricular sympathetic innervation delineated by ^{123}I-MIBG and inducible ventricular tachyarrhythmias in patients with LV dysfunction and previous myocardial infarction. In a multi-variable analysis, the 4 h ^{123}I-MIBG SPECT defect score was the only variable that showed a significant difference between patients with positive electrophysiological testing.

Nagahara et al.[25] recently investigated if alterations of cardiac autonomic innervation demonstrated with cardiac ^{123}I-MIBG imaging are related to lethal cardiac events, defined as an appropriate ICD shock against potentially fatal ventricular arrhythmias, and if sympathetic imaging in combination with conventional variables is useful for the selection of

patients who are at a higher risk for cardiac death and have the greatest need for ICD implantation. They prospectively followed 54 patients after ^{123}I-MIBG imaging, plasma concentration of brain natriuretic peptide (BNP), and LVEF measurements. The patients were divided into two groups based on the presence (n = 21) or absence (n = 33) of appropriate ICD discharge during a 15-month period. Patients with appropriate discharge had a significantly lower level of ^{123}I-MIBG activity and a higher plasma BNP level than those without such discharge. Univariate analysis revealed late ^{123}I-MIBG HMR, BNP level, and medication to be significant predictors. Multi-variate analysis showed late ^{123}I-MIBG HMR to be an independent predictor. ^{123}I-MIBG HMR <1.95 with a plasma BNP level >187 pg/mL or a LVEF <50% had significantly increased power to predict ICD shock. These data suggest that cardiac ^{123}I-MIBG imaging, in combination with plasma BNP concentration or cardiac function, can help in the identification of patients who are at greater risk of fatal arrhythmias and who would benefit most from an ICD.

Conclusions

In conclusion, a growing body of evidence supports the use of cardiac sympathetic innervation imaging to risk-stratify patients with HF, in particular, by using cardiac ^{123}I-MIBG imaging. Cardiac sympathetic imaging can help to improve the understanding of the mechanisms responsible for increased sympathetic activity in HF and how this hyperactivity exerts its deleterious actions, which may result in better therapy and outcome for patients with HF. Assessment of cardiac sympathetic activity would also contribute to more appropriate use of ICD implantation and may help to predict and prevent further lethal cardiac episodes.

References

1. Carrió I. Cardiac neurotransmission imaging. *J Nucl Med*. 2001;42:1062–1076
2. Flotats A, Carrió I. Cardiac neurotransmission SPECT imaging. *J Nucl Cardiol*. 2004;11:587–602
3. Bengel FM, Schwaiger M. Assessment of cardiac sympathetic neuronal function using PET imaging. *J Nucl Cardiol*. 2004; 11:603–616
4. Henneman MM, Bengel FM, van der Wall EE, et al Cardiac neuronal imaging: Application in the evaluation of cardiac disease. *J Nucl Cardiol*. 2008;15:442–455
5. Ungerer M, Bohm M, Elce J, et al Altered expression of beta–adrenergic receptor kinase and beta–adrenergic receptors in the failing human heart. *Circulation*. 1993;87:454–463
6. Merlet P, Delforge J, Syrota A, et al Positron emission tomography with 11C CGP–12177 to assess beta–adrenergic receptor concentration in idiopathic dilated cardiomyopathy. *Circulation*. 1993;87:1169–1178
7. Le Guludec D, Cohen–Solal A, Delforge J, et al Increased myocardial muscarinic receptor density in idiopathic dilated cardiomyopathy: an in vivo PET study. *Circulation*. 1997;96:3416–3422
8. Paul M, Schafers M, Kies P, et al Impact of sympathetic innervation on recurrent life–threatening arrhythmias in the follow–up of patients with idiopathic ventricular fibrillation. *Eur J Nucl Med Mol Imaging*. 2006;33:866–870
9. Merlet P, Valette H, Dubois–Rande JL, et al Prognostic value of cardiac metaiodobenzylguanidine imaging in patients with heart failure. *J Nucl Med*. 1992;33:471–477
10. Merlet P, Benvenuti C, Moyse D, et al Prognostic value of MIBG imaging in idiopathic dilated cardiomyopathy. *J Nucl Med*. 1999;40:917–923
11. Cohen–Solal A, Esanu Y, Logeart D, et al Cardiac metaiodobenzylguanidine uptake in patients with moderate chronic heart failure: relationship with peak oxygen uptake and prognosis. *J Am Coll Cardiol*. 1999;33:759–766
12. Nakata T, Miyamoto K, Doi A, et al Cardiac death prediction and impaired cardiac sympathetic innervation assessed by MIBG in patients with failing and nonfailing hearts. *J Nucl Cardiol*. 1998;5: 579–590
13. Wakabayashi T, Nakata T, Hashimoto A, et al Assessment of underlying etiology and cardiac sympathetic innervation to identify patients at high risk of cardiac events. *J Nucl Med*. 2001;42: 1757–1767
14. Ogita H, Shimonagata T, Fukunami M, et al Prognostic significance of cardiac ^{123}I metaiodobenzylguanidine imaging for mortality and morbidity in patients with chronic heart failure: a prospective study. *Heart*. 2001;86:656–660
15. Yamada T, Shimonagata T, Fukunami M, et al Comparison of the prognostic value of cardiac iodine–123 metaiodobenzylguanidine imaging and heart rate variability in patients with chronic heart failure: a prospective study. *J Am Coll Cardiol*. 2003;41:231–238
16. Anastasiou–Nana MI, Terrovitis JV, Athanasoulis T, et al Prognostic value of iodine–123–metaiodobenzylguanidine myocardial uptake and heart rate variability in chronic congestive heart failure secondary to ischemic or idiopathic dilated cardiomyopathy. *Am J Cardiol*. 2005;96:427–431
17. Kioka H, Yamada T, Mine T, et al Prediction of sudden death by using cardiac iodine–123 metaiodobenzylguanidine imaging in patients with mild to moderate chronic heart failure. *Heart*. 2007;93:1213–1218
18. Verberne HJ, Brewster LM, Somsen GA, et al Prognostic value of myocardial ^{123}I–metaiodobenzylguanidine (MIBG) parameters in patients with heart failure: a systematic review. *Eur Heart J*. 2008; 29:1147–1159
19. Agostini D, Verberne HJ, Burchert W, et al I–123–mIBG myocardial imaging for assessment of risk for a major cardiac event in heart failure patients: insights from a retrospective European multi–center study. *Eur J Nucl Med and Mol Imaging*. 2008;35:535–546
20. Pietila M, Malminiemi K, Ukkonen H, et al Reduced myocardial carbon–11 hydroxyephedrine retention is associated with poor prognosis in chronic heart failure. *Eur J Nucl Med*. 2001; 28:373–376
21. Kasama S, Toyama T, Sumino H, et al Prognostic value of serial cardiac ^{123}I–MIBG imaging in patients with stabilised chronic heart failure and reduced left ventricular ejection fraction. *J Nucl Med*. 2008;49:907–914
22. Nakata T, Wakabayashi T, Kyuma M, et al Cardiac metaiodobenzylguanidine activity can predict the long–term efficacy of

angiotensin–converting enzyme inhibitors and/or beta–adrenoceptor blockers in patients with heart failure. *Eur J Nucl Med Mol Imaging*. 2005;32:186–194

23. Gould PA, Kong G, Kalff V, et al Improvement in cardiac adrenergic function post biventricular pacing for heart failure. *Europace*. 2007;9:751–756
24. Bax JJ, Kraft OR, Buxton AE, et al^{123}I–mIBG Scintigraphy to predict inducibility of ventricular arrhythmias on cardiac electrophysiology testing: a prospective multicenter pilot study. *Circ Cardiovasc Imaging*. 2008;1:131–140
25. Nagahara D, Nakata T, Hashimoto A, et al Predicting the need for an implantable cardioverter defibrillator using cardiac metaiodobenzylguanidine activity together with plasma natriuretic peptide concentration or left ventricular function. *J Nucl Med*. 2008;49:225–233

Chapter 20

CARDIAC RESYNCHRONIZATION THERAPY: SELECTION OF CANDIDATES

Nico R. L. Van de Veire, Ernst E. van der Wall, and Jeroen J. Bax

CONTENTS

J. L. Zamorano et al. (eds.), *The ESC Textbook of Cardiovascular Imaging*
DOI: 10.1007/978-1-84882-421-8_20, © Springer-Verlag London Limited 2010

Introduction

Cardiac resynchronization therapy (CRT) is an established therapy for patients with advanced heart failure (HF), depressed left ventricular function, and wide QRS complex. A significant number of patients do not respond to CRT. Recent studies suggest that assessment of mechanical dyssynchrony may allow identification of potential CRT responders. In addition, the presence of scar tissue and venous anatomy may play a role in the selection of candidates. In this chapter the role of various cardiac imaging modalities addressing these issues in the selection of potential CRT candidates is discussed extensively.

Over the past decades, chronic HF has demonstrated an exponential increase, with a poor long-term outcome.[1] Despite the advances in pharmacological therapy, including ACE inhibitors, beta-blockers, and spironolactone, mortality remains high. After the first admission for HF, the 1-year survival is 63% and the 5-year survival is only 30%.[1–6] HF patients die either from progressive HF or sudden cardiac death.[7] In addition to the high mortality, morbidity is also substantial, with frequent re-hospitalizations for decompensated HF[3] and extensive co-morbidity.

Recently, non-pharmacological treatment options for end-stage HF patients have been explored, including exercise training, mitral valve surgery, surgical ventricular restoration, and device therapy.[8–10] More than a decade ago, atrial synchronized biventricular pacing or CRT has been introduced. In large randomized trials, CRT was associated with improved survival and reduced morbidity as compared to optimized medical therapy.[11–13] In the CARE-HF trial, 813 end-stage HF patients with depressed left ventricular ejection fraction (LVEF, ≤35%), NYHA class III–IV, and wide QRS complex were randomized to CRT or optimized medical therapy.[13] Significant reductions in HF deaths (10%) and re-hospitalizations for HF (52%) were observed in the CRT arm.

"Classic" Selection Criteria for CRT and the Role of Cardiac Imaging

Current European Society of Cardiology guidelines[14] recommend CRT in a well-defined subgroup of HF patients presented in Table 20.1. Biventricular pacing without ICD backup has a class I indication (level of evidence A), whereas patients who have a life expectancy >1 year have a class I indication (level of evidence B) for a biventricular pacemaker combined with an ICD.

Table 20.1. European Society of Cardiology criteria for cardiac resynchronization therapy

Symptomatic heart failure patients (NYHA classes III–IV) despite optimal medical treatment
Left ventricular ejection fraction ≤35%
Left ventricular dilatation, defined as:
Left ventricular end-diastolic diameter >55 mm
Left ventricular end-diastolic diameter >30 mm/m^2
Left ventricular end-diastolic diameter >30 mm/m (height)
Normal sinus rhythm
Wide QRS complex (≥120 ms)

Accordingly, adequate information on LVEF and/or LV dimensions is needed. LV internal diameters should be measured at the level of the mitral chordae using 2D or M-mode echocardiography.[15] For the echocardiographic assessment of LVEF, the biplane method of discs (Simpson's rule) is the currently recommended method of choice.[15] However, 2D approaches for the assessment of LV volumes (and EF) are based on geometric assumptions. To avoid this problem, several 3D echocardiographic techniques have been developed over the last decade. One possibility is the so-called tri-plane approach, in which apical 2-, 3-, and 4-chamber views are acquired during a single heart beat. With the use of end-systolic and end-diastolic still frames, and endocardial border tracings, a tri-plane method of discs algorithm is used to calculate LV volumes and EF (Fig. 20.1a). Alternatively, a true full 3D volume can be acquired, from which LV volumes and EF are derived (Fig. 20.1b). Accuracy and reproducibility of this approach can be further improved with intravenous contrast for LV endocardial border opacification (Fig. 20.1a).[16] Other non-invasive imaging modalities that can provide LV volumes and EF are gated single photon emission computed tomography (SPECT), magnetic resonance imaging (MRI), and multi-slice computed tomography (MSCT). The available gated SPECT processing software can measure the LV volumes and EF with high accuracy and reproducibility.[17] MRI is considered the gold standard for quantification of LV volumes and EF, with high accuracy and reproducibility in normal and dilated hearts.[18] MSCT can also reliably measure LV volumes and EF; due to the radiation and contrast burden, MSCT should currently not be used as a first-line imaging modality to assess LV volumes and EF.

The majority of the CRT trials used the "classic" selection criteria (Table 20.1), but resulted in 70% response rate to CRT.[19, 20] The non-response has been related to the lack of cardiac dyssynchrony, but also to the presence of extensive scar tissue in the left ventricle. In addition, venous anatomy

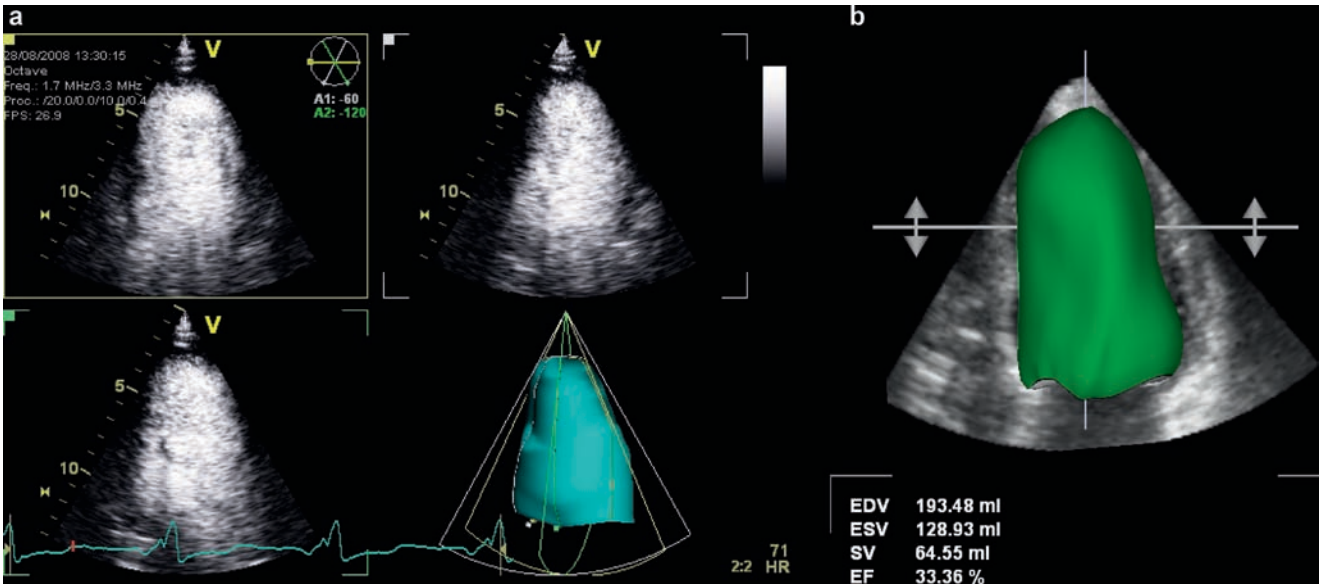

Fig. 20.1 **(a)** Using tri-plane imaging, apical 2-, 3-, and 4-chamber views are acquired during one single heartbeat. With the use of manual tracing of the endocardial borders at end-systole and end-diastole, LV volumes are generated using the tri-plane method of discs. Note that intravenous contrast was used in this particular patient to improve LV endocardial border opacification. **(b)** Example of a dilated LV generated from a full volume 3D data set; end-diastolic volume (EDV), end-systolic volume (ESV), stroke volume (SV) and ejection fraction (EF) are reported automatically

is important in response to CRT. These issues can be evaluated with different non-invasive imaging techniques.

Mechanical Dyssynchrony

Dyssynchronous activation of the heart is a common problem in HF patients and can be divided into three types (Table 20.2).

Atrio-ventricular dyssynchrony is the result of a prolonged atrio-ventricular conduction time. This delay reduces the diastolic filling period leading to suboptimal ventricular filling, which can be reversed by CRT.[21] In HF patients, delayed activation of the LV results in a timing difference between the activation of the left and right ventricle: inter-ventricular dyssynchrony. Finally, a notable portion of HF patients exhibit substantial dyssynchrony within the LV intra-ventricular dyssynchrony. All these forms of cardiac dyssynchrony affect LV haemodynamics and pumping efficiency.[22] Particularly LV dyssynchrony has been considered as an important component in the response to CRT.

Table 20.2. Types of mechanical dyssynchrony

Atrio-ventricular dyssynchrony
Inter-ventricular (LV vs. RV) dyssynchrony
Intra-ventricular (within LV) dyssynchrony

The presence of LV dyssynchrony has clear prognostic implications. Bader and colleagues evaluated 104 HF patients and demonstrated that patients with severe intra-ventricular dyssynchrony were at increased risk of cardiovascular events, irrespective of LVEF.[22] The following section will summarize the various non-invasive imaging modalities to evaluate inter and intra-ventricular dyssynchrony.

Echocardiographic Evaluation of Mechanical Dyssynchrony

Various echocardiographic techniques have been proposed for the evaluation of mechanical dyssynchrony (Table 20.3).

Conventional Techniques

Pitzalis and co-workers proposed a simple M-mode technique to evaluate LV dyssynchrony by measuring the delay between the systolic excursion of the septum and the posterior wall (Fig. 20.2), the so-called *septal to posterior wall motion delay* (SPWMD).[23] In the initial study (20 patients), the SPWMD was significantly larger in responders than non-responders to CRT. A cut-off value of 130 ms yielded 100% sensitivity and 63% specificity to predict CRT response. In a subsequent study, the same authors demonstrated that the cut-off value of 130 ms was a strong predictor of prognosis after CRT.[24] Marcus et al., however, obtained less favourable

Table 20.3. Overview of echocardiographic techniques available to quantify dyssynchrony (for some techniques cut-off values to predict response to CRT are indicated)

Conventional techniques
M-mode: septal to posterior wall motion delay (cut-off 130 ms)
Pulsed wave Doppler: inter-ventricular dyssynchrony (cut-off 40 ms)
Tissue Doppler imaging (TDI)
Opposing wall technique: difference between (antero-)septal and (postero-)lateral peak myocardial systolic velocity (cut-off 65 ms)
Multiple segments techniques: utilizes standard deviation of time to peak myocardial systolic velocity in multiple LV segments (cut-off 34.4 ms)
Automated tissue Doppler techniques: tissue synchronization imaging
Tri-plane TDI
Strain (rate) imaging
Tissue Doppler derived strain
2-dimensional strain or speckle tracking: delay in time to peak systolic radial strain among six mid-ventricular segments in the parasternal short-axis view (cut-off 130 ms)
Real-time 3D echocardiography
Standard deviation of the time to reach minimal regional volume in 17 LV segments, systolic dyssynchrony index (cut-off 6.4%)

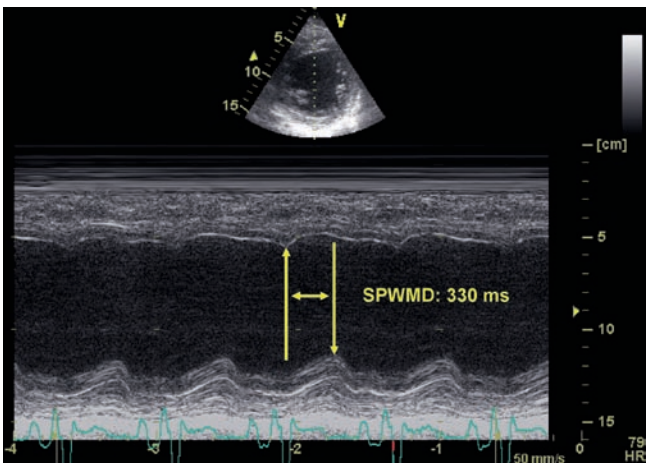

Fig. 20.2 The septal to posterior wall motion delay (SPWMD) measurement by M-mode echocardiography obtained from the short-axis view: a delay of 330 ms indicates significant intra-ventricular dyssynchrony

results with this technique.[25] The authors applied the SPWMD in 79 HF patients (72% ischaemic cardiomyopathy) and reported a sensitivity of 24% with a specificity of 66% to predict response to CRT. Importantly, in half of the patients, the SPWMD could not be assessed. Bleeker et al. demonstrated in 98 patients scheduled for CRT that the poor interpretability of SPWMD was the result of the absence of a clear systolic motion on M-mode echocardiography due to akinesia of the inter-ventricular septum and/or posterior wall, or a poor acoustic window in the para-sternal view.[26]

Pulsed wave Doppler echocardiography is the method of choice for assessment of *inter-ventricular dyssynchrony*. For this purpose, pulsed wave recordings across the aortic and pulmonary valves are obtained; aortic and pulmonary pre-ejection times are defined as the intervals between the onset of the QRS complex and the onset of aortic and pulmonary flow, respectively (Fig. 20.3). The difference between the aortic and pulmonary preejection times is considered a measure of inter-ventricular dyssynchrony.[27] Ghio et al. (using a cut-off value of 40 ms) reported that 72% of patients with QRS duration >150 ms exhibited inter-ventricular dyssynchrony.[28]

Tissue Doppler Imaging

Tissue Doppler imaging (TDI) is perhaps the most widely studied technique for assessment of LV dyssynchrony. TDI enables measurement of peak systolic velocities in different regions of the myocardium and, more importantly, the time intervals between electrical activity (QRS complex) and mechanical activity (segmental peak systolic velocity). The myocardial velocity curves can either be constructed online using pulsed wave TDI, or reconstructed offline from 2D colour-coded TDI. Because colour-coded TDI has some important practical advantages compared to pulsed wave TDI (Table 20.4), this section will primarily focus on colour-coded TDI techniques (Fig. 20.4).

Opposing Wall Technique

Bax et al. evaluated 85 HF patients who underwent CRT implantation with follow-up data obtained up to 1 year.[29] Intra-ventricular dyssynchrony was defined as the time difference between the peak systolic myocardial velocities of the septal and lateral wall, respectively (Fig. 20.5). Receiver operating characteristic curve analysis revealed that intra-ventricular dyssynchrony ≥65 ms was highly predictive of both clinical response (sensitivity/specificity 80%) and LV reverse re-modelling (sensitivity/specificity 92%). Penicka et al. defined LV dyssynchrony as the maximal electromechanical delay between three basal LV segments (septal, lateral, and posterior wall).[30] The authors described a cut-off value of 102 ms (88% accuracy) to predict CRT response defined as a relative increase in LVEF >25%. Gorcsan et al. studied 29 patients who underwent CRT with colour-coded TDI.[31] Differences in baseline time-to-peak velocities of

Table 20.4. Advantages of colour-coded TDI

Possibility for offline analysis
Possibility of analyzing multiple segments during one heart beat
More accurate display of peak myocardial systolic velocities

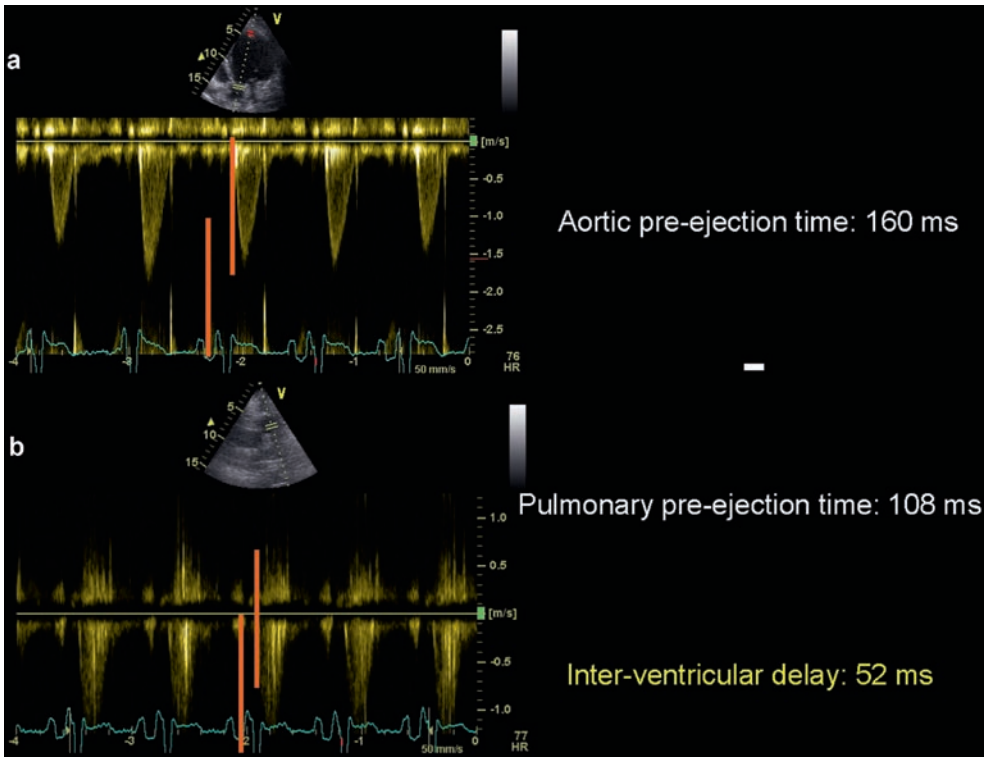

Fig. 20.3 **(a)** The aortic pre-ejection time is measured as the time difference between the onset of the QRS complex and the onset of aortic flow as obtained with pulsed wave Doppler imaging. **(b)** The pulmonary pre-ejection time is measured as the time difference between the onset of the QRS complex and the onset of pulmonary flow. The difference between the aortic and pulmonary pre-ejection times is a measure of *inter-ventricular dyssynchrony*: >40 ms indicates significant inter-ventricular dyssynchrony

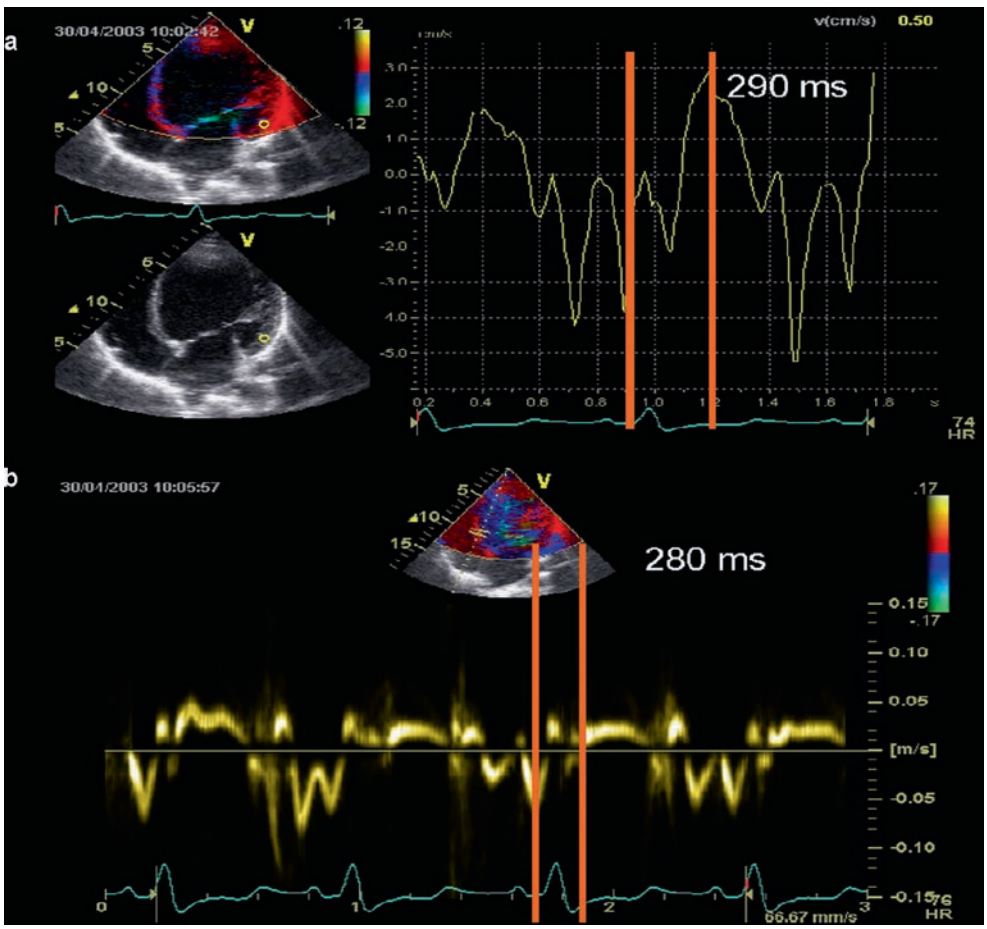

Fig. 20.4 **(a)** Mechanical activation time of a left ventricular segment can be assessed by measurement of the time interval between onset of QRS complex on the ECG and peak myocardial systolic velocity (290 ms) by colour-coded tissue Doppler imaging. **(b)** Assessment of mechanical activation by pulsed wave TDI uses the time interval between onset of QRS on the ECG and onset of mechanical contraction in the ejection phase, (280 ms) instead of peak myocardial systolic velocity

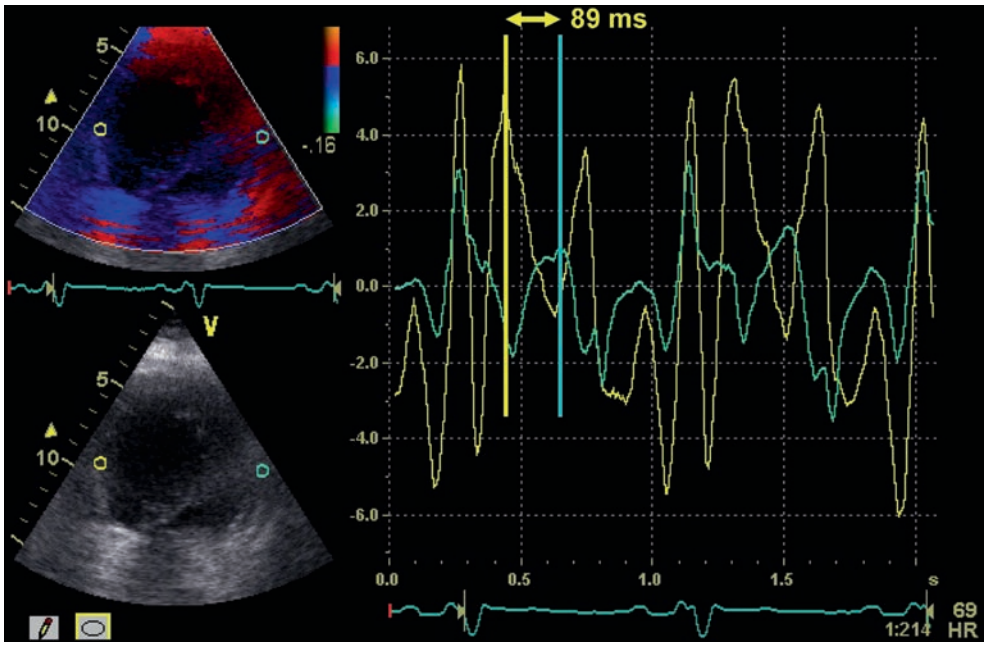

Fig. 20.5 Intra-ventricular dyssynchrony assessment by measuring the time difference between the peak myocardial systolic velocities of the septal (*yellow*) and lateral (*green*) wall on colour-coded tissue Doppler images; in this patient the LV dyssynchrony is 89 ms. A time difference exceeding 65 ms (significant intra-ventricular dyssynchrony) is predictive for CRT response

opposing ventricular walls were larger in patients with an acute haemodynamic improvement. A delay ≥ 65 ms between the anterior septum and the posterior wall had 87% sensitivity and 100% specificity for predicting an acute response.

Multiple Segment Techniques

Other studies have used a multiple segments approach to create various models of intra-ventricular dyssynchrony in order to predict a favourable response to CRT. Notobartolo and co-workers used a model with six basal LV segments.[32] The authors used colour-coded TDI to measure time to the highest peak velocity in either ejection phase or post-systolic shortening, and calculated the maximal time difference to generate the peak velocity difference. In 49 HF patients who underwent CRT, a peak velocity difference >110 ms at baseline predicted LV reverse re-modelling at 3 months follow-up with a sensitivity of 97% and a specificity of 55%. Yu et al. used a 12-segment model to evaluate LV dyssynchrony.[33] This method is more cumbersome as it requires colour-coded TDI images from three images (apical 2-, 3-, and 4-chamber views). From these 12 data points, a standard deviation can be calculated, representing a comprehensive assessment of LV dyssynchrony. Application of a cut-off value of 34.4 ms yielded a sensitivity and specificity to predict reverse LV re-modelling of 87 and 81%, respectively.

Automated TDI Techniques

An evolving parametric TDI-based technique to assess LV dyssynchrony is tissue synchronization imaging (TSI, General Electric Vingmed, Horten, Norway). TSI automatically calculates peak myocardial systolic velocities from colour-coded TDI data and displays the timings in colour-map format, permitting quick visualization of the early and late activated segments, displayed in green and yellow/orange, respectively (Fig. 20.6). Using a user-defined event-timing tool, time from onset of the QRS complex to the aortic valve opening and closure can first be measured in a separately recorded pulsed wave Doppler spectrum. This prevents the TSI system of measuring peak systolic velocities outside the ejection phase. In addition, a quantitative measurement tool allows calculation of the median time to peak myocardial systolic velocity within a 6 mm sample volume positioned manually within the 2-dimensional TSI image. Gorcsan et al. demonstrated in 29 patients who underwent CRT that differences in baseline time to peak myocardial systolic velocities of opposing ventricular walls by TSI were greater in patients with an acute haemodynamic improvement.[31] Van de Veire et al. evaluated intra-ventricular dyssynchrony both manually and with TSI in 60 HF patients who underwent CRT implantation.[34] An excellent correlation was observed between intra-ventricular dyssynchrony measured manually and automatically derived by TSI ($r = 0.95$, $p < 0.0001$). Using a cut-off value of 65 ms to define extensive LV dyssynchrony, TSI had a sensitivity of 81% with a specificity of 89% to predict reverse LV re-modelling. Yu and colleagues evaluated TSI (using the 12 segment LV model, Fig. 20.7) in 56 HF patients and reported a sensitivity of 82% with a specificity of 87% to predict CRT response.[35]

Tri-Plane Technique

Recently, a novel 3-dimensional probe (General Electrics, Vingmed, Horten, Norway) for tri-plane imaging became

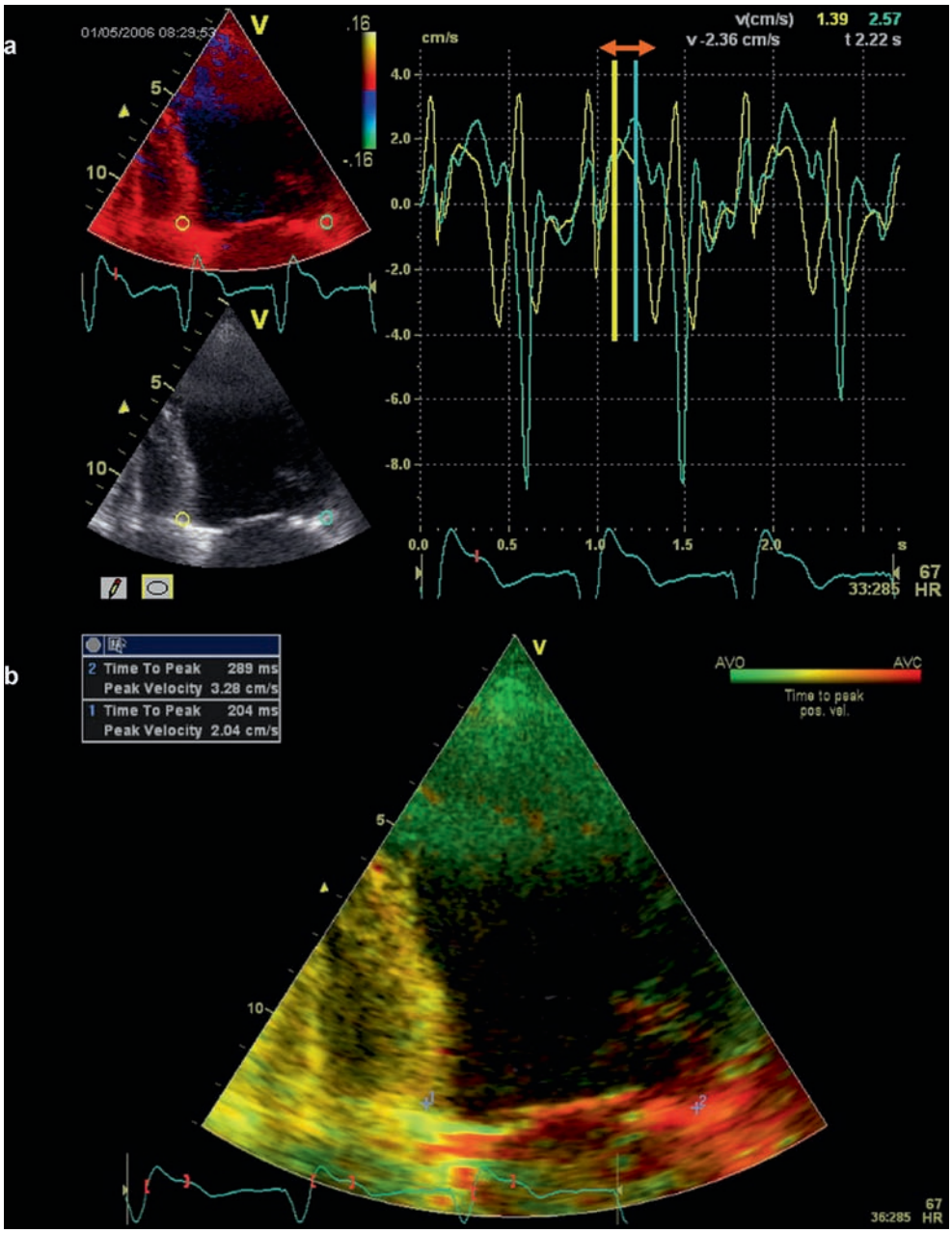

Fig. 20.6 **(a)** Example of septal and lateral velocity curves derived from colour-coded tissue Doppler imaging. The difference between the septal and lateral peak systolic myocardial velocity was 80 ms. **(b)** Automated measurement of the septal and lateral time to peak myocardial systolic velocity by tissue synchronization imaging in the same patient as **(a)** 204 and 289 ms, respectively. The *red* colour of the lateral wall indicates late mechanical activation in this region

commercially available. During a single heart beat, apical 2-, 3-, and 4-chamber views can be acquired, combined with colour-coded TDI. During post-processing, the TSI option can be applied to the TDI tri-plane dataset. By manually tracing the endocardial borders during post-processing (surface mapping), a 3D volume is generated semi-automatically, portraying the area of latest activation allowing quick visual identification of the most delayed LV segment (Fig. 20.8). Moreover, LVEF and LV volumes can also be assessed from the same tri-plane dataset. Van de Veire and co-workers applied the tri-plane approach (evaluating 12 segments) to predict the acute and long-term benefit of CRT.[36, 37] The authors evaluated 60 HF patients who underwent tri-plane echocardiography with simultaneous TDI acquisition before and 6 months after CRT implantation.[37] A cut-off value of 33 ms for baseline LV dyssynchrony (standard deviation of 12 segments) yielded a sensitivity and specificity to predict reverse LV re-modelling of 90 and 83%, respectively.

Strain (Rate) Imaging

In contrast to TDI, which only measures myocardial velocities, strain (rate) imaging examines the (rate of) myocardial deformation. Comparable to TDI, the extent of dyssynchrony can be quantified by measuring delays in time to peak systolic strain (Fig. 20.9). Due to the angle dependency of strain rate imaging and limited reproducibility, initial studies

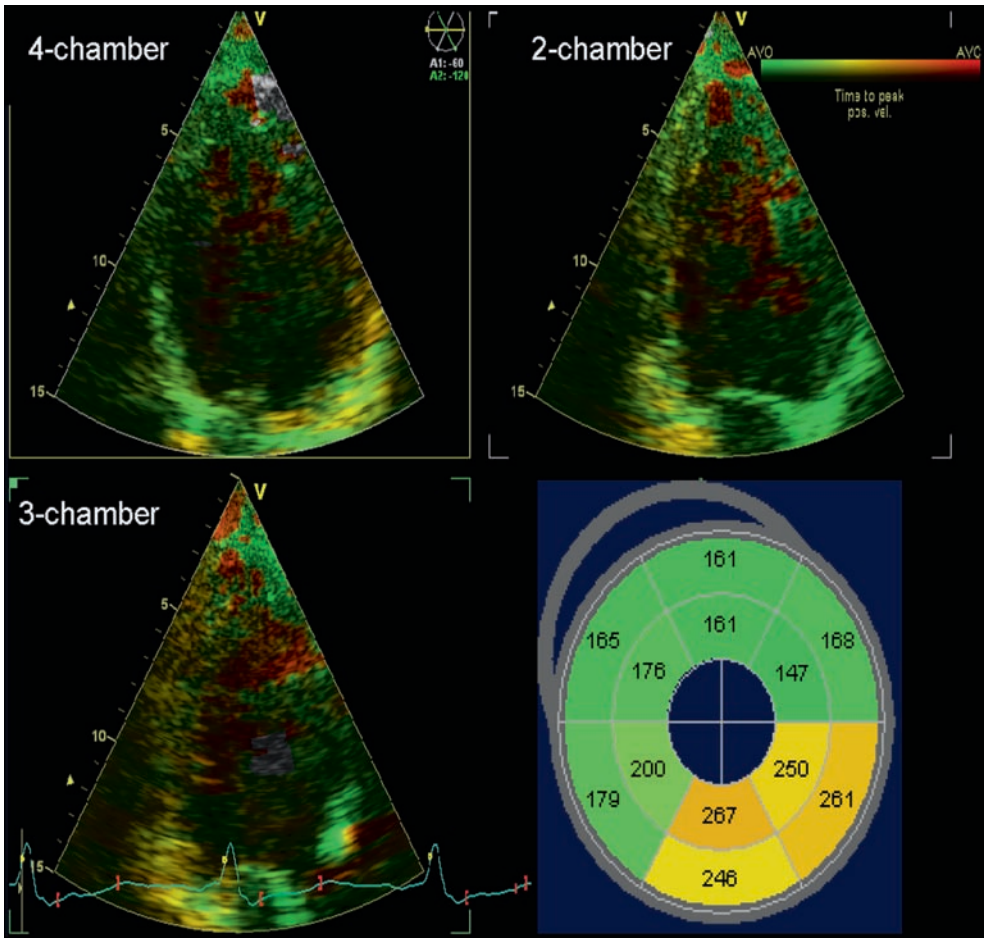

Fig. 20.7 Example of a tri-plane tissue synchronization imaging (TSI) dataset; in a single heart beat, the apical 2-, 3-, and 4-chamber views are provided and the TSI software automatically calculates time to peak myocardial systolic velocity in 12 LV segments. The latest activated segment can be quickly recognized by the yellow colour. A quantitative report of the individual activation times in 12 left ventricular segments is automatically generated in a bull's eye format (*lower right panel*). In this example the infero-lateral left ventricular segments are activated later (*yellow*) compared to other segments (*green*); accordingly, the latest mechanical activation occurred in the infero-lateral region

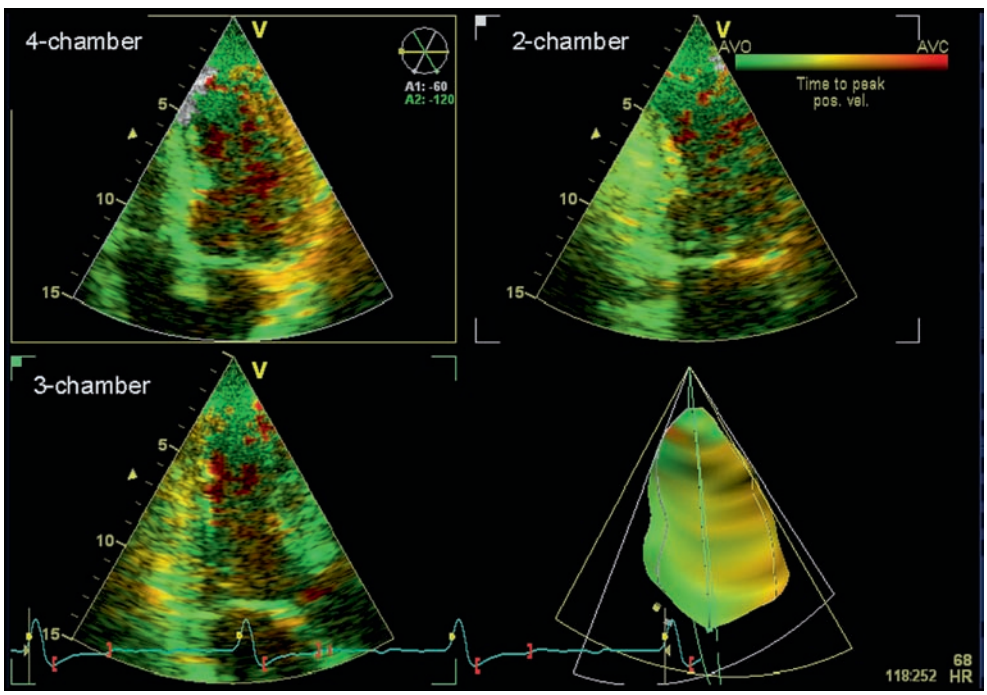

Fig. 20.8 3D presentation of the area of latest mechanical activation can be achieved by manually tracing the endocardial borders in each of the three apical views in a tri-plane TSI dataset. The software generates a 3D colour-coded volume (*lower right panel*). In this example, the orange colour in the infero-lateral left ventricular wall indicates later mechanical activation of this segment compared to the other segments (*green*)

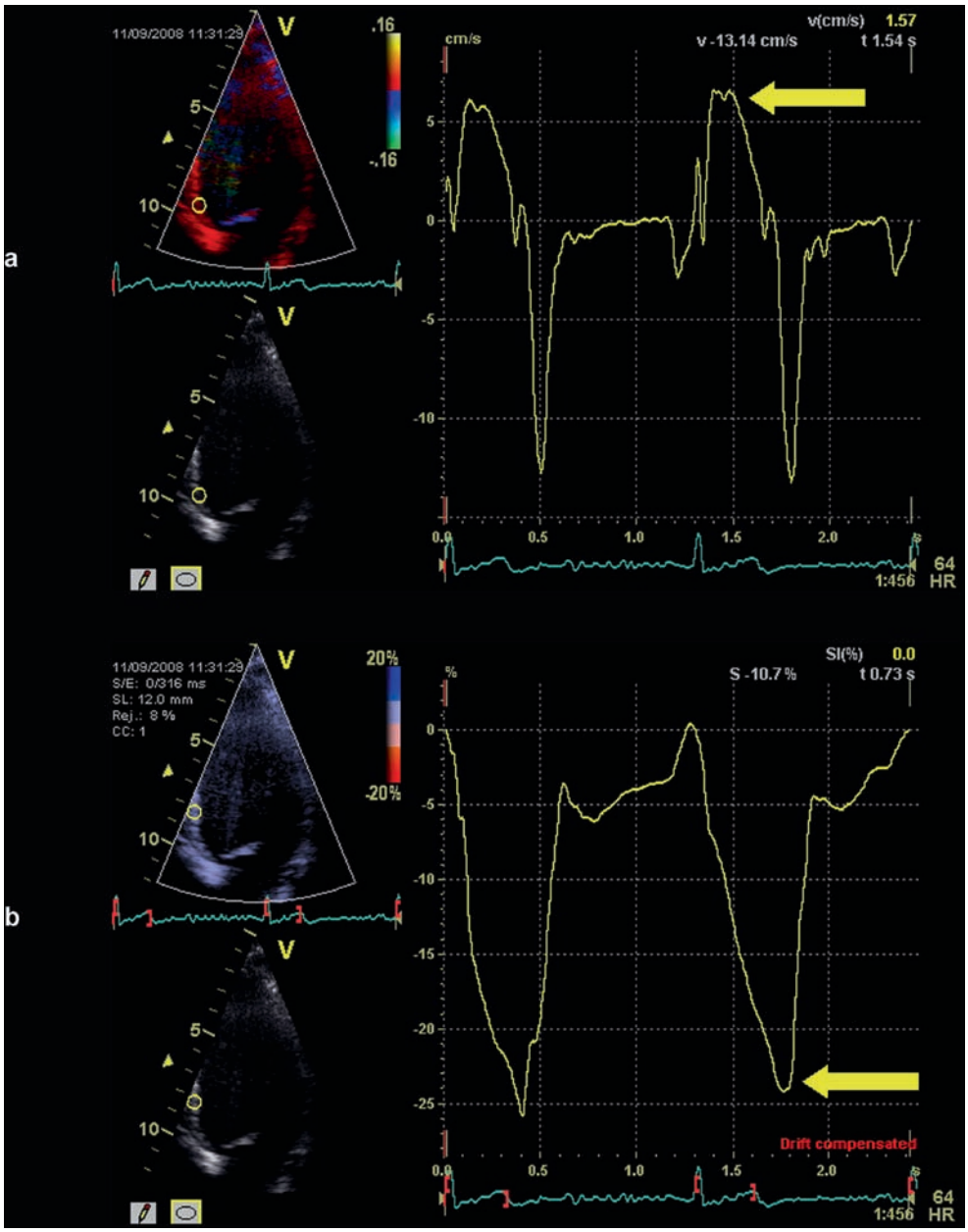

Fig. 20.9 **(a)** Identification of peak myocardial systolic velocity (*arrow*) in a tissue Doppler-derived velocity curve. **(b)** Identification of peak longitudinal (negative) strain (*arrow*) in a tissue Doppler-derived strain curve

employing this technique to measure LV dyssynchrony from the apical views (measuring longitudinal strain) reported low predictive values for CRT response.[32] One multi-centre study (with 256 patients who were followed for at least 3 months after CRT implantation) assessed both TDI-derived and strain-derived parameters of LV dyssynchrony, aiming to predict LV reverse re-modelling.[38] While TDI-derived parameters were highly predictive of reverse re-modelling, the longitudinal strain-derived measurements of LV dyssynchrony were not predictive.[38] More promising results have been obtained with radial strain measurements to quantify LV dyssynchrony from short-axis images. Dohi et al. reported in 38 HF patients that ≥130 ms difference in septal vs. posterior wall peak strain was predictive of acute improvement in stroke volume after CRT implantation (sensitivity 95%, specificity 88%).[39]

Speckle Tracking or 2D Strain

Speckle tracking is a new technique that tracks movements of natural acoustic markers (speckles) present on standard 2D images.[40] From the spatial and temporal data of each speckle, local 2D tissue velocity vectors are derived. Myocardial strain can be assessed from temporal differences in mutual distance of neighbouring speckles. From short-axis

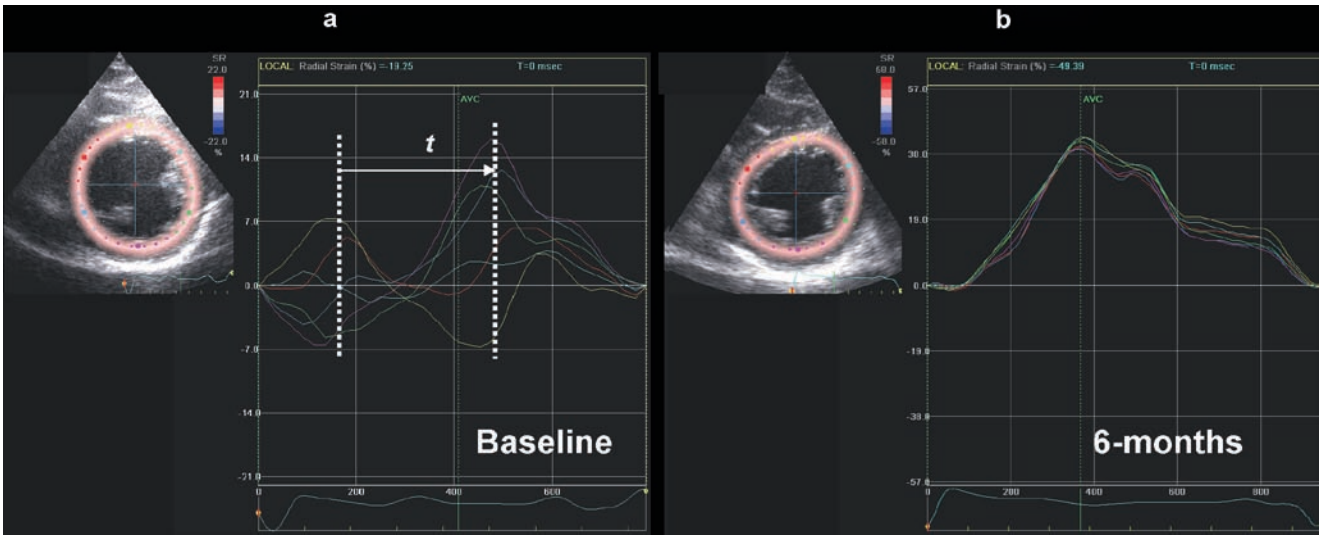

Fig. 20.10 **(a)** Short-axis of the left ventricle at the level of the papillary muscles, with reconstruction of six LV segments. Separate 2D strain time curves for each individual segment are depicted (the colour of the individual curves correspond to the individual segments). In this example, severe baseline intra-ventricular dyssynchrony was present as expressed by the delay in time to peak systolic radial 2D strain (*t*) >130 ms between the anterior-septal (*yellow*) and posterior wall (*purple*) peak strain. **(b)** Same patient as in **(a)**; complete resynchronization was observed 6 months after CRT implantation

images, circumferential and radial strain can be calculated, and from apical images, longitudinal strain can be derived. Speckle tracking may prove to be superior compared to TDI-derived strain because it is angle independent, allowing assessment of radial, circumferential, and longitudinal strain in all segments. The theoretical disadvantage of speckle tracking is its temporal resolution, which is lower than in TDI-derived strain, especially in dilated hearts requiring large sector size for imaging. Sufoletto and colleagues applied speckle tracking in 48 HF patients.[41] A delay >130 ms in time to peak systolic radial strain among six mid-ventricular segments (Fig. 20.10) predicted increase in LVEF >15% with a sensitivity of 89% and a specificity of 83% at 8 months after CRT. Delgado et al. performed speckle tracking in 161 patients at baseline and after 6 months of CRT.[42] A cut-off value of radial dyssynchrony ≥130 ms was able to predict response to CRT with a sensitivity of 83% and a specificity of 80%. In addition, a significant decrease in extent of LV dyssynchrony measured with radial strain (from 251 ± 138 to 98 ± 92 ms; $p < 0.001$) was demonstrated in responders.

Real-Time 3D Echocardiography

Real-time 3D echocardiography can provide simultaneous information on the timing of contraction in a large number of LV segments. Also, this technique provides detailed information on global and regional LV function. Regional volume-time curves can be derived for each of the LV segments (Fig. 20.11) (Videos 20.1 and 20.2). Intra-ventricular dyssynchrony is assessed by comparing the times to reach minimal regional volume for each LV segment. The standard deviation of the time to reach minimal regional volume for each of the LV segments (the so-called systolic dyssynchrony index, SDI) is used as a marker of global LV dyssynchrony. In addition, regional time differences between different segments allow identification of the area of latest mechanical activation. Kapetanakis et al. demonstrated the feasibility of real-time 3D echocardiography to assess LV dyssynchrony in 174 unselected patients referred for routine echocardiography.[43] Ajmone Marsan et al. studied 57 HF patients who underwent CRT implantation,[44] and demonstrated that the SDI was significantly larger in responders (9.7 ± 3.6% vs. 5.1 ± 1.8, $p < 0.0001$). A cut-off value for SDI of 6.4% yielded a sensitivity of 88% with a specificity of 85% to predict response to CRT.

Nuclear Imaging to Evaluate Mechanical Dyssynchrony

Several nuclear imaging techniques can be used for the assessment of mechanical dyssynchrony (Table 20.5).[45] Planar imaging techniques such as gated blood-pool ventriculography are less suitable for quantification of dyssynchrony because single view projections are associated with poor differentiation of ventricular regions of interest and are sensitive to extra-cardiac tissue overlap. As compared to gated-blood ventriculography, gated blood-pool SPECT acquires data at different angles. Time-activity curves are

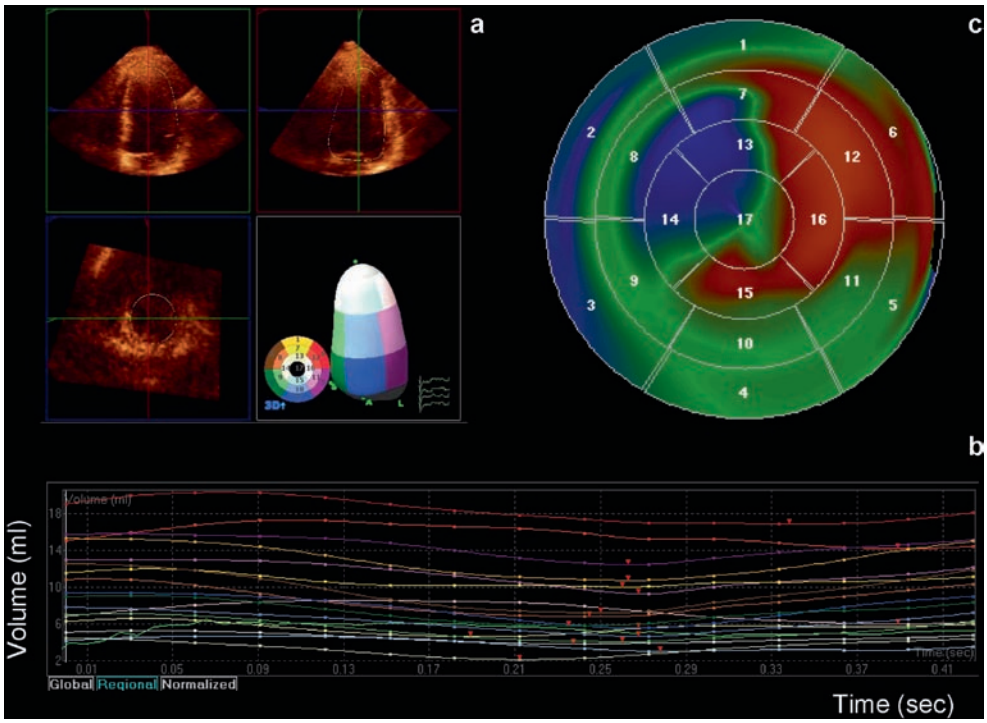

Fig. 20.11 **(a)** From a real-time 3D LV volume, a 17-segment model is derived by automated tracking of the endocardial wall. **(b)** From each of the 17 LV segments, a time/volume curve is derived. **(c)** Time to peak minimal volume of the segments is presented in a bull's eye plot. Colour-coding allows quick visual identification of the area of latest mechanical activation: *red* segments are activated latest; the *green* segments are activated earlier

Table 20.5. Nuclear imaging techniques for assessment of cardiac dyssynchrony

Gated blood-pool ventriculography
Gated blood-pool single photon emission computed tomography (SPECT)
Gated myocardial perfusion single photon emission computed tomography (GMPS)

generated by application of first Fourier harmonic function. From each time-activity curve, amplitude and phase are generated, wherein the highest phase reflects the latest conduction. Inter- and intra-ventricular dyssynchrony can be assessed by analysis of mean and standard deviation of the phase distribution, respectively. Botvinick and co-workers compared gated blood-pool ventriculography and SPECT and noted that gated blood-pool SPECT provided excellent differentiation and visualization of cardiac chambers and regional wall motion compared with planar projections.[46]

Chen et al. developed a novel approach for assessing LV dyssynchrony from GMPS. This count-based method allows extraction of amplitude (which reflects systolic wall thickening) and phase from the regional LV count changes throughout the cardiac cycle.[47] The phase information is related to the time interval when a region in the LV myocardial wall starts to contract (Figs. 20.12 and 20.13). Henneman et al. compared intra-ventricular dyssynchrony assessment with GMPS and phase analysis to intra-ventricular dyssynchrony assessment with TDI in 75 HF patients.[48] Of the four quantitative indices of phase analysis, histogram bandwidth and phase standard deviation correlated best with TDI-derived intra-ventricular dyssynchrony. In a subsequent study, intra-ventricular dyssynchrony derived from tri-plane TDI was related to phase analysis from GMPS in 40 HF patients. Excellent correlations between histogram bandwidth and phase standard deviation with the standard deviation of time to peak myocardial systolic velocity in 12 LV segments were shown.[49] Henneman et al. evaluated 42 HF patients who underwent CRT.[50] Responders had more extensive intra-ventricular dyssynchrony as reflected in a significantly larger histogram bandwidth and phase standard deviation. The optimal value for prediction of response to CRT was 135° for histogram bandwidth (sensitivity and specificity 70%) and 43° for phase standard deviation (sensitivity and specificity 74%). This novel technique can play a role in the identification of potential responders to CRT as it provides integrated information on LV function, LV dyssynchrony, extent of myocardial scar, ischaemia, and viability.

Magnetic Resonance Imaging to Evaluate Mechanical Dyssynchrony

Since the late 1980s, several MRI techniques have been developed for quantification and characterization of myocardial motion including myocardial tagging, strain-encoded

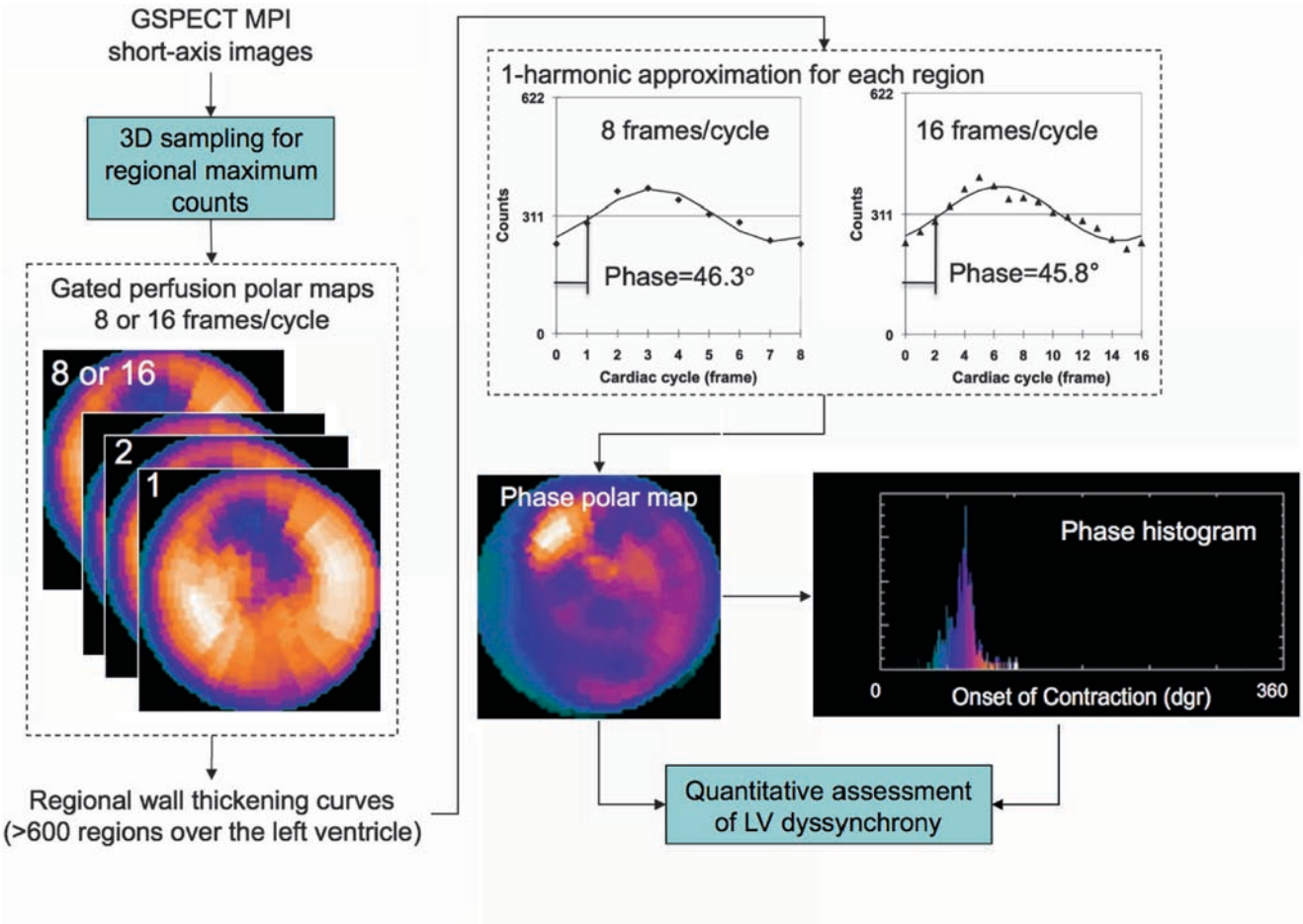

Fig. 20.12 Gated myocardial perfusion SPECT images are reconstructed and reoriented to gated short-axis images and subsequent search for regional maximal counts (3D sampling) is performed. For each LV short-axis section, count-based curves are generated from 8 or 16 discrete wall thickening points (*continuous line* represents approximation of first Fourier harmonic function). The distribution of phase angle (onset of mechanical contraction) within the left ventricle can be displayed in polar map and histogram format

MRI, and velocity-encoded MRI, which are reviewed elsewhere.[51, 52] Rüssel et al., for example, studied 29 HF patients with MRI.[53] Using myocardial tagging, two mechanical dyssynchrony parameters were defined: standard deviation in onset time and time to first peak of circumferential shortening. Two heterogeneity parameters were defined: coefficient of variation in end-systolic strain and difference between peak septal and lateral strain. The authors found that the heterogeneity parameters correlated best with acute response (as defined by a relative increase in maximum rate of LV pressure rise) to CRT. Westenberg et al. studied 20 HF patients with systolic LV dysfunction and a wide QRS complex, as well as ten normal individuals.[54] Both colour-coded TDI data and velocity-encoded MRI were performed to assess LV dyssynchrony (Fig. 20.14). Intra-ventricular dyssynchrony was not observed in normal individuals. In HF patients, the mean intra-ventricular dyssynchrony was 55 ± 37 ms on TDI and 49 ± 38 on MRI. Agreement between MRI and TDI for assessment of intra-ventricular dyssynchrony was excellent.

The clinical use of MRI to assess intra-ventricular dyssynchrony has been limited by cumbersome post-processing techniques. Cardiac devices further complicate the use of MRI since devices form a contraindication for MRI. New methods that provide easy and rapid MRI strain analysis and evidence supporting the MRI compatibility of modern implantable cardiac devices could expand the role of MRI in the selection process of CRT candidates.

Assessment of Viability and Scar Tissue

Recent observations have emphasized the importance of the presence and extent of scar tissue prior to CRT implantation. First, it is important to determine whether the target region for LV lead positioning contains scar tissue, and second, it is important to determine the extent of scar tissue in the entire left ventricle.[20] Various imaging techniques are available to detect scar tissue, including echocardiography, nuclear imaging, and MRI.

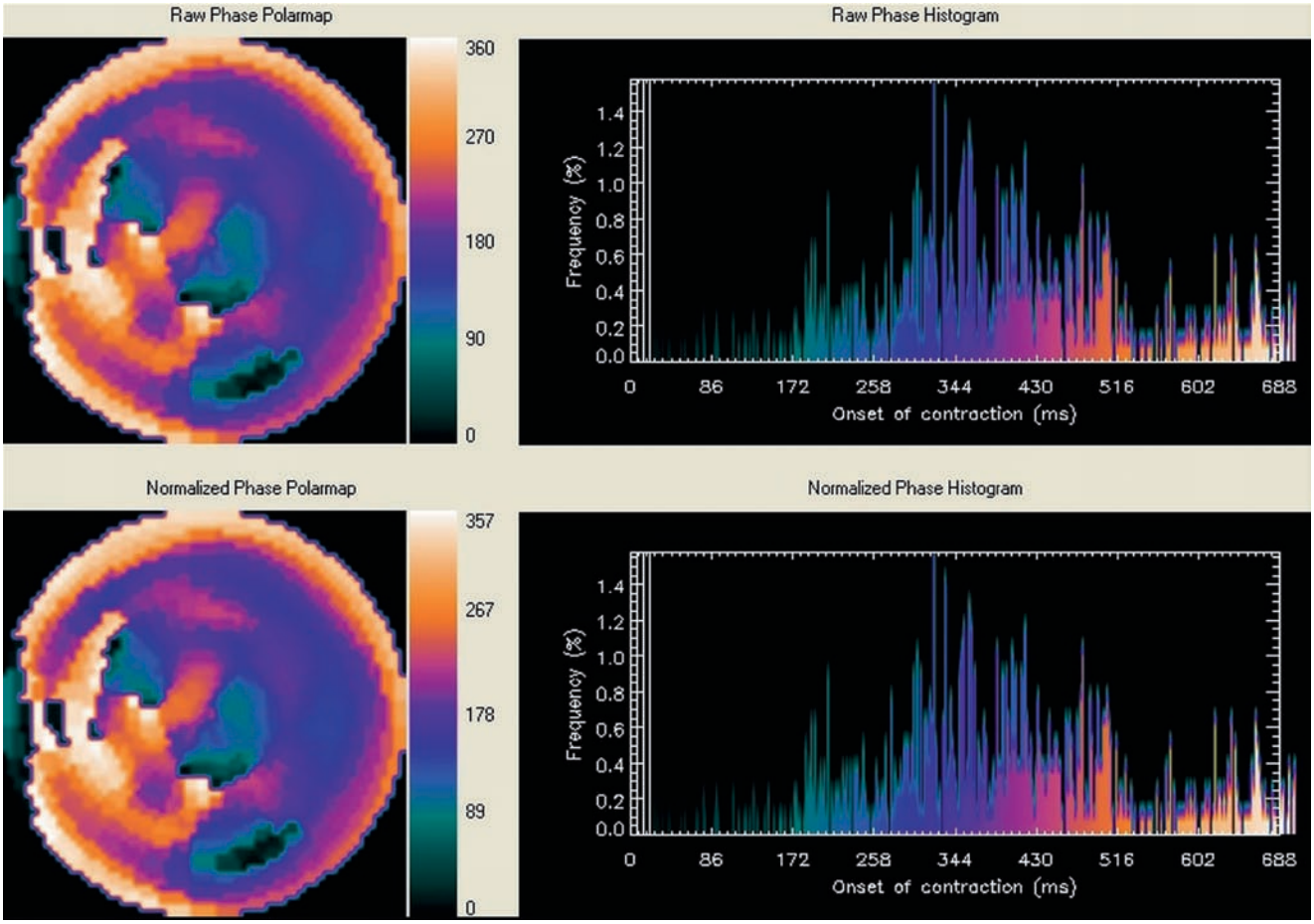

Fig. 20.13 Example of phase analysis with gated myocardial perfusion SPECT in a patient with extensive LV dyssynchrony. The heterogeneous phase angle distribution is reflected in the non-normalized (*upper*) and normalized (*lower*) heterogeneous colour-coding scale (polar map format) and a broad and moderate peaked histogram

Echocardiography to Evaluate Viability and Scar

Da Costa et al. prospectively enrolled 55 HF patients who subsequently underwent CRT implantation.[55] All patients underwent TDI to assess LV dyssynchrony, followed by low-dose dobutamine stress echocardiography to detect viability and scar tissue; both the magnitude of LV dyssynchrony and the extent of viable tissue were predictive of acute response to CRT. Ypenburg and colleagues confirmed these findings in 31 HF patients who underwent low-dose

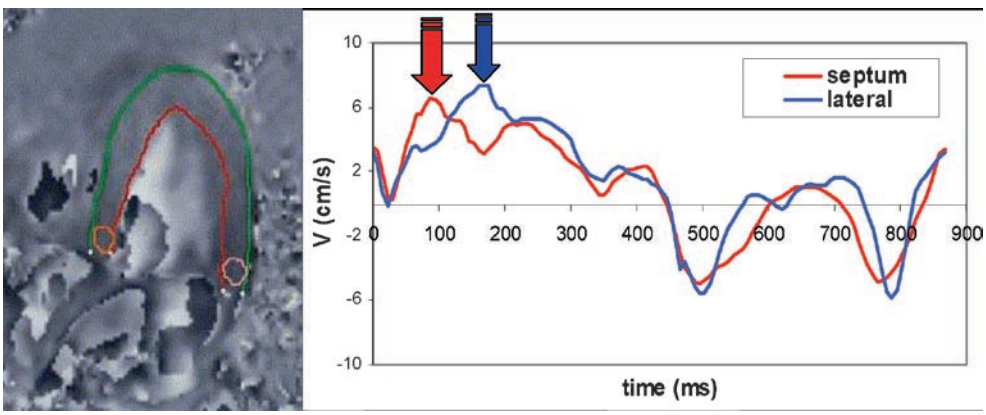

Fig. 20.14 Example of assessment of LV dyssynchrony with velocity-encoded MRI. Velocity curves from the basal segments of the septum (*red curve*) and lateral wall (*blue curve*) are shown: Note the significant delay between these two segments indicating LV dyssynchrony

dobutamine stress echocardiography with strain analysis before CRT implantation.[56] Global contractile reserve (≥7.5% increase in LVEF during dobutamine infusion) predicted LV reverse re-modelling and improvement in LV function after 6 months of CRT. Moreover, responders had viable tissue in the region where the LV lead was positioned, whereas non-responders had mostly non-viable tissue in this region. Hummel et al. used contrast echocardiography to assess viability and demonstrated that the presence of viability correlated well with improvement in LVEF after 6 months of CRT.[57]

Nuclear Imaging to Evaluate Viability and Scar

De Winter and co-workers evaluated 132 patients with ischaemic cardiomyopathy and depressed LV function using gated SPECT and demonstrated that scar tissue in the inferior, posterior, or lateral regions (where the LV pacing lead is often positioned) is frequently encountered in potential candidates for CRT and may limit response to CRT.[58] Ypenburg et al. determined the extent of viability with F18-fluorodeoxglucose (FDG) and SPECT imaging in 61 HF patients prior to CRT implantation.[59] Responders to CRT had more viable segments in the left ventricle as compared to non-responders (12 ± 3 vs. 7 ± 3 viable segments, $p < 0.01$), and the number of viable segments was directly related to the increase in LVEF after 6 months of CRT (Fig. 20.15). The optimal cut-off value to predict clinical response to CRT was 11 viable segments or more (in a 17-segment model), yielding a sensitivity of 74% and a specificity of 87%. Similar results were reported when technetium-99m tetrofosmin was used as viability marker.[60]

Magnetic Resonance Imaging to Evaluate Viability and Scar

Contrast-enhanced MRI allows precise determination of the spatial and trans-mural extent of scar tissue. Bleeker et al. explored this technique for assessment of scar tissue in 40 patients before undergoing CRT.[61] One-third of the patients had a trans-mural postero-lateral scar (Fig. 20.16). In contrast to patients without postero-lateral scar, these patients showed a low response rate and did not show improvement in clinical or echocardiographic parameters after CRT. In addition, LV dyssynchrony remained unchanged after CRT implantation in the presence of scar tissue. Ypenburg and co-workers subsequently emphasized that not only the location but also the extent of scar tissue (total scar burden) is important for response to CRT.[62] The authors demonstrated a significant correlation between the total scar burden at baseline on contrast-enhanced MRI and the change in LV end-systolic volume (ESV) after 6 months of CRT.

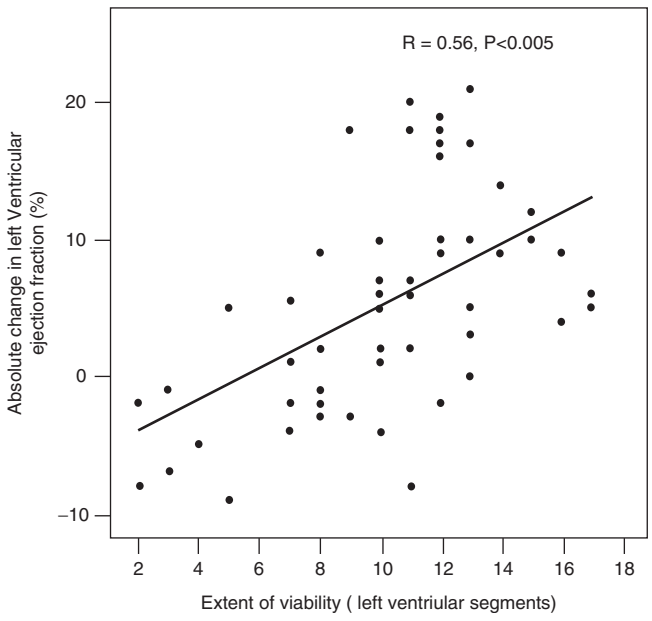

Fig. 20.15 Relationship between the extent of viability (number of viable segments) as assessed with FDG SPECT imaging and the absolute change in LV ejection fraction after 6 months of CRT. Modified from Ypenburg et al.[59]

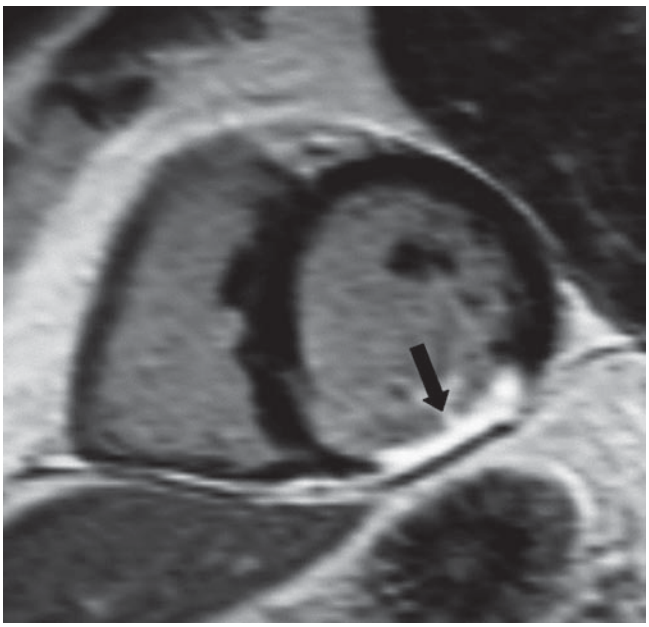

Fig. 20.16. Example of a patient with a trans-mural infarction (scar, *arrow*) located in the postero-lateral segment of the left ventricle (LV) as identified with contrast-enhanced magnetic resonance imaging

Imaging the Cardiac Veins

Anatomy of the Cardiac Veins

The most challenging part of a CRT device implantation through an endovascular approach is positioning the LV lead in a branch of the coronary sinus. Therefore, a detailed knowledge of the venous anatomy, as systematically described by von Lüdinghausen, is required (Fig. 20.17).[63] The first tributary of the coronary sinus is the posterior inter-ventricular vein or middle cardiac vein, running in the posterior inter-ventricular groove. The second tributary of the coronary sinus is the posterior vein of the left ventricle. The next tributary is the left marginal vein (LMV). The great cardiac vein continues as the anterior cardiac vein in the anterior inter-ventricular groove. Important inter-individual variations are observed regarding origin and presence of these tributaries. Pre-procedural knowledge on the cardiac venous anatomy of an individual patient could contribute significantly to the success of the LV lead implantation.

Invasive Venography

The gold standard to depict the cardiac venous system is invasive venography. Two techniques are available, including direct venography (direct manual injection of contrast in the guiding catheter) or occlusive venography (Fig. 20.18) (Video 20.3). Occlusive venography has more success to identify the anatomy, but may be related with more dissections, more contrast is needed, and the procedure time is generally longer.[64] Ideally, however, the information on venous anatomy should be available prior to CRT implantation. Non-invasive imaging techniques such as computed tomography (CT) and MRI may be able to provide this information as well.

Non-invasive Venography: Multi-slice CT and MRI

Various studies reported on the use of 16-slice CT to depict the cardiac veins.[64–67] Jongbloed and colleagues described a marked variability in venous anatomy among patients, confirming anatomical and invasive studies.[67] Meanwhile, 64-slice CT has become the standard to depict the cardiac structures offering a decreased acquisition time and higher spatial resolution. The feasibility of 64-slice MSCT to depict the cardiac venous system was recently demonstrated in 100 subjects referred for non-invasive angiography (Fig. 20.19, Video 20.4).[68] One of the hypotheses of this particular study was that the absence of cardiac veins may

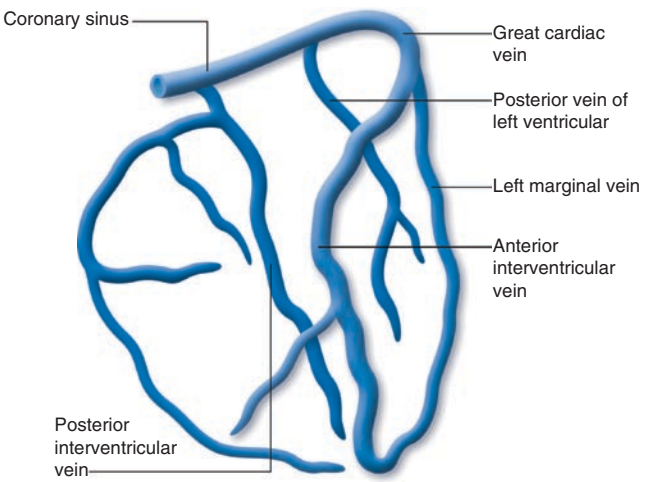

Fig. 20.17 The venous anatomy of the heart as described systematically by von Lüdinghausen. The first tributary of the coronary sinus is the posterior inter-ventricular vein or middle cardiac vein, running in the posterior inter-ventricular groove. The second tributary of the coronary sinus is the posterior vein of the left ventricle. The next tributary is the left marginal vein. The great cardiac vein continues as the anterior cardiac vein in the anterior inter-ventricular groove

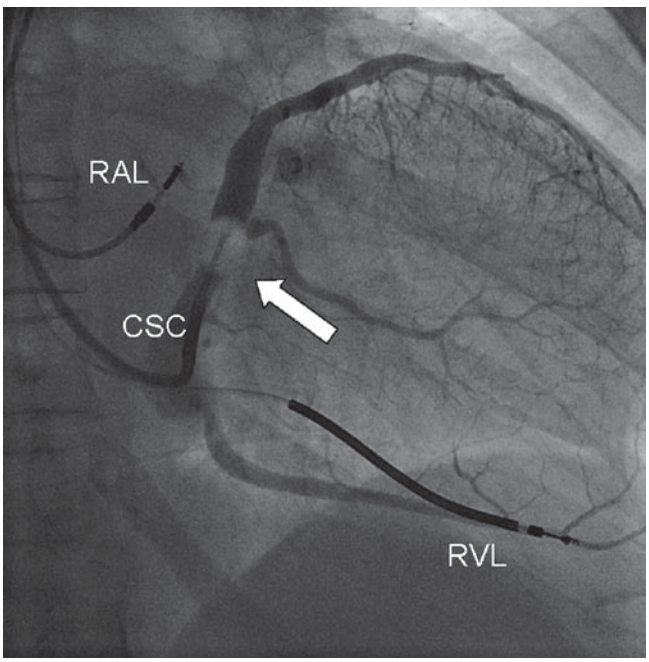

Fig. 20.18 Example of an invasive occlusive venogram during CRT implantation (right anterior oblique view). A catheter is positioned in the coronary sinus (CSC). An occlusion catheter is advanced through the guiding catheter and a balloon (*arrow*) is inflated with 1–1.5 mL air beyond the distal tip of the guiding catheter. The result is a detailed venogram. Note the right atrial (RAL) and right ventricular lead (RVL)

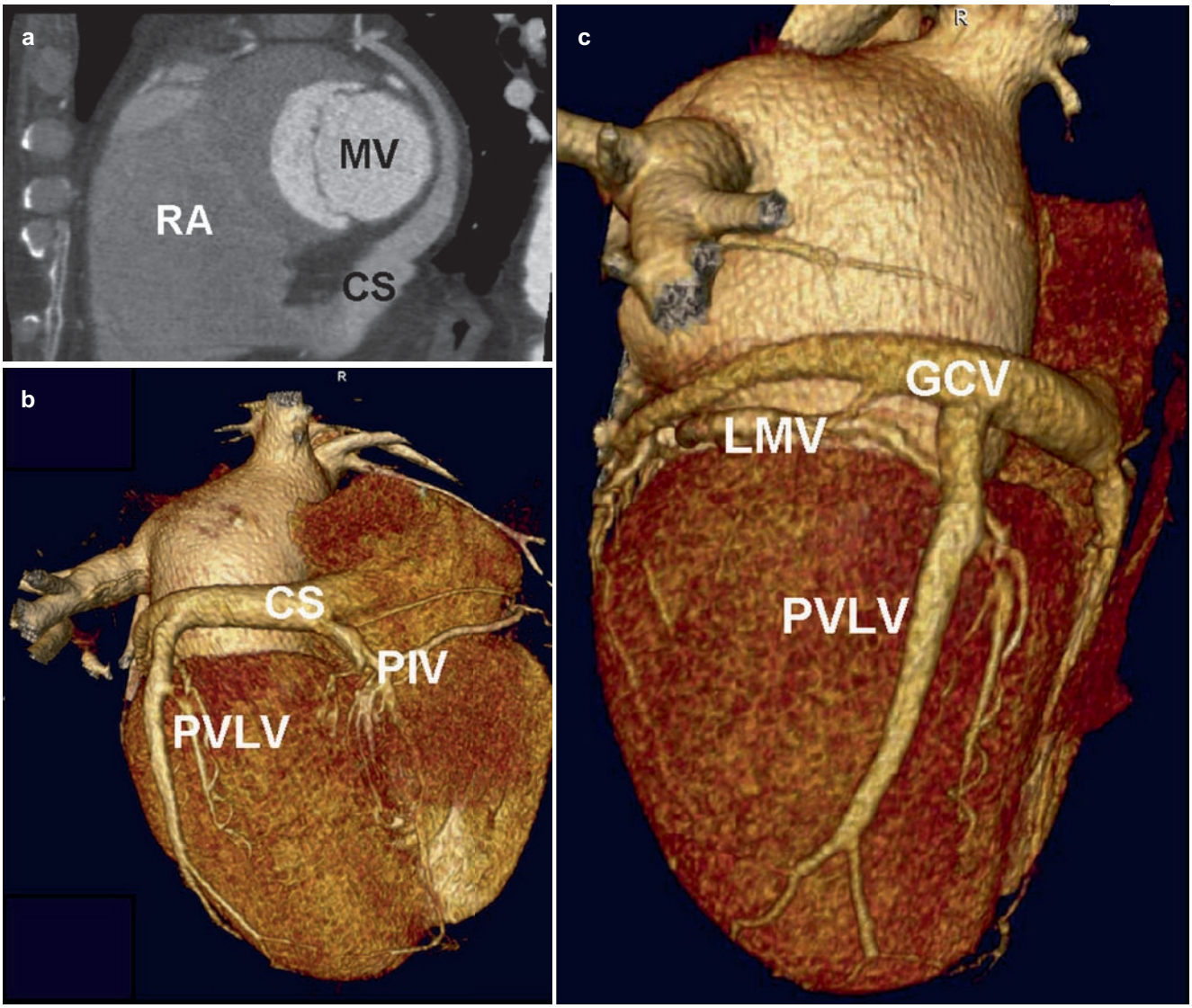

Fig. 20.19 Non-invasive venography using 64-slice CT. **(a)** Curved multi-planar reconstruction illustrating the coronary sinus (CS) originating from the right atrium (RA) and curving around the mitral valve (MV) plane. **(b)** Volume rendered reconstruction, posterior view illustrating the coronary sinus (CS), posterior inter-ventricular vein (PIV), and posterior vein of the left ventricle (PVLV). **(c)** Volume-rendered reconstruction, lateral view illustrating great cardiac vein (GCV), PVLV, and left marginal vein (LMV)

be related to scar formation secondary to a previous infarction in the region drained by these specific veins. Indeed, absence of the LMV was more frequently encountered in patients with a history of lateral infarction (Fig. 20.20), whereas patients with previous antero-lateral infarction were frequently lacking the LMV. Blendea et al., using high-speed rotational (invasive) venography, also noted a lower prevalence of the LMV in patients with a history of lateral infarction.[69] Absence of suitable cardiac veins may hamper trans-venous LV lead positioning, and a surgical approach could be preferred. In a preliminary study, 21 patients underwent both 64-slice CT venography in advance and invasive venography during CRT implantation.[70] There was an excellent correlation between CT venography and invasive venography.

Few preliminary reports have demonstrated the technical aspects of imaging the cardiac veins with MRI.[71, 72] Chiribiri et al. examined 16 volunteers and 7 patients with MRI.[72] The cardiac venous system was visualized in all subjects, and the variability of the cardiac venous system was again reported. MRI may be preferred over CT since radiation is absent with MRI, but further studies are needed before MRI venography can be integrated in clinical practice.

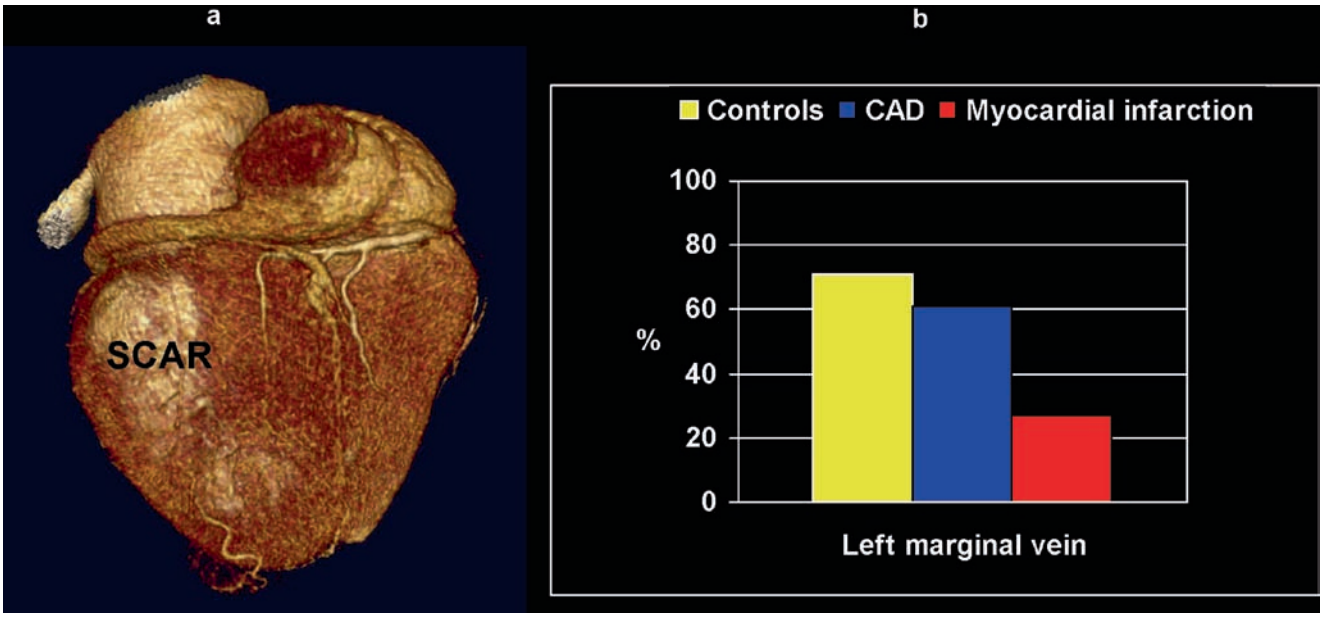

Fig. 20.20 **(a)** Volume-rendered reconstruction of 64-slice CT venography illustrating scar tissue and absence of the left marginal vein (LMV). **(b)** Analysis of 100 patients revealed that the LMV was significantly less observed in patients with a history of lateral infarction compared to controls ($p < 0.0001$) and compared to patients with coronary artery disease (CAD), without previous infarction ($p < 0.01$)

Summary: What Can Imaging Contribute to the Selection of CRT Candidates?

Assessing LV volumes and EF is essential according to the "classic" selection criteria for CRT. Echocardiography appears to be the method of choice, but nuclear imaging and MRI can be valid alternatives. Other pathophysiological issues such as cardiac dyssynchrony, viability/scar tissue, and venous anatomy can also be addressed with imaging modalities. Several echocardiographic dyssynchrony parameters have demonstrated the ability to distinguish CRT responders from non-responders with a high degree of accuracy in multiple, small, single-centre studies. There is, however, no consensus on which parameter to use in clinical practice. A prospective multi-centre study, the PROSPECT trial, tested the performance of 12 conventional and TDI echocardiographic dyssynchrony parameters to predict response to CRT in 498 patients with standard CRT indications.[73] The results of this trial were disappointing with the different echocardiographic approaches yielding only modest sensitivity and specificity to predict response to CRT.

Both technical and pathophysiological issues may be related to this failure to predict response to CRT. Technical issues include better training in data acquisition, and data analysis is needed. Moreover, better technology for assessment of LV dyssynchrony may be needed, and particularly strain (rate) imaging may be preferred, since many patients have ischaemic cardiomyopathy and TDI may not be ideal for dyssynchrony assessment in these patients. Pathophysiological issues include the presence of extensive scar tissue, limited venous anatomy, and suboptimal LV lead position.

Accordingly, various questions may be addressed in patients considered for CRT, and, based on the answers, it will be possible to identify patients with low and high likelihood of response to CRT.

Is substantial LV dyssynchrony present, and where is the area of latest mechanical activation? Patient selection based on dyssynchrony assessment showed a higher response rate compared to selection based on the current guidelines, but larger studies are needed to identify the best technology for dyssynchrony assessment. Echocardiography appears to be the technique of choice, but alternatives can be nuclear imaging and MRI.

Does the site of latest activation contain scar tissue? Scar tissue in the region of the LV pacing lead will result in the failure of responding to CRT. Contrast-enhanced MRI is the technique of choice, since this technique has the highest spatial resolution and provides information on the extent and trans-murality of scar tissue with high precision. Echocardiographic techniques and nuclear imaging can also provide information on scar tissue.

Are cardiac veins present in the region of latest activation (the preferred LV lead position)? Multi-slice CT can provide this information non-invasively. Recent data have demonstrated that patients with extensive previous infarction may lack certain veins. In patients with large previous infarction(s),

CT may be useful to define the precise venous anatomy. In patients without suitable veins in the region of latest mechanical activation, a surgical approach may be preferred. The importance of individually tailored LV lead position was illustrated by Murphy and co-workers who studied 54 patients with advanced HF treated with CRT.[74] At baseline, the area of maximal delay was identified using TSI. In 22 patients, the LV lead position corresponded to the segment of maximal delay. Reverse re-modelling was defined as >15% decrease in ESV at 6 months follow-up. The placing of the LV lead proximal to the site of maximal delay by TSI was significantly correlated with reverse re-modelling. Moreover, the extent of reverse re-modelling and improved systolic function was largest in the 22 patients with LV lead position corresponding to segment of maximal delay. Ypenburg and colleagues used speckle tracking radial strain analysis to identify the area of latest mechanical activation in 257 patients who underwent CRT.[75] Significant reverse re-modelling at 6 months follow-up was only noted in the group of patients with a concordant LV lead position (as determined from chest X-ray). In addition, a concordant LV lead position appeared to be an independent predictor of hospitalization-free survival after long-term CRT. Accordingly, the likelihood of a successful endovascular CRT implantation appears highest in patients with the classic selection criteria who also show significant dyssynchrony, exhibit viable tissue in the area of latest mechanical activation, and have a suitable coronary sinus tributary draining that area (Fig. 20.21).

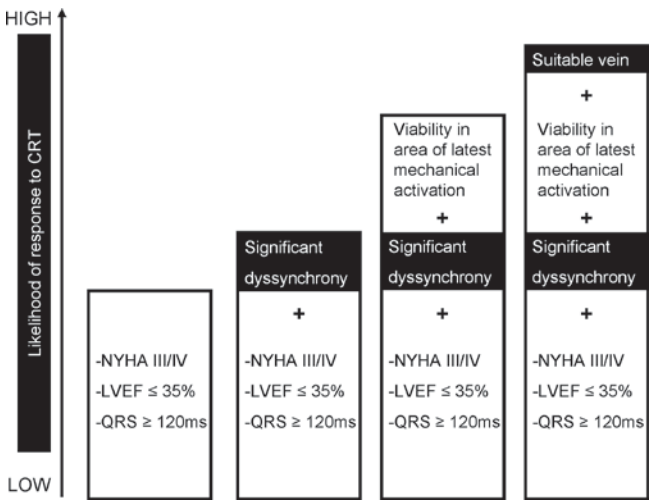

Fig. 20.21 Integrated cardiac imaging in CRT candidates can provide the clinician with important information such as the extent of LV dyssynchrony as well as the site of latest activation, the presence of viable tissue, and the details of venous cardiac anatomy. The likelihood of a favourable response to endovascular CRT implantation increases if the candidate has - on top of the classic selection criteria – an area of latest mechanical activation containing viable tissue drained by a suitable coronary sinus tributary

In summary, various non-invasive imaging techniques may play a role in the selection of patients for CRT. Echocardiography still appears to be the technique of choice to assess LV function and dyssynchrony, whereas other imaging techniques may provide additional information on scar tissue and venous anatomy.[76]

Video 20.1

Example of full volume 3D echocardiography in a heart failure patient. Left ventricular volumes are clearly dilated and LVEF is depressed (32%). From the 17 time/volume curves in 17 LV segments, the systolic dyssynchrony index is calculated (11.5%) indicating significant LV dyssynchrony

Video 20.2

Full volume 3D echocardiography is repeated post-CRT implantation. Left ventricular end-systolic volume has decreased significantly resulting in an improved systolic function (LVEF 48%). Note the resynchronization of the left ventricle, with a systolic dyssynchrony index of 1.9%

Video 20.3

Example of an invasive venogram during CRT implantation using an occlusive catheter

Video 20.4

The cardiac venous system can be evaluated non-invasively using 64-slice CT. The coronary sinus and its tributaries can be easily identified on this 3-dimensional, volume-rendered reconstruction of the heart

References

1. Bleumink GS, Knetsch AM, Sturkenboom MC, et al Quantifying the heart failure epidemic: prevalence, incidence rate, lifetime risk and prognosis of heart failure. *Eur Heart J*. 2004;25:1614–1619

2. Stewart S, MacIntyre K, Hole DJ, Capewell S, McMurray JJ. More "malignant" than cancer? Five-year survival following a first admission for heart failure. *Eur J Heart Fail*. 2001;3:315–322
3. Jessup M, Brozena S. Heart Failure. *N Engl J Med*. 2007;348: 2007–2018
4. Garg R, Yusuf S. Overview of randomized trials of angiotensin-converting enzyme inhibitors on mortality and morbidity in patients with heart failure. *JAMA*. 1995;273:1450–1456
5. Farrell MH, Foody JM, Krumholz HM. Beta-blockers in heart failure: clinical applications. *JAMA*. 2002;287:890–897
6. Pitt B, Zannad F, Remme WJ, et al for The Randomized Aldactone Evaluation Study Investigators. The effect of spironolactone on morbidity and mortality in patients with severe heart failure. *N Engl J Med*. 1999;341:709–717
7. Goldman S, Johnson G, Cohn J, Cintron G, Smith R, Francis G. Mechanism of death in heart failure. The vasodilator-heart failure trials. The V-Heft VA Cooperative studies group. *Circulation*. 1993;87:IV24-IV31
8. Myers J. Principles of exercise prescription for patients with chronic heart failure. *Heart Fail Rev*. 2008;13:61–68
9. Allen LA, Felker GM. Advances in the surgical treatment of heart failure. *Curr Opin Cardiol*. 2008;23:249–253
10. Jarcho JA. Biventricular pacing. *N Engl J Med*. 2006;355:288–294
11. Abraham WT, Fisher WG, Smith AL, et al MIRACLE Study Group. Multicenter InSync Randomized Clinical Evaluation. Cardiac resynchronization in chronic heart failure. *N Engl J Med*. 2002;346:1845–1853
12. Bristow MR, Saxon LA, Boehmer J, et al Comparison of medical therapy, pacing and defibrillation in heart failure (COMPANION) investigators. Cardiac resynchronization therapy with or without an implantable defibrillator in advanced chronic heart failure. *N Engl J Med*. 2004;350:2140–2150
13. Cleland JGF, Daubert JC, Erdmann E, et al Cardiac resynchronization-heart failure (CARE-HF) study investigators. The effect of cardiac resynchronization therapy on morbidity and mortality in heart failure. *N Engl J Med*. 2005;352:1539–1549
14. Vardas PE, Auricchio A, Blanc J-J, et al European Society of Cardiology; European Heart Rhythm Association. Guidelines for cardiac pacing and cardiac resynchronization therapy. The task force for cardiac pacing and cardiac resynchronization therapy of the European Society of Cardiology. Developed in collaboration with the European Heart Rhythm Association. *Eur Heart J*. 2007;28:2256–2295
15. Lang RM, Bierig M, Devereux RB. Recommendations for chamber quantification. *Eur J Echocardiogr*. 2006;7:79–108
16. Lang RM, Mor-Avi V, Zoghbi WA, Senior R, Klein AL, Pearlman AS. The role of contrast enhancement in the echocardiographic assessment of left ventricle. *Am J Cardiol*. 2002;90:28–34
17. Germano G, Kiat H, Kavanagh PB, et al Automatic quantification of ejection fraction from gated myocardial perfusion SPECT. *J Nucl Med*. 1995;36:2138–2147
18. Bellenger NG, Burgess MI, Ray SG, et al Comparison of left ventricular ejection fraction and volumes in heart failure by echocardiography, radionuclide ventriculography and cardiovascular magnetic resonance. Are they interchangeable? *Eur Heart J*. 2000;21:1387–1396
19. Mehra MR, Greenberg BH. Cardiac resynchronization therapy: caveat medicus! *J Am Coll Cardiol*. 2004;43:1145–1148
20. Bax JJ, Abraham T, Barold SS, et al Cardiac resynchronization therapy: part 1 – issues before device implantation. *J Am Coll Cardiol*. 2005;46:2153–2167
21. Auricchio A, Ding J, Spinelli JC, et al Cardiac resynchronization therapy restores optimal atrioventricular mechanical timing in heart failure patients with ventricular conduction delay. *J Am Coll Cardiol*. 2002;39:1136–1139
22. Bader H, Garrigue S, Lafitte S, et al Intra-left ventricular electromechanical asynchrony. A new independent predictor of severe cardiac events in heart failure patients. *J Am Coll Cardiol*. 2004;43: 248–256
23. Pitzalis MV, Iacoviello M, Romito R, et al Cardiac resynchronization therapy tailored by echocardiographic evaluation of ventricular asynchrony. *J Am Coll Cardiol*. 2002;40:1615–1622
24. Pitzalis MV, Iacoviello M, Romito R, et al Ventricular asynchrony predicts a better outcome in patients with chronic heart failure receiving cardiac resynchronization therapy. *J Am Coll Cardiol*. 2005;45:65–69
25. Marcus GM, Rose E, Viloria EM, et al VENTAK CHF/CONTAK-CD Biventricular Pacing Study Investigators. Septal to posterior wall motion delay fails to predict reverse remodeling or clinical improvement in patients undergoing cardiac resynchronization therapy. *J Am Coll Cardiol*. 2005;46:2208–2214
26. Bleeker GB, Schalij MJ, Boersma E, et al Relative merits of M-mode echocardiography and tissue Doppler imaging for prediction of response to cardiac resynchronization therapy in patients with heart failure secondary to ischemic or idiopathic dilated cardiomyopathy. *Am J Cardiol*. 2007;99:68–74
27. Rouleau F, Merheb M, Geffroy S, et al Echocardiographic assessment of the interventricular delay of activation and correlation to the QRS width in dilated cardiomyopathy. *Pacing Clin Electrophysiol*. 2001;24:1500–1506
28. Ghio S, Constantin C, Klersy C, et al Interventricular and intraventricular dyssynchrony are common in heart failure patients, regardless of QRS duration. *Eur Heart J*. 2004;25:571–578
29. Bax JJ, Bleeker GB, Marwick TH, et al Left ventricular dyssynchrony predicts response and prognosis after cardiac resynchronization therapy. *J Am Coll Cardiol*. 2004;44:1834–1840
30. Penicka M, Bartunek J, De Bruyne B, et al Improvement of left ventricular function after cardiac resynchronization therapy is predicted by tissue Doppler imaging echocardiography. *Circulation*. 2004;109:978–983
31. Gorcsan J III, Kanzaki H, Bazaz R, Dohi K, Schwartzman D. Usefulness of echocardiographic tissue synchronization imaging to predict acute response to cardiac resynchronization therapy. *Am J Cardiol*. 2004;93:1178–1181
32. Notabartolo D, Merlino JD, Smith AL, et al Usefulness of the peak velocity difference by tissue Doppler imaging technique as an effective predictor of response to cardiac resynchronization therapy. *Am J Cardiol*. 2004;94:817–820
33. Yu CM, Fung JW, Zhang Q, et al Tissue Doppler imaging is superior to strain rate imaging and postsystolic shortening on the prediction of reverse remodeling in both ischemic and nonischemic heart failure after cardiac resynchronization therapy. *Circulation*. 2004; 110:66–73
34. Van de Veire NR, Bleeker GB, De Sutter J, et al Tissue synchronisation imaging accurately measures left ventricular dyssynchrony and predicts response to cardiac resynchronisation therapy. *Heart*. 2007;93:1034–1039
35. Yu CM, Zhang Q, Wing-Hong Fung J, et al A novel tool to assess systolic asynchrony and identify responders of cardiac resynchronization therapy by tissue synchronization imaging. *J Am Coll Cardiol*. 2005;45:677–684
36. Van de Veire NR, Bleeker GB, Ypenburg C, et al Usefulness of triplane tissue Doppler imaging to predict acute response to cardiac resynchronization therapy. *Am J Cardiol*. 2007;100:476–482
37. Van de Veire NR, Yu CM, Ajmone-Marsan N, et al Triplane tissue Doppler imaging: a novel three-dimensional imaging modality that predicts reverse left ventricular remodeling after cardiac resynchronization therapy. *Heart*. 2008;94:e9
38. Yu CM, Gorcsan J III, Bleeker GB, et al Usefulness of tissue Doppler velocity and strain dyssynchrony for predicting left

ventricular reverse remodeling response after cardiac resynchronization therapy. *Am J Cardiol*. 2007;100:1263–1270
39. Dohi K, Sufoletto MS, Schwartzman D, Ganz L, Pinsky MR, Gorcsan J III. Utility of echocardiographic radial strain imaging to quantify left ventricular dyssynchrony and predict acute response to cardiac resynchronization therapy. *Am J Cardiol*. 2005;96:112–116
40. Leitman M, Lysyansky P, Sidenko S, et al Two-dimensional strain - a novel software for real-time quantitative echocardiographic assessment of myocardial function. *J Am Soc Echocardiogr*. 2004; 17:1021–1029
41. Suffoletto MS, Dohi K, Cannesson M, Saba S, Gorcsan J III. Novel speckle-tracking radial strain from routine black-and-white echocardiographic images to quantify dyssynchrony and predict response to cardiac resynchronization therapy. *Circulation*. 2006;113:960–968
42. Delgado V, Ypenburg C, van Bommel RJ, et al Assessment of left ventricular dyssynchrony by speckle tracking strain imaging comparison between longitudinal, circumferential and radial strain in cardiac resynchronization therapy. *J Am Coll Cardiol*. 2008;51: 1944–1952
43. Kapetanakis S, Kearny MT, Siva A, Gall N, Cooklin M, Monaghan MJ. Real-time three-dimensional echocardiography: a novel technique to quantify global left ventricular mechanical dyssynchrony. *Circulation*. 2005;112:992–1000
44. Ajmone Marsan N, Bleeker GB, Ypenburg C, et al Real-time three-dimensional echocardiography as a novel approach to assess left ventricular and left atrium reverse remodeling and to predict response to cardiac resynchronization therapy. *Heart Rhythm*. 2008;5:1257–1264
45. Boogers MM, Chen J, Bax JJ. Myocardial perfusion single photon emission computed tomography for the assessment of mechanical dyssynchrony. *Curr Opin Cardiol*. 2008;23:431–439
46. Botvinick EH, O'Connell JW, Kadkade PP, et al Potential added value of three-dimensional reconstruction and display of single photon emission computed tomographic gated blood pool images. *J Nucl Cardiol*. 1998;5:245–255
47. Chen J, Garcia EV, Folks RD, et al Onset of left ventricular mechanical contraction as determined by phase-analysis of ECG gated myocardial perfusion SPECT imaging: development of a diagnostic tool for assessment of mechanical dyssynchrony. *J Nucl Cardiol*. 2005;12:687–695
48. Henneman MM, Chen J, Ypenburg C, et al Phase analysis of gated myocardial perfusion SPECT compared to tissue Doppler imaging for the assessment of ventricular dyssynchrony. *J Am Coll Cardiol*. 2007;49:1708–1714
49. Ajmone NA, Henneman MM, Chen J, et al Left ventricular dyssynchrony assessed by two three-dimensional imaging modalities: phase analysis of gated myocardial perfusion SPECT and tri-plane tissue Doppler imaging. *Eur J Nucl Med Mol Imaging*. 2008;35: 166–173
50. Henneman MM, Chen J, Dibbets-Schneider P, et al Can LV dyssynchrony as assessed with phase analysis on gated myocardial perfusion SPECT predict response to CRT? *J Nucl Med*. 2007;48: 1104–1111
51. Lardo AC, Abraham TP, Kass DA. Magnetic resonance imaging. Assessment of ventricular dyssynchrony. Current and emerging concepts. *J Am Coll Cardiol*. 2005;46:2223–2228
52. Helm RH, Lardo AC. Cardiac magnetic resonance assessment of mechanical dyssynchrony. *Curr Opin Cardiol*. 2008;23:440–446
53. Rüssel IK, Zwanenburg JJ, Germans T, et al Mechanical dyssynchrony or myocardial shortening as MRI predictor of response to biventricular pacing. *J Magn Reson Imaging*. 2007;26:1452–1460
54. Westenberg JJ, Lamb HJ, van der Geest RJ, et al Assessment of left ventricular dyssynchrony in patients with conduction delay and idiopathic dilated cardiomyopathy: head-to-head comparison between tissue Doppler imaging and velocity-encoded magnetic resonance imaging. *J Am Coll Cardiol*. 2006;47:2042–2048
55. Da Costa A, Thévenin J, Roche F, et al Prospective validation of stress echocardiography as an identifier of cardiac resynchronization therapy responders. *Heart Rhythm*. 2006;3:406–413
56. Ypenburg C, Sieders A, Bleeker GB, et al Myocardial contractile reserve predicts improvement in left ventricular function after cardiac resynchronization therapy. *Am Heart J*. 2007;154:1160–1165
57. Hummel JP, Linder JR, Belcik JT, et al Extent of myocardial viability predicts response to biventricular pacing in ischemic cardiomyopathy. *Heart Rhythm*. 2005;11:1211–1217
58. De Winter O, Van de Veire N, Van Heuverswyn F, Van Pottelberge G, Gillebert TC, De Sutter J. Relationship between QRS duration, left ventricular volumes and prevalence of nonviability in patients with coronary artery disease and severe left ventricular dysfunction. *Eur J Heart Fail*. 2006;8:275–277
59. Ypenburg C, Schalij MJ, Bleeker GB, et al Extent of viability to predict response to cardiac resynchronization therapy in ischemic heart failure patients. *J Nucl Med*. 2006;47:1565–1570
60. Ypenburg C, Schalij MJ, Bleeker GB, et al Impact of viability and scar tissue on response to cardiac resynchronization therapy in ischaemic heart failure patients. *Eur Heart J*. 2007;28:33–41
61. Bleeker GB, Kaandorp TA, Lamb HJ, et al Effect of posterolateral scar tissue on clinical and echocardiographic improvement after cardiac resynchronization therapy. *Circulation*. 2006;113:969–976
62. Ypenburg C, Roes SD, Bleeker GB, et al Effect of total scar burden on contrast-enhanced magnetic resonance imaging on response to cardiac resynchronization therapy. *Am J Cardiol*. 2007;99:657–660
63. von Lüdinghausen M. The venous drainage of the human myocardium. *Adv Anat Embryol Cell Biol*. 2003;168:1–107
64. Abbara S, Cury RC, Nieman K, et al Noninvasive evaluation of cardiac veins with 16-MDCT angiography. *Am J Roentgenol*. 2005;185:1001–1006
65. Tada H, Naito S, Koyama K, Taniguchi K. Three-dimensional computed tomography of the coronary venous system. *J Cardiovasc Electrophysiol*. 2003;14:385
66. Mühlenbruch G, Koos R, Wildberger JE, Günther R, Mahnken AH. Imaging of the cardiac venous system: comparison of MDCT and conventional angiography. *AJR*. 2005;185:1252–1257
67. Jongbloed MRM, Lamb HJ, Bax JJ, et al Noninvasive visualization of the cardiac venous system using multislice computed tomography. *J Am Coll Cardiol*. 2005;45:749–753
68. Van de Veire N, Schuijf JD, De Sutter J, et al Non-invasive visualization of the cardiac venous system in coronary artery disease patients using 64-slice computed tomography. *J Am Coll Cardiol*. 2006;48:1832–1838
69. Blendea D, Shah RV, Auricchio A, et al Variability of coronary venous anatomy in patients undergoing cardiac resynchronization therapy: a high-speed rotational venography study. *Heart Rhythm*. 2007;4:1163–1164
70. Van de Veire NR, Ajmone-Marsan N, Schuijf JD, et al Non-invasive imaging of cardiac venous anatomy with 64-slice multi-slice computed tomography and non-invasive assessment of left ventricular dyssynchrony by 3-dimensional tissue synchronization imaging in patients with heart failure scheduled for cardiac resynchronization therapy. *Am J Cardiol*. 2008; 101:1023–1029
71. Nezafat R, Han Y, Peters DC, et al Coronary magnetic resonance vein imaging: imaging contrast, sequence, and timing. *Magn Reson Med*. 2007;58:1196–1206
72. Chiribiri A, Kelle S, Götze S, Visualization of the cardiac venous system using cardiac magnetic resonance. *Am J Cardiol*. 2008;101: 407–412
73. Chung ES, Leon AR, Tavazzi L, et al Results of the predictors of response to CRT (PROSPECT) trial. *Circulation*. 2008;117: 2608–2616

74. Murphy RT, Sigurdsson G, Mulamalla S, et al Tissue synchronization imaging and optimal left ventricular pacing site in cardiac resynchronization therapy. *Am J Cardiol*. 2006;97:1615–1621
75. Ypenburg C, van Bommel RJ, Delgado V, et al Optimal left ventricular lead position predicts reverse remodeling and survival after cardiac resynchronization therapy. *J Am Coll Cardiol*. 2008; 52:1402–1409
76. De Martino G, Messano L, Santamaria M, et al A randomized evaluation of different approaches to coronary sinus venography during biventricular pacemaker implants. *Europace*. 2005;7:73–76

Chapter 21

CARDIAC RESYNCHRONIZATION THERAPY: OPTIMIZATION AND FOLLOW-UP

Marta Sitges and Genevieve Anne Derumeaux

CONTENTS

J. L. Zamorano et al. (eds.), *The ESC Textbook of Cardiovascular Imaging*
DOI: 10.1007/978-1-84882-421-8_21, © Springer-Verlag London Limited 2010

Introduction

While the role of cardiac imaging in the selection of candidates for cardiac resynchronization therapy (CRT) remains controversial, it is well established that imaging is essential to establish an objective evidence of response to the therapy. Also, in the absence of other well-validated methodology, echocardiography stands as the reference method to optimize the programming of the device in many instances. In the present chapter, the role of cardiac imaging in optimizing the programming of CRT devices as well as the usefulness in the follow-up of patients treated with CRT will be discussed.

Optimization

Rationale for Optimizing the Programming of the Device

In patients with heart failure, the presence of a prolonged AV interval is not unusual. Also, left bundle branch block is present in up to one-third of these patients. Both prolonged AV interval and LBBB result in delayed ejection, and consequently, in shortened diastolic time (Fig. 21.1). This leads to shortened filling time, decreased pre-load, and the consequent decrease in stroke volume, which is especially important in patients with left ventricular systolic dysfunction. Restoring adequate AV interval and intra-ventricular conduction delays results in a longer filling time and an increased pre-load. However, excessively short AV delays may result in early closure of the mitral valve, impeding the whole contribution of the atrial contraction to left ventricular filling (A wave truncation). Consequently, finding the optimum AV delay that yields the longest diastolic filling time without truncating the atrial contribution to ventricular filling is of most interest.

On the other hand, devices now have the capability of programming the time sequence and intervals to stimulate both ventricles. Optimization of the inter-ventricular (VV) delay may be justified according to several issues. First, obtaining a good ventricular synchronization may constitute a goal to achieve and may explain why patients in atrial fibrillation also benefit from CRT, besides the benefit on diastolic filling due to optimized AV intervals. Additionally, the epicardial position of the lead implies that trans-mural activation, usually lasting for 30 ms, should be taken into account when considering time delays between both ventricles. Finally, delayed ventricular segments may be located at different sites of the left ventricle due to underlying myocardial scars or different conduction abnormalities; consequently, dyssynchrony may be corrected with different device programming.

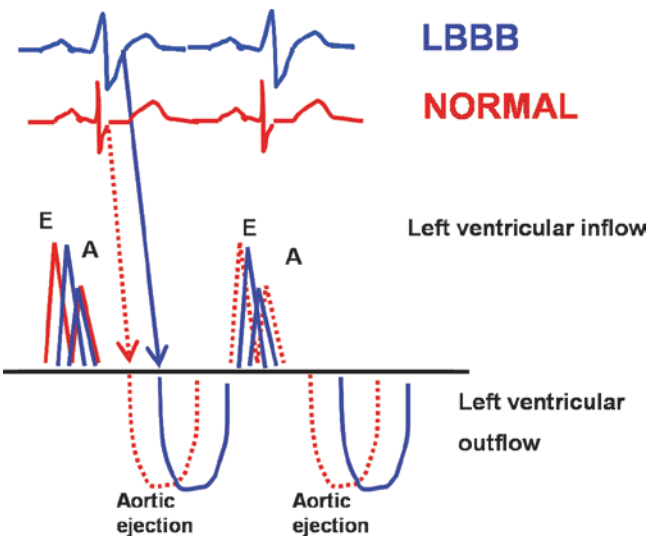

Fig. 21.1 Patients with LBBB have delayed aortic ejection as a consequence of their delayed conduction and mechanical contraction. Delayed aortic ejection results in shortened diastolic time, which, in turn, causes fusion of the E and A wave of the left ventricular filling flow

How to Optimize the Programming of CRT Devices with Imaging

Optimization of the AV Delay

The optimization of the AV interval involves different methodologies, the aim of which is to obtain the greatest diastolic filling time and the optimum haemodynamic effect. Echocardiography typically has been used for such purposes; however, there are also many other methods based on invasive approaches (assessment of dP/dt and cardiac output with catheters at the time of the implantation) and non-invasive approaches (impedance cardiography, intra-cardiac electrograms, endocardial acceleration detected by a micro-accelerometer, or algorithms based on electric intervals detected by the device). The big advantage of these latter methods is that they are incorporated in the device, can be performed automatically, and continuously allow for adaptative optimization of the AV interval according to physical activity or heart rate. The limitation is that these methodologies are not well validated and are limited to each vendor's device. On the other hand, experience demonstrating the benefits of AV interval optimization has been mainly limited to dual chamber pacing rather than CRT. However, most of the

large clinical trials proving the clinical benefit of CRT, such as the Multicenter InSync Randomized Clinical Evaluation (MIRACLE) or the Cardiac Resynchronization-Heart Failure (CARE-HF), have performed AV optimization with echocardiography. Accordingly, AV optimization using echocardiography is recommended and most commonly used.[1]

The most used echocardiographic method to optimize the AV delay is the iterative method. By the use of PW Doppler of the left ventricular inflow, diastolic filling time is measured from the onset of the E wave to the end of the A wave. The AV delay is reduced by 10–20 ms until the longest diastolic filling time is obtained without interrupting the A wave (Fig. 21.2). Another approach derived from dual chamber pacing in patients with AV block and not validated in CRT is the Ritter's method. This calculates the optimum AV interval by calculations derived from a setting with a very long AV delay and another one with a very short AV delay. For each AV delay, the time from QRS onset to the end of the A wave is determined, and the optimum AV delay is calculated by a formula $((AV_{opt}\text{-}AV_{long})-(QA_{short}\text{-}QA_{long}))$. This optimum AV corresponds to the longest diastolic filling time without interrupting the A wave, resulting in similar AV delays to those obtained by the iterative method but in a shorter procedure.

Another approach to optimize the AV delay with echocardiography has been proposed by determining the maximum mitral inflow or the aortic velocity-time integral, both as surrogates of the left ventricular cardiac output. In one study including 30 patients, the optimization of the AV delay with these four echocardiographic methods was compared to invasive dP/dt. The optimum AV delay invasively determined was largely concordant with the one determined by the maximum mitral velocity-time integral (97%), while there was no agreement with the AV delay determined by Ritter's method.[2] Agreement of dP/dt with the iterative method and the aortic velocity-time integral was modest (67 and 43%, respectively).

The AV delay has also been optimized by echocardiography with similar iterative methods that aim to obtain the largest cardiac output as determined by the left ventricular outflow tract velocity-time integral (as a surrogate of cardiac

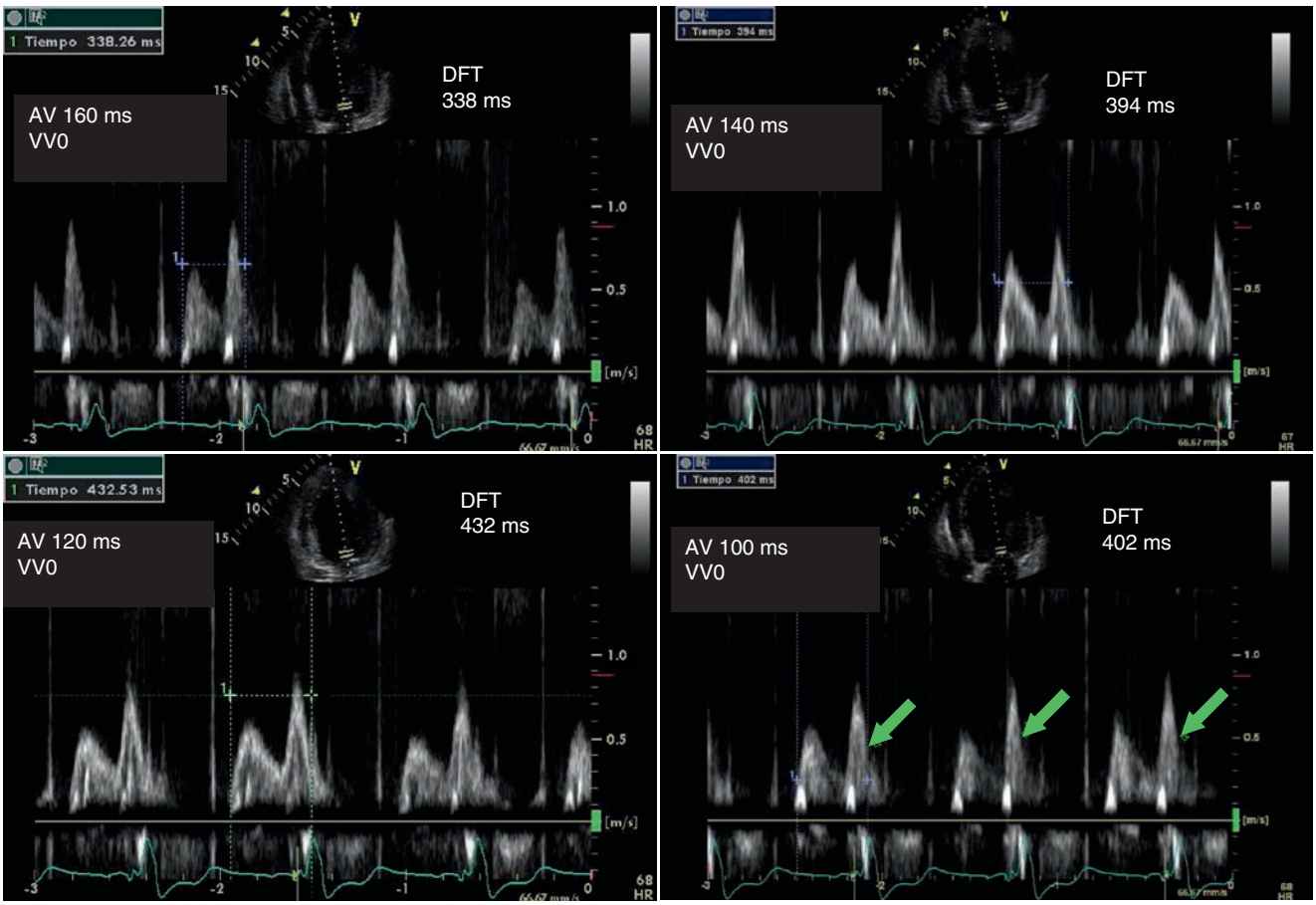

Fig. 21.2 Optimization of the AV interval according to the iterative method: The AV interval is progressively reduced at 20 ms intervals trying to obtain the largest diastolic filling time and, consequently, the largest left ventricular filling. As the AV interval decreases, the diastolic filling time increases until the A wave is early interrupted (*green arrows*). Accordingly, the optimum AV interval selected in this case patient was AV 120 ms, which yielded the largest diastolic filling time without interrupting the A wave

output) or the Doppler-derived left ventricular d*P*/d*t*, as well as the myocardial performance index (Tei index). Again, the widespread use and, especially, the validation and utility of the methodologies among CRT patients remain uncertain.

The Ishikawa echocardiographic method relies on the minimization or elimination of diastolic mitral regurgitation to select the optimum AV delay by substracting the duration of the diastolic mitral regurgitation to the AV delay programmed to induce it. Finally, other echocardiographic approaches such as the Meluzin and the Ismer methods combine electric data to optimize the AV delay and are rarely used in CRT.

Optimization of the VV Delay

The VV delay can be optimized by determining invasive left ventricular d*P*/d*t* or cardiac output by the surface ECG or by a variety of device-based algorithms or intra-cardiac electrograms. Echocardiography has also been used to optimize the VV delay either by empirically assessing the VV delay, which yields the largest cardiac output, or the best left ventricular synchrony. The most commonly used echocardiographic method for VV delay optimization is the evaluation of cardiac output determined by the left ventricular outflow tract velocity-time integral. Several VV delays are programmed at 20 ms interval, and the effect on cardiac output is tested (Fig. 21.3). Few authors have also used Tissue Doppler to evaluate left ventricular synchrony and optimize the VV delay, by testing the effect of several VV intervals on left ventricular dyssynchrony, assessed with tissue displacement, or strain rate traces of opposite myocardial walls (Fig. 21.4, Video 21.4). A small study has reported a good agreement between optimization of the VV interval according to either left ventricular outflow tract velocity-time integral or intra-ventricular dyssynchrony, indicating that the best intra-ventricular synchrony results in the best haemodynamics.[3]

Impact of Optimization of CRT Programming

Acute Effect of Optimization of the Programming of CRT Devices

Several groups have reported the beneficial acute effect of optimization of the CRT programming on haemodynamics and left ventricular dyssynchrony either by invasive or non-invasive methods. Early on the clinical application of CRT, Auricchio et al. already demonstrated an acute incremental benefit on cardiac output and pulse aortic pressure by small changes in the AV delay.[4] Similarly, optimized VV delay has resulted in larger d*P*/d*t* (up to 8% increase), especially by pre-activating the left ventricle (%).[5] When the VV delay has been optimized with echocardiography, mainly by using an iterative method to reach the largest aortic or left ventricular outflow tract velocity-time integral, an additional five point increase in left ventricular ejection fraction (LVEF) and a 20% in cardiac output have been reported; also an incremental reduction in dyssynchrony and a reduction in the number of ventricular segments with delayed contraction have been demonstrated.[6–9] On the other hand, selecting a non-optimal VV delay may have a deleterious impact, reducing cardiac output by even more than 25%.[6, 9]

Effect of Optimization of the Programming of CRT Devices on Clinical Outcomes

Despite compelling evidence that AV and VV delay optimization may have an acute haemodynamic beneficial effect, scarce evidence supports the clinical impact of such an optimization.

Few studies have evaluated the impact of optimizing the AV interval by echocardiography on clinical outcomes. Most

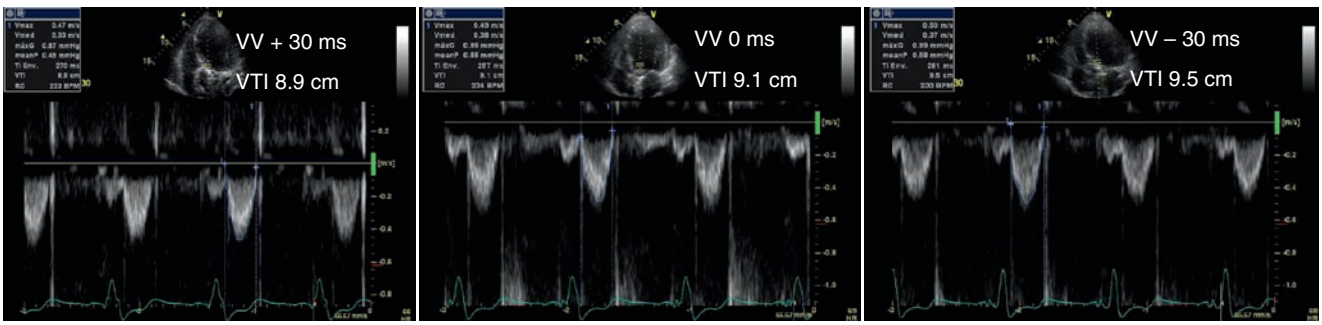

Fig. 21.3 Optimization of the VV interval according to the iterative method using left ventricular outflow tract velocity-time integral: The VV interval is tested to obtain the largest velocity-time integral. In this patient, despite a variation that was not large, optimum VV was set at −30 ms (left ventricular pre-activation at 30 ms) because this yielded the largest velocity-time integral

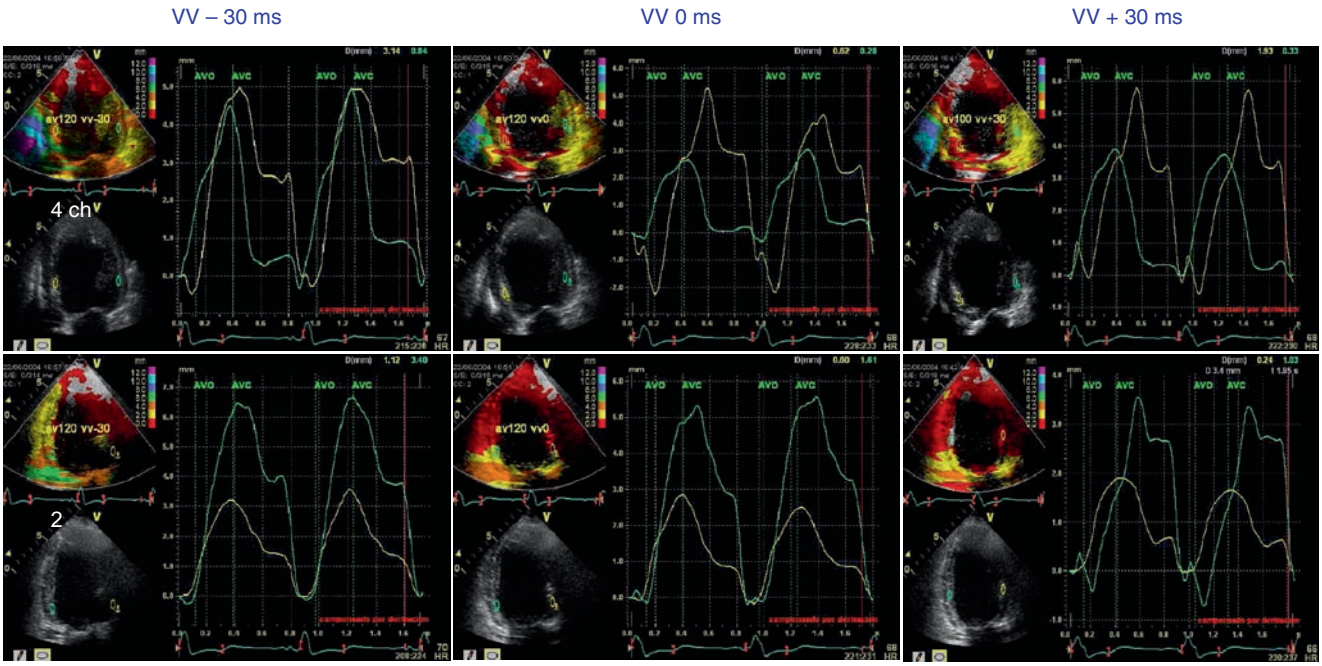

Fig. 21.4 Optimization of the VV interval according to the iterative method using left ventricular dyssynchrony: The superposition of the displacement of two opposing walls is evaluated both in the 4- and 2-chamber apical walls with tissue Doppler imaging. The superposition and the amount of displacement were maximal with the setting of a VV interval of −30 ms, especially patent in the 4-chamber traces. In the 2-chamber images, there are no significant changes among the different VV intervals. These images come from the same patient shown in Fig. 21.3. The selected optimum VV interval was the same either by the velocity-time integral or dyssynchrony assessment. Quantitative and semi-qualitative analysis of intra-ventricular dyssynchrony or quantification of aortic velocity-time integral provided useful information to select the optimum VV interval. However, only when visual assessment of left ventricular motion was analyzed (Video 21.4), no clear selection could be taken; there was a slight improvement on left ventricular motion with VV 0 ms and VV −30 ms as compared to without CRT (OFF) and to VV +30 ms. No significant difference could be observed between VV 0 and −30 ms

of them were carried among patients with dual-chamber pacemakers without heart failure, and none demonstrated an improvement on clinical outcomes; techniques used to optimize the delay and outcome definition were also different between authors. Among CRT patients, few studies have used optimization only of the AV interval and evaluated the clinical evolution. One study reported optimization of the AV delay by maximizing the left ventricular outflow tract velocity-time integral in 33 patients which resulted in improvements in functional capacity and plasma BNP;[10] however, this effect could have resulted simply from CRT, and the lack of a control group precludes conclusions regarding the effect of AV delay optimization alone. Only two small studies have analyzed the clinical impact of AV delay optimization in CRT as compared to a control group with CRT and an empirical AV delay of 120 ms. Sawhney et al.[11] compared AV delay optimization by echocardiography (iterative method using aortic velocity-time integral) to an empirical AV delay set at 120 ms in a randomized study of 40 patients with CRT, finding an improvement in quality of life and NYHA functional class without differences in LVEF or volumes, or in the distance walked in the 6 min walking test. Morales et al.[12] also studied 41 patients with CRT who were randomized to receive an empirical AV delay of 120 ms or to optimize their AV delay with echo Doppler-derived d*P*/d*t*. At 6-month follow-up, LVEF was significantly higher and NYHA functional class significantly lower in the AV-optimized group.

Regarding the clinical impact of VV interval optimization, reports have also been scarce. Mortensen et al. reported the acute beneficial effects on haemodynamics of VV delay optimization with echocardiography (left ventricular outflow tract velocity-time integral), but they were unable to show any additional clinical improvement in the optimized group as compared to the conventional simultaneous biventricular pacing at 3-month follow-up.[9]

In another study, the 6-month clinical outcome of 359 patients included in the InSync III Study and who received VV delay optimization with echocardiography (iterative method using the left ventricular outflow tract velocity-time integral) were also compared against the outcome of the patients included in the MIRACLE study. All patients received AV delay optimization with echocardiography. There was an incremental benefit on the distance walked in the 6 min walking test (median increase in the InSync 38 vs. 15% in the MIRACLE, $p < 0.0001$), while no differences in quality of life or in NYHA functional class could be demonstrated.[ff]

The only randomized study trying to demonstrate the beneficial clinical effect of VV delay optimization has been the RHYTHM II ICD study, which included 121 patients with CRT. AV delay was optimized in all patients. VV delay was optimized only in randomly assigned patients by using echocardiography (with the maximum aortic velocity-time integral). Similarly to previous findings, VV optimization conferred no benefit in the distance walked in the 6 min test, quality of life, NYHA functional class, or hospital admissions.[14] The results of these echocardiography-based optimization studies are in keeping with the observations found in another trial that used a device-based algorithm to optimize the VV delay; in this study, sequential pacing was equivalent, but not superior, to simultaneous biventricular pacing for the composite endpoint of peak oxygen consumption and left ventricular end-systolic dimension.[15]

Finally, the effect of optimizing both the AV and the VV delay was studied in a single centre study comparing two historical cohorts of CRT patients: the first 50 patients with an empirical AV delay set at 120 ms and simultaneous biventricular pacing and the next 51 patients undergoing a standardized systematic echocardiographic optimization of the programming of the AV and VV intervals.[3] In brief, the optimum AV delay was chosen among 160, 140, and 120 ms according to the one that yielded the longest diastolic filling time without truncating the A wave. Once the optimum AV delay was chosen, the VV interval was optimized and selected from 30 ms pre-activation of the right ventricle (+30 ms), simultaneous biventricular pacing (0 ms), and 30 ms pre-activation of the left ventricle (−30 ms); the optimum VV interval was selected as the one that resulted in larger superposition of the systolic displacement of two opposing ventricular walls with the use of Tissue Doppler (i.e. less dyssynchrony) (Fig. 21.4). Patients receiving optimization walked more distance in the 6 min test and showed larger left ventricular cardiac output at 6-month follow-up; however, there were no differences in NYHA functional class, quality of life, LVEF, and dimensions, and more importantly, in the rate of cardiac death or heart transplantation. Indeed, the primary endpoint, which was a combination of non-improvement in the 6 min walking test, heart transplantation, or cardiac death, was equivalent in both groups.

Limitations and Unresolved Questions

Many questions remain unanswered regarding optimization of the programming of CRT devices. Methodology is not completely standardized, despite most groups using the iterative method both for the AV and the VV delay, trying to obtain the largest diastolic filling time without truncating the A wave and the largest aortic velocity-time integral r, the best intra-ventricular dyssynchrony. However, still little is known about the interaction between the AV and VV delays programming. Indeed, most authors have reported a stepwise optimization usually starting with the AV and finishing with the VV. The impact of optimizing the VV first and then the AV delay is unknown.

Also, the equivalence between different methods is far from being established, especially regarding the programming of the AV delay. Another matter of controversy is the stability of the programming of the delay through follow-up when reverse ventricular re-modelling develops and potentially impacts on AV and VV delays. Should the AV and VV delays, therefore, periodically be optimized? How often?

Finally, the cost-efficacy of programming the device with imaging has to be taken into consideration. According to the time and resource consumption of the optimization procedure, routine empirical programming has been proposed leaving optimization for selected non-responder patients. Also, the role of optimization of the AV and VV delays in patients with narrow QRS receiving CRT is completely unexplored.

Because most of the major clinical trials demonstrating the beneficial effect of CRT have employed AV optimization, currently accepted recommendations are to routinely optimize AV delay with echocardiography with the Ritter's or the iterative method. Regarding VV delay optimization, no consensus exists, except that simple and widely available methods should be implemented.

Follow-Up of Patients Treated with CRT

Reversing Left Ventricular Re-modelling in Heart Failure

The deleterious action of incoordination on myocardial contractility and geometry has been extensively considered with the development of non-invasive cardiac imaging and has gained interest as the basis of effect of the resynchronization therapy. In heart disease, both intra- and inter-ventricular asynchronous activation have marked adverse consequence on ventricular pump function leading to prolonged contraction, reduced ejection time, delayed and prolonged relaxation, reduced diastolic filling time, and mitral regurgitation.[16] The overall result is left ventricular re-modelling, which is a dynamic process characterized by a progressive chamber dilatation, a distortion of cavity shape towards sphericity, a disruption of the mitral valve geometry with tenting and occurrence of mitral regurgitation, and deterioration in contractile function that culminates in heart failure.[17–19] The left ventricular re-modelling process is the final common pathway for all of the causes of heart failure and portends a poor prognosis.

Therefore, left ventricular re-modelling itself represents a new target for therapeutic interventions to attenuate progression of left ventricular re-modelling to heart failure.

Most of these deleterious effects can be improved by CRT. The two primary targets of CRT are modifying the pattern of left ventricular activation and the delay between atrial and ventricular systole. Synchrony of contraction is important because it results in more effective and energetically efficient ejection. Indeed, the clinical success of CRT attests to the importance of dyssynchrony in the pathophysiology of heart failure.

CRT often results in "reverse" re-modelling where left ventricular size and function progressively improve over time. "Reverse" re-modelling is, therefore, a new concept where deterioration in systolic function and left ventricular dilatation are not simply stopped, but partially reversed. Cardiac imaging techniques play a key role in the diagnosis of reverse re-modelling and especially echocardiography, which is easily applied in the follow-up of these patients. Currently used MRI systems still have the limitation on their application among patients with pacemakers.

Evidence for Reverse Re-modelling from Randomized Clinical Trials of CRT

CRT often results in reverse re-modelling where left ventricular size and function progressively improve over time (Fig. 21.5, Video 21.5). This is a CRT-dependent, dynamic process where subsequent cessation of CRT results in progressive deterioration in left ventricular function towards baseline values. Consistent findings both in small, uncontrolled trials and in large, randomized and double-blind CRT trials have been the incremental beneficial effects of CRT (i.e. improvement in exercise capacity, NYHA class, and quality of life) in patients with heart failure and optimal medical heart failure therapy. The changes in structural and functional left ventricular remodelling associated with CRT have also been documented in CRT studies by echocardiography and are coincident with improvement in symptoms and exercise capacity. The effects of CRT on reverse ventricular re-modelling are additive and to a larger degree than those observed with medical therapy.

The MIRACLE was the first large randomized double-blind study.[20] All 453 patients had heart failure therapy optimized prior to enrollment and if they remained in class III-IV, had LVEF ≤35%, QRS duration ≥130 ms, and an left ventricular end-diastolic diameter ≥55 mm. The MIRACLE study demonstrated that the benefits of CRT on 6-min walk distance, NYHA class, and quality of life occurred predominantly, but not exclusively, in the patients with objective improvement in left ventricular geometry and function. Significant reductions in left ventricular end-diastolic and end-systolic volumes were demonstrated at 3 and 6 months in the CRT group compared with the control group (inactive pacing), in which no change was observed from baseline values. In addition, left ventricular mass also significantly decreased, whereas left ventricular contractile function increased in the CRT group, but not in the control group. These beneficial effects on left ventricular re-modelling were sustained after 2-year follow-up.

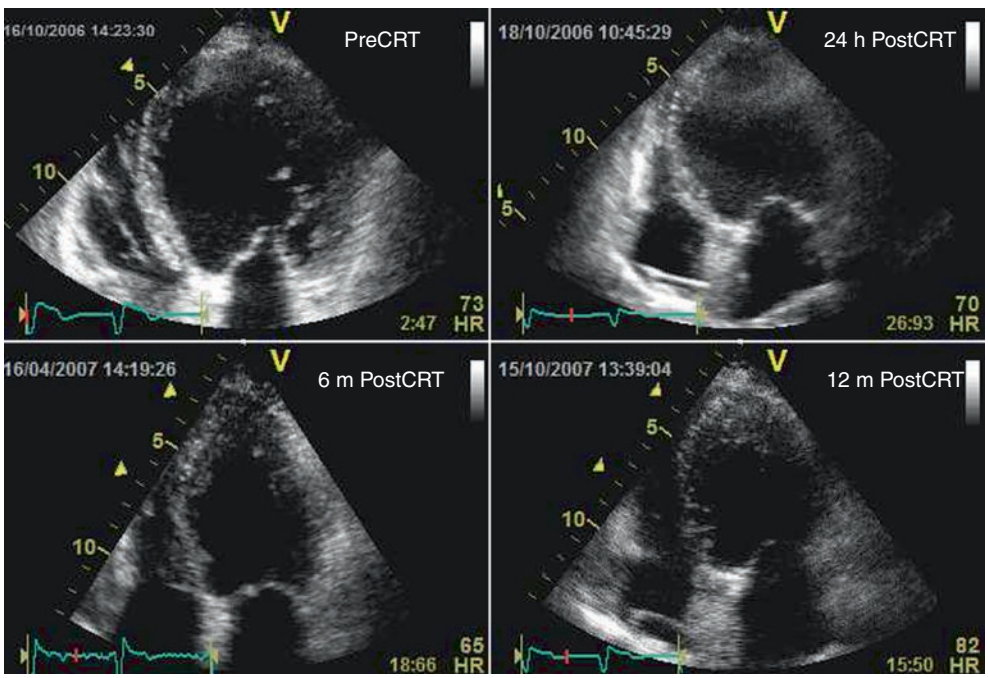

Fig. 21.5 Progressive left ventricular reverse re-modelling in a patient effectively treated with CRT: 4-chamber apical view of the left ventricle at baseline and after CRT at different time points during 1 year. The reduction in the left ventricular size can be progressively observed as well as the improvement in systolic function

Three clinical trials demonstrated that continuous (rather than intermittent) CRT induces a progressive and sustained reduction in left ventricular size and volumes. MUSTIC trial was the first to show sustained reduction in left ventricular size measured by echocardiography at 1 year in a small cohort of patients.[21] With the results of CARE-HF study, it is now evident that reverse left ventricular re-modelling and associated symptomatic improvement continues for at least 18 months after initiation of CRT.[22] The CARE-HF trial examined the effects of CRT alone on morbidity and mortality in 819 high-risk heart failure patients with ventricular dyssynchrony (LVEF ≤35%, QRS duration >150 ms or if QRS duration of 120–150 ms when there was echo-Doppler evidence of ventricular dyssynchrony).[22] CRT reduced the time to death or hospitalization by 37% ($p < 0.001$), and all cause mortality by 36% ($p < 0.002$) compared to medical therapy alone. This important study was the first to demonstrate conclusively that CRT alone can reduce mortality, presumably by favourable effects on left ventricular function. In addition, reverse left ventricular re-modelling was assessed at 3 and 18 months, showing a significant and sustained increase in LVEF (+3.7 and +6.9%, respectively) associated with a decrease in left ventricular end-systolic volume index (−18.2 and −26 mL/m^2, respectively) and in mitral regurgitation area.

Most of the landmark studies of CRT chose a LVEF ≤35% as an entry criterion, but recently the REVERSE study raised the threshold to 40% and showed that the benefit in terms of recovery of left ventricular function and in morbidity and mortality was similar to that observed in CARE-HF.[23] The REVERSE study enrolled 684 patients with NYHA functional class I or II, in sinus rhythm, with QRS duration ≥120 ms, left ventricular end-diastolic diameter ≥55 mm and LVEF ≤40%. After baseline evaluation, all patients underwent CRT implantation with or without ICD and were randomly assigned to active CRT (CRT-ON) or to control (CRT-OFF). The left ventricular end-systolic volume index improved (−18.4 ± 29.5 mL/m^2) in the CRT-ON group (n = 324) compared with the CRT-OFF group (−1.3 ± 23.4 mL/m^2; n = 163; $p < 0.0001$). The observed reduction in left ventricular end-systolic volume index in CRT-ON patients was three times greater in the non-ischaemic group than in patients with an ischaemic aetiology of heart failure, but was of similar magnitude in patients in NYHA functional class I and II. LVEF also improved significantly with active CRT, but not in the CRT-OFF group. It is noteworthy that 95% of patients included in the REVERSE trial received an angiotensin-converting enzyme inhibitor or an angiotensin I receptor blocker, and a beta-adrenergic blocker for ≥3 months, and that 60% received ≥50% of the target dose and ≥30% the full target dose of beta-adrenergic blocker. By comparison with the most recent HF trials and actual clinical practice, the pharmacological management in the REVERSE trial was optimal. This result suggests that CRT produces significant additive effects on ventricular re-modelling that occur in addition to HF drug therapy.

Predictors of Left Ventricular Reverse Re-modelling with CRT

The clinical response to CRT is variable, and, so far, its prediction from baseline variables has met with limited success. Left ventricular reverse re-modelling does not occur in all patients (Figs. 21.6 and 21.7, Videos 21.6a, b, and 21.7a, b). Between two-thirds and three-quarters of patients exhibit reverse left ventricular re-modelling with CRT. There is no current consensus on baseline clinical data that may predict an optimal left ventricular reverse re-modelling before device implantation. Among the number of possible mechanisms that have been proposed, the absence of mechanical left ventricular dyssynchrony, the advanced and irreversible left ventricular dysfunction, and the sub-optimal placement of the leads are the most likely causes.

Several studies have suggested a potential role for echocardiography to direct left ventricular lead placement through identification of the anatomic site of latest mechanical activation. Ansalone et al. were among the first to show that left ventricular lead placement concordant with the site

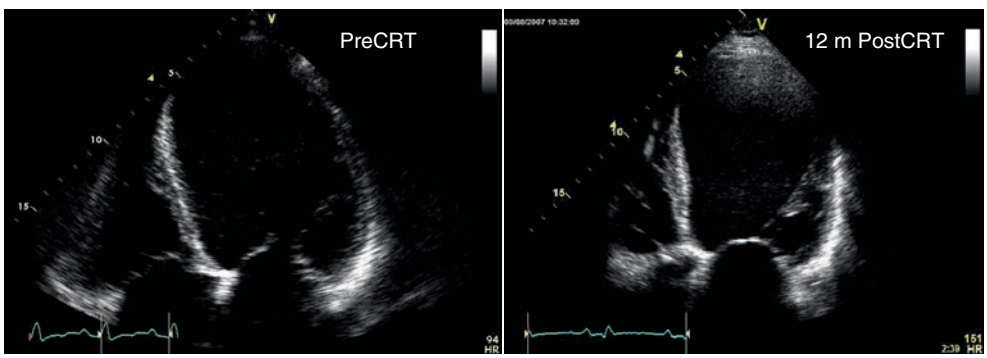

Fig. 21.6 An example of a patient who did not show reverse re-modelling after 12 months CRT: 4-chamber apical view of the left ventricle before (Video 21.6a) and 12 months (Video 21.6b) after CRT. No change is observed in the left ventricular dimensions or in its systolic motion

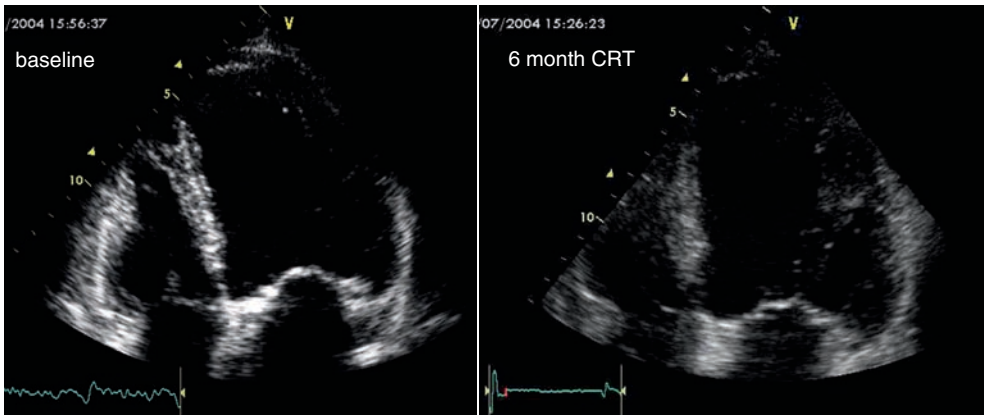

Fig. 21.7 An example of a patient who showed reverse re-modelling after 6 months CRT: 4-chamber apical view of the left ventricle before (Video 21.7a) and 6 months (Video 21.7b) after CRT. A significant reduction in the left ventricular size, and especially an improvement in its systolic function (particularly at the septum), can be observed

Table 21.1. Echocardiographic studies for detection of intra-ventricular dyssynchrony and prediction of LV reverse re-modelling

Measure of dyssynchrony	Responder definition	Number of patients (non-responders)	Correlation		Accuracy	
			r	p value	Sensitivity	Specificity
M-mode, SPWMD (>130 ms)	+5% LVEF	60 (53%)	0.69	<0.0001	92	78
PW tissue, difference of Ts between LV segments	Clinical	85 (26%)	ND	ND	80	80
Ts-4 (>65 ms)	−15% LVESV	ND	0.70	<0.001	92	92
TVI, TSI, Ts-SD>32.6 ms	−15% LVESV	30 (43%)	0.76	<0.001	100	100
TSI Ts-SD-12 (34.4 ms)	−15% LVESV	56 (46%)	0.61	<0.001	87	81
2D radial strain, septal-to-posterior wall delay in peak radial strain (>130 ms)	+15% LVEF	64 (24%)	ND	ND	89	83

From Cleland et al[26]
− reduction; + increase; *LVEF* left ventricular ejection fraction; *LVESV* left ventricular end systolic volume; *ND* no data could be obtained; *OR* odds ratio; *PW* pulsed wave; *SPWMD* septal-to-posterior wall mechanical delay; *TSI* tissue synchronization imaging; *Ts-SD* standard deviation of time to peak; *TVI* tissue velocity imaging

of latest velocity activation by tissue Doppler was associated with a more favourable response to CRT.[24] Suffoletto et al. utilized 2D speckle tracking to analyze left ventricular radial strain to identify the site of latest mechanical activation before CRT and also observed that the patients with concordant left ventricular lead placement had more favourable ventricular reverse re-modelling.[25]

Small, non-randomized studies have generated interest in markers of mechanical intra-ventricular dyssynchrony to predict reverse re-modelling (Table 21.1) as discussed in the previous chapter. A series of small observational trials has suggested that cardiac dyssynchrony measured by a variety of echocardiographic techniques might predict the response to CRT. However, a large prospective, observational study (PROSPECT [Predictors of Response to CRT] trial) was unable to find clinically useful predictors of the response to CRT over 6 months in terms of clinical status or improvement in left ventricular function.[27]

Recent studies have also pointed out a sub-group of patients identified as "super-responders." Those patients improved dramatically after CRT with almost complete symptomatic recovery and marked reverse remodelling, "suggesting some kind of heart failure remission phase" (Fig. 21.8, Video 21.8). In an observational longitudinal study recruiting 520 patients, Gasparini et al. observed 16 remissions per 100 person-years, usually reached within the first 2 years of CRT. The most powerful predictors of heart failure remission phase were found to be a baseline LVEF of 30–35%, a baseline left ventricular end-diastolic volume 180 mL, and non-CAD aetiology. The concomitance of all three factors was strongly predictive of the heart failure remission phase.[28]

In a prospective observational study conducted in 84 consecutive patients, 13% of patients treated with CRT for severe long lasting chronic heart failure showed a dramatic improvement in EF (>50%) and were considered as "hyper-responders." This improvement was mainly related to the

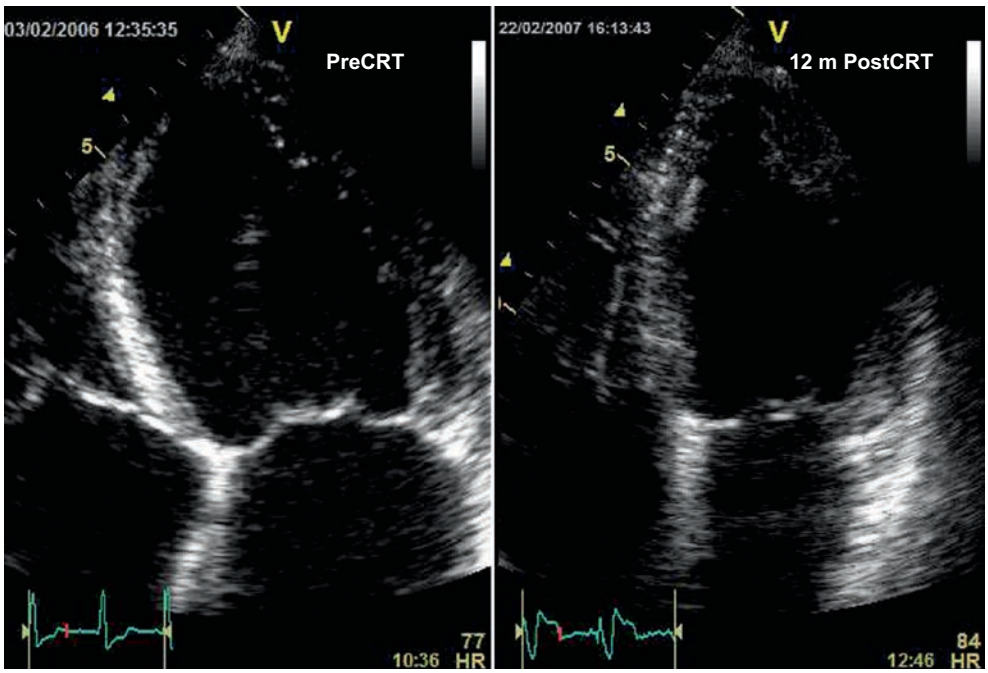

Fig. 21.8 An example of a patient who showed a super-response to CRT with normalization of left ventricular volumes and ejection fraction. The image shows a 4-chamber apical view of the left ventricle before and 12 months after CRT

aetiology of the underlying heart disease, as all hyper-responders had non-ischaemic dilated cardiomyopathy.[29]

In a recent multi-centre French study (Marseille, Bordeaux, Rennes), 186 patients were investigated before and 6 months after CRT by 2D strain. Super-responders were defined as a reduction of end-systolic volume of at least 15% and an EF > 50% and were compared to normal responder patients (reduction of end-systolic volume of at least 15%, but an EF < 50%). CRT super-responders (EF > 50%) were observed in 9% of the population and were associated with less-depressed left ventricular function as determined by strain analysis (global longitudinal strain: −12.8 ± 3% vs. −9 ± 2.6%, $p < 0.001$). Global longitudinal strain obtained by ROC curves was identified as the best parameter for predicting super-response with a cut-off value of −11% (Se = 80%, Spe = 87%, AUC = 0.89, $p < 0.002$) and was confirmed as an independent predictor by the logistic regression (RR: 21.3, $p < 0.0001$).[30]

On the other hand, the identification of non-responders is also crucial since non-responders represent approximately 30% of CRT patients, and CRT is an invasive treatment with potential complications. The aetiology of the underlying cardiomyopathy and the presence of left ventricular scar should be assessed before CRT. Clearly, a heavily scarred ventricle cannot recover as much contractile function despite stimulation. Patients with ischaemic heart disease are more likely to have substantial myocardial scar. Scar probably accounts for why patients with left ventricular dysfunction due to ischaemic heart disease have a worse prognosis and gain a smaller improvement in left ventricular function with CRT than patients who do not have ischaemic heart disease. Bleeker et al. suggested that in addition to the presence of left ventricular mechanical dyssynchrony, trans-mural scar tissue in the region of the left ventricular pacing lead (usually the postero-lateral left ventricular region) results in ineffective left ventricular stimulation and may prohibit functional response to CRT.[31] These authors suggested that in patients with ischaemic cardiomyopathy and history of previous myocardial infarction, assessment of scar tissue in the region targeted for left ventricular stimulation should be considered before CRT implantation. This observation was confirmed by other studies that evaluated the role of magnetic resonance imaging to quantify the importance of total scar burden for functional response to CRT.[32]

In addition to magnetic resonance imaging studies, Ypenburg et al. recently demonstrated that a >7.5% increase in LVEF during low-dose dobutamine echocardiography predicts left ventricular reverse re-modelling with a sensitivity of 76% and a specificity of 86% after 6 months of CRT.[33]

Effects of CRT on Mitral Regurgitation

Reduction of mitral regurgitation is one of the most immediate and often substantial effects of CRT, and reduction in mitral regurgitation by CRT is associated with an improved outcome.

CRT can reduce mitral regurgitation by improved temporal coordination of mechanical activation of the papillary muscles acutely and later improvements in left ventricular size and geometry from reverse re-modelling (Fig. 21.9, Video 21.9a-c). Indeed, there is some evidence that the decrease in the severity of mitral regurgitation precedes the reduction in

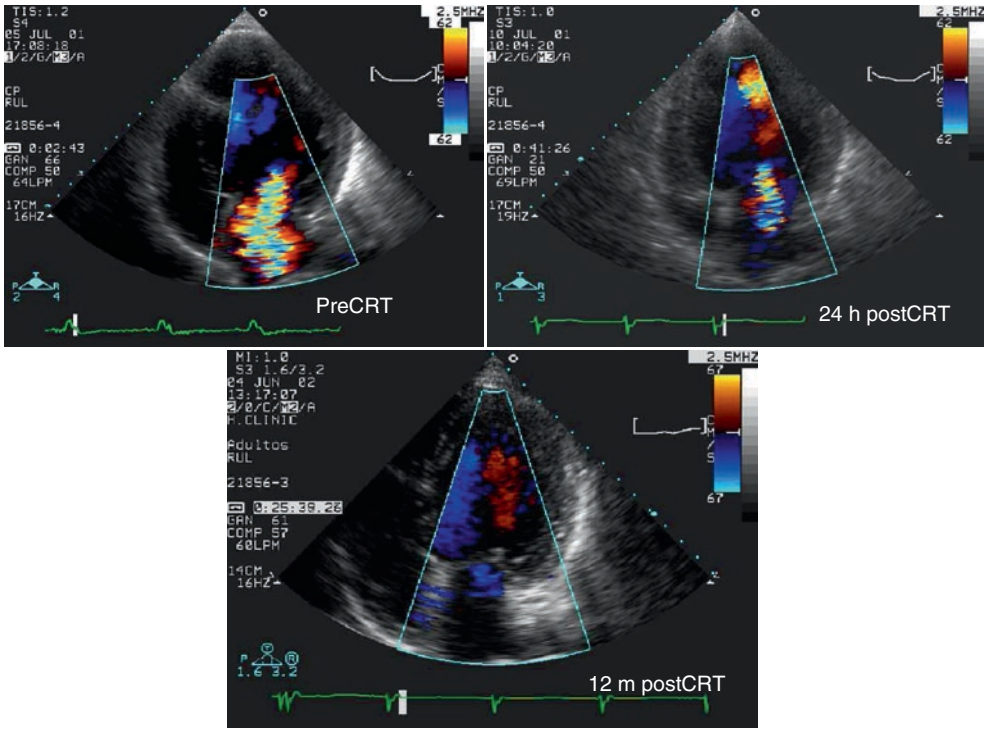

Fig. 21.9 An example of a patient who showed a progressive reduction in mitral regurgitation. The image shows a 4-chamber apical view with colour Doppler of the mitral valve and the left ventricle before (Video 21.9a), 24 h after (Video 21.9b) and 12 months (Video 21.9c) after CRT. A significant reduction in mitral regurgitation can be observed immediately after the activation of CRT. At 12 months follow-up, mitral regurgitation has virtually disappeared

left ventricular volumes and the associated changes in left ventricular and mitral valve architecture.[19] Breithardt et al. used the proximal isovelocity surface area method during both pacing-off and CRT in the first week after CRT to report a significantly reduced regurgitant volume from 32 ± 19 to 19 ± 9 mL, and effective regurgitant orifice area from 25 ± 19 to 13 ± 8 mm^2, with CRT.[34] Kanzaki et al. associated reductions in MR after CRT with acute improvements in the timing of mechanical activation of the papillary muscle sites, using mechanical strain activation mapping.[35]

In addition, the progressive reduction in left ventricular volumes and architecture with CRT are associated with restoration of mitral valve ventriculare annular diameter and mitral sub-valvular geometry towards normal. In the MIRACLE study, the severity of MR had decreased significantly with CRT at 3 months, and this improvement was maintained at 6 and 12 months. In contrast, no change was observed in the control group.[17] Reduction in volume and severity of mitral regurgitation and the increase in LVEF were consistently two- to threefold greater in non-ischaemic patients than in patients with ischaemic heart failure in spite of significantly larger baseline volumes and lower LVEF.[17]

Clinical Response and Reverse Re-modelling

In general terms, the clinical response to CRT is greater (up to 70% of patients in most studies) than the re-modelling response (up to 50% as described by most groups). Consequently, there is a correlation between re-modelling and clinical response in some patients, while others may show paradoxical responses.[36, 37]

In the MIRACLE trial, change in left ventricular end-diastolic volume and NYHA class correlated weakly, and reverse left ventricular re-modelling was greater in patients with non-ischaemic cardiomyopathy, whereas clinical outcomes improved irrespective of heart failure aetiology.[17] The paradox between the effects of CRT on left ventricular function and outcome in patients with ischaemic heart disease suggests that only some of the benefit of CRT is mediated by improving ventricular function. CRT reduces the risk of sudden cardiac death and it is possible that CRT suppresses arrhythmias directly or by even small improvements in cardiac function.

Yu et al. showed in 141 patients who received CRT that those who decreased left ventricular end-systolic volume by at least 10% at 3–6 months had a more favourable long-term clinical outcome, including lower all-cause mortality (7 vs. 31%), cardiovascular mortality (2 vs. 24%), and heart failure events (12 vs. 33%; all $p < 0.005$).[38]

A recent report from the CARE-HF study investigated the prediction of the long-term effects of CRT on mortality from baseline variables and from the early response to CRT.[39] This analysis demonstrated that mitral regurgitation and NT-proBNP measured 3 months after CRT were powerful independent factors of long-term survival in the CARE-HF study. The authors concluded that patients who improve their cardiac function after CRT have a better prognosis, but, at the same time, that this is a mechanism of a relatively small

proportion of the effect of CRT on long-term mortality. Therefore, an improvement in cardiac function and left ventricular re-modelling after CRT may be a "welcome sign but an unreliable surrogate for long-term response."[39]

Conclusion

Currently, cardiac imaging has an essential role in the follow-up of patients treated with CRT as it provides an objective evidence of the extent of response to the therapy, which is, in turn, related to the prognosis of these patients. Imaging may also be of help in assessing the cause of non-response such as the lack of mechanical resynchronization or suboptimal device programming. In this sense, echocardiography has also shown its usefulness for the optimization of AV and VV intervals, at least in the acute term. Further studies, however, are necessary to clarify and establish if there is any clinical impact of such an echocardiography-guided CRT device programming in the longer term.

References

1. Gorcsan J III, Abraham T, Agler DA, et al Echocardiography for cardiac resynchronization therapy: recommendations for performance and reporting – a report from the American Society of Echocardiography Dyssynchrony Writing Group endorsed by the Heart Rhythm Society. *J Am Soc Echocardiogr*. 2008;21:191–213
2. Jansen AH, Bracke FA, van Dantzig JM, et al Correlation of echo-Doppler optimization of atrioventricular delay in cardiac resynchronization therapy with invasive hemodynamics in patients with heart failure secondary to ischemic or idiopathic dilated cardiomyopathy. *Am J Cardiol*. 2006;97:552–557
3. Vidal B, Sitges M, Marigliano A, et al Optimizing the programation of cardiac resynchronization therapy devices in patients with heart failure and left bundle branch block. *Am J Cardiol*. 2007;100: 1002–1006
4. Auricchio A, Stellbrink C, Block M, et al Effect of pacing chamber and atrioventricular delay on acute systolic function of paced patients with congestive heart failure. The Pacing Therapies for Congestive Heart Failure Study Group. The Guidant Congestive Heart Failure Research Group. *Circulation*. 1999;99:2993–3001
5. Perego GB, Chianca R, Facchini M, et al Simultaneous vs. sequential biventricular pacing in dilated cardiomyopathy: an acute hemodynamic study. *Eur J Heart Fail*. 2003;5:305–313
6. Sogaard P, Egeblad H, Pedersen AK, et al Sequential versus simultaneous biventricular resynchronization for severe heart failure: evaluation by tissue Doppler imaging. *Circulation*. 2002;106: 2078–2084
7. Leon AR BS, Liang CS, Abraham WT, Chinchoy E, Hill MRS, US InSync III Investigators and Coordinators. Interventricular delay increases stroke volume in cardiac resynchronization patients. *Eur Heart J*. 2002;23(abstr suppl):529
8. Bordachar P, Lafitte S, Reuter S, et al Echocardiographic parameters of ventricular dyssynchrony validation in patients with heart failure using sequential biventricular pacing. *J Am Coll Cardiol*. 2004;44:2157–2165
9. Mortensen PT, Sogaard P, Mansour H, et al Sequential biventricular pacing: evaluation of safety and efficacy. *Pacing Clin Electrophysiol*. 2004;27:339–345
10. Hardt SE, Yazdi SH, Bauer A, et al Immediate and chronic effects of AV-delay optimization in patients with cardiac resynchronization therapy. *Int J Cardiol*. 2007;115:318–325
11. Sawhney NS, Waggoner AD, Garhwal S, Chawla MK, Osborn J, Faddis MN. Randomized prospective trial of atrioventricular delay programming for cardiac resynchronization therapy. *Heart Rhythm*. 2004;1:562–567
12. Morales MA, Startari U, Panchetti L, Rossi A, Piacenti M. Atrioventricular delay optimization by doppler-derived left ventricular d*P*/d*t* improves 6-month outcome of resynchronized patients. *Pacing Clin Electrophysiol*. 2006;29:564–568
13. Leon AR, Abraham WT, Brozena S, et al Cardiac resynchronization with sequential biventricular pacing for the treatment of moderate-to-severe heart failure. *J Am Coll Cardiol*. 2005;46:2298–2304
14. Boriani G, Muller CP, Seidl KH, et al Randomized comparison of simultaneous biventricular stimulation versus optimized interventricular delay in cardiac resynchronization therapy. The Resynchronization for the HemodYnamic Treatment for Heart Failure Management II implantable cardioverter defibrillator (RHYTHM II ICD) study. *Am Heart J*. 2006;151:1050–1058
15. Rao RK, Kumar UN, Schafer J, Viloria E, De Lurgio D, Foster E. Reduced ventricular volumes and improved systolic function with cardiac resynchronization therapy: a randomized trial comparing simultaneous biventricular pacing, sequential biventricular pacing, and left ventricular pacing. *Circulation*. 2007;115:2136–2144
16. Leclercq C, Kass DA. Retiming the failing heart: principles and current clinical status of cardiac resynchronization. *J Am Coll Cardiol*. 2002;39:194–201
17. Sutton MG, Plappert T, Hilpisch KE, Abraham WT, Hayes DL, Chinchoy E. Sustained reverse left ventricular structural remodelling with cardiac resynchronization at one year is a function of etiology: quantitative Doppler echocardiographic evidence from the Multicenter InSync Randomized Clinical Evaluation (MIRACLE). *Circulation*. 2006;113:266–272
18. Sutton MS, Keane MG. Reverse r emodelling in heart failure with cardiac resynchronisation therapy. *Heart*. 2007;93:167–171
19. Yu CM, Chau E, Sanderson JE, et al Tissue Doppler echocardiographic evidence of reverse remodelling and improved synchronicity by simultaneously delaying regional contraction after biventricular pacing therapy in heart failure. *Circulation*. 2002;105:438–445
20. Abraham WT, Fisher WG, Smith AL, et al Cardiac resynchronization in chronic heart failure. *N Engl J Med*. 2002;346:1845–1853
21. Linde C, Leclercq C, Rex S, et al Long-term benefits of biventricular pacing in congestive heart failure: results from the multisite stimulation in cardiomyopathy (MUSTIC) study. *J Am Coll Cardiol*. 2002;40:111–118
22. Cleland JG, Daubert JC, Erdmann E, et al The effect of cardiac resynchronization on morbidity and mortality in heart failure. *N Engl J Med*. 2005;352:1539–1549
23. Linde C, Abraham WT, Gold MR, St John Sutton M, Ghio S, Daubert C. Randomized trial of cardiac resynchronization in mildly symptomatic heart failure patients and in asymptomatic patients with left ventricular dysfunction and previous heart failure symptoms. *J Am Coll Cardiol*. 2008;52:1834–1843
24. Ansalone G, Giannantoni P, Ricci R, Trambaiolo P, Fedele F, Santini M. Doppler myocardial imaging to evaluate the effectiveness of pacing sites in patients receiving biventricular pacing. *J Am Coll Cardiol*. 2002;39:489–499
25. Suffolettoms, Dohi K, Cannesson M, Saba S, Gorcsan J III. Novel speckle-tracking radial strain from routine black-and-white echocardiographic images to quantify dyssynchrony and predict response

to cardiac resynchronization therapy. *Circulation*. 2006;113: 960–968
26. Cleland JCF, Cullington D, Khaleva O, Tageldien A. Cardiac resynchronization therapy: dyssynchrony imaging from a heart failure perspective. *Curr Opin Cardiol*. 2008;23:634–645
27. Chung ES, Leon AR, Tavazzi L, et al Results of the predictors of response to CRT (PROSPECT) trial. *Circulation*. 2008;117: 2608–2616
28. Gasparini M, Regoli F, Ceriotti C, et al Remission of left ventricular systolic dysfunction and of heart failure symptoms after cardiac resynchronization therapy: temporal pattern and clinical predictors. *Am Heart J*. 2008;155:507–514
29. Castellant P, Fatemi M, Bertault-Valls V, Etienne Y, Blanc JJ. Cardiac resynchronization therapy: "nonresponders" and "hyperresponders". *Heart Rhythm*. 2008;5:193–197
30. Zaroui A, Réant P, Donal E, et al Identification and characterization of super-responders to cardiac resynchronization therapy: an echocardiographic study. *Circulation*. 2008;118(suppl):abstract 2819
31. Bleeker GB, Kaandorp TA, Lamb HJ, et al Effect of posterolateral scar tissue on clinical and echocardiographic improvement after cardiac resynchronization therapy. *Circulation*. 2006;113:969–976
32. Ypenburg C, Roes SD, Bleeker GB, et al Effect of total scar burden on contrast-enhanced magnetic resonance imaging on response to cardiac resynchronization therapy. *Am J Cardiol*. 2007;99:657–660
33. Ypenburg C, Sieders A, Bleeker GB, et al Myocardial contractile reserve predicts improvement in left ventricular function after cardiac resynchronization therapy. *Am Heart J*. 2007;154:1160–1165
34. Breithardt OA, Sinha AM, Schwammenthal E, et al Acute effects of cardiac resynchronization therapy on functional mitral regurgitation in advanced systolic heart failure. *J Am Coll Cardiol*. 2003;41: 765–770
35. Kanzaki H, Bazaz R, Schwartzman D, Dohi K, Sade LE, Gorcsan J III. A mechanism for immediate reduction in mitral regurgitation after cardiac resynchronization therapy: insights from mechanical activation strain mapping. *J Am Coll Cardiol*. 2004;44:1619–1625
36. Bleeker GB, Bax JJ, Fung JW, et al Clinical versus echocardiographic parameters to assess response to cardiac resynchronization therapy. *Am J Cardiol*. 2006;97:260–263
37. Vidal B, Sitges M, Marigliano A, et al Relation of response to cardiac resynchronization therapy to left ventricular reverse remodelling. *Am J Cardiol*. 2006;97:876–881
38. Yu CM, Bleeker GB, Fung JW, et al Left ventricular reverse remodelling but not clinical improvement predicts long-term survival after cardiac resynchronization therapy. *Circulation*. 2005;112:1580–1586
39. Cleland J, Freemantle N, Ghio S, et al Predicting the long-term effects of cardiac resynchronization therapy on mortality from baseline variables and the early response a report from the CARE-HF (cardiac resynchronization in heart failure) Trial. *J Am Coll Cardiol*. 2008;52:438–445

Section 5

Cardiomyopathies

Chapter 22

HYPERTROPHIC CARDIOMYOPATHY

Frank A. Flachskampf, Ruxandra T. Beyer, and Petros Nihoyannopoulos

CONTENTS

J. L. Zamorano et al. (eds.), *The ESC Textbook of Cardiovascular Imaging*
DOI: 10.1007/978-1-84882-421-8_22, © Springer-Verlag London Limited 2010

Introduction

Hypertrophic cardiomyopathy (HCM) is a genetically determined disease with familial and spontaneous occurrence. The disease is often asymptomatic. Symptoms typically develop in young adulthood or later. With advanced disease, the leading symptoms are dyspnea, angina, and syncope. Because of the risk of syncope and of ventricular arrhythmias and sudden death, detection is important even in the absence of symptoms in daily life.

On physical examination, the most prominent sign is a systolic murmur over the base of the heart at the left sternal border, which is not transmitted to the carotids. The ECG usually shows signs of left ventricular hypertrophy with strain or left bundle branch block.

The echocardiographic hallmark of HCM is an increase in wall thickness of the left ventricle (LV), with a corresponding increase in LV mass (Table 22.1). This increase is extremely variable, both in localization and extent. In fact, localized thickening has been observed in all regions of the LV with this disease, although the most frequent site is the septum. Besides an increase in wall thickness, classical echo signs of the disease include a particular echo texture ("granular sparkling") of the diseased myocardium, changes in mitral valve morphology with increased leaflet size, an anterior shift in papillary muscle position, signs of dynamic systolic LV outflow tract obstruction including narrowing of the LV outflow tract, systolic anterior motion (SAM) of the mitral valve, mid-systolic closure of the aortic valve, occurrence of a systolic outflow tract gradient or, less frequently, a systolic gradient at the mid-ventricular level, and mitral regurgitation. The latter signs indicate the presence of the obstructive form of the disease, denominated hypertrophic obstructive cardiomyopathy. However, the degree of obstruction often fluctuates, depending on the sympathetic drive, load conditions, and other factors, and at least a low degree of obstruction is a very frequent finding, even if the full-blown picture of hypertrophic obstructive cardiomyopathy is not present.

Myocardial longitudinal velocities and deformation parameters (strain and strain rate) are dramatically decreased, in spite of frequently normal ejection fraction. These parameters have been used for the diagnosis of "subclinical" disease before or without the development of visible increases in wall thickness.

Pathophysiology of HCM

Hypertrophy

Degree and location of increased LV wall thickness vary significantly, ranging from the "typical" sigmoid shape of the septum with "asymmetric hypertrophy" (ratio of end-diastolic septal to posterior wall thicknesses >1:1.3) to apical hypertrophy or bizarre localized myocardial "bumps" (Fig. 22.1). Hypertrophy is usually concentric (without increase in cavity diameter), although eccentric hypertrophy with impaired LV ejection fraction has been described in end-stage HCM. A pronounced, localized increase in wall thickness is suggestive of HCM, except for the basal septal bulge often found in long-standing hypertension. In any case, differentiation from long-standing severe hypertensive heart disease is difficult based on wall thickness or mass alone, except that very large increases in wall thickness and mass (e.g. end-diastolic thicknesses in excess of 20 mm) are indicative of cardiomyopathy. An overlapping form of "hypertensive HCM of the elderly" has been described.[1] Thus, in the presence of substantial hypertension, the differential diagnosis of hypertensive heart disease cannot be excluded in a patient with extensive wall hypertrophy. Similarly, aortic stenosis or infiltrative cardiomyopathy (e.g. cardiac amyloidosis) can produce left ventricular hypertrophy which is difficult to distinguish from HCM. Recently, reduced peak systolic longitudinal deformation (strain) averaged over all LV walls was reported to distinguish hypertensive from cardiomyopathic hypertrophy, with values for deformation (strain) <10.6% (in absolute value, neglecting the negative

Table 22.1. Echo signs of HCM. Note that none of these signs is absolutely specific for the diagnosis of HCM

LV wall thickness increase and hypertrophy, especially, but not exclusively, with asymmetric septal hypertrophy (septal/posterior end-diastolic wall thickness >1.3) in the absence of other causes of hypertrophy
Decreased basal longitudinal myocardial velocities (e' < 13.5 cm/s)
LV systolic outflow tract obstruction or mid-ventricular obstruction
SAM of the mitral valve with or without septal contact of leaflet tips
Mid-systolic closure of aortic valve
Presence of an increased systolic flow velocity (>2 m/s) in the LV outflow tract, with a late systolic peak. In some instances, the obstruction is mid-ventricular

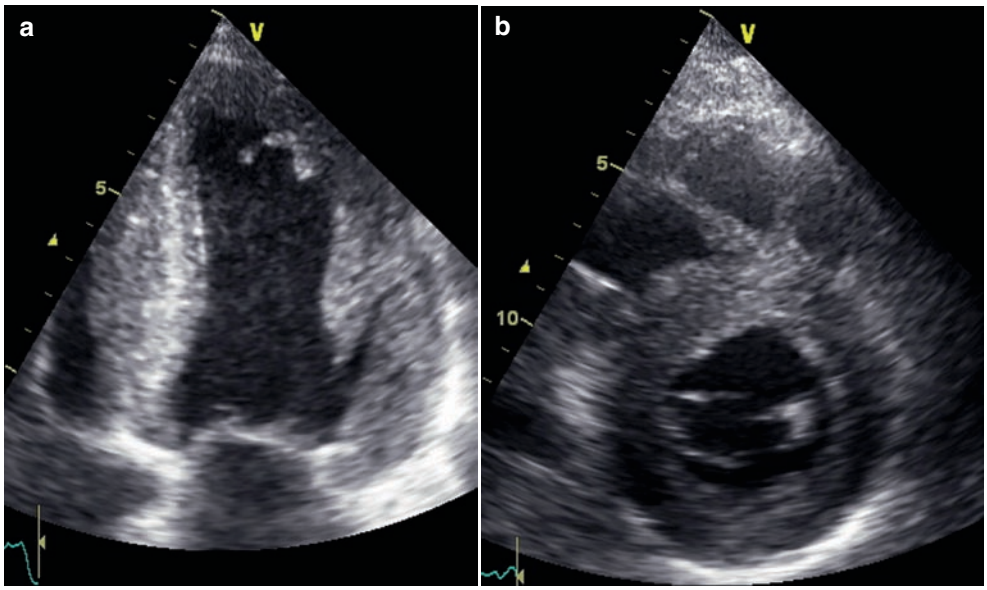

Fig. 22.1 **(a)** End-diastolic apical four-chamber view of patient with HCM. The maximal septal thickness is 31 mm, and the lateral wall is also massively thickened. Note bright echo texture of septal myocardium. **(b)** Diastolic parasternal short-axis view of LV of same patient

sign) predicting HCM with a sensitivity of 85% and specificity of 100%. A ratio of end-diastolic septal to posterior wall thickness >1.3 combined with evaluation of systolic strain yielded a predictive accuracy of 96%.[2]

Apical HCM is more frequently seen in Asia, especially in Japan, than in Western countries. In this subset of HCM, there is systolic apical cavity obliteration (Fig. 22.2), and giant negative T-waves are seen in the precordial ECG leads. LV contrast echocardiography may aid in the delineation of apical hypertrophy. Apical aneurysms, which occur in only approximately 2% of patients with HCM,[3] are mostly associated with apical or mid-ventricular hypertrophy and seem to affect prognosis negatively. These aneurysms, which are usually small, may escape 2D echo detection because of foreshortening of the LV apex. Paradoxical diastolic flow directed towards the mitral valve may be present, and can be detectable by Doppler imaging.[4, 5]

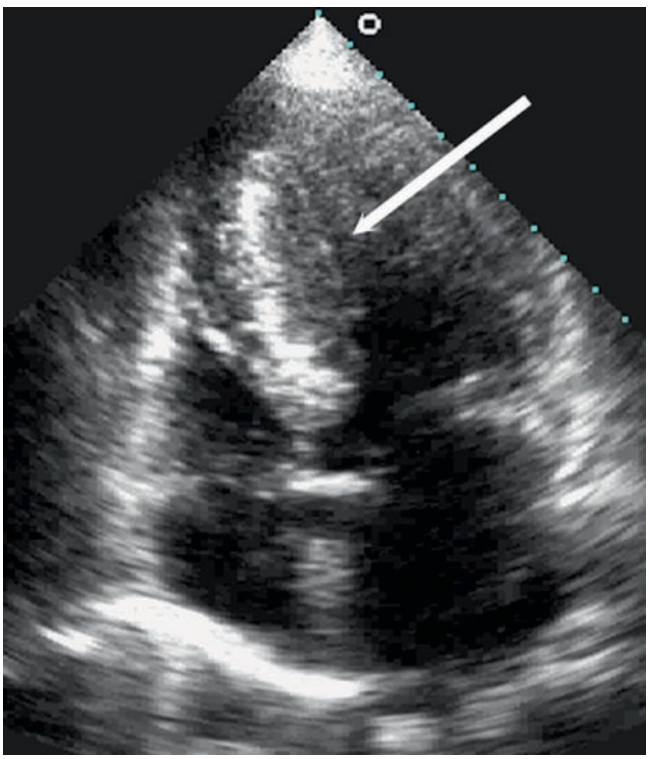

Fig. 22.2 Apical four-chamber view of apical HCM with LV cavity obliteration in systole (*apical arrow*)

The basic functional disorder in HCM occurs during diastole with impaired relaxation, filling, and compliance of the ventricles. Far from being uniform, myocardial dysfunction is regional and irregular, depending on the extent and distribution of the underlying myofibrillar lesions. Early studies using M-mode echocardiography showed that the rates of filling and relaxation of the LV were abnormal in patients with HCM.[6–8] However, pulsed-wave Doppler echocardiographic recordings of trans-mitral flow are easier to obtain and provide a good overall estimate of diastolic filling abnormalities of the LV.[9, 10] In HCM patients, the period during which the heart is isovolumic is often prolonged, LV filling is slow, and the proportion of filling volume resulting from atrial systole may be increased. As long as left atrial pressures are still normal, impaired ventricular relaxation results in prolonged isovolumic relaxation time, slower early ventricular filling (E-wave), and a compensatory exaggerated atrial systolic filling (A-wave), with a reduced E/A ratio.[10,11] In more severe cases, with increased mean diastolic left atrial pressure (>15 mmHg), rapid filling is increased with a consequent reduction of the atrial contribution, giving the wrong impression of "normalization" of LV filling (pseudo-normalization). Such "normalization" of the diastolic filling pattern in HCM can also happen in the presence of significant mitral regurgitation. With more advanced

disease, compliance decreases further and LV filling pressures rise, and there is accelerated and shortened rapid early filling and normal or reduced late filling similar to patients with restrictive cardiomyopathy. It is therefore understandable that in a non-homogeneous HCM population where patients exhibit different degrees of functional disability, they will be presenting with a spectrum of mitral and pulmonary venous inflow waveforms. Colour Doppler flow imaging can distinguish the high pre-systolic inflow velocity (A-wave) from the lower velocity of the early diastolic filling flow (E-wave) by the increased brightness of the red-orange colour occurring in late diastole, which also often aliases. Since patients with HCM usually have small LV cavity dimensions, the higher velocity in late diastole may be seen into the LV cavity and even on occasion reaching the cardiac apex.

The texture of myopathic walls, especially the septum, has been described as "granular sparkling," highlighting the increased brightness and strong speckle pattern of the myocardium (Figs. 22.1 and 22.2). A stringent definition of this descriptive term, however, does not exist, and the finding is rather unspecific, also occurring in severe hypertrophy of other aetiologies.

Obstruction

Basal septal hypertrophy, per se, leads to a narrowing of the outflow tract during systole (Figs. 22.3 and 22.4). In addition, in the full-blown picture of obstructive HCM, the attachment of the papillary muscles is shifted anteriorly, thus contributing to the narrowing of the LV outflow tract. HCM also frequently affects the mitral valve, with enlargement especially of the anterior leaflet.[12] This leaflet partakes in the obstructive mechanism, moving – together with the whole mitral apparatus – anteriorly towards the septum in systole, a phenomenon termed systolic anterior motion (SAM) (Figs. 22.3–22.6). The extent of the SAM is variable between patients and also in a given patient according to sympathetic drive, load conditions, and medication. The ultimate mechanism of this characteristic sign of obstruction is still debated, but elegant work from Robert A. Levine's group in Boston makes it likely that the mechanism is slack in the chordal tethering of the enlarged anterior mitral leaflet, at least partly due to the malposition of the papillary muscles, which allows leaflet tissue to be dragged into the outflow tract by the blood propelled towards the aortic valve.[13, 14] An alternative mechanism that has been proposed is a Venturi force sucking the mitral leaflet towards the septum by the increased flow velocity in the outflow tract.[15] The latter mechanism observes the SAM as a consequence, and not as a cause of LV outflow tract obstruction, whereas the former explanation implies a causal contribution of SAM to obstruction.

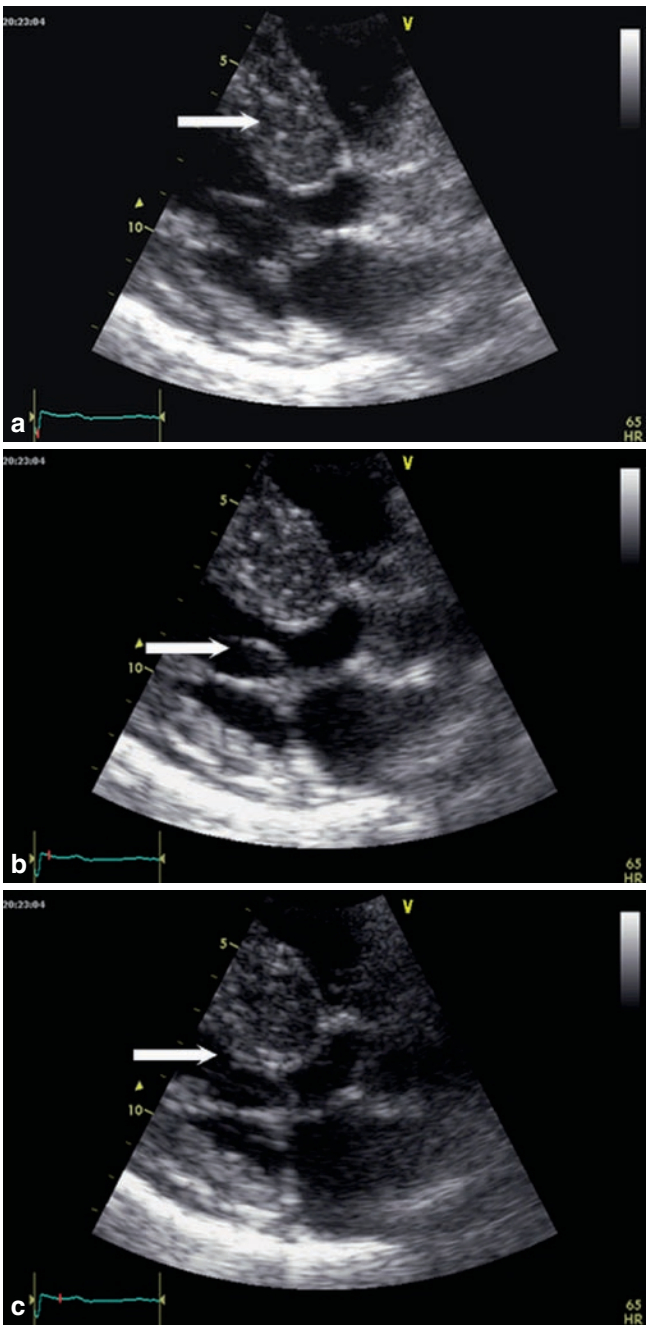

Fig. 22.3 Typical example of hypertrophic obstructive cardiomyopathy. Parasternal long-axis view (zoom). **(a)** End-diastole: End-diastolic frame showing thickened septum (20 mm) (*arrow*). Note that the posterior wall is less thickened (12 mm). **(b)** Early systole: The tip of the anterior mitral leaflet (*arrow*) approaches the septum. **(c)** Mid-systole: Septal contact of the anterior leaflet (*arrow*). Note the narrowed outflow tract

Although LV obstruction in HCM is most frequent at the outflow tract level (Figs. 22.7–22.9), mid-ventricular obstruction at the papillary muscle level is not uncommon and can be detected and distinguished from classical obstructive

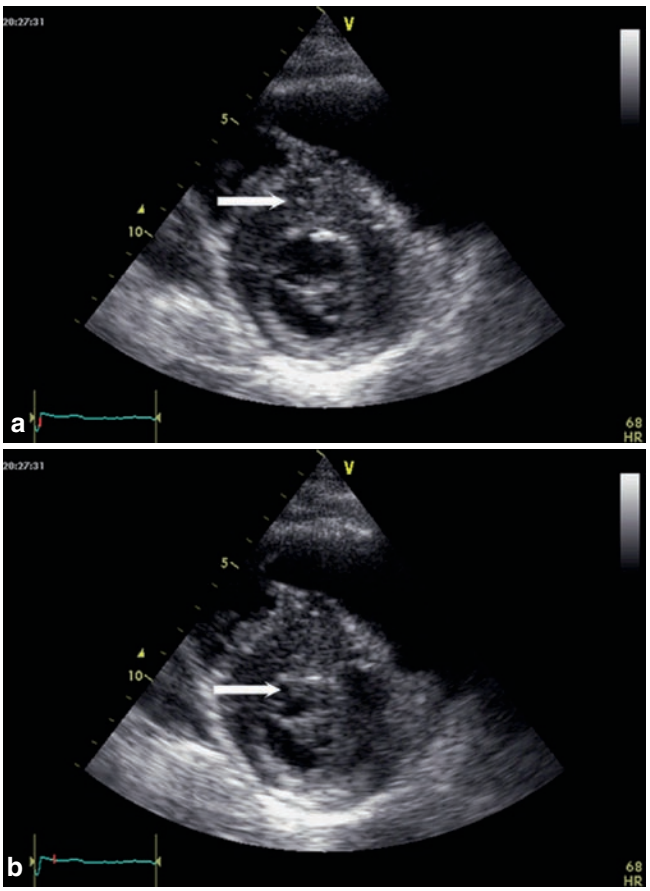

Fig. 22.4 Basal parasternal short-axis view of hypertrophic obstructive cardiomyopathy. Note "asymmetrically" thickened septum (end-diastole) (*arrow* in **(a)**). In early systole, the anterior leaflet is seen to obstruct the outflow tract (*arrow* in **(b)**)

HCM by registering systolic flow turbulence at the mid-ventricular (papillary) muscle level rather than at the outflow tract level by colour and spectral Doppler imaging.

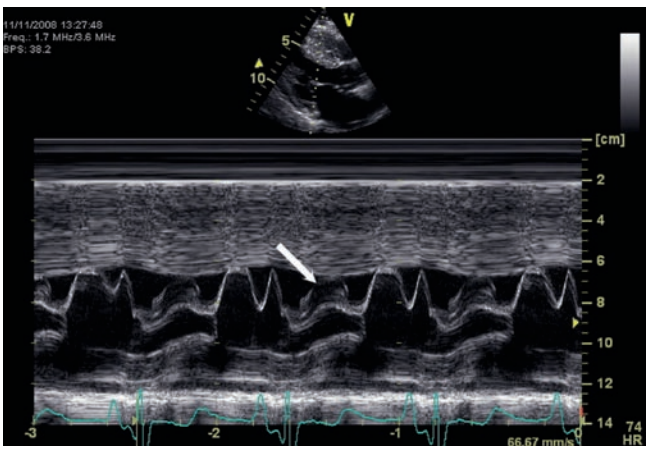

Fig. 22.5 M-mode of mitral valve in hypertrophic obstructive cardiomyopathy. Note typical SAM pattern (*arrow*) with mid-systolic contact with the massively thickened septum

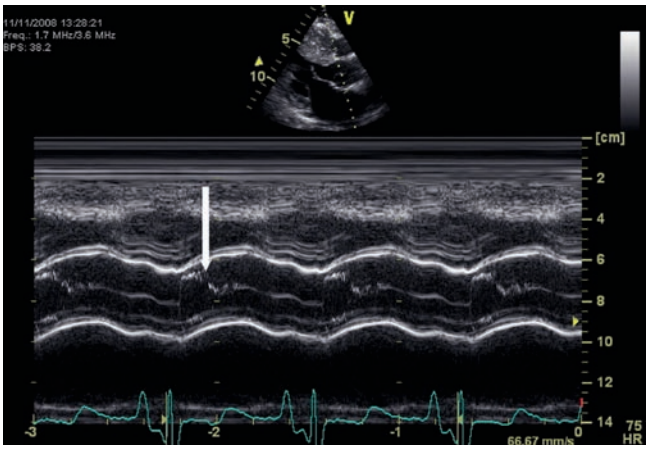

Fig. 22.6 M-mode of the aortic valve in hypertrophic obstructive cardiomyopathy. Note mid-systolic partial closure of the aortic valve due to increasing obstruction (*arrow*)

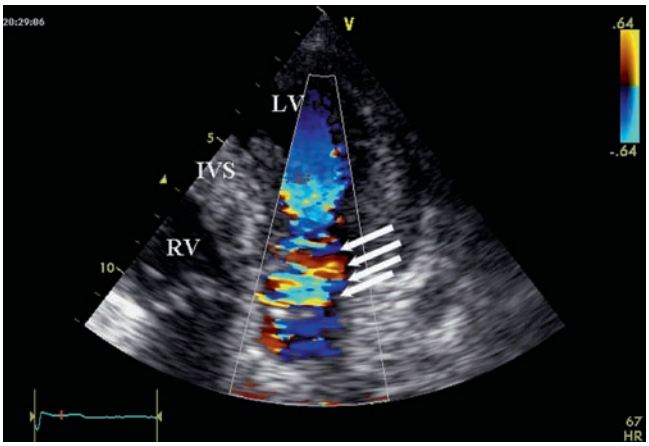

Fig. 22.7 Apical five-chamber view in hypertrophic obstructive cardiomyopathy. Colour Doppler mapping in systole shows flow acceleration and turbulence in the LV outflow tract (*arrows*). *IVS*: ventricular septum; *LV*: left ventricle; and *RV*: right ventricle

Changes in Mitral Valve Morphology and Function

As mentioned earlier, analyses of autopsy material have shown that mitral leaflet sizes are increased in patients with obstructive HCM, and that papillary muscle position and morphology are often abnormal, with anterior and medial displacement and hypertrophy. These changes are related to SAM, obstruction, and the occurrence of mitral regurgitation, which is present to some degree in nearly all obstructive HCM patients and may be severe.

Myocardial Velocity and Deformation

In spite of usually preserved LV ejection fraction (which mainly represents radial systolic inward motion), the

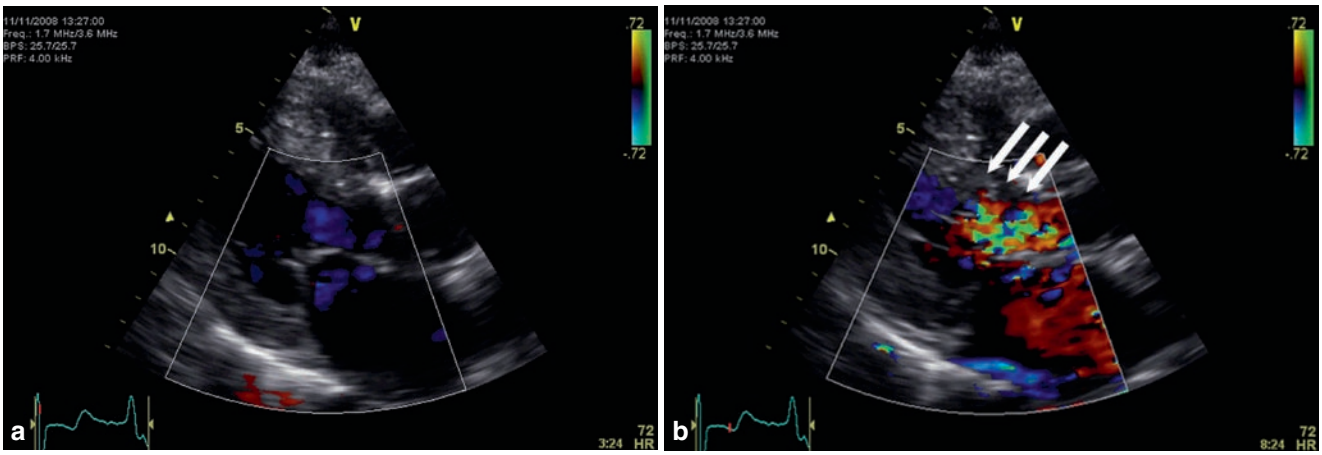

Fig. 22.8 Parasternal long-axis view in hypertrophic obstructive cardiomyopathy. **(a)** End-diastolic frame for orientation. **(b)** Colour Doppler mapping in systole shows flow acceleration and turbulence in the LV outflow tract, well proximal of the aortic valve (*arrows*)

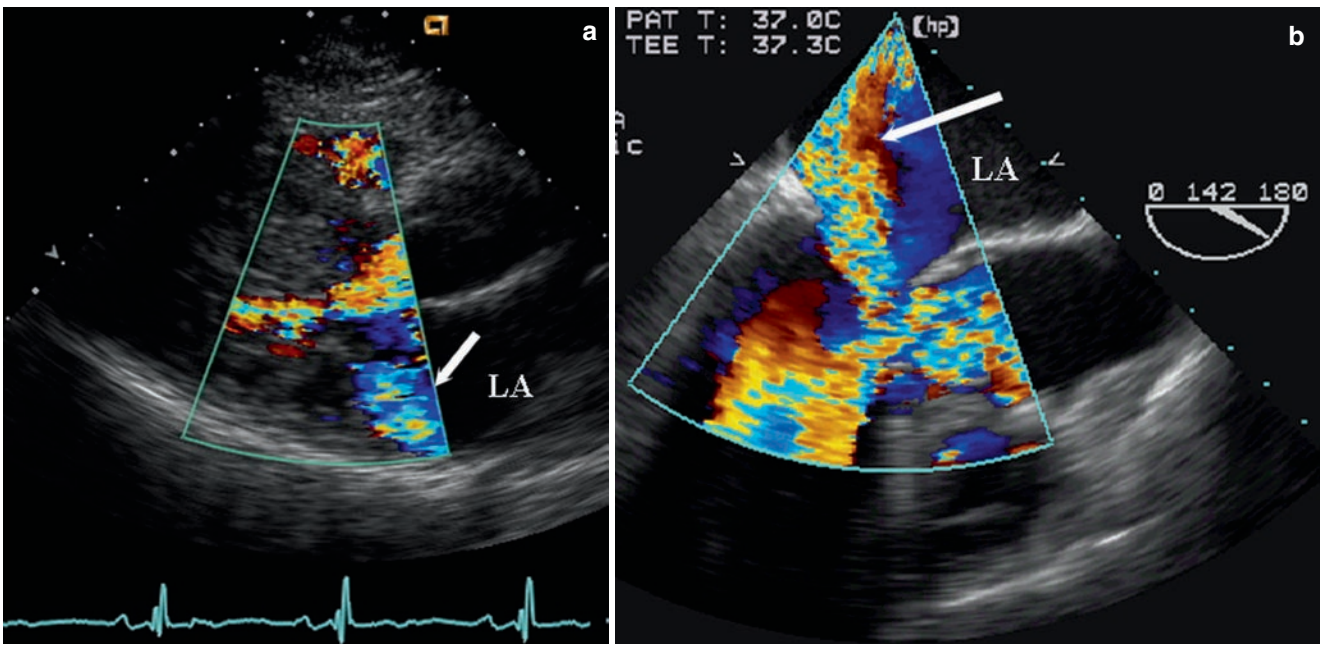

Fig. 22.9 Hypertrophic obstructive cardiomyopathy with severe mitral regurgitation (*arrow*). **(a)** Parasternal long-axis view. **(b)** Trans-oesophageal long-axis view. Note also systolic high-velocity flow (turbulence) in the LV outflow tract

longitudinal systolic and early diastolic velocities of the LV myocardium are decreased, which is best detected at the mitral annulus level (Fig. 22.10). In a study of 36 individuals who were genotyped and positive for a familial HCM form and 36 controls, a decrease of early diastolic tissue velocity, *e′* (averaged from basal septal, lateral, anterior, and posterior walls) <13.5 cm/s had a sensitivity of 75% and a specificity of 86% to detect individuals genetically positive for HCM, although half of the 36 genetically positive individuals were asymptomatic and without hypertrophy on echo (Fig. 22.11). Similar data were reported from another group.[16, 17] Myocardial longitudinal deformation (strain) is decreased at the site of hypertrophy; in a recent publication, mid-septal maximal strain was −1.3 ± 8.2% in HCM (including some patients with reversed mid-septal strain: i.e. systolic elongation) vs. 17.6 ± 5.0% in controls, with an inverse correlation between mid-septal wall thickness and strain[18] and averaged peak systolic longitudinal strain <10.6% has been used to distinguish HCM from hypertensive hypertrophy.[2] In the HCM associated with Friedreich's ataxia, a neurodegenerative disease, significantly lower systolic and particularly early diastolic strain rates were noted in homozygously affected patients

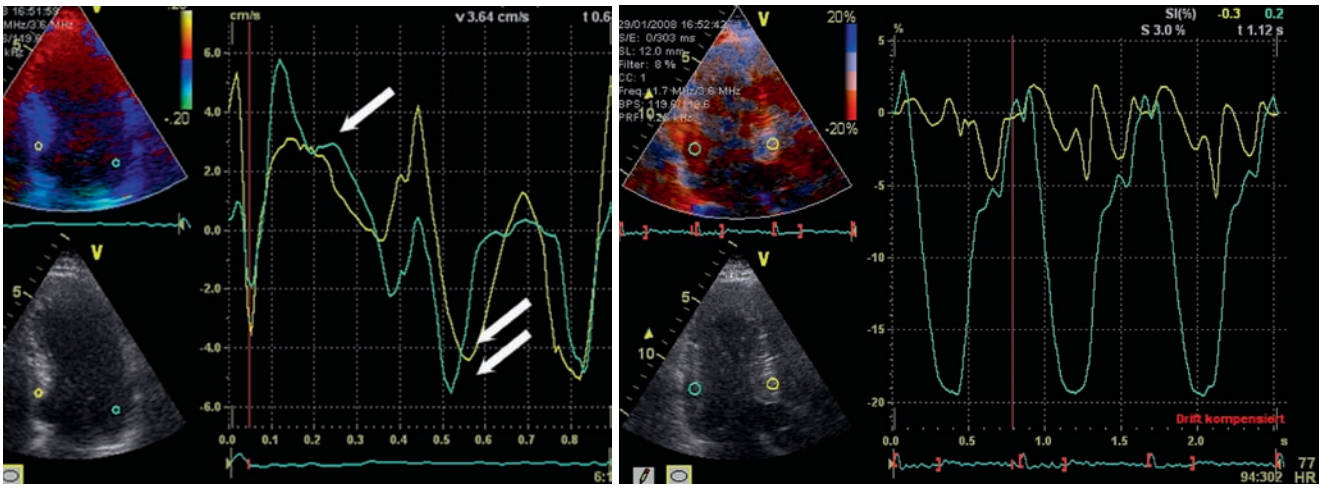

Fig. 22.10 Deformation imaging in HCM. Left, longitudinal tissue velocities of basal septum (*yellow*) and lateral wall (*green*). Systolic (*single arrow*) and early diastolic velocities (*double arrows*) are severely depressed (<6 cm/s). Right, longitudinal strain from hypertrophied septum (*green*) and lateral of wall of normal thickness (*yellow*). Note severely depressed longitudinal peak strain in the septum (<5%)

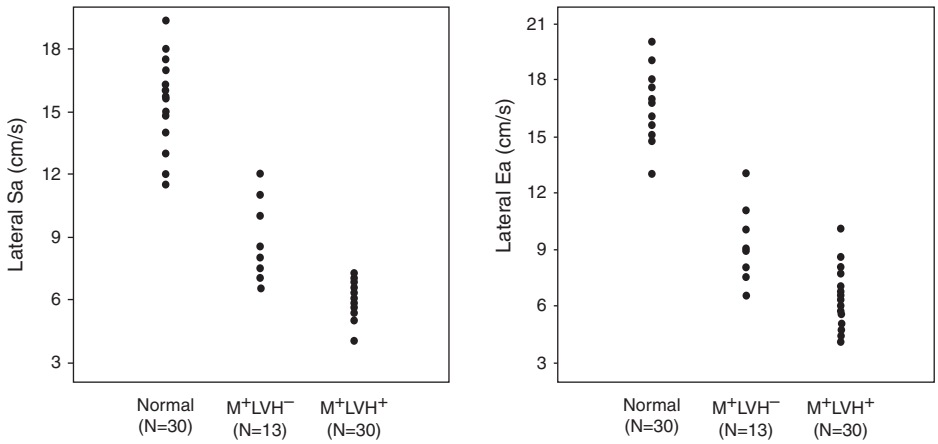

Fig. 22.11 Tissue Doppler parameters in the detection of sub-clinical HCM. Longitudinal tissue velocities in normal, genetically affected patients *without* phenotypically manifest hypertrophy (M+/LVH−), and genetically affected patients *with* echocardiographic hypertrophy (M+/LVH+). The *left panel* shows peak systolic longitudinal velocities (Sa), the *right panel* early diastolic velocities (Ea), measured at the lateral mitral annulus region. The differences are statistically significant. Reproduced with permission from Nagueh et al.[16]

than in age-matched controls.[19] Note, however, that such decreases in tissue velocities and deformation indices also occur in infiltrative cardiomyopathies (see Chap. 23) and hypertrophic re-modelling of other etiologies. In obstructive HCM, there may be a very short mid-systolic deceleration of longitudinal tissue velocity detectable, corresponding to mid-systolic aortic closure (see later).

Diagnosis

The most recent pertinent recommendations of the European Society of Cardiology stipulate the following:

> The clinical diagnosis of HCM is established most easily and reliably with 2D echocardiography by demonstrating left ventricular hypertrophy (LVH) (typically asymmetric in distribution, and showing virtually any diffuse or segmental pattern of left ventricular [LV] wall thickening). Left ventricular wall thickening is associated with a non-dilated and hyper-dynamic chamber (often with systolic cavity obliteration) in the absence of another cardiac or systemic disease (e.g. hypertension or aortic stenosis) capable of producing the magnitude of hypertrophy evident and independent of whether or not LV outflow obstruction is present.[20]

Increases in wall thickness of the LV are a very frequent echocardiographic finding and mostly due to hypertension. Exercise also leads to modest increases in wall thickness, but a study in 947 world-class athletes found an end-diastolic wall thickness >12 mm in only 1.7% of them, with a maximum of 16 mm.[21] Thus, substantial increases in wall thickness in the absence of hypertension are always suspicious of HCM. The pattern of "asymmetric septal hypertrophy" is particularly typical of obstructive HCM, but balanced concentric hypertrophy may also occur, and localized increases in wall thickness (e.g. in circumscribed regions of the LV

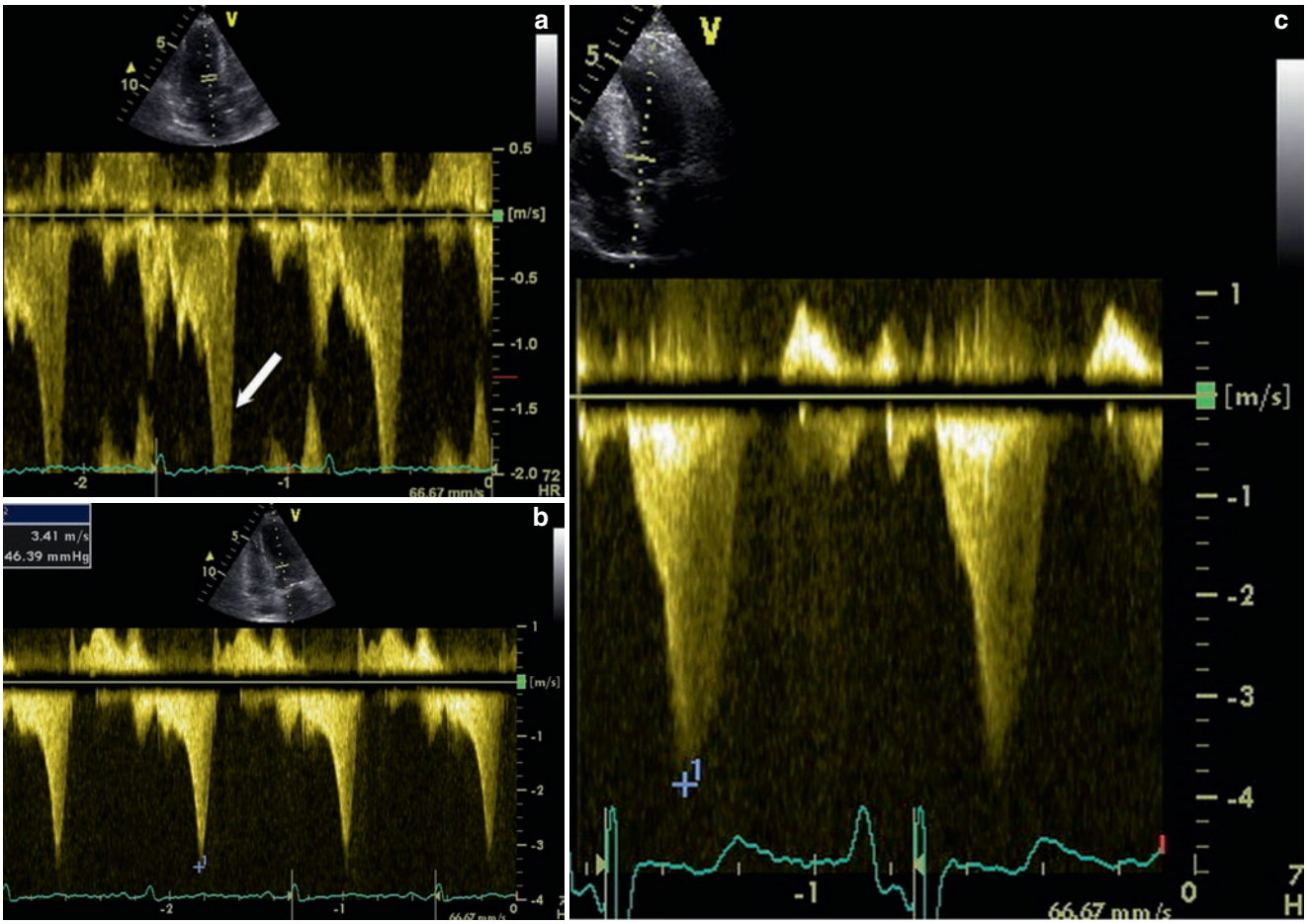

Fig. 22.12 **(a)** Pulsed Doppler recording of systolic flow in the LV in a patient with hypertrophic obstructive cardiomyopathy. Note that sample volume is about 25 mm distant from the aortic valve, well within the LV. Systolic flow velocities towards the outflow tract (*arrow*) are clearly elevated (>2 m/s) and there is aliasing. **(b)** Continuous-wave Doppler recording of outflow tract velocities in the same patient. Note late- peaking elevated velocities (peak gradient, 46 mmHg). **(c)** Continuous-wave Doppler recording of outflow tract velocities from another patient with hypertrophic obstructive cardiomyopathy and a peak gradient of 60 mmHg

free wall) have been described as well. A particular form of HCM has been described predominantly in Asian patients, but also in others, where hypertrophy is confined to the LV apex. Typically, these patients have deep negative symmetric T-waves in their precordial ECG leads.

Obstruction can be suspected in the presence of "turbulent" intra-ventricular flow on colour Doppler, which also precisely identifies the location of maximal flow acceleration and, thus, obstruction (Figs. 22.7–22.9). This is especially important if interventional therapy is contemplated. The findings can be corroborated by carefully moving the sample volume of the pulsed-wave Doppler in an apical long-axis or five-chamber view along the septum from the LV cavity towards the outflow tract identifying the location of obstruction where the peak systolic flow velocity starts to abruptly increase and aliasing occurs. Peak outflow tract velocities should be acquired by continuous-wave Doppler and typically show a late systolic maximum, giving the spectral curve a "dagger shape" (Fig. 22.12). Peak velocities vary with the degree of obstruction, but can exceed 5 m/s. It is common practice to report the peak velocities or gradients and not mean gradients in this disease. The normal upper limit of LV outflow tract velocities is not well defined, but generally assumed to be 1.5 m/s; on the other hand, a peak sub-aortic flow velocity of >2.7 m/s or a gradient of >30 mmHg are currently recommended by guidelines to diagnose the obstructive form of HCM.[20] If borderline velocities are detected, measurement after physical exercise or after administering sublingual nitroglycerine (one to two puffs) may be considered. Shape and timing distinguishes the continuous-wave signal of outflow tract obstruction from the signal of concomitant mitral regurgitation, which may be similar in peak velocity, but starts earlier and finishes later than the obstruction signal and has a symmetric shape. Often one can see both spectra superimposed. If in doubt, mitral regurgitation should be recorded by pulsed Doppler at the mitral

annulus level and the timing compared to the signal in question.

Morphologic signs of obstruction are:

- SAM, which can vary from a barely perceptible buckling to clear contact between the anterior mitral leaflet and the septum during systole. A SAM confined to the chordae (chordal SAM) is a more unspecific finding not diagnostic of obstructive HCM. Even leaflet SAM, however, can occur in a number of other situations than obstructive HCM, namely during dobutamine stress in otherwise normal ventricles with excellent function, in states of volume depletion or external compression of the LV (e.g. by a large right ventricle), and after surgical mitral valve repair with a ring.
- Mid-systolic (incomplete) closure of the aortic valve, best seen by M-mode (Fig. 22.6), due to the mid-systolic peak in obstruction.

Additional confirmation of HCM may be sought from tissue Doppler and deformation imaging (Fig. 22.10). Both show markedly decreased velocities and deformation parameters in the presence of HCM, in spite of preserved ejection fraction, and – based on published studies in small numbers of patients – may be able to detect HCM before hypertrophy becomes apparent or in genetically, but not phenotypically, affected individuals. Special attention should be paid to a decrease in e´ velocity when screening relatives of patients with HCM. However, these changes are not specific and also found in other cardiomyopathies or hypertrophy of other origins.

Pitfalls

An erroneous diagnosis of presence or absence of HCM can occur due to the following mistakes[22]:

- LVH due to hypertension (often with a basal septal bulge), aortic stenosis, infiltrative cardiomyopathy, or heavy exercise. LV non-compaction may mimic HCM. This is a cardiomyopathy characterized by a two-layered LV wall structure with a heavily trabecularized inner layer (the non-compacted layer) showing prominent inter-trabecular spaces and a thickness at least twice as large as the compacted outer layer.[23]
- Over-reliance on M-mode measurements of septal and posterior wall thickness. M-mode measurements frequently are oblique to the true short axis of the LV. Attention to this problem, measurements from 2D images or from anatomic M-mode help avoid this problem.
- Apical hypertrophy may go undetected due to near-field artefact. Insufficient delineation of the lateral wall may also obscure localized hypertrophy. In cases of doubt, left heart contrast injection is helpful.
- In conditions of volume depletion, during dobutamine stress or in acute anterior myocardial infarction, unspecific systolic ventricular gradients may occur. These do not indicate the presence of cardiomyopathy.

While recording LV (outflow tract) gradients by continuous-wave Doppler, care must be taken not to confound them with mitral regurgitation signals. Mitral regurgitation starts earlier (immediately after the end of the transmitral A-wave) and ends later (at the onset of the transmitral E-wave). If in doubt, the timing of the systolic high velocity signal on continuous-wave Doppler assumed to be due to ventricular obstruction should be compared with the timing of pulsed-wave recordings of mitral regurgitation and outflow tract velocities.

Imaging in Guiding the Therapy of Hypertrophic Obstructive Cardiomyopathy

While medical therapy with beta-blockade and calcium antagonists is the first therapeutic step in symptomatic individuals, percutaneous septal alcohol ablation or surgical septal myectomy/myotomy are performed in patients with persisting severe symptoms. Echo is used in a few centres performing percutaneous alcohol ablation to define the perfusion territory of the targeted septal branch of the left anterior descending artery (Figs. 22.13 and 22.14).[18] For this purpose, echo contrast is injected during coronary angiography into the respective septal branch through the lumen of an over-the-wire balloon catheter after guidewire removal. The balloon is inflated to prevent spillover of contrast into the left anterior descending artery. Impressive variability in the perfusion territory of such branches has been reported. The delineation of the perfusion territory serves to identify:

(a) whether the corresponding septal area is adjacent to the region of flow acceleration;
(b) other structures perfused by the septal branch (e.g. right ventricular myocardial regions, papillary muscles, and other areas), which would be jeopardized by the planned alcohol ablation.

In the largest reported series of 322 patients who had intracoronary echo contrast application (Levovist®) before intended septal ablation, in 18 (6%) patients the procedure was aborted because atypical perfusion territories were found at risk (right and left papillary muscles, right ventricular free wall) by the septal contrast injection.

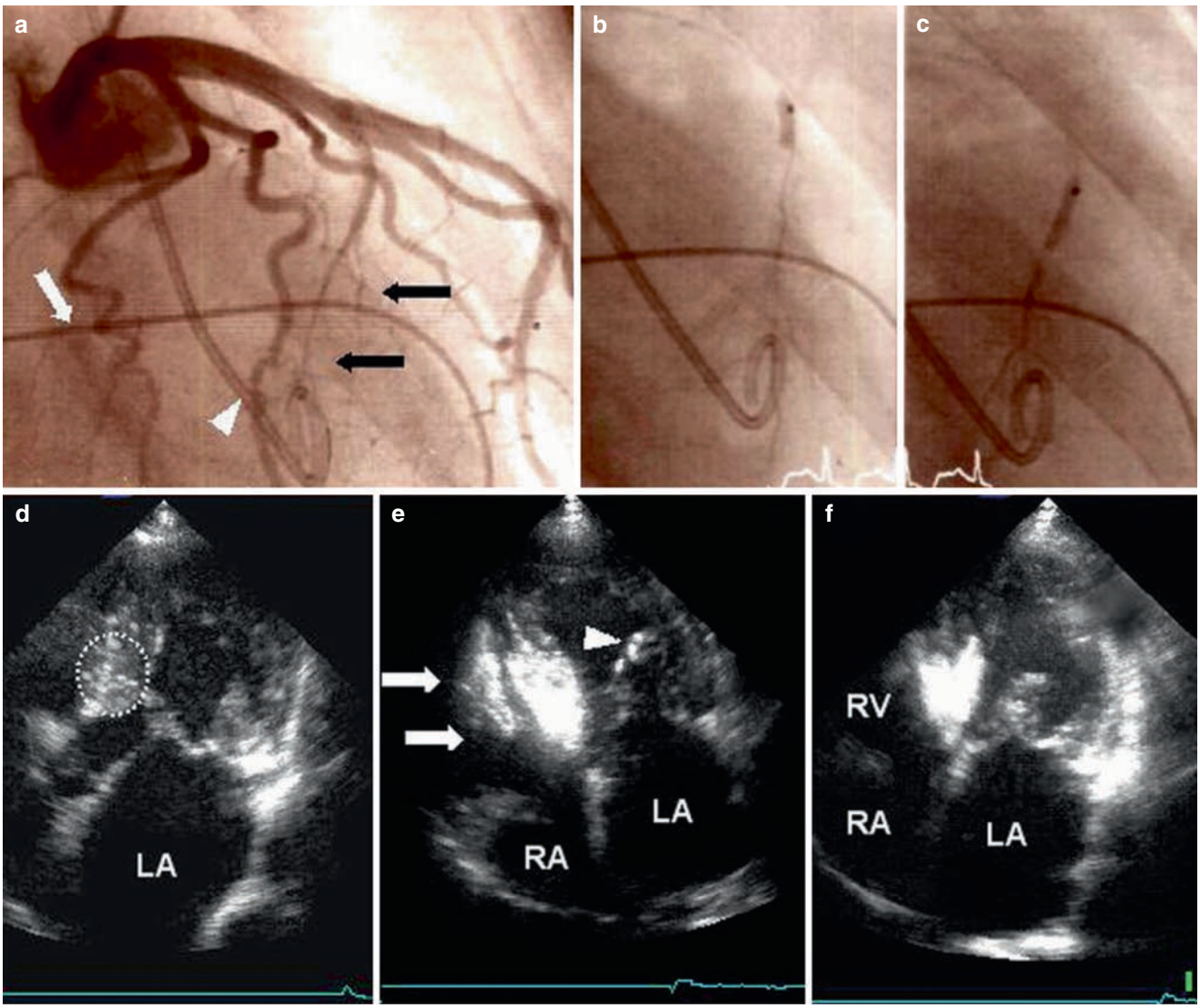

Fig. 22.13 Interventional and echocardiographic sequence of a (super-selective) septal ablation procedure for symptomatic hypertrophic obstructive cardiomyopathy. Angio sequence: first major septal perforator artery with two sub-branches (*black arrows*), as the presumed target vessel **(a)**, *white arrow*, lead of the temporary pacemaker; *white arrow*, pigtail catheter in the LV, balloon within the proximal part of the septal perforator, **(b)** distal vessel bed with two sub-branches contrasted angiographically, **(c)** balloon advanced super-selectively into the left/basal sub-branch. Corresponding echo sequence: Sub-aortic septum as target region in typical SAM-associated, sub-aortic obstruction (**d**, *dotted line*), **(e)** test injection of the echo contrast agent in balloon position of **(b)** highlighting the basal half of the septum plus a right ventricular papillary muscle (*white arrows*), **(f)** after super-selective balloon position of **(c)**, correct opacification of the target region is achieved. Reproduced with permission from Faber et al.[25] *RA* right atrium; *RV* right ventricle; *LA* left atrium

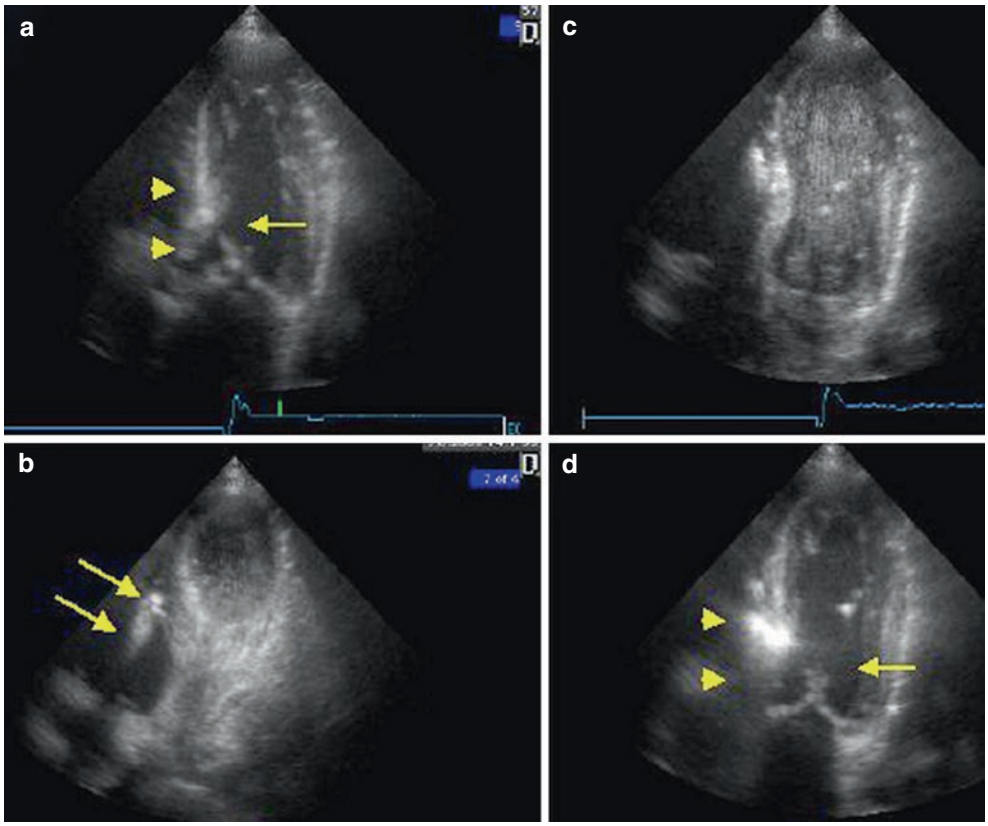

Fig. 22.14 Variety of structures at risk for alcohol-induced necrosis as detected by intra-procedural echocardiography. **(a)** Baseline four-chamber view in a patient who had myectomy 5 years ago and underwent septal ablation because of class III symptoms and significant SAM-associated (*arrow*) recurrent obstruction. Target region marked by *arrowheads*. Test injection into the first presumed target vessel produces opacification of a right papillary muscle (**(b)**, *arrows*), test injection into a second septal perforator leads to LV cavity contrast **(c)** without any opacification within the target region, injection into the third target vessel correctly highlights the target region (**d**, *arrowheads*). Reproduced with permission from Faber et al.[25]

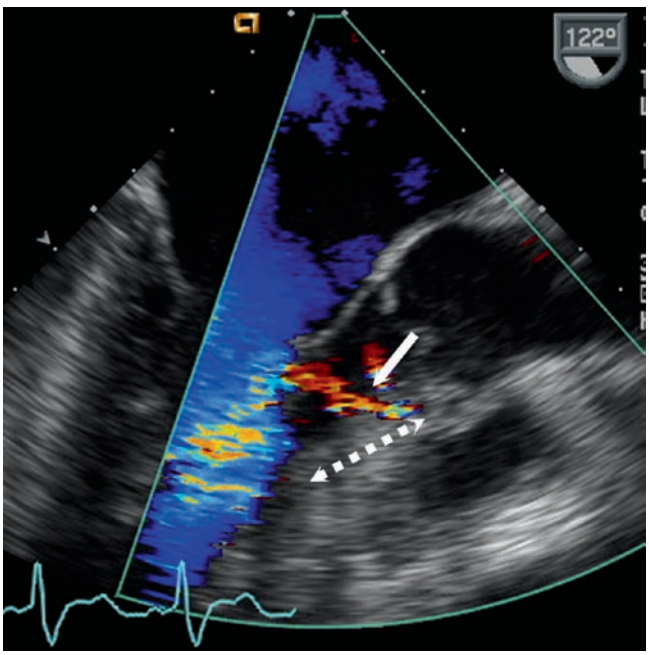

Fig. 22.15 Coronary fistula (*solid arrow*) with diastolic flow into the LV after surgical myectomy/myotomy in a patient with hypertrophic obstructive cardiomyopathy. The *dotted double arrow* delineates the approximate extent of the myectomy. Trans-oesophageal long-axis view

During surgical myectomy/myotomy, intra-operative echo can guide the surgeon as to the necessary extent of removal of septal myocardium, while avoiding creation of a ventricular septal defect. Sometimes, after myectomy small fistulas can be seen from coronary branches that have been cut and now drain into the left ventricle (Fig. 22.15).

References

1. Topol EJ, Traill TA, Fortuin NJ. Hypertensive hypertrophic cardiomyopathy of the elderly. *N Engl J Med*. 1985;312:277–283
2. Kato TS, Noda A, Izawa H, et al Discrimination of nonobstructive hypertrophic cardiomyopathy from hypertensive left ventricular hypertrophy on the basis of strain rate imaging by tissue Doppler ultrasonography. *Circulation*. 2004;110:3808–3814
3. Maron MS, Finley JJ, Bos JM, et al Prevalence, clinical significance, and natural history of left ventricular apical aneurysms in hypertrophic cardiomyopathy. *Circulation*. 2008;118:1541–1549
4. Nakamura T, Matsubara K, Furukawa K, et al Diastolic paradoxic jet flow in patients with hypertrophic cardiomyopathy: evidence of concealed apical asynergy with cavity obliteration. *J Am Coll Cardiol*. 1992;19:516–524
5. Matsubara K, Nakamura T, Kuribayashi T, Azuma A, Nakagawa M. Sustained cavity obliteration and apical aneurysm formation in

apical hypertrophic cardiomyopathy. *J Am Coll Cardiol*. 2003;42:288–295 Erratum in: *J Am Coll Cardiol*. 2003;42:1338
6. Hanrath P, Mathey DG, Siegert R, et al Left ventricular relaxation and filling pattern in different forms of left ventricular hypertrophy: an echocardiographic study. *Am J Cardiol*. 1980;45:15–23
7. Sanderson JE, Trail TA, St John Sutton MG, et al Left ventricular relaxation and filling in hypertrophic cardiomyopathy: an echocardiographic study. *Br Heart J*. 1978;40:596–601
8. St John Sutton MG, Tajik AJ, Gibson DG, et al Echocardiographic assessment of left ventricular filling and septal and posterior wall dynamics in idiopathic hypertrophic subaortic stenosis. *Circulation*. 1978;57:512–520
9. Takenaka K, Dabestani A, Gardin JM, et al Left ventricular filling in hypertrophic cardiomyopathy: a pulsed Doppler echocardiographic study. *J Am Coll Cardiol*. 1986;7:1263–1271
10. Maron BJ, Spirito P, Green KJ, Wesley YE, Bonow RO, Arce J. Non-invasive assessment of left ventricular diastolic function by pulsed Doppler echocardiography in patients with hypertrophic cardiomyopathy. *J Am Coll Cardiol*. 1987;10:733–742
11. Nihoyannopoulos P, Karatasakis G, Frenneaux M, McKenna WJ, Oakley CM. Diastolic function in hypertrophic cardiomyopathy; relation to exercise capacity. *J Am Coll Cardiol*. 1992;19:536–540
12. Klues HG, Maron BJ, Dollar AL, Roberts WC. Diversity of structural mitral valve alterations in hypertrophic cardiomyopathy. *Circulation*. 1992;85:1651–1660
13. Jiang L, Levine RA, King ME, Weyman AE. An integrated mechanism for systolic anterior motion of the mitral valve in hypertrophic cardiomyopathy based on echocardiographic observations. *Am Heart J*. 1987;113:633–644
14. Levine RA, Vlahakes GJ, Lefebvre X, et al Papillary muscle displacement causes systolic anterior motion of the mitral valve. Experimental validation and insights into the mechanism of subaortic obstruction. *Circulation*. 1995;91:1189–1195
15. Maron BJ, Bonow RO, Cannon RO III, et al Hypertrophic cardiomyopathy: interrelations of clinical manifestations, pathophysiology and therapy: *N Engl J Med*. 1987;316:780–789;844–852
16. Nagueh SF, Bachinski LL, Meyer D, et al Tissue Doppler imaging consistently detects myocardial abnormalities in patients with hypertrophic cardiomyopathy and provides a novel means for an early diagnosis before and independently of hypertrophy. *Circulation*. 2001;104:128–130
17. Ho CY, Sweitzer NK, McDonough B, et al Assessment of diastolic function with Doppler tissue imaging to predict genotype in preclinical hypertrophic cardiomyopathy. *Circulation*. 2002;105:2992–2997
18. Yang H, Sun JP, Lever HM, et al Use of strain imaging in detecting segmental dysfunction in patients with hypertrophic cardiomyopathy. *J Am Soc Echocardiogr*. 2003;16:233–239
19. Dutka DP, Donnelly JE, Palka P, Lange A, Nunez DJ, Nihoyannopoulos P. Echocardiographic characterization of cardiomyopathy in Friedreich's ataxia with tissue Doppler echocardiographically derived myocardial velocity gradients. *Circulation*. 2000;102:1276–1282
20. Maron BJ, McKenna WJ, Danielson GK, et al; American College of Cardiology Foundation Task Force on Clinical Expert Consensus Documents; European Society of Cardiology Committee for Practice Guidelines. American College of Cardiology/European Society of Cardiology Clinical Expert Consensus Document on Hypertrophic Cardiomyopathy. A report of the American College of Cardiology Foundation Task Force on Clinical Expert Consensus Documents and the European Society of Cardiology Committee for practice guidelines. *Eur Heart J*. 2003;24:1965–1991
21. Spirito P, Pelliccia A, Proschan MA, et al Morphology of the "athlete's heart" assessed by echocardiography in 947 elite athletes representing 27 sports. *Am J Cardiol*. 1994;74:802–806
22. Prasad K, Atherton J, Smith GC, McKenna WJ, Frenneaux MP, Nihoyannopoulos P. Echocardiographic pitfalls in the diagnosis of hypertrophic cardiomyopathy. *Heart*. 1999;82(suppl 3):III8-III15
23. Oechslin E, Jenni R. Isolated left ventricular non-compaction: increasing recognition of this distinct, yet 'unclassified' cardiomyopathy. *Eur J Echocardiogr*. 2002;3:250–251
24. Faber L, Seggewiss H, Welge D, et al Echo-guided percutaneous septal ablation for symptomatic hypertrophic obstructive cardiomyopathy: 7 years of experience. *Eur J Echocardiogr*. 2004;5:347–355
25. Faber L, Seggewiss H, Gleichmann U. Percutaneous transluminal septal myocardial ablation in hypertrophic obstructive cardiomyopathy: results with respect to intraprocedural myocardial contrast echocardiography. *Circulation*. 1998;22:2415–2421

Chapter 23

INFILTRATIVE CARDIOMYOPATHY

Joseph B. Selvanayagam, Majo Joseph, and Stefan Neubauer

CONTENTS

J. L. Zamorano et al. (eds.), *The ESC Textbook of Cardiovascular Imaging*
DOI: 10.1007/978-1-84882-421-8_23, © Springer-Verlag London Limited 2010

Introduction

Infiltrative cardiomyopathy can result from a wide spectrum of both inherited and acquired conditions with varying systemic manifestations. They usually portend an adverse prognosis, although in rare instances (e.g. Fabry's disease) early diagnosis can result in potentially curative treatment. Cardiac amyloid remains the archetypal infiltrative cardiomyopathy and is discussed in great detail in this chapter. Non-invasive imaging modalities, principally echocardiography and cardiovascular magnetic resonance (CMR), play a pivotal role in the early diagnosis and management of all types of infiltrative cardiomyopathy.

Amyloidosis

Amyloidosis is a clinical disorder caused by extracellular deposition of insoluble abnormal fibrils, derived from aggregation of mis-folded, normally soluble, protein.[1, 2] About 20 different unrelated proteins are known to form amyloid fibrils in vivo, which share a pathognomonic ultrastructure.[3] Systemic amyloidosis, in which amyloid deposits are present in the viscera, blood vessel walls, and connective tissues, is usually fatal and is the cause of about 1 per 1,000 deaths in developed countries. There are also various localized forms of amyloidosis in which the deposits are confined to specific foci or to a particular organ or tissue. "Cardiac amyloidosis" describes involvement of the heart by amyloid deposition, whether as part of systemic amyloidosis (as is most commonly the case) or as a localized phenomenon.

Amyloid Subtype Classification

Systemic AA amyloidosis, formerly known as secondary amyloidosis, rarely involves the heart. Systemic AL amyloidosis, previously known as primary amyloidosis, is the most commonly diagnosed form of clinical amyloid disease in developed countries. AL fibrils are derived from monoclonal immunoglobulin light chains and consist of the whole or part of the variable (VL) domain. The heart is affected pathologically in up to 90% of AL patients, in 50% of whom diastolic heart failure with physical signs of right heart failure is a presenting feature. Conversely, less than 5% of patients with AL amyloidosis involving the heart have clinically isolated cardiac disease. Death in more than half of these patients is due to either heart failure or arrhythmia.

There are two additional variants of systemic AL amyloidosis: Hereditary systemic amyloidosis is caused by deposition of amyloid fibrils derived from genetic variants of transthyretin (TTR), apolipoprotein A-I, lysozyme, or fibrinogen A α-chain and other extremely rare variants. Clinical syndromes include cardiomyopathy, nephropathy, or neuropathy, although the heart is most prominently involved in variant TTR type, which is associated with more than 100 different TTR mutations and most often with associated neuropathy. This entity is not rare, and indeed, the amyloidogenic TTR Val122Ile variant is present in 4% of African-Americans, and 23% of African-Americans with cardiac amyloidosis have this variant.

Senile systemic amyloidosis (SSA) is caused by deposition of amyloid fibrils derived from normal wild-type TTR, and it almost always presents as a slowly progressive, infiltrative amyloid cardiomyopathy. It is exceptionally rare below the age of 60 years, but its prevalence ranges from 25%– to 36% over the age of 80 years. There is a large male predominance, and it has a major predilection for the heart.

Echocardiography

Echocardiography can show several features that are suggestive of cardiac amyloidosis (Fig. 23.1), although the classical features are commonly present in the later stages of the disease[4,5] and there is a wide spectrum of echocardiographic findings. It cannot confirm diagnosis in isolation, and the images should be interpreted in the context of the clinical picture and other investigations. AA amyloid very rarely affects the heart and the common types that do (i.e. AL and variant/wild-type TTR types) cannot be distinguished by echo. Although extremely rare, hereditary apolipoprotein A-I amyloidosis can involve the heart, again producing similar echocardiographic abnormalities.

The most common echocardiographic feature is increased thickness of the left ventricular (LV) wall, particularly in the absence of hypertension. This is often referred to incorrectly as "hypertrophy," as the pathological process is infiltration, and not myocyte hypertrophy. This feature has poor specificity for amyloidosis because of its occurrence in other conditions (e.g. hypertensive heart disease, hypertrophic cardiomyopathy, and other infiltrative cardiac diseases, such as glycogen storage diseases (GSD), sarcoidosis, and haemochromatosis). *The combination of increased LV mass in the absence of high electrocardiography (ECG) voltages may be more specific for infiltrative diseases* of which amyloid is the commonest (Fig. 23.2).[3] High sensitivity (72% to 79%) and specificity (91% to 100%) have been reported for this combination,[6, 7] although some study sizes are small and may be influenced by referral bias.

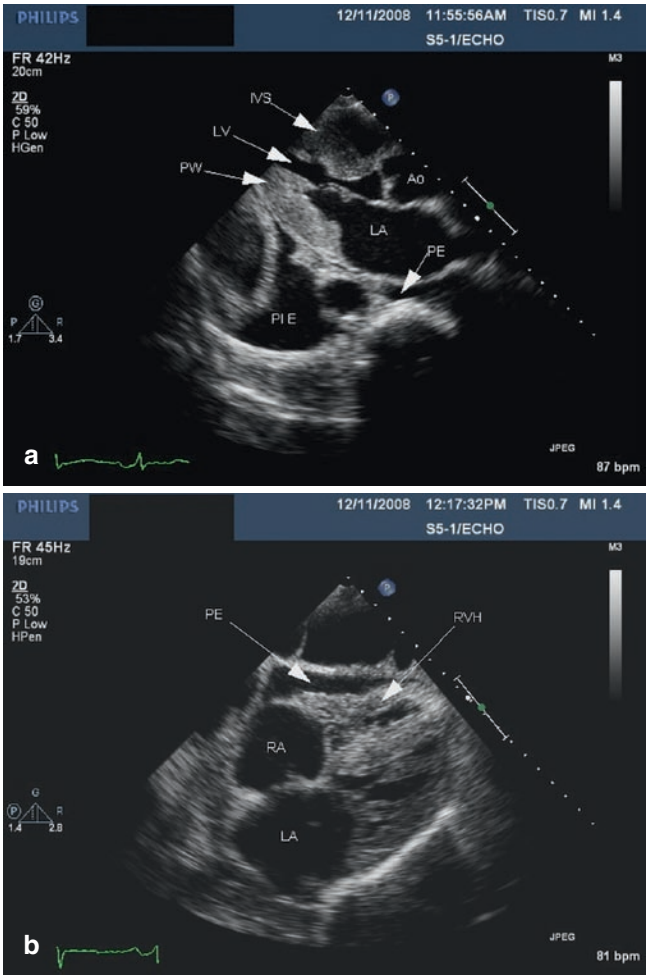

Fig. 23.1 (a). 2D echocardiogram (parasternal long-axis view) showing marked concentric LVH (*IVS*: inter-ventricular septum, and *PW*: posterior wall) and a non-dilated LV cavity. There is also left atrial enlargement (LA) and a small pericardial (PE) and larger pleural effusion (PE). **(b)** 2D echo (sub-costal view) highlighting markedly increased RV thickness (*RVH*: right ventricular hypertrophy). There is also bi-atrial enlargement (*RA*: right atrium; *LA* =: left atrium), and the presence of a small pericardial effusion (PE). **(c)** Spectral Doppler of mitral inflow of the same patient with advanced amyloid heart disease. There is a restrictive pattern with marked shortening of DT and diminution of atrial contribution with E/A ratio > 2. **(d)** Tissue Doppler velocity (apical window) of the medial mitral annulus in the same patient showing marked decrease in E′ (early-diastolic wave). The E/E′ ratio was calculated at 28, which corresponds to significant elevation in left-sided filling pressures. There is also a striking decrease in the systolic-positive wave(s) illustrating a significant decrease in longitudinal contractile function

Increased echogenicity of the myocardium, particularly with a granular or "sparkling" appearance, has been reported in several studies.[8] However, this can occur in other causes of left ventricular hypertrophy (LVH)[6, 9] and, although high specificity rates are quoted (71% to 81%),[6, 9] the populations studied were those referred with suspected amyloid, and this specificity may not be reflective of "real-life" practice. Moreover, sensitivity tends to be low with this pattern seen in 26% to 36% of cardiac amyloid cases[10, 11] apart from a single study suggesting a sensitivity of 87%.[9] It should be noted that this granular pattern only applies to standard echocardiographic imaging, without tissue harmonics being applied, as this increases myocardial echogenicity in general. Newer echocardiographic image processing techniques may also reduce the granular appearance. Thus, *although increased echogenicity is common in amyloid, its usefulness as a discriminating factor is limited.*

LV systolic function is usually normal until late stages of the disease process. Systolic function can be hyper-dynamic in some cases (hence, can be mistaken for hypertrophic or hypertensive cardiomyopathy) in initial stages, but in advanced stages systolic function can be depressed without cavity dilation resulting in marked reduction in stroke volume and cardiac output.

Diastolic dysfunction, however, is the fundamental abnormality in cardiac amyloidosis and is abnormal prior to systolic dysfunction, which is often normal even with advanced symptoms. Early in the disease process, there may be an abnormal relaxation pattern with progression to a restrictive pattern in advanced and symptomatic disease (Fig. 23.1c). Not only do diastolic parameters correlate with the severity of the symptoms, but they are also prognostic with a restrictive filling pattern (DT < 150 msec, see Fig. 23.1c) associated with a mortality of 50% at 1 year. Atrial enlargement is a common finding in amyloid heart disease and reflects the abnormal diastolic function.

Tissue Doppler imaging can measure regional myocardial motion and velocity and can detect changes in systolic and diastolic function prior to more conventional measurements of cardiac dysfunction (Fig. 23.1d). However, tissue Doppler velocity imaging suffers from the confounding effects of tethering and translation and, hence, newer techniques that assess regional longitudinal myocardial deformation, such as strain and strain rate, may be more sensitive. These tissue myocardial changes may be present prior to increased LV wall thickness and symptoms, and hence may have a role in preclinical detection.

Other echocardiographic features are the result of diffuse infiltration with resultant increased wall thickness of the right ventricle (RV), cardiac valves, and inter-atrial septum (Fig. 23.1). Although cardiac valves may be focally or diffusely thickened, significant dysfunction is not common. Inter-atrial septal thickening along with speckling is a distinctive sign of amyloid with high specificity. RV abnormalities are common and may manifest as systolic or more commonly diastolic dysfunction. RV dilation, if present, may reflect a more advanced disease process and is associated with a more adverse prognosis. Atrial involvement with demonstrable dysfunction using strain echocardiography has also been observed and may be contributory to cardiac symptoms in

Fig. 23.1 (continued)

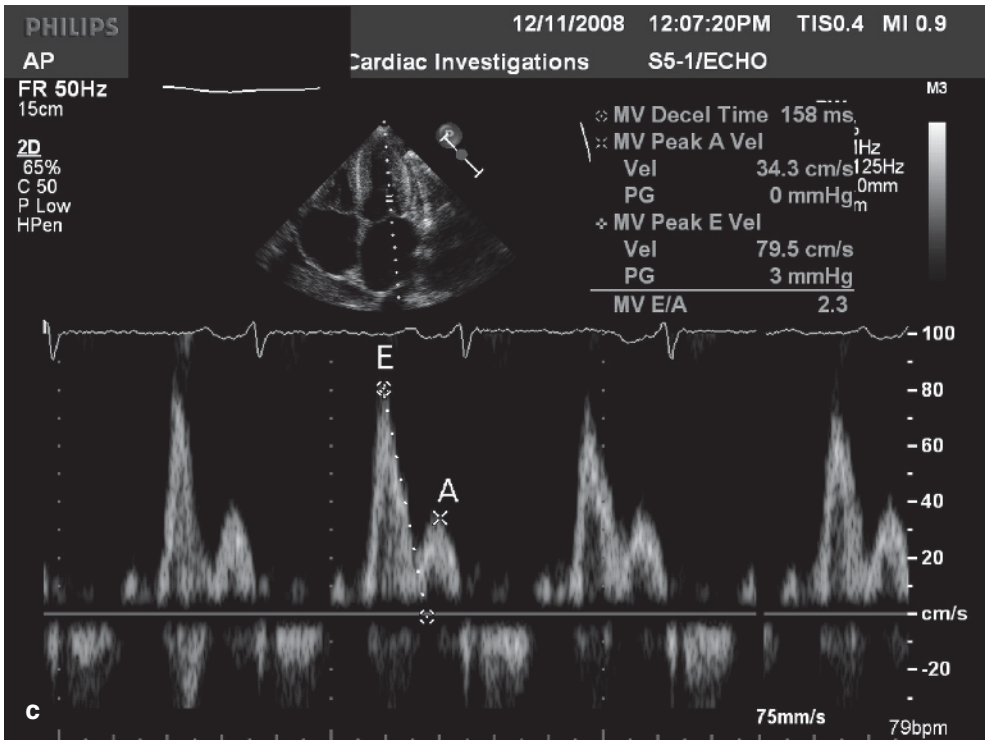

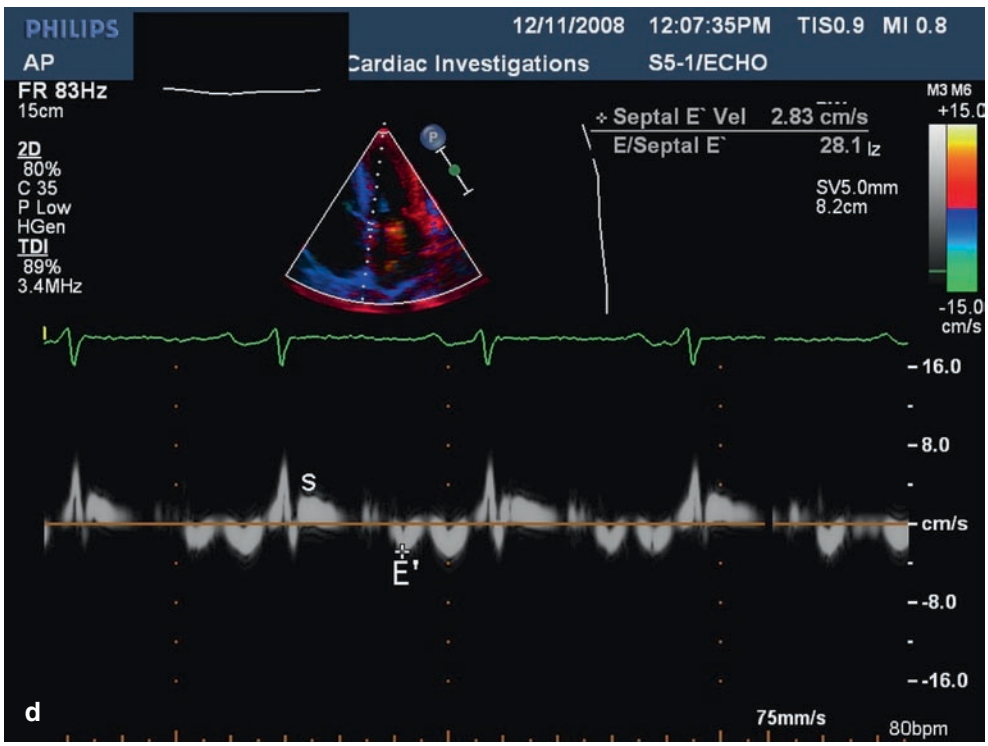

primary amyloidosis. Small-to-moderate-sized pericardial effusion due to pericardial involvement is also common, particularly in end-stage disease.

Despite the number of echocardiographic features found in amyloid heart disease, none, taken individually, are diagnostic, and they can be seen in other cardiac diseases. The diagnosis is still based on the combination of various echocardiographic findings with the integration of clinical findings and (where available) further imaging with CMR (see below). However, marked myocardial hypertrophy along with valvular thickening, abnormality of diastolic function (particularly restrictive physiology), and presence of pericardial effusion in combination with characteristic ECG findings makes amyloid disease an important diagnostic consideration.

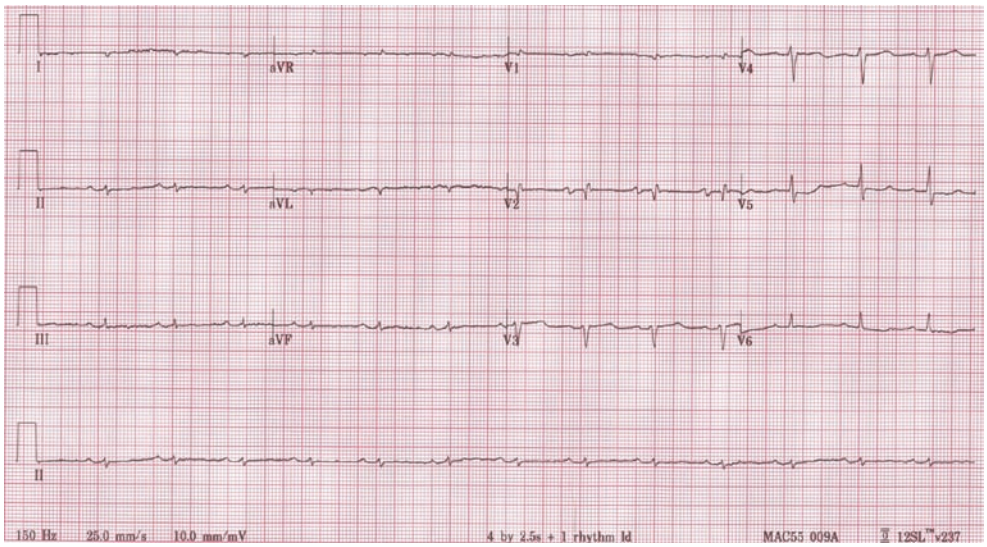

Fig. 23.2 12 Twelve-lead ECG demonstrating small voltages in limb and chest leads (in same patient as Fig. 23.1). There is also poor R-wave progression in the anterior leads (pseudo-infarct pattern). This appearance in combination with marked LV thickness on echocardiogram (see Fig. 23.1a) in the same patient is strongly suggestive of an infiltrative cardiomyopathy (cardiac amyloid)

CMR Imaging

A strength of CMR using late-gadolinium enhancement (LGE) technique is the ability to "phenotype" various forms of cardiomyopathy with high spatial resolution and reproducibility. Maceira et al. studied 29 patients with systemic amyloidosis and 16 hypertensive controls using gadolinium-enhanced CMR.[12] Amyloidosis was associated with qualitative global and sub-endocardial gadolinium enhancement of the myocardium. Sub-endocardial longitudinal relaxation time (T1) in amyloid patients was shorter than in controls and was correlated with markers of increased myocardial amyloid load, such as (LV) mass, wall thickness, inter-atrial septal thickness, and diastolic function. Global sub-endocardial LGE was found in approximately two-thirds of patients. Based on pathological correlates in a patient from this study, the *CMR hyperenhancement probably represents interstitial expansion from amyloid infiltration.*

Perugini et al.. studied an Italian population of patients with histologically proven systemic amyloidosis and echocardiographic diagnosis of cardiac involvement.[13] Gadolinium enhancement by CMR was detected in 16 of 21 (76%) patients. In contrast to the study of Maciera et al. in which the pattern of late enhancement was global and subendocardial, Perugini et al.. reported a much more variable pattern of late enhancement that could be localized or diffuse and subendocardial or trans-mural. Trans-mural extension of hyperenhancement (i.e. how much of the LV wall thickness was enhanced) within each patient significantly correlated with (LV) end-systolic volume. The number of enhanced segments correlated with LV end-diastolic volume, end-systolic volume, and left atrial size. *An especially unique feature of LGE appearances in this population is the blood pool appearing atypically dark.* This reflects the similar myocardial and blood T1 values due to high myocardial uptake and fast blood pool washout of the contrast agent. Although yet to be proved, imaging with a highly reproducible and quantifiable technique such as CMR may help to estimate the prevalence of cardiac involvement in systemic amyloidosis when cardiac morphological changes are not apparent by echocardiography. Screening of subclinical early cardiac involvement may become possible if delayed enhancement proves to have adequate sensitivity in detecting early amyloid infiltration. Improved non-invasive surveillance may also potentially aid in the evaluation of new chemotherapeutic agents. Figure 23.3 illustrates the typical CMR features of amyloid heart disease.

Radiolabelled Serum Amyloid P Component Scintigraphy

Serum amyloid P (SAP) is a highly conserved, invariant plasma glycoprotein of the pentraxin family that becomes specifically and highly concentrated in amyloid deposits of all types as a result of its calcium-dependent binding to all types of amyloid fibril. Following intravenous injection, radiolabelled SAP distributes between the circulating and the amyloid bound SAP pools in proportion to their size and can then be imaged and quantified.[14] *This safe non-invasive method provides unique information on the diagnosis, distribution, and extent of amyloid deposits throughout the body, and serial scans monitor progress and response to therapy.* Serial SAP scans have unequivocally demonstrated that amyloid deposits of all types regress in a proportion of patients when the supply of the respective amyloid fibril

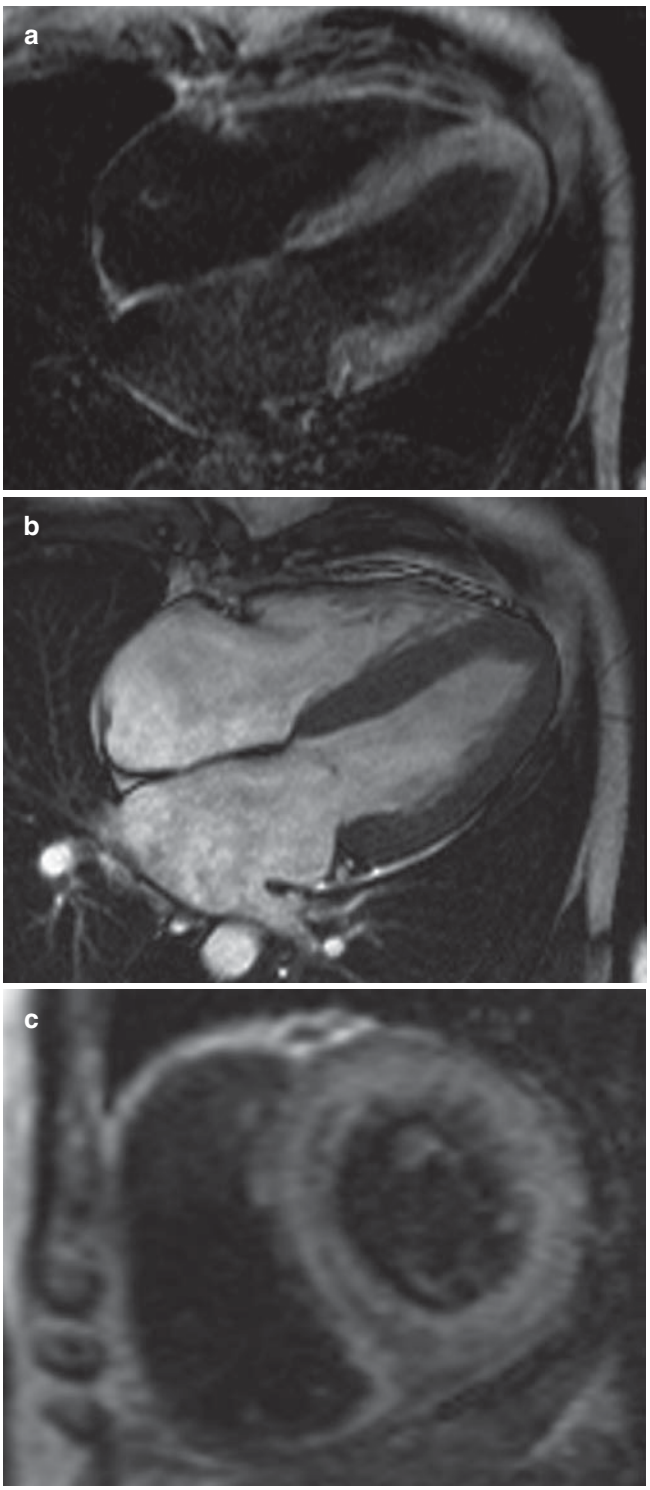

Fig. 23.3 CMR-delayed enhancement (**a**, horizontal long-axis view and **c**, short-axis view) and cine (**b**, horizontal long-axis view) images from a patient with cardiac amyloidosis. Images show typical CMR features: global increase in wall thickness/mass and diffuse biventricular and biatrial sub-endocardial late-gadolinium hyper-enhancement

precursor protein is sufficiently reduced. Unfortunately, planar SAP scintigraphy is unable to image amyloid in the moving heart.

Sarcoidosis

Sarcoidosis is a systemic disorder of unknown etiology involving granulomatous infiltration of various organs including the heart. The pathophysiology is thought to be related to an excessive cell-mediated immune response to an unknown antigen with accumulation of mononuclear inflammatory cells, mostly CD4 + lymphocytes.[15] The resultant inflammatory response produces tissue injury and fibrosis that may be focal or diffuse.

There is a striking variance in prevalence, with the disease more common in Blacks and Scandinavians.[16] Cardiac involvement occurs in up to 30–40% in post-mortem studies [17, 18] and is associated with poorer prognosis, particularly if patients exhibit cardiac symptoms.[19] Clinically, cardiac involvement occurs in 5%, and its presentation may include rhythm disturbance (particularly heart block), cardiac failure, cor pulmonale, and even sudden death.[20] However, diagnosis of cardiac involvement is difficult because of the numerous different manifestations of the disease process and the lack of sensitivity or specificity of various cardiac imaging tests. The Japanese Ministry of Health and Welfare guidelines for diagnosis of cardiac sarcoid, which incorporates the use of ECG, cardiac imaging, and histopathology, is the most well known and currently presides as the reference standard. More recently, Mehta et al. found that including advanced cardiac imaging with positron emission tomography (PET) scanning or CMR increased sensitivity above the previously established criteria.[21]

Echocardiography

Sarcoid involvement of the heart is a great masquerader and may present with a variety of echocardiographic abnormalities, including wall motion abnormalities (particularly regional thinning and aneurysms),[22] systolic and diastolic dysfunction, pulmonary hypertension, and pericardial effusions. Case reports have sarcoidosis mimicking coronary artery disease, Takotsubo cardiomyopathy, RV cardiomyopathy[23], hypertrophic cardiomyopathy, and valvular dysfunction. However, in most cases of systemic sarcoidosis, there are no distinctive morphological or functional abnormalities of the heart. Tissue Doppler[4] and ultrasonic tissue characterization by myocardial integrated backscatter[5] have demonstrated abnormalities in the absence of other 2D echocardiographic features and, hence, may have the ability to diagnose early cardiac involvement. Figure 23.4 shows an echocardiographic example of a patient with cardiac sarcoidosis.

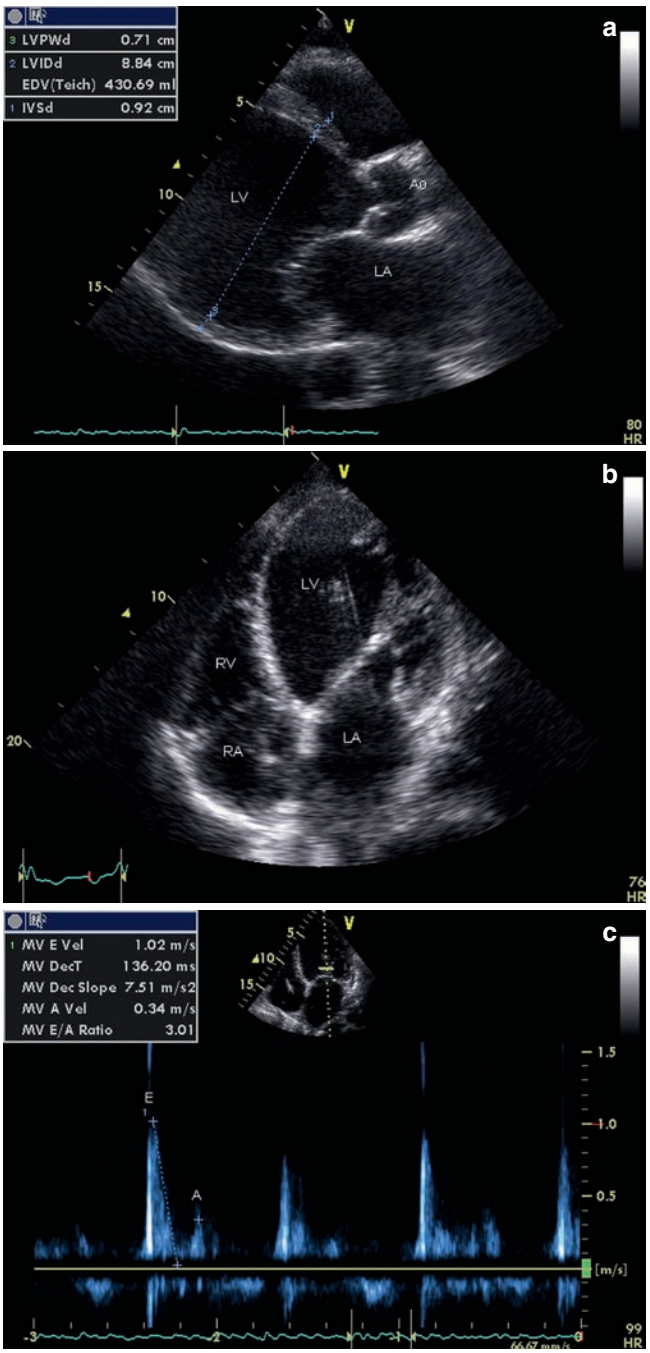

Fig. 23.4 **(a)** 2D parasternal long-axis view of a patient with biopsy-proven cardiac sarcoidosis. The appearance is typical of a dilated cardiomyopathy with globally reduced contraction. The end-diastolic dimension (LVEDd) is increased and there is normal thickness of the posterior wall (LVPWd) and the interventricular septum (IVSd). *LV* : left ventricle; *Ao* =: aorta; and *LA* : left atrium. **(b)** 2D echocardiogram of an apical four chamber showing an LV that is significantly dilated and spherical in shape. This patient had endomyocardial biopsy-proven sarcoidosis, but the appearance is indistinguishable from a typical dilated cardiomyopathy. *RV* : right ventricle; *RA* : right atrium; and *LA* : left atrium. **(c)** Pulse-wave Doppler of mitral valve (MV) inflow in a patient with dilated cardiomyopathy due to sarcoidosis showing a restrictive filling pattern with a E (early-diastolic filling) to A (late-diastolic filling due to atrial contraction) ratio of greater than 2 and a short DT

Nuclear Imaging

Thallium-201 scintigraphy in sarcoidosis can be distinctive with a pattern of reverse redistribution in which a resting perfusion defect improves with stress imaging. This can be helpful in differentiating sarcoid heart disease from an ischaemic cause.[24] However, these findings are non-specific, particularly in the absence of cardiac symptoms, and, hence, are of limited value as a screening test. Gallium-67 scintigraphy has also been used to diagnose cardiac sarcoid as it accumulates in the presence of active inflammation. Hence, the absence of uptake may not exclude sarcoid involvement but suggests lack of active disease and has been shown to predict response to corticosteroid therapy.[25] More recently, a study by Ishimaru et al.. using (18)F-fluoro-2-deoxyglucose positron emission tomography ((18)F-FDG PET) demonstrated focal myocardial uptake in cardiac sarcoidosis.[26]

CMR Imaging

The superior spatial resolution of CMR is particularly useful in identifying even small areas of myocardial oedema and fibrosis leading to post-inflammatory scarring that is typically seen in cardiac sarcoidosis. Both global and regional contractile dysfunction have been described, although, similar to cardiac amyloidosis, the (LGE) technique has been most widely evaluated in clinical studies using CMR. In the largest study to date, Smedma and colleagues evaluated the utility of LGE in 58 patients with biopsy-proven pulmonary sarcoidosis, 25% of whom also had symptoms suggestive of cardiac involvement.[27] All patients underwent clinical assessment, 12-lead (ECG), ambulatory ECG monitoring, trans-thoracic echocardiography,[201]thallium single-photon emission computed tomography (SPECT), and CMR (cine and LGE). The modified Japanese Ministry of Health criteria was used as the gold standard. CMR revealed LGE, mostly involving the epicardium of basal and lateral segments in 73% of patients diagnosed with cardiac involvement by the Japanese criteria. In about half of these patients, scintigraphy was normal, while patchy LGE was present underlining the differences in spatial resolution. This study is limited in that only a minority of patients had correlation between LGE-CMR results and endomyocardial biopsy. Other studies have confirmed the predilection of LGE for the basal-lateral segments, although sub-endocardial or trans-mural hyper-enhancement also has been observed, mimicking the ischaemic pattern. The long-term prognostic implications of LGE in cardiac sarcoidosis are not yet available.

Apart from LGE, both functional and anatomical ("white blood" and "black blood") CMR sequences can help in

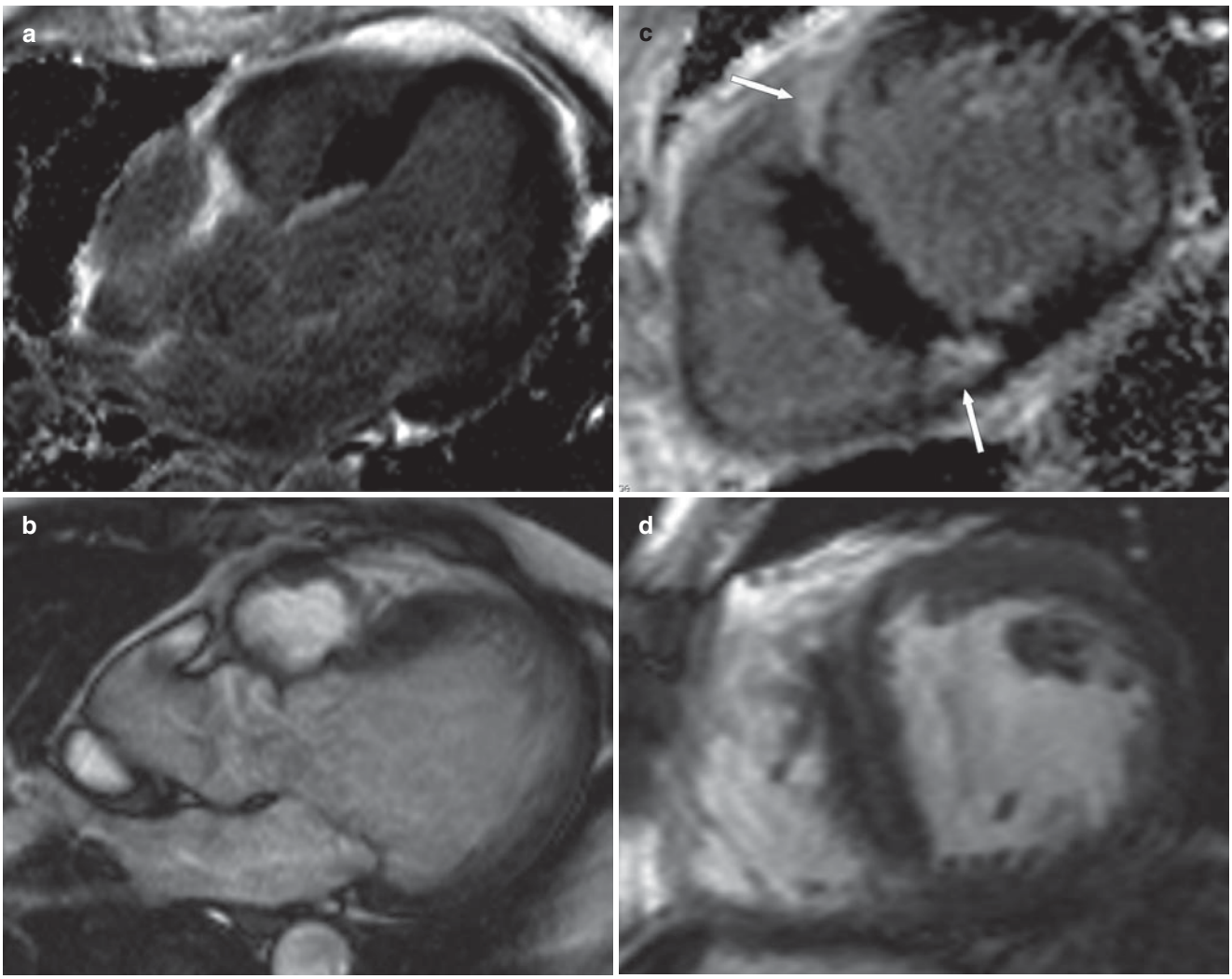

Fig. 23.5 CMR-delayed enhancement (**a**, LV outflow tract view and **c**, short-axis view) and cine (**b**, Lleft ventricularV outflow tract view and **d**, short-axis view) images from a patient with cardiac sarcoidosis. Images show typical CMR features: septal wall thinning, increased overall LV mass, and patchy late-gadolinium hyper-enhancement (*white arrows*)

detecting cardiac sarcoid by demonstrating some of its characteristic features – septal thinning, LV/RV dilation and systolic dysfunction, and pericardial effusion[28,29] (see Fig. 23.5). T2-weighted sequences may also help in identifying myocardial oedema.[30] CMR also identifies pulmonary features of sarcoid, such as enlarged hilar lymph nodes and lung fibrosis.

Anderson–Fabry Disease

Fabry's disease is an X-linked condition with systemic and cardiac manifestations. It is an enzyme deficiency of α-galactosidase[31] that results in accumulation of glycosphingolipids in lysosomes of various cells and organs including the heart. Cardiac involvement is frequent[32] and results in myocyte vacuolation, hypertrophy, and regional fibrosis.[33,34] This can result in heart failure and conduction abnormalities and is an important cause of death in these patients.[35] Currently, the diagnosis is based on one or more of biochemical testing, genetic mapping, and endomyocardial biopsy. However, imaging of the myocardium has been explored as a non-invasive way of early screening and diagnosing patients. *Correct diagnosis is of vital importance because, unlike many other forms of infiltrative cardiomyopathy, the condition is potentially reversible with treatment by enzyme replacement therapy.*[36] Fabry's cardiomyopathy is not as rare as initially thought and can be difficult to distinguish from other forms of infiltrative or hypertrophic cardiomyopathies. A recent study discovered that 6% of male patients diagnosed with hypertrophic cardiomyopathy in fact have Fabry's disease on biochemical and genetic testing.[37] Another study found

that Fabry's disease was present in 10% of patients referred to their cardiac unit with unexplained hypertrophy.[38]

Echocardiography

The principal echocardiographic finding is concentric LVH with often initially preserved systolic function and without cavity dilation. The main functional abnormality, as in other infiltrative cardiomyopathies, is abnormal diastology, although restrictive physiology is also possible, but not as common. Cardiac valves may be thickened, but severe valve dysfunction is rare. There is also increased incidence of aortic root dilation.[39]

Recent studies using tissue Doppler imaging have shown a reduction in both relaxation and contraction tissue Doppler velocities in patients (see Fig. 23.6). These findings are detectable before the onset of LVH and other morphological changes.[40] Strain and strain rate imaging reflect regional myocardial function and contractility, respectively. They are also reduced early in the disease process and can be reversed with treatment.[36] Strain imaging has the advantage over tissue Doppler velocity in that it can detect regional heterogeneity in myocardial function, which is characteristic of Fabry's with strain abnormalities being most pronounced in the inferolateral wall.[41] Interestingly, this is also the area where LGE CMR abnormalities are most pronounced (see below).

More recently, Pieroni and colleagues[42] have described the so-called binary sign, which is an abnormal appearance of the LV endocardial border thought to be related to glycosphingolipid compartmentalization. They found this to be both a specific and sensitive mark for Fabry's disease. However, other authors have disputed this finding and suggested that this binary appearance is non-specific and affected by instrumental settings.[43]

As with other infiltrative and storage cardiomyopathies, the progression and spectrum of disease are not static. In the initial stages, standard morphological and functional changes may not be apparent, and, hence, these newer tissue imaging techniques could provide earlier diagnosis with prompt consideration for enzyme replacement. Regardless, the higher than expected incidence of Fabry's should alert the imaging clinician to this diagnosis in anyone with unexplained LVH.

CMR

Systematic reporting of CMR features in this disease (Fig. 23.7b, c, Video 23.7a) is sparse. Moon et al. have reported LGE patterns in a unique distribution involving the basal inferolateral wall, sparing the endocardium, in 50% of

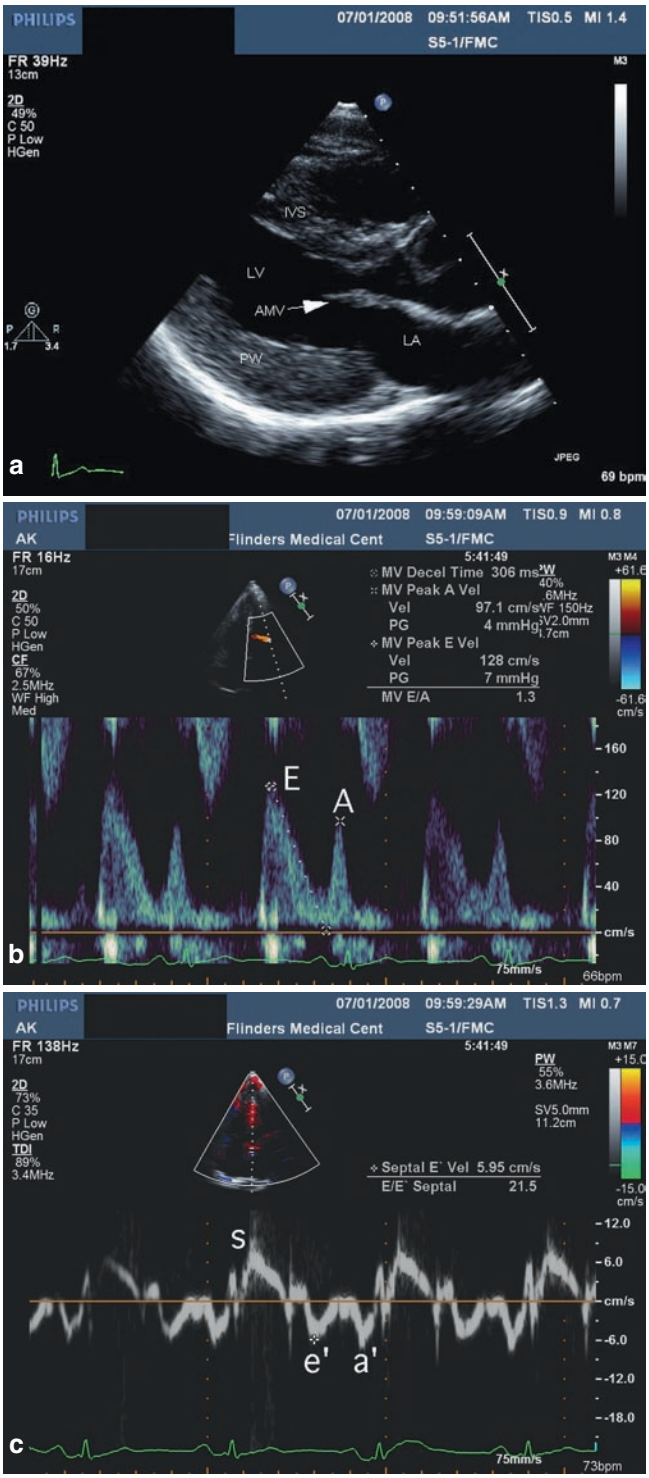

Fig. 23.6 **(a)** 2D echocardiogram of a parasternal long-axis view in a patient with Fabry's disease demonstrating marked concentric LVH without cavity dilation. Thickening of the anterior mitral valve (AMV) is also seen. *PW* : posterior wall; *IVS*: interventricular septum; *LA* : left atrium; and *LV*: left ventricular cavity. **(b)** Doppler imaging: **(a)** Pulsed-wave Doppler of mitral inflow demonstrating ventricular (E-wave) and atrial filling (A-wave). **(b)** Tissue Doppler imaging of basal septum showing contractile (S) and relaxation velocities (E′ and A′). The E′ is markedly reduced with increased E/E′ demonstrating an elevated LV filling pattern of diastolic dysfunction

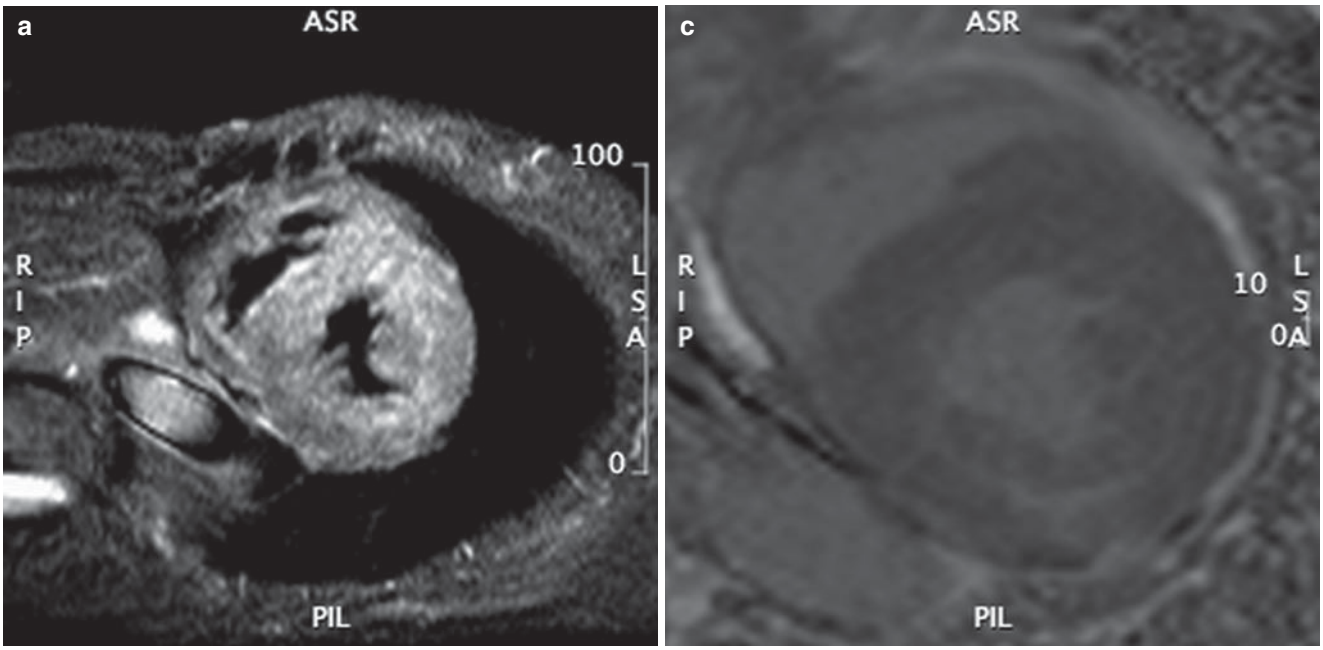

Fig. 23.7 CMR tissue characterization in a patient with Fabry's disease and cardiac involvement (LV mass index 138 g/m^2 (NR: 35–64). **(a)** T2 STIR short- axis showing homogeneous signal indicating absence of oedema and short-axis PSIR late enhancement. **(b)** Infero-lateral uptake in a non-ischaemic distribution pattern

affected patients.[44] LGE in this respect probably represents interstial expansion secondary to replacement fibrosis, although why this region of the myocardium is favoured is unclear. Nevertheless, the finding of substantial areas of myocardial fibrosis by CMR LGE may in future have important implications for the treatment of Fabry's disease, as enzyme replacement therapy may be less effective in patients with extensive areas of myocardial scarring. Prolongation of myocardial T2 relaxation time has also been shown in studies of patients with genotype-positive Fabry's disease, probably related to the marked deposition of glycolipid in the myocardium.[45] This has been suggested by some as a useful marker of this disease. However, there is a wide overlap in myocardial T2 values of Fabry's disease patients when compared with patients with LVH from other causes, such that T2 times *alone* are unlikely to be useful in clinching the diagnosis.[45]

Other Infiltrative Cardiomyopathies

In glycogen storage diseases (GSD), deficiencies in enzymes responsible for metabolizing muscle glycogen not only cause systemic diseases but also can involve the myocardium. Many types have been described, most of which can involve the heart, although in a number of cases (e.g. GSD Type 2a Pompe's disease) the disease is invariably fatal in early infancy and is unlikely to be encountered by the adult cardiologist. Danon disease (GSD Type 2b), characterized by an X-linked dominant inheritance pattern, can present in childhood and early adulthood. Among males, the key features are cardiomyopathy, skeletal myopathy, and intellectual disability ranging from mild learning problems to mental retardation. In a recent seminal study, Arad et al.. showed that cardiac disease can be the initial and predominant manifestation of defects in human glycogen metabolism.[46] It was found that specific glycogen metabolism mutations, LAMP2 and PRKAG2, cause multi-system glycogen-storage disease and can also present as primary cardiomyopathy mimicking hypertrophic or infiltrative cardiomyopathy.

Haemochromatosis can also be considered an infiltrative cardiomyopathy because it is a deposition disease in which iron is deposited intracellularly, causing cell damage with associated cardiac dysfunction. Echocardiography demonstrates features of dilated cardiomyopathy including LVleft ventricular dilation and global systolic dysfunction. Cardiac involvement is progressive and in the later stages can manifest restrictive physiology that clinically can mimic constrictive disease. Non-invasive determination of the cardiac iron load is possible using CMR by measuring myocardial relaxation time T2*.

Myocardial T2* correlates well with cardiac iron concentration measured from biopsy specimens and T2* values < 20 ms are associated with heart failure in patients with β-thalassemia major.

Summary

The evaluation and management of patients with infiltrative cardiomyopathy remains clinically challenging. Cardiac involvement in amyloidosis and sarcoidosis is associated with a more adverse prognosis and hence early identification is warranted.

Echocardiography, though able to detect gross morphological and functional abnormalities, lacks specificity and sufficient sensitivity. Newer methods using tissue imaging may prove to have a role in the future by their ability to define focal abnormalities and detect subclinical disease. Nuclear imaging is helpful in differentiating sarcoid from other cardiac diseases when symptoms are present as well as predicting response to treatment. More recently, cardiac MRI has shown promise for all types of infiltrative cardiomyopathy, in not only identifying typical morphological and functional changes, but also in assessing disease activity. However, *no imaging technique stands alone,* and even the "gold standard" of endomyocardial biopsy may often not be conclusive, given the focal nature of cardiac infiltration in some cases. The integration of clinical assessment, tissue biopsy, and cardiac imaging will still need to form the basis of any future diagnostic framework.

References

1. Merlini G, Westermark P. The systemic amyloidoses: clearer understanding of the molecular mechanisms offers hope for more effective therapies. *J Intern Med*. 2004;255:159–178
2. Selkoe DJ. Folding proteins in fatal ways. *Nature*. 2003;426:900–904
3. Hamer JP, Janssen S, van Rijswijk MH, Lie KI. Amyloid cardiomyopathy in systemic non-hereditary amyloidosis. Clinical, echocardiographic and electrocardiographic findings in 30 patients with AA and 24 patients with AL amyloidosis. *Eur Heart J*. 1992;13:623–627
4. Fahy GJ, Marwick T, McCreery CJ, Quigley PJ, Maurer BJ. Doppler echocardiographic detection of left ventricular diastolic dysfunction in patients with pulmonary sarcoidosis. *Chest*. 1996;109:62–66
5. Hyodo E, Hozumi T, Takemoto Y, et al Early detection of cardiac involvement in patients with sarcoidosis by a non-invasive method with ultrasonic tissue characterisation. *Heart*. 2004;90:1275–1280
6. Rahman JE, Helou EF, Gelzer-Bell R, et al Noninvasive diagnosis of biopsy-proven cardiac amyloidosis. *J Am Coll Cardiol*. 2004;43:410–415
7. Carroll JD, Gaasch WH, McAdam KP. Amyloid cardiomyopathy: characterization by a distinctive voltage/mass relation. *Am J Cardiol*. 1982;49:9–13
8. Selvanayagam JB, Hawkins PN, Paul B, Myerson SG, Neubauer S. Evaluation and management of the cardiac amyloidosis. *J Am Coll Cardiol*. 2007;50:2101–2110
9. Falk RH, Plehn JF, Deering T, et al Sensitivity and specificity of the echocardiographic features of cardiac amyloidosis. *Am J Cardiol*. 1987;59:418–422
10. Hongo M, Kono J, Yamada H, et al Doppler echocardiographic assessments of left ventricular diastolic filling in patients with amyloid heart disease. *J Cardiol*. 1991;21:391–401
11. Cacoub P, Axler O, De Zuttere D, et al Amyloidosis and cardiac involvement. *Ann Med Interne (Paris)*. 2000;151:611–617
12. Maceira AM, Joshi J, Prasad SK, et al Cardiovascular magnetic resonance in cardiac amyloidosis. *Circulation*. 2005;111:186–193
13. Perugini E, Guidalotti PL, Salvi F, et al Noninvasive etiologic diagnosis of cardiac amyloidosis using 99mTc-3,3-diphosphono-1,2-propanodicarboxylic acid scintigraphy. *J Am Coll Cardiol*. 2005;46:1076–1084
14. Hawkins PN. Serum amyloid P component scintigraphy for diagnosis and monitoring amyloidosis. *Curr Opin Nephrol Hypertens*. 2002;11:649–565
15. Iannuzzi MC, Rybicki BA, Teirstein AS. Sarcoidosis. *N Engl J Med*. 2007;357:2153–2165
16. Dubrey SW, Bell A, Mittal TK. Sarcoid heart disease. *Postgrad Med J*. 2007;83:618–623
17. Silverman KJ, Hutchins GM, Bulkley BH. Cardiac sarcoid: a clinicopathologic study of 84 unselected patients with systemic sarcoidosis. *Circulation*. 1978;58:1204–1211
18. Thomsen TK, Eriksson T. Myocardial sarcoidosis in forensic medicine. *Am J Forensic Med Pathol*. 1999;20:52–56
19. Roberts WC, McAllister HA, Jr. Ferrans VJ. Sarcoidosis of the heart. A clinicopathologic study of 35 necropsy patients (group 1) and review of 78 previously described necropsy patients (group 11). *Am J Med*. 1977;63:86–108
20. Deng JC, Baughman RP, Lynch JP, 3rdIII. Cardiac involvement in sarcoidosis. *Semin Respir Crit Care Med*. 2002;23:513–527
21. Mehta D, Lubitz SA, Frankel Z, et al Cardiac involvement in patients with sarcoidosis: diagnostic and prognostic value of outpatient testing. *Chest*. 2008;133:1426–1435
22. Burstow DJ, Tajik AJ, Bailey KR, DeRemee RA, Taliercio CP. Two-dimensional echocardiographic findings in systemic sarcoidosis. *Am J Cardiol*. 1989;63:478–482
23. Yared K, Johri AM, Soni AV, et al Cardiac sarcoidosis imitating arrhythmogenic right ventricular dysplasia. *Circulation*. 2008;118:e113–e115
24. Fields CL, Ossorio MA, Roy TM, Denny DM, Varga DW. Thallium-201 scintigraphy in the diagnosis and management of myocardial sarcoidosis. *South Med J*. 1990;83:339–342
25. Okayama K, Kurata C, Tawarahara K, Wakabayashi Y, Chida K, Sato A. Diagnostic and prognostic value of myocardial scintigraphy with thallium-201 and gallium-67 in cardiac sarcoidosis. *Chest*. 1995;107:330–334
26. Ishimaru S, Tsujino I, Takei T, et al Focal uptake on 18F-fluoro-2-deoxyglucose positron emission tomography images indicates cardiac involvement of sarcoidosis. *Eur Heart J*. 2005;26:1538–1543
27. Smedema JP, Snoep G, van Kroonenburgh MP, et al Evaluation of the accuracy of gadolinium-enhanced cardiovascular magnetic resonance in the diagnosis of cardiac sarcoidosis. *J Am Coll Cardiol*. 2005;45:1683–9160
28. Doughan AR, Williams BR. Cardiac sarcoidosis. *Heart*. 2006;92:282–288
29. Serra JJ, Monte GU, Mello ES, et al Images in cardiovascular medicine. Cardiac sarcoidosis evaluated by delayed-enhanced magnetic resonance imaging. *Circulation*. 2003;107:e188–e189
30. Vignaux O, Dhote R, Duboc D, et al Clinical significance of myocardial magnetic resonance abnormalities in patients with sarcoidosis: a 1-year follow-up study. *Chest*. 2002;122:1895–1901
31. Brady RO, Gal AE, Bradley RM, Martensson E, Warshaw AL, Laster L. Enzymatic defect in Fabry's disease. Ceramidetrihexosidase deficiency. *N Engl J Med*. 1967;276:1163–1167
32. Kampmann C, Baehner F, Whybra C, et al Cardiac manifestations of Anderson-Fabry disease in heterozygous females. *J Am Coll Cardiol*. 2002;40:1668–1674

33. Chimenti C, Pieroni M, Morgante E, et al Prevalence of Fabry disease in female patients with late-onset hypertrophic cardiomyopathy. *Circulation*. 2004;110:1047–1053
34. Funabashi N, Toyozaki T, Matsumoto Y, et al Images in cardiovascular medicine. Myocardial fibrosis in Fabry disease demonstrated by multislice computed tomography: comparison with biopsy findings. *Circulation*. 2003;107:2519–2520
35. MacDermot KD, Holmes A, Miners AH. Natural history of Fabry disease in affected males and obligate carrier females. *J Inherit Metab Dis*. 2001;24 (Ssuppl 2):13–14; discussion 11–12
36. Weidemann F, Breunig F, Beer M, et al Improvement of cardiac function during enzyme replacement therapy in patients with Fabry disease: a prospective strain rate imaging study. *Circulation*. 2003;108:1299–1301
37. Sachdev B, Takenaka T, Teraguchi H, et al Prevalence of Anderson-Fabry disease in male patients with late onset hypertrophic cardiomyopathy. *Circulation*. 2002;105:1407–1411
38. Nakao S, Takenaka T, Maeda M, et al An atypical variant of Fabry's disease in men with left ventricular hypertrophy. *N Engl J Med*. 1995;333:288–293
39. Linhart A, Palecek T, Bultas J, et al New insights in cardiac structural changes in patients with Fabry's disease. *Am Heart J*. 2000;139: 1101–1108
40. Pieroni M, Chimenti C, Ricci R, Sale P, Russo MA, Frustaci A. Early detection of Fabry cardiomyopathy by tissue Doppler imaging. *Circulation*. 2003;107:1978–1984
41. Weidemann F, Breunig F, Beer M, et al The variation of morphological and functional cardiac manifestation in Fabry disease: potential implications for the time course of the disease. *Eur Heart J*. 2005;26:1221–1227
42. Pieroni M, Chimenti C, De Cobelli F, et al Fabry's disease cardiomyopathy: echocardiographic detection of endomyocardial glycosphingolipid compartmentalization. *J Am Coll Cardiol*. 2006;47:1663–1671
43. Kounas S, Demetrescu C, Pantazis AA, et al The binary endocardial appearance is a poor discriminator of Anderson-Fabry disease from familial hypertrophic cardiomyopathy. *J Am Coll Cardiol*. 2008;51: 2058–2061
44. Moon JCC, Sachdev B, Elkington AG, et al Gadolinium enhanced cardiovascular magnetic resonance in Anderson-Fabry disease 1: evidence for a disease specific abnormality of the myocardial interstitium. *European Heart Journal*. 2003;24:2151–2155
45. Imbriaco M, Spinelli L, Cuocolo A, et al MRI characterization of myocardial tissue in patients with Fabry's disease. *AJR Am J Roentgenol*. 2007;188:850–853
46. Arad M, Maron BJ, Gorham JM, et al Glycogen storage diseases presenting as hypertrophic cardiomyopathy. *N Engl J Med*. 2005; 352:362–372

Chapter 24

DILATED CARDIOMYOPATHY

Massimo Lombardi, Danilo Neglia, Petros Nihoyannopoulos, and Albert C. van Rossum

CONTENTS

J. L. Zamorano et al. (eds.), *The ESC Textbook of Cardiovascular Imaging*
DOI: 10.1007/978-1-84882-421-8_24, © Springer-Verlag London Limited 2010

Introduction

Dilated cardiomyopathies, either familial-genetic or non-familial-genetic, in origin are characterized by dilatation of one or both ventricles and/or ventricular systolic dysfunction. The modern imaging techniques allow assessing the primary myocardial defect in force generation as well as abnormalities in the metabolic, perfusion, and structural patterns. The diagnostic and the prognostic role of the three most used techniques (echocardiography, nuclear technologies, and cardiac magnetic resonance, CMR) are discussed with the purpose of integrating the specific information that can be achieved by each of them.

According to a recent statement of the European Society of Cardiology, dilated cardiomyopathy (DCM) is defined by the presence of left ventricular dilatation and left ventricular systolic dysfunction in the absence of abnormal loading conditions (hypertension, valve disease) or coronary artery disease (CAD) sufficient to cause global systolic impairment. Right ventricular dilation and dysfunction may be present, but are not necessary for the diagnosis.[1]

The DCM phenotype may be characterized by a primary myocardial defect in force generation and transmission (mainly linked to genetic causes), by some amount of myocardial inflammation and cell damage (mainly due to infective immunologic or toxic mechanisms), and by specific abnormalities of myocardial function, perfusion, and metabolism, which are the only recognizable alterations in patients without a clear genetic or inflammatory cause of DCM (the most frequent presentation of the disease).

In this chapter, besides DCM with or without evidence of genetic-familial or inflammatory cause, other forms of myocardial disease such as cardiomyopathy associated with pregnancy and parturition, isolated left ventricle non-compaction, or Tako-tsubo disease are discussed. They all are, in fact, characterized by dilatation and/or functional impairment of ventricular cavity, and they all receive a strong diagnostic support from the different imaging technologies.

Today the cardiologist can utilize different diagnostic imaging tools, such as echocardiography, nuclear technologies, and magnetic resonance. They all have tremendous and unique capabilities; it is highly recommended to integrate the information provided by each of them but avoid overlap and duplication.

Dilated Cardiomyopathy

Determining whether newly recognized left ventricle (LV) dysfunction is due to CAD or DCM is a critical early step in the risk stratification and management of patients with or without overt heart failure. Generally, this diagnosis can be anticipated on a clinical ground, but it is conclusively achieved by demonstration of the presence or absence of significant stenosis of the main coronary arteries at invasive coronary angiography. Also, non-invasive evaluation of coronary morphology by multi-slice computed tomography (MSCT) has been proposed by several groups and is likely to be systematically used for this purpose in the near future.

The electrocardiogram is often abnormal and may show intra-ventricular conduction abnormalities and bundle branch block. At least 25% of patients affected by DCM in Western countries have evidence for familial disease with predominantly autosomal dominant inheritance. Familial disease should also be suspected when there is a family history of premature cardiac death or conduction system disease or skeletal myopathy. Autosomal dominant forms of the disease are caused by mutations in cytoskeletal, sarcomeric protein/Z-band, nuclear membrane, and intercalated disc protein genes. X-linked diseases associated with DCM include muscular dystrophies (e.g. Becker and Duchenne) and X-linked DCM. DCM may also occur in patients with mitochondrial cytopathies and inherited metabolic disorders (e.g. haemochromatosis).[2]

DCM can occur at a late stage following cardiac infection and inflammation. In contrast to active or fulminant myocarditis, which is by definition an acute inflammatory disorder of the heart, often with preserved left ventricular size, inflammatory DCM is defined by the presence of chronic inflammatory cells in association with left ventricular dilatation and reduced ejection fraction; histology and/or immunocytochemistry are, therefore, necessary for the diagnosis.

Even if a direct cause of DCM remains frequently unrecognized, the condition may represent the final result of a variable combination of familial, immunological, toxic, or infectious mechanisms. The natural history is not well established, and the ventricular impairment in some instances may be reversible. An early diagnosis is crucial to institute early management.

Echocardiography

Two-Dimensional Echocardiography

Two-dimensional echocardiography can quickly establish the diagnosis of left ventricular systolic dysfunction by demonstrating ventricular dilatation as well as systolic dysfunction (Figs. 24.1 and 24.2). This is typically diffuse, and often involves both the left and right ventricles. However, the left ventricular dimensions frequently remain normal, and the only abnormality may be diffuse ventricular dysfunction (Video 24.1). This may well represent a milder form or an earlier stage of cardiomyopathy. Regular follow-up with repeated echocardiographic examinations will be able to demonstrate changes of ventricular dimensions, and

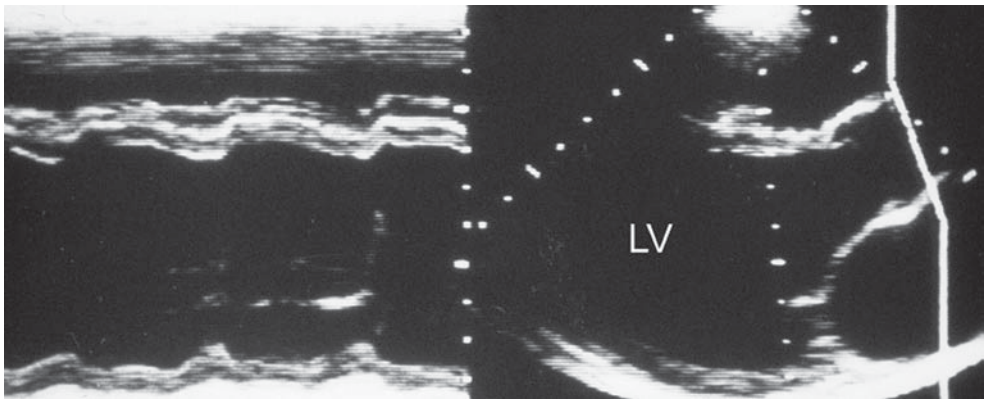

Fig. 24.1 M-mode echocardiogram (*left*) and 2D parasternal long axis (*right*) from a patient with dilated cardiomyopathy and heart failure. There is much dilation of the LV with global reduction of ejection fraction estimated at 30%

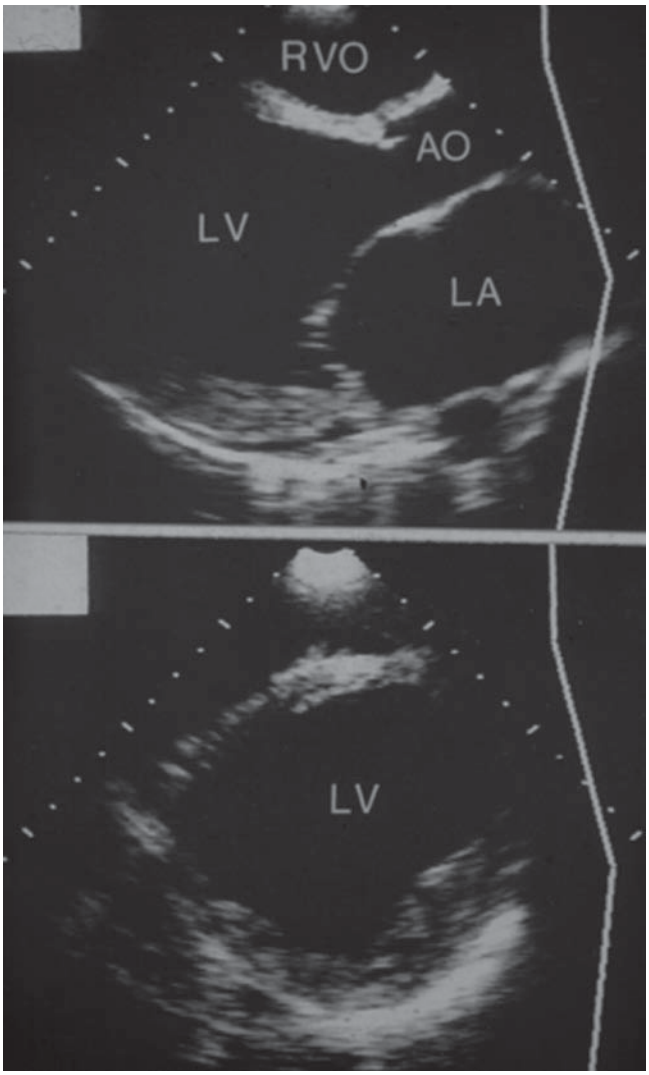

Fig. 24.2 Parasternal long-axis (*top*) and short-axis (*bottom*) from a patient with dilated cardiomyopathy. Note the marked dilatation of the left ventricle

echocardiography is ideally suited for such longitudinal studies.

Both patients with CAD and DCM may present with symptoms of heart failure. It is obviously crucial to separate the two conditions as treatment is very different. This is difficult to achieve with echocardiography alone. Typically, patients with CAD have dilated ventricles with regional wall motion abnormalities, while DCM patients present with a more diffuse dilatation. The right ventricle is not often involved in CAD unless there is proximal right coronary artery occlusion, while in DCM it is frequently affected. Occasionally, the myocardium may be thin and echogenic in case of an old myocardial infarction, which will imply scar tissue. In addition, CAD patients tend to be older than 40 years of age, while DCM patients are younger.

Quantifying left ventricular size and function are obviously important for patient follow-up, and echocardiography is ideally suited for regular assessment. LV dimensions are usually enough, but assessing left ventricular volumes may offer a better way to assess severity. Importantly, many treatment options such as institution of ACE inhibitors or candidates for cardiac resynchronization therapy (CRT) need to have precise estimates of ejection fraction, and 2D echocardiography provides the first-line estimate of LV volumes. The recommended method to measure EF is the modified Simpson's method from two apical planes. If, however, no clear endocardial border delineation is obtained, it is recommended to use ultrasound contrast agents[3] (Fig. 24.3) or real-time 3D echocardiography (Fig. 24.4)[4] in order to accurately calculate LV volumes and ejection fraction (Video 24.2).

Doppler Echocardiography

Mitral Regurgitation

Left ventricular dilatation will lead to mitral annular enlargement, which will cause the mitral leaflets not to appose properly and consequently lead to functional mitral regurgitation. This can be visualized with colour Doppler and quantified as necessary. While in some occasions the causal link between mitral regurgitation and dilated ventricle may be difficult to establish, the association of a globally hypokinetic LV with mitral regurgitation in the presence of otherwise structurally normal mitral leaflets points to primary myocardial disease.

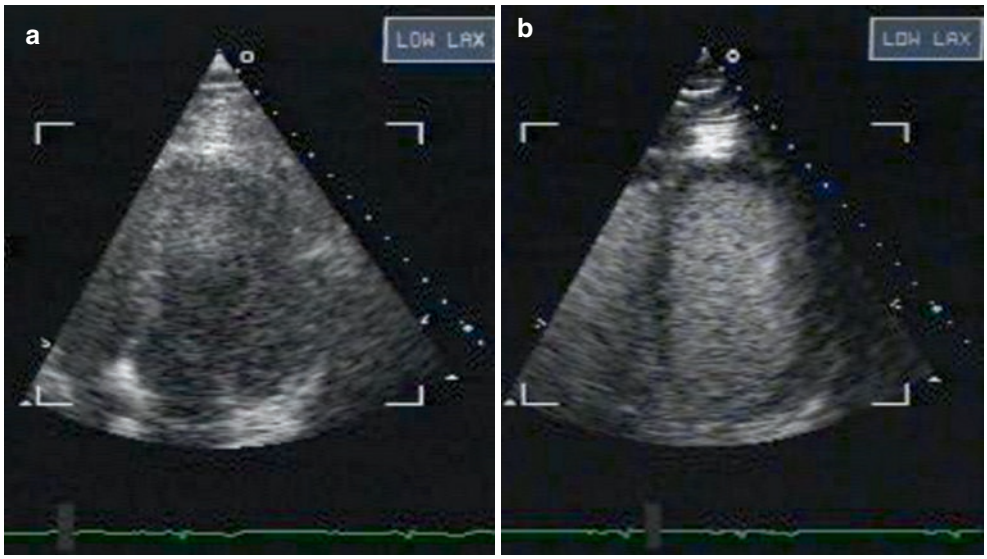

Fig. 24.3 Apical projections from a patient with poor apical imaging with no endocardial border delineation (*left panel,* **a**). The same patient after 0.3 mL of Sonovue® injection (*right panel*, **b**). The entire endocardium is now clearly visualized

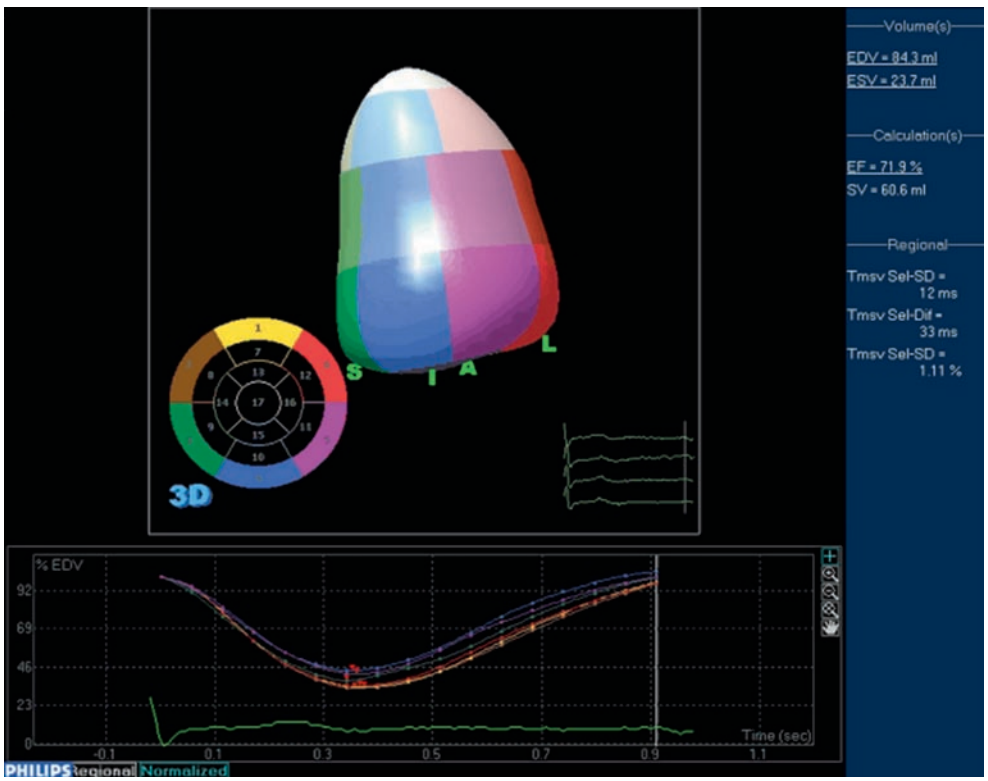

Fig. 24.4 Real-time 3D echocardiography from a patient with normal heart

Rarely the mitral regurgitation is severe in dilated cardiomyopathies, and when this happens, it is more difficult to rule out mitral regurgitation as the prime culprit of LV dysfunction.

Estimate of LV Pressures

With the use of continuous wave Doppler, an estimate of intra-ventricular pressures could be ascertained and, in particular, the right ventricular pressures. In the presence of a tricuspid regurgitant jet, the RV pressures can be calculated as a useful measure of the severity of mitral regurgitation.

With pulse-wave Doppler, the assessment of diastolic LV function can be ascertained and an estimation of LV filling pressures obtained. Trans-mitral velocities profiles may be used to obtain longitudinal follow-up data on disease progression. Abnormally slow LV relaxation, with low LA pressure, gives rise to a pattern of slow acceleration of mitral flow in early diastole (E wave) with the opposite end of the spectrum being patients with seriously compromised LV, giving rise to

a very high early velocity (E wave) across the mitral valve, which represent the dip-and-plateau pressure contour at cardiac catheterization. This pattern usually is accompanied by a diminutive A wave during atrial filling. Between these two ends of the spectra is the normal filling pattern with the early filling velocity somewhat larger than the atrial flow velocity.

Intra-cardiac Flow and Risk of Embolization

Ventricular dilatation with diffuse hypokinesia in patients with DCM, together with the low intra-ventricular velocities, constitutes a major risk for the development of intra-ventricular thrombi with the risk of systemic embolization. Echocardiography can readily identify the presence of an intra-ventricular thrombus and lead to prompt anticoagulant treatment. Thrombi are usually attached at the apex (Fig. 24.5) and may be laminar or protruding with a narrow point of attachment on the endocardial surface.

Deformation Imaging

Tissue Doppler may be used to detect regional or global myocardial dysfunction, particularly in patients with normal chamber dimensions. Tissue Doppler may be used by measuring mitral annular velocities as well as myocardial velocity gradients or left ventricular strain and strain rate. Mean tissue Doppler velocities and radial strain rate of the LV posterior wall at peak systole and early diastole may be reduced, while conventional echocardiography may be normal.[5]

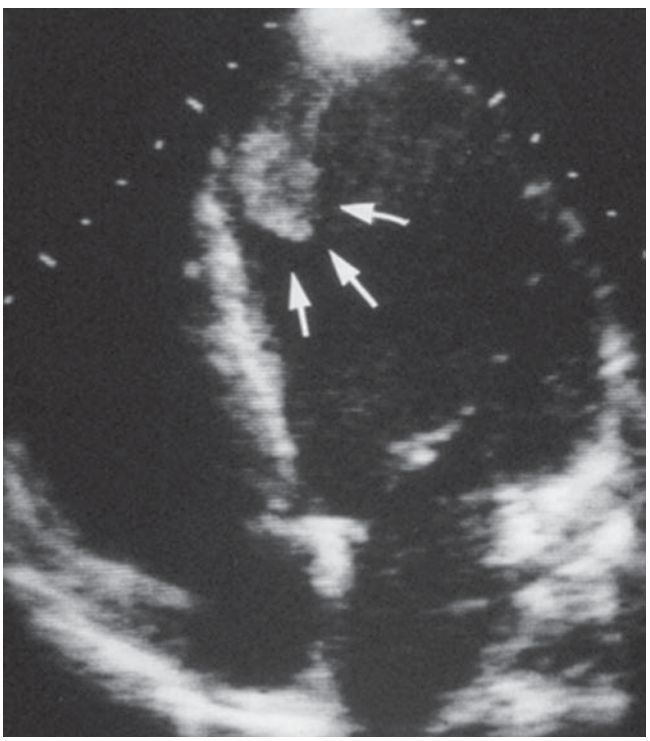

Fig. 24.5 Apical 4-chamber view from a patient with dilated cardiomyopathy. Note the presence of an apical thrombus (*arrows*). The patient was not receiving anticoagulation

The early diastolic mitral annular velocity (*E*m) is a good indicator of diastolic function.

At ³10 cm/s, diastolic function is usually normal, but at ≤8 cm/s it will imply diastolic dysfunction.

Perhaps a more precise way to establish early ventricular dysfunction and predict elevation of LV filling pressures is by using the ratio of early trans-mitral diastolic velocity (E wave) over the early mitral annular velocity (*E*m). *An E/E*m > *10 will imply elevated filling pressures with high sensitivity and specificity.*

Doppler-based strain imaging has found only limited access into clinical practice due to a number of limitations including dependency, a low signal-to-noise ratio, limited spatial resolution, and potential interactions by cardiac translational motion and tethering. Tracking of acoustic markers from frame-to-frame on the basis of 2D echocardiography can accurately determine regional and global LV function, including incremental function parameters like LV rotation and torsion.[6] This novel technique overcomes most of the limitations of conventional tissue Doppler-based strain imaging (Fig. 24.6). This type of quantitation may well be more accurate in predicting outcome than the more traditional ejection fraction.

One particular application of tissue Doppler is in patients who have been identified as suffering from a genetic condition that may lead to left ventricular dysfunction and dilatation such as patients with Duchenne muscular dystrophy in whom it might be useful to detect early left ventricular dysfunction, prior to any clinical manifestation of heart failure.[7] This may have therapeutic implications such that an early treatment might prevent left ventricular re-modelling.

Family Screening

Family screening is important, and echocardiography is ideally suited for this. Large series of asymptomatic relatives have shown that 29% had abnormal echocardiograms. Among affected relatives, symptoms can be quite variable. The majority of affected relatives may be asymptomatic and cannot be identified by relying on history alone. Echocardiography, therefore, plays an important role for the early recognition of affected family members, which may promote the early institution of treatment in an attempt to prevent ventricular re-modelling.

Nuclear Imaging

Abnormalities in the myocardial energy production process, which can be recognized in the DCM heart not specifically linked to specific etiologies, are relevant determinants of

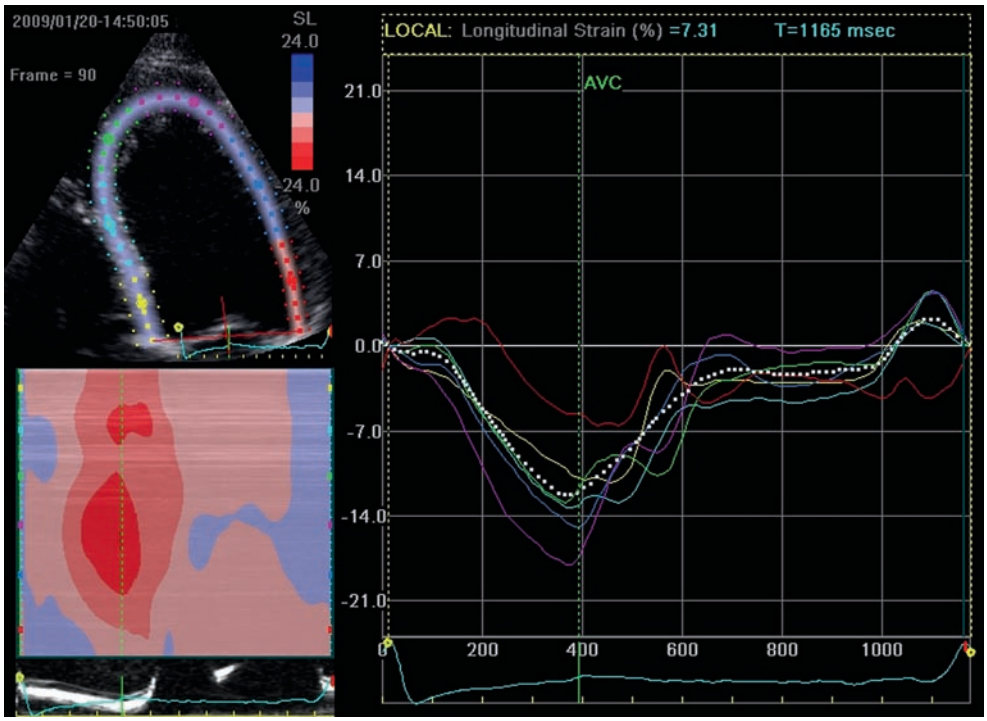

Fig. 24.6 Apical 4-chamber view from a patient with dilated cardiomyopathy. Using speckle tracking it is possible to quantify the longitudinal strain in that patient in every segment and express it as global longitudinal strain (*dotted line*). Here it is clearly reduced

progressive cardiac failure. This pathogenesis is common to other cardiovascular disorders and could be linked to inappropriate perfusion due to coronary endothelial and microvascular abnormalities, abnormal mithocondrial function, or metabolic derangement. These mechanisms, together with alterations in myocardial innervation, may contribute to the progressive myocardial damage and could represent reversible targets of treatment.

Myocardial Perfusion Imaging

It has an elevated accuracy to exclude CAD in patients with LV dysfunction; thus, in the absence of rest or stress-induced perfusion defects at single photon emission computed tomography (SPECT) or positron emission tomography (PET) imaging, the likelihood of significant CAD as a cause of LV dysfunction is extremely low.[8] Conversely, the specificity is suboptimal mainly due to the frequent occurrence of regional perfusion abnormalities in a significant number of patients with LV dysfunction without detectable CAD (Video 24.3). PET has the specific advantage of precisely measuring the absolute myocardial blood flow (MBF, mL/min/g) at rest and during pharmacologic stress (i.v. dipyridamole or adenosine) and, hence, to measure regional and global MBF reserve. Using $^{15}O\text{-}H_2O$ or $^{13}N\text{-}NH_3$ as flow tracers in rest-stress protocols, quantitative evaluation of MBF in patients with DCM often demonstrates a diffuse impairment of myocardial perfusion and MBF reserve, which is interpreted as a result of coronary micro-vascular dysfunction, abnormal myocardial contractility, and wall stress, but is independent of myocardial fibrosis. A global and severe reduction in MBF reserve may occur even in the earlier stages of DCM, and is a distinctive marker of the severity of the disease and of an increased risk of progressive myocardial dysfunction, heart failure, and sudden death[9] (Fig. 24.7). It must be kept in mind that a similar pattern of globally depressed myocardial perfusion may also hinder a multi-vessel CAD, which still needs to be ruled out.

Myocardial Metabolic Imaging

The assessment of myocardial metabolism using ^{18}F-FDG in patients with LV dysfunction is the most frequent clinical application of cardiac PET. It can be combined either with a $^{13}N\text{-}NH_3$ PET or a SPECT perfusion study. It allows identifying different characteristics of the dysfunctional myocardium based on the relationship between glucose metabolism and perfusion at rest. Residual metabolic activity is an indicator of myocardial viability and, thus, of potential reversibility of myocardial dysfunction. Increased regional FDG uptake relative to myocardial perfusion (perfusion/metabolism mismatch) indicates viability, while regional reduction of FDG uptake in proportion to perfusion (perfusion/metabolism match) indicates irreversibly damaged myocardium. It was generally believed that the demonstration of a regional "match" or "mismatch" pattern in patients with newly discovered LV dysfunction could help to identify a CAD etiology. Actually, regionally matched perfusion and metabolic defects indicating myocardial scar as well as regional flow metabolic "mismatch" indicating ischaemia can be frequently

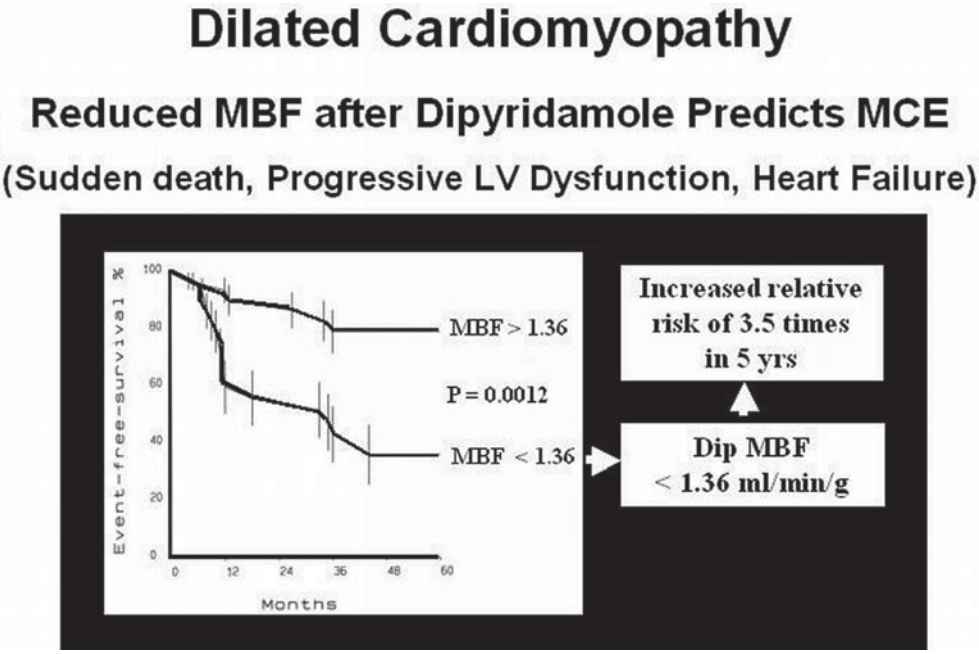

Fig. 24.7 In patients with DCM and without overt heart failure, the extent of myocardial blood flow impairment at rest and during stress, measured by PET, predicts major cardiovascular events (MCE) at follow-up[8]

found in patients with idiopathic DCM[10] (Fig. 24.8), even if data on the potential prognostic meaning of these findings in DCM are still very few.

Additional purpose of metabolic imaging in DCM is to assess abnormalities of intermediate myocardial metabolism, which may further impair and/or be a consequence of reduced contractile performance of the myocardium. Myocardial free fatty acid (FFA) metabolism is decreased and glucose metabolism increased in patients with DCM proportionally to the severity of LV dysfunction. This compensatory metabolic shift towards the more efficient fuel glucose, as well as the effects of metabolic treatment, can be documented by PET imaging using [^{11}C]glucose, [^{11}C]palmitate, and [^{11}C]acetate.[11, 12] Myocardial metabolism in DCM, like myocardial perfusion, may not only be globally but also regionally abnormal, improving after chronic treatment with beta-blockers. Myocardial metabolic efficiency can be assessed by combining the PET measurement of oxidative metabolic rate (washout constant (k) from ^{11}C-acetate myocardial time-activity curve) and independent measurements of stroke work. By this approach in DCM patients, oxidative metabolism and metabolic efficiency were shown to be reduced in proportion to the reduction of LV function and of the integrity of pre-synaptic innervations as assessed using ^{11}C-hydroxyephedrine PET imaging.[13]

DCM and Left Bundle Branch Block

Patients with DCM frequently present with left bundle branch block (LBBB), causing asynchronous activation of the left ventricle (early septal contraction against a relaxed left ventricle), which may further deteriorate cardiac function. CRT re-coordinates ventricular activation and may translate into improvement of cardiac function, symptoms, and prognosis. SPECT and PET imaging in patients with DCM and LBBB are helpful to recognize the efficacy of CRT. The septal-to-lateral perfusion ratio may be reduced in DCM with LBBB, when evaluated with ^{99m}Tc-sestamibi and SPECT or with ^{15}O-H_2O and PET, normalizing after CRT.[14] However, septal perfusion has also been demonstrated to be normal, when evaluated with ^{13}N-NH_3 and PET, without changes after CRT. Independently from regional distribution at rest, absolute measurement of MBF by PET demonstrates that an increase in hyperaemic MBF and MBF reserve after CRT is associated with improvement in LV wall stress and contractile function.[14] The effects of CRT on regional myocardial metabolism may be even more evident. In fact, LBBB is frequently associated with a reduced uptake of FDG in the septal wall, which normalizes after CRT expressing a more homogeneous myocardial oxygen consumption and improved metabolic efficiency.[15] There is preliminary evidence that a "reverse mismatch" pattern in the septum, i.e. preserved perfusion with reduced FDG uptake in patients with DCM and LBBB, may predict a favourable prognosis after CRT.

DCM and Pharmacological Treatment

Nuclear imaging can also be used to assess and somewhat predict the efficacy of pharmacologic treatment in DCM. The favourable effect of carvedilol, other beta-blocker, and trimetazidine on myocardial perfusion and metabolism has been assessed by nuclear medicine technologies. However, the demonstration of the role of PET or SPECT specific patterns of myocardial perfusion and metabolism to predict response to treatment and outcome in DCM requires further extensive confirmative clinical research.

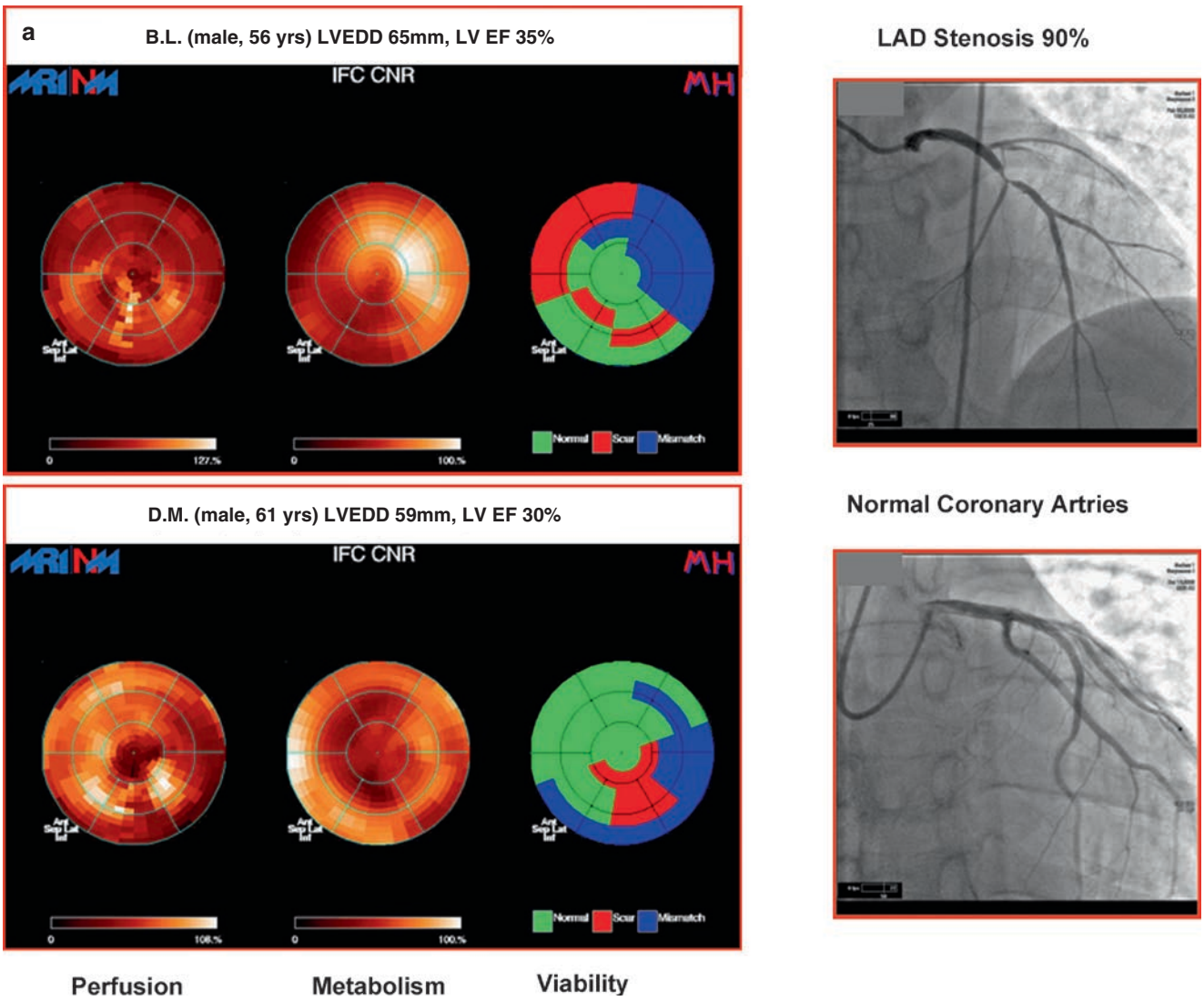

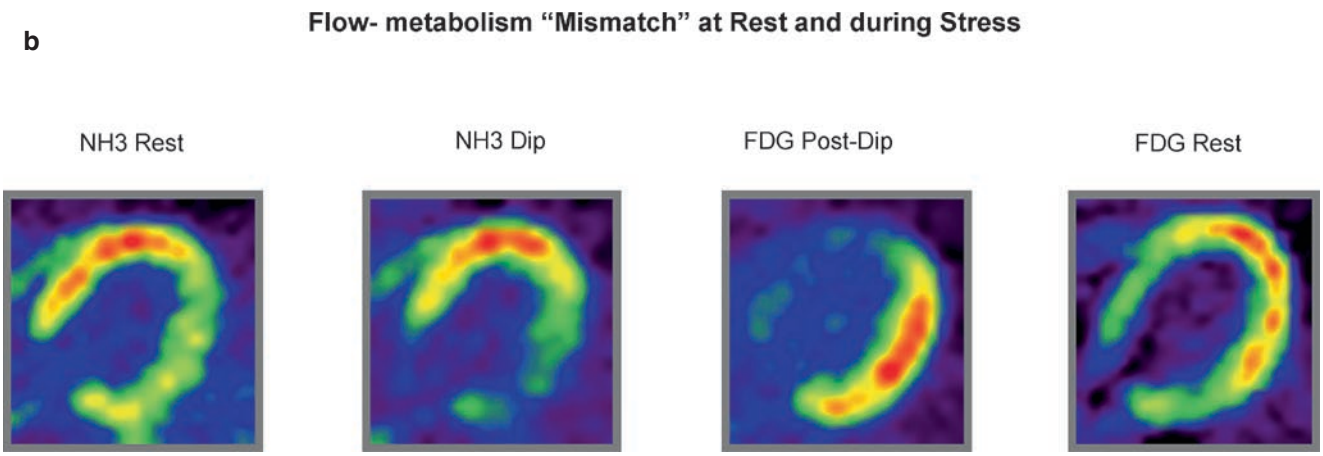

Fig. 24.8 Flow-metabolism regional "match" and "mismatch" patterns typically observed by ^{13}N-NH_3 and ^{18}F-FDG PET study in patients with LV dysfunction due to CAD (Fig. 24.8 *part* **a**, *upper panel*) can be frequently observed also in patients with DCM (Fig. 24.8 *part* **a**, *lower panel*). A regional "mismatch" pattern suggesting myocardial ischaemia can be documented in DCM patients injecting the metabolic tracer FDG, either at rest or after dipyridamole stress (Fig. 24.8 *part* **b**)

Nuclear Imaging of Cardiac Function

Cardiac function may be obtained by gated acquisitions of perfusion and metabolic imaging studies or by equilibrium radionuclide ventriculography (ERNV). The addition of gating to myocardial perfusion scintigraphy or FDG PET studies has been demonstrated to be of great clinical value in CAD as well as in DCM.[16] ERNV still excels in the evaluation of right and left ventricular function and is often indicated in candidates for CRT to assess cardiac dyssynchrony by phase analysis.

Future Developments: Integrated Nuclear and CT Imaging in DCM

The role of nuclear imaging in the evaluation of patients with DCM could be expanded in the near future as a consequence of the diffusion of newer hybrid SPECT or PET/multi-detector CT scanners. Thus, in addition to the functional assessments obtained with SPECT and/or PET (i.e. myocardial perfusion, metabolism, and innervation), the new hybrid SPECT-PET/CT technology allows non-invasive anatomic exclusion of underlying coronary atherosclerosis in the same session (Fig. 24.9). Moreover, the analysis of the ventriculographic phase of CT could add a detailed evaluation of regional and global ventricular function. Independently from the availability of hybrid scanners, however, SPECT or PET may be combined with multi-detector CT in a new conceptual framework to provide a unique non-invasive work-up to exclude CAD, predicting risk, addressing treatment, and testing its efficacy. In addition, this approach might help to study the relationships between non-obstructive atherothrombosis, microvascular disease, and progressive myocardial dysfunction and to evaluate new medical treatments targeted to alter or reverse the progression of heart failure. Prospective outcome

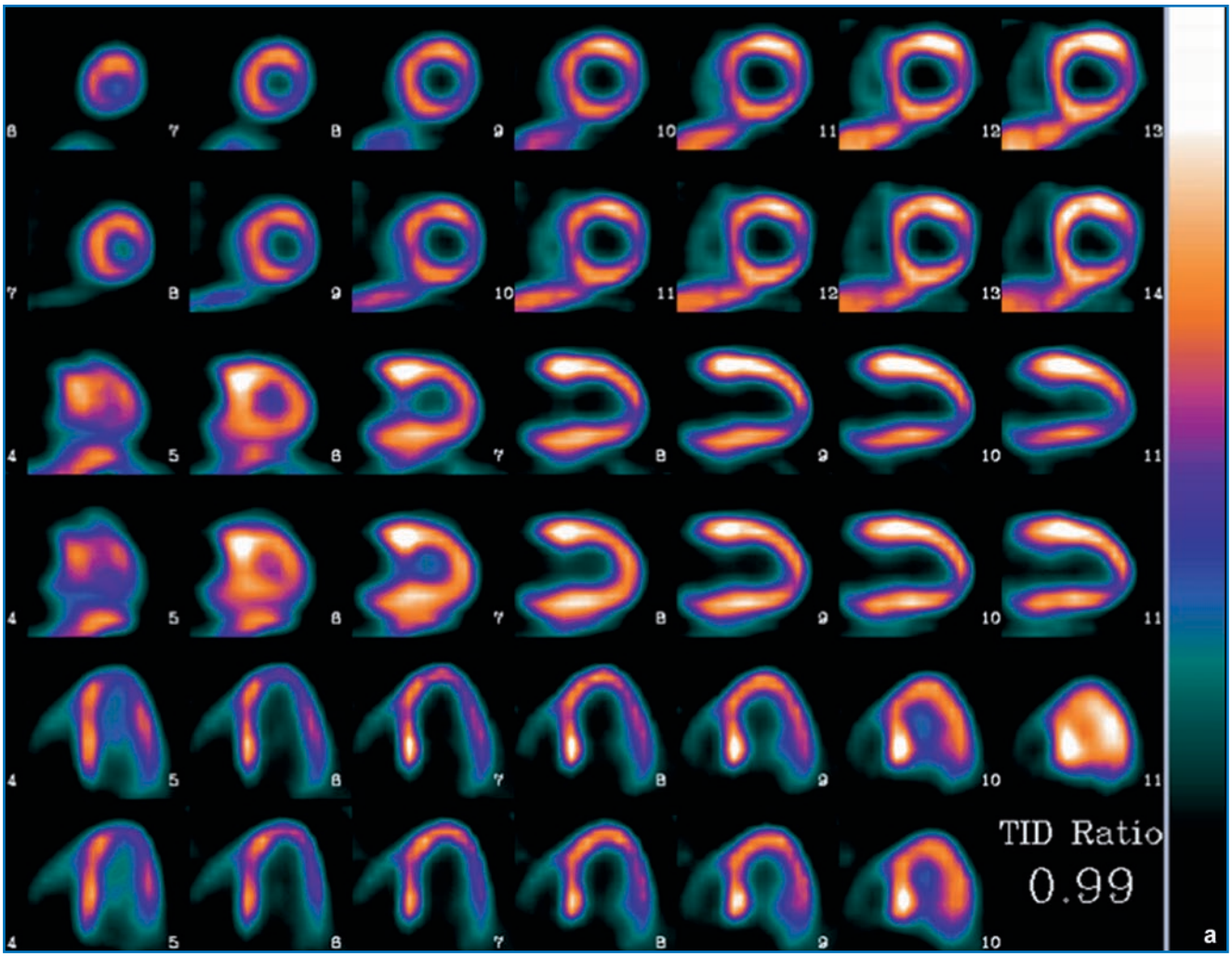

Fig. 24.9 A perfusion ^{13}N-NH_3 PET study at rest (*upper images*) and during dipyridamole stress (*lower images*), performed in a patient with recent onset LBBB and LV EF 38% to exclude CAD as a cause of LV dysfunction, is shown in Fig. 24.4a. A non-reversible perfusion defect involving the middle-apical portions of the lateral wall is evident both at rest and during stress. CTA performed soon after the PET study shows angiographically normal coronary arteries allowing the diagnosis of DCM **(b)**

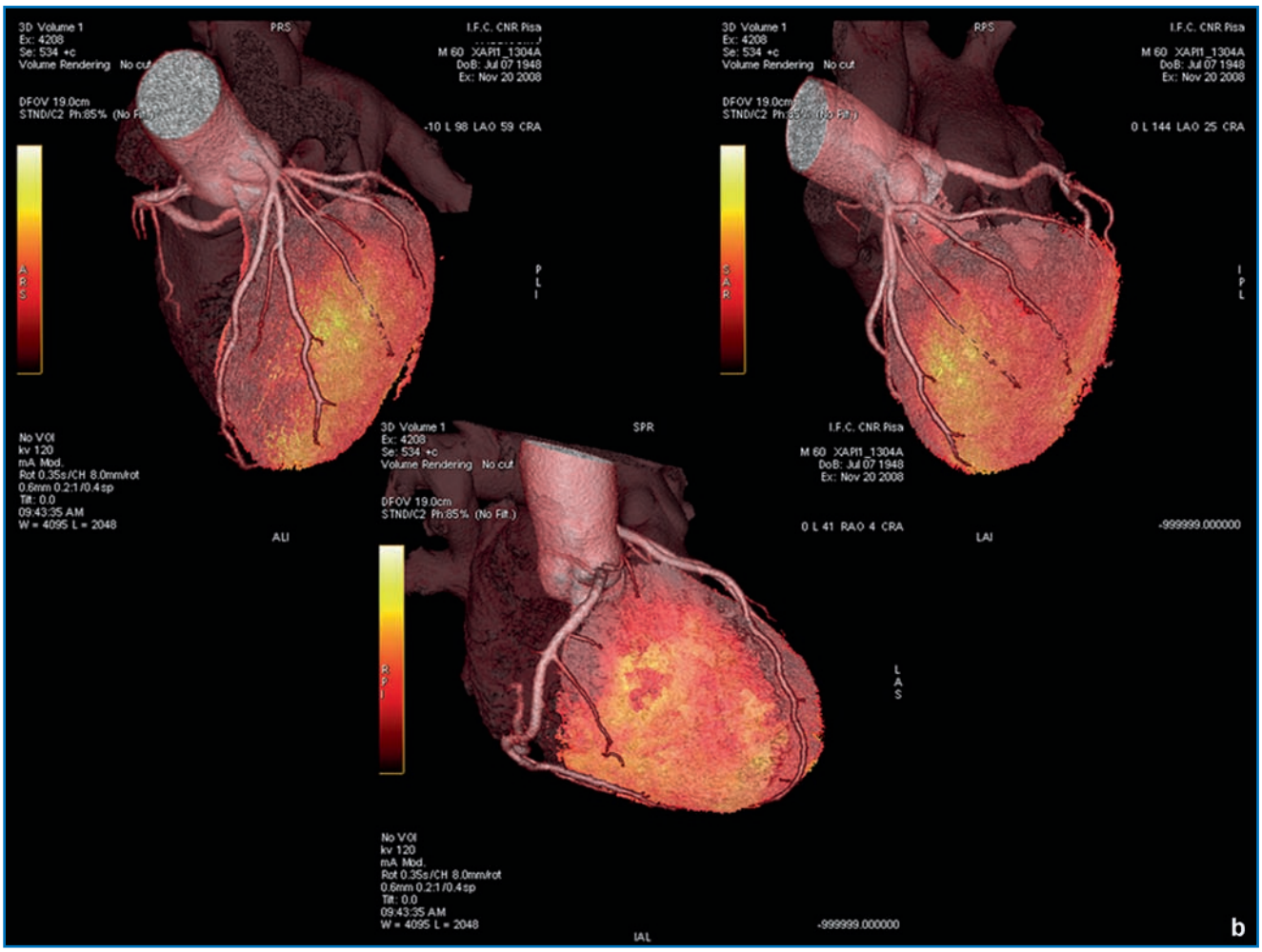

Fig. 24.9 (b) (continued)

studies are warranted to assess the value of this new approach in the evaluation of patients with DCM, also taking into account cost-benefit and radiation exposure issues.

Cardiac Magnetic Resonance

The value of CMR in the diagnosis of DCM relies on two cornerstones: one is the detailed determination of LV function using fast cine techniques (steady state free precession - SSFP), and the other is the assessment of myocardial texture based on the application of techniques that accentuate differences in relaxation properties of the myocardium. The second may help to differentiate normal myocardium from pathologic processes associated with oedema, fibrosis, haemorrhage, iron, and protein deposition using T1- and T2-weighted imaging, late gadolinium enhancement (LGE), T2-star imaging, and combinations of these techniques, respectively. Generally, the detailed functional measurement is useful to confirm a previous abnormal finding on echocardiography, whereas the assessment of pathological myocardial texture is unique to CMR and may provide a key to the etiology of an "idiopathic" cardiomyopathy.

CMR Characteristics of Non-Ischaemic Dilated Cardiomyopathy

Using SSFP cine imaging, the diagnosis of LV dilation is made when the LV end diastolic volume exceeds 235 mL or 112 mL/m^2 in males and 174 or 99 mL/m^2 in females.[17] The superior quality of images obtained by this technique facilitates the detection of regional abnormalities allowing an easier differentiation between ischaemic and non-ischaemic LV impairment. Nonetheless, this task may remain difficult in advanced ischaemic disease when extreme LV re-modelling with subsequent LV dilation has developed. Then, additional use of LGE is likely to be decisive based on the pattern of hyper-enhancement representing necrosis and fibrosis. Hyper-enhancement in ischaemic cardiomyopathy characteristically spreads from the subendocardium up to the epicardium and is confined to the perfusion territories of the coronary arteries. The prevalence of a

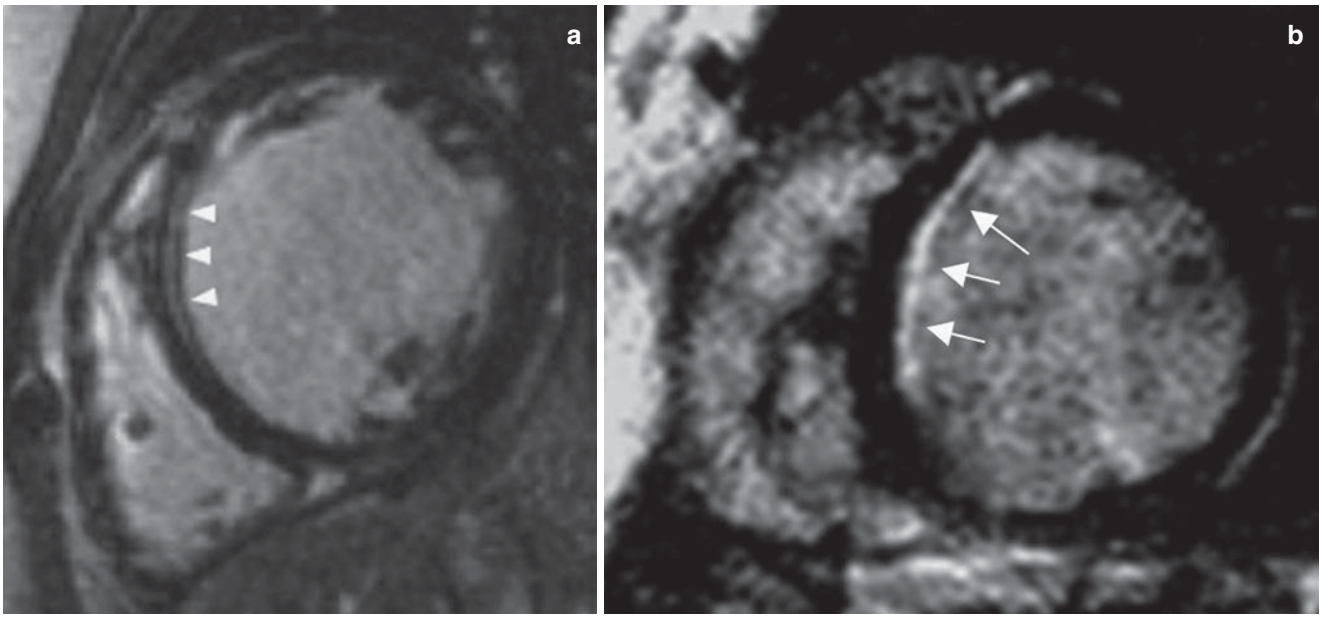

Fig. 24.10 Short-axis late gadolinium-enhanced images in two patients with heart failure, dilated LV and poor EF. *Patient A* (*left panel*) shows a subtle intra-septal stripe of hyper-enhancement (*arrows*) that may be present in up to 1/3 of patients with dilated cardiomyopathy. *Patient B* (*right panel*) demonstrates bright sub-endocardial hyper-enhancement (*arrows*), typical of ischaemic origin due to coronary artery disease

sub-endocardial enhancement pattern in ischaemic cardiomyopathy is between 81 and 100%. In non-ischaemic DCM, hyper-enhancement was either absent (59–88% of cases) or appeared as stripes of hyper-enhancement in the midwall of the myocardium not related to specific coronary artery perfusion territories (9–28% of the cases) (Fig. 24.10). A minority of patients without obstructive CAD, however, may demonstrate the typical ischaemic sub-endocardial enhancement pattern. It has been postulated that this may result from missed infarcts due to transient occlusion and recanalization of the infarct-related vessel or vasospasm. Interestingly, the midwall enhancement pattern was shown to be present in patients with biopsy proven active and borderline myocarditis. This finding points to an etiology of sustained myocarditis in at least a number of dilated cardiomyopathies so far classified as being of unknown origin.

Recently, midwall enhancement was shown to be a predictor of adverse outcome in terms of combined endpoints for all cause mortality and hospitalization for heart failure, sudden cardiac death (SCD), inducible ventricular arrhythmias, and appropriate ICD firing in patients with non-ischaemic DCM.[18–20] Moreover, the predictive value of midwall fibrosis remained significant after correction for left ventricular volumes and ejection fraction. Thus, LGE may play an important role to refine selection of ICD implantation in patients at risk. Future studies will need to corroborate these expectations.

Cardiac muscle involvement leading to progressive DCM is common in neuromuscular disorders and occurs in up to 90 and 70% of patients with Duchenne and Becker muscular dystrophy, respectively. In paediatric patients with Duchenne, occult regional cardiac dysfunction with reduced circumferential strain was detected using CMR tagging when these patients still exhibited normal LV volumes and ejection fractions.[21] In a study involving 74 patients (range of 7.7–26.4 years), 32% was found to have LGE involving the postero-basal sub-epicardial region of the LV with a possible trans-mural and inferior or left lateral spreading.[22] In patients with Becker muscular dystrophy, LGE has been demonstrated in 11 of 15 patients (73%, range 11–56 years), with a similar regional extension (Fig. 24.11). CMR revealed abnormal findings including wall motion abnormalities, reduced LVEF, and LGE in 80% of patients, compared to 53% by echocardiography.[23] In both studies LGE was associated with higher age and adverse LV re-modelling with decreased ejection fraction, but serial studies are needed to clarify whether LGE precedes LV dysfunction and may serve as an early marker for the initiation of heart failure management.

DCM and Recognized Inflammatory Disease

Myocarditis is strongly suspected when a patient, previously normal, is suddenly in congestive cardiac failure, often as a result of a flu-like illness. Following standardization of the histopathological diagnosis of myocarditis by the Dallas criteria,[24] evidence of myocarditis in DCM varies between 18 and 55%. The therapeutic implications, however, are limited as the mere presence of inflammatory infiltrates does not necessarily signify active myocarditis.

Myocarditis due to viral infection is a more frequent finding in DCM than is clinically obvious and can be identified as a cause of disease in almost 10% of cases. Inflammatory DCM is defined by the presence of chronic inflammatory cells in association with left ventricular dilatation, and reduced ejection

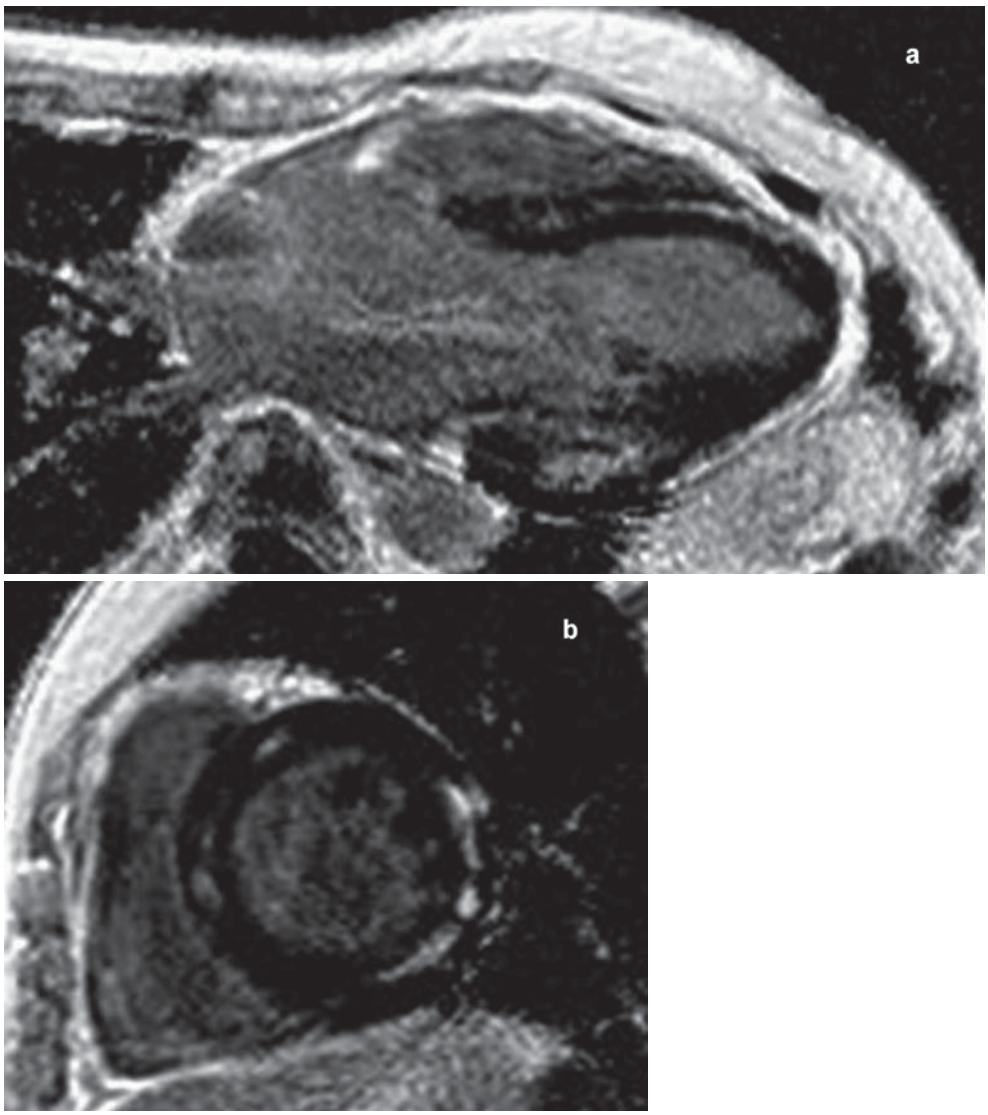

Fig. 24.11 Example of late gadolinium enhancement in patient with Becker's muscular dystrophy. **(a)** 3-chamber view. **(b)** Short-axis view. Hyper-enhancement is predominately apparent in the basal lateral wall, and to a lesser degree, in the inter-ventricular septum

fraction; histology, and/or immunocytochemistry are, therefore, necessary for the diagnosis. Myocarditis increases the risk of SCD in young adults during sports, and accounts for approximately 10% of SCD in macroscopically normal hearts. The diagnosis may be difficult to establish and is generally based on a diversity of clinical signs supported by electrocardiographic and laboratory abnormalities. Endomyocardial biopsy still is considered the gold standard for diagnosis, but this method has limited sensitivity inherent to the focal nature of myocarditis.

Echocardiography

Myocarditis

Myocarditis is suspected when a patient is acutely ill and echocardiography demonstrated a non-dilated LV with global hypokinesia. Often, however, there is only regional ventricular dysfunction involving the septum or even the right ventricle, which may be more difficult to detect. When this regional ventricular dysfunction is present, it is difficult to rule out an acute coronary syndrome. The patient's age and the clinical picture, however, should make the differential diagnosis.

Echocardiography in Cardiac Damage by Exogenous Toxins

A variety of substances can affect the heart leading to DCM. Perhaps the most common toxin is alcohol. Macrocytosis is a useful indicator of chronically high alcohol consumption even in the absence of abnormal liver function. A raised gamma-glutamyltransferase (gamma GT) may be an indicator of only recent rather than long-term alcohol intake, whereas raised levels of other liver enzymes may be due to chronic alcohol hepatitis.

There is an individual susceptibility to the adverse effects of alcohol on the myocardium, which may well be genetically predisposed. The heart is typically markedly dilated

with global ventricular dysfunction, but it may show dramatic improvement after a patient has stopped drinking.

Anthracyclines given as doxorubicin have important toxic subcellular effects that can eventually lead to intracellular calcium overload and depressed cardiac function. The echocardiographic findings are again those similar to DCM with global ventricular dysfunction. As in all dilated cardiomyopathies, it is important to look for the presence in LV thrombus as those patients with dilated ventricles may be prone to thromboembolism.

Echocardiography and Sarcoidosis

Sarcoidosis is a systemic immunological disorder characterized by multiple non-caseating granulomas. Cardiac involvement occurs in 20–60% of patients, of which approximately 30% will develop LV dilation and concomitant symptoms of heart failure, (supra)ventricular arrhythmias, and/or conduction disorders.

Echocardiographic abnormalities include regional wall motion abnormalities, ventricular aneurysms, pericardial effusion, left ventricular systolic or diastolic dysfunction, valvular abnormalities, and abnormal wall thickness (either thinning or thickening); however, none of these abnormalities is specific to cardiac sarcoidosis, and additional testing such as MRI may be necessary to rule out alternative etiologies. In a small study population of 22 patients, ultrasonic tissue characterization with integrated backscatter showed a significant improvement in sensitivity over 2D echocardiography.[25] Further studies will be necessary to confirm the usefulness of this technique. Other techniques such as strain imaging have not been investigated.

Nuclear Imaging

SPECT Imaging

SPECT imaging, coupled with imaging agents of chronic inflammation or labelled antibodies, may be used in myocarditis and inflammatory DCM.[26] Gallium-67 citrate scintigraphy has been tested in DCM patients showing that 87% of patients with hystologically proven myocarditis had a positive gallium-67 scan, while histology was positive only in 1.8% in the negative scintigraphic group. Indium-111 radiolabelled antimyosin (AM) antibodies have been shown to detect myocardial necrosis in human myocarditis. Using planar and SPECT cardiac imaging, the sensitivity of AM imaging for the detection of histologically proven myocaditis is very high (91–100%) with a high negative predictive value (93–100%). By contrast, the specificity and positive predictive value of this approach are below 50%. However, a positive AM scan can predict more than myocardial biopsy a subsequent improvement in ejection fraction in acute onset DCM patients. Limitations to this technique include its current limited availability, radiation exposure, and 48-h delays in obtaining imaging after injection to prevent blood pool effect.

Chagas' Disease

Chagas' disease, an infective syndrome endemic in South America and caused by Trypanosoma Cruzi, may be characterized by DCM in the late chronic phase of the disease associated with severe ventricular arrhythmias. Chagas' myocarditis and/or DCM has several distinctive features in comparison with DCM due to viral myocarditis. Radionuclide functional imaging by ERNV and perfusion imaging by SPECT may detect LV regional wall motion abnormalities and perfusion defects in the absence of epicardial CAD, while RV dyssynergy is common in asymptomatic patients with no other clinical signs of heart failure. An association between regional defects in sympathetic denervation detected by ^{123}I-MIBG and perfusion defects detected by ^{201}Tl scintigraphy has also been shown.

Sarcoidosis

In sarcoidosis, myocardial SPECT with ^{99m}Tc-sestamibi has been used to detect myocardial involvement. Perfusion defects are more common in the RV than in the LV and correlate with atrio-ventricular block, heart failure, and ventricular tachycardia of RV origin. These defects are frequently reversible, which makes it unlikely that they represent granulomatosis or fibrosis. ^{67}Ga scintigraphy has been used in sarcoidosis as a marker of the activity and extent of the disease and for predicting the efficacy of corticosteroids, but has been largely replaced by serial other tests.

Churg-Strauss Syndrome

In Churg-Strauss syndrome, there is systemic vasculitis with eosinophilic myocardial infiltration and cardiomyopathy. A regional pattern of enhanced ^{18}F-FDG uptake with reduced ^{13}N-NH_3 uptake (the pattern of flow-metabolism mismatch) can be observed, which can be reversible after anti-inflammatory treatment and predicts improvement of cardiac function (Fig. 24.12).

Takayasu Arteritis

Takayasu arteritis, myocardial damage, and dilatation may ensue as a consequence of large and small coronary vessels involvement. Tc-99m sestamibi and F-18 FDG SPECT may manifest myocardial ischemic damage.

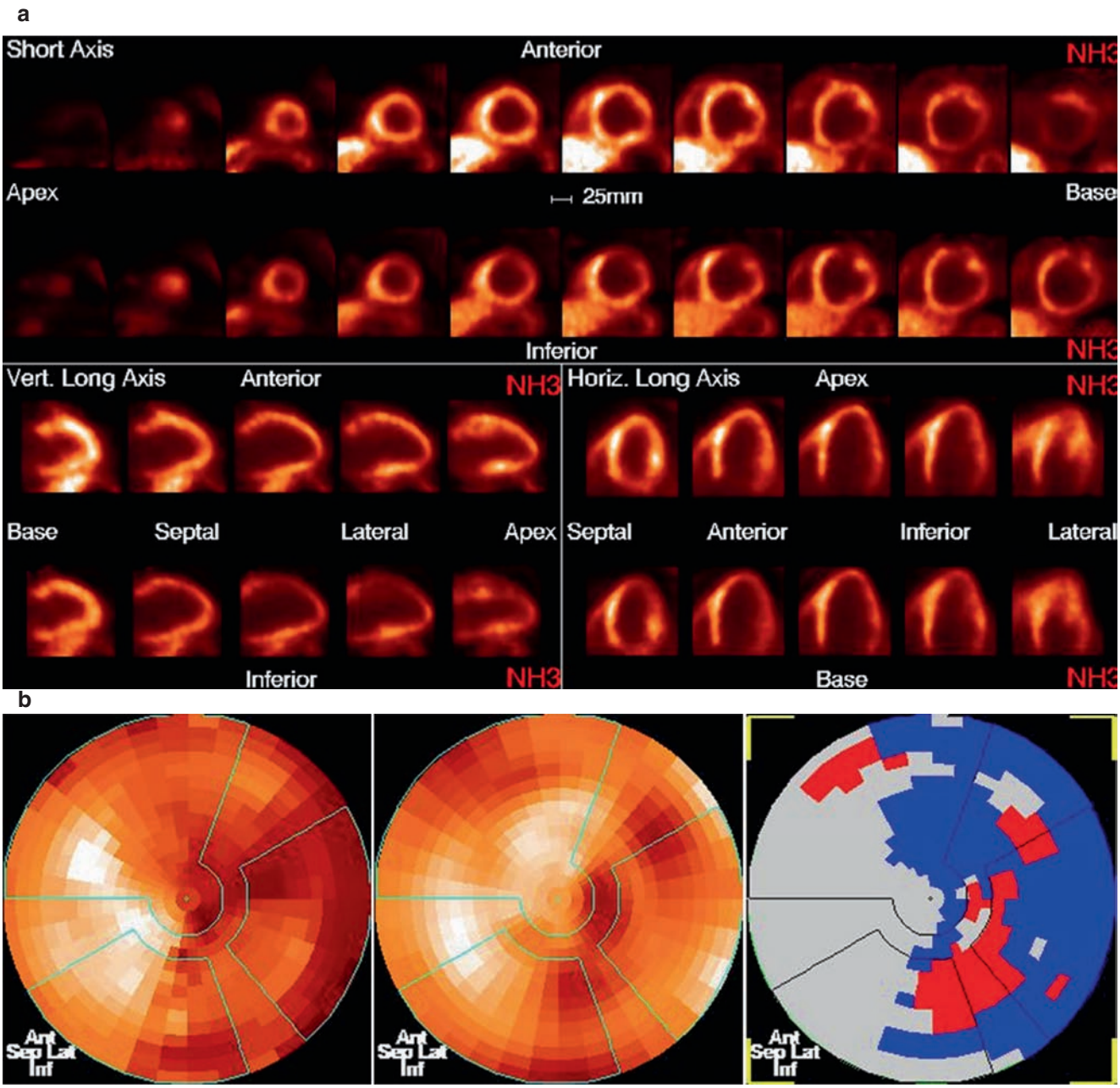

Fig. 24.12 A perfusion ^{13}N-NH$_3$ PET study performed at rest (*upper images*) and during dipyridamole stress (*lower images*) in a patient with an active phase of Churg-Strauss' disease is shown in Fig. 24.12a. A perfusion defect involving the basal portion of the lateral wall is evident in both conditions, while a stress-induced perfusion defect is present in the middle and apical portions of the anterior wall of the LV. Resting ^{13}N-NH$_3$ perfusion images are compared with ^{18}F-FDG metabolic images acquired injecting the tracer after oral glucose loading in a different day in a typical viability study (Fig. 24.12b). Extensive "mismatch" pattern indicating ischaemia is evident in the antero-lateral wall of the LV with some "match" area indicating myocardial necrosis

Kawasaki Disease

In children, Kawasaki disease cardiovascular manifestations can be prominent in the acute phase and are the leading cause of long-term morbidity and mortality. During this phase, the pericardium, myocardium, endocardium, valves, and coronary arteries all may be involved. Nuclear stress perfusion imaging for reversible ischaemia is indicated to assess the existence and functional consequences of coronary artery abnormalities in children with Kawasaki disease and coronary aneurysms. Myocarditis has been demonstrated in autopsy and myocardial biopsy studies to be a common feature of early Kawasaki disease. Myocardial inflammation has been documented in 50–70% of patients using 67Ga citrate SPECT scans and 99mTc-labelled white blood cell scans.

DCM Due to Cardiotoxic Drugs

In DCM due to cardiotoxic drugs (i.e. doxorubicine), ERNV provides initial and longitudinal quantitative assessment of LV function. EF should be measured in all patients before receiving doxorubicin; those with preexisting heart disease and/or LV dysfunction are at greater risk of congestive heart failure. Continued use of doxorubicin after LV dysfunction causes progressive chamber dilatation and deterioration in systolic function.

Cmr

Techniques

Several CMR techniques are used in non-invasive detection of myocarditis, including T2-weighted oedema imaging, T1-weighted spin-echo early gadolinium enhancement, and LGE.[27, 28] When these techniques were compared in patients with clinically suspected acute myocarditis, T2-weighted imaging demonstrated the highest sensitivity (84%) and LGE the highest specificity (100%); the best diagnostic accuracy, however, was obtained when any two of the three techniques were positive in the same patient (85%). The pattern of LGE in the acute phase of myocarditis typically has multiple foci within the lateral wall of the LV, originating primarily from the epicardium (Fig. 24.13) (Video 24.4). When biopsies were taken from the region of contrast enhancement, histopathologic analysis revealed active myocarditis, which was less consistently observed when the biopsy specimens could not be retrieved from the hyper-enhanced regions. This suggests that CMR-guided biopsy may lead to a higher yield of positive findings than routine right ventricular biopsy in patients with acute myocarditis. In patients with chronic DCM, however, such a correlation has not been shown.

Differences in sensitivity of CMR techniques presumably are related to temporal changes of the inflammatory and healing process. Histologically, oedema and islets of necrosis are dispersed throughout the myocardium in the acute and subacute phase of inflammation and ongoing healing of the myocardium.[27] Depending on the time frame after onset of inflammation, oedema sensitive T2-weighted signal or necrosis and fibrosis sensitive LGE signal may both concur, or one of the two may prevail.[28] After healing, LV ejection fractions and dimensions often restore, and the areas of hyperenhancement almost completely resolve. Similar to the shrinkage of myocardial infarct size in the chronic phase, shrinkage

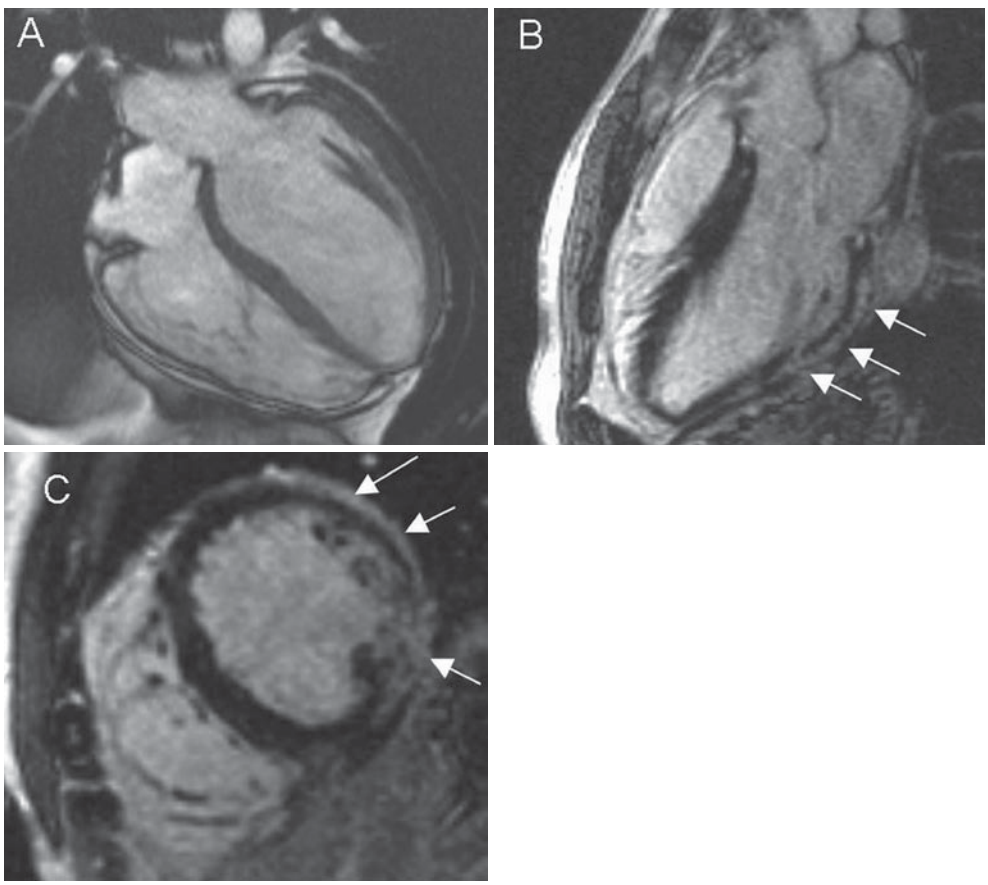

Fig. 24.13 Patient presenting with clinical signs of acute myocarditis. **(a)** SSFP cine 4-chamber view demonstrating slightly dilated LV with EF 47%. **(b)** Late gadolinium-enhanced 3-chamber view with postero-lateral epicardial hyper-enhancement. **(c)** Late gadolinium-enhanced short-axis view with epicardial hyper-enhancement and inferolateral trans-mural progression

of the islets of fibrotic areas to sizes smaller than the dimensions of a voxel has been suggested as an underlying mechanism of the resolution of hyper-enhancement. However, in some patients in whom LV dysfunction and dilation persist, a small remnant mid-ventricular rim of subtle hyper-enhancement may be observed that was shown to be associated with biopsy-proven active and borderline myocarditis, according to the Dallas criteria. This rim is more often found in patients with idiopathic DCM, and may reflect the patchy areas of replacement fibrosis after sustained myocarditis. The presence of hyper-enhancement 4 weeks after the onset of acute myocarditis does not seem to have a significant prognostic value.

Chagas' Disease

Sometimes cardiac involvement develops decades after the initial infection in 30–40% of patients. The clinical course of the disease can be subdivided into three stages, an acute stage with fever and headache, an indeterminate phase in which patients are asymptomatic, and a chronic phase in which the heart is the most frequently affected organ resulting in heart failure and the onset of potentially life threatening ventricular arrhythmias. Localized aneurysm formation can be detected using SSFP cine imaging with predilection sites at the apex and basal inferolateral wall, which are difficult to evaluate with echocardiography (Fig. 24.14) (Video 24.5). Using LGE areas of hyper-enhancement can be observed within these regions in 20% of seropositive patients with indeterminate phase of the disease, 85% with clinical Chagas' heart disease, and 100% with Chagas' heart disease and ventricular tachycardia.[29] The hyper-enhancement pattern is indistinguishable from the ischaemic pattern, and predilection sites are thought to be terminal portions of the micro-circulation, which are most vulnerable to become ischaemic in recurrent episodes of inflammatory disease and subsequent vasodilatation. Another advantage of CMR in evaluating Chagas' disease is its capability to visualize thrombus that may develop within the aneurysms.

Sarcoidosis

The non-caseating granulomas within the myocardium implicate an increase of extra-cellular space; hyper-enhancement on LGE CMR is likely to occur. Hyper-enhancement was reported to be present in 19 of 58 patients (33%) with biopsy-proven pulmonary sarcoidosis and in all patients with cardiac involvement, according to guideline criteria.[30] Hyper-enhanced areas are focal, epicardial, or confluent trans-mural, and predominantly located in the basal and lateral LV segments (Fig. 24.15), thereby showing similarity to LGE in myocarditis. Interestingly, the areas of hyper-enhancement were also present in patients with no LV dilation, indicating that CMR may help preventing the development of heart failure by early detection of cardiac involvement, which accounts for up to 85% of mortality in this patient group.

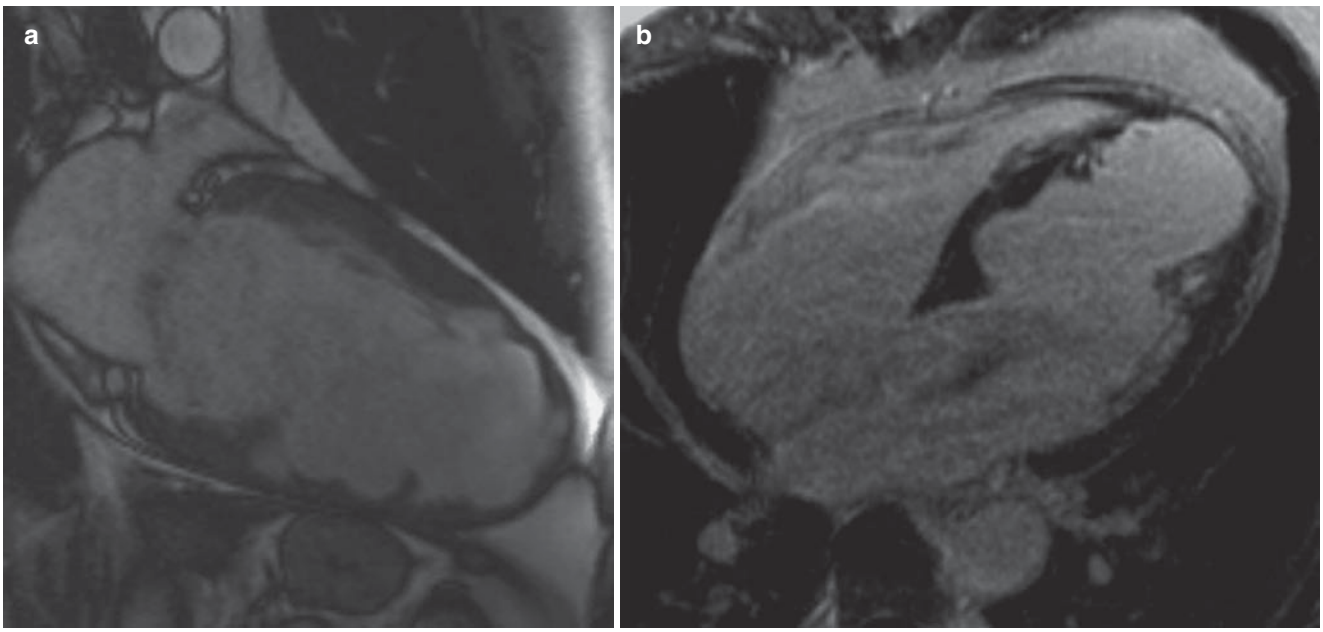

Fig. 24.14 Chronic stage of Chagas' disease with cardiac involvement. **(a)** SSFP (cine) 2-chamber view. **(b)** Late gadolinium-enhanced 4-chamber view. The LV is dilated with manifestation of several small aneurysms, and a large apical aneurysm with trans-mural hyper-enhancement due to fibrosis

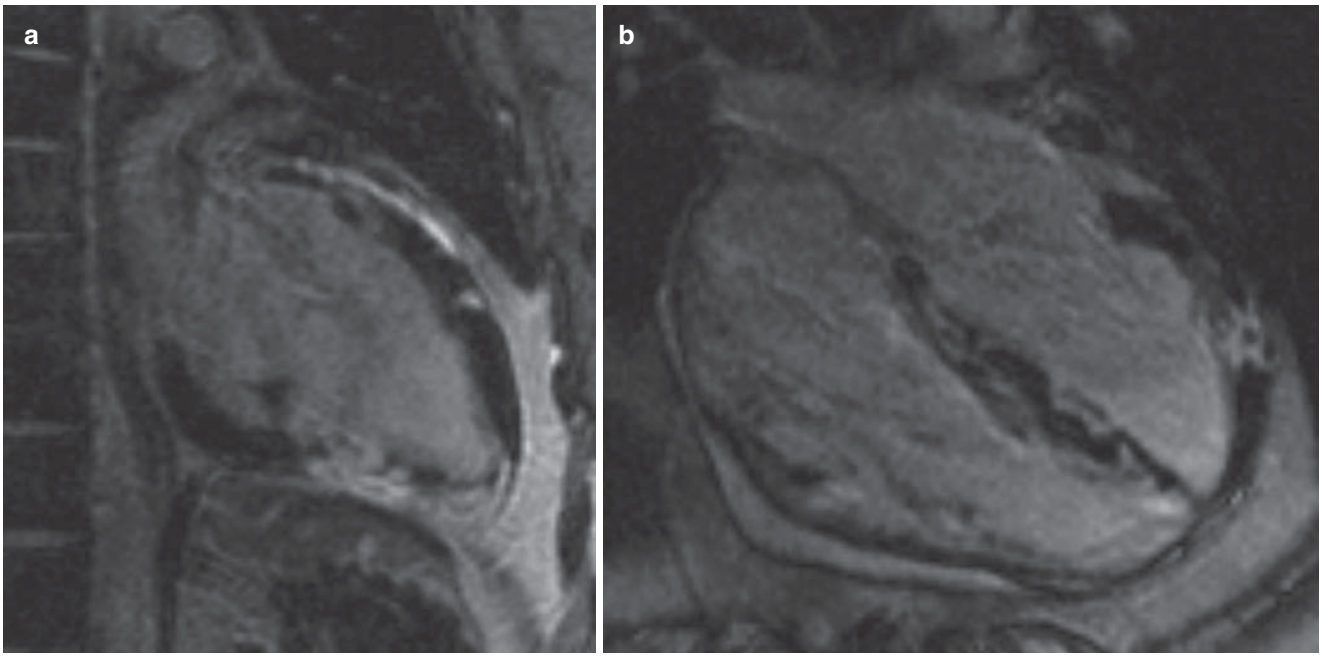

Fig. 24.15 Late gadolinium enhancement in patient with cardiac sarcoidosis. Multiple focal areas of hyper-enhancement are observed in the epicardium and midwall, which partially become confluent and trans-mural **(a)** image obtained in modified 2-chamber view of the left ventricle. **(b)** image obtained in horizontal long axis of the left ventricle"

Cardiomyopathy Associated with Pregnancy and Parturition

Peripartum cardiomyopathy typically occurs during the third trimester of pregnancy or during the first 6 months post-partum without obvious cause and without prior evidence of heart disease. Because it is rare, the literature is limited and filled with anecdotal cases and heterogeneous material. Heart failure with peripheral oedema and ventricular dilatation may be sudden and catastrophic or more insidious. An immunological interaction between mother and fetus can be postulated. This may be responsible for "myocarditis" frequently found on biopsy with interstitial and perivascular lymphocytic infiltration in the presence of myocyte necrosis with or without fibrosis.

The echocardiographic findings are usually those of a non-dilated left ventricle with global hypokinesia (increased end-systolic dimensions), similar to myocarditis. Occasionally, the differential diagnosis with viral myocarditis is difficult and should rely mainly on clinical grounds. It is important to look for LV thrombus as this will carry a high risk for embolization and anticoagulation may be needed. When LV dysfunction is discovered in the context of arrhythmias and congestive cardiac failure during the third trimester or immediately post-delivery, the diagnosis is straightforward. Careful follow-up is mandatory as the disease can deteriorate rapidly with ventricular dilatation and further ventricular dysfunction or can improve from severe hypokinesia to mild ventricular dysfunction and reduced ventricular size to complete recovery.

Typically, peripartum cardiomyopathy can evolve in three ways of approximately equal thirds: 30% of patients may return to normal in up to a year post-delivery, 30% may deteriorate and evolve into DCM, and 30% may remain unchanged. The remaining 10% of patients may be in any intermediate stage. Persisting cardiomegaly at 6 months is usually associated with high mortality and the women may be candidates for cardiac transplantation.

Isolated Left Ventricular Non-Compaction

Its existence is still debated as to whether or not this is a true cardiomyopathy. It was described approximately a decade ago in patients presenting with symptoms of heart failure. It is characterized by prominent myocardial trabeculations with deep inter-trabecular recesses that lie in continuity with the left ventricular cavity.

During early embryogenesis, ventricular trabeculations develop in the distal left ventricle soon after looping and serve primarily as a means to increase myocardial oxygenetaion in the absence of effective coronary circulation. At the same time, when ventricular septation occurs, the trabeculae start to condense (compact) in their portions adjacent to the

outer myocardium, adding to its overall ventricular thickness. At 6 weeks of pregnancy, there are abandoned fine trabeculae that may be present. At 12 weeks, the trabeculae begin to solidify at a time when ventricular septation is completed. In the early fetal period, the compact layer forms most of the myocardial mass. Failure of the left ventricle to condense (become compacted) may result in the isolated left ventricular non-compaction.

The precise etiology for this remains unknown, but it would appear that this is a non-specific condition and can be presented in families with various forms of X-linked dilated cardiomyopathies and also associated with conditions that generate ventricular pressure overload. Whether or not isolated left ventricular non-compaction represents a distinct cardiomyopathy remains a matter of debate. As genetic evidence emerges, it appears that this is a heterogenous and non-specific disorder that may be associated with a variety of conditions such as dilated cardiomyopathies or hypertensive heart disease, restrictive cardiomyopathies, and with neuromuscular disorders. It has been characterized by an extensive layer of non-compacted myocardium aligning a compact layer of myocardium and is typically located in the apical and lateral regions of the LV. Clinical presentation is often heart failure, but also arrhythmia and thromboembolic events. Isolated left ventricular non-compaction may be presented in neonates and children, but also in young adults. It is rarely seen in middle or advanced ages. Accurate diagnosis is important as its clinical morbidity includes heart failure caused by progressive left ventricular dysfunction, arrhythmias, and systemic or pulmonary embolism.

Echocardiography

The diagnosis is made by echocardiography in the vast majority of patients by the combination of the clinical picture of breathlessness or palpitations and the echocardiographic appearance of coarsely trabeculated left ventricle, often distally, presenting with a degree of sub-endocardial recesses. The affected ventricle may present with two layers, a compact (solid) epicardial layer and an endocardial layer consisting of prominent trabecular meshwork and deep intertrabecular spaces/recesses. This is best visualized in apical 4-chamber projections and parasternal short-axis views.

Pet

PET with ^{13}N-NH_3 has been shown to demonstrate restricted myocardial perfusion and decreased flow reserve in these myocardial areas in children. The myocardial perfusion defects may contribute to myocardial damage and possibly to arrhythmias and pump failure.

Mri

With the advent of high-resolution imaging techniques such as CMR, abnormal trabeculation is more easily recognized, requiring stricter criteria for diagnosis of non-compaction than the previously defined echocardiographic criteria of a non-compacted to compacted layer ratio >2in end-systole. Based on a comparison between CMR images of patients with several forms of cardiomyopathy and hypertrophy, and a limited number of patients with previously demonstrated non-compaction cardiomyopathy, a non-compacted to compacted ratio >2.3 in end-diastole has been proposed, yielding a sensitivity of 86% and specificity of 99%[31] (Fig. 24.16) (Videos 24.6 and 24.7). However, in our experience, measuring non-compacted to compacted ratios >2.3 are also frequently found in other cardiomyopathies, such as ischaemic DCM and HCM and even in healthy volunteers. Also, crypt formation has been described in genetically proven carriers of hyper-trophic cardiomyopathy (Fig. 24.17) (Videos 24.8 and 24.9).[32] Although by CMR clearly distinct from the typical hyper-trabecularization pattern of non-compaction cardiomyopathy, prominent crypts may have been misdiagnosed by echocardiography as non-compaction cardiomyopathy in the past. Therefore, further refinement of the criteria to diagnose LV non-compaction cardiomyopathy with CMR is necessary. Of note, no hyper-enhancement has been reported so far in this particular patient group.

Tako-Tsubo

Tako-tsubo cardiomyopathy was described in 1990 as a unique clinical entity among acute coronary syndromes characterized by sudden onset of chest symptoms, electrocardiographic changes consistent with myocardial ischaemia, and transient left ventricular dysfunction (apical or mid segment, or both) without significant coronary stenosis by angiography[33, 34], which is often normal. This rare clinical variant is unique and has a favourable prognosis compared with other causes of acute coronary syndromes, despite the similarity in presentation. To date, the precise etiologic basis of this syndrome is not clear. Tako-tsubo cardiomyopathy has been linked to an excess sympathetic nervous activity, which is proposed as a central mechanism in the pathogenesis of transient left ventricular apical dysfunction (apical ballooning syndrome). Acute multi-vessel coronary vasospasm (epicardial or micro-vascular), abnormalities in coronary endothelial function, and catecholamine-mediated cardiotoxicity have been also claimed.

These patients may present with acute onset chest pain, heart failure, and cardiogenic shock, and at heart catheterization, have angiographically normal coronary vessels and typical dyssinergy of the LV apex.

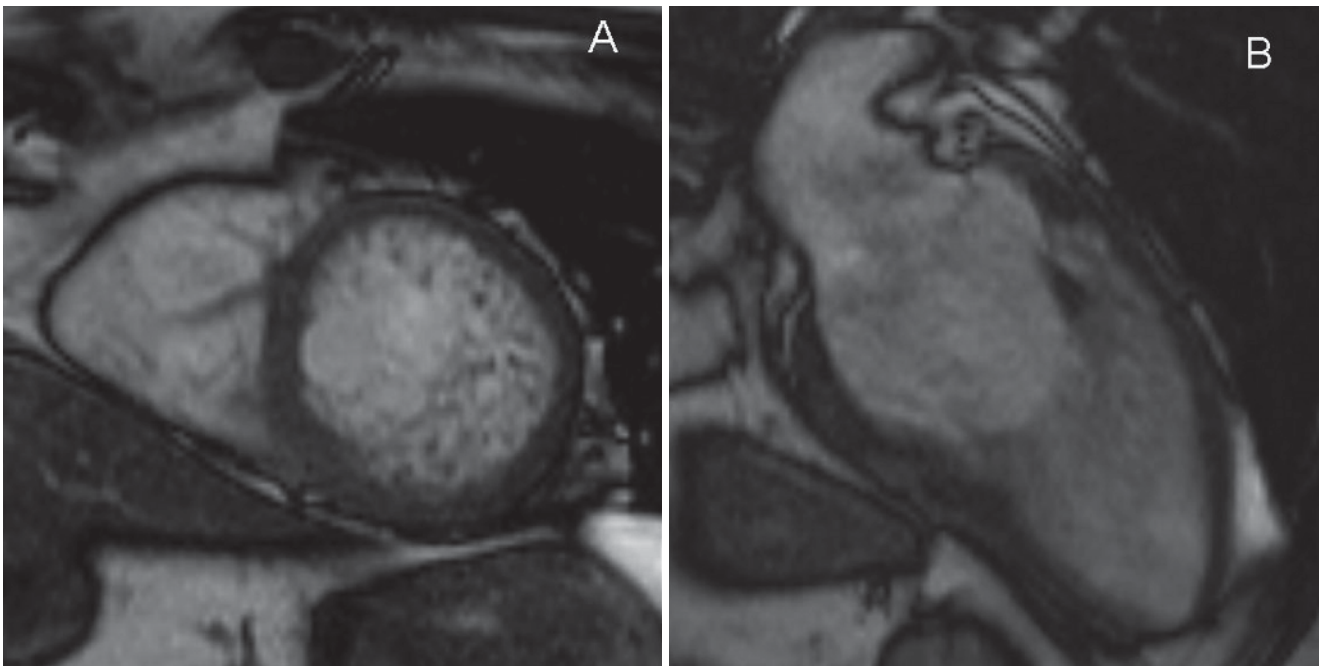

Fig. 24.16 Patient with non-compaction cardiomyopathy demonstrating meshwork of trabeculae predominantly in the apex. The end-diastolic non-compacted to compacted ratio exceeds 2.3. **(a)** Short-axis view. **(b)** 2-chamber view

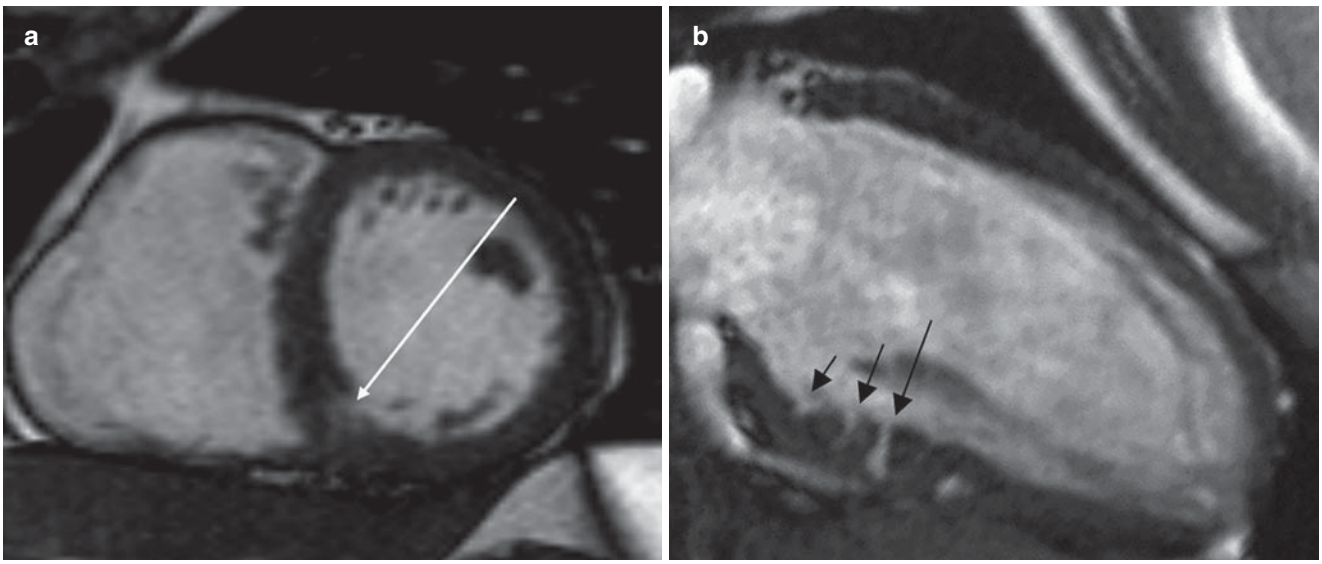

Fig. 24.17 Myocardial crypts in the inferoseptal wall as observed in genetically proven carrier of hypertrophic cardiomyopathy mutation. The appearance is clearly distinct from hyper-trabecularization in non-compaction cardiomyopathy (see Fig. 24.16). **(a)** Short axis view with line indicating the transaction of modified 2-chamber view as seen in **(b)**, and *arrows* pointing the crypts

Echocardiography

Echocardiography is typical of an extensive acute left coronary artery syndrome with extensive apical akinesia or even dyskinesia (Fig. 24.18). The diagnosis, however, is based on the natural history of the disease, which is based on the restoration of the ventricular function within 2–4 weeks.[33, 34]

Nuclear Imaging

SPECT imaging can be used to evaluate myocardial damage and the pathogenesis of the syndrome. Using myocardial ^{123}I-MIBG to evaluate adrenergic innervations and ^{99m}Tc-MIBI to assess myocardial perfusion in patients with angiography proven typical ballooning syndrome, it has been shown

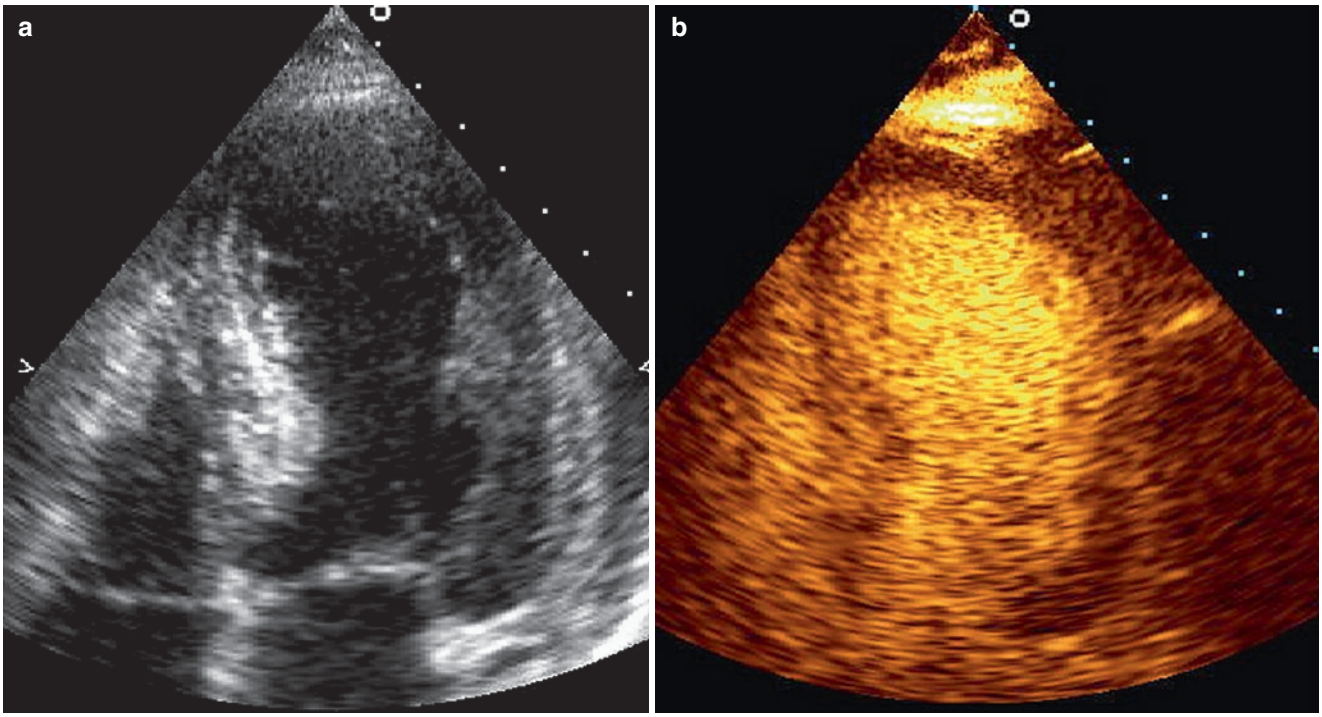

Fig. 24.18 Systolic frames from apical 4-chamber projections in a patient with Tako-Tsubo cardiomyopathy. On the *left panel,* gray-scale imaging shows apical ballooning. On the *right panel,* contrast study a few seconds later demonstrates better the apical aneurysm

a decreased heart-to-mediastinum ratios of ^{123}I-MIBG at early (20 min) and delayed (4 h) image, with an increased cardiac washout rate indicating a functional alteration in presynaptic sympathetic neurotransmission. The neuronal tracer was evidently reduced in the akinetic apex and the perfusion tracer showed a modest defect. It has been also documented that the severity of the apical perfusion defects, evidenced by measurements of the TIMI myocardial perfusion grade at angiography, correlates with the extent of acute myocardial injury suggesting a catecholamine-mediated endothelial/micro-vascular dysfunction as a pathogenetic mechanism in this disease. SPECT and PET perfusion-metabolic studies in these patients have shown a sort of "reverse mismatch" pattern (FDG defect in excess of perfusion defect) at the apex suggesting that the myocardial damage caused by sympathetic overload may involve abnormalities of both perfusion and glucose metabolism with a scintigraphic "fingerprint" of reversibility.

Mri

Using CMR, the apical ballooning syndrome is characterized by wall motion abnormalities and increased T2-weighted signal indicating oedema, without signs of LGE[35] (Fig. 24.19). It is worth noting that the pattern of oedema during the acute phase of Tako-tsubo is different from the other ischaemic acute syndromes. Thus, CMR is particularly useful to confirm a suspected diagnosis of the apical ballooning syndrome since it can differentiate this syndrome from other ACS-mimicking syndromes with normal coronary arteries as myocarditis and infarction due to coronary embolization.

Video 24.1

Apical 4-chamber view from a patient who presented with an out of hospital cardiac arrest. The LV is not dilated with full-thickness myocardium and marked global hypokinesia. Contrast-enhanced CMR did not show any myocardial scar

Video 24.2

Real-time 3D echocardiographic images from a patient with dilated cardiomyopathy. With some simple identification of endocardial borders, the system calculates the left ventricular volumes automatically

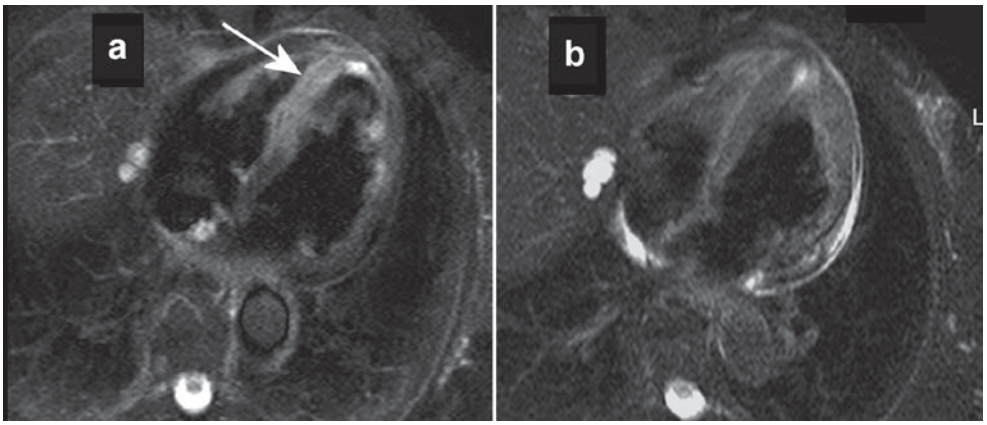

Fig. 24.19 A case of Tako Tsubo. **(a)** T2 image obtained during the acute phase. A clear enhancement of the signal due to the presence of myocardial oedema at the level of the inter-ventricular septum is evident (*arrow*). **(b)** At the same level, the T2 image obtained 3 months later, no signal abnormality could be observed. With kind permission of Dr. Lorenzo Montu, Humanitas, Milano, Italy

Video 24.3

Report of a PET perfusion study ($^{13}NH_3$ as a flow tracer) combined with a CT coronary angiography study performed at IFC-CNR and FGM in Pisa. The study was done in a male patient, 60 years old, with cardiovascular risk factors, recent onset of LBBB and moderate LV dysfunction (LVEF 33% at 2D-Echo) for differential diagnosis between ischaemic or primitive dilated cardiomyopathy. The video clip shows a fusion image of volumetric reconstruction of perfusion PET data obtained during dipyridamole stress and of reconstructed CT angiography data in the diastolic phase of the cardiac cycle. A clear and wide perfusion defect is evident involving the lateral-inferior wall of the left ventricle in the presence of angiographycally normal epicardial coronary vessels. A similar flow defect was also evident in resting conditions. Absolute myocardial blood flow was severely reduced in all myocardial regions both at rest (range 0.35–0.51 mL/min/g, Normal Values >0.6 mL/min/g) and during dipyridamole stress (range 0.52–0.72 mL/min/g) with reduced myocardial perfusion reserve (range 1.38–1.52, normal values >2.5). The diagnosis of primitive dilated cardiomyopathy associated with coronary micro-vascular dysfunction was confirmed at invasive catheterization

Video 24.4

Acute myocarditis. Cine images (SSFP) in 4-chamber view demonstrating slightly dilated LV with EF 47%

Video 24.5

Chagas' disease. Cine images/SSFP) on 2-chamber view. The LV is dilated with manifestation of several small aneurysms and a large apical aneurysm with trans-mural hyperenhancement due to fibrosis

Video 24.6

Patient with non-compaction cardiomyopathy (cine images-SSFP - short axis) demonstrating meshwork of trabeculae predominantly in the apex. The end-diastolic non-compacted to compacted ratio exceeds 2.3

Video 24.7

Patient with non-compaction cardiomyopathy (cine images - SSFP - vertical long axis) demonstrating meshwork of trabeculae predominantly in the apex. The end-diastolic non-compacted to compacted ratio exceeds 2.3

Video 24.8

Myocardial crypts in the proximal infero-septal wall as observed in genetically proven carrier of hypertrophic

cardiomyopathy mutation (cine images -SSFP - modified 2-chamber view)

Video 24.9

Myocardial crypts in the proximal infero-septal wall as observed in genetically proven carrier of hypertrophic cardiomyopathy mutation (cine images - SSFP - short axis view)

References

1. Elliott P, Andersson B, Arbustini E, et al Classification of the cardiomyopathies: a position statement from the European Society of Cardiology Working Group on Myocardial and Pericardial Diseases. *Eur Heart J*. 2008;29:270–276
2. MacRae CA. Genetics and dilated cardiomyopathy: limitations of candidate gene strategies. *Eur Heart J*. 2000;21:1817–1819
3. Senior R, Becher H, Monaghan M, et al Contrast echocardiography: evidence-based guidelines for clinical use recommended by European Association of Echocardiography. *Eur J Echocardiogr*. 2009;10(2):194–212
4. Mor-Avi V, Jenkins A, Kühl HP, et al Real-time 3-dimensional echocardiographic quantification of LV Volumes. *JACC Imaging*. 2008;1:413–423
5. Dutka DP, Donnelly JE, Palka P, et al Echocardiographic characterization of cardiomyopathy in Friedreich's ataxia with tissue doppler echocardiographically derived myocardial velocity gradients. *Circulation*. 2000;102:1276–1282
6. Amundsen BH, Helle-Valle T, Edvardsen T, et al Noninvasive myocardial strain measurement by speckle tracking echocardiography: validation against sonomicrometry and tagged magnetic resonance imaging. *J Am Coll Cardiol*. 2006;47:789–793
7. Giatrakos N, Kinali, M, Stephens DA, et al Cardiac tissue velocities and strain rate in the early detection of myocardial dysfunction of asymptomatic boys with Duchenne muscular dystrophy; relation to clinical outcome. *Heart*. 2006:92;840–842
8. Klocke FJ, Baird MG, Bateman T, et al ACC/AHA/ASNC Guidelines for the clinical use of cardiac radionuclide imaging. A report of the American College of Cardiology/American Heart Association Task Force on Practice Guidelines (ACC/AHA/ASNC Committee to Revise the 1995 Guidelines for the Clinical Use of Cardiac Radionuclide Imaging). *J Am Coll Cardiol*. 2003;42(7):1318–1333
9. Neglia D, Michelassi C, Trivieri MG, et al Prognostic role of myocardial blood flow impairment in idiopathic left ventricular dysfunction. *Circulation* 2002;105:186–193
10. van den Heuvel AFM, van Veldhuisen DJ, van der Wall EE, et al Regional myocardial blood flow reserve impairment and metabolic changes suggesting myocardial ischemia in patients with idiopathic dilated cardiomyopathy. *J Am Coll Cardiol*. 2002;35:19–28
11. Dávila-Román VG, Vedala G, Herrero P, et al Altered myocardial fatty acid and glucose metabolism in idiopathic dilated cardiomyopathy. *J Am Coll Cardiol*. 2002;40:271–277
12. Tuunanen H, Engblom E, Naum A, et al Trimetazidine, a metabolic modulator, has cardiac and extracardiac benefits in idiopathic dilated cardiomyopathy. *Circulation*. 2008;118:1250–1258
13. Bengel FM, Permanetter B, Ungerer M, et al Alterations of the sympathetic nervous system and metabolic performance of the cardiomyopathic heart. *Eur J Nucl Med*. 2002;29(2):198–202
14. Knaapen P, van Campen LM, de Cock CC, et al Effects of cardiac resynchronization therapy on myocardial perfusion reserve. *Circulation*. 2004;110:646–651
15. Lindner O, Sörensen J, Vogt J, et al Cardiac efficiency and oxygen consumption measured with 11C-acetate PET after long-term cardiac resynchronization therapy. *J Nucl Med*. 2006;47:378–383
16. Hesse B, Lindhardt TB, Acampa W, et al EANM/ESC guidelines for radionuclide imaging of cardiac function. *Eur J Nucl Med Mol Imaging*. 2008;35:851–885
17. Alfakih K, Plein S, Thiele H, Jones T, Ridgway JP, Sivananthan MU. Normal human left and right ventricular dimensions for MRI as assessed by turbo gradient echo and steady-state free precession imaging sequences. *J Magn Reson Imaging*. 2003;17:323–329
18. Assomull RG, Prasad SK, Lyne J, et al Cardiovascular magnetic resonance, fibrosis, and prognosis in dilated cardiomyopathy. *J Am Coll Cardiol*. 2006;48:1977–1985
19. Nazarian S, Bluemke DA, Lardo AC, et al Magnetic resonance assessment of the substrate for inducible ventricular tachycardia in nonischemic cardiomyopathy. *Circulation*. 2005;112:2821–2825
20. Wu KC, Weiss RG, Thiemann DR, et al Late gadolinium enhancement by cardiovascular magnetic resonance heralds an adverse prognosis in nonischemic cardiomyopathy. *J Am Coll Cardiol*. 2008;51:2414–2421
21. Ashford MW Jr, Liu W, Lin SJ, et al Occult cardiac contractile dysfunction in dystrophin-deficient children revealed by cardiac magnetic resonance strain imaging. *Circulation*. 2005;112:2462–2467
22. Puchalski MD, Williams RV, Askovich B, et al Late gadolinium enhancement: precursor to cardiomyopathy in Duchenne muscular dystrophy? *Int J Cardiovasc Imaging*. 2009;25:57–63
23. Yilmaz A, Gdynia HJ, Baccouche H, et al Cardiac involvement in patients with Becker muscular dystrophy: new diagnostic and pathophysiological insights by a CMR approach. *J Cardiovasc Magn Reson*. 2008;8:50
24. Aretz HT, Billingham ME, Edwards WD, et al Myocarditis: a histopathologic definition and classification. *Am J Cardiovasc Pathol*. 1987;1:3–14
25. Hyodo E, Hozumi T, Takemoto Y, et al Early detection of cardiac involvement in patients with Sarcoidosis by a non-invasive method with ultrasonic tissue characterisation. *Heart*. 1987;90(11):1275–1280
26. Skouri HN, Dec GW, Friedrich MG, Cooper LT. Noninvasive imaging in myocarditis. *J Am Coll Cardiol*. 2006;48:2085–2093
27. Mahrholdt H, Goedecke C, Wagner A, et al Cardiovascular magnetic resonance assessment of human myocarditis: a comparison to histology and molecular pathology. *Circulation*. 2004;109:1250–1258
28. Abdel-Aty H, Boyé P, Zagrosek A, Wassmuth R, et al Diagnostic performance of cardiovascular magnetic resonance in patients with suspected acute myocarditis: comparison of different approaches. *J Am Coll Cardiol*. 2005;45:1815–1822
29. Rochitte CE, Oliveira PF, Andrade JM, et al Myocardial delayed enhancement by magnetic resonance imaging in patients with Chagas' disease: a marker of disease severity. *J Am Coll Cardiol*. 2005;46:1553–1558
30. Smedema JP, Snoep G, van Kroonenburgh MP, et al Evaluation of the accuracy of gadolinium-enhanced cardiovascular magnetic resonance in the diagnosis of cardiac sarcoidosis. *J Am Coll Cardiol*. 2005;45:1683–1690
31. Petersen SE, Selvanayagam JB, Wiesmann F, et al Left ventricular non-compaction: insights from cardiovascular magnetic resonance imaging. *J Am Coll Cardiol*. 2005;46:101–105
32. Germans T, Wilde AA, Dijkmans PA, et al Structural abnormalities of the inferoseptal left ventricular wall detected by cardiac magnetic resonance imaging in carriers of left ventricular hypertrophic cardiomyopathy mutations. *J Am Coll Cardiol*. 2006;48:2518–2523
33. Tsuchihashi K, Ueshima K, Uchida T, et al Angina pectoris-myocardial infarction investigations in Japan. Transient left ventricular apical ballooning without coronary artery stenosis: a novel heart

syndrome mimicking acute myocardial infarction. *J Am Coll Cardiol*. 2001;38(1):11–18

34. Bybee KA, Kara T, Prasad A, et al Systematic review: transient left ventricular apical ballooning: a syndrome that mimics ST-segment elevation myocardial infarction. *Ann Intern Med*. 2004;141(11):858–865
35. Eite I, Behrendt F, Schindler K, et al Differential diagnosis of suspected apical ballooning syndrome using contrast-enhanced magnetic resonance imaging. *Eur Heart J*. 2008;29: 2651–2659

Chapter 25

ARRHYTHMOGENIC RIGHT VENTRICULAR CARDIOMYOPATHY/ DYSPLASIA (ARVC/D)

Petros Nihoyannopoulos, Covadonga Fernández-Golfín, and Juhani Knuuti

CONTENTS

J. L. Zamorano et al. (eds.), *The ESC Textbook of Cardiovascular Imaging*
DOI: 10.1007/978-1-84882-421-8_25, © Springer-Verlag London Limited 2010

Introduction and Definitions

The right ventricle may be the seat of ventricular tachycardia of left bundle branch block pattern.[1] Recent interest has centred on its pathophysiology because early reports suggested that an apparent absence of gross organic heart disease indicated a more favourable prognosis.[2] The term "arrhythmogenic right ventricular cardiomyopathy" was first proposed in 1977 by Fontaine et al,[3] when he demonstrated that right ventricular tachycardia can have adverse electrophysiological features and may be associated with right-sided structural disorders. These include right ventricular dysplasia and coronary artery disease and cardiomyopathy affecting one or both ventricles.

ARVC/D is a cardiomyopathy affecting primarily the right ventricle (RV).[4] However, it has been increasingly recognized that the left ventricle (LV) is also affected in several patients. It is a heterogeneous group of conditions characterized by right ventricular dysfunction and dilatation from very subtle abnormalities located at the RV to a most extensive RV and LV dysfunction.

The most common presentation is patients complaining of arrhythmias, specifically with ventricular tachycardia originating from the RV with the characteristic LBBB morphology, which could be life-threatening. ARVC/D is an important cause of sudden death in individuals <30 years of age and has been found in up to 20% of sudden deaths in young people.[4]

ARVC/D is an autosomal dominant disease with variable penetrance and incomplete expression. It is characterized by adipose replacement of myocardial tissue in the right ventricular wall in a spotty or diffuse process that starts on the right ventricular sub-epicardium and progresses to the endocardium with fibro-fatty replacement of myocytes and thinning of the wall (Fig. 25.1). Men are more frequently affected than women, and the condition is usually discovered between the second and fourth decade of life.

The regions of the RV most frequently involved are the RV inflow area, the apex, and the infundibulum. These three areas form the "triangle of dysplasia" (Fig. 25.2). When the LV is also involved, the fibro-fatty replacement can affect both the septum and left ventricular free wall.

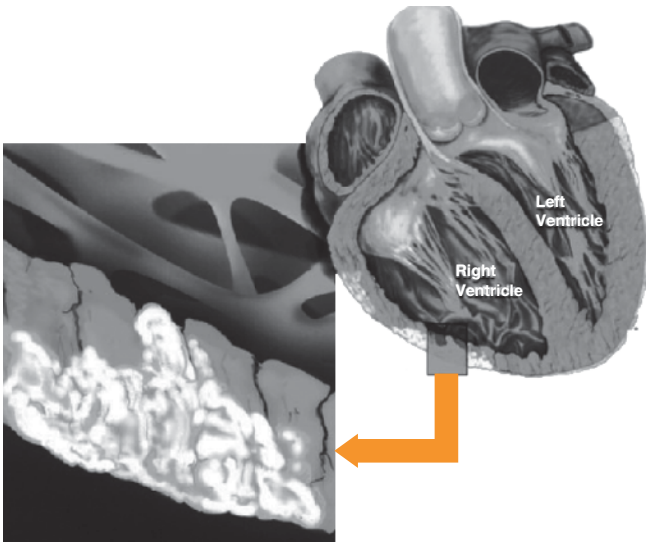

Fig. 25.1 Diagrammatic representation of the histology in arrhythmogenic right ventricular cardiomyopathy

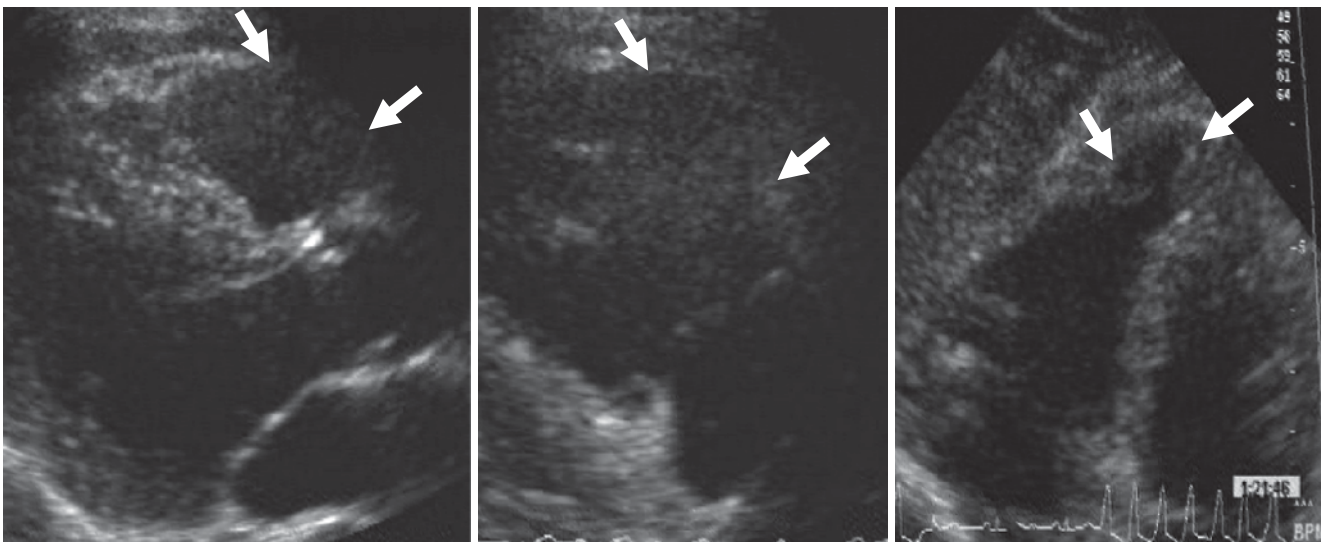

Fig. 25.2 Echocardiographic views from a patient with ARVC/D illustrating the "triangle of dysplasia." On the *left panel*, the outflow track seen from parasternal long-axis view (*arrows*) demonstrates a subtle thinning of the free wall. In the *middle panel*, the RV inflow track view shows the localized akinetic region in the free wall (*arrows*). On the *right panel*, apical four-chamber projection demonstrates an apical aneurysm on the RV (*arrows*)

Criteria for Diagnosis of ARVC/D

A definite diagnosis of ARVC/D requires the histological finding of trans-mural fibro-fatty replacement of RV myocardium. However, in the leaving, patient histological diagnosis is difficult, as small amounts of adipose tissue also present in the epicardial layer as well as within the RV myocardium in normal subjects, and increases with the advancing age. A consensus group has, therefore, proposed a number of major and minor diagnostic criteria (Table 25.1).[5] To qualify as ARVC/D, a patient must demonstrate two major, or one major plus two minor, or four minor criteria.

Table 25.1. Criteria for diagnosis of ARVC

Global or regional dysfunction and structural alterations
Major
Severe dilatation and reduction of RV ejection fraction with no (only mild) LV impairment
Localized RV aneurysms (akinetic or dyskinetic areas with diastolic bulging)
Severe segmental dilatation of the RV
Minor
Mild global RV dilatation or reduced ejection fraction with normal LV
Mild segmental dilatation of the RV
Regional RV hypokinesia
Tissue characterization of walls
Major
Fibrofatty replacement of myocardium on endomyocardial biopsy
Re-polarization abnormalities
Minor
Inverted T-waves in right precordial leads (V2 and V3) in people aged more than 12 years in absence of RBBB
De-polarization/conduction abnormalities
Major
Epsilon waves or localized prolongation (>110 ms) of the QRS complex in right precordial leads (V1 to V3)
Minor
Late potentials (signal averaged ECG)
Arrhythmia
Minor
LBBB type ventricular tachycardia (sustained and non-sustained)
Frequent ventricular extrasystoles (more than 1,000/24 h) on Holter
Family history
Major
Familial disease confirmed at necropsy or surgery
Minor
Familial history of premature sudden death (<35 years) due to suspected RV dysplasia
Familial history (clinical diagnosis based on present criteria)

Global or Regional Right Ventricular Dysfunction

Of the major criteria, the global or regional right ventricular dysfunction may be best evaluated with any accepted imaging technique such as RV angiography, nuclear medicine, echocardiography, or cardiac magnetic resonance (CMR). However, RV evaluation is normally performed by means of comprehensive echocardiography and CMR imaging.

Echocardiography

Echocardiography in expert hands can identify subtle RV abnormalities in the form of RV free wall thinning (Fig. 25.3) or RV apical aneurysms (Fig. 25.4) by careful and systematic evaluation of the RV.[6–8] Echocardiography is probably the diagnostic test of choice, but needs to be performed comprehensibly by experts following standardized protocols for the detailed imaging of the right ventricle.[8] As ARVC/D affects primarily the RV, it is important to perform all right ventricular views, which include the RV inflow and outflow views.

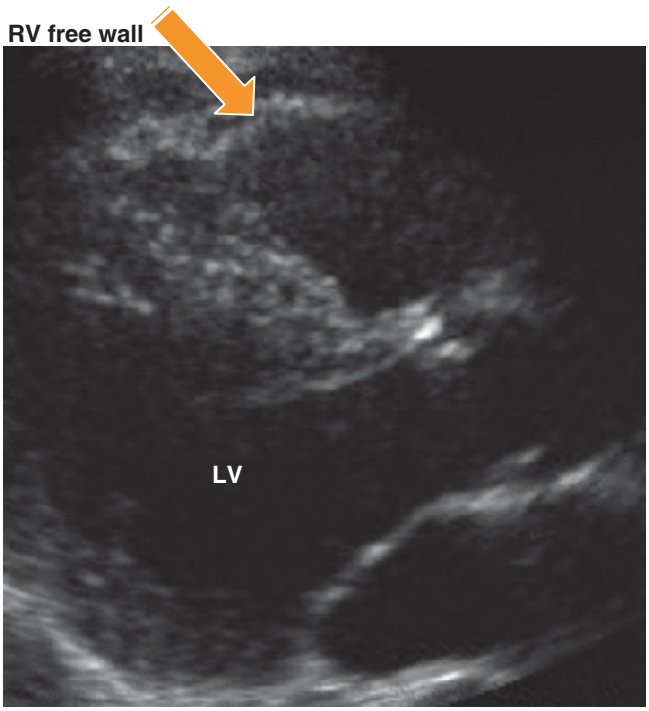

Fig. 25.3 Parasternal long-axis projection from a patient with ventricular tachycardia demonstrating a non-dilated RV outflow, but a localized RV free wall thinning (*arrow*) and absent contraction, suggestive of ARVC/D

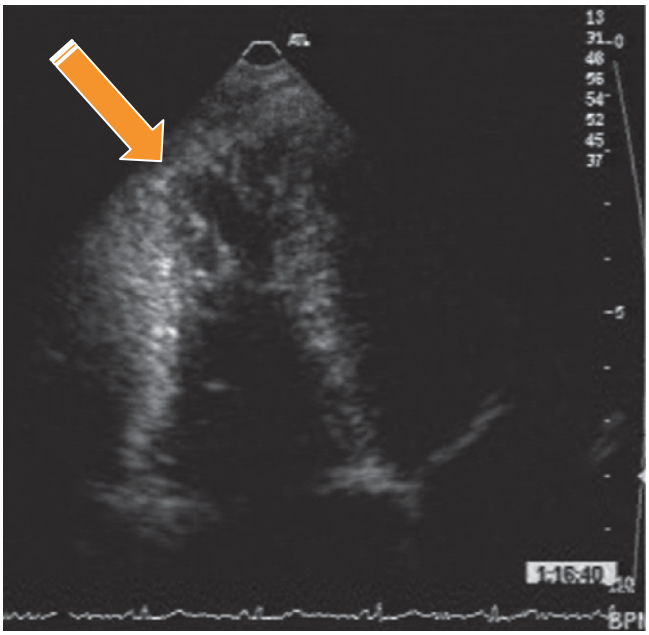

Fig. 25.4 Same patient as in Fig. 25.3. Apical four-chamber demonstrating the discrete aneurysm at the apex (*arrow*)

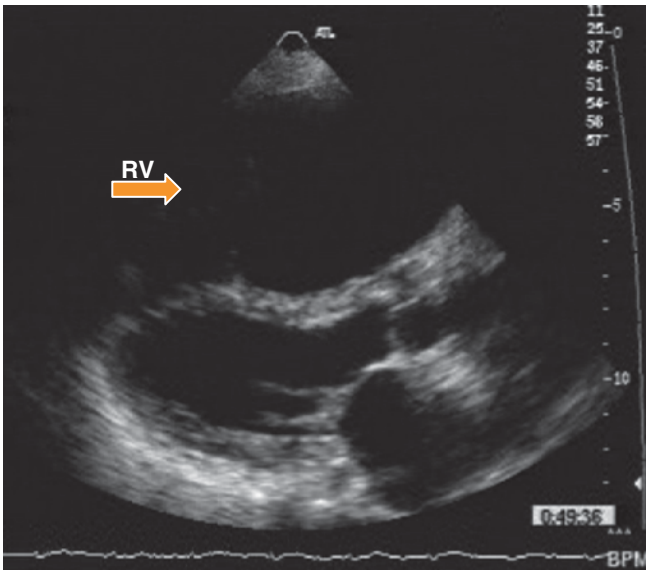

Fig. 25.6 Parasternal long-axis view from a patient with advanced ARVC/D demonstrating a dilated RV (*arrow*) with marked global hypokinesia. Notice that the LV size is normal

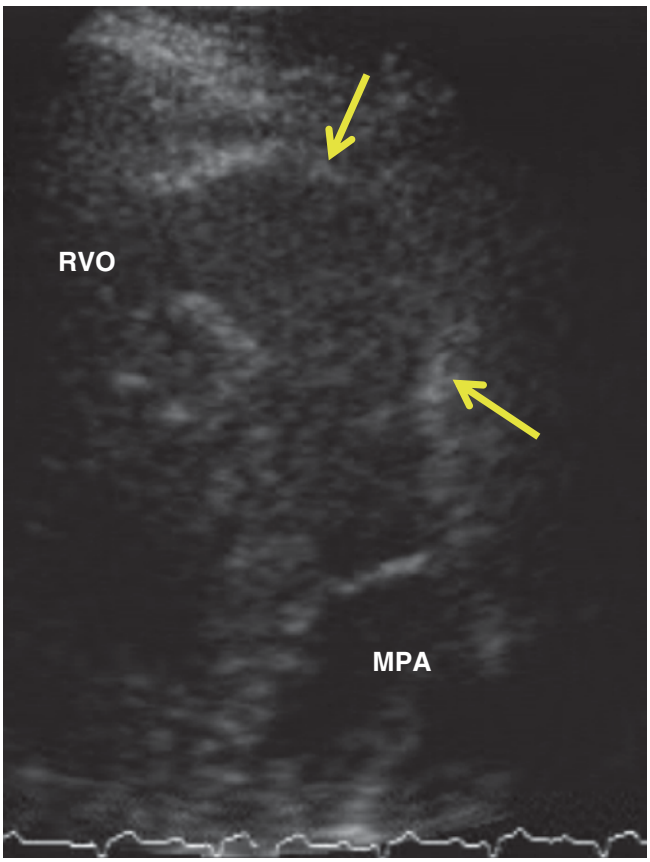

Fig. 25.5 Right ventricular outflow track view demonstrating a clear aneurysm below the pulmonary valve (*arrows*) taking the form of a "mushroom"

The typical presentation will be that of a young patient with ventricular arrhythmias of right ventricular origin. This patient will be first referred for an echocardiographic examination, which will have to be conducted in an expert department to look for subtle RV abnormalities. The earliest abnormalities that can be detected may be focal areas of myocardial dysfunction, which may involve the RV inflow, apex, and/or the RV outflow tract. Those three locations constitute the "triangle of dysplasia." These areas, however, may easily be missed if particular attention has not been paid. The more obvious and pathognomonic abnormalities are those of localized aneurismal regions of the triangle of dysplasia in the form of systolic bulges (Fig. 25.5). As long as the RV inflow and outflow tract projections are carefully recorded, missing those regional dyskinetic regions will be difficult. In a more advanced stage of ARVC/D, extended areas of RV free wall may become thin and akinetic, which, together with RV dilatation, will form the "typical" pattern of ARVC/D (Figs. 25.6 and 25.7). Ultimately, the whole of the RV will be thinned, dilated, and hypokinetic. The diagnosis is difficult to miss and is straightforward with any imaging modality. Last, in the most severe and advanced cases, the LV will also become involved and could mimic that of non-specific dilated cardiomyopathy. Global RV dysfunction is most common in patients with cardiac arrest, although this is not necessarily true in patients with first presentation. Figures 25.5 and 25.6 are from a 55-year-old lady with ARVC/D. The marked dilatation of the RV will lead to functional tricuspid regurgitation (Fig. 25.8). The differential diagnosis with pulmonary hypertension is straightforward by directing the continuous wave Doppler beam along the tricuspid regurgitant jet in order to

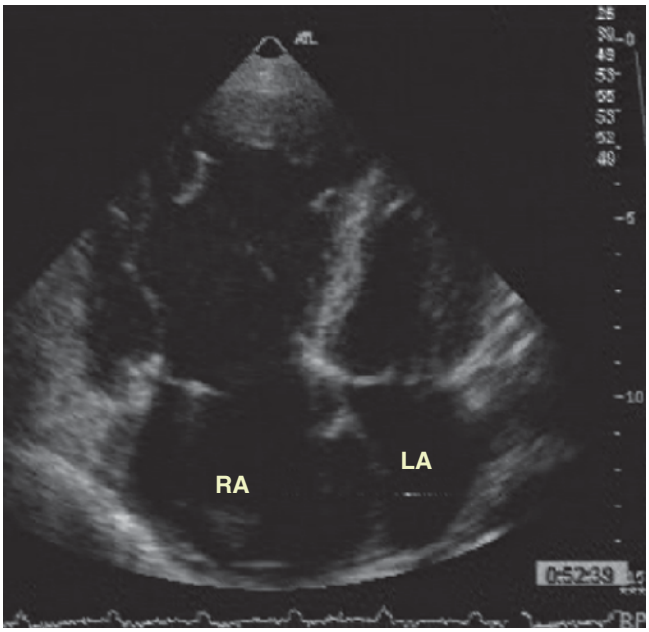

Fig. 25.7 Apical four-chamber view from the same patient as in Fig. 25.6 demonstrating the markedly dilated RV. This patient can be compared with patient in Fig. 25.4 where the aneurysm was very discrete

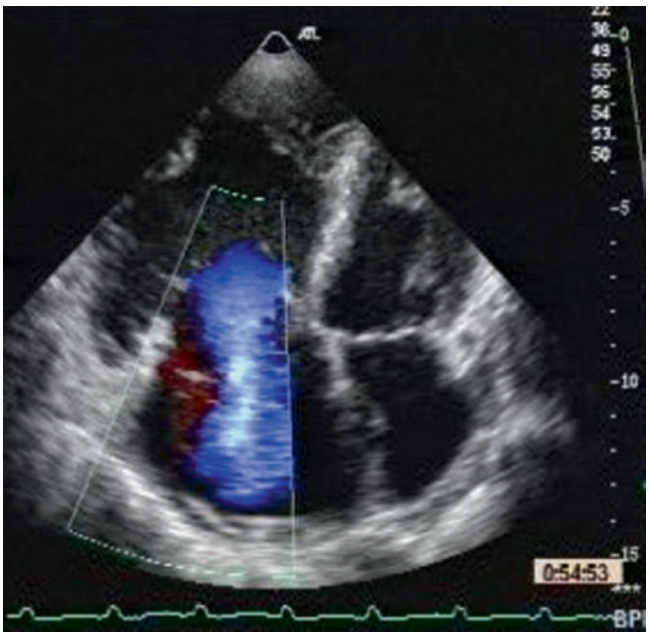

Fig. 25.8 Apical four-chamber projection with colour Doppler demonstrating the presence of almost free tricuspid regurgitation secondary to the marked dilatation of the tricuspid annulus. Notice the low velocity flow as seen by the deep blue colour of the velocity jet

estimate the RV systolic pressures. Video 25.1 shows a discrete RV apical aneurysm while the patient developed her usual arrhythmia.

Cardiac Magnetic Resonance

In recent years, MRI scanners and imaging protocols have rapidly been developed.[9] At present, imaging is generally performed on 1.5 T systems using dedicated cardiac phased-array coils with multiple elements and ECG triggering, although 3-T scanners offering better spatial resolution will rapidly develop. CMR evaluation of ARVC/D was initially focussed on the detection of fat tissue infiltration at the level of RV free wall. First reports in the early 90s[10, 11] included T_1-weighted spin echo images showing bright signal intensity corresponding to RV free wall fatty infiltration. After a period of initial enthusiasm that almost gave CMR the same value as histology for the detection of fat replacement, both in formalin-fixed hearts and in vivo,[12, 13] the role of CMR in the detection of fat was redefined. Since fat infiltration has been described in normal hearts and CMR tissue characterization (fat infiltration) is often difficult, the clinical and diagnostic utility at present is limited (Table 25.2).[14, 15]

CMR abnormalities described in patients with ARVC/D (Table 25.3) can be divided into two groups: functional anomalies and morphological changes, both most commonly found in the "triangle of dysplasia."

Functional Evaluation

As with echocardiography, among functional abnormalities described by CMR in ARVC/D, dilatation and RV systolic dysfunction are most commonly found in patients who meet Task Force criteria. Other abnormalities include regional wall motion abnormalities (hypokinesia or akinesia) and focal aneurysm with persistent diastolic bulging (Table 25.1). CMR allows the evaluation of RV volumes and global and regional function. ECG-gated breath-hold gradient echo sequences (steady state free precession) achieve excellent

Table 25.2. CMR advantages for the evaluation of ARVC/D

Non-invasive
Absence of ionizating radiation
Non-iodated contrast agents
High spatial and temporal resolution
Multiple planes
High contrast between blood pool and myocardium
No acoustic window problems
High reproducibility on RV volume and function parameters
Tissue characterization

ARVC/D arrhythmogenic right ventricular cardiomyopathy/dysplasia

Table 25.3. CMR findings on ARVC/D

	Task force criteria		
	Major	Minor	None
Functional abnormalities			
Severe RV dilatation	+		
RV severe systolic dysfunction without LV involvement	+		
Localized RV aneurysm (akinetic, dyskinetic areas with diastolic bulging)	+		
Severe segmental dilatation of RV	+		
Mild global RV dilatation		+	
Mild RV ejection fraction reduction		+	
Mild segmental dilatation RV		+	
Regional RV hypokinesia		+	
Morphological abnormalities			
RV free wall thinning			+
RV moderator band or trabeculae hyperthrophy			+
RVOT enlargement			+
RV fat infiltration			+
Delayed enhancement (intra-myocardial fibrosis)			+

CMR cardiac magnetic resonance; *ARV/CD* arrythmogenic right ventricular cardiomyopathy/dysplasia; *RV* right ventricle; *LV* left ventricle; *RVOT* right ventricular outflow tract

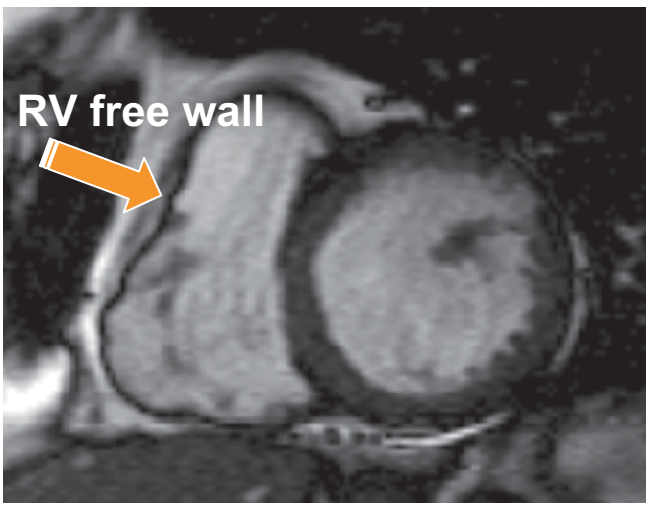

Fig. 25.9 Cardiac magnetic resonance imaging from a patient with ARVC/D. Note the clarity of the thinned RV free wall (*arrow*) and the dilation of the RV cavity

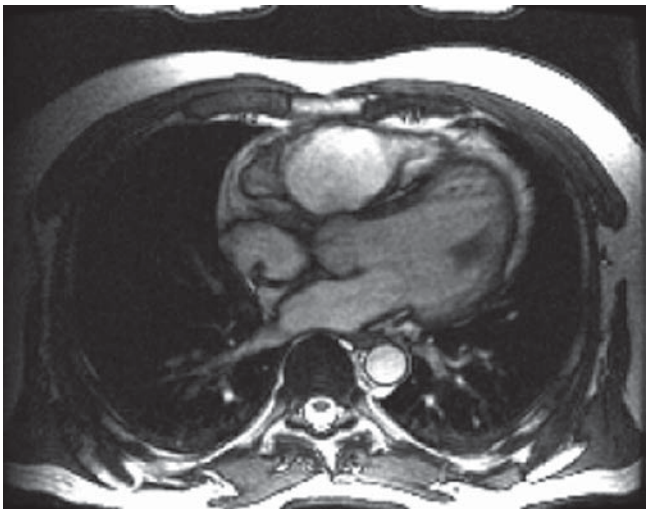

Fig. 25.10 Gradient echo sequence, axial plane showing a dilated and akinetic right ventricular outflow tract

contrast between blood and myocardium with good delineation of RV endocardial borders. Image planes include classical long-axis cardiac views, as well as RV outflow tract (RVOT), short axis, and axial images from the level of the RVOT to the diaphragm (Video 25.2). RV volume and systolic function are calculated from serial short-axis cine loops tracing end-diastolic and end-systolic areas. Suppression of premature ventricular beats with anti-arrhythmic therapy is recommended to avoid blurring, and age, height, and weight should be recorded in all cases. RV volumes and ejection fraction (EF) should be matched according to age, sex, and body surface area. Ventricular dilatation is defined when end-diastolic volume (EDV) is above 117% predicted.[16] Wall motion abnormalities are subjectively assessed in order to detect localized aneurysm defined as akinetic or dyskinetic regions of the RV wall showing diastolic bulging (Videos 25.3 and 25.4). Since normal variations of RV regional function are frequently seen on healthy subjects (Video 25.5), especially on axial planes and near moderator band insertion,[17] the significance of their presence should be interpreted with caution. For this reason, performance and interpretation of ARVC/D suspected CMR should be limited to high volume centres that are expert in CMR and familiar with the disease in order to avoid false positive ARVC/D diagnosis.

Morphological Evaluation

Morphological abnormalities include focal wall thinning (Video 25.1), moderator band or trabeculae hypertrophy, RVOT enlargement, and intra-myocardial fibro–fatty infiltration. Although a first approach to wall thickness and RVOT diameter can be done using previously described ECG gated

fast gradient echo sequences, a better spatial resolution is achieved by the use of black blood spin echo sequence. Current black blood sequences use a breath-hold fast spin echo with a dual magnetization preparation pulse (double inversion-recovery), which provides end-diastolic T_1-weighted images for detailed morphological analysis (Video 25.2). Fat infiltration is also evaluated with this sequence; since signal intensity of fat on T_1-weighted images is high (bright), much higher than normal myocardium, the presence of a bright focal or diffuse area within the right or left ventricular myocardium suggests fat infiltration. However, high signal intensity on T_1-weighted images is not specific of fat; proximity to surface coil, motion-related artefacts, and other technical issues may cause projection of high signal intensity onto the myocardium causing the false diagnosis of fatty infiltration. Along with T_1-weighted images, a fat suppressed sequence should always be performed. The presence of a bright signal spot within the myocardium on T_1-weighted images that darkens or disappears on fat suppressed images is diagnostic of fatty infiltration (Fig. 25.11). High spatial resolution on spin echo images is mandatory.[18] Even though fat detection with CMR is not a Task Force criterion for the diagnosis of ARVC/D, most CMR protocols include T_1-weighted and T_2-weighted STIR (fat suppression) images on axial and short-axis planes. Importantly, planning of both sequences should be the same, so the very same image can be seen without and with fat suppression. This approach has proved to increase inter-observer agreement and confidence in diagnosis and evaluation of intra-myocardial fatty infiltration in patients suspected to have ARVC/D.[19] Fat RV infiltration detected with cine CMR has also been described in patients without any other ARVC/D abnormalities[20] and its presence should be evaluated with caution (Fig. 25.12).

Delayed Enhancement

In recent years, delayed enhancement imaging in the CMR evaluation of patients with ARVC/D for detecting fibrosis has gained acceptance. Studies have shown that delayed-enhancement can be detected in biopsy-proven ARVC/D patients in areas with wall thinning and regional dysfunction.[21, 22] Fibro–fatty infiltration is more common in ARVC/D patients than fatty infiltration alone. Detection of fibrotic tissue using delayed enhancement may be more important than the detection of fat replacement alone (Figs. 25.13 and 25.14). However, prognostic implication and its clinical utility for diagnosis and prognostic purposes are not defined yet. At present, inclusion on CMR protocols (Table 25.4), which are already long and technically demanding, is a question of debate. Further studies are needed in order to address these issues and to establish the feasibility of delayed enhancement detection within the thin RV wall.

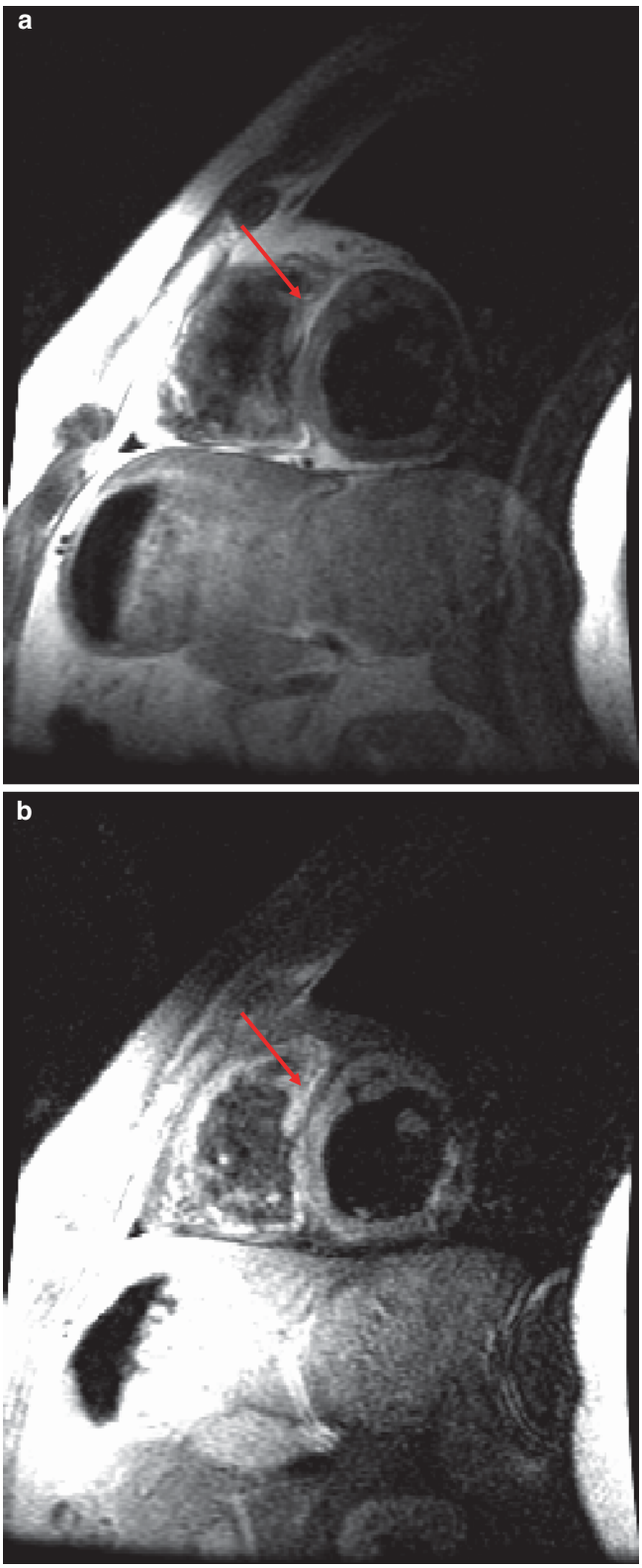

Fig. 25.11 **(a)** Fat spin echo T_1-weighted image showing high signal intensity suggestive of fat infiltration in the septum (*arrow*). **(b)** Same image as Fig. 25.7 with fat suppression. Septal high signal intensity has disappeared, confirming the diagnosis of fat infiltration in this patient diagnosed of arrhythmogenic right ventricular dysplasia

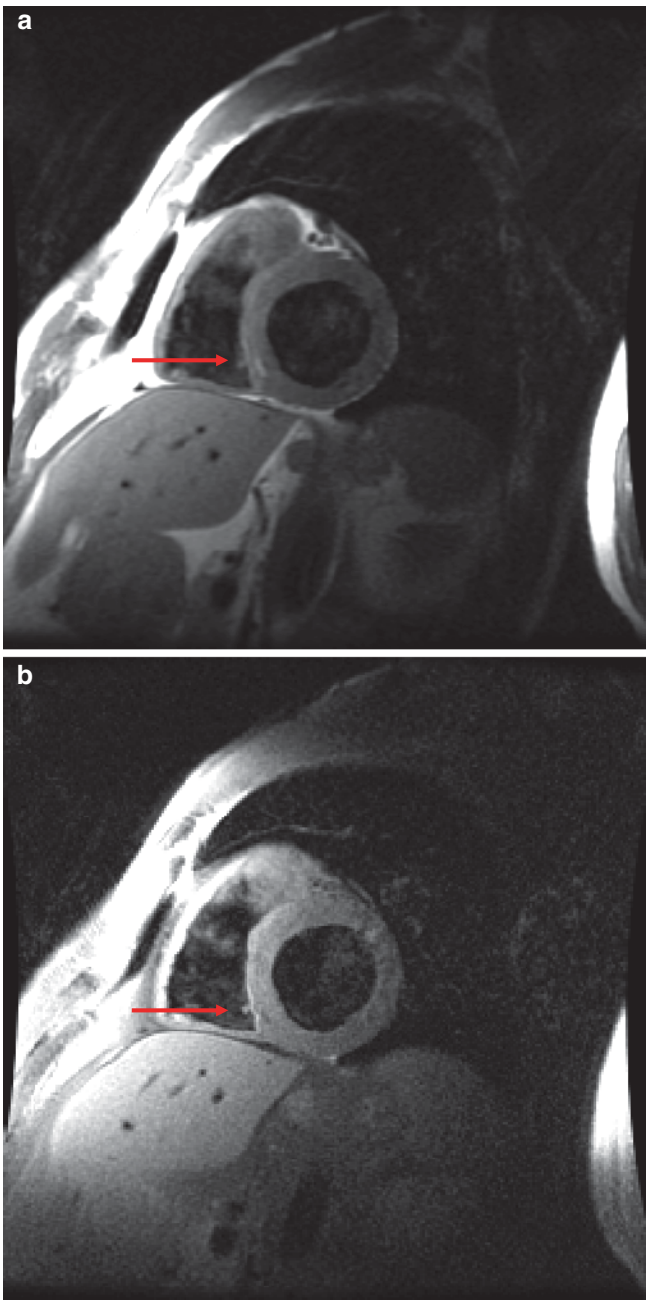

Fig. 25.12 **(a)** T_1-weighted image of a patient with unexplained syncope. Linear high signal intensity is noted in the inferior septum (*arrow*) that disappears on fat suppressed images **(b)** corresponding to fat infiltration. No other abnormalities were noted

CMR Limitations

Despite the excellent image quality and reproducibility, CMR has some disadvantages; the data acquisition and analysis require expertise and are rather time-consuming, without clear validated and standardized protocols. Some patients groups, such as claustrophobic or patients with pacemakers, cannot undergo CMR. The lack of widespread availability of CMR scanners, however, may constitute the most significant limitation of this technique. In ARVC/D, localized RV aneurysms may be detected with CMR, but they can also be missed when the plane of section is outside a localized aneurysm.

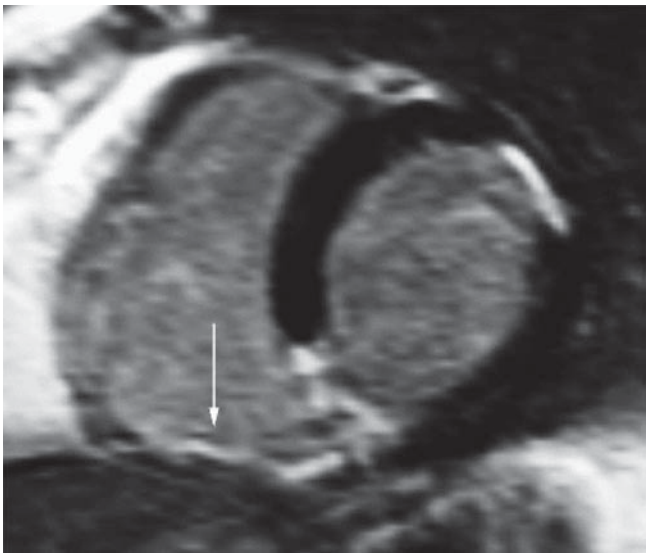

Fig. 25.13 Delayed gadolinium enhancement from a patient with ARVC/D. Short-axis projection demonstrating the scar in the inferior-basal portion of the RV, but also extending into the LV. Image obtained with permission from Bleeker et al[9]

Other Imaging Techniques

Recently, multi-detector computed tomography (MDCT) was used in the evaluation of patients suspected to have ARVC/D. Also patients with pacemaker and cardioverter-defibrillators can be studied using CT, which at present cannot be imaged with CMR. Increased RV trabeculation and RV intra-myocardial fat and scalloping were associated with ARVC/D. RV volumes. Also, RV inlet dimensions and RV outflow tract surface area are increased in patients with ARVC/D. Further studies are warranted to ensure the accuracy of CT in the detection of ARVC/D.[23] Also, multi-detector CT can be used to detect fibro–fatty infiltrations. However, with increasing experience, it became apparent that the differentiation of myocardial fibro–fatty infiltration from the fatty tissue normally present in the pericardium is inaccurate, unless, of course, the infiltration is extensive. Furthermore, myocardial fat can be present not only in ARVC/D, and is often related to aging, prior myocardial infarction, and chronic ischaemia.[24] The separation between myocardial infiltration and normal pericardial fat is almost impossible in the presence of thinned RV free wall.

The recent development of radionuclide blood-pool SPECT imaging also allows regional assessment of the left and right ventricular function. In one prospective study it was found that detecting localized dysfunction by

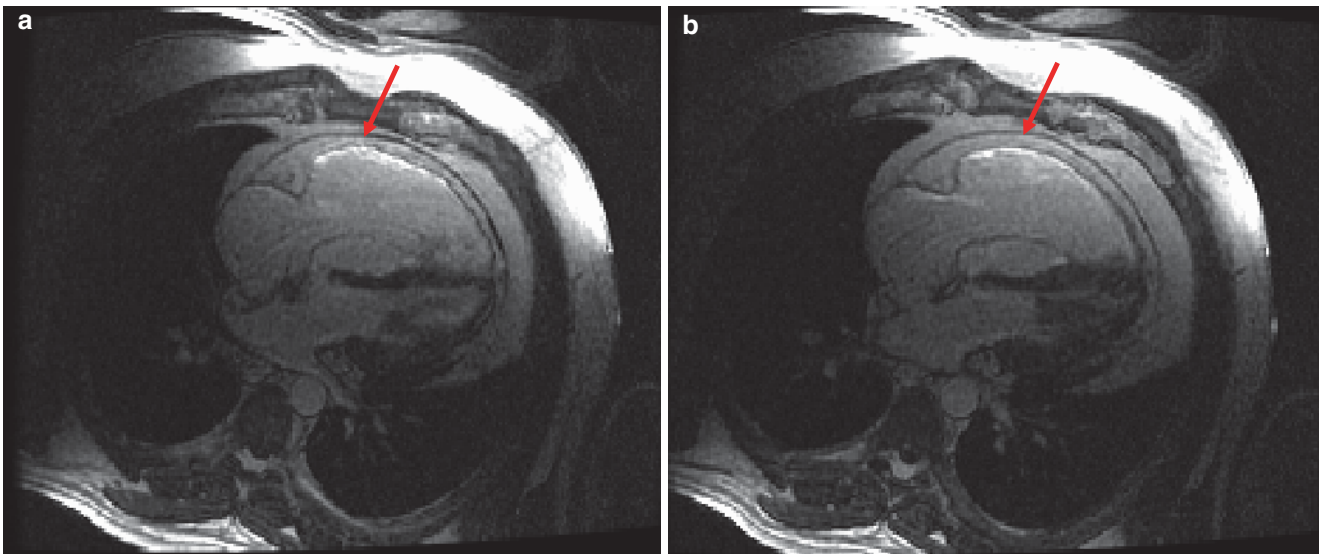

Fig. 25.14 Double inversion-recovery sequence after gadolinium injection showing diffuse right ventricular wall enhancement (*arrows*) indicative of myocardial fibrosis **(a, b)**

Table 25.4. Basic CMR study protocol for ARVC/D

Localizers (real time, three plane)			
four-chamber, two-chamber, LVOT and RVOT	Gradient echo sequence (SSFP)	7 mm/3 mm 8 mm/2 mm	Functional assessment (global and regional)
Sequential short-axis slices from base to apex	Gradient echo sequence (SSFP)	7 mm/3 mm 6 mm/4 mm	Ventricular volumes, mass, EF. Global and regional RV function
Axial sequential cine images from RVOT to the diaphragm	Gradient echo sequence (SSFP)	7 mm/3 mm 6 mm/4 mm	Regional RV functional evaluation (RVOT)
Black blood T_1 images, sequential short-axis view	T_1-weighted double inversion–recovery fast spin echo	6 mm/4 mm FOV 26–28	Fat infiltration (intra-myocardial high signal intensity)
Black blood T_1 fat suppressed images, short axis	T_1-weighted double inversion–recovery fast spin echo with fat suppression	Same planning as T_1-weighted images, same parameters	Fat infiltration (suppression of intra-myocardial high signal intensity)
Same sequences (5 and 6) on axial plane from RVOT to the diaphragm			
Delayed enhancement (optional)	Inversion recovery prepared breath-hold cine gradient-echo images	6–7 mm/4–3 mm 8 mm/2 mm	Intra-myocardial fibrosis (fibro-fatty infiltration)

CMR cardiac magnetic resonance; *ARVC/D* arrythmogenic right ventricular cardiomyopathy/dysplasia; *RV* right ventricle; *LV* left ventricle; *RVOT* right ventricular outflow tract; *SSFP* steady state free precession; *FOV* field of view

gated SPECT was accurate in the detection of ARVC (sensitivity 100%, specificity 81%),[25] but, obviously, more studies are needed to assess the value of this technique in this setting.

An interesting alternative to detect right ventricular involvement in ARVC/D is using imaging of cardiac neural innervation. In two earlier studies, this method was found to be a very sensitive marker of ARVC/D,[26, 27] but no large prospective trials have been published.

Histological Demonstration of Fibro–Fatty Replacement of Myocardium

The second major criterion for the diagnosis of ARVC/D is the histological demonstration of fibro–fatty replacement of myocardium on endomyocardial biopsy. The problem, however, with endomyocardial biopsy is that it is difficult to perform in patients with thinned wall running the danger of perforating the myocardium and performing pericardium

biopsy instead, leading to misleading diagnosis. Furthermore, in its earlier stages of the disease progression, the fibro-fatty replacement has a patchy distribution, thereby making myocardial biopsy even less helpful.

Repolarization and Depolarization/Conduction Abnormalities

The remaining diagnostic criteria are based on the electrical characteristics and depolarization/conduction abnormalities of these patients. Repolarization abnormalities only constitute a minor criterion. They are in the form of T-wave inversion in leads V1 to V3 in the absence of a complete RBBB. Nevertheless, when present, they are very useful in raising the suspicion of ARVC/D and are present in up to 50% of cases.

Depolarization/conduction abnormalities constitute a major criterion when the characteristic epsilon wave or localized prolongation (>110 ms) of the QRS complex in leads V1 to V3 is present. In routine clinical practice, however, those waves are rarely seen or difficult to diagnose. Arrhythmia also constitutes a minor criterion and is in the form of left bundle branch block type ventricular tachycardia (sustained or non-sustained). ECG, Holter, and exercise testing are useful to unveil these arrhythmias.

Family History

The final, and perhaps the most significant major diagnostic criterion, is the presence of familial disease confirmed at necropsy or surgery (hard evidence). Because of the genetic character of ARVC/D, it is important to screen all members of the family once the diagnosis has been made. This can be performed non-invasively by routine ECG and echocardiography.

Conclusions

Arrhythmogenic RV cardiomyopathy has been recognized as an important cause of sudden death in association with exercise and athletic participation. Physicians should consider this condition in young subjects who die suddenly or in people with unexplained cardiac arrhythmias. Diagnosis relies predominantly on imaging using echocardiography and CMR, which are complementary as long as they are performed by experts. Management involves the suppression of malignant arrhythmias with anti-arrhythmic medication, but is increasingly directed towards placement of automatic implantable defibrillators as the most effective treatment to prevent sudden cardiac death.

Video 25.1

Sub-costal projection from a patient with ARVC/D demonstrating a discrete RV apical aneurysm. During the examination, the patient spontaneously reproduced her usual arrhythmia

Video 25.2

Gradient echo sequence, axial plane showing a dilated and akinetic right ventricular outflow tract

Video 25.3

Gradient echo sequence, short-axis view showing severe right ventricular dilatation and dysfunction. Right ventricular wall thinning is also noted in this patient diagnosed right ventricular dysplasia

Video 25.4

Cine gradient echo sequences, four-chamber view showing and enlarged right ventricle with right ventricular regional dysfunction. Basal and mid segments of right ventricular free wall are akinetic

Video 25.5

Cine images, four-chamber view of a patient evaluated for possible ARVC/D without any Task Force criteria. Cardiac magnetic resonance was normal, but mild regional abnormality was noted at the right ventricular mid free wall which is a normal variant

References

1. Foale RA, Nihoyannopoulos P, Ribeiro P, et al Right ventricular abnormalities in ventricular tachycardia of right ventricular origin: relation to electrophysiological abnormalities. *Heart*. 1986;56: 45–54
2. Pietras RJ, Mautner R, Denes P, et al Chronic recurrent right and left ventricular tachycardia: comparison of clinical, haemodynamic and angiographic findings. *Am J Cardiol*. 1977;40:32–37
3. Fontaine G, Frank R, Vedel J, Grosgogeat Y, Cabrol C, Facquet J. Stimulation studies and epicardial mapping in ventricular tachycardia: study of mechanisms and selection for surgery. In: Kulbertus HE, ed. *Reentrant Arrhythmias*. Lancaster, PA: MTP Publishing. 1977:334–350
4. Corrado D, Basso C, Thiene G. Arrhythmogenic right ventricular cardiomyopathy: diagnosis, prognosis, and treatment. *Heart*. 2000;83:588–595
5. McKenna WJ, Thiene G, Nava A, et al Diagnosis of arrhythmogenic right ventricular dysplasia/cardiomyopathy: task force of the working group myocardial and pericardial disease of the European Society of Cardiology and the Scientific Council on Cardiomyopathies of the International Society and Federation of Cardiology. *Br Heart J*. 1994;71:215–218
6. Ho SY, Nihoyannopoulos, P. Anatomy, echocardiography, and normal right ventricular dimensions. *Heart*. 2006;92:i2–i13
7. Bleeker GB, Steendijk P, Holman ER, et al Acquired right ventricular dysfunction. *Heart*. 2006;92:i14–i18
8. Foale RA, Nihoyannopoulos P., McKenna WJ, et al The echocardiographic measurements of the normal adult right ventricle. *Br Heart J*. 1986;56:33–44
9. Bleeker GB, Steendijk P, Holman ER, et al Assessing right ventricular function: the role of echocardiography and complementary technologies. *Heart*. 2006;92:i19-i26
10. Blake LM, Scheinman MM, Higgins CB. MR feature of arrhythmogenic right ventricular dysplasia. *AJR*. 1994;162:809–812
11. Aufferman W, Wichter T, Breihardt G, Joachimsen K, Peters PE. Arrhythmogenic right ventricular disease: MR imaging vs angiography. *AJR*. 1993;161:549–555
12. Basso C, Thiene G, Corrado D, et al Arrhythmogenic right ventricular cardiomyopathy. Dysplasia, dystrophy, or myocarditis? *Circulation*. 1996;94:983–991
13. Menghetti L, Basso C, Nava A, et al Spin-echo nuclear magnetic resonance for tissue characterisation in arrhythmogenic right ventricular cardiomyopathy. *Heart*. 1996;76:467–470
14. MR imaging of arrhythmogenic right ventricular cardiomyopathy: morphologic findings and interobserver reliability. *Cardiology*. 2003;99:153–162
15. Tandri H, Calkins H, Marcus FI. Controversial role of magnetic resonance imaging in the diagnosis of arrhythmogenic right ventricular dysplasia. *Am J Cardiol*. 2003;92:649
16. Sen-Chowdhry S, Prasad SK, Syrris P, et al Cardiovascular magnetic resonance in arrhythmogenic right ventricular cardiomyopathy revisited comparison with task force criteria and genotype. *J Am Coll Cardiol*. 2006;48:2132–2140
17. Sievers B, Addo M, Franken F, Trappe HJ. Right ventricular wall motion abnormalities found in healthy subjects by cardiovascular magnetic resonance imaging and characterized with a new segmental model. *J Cardiovasc Mag Reson*. 2004;6:601–608
18. Castillo E, Tandri H, Rodriguez ER, et al Arrhythmogenic right ventricular dysplasia: ex vivo and in vivo fat detection with black-blood MR imaging. *Radiology*. 2004;232:38–48
19. Abbara S, Migrino RQ, Sosnovik DE, et al Value of fat suppression in the MRI evaluation of suspected arrhythmogenic right ventricular dysplasia. *AJR*. 2004;182:587–591
20. Macedo R, Prakasa K, Tichnell C, et al Marked lipomatous infiltration of the right ventricle: MRI findings in relation to arrhythmogenic right ventricular dysplasia. *AJR*. 2007;188: W423–427
21. Tandri H, Saranathan M, Rodríguez ER, et al Noninvasive detection of myocardial fibrosis in arrhythmogenic right ventricular cardiomyopathy using delayed-enhancement magnetic resonance imaging. *J Am Coll Cardiol*. 2005;45:98–103
22. Hunold P, Wieneke H, Bruder O, et al Late enhancement: a new feature in MRI of arrhythmogenic right ventricular cardiomyopathy? *J Cardiovasc Magn Reson*. 2005;7:649–655
23. Bomma C, Dalal D, Tandri H, et al. Evolving role of multidetector computed tomography in evaluation of arrhythmogenic right ventricular dysplasia/cardiomyopathy. *Am J Cardiol*. 2007;100: 99–105
24. Mariano-Goulart D, Déchaux L, Rouzet F, et al Diagnosis of diffuse and localized arrhythmogenic right ventricular dysplasia by gated blood-pool SPECT. *J Nucl Med*. 2007;48:1416–1423
25. Jacobi AH, Gohari A, Zalta B, Stein MW, Haramati LB. Ventricular myocardial fat: CT findings and clinical correlates. *J Thorac Imaging*. 2007;22:130–135
26. Takahashi N, Ishida Y, Maeno M, et al Noninvasive identification of left ventricular involvements in arrhythmogenic right ventricular dysplasia: comparison of 123I-MIBG, 201TlCl, magnetic resonance imaging and ultrafast computed tomography. *Ann Nucl Med*. 1997;11:233–241
27. Lerch H, Bartenstein P, Wichter T, et al Sympathetic innervation of the left ventricle is impaired in arrhythmogenic right ventricular disease. *Eur J Nucl Med*. 1993;20:207–212

Section 6

PERI- MYOCARDIAL DISEASE

Chapter 26

PERICARDIAL EFFUSION AND CARDIAC TAMPONADE

Paul Leeson and Harald Becher

CONTENTS

J. L. Zamorano et al. (eds.), *The ESC Textbook of Cardiovascular Imaging*
DOI: 10.1007/978-1-84882-421-8_26, © Springer-Verlag London Limited 2010

Introduction

Echocardiography is the modality of choice for initial diagnosis, investigation, and monitoring of pericardial effusions. Echocardiography also identifies changes in cardiac function suggestive of cardiac tamponade and can be used to plan the removal of fluid by pericardiocentesis. Cardiac CT and MR provide further detailed pericardial imaging, as well as information on fluid characteristics and localized effusions. Furthermore, they are particularly suited to investigation of related pathology whether pericardial, cardiac, or within their wider field of view.

Background to Pericardial Effusions and Cardiac Tamponade

Pericardial Space

A *pericardial effusion* is an accumulation of fluid within the pericardial space created by the *serous pericardium.* The *serous pericardium* consists of two membranes: one lines the inside of the *fibrous pericardium* and the other extends over the outer surface of the heart (*visceral pericardium*). The serous membranes are continuous with each other and, therefore, form a deflated sac. This provides a potential space for fluid to accumulate and as the amount of fluid increases, there is an associated increase in intra-pericardial pressure.[1]

The vascular connections to the heart pass through the pericardium via two irregular holes. One hole accommodates the great vessels – aorta and pulmonary artery – and the other, the venous connections – pulmonary veins and vena cava. At each point, the *serous pericardium* has to wrap around the blood vessels and, therefore, two pockets (or sinuses) are created, the *transverse sinus* between aorta and pulmonary artery, and the *oblique sinus* between the pulmonary veins on the back of the left atrium.[2] These are of particular importance in pericardial effusions because collections can localize in the sinuses. These localized collections may cause clinical symptoms because of restricted flow in the associated blood vessels, such as pulmonary vein flow when fluid localizes in the oblique sinus.

Causes of Pericardial Effusions

Normally within the pericardial space, there is a small amount of pericardial fluid, around 10–15 mL. This fluid is a transudate produced by the visceral pericardium and ensures that the two layers of serous membrane move freely over each other to allow unrestricted motion of the cardiac chambers during systole and diastole. Diagnosis of a pericardial effusion implies the presence of an abnormal increase in fluid within the pericardial space.[3]

Pericardial fluid accumulates for reasons similar to fluid accumulation in any other body space and typically is either a transudate or exudate. The most common cause of effusion is in response to pericardial inflammation, as in pericarditis or post-cardiac surgery. If infective, the effusion may be purulent. Effusions also occur in response to malignant processes, both those in direct proximity to the heart such as pericardial or cardiac and also those more distant such as breast or lung.[4] Metabolic changes such as hypothyroidism or uremia can also lead to fluid collection, and rarely effusions occur due to abnormalities in lymphatic drainage, described as a chylous effusion. Haemopericardium occurs after coronary surgery and if there is any other pathological or iatrogenic cardiac or coronary rupture that allows blood to be released into the pericardial space.

The characteristics or location of an effusion, as well as the presence of intra-pericardial structures, may help determine the underlying diagnosis. Fibrin strands or loculated effusions are often seen in response to inflammation, whereas haematoma is very suggestive of a haemopericardium. Irregular or invasive masses may suggest tumour, cyst, or fungal infection.

Size of Pericardial Effusions

Pericardial effusions vary significantly in size and haemodynamic effect. These two factors are not directly related, and haemodynamic effects are more closely related to the speed of fluid accumulation. In conditions such as malignancy, where fluid has accumulated over several months, the pericardium has had time to adapt and accommodates larger volumes before haemodynamic problems occur.[4] In sudden fluid accumulation, which can occur following iatrogenic cardiac or coronary puncture, only a small amount of fluid is required to limit cardiac function.

Global effusions are usually graded as *mild*, *moderate*, or *large*, based on their depth, which is the distance between pericardial and cardiac surface.[5] This depth is sometimes used to approximate volume. Less than 0.5 cm usually equates to around 50–100 mL of fluid, whereas a depth of 0.5–1 cm is considered a mild effusion and is associated with volumes of around 100–250 mL. A moderate effusion is usually 1–2 cm, or 250–500 mL, and a large effusion tends to be more than 2 cm deep and is associated with over 500 mL of fluid. These approximations do not hold for localized or loculated effusions.

Cardiac Tamponade

Pericardial effusions have haemodynamic consequences when they restrict normal cardiac function.[2,4] The presence of *cardiac tamponade* specifically refers to diagnosis of the severe haemodynamic compromise that leads to clinical symptoms and signs. This diagnosis is based on tachycardia (>100 bpm), hypotension (<100 mmHg systolic), pulsus paradoxus (>10 mmHg drop in blood pressure on inspiration), and a raised JVP with prominent x descent.[5]

For clinical symptoms to emerge, the effusion must be sufficient to increase intra-pericardial pressure to levels greater than intra-cardiac pressure. The first visible signs of haemodynamic impact, therefore, occur in chambers at lower pressure and at points within the cardiac cycle when pressure is at a minimum. After a general reduction in chamber size, the right atrium starts to appear to collapse in atrial systole. As intra-pericardial pressure increases further, parts of the right ventricle start to collapse at the end of ventricular systole. The combination of rapid atrial collapse in atrial systole followed by rapid ventricular collapse at the end of ventricular systole creates the appearance of a swinging right atrium and ventricle.[6] Cardiac efficiency is impaired as a result, and blood flow through the heart becomes limited, eventually leading to symptoms.

Intra-cardiac pressure is also affected by respiration, which is normally associated with a swing of 5 mmH_2O in intra-thoracic pressure. During inspiration, there is an increase in blood flow into the lungs, which increases flow into the right heart and reduces flow into the left heart. Expiration forces blood out of the lungs into the left heart and reduces flow into the right heart. These changes in flow can normally be identified by a small variation in blood pressure with respiration. As intra-pericardial pressure begins to approach intra-cardiac pressure and influence blood flow into the right heart, the drop in blood pressure with inspiration becomes more exaggerated and is described as pulsus paradoxus when it exceeds 10 mmHg.[5,6]

Imaging Pericardial Effusions

Overview

Pericardial imaging is usually based on a staged, multimodality approach. The combination of echocardiography, cardiac CT, and cardiac MR provides sufficient spatial resolution to visualize the pericardium, a wide field of view to look for associated pathology within the chest, a high temporal resolution to provide detailed information on myocardial function (and acute changes in function), and a means to differentiate tissue characteristics, such as calcium, blood, tumour, and fibrosis. However, echocardiography is usually the main modality used in the management of pericardial effusions, with cardiac CT and cardiac MR reserved for patients in whom there is a need to investigate possible underlying diagnoses, such as malignancy, or there is concern about localized effusions. Alternatively, assessment of effusions by cardiac MR and cardiac CT may be carried out as part of image acquisition for broader cardiac pathology or effusions may be noted incidentally. The key roles of cardiovascular imaging when there is a pericardial effusion are to identify the size and location of the effusion, likely cause, haemodynamic effects, and the best approaches to remove the effusion (*pericardiocentesis*).

Chest X-ray

The chest X-ray remains the standard first-line investigation in patients with chest pain or shortness of breath. The predominant symptom of a pericardial effusion is shortness of breath and, therefore, very frequently, the chest X-ray is the first image acquired before the diagnosis is made. The strengths of the chest X-ray are its wide availability, wide field of view to pick up alternative or related pathology such as chest infection, ability to provide an outline of cardiovascular structures against the lung, and ability to pick up calcification.[7] The pericardium itself is not normally visible on the chest X-ray, except when it becomes calcified, and in the majority of patients the most useful information is obtained from changes in the shape of the cardiac silhouette (Fig. 26.1). *Pericardial effusions* classically cause a large, globular heart.[8] Such a finding should prompt further imaging with echocardiography. Other information may be gathered from the chest X-ray about possible underlying or alternative pathologies such as chest infections, tuberculosis, or malignancy.

Echocardiography

Advantages and Disadvantages of Echocardiography

Identification of a pericardial effusion was one of the first uses of echocardiography, and echocardiography remains the imaging modality of choice for initial investigation of pericardial effusion.[9] This is because it is readily available at the bedside, in the clinic, and, increasingly, in the community. Echocardiography has the spatial and temporal resolution to provide information on quantity and position of fluid accumulation within the pericardial space, combined with related

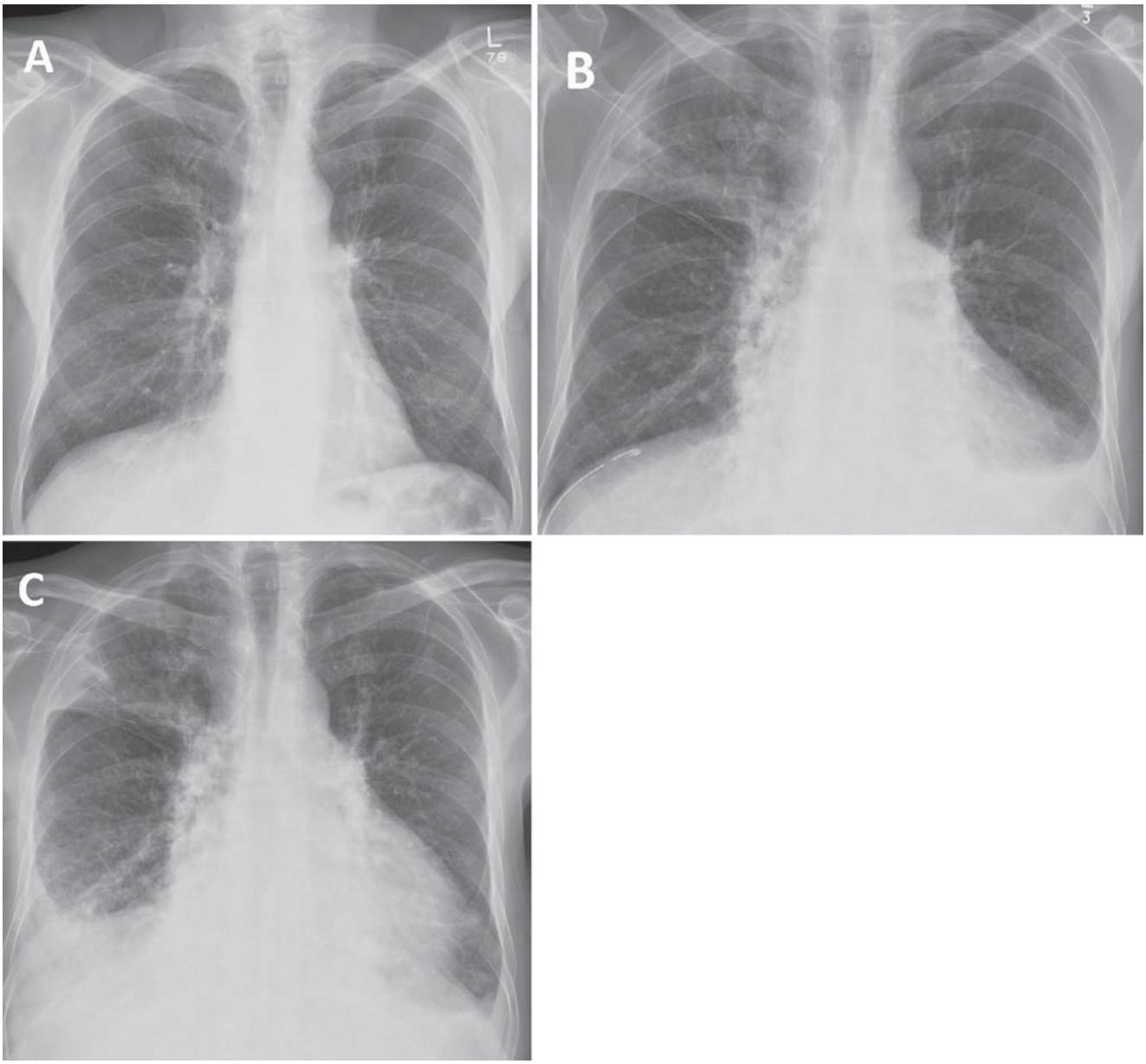

Fig. 26.1 Series of chest X-rays **(a-c)** of the same patient taken over 6 months. Note the gradual change in shape of the cardiac silhouette into a *globular heart* as a pericardial effusion develops. In the final image **(c)** a thin lower attenuation band can be noted around the lateral border of the heart consistent with the fluid layer within the pericardium. Images courtesy of Radiology Department, John Radcliffe Hospital, Oxford

changes in haemodynamics.[5] Information on cardiac size, function, and mass can be collected at the same time. In combination with trans-oesophageal imaging, the whole of the pericardial space can be viewed, including the sinuses.[6, 9] Presence of thrombus or fibrin can also be noted from changes in echo characteristics, and masses associated with the pericardium can be identified. Echocardiography may be limited by body habitus and is not able to differentiate accurately fluid types or assess pericardial thickness. The modality also lacks the field of view to assess related pathology in the lungs. However, echocardiography is particularly useful in the emergency setting when there is concern about acute haemodynamic compromise due to pericardial fluid accumulation, for which it can also be used to aid pericardial drainage.

Appearances on Echocardiography

Part of the pericardium and pericardial space can be seen in all standard echocardiography views (Fig. 26.2, Videos 26.2A-D). However, the best trans-thoracic views to see a pericardial effusion are usually the parasternal long and short

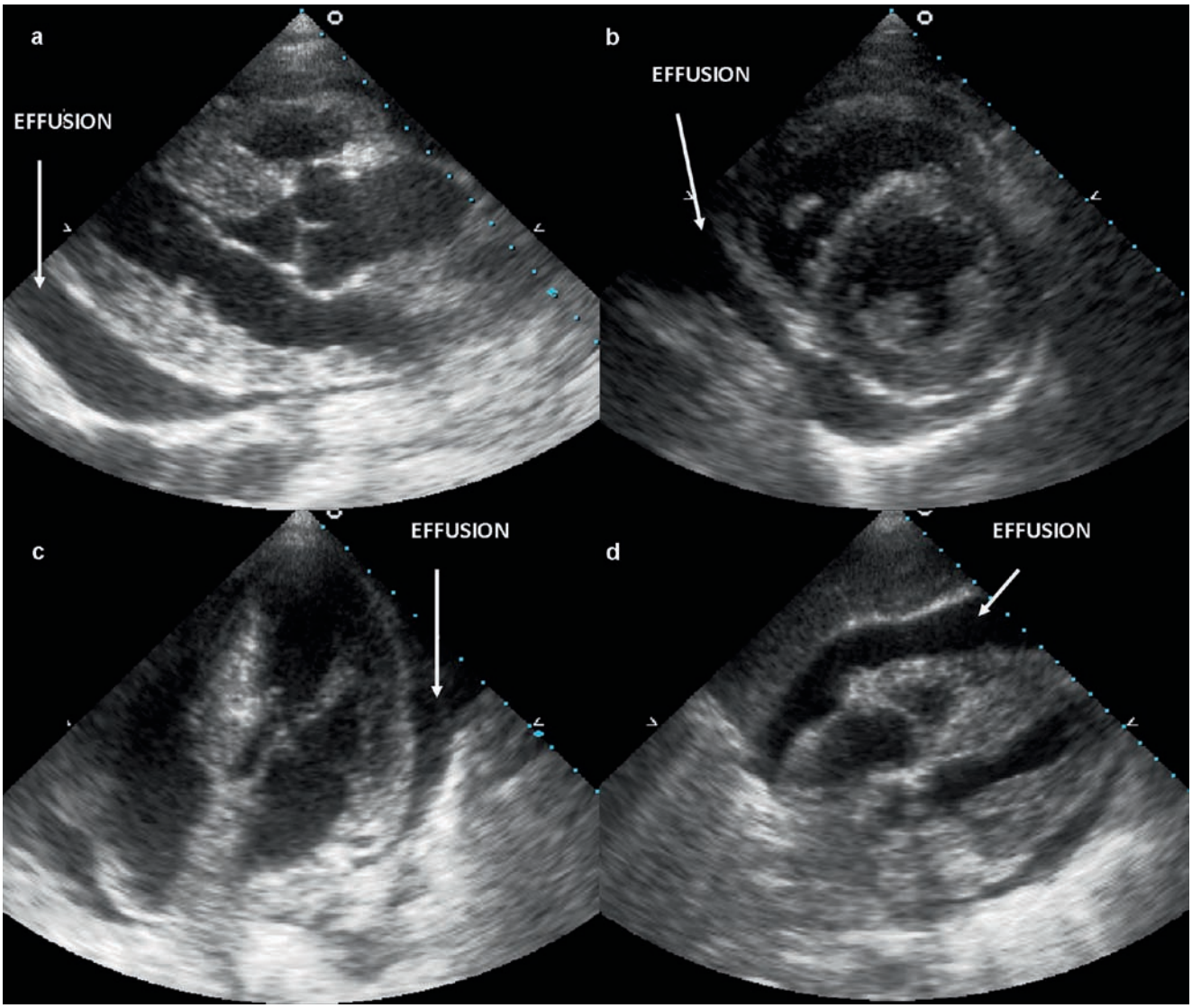

Fig. 26.2 Four standard echocardiography views. A pericardial effusion can be noted in each view. Images courtesy of Echocardiography Department, John Radcliffe Hospital, Oxford

axes, apical four-chamber, and sub-costal views. During trans-eosphageal echocardiography, the most useful additional views are the four-chamber view (mid-oesophageal 0°-view) as it allows assessment of localized collections around the pulmonary veins and right heart, and the aortic valve views (mid-oesophageal short-axis 50°- and long-axis 135°-views) to assess the transverse sinus.[5]

The pericardial surfaces may be apparent as a thin, slightly brighter line around the heart (Fig. 26.3, Video 26.3). The acoustic properties of the pericardium are close to those of surrounding tissues, and, therefore, it is difficult to see, which makes measures inaccurate. Gross changes in thickness or calcifications (which are seen as echo-lucent areas with associated shadowing) may be seen. The normal pericardial space is a thin black line around the heart, and there should only be a few millimeters of fluid.[10] A pericardial effusion will be seen as an abnormal increase in size of this echo-lucent space. Pleural fluid has a similar appearance, and it is important to differentiate this from a pericardial collection. This can usually be achieved because the pericardium is visible (Fig. 26.3) or from the position of the collection relative to the aorta.[11] As the pericardium lies between the aorta and the heart, pericardial fluid will track along the inferolateral surface of the heart, whereas pleural fluid will track around the aorta (Fig. 26.3). Echocardiography will be able to assess the size, location, possible underlying diagnosis, and haemodynamic effects of an effusion. Furthermore, it will be able to determine whether the effusion is global, localized, or loculated (Fig. 26.4).

Echocardiography can approximate volume of fluid based on depth, with more accurate volume measures obtainable from planimetry of pericardial and cardiac borders

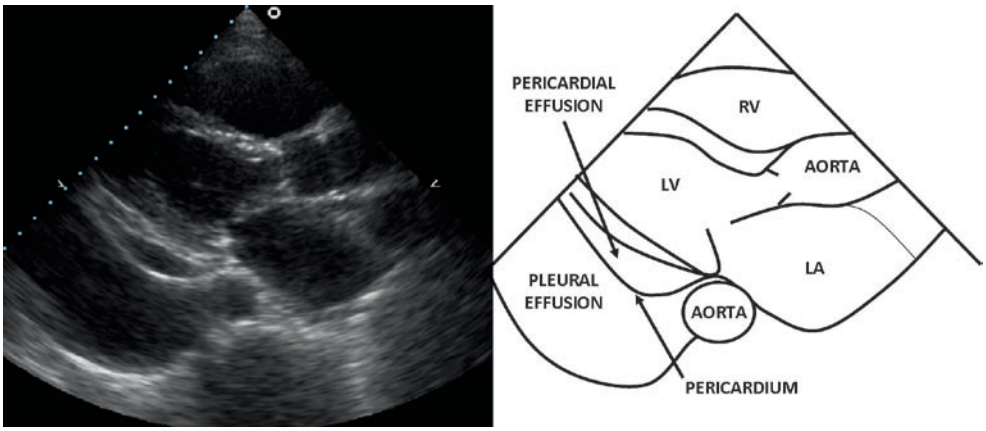

Fig. 26.3 Example of a pleural and pericardial collection. Note the bright white pericardium and how the pericardial fluid passes between aorta and heart, whereas the pleural fluid lies outside the aorta. Images courtesy of Echocardiography Department, John Radcliffe Hospital, Oxford

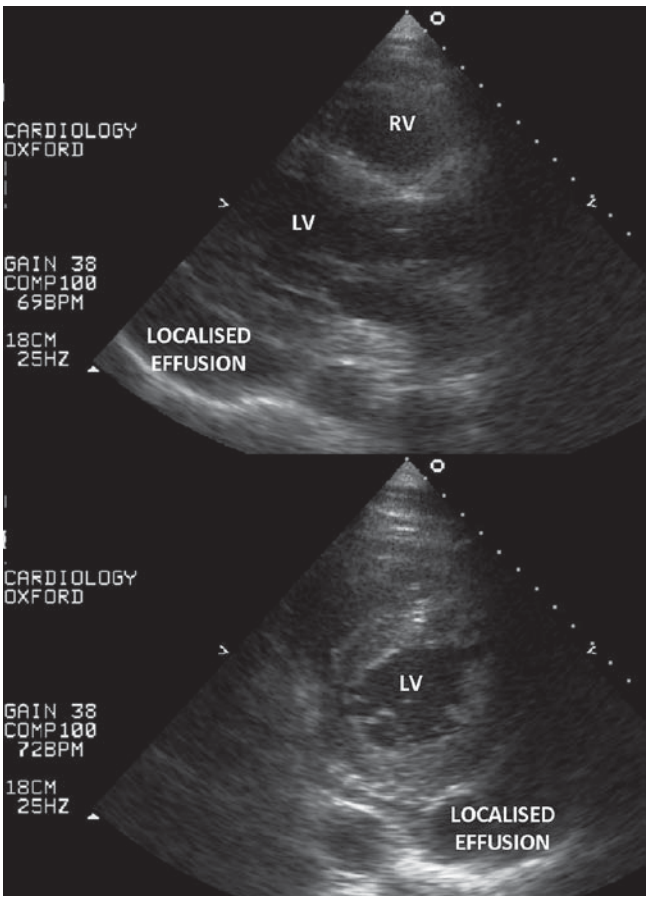

Fig. 26.4 Parasternal long-axis and parasternal short-axis views of a pericardial effusion localized against the inferolateral wall of the left ventricle. Images courtesy of Echocardiography Department, John Radcliffe Hospital, Oxford

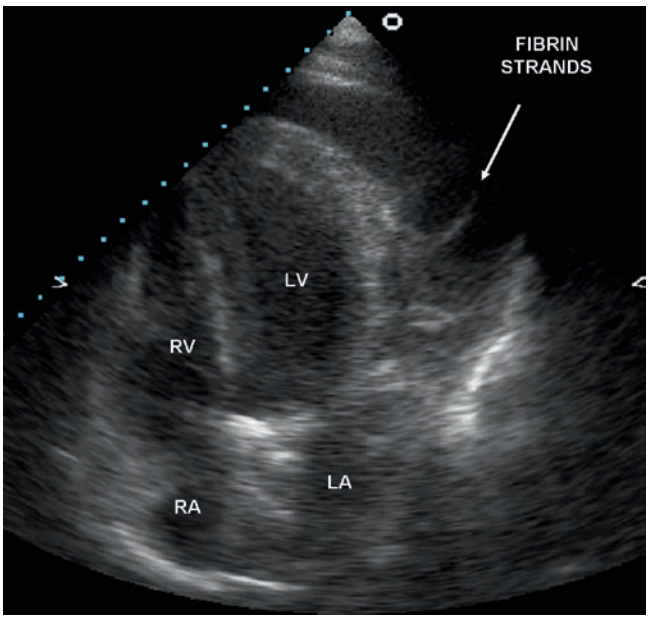

Fig. 26.5 Apical four-chamber view with fibrin strands evident within the effusion along the lateral wall of the left ventricle. Images courtesy of Echocardiography Department, John Radcliffe Hospital, Oxford

in apical views or from 3D echocardiography. Pericardial fluids (serous, blood, or pus) are all seen as black echolucent areas, and it is difficult to differentiate between fluid types with echocardiography. Strands (fibrin) can easily be seen (Fig. 26.5, Video 26.5), and haemotoma may be evident, although it has similar echocardiographic density to myocardium. Trans-eosphageal echocardiography may be particularly useful for the assessment of possible localized effusions in patients with haemodynamic problems after cardiac surgery (Fig. 26.6, Video 26.6).

Cardiac Tamponade and Echocardiography

Echocardiography is of great importance for the assessment of cardiac tamponade. A key feature that can be identified with echocardiography is the 2D evaluation of the abnormal collapse of the right atrium and ventricle (Fig. 26.7, Video 26.7). The first part of the heart to be affected is the right atrium at end diastole. As pressure increases further, the right ventricle starts to be affected and collapses at end systole.[5] Clinical haemodynamics usually intervenes before intra-pericardial pressure is sufficient to influence the left ventricle and atrium.

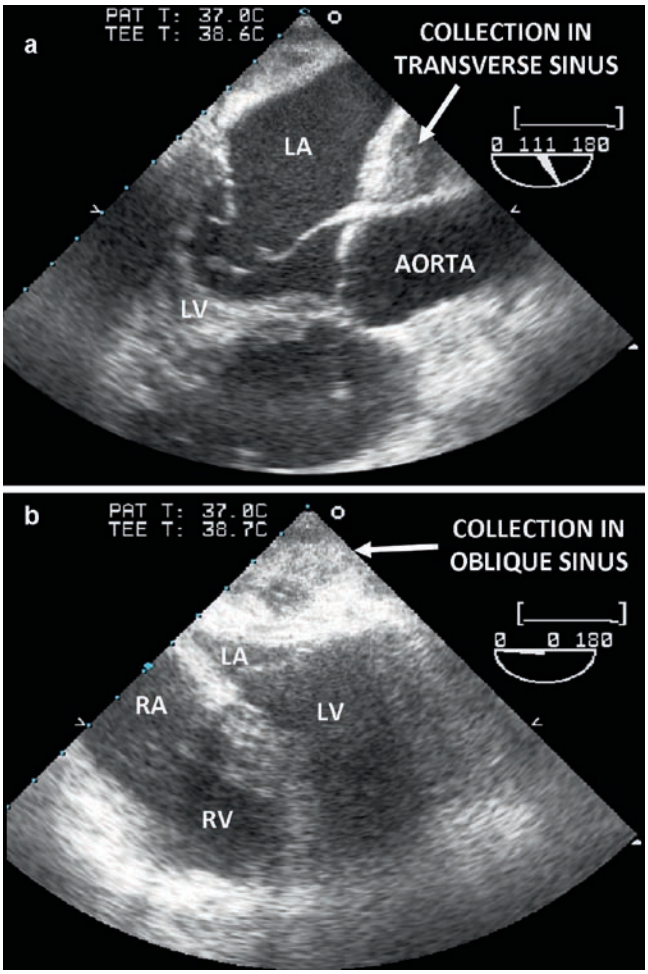

Fig. 26.6 Trans-oesophageal echocardiography views of localized collections. **(a)** a 135° long axis view of the aortic valve. As well as the oblique sinus collection, fluid and haemotoma are also present in the transverse sinus between aorta and left atrium. **(b)** a 0° four-chamber view with a localised, haemotoma-filled collection behind the left atrium consistent with an oblique sinus collection. Images courtesy of Echocardiography Department, John Radcliffe Hospital, Oxford

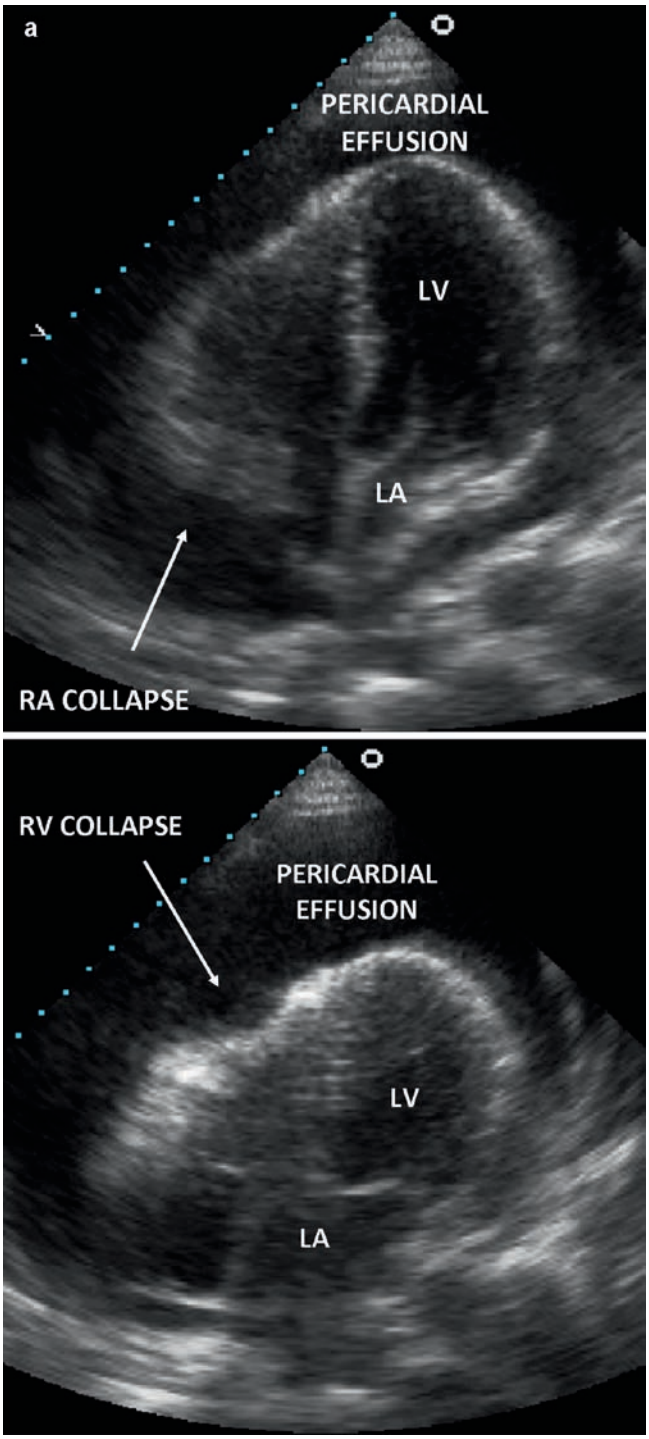

Fig. 26.7 Apical four-chamber view of a large global pericardial effusion. The image is stopped in end diastole and end systole to demonstrate right atrial and right ventricular collapse, respectively. This observation is supportive of cardiac tamponade. Images courtesy of Echocardiography Department, John Radcliffe Hospital, Oxford

Cardiac tamponade is associated with pulsus paradoxus, which is the abnormal exaggeration of the variation in systolic blood pressure with respiration. This occurs due to changes in blood flow through the heart, and, therefore, Doppler is ideally suited to identify these variations in blood flow.[6] To demonstrate the respiratory variation, Doppler inflow across one of the valves can be measured and change in E-wave recorded (Fig. 26.8). Respiration can be tracked using a physio trace or annotated on the recording. Normally, peak flow across the mitral valve varies by <15 and <25% at the tricuspid valve (Fig. 26.9). Greater than this supports tamponade, but clinical signs are usually associated with >40% variation at the mitral valve. Exaggerated flow changes through the heart during respiration can also be demonstrated in the left and right ventricle outflow tracts (increased flow in inspiration on the right and in expiration on the left) with variation of greater than 10%. Increases in filling pressures may also be evident with dilatation of the inferior vena cava and hepatic veins. Septal motion

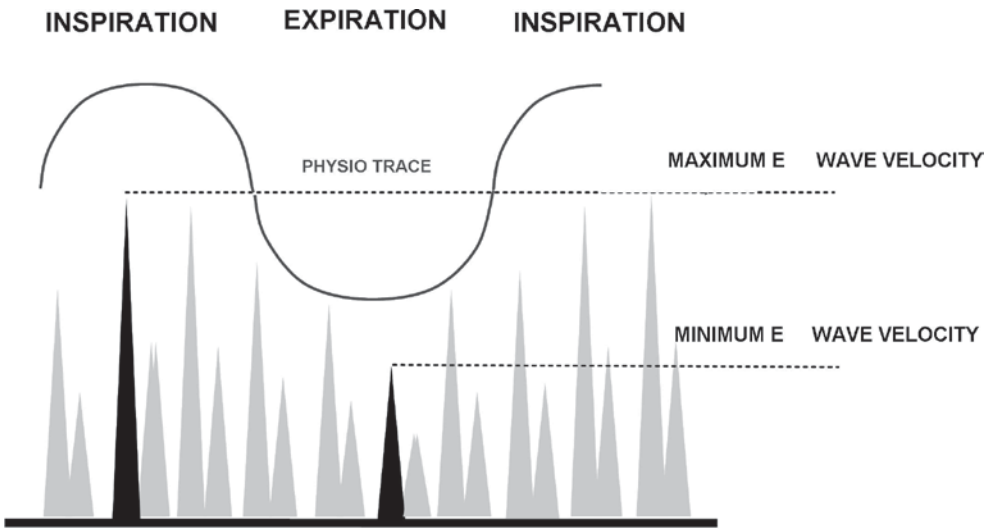

Fig. 26.8 Figure to demonstrate measurement of variation in E-wave velocity on inspiration and expiration. Reproduced with permission from Leeson et al[5]

may be abnormal with fluttering of the septum as left and right ventricles fill during diastole, probably due to waves of competitive filling of the two ventricles. This is reported as early diastolic notching on M-mode.

Cardiac CT

Advantages and Disadvantages of Cardiac CT

Cardiac CT provides a modality when more detailed imaging of pericardial pathology is required and may be particularly useful to assess loculated or localized effusions not well visualized on echocardiography.[12, 13] Furthermore, CT may be indicated to investigate underlying causes such as malignancy. Effusions may be identified on CT as an incidental finding during chest CT imaging for investigation of symptoms such as shortness of breath. Strengths of cardiac CT are its ability to easily identify calcification including micro-calcifications, provide soft tissue contrast with tissue characterization—including fluid assessment based on attenuation—and a wide field of view to identify associated chest pathology. Multi-detector CT has enabled motion-free imaging of the pericardium to improve resolution, multi-planar reformation, and options to assess associated changes in cardiac function.[14] Without gating, motion artefacts can make measurements difficult including complicating differentiation of thickened pericardium from fluid. The major limitations of cardiac CT are the requirement for ionizing radiation and use of iodinated contrast agents.

Appearances on Cardiac CT

The normal *pericardial surfaces* are seen as a thin grey line of soft-tissue density usually well delineated between the pericardial and epicardial fat layers.[3, 14] Therefore, the pericardium is most evident on the anterior surface of the heart in front of the right ventricle and right atrium where the fat is more prominent and there is an area of ventral mediastinal fat. *Pericardial fluid* usually has attenuation characteristics of water and is seen as a thin line between the pericardial surfaces and the heart (Fig. 26.10). Attenuation characteristics may allow differentiation of the contents of an effusion. The more common *transudate* effusions have the attenuation of water, whereas those with higher protein content such as *haemopericardium,* purulent exudates, malignancy, or chylous effusions have high attenuation.[3, 13] The attenuation of haemopericardium varies with age with a gradual reduction over time and the emergence of mixed areas due to the presence of thrombus. Inflammatory effusions may be associated with contrast uptake by the pericardium.[14] A limitation of cardiac CT is the differentiation of a small effusion from pericardial thickening or when the effusion is the same attenuation as pericardium because of volume averaging. Because the whole heart is seen in every acquisition, loculated or localized effusions and those around the anterior heart can be imaged within a standard protocol.[12] Another feature of cardiac CT is the wide field of view, which can be used to assess related pathology in the lungs and also more clearly define the extent of masses associated with the pericardium. Cardiac CT is, therefore, particularly useful for more detailed assessment of pericardial pathology associated with the effusion, in particular, pericardial thickness (Fig. 26.11), calcification, and size, extent, and functional effects of pericardial masses (Fig. 26.12).

Cardiac Tamponade and Cardiac CT

Cardiac tamponade should have been identified clinically and on echocardiography. However, multi-detector CT allows visualization of the cardiac cycle and may identify chamber collapse or changes in cardiac chamber size. If these findings

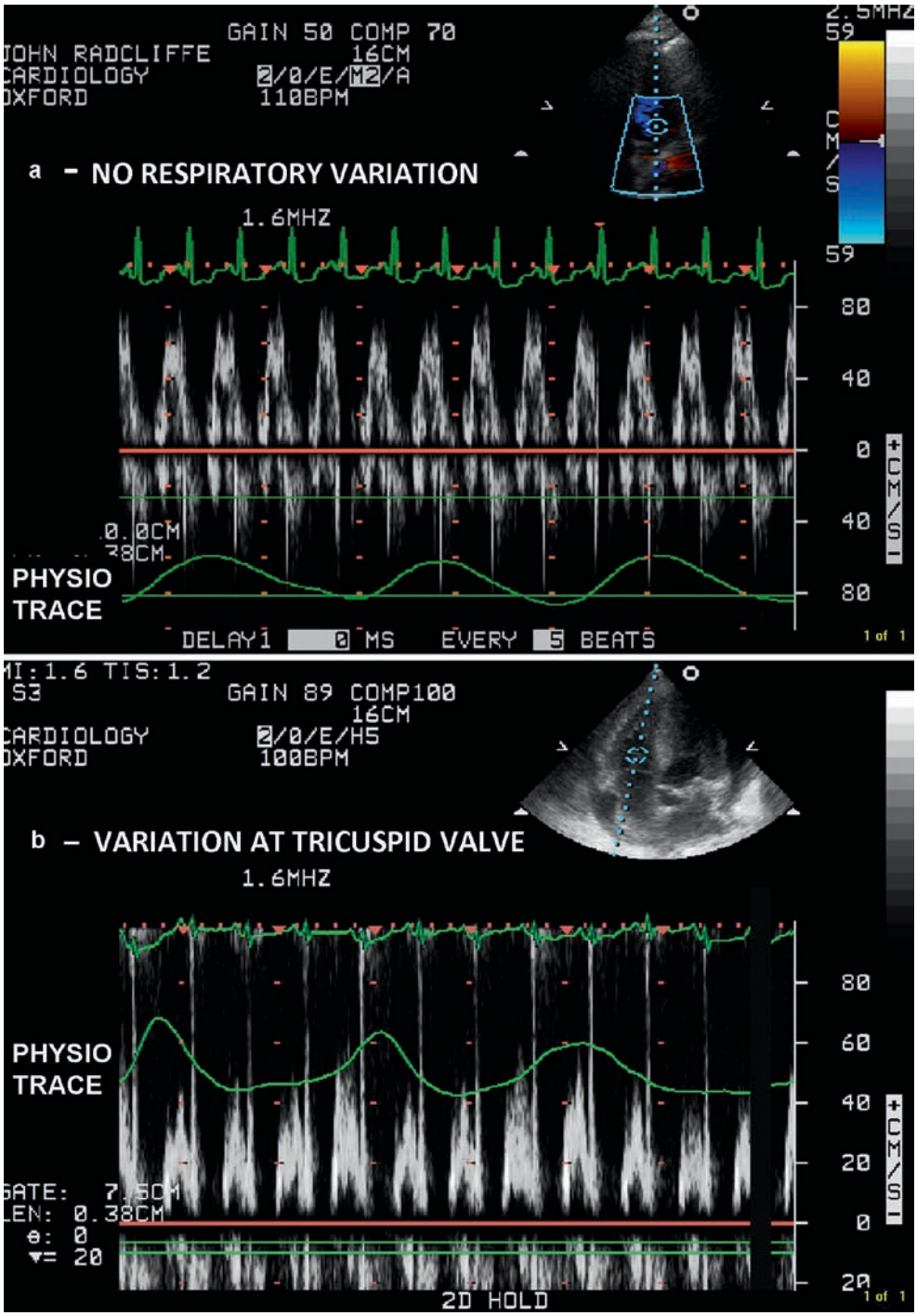

Fig. 26.9 Doppler recordings of normal (minimal) respiratory variation in tricuspid inflow and an exaggerated variation in inflow in a patient with a pericardial effusion. Images courtesy of Echocardiography Department, John Radcliffe Hospital, Oxford

are noted to be present during CT examination, urgent referral for treatment is warranted.

Cardiac MR

Advantages and Disadvantages of Cardiac MR

Cardiac MR provides a modality for more detailed assessment of pericardial effusions.[15] Cardiac MR can be useful to diagnose localized effusions around the right atrium, aorto-pericardial reflection, and posterior to the left ventricle.[16] Effusions may also be evaluated by cardiac MR as part of other cardiac pathology being imaged or noted incidentally. Strengths of cardiac MR are its ability to provide unrestricted planes of view, differentiation of tissue and fluid characteristics based on T_1 and T_2 characteristics, and provision of functional cardiac imaging.[17, 18] Assessment of the myocardium, alongside the pericardium, and the use of gadolinium contrast can provide

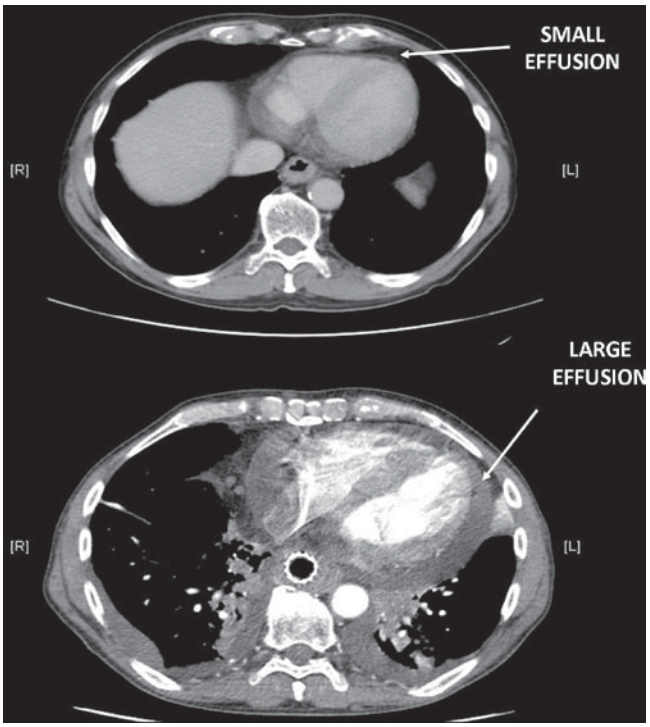

Fig. 26.10 Two standard transverse CT slices demonstrate a small and a large effusion. Note the attenuation characteristics of the effusion. Images courtesy of Radiology Department, John Radcliffe Hospital, Oxford

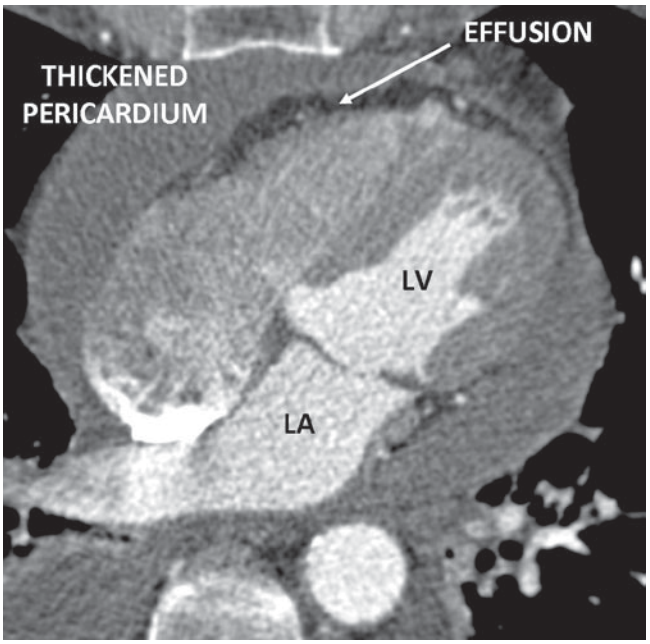

Fig. 26.11 A patient with a grossly thickened pericardium and small effusion. Images courtesy of Dr Ed Nicol, Royal Brompton Hospital, London

important information on cardiomyopathic processes that may complicate a pericardial effusion.[19, 20] Cardiac MR has a wide field of view to study related chest pathology or

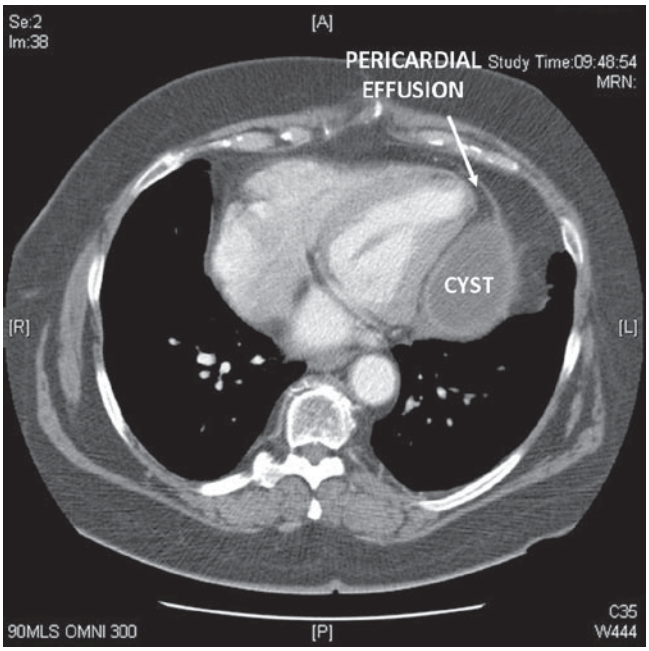

Fig. 26.12 A patient with a pericardial cyst associated with an effusion. Images courtesy of Radiology Department, John Radcliffe Hospital, Oxford

define extent of pericardial masses, and avoids ionizing radiation.

Appearances on Cardiac MR

The normal pericardium is visible as a thin dark line on most cardiac MR sequences. It is dark on both T_1- and T_2-weighted sequences because it is fibrous, with a low water content.[20] Fat has different magnetic resonance characteristics, and, therefore, the pericardial and epicardial fat help delineate the pericardium.[21] Transudates will have low-signal on T_1 and high-signal on T_2 with complex exudative effusions exhibiting greater signal intensity on T_1 (Fig. 26.13, Video 26.13). SSFP-cine imaging is associated with greater signal intensity in the presence of a greater T_2/T_1 ratio, and, therefore, transudates tend to have high intensity (Fig. 26.13). On inversion recovery, gadolinium late enhancement imaging effusions appear strikingly black (Fig. 26.14). The wide field of view means cardiac MR provides detailed assessment of loculated effusions, particularly around the aortic-pericardial reflection and at the left ventricular apex.[16] In sequences with high signal from the pericardial fluid, it is important to differentiate the effusion from the epicardial and pericardial fat. The presence of inflammatory or protein rich material within the effusion also creates patchy changes in signal intensity (Fig. 26.15, Video 26.15). The wide field of view allows detailed assessment of size, and extent of pericardial masses and tissue characteristics can be used to aid diagnosis.[22, 23]

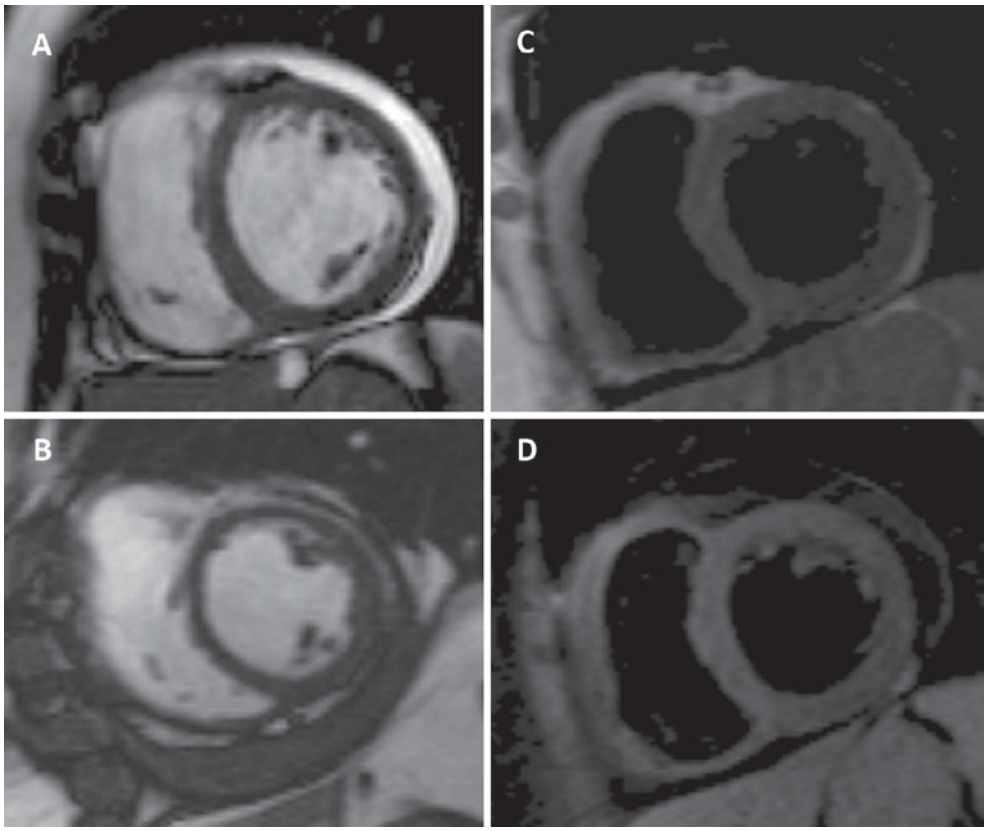

Fig. 26.13 Four short-axis views demonstrate the appearances of an effusion on **(a, b)** SSFP-imaging and T_1 turbo spin echo image without **(c)** and with **(d)** fat saturation. Images courtesy of Oxford Centre for Clinical Magnetic Resonance Research

Cardiac Tamponade and Cardiac MR

Cine images of cardiac function and free-breathing sequences allow identification of haemodynamic changes such as chamber size and collapse associated with pericardial fluid. In cardiac tamponade, there could also be dilatation of the inferior vena cava, and free breathing sequences may demonstrate abnormal septal motion. The classic right heart signs of ventricular and atrial collapse can also be imaged, but should prompt referral for treatment (Fig. 26.16, Video 26.16).[24]

Other Modalities

The pericardium is not seen during angiography, and, because of the "windowing" used, the cardiac silhouette is also not as clear as on chest radiography. Therefore, changes in size of the cardiac silhouette that may be present in pericardial effusions are more subtle. In iatrogenic pericardial effusion following intervention on a coronary artery, the pericardial space may become evident due to accumulation of contrast around the heart. During pericardiocentesis, contrast can be purposefully injected to identify the pericardial space and fluoroscopy can be used to guide needle position.

Pericardial effusions are not seen on nuclear perfusion imaging. FDG-PET is not indicated for investigation of pericardial disease, but as FDG-PET measures metabolic activity, changes in uptake within the pericardium can occur[25] in pericardial tumours or in chronic inflammatory pericarditis. It is usually difficult to distinguish uptake from that seen in the myocardium. However, this may be simplified if a pericardial effusion is present and separates the peri- and myocardium.

Pericardiocentesis

Overview

Pericardiocentesis is used to drain pericardial effusions for diagnostic purposes or to treat cardiac tamponade. The aims of pericardiocentesis are to enter the pericardial space with a needle and insert a drain via a Seldinger technique. Imaging can help by guiding the insertion of the needle, confirming position of the needle or drain within the pericardial space, and monitoring removal of fluid.

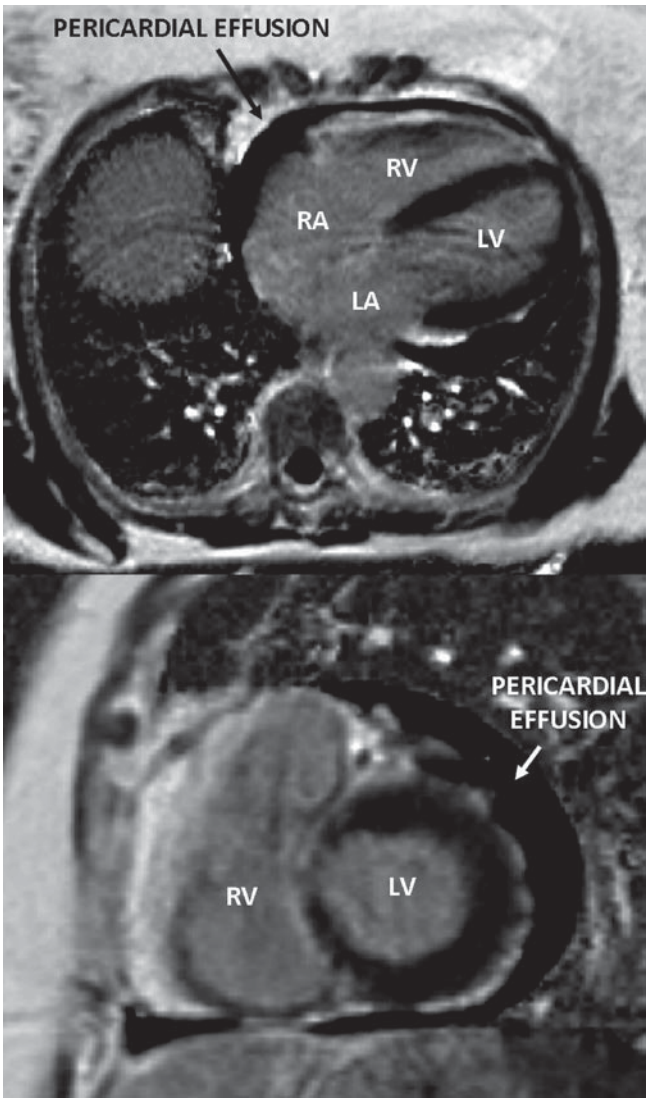

Fig. 26.14 Pericardial effusion appearances following gadolinium on an inversion recovery sequence. Images courtesy of Oxford Centre for Clinical Magnetic Resonance Research

Chest X-ray and Angiography

Fluoroscopy can aid pericardial drainage because the needle is clearly seen on screening. The needle can be followed according to the landmarks of the ribs and spines to a position where the pericardial space should be present.

Echocardiography

Echocardiography is the modality of choice for imaging-guided pericardiocentesis. Pericardiocentesis is usually done from sub-costal or apical positions, and echocardiography allows preprocedural evaluation of location and depth of fluid in these positions.[5] During the procedure, the angle of the echo probe used to achieve images can be used as a guide to the angle to be used for the needle. Imaging can then be maintained from the alternative position (apical or sub-costal), and the needle can sometimes be seen advancing into pericardial space (Fig. 26.17, Video 26.17). If it is not clear if the needle is in the pericardial space, injection of a small amount of agitated saline contrast down the needle should be seen filling the pericardial space.

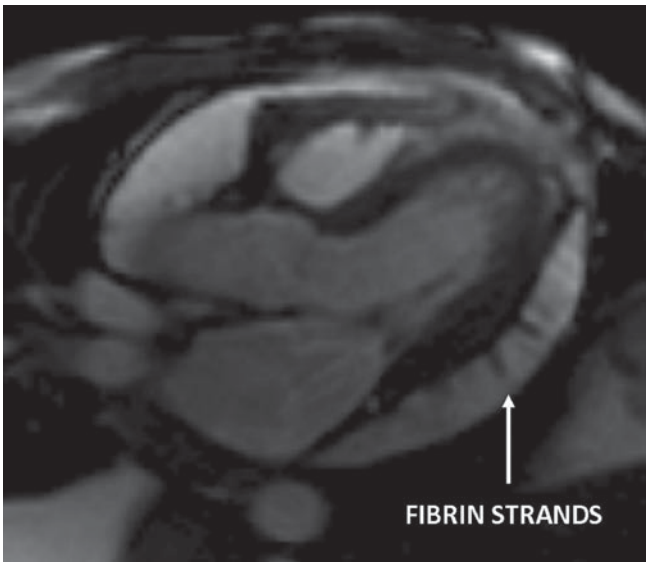

Fig. 26.15 SSFP left ventricular outflow tract view demonstrates the high intensity effusion and strands of low intensity along the lateral wall consistent with fibrin strands. Images courtesy of Oxford Centre for Clinical Magnetic Resonance Research

Conclusions

The pericardium has a key function to maintain cardiac efficiency and function by allowing free movement of the heart. Impairment of this normal function due to the accumulation of a pericardial effusion can lead to a range of symptoms from mild discomfort to haemodynamic collapse. Presentation with pericardial effusion can present a diagnostic conundrum because of the similarities between symptoms and other pathologies, for example, chest pain of pericardial or cardiac origin, breathlessness of chest disease, heart failure, or cardiomyopathies. Multi-modality cardiovascular imaging is an essential and incredibly powerful tool to aid diagnosis. Echocardiography provides the modality of choice for immediate, simple assessment of pericardial effusions and evaluation of possible cardiac tamponade. Furthermore, echocardiography can guide intervention and provide follow-up assessments. Cardiac CT and MR provide means for detailed investigation of localized effusions and also of wider pathology that may be related to the presence of a pericardial effusion.

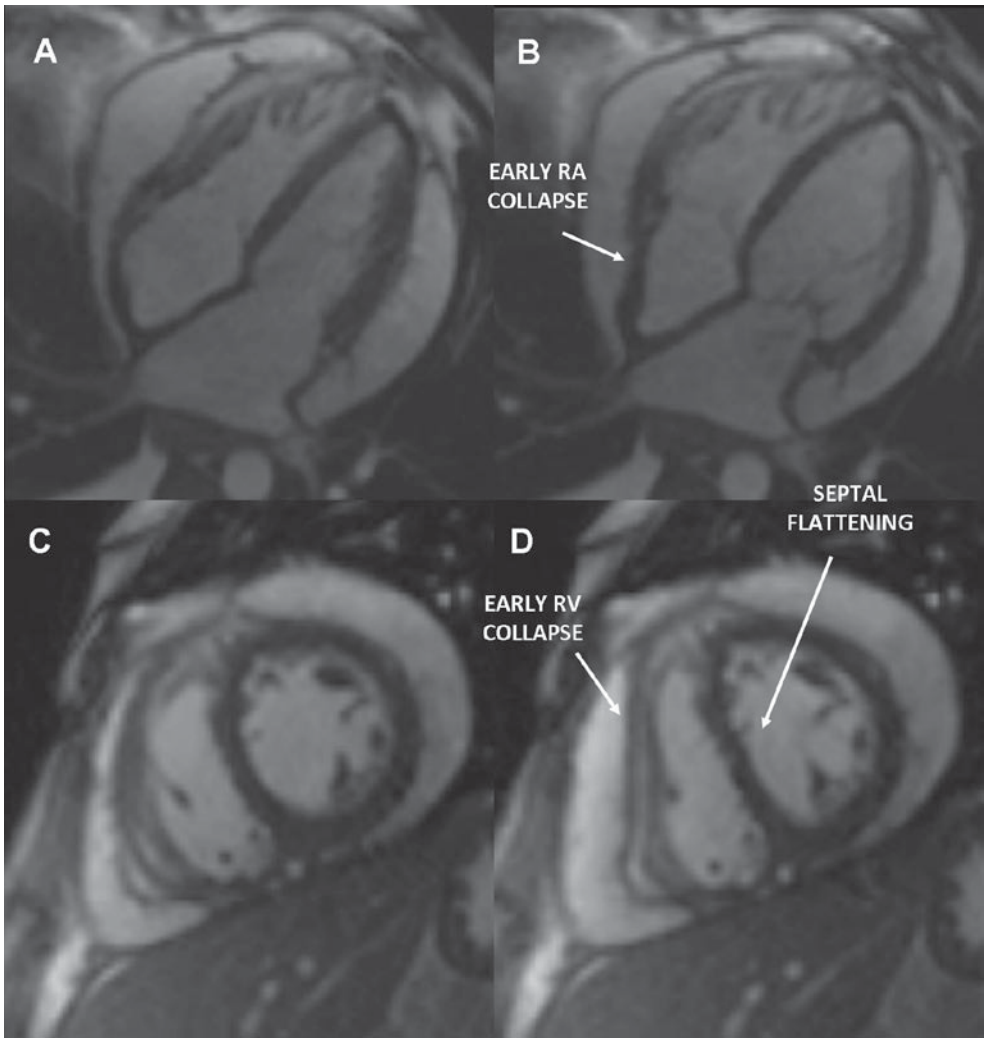

Fig. 26.16 SSFP views of a large global effusion with evidence of mild right atrial collapse in end-diastole and right ventricular collapse in late systole. Images courtesy of Oxford Centre for Clinical Magnetic Resonance Research

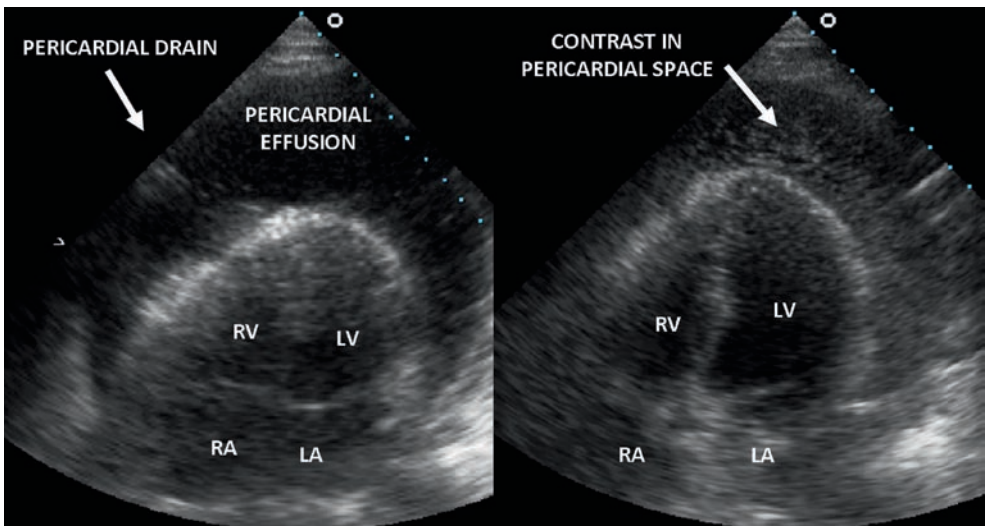

Fig. 26.17 Apical four-chamber echocardiography views acquired during pericardiocentesis. In **(a)** a part of the pericardial drain is just visible, and in **(b)** agitated saline contrast has been injected down the pericardiocentesis needle to confirm position of the needle within the pericardial space. Images courtesy of Echocardiography Department, John Radcliffe Hospital, Oxford

References

1. Stephen WM. Imaging pericardial disease. *Radiol Clin North Am*. 1989;27:1113
2. Breen JF. Imaging of the pericardium. *J Thorac Imaging*. 2001;16(1):47–54
3. Kim JS, Kim HH, Yoon Y. Imaging of pericardial diseases. *Clin Radiol*. 2007;62(7):626–631
4. Camm A, Luscher T, Serruys P. *ESC Textbook of Cardiovascular Medicine*. Oxford, UK: Blackwell Publishing; 2006
5. Leeson P, Mitchell A, Becher H. *Echocardiography*. Oxford: Oxford University Press; 2007
6. Merce J, et al Correlation between clinical and Doppler echocardiographic findings in patients with moderate and large pericardial effusion: implications for the diagnosis of cardiac tamponade. *Am Heart J*. 1999;138(4 Pt 1):759–764
7. Weinreb JC, et al ACR clinical statement on noninvasive cardiac imaging. *J Am Coll Radiol*. 2005;2(6):471–477
8. Carsky EW, Azimi F, Mauceri R. Epicardial fat sign in the diagnosis of pericardial effusion. *JAMA*. 1980;244(24):2762–2764
9. Feigenbaum H. Echocardiographic examination of the left ventricle. *Circulation*. 1975;51(1):1–7
10. Feigenbaum H, Armstrong WF, Ryan T. *Feigenbaum's Echocardiography*. 6th ed. Philadelphia, PA: Lippincott Williams & Wilkins; 2004
11. Otto CM. *Textbook of Clinical Echocardiography*. 3rd ed. Philadelphia, PA: Saunders; 2004
12. Levy-Ravetch M, et al CT of the pericardial recesses. *AJR*. 1985;144:07–714
13. Lopez Costa I, Bhalla S. Computed tomography and magnetic resonance imaging of the pericardium. *Semin Roentgenol*. 2008;43(3): 234–245
14. Wang ZJ, et al CT and MR imaging of pericardial disease. *Radiographics*. 2003;23 Spec No: S167–S180
15. Jeudy J, White CS. Cardiac magnetic resonance imaging: techniques and principles. *Semin Roentgenol*. 2008;43(3):173–182
16. Mulvagh SL, et al Usefulness of nuclear magnetic resonance imaging for evaluation of pericardial effusions, and comparison with two-dimensional echocardiography. *Am J Cardiol*. 1989;64(16):1002–1009
17. Lardo AC, et al *Cardiovascular Magnetic Resonance: Established and Emerging Applications*.London: Taylor and Francis; 2003
18. Misselt AJ, et al MR imaging of the pericardium. *Magn Reson Imaging Clin N Am*. 2008;16(2):185–199, vii
19. Leeson CP, et al Atrial pathology in cardiac amyloidosis: evidence from ECG and cardiovascular magnetic resonance. *Eur Heart J*. 2006;27:1670
20. Smith WH, et al Magnetic resonance evaluation of the pericardium. *Br J Radiol*. 2001;74(880):384–392
21. Maksimovic R, et al Magnetic resonance imaging in pericardial diseases. Indications and diagnostic value. *Herz*. 2006;31(7):708–714
22. Sechtem U, Tscholakoff D, Higgins CB. MRI of the abnormal pericardium. *AJR*. 1986;147(2):245–252
23. Sechtem U, Tscholakoff D, Higgins CB. MRI of the normal pericardium. *AJR*. 1986;147(2):239–244
24. Olson MC, et al Computed tomography and magnetic resonance imaging of the pericardium. *Radiographics*. 1989;9(4):633–649
25. Strobel K, Schuler R, Genoni M. Visualization of pericarditis with fluoro-deoxy-glucose-positron emission tomography/computed tomography. *Eur Heart J*. 2008;29(9):1212

Chapter 27

CONSTRICTIVE PERICARDITIS AND RESTRICTIVE CARDIOMYOPATHY

Frank Rademakers

CONTENTS

J. L. Zamorano et al. (eds.), *The ESC Textbook of Cardiovascular Imaging*
DOI: 10.1007/978-1-84882-421-8_27, © Springer-Verlag London Limited 2010

Introduction

Constrictive pericarditis (CP) and restrictive cardiomyopathy (RCMP) have some similarities in presentation, but their pathophysiology, clinical features, and, more importantly, therapeutic approach are quite different.[1] It is therefore imperative that the correct diagnosis be made before installing a therapy, which, if applied for the wrong diagnosis, could be deleterious to the patient.

In some patients, various components of fluid accumulation, constriction, and abnormalities in myocardial compliance and function can coexist, making the diagnostic process extremely difficult.[2]

To better understand the contribution of various imaging modalities, the pathophysiology and the clinical presentation with symptoms and signs will be reviewed. For completeness and since some transitions exist, tamponade will also be covered.[3] Most diagnostic signs on imaging are direct illustrations and consequences of the underlying physiopathology.

Pathophysiology

The normal human pericardium is a relatively stiff sac, enveloping the heart and returning on itself at the origins of the vessels; it is attached to the adventitia of the arteries and to the sternum, vertebral column, and diaphragm.[4] The pressure in the pericardium, although still under debate, is between 0 and 3 mmHg and slightly less than right atrial pressure (RAP); as such, it counteracts the distension pressure of the cardiac cavities and mostly so for the thin walled, low pressure right heart where the structure of the wall itself resists volume and shape changes less and where the relaxation process in the myocardium contributes less to overall filling than in the left heart (suction pump). The driving force for the expansion of a heart cavity is the active relaxation generating a negative force during the brief, early diastolic suction period and the difference between the intra-cavitary and pericardial pressure during the passive dilation or diastasis period and during active atrial contraction.

When fluid accumulates in the pericardium, the pressure in the pericardium increases, the trans-mural diastolic distending pressures of the atria drop to 0 (tamponade sets in), and the increased atrial pressures equalize. As the effect of a decreased distension pressure is more pronounced in the right heart, a compression of the right atrium and ventricle occurs at the time of lowest intra-cavitary pressure, i.e. early diastole, impeding early filling, and consequently limiting total filling volume and ultimately stroke volume; with increasing pericardial volume and pressure, the atrium remains collapsed throughout diastole. Left ventricular filling and output become compromised by the decreased right heart output and the increased left-right interaction (Fig. 27.1). The increase in pericardial pressure depends on the speed of fluid accumulation since the pressure-volume relation of the pericardium is relatively flat in the first part, but becomes exponential thereafter. With slow accumulation, the pericardium can grow and adapt to accommodate large amounts of fluid with only a small increase in pressure. Every acute intervention that increases the venous return to the heart increases total heart volume and, as such, intrapericardial total volume and pressure; if this occurs on the steep portion of the pericardial P–V relation, it will ensue in an upward shift of the LV diastolic P–V relation. On the other hand, a significant hypo-volemia with overall small heart cavities can mask the haemodynamic effects and clinical signs of tamponade.

Overall, the volume change of the pericardial sac during a cardiac cycle is limited, with a small increase during diastole and a decrease during ejection; for the largest part, blood volume is shifted between the atria and the ventricles, with ejection of the ventricles and filling of the atria during systole and emptying of the atria and filling of the ventricles during diastole. On the other hand, since the left and right heart occupy the pericardial sac together, a ventricular interdependence or coupling exists, i.e. the more space one side of the heart occupies, less is available for the other side, leading to increased diastolic pressures in the contralateral part (Fig. 27.2). This interdependence is present in normal circumstances during breathing and is exaggerated by fluid accumulation in the pericardium or by pericardial stiffening. The depth and speed of respiration also significantly determine the size of the effect on cardiac haemodynamics and should be recorded during imaging (increased apparent interdependence in COPD patients). The effect of a stiffened pericardium is not apparent at the smallest heart volume, i.e. during early, fast filling, but becomes apparent during subsequent diastasis and atrial contraction.

During inspiration, pressure in the thorax and the pericardium drops, and flow towards (inferior vena cava) and from the right heart increases (with an increased total right heart volume and pressure), while the reverse occurs on the left side (when exaggerated this causes pulsus paradoxus); during expiration, the opposite changes take place (Fig. 27.3).

While cardiac tamponade counteracts distension pressures throughout the entire filling period, the restraint in CP is nearly absent during early filling when overall cardiac volume is lowest, but rapidly increases thereafter, giving rise to the characteristic square root sign on LV pressure traces. Another characteristic of CP is the belated transmission of changes in intra-thoracic pressures to the intra-pericardial structures, creating the exaggerated acute changes in filling

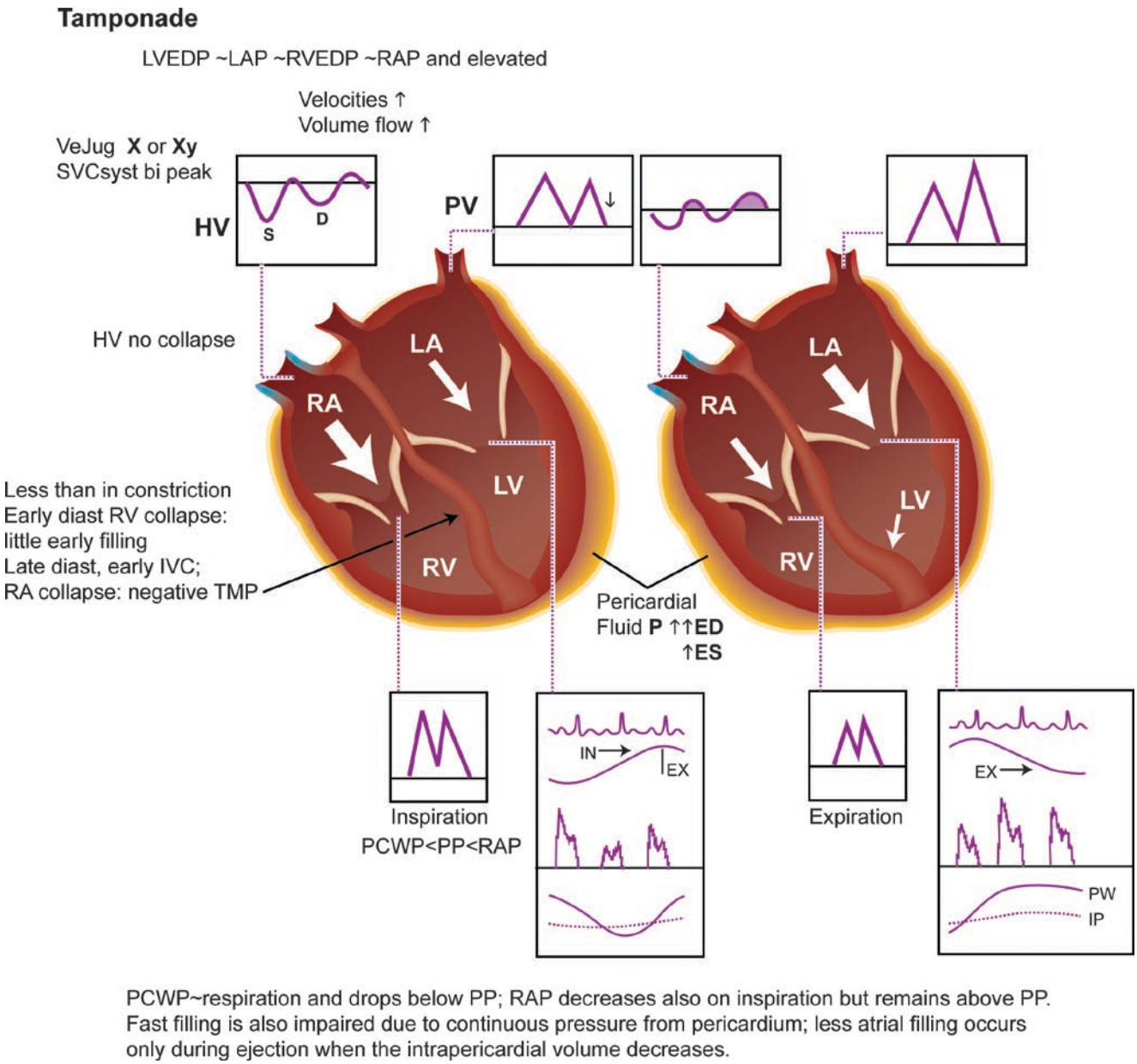

Fig. 27.1 Haemodynamic characteristics of cardiac tamponade. Various pressures and flow patterns are illustrated during inspiration on the left and expiration on the right. *RA* right atrium; *LA* left atrium; *RV* right ventricle; *LV* left ventricle; *LVEDP* left ventricular end-diastolic pressure; *LAP* left atrial pressure; *RVEDP* right ventricular end-diastolic pressure; *RAP* right atrial pressure; *SVC* superior vena cava; *HV* hepatic vein; *PV* pulmonary vein, *diast* diastole; *IVC* isovolumic contraction phase; *PCWP, PW* pulmonary capillary wedge pressure; *IP, PP* pleural pressure; *P* pressure; *ED* end diastole; *ES* end systole; *in* inspiration; *ex* expiration; *TMP* trans-mural pressure

gradients at the onset of the inspiratory and expiratory motions. During inspiration, the increased venous return is not coupled to the characteristic drop in RA pressure and systemic venous pressure may actually increase, i.e. Kussmaul's sign in the superior caval vein (SVC) (Fig. 27.4). In other words, in patients with CP, the pulmonary wedge pressure is influenced by the inspiratory fall in thoracic pressure, while the left ventricular pressure is shielded from respiratory pressure variations by the stiff pericardium. Thus, inspiration lowers the pulmonary wedge pressure and, presumably, left atrial pressure (LAP), but not left ventricular diastolic pressure, thereby decreasing the pressure gradient for ventricular filling. The less favourable filling pressure gradient during inspiration explains the decline in filling efficiency. Reciprocal changes occur in the volume of right ventricular filling (Fig. 27.5). These reciprocal changes are mediated by the ventricular septum, not by increased systemic venous return. Thus, ventricular interdependence can

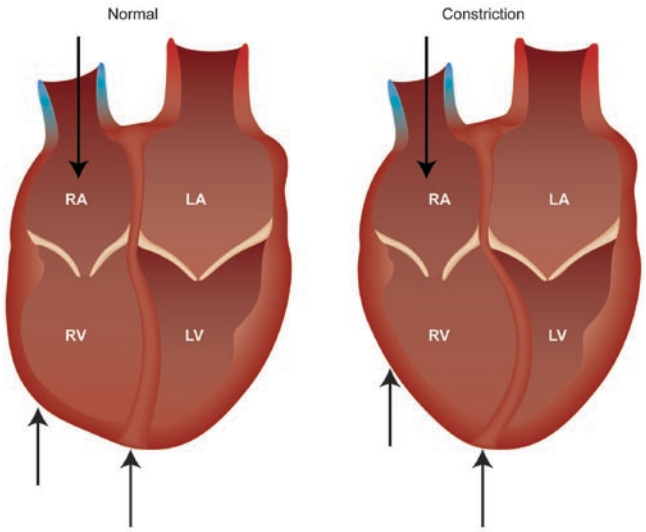

Fig. 27.2 Ventricular interdependence in normal conditions during inspiration with increased filling of the right heart and in pericardial constraint leading to a shift of the inter-ventricular septum towards the left

be seen as a more continuous and a more sudden effect, governed by either slower volume shifts or by more sudden pressure shifts. When the pressure gradient between the left and right heart shifts, the structure separating the two, i.e. the inter-atrial and inter-ventricular septum, can move; in normal conditions, the pressures on the left are higher than on the right, leading to the characteristic shape of the septa; with pericardial constriction, a sudden shift of the prevailing pressure gradient between left and right ventricle during early diastole causes a septal bouncing motion that is characteristic for this condition.

Since respiratory interdependence in CP decreases at higher absolute LA pressures and with the severity of constriction, examining a patient in the upright position (decrease of filling pressures) can unmask interdependence in such cases.

In comparison to CP, tamponade exhibits a more marked pulsus paradoxus and a fall in RAP with onset of inspiration (no Kussmaul's sign) because the intra-thoracic pressure changes are readily transmitted to the intra-cardiac cavities. CP more then tamponade is mimicked by acute RV

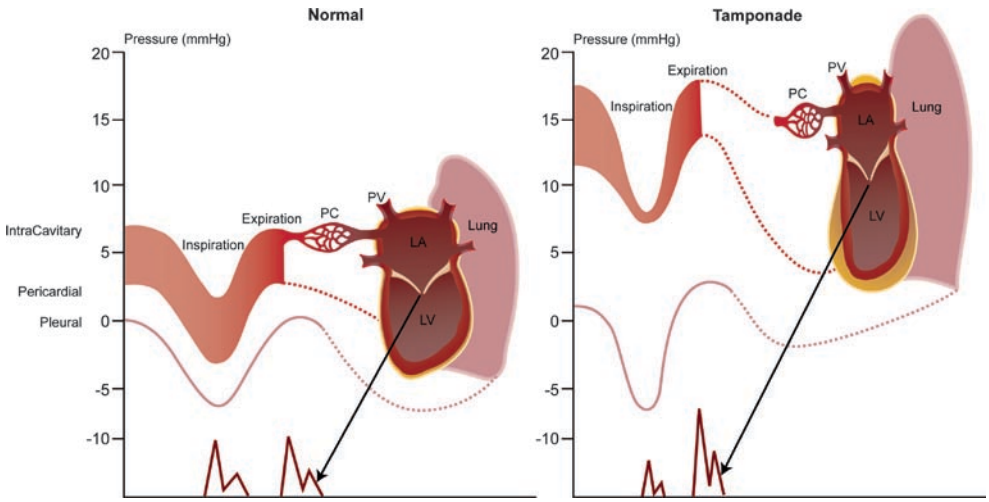

Fig. 27.3 Variation in pressures in the vasculature and cavities in the pericardium and in the pleural space during in- and expiration in the normal situation (*left*) and in conditions of pericardial constraint (*right*); in the former, the gradients remain the same with a constant trans-mural filling pressure and inflow over the mitral valve as a consequence; in the latter, the gradients vary with a decrease during inspiration and a subsequent variation in the mitral inflow pattern

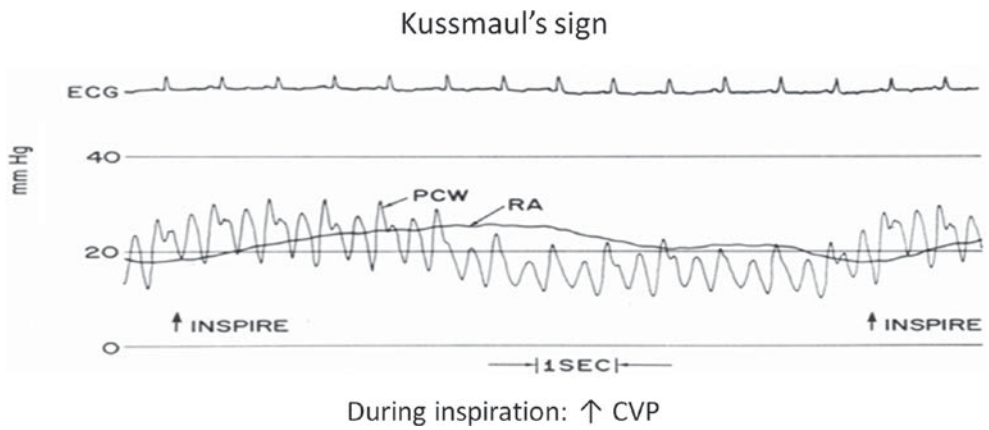

Fig. 27.4 Kussmaul's sign with a paradoxical increase of right atrial pressure during early inspiration due to the belated transmission of decreased intra-thoracic pressure to the intra-pericardial structures. *RA* right atrium; *CVP* central venous pressure; *PCW* pulmonary capillary wedge pressure

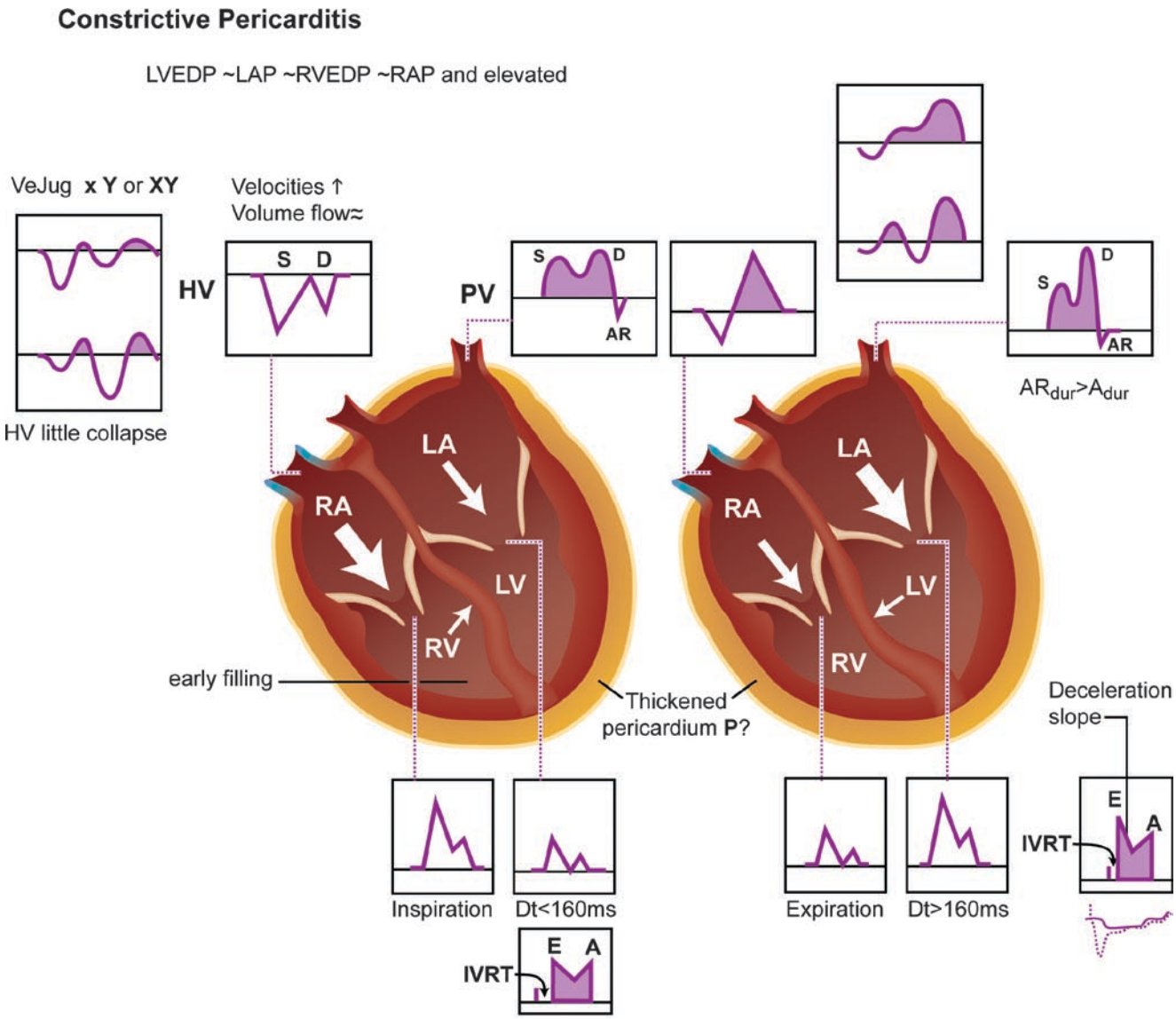

Fig. 27.5 Haemodynamic characteristics of pericardial constriction. Various pressures and flow patterns are illustrated during inspiration on the left and expiration on the right. *RA* right atrium; *LA* left atrium; *RV* right ventricle; *LV* left ventricle; *LVEDP* left ventricular end-diastolic pressure; *LAP* left atrial pressure; *RVEDP* right ventricular end-diastolic pressure; *RAP* right atrial pressure; *SVC* superior vena cava; *HV* hepatic vein; *VeJug* jugular vein; *PV* pulmonary vein; *diast* diastole; *IVC* isovolumic contraction phase; *PCWP, PW* pulmonary capillary wedge pressure; *P* pressure; *ED* end diastole; *ES* end systole; *TMP* trans-mural pressure; *s* systolic; *d* diastolic; *AR* atrial reversal; *dur* duration; *E* early filling velocity; *A* atrial contraction velocity; *Dt* decelaration slope of early filling velocity; *IVRT* isovolumic relaxation time

infarction (sudden dilatation of right heart cavities with increased pericardial pressure and restraint).

CP must also be differentiated from RCMP,[5] where the compliance problem resides within the myocardium, and from exaggerated respiratory variations and ventricular interdependence, occurring with increased intra-thoracic pressure swings in COPD,[6] marked obesity, recent thoracotomy, and marked dyspnea from another cause. Hepatic vein and SVC flows can help to differentiate (Fig. 27.6).

CP and RCMP share the following features: non-dilated ventricles, ventricular filling limited to early diastole, high venous pressures with dilated inferior caval vein and reduced respiratory collapse, diastolic flow into the pulmonary artery, and ventricular dip-plateau. Important differences are the

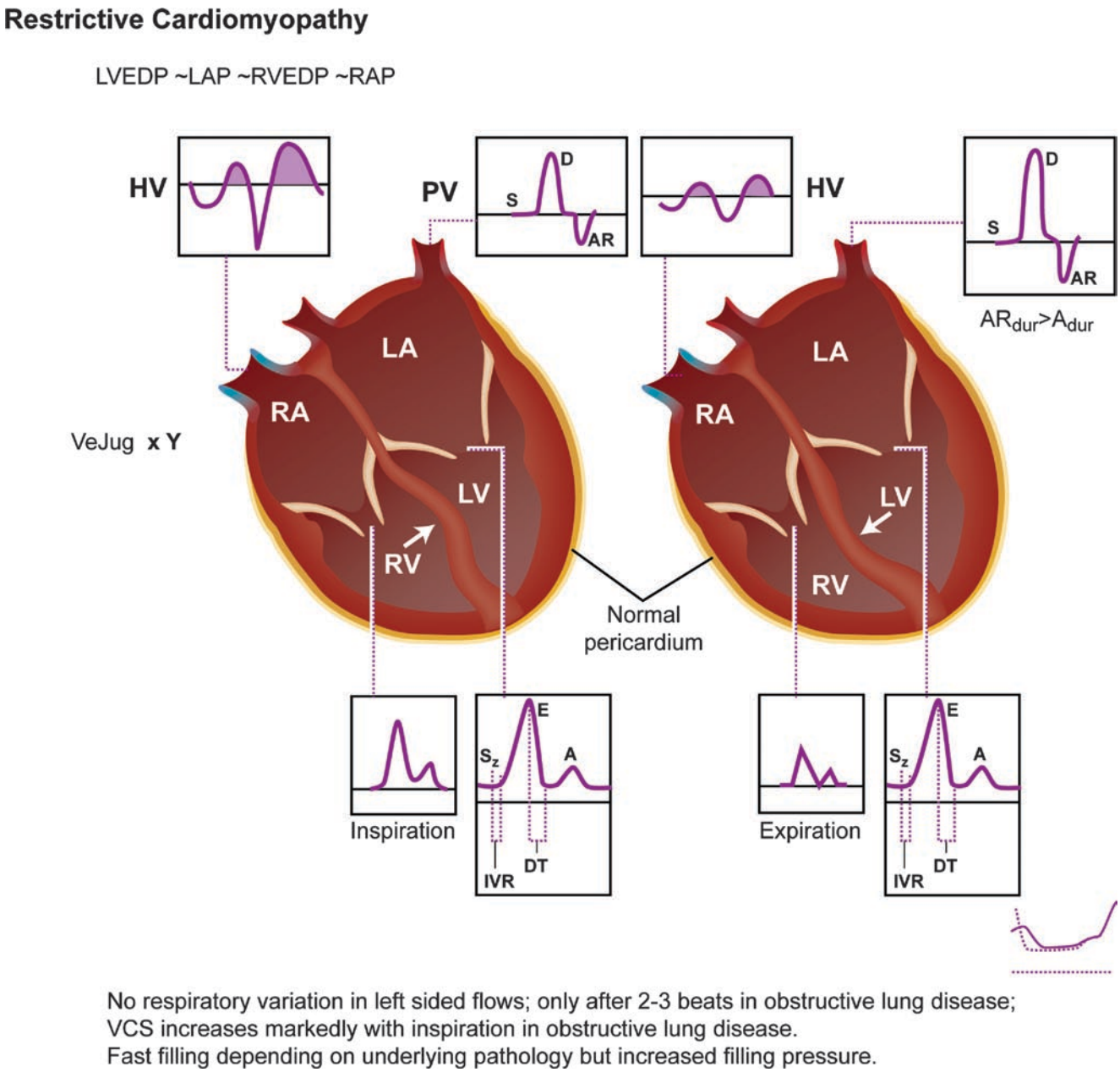

Fig. 27.6 Haemodynamic characteristics of restrictive cardiomyopathy. Various pressures and flow patterns are illustrated during inspiration on the left and expiration on the right. *RA* right atrium; *LA* left atrium; *RV* right ventricle; *LV* left ventricle; *LVEDP* left ventricular end-diastolic pressure; *LAP* left atrial pressure; *RVEDP* right ventricular end-diastolic pressure; *RAP* right atrial pressure; *HV* hepatic vein; *VeJug* jugular vein; *PV* pulmonary vein; *IVC* isovolumic contraction phase; *PCWP, PW* pulmonary capillary wedge pressure; *P* pressure; *ED* end diastole; *ES* end systole; *TMP* trans-mural pressure; *s* systolic; *d* diastolic; *AR* atrial reversal; *dur* duration; *E* early filling velocity; *A* atrial contraction velocity; *AT* acceleration slope of early filling velocity; *DT* deceleration slope of early filling velocity; *IR* isovolumic relaxation time; *S2* second heart sound

larger atria in RCMP, the more pronounced respiratory changes in filling with increased interdependence in CP, the decrease of tricuspid DT in RCMP, the early diastolic septal inversion (bounce) in CP, and the hepatic vein reversal on atrial contraction, which is more pronounced in expiration in CP and in inspiration in RCMP. A lower left ventricular filling pressure gradient with CP also leads to a delay in mitral valve opening, and, therefore, a longer iso-volumic relaxation time during inspiration. Prolonged iso-volumic relaxation of the left ventricle is a feature of both restrictive and constrictive pathology, but this finding varies with respiration in CP but not RCMP.

These pathophysiologic characteristics of the various pericardial syndromes can be studied with the different imaging modalities, but it is crucial to be able to register morphology as well as function and flow, mainly during the different phases of the respiratory cycle.

Clinical Findings

History

A prior history of pericarditis (e.g. tuberculosis, connective tissue disease, malignancy), trauma, or cardiac surgery makes the diagnosis of CP more likely.

A history of an infiltrative disease that may involve the heart muscle (e.g. amyloidosis, haemochromatosis, or sarcoidosis) or a therapy that can cause myocardial apoptosis and fibrous replacement (chemotherapy) favors the diagnosis of RCMP. On the other hand, prior mantle radiation or cardiac surgery can result in both pericardial restriction and/or RCMP.

Physical Examination

Using only a systemic venous pressure tracing or observing the venous neck pulse, it is not possible to distinguish between CP, RCMP, and tricuspid regurgitation with an enlarged compliant right atrium, right heart failure (e.g. due to right ventricular infarction or pulmonary hypertension), or circulatory overload with systemic congestion. The contour of the jugular venous pulse in all these conditions is dominated by a deep, steep Y descent.

The abrupt cessation of early diastolic filling may be manifested in either CP or RCMP by an early diastolic sound, which is called a pericardial knock in patients with CP.

Kussmaul's Sign

The presence of Kussmaul's sign (Fig. 27.4) is often sought in patients with suspected CP. Kussmaul's sign represents the lack of the expected inspiratory decline in jugular venous pressure due to a decrease in effective operative compliance of the right ventricle. In severe cases, the pressure actually increases with inspiration. In most cases of CP studied during quiet respiration, Kussmaul's sign takes a forme fruste; respiratory variation of the mean central venous pressure is absent rather than reversed. Importantly, Kussmaul's sign is also observed in right heart failure or systemic venous congestion of any cause, and in severe tricuspid regurgitation. Doppler flow measured in the superior vena cava or the jugular vein is the imaging correlate of this clinical sign.

In contrast, the venous pulse in cardiac tamponade (with a continuous counteraction of filling) has a truly abnormal waveform characterized by attenuation of the Y descent, or replacement of it by an upwardly sloping segment. In addition, Kussmaul's sign is usually absent in tamponade.

Non-invasive Testing

Electrocardiogram

The electrocardiogram may be helpful. Depolarization abnormalities (such as bundle branch block), ventricular hypertrophy, pathologic Q waves, or impaired atrio-ventricular conduction strongly favour RCMP. Low voltage and isolated repolarization abnormalities can occur in both conditions, although the latter are more common in CP. Atrial fibrillation is common in the late stages of both diseases.

Chest X-Ray

Calcification of the pericardium (excepting scattered plaques) strongly suggests CP (Fig. 27.7). However, the absence of calcification is equally compatible with either diagnosis, since pericardial stiffening can occur without calcification. Mild cardiomegaly on chest X-ray is common in both conditions, but more prominent in RCMP. It is due to atrial rather than ventricular enlargement.

Plasma BNP

Plasma concentrations of B type natriuretic peptide (BNP) are increased in patients with left ventricular dysfunction and wall stretch. Wall stretch is increased in RCMP. However, in CP, the myocardium is normal, and stretch is limited by the thickened pericardium. These physiologic differences suggest that measurement of plasma BNP might have value in distinguishing between these two disorders.

Although evidence is still limited, this hypothesis is generally confirmed with significantly elevated BNP in RCMP and low BNP in patients with idiopathic CP.[7] However, moderate elevations in plasma BNP were also noted in patients with CP due to overt etiologies (e.g. cardiac surgery or mantle radiation).

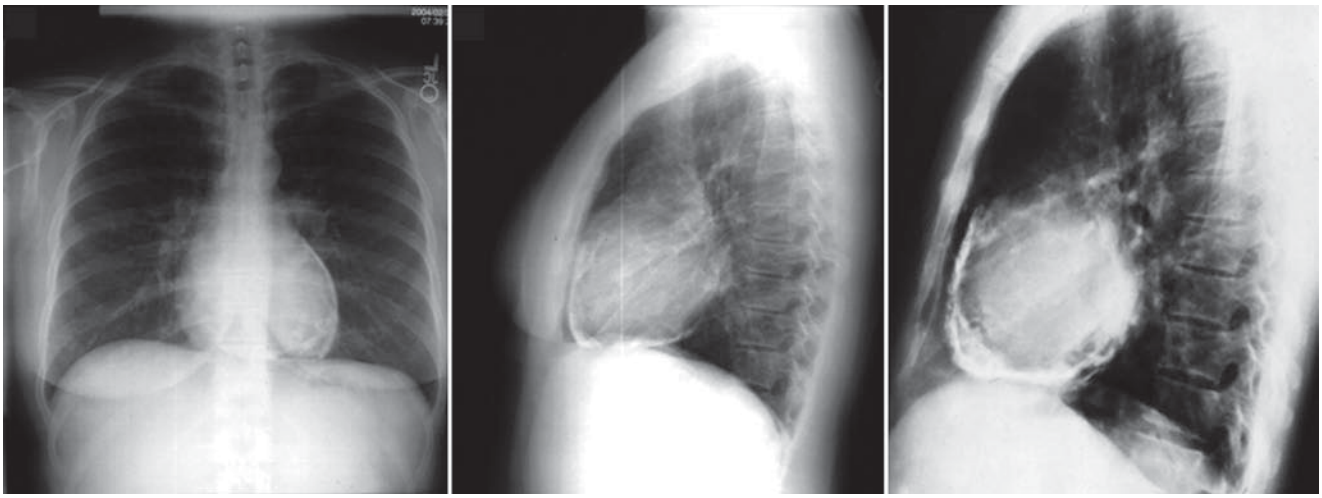

Fig. 27.7 Pericardial calcifications on chest X-ray

Echocardiography

The parietal pericardium produces one of the most strongly reflective or echo-producing areas of the heart, and it normally moves anteriorly with the epicardium; if the gain on the echo machine is lowered, only the signals from the strongest reflector in the tracing, the pericardium, remain (Fig. 27.8). TOE (trans-oesophageal echocardiography) can be of help to establish pericardial thickening.[8, 9]

Pericardial thickness exceeding 3–5 mm is highly suggestive of CP. However, constriction can also be caused by a thin tight peel of visceral pericardium. Thus, a normal appearing parietal pericardium does not rule out CP.[10]

In addition, patients who have had radiation therapy or open heart surgery may have areas of thickened pericardium that do not cause haemodynamic compromise, while on the other hand, radiation can cause myocardial restriction.

When evaluating an effusion by 2D echocardiography, its presence, size, haemodynamic importance, and distribution are noted in each of the standard imaging windows. An echo free space between pericardial layers is the hallmark of a pericardial effusion. It is important to remember that not all pericardial spaces represent effusion. Pericardial fat is the most common source of non-effusive pericardial space. This normal but highly variable tissue is most commonly seen anterior to the heart in the parasternal long-axis view and in the sub-costal views. The best clues to its identity as fat are its absence posteriorly, normal motion of the pericardium, low intensity echoes within the space, and, perhaps most importantly, absence above the right atrium in the 4-chamber view and just posterior to the base of the left ventricle.

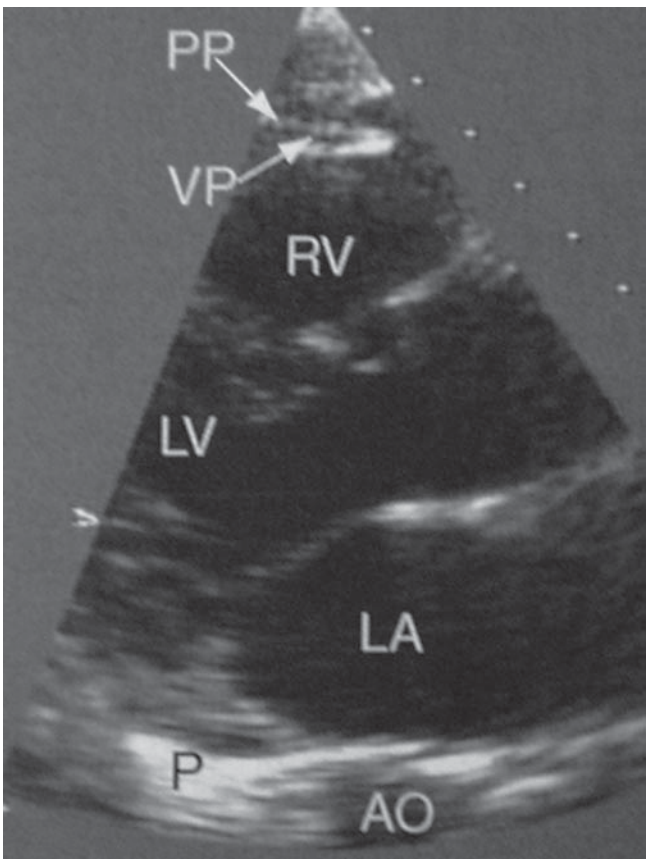

Fig. 27.8 2D echocardiogram with the bright echo signals at the anterior and posterior surface of the heart representing the pericardial structures. *RV* right ventricle; *LV* left ventricle; *AO* aorta; *P* posterior pericardium; *PP* parietal pericardium; *VP* ventricular pericardium

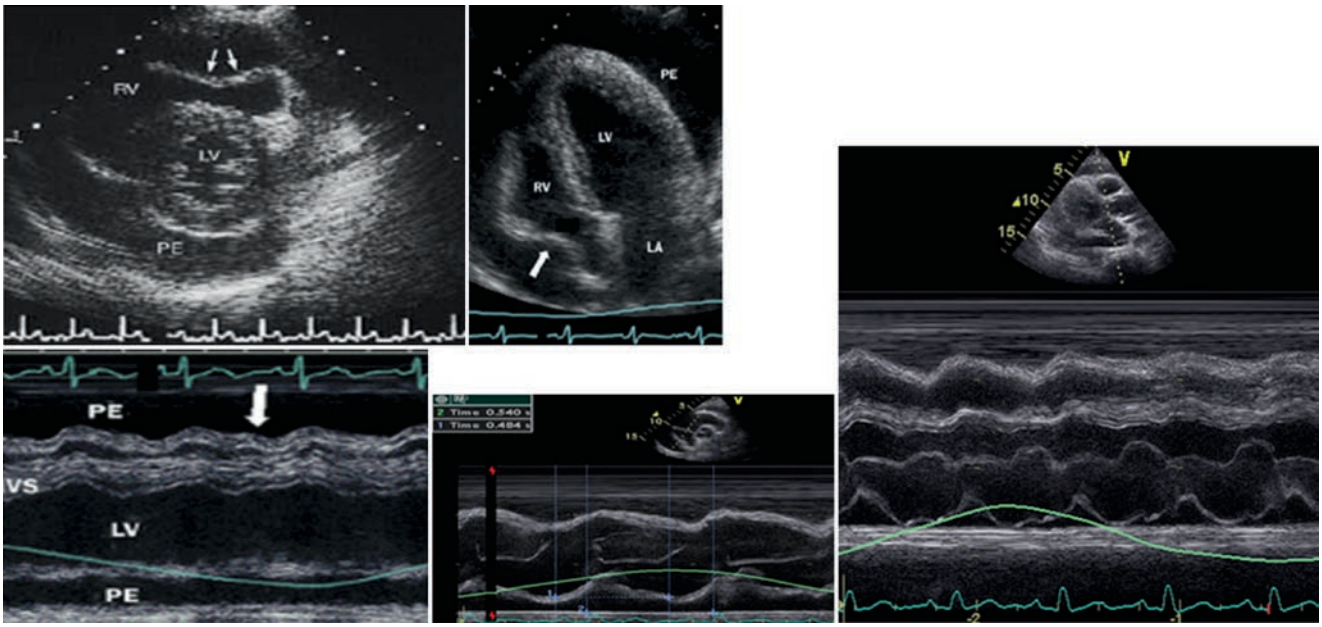

Fig. 27.9 Right atrial (*left* and *middle*) and left atrial collapse with tamponade. *Top panels* show 2D and *lower panels* M-mode tracings. *PE* pericardial effusion; *RV* right ventricle; *LV* left ventricle; *IVS* inter-ventricular septum; *LV* left ventricle

Pericardial tamponade has certain features that are usually present on the 2D echocardiogram:

- Moderate or large effusion
- Right atrial expiratory collapse (Fig. 27.9)
- Right ventricular expiratory compression collapse
- IVC plethora with diminished respiratory response
- Left atrial compression
- Small chamber volumes (especially the right ventricle)
- Reciprocal size changes with respiration between right and left ventricles and mitral and tricuspid valves

Many of the right ventricular findings may be absent in a patient with significant pulmonary artery hypertension.

CP exhibits the following features that are supportive of the diagnosis, but not necessarily diagnostic:

- Pericardial thickening and adhesion: lack of "sliding"; heart motion transmitted to other organs ("tugging")
- Septal bounce – abrupt transient rightward movement
- IVC plethoric and unresponsive to respiration; hepatic veins dilated (Fig. 27.10)
- Left and right ventricular size decreased; heart tubular in shape
- Mild biatrial enlargement

Septal bounce is the 2D counterpart of the M-mode septal notch and is often the first and best clue that constriction is present. This early diastolic incoordinate septal motion occurs towards the apex, but is indistinguishable from the incoordinate contraction/relaxation pattern seen in left bundle branch block or pacing from the right ventricular apex. Once the septal bounce is noted, constriction must be excluded as a possible diagnosis.

RCMP findings on 2D echocardiography, in comparison to CP, include:

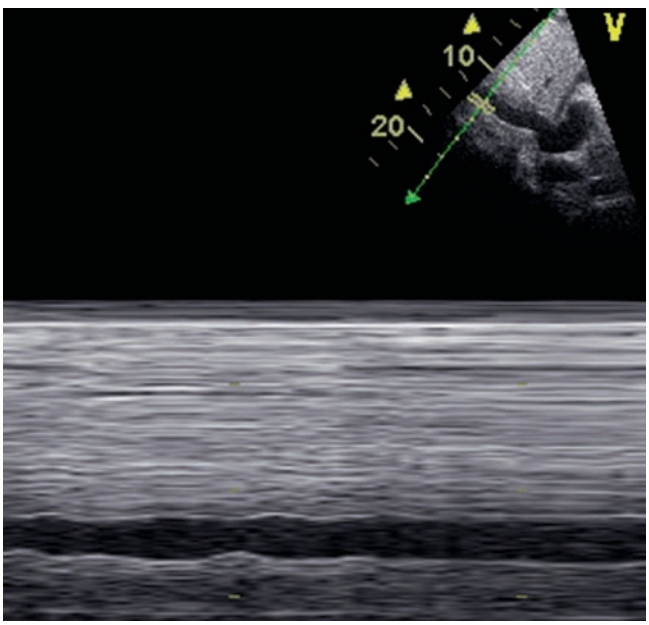

Fig. 27.10 M-mode through a hepatic vein illustrating the increased diameter and the lack of respiratory variation

- Absence of pericardial adhesion and thickening
- Left ventricular mass that is normal or increased; myocardial reflectance increased
- Moderate to severe biatrial enlargement
- Frequent AV valve regurgitation
- Signs of pulmonary hypertension
- AV valve excursion on M-mode unaffected by respiration

Doppler Echocardiography

Since RCMP and CP share important haemodynamic characteristics, they have a number of Doppler characteristics in common. Most notable is a restrictive mitral inflow or ventricular filling pattern with striking E dominance and a short deceleration (DT) time. These findings indicate early rapid filling and are seen in both entities.

Colour M-mode Doppler, on the other hand, shows an excessively rapid transit of blood flow from the mitral and tricuspid (Fig. 27.11) orifice to the apex in CP, whereas the transit is much slower than normal in RCMP.

It is mainly the changes with respiration, described in the pathophysiology section, that can help in establishing the correct differential diagnosis between CP and RCMP.[11, 12] These include respiratory changes in the mitral E velocity (early diastolic left ventricular filling increases with expiration) and reciprocal changes in right-sided Doppler flows (Fig. 27.12).[13]

The respiratory variation in ventricular filling velocity in RCMP is usually minimal (less than 10%). On the other hand, patients with CP may have variations as high as 30–40%, and almost always at least 15% with clinically significant constriction. However, the ventricular filling velocity is highly influenced by preload; thus, when LAP is greatly elevated, respiratory variation in this parameter may not be seen in patients with CP. Reducing preload by head-up tilting may bring out the abnormality in such cases. Although some have suggested that respiratory variation can be assessed in patients with atrial fibrillation, the presence of highly variable RR-interval makes the diagnosis of CP difficult.[14]

Respiratory variation in mitral E velocity, like pulsus paradoxus, can also be present in patients with chronic obstructive pulmonary disease. In an attempt to distinguish between these disorders, the pulse-wave Doppler recordings of mitral and superior vena cava flow velocities can be of help. The patients with pulmonary disease have a marked increase in inspiratory superior vena cava systolic flow velocity

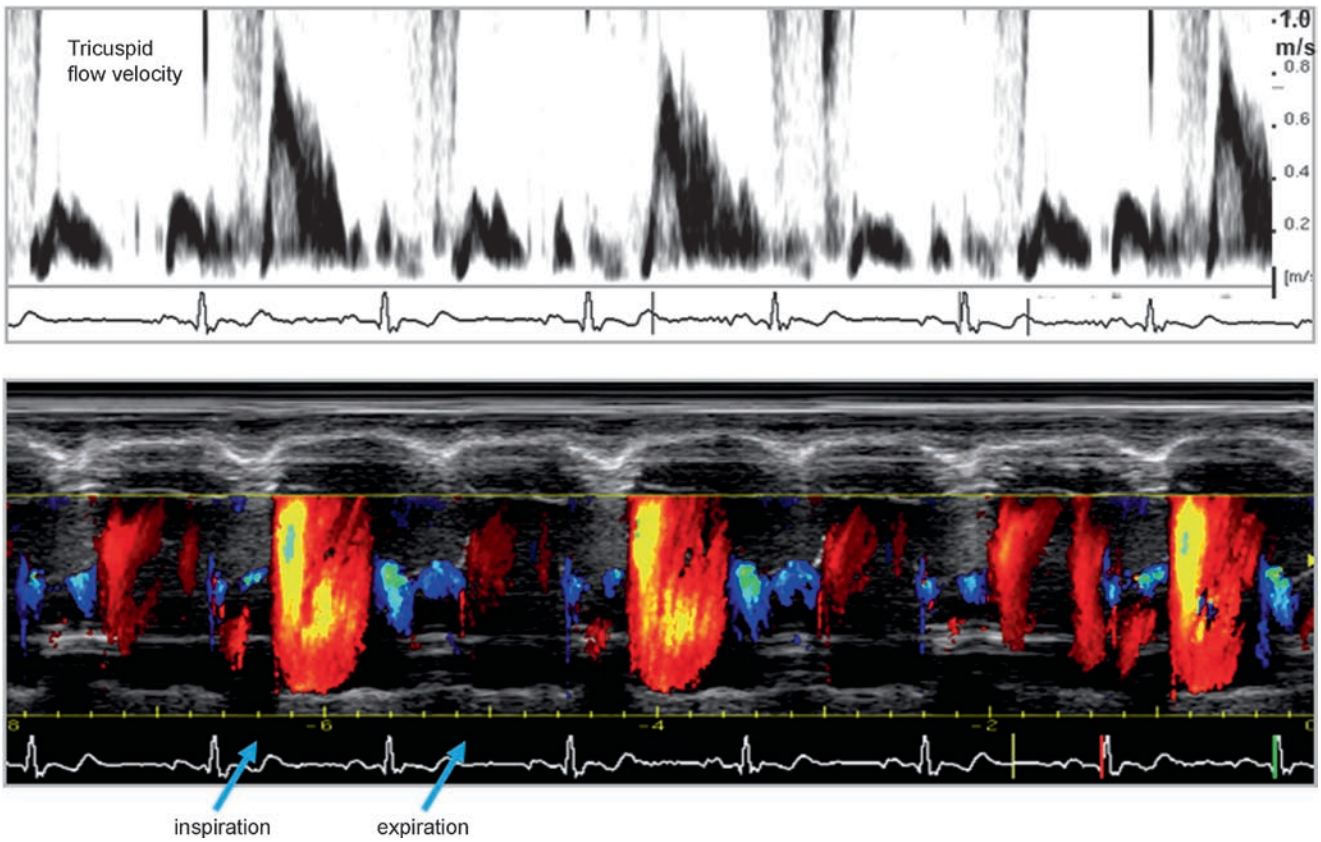

Fig. 27.11 Tricuspid Doppler flow and colour M-mode of the right ventricle in a patient with constrictive pericarditis. Flow in the right ventricle is very fast and limited to early diastole; also notice the large variation with respiration

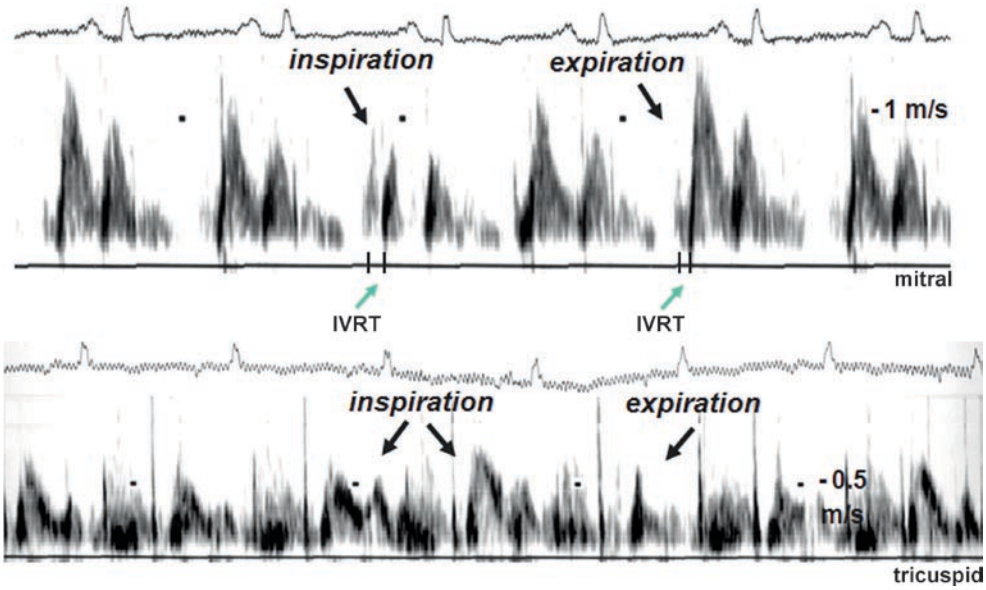

Fig. 27.12 The variation in mitral and tricuspid inflow with respiration in a patient with constrictive pericarditis. Not only peak velocities but also deceleration varies considerably: mitral DT 120–70–160–125 ms, tricuspid DT 140–180–100–140 ms

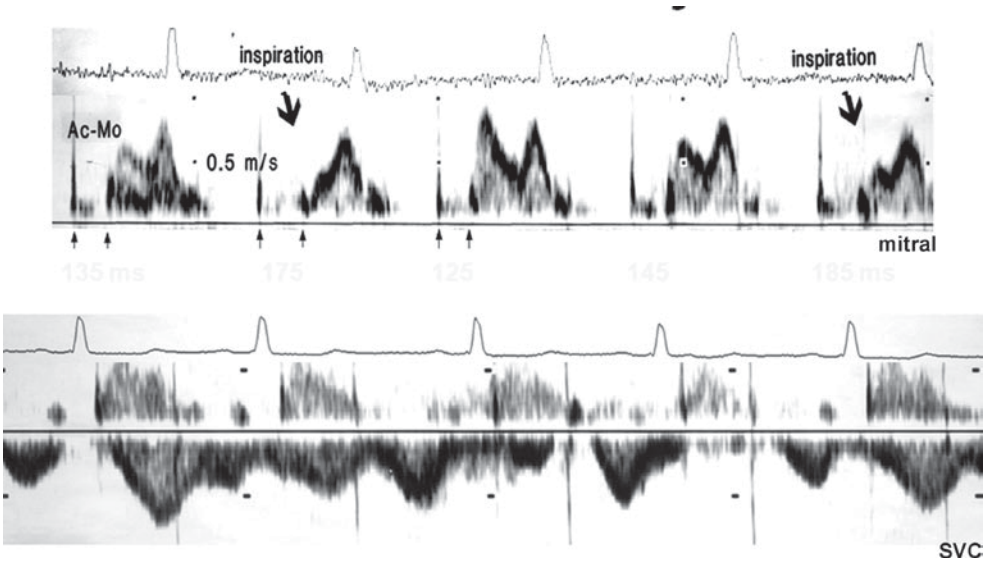

Fig. 27.13 A case of left ventricular hypertrophy and pulmonary obstructive disease: similar to constrictive pericarditis, a significant variation exists in mitral inflow velocities with respiration; in contrast to constriction (Fig. 27.14), the flow in the superior vena cava (SVC) also varies significantly with respiration

(Fig. 27.13), which is not seen to that extent in those with CP (Fig. 27.14).

There are both false positive and false negative results when examining the respiratory variation of the mitral flow velocity to differentiate CP from RCMP. Measurement of other parameters may be helpful:

- The hepatic venous flow may be of diagnostic utility. In patients with CP, there will be a reversal of forward flow during expiration (Fig. 27.14), since the right ventricle becomes less compliant as the left ventricle fills more.
- Atrial and ventricular diastolic compliance are determined by the pericardium in patients with CP. Furthermore, blood can transfer easily from atrium to ventricle because no change in total cardiac volume occurs. By contrast, the ventricles of patients with RCMP are much stiffer than the atria. The atria typically enlarge considerably and sometimes massively, and ultimately fail. Thus, late ventricular filling velocity is reduced in patients with RCMP, and diastolic flow reversals occur; in comparison, flow reversal in CP occurs either in systole or in both systole and diastole.[15]

Tissue Doppler Imaging

Pulsed-wave tissue Doppler imaging may help to distinguish between RCMP and CP by measuring the myocardial velocity gradient or strain, which is an index of myocardial

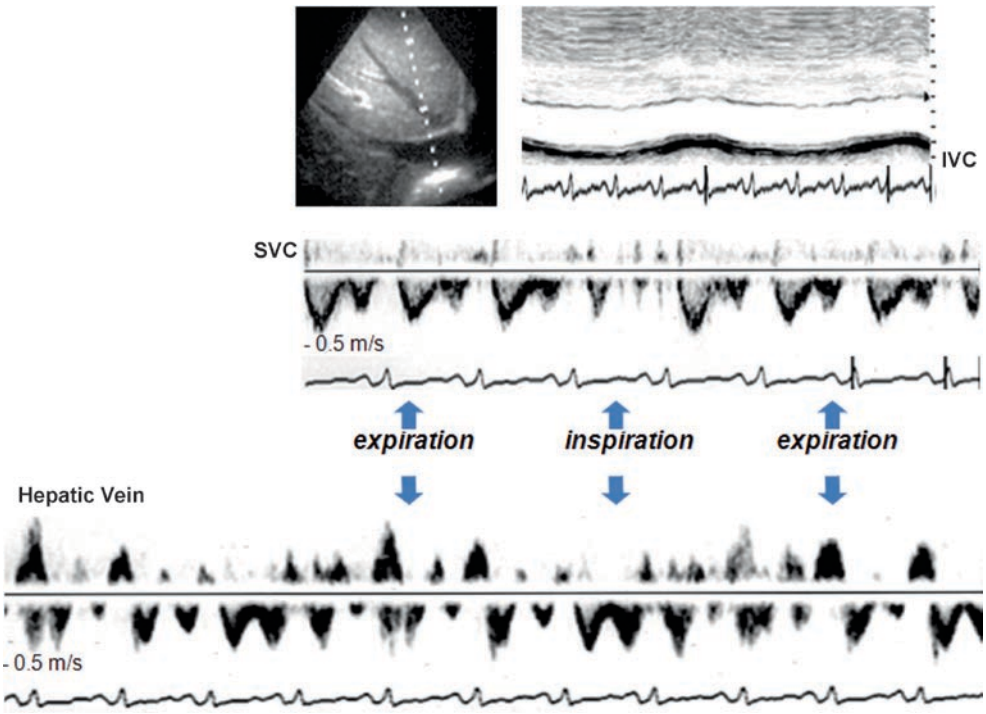

Fig. 27.14 Patient with constrictive pericarditis shows the absence of diameter variation (with respiration) of the inferior vena cava (IVC), the lack of significant variation in flow velocities of the superior vena cava (SVC), and the significant flow variation in the hepatic vein with reversal of flow during expiration

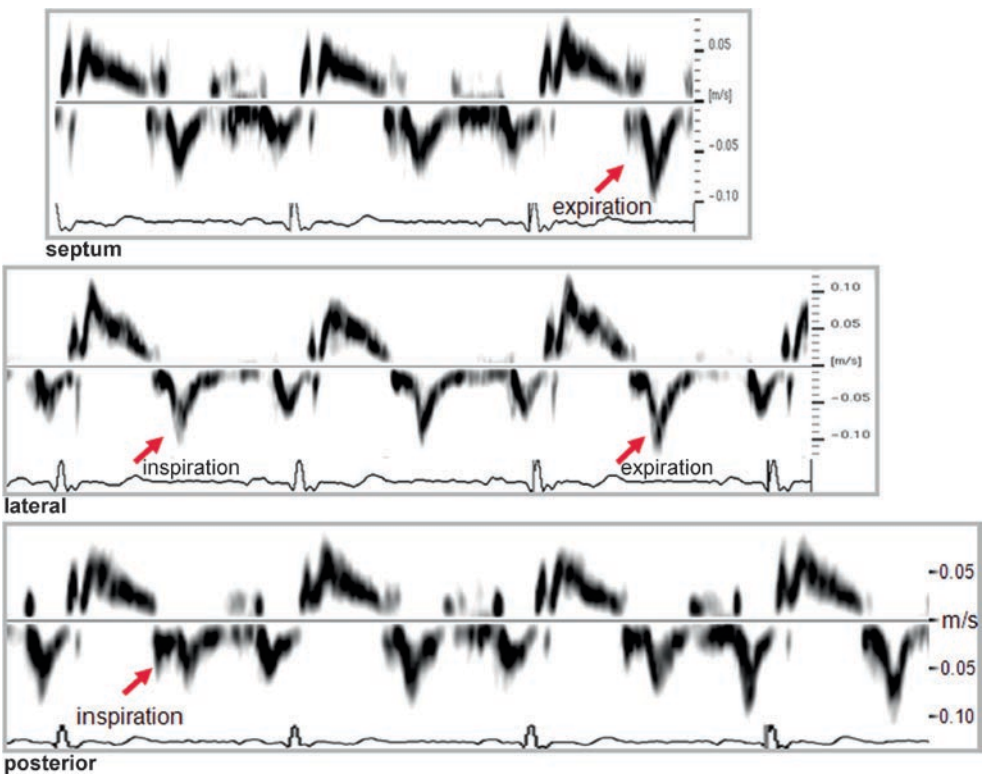

Fig. 27.15 Tissue Doppler traces in a patient with constrictive pericarditis showing normal systolic velocities; diastolic velocities are in the non-diagnostic range and vary with respiration

contraction and relaxation that quantifies the spatial distribution of intra-mural velocities across the myocardium.[16]

Doppler myocardial velocities (Fig. 27.15), as measured from the left ventricular posterior wall on the apical view in early diastole and during ventricular ejection, were significantly lower in patients with a RCMP compared to those with CP and to normal controls.[17]

The early diastolic Doppler tissue velocity at the mitral annulus (E') can also be helpful in diagnosis.[18] The transmitral E' is decreased in RCMP due to an intrinsic decrease in

myocardial contraction and relaxation, while the transmitral E' is increased in CP because the longitudinal movement of the myocardium is enhanced in compensation of the limited radial motion.[19, 20]

A high E' velocity (>12 cm/s) usually indicates CP, while a low E' velocity (<8 cm/s) usually indicates restrictive myocardial disease. However, a large number of patients fall in between these numbers, and diagnosis in them is still not clear (Fig. 27.15). Also the time difference between mitral inflow and E' can be helpful.[21]

Coronary Blood Flow

Patients with either CP or RCMP have reductions in coronary flow reserve and peak hyperaemic flow velocity compared to normal.[22] However, coronary flow in CP shows a rapid acceleration and more rapid deceleration (velocity half-time < ms or corrected by $\sqrt{RR} < 9.5$) of diastolic blood flow compared to RCMP. This variance may be based upon differences in the pathogenesis of these diseases, such as pericardial and epicardial vs. myocardial involvement.

CT

Computed tomographic (CT) scanning of the heart, obtained by rapid scanning gated to the cardiac cycle, is extremely useful in the diagnosis of CP.[23] Findings include increased pericardial thickness and calcification (Figs. 27.16 and 27.17). A normal appearance or non-visualization of the pericardium does not rule out the diagnosis.

Other findings include dilatation of the inferior vena cava, deformed ventricular contours, and angulation of the ventricular septum. CT imaging may also be used to examine the

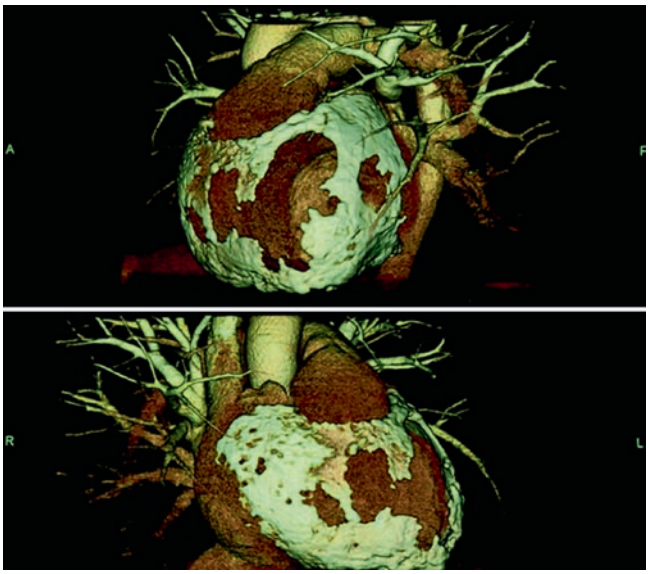

Fig. 27.17 Reconstruction of a cardiac CT scan with severe calcifications over the left and right ventricles

effect of cardiac motion transmitted to the surrounding pulmonary parenchyma. Failure of the immediately adjacent pulmonary structures to pulsate during the cardiac cycle, in the presence of a regionally or globally thickened pericardium, is virtually diagnostic of constrictive physiology.

Magnetic Resonance Imaging

Gated cardiac magnetic resonance imaging (CMR) provides direct visualization of the normal pericardium, which is composed of fibrous tissue and has a low MRI signal intensity (Fig. 27.18).[24] CMR can be seen as the diagnostic procedure of choice for the detection of certain pericardial diseases, including CP, since it can clearly visualize the morphologic

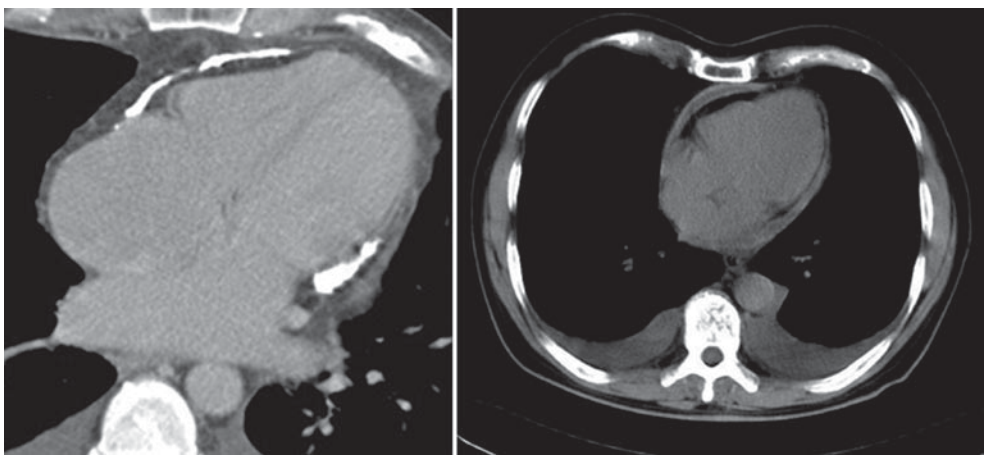

Fig. 27.16 Two CT scans of patients with constrictive pericarditis. On the left, several calcifications (high signal intensity) can be seen; on the right, the pericardium is severely thickened

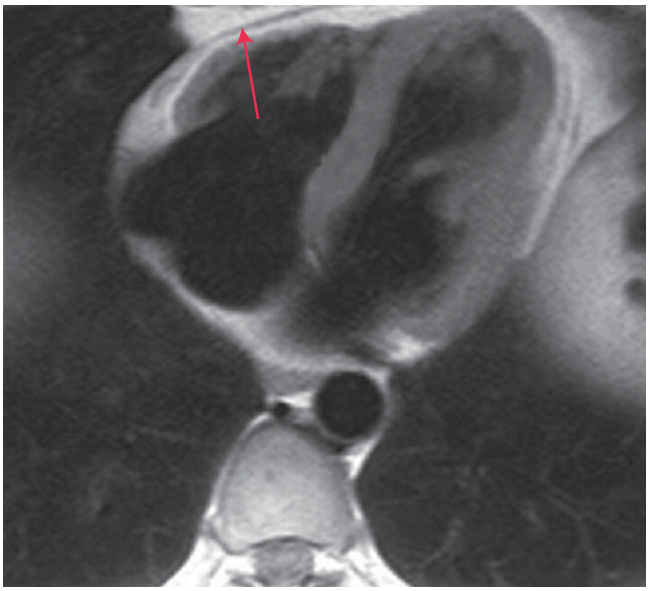

Fig. 27.18 Appearance of normal pericardium over the right ventricle on a CMR image. *Arrow* points at normal thickness pericardium

features of the disease as well as the functional and flow characteristics. Typical features include increased pericardial thickening (Figs. 27.19–27.21) and dilatation of the inferior vena cava. The occurrence of the septal bounce in PC can be nicely shown, as well as the dependence on the respiratory cycle (Fig. 27.22).[25]

Cardiac Catheterization

In some cases, particularly when there are multiple potential etiologies for heart failure, invasive cardiac catheterization is required to establish the diagnosis. Elevation and equalization of diastolic filling pressures occur in patients with CP. Although these haemodynamic findings may also occur in patients with other cardiac disorders, their presence is required for the diagnosis of constriction. Diastolic equalization may not be present in patients with constriction due to diuresis and a low volume state. In these patients, however, the cardiac output will be low. Therefore, the presence of normal cardiac output with normal filling pressures precludes the presence of haemodynamically significant constriction.

The dip and plateau configuration of ventricular pressure (also called the square root sign) during diastole corresponds to a rapid early filling, aided by augmented suction followed by a hampered further filling caused by rapidly increasing pressures. The dip and plateau is often grossly exaggerated by underdamping when recorded using a conventional fluid-filled catheter and external transducer.

Clinical Syndromes

Pericarditis

The diagnosis of pericarditis is clinical (history, cardiac auscultation) and by typical ECG changes. Chest X-ray is normal in most cases but can point to causative pulmonary abnormalities. The presence of pericardial fluid can be shown most easily by echocardiography, but epicardial and pericardial fat (which is not always proportional to subcutaneous fat) can be mistaken for fluid. Also, pericardial fluid is not synonymous to pericarditis; nor is the absence of fluid a criterion to exclude the disease. CMR and CT can nicely show fluid and can more easily make the distinction between fluid

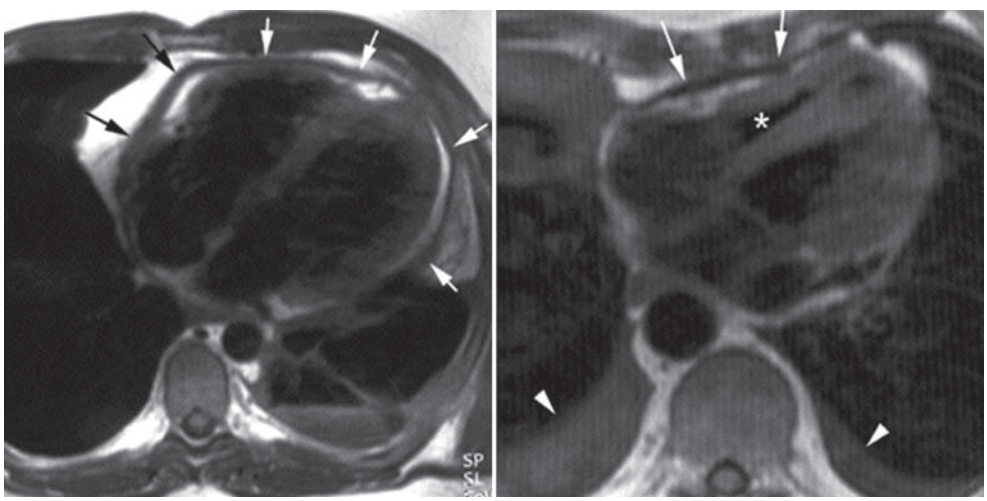

Fig. 27.19 Some typical features of constrictive pericarditis on CMR: thickening of the pericardium (low signal intensity), which is irregular (*black* = thickened, *white arrows* normal thickness on left image); narrowed, tubular shaped right ventricle (*asterisk* on right image); pleural effusion (*short arrow* on right image); and slightly thickened pericardium over right heart (*white arrow* on right image). High intensity signal around pericardium on left image is pericardial fat

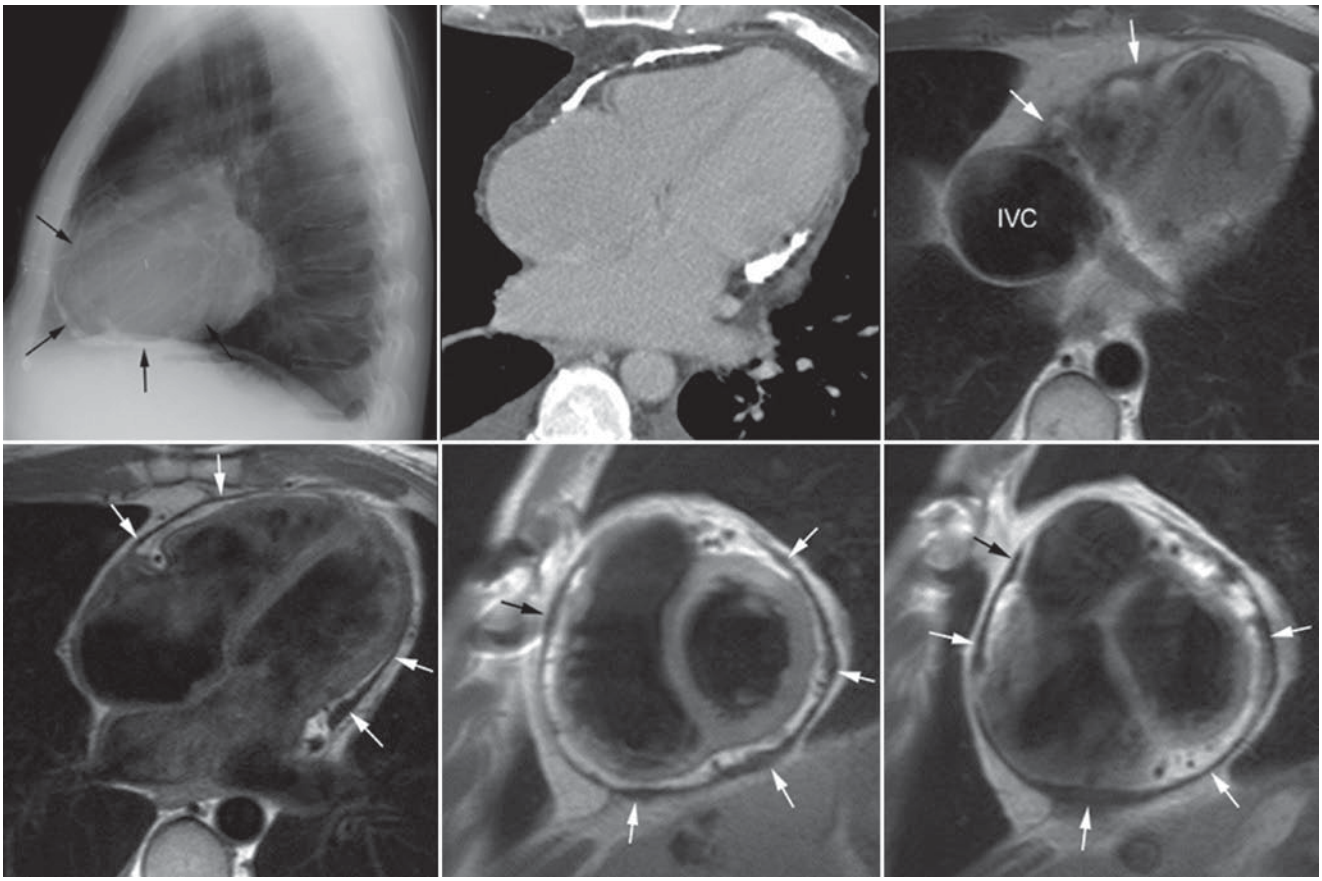

Fig. 27.20 Findings on chest X-ray, CT, and CMR of a patient with constrictive pericarditis and calcified pericardium. The low signal intensity, thickened pericardium on CMR corresponds to the calcified areas on CT (*top middle* and *top right* image). Note the pericardial fat with high signal intensity on the CMR images; *arrows* point at different areas of thickened percardium

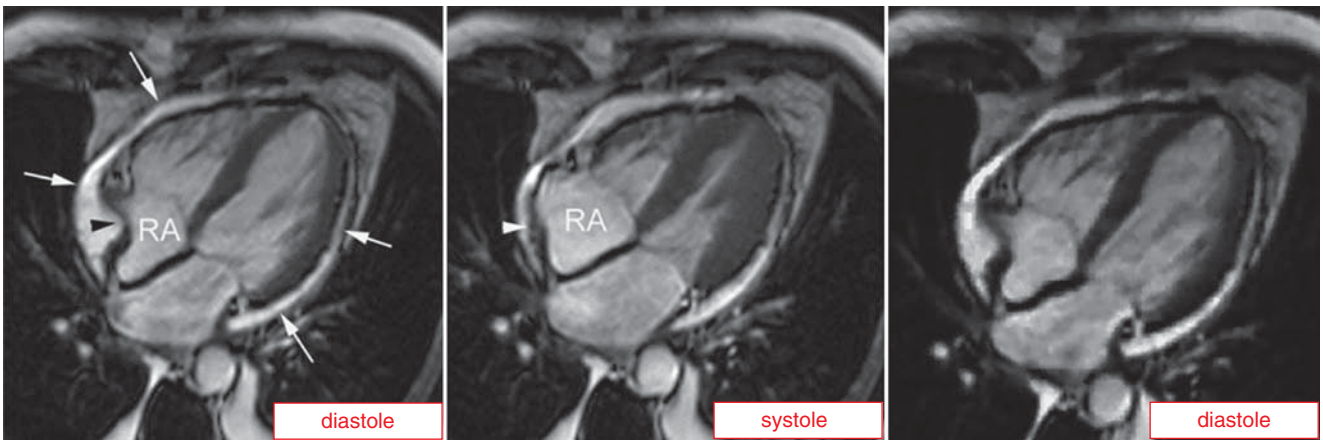

Fig. 27.21 Collapse of the right atrium at early diastole as illustrated with CMR left image: white arrows point at pericardial fluid; *black arrow* points at collapsed RA during diastole middle image: *white arrow* point at non-collapsed RA wall during systole

and fat. Increased signal of the pericardium after Gd administration on CMR is indicative of acute inflammation and can strengthen the diagnosis. Pericardial thickness (abnormal ≥4 mm) can be measured on echo, if extensive, but is more reliable on CT and CMR (the latter is to be preferred if a pericardial effusion coexists).

Pericardial Effusion and Tamponade

The presence of fluid in the pericardial sac is normal, and the effect on cardiac performance depends on the speed of accumulation: a rapid increase of 150–200 mL can cause symptoms, while a slow buildup of 2L can go unnoticed until

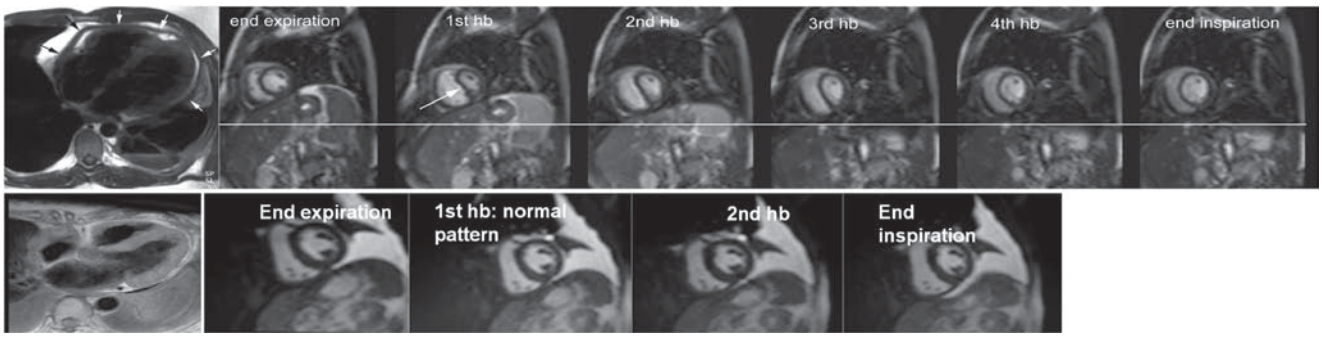

Fig. 27.22 Variation in septal shape with respiration as measured with real-time CMR imaging in a patient with constrictive pericarditis (*top*) and a patient with restrictive cardiomyopathy (*bottom*). Notice the significant inversion of septal shape with the onset of inspiration in CP, which disappears by end inspiration; no such shape change occurs in RCMP

non-cardiac structures (lung, bronchi, trachea) become compressed. It is, therefore, more important to evaluate the impact on function and the evolution over time, than the amount of fluid at one given instance. In the differential diagnosis between pericardial and pleural effusion, the "separation" of the descending aorta from the left atrium in the parasternal long-axis echo view (pericardial effusion) can be of help.

Pericardial fluid can be identified with most techniques, but it is important to report on the extent, location, and characteristics of the fluid (better with CMR; multiple sequences for fluid characterization) and to quantify the haemodynamic consequences.

Effusive Constrictive

The pericardial cavity is typically obliterated in patients with CP. Thus, even the normal amount of pericardial fluid is absent. However, pericardial effusion may be present in some cases (Fig. 27.23). In this setting, the scarred

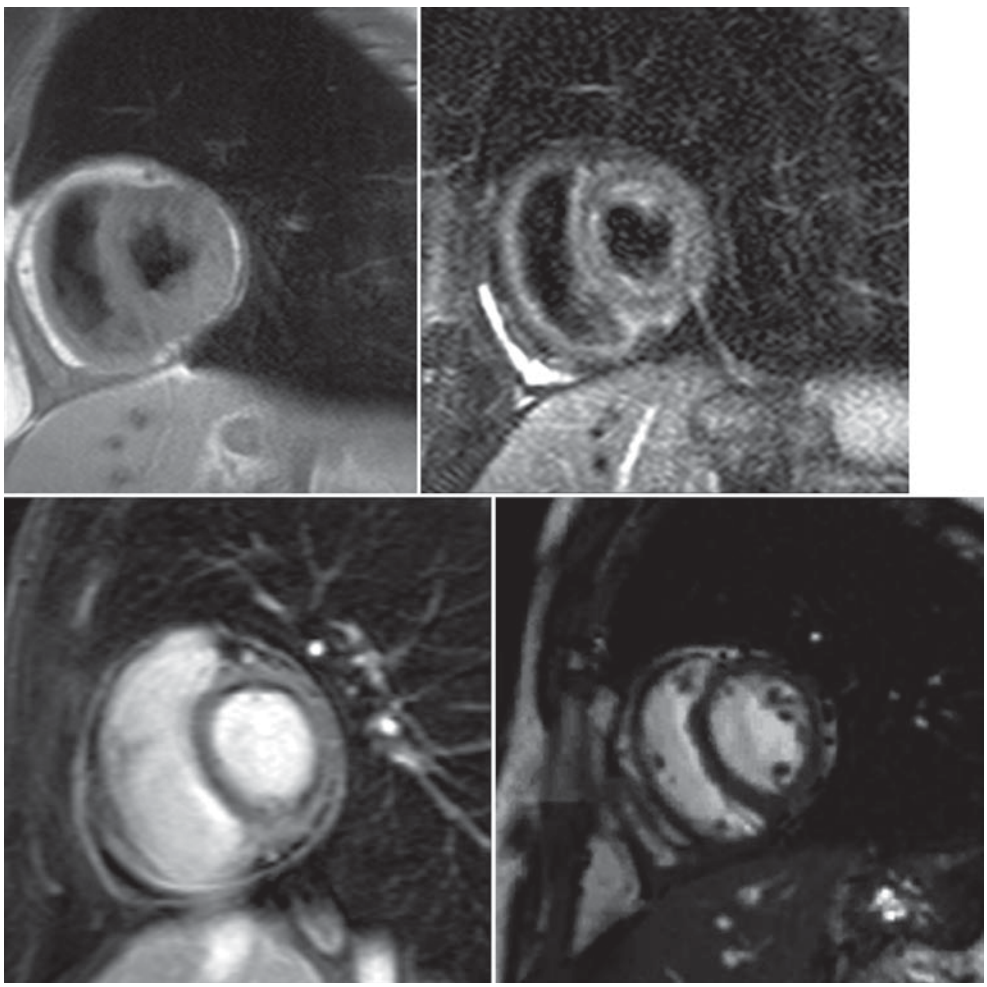

Fig. 27.23 The characteristics of effusive-constrictive pericarditis on black blood (*top left*), white blood (*bottom left*), T2 weighted (*top right*), and SSFP (*bottom right*) images: thickened pericardium, small pericardial effusion, slightly flattened inter-ventricular septum

pericardium not only constricts the cardiac volume, but can also put pericardial fluid under increased pressure, leading to signs suggestive of cardiac tamponade. This combination is called effusive CP.[26]

The diagnosis of effusive CP often becomes apparent during pericardiocentesis in patients initially considered to have uncomplicated cardiac tamponade. Unexpected persistence of the v wave of RAP is a clue to the possibility of effusive CP that may be present before pericardiocentesis. After pericardiocentesis, despite lowering of the pericardial pressure to near 0, persistence of elevated RAP suggests the presence of effusive constrictive disease. The diagnosis has been defined by the failure of the RAP to fall by 50% or to a level below 10 mmHg after pericardiocentesis.

Patients with effusive CP usually present with clinical features of pericardial effusion or CP or both.

A number of clinical clues suggest that a patient with manifestations of CP may actually have effusive CP.

- Pulsus paradoxus is often present; this finding is uncommon in classical CP because the inspiratory decline in intra-thoracic pressure is not transmitted to the right heart chambers
- A pericardial knock is absent
- The Y descent is less marked than expected
- Kussmaul's sign is frequently absent

Constrictive Pericarditis

Although thickening of the pericardium can be shown by CMR or CT, a normal thickness does not exclude CP due to increased stiffness without thickening. Showing the typical haemodynamic features of constriction is, therefore, important. Calcification of the pericardium is best seen on X-ray or CT, since on CMR calcium is visualized as hypo-intense regions, which can be mistaken for pericardial fluid or thickening only. A specific CMR application is the use of tagging, where non-invasive lines or a grid are inscribed on the heart: in non-CP (even with a thickened pericardium) the heart moves during the cardiac cycle independently from the pericardium, so the tags "break" at the pericardial interface, whereas in CP the tags cross the pericardium and remain uninterrupted from the myocardium to the pericardium during the cardiac cycle (Fig. 27.24).[27]

Haemodynamic Measurements

Both for tamponade and CP, these are most easily obtained by echocardiography because this real-time technique allows imaging during the different phases of the respiratory cycle; registration of the respiratory trace is important because differentiation between changes occurring on the first beat after onset of in- or expiration (CP) should be differentiated from changes after two or three beats (COPD, exaggerated respiratory motion). With the advent of real-time imaging and flow measurements on CMR, this technique can also be used. Visualization of the abnormal septal motion with CP is often easier in a true short-axis image and can be nicely visualized on CMR.

The characteristics of tamponade, CP, and restriction are graphically summarized in Figs. 27.1, 27.5, and 27.6. Each figure shows the flow curves on the right (hepatic veins, superior vena cava, if appropriate, and tricuspid) and on the left (pulmonary vein, mitral) during inspiration (left) and expiration (right), as well as some other haemodynamic characteristics (caval collapse, jugular vein, pericardial and intra-cavitary pressures).

In the differential diagnosis between CP and RCMP, nuclear studies and newer echo-Doppler parameters can also help: in CP, intrinsic systolic and early diastolic function are

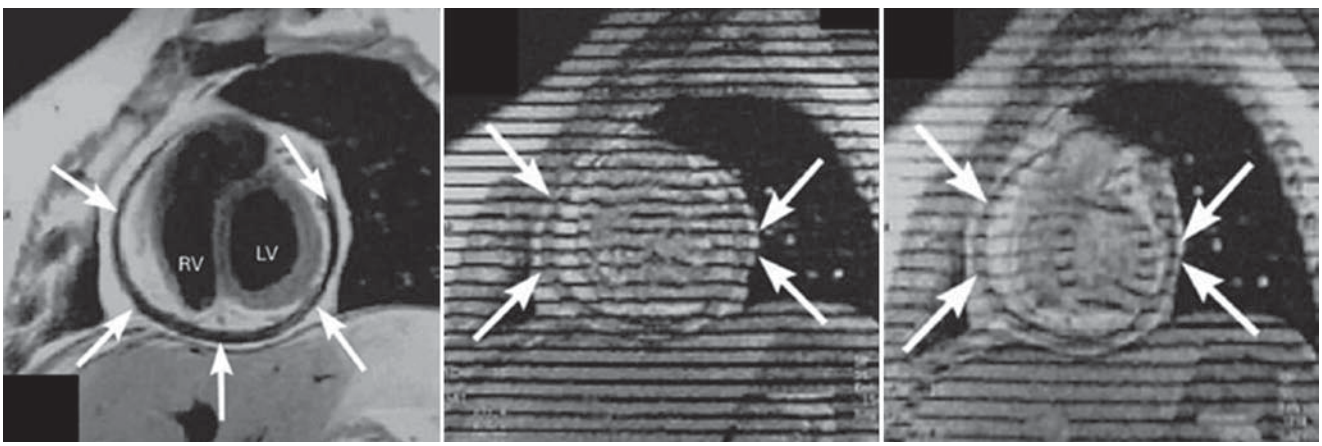

Fig. 27.24 CMR study of a patient with constrictive pericarditis. The *left* image arrows point at the thickened pericardium; the two images on the *right* are line-tagged images at end diastole (when tags are put down, *middle* image) (*arrows* point at uninterrupted tag lines at the level of the pericardium) and at end systole: the tag lines remain uninterrupted at the pericardium, showing the adhesion of the epi- and pericardial structures

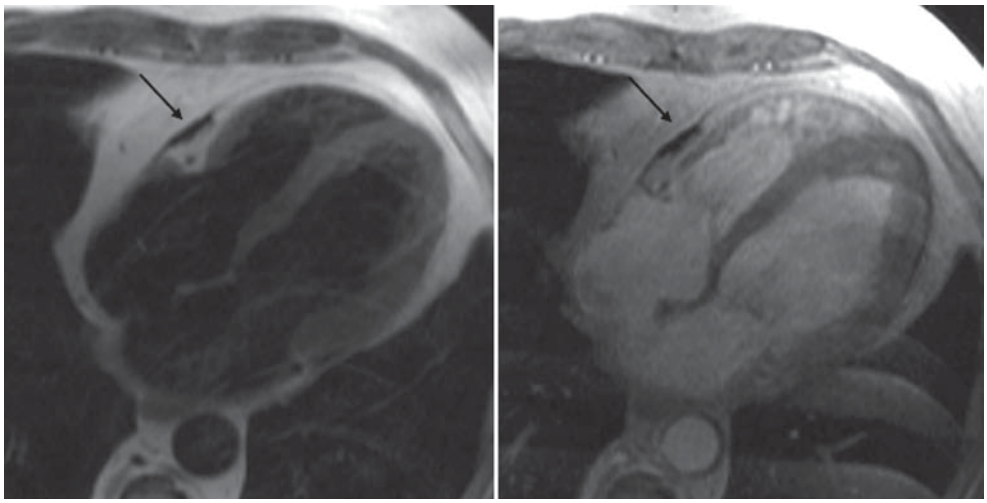

Fig. 27.25 Focal pericardial thickening (*arrow*) in a patient with clinical features of right-sided constriction (T1 weighted spin echo on the left, cine image on the right); notice the somewhat narrowed aspect of the right ventricle

normal (certainly early in the evolution of the disease), whereas in RCMP, intrinsic diastolic function is abnormal from the onset. Early filling velocity, as measured by nuclear techniques, is abnormal in RCMP but remains normal in PC. In a similar manner, long-axis shortening and lengthening, as measured by M-mode or TDI of the annulus, is normal in CP, except when the valve annulus has become attached to the pericardium. Also, colour Doppler intra-cavitary flow propagation as measured by colour-Doppler M-mode remains normal in CP, whereas it is depressed in RCMP.

Diagnostic problems remain in cases with atrial arrhythmia's (atrial fibrillation), a combination of COPD and LV myocardial restriction, and in the post-radiation patient, where constriction and restriction can coexist.

Regional Tamponade and Constriction

A regional fluid accumulation, pericardial adhesion, or a combination (effusive constrictive) can be very difficult to diagnose with haemodynamic features limited to the underlying cavity rather than the entire heart and often occurring over the right ventricle (tubular-shaped). CMR is generally the best way to identify the localized thickening (Fig. 27.25) and adhesion (tagging).

Summary

Differential diagnosis in pericardial disease remains difficult and challenging to the clinician. When a discrepancy exists between clinical findings and haemodynamic evaluation with imaging, multiple modalities should be combined and, if a very low or very high atrial pressure is suspected, an intervention to increase or lower this pressure can be required to unmask characteristic findings during respiration and with respect to ventricular interdependence.

References

1. Maisch B, Seferovic PM, Ristic AD, et al Guidelines on the diagnosis and management of pericardial diseases executive summary; The Task force on the diagnosis and management of pericardial diseases of the European society of cardiology. *Eur Heart J*. 2004;25:587
2. Hancock EW. Differential diagnosis of restrictive cardiomyopathy and constrictive pericarditis. *Heart*. 2001;86(suppl 3):343–349
3. Goldstein JA. Cardiac tamponade, constrictive pericarditis, and restrictive cardiomyopathy. *Curr Probl Cardiol*. 2004;29(suppl 9):503–567
4. Shabetai R. *The Pericardium*. Norwell, MA: Kluwer; 2003:227
5. Lavine SJ. Genesis of the restrictive filling pattern: pericardial constraint or myocardial restraint. *J Am Soc Echocardiogr*. 2004;17(suppl 2):152–160
6. Boonyaratavej S, Oh JK, Tajik AJ, et al Comparison of mitral inflow and superior vena cava Doppler velocities in chronic obstructive pulmonary disease and constrictive pericarditis. *J Am Coll Cardiol*. 1998;32:2043
7. Babuin L, Alegria JR, Oh JK, et al Brain natriuretic peptide levels in constrictive pericarditis and restrictive cardiomyopathy. *J Am Coll Cardiol*. 2006;47:1489
8. Ling LH, Oh JK, Tei C, et al Pericardial thickness measured with transesophageal echocardiography: feasibility and potential clinical usefulness. *J Am Coll Cardiol*. 1997;29:1317
9. Abdalla IA, Murray RD, Lee JC, White RD, Thomas JD, Klein AL. Does rapid volume loading during transesophageal echocardiography differentiate constrictive pericarditis from restrictive cardiomyopathy? *Echocardiography*. 2002;19(suppl 2):125–134
10. Talreja DR, Edwards WD, Danielson GK, et al Constrictive pericarditis in 26 patients with histologically normal pericardial thickness. *Circulation*. 2003;108:1852
11. Hatle LK, Appleton CP, Popp RL. Differentiation of constrictive pericarditis and restrictive cardiomyopathy by Doppler echocardiography. *Circulation*. 1989;79:357

12. Hurrell DG, Nishimura RA, Higano ST, et al Value of dynamic respiratory changes in left and right ventricular pressures for the diagnosis of constrictive pericarditis. *Circulation*. 1996;93:2007
13. Oh JK, Hatle LK, Seward JB, et al Diagnostic role of Doppler echocardiography in constrictive pericarditis. *J Am Coll Cardiol*. 1994;23:154
14. Tabata T, Kabbani SS, Murray RD, et al Difference in the respiratory variation between pulmonary venous and mitral inflow Doppler velocities in patients with constrictive pericarditis with and without atrial fibrillation. *J Am Coll Cardiol*. 2001;37:1936
15. Klein AL, Cohen GI, Pietrolungo JF, et al Differentiation of constrictive pericarditis from restrictive cardiomyopathy by Doppler transesophageal echocardiographic measurements of respiratory variations in pulmonary venous flow. *J Am Coll Cardiol*. 1993;22(suppl 7):1935–1943
16. McCall R, Stoodley PW, Richards DA, Thomas L. Restrictive cardiomyopathy versus constrictive pericarditis: making the distinction using tissue Doppler imaging. *Eur J Echocardiogr*. 2008;9(suppl 4):591–594
17. Palka P, Lange A, Donnelly JE, Nihoyannopoulos P. Differentiation between restrictive cardiomyopathy and constrictive pericarditis by early diastolic doppler myocardial velocity gradient at the posterior wall. *Circulation*. 2000;102:655
18. Ha JW, Oh JK, Ling LH, et al Annulus paradoxus: transmitral flow velocity to mitral annular velocity ratio is inversely proportional to pulmonary capillary wedge pressure in patients with constrictive pericarditis. *Circulation*. 2001;104:976
19. Ha JW, Ommen SR, Tajik AJ, et al Differentiation of constrictive pericarditis from restrictive cardiomyopathy using mitral annular velocity by tissue Doppler echocardiography. *Am J Cardiol*. 2004; 94(suppl 3):316–319
20. Garcia MJ, Rodriguez L, Ares M, Griffin BP, Thomas JD, Klein AL. Differentiation of constrictive pericarditis from restrictive cardiomyopathy: assessment of left ventricular diastolic velocities in longitudinal axis by Doppler tissue imaging. *J Am Coll Cardiol*. 1996;27(suppl 1):108–114
21. Choi EY, Ha JW, Kim JM, et al Incremental value of combining systolic mitral annular velocity and time difference between mitral inflow and diastolic mitral annular velocity to early diastolic annular velocity for differentiating constrictive pericarditis from restrictive cardiomyopathy. *J Am Soc Echocardiogr*. 2007;20(suppl 6): 738–743
22. Akasaka T, Yoshida K, Yamamuro A, et al Phasic coronary flow characteristics in patients with constrictive pericarditis: comparison with restrictive cardiomyopathy. *Circulation*. 1997;96:1874
23. Isner JM, Carter BL, Bankoff MS, et al Differentiation of constrictive pericarditis from restrictive cardiomyopathy by computed tomographic imaging. *Am Heart J*. 1983;105(suppl 6):1019–1025
24. Sechtem U, Tscholakoff D, Higgins CB. MRI of the normal pericardium. *AJR Am J Roentgenol*. 1986;147:239
25. Francone M, Dymarkowski S, Kalantzi M, et al Assessment of ventricular coupling with real-time cine MRI and its value to differentiate constrictive pericarditis from restrictive cardiomyopathy. *Eur Radiol*. 2006;16:944
26. Haley JH, Tajik AJ, Danielson GK, Schaff HV. Transient constrictive pericarditis: causes and natural history. *J Am Coll Cardiol*. 2004;43:271
27. Kojima S, Yamada N, Goto Y. Diagnosis of constrictive pericarditis by tagged cine magnetic resonance imaging. *N Engl J Med*. 1999;341:373

Chapter 28

MYOCARDITIS

Heiko Mahrholdt, Ali Yilmaz, and Udo Sechtem

CONTENTS

J. L. Zamorano et al. (eds.), *The ESC Textbook of Cardiovascular Imaging*
DOI: 10.1007/978-1-84882-421-8_28, © Springer-Verlag London Limited 2010

Introduction

The symptoms and signs of myocarditis are non-specific. Thus, myocarditis is a differential diagnosis in many patients with heart complaints. As myocarditis may accompany common viral infections of the upper respiratory and gastrointestinal tracts and mild ECG changes are not uncommon in such patients, the diagnosis needs to be considered in large patient cohorts. Establishing the correct diagnosis is of importance as the disease may lead to sudden cardiac death or dilated cardiomyopathy.

Clinical tools such as history taking, physical examination, blood tests, ECG, and chest X-ray are not sufficient to ascertain the diagnosis of myocarditis;[1] additional information from cardiac imaging techniques or endomyocardial biopsy are necessary to confirm or exclude the disease. In daily clinical routine, however, the use of biopsy is limited to severely ill patients with reduced left ventricular function due to its invasiveness and potential complications. Thus, this chapter reviews how non-invasive cardiac imaging techniques can be used in clinical practice to diagnose myocarditis.

Imaging Modalities Other Than Cardiovascular Magnetic Resonance Imaging

Echocardiography

Echocardiography still represents the first-choice imaging modality in patients with a clinical suspicion of myocarditis because it offers the acquisition of comprehensive anatomic and functional data very quickly at the bedside of the patient. Especially in haemodynamically unstable patients in whom clinical state precludes the application of other, potentially more accurate, imaging modalities such as cardiac magnetic resonance imaging, echocardiography is the most helpful imaging tool.

Recent developments have broadened the armamentarium of echocardiographic methods: apart from traditional M-mode and 2D echocardiography, new techniques such as tissue Doppler, strain-rate imaging, or contrast-enhanced echocardiography have become available for evaluation of patients with clinical symptoms suggestive of myocarditis. However, the value of these new echocardiographic imaging techniques in patients with myocarditis is yet unknown because data in larger patient groups are not available. Using M-mode and 2D echocardiography in patients with histologically proven myocarditis, a multitude of different echocardiographic patterns comprising dilated, hypertrophic, restrictive, or even ischaemic cardiomyopathy can be detected, but these echocardiographic features are non-specific in comparison to biopsy results.[2]

However, echocardiography may help to differentiate between fulminant and non-fulminant acute myocarditis. While fulminant myocarditis is characterized by a rapid onset of illness with severe haemodynamic compromise, nonfulminant acute myocarditis is believed to have a less distinct presentation with less severe haemodynamic compromise, but with a greater likelihood to progress to dilated cardiomyopathy. Using echocardiography, normal left ventricular diastolic diameters combined with an increased thickness of the inter-ventricular septum (Fig. 28.1) and/or an impaired right ventricular systolic function at initial presentation are more suggestive of fulminant myocarditis.[3] Those patients who initially suffer from fulminant myocarditis with severe impairment of cardiac function are more likely to recover quickly, while those patients presenting with non-fulminant myocarditis are more prone to develop progressive cardiac dysfunction.

Myocardial Scintigraphy

Two scintigraphic methods, gallium-67 scintigraphy and indium-111 radiolabelled antimyosin imaging (Fig. 28.2), have been used in the past for diagnosis and evaluation of prognosis in patients with clinical suspicion of myocarditis. These techniques have a high sensitivity,[5, 6] but data are only available from patients with severely impaired left ventricular (LV) function (indicating severe forms of myocarditis), and the gold standard against which the sensitivity of the techniques was evaluated was endomyocardial biopsy without immune histology, which itself suffers from a low sensitivity.[1] Gallium-67 is a non-specific marker of inflammation. Gallium imaging should be performed 72 h after the injection of the tracer to avoid false positive results from remaining gallium circulating in the blood. In clinical practice, due to this disadvantage, gallium scintigraphy is rarely used today.

The disease process of myocarditis is histologically characterized by myocardial inflammation with accumulation of immune cells leading to myocardial damage with necrosis of cardiomyocytes. Since necrotic cardiomyocytes lose the integrity of their cell membranes, intracellular proteins such as myosin are exposed to the extra-cellular space. Indium-111-labelled antimyosin is able to localize and visualize those myocardial areas. In practice, antimyosin antibodies are coupled with indium-111 and administered intravenously. Scintigraphic imaging (single photon emission computed tomography, SPECT) is performed 48 h after intravenous

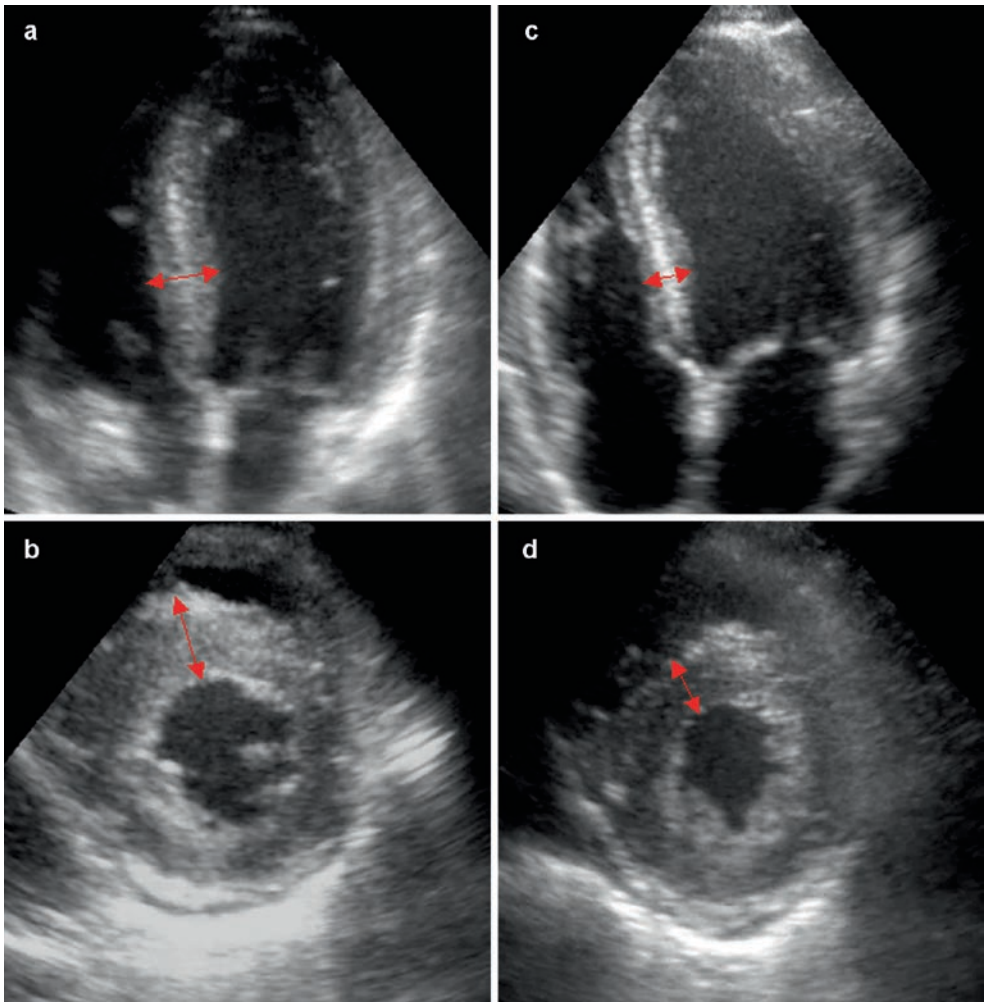

Fig. 28.1 2D echocardiographic images of a patient presenting with fulminant myocarditis. An increased thickness of the inter-ventricular septum is seen at acute onset in the long- **(a)** and short-axis **(b)** views. Five days after presentation, the thickness of the septum has already decreased **(c, d)**

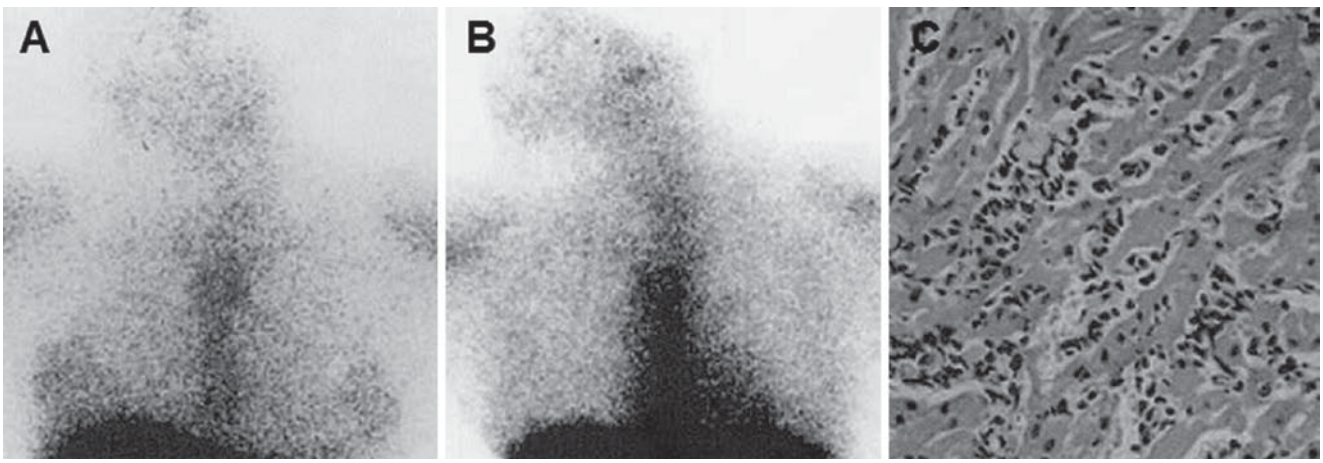

Fig. 28.2 Antimyosin scan of a healthy patient with normal findings **(a)**. Significant myocardial antimyosin uptake in a patient with myocarditis **(b)** with the corresponding right ventricular endomyocardial biopsy **(c)** demonstrating lymphomononuclear cell infiltrate diagnostic of myocarditis. Reprinted by permission of the Society of Nuclear Medicine from Martin et al.[4], Fig. 1

administration of the radionuclide. Qualitative or (semi-) quantitative analysis of the scans is then performed. The semi-quantitative calculation of the heart-to-lung ratio may be used to objectively assess the extent of antimyosin-coupled indium-111-labelled radionuclide accumulation in the myocardium. Although a cut-off heart-to-lung ratio <1.6 has

been suggested to be normal, such a cut-off value needs to be established individually in each centre by studying a healthy control group.

The strength of scintigraphy in the work-up of myocarditis is based on many studies, suggesting that a positive biopsy result (indicative of myocarditis) is almost always associated with a positive scintigraphic result, while a negative scintigraphic result excludes a biopsy-based diagnosis of myocarditis with a high degree of reliability. However, the specificity (31–44%) and the positive predictive value (28–33%) of indium-111 scintigraphy are quite low.[5] In consideration of this limited specificity, the radiation burden, and the practical difficulties of myocardial scintigraphy, the use of scintigraphic techniques has declined over the past years.

Multi-detector-Computed Tomography

The diagnostic capacity of multi-detector-computed tomography (MDCT) has tremendously increased with recent technological advancements. MDCT-based coronary angiography is becoming increasingly popular for non-invasive evaluation of coronary artery disease comprising the assessment of coronary diameters, plaque calcification, and vessel wall pathology. Hence, MDCT coronary angiography is increasingly used in low- and intermediate-risk patients presenting with chest pain suggestive of coronary artery disease. As myocarditis may be a differential diagnosis in these patients, tissue information from MDCT images would be helpful not only to rule out coronary disease, but to also establish the diagnosis of myocarditis.

Preliminary investigations suggest that contrast-enhanced MDCT may be helpful for myocardial tissue characterization. Such delayed enhancement (DE)-MDCT images are acquired 5–10 min after contrast injection with a lower tube current and voltage compared to MDCT coronary angiography in order to reduce radiation dose and perhaps also increase signal-to-noise. In a similar way as in DE-CMR, myocardial damage in myocardial infarction presents as subendocardial or trans-mural contrast enhancement.[7]

The combination of MDCT coronary angiography and DE-MDCT can be used to differentiate ischaemic from non-ischaemic cardiomyopathy (Fig. 28.3): ischaemic myocardial damage is characterized by subendocardial or transmural DE, while non-ischaemic forms are characterized by epicardial or intra-mural patterns of DE.[7] Preliminary data suggest that diagnostic agreement of MDCT with contrast-enhanced cardiovascular magnetic resonance (CMR) is excellent.[7] In acute myocarditis, DE-MDCT is also able to detect patterns of damage in the epicardial portion of the left ventricular myocardium similar to contrast-enhanced CMR.[8]

A combined procedure of MDCT coronary angiography and DE-MDCT could become attractive for the diagnosis of acute myocarditis in the emergency department, since it allows the acquisition of comprehensive data in a single study within 15 min. However, the clinical use of such a combined procedure is limited due to the radiation burden (up to 20 mSv with ~30% from DE-MDCT) with the high risk of radiation-induced cancer, especially in the young patients who present with myocarditis. The lower image quality as compared to LGE-CMR may also result in a lower sensitivity of detecting very small areas of myocardial damage.

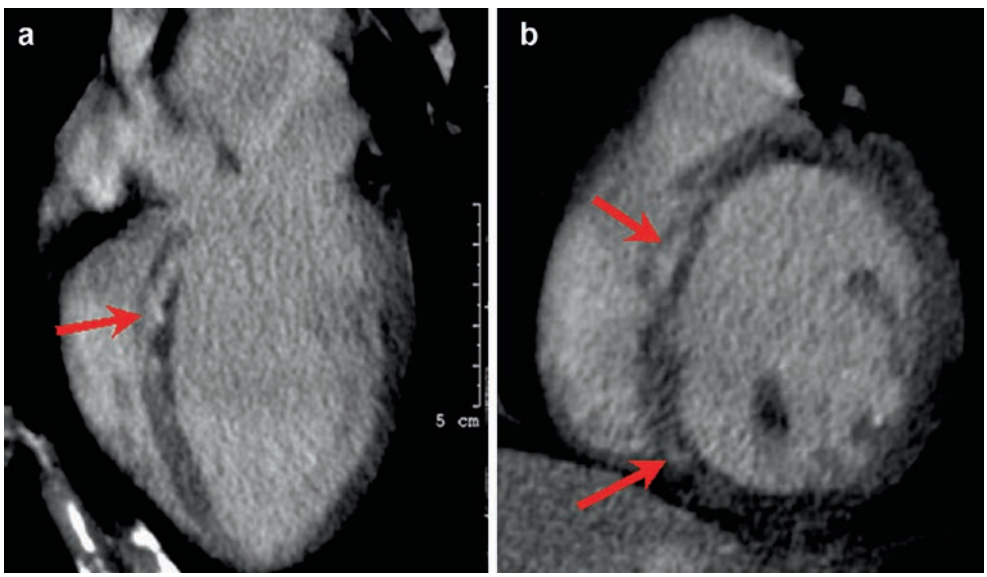

Fig. 28.3 Delayed-enhancement (DE) multi-detector-computed tomography in patient with myocarditis demonstrating intra-mural DE in the septal wall in a long- **(a)** and short-axis **(b)** view. Kindly provided by le Polain de Waroux et al.[7]

Cardiovascular Magnetic Resonance Imaging

Due to its non-invasiveness, the lack of radiation exposure, its image quality, which helps in assessing and quantifying cardiac function, and its high tissue contrast, which can be modified using various pulse sequences, CMR has become an important technique for evaluating patients with suspected myocarditis. In many institutions, CMR is now routinely applied clinically in such patients and many reports confirmed the feasibility and diagnostic accuracy of CMR protocols.

Anatomic and Functional Abnormalities

CMR has few advantages as compared to echocardiography for depicting anatomic and functional abnormalities in patients with suspected myocarditis. However, in patients with a suboptimal ultrasound window, in those in whom a 3D visualization of the ventricles is needed to detect subtle abnormalities of regional anatomy and function, and in those in whom details of the right ventricle are of interest, CMR should be employed.

Similar to echocardiography, CMR detects an increase in myocardial mass in patients with fulminant myocarditis and is able to document normalization of mass with disappearance of myocardial oedema. CMR is more sensitive than echocardiography in depicting small and often localized pericardial effusions that may be found adjacent to the myocardial region mostly affected by myocardial inflammation. The presence of pericardial effusion in a patient suspected to have myocarditis supports ongoing active inflammation.

Tissue Characterization

The following three tissue features potentially associated with acute myocardial inflammation may be visualized by CMR:

1. Hyperaemia seems to be the cause of an increased signal on T1-weighted spin-echo images following gadolinium administration (elevated global relative enhancement (GRE))
2. Tissue oedema, which may result in an elevated T2 signal
3. Myocardial necrosis or scarring, as indicated by the presence of late gadolinium enhancement (LGE)

Hyperaemia CMR (Early Myocardial Gadolinium Enhancement Ratio)

The myocardium in patients with the clinical manifestations of acute myocarditis shows hyper-enhancement relative to skeletal muscle on T1-weighted contrast-enhanced images in the early wash-out period (Fig. 28.4).[9] Scanning is started immediately following the first pass of contrast media, such as gadolinium diethylenetriamine pentaacetic acid (Gd-DTPA), using a standard fast spin-echo pulse sequence with sufficient T1 weighting, and is completed at 5 min after the injection.[10]

The mechanism of signal increase may be related to tissue hyperaemia because vasodilatation is a typical feature of inflamed tissue. Tissue hyperaemia may lead to faster distribution of contrast medium into the interstitial space. However, it is also conceivable that the increased T1 signal is caused by the same mechanism of tissue destruction, which explains the LGE effect. Whatever the exact cause, an increased T1 signal can be observed during the first minutes after injection of the contrast agent. It is usually difficult to appreciate the

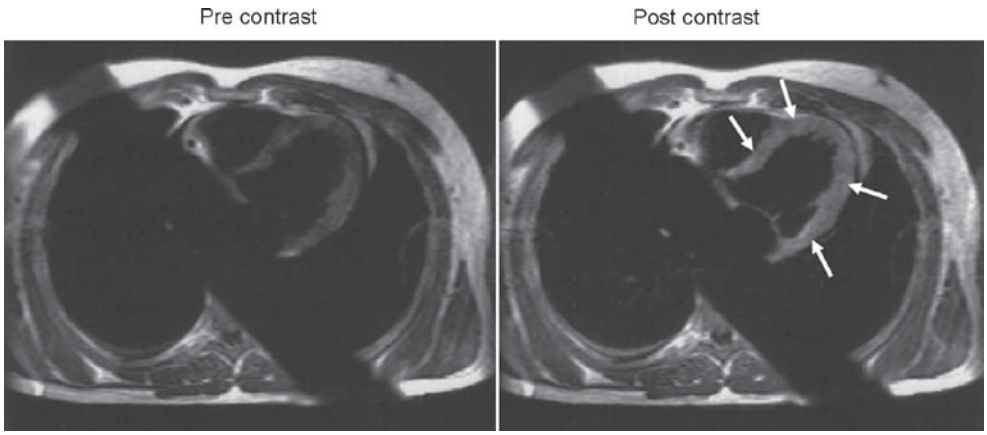

Fig. 28.4 T1-weighted cross-sectional views at the mid-ventricular level of a patient with myocarditis. The *left panel* displays a view obtained before gadopentate dimeglumine (Gd-DTPA). The *right panel* depicts the same view after the administration of 0.1 mmole/kg Gd-DTPA. Note diffuse signal enhancement in the left ventricle. Reprinted with permission from Friedrich et al.[9]

Table 28.1. Sensitivity and specificity of global relative enhancement (T1 spin-echo) in myocarditis

Sensitivity	*n*	Sensitivity (%)	Specificity	*n*	Specificity (%)
Friedrich et al.[9]	19	84[a]	Friedrich et al.[1]	34	90[a]
Abdel-Aty et al.[11]	25	80[a]	Abdel-Aty et al.[7]	23	74[a]
Laissy et al.[12]	20	85[a]			
Laissy et al.[13]	24	100[a]	Laissy et al.[13]	7	100[a]
Gutberlet et al.[14]	48	63[b]	Gutberlet et al.[14]	35	86[b]
Total	136	79		99	86

[a]Sensitivity and specificity to detect inflammation as defined by clinical picture
[b]Sensitivity and specificity to detect inflammation as defined by immunohistochemistry

diffuse rise in signal intensity on these images, and, thus, quantification of signal changes is necessary. As spin-echo imaging often yields low contrast between inflamed and normal myocardium and suffers from image artefacts, it turned out to be advantageous to relate the signal increase in the myocardium to that observed in neighbouring skeletal muscle.[9] Thus, relative enhancement depends on the assumption that skeletal muscle is normal, which may be erroneous if the inflammation also involves skeletal muscles. Although early gadolinium enhancement ratio suffers from several artefacts, several studies confirm the diagnostic usefulness of this parameter (Table 28.1). Nevertheless, this pulse sequence is only used in a few centres around the world.

Oedema Imaging by CMR

Acutely inflamed tissue shows an increase in water content due to oedema formation. Isolated oedema usually indicates reversible myocardial injury. However, oedema also accompanies necrosis as shown in myocardial infarction. Once myocarditis has healed, oedema should disappear.

T2-weighted CMR[10] today is usually performed by short inversion time recovery (STIR) pulse sequences. These pulse sequences are sensitive to the long T2 of water protons to generate images with a higher signal intensity of oedematous myocardial tissue as compared to non-inflamed muscle tissue in the vicinity. Depending on the distribution of oedema within the left ventricular myocardium, there may be visible regional signal differences within an image. Regions with a signal intensity of more than two standard deviations above the mean of normal appearing myocardial tissue within the same slice are regarded as indicative of regional oedema. One has to be careful not to look at too small regions as signal inhomogeneity on T2 images in normals may be considerable. However, due to the often diffuse nature, especially in less aggressive inflammation, quantitative analysis of the signal of the entire slice of myocardium may have advantages as compared to visual analysis. Signal intensity of the myocardium is normalized to that of nearby skeletal muscle, and ratios of 1.9 or higher are regarded as indicative of oedema. However, this cut-off ratio is based on small-sized studies and every centre is advised to establish its own cut-off value.

An obvious drawback of this type of analysis is the dependence on the absence of inflammation in the skeletal muscle, which is not uncommon in systemic viral illness. Another shortcoming of T2-weighted CMR is that in patients with arrhythmias or motion artefacts from breathing image, quality may not allow reliable visualization or quantification of oedema. Moreover, in studies looking at the diagnostic value of T2 oedema imaging, it is usually not specifically mentioned how the diagnosis was made (visually or by quantification or by both methods). The results of several studies are shown in Table 28.2.

Necrosis and Fibrosis Imaging by CMR (Late Gadolinium Enhancement)

The more severe forms of myocarditis may result in tissue necrosis, which is often focal in nature, just as the disease itself. New contrast-enhanced CMR techniques employing inversion pulses to null the signal of normal myocardium were initially developed for infarct imaging (Fig. 28.5). However, they also show necrotic or fibrotic myocardium in patients with myocarditis as bright areas and provide high contrast between diseased and normal myocardium. Imaging is performed at about 5–10 min after contrast injection (LGE). The mechanism by which contrast enhancement can be explained is as follows. When serious membrane damage has occurred in early necrosis, gadolinium molecules enter the intracellular space. This results in an increased volume of distribution for the contrast agent within a voxel of tissue with an associated increase in signal intensity. In the chronic stage of myocarditis, areas of scar are histologically characterized by abundant loose connective tissue with a few

Table 28.2. Sensitivity and specificity of T2-weighted imaging in myocarditis

Sensitivity	*n*	Sensitivity (%)	Specificity	*n*	Specificity (%)
Rieker et al.[15]	11	100[a]			
Abdel-Aty et al.[7]	25	84[a]	Abdel-Aty et al.[1]	23	74[a]
Laissy et al.[12]	20	62[a]			
Laissy et al.[13]	24	61[a]			
Gutberlet et al.[14]	48	67[b]	Gutberlet et al.[14]	35	69[b]
Total	128	71		58	71

[a]Sensitivity and specificity to detect inflammation as defined by clinical picture
[b]Sensitivity and specificity to detect inflammation as defined by immunohistochemistry

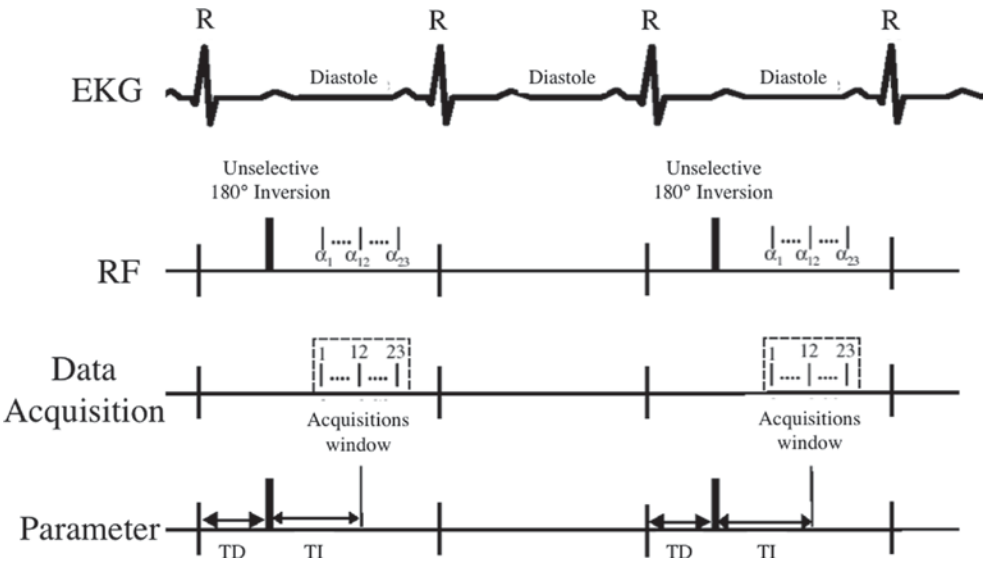

Fig. 28.5 Schematic diagram of the inversion recovery gradient echo pulse sequence used for late gadolinium enhancement imaging. Reprinted with permission from Simonetti et al.[16]

fibrocytes. Again, voxels within such areas of myocardium exhibit a higher concentration of contrast medium as compared to normal myocardial tissue. In contrast to necrotic or fibrotic tissue, densely packed myocytes forming most of the normal myocardium are not accessible to gadolinium compounds. Hence, the volume of distribution and the concentration of the contrast agent within a voxel remain low.

When such inversion recovery gradient echo techniques are used in patients with clinically suspected myocarditis (history of respiratory or gastrointestinal symptoms with 8 weeks of admission in combination with fatigue/malaise, chest pain, dyspnea, or tachycardia plus ECG changes such as conduction block, ST abnormalities, supra-ventricular tachyarrhythmia, or ventricular tachycardia), LGE is found in up to 90% of the patients.[17] The regions of LGE have a patchy distribution throughout the left ventricle. They are frequently located in the lateral free wall (Fig. 28.6) and originate from the epicardial quartile of that wall. Another frequently seen pattern is the mid-wall stria pattern in the basal inter-ventricular septum in patients with chronic myocarditis.[18] LGE CMR also has a good sensitivity in patients with a more chronic form of myocarditis by clinical criteria.[19] However, in this series of biopsy confirmed patients with chronic myocarditis, borderline myocarditis - the less severe form of the disease by the DALLAS criteria - was less often associated with LGE than active myocarditis by the DALLAS criteria.[19]

If scarring occurs in acute myocarditis, it will remain visible on LGE images when the acute inflammation has long subsided. Chronic scar following acute myocarditis is often significantly smaller than in the acute stage due to scar shrinking. When the initial areas of scarring are just large enough to be visible, scar shrinking may lead to disappearance of LGE in some patients (Fig. 28.7).

LGE-CMR is the most widely used approach in the diagnosis of myocarditis, and this is reflected in the literature. Table 28.3 shows the results of published studies including the average weighted sensitivity and specificity.

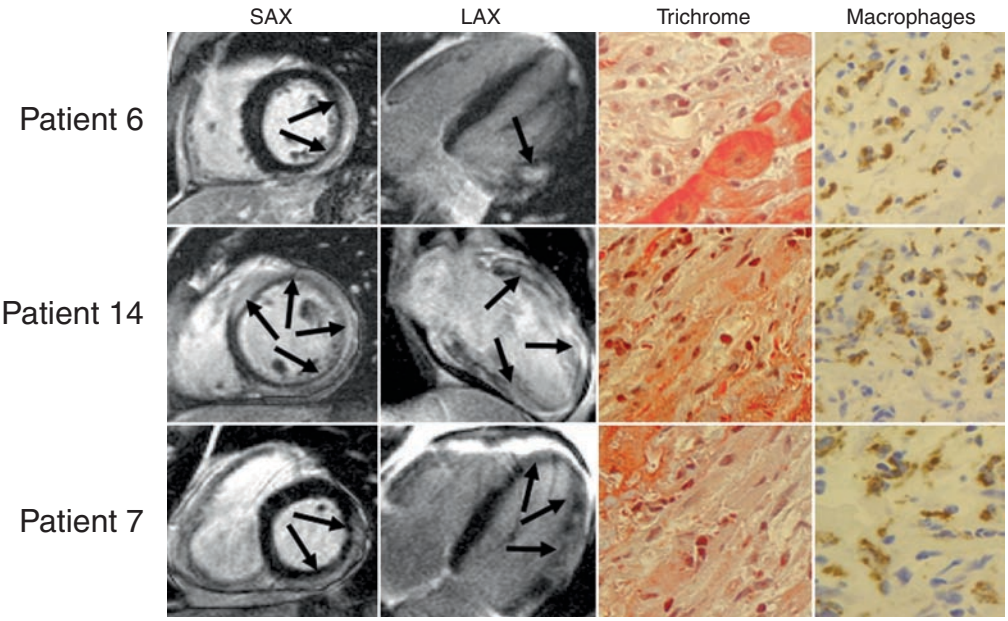

Fig. 28.6 Late gadolinium-enhanced (LGE) CMR images and histopathology of typical patients in whom biopsies were obtained from the area of contrast enhancement. The panels show cases of active myocarditis with myocyte damage as well as infiltration of macrophages. Note that contrast enhancement is often located in the sub-epicardial region of the postero-lateral wall. Reprinted with permission from Mahrholdt et al.[17]

Which CMR Pulse Sequences Should Be Used?

A disadvantage of the LGE CMR technique is the inability to demonstrate diffuse myocardial changes as encountered in diffuse acute myocarditis with diffuse oedema formation. In addition, localized oedema without accompanying myocyte death will not result in enough increase in extracellular space to cause LGE.[24] Thus, the sensitivity of LGE to detect milder forms of myocarditis may be suboptimal.

CMR imaging optimized at detecting hyperaemia or oedema may be more sensitive to identify patients with acute myocarditis. A study comparing early gadolinium enhancement, oedema imaging, and LGE using the appropriate pulse sequences in patients with cardiac symptoms suggestive of myocarditis made the following observations[11]:

1. T1-weighted early gadolinium enhancement (using a turbo spin echo sequence) yields a significantly higher global myocardial relative enhancement in patients compared to volunteers. A cut-off value of 4.0 has a sensitivity of 80% and a specificity of 73% to identify myocarditis.
2. T2-weighted oedema imaging (using a triple inversion recovery pulse sequence) shows significantly higher global myocardial signal intensity in patients than in volunteers, although there is overlap. A cut-off value of 1.9 has a sensitivity of 84% and a specificity of 74% to identify the disease.
3. Necrosis LGE imaging (using an inversion recovery gradient echo pulse sequence) has a lower sensitivity of only 44% (Fig. 28.8), but the specificity is high (100%).
4. The best diagnostic performance was obtained when myocarditis was diagnosed in patients in whom any two of the criteria obtained by the three techniques were positive.[11]

One needs to remember, however, that in this series the gold standard for identifying myocarditis was the clinical presentation of the patient and endomyocardial biopsy was not performed. In addition, gRE imaging does not work equally well in all centres.

When performing the same CMR protocol consisting of a T1-weighted gRE, a T2-weighted oedema, and a LGE pulse sequence in patients with clinically suspected **chronic** myocarditis, increased myocardial gRE (obtained from the T1 images) and increased oedema ratio (obtained from the T2 images) are common findings, whereas LGE is less often detected than reported for acute myocarditis.[14] This suggests that clinically active inflammation is usually associated with T2 signal elevation, as well as an increase in gRE ratio irrespective of whether the onset of clinical symptoms has been recent or whether the clinical presentation is a more chronic one. One may also conclude that scar in chronic myocarditis may have shrunk to an extent that LGE-CMR has reduced sensitivity (see Fig. 28.7). Also in chronic myocarditis, the approach of diagnosing myocarditis by CMR when two out of the three pulse sequences performed resulted in pathologic results yielded the best accuracy.[14]

Follow-Up of Patients with Myocarditis by CMR

Clinical improvement of myocarditis patients is paralleled by normalization of gRE and oedema ratio in many patients.[25] Serial assessment of the relative T2 signal, gRE

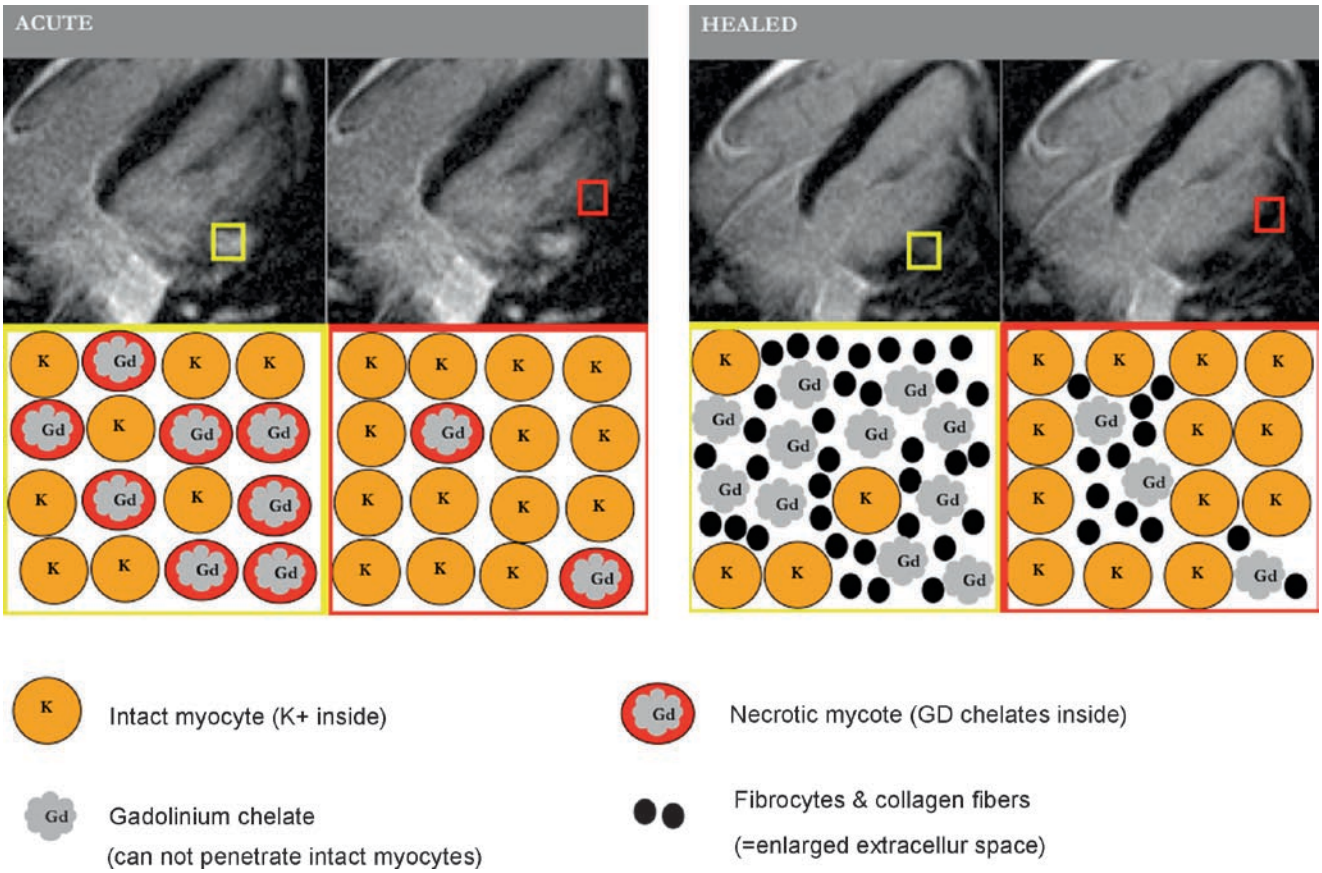

Fig. 28.7 Mechanism of contrast enhancement in the setting of acute and healed myocarditis. *Upper images* show LGE images using inversion recovery gradient echo images, *bottom images* show a schematic view of the mechanism of contrast enhancement in an area with frequent myocyte necrosis (*left* and *right panel*, *yellow frames*), as well as in an area with occasional myocyte necrosis (*left* and *right panel*, *red frames*). Just as in infarcts, acute necrosis in the setting of myocarditis (*left panel*) is characterized by ruptured sarcolemmal membranes and surrounding interstitial oedema, allowing the contrast agent to accumulate in the interstitium as well as to diffuse into the intracellular space, resulting in crisp contrast enhancement in areas with a lot of necrosis (*left panel, yellow frames*), and more diffuse enhancement in areas with occasional myocyte necrosis (*left panel, red frames*). Thus, the general mechanism of hyper-enhancement in myocarditis is the same as in infarction. During healing, some amount of interstitial oedema persists, and necrotic myocytes are slowly replaced by fibrous tissue, comparable to small chronic infarcts. Thus, hyper-enhancement will remain present during this phase of the disease. However, when healing is completed (*right panel*), oedema has resolved while scars shrink and remodel over time (*right panel, yellow frame*). Consequently, in areas with occasional myocardial necrosis (*right panel, red frames*), voxels may now contain so many previously bordering surviving myocytes that contrast enhancement in these voxels may not be visible any longer (*right panel red frames*), resulting the area of contrast enhancement to decrease significantly. This effect is likely magnified by the patchy distribution of scars in myocarditis and the fact that interstitial oedema mainly occurs in areas of myocardial necrosis. Thus, all areas of visible hyper-enhancement may disappear in some cases after healing, just leaving minimal diffuse signal enhancement

ratio, and LGE at initial presentation and after 18 months in 36 patients diagnosed with acute myocarditis by clinical criteria showed a decrease in the mean T2 signal ratio from 2.4 to 1.9, a decrease in the gRE signal ratio from 7.6 to 4.4, and a decrease in the amount of LGE from 38 to 22% of left ventricular mass. These findings are in line with previous publications describing the individual time courses of each of those CMR parameters[26, 27] in myocarditis patients. Hence, the CMR approach combining a contrast-enhanced T1-weighted pulse sequence, a T2-weighted sequence, and a LGE pulse sequence may be capable of differentiating reversible and healing (elevated T1 gRE ratio and T2 oedema ratio, which normalizes over time) myocarditis and irreversible myocardial damage with or without ongoing inflammation (persistent LGE with or without accompanying elevations of T1 gRE ratio and T2 oedema ratio) non-invasively.

In patients with ongoing cardiac symptoms, the clinical question is often whether the acute inflammatory process has healed. If none or just one of T2 or gRE ratios is elevated, this constellation may have a very high negative predictive value for excluding ongoing active myocarditis in living patients.[25]

However, data on the value of CMR in identifying healed from ongoing active myocarditis are far from being conclusive. The largest study examining patients with clinically suspected chronic myocarditis by CMR and endomyocardial

Table 28.3. Sensitivity and specificity of LGE-CMR in myocarditis

Sensitivity	*n*	Sensitivity (%)	Specificity	*n*	Specificity (%)
Rieker et al.[15]	11	45[a]	Rieker et al.[15]	10	100[a]
Mahrholdt et al.[17]	32	88	Roiditi et al.[20]	8	100[a]
Abdel-Aty et al.[11]	25	44[a]	Abdel-Aty et al.[7]	23	100
Hunold et al.[21]	6	100			
Laissy et al.[12]	24	79[a]	Laissy et al.[13]	31	97[a]
Ingkanisorn et al.[22]	21	100[a]			
DeCobelli et al.[19]	23	84[b]			
Gutberlet et al.[14]	48	27[b]	Gutberlet et al.[14]	35	80[b]
Mahrholdt et al.[18]	87	95[b]			
Yilmaz et al.[23]	71	46[b]			
Total	348	68		107	93

[a]Sensitivity and specificity to detect inflammation as defined by clinical picture
[b]Sensitivity and specificity to detect inflammation as defined by immunohistochemistry

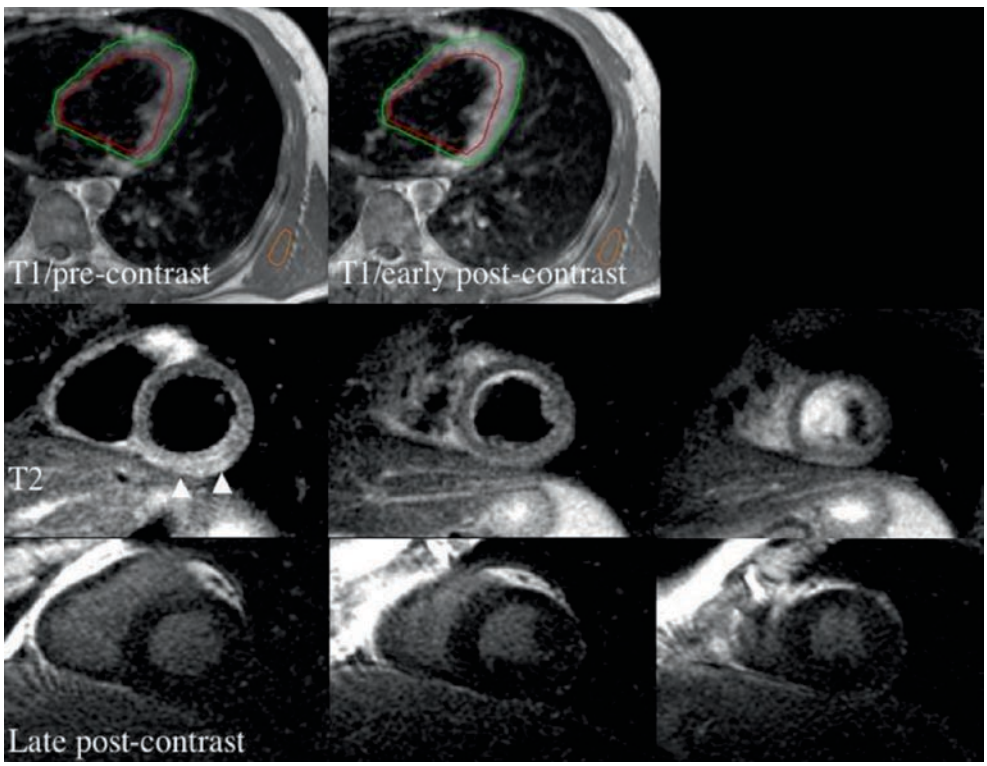

Fig. 28.8 CMR findings in a patient with acute chest pain and ST-elevations in II, III, aVF as well as negative T-waves in II, III, aVF, V5–V6. The patient also had mild elevation of cardiac markers. *Top*. Pre-and post-contrast axial T1-weighted spin echo images of the same slice. Global relative enhancement was elevated (4.1). *Middle*. T2-weighted images in three short-axis slices. Note the postero-lateral focal high T2 signal (*arrowheads*) in the basal slice with apparent focal increase in myocardial thickness. *Bottom*. Corresponding late enhancement images: no evidence of late gadolinium enhancement. Reprinted with permission from Abdel-Aty et al.[11]

biopsy[14] found absence of T2 elevation in 33%, and no elevated gRE ratio in 37% of those shown to have inflammation by histology. Hence, there will be several patients with persisting inflammation who will have elevation of only one of these two CMR parameters.

CMR or Endomyocardial Biopsy?

Biopsies obtained from the area of LGE show acute or borderline myocarditis[17] in a higher percentage than reported from biopsies taken randomly (usually from the right ventricle) in the literature. These recent findings may be explained by the fact that more LGE may be associated with more intense inflammation permitting the operator to direct the bioptome towards the area of maximum injury. Myocarditis is found less consistently in patients in whom the biopsy cannot be obtained from the region of contrast enhancement.[17] Thus, CMR-guided biopsy in the right or the left ventricle may result in a higher yield of positive findings than routine right ventricular biopsy (Fig. 28.9). Routine performance of LV biopsy in patients with suspected myocarditis may have advantages over RV biopsy as maximum inflammation often occurs in the postero-lateral wall of the LV, which is easily accessible for the bioptome (Fig. 28.10).

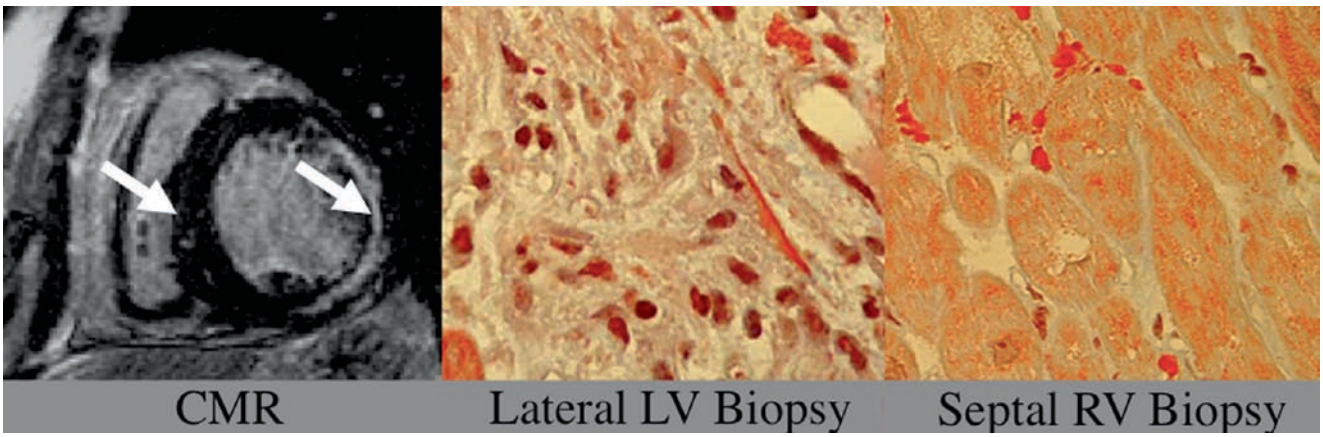

Fig. 28.9 Mechanism how CMR guidance can improve sensitivity of endomyocardial biopsy by avoiding sampling errors. The left ventricular biopsy was obtained near the focus of myocardial damage as indicated by LGE CMR (*white arrow, left panel*) and reveals acute myocarditis (*mid panel*), whereas the right ventricular biopsy, which was obtained from the septum (*black arrow*, no LGE), shows completely normal myocytes (*right panel*)

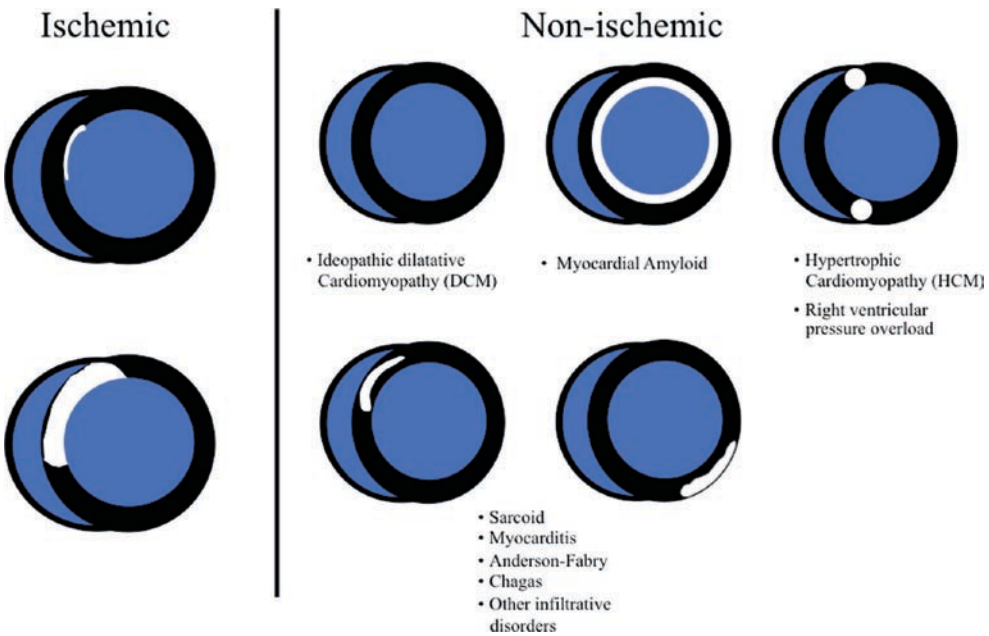

Fig. 28.10 Late gadolinium enhancement patterns that one may encounter in clinical practice. If hyper-enhancement is present, the endocardium should be involved in patients with ischaemic disease. Isolated mid-wall or epicardial hyper-enhancement strongly suggests a "non-ischaemic" etiology. Modified with permission from Mahrholdt et al.[28]

However, the higher sensitivity of endomyocardial biopsy recently reported in some CMR studies[17, 18] is in part also due to the fact that the definition of borderline myocarditis has been broadened by the routine availability of immunohistochemistry and that an increase of the number of activated macrophages and/or lymphocytes to >14/high power field is now a widely accepted criterion for making the diagnosis of borderline myocarditis.[29] This new definition represents an extension of the original DALLAS criteria, and an increased sensitivity of endomyocardial biopsy can hence be expected.

When managing patients with inflammatory heart disease today, it should be kept in mind that endomyocardial biopsy remains the only technique that can directly assess the presence and intensity of myocardial inflammation in vivo. Therefore, it is the technique of choice if clinically indicated to differentiate between active and healed myocarditis. Endomyocardial biopsy also provides information on the underlying cause of inflammation, such as viral or bacterial infection of the myocardium, or myocardial autoimmune processes, on the presence of giant cells, or Churg Strauss syndrome.[30] This information cannot be obtained by CMR imaging, but is essential for patient management decisions. The importance of endomyocardial biopsy is reflected in the current guidelines,[30] recommending it in basically all patients developing non-ischaemic heart failure as well as for several other non-ischaemic conditions.

Clinical Recommendations

The optimal CMR approach for diagnosing myocarditis may depend on the clinical presentation of the patient. The patient with less impressive symptoms may be more likely to have pathologic hyperaemia and oedema imaging with normal LGE. Recent expert consensus suggests that CMR should be performed in patients who are symptomatic, have clinical evidence suggesting myocarditis, and in whom CMR will likely affect clinical management.[10] A positive diagnosis of myocarditis may result in a recommendation to refrain from exercise, betablockade may be instituted in patients with arrhythmias, and clinical follow-up may be scheduled. Some patients may require additional follow-up by echocardiography or CMR. In patients with occupations associated with strenuous exercise, the indication to perform CMR should even be broader because the consequences of having the disease are more severe. In these patients, clinical symptoms may be absent, and the mere presence of an abnormal ECG should trigger a request of performing CMR (Table 28.4).

In most centres, only two sets of images (T2 oedema and LGE) are acquired (Table 28.5), whereas myocardial GRE is not measured due to the fact that T1-weighted spin-echo images are often of poor quality. When all three sets of images are acquired, myocarditis is defined to be present when at least two of the three sets of images show pathologic results.[10] Other centres feel that LGE is the most stable pulse sequence with the fewest number of artefacts, and they rely on the result of this set of images alone. This approach may result in some under-diagnosis of myocarditis, but has a good specificity. These different approaches at different centres reflect the fact that there are still not enough data available at the moment, especially in patients who also had endomyocardial biopsy, to give final recommendations on CMR in patients with suspected myocarditis.

Table 28.4. Indications for CMR in myocarditis

Suspected myocarditis based on various combinations of clinical symptoms such as fatigue, palpitations, arrhythmias, unexplained dyspnea, unexplained chest pain in the absence of coronary artery disease or any other structural heart disease, and/or abnormal resting ECG
Clinical presentation with acute coronary syndrome in the absence of coronary artery disease or culprit lesion
Clinical presentation with successful resuscitation after sudden cardiac death in the absence of coronary artery disease or any structural heart disease
Clinical presentation with new onset of heart failure in the absence of coronary artery disease or any structural heart disease
CMR guidance of endomyocardial biopsy to increase sensitivity
Follow-up of known myocarditis
Follow-up of known myocarditis after antiviral or immunosuppressive treatment

Table 28.5. CMR protocol for work-up of myocarditis

Requirements
Patient should be able to hold his/her breath for 15–20 s
Limited diagnostic performance with frequent extrasystoles (>10/min), atrial fibrillation
Step 1: LV structure and function module
Scout imaging - axial, coronal, sagittal
Axial (8–10 mm) set of steady state free precession (SSFP) or half Fourier single shot turbo spin echo images through the chest
Scout to line up short-axis images – this can either be a single shot image or a cine acquisition
2-chamber long axis (also called the vertical long axis) prescribed off an axial view showing the apex and mitral valve, bisecting the mitral valve and apex
Horizontal long axis prescribed off the 2-chamber long axis, again bisecting the apex and centre of the mitral valve
Steady-state free-precession short-axis cine images from the mitral valve plane through the apex, prescribed from the previously acquired horizontal long-axis image
Slice thickness 6–8 mm, with 2 mm inter-slice gaps
Temporal resolution <45 ms between phases
Parallel imaging used as available, speed up factor 2×
Steady-state free-precession long-axis cine images
4-chamber long axis, prescribed off a basal short-axis image, bisecting the inter-ventricular septum
2-chamber long axis, prescribed off a basal short-axis image, bisecting the anterior and inferior walls
3-chamber long axis, prescribed off the most basal short axis including the plane of the LVOT, bisecting the LVOT and the postero-lateral wall
Analysis
All short-axis images are evaluated with computer aided analysis packages for planimetry of endocardial and epicardial borders at end-diastole and end-systole
The inclusion or exclusion of papillary muscles in the LV mass should be the same as that used in normal reference ranges used for comparison
Care must be used at the 1 or 2 most basal slices. Due to systolic movement of the base towards the apex, the end-systolic phase will include only left atrium. However, this slice at end-diastole will include some of the LV mass and volume
Step 2: T2-weighted black blood imaging module
Breath-hold, segmented fast spin-echo imaging with dark blood preparation (double inversion recovery)
Perform imaging prior to contrast administration
Selected slices based on cine imaging findings (e.g. 2- and 4-chamber long-axis and three representative short-axis slices)
Adjust readout to middiastole
Slice thickness 8 mm slice thickness of dark blood prep should be greater than the base-apex motion of the mitral annulus
Analysis
Visual analysis of all T2-weighted images for focal signal enhancement matching morphological abnormalities, wall motion abnormalities, and/or regions of late gadolinium enhancement. **Caution**: Sub-endocardial slow flow artefact
Quantitative analysis comparing average signal intensity (SI) with the average signal intensity of skeletal muscle. Depending on the individual scanner (at least 20 healthy volunteers must be scanned and evaluated before starting to evaluate patients), the normal ratio $SI_{myocardium}/SI_{skeletal\ muscle}$ is reported to be <1.8–2.0[11]
Step 3: late gadolinium enhancement
Need at least 10 min wait after contrast administration (0.15–0.2 mmole/kg). Note: The delay may be shorter than 10 min if lower doses are used as blood pool signal falls below that of late enhanced myocardium

(*continued*)

Table 28.5. (continued)

Requirements
2D segmented inversion recovery GRE imaging during diastolic stand-still
Same views as for cine imaging (short- and long-axis views)
Slice thickness, same as for cine imaging
In-plane resolution, ~1.4–1.8 mm
Acquisition duration per R-R interval below 200 ms, but should be less in the setting of tachycardia
Inversion time set to null normal myocardium. Alternative is to use fixed TI with a phase-sensitive sequence
Read-out is usually every other heartbeat, but can be modified to every heartbeat in the setting of bradycardia, and every third heart beat in the setting of tachycardia or arrhythmia
Optional: Single-shot imaging (SSFP readout) performed as backup for patients with irregular heart beat, difficulty breath-holding
Analysis - Examine the "pattern" of enhancement as certain non-ischaemic myocardial diseases have predilection for scarring in various myocardial regions (Fig. 28.10)

References

1. Magnani JW, Dec GW. Myocarditis: current trends in diagnosis and treatment. *Circulation*. 2006;113:876–890
2. Pinamonti B, Alberti E, Cigalotto A, et al Echocardiographic findings in myocarditis. *Am J Cardiol*. 1988;62:285–291
3. Felker GM, Boehmer JP, Hruban RH, et al Echocardiographic findings in fulminant and acute myocarditis. *J Am Coll Cardiol*. 2000;36:227–232
4. Martin ME, Moya–Mur JL, Casanova M, et al Role of noninvasive antimyosin imaging in infants and children with clinically suspected myocarditis. *J Nucl Med*. 2004;45:429–437
5. Narula J, Khaw BA, Dec GW, et al Diagnostic accuracy of antimyosin scintigraphy in suspected myocarditis. *J Nucl Cardiol*. 1996;3:371–381
6. O'Connell JB, Henkin RE, Robinson JA, Subramanian R, Scanlon PJ, Gunnar RM. Gallium–67 imaging in patients with dilated cardiomyopathy and biopsy–proven myocarditis. *Circulation*. 1984;70:58–62
7. le Polain de Waroux JB, Pouleur AC, Goffinet C, Pasquet A, Vanoverschelde JL, Gerber BL. Combined coronary and late–enhanced multidetector–computed tomography for delineation of the etiology of left ventricular dysfunction: comparison with coronary angiography and contrast–enhanced cardiac magnetic resonance imaging. *Eur Heart J*. 2008;29:2544–2551
8. Redheuil AB, Azarine A, Garrigoux P, Mousseaux E. Images in cardiovascular medicine. Correspondence between delayed enhancement patterns in multislice computed tomography and magnetic resonance imaging in a case of acute myocarditis. *Circulation*. 2006;114:e571–e572
9. Friedrich MG, Strohm O, Schulz–Menger J, Marciniak H, Luft FC, Dietz R. Contrast media–enhanced magnetic resonance imaging visualizes myocardial changes in the course of viral myocarditis. *Circulation*. 1998;97:1802–1809
10. Friedrich MG, Sechtem U, Schulz–Menger J, et al Cardiovascular magnetic resonance in myocarditis. *J Am Coll Cardiol*. 2009;53(suppl 17):1475–1487
11. Abdel–Aty H, Boyé P, Zagrosek A, Wassmuth R, et al The sensitivity and specificity of contrast–enhanced and T2–weighted cardiovascular magnetic resonance to detect acute myocarditis. *J Am Coll Cardiol*. 2005;45:1815–1822
12. Laissy JP, Messin B, Varenne O, et al MRI of acute myocarditis: a comprehensive approach based on various imaging sequences. *Chest*. 2002;122(suppl 5):1638–1648
13. Laissy JP, Hyafil F, Feldman LJ, et al Differentiating acute myocardial infarction from myocarditis: diagnostic value of early– and delayed–perfusion cardiac MR imaging. *Radiology*. 2005;237 (suppl 1):75–82
14. Gutberlet M, Spors B, Thoma T, et al Suspected chronic myocarditis at cardiac MR: diagnostic accuracy and association with immunohistologically detected inflammation and viral persistence. *Radiology*. 2008;246:401–409
15. Rieker O, Mohrs O, Oberholzer K, Kreitner KF, Thelen M. [Cardiac MRI in suspected myocarditis]. *Rofo Fortschr Geb Rontgenstr Neuen Bildgeb Verfahr*. 2002;174(suppl 12):1530–1536
16. Simonetti OP, Kim RJ, Fieno DS, et al An improved MRI technique for the visualization of myocardial infarction. *Radiology*. 2001;218: 215–223
17. Mahrholdt H, Goedecke C, Wagner A, et al Cardiovascular magnetic resonance assessment of human myocarditis: a comparison to histology and molecular pathology. *Circulation*. 2004;109: 1250–1258
18. Mahrholdt H, Wagner A, Deluigi C, et al Presentation, patterns of myocardial damage and clinical course of viral myocarditis. *Circulation*. 2006;114:1581–1590
19. DeCobelli CF, Pieroni M, Esposito A, et al Delayed gadolinium–enhanced cardiac magnetic resonance in patients with chronic myocarditis presenting with heart failure or recurrent arrhythmias. *J Am Coll Cardiol*. 2006;47:1649–1654
20. Roditi GH, Hartnell GG, Cohen MC. MRI changes in myocarditis – evaluation with spin echo, cine MR angiography and contrast–enhanced spin echo imaging. *Clin Radiol*. 2000;55:752–758
21. Hunold P, Schlosser T, Vogt FM, et al Myocardial late enhancement in contrast–enhanced cardiac MRI: distinction between infarction scar and noninfarction–related disease. *AJR Am J Roentgenol*. 2005;184:1420–1426
22. Ingkanisorn WP, Paterson I, Calvo KR, et al Cardiac magnetic resonance appearance of myocarditis caused by high dose IL–2: similarities to community–acquired myocarditis. *J Cardiovasc Magn Res*. 2006;8:353–360
23. Yilmaz A, Mahrholdt H, Athanasiadis A, et al Coronary vasospasm as the underlying cause for chest pain in patients with PVB19 myocarditis. *Heart*. 2008;94:1456–1463

24. Li G, Xiang B, Dai G, et al Tissue edema does not change gadolinium–diethylenetriamine pentaacetic acid (Gd–DTPA)–enhanced T1 relaxation times of viable myocardium. *J Magn Reson Imaging*. 2005;21:744–751
25. Zagrosek A, Abdel–Aty H, Boyé P, et al Cardiac magnetic resonance monitors reversible and irreversible myocardial injuries in myocarditis. *J Am Coll Cardiol Imag*. 2009;2(suppl 2): 131–138
26. Wagner A, Schulz–Menger J, Dietz R, Friedrich MG. Long–term follow–up of patients paragraph sign with acute myocarditis by magnetic paragraph sign resonance imaging. *MAGMA*. 2003;16:17–20
27. Zagrosek A, Wassmuth R, Abdel–Aty H, Rudolph A, Dietz R, Schulz–Menger J. Relation between myocardial edema and myocardial mass during the acute and convalescent phase of myocarditis – a CMR study. *J Cardiovasc Magn Reson*. 2008;10:19
28. Mahrholdt H, Wagner A, Judd RM, et al Delayed enhancement cardiovascular magnetic resonance assessment of non–ischaemic cardiomyopathies. *Eur Heart J*. 2005;26:1461–1474
29. Baughman KL. Diagnosis of myocarditis: death of Dallas criteria. *Circulation*. 2006;113:593–595
30. Cooper LT, Baughman KL, Feldman AM, et al The role of endomyocardial biopsy in the management of cardiovascular disease: a scientific statement from the American Heart Association, the American College of Cardiology, and the European Society of Cardiology Endorsed by the Heart Failure Society of America and the Heart Failure Association of the European Society of Cardiology. *Eur Heart J*. 2007;28:3076–3093

Chapter 29

CARDIAC MASSES AND TUMOURS

Peter Buser, Thomas Buck, and Björn Plicht

CONTENTS

J. L. Zamorano et al. (eds.), *The ESC Textbook of Cardiovascular Imaging*
DOI: 10.1007/978-1-84882-421-8_29, © Springer-Verlag London Limited 2010

Introduction

Cardiac tumours represent a rare but important cause of morbidity and mortality in clinical cardiology and are often challenging for diagnostic cardiac imaging. There is a broad spectrum of differential diagnoses for cardiac masses (Table 29.1). This chapter is mainly focussed on the diagnosis of primary and secondary cardiac tumours and intra-cardiac thrombi. Primary cardiac tumours are rare, with a prevalence between 0.001 and 0.3%.[1] Based on autopsy studies, secondary cardiac tumours, including metastases from distant malignomas or local invasion from neoplasms in the chest, are at least 20 times more common.[2] Three quarters of the primary cardiac tumours are benign, and nearly half of those are myxomas, the rest being lipomas, papillary fibroelastomas, haemangiomas, and rhabdomyomas. Ninety-five percent of the malignant primary cardiac tumours are sarcomas, and the more common types are angiosarcomas (37%), undifferentiated sarcomas (24%), malignant fibrous histiocytomas (11–24%), leiomyosarcomas (8%), and osteosarcomas (3–9%).[3]

The treatment for different types of cardiac masses differs greatly. Diagnostic imaging of cardiac tumours provides important clinical decision-making information such as origin, size, extension, morphology and mobility of the tumour, involvement of cardiac chambers, valves, myocardium and pericardium, invasiveness, vascularization, and tissue characterization. Echocardiography is usually the first imaging modality providing high sensitivity in detecting cardiac masses, particularly by trans-oesophageal approach, and detailed analysis of mass characteristics by the use of different imaging modalities including 3D imaging, tissue Doppler imaging, and contrast imaging. A large number of cardiac tumours, in fact, are detected incidentally during routine echocardiographic examinations. Cardiac magnetic resonance (CMR) offers distinct advantages in diagnosing cardiac masses and tumours including 3D and multi-planar views, a large field of view, excellent contrast resolution, adequate temporal and high spatial resolution, and the unique potential to characterize specific tissues based on their signal intensity with different imaging sequences and during contrast enhancement (Table 29.2). In patients with contraindications for CMR, cardiac CT is an alternative, although irradiation exposure has to be taken into account.

Table 29.1. Differential diagnosis of cardiac masses

Primary cardiac tumours	
Benign	Myxoma
	Lipoma
	Papillary fibroelastoma
	Rhabdomyoma
	Fibroma
Malignant	Angiosarcoma
	Malignant fibrous histiocytoma
	Leiomyosarcoma
	Rhabdomyosarcoma
	Osteosarcoma
	Liposarcoma
	Primary cardiac lymphoma
Secondary cardiac tumours, metastases	
Thrombus	
Vegetation	
Abscess	
Anatomic variants (crista terminalis etc.)	
Focal myocardial hypertrophy	
Lipomatous hypertrophy of inter-atrial septum	
Cysts (bronchogenic, pericardial)	

Primary Cardiac Tumours

Primary Benign Cardiac Tumours

Myxoma

Myxomas comprise approximately 50% of primary benign cardiac tumours. They typically arise from the inter-atrial septum or the fossa ovalis, although they can arise from any endocardial area. Seventy-five percent of myxomas are located within the left atrium, 20% in the right atrium, and rarely any in the ventricles.[4] Myxomas typically manifest as intra-cardiac masses attached to the endocardium by a narrow pedicle, although broad-based and immobile masses have been reported. Myxomas may be lobular and smooth and may have villous extensions. They frequently have organized thrombi on the surface. Internally, myxomas are heterogeneous and frequently contain cysts, necrosis, haemorrhage, and calcifications.[5] *Most cardiac myxomas are sporadic, but occasionally, they occur multiply and as a familial disorder and* may include the LAMB (lentigines, atrial myxoma, mucocutaneous myxomas, and blue naevi) and the NAME (naevi, atrial myxoma, myxoid neurofibromas, and ephelides) syndromes, which are listed under the nomenclature of the Carney complex and are associated with the germline mutation PRKAR1A.[6] Patients with cardiac myxomas often present with signs and symptoms of cerebral or systemic embolism, haemodynamic obstruction, or signs of systemic disease such as fatigue, arthralgias, weight loss, high sedimentation rate, and anaemia due to IL-6 and TNF production.

Table 29.2. MR characteristics of primary cardiac tumours. Typical signal intensities on T_1-(T_1-TSE) and T_2 -(T_2-TSE)weighted images, bright blood gradient echo (GE) cine sequences, and uptake of contrast media

	T_1-TSE	T_2-TSE	GE	Contrast
Primary benign cardiac tumours				
Myxoma	↔	↑	↓	+
Lipoma	↑	↑	↑	−
Fibroelastoma	↔	↑	↔	+
Haemangioma	↔	↑	↔	+
Rhabdomyoma	↔/↑	↔/↑	↔	As myocardium
Fibroma	↔/↑	↔/↓	↔	−
Primary malignant cardiac tumours				
Angiosarcoma	Inh	inh	inh	+
Leiomyosarcoma	Var	var	var	+
Osteosarcoma	Inh	inh	inh	+
Liposarcoma				
Lymphoma	↔	↔	↔	inh
Thrombus				
Fresh thrombus				
Older thrombus				

Tumour signal intensity relative to signal intensity of myocardium: ↑ hyper-intense; ↓ hypo-intense; ↔ iso-intense; *inh* inhomogeneous signal intensity within the tumour; *var* variable signal intensity with same histology

In echocardiographic imaging, myxomas are usually isodense to the myocardium. Trans-oesophageal echocardiography has a higher sensitivity in detecting myxomas compared to trans-thoracic echocardiography, especially in the case of small myxomas, and should be performed in any case with suspicion for intra-cardiac tumour or source of embolism. Differentiation between myxoma and thrombus can be difficult. Compared to thrombi, myxomas usually are single masses and are typically located at the inter-atrial septum near the aortic root (Fig. 29.1, Video 29.1a, b, and d). Morphology, mobility, and attachment to endocardium do not provide reliable discrimination between myxomas and thrombi. The presence of a tumour in the pulmonary veins, renal veins, or vena cava extension has been described as a useful aid in the differentiation of a malignant neoplasm from myxoma because myxomas with venous involvement have not been reported.[7] Although usually presenting as a homogeneous, gelatinous mass, a myxoma can present an inhomogeneous echo due to intra-tumoural haemorrhage, necrosis, or calcification. Sometimes cystic formations can be displayed. Detection of flow within the myxoma by colour Doppler with a sufficiently reduced pulse repetition frequency is indicating vascularization and making thrombus less likely (Fig. 29.2, Video 29.2). However, colour Doppler is not sensitive in detecting vascularization in every myxoma. In large left atrial myxomas occluding the mitral valve during diastolic filling, functional mitral stenosis can be detected by colour Doppler and continuous wave Doppler measurement of elevated pressure gradient (Fig. 29.1, Video 29.1a, b, and d).

On CMR examination, cardiac myxomas are usually isointense to the myocardium on T_1-weighted images and hyper-intense on T_2-weighted images. Less commonly, they can appear heterogeneous on both T_1-weighted and T_2-weighted images due to the presence of haemorrhage, necrosis, and calcification (Fig. 29.3, Video 29.3). With cine CMR low signal intensity, mobile masses are revealed, and the origin, size, mobility, extension into the different cardiac chambers, and haemodynamic obstruction can be depicted. After intravenous injection of contrast, media myxomas usually show a heterogeneous contrast enhancement to some degree.

With cardiac CT, myxomas usually have heterogeneous low attenuation reflecting gross pathologic features. Calcifications can be found frequently.

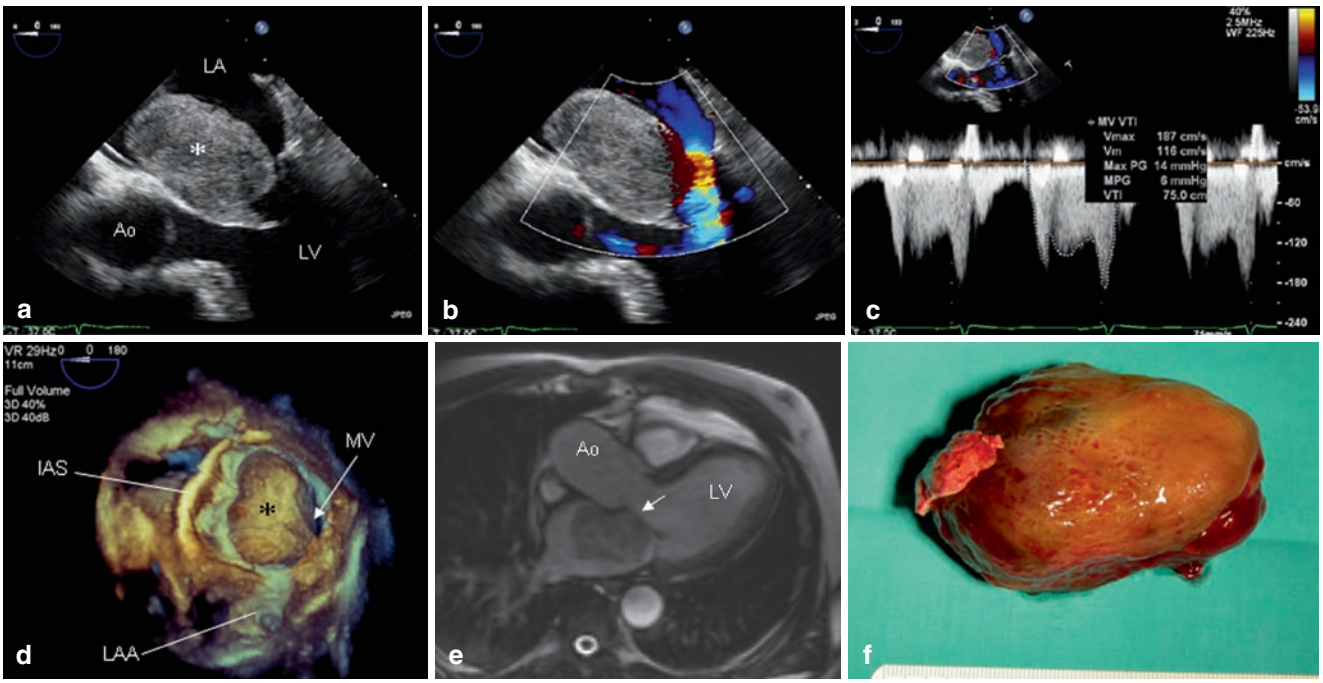

Fig. 29.1 Large left atrial myxoma (6.5 × 3.4 cm) with typical origin at the basal inter-atrial septum in a 60-year-old male patient with history of two recent cerebral embolic strokes. **(a–c)** Trans-oesophageal echocardiographic imaging shows the myxoma (*asterisk*) as a highly mobile mass of heterogeneous texture and isodensity relative to the myocardium. Large myxomas can occlude the mitral valve during diastolic filling with flow obstruction demonstrated by colour Doppler **(b)**, causing functional mitral stenosis with mean PG of 6 mmHg measured by continuous wave Doppler in this case **(c)**. Real-time 3D echocardiographic imaging **(d)** reveals the true extension of the myxoma (*asterisk*) in relation to the left atrium and mitral valve. In cardiac MR, **(e)** the myxoma (*arrow*) appears as a hypo-intense mass with heterogeneous texture **(f)**. Photographic representation of the re-sected myxoma shows a glassy-elastic tumour with a vascularized, myxoid matrix in histology proving myxoma. *LA* left atrium; *Ao* aorta; *LV* left ventricle; *IAS* inter-atrial septum; *LAA* left atrial appendage; *M* mitral valve

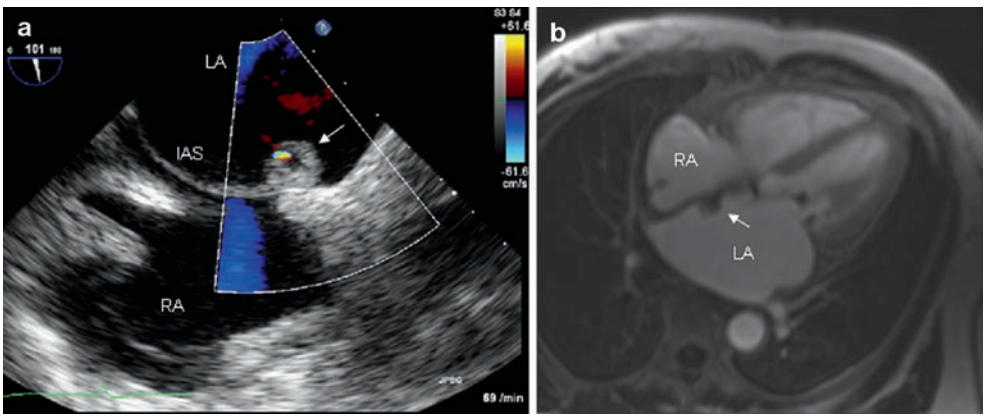

Fig. 29.2 Small left atrial myxoma (1.2 × 1.1 cm) with typical origin at the fossa ovalis in a 62-year-old female patient with moderate-to-severe mitral stenosis. In the severely dilated left atrium with spontaneous echo contrast, the mass (*arrow*) was initially diagnosed as a thrombus. But evidence of flow by trans-oesophageal colour Doppler echocardiography **(a)** within the mass indicating vascularization of the tumour proven to be a myxoma by histology. Cardiac MR representation **(b)** of the myxoma in the same patient (*arrow*). *LA* left atrium; *IAS* inter-atrial septum; *RA* right atrium

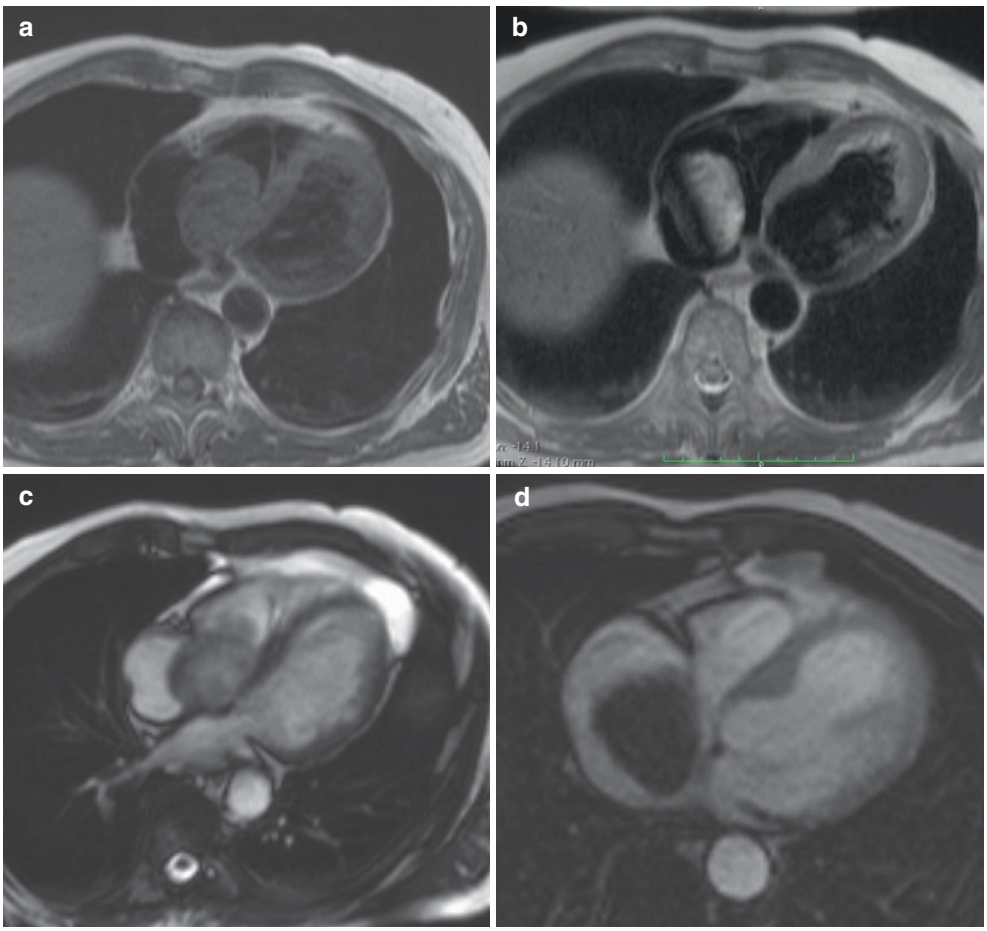

Fig. 29.3 Typical tissue signal intensities of a right atrial myxoma with different CMR sequences. **(a)** T_1-weighted image with iso-intense signal of the myxoma relative to myocardium. **(b)** T_2-weighted image shows heterogeneous signal intensity with hyper-intense parts of the myxoma relative to myocardium. **(c)** Cine TRUFI image shows heterogeneous signal intensity of the myxoma. **(d)** Contrast-enhanced image early after contrast administration shows enhancement of the normal myocardium, but no enhancement of the myxoma

Papillary Fibroelastoma

Papillary fibroelastomas are the second most common benign primary cardiac tumour after myxoma and represent 10% of all primary cardiac tumours.[3,5] On histology, a collection of nonvascular fronds of dense connective tissue lined by endothelium are found.[3] The reported prevalence varies considerably, because papillary fibroelastomas are usually asymptomatic and may, therefore, be underrepresented in patient series. When symptoms occur, they are usually related to embolization from thrombi on the tumour surface, but embolization of parts of the fibroelastoma is not unlikely. Ninety percent of fibroelastomas occur on valve surfaces, and they are slightly more common on the aortic (29%) and the mitral valves (25%) than on the pulmonary (13%) and tricuspid valves (17%). However, this may be influenced by the increased prevalence of symptoms associated with the left-sided valves. 16% of fibroelastomas arise from non-valvular surfaces.[3] Fibroelastomas are usually small (<1 cm) tumours, although they have been reported as large as 5 cm.

In echocardiographic imaging, papillary fibroelastomas typically present as small, mobile masses. They have a characteristic stippled edge with a shimmer or vibration at the tumour-blood interface.[8] Finger-like projections can produce the impression of a sea anemone. Most likely they are attached to the endocardium either on the aortic or left ventricular side of the aortic valve or neighbouring endocardium (Fig. 29.4, Video 29.4a, b, Videos). Due to their small size, fibroelastomas are rarely detected by transthoracic echocardiography. Even in trans-oesophageal echocardiography, fibroelastomas are usually incidental findings. Fibroelastomas often appear alike infectious vegetations or Lambl's excrescenses, which makes differentiation difficult.

On CMR examination, papillary fibroelastomas are often hard to depict due to their small size, adherence to valvular, and therefore, rapidly moving structures. They are mostly detected on cine CMR as small tumours with low signal intensity attached to moving valves. In sporadic case reports, fibroelastomas have been shown to have intermediate signal intensity on T_1-weighted images and intermediate to low signal intensity on T_2-weighted images.[9–11] On delayed enhancement images after administration of Gd-DTPA, a hyper-intense signal intensity caused by the fibroelastic tissue has been reported.[9]

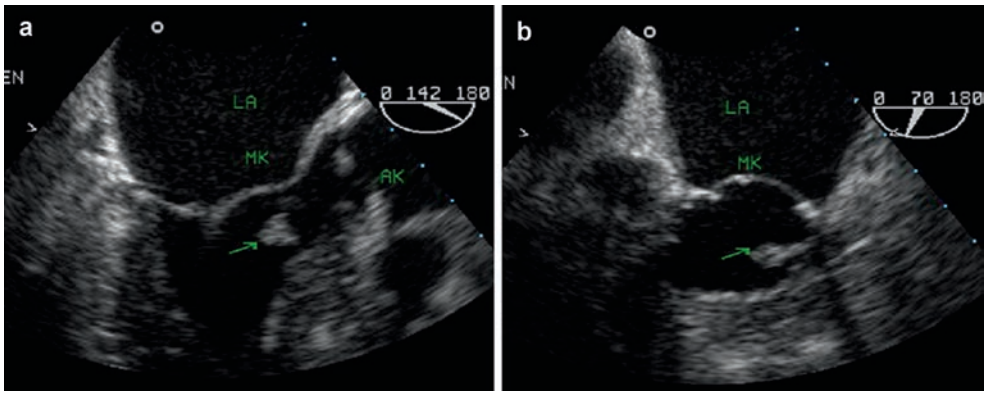

Fig. 29.4 Trans-oesophageal echocardiographic representation of a histological proven papillary fibroelastoma (*arrow*) as an incidental finding in a 56-year-old male with origin from the endocardium at the antero-lateral wall of the left ventricular outflow tract shown in long-axis **(a)** and short-axis **(b)** views of the aortic outflow tract. *LA* left atrium; *MK* mitral valve; *AK* aortic valve

With cardiac CT, papillary fibroelastomas can be found occasionally. With ECG-gated contrast enhanced 64-slice spiral CT, a well-defined, pedunculated, mobile, spherical structure with a density of 64 ± 21 Houndsfield units has been described.[10]

Lipoma and Lipomatous Hypertrophy of the Inter-atrial Septum

Primary cardiac lipomas are benign neoplasms composed of mature adipose tissue and are histologically similar to extracardiac soft-tissue lipomas.[3] In autopsy studies they constitute 8–12% of primary cardiac tumours. This, however, may not represent the true prevalence, since small lipomas may remain undiagnosed in asymptomatic patients, and, on the other hand, lipomatous hypertrophy of the inter-atrial septum has been included in reports of cardiac lipomas. Lipomatous hypertrophy of the inter-atrial septum is defined as "any deposit of fat in the atrial septum which exceeds 2 cm in transverse dimension,"[3] is caused by an increase in the number of adipocytes, spares the fossa ovalis, is associated with advanced age and obesity, and does not represent a true cardiac neoplasy. Lipomas are encapsulated, homogeneous fatty tumours. They may arise from the epicardium, from the endocardium, or from the inter-atrial septum.[12–14] They grow as broad-based, pedunculated masses into any of the cardiac chambers and may reach giant sizes and weigh up to 4,800 g.[15] Many patients are asymptomatic, and the tumour is found incidentally because of chest X-ray abnormalities or heart murmur. Symptoms include shortness of breath, signs of haemodynamic obstruction, or arrhythmias.

In echocardiographic imaging, the finding of cardiac tumours suspicious of being primary cardiac lipomas is extremely rare. Because those tumours are commonly considered benign, they are not surgically resected, and therefore definite histological evidence of a lipoma is lacking (Fig. 29.5, Video 29.5a-c). In echocardiography, lipomas usually appear

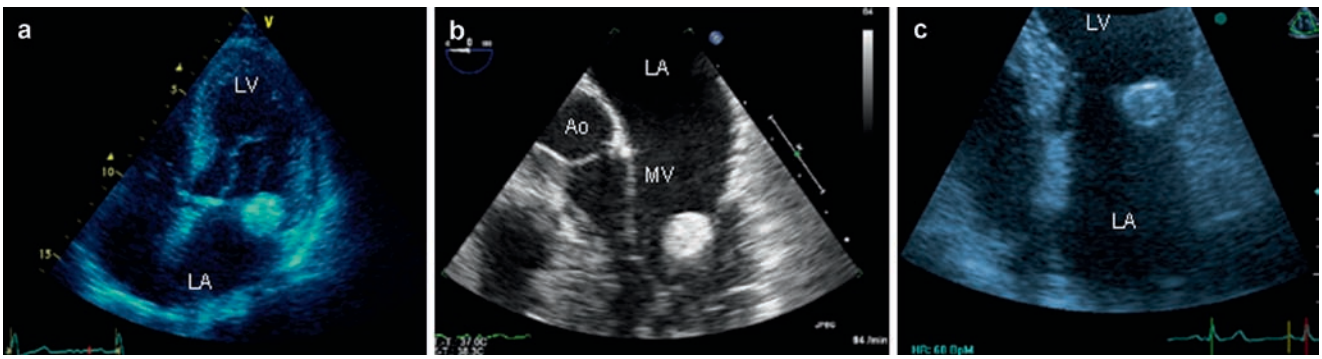

Fig. 29.5 Three examples of cardiac masses with similar echocardiographic appearance located at the posterior mitral leaflet or mitral ring. Because masses were considered benign, histology is unknown. **(a)** A 60-year-old patient with chronic dialysis with transthoracic echocardiography showing shadowing of the echolucent, immobile mass at the posterior mitral ring being most evident of severe mitral ring calcification. **(b)** A 37-year-old otherwise healthy female patient with the incidental echocardiographic finding of a hyperintense, highly mobile mass on the posterior mitral leaflet without shadowing. All criteria summarized make the mass most likely to be a haemangioma or fibroma. **(c)** Trans-thoracic echocardiographic detection of a mobile mass at the posterior mitral ring with a hyperdense outer region and a more isodense centre region and discrete echo shadowing as a incidental finding in a 56-year-old otherwise healthy patient. Differential diagnosis includes mitral ring calcification as well as lipoma, haemangioma, or fibroma. *LV* left ventricle; *LA* left atrium; *MV* mitral valve; *Ao* aorta

as sharply circumscribed, hypo-dense masses broadly attached on the adjacent wall. There is no shadowing, necrosis, or intra-tumoural haemorrhage as a discriminating criterion to sclerotic masses. In contrast, lipomatous hypertrophy of the inter-atrial septum is a more frequent finding in trans-thoracic and trans-oesophageal echocardiography, however, without further diagnostic or therapeutic consequences. Characteristic thickening of the inter-atrial septum of more than 2 cm spares the fossa ovalis. In rare cases, vena cava inflow obstruction can occur. A tangential imaging by a multi-plane probe is important to distinguish between true septal hyper-trophy and malprojection mimicking hypertrophy.

On CMR examination, the diagnosis of a lipoma can be made with a high degree of certainty. On T_1-weighted images, lipomas have a homogeneous increased signal intensity that is comparable to the signal intensity of subcutaneous fat. Necrosis, haemorrhages, and calcifications are not found. On T_2-weighted images, they appear with intermediate signal intensity. By application of a fat saturation, preparation pulse with T_1-weighted sequences signal intensity is decreased parallel to subcutaneous fat. Cardiac lipomas are not enhanced with the administration of contrast media (Fig. 29.6).

On cardiac CT, lipomas appear as homogeneous, low-attenuation masses with approximately −50 Houndsfield units.

Haemangioma

Haemangiomas are benign vascular tumours that represent less than 2% of all cardiac tumours and 5–10% of benign cardiac tumours. They are classified according to the size of their vascular channels into capillary, cavernous, or venous haemangiomas.[16] They can occur in any cardiac location and arise from the epicardium, endocardium, myocardium, and pericardium. Cardiac haemangiomas are often clinically

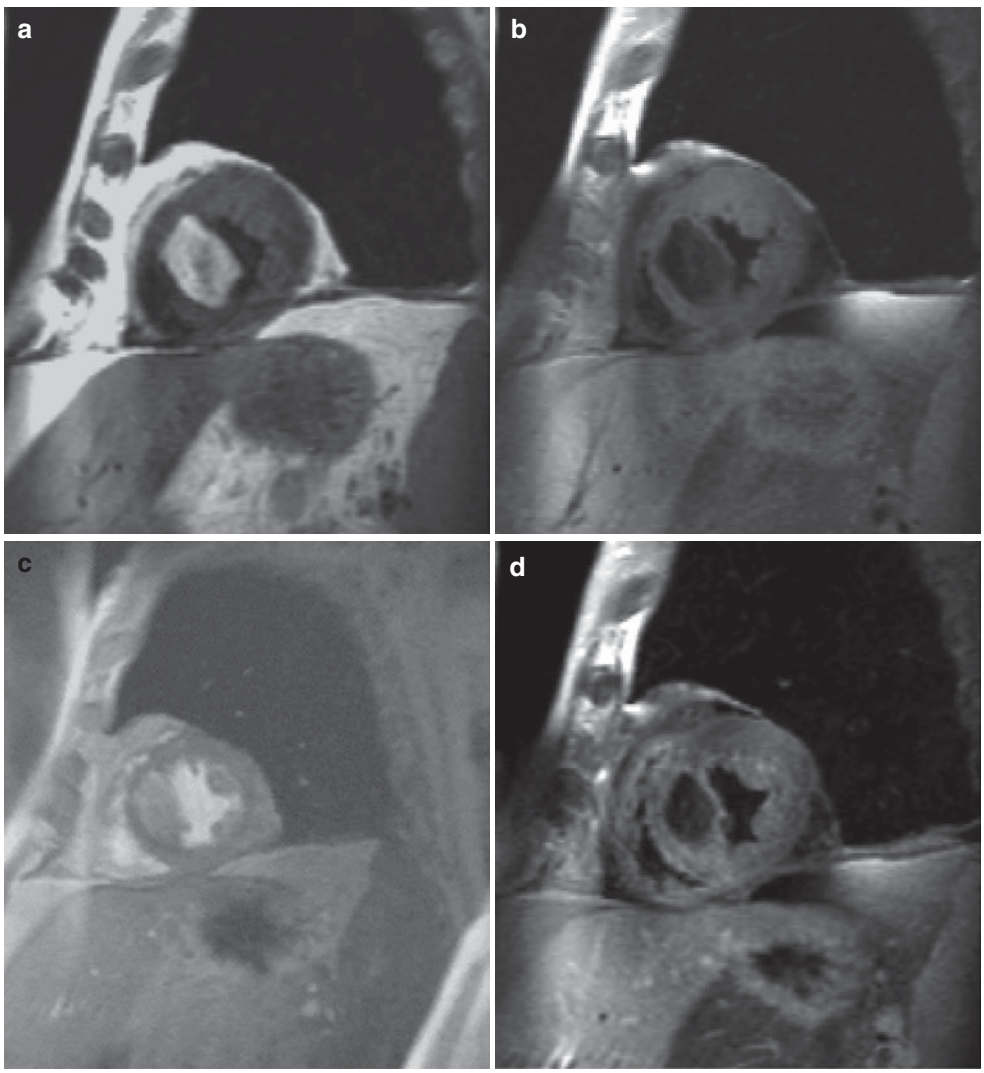

Fig. 29.6 Typical tissue signal intensities with different CMR sequences of a lipoma located within the inter-ventricular septum. **(a)** T_1-weighted image shows hyper-intense signal of the lipoma which is similar to subcutaneous fat; **(b)**: T_1-weighted image with preparation pulse for fat saturation shows hypo-intense signal of the lipoma relative to myocardium. Similar signal loss of subcutaneous fat; **(c)** cine TRUFI image shows iso-intense signal of the lipoma relative to myocardium; **(d)**: T_1-weighted image with preparation pulse for fat saturation after contrast administration shows no contrast enhancement of the lipoma

insignificant, exist unrecognized, and are mostly diagnosed incidentally. Symptoms depend on the location within the heart and the extent of the tumour. Conduction disturbances, AV-block, arrhythmias, pericardial effusion, and angina have been reported.[17]

Echocardiographic finding of cardiac tumours suspicious of being haemangiomas is extremely rare, and, similar to lipomas, histological evidence usually is lacking. They are varying in size between less than 1 and more than 8 cm and are pediculated, non-calcified but hyper-dense, and most often attached to the left or right ventricular wall, but can occur in any cardiac cavity.[18]

On CMR examination, cardiac haemangiomas show intermediate signal intensity on T_1-weighted images, which is comparable to myocardium. On T_2-weighted images, high signal intensity is typically observed. Cardiac haemangiomas enhance intensely and very rapidly after administration of contrast media indicating a high vascularity. However, early enhancement after gadolinium administration can be inhomogeneous because of interspersed calcifications and fibrous septations within the tumour.[19]

On unenhanced cardiac CT, haemangiomas are shown as well-delineated masses heterogeneous to low density. They are intensely enhanced after intravenous contrast administration.[19]

Rhabdomyoma

Rhabdomyomas are the most common primary cardiac tumour in children. They are myocardial hamartomas, and up to 50% occur in association with tuberous sclerosis.[20] Most frequently, rhabdomyomas are located in the myocardium of both ventricles and multiplicity is common. The size of the tumours may vary from miliary nodules measuring less than 1 mm up to masses of 10 cm diameter, and they tend to disappear spontaneously, although occasionally surgical resection is necessary.

Echocardiography may be diagnostic of an intra-cardiac mass by demonstrating the presence of an intra-cavitary, echodense structure. Rhabdomyomas will more frequently be lobulated in shape and ventricular in origin.[21] When occurring intra-mural, a circumscribed ventricular wall thickening of the left and/or right ventricle can be detected. Multi-focal lesions are common.

On CMR examination, rhabdomyomas show a homogeneous iso-intense signal on T_1-weighted images compared to the surrounding myocardium. On T_2-weighted images, hyper-intense signal is observed within the mass, which is different from the surrounding myocardium. Perfusion imaging shows complete opacification of the full thickness of the mass with almost immediate opacification of the central portion. Early gadolinium uptake is more intense compared to the surrounding myocardium, and abnormal late gadolinium enhancement may be observed across the entire thickness of the mass.[22]

Fibroma

Cardiac fibroma is a congenital neoplasm and is the second most common cardiac tumour in children. It is the paedriatic cardiac tumour most commonly resected. However, 15% of cardiac fibromas occur in adolescence and adults. There is an increased risk of cardiac fibromas in patients with Gorlin syndrome, which is characterized by multiple nevoid basal cell carcinomas of the skin, jaw cysts, and bifid ribs. Less than 14% of these patients have cardiac fibromas (20). The morphological features of cardiac fibromas are characteristically solitary, circumscribed, firm, grey–white, and often centrally calcified. The cellularity of the lesion decreases as fibrosis and the patient's age increase. Common clinical manifestations in patients with cardiac fibromas are heart failure, arrhythmias, and sudden death. Cardiac fibromas are usually located within the myocardium of the ventricles, and the inter-ventricular septum and the lateral wall of the left ventricle are most commonly involved. The size of the tumours is rather large and varies between 2 and 5 cm.

In the echocardiographic evaluation, cardiac fibromas appear as non-contractile solid masses often attached to the left ventricular septum and well demarcated from the surrounding myocardium by multiple calcifications.

On CMR examination, cardiac fibromas may manifest as a discrete mural mass or focal myocardial thickening. These lesions appear iso-intense to hyper-intense relative to myocardium on T_1-weighted images and hypo-intense with T_2-weighted images, findings which are characteristic for fibrous tissue. After intravenous administration of gadolinium, contrast media cardiac fibromas do not show enhancement during first-pass perfusion, suggesting a low vascularity. However, 10 min after contrasts administration, intense late gadolinium enhancement was observed reflecting an increased extracellular volume of distribution within the ventricular myocardium.[23]

Primary Malignant Cardiac Tumours

The majority of primary malignant cardiac tumours are sarcomas. Primary cardiac sarcomas by definition are confined to the heart or pericardium at the time of diagnosis. The most common types are angiosarcoma (37%), unclassified or undifferentiated sarcoma (24%), malignant fibrous histiocytoma (11–24%), leiomyosarcoma (8%), and osteosarcoma (3–9%).[3] Primary cardiac sarcomas most commonly metastasize to the lungs, but also to the lymph nodes, bone, liver,

brain, bowel, spleen, adrenal glands, pleura, diaphragm, kidneys, thyroid, and skin.[24]

Cardiac sarcomas that typically affect the left atrium are malignant fibrous histiocytoma, osteosarcoma, and leiomyosarcoma. Patients present with symptoms of mitral valve obstruction such as dyspnea and heart failure.

Approximately 80% of cardiac angiosarcomas occur in the right atrium and involve the pericardium. Therefore, symptoms of right-sided heart inflow obstruction or cardiac tamponade are common.

Angiosarcoma

Echocardiographic imaging helps to differentiate between benign myxomas and malignant infiltrative growing angiosarcomas by evidence of infiltration of the cardiac wall. With the evidence of hemorrhagic pericardial effusion, a malignant tumour should be considered. Angiosarcomas appear as an inhomogeneous mass with hypo-dense necrotic and haemorrhagic zones, usually located in the right atrium. A possible infiltration of the pericardium, the tricuspid valve, and the vena cava can be displayed.

On CMR examination, angiosarcomas are depicted as large, heterogeneous, invasive right atrial masses frequently with extensive pericardial involvement and haemorrhagic pericardial effusion. Pericardial and extra-cardiac invasion, valvular destruction, tumour necrosis, and metastases are frequently seen. Cardiac angiosarcomas have a marked heterogeneity of signal intensity on T_1-weighted and T_2-weighted images. Hyper-intense foci in T_1-weighted images may correspond to intra-tumoural haemorrhage, whereas hyper-intense foci on T_2-weighted images may represent cystic or necrotic parts of the tumour.[25] Vascular structures within the tumour may appear hyper-intense on cine sequences, which has been described as "cauliflower" appearance.[16] Cardiac angiosarcomas typically show diffuse and intense contrast enhancement that has been described as "sunray" appearance.[26]

Other Sarcomas

Undifferentiated sarcoma, malignant fibrous histiocytoma, leiomyosarcoma, rhabdomyosarcoma, osteosarcoma, fibrosarcoma, and liposarcoma are rare primary malignant cardiac tumours. However, approximately 10% of surgically resected cardiac tumours are primary sarcomas.

For the echocardiographic evaluation of the other cardiac sarcomas, the same rules may be applied as for angiosarcomas, except they are not characteristically located within the right atrium, but elsewhere in the heart predominantly within the left atrium. They typically originate from the roof of the left atrium as a criterion of discrimination from myxomas

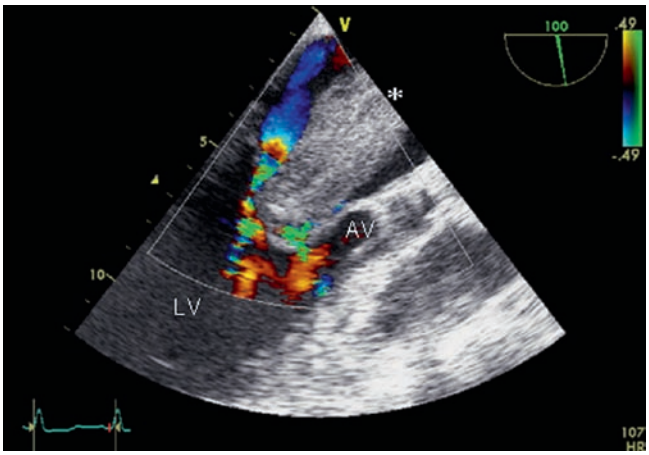

Fig. 29.7 Undifferentiated primary cardiac sarcoma (*asterisk*) in a 67-year-old female patient with the history of progressive dyspnea due to functional mitral stenosis caused by diastolic occlusion of mitral inflow by the large sarcoma shown by colour Doppler. Note the similar appearance of the sarcoma in trans-oesophageal echocardiographic imaging compared to the myxoma in Fig. 29.1 except of the sarcoma's origin from the left atrial roof. *LV* left ventricle; *AV* aortic valve

(Fig. 29.7, Video 29.7), as well as infiltration of the surrounding cardiac wall or pericardial structures (Fig. 29.8, Video 29.8). They appear as large, mobile, and inhomogeneous masses with zones of necrosis and haemorrhage and are indistinguishable from angiosarcoma. Only osteosarcomas can be differentiated by typically showing calcification.

On CMR examination, cardiac sarcomas are typically shown as large, heterogeneous, broad-based masses that frequently occupy most of the affected cardiac chamber or multiple chambers (Video 29.9). Pericardial and extra-cardiac invasion, tumour necrosis, and metastases are all characteristic features of malignant lesions. Cardiac sarcomas enhance heterogeneously with non-enhancing areas corresponding to necrosis.

Cardiac CT is very helpful in the evaluation of cardiac osteosarcoma because it typically shows calcifications.[3]

Primary Cardiac Lymphoma

Primary cardiac lymphoma involves only the heart or pericardium at the time of diagnosis with no evidence of extracardiac lymphoma.[3] Although 16–28% of patients with disseminated lymphoma have cardiac involvement, primary cardiac lymphoma is very rare. It is seen mostly in immunocompromised patients, particularly in association with the acquired immunodeficiency syndrome.

In the echocardiographic evaluation, an immobile, sometimes polypoid, mass appears predominantly in the right atrium. It is commonly combined with a pericardial effusion.

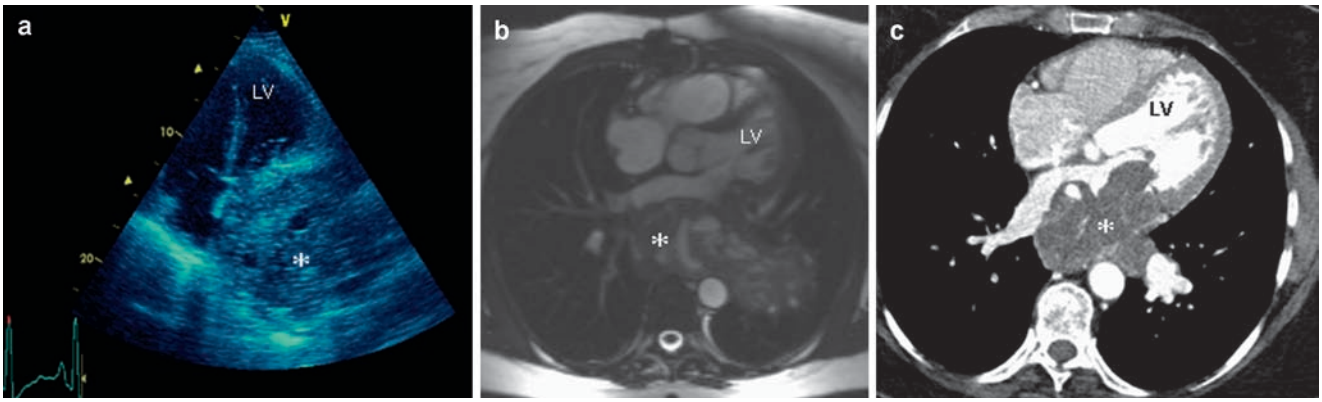

Fig. 29.8 Large rhabdomyosarcoma (*asterisk*) first detected by transthoracic echocardiography **(a)** in an 83-year-old female patient with signs of progressive dyspnea. The tumour that fills out the entire dilated left atrium in echocardiography appears of heterogeneous texture with hypo-dense zones of necrosis and hyper-dense sclerotic spots. Cardiac MR **(b)** revealed a large rhabdomyosarcoma (7.0 × 13.1 cm) with cystic areas and strong contrast agent uptake in border regions as well as with extensive infiltration of the left lung and less infiltration of the right lung, but no metastases. Cardiac CT **(c)** 1 month after cardiac MR **(b)** reveals rapid progression of tumour size now being 9.1 × 14.3 cm with progressive building of a wall around the left lung hilus and compression of the oesophagus. *LV* left ventricle

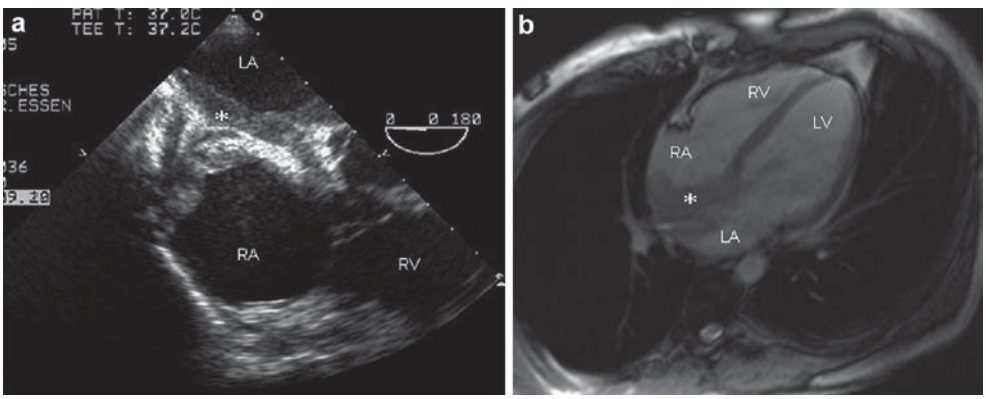

Fig. 29.9 Primary cardiac lymphoma in a 25-year-old male patient with acute myeloid leukemia. Trans-oesophageal echocardiographic imaging **(a)** shows massive growth of a heterogeneous tumour mass (*asterisk*) within the inter-atrial septum with infiltration of the right atrial roof. Cardiac MR **(b)** reveals tumour manifestation beginning in the right atrial roof or superior vena cava entrance, which is walled in by the tumour, and tumour growth up to pulmonary artery descending aorta, into the posterior right atrial wall and the inter-atrial septum and caudal up to the inferior vena cava and coronary sinus. The tumour (*asterisk*) is clearly hyper-intense on the T2-weighted image and enhances markedly after contrast administration, but no myocardial late enhancement was found. *LA* left atrium; *RA* right atrium; *RV* right ventricle; *LV* left ventricle

Infiltration of the cardiac structures can occur (Fig. 29.9, Video 29.10).

On CMR examination, poorly marginated and heterogeneous lesions are observed, which are iso-intense to slightly hypo-intense on T_1-weighted images and iso-intense on T_2-weighted images relative to myocardium. Contrast administration produces a heterogeneous pattern of enhancement.[20]

With cardiac CT, primary cardiac lymphomas are hypo-attenuating or iso-attenuating relative to myocardium and demonstrate heterogeneous enhancement after intravenous contrast administration.[27]

Secondary Cardiac Tumours, Metastases

Tumours within the chest can cause displacement and compression of the heart or infiltrate the heart and pericardium directly. High-resolution imaging of such tumours and proof of infiltration are important because such tumours are usually non-resectable. Cardiac metastases can arise from almost any malignant tumour, and melanomas have been reported to have the highest frequency of seeding into the heart at autopsy.

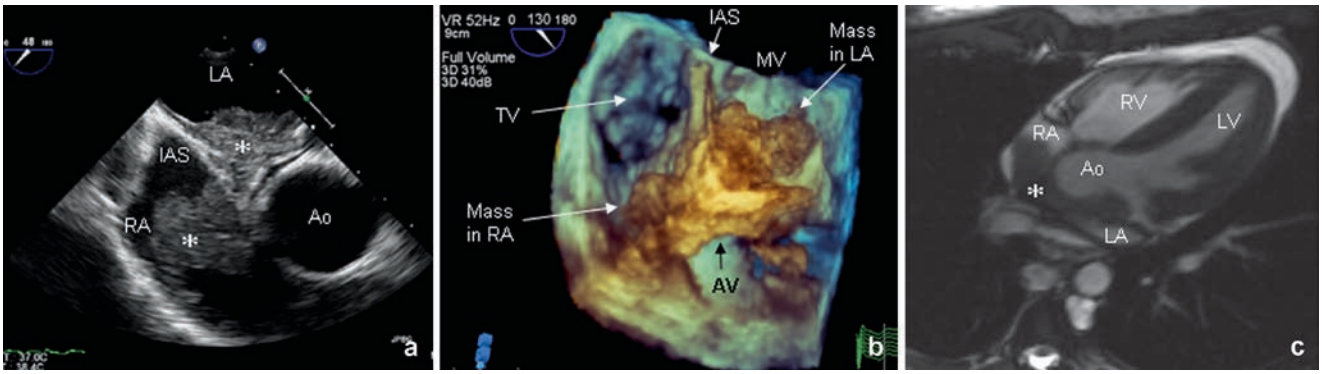

Fig. 29.10 Highly malignant, cerebellary non-Hodgkin lymphoma in a 19-year-old male patient with secondary cardiac lymphoma manifestation in both atria. Trans-oesophageal echocardiographic imaging shows growth of lymphoma masses (*asterisks*) of heterogeneous texture on both sides of the inter-atrial septum (IAS) **(a)**. Real-time 3D echocardiography **(b)** provides greater information on the location and extent of lymphoma manifestation. Cardiac MR **(c)** shows lymphoma growth iso-intense to the myocardium into left and right atrium (*asterisk*), as well as sub-total occlusion of vena cava superior causing thrombus formation into right vena subclavia, left vena brachiocephalica, and right vena jugularis. *LA* left atrium; *RA* right atrium; *Ao* aorta; *RV* right ventricle; *TV* tricuspid valve; *MV* mitral valve; *LV* = left ventricle

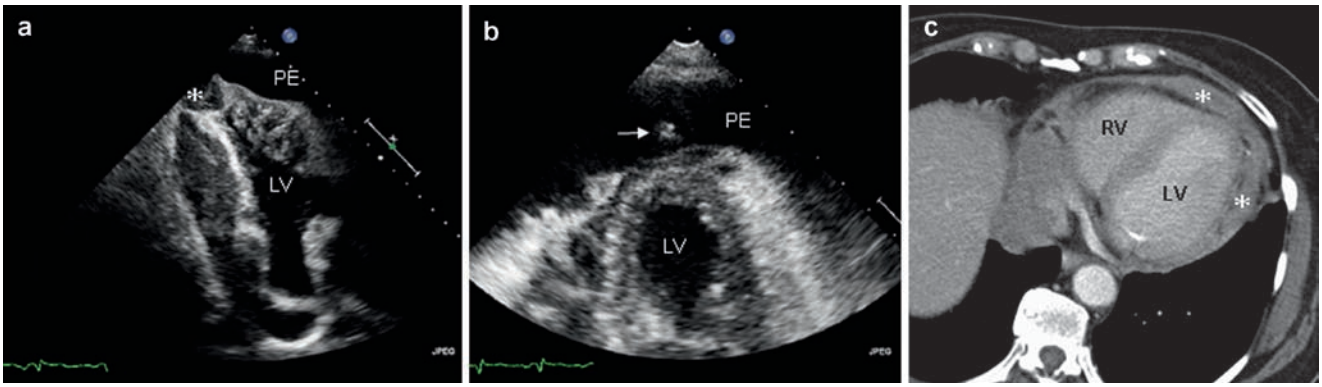

Fig. 29.11 Secondary cardiac manifestation of a low-malignant non-Hodgkin lymphoma in a 77-year-old female patient. Transthoracic echocardiography shows massive intra-pericardial lymphoma growth with compression of the right heart chambers, as well as infiltrative growth into right ventricular apex (*asterisk*) **(a)**. At the time of echocardiographic examination, cardiac lymphoma manifestation was unknown, and diagnosis of haemodynamic important pericardial effusion (PE) was priority. Surprisingly, echo-guided pericardiocentesis **(b)** with the needle tip safely placed in the echo-free pericardial space (*arrow*) did not allow fluid aspiration. Cardiac CT **(c)** revealed the diagnosis of circular intra-pericardial lymphoma growth (*asterisks*) as the explanation of the punctio sicca. *PE* pericardial effusion; *LV* left ventricle; *RV* right ventricle

Secondary cardiac lymphoma show similar echocardiographic characteristics as primary cardiac lymphomas (Figs. 29.10 and 29.11, Videos 29.11a, b, and 29.12a, b). Common echocardiographic findings associated with cardiac metastases are malignant pericardial effusion sometimes with enclosed tumour masses with partially bizarre surface structures. The infiltrated cardiac walls appear with a hyper-dense thickening (Figs. 29.12 and 29.13, Videos 29.13 and 29.14). Wall motion abnormalities in these regions are common. Application of echo contrast agents can reveal the tumour perfusion and helps discrimination of the metastasis from the surrounding tissue (Fig. 29.14, Video 29.15a, b).

On CMR examination, the extension of tumours within the chest (Fig. 29.15, Video 29.16), their relation to cardiac structures, signs of invasion (Video 29.17), evidence of haemorrhagic, and serous pericardial effusion can be demonstrated very effectively due to the large field of view and the high contrast resolution. This information is necessary to assess potential resectability of the tumour (Video 29.18). Cardiac CT, with its excellent spatial resolution, may provide comparable information as CMR; however, CMR has been shown to be even more effective in demonstrating invasion of the pericardium and myocardium.[28]

Thrombus

Thrombi represent the most frequently found intra-cardiac masses. Mitral valve disease and atrial fibrillation are the predominant risk factors for thrombus formation within the

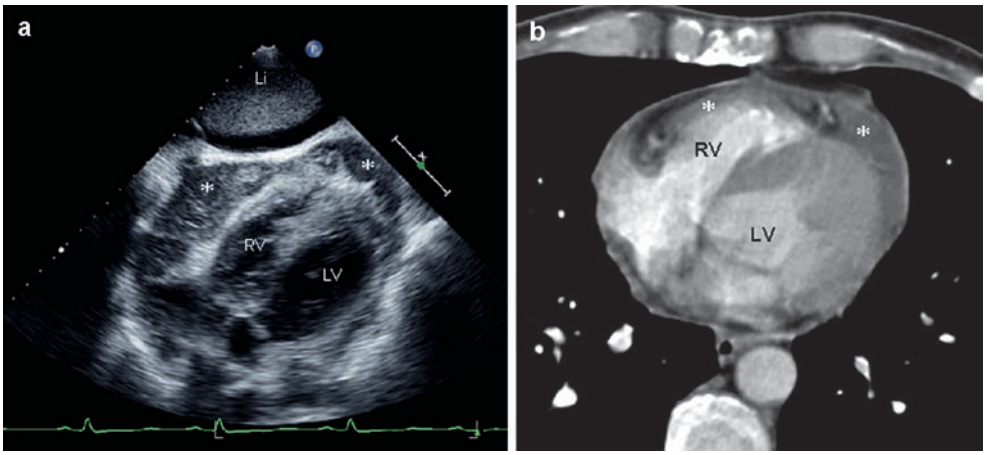

Fig. 29.12 Secondary cardiac manifestation of thymus carcinoma in a 52-year-old male patient with infiltrative pericardial and myocardial growth. Trans-thoracic echocardiographic image from a subcostal view **(a)** shows the tumour (*asterisks*) hypo-dense relative to the myocardium and with heterogeneous appearance. **(b)** Cardiac CT shows the tumour reaching from above the aortic arch to the heart apex with displacement of the entire heart and marked intrapericardial *growth* (*asterisks*) and compression of right heart chambers. *Li* liver; *RV* right ventricle; *LV* left ventricle

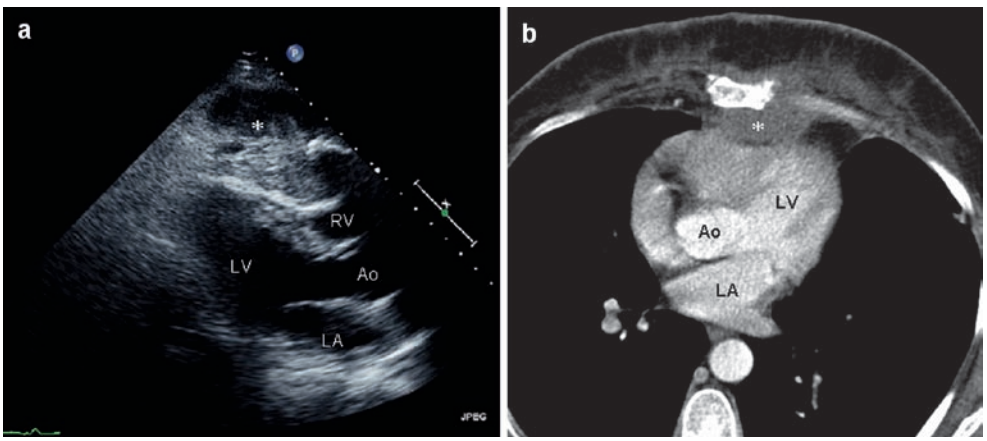

Fig. 29.13. Sternal metastasis of breast carcinoma in a 47-year-old female patient with marked displacement of the heart and compression of right heart chambers. Trans-thoracic echocardiographic imaging in a parasternal view **(a)** shows an isodense tumour mass of heterogeneous appearance (*asterisk*) with infiltrative growth into right heart pericardium. Cardiac CT with contrast application **(b)** shows the large sternal metastasis (8.2 × 6.4 cm) (*asterisk*) with infiltrative growth into the mediastinum and pericardium. *LV* left ventricle; *R* right ventricle; *LA* left atrium; *Ao* aorta

left atrium, especially within the left atrial appendage. Thrombi within the left ventricle are typically found in areas of severe wall motion abnormalities such as akinetic, dyskinetic, or aneurysmal myocardial segments after myocardial infarction. Severe impairment of global left ventricular function may also increase the risk for thrombus formation within the left ventricular cavity. Thrombus morphology correlates with the risk for systemic embolization: mobile or exophytically growing thrombi carry a risk of 50% for systemic embolism, whereas this risk is 10% for immobile, mural thrombi. Right-sided thrombi are found less frequently and may represent transitory thrombi in patients with deep vein thrombosis and pulmonary embolism. However, in patients with rather rare systemic diseases such as Behcet disease, Löffler's endocarditis, Churg-Strauss syndrome, and coagulopathies, thrombi can be found in all cardiac chambers.

Echocardiographic appearance of intra-cardiac thrombi is heterogeneous. Because thrombi can mimic any other cardiac mass, echocardiography cannot reliably differentiate between thrombi and tumours (Figs. 29.18–29.22, Videos 29.19a, b, 29.20a–d, 29.21–29.23a–c). Thrombi show a different echodensity, depending on age and degree of thrombus organization (Fig. 29.19, Video 29.20). Even vascularization can be found in some cases. Sometimes a layering phenomenon can be found, indicating appositional thrombus growth. Confounding risk factors for thrombus

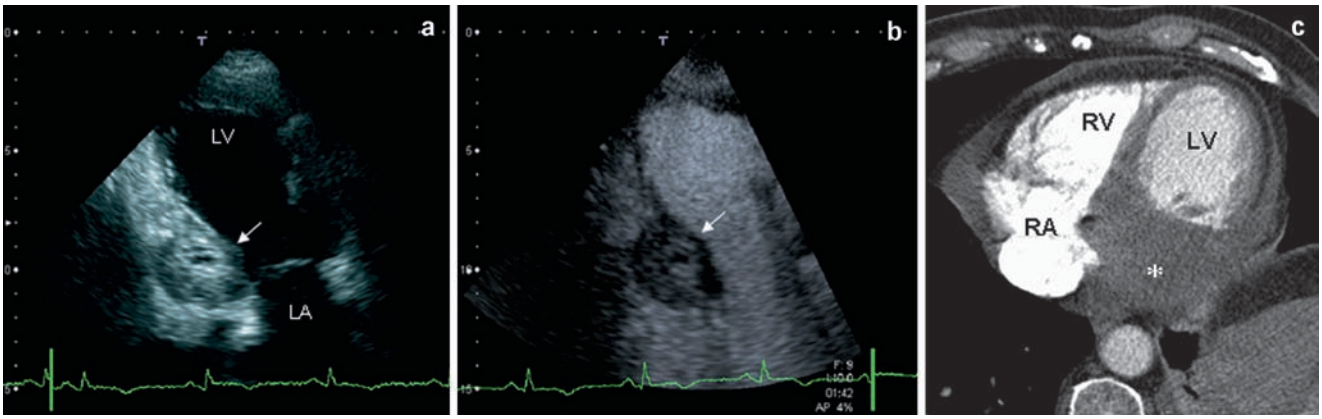

Fig. 29.14 Cardiac metastasis of urothel carcinoma in a 70-year-old male patient. In trans-thoracic echocardiography, the metastasis located in the basal inferior wall of the left ventricle (*arrow*) appears with a typical pattern of a hypo-dense outer region that is clearly demarcated from myocardial tissue and a hyper-dense central region **(a)**, which enhances markedly after myocardial contrast application **(b)** indicating central perfusion of the metastasis. **(c)** Cardiac CT shows the metastasis (*asterisk*) as a homogeneous mass, which is iso-intense relative to the myocardium. *LV* left ventricle; *LA* left atrium; *RV* right ventricle; *RA* right atrium

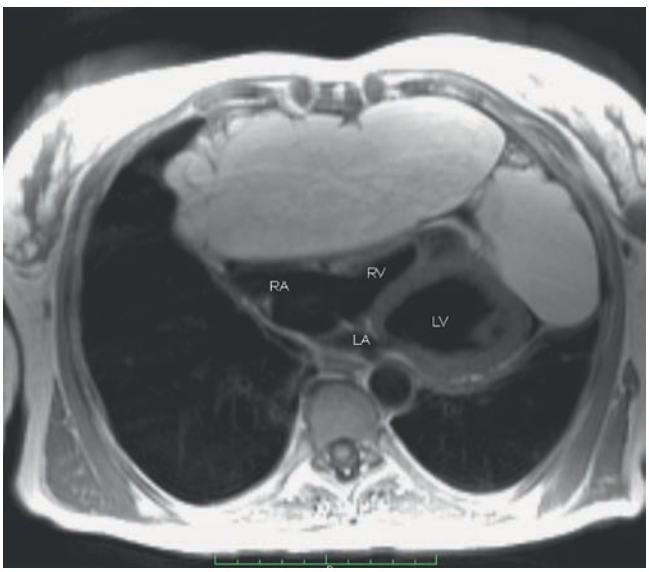

Fig. 29.15 T_1-weighted image of metastases in the chest of a cystadeno-carcinoma. Huge fluid containing cysts with septations are shown to compress and dislocate the cardiac chambers without signs of tumour invasion. The patient suffered from severe dyspnea

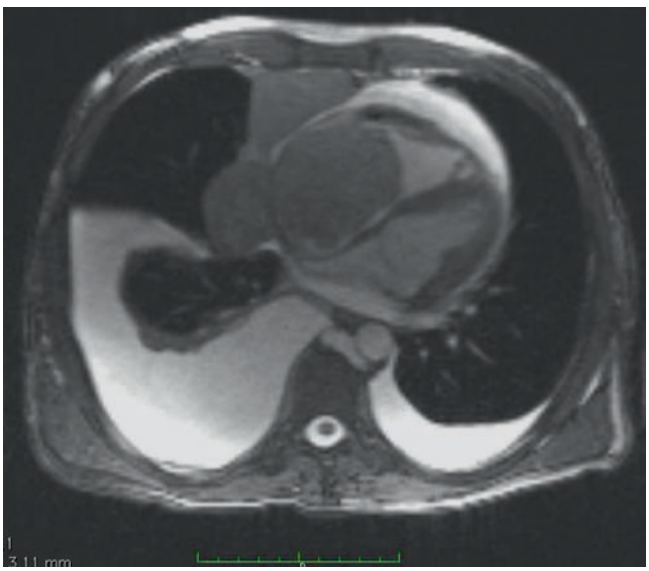

Fig. 29.16 Cine CMR of a thymus carcinoma invading the right atrium from the anterior mediastinum and obstructing the right ventricular inflow on the level of the tricuspid valve. Pericardial and pleural effusion

formation, such as wall motion abnormalities (Fig. 29.20, Video 29.21), atrial dilatation (Fig. 29.18, Video 29.19), and slow flow with spontaneous echo contrast (Fig. 29.18, Video 29.19), allow differentiation to cardiac tumours. Reduced velocities within the left atrial appendage due to atrial fibrillation can be detected by pulsed wave Doppler and can predict the risk for thrombus formation (Fig. 29.22, Video 29.23).

On CMR examination, the appearance of thrombus is dependent on the composition and physico–chemical properties of its components. Paramagnetic haemoglobin degradation products, such as intra-cellular methaemoglobin, haemosiderin, and ferromagnetic ferritin, accumulate with ageing of the thrombus. On T_1-and T_2-weighted images, these haemoglobin degradation products are hypo-intense. Detection and characterization of thrombi with dark-blood prepared T_1-and T_2-weighted images is, however, sub-optimal because slow blood flow around thrombi may produce slow flow artefact, thereby impeding the detection of thrombi. With cine sequences, however, fresh thrombus may show

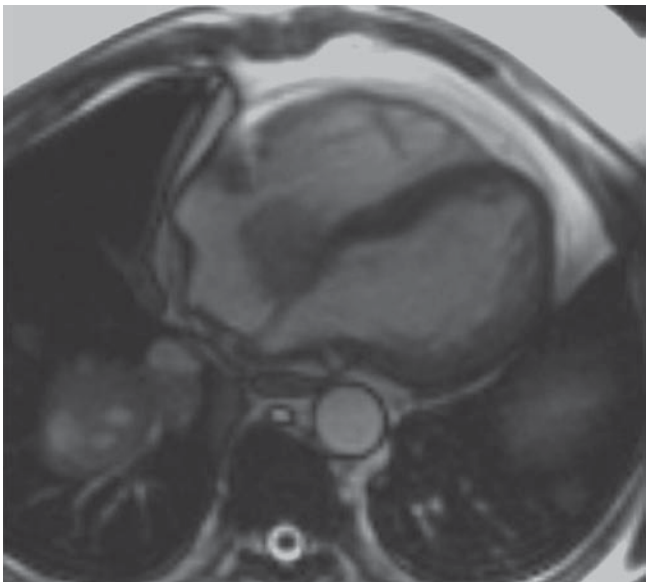

Fig 29.17 Cine CMR showing a metastasis of a melanoma attached to the right-sided inter-atrial septum. One large and several smaller metastases in both lungs are also demonstrated

hyper-intense signal intensity (Fig. 29.23) and sub-acute and old thrombi low signal intensity (Fig. 29.24). Thrombi generally do not enhance after administration of contrast media; however, chronic organized thrombi may occasionally show patchy peripheral contrast uptake.[29] Delayed contrast CMR has been shown to be highly helpful in detecting intra-cardiac thrombi, which have very low signal intensity (black) with this technique. On the other hand, adjacent infarcted myocardium shows very high signal intensity (white). During first pass of the contrast media through the cardiac chambers, left ventricular cavity is strongly enhanced with abnormal intra-ventricular structures appearing dark in comparison.[30] Contrast-enhanced inversion recovery CMR allows visualization of small thrombi (<1 cm), although some may be missed due to flow turbulence in proximity to dysfunctional myocardial wall segments or lack of contrast between a mural thrombus and the adjacent myocardium. In this case, a combination of cine CMR sequences and contrast-enhanced inversion recovery CMR sequences may overcome that problem.[31]

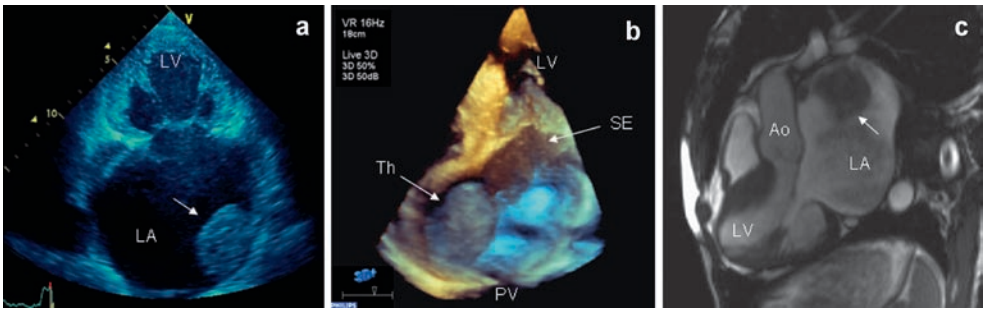

Fig. 29.18 Left atrial thrombus in a monstrous dilated left atrium (10.0 × 10.5 cm) in a 46-year-old male patient with long-standing hypertrophic restrictive cardiomyopathy. Transthoracic echocardiographic imaging **(a)** shows the isodense appearance of the large immobile thrombus (4 × 5 cm) (*arrow*) broadly attached to left atrial wall. Note the marked spontaneous echo contrast (SE) passing from the left atrium through the mitral valve. Real-time 3D echocardiography reveals the true shape and size of the thrombus (Th) **(b)** and its exact location relative to pulmonary vein (PV) entrance. **(c)** Cardiac MR shows the thrombus (*arrow*) with hypo-intense appearance and no contrast uptake after contrast application. *LV* left ventricle; *LA* left atrium; *Ao* aorta

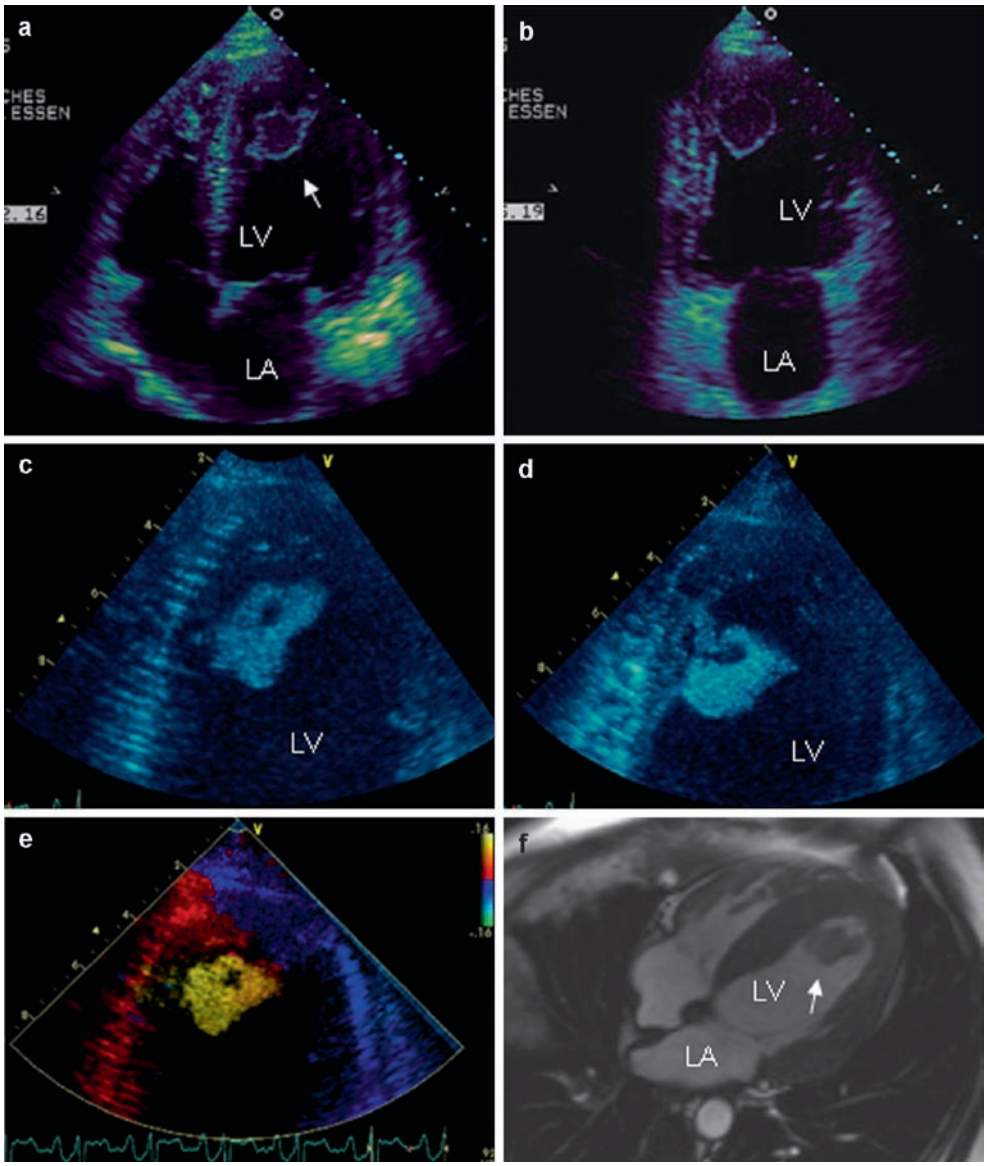

Fig. 29.19 Apical left ventricular thrombus in a 32-year-old male patient with thrombophilia due to factor × mutation. Transthoracic echocardiographic imaging in apical 4-chamber **(a)** and 2-chamber view **(b)** shows typical appearance of a fresh thrombus (*arrow*) with hyper-dense outer border and hypo-dense centre. The jelly-like thrombus is highly mobile and deformable and only partly attached to the infero-apical wall. After a 10-day follow-up under intensive anti-coagulation, the thrombus became markedly more organized and stiffer **(c, d)**. Colour-coded tissue Doppler imaging (TDI) provides still image documentation of incoherent thrombus motion relative to cardiac tissue **(e)**. In cardiac MR **(f)** the jelly-like thrombus (*arrow*) appears to be only attached by thin threadlike structures to the apical wall. *LV* left ventricle; *LA* left atrium

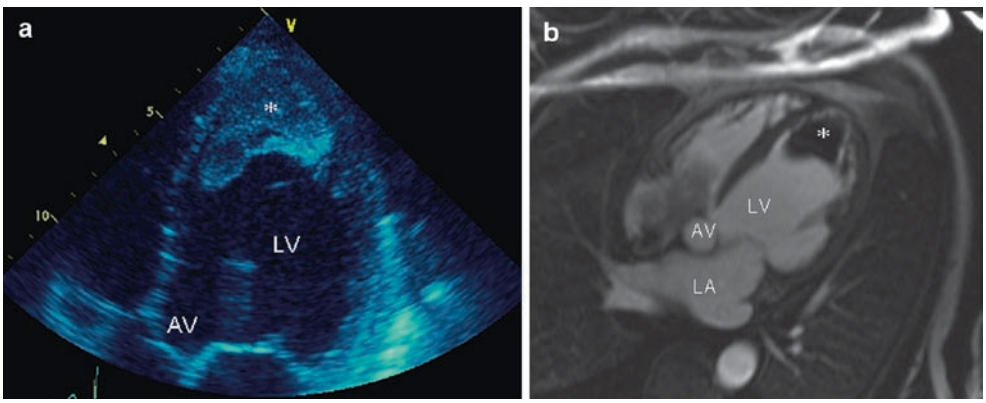

Fig. 29.20 Large thrombus formation in an apical left ventricular aneurysm in a 54-year-old male patient after apical myocardial infarction. Transthoracic echocardiographic imaging **(a)** shows a large immobile thrombus (*asterisk*) with heterogeneous appearance with hypo-dense areas and hyper-dense sclerotic spots. Cardiac MR **(b)** shows the thrombus (*asterisk*) with hypo-intense appearance and no contrast uptake after contrast application. *AV* aortic valve; *LV* left ventricle; *LA* left atrium

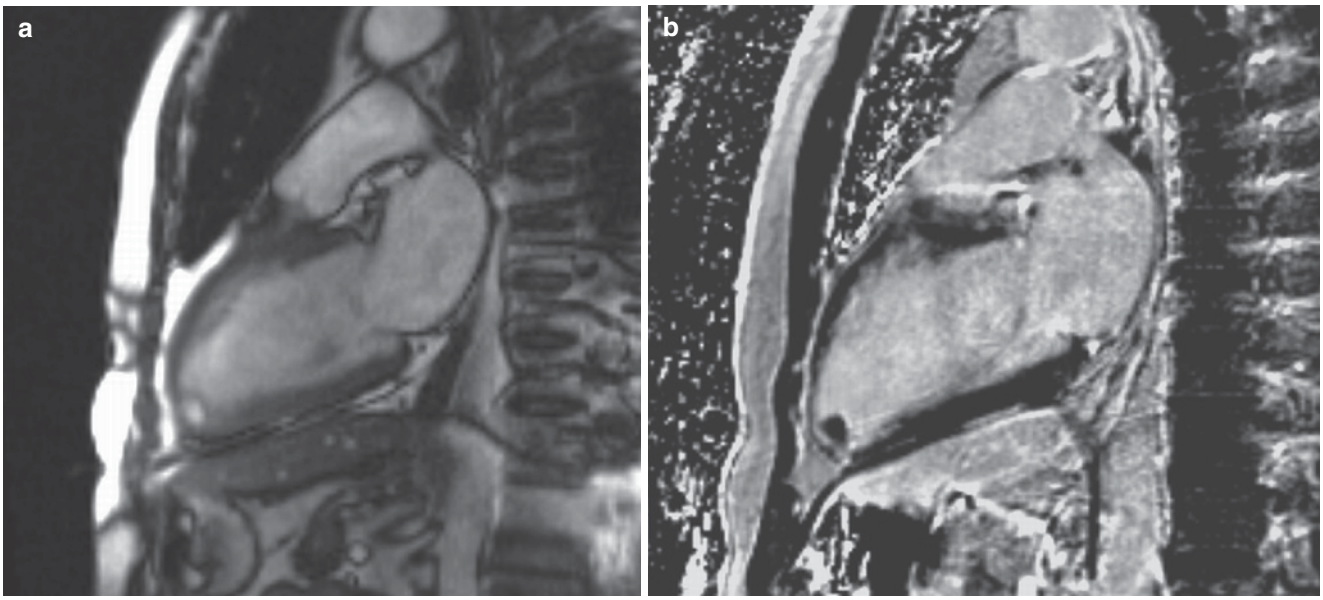

Fig. 29.21 Multiple right atrial thrombi in a 60-year-old male patient with history of cerebral transient ischaemia attacks. Trans-oesophageal echocardiographic imaging **(a)** shows multiple mobile hypo-dense thrombi attached to the right-sided inter-atrial septum and right atrial walls. In cardiac MR **(b)** 2 days later only one thrombus (*arrow*) was detectable, shown hypo-intense in TrueFISP-Sequences. *LA* left atrium; *RA* right atrium

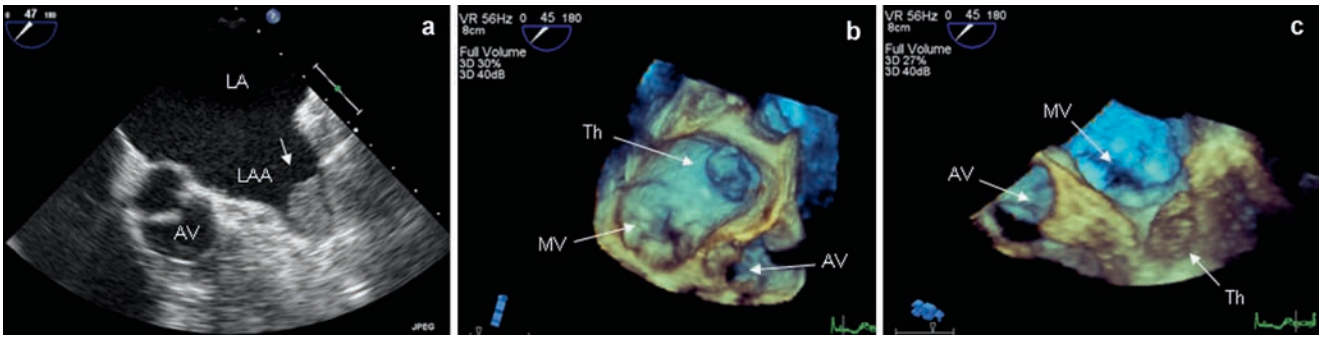

Fig. 29.22 Cardiac thrombus in the left atrial appendage in a 74-year-old male patient with moderate-severe mitral stenosis and dilated left atrium. Trans-oesophageal echocardiographic imaging in 2D mode **(a)** shows a 1.0 × 1.9 cm large isodense, slightly mobile thrombus (*arrow*) in the left atrial appendage (LAA). Real-time 3D imaging provides improved orientation by showing neighbouring cardiac structures in an enface view from left atrium to mitral valve (MV) **(b)**, as well as exact dimension of the thrombus (Th) within the appendage **(c)**. *LA* left atrium; *AV* aortic valve

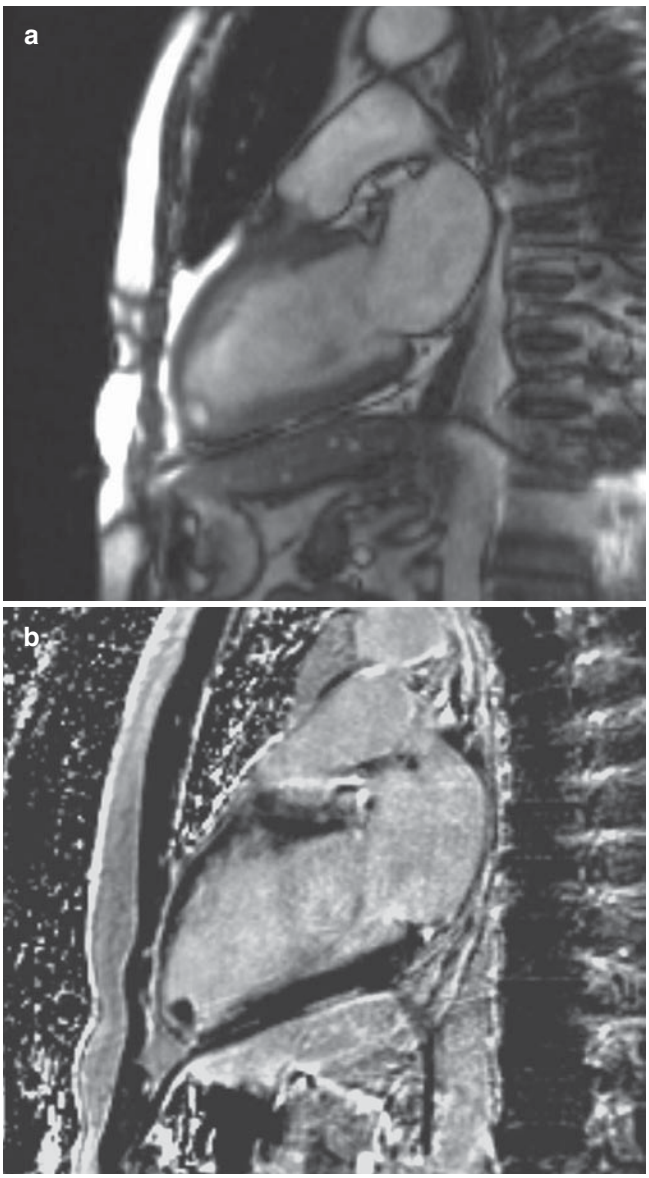

Fig. 29.23 Fresh thrombus in the left ventricular apex assessed with CMR. **(a)** A single image frame from a cine CMR loop in a left ventricular long-axis 2-chamber view shows the thinned wall of the left ventricular apex after myocardial infarction containing a thrombus depicted as a bright spherical mass surrounded by a dark rim. **(b)** With late gadolinium enhancement, the infarcted area of the left ventricular apex is depicted as hyper-intense (*white* = scar) and the thrombus black without any uptake of contrast media

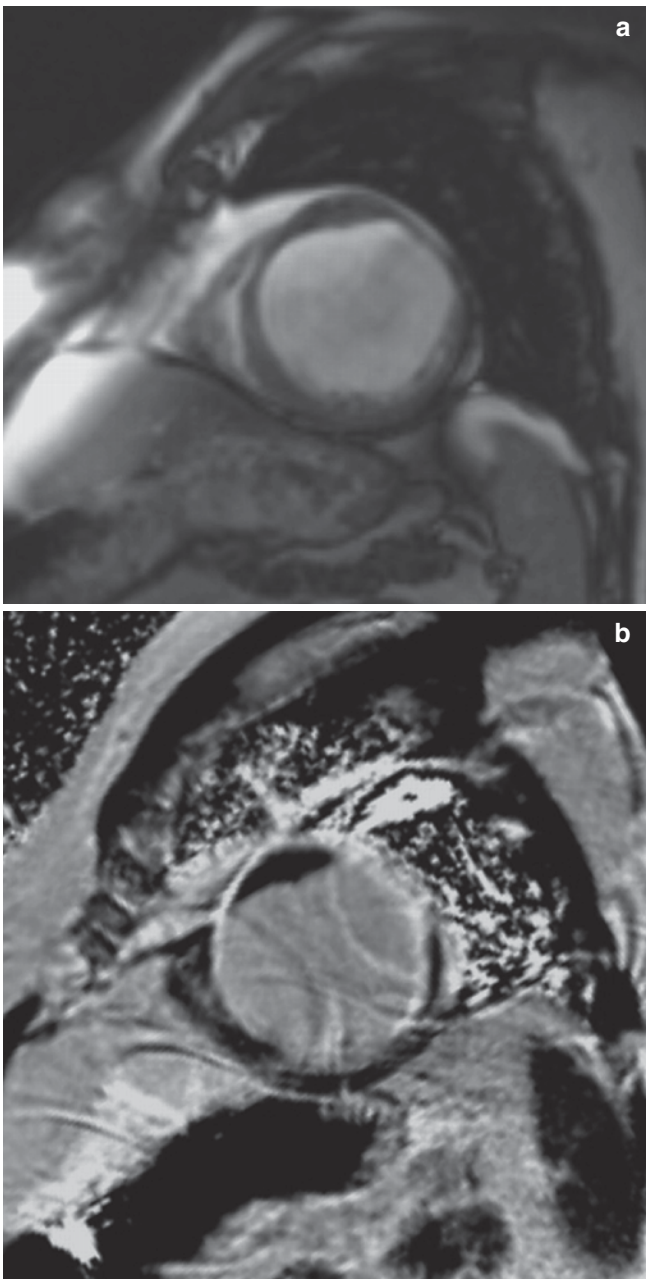

Fig. 29.24 Chronic mural thrombus in a patient with chronic antero-septal myocardial infarction and heart failure as assessed by CMR. **(a)** A single image frame from a cine CMR loop in a left ventricular short-axis view shows the thinned antero-septal wall with chronic myocardial infarction and a hypo-intense mural mass (thrombus) in the infarct zone. **(b)** With late gadolinium enhancement, the infarct area (*white* = scar) is depicted transmurally in the antero-septal segments and sub-endocardially (=non-transmural) in the lateral segment. In the antero-septal segments, the mural thrombus is depicted as hypo-intense (*black*) inside the *white* myocardial scar without any uptake of contrast media

References

1. Butany J, Nair V, Naseemuddin A, Nair GM, Catton C, Yau T. Cardiac tuomours: diagnosis and management. *Lancet Oncol*. 2005;6:219–228
2. Lam KY, Dickens P, Chan AC. Tumours of the heart. A 20-year experience with a review of 12,485 consecutive autopsies. *Arch Pathol Lab Med*. 1993;117:1027–1031
3. Burke A, Virmany R. Tumours of the heart and great vessels. In: *Atlas of Tumour Pathology. 3rd Series, fasc 16*. Washington, DC: Armed Forces Institute of Pathology; 1996
4. Araoz PA, Mulvagh SL, Tazelaar HD, Julsrud PR, Breen JF. CT and MR imaging of benign primary cardiac neoplasm with echocardiographic correlation. *Radiographics*. 2000;20:1303–1319
5. Tazelaar HD, Locke TJ, McGregor CG. Pathology of surgically excised primary cardiac tumors. *Mayo Clin Proc*. 1992;67:957–965
6. Stergiopoulos SG, Stratakis CK. Human tumours associated with Carney complex and germline PRKAR1A mutations: a protein kinase A disease. *FEBS Lett*. 2003;546:59–64
7. Edwards LC III, Louie EK. Transthoracic and transesophageal echocardiography for evaluation of cardiac tumours, thrombi, and valvular vegetations. *Am J Cardiac Imaging*. 1994;8:45–48
8. Klarich KW, Enriquez-Sarano M, Gura GM, Edwards WD, Tajik AJ, Seward JB. Papillary fibroelastoma: echocardiographic characteristics for diagnosis and pathologic correlation. *JACC*. 1997; 30:784–790
9. Kelle S, Chiribiri A, Meyer R, Fleck E, Nagel E. Papillary fibroelastoma of the tricuspid valve seen on magnetic resonance imaging. *Circulation*. 2008;117:e190-e191
10. Lembcke A, Meyer R, Kivelitz D, et al Papillary fibroelastoma of the aortic valve. Appearance in 64-slice spiral CT, magentic resonance imaging and echocardiography. *Circulation*. 2007;115:e3-e6
11. Kondruweit M, Schmid M, Strecker T. Papillary fibroelastoma of the mitral valve: appearance in 64-slice spiral CT, magnetic resonance imaging and echocardiography. *Eur Heart J*. 2008;29:831
12. Grande AM, Minizioni G, Perderzolli C, et al Cardiac lipomas. Description of 3 cases. *J Cardiovasc Surg*. 1998;39:813–815
13. Vanderheyden M, De Sutter J, Wellens F, Andries E. Left atrial lipoma: case report and review of the literature. *Acta Cardiol*. 1998;53:31–32
14. Mousseaux E, Idy-Peretti I, Bittoun J, et al MR tissue chracterization of a right atrial mass: diagnosis of a lipoma. *J Comput Assist Tomogr*. 1992;16:148–151
15. Lang-Lazdunski L, Oroudji M, Pansard Y, Vissuzaine C, Hvass U. Successful resection of giant intrapericardial lipoma. *Ann Thorac Surg*. 1994;58:238–240
16. Krombach GA, Saeed M, Higgins CB. Cardiac masses. In: Higgins CB, de Roos A, eds. *Cardiovascular MRI and MRA*. Philadelphia, PA: Lippincott Williams & Wilkins, 2003:136–144
17. Kober G, Magedanz A, Mohrs O, et al Non-invasive diagnosis of a pedunculated left ventricular hemangioma. *Clin Res Cardiol*. 2007;96:227–231
18. Kojima S, Sumiyoshi M, Suwa S, et al Cardiac hemangioma: a report of two cases and review of the literature. *Heart Vessels*. 2003;18:153–156
19. Oshima H, Hara M, Kono T, Shibamoto Y, Mishima A, Akita S. Cardiac hemangioma of the left atrial appendage: CT and MR findings. *J Thorac Imag*. 2003;18:204–206
20. Grebenc ML, Rosado de Christenson ML, Burke AP, Green CE, Galvin JR. Primary cardiac and pericardial neoplasms: radiologic-pathologic correlation. *Radiographics*. 2000;20:1073–1103
21. Fischer DR, Beerman LB, Prak SC, Bahnson HAT, Fricker FJ, Mathews RA. Diagnosis of intracardiac rhabdomyoma by two-dimensional echocardiography. *Am J Cardiol*. 1984;53:978–979
22. Wage R, Kafka H, Prasad S. Cardiac rhabdomyoma in an adult with previous presumptive diagnosis of septal hypertrophy. *Circulation*. 2008;117:e469-e470
23. Yan AT, Coffey DM, Li Y, et al Myocardial fibroma in Gorlin syndrome by cardiac magnetic resonance imaging. *Circulation*. 2006;114:e376-e379
24. Burke AP, Cowan D, Virmani R. Primary sarcomas of the heart. *Cancer*. 1992;69:387–395
25. Frank H. Cardiac and paracardiac masses. In: Manning W, Pennell D, eds. *Cardiovascular Magnetic Resonance*. New York: Churchill Livingstone; 2002:342–454
26. Kaminaga T, Takeshita T, Kimura I. Role of magnetic resonance imaging for the evaluation of tumours in cardiac region. *Eur Radiol*. 2003;13:L1-L10
27. Ceresoli Gl, Ferreri AJ, Bucci E, Ripa C, Ponzoni M, Villa E. Primary cardiac lymphoma in immunocompetent patients. *Cancer*. 1997;80:1497–1506
28. Mader MT, Poulton TB, White RD. Malignant tumours of the heart and great vessels: MR imaging appearance. *Radiographics*. 1997; 17:145–153
29. Paydarfar D, Krieger D, Dib N, et al In vivo magnetic resonance imaging and surgical histopathology of intracardiac masses: distinct features of subacute thrombi. *Cardiology*. 2001;95:40–47
30. Attili AK, Espinosa L, Gebker R. AJR teaching file: left ventricular mass in a patient with ischemic heart disease. *AJR*. 2007;188: S31–S34
31. Barkhausen J, Hunold P, Eggebrecht H, et al Detection and characterization of intracardiac thrombi on MR imaging. *AJR*. 2002;179: 1539–1544

Section 7

ADULT CONGENITAL HEART DISEASE

Chapter 30

THE ROLE OF ECHOCARDIOGRAPHY IN ADULT CONGENITAL HEART DISEASE

Edgar Tay, Mark Friedberg, Michael A. Gatzcollis, and Luc Mertens

CONTENTS

J. L. Zamorano et al. (eds.), *The ESC Textbook of Cardiovascular Imaging*
DOI: 10.1007/978-1-84882-421-8_30, © Springer-Verlag London Limited 2010

Introduction

Congenital malformations of the heart affect at least 1% of newborn infants. Without intervention, the prognosis for more complex forms is poor. Over the last few decades, advances in paedriatic cardiology and cardiac surgery have significantly improved patient management, and the majority of patients now survive into adulthood.[1, 2] This has led to new challenges as increasing numbers of congenital heart patients pass into the care of adult cardiac services. The need for expert knowledge to appropriately investigate the variable cardiovascular anatomy and pathophysiology and to manage this patient group has led to the expanding cardiological subspecialty of adult congenital heart disease (ACHD). This also poses new challenges with regard to cardiac imaging.

Overview of the Main Non-invasive Imaging Modalities

The different non-invasive modalities are, to a large extent, complementary. More than one modality is likely to be needed to address all the relevant clinical questions, particularly in the more complex cases.

Chest X-Ray

Chest X-ray (postero-anterior ± lateral) provides an inclusive overview of the heart, mediastinum, pulmonary vessels, lung fields, and thoracic skeleton. It remains a valuable and inexpensive modality, with only a low dose of ionizing radiation, for the serial comparison of heart size, pulmonary vascularity, and peripheral lung fields in ACHD.

Trans-thoracic Echocardiography (TTE)

TTE is generally the first-line cardiovascular imaging modality because of its convenience, availability, real-time acquisition, relatively modest cost, and safety. Its usefulness is, however, operator-dependent, particularly in ACHD. Limited echocardiographic windows and suboptimal penetration of ultrasound represent important limitations in adults who have undergone cardiovascular surgery.

Trans-oesophageal Echocardiography (TOE)

TOE has the advantage of clear access to more posterior parts of the heart, particularly for visualization of valves and the atrial septum. A disadvantage, however, is its invasive nature, generally requiring sedation or anaesthesia, making it less acceptable for serial investigation. The field of view provided by TOE is relatively narrow with limited access to extra-cardiac structures, and the alignment of the Doppler beam with unusually oriented flow jets can be challenging.

Cardiovascular Magnetic Resonance (CMR)

CMR is not restricted by body size or poor acoustic windows, and is versatile, offering a repertoire of velocity mapping and tissue contrast options, without any ionizing radiation. The versatility, however, presents challenges and consistency of methods between studies or between centres should not be assumed. CMR is widely regarded as the gold standard for measurements of right as well as left ventricular volumes, although analysis takes time and requires rigorously consistent methods of acquisition and measurement that may be hard to maintain in practice.

Multi-slice Computed Tomography (MSCT)

MSCT also offers robust spatial localization plus excellent spatial resolution in much shorter investigation times than CMR. It is well suited for imaging the epicardial coronary arteries and aorto-pulmonary collateral arteries and for the investigation of parenchymal lung disease, if present. ECG-gated cine MSCT allows measurements of biventricular size and function, albeit at a lower temporal resolution than CMR and subject to adequate opacification of the intra-ventricular blood volumes. In patients with a pacemaker or ICD, CT provides an alternative to CMR. The main drawback of MSCT is exposure to a substantial dose of ionizing radiation. Other drawbacks compared with CMR include less versatile tissue contrast and an inferior ability to evaluate cardiovascular physiology.

Describing Abnormal Cardiovascular Connections

For the description of anatomy, a common methodology can be used by all imaging techniques. This is called the segmental approach.[3] The heart is viewed as consisting of certain segments (the systemic and pulmonary veins, the atria, the ventricles, and the great vessels), which are defined by unique morphological characteristics. The segments are identified, and the connections between the segments are described. These are the veno–atrial connections, the atrio-ventricular connections, and the ventriculo-arterial connections.

Segmental analysis begins by defining the cardiac position and atrial arrangement (situs). The cardiac position may be levocardia, dextrocardia, or mesocardia. The atrial situs is "usual" (situs solitus, i.e. a right atrium on the right and a left atrium on the left), or "inverted" (situs inversus), or there can be bilateral duplication of one type of atrium known as right or left atrial "isomerism." Isomerism is generally associated with accompanying malformations. Atrio-ventricular and ventriculo-arterial connections are described as concordant (e.g. RA to RV or LV to aorta), discordant (e.g. LA to RV), double inlet (e.g. double inlet left ventricle), or single inlet (left AV-valve atresia). This requires identification of the ventricular chambers as morphological left or right ventricles, which is based on unique morphological characteristics for each ventricle. The great vessels are also identified, and the ventriculo-arterial connections are described. These connections can be concordant (normal), discordant (transposition of the great arteries), double outlet (double outlet RV), or single outlet (pulmonary atresia, common arterial trunk). Finally, communications between the left and right side are described (VSD, ASD, PDA).

The Role of Echocardiography in Different Congenital Defects

Atrial Septal Defects (ASD)

ASDs are common even in the adult population. When diagnosing patients with ASDs, the following should be addressed.

Type and Location of the ASD

- Secundum ASD (70%): The defect is localized centrally in the intra-atrial septum (Fig. 30.1, Video 30.1a, b). There can be multiple defects and the defect can be fenestrated.
- Primum ASD (11%) (Fig. 30.2, Video 30.2): Belongs to the spectrum of atrio-ventricular septal defects. This is associated with an abnormal left atrio-ventricular valve ("cleft" AV-valve).
- Sinus venosus ASD (SVC 5.3–10%, IVC 2%): This defect is located outside the limbus of the fossa ovalis, on the right septal surface adjacent to the drainage site of the superior (or inferior) vena cava. This is commonly associated with partially anomalous venous return of the right pulmonary veins.
- Coronary sinus ASD: This defect is in the wall that separates the coronary sinus from the left atrium (LA). It may be fenestrated or completely absent. An enlarged coronary sinus with a dropout between the LA and the coronary sinus is seen. The best view is a posteriorly tilted 4-chamber view.

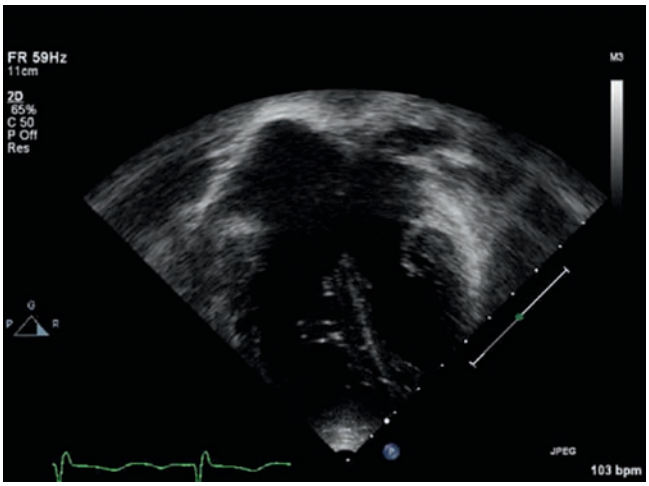

Fig. 30.2 Large primum defect. The left and right AV-valve are inserted at the same level, and this is associated with abnormal left AV-valve anatomy ("cleft" mitral valve)

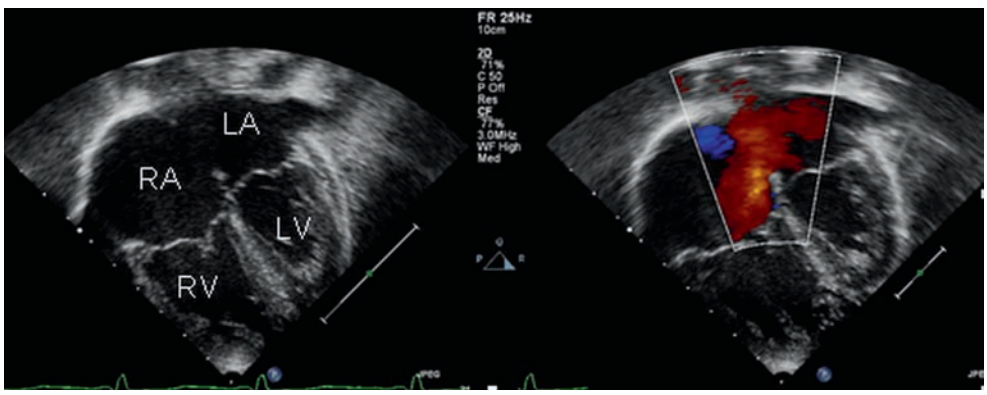

Fig. 30.1 Large secundum ASD. There is a large central defect with secondary right atrial and right ventricular dilatation

Size and Haemodynamic Effects

The atrial left-to-right shunt can cause right heart dilatation and can be associated with pulmonary hypertension. Signs of a haemodynamical significant ASD are:

- Right atrial and right ventricular (RV) dilatation.
- Abnormal "paradoxical" septal motion.
- Elevated right ventricular pressure.
- The right-to-left shunt can be quantified using the continuity equation (RVOT VTI × RVOT area/LVOT VTI × LVOT area), and a Qp/Qs > 2/1 is generally considered to be haemodynamically significant.

Associated Anomalies

A full segmental analysis needs to be performed because nearly any congenital anomaly can be associated with an ASD.[4] It is important to exclude pulmonary venous anomalies and interrupted IVC before interventional closure.

Mostly ASDs can be diagnosed using transthoracic imaging. However, if right heart dilatation is found without identifying an ASD, additional imaging including TOE or cardiac MRI can be indicated to diagnose a sinus venosus defect or anomalous pulmonary venous connections.

Imaging is important during interventional closure of secundum ASDs. Currently, interventional closure is monitored either by TOE or intra-cardiac echocardiography (ICE).[5] Before device closure, adequacy of the ASD rims needs to be defined. The role of 3D TOE is very promising.[6, 7]

Post-intervention or after surgical closure of ASDs, the following aspects are important;

- Residual atrial shunt
- Position of the device relative to other cardiac structures
- Residual RV dilatation
- Presence of pulmonary hypertension
- AV-valve regurgitation (especially after ASD primum correction)

Ventricular Septal Defects (VSD)

Imaging should define the following.

Type of VSD

- *Perimembranous* VSDs (60%) are localized in the membranous part of the septum and are characterized by fibrous continuity between the leaflets of the atrio-ventricular and arterial valve (Fig. 30.3, Videos 30.3a, b). These defects may have inlet, trabecular, or outlet extensions. Anterior deviation of the outlet part of the septum can cause right ventricular outflow tract obstruction (RVOTO) (tetralogy of Fallot). Posterior deviation can cause left ventricular outflow tract obstruction and can be associated with aortic arch anomalies (coarctation, interrupted aortic arch).
- *Muscular* VSD (20%) defects are localized in the muscular septum. The muscular VSDs can be divided into the inlet, trabecular, or outlet types. There may occasionally be multiple defects.
- *Doubly committed* VSDs (5%) are localized just below the aortic and pulmonary valve and are characterized by fibrous continuity between the aortic and pulmonary valve.

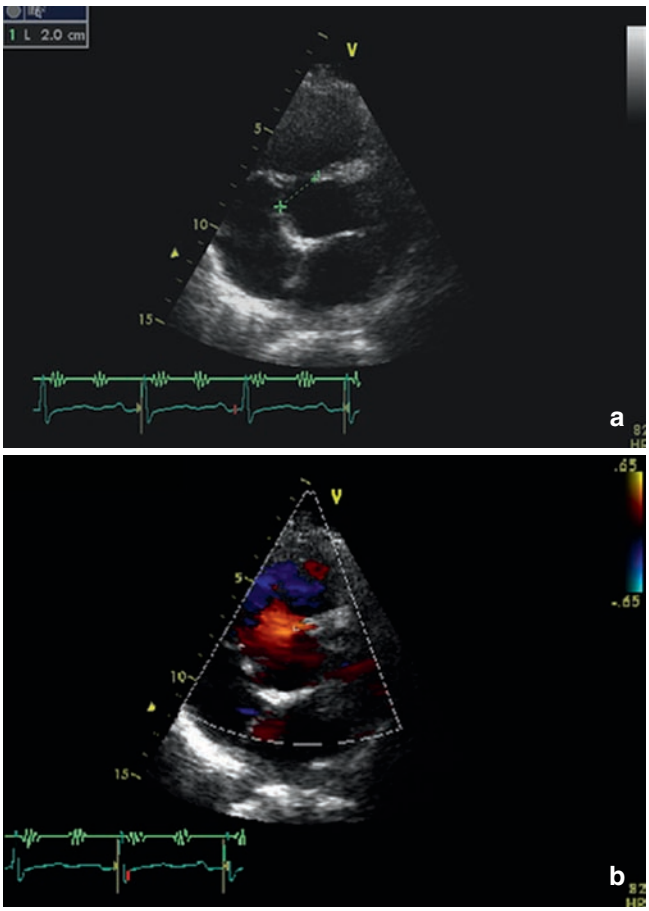

Fig. 30.3 **(a)** Perimembranous VSD as shown on a parasternal short-axis view. Typically the VSD is adjacent to the septal leaflet of the tricuspid valve. **(b)** Perimembranous VSD colour Doppler image of left to right shunt

Assessment of Defect Size and Haemodynamic Significance

- Size of the VSD should be measured in at least two dimensions. A VSD is small (<5 mm), moderate (5–10 mm), or large (>10 mm).
- The left-to-right shunt can cause left atrial and left ventricular dilatation. LA size and volume and LV dimensions should be measured. There can be associated secondary mitral insufficiency.

- A VSD can be associated with pulmonary arterial hypertension (PHT). RV pressures should be assessed based on calculating the VSD pressure Doppler gradient or tricuspid regurgitant jet. Obstructive PHT can develop and result in right-to-left shunting across the VSD (Eisenmenger's syndrome).
- The shunt can be calculated and a Qp/Qs > 1.5–2.0/1 is considered haemodynamically significant.

Associated Anomalies

Any congenital heart defect can be associated with a VSD. A full segmental analysis is crucial. Important associated lesions are:

- Aortic cusp prolapse with progressive AR
- Development of double chamber right ventricle (DCRV) due to hypertrophic RV muscle bands

Except for muscular defects, most defects are closed surgically if indicated. Post-surgical closure of a VSD, the following needs to be assessed:

- Residual VSDs
- Sub-aortic stenosis
- Sub-pulmonary stenosis
- Aortic insufficiency

Most VSD can be imaged using transthoracic imaging. Rarely TOE or other imaging modalities may be indicated.

Atrio-ventricular Septal Defect

Most adult patients with AVSDs have been diagnosed and surgically corrected during childhood. Unoperated AVSDs with large ventricular components are commonly associated with obstructive pulmonary hypertension (Eisenmenger syndrome).

Imaging unoperated AVSDs involves the following.

Identifying the Morphology[8, 9]

- Types of AVSDs: A *partial* AVSD is similar to a primum ASD. An *intermediate* AVSD is characterized by a primum ASD, a small restrictive VSD, separate right and left AV valves, and a trileaflet left AV valve. A *complete* AVSD has a primum ASD, a non-restrictive VSD, and a common AV valve (Fig. 30.4, Video 30.4).
- There is lack of offset between the left and right atrioventricular valves (AV) in the apical 4 chamber.
- The LVOT is elongated in the parasternal long axis. This is due to the presence of a single AV junction and unwedging of the aorta.

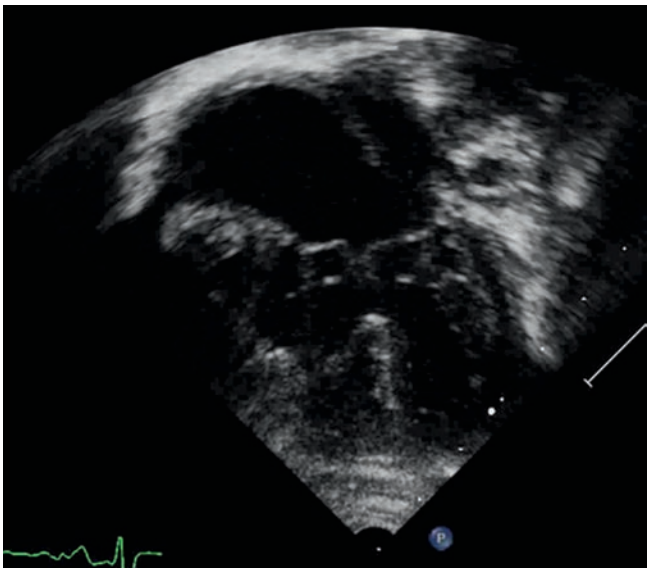

Fig. 30.4 Complete atrio-ventricular septal defect. There is a single AV-valve at the entrance of both ventricles. There is a large atrial primum component and a large inlet ventricular septum defect.

- The AV valve is made up of five leaflets. AV-valve anatomy and AV-valve regurgitation can be present and need to be assessed carefully. Regurgitation can be centrally between the superior and inferior bridging leaflets or located in the commisures between the right sided and/or left-sided AV-valve components.

Haemodynamic Assessment

- The atrial and ventricular shunt can result in atrial as well as ventricular dilatation.
- There can be associated pulmonary hypertension.
- Qp/Qs can be measured.

Associated Lesions

Different congenital lesions (like coarctation, tetralogy of Fallot, atrial isomerism, etc.) can be associated with an AVSD and complete sequential segmental analysis is required.

Post-surgical assessment includes:

- Assessment of residual atrial and ventricular shunts.
- Assessment of left and right AV valve function. Variable degrees of left-sided or right-sided AV-valve stenosis or regurgitation can be present. Careful assessment of the AV valves and description of the mechanisms involved in valve dysfunction are important.
- Left ventricular outflow obstruction can be present.
- Pulmonary arterial hypertension.

Patent Ductus Arteriosus

A persistent ductus arteriosus is not an uncommon lesion in adulthood. The left-to-right shunt causes left ventricular volume overload. If large, it may cause obstructive pulmonary hypertension and the Eisenmenger syndrome.

Imaging a patent ductus arteriosus involves identifying:

- Presence of a PDA and its size
- Direction of flow: left-to-right, bidirectional, right-to-left
- Secondary effects of PDA: left atrial and ventricular dilatation, presence of pulmonary hypertension
- Associated congenital defects

Identifying the PDA (*Fig. 30.5*)

In a left aortic arch, the duct is usually located between the descending aorta and the left pulmonary artery (PA). If the arch is right sided, the duct can be present between the descending aorta and the right PA, but more commonly connects the left subclavian artery and the left PA. This variability in location of the duct makes the echocardiographic diagnosis sometimes difficult.

Direction of Flow (*Fig. 30.6*)

The shunt size and direction can be assessed by colour Doppler, pulsed Doppler, and CW Doppler. If the PVR is normal, the flow is left to right (L→R) and continuous. Flow velocity is high in a restrictive PDA. The peak and mean gradient between the aorta and PA can be measured. With increasing PVR, flow becomes bidirectional with R→L flow in systole and L→R shunting in diastole. With progressive pulmonary vascular disease, the shunt can be exclusively R→L.

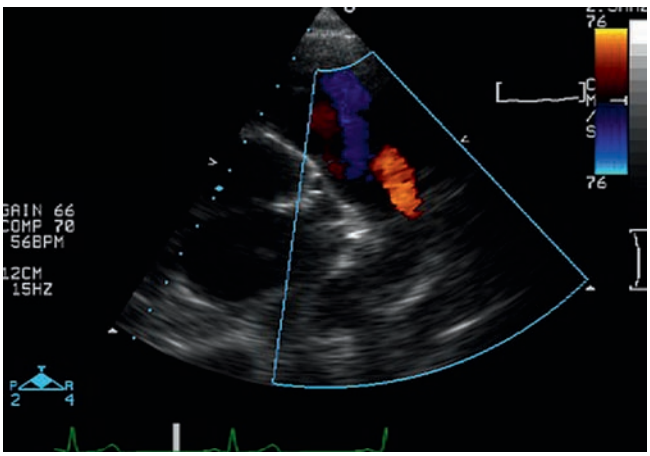

Fig. 30.5 Patent ductus arteriosus. Colour flow Doppler demonstrating aortic to pulmonary flow in the short-axis view. The *red* colour represents the diastolic flow though the arterial duct

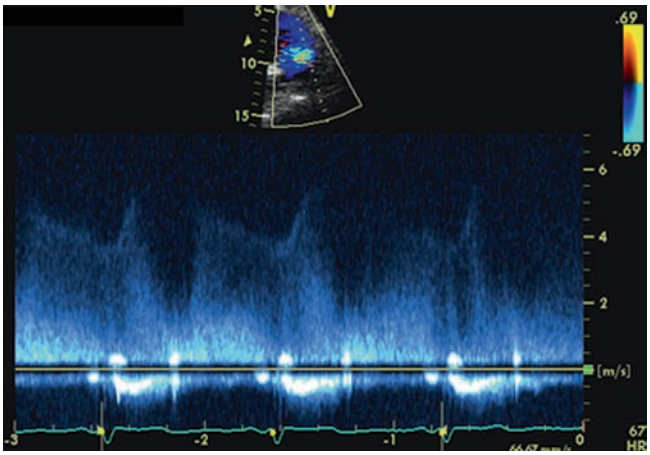

Fig. 30.6 Patent ductus arteriosus. There is continuous L→R shunting from the aorta to the pulmonary artery through the duct. The high velocity across the duct excludes the presence of significant pulmonary hypertension

Associated Anomalies

In the adult population, isolated PDA is the most common presentation, but associated congenital anomalies need always be excluded.

Secondary Haemodynamic Effects

- Left atrial and left ventricular dilatation
- Secondary mitral regurgitation
- Pulmonary hypertension

A duct can be closed surgically or interventionally by placement of a coil or a device.[10] After duct closure, the following should be evaluated:

- Residual shunt through the duct
- Residual pulmonary hypertension
- Residual LV dilatation and mitral regurgitation
- Obstruction on the left PA after coil/device placement

A patent ductus arteriosus can usually be diagnosed using echocardiography. Rarely cardiac MRI or cardiac CT might be required, especially in the case of unusual origin of the duct.

Coarctation of the Aorta

In classic coarctation, there is a narrowing of the aorta located distal to the origin of the left subclavian artery at the arterial

duct.[11] This narrowing typically is discrete, but can be associated with long segment hypoplasia. Coarctation alone is termed simple, and complex if associated with other lesions. The diagnosis should be clinical with arterial hypertension associated with poor or absent femoral pulses. Typically large collaterals develop providing blood supply to the lower part of the body.

Imaging should provide:

- Diagnosis of coarctation
- Location and severity
- Assessment of the secondary effects: left ventricular hypertrophy, left ventricular dysfunction, coronary artery disease
- Identifying associated lesions, especially bicuspid aortic valve, mitral valve disease (parachute mitral valve), and left ventricular outflow tract obstruction

Diagnosing and Locating Coarctation of the Aorta

The best screening method for diagnosing coarctation of the aorta is scanning the abdominal aorta in a sub-costal long-axis view (Fig. 30.7). If there is a decreased systolic flow with diastolic run-off, this is suggestive of the presence of a narrowing on the thoracic aorta. To identify the location of the narrowing, the supra-sternal view should be used, but this very often gives only very limited windows in adult patients (Fig. 30.8, Video 30.8). Colour flow Doppler can be helpful.

Haemodynamic Significance

CW Doppler is used to interrogate the narrowed segment. The coarctation is significant if high velocities and antero-grade diastolic flow are seen (diastolic runoff) (Fig. 30.9).

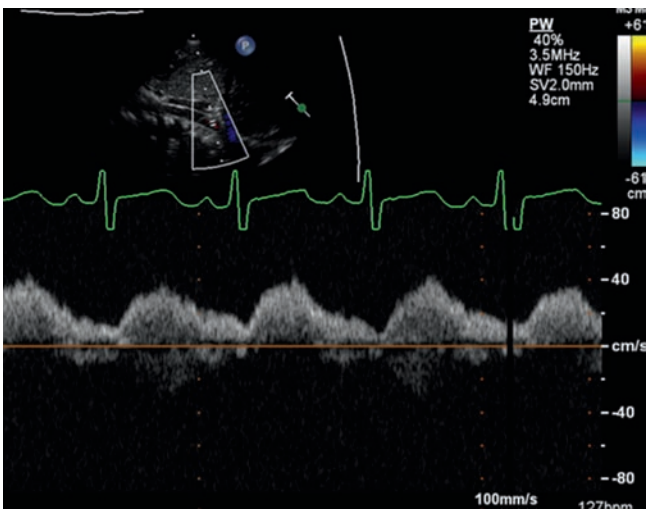

Fig. 30.7 Coarctation of the aorta. Abdominal aortic flow in aortic coarctation. Typically there is a continuous flow pattern in the abdominal aorta, instead of the normal pulsatile pattern

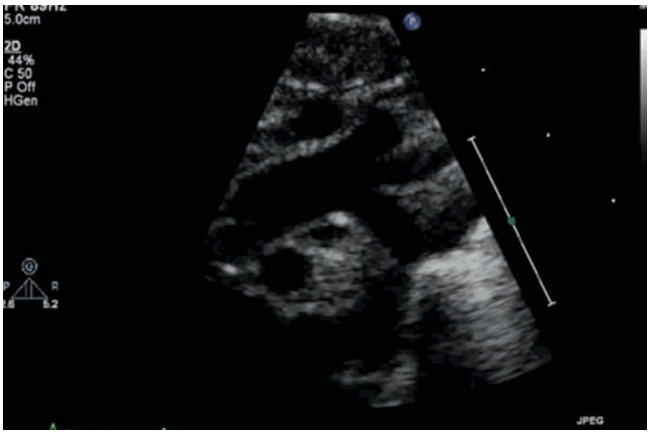

Fig. 30.8 Coarctation of the aorta. The coarctation with an obvious posterior shelve is located just distal to the origin of the left subclavian artery. There is a localized narrowing in the juxtaductal region with a prominent posterior shelve

Caveats

- PDA or collaterals may reduce the gradient across the coarctation.
- The simplified Bernoulli equation is less accurate for long lesion or segments with multiple stenosis.
- Patients with coarctation often have multiple obstructive lesions in series that lead to an increased peak velocity proximal to the coarctation. For this reason, the expanded Bernoulli equation should be used if the proximal velocity exceeds 1 m/s: Peak gradient = $4v^2_{\text{max-coarctation}} - 4v^2_{\text{max-precoarctation}}$.

Secondary Effects

LV wall thickness and mass should be measured. LV systolic and diastolic function should be assessed.

In adults with coarctation, additional imaging techniques such as cardiac MRI or cardiac CT are necessary to better describe the arch anatomy prior to any interventional or surgical treatment.[12]

Right Ventricular Outflow Tract Obstruction

This is classified into valvular and sub-valvular stenosis.

Valvular Stenosis

In the assessment of pulmonary valve stenosis, the following points are important:

- *Morphology*. The valves may be unicuspid, bicuspid, tricuspid, or quadricuspid. The most common type in

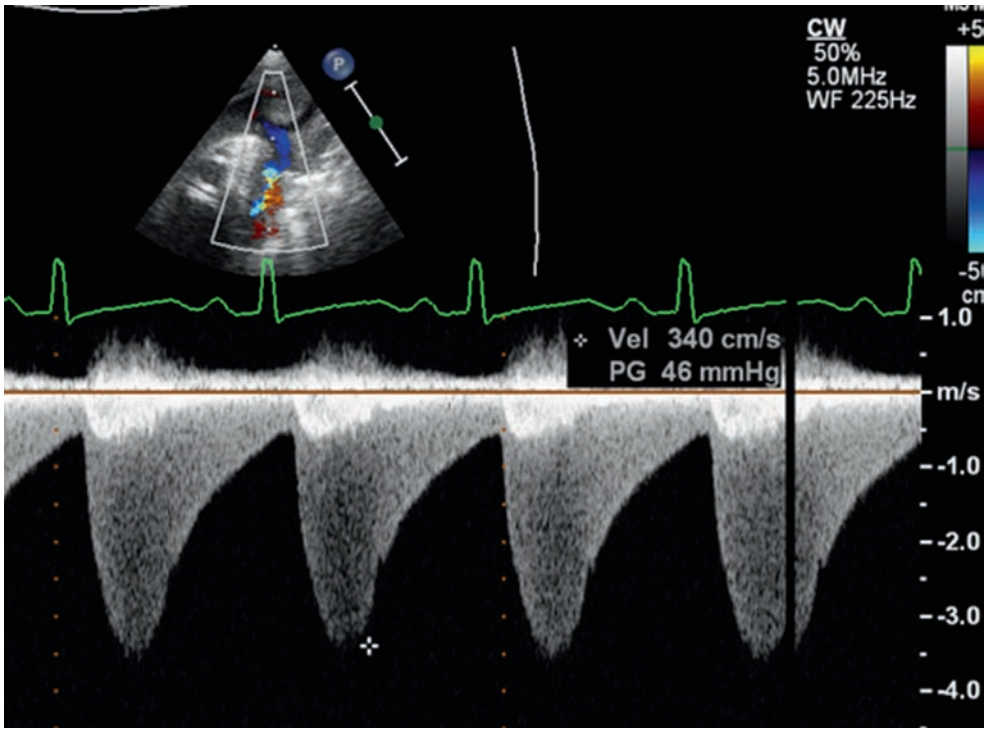

Fig. 30.9 Coarctation of the aorta. Continuous wave Doppler through the coarctation region. The typical "sawtooth" pattern is identified with the typical diastolic run-off

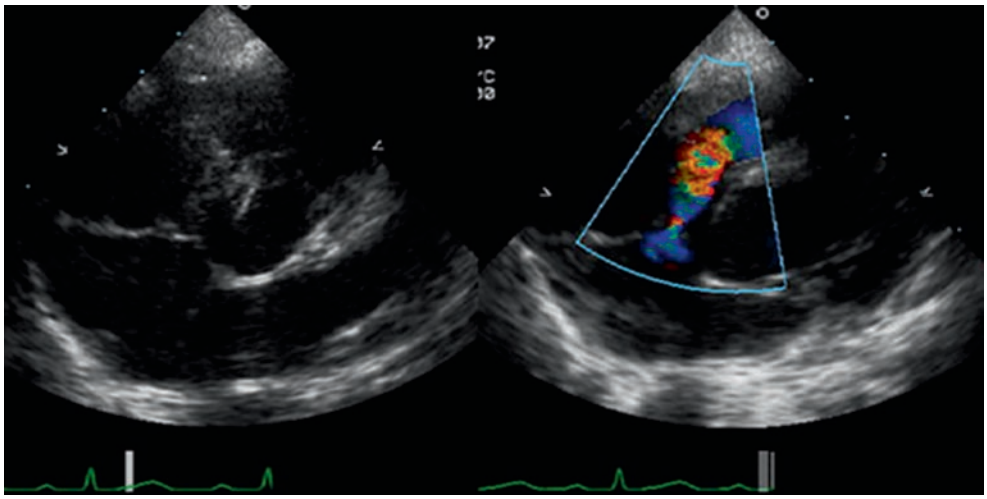

Fig. 30.10 Double-chambered right ventricle. A hypertrophied muscle band is noted with flow acceleration. This patient also had a spontaneously closed perimembranous ventricular septal defect

isolated pulmonary valve stenosis is the acommisural type. The annulus size should be measured.

- *Degree of severity*. Stenosis is severe if the Doppler CW peak gradient measures > 80 mmHg. Right ventricle hypertrophy reflects severity. Associated L-R shunts (e.g. ASD) increases flow across the valve and can lead to overestimation of the gradient. Conversely RV dysfunction, TR and R-L shunting can result in under-estimation of the stenosis.
- *PA dilatation*. PA dilatation is often associated with isolated PS.
- *Associated anomalies*. PFOs or secundum ASDs are frequent.

Sub-valvular Stenosis

This includes infundibular stenosis or DCRV.

- DCRV is characterized by muscle bundles dividing the RV into a proximal and distal chamber. DCRV is differentiated from infundicular stenosis in that the obstruction is located lower within the body of the RV. A concomitant perimembranous VSD may be identified (Fig. 30.10, Video 30.10).
- Infundibular stenosis is located at the lower portion of the pulmonary infundibulum where the infundibulum unites with the trabecular portion of the RV.

Left Ventricular Outflow Tract Obstruction (LVOTO)

This includes valvular aortic stenosis, sub-valvular stenosis, and supra-valvular stenosis.

Valvular Aortic Stenosis

This constitutes 70% of the obstructions in the LVOT. The evaluation of patients with congenital aortic stenosis is similar to patients with acquired stenosis. We refer to the chapter on aortic stenosis in this book.

Sub-aortic Stenosis

This is a narrowing below the aortic valve (Fig. 30.11). Three subtypes can be identified: a membranous form, a fibromuscular ridge, and a fibromuscular tunnel. Colour flow Doppler detects turbulence, while pulse wave Doppler helps to localize the origin of acceleration. M-mode and 2D imaging may demonstrate early systolic closure of the aortic valve or fluttering of the aortic valves. Continuous wave Doppler should be used to assess the peak and mean gradients across the lesion.

In the adult congenital clinic, subaortic stenosis can be seen after VSD closure, after the repair of double outlet right ventricle, after the Rastelli procedure, and in patients with AVSD.

Supra-valvular Stenosis

This is a more rare form of left ventricular outflow tract obstruction. The stenosis can be membranous, hourglass-shaped, or be associated with hypoplasia of the ascending aorta (20%). The aortic valve is involved in 30% of cases due to valve dysplasia, fibrosis, or thickening, and aortic regurgitation may be present. The coronary arteries may be involved in the narrowing. Associated pulmonary branch stenosis is not uncommon.

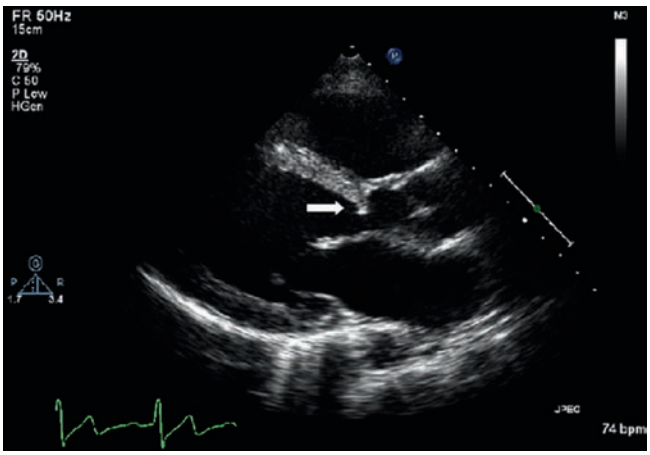

Fig. 30.11 Subaortic stenosis caused by a fibromuscular ridge (*arrow*)

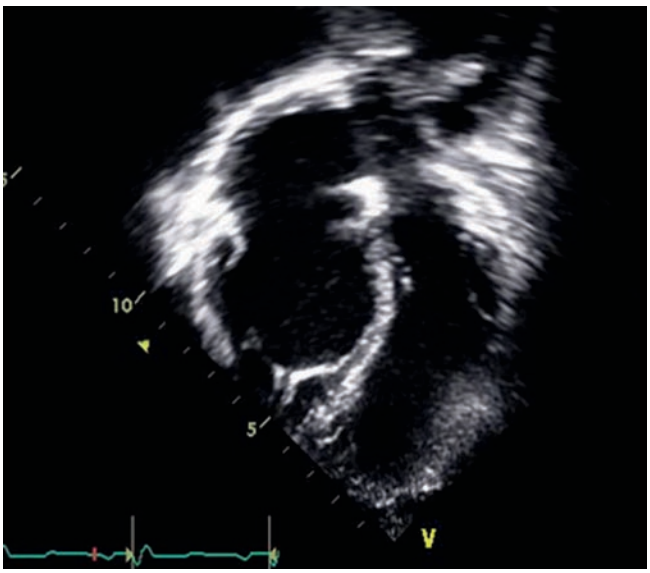

Fig. 30.12 Ebstein's anomaly. Apical 4-chamber shows apical displacement of the septal leaflet

Ebstein's Anomaly

Ebstein's anomaly of the tricuspid valve is defined by apical displacement of the septal and post-inferior leaflets of the tricuspid valve (Fig. 30.12, Video 30.12).[13] Typically, the tricuspid valve orifice is rotated superiorly towards the RVOT. The anterosuperior leaflet is large and redundant (sail-like). This is associated with variable degrees of tricuspid stenosis and regurgitation (Fig. 30.13, Video 30.13). An ASD or PFO may be associated with Ebstein's disease. Due to variability in the apical displacement, variable degrees of atrialization of the right ventricular cavity are present.

Congenital Mitral Valve Anomalies

These are rare abnormalities. Evaluation of mitral stenosis and insufficiency is discussed in the corresponding chapters. Common congenital types include the following.

Parachute Mitral Valve

This defect involves the attachment of the chordae tendinae to a single papillary muscle (most commonly the post-medial papillary muscle).

Double Orifice Mitral Valve

This defect is characterized by two separate mitral valve orifices. The first type is associated with AVSD. The second

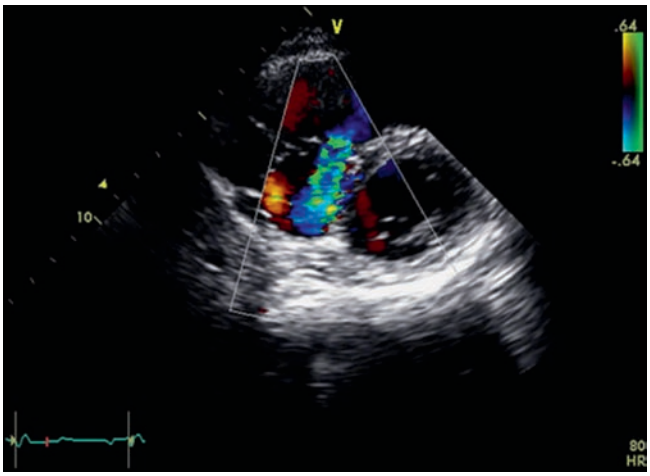

Fig. 30.13 Tricuspid regurgitation associated with Ebstein's disease

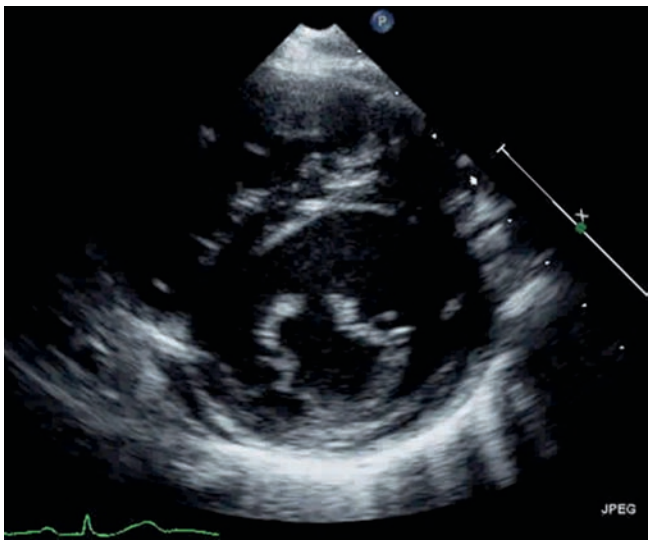

Fig. 30.14 Isolated cleft in the anterior leaflet of the mitral valve. Short-axis view at the level of the valve leaflets

type is caused by reduplication of the mitral valve orifice with two orifices, each having their own chordal attachments and papillary muscles.

Isolated Cleft in the Mitral Valve

This is a cleft in the anterior mitral leaflet not associated with an AVSD (Fig. 30.14).

Supra-valve Mitral Ring

This is a shelf-like structure found above the mitral valve. This ring originates from the fibrous annulus.

Cor Triatriatum Sinister

A fibromuscular membrane divides the LA into two separate chambers. The proximal chamber receives the four pulmonary veins. The left atrial appendage is located below the membrane. Occasionally, several orifices in the membrane may be seen. There may be obstruction caused by the membrane, and a mean gradient of >10 mmHg (using CW Doppler) is consistent with severe stenosis. In up to 50% of cases, there may be an ASD/PFO. This usually communicates with the distal chamber. Dilated pulmonary veins and associated pulmonary arterial hypertension also suggest significant stenosis. Anomalous pulmonary venous drainage may be an association.

Tetralogy of Fallot and Tetralogy of Fallot with Pulmonary Atresia

Tetralogy of Fallot is classically defined as the combination of a large outlet VSD with overriding of the aorta associated with various degrees of RVOTO and secondary right ventricular hypertrophy. The key anatomical feature of Tetralogy of Fallot is anterocephalad deviation of the outlet septum causing various degrees of muscular/infundibular RVOT obstruction (Fig. 30.15, Video 30.15a, b). This is associated with variable degrees of pulmonary valve obstruction and hypoplasia of PA branches. Tetralogy of Fallot with pulmonary atresia can be considered as an extreme form where no connection is present between the RV and the pulmonary circulation. The pulmonary perfusion can be duct-dependent to central pulmonary arteries or be dependent on aortapulmonary collaterals.[14]

Pre-operative Echocardiographic Assessment

This includes:

- Size and localization of VSD + degree of aortic override (Fig. 30.16, Video 30.16): perimembranous to outlet (92%), doubly committed (5%), inlet VSD, or atrioventricular septal defect (2%). If aorta overrides the VSD by more than 50%, this is called a double outlet RV.
- Localization + severity of RVOT obstruction: infundibular, valvular, and/or supra-valvular (Fig. 30.17).
- Image the pulmonary arteries. The size of the central and proximal right and left PA, PA abnormalities: absence of central pulmonary arteries, aorta-pulmonary collaterals, and discontinuity between RPA and LPA.
- Coronary artery abnormalities: LAD from RCA, prominent conal branch from RCA.
- Aortic arch: right/left arch, aortapulmonary collaterals.

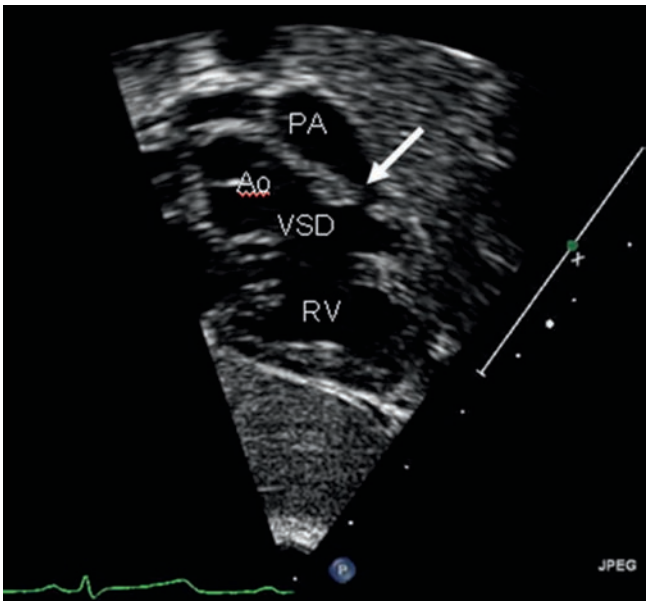

Fig. 30.15 Tetralogy of Fallot. Subxyphoid short axis view in infant. Anterior deviation of the outlet septum. Sub-costal view imaging the right ventricular outflow tract (RVOT). The *arrow* indicates the antero-cephalad deviation of the outlet septum, causing RVOTO

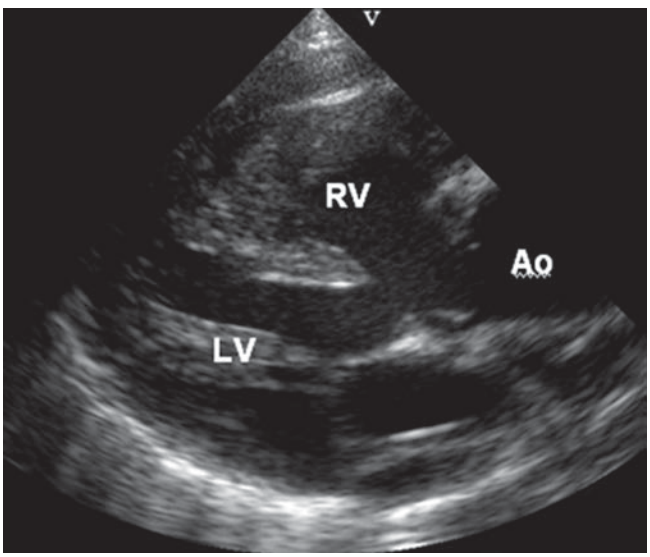

Fig. 30.16 Tetralogy of Fallot. Parasternal long-axis view demonstrating the ventricular septal defect extending to the outlet part of the septum and the overriding aorta

- Associated abnormalities such as ASDs, left superior vena cava (SVC), additional VSDs, and abnormal pulmonary venous return.

Role of Echocardiography in Pre-operative Imaging

- Defining intra-cardiac anatomy
- Identifying sources of pulmonary blood flow

Role of Cardiac MRI

- PA anatomy, especially if complex pulmonary perfusion
- Aortic arch: laterality, aortapulmonary collaterals
- Coronary anatomy or associated coronary lesions

Role of Angiography

- Pulmonary perfusion if complex, especially patients with pulmonary atresia.
- Coronary anatomy and associated coronary atherosclerosis.

Post-operative Imaging

Post-operative evaluation should include the following:

- Residual RVOT obstruction
- Degree of pulmonary regurgitation (qualitative assessment)
- Residual VSD
- Right ventricular dilatation and RV function
- Peripheral PA stenosis
- Aortic insufficiency
- Left ventricular function

One of the most common problems after tetralogy of Fallot repair is the occurrence of pulmonary regurgitation resulting in progressive RV dilatation and dysfunction (Fig. 30.18, Video 30.18). Timely replacement of the pulmonary valve can prevent irreversible damage to the right ventricle, but timing of the valve replacement is still very controversial. This is partly due to the lack of a good reproducible echocardiographic technique to quantify pulmonary regurgitation and right ventricular function.[15] Cardiac magnetic resonance has become the technique of choice for this indication, and is used frequently to assess the post-operative patient.

Role of Echocardiography in Post-operative Imaging

- Result of intra-cardiac repair: VSD patch, RVOT obstruction
- RV size and function

Role of Cardiac MRI

- RV size and function
- Pulmonary valve function: quantification of insufficiency
- PA anatomy

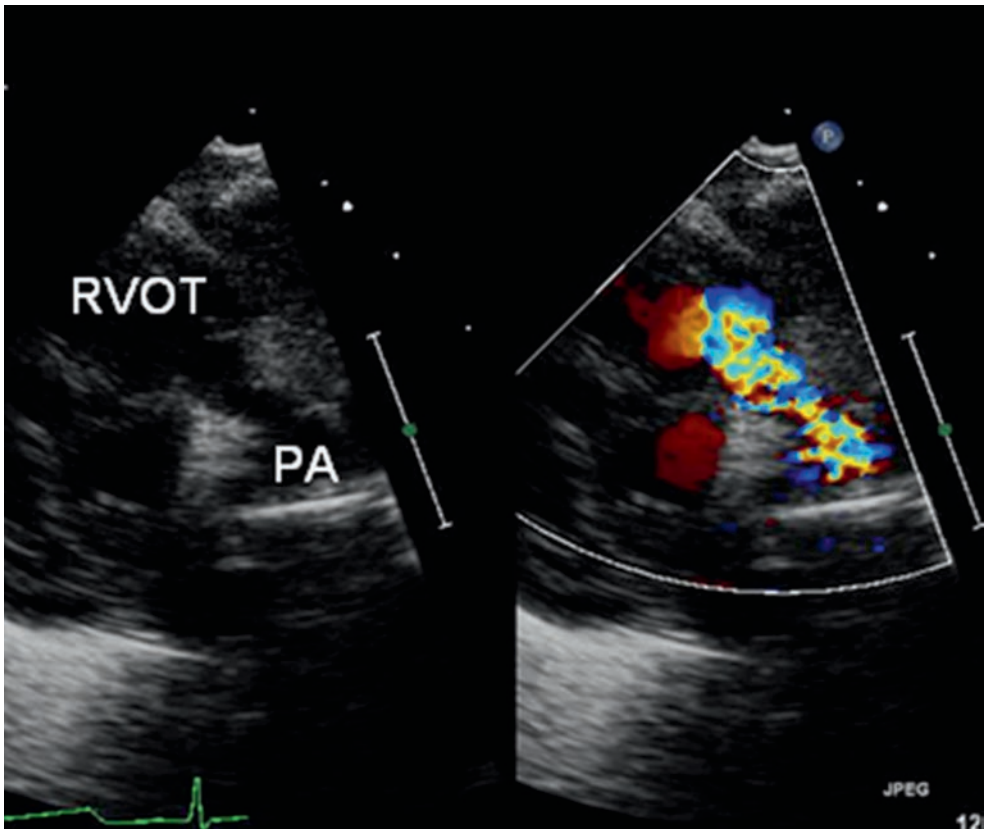

Fig. 30.17 Tetralogy of Fallot. Parasternal long-axis view tilted towards the right ventricular outflow tract. There is flow acceleration from below the valve, at the valve, and also at supra-valvular level

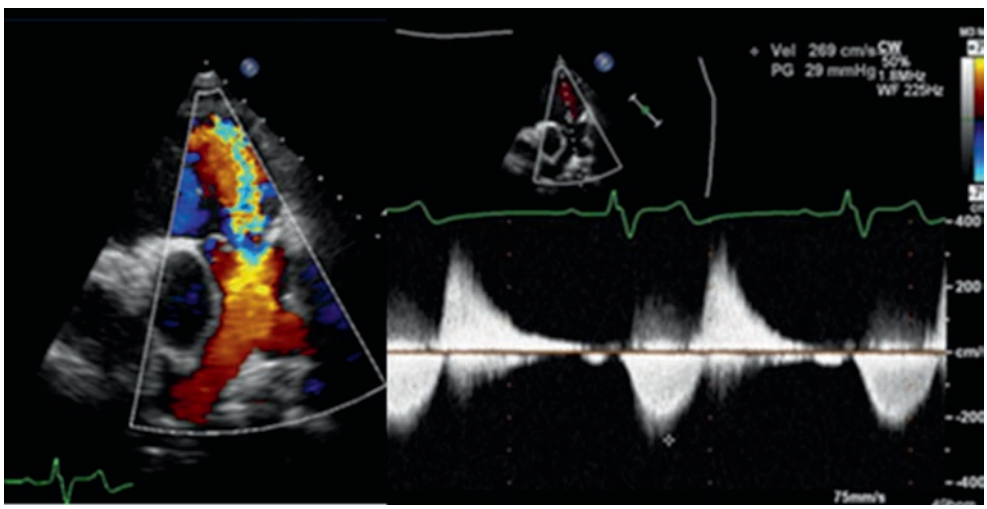

Fig. 30.18 Tetralogy of Fallot. Post-operative image. Severe pulmonary regurgitation after tetralogy of Fallot repair. The *left panel* shows a diastolic frame with a wide regurgitant jet at valve level and backflow originating from distally into the pulmonary branches. The Doppler shows the short deceleration time typical for severe pulmonary regurgitation with flow only in early and middiastole

Common Arterial Trunk

This is characterized by one arterial trunk originating from the heart supplying coronary, pulmonary, and systemic circulation. There is usually a large associated VSD, and the truncal valve has variable anatomy with variable degrees of stenosis and insufficiency. Most patients presenting in adulthood will have undergone surgical repair with VSD closure and connecting the right ventricle to the pulmonary arteries with a (valved) conduit. Those patients who have not undergone surgery and survived will have developed Eisenmenger's syndrome.

Post-operative evaluation of common arterial trunk includes:

- Looking for residual VSDs.
- Assessing truncal valve function: stenosis and insufficiency. The truncal valve may be tricuspid, quadricuspid, or bicuspid. Occasionally, the valve may have been replaced with a prosthetic valve.

- Measuring the size of the neoaorta.
- Assessing the right ventricular conduit: obstruction and regurgitation.
- Looking for pulmonary branch stenosis.
- Assessing biventricular function.

This evaluation can generally be performed using echocardiography. For right ventricular function analysis or for viewing pulmonary branch stenosis, cardiac MRI may be required.

Transposition of the Great Arteries

In transposition of the great arteries (TGA), the aorta arises from the morphological right ventricle (RV) and the PA from the morphological left ventricle (LV) resulting in ventriculo-arterial discordance.[16] In this paragraph, we will discuss transposition with atrio-ventricular concordance. The following anatomical features are relevant for preoperative assessment:

- VSD in up to 50% of all patients
  Perimembranous in 33%
  Malalignment defect (often associated with obstruction of one of the outflow tracts) in 30%
  Muscular defect in 25%
  Atrio-ventricular inlet defect (5%) or doubly committed defect (5%)
- Left ventricular outflow tract obstruction (sub-pulmonary and pulmonary stenosis) caused by different mechanisms
- Variable coronary artery anatomy - The most common coronary variant is the circumflex originating from the right coronary artery (18%). Single coronary artery or intra-mural coronary is significant risk factor.

The treatment for simple TGA has undergone an historical evolution as the atrial switch procedure (Senning or Mustard operation) that was performed until the mid-1980s-early 1990s has been replaced by the arterial switch operation afterwards.[17] For TGA with VSD and LVOT obstruction, the Rastelli operation is performed. This was recently replaced by the Nikaidoh procedure in selected cases.

Echocardiographic Evaluation After the Atrial Switch Procedure (Senning or Mustard)

Imaging after an atrial switch operation requires[18] the following.

- Identifying the venous pathways to rule out baffle obstruction or baffles leaks (Fig. 30.19, Video 30.19)–Systematic imaging needs to be performed on each venous pathway. In those with poor windows, alternative imaging modalities might be required. TOE has been used extensively in atrial switch patients, but cardiac MRI is a good alternative. Contrast echocardiography with injection of agitated saline through a peripheral intravenous cannula can be helpful to detect baffle problems.
- Tricuspid regurgitation and systemic RV function–Progressive tricuspid regurgitation and systemic RV dysfunction are common problems after the atrial switch procedure (Fig. 30.20, Video 30.20). Quantification of systemic RV function by echocardiography remains challenging. In most clinical settings, assessment of global RV systolic function is qualitative. Newer quantitative methods include fractional area change, tissue Doppler imaging, isovolumic acceleration of the RV free wall, and strain calculation in the RV free wall. Cardiac MRI remains the gold standard for the quantitative evaluation of RV function.

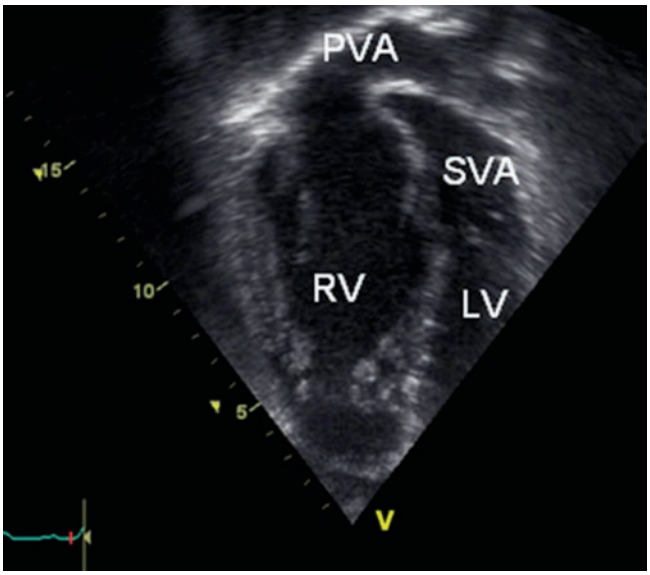

Fig. 30.19 Apical 4-chamber view of patient after the Senning operation. Notice the baffle in the atrium. The pulmonary venous atrium (PVA) is directing the pulmonary venous blood to the right ventricle. The systemic venous blood is directed through the systemic venous atrium (SVA) to the left ventricle. The RV is the systemic ventricle after this operation

Echocardiographic Evaluation After the Arterial Switch Procedure

Imaging after the arterial switch procedure involves the following:

- Imaging the neo-aortic root and valve Progressive neo-aortic root dilatation and neo-aortic valve regurgitation can occur. Neo-aortic regurgitation using the same echocardiographic methods as for aortic regurgitation.
- Imaging the RV outflow tract and pulmonary arteries–Stenosis on the RV outflow tract at any level is the most

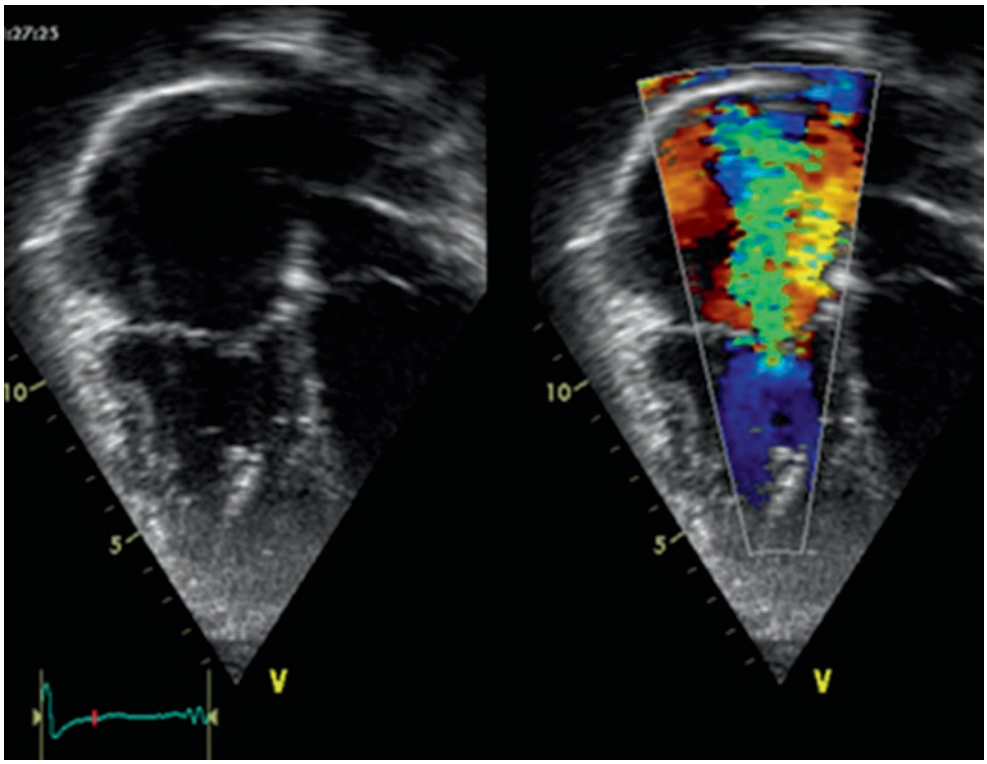

Fig. 30.20 Severe tricuspid regurgitation after the Senning operation. The RV is dilated and hypertrophied. Notice the broad jet of regurgitation

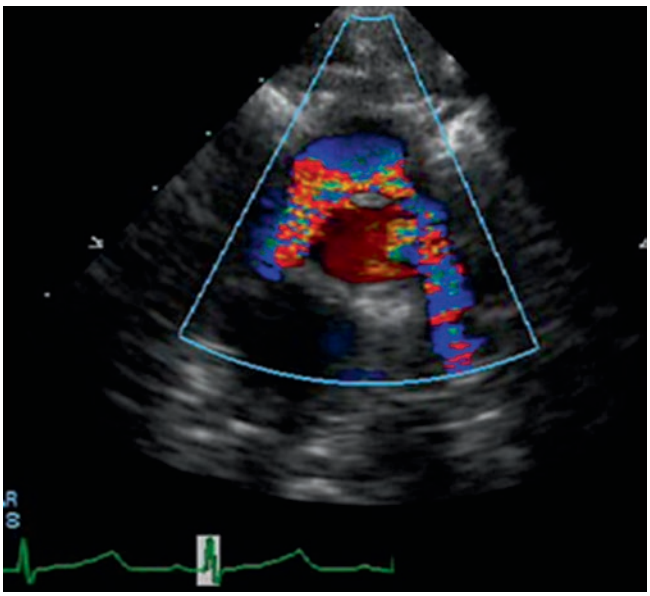

Fig. 30.21 The arterial switch operation. Position of the pulmonary arteries after the arterial switch procedure. Notice that the bifurcation is located anteriorly to the aorta

common cause for late re-operation after ASO. The obstruction can occur at any level, but most commonly at the suture line of the neo-main pulmonary arterial anastomosis. For imaging, it should be taken into account that due to the Lecompte manoeuvre, the pulmonary bifurcation is anterior to the aorta (Fig. 30.21, Video 30.21). Peak velocities ≤ 2m/s (predicted maximum instantaneous gradient ≤16 mmHg) across the distal main PA and branch pulmonary arteries are within normal limits after ASO.

- Imaging the coronary arteries–During the switch procedure, a coronary transfer is performed with re-implantation of the coronaries in the neo-aortic root. Coronary stenosis, and especially kinking, can occur resulting in myocardial ischaemia. Careful monitoring of global and regional myocardial performance is important. Dobutamine stress echocardiography can be used to identify perfusion problems. Direct visualization of the coronaries is possible using cardiac MRI and cardiac CT. Coronary angiography should be considered in patients in whom coronary stenosis or occlusion is highly suspected.
- Ventricular size and function–Evaluation of left ventricular size and function is required in every patient after the switch procedure.

Echocardiographic Evaluation After the Rastelli Procedure

In the Rastelli procedure, the VSD is closed creating a tunnel between the left ventricle and the aorta, and the right ventricle is connected with a conduit to the pulmonary arteries. Imaging the patients after the Rastelli procedure involves the following:

- Evaluation of the conduit and branch pulmonary arteries by 2D, colour, and Doppler using several views.

- Evaluation of the LV-to-aortic valve pathway for obstruction and aortic regurgitation.
- Evaluation of left ventricular function as LV dysfunction is a potential late complication after the Rastelli operation.
- Exclude the presence of residual VSDs.

Double Outlet RV

In double outlet right ventricle by definition at least 50% of each great vessel arises from the right ventricle.[14] This includes a wide spectrum of lesions from tetralogy of Fallot to patients with functionally univentricular hearts. As with tetralogy of Fallot patients, many of the adult patients seen in the cardiology clinic will have undergone corrective or palliative surgery.

Pre-operative Assessment

Detailed segmental analysis is required including:

- Location and size of the VSD. The VSD is usually large and unrestrictive, and can be located in four different positions: sub-aortic, sub-pulmonary, doubly committed, or remote.
- Variable position of the great vessels with normal relationship or malposition. The relationship needs to be defined for each individual patient.
- Variable degrees of outflow tract obstruction with sub-pulmonary of sub-aortic obstruction.
- Associated lesions like aortic coarctation, ASD.

Post-operative Assessment

Depending on the underlying anatomy, different types of surgical repairs are performed, and the post-operative assessment will be dependent on the surgery performed. For patients with sub-aortic VSD, this is often similar to post-operative tetralogy of Fallot repair assessment. For more complex lesions, other types of surgery are performed like arterial switch and VSD closure.

Congenitally Corrected Transposition of the Great Arteries

In ccTGA, oxygenated pulmonary venous blood enters the left atrium, which connects through the tricuspid valve to the morphological right ventricle.[18] Systemic venous deoxygenated blood enters the right atrium, which connects to the morphologic left ventricle through the mitral valve (atrio–ventricular discordance). The aorta arises leftward from the morphological right ventricle and the PA from the morphologic left ventricle (ventricular–arterial discordance). In 20% of cases, there is dextrocardia. Associated abnormalities dictate a highly variable clinical spectrum.[19]

Determination of Anatomy

General (Figs. 30.22–30.24, Videos 30.22 and 30.23)

- Situs and segmental anatomy.
- In usual situs, the tricuspid valve is on the left (4-chamber view).
- Mitral–pulmonary fibrous continuity (parasternal long-axis view).
- Ventricles, septum, and great vessels are more vertically oriented than usual (requires vertical rotation of transducer in parasternal planes).
- Sub-pulmonary morphologic left ventricle may appear "pancaked" (parasternal short-axis view).
- Great arteries arise in parallel and superiorly with vertical orientation (modified parasternal long-axis).
- Aorta arises leftward, anterior, and superior from the morphologic right ventricle (high parasternal short-axis).

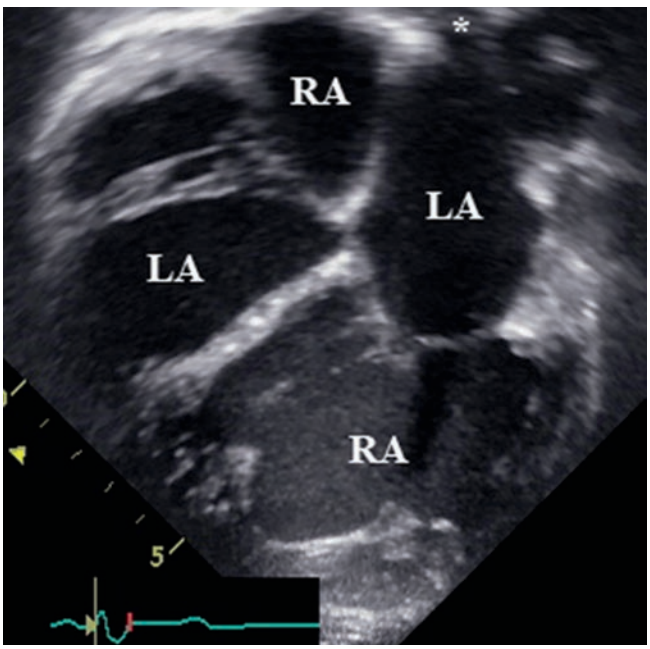

Fig. 30.22 ccTGA. Apical 4-chamber view in a patient with congenitally corrected transposition of the great arteries (atrio-ventricular; ventricular arterial discordance). The pulmonary veins (*asterisk*) drain into the left atrium, which connects through the more apically displaced tricuspid valve to the morphologic right ventricle (RV), situated on the left. The right atrium (RA) connects through the mitral valve to the morphologic left ventricle situated on the right

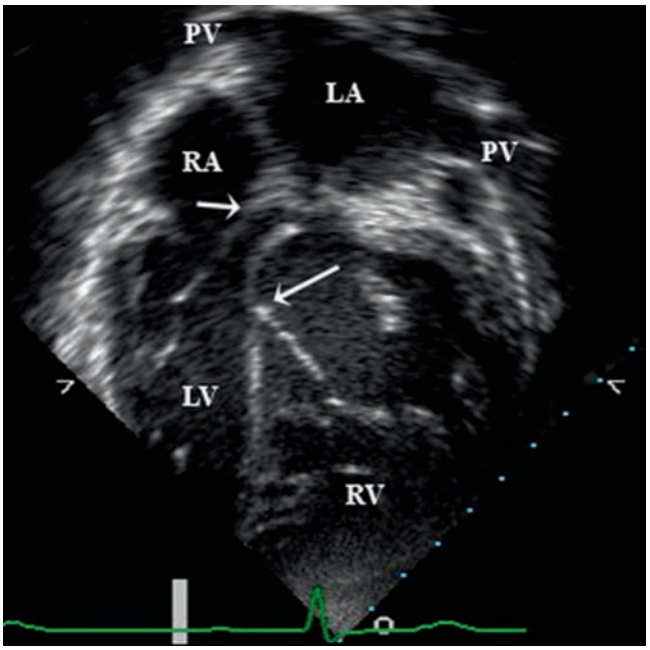

Fig. 30.23 ccTGA Ebstein. Apical 4-chamber view in a patient with congenitally corrected transposition of the great arteries (atrioventricular; ventricular arterial discordance). The tricuspid valve has an Ebstein's like pathology with abnormal apical displacement (*long arrow*). The mitral valve attachment is shown by the *short arrow*. *PV* pulmonary vein; *RA* right atrium; *LA* left atrium; *RV* right ventricle; *LV* left ventricle

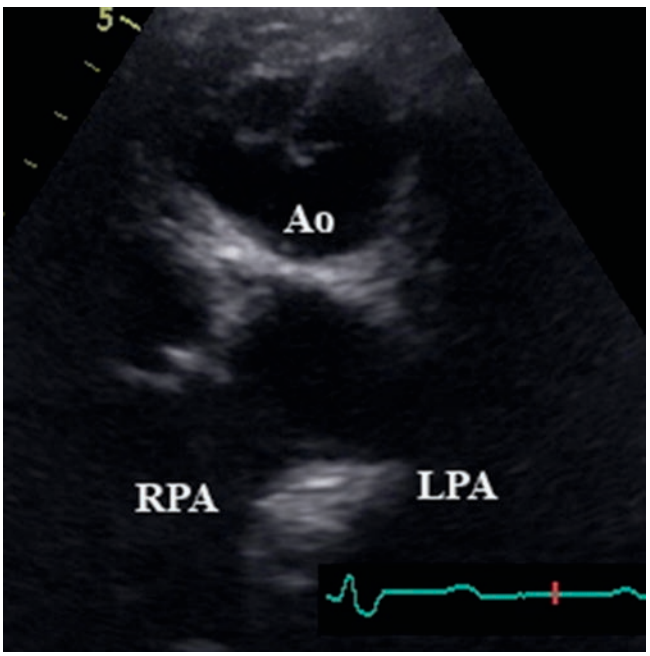

Fig. 30.24 ccTGA short-axis view. High parasternal short-axis view in a patient with congenitally corrected transposition of the great arteries. The aorta (AO) is seen anterior and slightly leftward of the pulmonary artery, which is posterior and branches into the left (LPA) and right (RPA) pulmonary arteries

Common Associated Anomalies

- *VSD (~60–70%)*. Commonly perimembranous (apical 4-chamber and parasternal long axis).
- *Left ventricular outflow tract and pulmonary stenosis (~40–70%)*. Commonly sub-valvular (aneurismal valve tissue, chords, discrete fibrous obstruction) and valvar.
- *Tricuspid valve abnormalities (~83–90)*. Variable pathology (increased apical displacement of septal leaflet (Ebstein's like), thickened/malformed leaflets, straddling). Tricuspid regurgitation is common.
- *Mitral valve abnormalities (~50%)*. Cleft mitral valve. Straddling through the VSD.
- *Atrial septal defect (43%)*.
- *Other associated lesions*: aortic stenosis, aortic coarctation, left atrial isomerism, coronary artery variants, and complete heart block.

Role of Echo Before and After Surgery

- Assess tricuspid valve for possible repair or replacement.
- Evaluate right ventricular function.
- Assess feasibility of biventricular repair or need for PA banding.
- After PA banding, assess left ventricular function, hypertrophy, and tricuspid regurgitation.
- After atrial switch and Rastelli procedures, assess leak or obstruction across baffles.
- Assess for worsening ventricular function and atrioventricular valve regurgitation.

Trans-oesophageal Echocardiography

- Pre-operative anatomical assessment
- Intra-operative monitoring of PA banding (gradient, left ventricular function)
- Intra-operative assessment of repair

Role of MRI

- Anatomy when echo windows are poor
- Systemic right ventricular function
- Atrio-ventricular valve regurgitation
- Left ventricular mass after PA banding

The Functionally Univentricular Heart

This is a wide anatomic spectrum of patients with a functionally single ventricle (left or right morphology) that supports systemic circulation.[20, 21] A second rudimentary ventricle invariably is present. Sometimes two adequately sized

ventricles are present, but anatomy prevents septation (e.g. straddling atrio-ventricular valves).

2D Echocardiography: General

- Situs and segmental anatomy.
- Systemic and pulmonary venous connections.
- Categorize: double inlet ventricles (DILV, DIRV), single inlet ventricles (absent right/ left connection), or common inlet (unbalanced AVSD). See Figs. 30.25–30.28, Video 30.25.
- Determine ventricular looping (D or L) and morphology (left/right) (multiple imaging planes required).
- Rule of thumb: a small superior and rightward sub-arterial outlet chamber is typically a morphologic RV. A small inferior-posterior rudimentary chamber is typically a morphologic LV.
- VSD location and restriction.
- Ventricular–arterial alignment (concordant or discordant).
- Atrio-ventricular valve straddling (tricuspid valve more common) across VSD (usually muscular).
- Atrio-ventricular valve stenosis/ regurgitation (2D + colour-flow).
- Ventricular function and pulmonary hypertension.
- Restriction at atrial septum (for specific lesions, i.e. absent right/ left connection).

Role of TOE

- Assess ventriclar/valvar morphology and function when transthoracic windows are inadequate.

Role of MRI

- Systemic and pulmonary venous anomalies.
- Aortic arch malformations.
- Branch pulmonary arteries.
- Ventricular function.

The Fontan Circulation

In the Fontan operation, the systemic venous blood is directed to the pulmonary arteries, bypassing the heart.[22] Since its introduction, the Fontan operation has undergone many modifications. Currently, the total cavopulmonary connection with the lateral tunnel or the use of an extra-cardiac conduit is the most commonly used. A fenestration is often placed between the systemic venous pathway and the pulmonary venous atrium. The fenestration allows a right-to-left shunt that decompresses the systemic venous pathway and maintains adequate cardiac output.

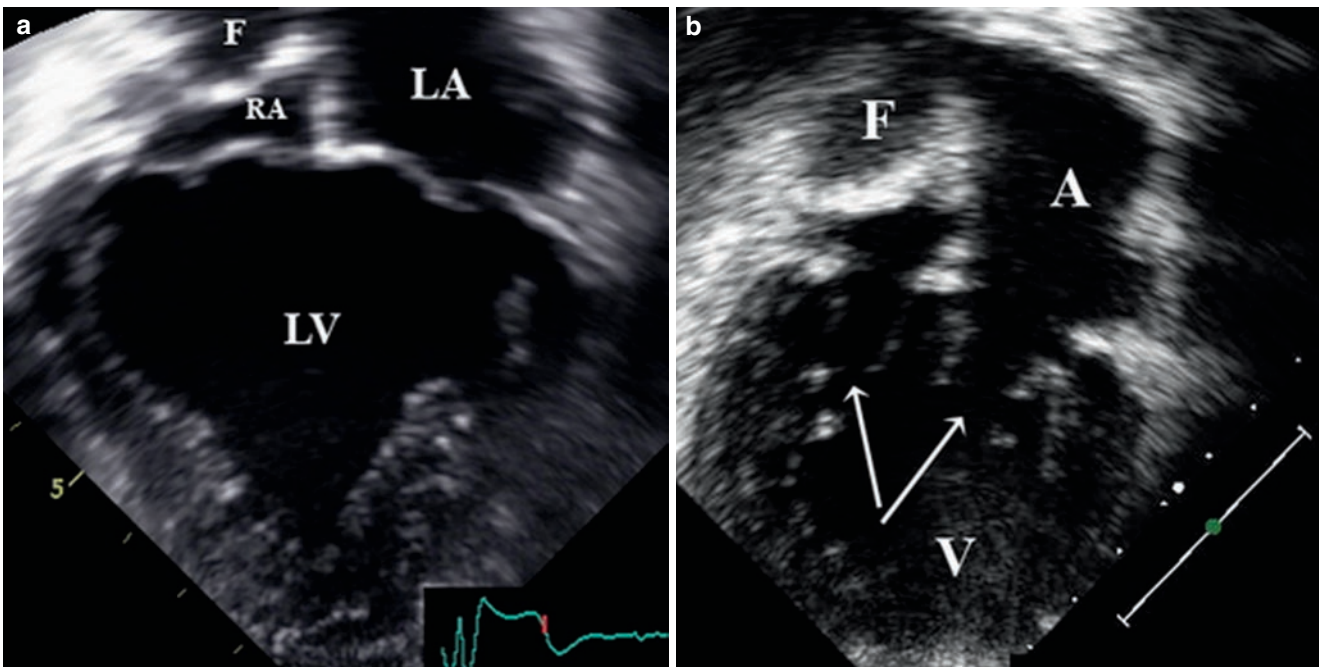

Fig. 30.25 Double inlet left ventricle. Apical view of double inlet left ventricle. **(a)** In this systolic frame, two separate AV valves connect the left atrium (LA) and right atrium (RA) to a single ventricle of left ventricular morphology (LV). The Fontan (F) connection is seen posteriorly. **(b)** Diastolic frame from an apical 4-chamber view in a patient with double inlet left ventricle. The right atrium and left atrium (A) connect via separate atrio-ventricular valves (*arrows*) to the dominant left ventricle (V). The Fontan circuit (F) is seen behind the right atrial cavity

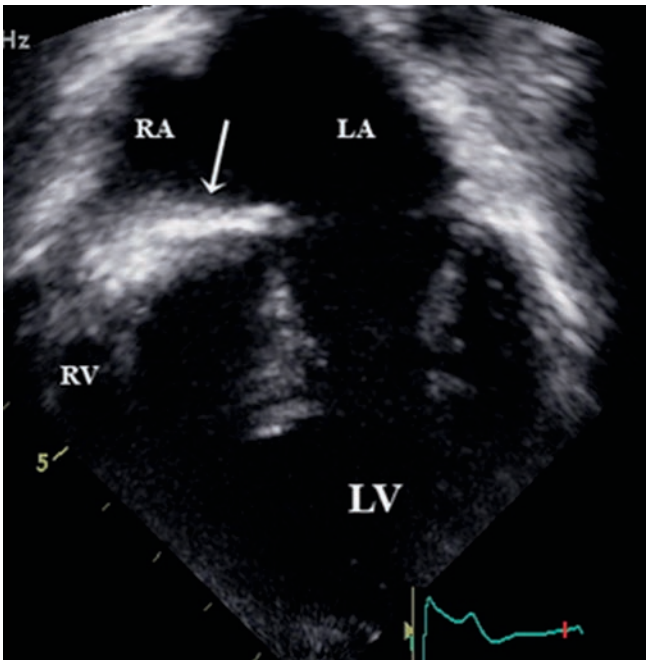

Fig. 30.26 Tricuspid atresia. Apical 4-chamber view in patient with absent right atrio-ventricular connection (tricuspid atresia). The absent right atrio-ventricular connection is seen echocardiographically as an echogenic border between the right atrium and small right ventricle (*arrow*). The atrial communication between the right (RA) and left atria (LA) is widely patent. The mitral valve and left ventricle (LV) dominate the image. The right ventricle (RV) is barely seen in this image

Imaging a patient after the Fontan operation should include the following:

Visualizing the Fontan Connections

The patency of the connections and absence of obstruction and thrombi should be assessed.
This involves:

- Evaluation of the superior cavopulmonary anastomosis (Fig. 30.29, Videos 30.29a, b), as well as the entire IVC to PA connection.
- Flow measurements in the SVC and IVC. In general, there is low-velocity flow with increase in flow velocities with inspiration.
- Evaluation of the patency and size of the fenestration. The mean gradient across the fenestration provides an estimate of the trans-pulmonary pressure gradient.
- In case of an intra-cardiac-type of connection, baffle leak should be excluded.
- Flow to both pulmonary arteries should be assessed using colour Doppler and pulsed Doppler.

Visualization of the entire conduit might be extremely difficult, and a TOE or MRI is an excellent non-invasive alternative.

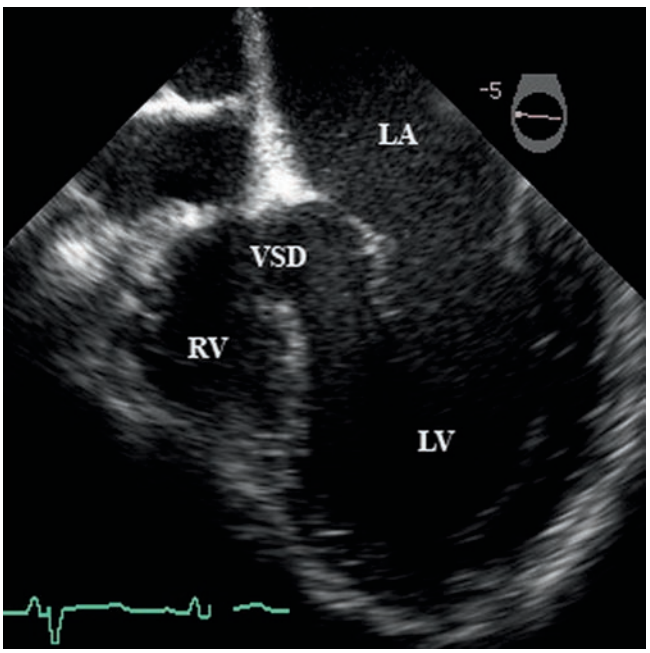

Fig. 30.27 Tricuspid atresia. 4-chamber view obtained at trans-oesophageal echocardiography in patient with absent right atrio-ventricular connection (tricuspid atresia). The left atrium (LA) connects through the mitral valve to the left ventricle (LV). No atrio-ventricular valve is discernable on the right and the absent connection is seen echocardiographically as an echogenic border between the right atrium and small right ventricle (RV). The posterior aspect of ventricular septal defect (VSD) is seen and is non-restrictive

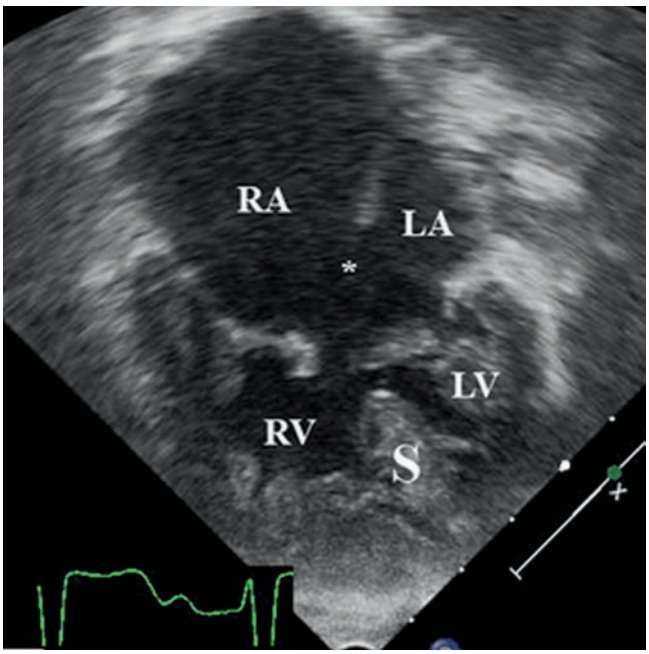

Fig. 30.28 Unbalanced AVSD. Apical 4-chamber view in a patient with unbalanced atrio-ventricular septal defect. The right atrium (RA) is considerably larger than the left atrium (LA). The large primum atrial septal defect is denoted with an *asterisk*. The common atrio-ventricular valve opens preferentially to the right ventricle (RV), which is dominant. The left ventricle (LV) is small. The ventricular septal defect is seen as the space between the inter-ventricular septum (S) and the atrio-ventricular valve

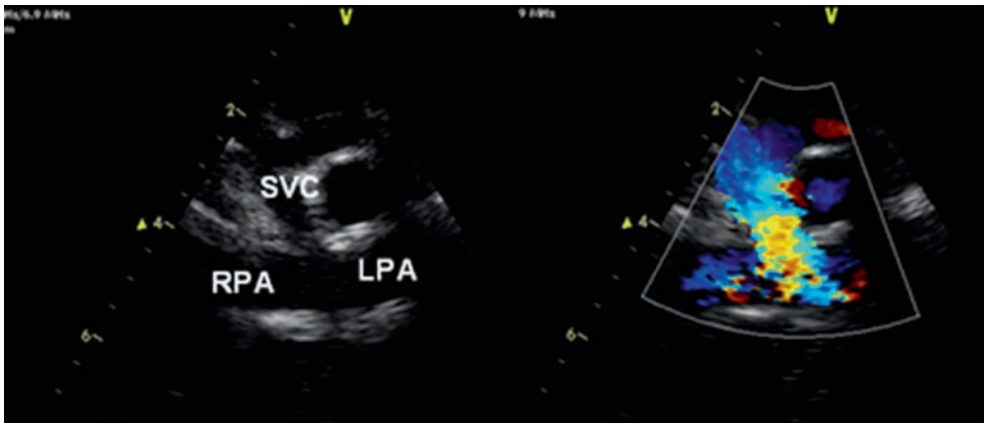

Fig. 30.29 Bidirectional cavopulmonary anastomosis (bidirectional Glenn shunt). Supra-sternal view. The superior vena cava (SVC) is connected end-to-side to the right pulmonary artery (RPA). The functionally proximal left PA can be visualized. With colour Doppler, the flow through the connection and the proximal pulmonary arteries can be imaged

Visualizing the Pulmonary Veins

Pulmonary venous obstruction should be excluded. All four pulmonary veins should, therefore, be identified after the Fontan operation, and pulmonary venous flow should be evaluated using colour Doppler and pulsed Doppler techniques. If pulmonary vein problems are suspected, additional imaging techniques such as cardiac CT, MRI, and cardiac catheterization are required.

AV-Valve Function

Low atrial pressure is a condition for optimal Fontan function. AV-valve stenosis and more commonly AV-valve regurgitation should be evaluated.

Ventricular Function Assessment

Ventricular function assessment is important part of postoperative Fontan evaluation, but due to the lack of quantitative techniques, it is largely a subjective qualitative approach. Also, the evaluation of diastolic function is extremely difficult due to abnormal AV-valve anatomy and abnormal pulmonary venous flow.

Detection of Aortic-to-Pulmonary Collateral Flow

An estimated 80% of patients undergoing Fontan-type operations already have, or subsequently develop, systemic arterial-to-pulmonary arterial collaterals as a consequence of preoperative or continued hypoxemia. Competitive flow from these aortopulmonary vessels can elevate right-sided pressures, thereby reducing systemic venous flow to the pulmonary arteries. These collaterals can be detected from the supra-sternal aortic views, but CT, MRI, and angiography are more sensitive non-invasive techniques for detecting collateral flow.

Eisenmenger's Syndrome

Characterized by irreversible pulmonary vascular disease as a result of a systemic-to-pulmonary communication (e.g. ASD, non-restrictive VSD, non-restrictive PDA, atrioventricular septal defect, aortopulmonary window, surgical systemic-to-pulmonary shunt). An initial left-to-right shunt reverses direction following an increase in pulmonary vascular resistance and arterial pressures.[23]

Clinical Questions to Be Answered by Echo

- Severity of pulmonary hypertension
- Direction of shunting across an intra-cardiac communication
- Underlying lesion
- Associated lesions
- Right and left ventricular function

Transthoracic Echocardiogram

- Right ventricular hypertrophy (4-chamber, parasternal long and short axis), flattening and bowing of the inter-ventricular septum in systole. ("D" sign [PSAX] Fig. 30.30). Diastolic flattening with disease progression.
- PA systolic pressure can be estimated using the modified Bernouli equation: RVSp mmHg = TR peak velocity (m/s) × 4 + estimated right atrial pressure (4-chamber apical view, parasternal long axis with posterior angulation, short axis at aortic valve level). Account for any gradient across the RVOT.
- Mean PA pressure estimated from peak early diastolic pulmonary regurgitation velocity and the diastolic PA pressure estimated from the end diastolic pulmonary regurgitation velocity.
- Qualitative and quantitative assessment of right ventricular function. With disease progression, right ventricular

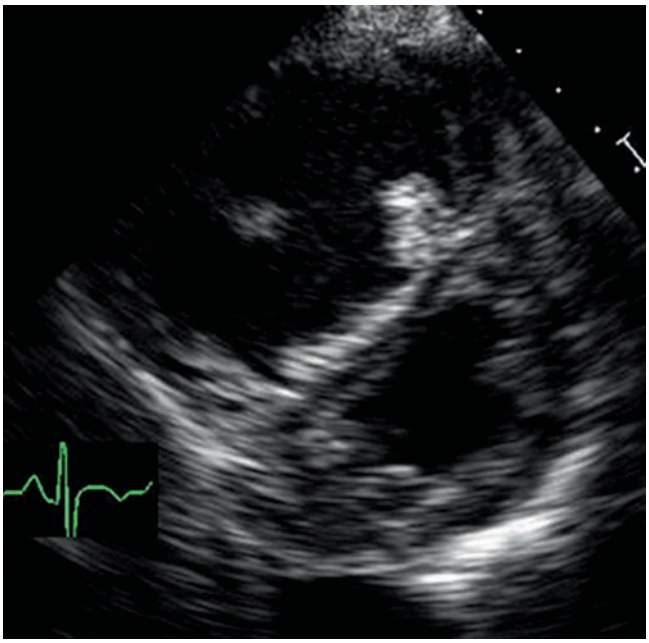

Fig. 30.30 Septal flattening in pulmonary hypertension. Parasternal short-axis view. The inter-ventricular septum is flat in systole due to the elevated pulmonary pressures. Due to the flattening, the LV has the configuration of a capital D

enlargement and dysfunction (parasternal long- and short-axis views, 4-chamber view).
- Left ventricular function (prognostic factor).
- Worsening tricuspid regurgitation (increasing afterload, annular dilatation, and right ventricular dysfunction) and right atrial enlargement (4 chamber).
- Underlying structural defect, coexisting structural abnormalities, surgical shunts (multiple planes).
- Obstruction or aneurysm in main PA and proximal branches.
- Colour flow Doppler helps define the anatomical defect and direction of shunting.
- Increased right-to-left shunting during supine bicycle ergometry, although the shunt may be small and difficult to demonstrate due to a low gradient. Contrast echo can enhance visualization of the shunt.

Trans-oesophageal Echocardiography

- Can be performed relatively safely and is usually well tolerated (even when baseline oxygen saturation levels are <80%).
- May be useful for detecting ASDs/patent ductus arteriosus and for imaging posterior structures (pulmonary veins).
- Should be performed in lung transplant candidates (detect unsuspected intra-cardiac defects/shunts, proximal PA thrombus).

Magnetic Resonance Imaging

- Not routinely required, but may be useful in selected cases for anatomical definition and to estimate magnitude of right-to-left shunt.

Special Topics in Adult Congenital Imaging

Echocardiography in the Pregnant Woman with Congenital Heart Disease

- Increased blood volume is reflected in increased cardiac chamber sizes.
- Physiologic pulmonary and tricuspid regurgitation and trivial mitral regurgitation are common.

Roles of Echocardiography in the Pregnant Woman with CHD[24]

Risk Stratification

High-risk patients include significant aortic stenosis (mean gradient >30–40 mmHg, valve area <0.7 cm^2 before pregnancy), significant aortic coarctation, significant mitral stenosis (valve area <2 cm^2), reduced systemic ventricular function (EF < 40%), mechanical prosthetic valve, Marfan's syndrome (especially when ascending aorta diameter > 44 mm), and cyanotic heart disease. Pregnancy is contraindicated in Eisenmenger physiology and significant pulmonary hypertension.

Lesion Specific Evaluation

Fetal echocardiography to evaluate structural heart disease in offspring.

Trans-thoracic Echocardiography in Selected Conditions

Lesions with potential RVOTO (e.g. TOF, DORV, etc.) (parasternal views)

- Assess right heart failure and increased tricuspid regurgitation.
- Assess RVOTO /pulmonary stenosis.

Ebstein's Anomaly (4 Chamber)

- Assess right heart failure and increased tricuspid regurgitation.
- Assess of a bioprosthetic valve degeneration and mechanical valve thrombosis.

Complex Post-operative Circulation

- Risk stratification is difficult in complex post-operative circulations (e.g. Fontan, Mustard/Senning).
- Assess ventricular function, residual lesions, baffle leak, baffle obstruction, and valvar stenosis/regurgitation.

Trans-oesophageal Echocardiography

- May be performed during pregnancy.
- Sedation may be given with fentanyl and midazolam.

Role of MRI

- Assess systemic or right ventricular function when echo windows are inadequate.
- Measure aortic root dimensions.

Tissue Doppler, Strain, and Strain Rate in Congenital Heart Disease

Quantification of ventricular function in patients with congenital heart disease can be very challenging using echocardiography. For the assessment of right ventricular function as well as single ventricular function, most of the time subjective visual assessment of ventricular function (eyeballing) is used. Alternative more quantitative methods should be used for follow-up and early detection of ventricular dysfunction.

Potential applications for tissue Doppler techniques currently are as follows[25]:

- Tissue Doppler velocities
  Diastolic function assessment.
  Isovolumetric acceleration seems to offer a relative load-independent measurement of cardiac contractility. It has been used in post-operative tetralogy patients and atrial switch patients. Due to its heart rate sensitivity, it has been used to study force-frequency relationships in post-operative patients with congenital heart disease.
  Further validation of its use in a clinical setting is required.
  Evaluation of dyssynchrony.
- Strain an strain rate imaging

  Evaluation of right ventricular systolic function
  Systemic right ventricle (CCTGA or after atrial switch)
  After tetralogy of Fallot correction
  Functionally single ventricle of RV morphology
  Evaluation of global and regional left ventricular function
  Evaluation of dyssynchrony

3D Echocardiography in Congenital Heart Disease

3D echo is useful for anatomical definition and for functional assessment, facilitating spatial recognition of intra-cardiac anatomy, thereby enhancing diagnostic confidence. 3D echocardiography is an emerging application. Full volume data acquisition in a single cardiac cycle and 3D myocardial strain are now being applied. Trans-oesophageal 3D echocardiography facilitates perioperative assessment.

Functional Assessment

- Compares well with MRI for the measurement of left ventricular volumes, ejection fraction, and mass.
- Reliable for the assessment of right ventricular volumes and functionally single ventricles (right or left ventricular morphology) using summation of discs. Semi-automatic algorithms for RV volumes are now available.[26]
- Growing role in the assessment and management of right ventricular volumes in tetralogy of Fallot, double outlet right ventricle (Fig. 30.31), atrial switch procedures, and congenitally corrected transposition of the great vessels.

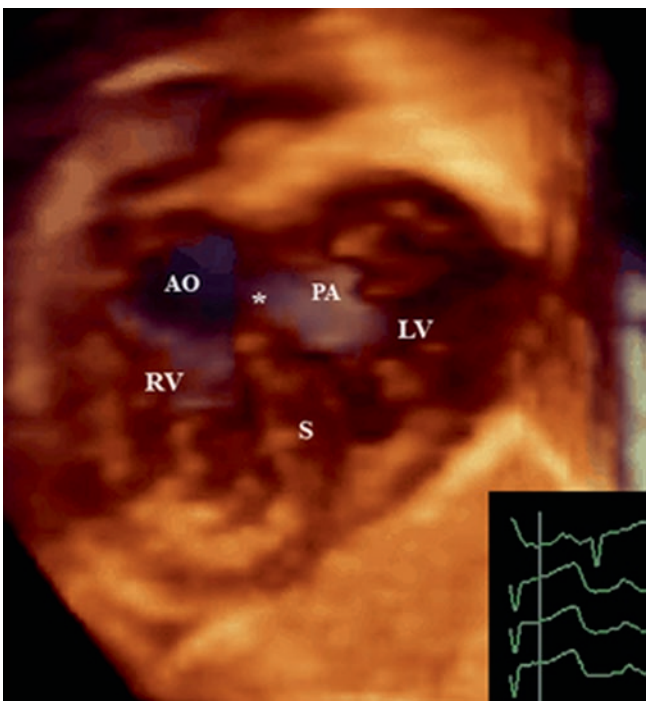

Fig. 30.31 3D image of double outlet RV. Sub-costal saggital plane in a patient with double outlet right ventricle and malposed great vessels. The aorta (AO) is seen arising far rightward and the pulmonary artery (PA) leftward and posterior. An asterisk denotes the VSD. The septum is marked by an *S*. Planning of surgical repair via an arterial switch procedure and VSD closure vs. an intra-cardiac baffle from the LV to AO across the VSD is facilitated by this kind of imaging

Assessment of Atrio-ventricular Valve Regurgitation (4 Chamber)

- Allows visualization of entire regurgitant jet.
- Orthogonal planes placed through the jet yield true vena contracta jet area.
- Ability to overlay colour Doppler on transparent grey-scale image and transient suppression of the colour image facilitate understanding of regurgitant mechanism.

3D Echo in Specific Lesions

Atrial Septal Defect (4-Chamber View, Sub-costal When Available)

- Shows true dimensions of the defect.
- Demonstrates changes in ASD size in systole and diastole.
- Shows ASD rims facilitating intervention planning.
- Shows position of device after intervention.
- Displays residual shunts (colour Doppler).

Enhances Visualization and Assesses True VSD Dimensions

- Guides transcatheter closure of muscular defects.
- Intra-operative visualization of apical and anterior muscular defects.

Atrio-ventricular Valves (4-Chamber, Parasternal Long-Axis)

- Assessment of mitral valve in congenital mitral stenosis.
- Assessment of the common atrio-ventricular valve and "cleft" in atrio-ventricular septal defects.
- Demonstrates mechanism of atrio-ventricular regurgitation.
- Perioperative assessment of atrio-ventricular valve regurgitation/stenosis.

Ebstein's Anomaly (Sub-costal When Available, 4 Chamber, Parasternal Views)

- Demonstrates tricuspid anatomy in single acquisition.
- Demonstrates extent of tricuspid regurgitation.

Left Ventricular Outflow Tract Obstruction (Parasternal Long Axis)

- Shows circumference and location of sub-aortic membranes.
- Shows relation of membrane to neighbouring structures.

Double Outlet Right Ventricle (Sub-costal When Available, Apical with Anterior Angulation, Parasternal)

- Defines relations of the great arteries to the ventricles, the VSD, and each other, facilitating surgical planning.
- Demonstrates straddling of AV valves.
- Demonstrates sub-pulmonary/ pulmonary stenosis.

Intra-cardiac Ultrasound (ICE)

- Used predominantly for guidance of electrophysiological and percutaneous congenital heart interventions in the catheterization laboratory (most commonly ASD/PFO closure) (4-chamber view).[27]
- Effective and comparable in cost to TOE.
- Catheter positioned in right atrium and used to display transverse planes at multiple levels and long-axis 4-chamber plane (Fig. 30.32).

Transducer orientation depends on the horizontal plane of the body and short axis of the right atrium.

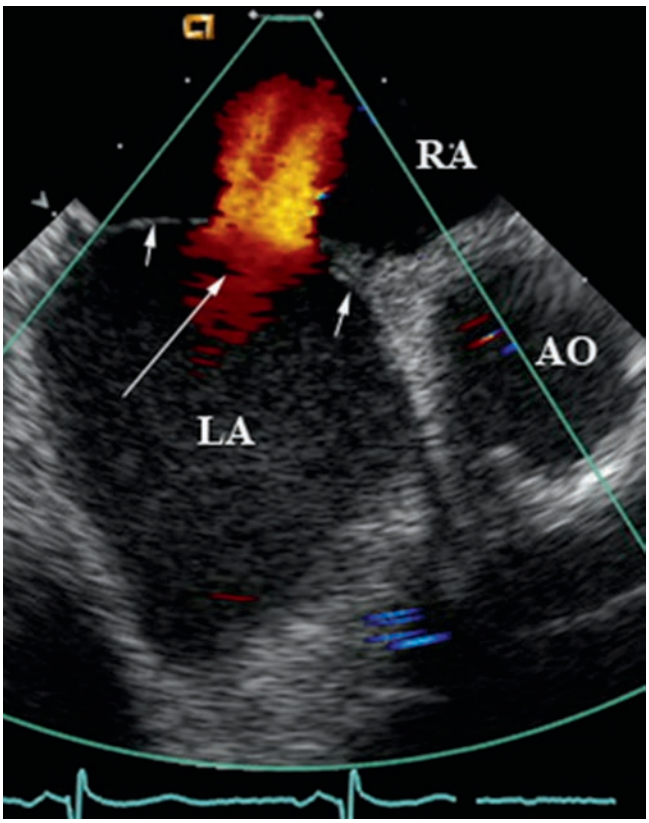

Fig. 30.32 Intra-cardiac echocardiography. Short-axis view at the level of the aortic valve (AO) obtained during intra-cardiac imaging of a secundum atrial septal defect. Colour flow (*long arrow*) depicting flow from the left atrium (LA) to the right atrium (RA) is seen. The rims bordering the defect (*short arrows*) are clearly seen

Video 30.1

(a) Secundum ASD. Apical four-chamber view of a secundum ASD. Notice the central position of the ASD within the intra-atrial septum and the T-signs at the margins. The right ventricle is dilated. (b) Secundum ASD. Apical four-chamber view of a secundum ASD with colour-flow imaging. Notice the large left-to-right shunt across the intra-atrial septum.

Video 30.2

Primum ASD. Apical four-chamber view of a primum atrial septal defect. The defect is located in the inferior part of the intra-atrial septum. Note that both AV-valves are implanted at the same level. There was an abnormal left AV-valve.

Video 30.3

(a) Perimembranous VSD. Parasternal short-axis view with on 2-D imaging a large perimembranous VSD. (b) Colour-Doppler image of a perimembranous VSD.

Video 30.4

Atrio-ventricular septum defect. Apical four-chamber view. Notice the combination of a primum atrial septal defect with an inlet VSD and a single AV-valve between the atria and the ventricles.

Video 30.5

Coarctation of the aorta. Notice the presence of a localized coarctation in this patient with continuous flow pattern in the juxtaductal region.

Video 30.6

Double-chambered right ventricle. Sub-costal view where the hypertrophied muscle bundle dividing the right ventricle into a high pressure and low pressure part with the presence of right ventricular outflow tract obstruction as can be seen on the colour image.

Video 30.7

Ebstein's anomaly. Apical four-chamber view of patient with Ebstain's anomaly. Notice that the septal leaflet of the tricuspid valve hinges distally towards the apex of the right ventricle and the sail-like appearance of the anterior leaflet of the tricuspid valve.

Video 30.8

Ebstein's anomaly. Parasternal short-axis view looking at the tricuspid valve. Notice that the inflow across the tricuspid valve is also rotated towards the right ventricular outflow tract. There is mild tricuspid regurgitation.

Video 30.9

(a, b) Tetralogy of Fallot. Sub-costal sagital view. Notice the large ventricular septal defect and the anterior deviation of the outlet septum causing right ventricular outflow tract obstruction. (b) Colour Doppler has been added.

Video 30.10

Tetralogy of Fallot. Parasternal long-axis view. Notice large ventricular septal defect extending to the outlet septum with about 40% of aortic override.

Video 30.11

Severe pulmonary regurgitation after Tetralogy of Fallot repair. Parasternal short-axis view. Notice the broad jet of pulmonary regurgitation which starts in the pulmonary artery branches. The right ventricular outflow tract (RVOT) is also dilated, which is related to the wide and dilated right ventricular outflow tract RVOT patch.

Video 30.12

Right ventricular dilatation related to severe pulmonary regurgitation after Tetralogy of Fallot repair. Apical four-chamber view. Notice the dilatation of the right ventricle. Qualitative assessment of right ventricular function suggest preserved systolic function in this patient.

Video 30.13

Patient after the Mustard operation with severe tricuspid regurgitation. Apical four chamber view. Notice the tricuspid regurgitation and mild RV dysfunction.

Video 30.14

Patient after the arterial switch operation. Parasternal short-axis view. Notice the position of the pulmonary artery in front of the aorta after the Lecompte manoeuver. The right pulmonary artery is to the right and the left pulmonary artery to the left of the aorta.

Video 30.15

Congenitally corrected transposition of the great arteries. Apical four-chamber view. In this view, the morphological right ventricle is on the left (notice the septal attachments of the tricuspid valve, the moderator band, and the coarse trabeculations).

Video 30.16

Congenitally corrected transposition of the great arteries. Parasternal short-axis view with the aorta located anterior and to the left of the pulmonary artery. The pulmonary artery bifurcation can be noted.

Video 30.17

Double inlet left ventricle. Apical fourchamber view. Two separate AV-valves are connected to a single ventricle which has left ventricular morphology. Notice the presence of the extra-cardiac Fontan conduit.

Video 30.18

Bidirectional Glenn shunt. Supra-sternal view. Look at the connection between the right superior vena cava and the right pulmonary artery. There is laminar flow on the connection. Flow can also be seen in the proximal left pulmonary artery.

Video 30.19

Total cavopulmonary connection. Supra-sternal view. The bidirectional Glenn shunt can be seen and also the connection between the extra-cardiac conduit and the pulmonary artery (the red flow moving into the pulmonary artery).

References

1. Hoffman JI, Kaplan S. The incidence of congenital heart disease. *J Am Coll Cardiol*. 2002;39(suppl 12):1890–1900
2. Hoffman JI, Kaplan S, Liberthson RR. Prevalence of congenital heart disease. *Am Heart J*. 2004;147(suppl 3):425–439
3. Anderson RH, Ho SY. Sequential segmental analysis: description and characterization for the millennium. *Cardiol Young*. 1997;7:98–116
4. Ferreira Martins JD, Anderson RH. The anatomy of interatrial communications – what does the interventionist need to know? *Cardiol Young*. 2000;10(suppl 5):464–473
5. Bartel T, Konorza T, Arjumand J, et al Intracardiac echocardiography is superior to conventional monitoring for guiding device closure of interatrial communications. *Circulation*. 2003;107(suppl 6):795–797
6. Handke M, Heinrichs G, Moser U, et al Transesophageal real–time three–dimensional echocardiography methods and initial in vitro and human in vivo studies. *J Am Coll Cardiol*. 2006;48(suppl 10):2070–2076
7. van den Bosch AE, Ten Harkel DJ, McGhie JS, et al Characterization of atrial septal defect assessed by real–time 3–dimensional echocardiography. *J Am Soc Echocardiogr*. 2006;19(suppl 6):815–821
8. Smallhorn JF, Tommasini G, Anderson RH, Macartney FJ. Assessment of atrioventricular septal defects by two dimensional echocardiography. *Br Heart J*. 1982;47(suppl 2):109–121
9. Smallhorn JF. Cross-sectional echocardiographic assessment of atrioventricular septal defect: basic morphology and preoperative risk factors. *Echocardiography*. 2001;18:415–432
10. Giroud JM, Jacobs JP. Evolution of strategies for management of the patent arterial duct. *Cardiol Young*. 2007;17(suppl 2):68–74
11. Matsui H, Adachi I, Uemura H, Gardiner H, Ho SY. Anatomy of coarctation, hypoplastic and interrupted aortic arch: relevance to interventional/surgical treatment. *Exp Rev Cardiovasc Ther*. 2007;5(suppl 5):871–880
12. Knauth Meadows A, Ordovas K, Higgins CB, Reddy GP. Magnetic resonance imaging in the adult with congenital heart disease. *Semin Roentgenol*. 2008;43(suppl 3):246–258

13. Paranon S, Acar P. Ebstein's anomaly of the tricuspid valve: from fetus to adult: congenital heart disease. *Heart*. 2008;94(suppl 2):237–243
14. Bashore TM. Adult congenital heart disease: right ventricular outflow tract lesions. *Circulation*. 2007;115(suppl 14):1933–1947
15. Redington AN. Determinants and assessment of pulmonary regurgitation in tetralogy of Fallot: practice and pitfalls. *Cardiol Clin*. 2006;24(suppl 4):631–639; vii
16. Anderson RH, Weinberg PM. The clinical anatomy of transposition. Cardiology in the young. 2005;15(suppl 1):76–87
17. Pretre R, Tamisier D, Bonhoeffer P, et al Results of the arterial switch operation in neonates with transposed great arteries. *Lancet*. 2001;357(suppl 9271):1826–1830
18. Warnes CA. Transposition of the great arteries. *Circulation*. 2006;114(suppl 24):2699–2709
19. Graham TJ, Bernard Y, Mellen B, et al Long–term outcome in congenitally corrected transposition of the great arteries: a multi-institutional study. *J Am Coll Cardiol*. 2000;36:255–261
20. Cook AC, Anderson RH. The functionally univentricular circulation: anatomic substrates as related to function. *Cardiol Young*. 2005;15(suppl 3):7–16
21. Anderson RH, Cook AC. Morphology of the functionally univentricular heart. *Cardiol Young*. 2004;14(suppl 1):3–12
22. Gewillig M. The Fontan circulation. *Heart*. 2005;91(suppl 6): 839–846
23. Vongpatanasin W, Brickner M, Hillis L, Lange R. The Eisenmenger syndrome in adults. *Ann Intern Med*. 1998;128:745–755
24. Siu SC, Colman JM. Heart disease and pregnancy. *Heart*. 2001;85(suppl 6):710–715
25. Mertens L, Ganame J, Eyskens B. What is new in pediatric cardiac imaging? *Eur J Pediatr*. 2008;167:1–8
26. Niemann PS, Pinho L, Balbach T, et al Anatomically oriented right ventricular volume measurements with dynamic three–dimensional echocardiography validated by 3–Tesla magnetic resonance imaging. *J Am Coll Cardiol*. 2007;50(suppl 17): 1668–1676
27. Zanchetta M, Onorato E, Rigatelli G, et al Intracardiac echocardiography-guided transcatheter closure of secundum atrial septal defect: a new efficient device selection method. *J Am Coll Cardiol*. 2003;42:1677–1682.

Chapter 31

THE ROLES OF CMR AND MSCT IN ADULT CONGENITAL HEART DISEASE

Philip Kilner, Ed Nicol, and Michael Rubens

CONTENTS

J. L. Zamorano et al. (eds.), *The ESC Textbook of Cardiovascular Imaging*
DOI: 10.1007/978-1-84882-421-8_31, © Springer-Verlag London Limited 2010

Introduction

Both CMR and MSCT give almost unrestricted access to intra-thoracic structures, which is important as ultrasonic access may be limited in ACHD patients, many of whom have had previous cardiothoracic surgery. MSCT, generally using intra-vascular contrast, gives superior spatial resolution in much shorter study times than CMR, although the radiation dose is a concern in this relatively young patient group that may require repeated studies. CMR offers unrivaled versatility of acquisition methods without ionizing radiation, enabling biventricular functional assessment, flow measurements, myocardial viability assessment, angiography, and more. For these reasons, a dedicated CMR service should be regarded as a necessary facility in a centre specializing in ACHD care. However, the short acquisition time and high spatial resolution of contrast-enhanced MSCT is advantageous, notably for imaging the epicardial coronary arteries and other narrow structures. MSCT also shows conduit calcification or stent location clearly, and retrospective ECG-gated multi-phase reformatting allows measurements of biventricular size and function, providing an alternative to CMR in patients with a pacemaker or ICD. To realize their full potential and avoid pitfalls, CMR and MSCT of ACHD require training and experience. Appropriate understanding is needed for the evaluation of congenitally and surgically altered circulatory function as after Fontan operations, surgery for transposition of the great arteries, or tetralogy of Fallot (ToF) repair. For these and other more complex cases, CMR and MSCT should ideally be undertaken by experienced congenital cardiovascular imaging specialists committed to long-term collaboration with the cardiologists and surgeons managing ACHD patients in a tertiary referral centre.

The relatively unrestricted access provided by CMR and MSCT allows the assessment of clinically important regions that may lie beyond ultrasonic access. These include the pulmonary veins and the sinus venosus regions of the atrial septum, the right ventricular free wall and outflow tract, the pulmonary arteries, and the whole aorta and the para-mediastinal regions, which may be crossed by aorto-pulmonary collateral arteries.[1,2] Both CMR and MSCT allow 3D contrast-enhanced angiography and regional or global assessment of biventricular function with good blood-tissue differentiation. MSCT offers the better spatial resolution and does not require specific predetermination of imaging planes as there is a complete volume of data that can be rotated and cut to any desired plane. CMR offers the possibility of "dynamic" angiography, visualizing the sequential opacification of successive vascular regions. Besides freedom from radiation, the key additional strengths of CMR lie in its high temporal resolution, measurements of flow volumes, and characterization of tissues, if needed.

Comprehensive CMR Acquisition in ACHD

Except in straightforward cases where the questions to be answered are well defined, it is prudent in a baseline or pre-surgical CMR study to perform a comprehensive examination that will allow review of the structure and function of the myocardium, valves, and vessels through all regions of the heart and mediastinum. A stack of multiple transaxial ± coronal cines is simple and relatively quick to acquire using a contemporary CMR system. Such cine stacks are easily reviewed using suitable image display software. Dynamic contrast-enhanced angiography and non-contrast 3D steady-state free-precession (SSFP) imaging can also be valuable, although these do not, on their own, yield cyclic functional information. Cine images should also be aligned with each inflow and outflow valve and with any shunt flow so that inter-connections can be established and described according to sequential segmental analysis (see previous chapter).

Measurements of Right and Left Ventricular function

Both CMR and MSCT allow volumetric analysis of both ventricles without geometric assumptions, which is particularly important given the variability of RV shape in ACHD.[3] However, the myocardium of the RV is extensively trabeculated in most individuals, with only a relatively thin layer of compact myocardium in the free wall. This makes reproducible delineation of the RV blood–muscle boundary challenging. For CMR, the most reproducible approach is probably to place a relatively smooth boundary line (contributing to a reconstructed 3D surface) between the trabeculated and compact layers of the RV free wall.[4] However, this boundary can be hard to define where trabeculations come together in systole. In MSCT, a more rapid and robust semi-automated boundary detection based on attenuation (or signal) differences between the (opacified) blood and myocardium is routinely used (Fig. 31.1). It may become feasible to apply a similar method to CMR cines, which could potentially be more accurate, although not necessarily directly comparable with the simplified, manually placed boundary method.

Additional considerations affecting RV volume measurements are the movements of the atrio-ventricular junction, which can contribute a significant part of the RV stroke volume, and the difficulty of locating pulmonary annular level after infundibular resection or patching in repairs of ToF. We

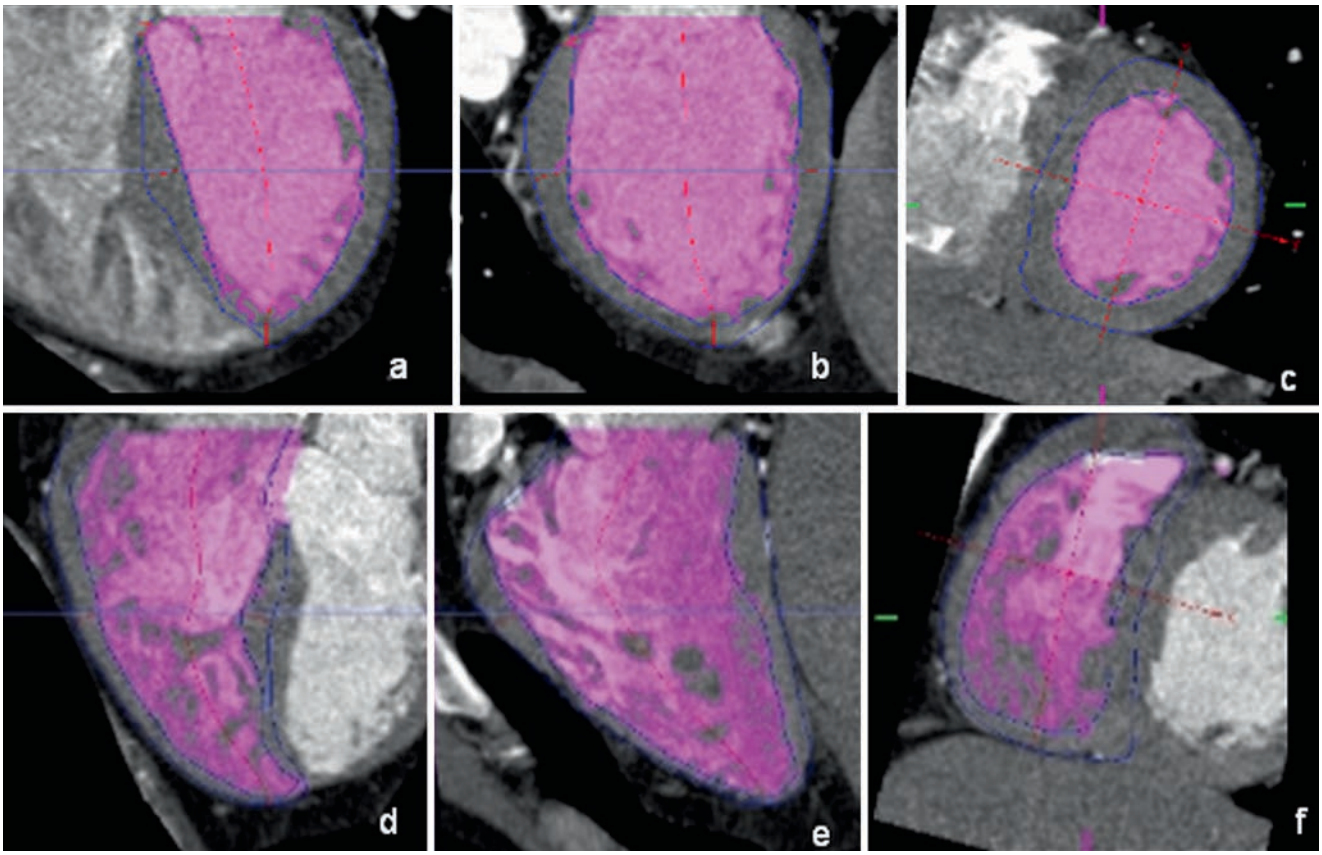

Fig. 31.1 Oblique long- and short-axis planes reformatted from MSCT data after a single injection of contrast, which also gave opacification of the coronary and pulmonary arteries. In the left ventricle **(a–c)** and right ventricle **(d–f)**, the opacified blood regions identified for volume calculation are coloured *pink*

recommend that an aneurysmal or akinetic RV outflow tract is included in the RV volume, up to the expected level of the pulmonary valve.

It needs to be emphasized that, for serial comparisons of RV function, consistent methods of delineation need to be used. Contour data for volumetric analysis should ideally be stored in a database and remain available for comparison at the time of follow-up.

Flow Measurements by CMR

The measurement of volume flow in a large vessel is potentially an unrivaled strength of CMR. Through-plane velocity mapping of ascending aortic and main pulmonary artery (PA) flow (Fig. 31.2) allows calculations of left- and right-sided output and, therefore, of shunting and of the amount of regurgitation of the outflow valves. For these derived values, however, the measurements of velocity need to have a high standard of accuracy. This is not easy to achieve on all CMR systems, and care may be needed to minimize or correct errors introduced by background phase offset errors, particularly when the vessel is dilated.[5]

Jet Velocities and Calculations of Pressure Difference

Measurements of the velocities of post-stenotic jets or of relatively broad regurgitant jets are feasible by phase contrast CMR as long as the velocity mapping slice is located to transect the jet immediately downstream of the orifice, so that voxels lie completely within the coherent jet core. As with Doppler ultrasound, pressure differences may be estimated by applying the modified Bernoulli equation. However, the velocities of narrow jets through mildly regurgitant tricuspid or pulmonary valves, which are used in echocardiography for estimations of RV or PA pressure, are unlikely to be accurately measured by CMR.

The Roles of CMR or MSCT in Specific Diagnostic Groups

Note: Further anatomical and pathophysiological background can be found in the corresponding subsections of the preceding chapter on echocardiographic investigation.

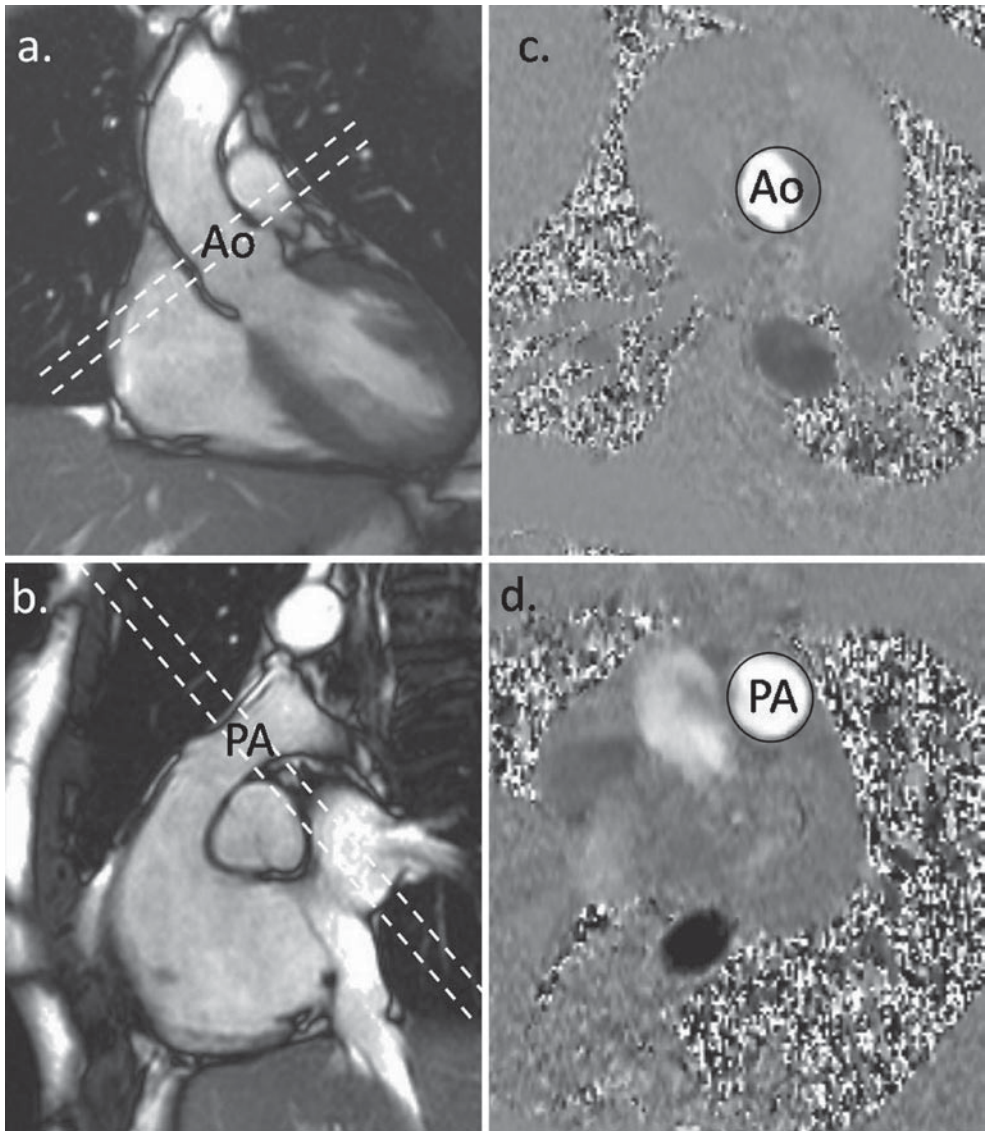

Fig. 31.2 CMR cine images **(a, b)** aligned with the ascending aorta (Ao) and main pulmonary artery (PA). Systolic frames of through-plane phase contrast velocity maps **(c, d)**, located as indicated by the dotted lines from which the volumes of aortic and pulmonary flow (and regurgitant volume, if present) can be derived

Atrial Septal Defects (ASD)

While echocardiography is the first-line modality, CMR and MSCT (Fig. 31.3a) can address unanswered questions about the location and size of unusual defects, biventricular size and function, and any associated anomalies, notably the possibility of anomalous pulmonary venous drainage.[6] With CMR, the amount of shunting (Qp:Qs measurement) can also be assessed. A contiguous transaxial stack of cines and pulmonary venous angiography allow visualization of all pulmonary veins and any sinus venosus defect. A contiguous atrial short axis stack, parallel to ventricular short axis planes, progressing from the A-V junction to the SVC, is suitable for visualization of an ASD, followed by through-plane velocity mapping of transecting flow through the defect. Both these views can be obtained by rotating and slicing the MSCT dataset to the required plane.

However, for the identification or exclusion of a small ASD or patent foramen ovale, CMR and MSCT are likely to be less effective than a (repeat) contrast echo study.

Ventricular Septal Defects (VSD)

VSDs can usually be visualized by echocardiography. They are easily identified by MSCT (Fig. 31.3b). CMR can add Qp:Qs measurement, if required (Fig. 31.1). The commonest way of identifying a small VSD by CMR is by the presence of a systolic jet on the RV side of the septum, seen in one of the ventricular short-axis cines that are acquired routinely for ventricular function measurement. The suspected jet should then be cross-cut with additional cine images. Mapping of velocities through a plane transecting the VSD jet can contribute to sizing of the defect.

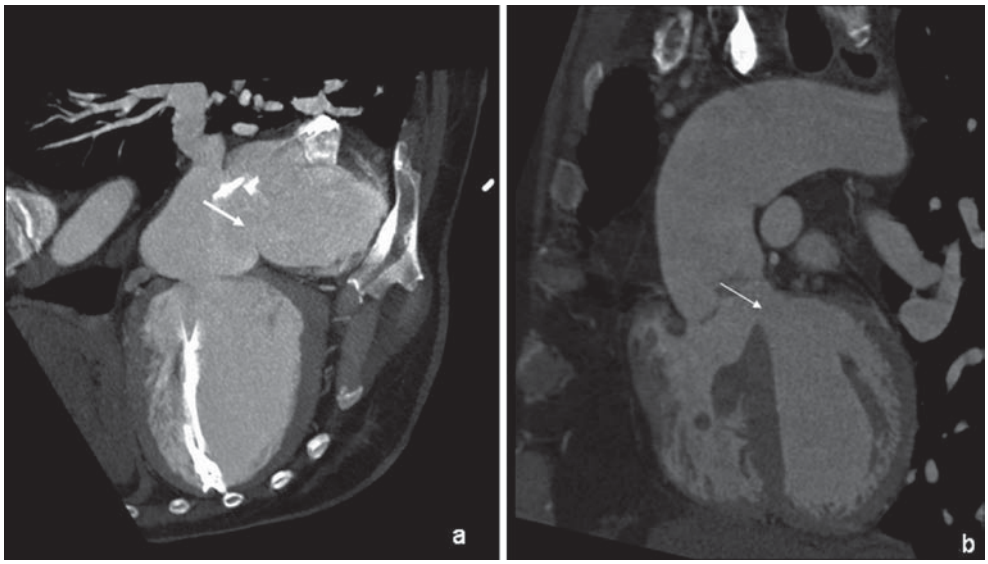

Fig. 31.3 Reformatted MSCT images showing an atrial septal defect (*broad white arrow in* **(a)**). Note the atrial and ventricular pacing leads that pass through the ASD and terminate in the left atrium and left ventricle, respectively. **(b)** Ventricular septal defect (*thin white arrow*) in a patient with tetralogy of Fallot

Atrio-ventricular Septal Defect

CMR and MSCT can provide additional views of any (residual) defect or associated anomaly, and CMR can quantify any residual shunt or regurgitation of the left A-V valve.

Patent Ductus Arteriosus

Either CMR or MSCT can show the size of a duct and any associated abnormalities of anatomy or ventricular function. For screening, a routine contiguous coronal stack of SSFP (bright blood) images, one slice per heart beat, is recommended as part of every ACHD CMR study. The jet through a small PDA can be identified in the distal pulmonary trunk in such images, and then interrogated further by cine imaging and velocity mapping, including Qp:Qs measurement. Note: When the shunt is from aorta to the distal PAs, the ascending aortic flow will be more than the MPA flow, whereas distal to the PDA, the actual pulmonary flow will be correspondingly greater than the systemic.

Coarctation of the Aorta

CMR or MSCT contrast-enhanced angiography is helpful in the assessment of native coarctation diagnosed beyond childhood with a view to balloon dilatation and stenting or surgery. Either modality also allows visualization of recoarctation or aneurysm formation after repair. CMR can probably offer the more thorough assessment of any associated pathology, such as stenosis or regurgitation of a bicuspid aortic valve, dilatation of the ascending aorta, or LV hypertrophy. The aortic arch with coarctation may not lie in a single plane, and when using cine imaging and velocity mapping, it is necessary to identify planes best orientated for the depiction and measurement of any jet flow through the coarctation. The presence of diastolic prolongation of forward flow, or a diastolic tail, is a useful sign of significant coarctation, which can be demonstrated by plotting a velocity–time curve of jet flow beyond the coarctation.[7] Following stent insertion for coarctation (Fig. 31.4), MSCT may better visualize the stent position and possible intra-stent stenosis due to the signal drop out that may occur with CMR.

Berry aneurysms of the circle of Willis or other cerebral vessels occur in up to 10% of patients with coarctation bearing the risk of rupture.[8] As rupture of a cerebral aneurysm is associated with high mortality, screening for cerebrovascular aneurysms by MRI may be wise, particularly, if symptoms develop.

Right Ventricular Outflow Tract (RVOT) Obstruction and Double-Chambered RV

The main contributions of CMR or MSCT lie in demonstrating the level(s) of RVOT obstruction, particularly in adults with poor acoustic windows. Stenosis may be present at more than one level of the RVOT, or in the pulmonary arteries (Fig. 31.5). Of note, a mild degree of pulmonary stenosis can result in marked post-stenotic dilatation, usually affecting the pulmonary trunk and LPA.

Sub-infundibular stenosis or double-chambered RV can be well demonstrated by CMR. The obstructing muscular

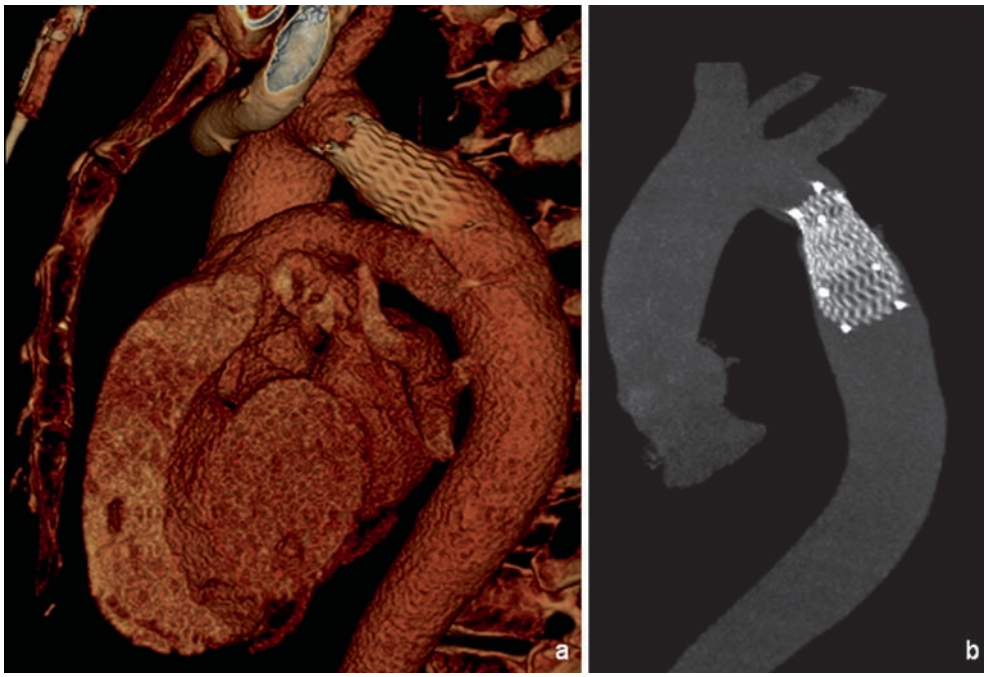

Fig. 31.4 Aortic coarctation with stent imaged by MSCT. Both volume-rendered projection **(a)** and maximal intensity projection **(b)** show the position of the stent and allow its dimensions to be measured

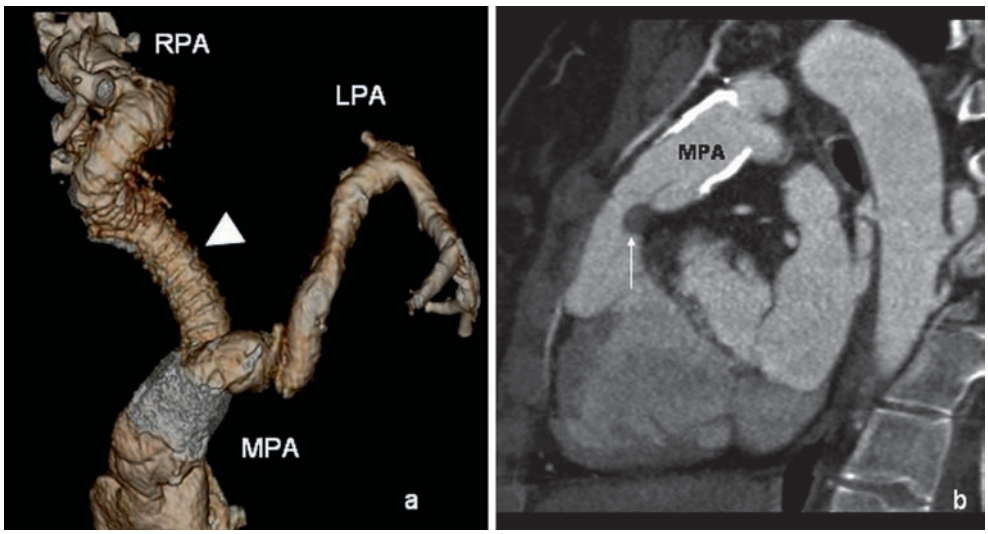

Fig. 31.5 The MSCT volume-rendered image **(a)** shows a heavily calcified main pulmonary artery homograft conduit (MPA) and a corrugated tubular conduit (*white arrowhead*) to the right pulmonary arterial branches (RPA) after unifocalization surgery for pulmonary atresia with aorto–pulmonary collateral arteries. **(b)** subpulmonary stenosis (*white arrow*) proximal to the calcified homograft

bands or fibromuscular ridge between the hypertrophied body of the RV and the non-hypertrophied and non-obstructive infundibulum and the resulting systolic jet should be well seen on at least one of the routine ventricular short-axis cines (Fig. 31.6, Video 31.6a–e). Mapping of velocities through a plane transecting the jet together with visualization of the degree of upstream RV hypertrophy and septal flattening allows an assessment of severity. However, an associated VSD with its jet usually arising close to the tricuspid valve into the trabeculated, high pressure part of the RV may be hard to identify on CMR.

Left Ventricular Outflow Tract Obstruction (LVOTO) and Aortic Regurgitation

While echocardiography remains the first line of investigation, CMR cine imaging and jet velocity mapping can be valuable in assessing the level(s) and nature of obstruction, which may be present at more than one level. In the case of hypertrophic obstructive cardiomyopathy, late gadolinium imaging can contribute to an assessment of myocardial fibrosis, which may be relevant to prediction of the risk of arrhythmia.

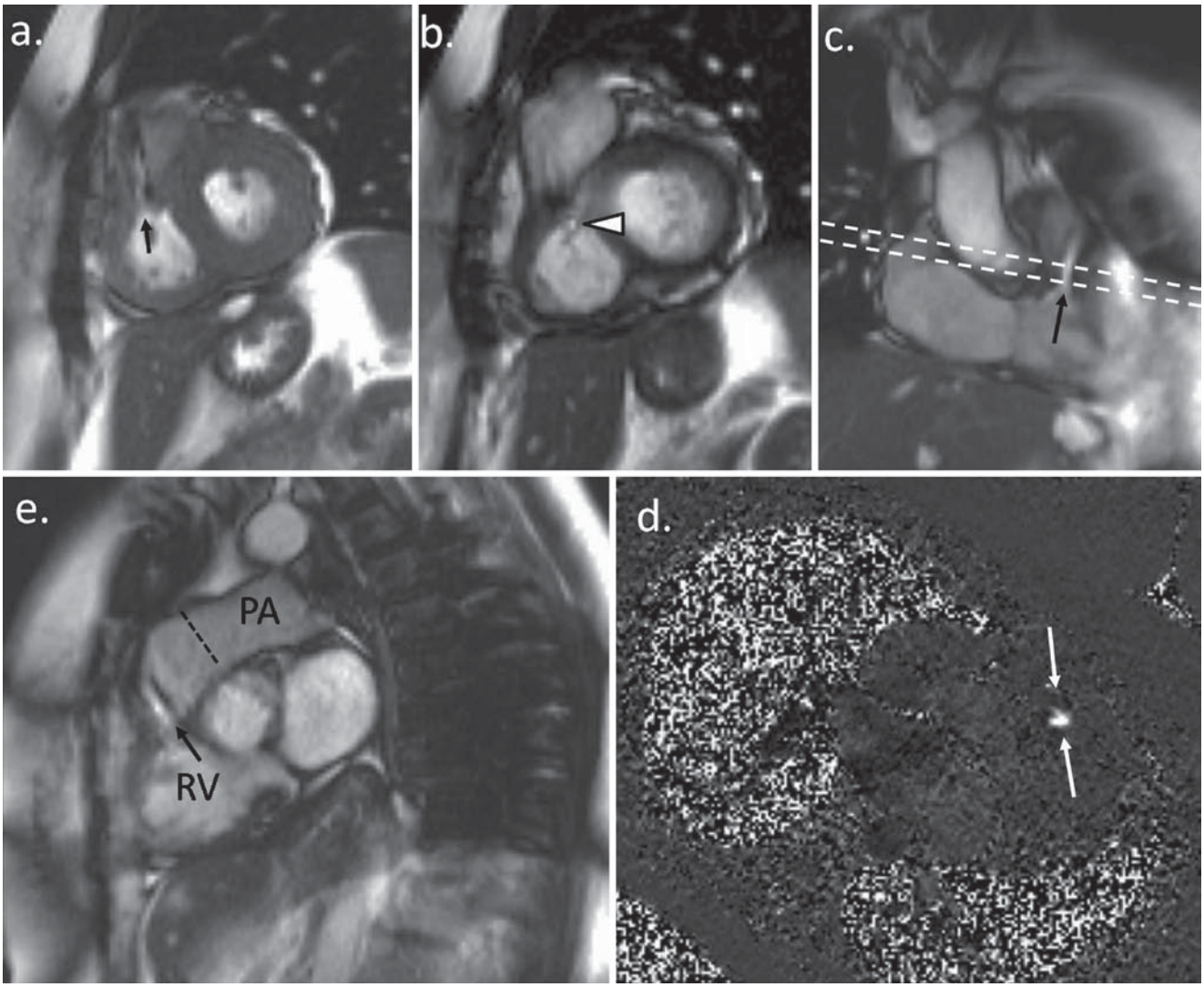

Fig. 31.6 Double-chambered right ventricle or sub-infundibular stenosis identified by CMR in a 53-year-old male. A routine short-axis SSFP cine **(a)** shows a systolic jet (*arrowed*) directed from the hypertrophied sinus of the RV into the non-hypertrophied infundibulum. A slightly more basal short-axis cine **(b)** shows a systolic bright spot (*arrowhead*) indicative of flow through a small perimembranous VSD. The oblique coronal cine **(c)** is aligned with the jet in **(a)**. The *dotted lines* indicate the slice location of through-plane jet velocity mapping **(d)**, which recorded a peak systolic velocity of 3.8 m/s. An oblique sagittal RVOT cine **(e)** shows the RV jet in relation to the unobstructed infundibulum and pulmonary valve, whose level is marked by the *dotted line*. The patient went on to have surgical relief of the sub-infundibular stenosis and closure of the VSD by a right atrial approach, conserving the native pulmonary valve

Assessment of aortic valve stenosis by MSCT has been found to show good correlation of transthoracic echocardiography[9] and trans-oesophageal echocardiography, and there is no reason to believe that the same should not be true for other valves. Any calcification of valve structures can be seen, and cardiac gating also allows assessment of valve leaflet mobility and valve orifice dimensions through the cardiac cycle.

The amount of aortic regurgitation can be measured using CMR by mapping velocities through a plane transecting the ascending aorta. For reproducibility and longitudinal comparison, the plane is probably best located immediately above the sino-tubular junction. Although this approach is clinically valuable, the derived measurements of aortic regurgitation are highly susceptible to any background phase offset errors, which may need to be minimized or corrected.[4] Furthermore, upward diastolic movement of the aortic root relative to a fixed velocity mapping plane can result in significant under-estimation of the regurgitant fraction if the root is mobile and dilated. In isolated aortic regurgitation, the excessive LV stroke volume relative to that of the RV can also quantify the regurgitation, as long as the volumes are accurately measured.

CMR Assessment After Ross Operation

The commonest post-operative complications are stenosis or regurgitation of the RV-PA homograft conduit. Stenosis may be due to shrinkage of the homograft tube or a suture line, or to stiffening of the valve leaflets. Any jet formation should be visualized by cine imaging and quantified by velocity mapping, and regurgitation measured by velocity mapping.[10] The autograft valve in aortic position should also be assessed for possible dilatation and regurgitation, particularly beyond the first decade after operation. Visualization of the re-implanted coronary arteries may be indicated using MSCT or CMR 3D SSFP acquisition (see below). If there is a question of post-surgical LV ischaemia or infarction, perfusion imaging and/or late gadolinium enhancement may be considered.

Ebstein's Anomaly and Tricuspid Regurgitation

CMR or MSCT allows thorough visualization of RA–RV anatomy, the ASD if present, tricuspid valve displacement and malfunction, and the size and contractility of the functional part of the RV (Fig. 31.7, Video 31.7a–d). A stack of transaxial CMR cines, supplemented by 4-chamber and sagittal RVOT cines, is recommended. Transaxial cines may be used for volume measurements of the functional part of the Ebstein RV, which can be hard to delineate in short-axis slices. In spite of atrialization, higher RV volumes than normal may be found in the presence of severe tricuspid regurgitation. The severity of tricuspid regurgitation can be assessed using through-plane velocity mapping, the VENC typically set at 250 cm/s, to depict the cross-section of the regurgitant stream through a plane transecting the jet on the right atrial side of the orifice. A TR jet cross-section, reflecting the regurgitant defect, of 6 × 6 mm or more can be regarded as severe. An ASD, due in this setting to distension and gaping of a PFO, can be present in about 50% of adult Ebstein patients and should be sought with an atrial short-axis cine stack. If present, the resting shunt can be measured by aortic and pulmonary velocity mapping. Cines may show diastolic compression of the LV by the dilated right heart, which can impair LV filling and so limit the cardiac output.

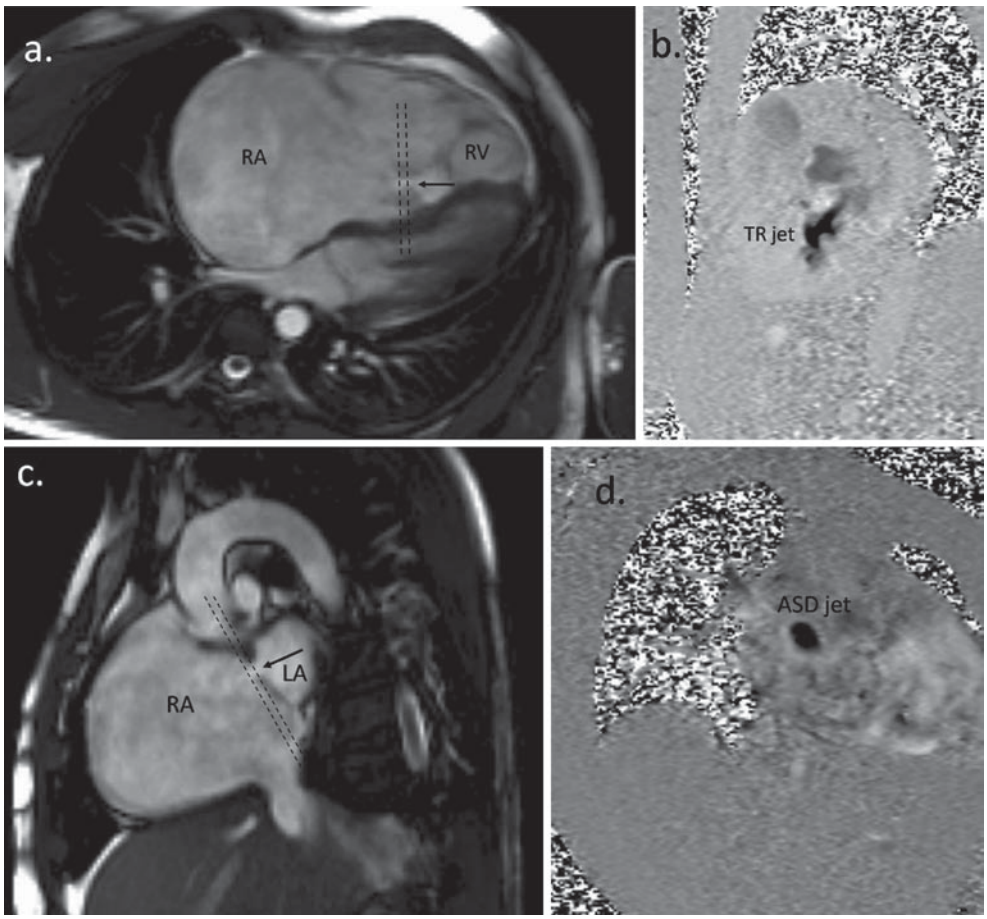

Fig. 31.7 Ebstein's anomaly imaged by CMR. Cine imaging in a 4-chamber plane **(a)** shows regurgitation (*arrow*) through the dysplastic tricuspid valve. The *dotted lines* indicate the plane through which velocities were mapped **(b)** to depict the cross sectional size of tricuspid regurgitant jet (TR), assessed in this case as severe. An atrial short-axis cine in the same patient **(c)** shows bidirectional flow through an atrial septal defect (*arrow*). The *dotted lines* indicate the plane through which velocities were mapped **(d)** to depict the cross section of the ASD jet

Congenital Mitral Valve Dysfunction

While echocardiography remains the first line of investigation, CMR can contribute to the measurement of regurgitation and assessments of the structural cause and of any associated myocardial or other pathology. For identification of tethering, prolapse, or failure of coaptation, a contiguous stack of 5 mm thick cine images aligned perpendicular to the central part of the line of mitral coaptation is recommended.[11] Regurgitant or stenotic jets are visible on cine imaging, although appearances depend on the jet size and characteristics and on the relative location and orientation of the imaging slice. Planimetry of an orifice, or rather of the cross section of the jet immediately downstream of the orifice, is feasible in some, but not all, cases, depending on the structure of the jet and the relative thickness and location of the imaging slice. Jet velocity mapping can contribute to quantification of stenosis and the time course of jet flow. In the absence of another regurgitant or shunt lesion, mitral regurgitation can be quantified using ventricular stroke volume difference. However, a more widely applicable approach is to subtract the aortic outflow volume from the LV stroke volume.

Cor Triatriatum Sinister

Echocardiography is likely to be satisfactory, but a stack of contiguous CMR cines will show the intra-atrial membrane well, if orientated orthogonal to it. Transaxial or 4-chamber orientations may be suitable. Transaxial cines can also show any anomalous pulmonary venous drainage. As in the case of an ASD, mapping of velocities through a plane orientated parallel and close to the membrane on its downstream side can delineate flow through the orifice(s).

Repaired Tetralogy of Fallot

CMR has become the modality of choice for the assessment and follow-up of adults with repaired ToF. CMR measurements of RV and LV function, pulmonary regurgitation (PR), RVOT obstruction, conduit or PA stenoses, and possible residual shunting all contribute to decisions on management, notably the possibility of pulmonary valve replacement, for PR. Where CMR is unavailable or contraindicated, MSCT can provide morphological assessment and ventricular function, but not the flow or shunt data. The pathophysiology of PR differs from that of aortic regurgitation because of the situation of the sub-pulmonary right heart, connected in series with the more powerful left heart via the low-resistance pulmonary and high-resistance systemic vasculature. Free PR, with little or no effective valve function, is common after repair of ToF. It may be tolerated without symptoms for decades and is typically associated with a regurgitant fraction of ~40% (Fig. 31.8, Video 31.8a–c). However, RV dysfunction, arrhythmia, and premature death can result. Surgical pulmonary valve replacement is considered in such patients in most centres, but deciding when to operate remains controversial, particularly if the patient is asymptomatic and bearing in mind that a homograft replacement may only function effectively for 15 or 20 years [12]. Once a conduit is in position, however, progressive stenosis or regurgitation may be treatable by percutaneous placement of a stented valve within the relatively rigid tube of the conduit.[13, 14] Studies by Therrien et al[15] and Oosterhof et al[16] compared CMR measurements of RV volumes before and after surgical pulmonary valve replacement, finding that patients with preoperative indexed RV end-diastolic volumes above about 60 mL/m^2 and end-systolic volumes above about 82 mL/m^2 failed to recover to the normal RV volume range. Although this may be taken as a guide to RV volumes that should not be exceeded when waiting to replace a pulmonary valve, there are more factors to be considered. Even in the absence of an effective pulmonary valve, the amount of regurgitation depends on factors upstream and downstream. In occasional cases, the rugurgitant fraction can exceed 50%, which may be attributable to an unusually large and compliant RV, large and compliant pulmonary arteries whose elastic recoil contributes to the regurgitation, branch PA stenosis, or elevated peripheral resistance limiting the distal escape of flow, or combinations of these.[17] Contrast-enhanced 3D angiography may be used for the visualization of PA branch stenosis, and appropriately aligned cines can visualize jet formation and the reduced systolic expansion of PA branches distal to a stenosis that is obstructive enough to require relief, either percutaneously or at the time of surgery. Surgeons can resect any akinetic region of the RVOT that may have resulted from previous infundibular resection or patching, and so regional as well as global RV function need to be described. Tricuspid regurgitation needs to be identified and assessed, as does any residual VSD patch leak and consequent shunting. Global and regional LV function and any aortic root dilatation or aortic regurgitation also need assessment.[18] So in summary, the evaluation of repaired ToF requires thorough assessment of the left and right heart, extending to the branch PAs. Each measurement should be interpreted in the context of circulatory factors upstream and downstream.

Common Arterial Trunk

CMR or MSCT can be useful in visualizing either the native pulmonary arterial branches or the conduit(s) following repair

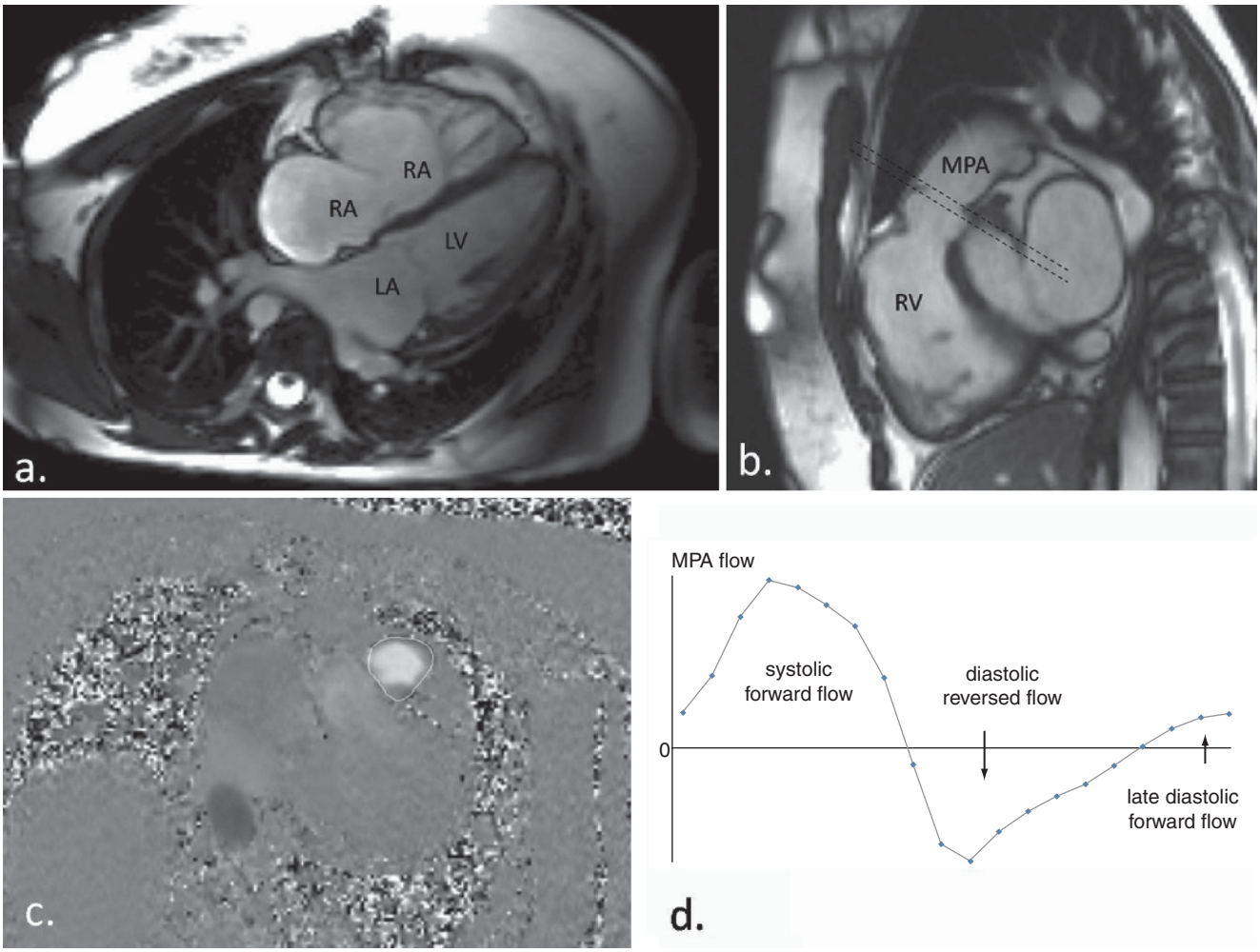

Fig. 31.8 Repaired tetralogy of Fallot imaged by CMR. The 4-chamber cine **(a)** shows evidence of mild tricuspid regurgitation. An oblique sagittal RVOT cine **(b)** shows evidence of pulmonary regurgitation, without effective valve function. The *dotted lines* indicate the slice through which pulmonary flow velocities were mapped (**(c)**, with the MPA outlined). **(d)** Pulmonary flow curve derived from the velocity data, from which a regurgitant fraction of 38% was calculated. Note the late diastolic forward flow occurring as atrial systole delivers flow forwards through the fully expanded right ventricle

and can help to quantify biventricular function. CMR can additionally quantify any regurgitation of the truncal valve.

Transposition of the Great Arteries (TGA)

TGA Treated by Atrial Switch Operation (Mustard or Senning)

CMR or MSCT can assess the atrial pathways and systemic RV function.[19] With CMR experience, oblique cines and velocity maps can be aligned with respect to systemic and pulmonary venous atrial pathways (Fig. 31.9, Video 31.9 a-d). Comprehensive coverage can, however, be achieved using a stack of contiguous transaxial or coronal cines or a 3D SSFP sequence. Baffle leaks may not be easy to identify by CMR, the suture line being long and non-planar, but measurement of Qp:Qs may be helpful.

TGA Treated by Arterial Switch Operation

CMR or MSCT allows assessment of any RVOT or supravalvular PA stenosis, branch PA stenosis, and function of both ventricles and the neo-aortic valve. MSCT or CMR can contribute to assessment of the patency of the re-implanted coronary arteries, and CMR perfusion imaging may be considered.[20]

TGA Treated by Rastelli Operation

CMR or MSCT allows assessment of possible stenosis or incompetence of the RV-to-PA conduit, the LVOT, of biventricular function, and, with CMR, possible residual shunt.

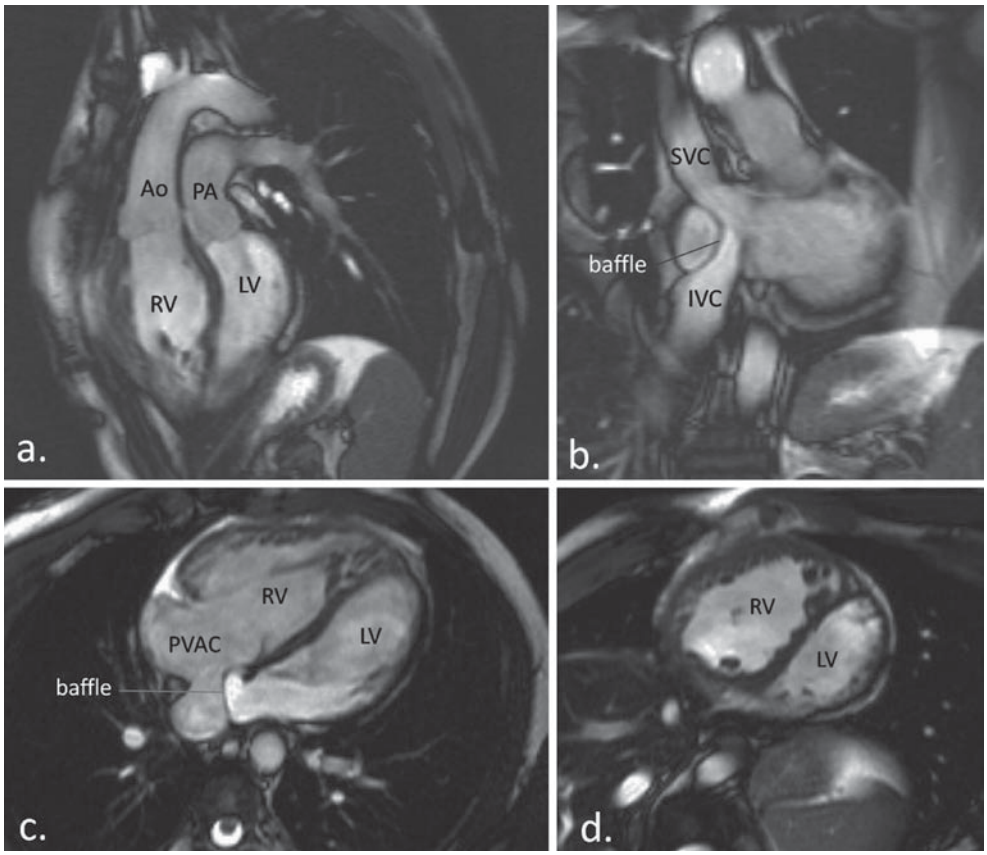

Fig. 31.9 Transposition of the great arteries after an atrial switch procedure (Mustard operation). An oblique sagittal cine **(a)** is aligned to show the discordant ventriculo-arterial connections. An oblique coronal cine **(b)** is aligned with the superior vena cava (SVC) and inferior vena cava (IVC) pathways, passing to the left of the surgically placed baffle, towards the sub-pulmonary left ventricle. An oblique long-axis cine **(c)** shows the pulmonary venous atrial compartment (PVAC), which carries blood from the pulmonary veins to the right ventricle. A mid short-axis cine **(d)** shows the expected hypertrophy of the systemic right ventricle

Double Outlet RV

CMR or MSCT can be valuable, particularly after surgery if a conduit, PA branch stenosis, residual shunting, or ventricular dysfunction need assessment.

Congenitally Corrected Transposition of the Great Arteries

Either CMR or MSCT can demonstrate the abnormal anatomy and connections well, which can be helpful in adults with poor acoustic windows. A useful way of distinguishing which ventricle is morphologically the RV is to compare the two surfaces of the inter-ventricular septum. The LV surface is relatively smooth, with few trabeculations arising from it, in contrast to the RV side, which gives rise to the moderator band and multiple trabeculations in the apical region (Fig. 31.10, Video 31.10a–c).

The Functionally Univentricular Heart

In patients with poor acoustic windows, any of the diagnostic issues listed in the preceding chapter can be addressed by CMR or MSCT and also systemic or pulmonary venous anomalies, aortic arch malformations, and branch PA stenoses. The global and regional function of the volume loaded dominant ventricle can be assessed with either modality with late gadolinium scar imaging by CMR, if required.

The Fontan Circulation

Fontan operations, performed in children in whom the abnormal cardiac anatomy precludes biventricular repair, result in a fundamental departure from normal circulatory dynamics. The systemic and pulmonary vascular beds are connected in series downstream of the single functional ventricle, thereby eliminating shunting at the cost of a critically elevated systemic venous pressure that is required to maintain flow through the lungs. Earlier procedures incorporated the right atrium between the caval veins and pulmonary arteries, whereas total cavo-pulmonary connection, connecting inferior vena cava (IVC) flow to the PAs via a lateral tunnel or extra-cardiac conduit, has been favoured in recent years. CMR or MSCT allows assessment of the Fontan cavo–(atrio)–pulmonary connections, branch pulmonary arteries, pulmonary veins (which can be compressed by a dilated right atrium after an atrio-pulmonary connection), the atrio-ventricular valve(s), the ventricle(s), the ventricular outflow tract, and

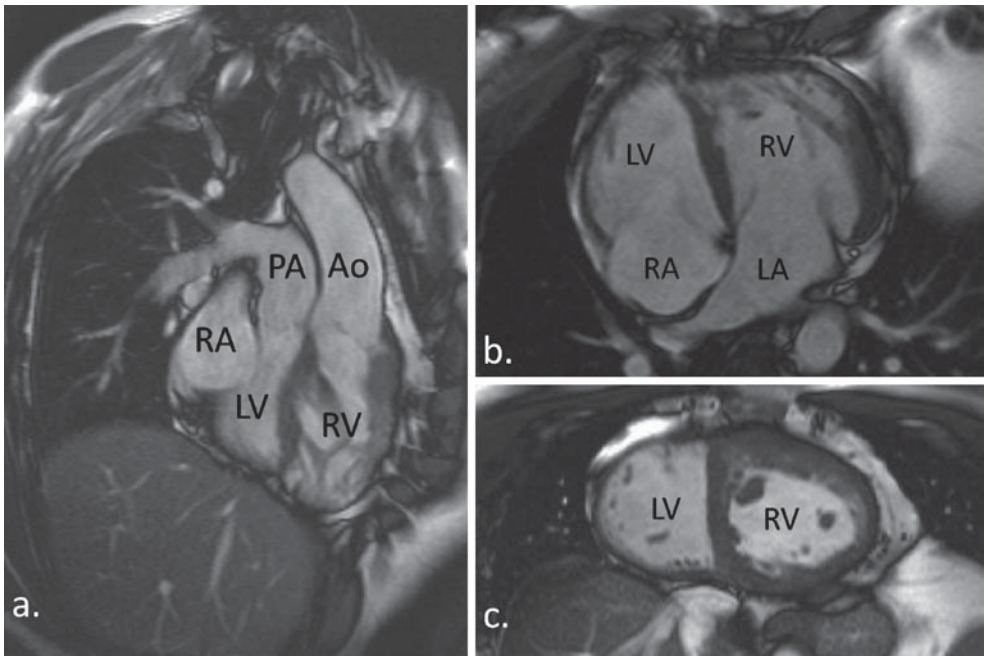

Fig. 31.10 Unoperated "congenitally corrected" transposition of the great arteries imaged by CMR. Both the atrio-ventricular and the ventriculo–arterial connections are discordant **(a, b)**. Note the expected apical displacement of the septal insertion of the tricuspid valve of the RV relative to that of the mitral valve of the LV. In the short axis cine **(c)** note that, as in Fig. 31.9, the left ventricular cavity can be identified as the one on the smoother, less trabeculated side of the ventricular septum

any residual leaks (with CMR) or collateral vessels. Comprehensive coverage using a stack of contiguous transaxial SSFP cines is recommended, which is generally suitable for the identification of any intra-atrial thrombus or suspected stenosis of the cavo–pulmonary connections. Velocity mapping can be used to assess flow through a suspected narrowing. In this setting, a peak jet velocity exceeding 1 m/s may represent significant stenosis. Should contrast injection for either MSCT or CMR angiography be considered, the connection of the SVC to the PAs and its relation to IVC flow should be borne in mind. Injection from a leg or else non-contrast CMR 3D SSFP imaging may be preferable. Evaluation of myocardial fibrosis by LGE may contribute to the assessment impaired ventricular function, if present.

Pulmonary Arterial Hypertension Including Eisenmenger's Syndrome

Although neither CMR or MSCT can measure pulmonary arterial pressures, good visualization of any RV hypertrophy, ventricular septal flattening, and any limitation of the systolic expansion of distended PAs means that the presence of pulmonary hypertension can be inferred and qualitatively assessed by CMR. CMR and MSCT also allow measurements of cardiac output, RV function, and hypertrophy, and CMR can be used, after gadolinium injection, for the assessment of RV or septal fibrosis. In Eisenmenger's syndrome, either modality can give valuable information on the underlying malformation(s), and CMR allows shunt calculation at rest. Contrast PA angiography, particularly by MSCT, is used to identify any pulmonary arterial thrombus (Fig. 31.11).[21]

Coronary Artery Anomalies and Acquired Coronary Disease

Contrast-enhanced MSCT is superior to CMR for the assessment of coronary artery patency and calcification, if present (Fig. 31.12).[22] Both techniques are also able to determine global and regional myocardial function. The origin and proximal course of the coronary arteries can be visualized in most patients by CMR using cardiac gated 3D SSFP angiography, with fat suppression and without contrast agent and either diaphragm navigator or breath-hold acquisition. However, the strength of CMR in this field lies in the complementary information that can be obtained on myocardial viability and perfusion.[23]

Prospects for Further Development

Both CMR and MSCT continue to be developed and refined. There are particular needs for reliable and user-friendly post-processing tools for the analysis of multi-dimensional image data. For example, rapid and reproducible segmentation and analysis of biventricular volumes from images of either modality would be a major step forward.

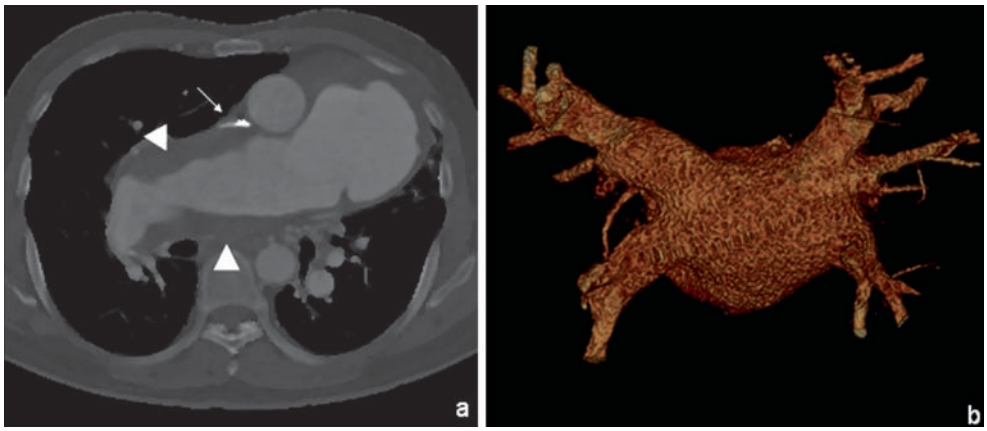

Fig. 31.11 Pulmonary arterial and pulmonary venous anatomy imaged by MSCT. **(a)** Dilated main and right pulmonary arteries with both mural calcification (*white arrow*) and in situ thrombus (*white arrowheads*). The ratio of the diameters of the pulmonary arteries to the aorta is more than 1, an indicator of pulmonary hypertension. **(b)** Normal pulmonary venous drainage into the left atrium

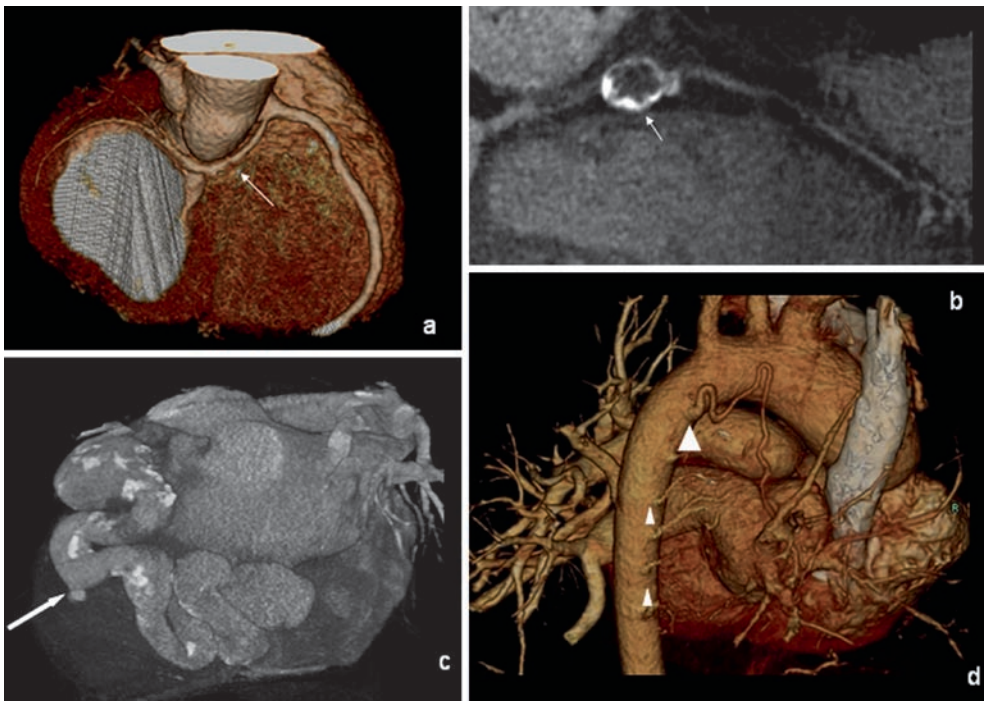

Fig. 31.12 Coronary anomalies imaged by MSCT include **(a)** aberrant coronary arteries, with the left circumflex artery (*white arrow*) arising from the right coronary artery, **(b)** coronary artery aneurysm in Kawasaki disease (note lack of contrast enhancement of aneurysm due to thrombus within it), and **(c)** a dilated and tortuous coronary arterio–venous fistula via a left circumflex artery (*white arrow*) that drains directly to the coronary sinus. **(d)** Aorto–pulmonary collateral arteries (*arrowheads*) arising from the descending aorta and supplying parts of the right lung

CMR is an inherently versatile modality. The repertoire of radio pulse and magnetic gradient sequences and their uses with respect to tissue characteristics, movements, flows, and contrast agents is being steadily extended and refined. "Comprehensive" image acquisitions can potentially be less operator dependent, delivering an inclusive dataset for subsequent review and measurement. However, prolonged acquisitions have to be gated or synchronized with respect to respiratory as well as cardiac cycles. Rapidly acquired 4D (time resolved 3D) CMR acquisitions have yet to achieve sufficient robustness and freedom from artefacts for clinical value. Comprehensive (3D, 3-directionally encoded and time resolved) velocity mapping has been implemented.[24] and processed to give dynamic streamline or particle trace displays reconstructed from data acquired of many heart and respiratory cycles, but limitations include acquisition periods of 30 min or more, and the inability of this approach to accurately measure a wide range of velocities in the presence of jet flow.

Real-time CMR acquisition requires neither cardiac nor respiratory gating and has a place in the imaging of breathing–related modifications of heart movement, for example, breathing dependent deviation of the ventricular septum in constrictive pericarditis[25] and improvements may bring further uses.

There is a major drive to reduce the ionizing radiation dose from MSCT with new and novel protocols and algorithms now standard on all new MSCT machines. Many of the newest generation of MSCT scanners have now complete cardiac coverage (256/320 detectors), allowing full

angiography with no or minimal gantry movement, and the possibility of contrast tracking allowing some flow data to be gained. This has led to a 50–90% reduction in ionizing radiation dose with the latest scanners delivering approximately 1 mv for a CTA and less than 5 MsV for a combined CT coronary, pulmonary, and aortic angiogram.

One of the additional limitations of MSCT in patients with congenital heart disease has been the lack of tolerance to pharmacological rate control (usually β-blockers), and with the latest iteration of MSCT, the temporal resolution has been reduced, albeit not to the current rate of CMR.

MSCT continues to develop rapidly and is likely to remain a significant modality in the assessment of adult congenital heart disease, particularly for the assessment of coronary artery pathology and pulmonary hypertension and if CMR is unable to be performed or unavailable locally.

References

1. Fratz S, John H, Annika S, et al Routine clinical cardiovascular magnetic resonance in pediatric and adult congenital heart disease: patients, protocols, questions asked and contributions made. *J Cardiovasc Magn Reson.* 2008;10:46
2. Nicol ED, Gatzoulis M, Padley SP, Rubens M. Assessment of adult congenital heart disease with multi-detector computed tomography: beyond coronary lumenography. *Clin Radiol.* 2007;62(suppl 6):518–527
3. Lembecke A, Dohmen PM, Dewey M, et al Evaluation of right ventricular volumes and function: comparison with magnetic resonance imaging. *Ann Thorac Surg*. 2005;79:1344–1351
4. Winter MM, Bernink FJ, Groenink M, et al Evaluating the systemic right ventricle by CMR: the importance of consistent and reproducible delineation of the cavity. *J Cardiovasc Magn Reson.* 2008; 10(suppl 1):40
5. Chernobelsky A, Shubayev O, Comeau CR, Wolff SD. Baseline correction of phase contrast images improves quantification of blood flow in the great vessels. *J Cardiovasc Magn Reson.* 2007;9: 681–685
6. Piaw CS, Kiam OT, Rapaee A, et al Use of non-invasive phase contrast magnetic resonance imaging for estimation of atrial septal defect size and morphology: a comparison with transesophageal echo. *Cardiovasc Intervent Radiol.* 2006;29:230–234
7. Nielsen JC, Powell AJ, Gauvreau K, Marcus EN, Prakash A, Geva T. Magnetic resonance imaging predictors of coarctation severity. *Circulation*. 2005;111(5):622–628
8. Connolly HM, Huston J III, Brown RD Jr, Warnes CA, Ammash NM, Tajik AJ. Intracranial aneurysms in patients with coarctation of the aorta: a prospective magnetic resonance angiographic study of 100 patients. *Mayo Clin Proc.* 2003;78:1491–1499
9. Pouleur AC, le Polain de Waroux JB, Pasquet A, Vanoverschelde JL, Gerber BL. Aortic valve area assessment: multidetector CT compared with cine MR imaging and transthoracic and transesophageal echocardiography. *Radiology.* 2007;244:745–754
10. Crowe ME, Rocha CA, Wu E, Carr JC. Complications following the Ross procedure: cardiac MRI findings. *J Thorac Imaging.* 2006; 21:213–218
11. Gabriel RS, Kerr AJ, Raffel OC, Stewart RA, Cowan BR, Occleshaw CJ. Mapping of mitral regurgitant defects by cardiovascular magnetic resonance in moderate or severe mitral regurgitation secondary to mitral valve prolapse. *J Cardiovasc Magn Reson.* 2008;10:16
12. Henkens IR, van Straten A, Schalij MJ, et al Predicting outcome of pulmonary valve replacement in adult tetralogy of Fallot patients. *Ann Thorac Surg.* 2007;83:907–911
13. Lurz P, Coats L, Khambadkone S, et al Percutaneous pulmonary valve implantation: impact of evolving technology and learning curve on clinical outcome. *Circulation.* 2008;117:1964–1972
14. Frigiola A, Tsang V, Nordmeyer J, et al Current approaches to pulmonary regurgitation. *Eur J Cardiothorac Surg.* 2008;34(3):576–580
15. Therrien J, Provost Y, Merchant N, Williams W, Colman J, Webb G. Optimal timing for pulmonary valve replacement in adults after tetralogy of Fallot repair. *Am J Cardiol.* 2005;95(6):779–782
16. Oosterhof T, van Straten A, Vliegen HW, et al Preoperative thresholds for pulmonary valve replacement in patients with corrected tetralogy of Fallot using cardiovascular magnetic resonance. *Circulation.* 2007;116:545–551
17. Chaturvedi RR, Redington AN. Pulmonary regurgitation in congenital heart disease. *Heart.* 2007;93:880–889
18. Geva T, Sandweiss BM, Gauvreau K, Lock JE, Powell AJ. Factors associated with impaired clinical status in long-term survivors of tetralogy of Fallot repair evaluated by magnetic resonance imaging. *J Am Coll Cardiol.* 2004;43:1068–1074
19. Salehian O, Schwerzmann M, Merchant N, Webb GD, Siu SC, Therrien J. Assessment of systemic right ventricular function in patients with transposition of the great arteries using the myocardial performance index: comparison with cardiac magnetic resonance imaging. *Circulation.* 2004;110:3229–3233
20. Taylor AM, Dymarkowski S, Hamaekers P, et al MR coronary angiography and late-enhancement myocardial MR in children who underwent arterial switch surgery for transposition of great arteries. *Radiology.* 2005;234:542–547
21. Nicol ED, Kafka H, Stirrup J, Padley SP, Rubens MB, Kilner PJ, Gatzoulis MA. A single, comprehensive non-invasive cardiovascular assessment in pulmonary arterial hypertension: combined computed tomography pulmonary and coronary angiography. *Int J Cardiol*. 2009;136:278–88
22. Leschka S, Alkhadi H, Plass A, et al Accuracy of MSCT coronary angiography with 64 –slice technology:first experience. *Eur Heart J*. 2005;26:1482–1487
23. Wu HD, Kwong RY. Cardiac magnetic resonance imaging in patients with coronary disease. *Curr Treat Options Cardiovasc Med.* 2008;10(1):83–92
24. Markl M, Harloff A, Bley TA, et al Time-resolved 3D MR velocity mapping at 3T: improved navigator-gated assessment of vascular anatomy and blood flow. *J Magn Reson Imaging.* 2007;25: 824–831
25. Francone M, Dymarkowski S, Kalantzi M, Rademakers FE, Bogaert J. Assessment of ventricular coupling with real-time cine MRI and its value to differentiate constrictive pericarditis from restrictive cardiomyopathy. *Eur Radiol.* 2006;16:944–951

Section 8

Aortic Disease: Aneurysm and Dissection

Chapter 32

ROLE OF ECHOCARDIOGRAPHY

José Luis Zamorano and Perez de Isla

CONTENTS

J. L. Zamorano et al. (eds.), *The ESC Textbook of Cardiovascular Imaging*
DOI: 10.1007/978-1-84882-421-8_32, © Springer-Verlag London Limited 2010

Introduction

Aortic aneurysms and aortic dissection are relatively frequent entities and their prognosis is sometimes fatal. Transthoracic and trans-oesophageal echocardiography (TOE) are two of the main diagnostic tools for diagnosis, prognostic evaluation, and surgical assessment. In this section, the potential use of echocardiography for patients with suspected or demonstrated aortic aneurysm dissection will be discussed.

Role of Echo in Aortic Disease

Aortic Aneurism

An aortic aneurysm is a localized dilatation of the aorta greater than 50% the normal diameter, and it should include the three layers of the wall.[1] A pseudoaneurysm in which there is a lack of one or more of the aortic walls is a different pathologic entity. There are two major morphologic types of aneurysm morphology: fusiform and saccular.

Causes of aortic aneurysm include hypertension, atherosclerosis, aortic stenosis, bicuspid aortic valve, and the Marfan syndrome, among others. Several conditions are associated with different patterns of aortic dilatation. For instance, hypertension is associated with enlargement at the sino-tubular junction and tubular ascending aorta, congenital aortic stenosis is associated with more significant post-stenotic dilatation, and Marfan syndrome is associated to symmetric dilatation of the three sinuses of Valsalva.

Echocardiography is a very useful diagnostic tool for aortic aneurysm assessment.[1–4] Transthoracic echocardiography (TTE) is the first-choice diagnostic tool for this indication, and TOE is used if additional information is required. Echocardiography is also recommended to evaluate aortic root dilation in Marfan syndrome and connective tissue syndromes, and in those patients with bicuspid aortic valve due to its association with aortic root and ascending aorta dilatation. Nevertheless, there are two settings in which TOE is preferred: aortic evaluation in emergency situations and when coexistent dissection is suspected (Figs. 32.1–32.3, Videos 32.1 and 32.2).

Aortic valve replacement and aortic root reconstruction or replacement are indicated in patients when the degree of dilatation of the aorta or aortic root reaches or exceeds 5.0 cm by echocardiography. Patients with bicuspid aortic valves and dilatation of the aortic root or ascending aorta with a diameter greater than 4.0 cm should undergo serial evaluation. Aortic root reconstruction or replacement is indicated in patients with bicuspid aortic valves if the diameter of the

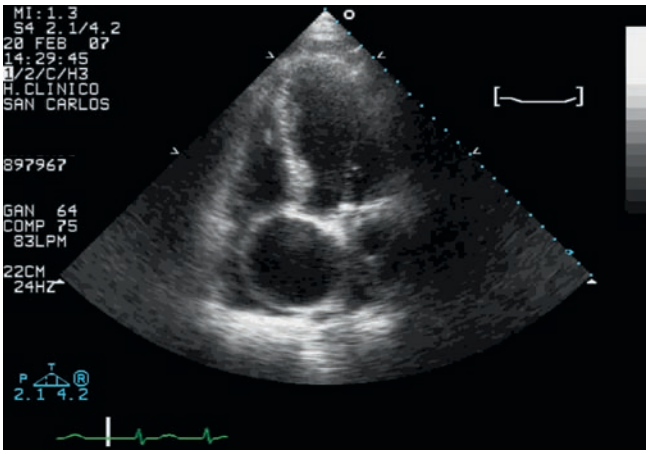

Fig. 32.1 Transthoracic echocardiography (TTE). Four-chamber view. A large ascendant aorta aneurysm can be clearly seen. Right atrium compression is evident

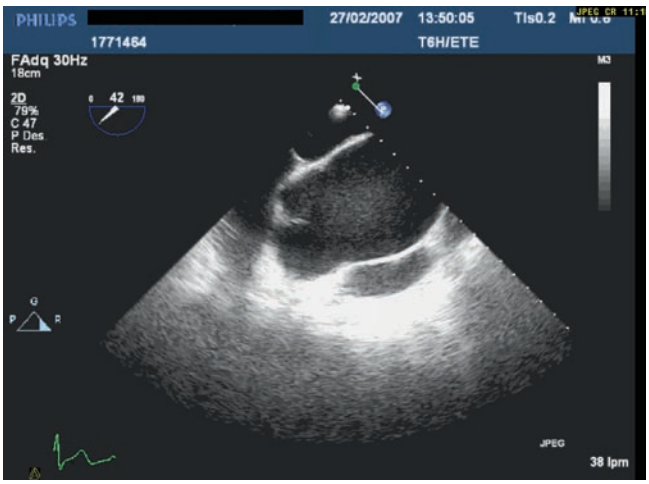

Fig. 32.2 TTE. Paraesternal long-axis view. Aortic aneurysm with Valsalva sinuses involvement is frequently seen in patient under the diagnosis of Marfan Syndrome

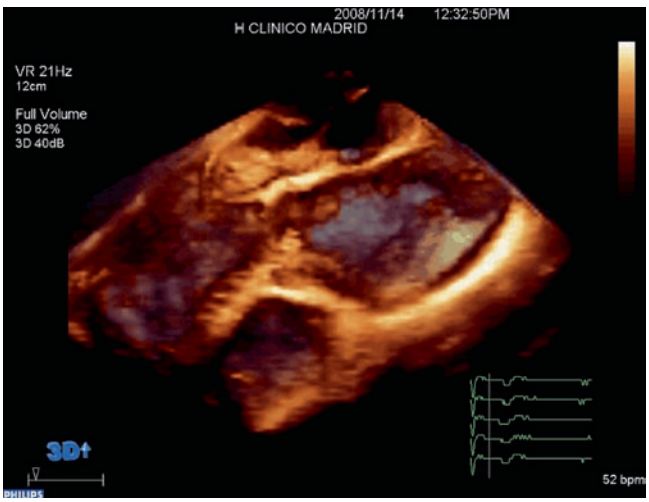

Fig. 32.3 Real-time 3D trans-oesophageal echocardiography (TOE) may help in some circumstances to evaluate the morphologic characteristics of aortic aneurisms

aortic root or ascending aorta is greater than 5.0 cm or if the rate of increase in diameter is 0.5 cm per year or more. In patients with bicuspid valves undergoing aortic valve replacement, severe aortic regurgitation, or aortic stenosis, surgery of the aorta is indicated if the diameter of the aortic root or ascending aorta is greater than 4.5 cm.[3, 5]

Aortic Dissection

Aortic dissection is a dramatic and sometimes fatal problem. Immediate mortality is 1% within 1 h, and the 2-week survival rate is only 25% in patients without treatment. It is characterized by the formation of a false lumen in the tunica media of the aorta wall. Depending on the anatomic characteristics, different types of aortic dissection can be differentiated, each with its own clinical, therapeutic, and prognostic implications.[6]

According to the Stanford classification of aortic dissection, there are two main types: Type A and Type B.[7, 8] An aortic dissection is Type A if it includes the ascending aorta, and Type B if it does not involve the ascending aorta. Otherwise, the De Bakey classification subdivides the dissection process into a Type I dissection if it involves the entire aorta, a Type II dissection if it involves the ascending aorta, and a Type III dissection if it involves the descending aorta.[8] Intra-mural haematoma (IH) and aortic ulcers may be signs of evolving dissections or dissection subtypes. Based on these findings, a new differentiation has been proposed[9]: Class 1: Classical aortic dissection with an intimal flap between true and false lumen; Class 2: Medial disruption with formation of IH/haemorrhage; Class 3: Discrete/subtle dissection without haematoma, eccentric bulge at tear site; Class 4: Plaque rupture leading to aortic ulceration, penetrating aortic atherosclerotic ulcer with surrounding haematoma, usually sub-adventitial; and Class 5: Iatrogenic and traumatic dissection. All classes of dissection can also be classified into acute and chronic: chronic dissections are considered to be present if more than 14 days have elapsed since the acute event or if they are found occasionally.

A typical aortic dissection begins with the tearing of the aortic intima, which exposes the diseased underlying medial layer to the pulsating blood flow (Figs. 32.4 and 32.5 and Video 32.3). The blood then penetrates this layer, dissecting it. This dissection can then extend distally for a variable distance, creating a false lumen. Shearing forces can then cause the tearing of the internal part of the dissected aorta wall, producing additional entry and exit zones. The most common locations for primary intimal tears are in the ascending aorta 1–5 cm above the right sinus of Valsalva (65% of cases), in the proximal descending aorta under the left subclavian artery (20%), in the transverse aortic arch (10%), and in the distal thoracic-abdominal aorta (5%).[10]

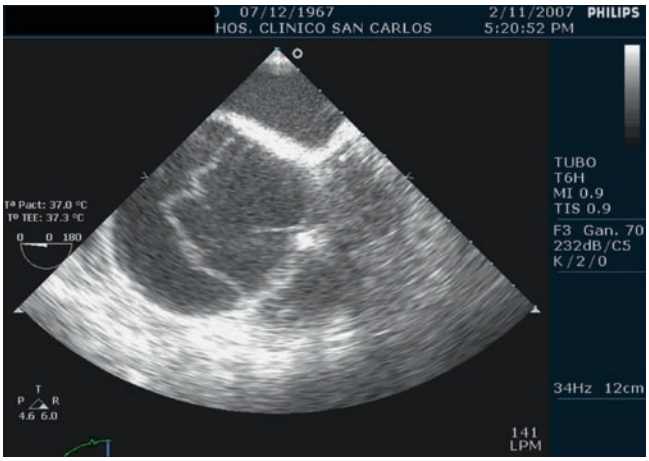

Fig. 32.4 TOE. Intimal flap is the more characteristic finding in aortic dissections. This image was acquired during the ventricular systole

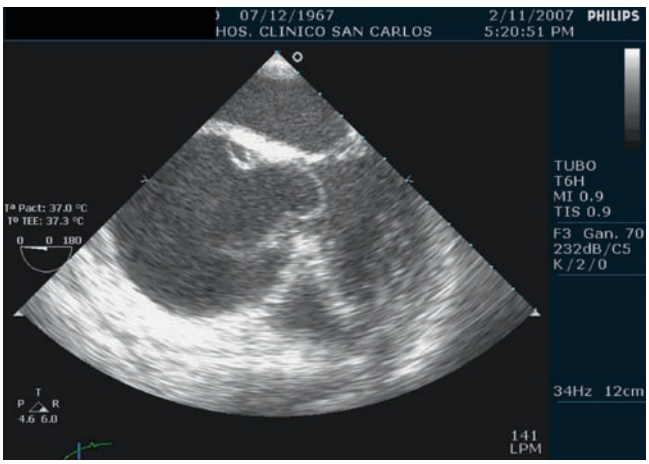

Fig. 32.5 Same case as in Fig. 32.4. Aortic dissection may be associated to many other complications, such as aortic regurgitation. In this case the intimal flap is the cause of the aortic valve incompetence. This image was acquired during the ventricular diastole

Echocardiography is the first step in the diagnosis of patients with a suspected aortic dissection. The diagnosis of aortic dissection by echocardiography requires the demonstration of a true and a false lumen separated by an intimal flap. Echocardiographic evaluation is very useful to assess an aortic dissection[11] and even may help determine the potential for aortic valve-sparing surgery in some cases. Advantages of TOE over TTE for the detection of aortic dissection include the close proximity of the oesophagus to the thoracic aorta and the fact that it is a portable procedure and may provide diagnostic information within minutes. It may be particularly useful in unstable patients who cannot undergo magnetic resonance imaging (MRI) or CT. TOE allows avoiding the limitations of TTE imposed by thoracic deformations, obesity, and pulmonary diseases. If, after TTE examination, the

need for surgery is clear, it should be necessary to stabilize the patient by intubation and mechanical ventilation before performing this procedure. TOE may also be used during surgery to obtain further details.

The main diagnostic finding that TOE provides in a patient with an aortic dissection is intimal dissection flaps. M-mode ultrasound allows the detection and differentiation of intimal flaps in the aorta. Enlargement of the aortic wall, dilation of the aortic root, and enlargement of the posterior wall are possible. M-mode ultrasound has also been described as useful for differentiating between real flaps and artefacts. Thus, M-mode echocardiography may help to avoid a wrong diagnosis by demonstrating a lack of relation between movement of the intimal flap and the aortic wall.[12]

- Identification of the true and false lumens: The presence of flow does not absolutely distinguish the true lumen from the false lumen. The true lumen is characterized by the following: it is of reduced size, shows greater pulsatility during systole, the presence of echocontrast is rare, clotting is also rare, and communication is from true lumen to false lumen during systole (Table 32.1, Figs. 32.6 and 32.7 and Videos 32.4–32.6).
- Differentiation between communicating and non-communicating dissection: according to how the flow is visualized in the false lumen and how tears are detected in the intimal flap, it is possible to differentiate between communicating and non-communicating dissections. When communication exists, the intimal flap shows wide movements during the cardiac cycle, whereas movements are reduced in non-communicating dissections.
- Localizing entry and communication points.
- Pericardial effusion: the effusion of fluid in the pericardium and/or the pleural space is a sign of poor prognosis (Fig. 32.8).[12]
- Coronary artery ostium involvement.
- Involvement of lateral branches of the aorta.
- Aortic valve involvement: TOE may evaluate the severity and mechanism of aortic regurgitation that complicates acute Type A dissections. In case aortic valve is normal and aortic regurgitation is secondary to a repairable aortic lesion, the patient may undergo aortic valve repair, but if there are non-repairable abnormalities, the patient should undergo valve replacement (Video 32.3).
- Thrombosis in the false lumen (Fig. 32.9 and Video 32.7).

The diagnostic accuracy TOE for the identification of aortic dissection has been studied in several works. A great proportion of the information is based on monoplane TOE studies. The sensitivity of TOE for the diagnosis of aortic dissection is greater than 97%. However, the specificity of TOE may be inferior to 85%.[13, 14] The low specificity is due to false positive findings in the ascending aorta, but these artefacts can be identified by the use of M-mode imaging, resulting in an increase in specificity to almost 100%.[13] In some circumstances, other entities such as the complicated atherosclerotic plaque shown in this video should be distinguished from aortic dissections (Video 32.8).

In acute Type A dissection, surgery is indicated, and its aim is to prevent aortic rupture and pericardial tamponade, and to relieve aortic regurgitation. Surgery in acute Type B dissection is indicted if persistent or recurrent chest pain appears, and if there is aortic expansion, periaortic haematoma, or mediastinal haematoma.[2]

Other Types of Acute Aortic Syndromes

Intra-mural Haematoma

An IH is caused by either a rupture of the aortic vasa vasorum which provokes a bleeding that separates medial wall

Table 32.1. Diagnostic characteristics of true and false lumen in a classic aortic dissection

Size	False lumen Large	True lumen Small
Systolic expansion	No	Yes
Systolic flow	High velocity/bidirectional	Low velocity/forward
Spontaneous contrast	Frequent	Absent
Wall	Thin	Tic
Thrombosis	Yes	No

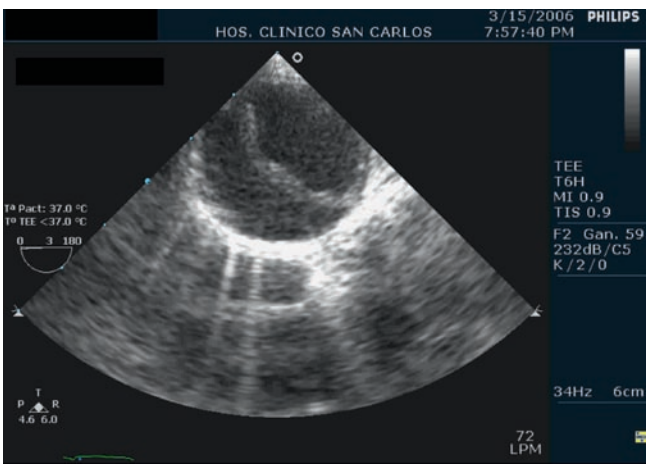

Fig. 32.6 TOE at the level of the thoracic descendent aorta. True and false lumen can be appreciated. Several echocardiographic findings are very useful to distinguish between both lumens. See text and Table 32.1 for more details

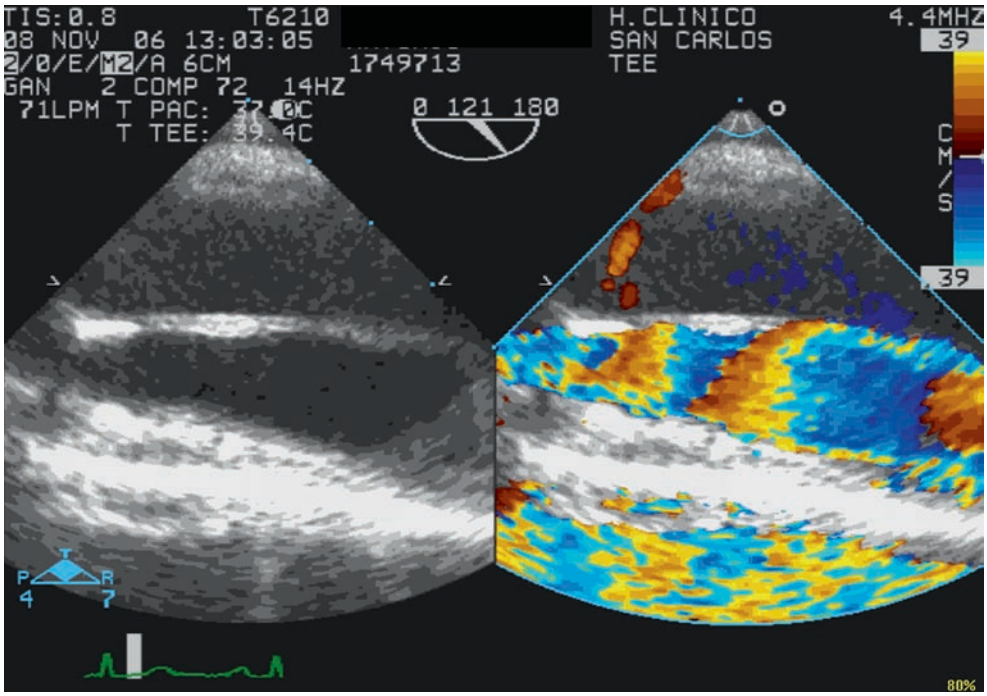

Fig. 32.7 TOE at the level of the thoracic descendent aorta. Colour Doppler is a very helpful diagnostic tool for identifying true and false lumen. See text for more details

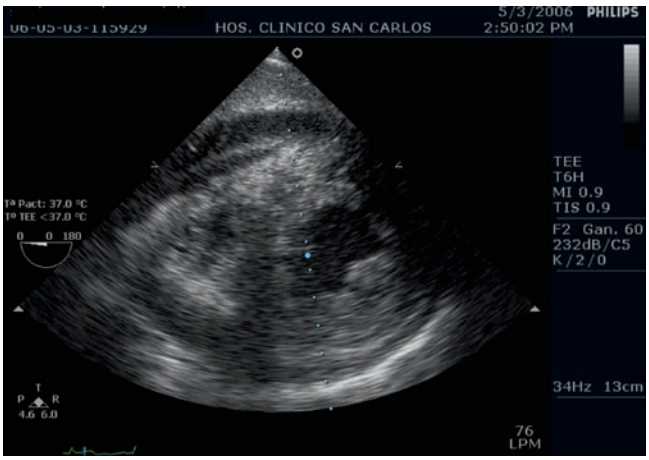

Fig. 32.8 Pericardial effusion is a sign of poor prognosis

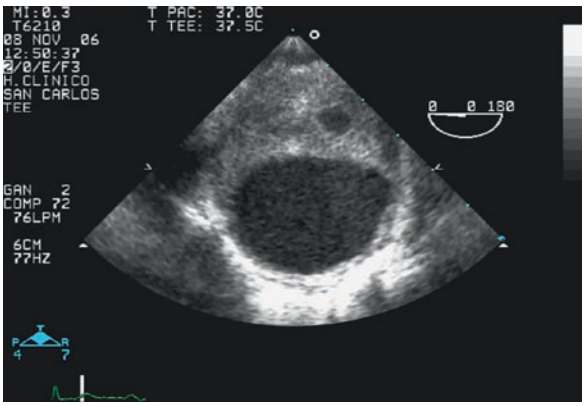

Fig.32.9 TEE at the level of the thoracic descendent aorta. In this case, the identification of the true lumen is easy, because the false lumen is partially thrombosed

layers, or less commonly, by a penetrating atherosclerotic ulcer. The rupture of the vasa vasorum may be the result of normal-appearing vasa vasorum that are not supported by the surrounding aortic media, or the result of the rupture of diseased vasa vasorum.

TOE allows IHs to be detected as the first events in aortic dissection.[15,16] The diagnostic characteristics of IH are multiple layers of aorta wall divided by the haemorrhage, thickening of the wall superior to 0.5 cm, an increased distance between the lumen and the oesophagus, and a peri-aortic area with no echo. IH typically shows a localized thickening of the aorta wall with echo-free central intra-mural spaces limited to one or two scanning planes. The calcification of the intima helps considerably to distinguish this entity of an intra-luminal thrombus. IHs can cause typical dissection in 30% of patients[17] or scar spontaneously. In these patients, no false lumen is detected. One of the main characteristics of IH is its dynamic nature with the possibility of its developing into a classic aortic dissection or an aortic rupture. Reabsorption may even occur (10% of cases).

IH is defined in echocardiography by a circular or semicircular thickening of the aorta wall (superior to 7 mm) with a density similar to clots, and no evidence of internal flow or of intimal tear. This thickening provokes a central displacement of the intima (sometimes calcified) and a reduction in the diameter of the aortic lumen. In approximately two-thirds of cases, echolucent zones representing fluid-filled areas are observed inside the haematoma. When these echo-free zones are located

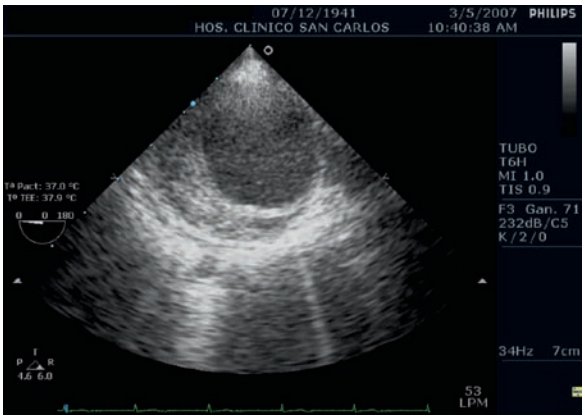

Fig. 32.10 TOE at the level of the thoracic descendent aorta. An intramural haematoma is appreciated. This entity is another type of manifestation of the acute aortic syndrome

below the intima, the image of a flap can be identified, which, unlike in classic aortic dissection, remains still. Nevertheless, this frequently makes it almost impossible to differentiate IH from a non-communicating dissection. Distinction from acute atherosclerosis of the aorta can also be difficult, especially when these lesions are associated with a clot (Fig. 32.10 and Videos 32.9 and 32.10).

Penetrating Aortic Ulcer

Atherosclerotic lesions may cause erosion at the aorta surface. This erosion may lead to a penetrating aortic ulcer (PU). PUs usually affect patients of advanced age who are hypertensive and have diffuse atherosclerosis. They are usually located in the descending thoracic aorta, and their clinical presentation is normally very similar to classic aortic dissection or IH.

PU follows a very variable course and can lead to aortic dissection, aortic aneurysm, or even rupture. A common development is the progressive dilation of the aorta, but if ulceration continues to deepen, it can cause a pseudoaneurysm or even aortic rupture.[18–20]

Ultrasound diagnosis is based on identifying an image that resembles a crater with irregular edges standing out from an aorta wall with atherosclerosis. As a diagnostic criterion and to differentiate it from IH, some authors include the identification of blood flow in the interior and at the edges of the ulcer. In addition, they consider that the disappearance of this flow during follow-up can be a sign of stabilization of the plaque, especially when accompanied by an improvement in symptoms. The identification of a thickening of the wall with echolucent images in its interior and central displacement of intimal calcifications allows one to diagnose an IH associated with a PU.

Pitfalls and Limitations of the Technique

TTE has some limitations and disadvantages for the aortic dissection diagnosis and evaluation. One main problem is its inability to adequately visualize the distal ascending, transverse, and descending thoracic aorta. Thus, TTE is important in suspected aortic dissection primarily for the diagnosis of cardiac complications of dissection such as cardiac tamponade and aortic regurgitation.

One limitation of monoplane TOE is its inability to visualize the upper portion of the ascending aorta due to the interposed trachea. It is not known if multi-plane TOE is better than biplane TOE for aortic dissection assessment. However, the flexibility of multi-plane TOE for patients with an abnormal aortic anatomy makes it eligible.

Prognostic Information Provided by Echo

In the case of aortic aneurisms, size[21,22] and the presence of wall complications are the main prognostic factors that echocardiography provides. In the case of aortic dissections, many prognostic features may be analyzed by means of echocardiography.

The prognosis is clearly impaired in case of ascendant aorta involvement (Standford Type A dissections). In case of isolated descendent aorta dissections, there are many echocardiographic findings associated with a worse prognosis: presence of associated complications, associated heart disease, and presence of haemothorax. Nevertheless, aortic arch involvement and dissection extension to the abdominal segments are not associated with a worse prognosis.[23]

Imaging in Decision Making: Echo vs. MRI and CT

Non-echographic Diagnostic Techniques for Aortic Aneurysm Evaluation

MRI and computed tomography (CT) are recommended if the aortic root or ascending aorta cannot be adequately measured by echocardiography. Yearly echocardiography, MRI, or CT is recommended for patients with bicuspid aortic valves and dilatation of the aortic root or ascending aorta (diameter greater than 4 cm, with consideration of a lower threshold for patients of small stature). Computed tomography and MRI

are actually the preferred tests to establish the diagnosis of an aortic aneurysm and assess its characteristics. In those patients with bicuspid aortic valves, computed tomography and MRI are indicated if echocardiography is not able to provide accurate information. Contrast angiography provides accurate information of luminal features and is the best method for evaluating branch vessel pathology.

Non-echographic Diagnostic Techniques for Aortic Dissection Evaluation

The use of CT for aortic dissection evaluation requires intravenous contrast injection. Advantages of CT are ready availability, identification of intra-luminal thrombus, and pericardial effusion. Disadvantages of standard CT are that the intimal flap is seen in less than 75% of cases, and that the site of entry is rarely identified[24] and aortic regurgitation cannot be evaluated (Table 32.2).

MRI is a highly accurate technique for evaluating the thoracic aorta in patients with suspected aortic dissection. The sensitivity and specificity of MRI may be as high as 98 and 85%, respectively.[5] MRI is safe for stable patients with aortic dissection, and MR contrast agents are safer than CT contrast agents. It may also provide information regarding branch vessels and is able to assess aortic regurgitation. MRI is not usually readily available in emergency departments at many institutions, and there are concerns about patient inaccessibility while undergoing this technique.

Choosing the best diagnostic test for suspected aortic dissection requires taking into account the information needed and the experience with the imaging modality at each centre. Thoracic MRI, thoracic CT, and multi-plane TOE are the most commonly preferred methods for aortic dissection assessment (Table 32.2).

Video 32.1

TTE. Four-chamber view. A large ascendant aorta aneurysm can be clearly seen. Right atrium compression is evident

Video 32.2

Real-time 3D TOE may help in some circumstances to evaluate the morphologic characteristics of aortic aneurisms

Video 32.3

TOE. Intimal flap is the more characteristic finding in aortic dissections. It is necessary to keep always in mind that aortic dissection may be associated to many other complications, such as aortic regurgitation. In this case the intimal flap is the cause of the aortic valve incompetence

Video 32.4

TOE at the level of the thoracic descendent aorta. True and false lumen can be appreciated. Several echocardiographic findings are very useful to distinguish between both lumens. See text and Table 32.1 for more details

Table 32.2. Characteristics of the main diagnostic techniques used for the aortic dissection diagnosis and assessment.

	MRI	TTE	CT	TOE
Diagnostic accuracy	+++	+	+++	+++
Extension assessment	+++	–	+++	++
Main tear evaluation	++	–	+	+++
Secondary tears evaluation	+	–	–	+++
Aortic regurgitation assessment	++	+++	–	+++
Pericardium assessment	+++	+++	++	+++
Lateral arterial branches involvement	+++	+	+++	++

CT computed tomography; *MRI* magnetic resonance imaging; *TOE* trans-oesophageal echocardiography; *TTE* transthoracic echocardiography

Video 32.5

TOE at the level of the thoracic descendent aorta. Colour Doppler is a very helpful diagnostic tool for identifying true and false lumen. See text for more details

Video 32.6

Another case similar to Video 32.5

Video 32.7

TOE at the level of the thoracic descendent aorta. In this case, the identification of the true lumen is easy, because the false lumen is partially thrombosed

Video 32.8

In some circumstances, other entities, such as the complicated atherosclerotic plaque shown in this video, should be distinguished from aortic dissections

Video 32.9

TOE at the level of the thoracic descendent aorta. An intramural haematoma is appreciated. This entity is another type of manifestation of the acute aortic syndrome

Video 32.10

Another example of intra-mural haematoma

References

1. Johnston KW, Rutherford RB, Tilson MD, et al Suggested standards for reporting on arterial aneurysms. Subcommittee on Reporting Standards for Arterial Aneurysms, Ad Hoc Committee on Reporting Standards, Society for Vascular Surgery and North American Chapter, International Society for Cardiovascular Surgery. *J Vasc Surg*. 1991;13:452
2. Erbel R, Alfonso F, Boileau C, et al; Task Force on Aortic Dissection, European Society of Cardiology. Diagnosis and management of aortic dissection. *Eur Heart J*. 2001;22:1642-1681
3. Bonow RO, Carabello BA, Chatterjee K, et al; American College of Cardiology/American Heart Association Task Force on Practice Guidelines. 2008 focused update incorporated into the ACC/AHA 2006 guidelines for the management of patients with valvular heart disease: a report of the American College of Cardiology/American Heart Association Task Force on Practice Guidelines (Writing Committee to revise the 1998 guidelines for the management of patients with valvular heart disease). Endorsed by the Society of Cardiovascular Anesthesiologists, Society for Cardiovascular Angiography and Interventions, and Society of Thoracic Surgeons. *Circulation*. 2008;118:e523-e661
4. Miller DC, Stinson EG, Oyer P, Rossiler S, Shumway NE. Operative treatment of aortic dissections: experiences with 125 patients over 16 year period. *Thorac Cardiovasc Surg*. 1979;78:365-375
5. Cheitlin, MD, Armstrong, WF, Aurigemma, GP, et al ACC/AHA/ASE 2003 guideline update for the clinical application of echocardiography: summary article: a report of the American College of Cardiology/American Heart Association Task Force on Practice Guidelines (ACC/AHA/ASE Committee to Update the 1997 Guidelines for the Clinical Application of Echocardiography). Circulation 2003; 108:1146. *J Am Coll Cardiol*. 2008;52(suppl 13):e1-e142 [No abstract available]
6. Crawford ES, Svensson LG, Coselli JS, Safi HJ, Hess KR. Surgical treatment of aneurysm and/or dissection of the ascending aorta, transverse aortic arch, and ascending aorta and transverse aortic arch. Factors influencing survival in 717 patients. *J Thorac Cardiovasc Surg*. 1989;98:659-674
7. De Bakey ME, McCollum CH, Crawford ES, et al Dissection and dissecting aneurysms of the aorta: twenty-year follow-up of five hundred and twenty-seven patients treated surgically. *Surgery*. 1982;92:1118-1134
8. Svensson LG, Labib SB, Eisenhauer AC, Butterly JR. Intimal tear without hematoma. *Circulation*. 1999;99:1331-1336
9. Roberts W. Aortic dissection: anatomy, consequences and causes. *Am Heart J*. 1991;101:195-214
10. Erbel R, Engberding R, Daniel W, et al Echocardiography in diagnosis of aortic dissection. *Lancet*. 1989;1:457
11. Cigarroa JE, Isselbacher EM, De Sanctis RW, Eagle K. Diagnostic imaging in the evaluation of suspected aortic dissection. *N Engl J Med*. 1993;328:35-43
12. Evangelista A, Garcia-del-Castillo H, Gonzalez-Alujas T, et al Diagnosis of ascending aortic dissection by transesophageal echocardiography: utility of M-mode in recognizing artifacts. *J Am Coll Cardiol*. 1996;27:102
13. Nienaber CA, von Kodolitsch Y, Nicolas V, et al The diagnosis of thoracic aortic dissection by noninvasive imaging procedures. *N Engl J Med*. 1993;328:1
14. Nienaber C, Kodotisch Y, Petersen B, Spielman R. Intramural haemorrage of the thoracic aorta. Diagnostic and therapeutic implications. *Circulation*. 1995;92:1465-1472
15. Khandheria BJ. Aortic dissection: the last frontier. *Circulation*. 1993;87:1765-1768
16. Robbins RC, Mitchell R, Latter D, Moon MR, Miller CM. Management of patients with intramural haematoma of the thoracic aorta. *Circulation*. 1993;88:1-10
17. Moskowitz HD, Lampert C, Jacobs LE, Kotler MN. Penetrating atherosclerotic aortic ulcers. *Am Heart J*. 1994;128:1210-1217
18. Montgomery DH, Ververis JJ, McGorisc G, Frohwein S, Martin RP, Taylor WR. Natural history of severe atheromatous disease of the thoracic aorta: a transesophageal echocardiography study. *J Am Coll Cardiol*. 1996;27:95-101

19. Atar S, Nagai T, Birnbaum Y, Harold JG, Luo H, Naqvi TZ, et al Transesophageal echocardiography Doppler findings in patients with penetrating atherosclerotic aortic ulcers. *Am J Cardiol*. 1999;83:133-135
20. Clouse WD, Hallett JW, Schaff HV, et al Improved prognosis of thoracic aortic aneurysms: a population-based study. *JAMA*. 1998;280:1926
21. Juvonen T, Ergin MA, Galla JD, et al Prospective study of the natural history of thoracic aortic aneurysms. *Ann Thorac Surg*. 1997;63:1533
22. Glower DD, Fann JL, Speier RH, Morrison L, White WD, Smith LR, et al Comparison of medical and surgical therapy for uncomplicated descending aortic dissection. *Circulation*. 1990;82(suppl IV):39-46
23. Vasile N, Mathieu D, Keita K, et al Computed tomography of thoracic aortic dissection: accuracy and pitfalls. *J Comput Assist Tomogr*. 1986;10:211
24. Nienaber CA, von Kodolitsch Y, Nicolas V, et al The diagnosis of thoracic aortic dissection by noninvasive imaging procedures. *N Engl J Med*. 1993;328:1.

Chapter 33

ROLE OF MAGNETIC RESONANCE IMAGING IN AORTIC DISEASE

Arturo Evangelista and Jérôme Garot

CONTENTS

J. L. Zamorano et al. (eds.), *The ESC Textbook of Cardiovascular Imaging*
DOI: 10.1007/978-1-84882-421-8_33,

Introduction

MRI is a non-invasive imaging technique that permits the most complete study of aortic disease. It offers morphological, functional, and biochemical information. Technological advances, e.g. the implementation of faster gradients, newer sequences, and ultrafast MR angiography, have led to MRI being the modality of choice for imaging aortic diseases. Conventional ECG-gated spin-echo imaging and cine gradient-echo have earned MRI the reputation of being the ideal tool for evaluating the aorta. Contrast-enhanced 3D MR angiography permits rapid acquisition and multi-planar imaging with minimal dephasing artefacts. Phase-contrast imaging is another technique that enables flow in the great vessels to be evaluated with accurate quantification of peak velocity and forward and regurgitant flow.

MRI is increasingly becoming the first-line technique for evaluating diseases in the thoracic aorta.[1, 2] MRI possesses the capability for multi-planar imaging; it uses a non-toxic contrast agent and does not involve ionizing radiation. With recent advances in gradient hardware, much shorter repetition times (TRs) are now achievable, resulting in significant increases in acquisition speed.

Magnetic Resonance Imaging Techniques

Black-Blood Sequences

Blood circulating through the aorta is black on conventional spin-echo and turbo spin-echo sequences owing to the emptying signal produced by the transit time effect of moving blood in the short phase. These sequences provide great morphological information on the aortic wall and adjacent structures. T1- or T2-weighted images are useful for characterization of wall tissue, permitting assessment of the haematic content of the intra-mural haematoma or the lipid content of the atherosclerosed plaque. Post-contrast T1 imaging with fat suppression is useful in the diagnosis of some entities such as aortitis or mycotic aneurysms. ECG triggering is essential in minimizing motion and pulsability artefacts. A slice of 3–8 mm and echo time (TE) of 20–30 msec are standard, while TR is determined from the R-R′ interval of the ECG. ECG-triggered, breath-hold turbo-spin echo (TSE) has been the cornerstone of black-blood MRI for aortic disease. A double inversion-recovery technique is used to abolish the blood signal. The black-blood appearance is the result of nullifying the blood flowing into the slice by the first 180° inversion pulse at a specific inversion time (IT). Imaging occurs during mid to late diastole and the entire image is acquired over several heartbeats. Spin-echo single-shot (HASTE or SS-FSE) sequences permit correct morphological assessment of the aorta with very rapid acquisition times. Recently, a fast diffusion-prepared (DP) balanced SSFP-based magnetic resonance technique that allows for 3D dark blood imaging has been described. Since this is a 3D technique, the images offer improved slice resolution and more intuitive visualization of the thoracic aorta compared to 2D methods.

Cine-MR Sequences

Cine-MR images are acquired using gradient-echo sequences that provide excellent contrast between blood and surrounding tissue without the use of contrast agents. Contrast to noise depends on T2/T1 differences, which, with short TRs, are high for blood and low for tissues. Mainly due to their high temporal resolution, it is possible to obtain images of multiple phases of the heart cycle and visualize blood flow both in systole and diastole. Gradient-echo sequences generate images of brilliant blood. The emptying signal determines turbulent flow in haemodynamically significant stenosis or valvular regurgitation that may be useful in the detection of aortic coarctation or valvular disease. Steady-state free–precession sequences (True FISP, Fiesta or Balanced FFE) are those most commonly used. They are normally used for the functional study of cardiac chambers, although their use is widely extended to the study of the aorta. Their main characteristic is that they permit high-contrast images with very short acquisition times since they have very low TR.

Flow Mapping

Accurate quantitative information on blood flow is obtained from modified gradient-echo sequences with parameter reconstruction from the phase, rather than the amplitude of the MR signal; this is also known as flow-mapping or phase contrast or velocity-encoded cine MRI.

Velocity-encoded cine-MRI sequences provide great functional information owing to their capacity to quantify flow. Quantification of both flow velocity and volume permits physiopathological assessment of blood flow alterations in different aortic diseases. With this technique, the information is processed using signal magnitude images and phase images. Signal magnitude images are in brilliant blood and offer better anatomical assessment, while phase images show a map of flow velocities and direction. Using post-processing techniques, it is possible to obtain curves of flow vs. time, velocity vs. time, and peak velocity vs. time. Quantitative

data on flow velocity and flow are estimated by multiplying the spatial mean velocity and cross-sectional area of the vessel. In this manner, the haemodynamic repercussion can be quantified in different situations such as aortic coarctation or valvular disease and also in the analysis of flow patterns of aortic dissection in true and false lumina.

Contrast-Enhanced MR Angiography (CE-MRA)

CE-MRA images are obtained by T1-weighted 3D-gradient echo sequences following endovenous contrast administration, utilizing the shortening effect of T1 of contrast with gadolinium. These sequences offer important anatomical information on both the aorta and main vessels originating from it. This technique is suitable for the depiction of abnormalities such as penetrating atherosclerotic ulcers, dissection, coarctation, and aneurysm. The acquired images must be re-evaluated by post-process MIP and MPR reconstructions. By the application of ultrarapid spoiled gradient-echo sequences in steady-state free-precession and the implantation of parallel acquisition techniques, we can obtain multiphasic time-resolved 3D MRA images with high temporal and spatial resolution. These sequences are very useful in aortic dissection or shunts. In multi-phase time-resolved 3D MRA sequences, contrast injection is started at the same time as the image acquisition, utilizing the first set of images as a mask for posterior subtraction using post-processing techniques and MIP and MPR reconstruction.

Normal Aorta

The aorta is the largest and strongest artery in the body. Its wall comprises three layers: the thin inner layer or intima; a thick middle layer or media; and a rather thin outer layer, the adventitia. In the human adult, normal diameter is considered to be within the limits of 40 mm in the aortic root, 37 mm in the ascending aorta, and 28 mm in the descending aorta. Although normal aortic dimensions should be normalized to body size, few studies refer to normal values indexed by body surface. In a recent study[3] including 120 healthy volunteers, 10 of each gender in each decile from 20 to 80 years, aortic root measurement was assessed by MRI. Diastolic cusp-commissure dimensions showed evidence of an increase of 0.9 mm per decade in men and 0.7 mm per decade in women. The elastic properties of the aorta contribute crucially to its normal function. However, elasticity and distensibility of the aorta decline with age. The loss of elasticity and aortic compliance probably account for the increase in pulse pressure commonly seen in elderly persons and are accompanied by progressive dilatation of the aorta. This loss of elasticity is caused by structural changes, including an increase in collagen content and formation of intimal atherosclerosis.

Diagnosis of Thoracic Aortic Disease

Atherosclerosis

MRI is a non-invasive imaging modality that can visualize and characterize the composition of atherosclerotic plaques and differentiate tissue structure on the basis of proton magnetic properties with excellent soft tissue contrast. MRA sequences are highly useful for the detection of aortic atheromatosis, although they offer only information on repercussions of the plaque in the aortic lumen in the form of stenosis, which occurs in advanced stages of the disease. For detection of atheromatous plaques, alterations occurring in the aortic wall must be observed. TSE sequences in black blood are very useful in the identification and characterization of the plaque and for distinguishing its constituent components in vivo. Being composed of cholesterol esters, the lipid nucleus has a short T2 and will be hypo-intense in T2-weighted images, while the fibrocellular components are hyper-intense in T2-weighted images compared to the lipid nucleus. Calcium deposits can be appreciated as hypo-intense regions within the plaque on T1-, proton density-, and T2-weighted images. The fibrous cap and lipid core, organized thrombus and fresh thrombus, or calcification and necrotic areas have been imaged in studies performed both in vitro and in vivo. Fayad et al[4] showed that MRI evaluation of the aorta compared well with TOE imaging for the assessment of aortic atherosclerotic plaque thickness, extent, and composition. Furthermore, high resolution non-invasive MRI demonstrates regression of aortic atherosclerotic lesions due to lipid lowering by simvastatin.[5]

One promising aspect to be considered is the capability of MRI to detect inflammatory activity of atheromatous plaque with the administration of contrast media. Inflammatory phenomena that determine the accumulation of macrophages can be demonstrated as hyper-uptake of gadolinium chelates in the plaque. This uptake is also produced with the use of other contrasts such as ultrasmall superparamagnetic particles of iron oxides (USPIO) by macrophages of the atheromatous plaque[6, 7] (Fig. 33.1).

Although commonly opposed as a limitation compared to TOE, MRI offers the possibility of assessing mobile atherosclerotic debris within the aortic lumen through the use of SSPF cine.

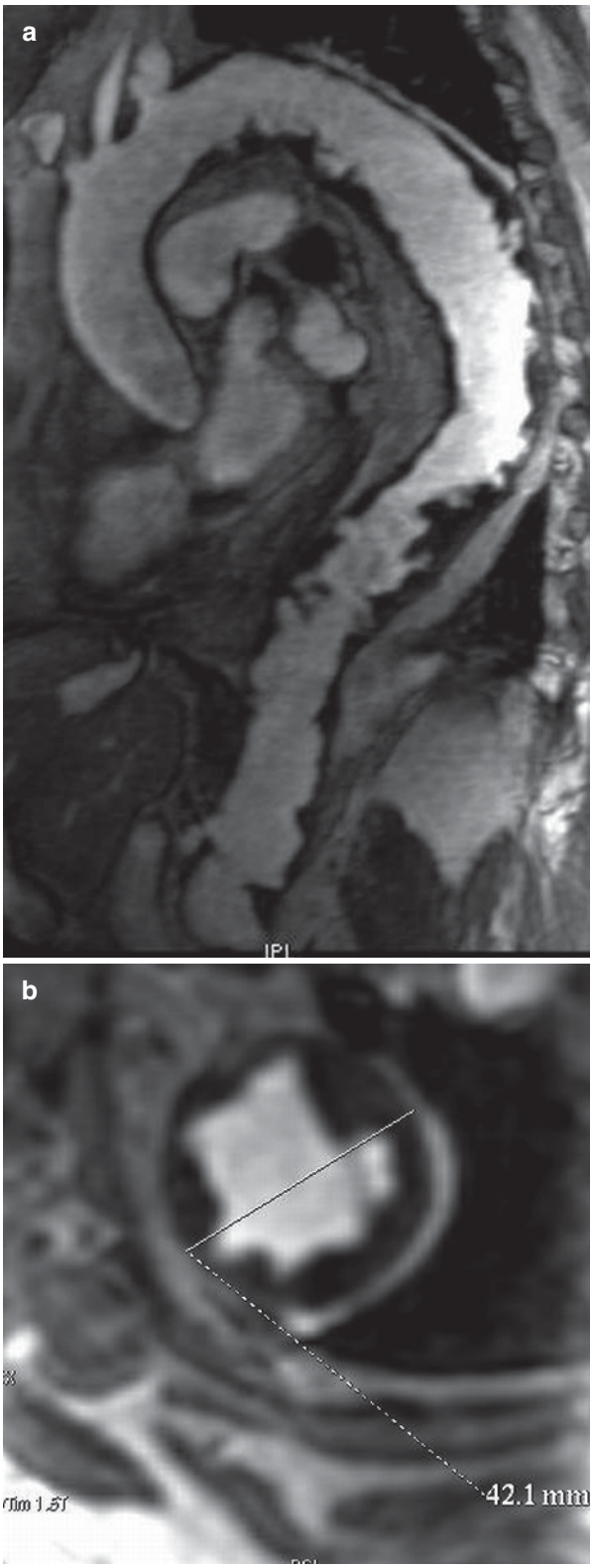

Fig. 33.1 Images extracted from a series of 3D MRA images of the thoracic aorta, in parasagittal **(a)** and transverse **(b)** views, in a patient with severe and extensive atheroma of the aorta, 48 h after injection of USPIO. The uptake of USPIO by active macrophages of the atheromatous plaque leads to a signal void within the aortic wall

Aortic Aneurysms

The basic information to be obtained is aortic diameter, aneurysm extension, and their relationships with the main arterial branches. CE-MRA offers excellent demonstration of the whole aortic anatomy, and is very efficacious for the identification and characterization of aneurysms. It is recommendable to combine MRA images with spin-echo in black-blood images (Fig. 33.2), which are very useful for detecting alterations in the wall and adjacent structures that could go unnoticed if only MRA images are acquired. In mycotic aneurysm, post-contrast T1-weighted images permit identification of inflammatory changes in the aortic wall and adjacent fat, secondary to bacterial infection. Atherosclerotic lesions are visualized as areas of increased thickness with high signal intensity and irregular profiles. Periaortic haematoma and areas of high signal intensity within the thrombus may indicate instability of the aneurysm and are well depicted on spin-echo images. The information provided by MRA in aortic aneurysm assessment is similar to that offered by current CT equipment with multi-detections. Both methods permit accurate determination of aortic diameters in sagittal plane. Furthermore, pre-processing techniques (MIP, MPR, and rendering volume) facilitate visualization of the aorta in its entirety together with the relationship of its principal branches, and are highly useful when planning treatment. The advantage of MRI over CT is that it is a non-ionizing technique that permits serial follow-up studies to be conducted innocuously. For correct monitoring, it is necessary to measure aortic diameter in the same location and same

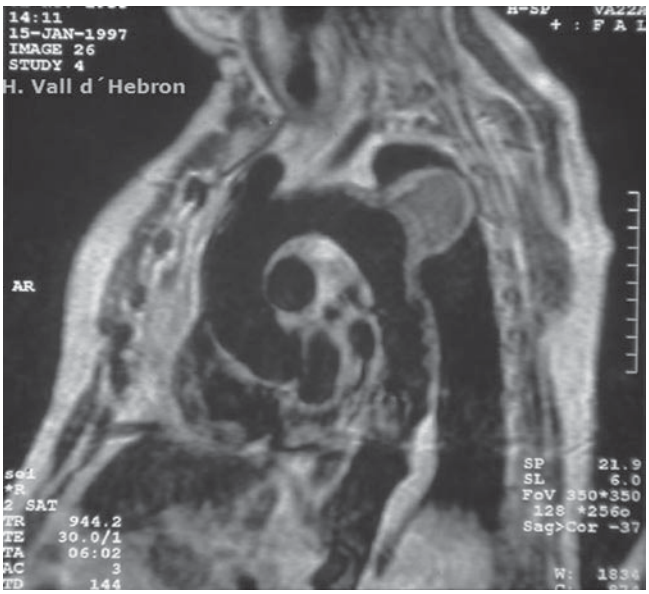

Fig. 33.2 T1-weighted black-blood image in sagittal view showing a thrombosed saccular aneurysm in proximal descending aorta

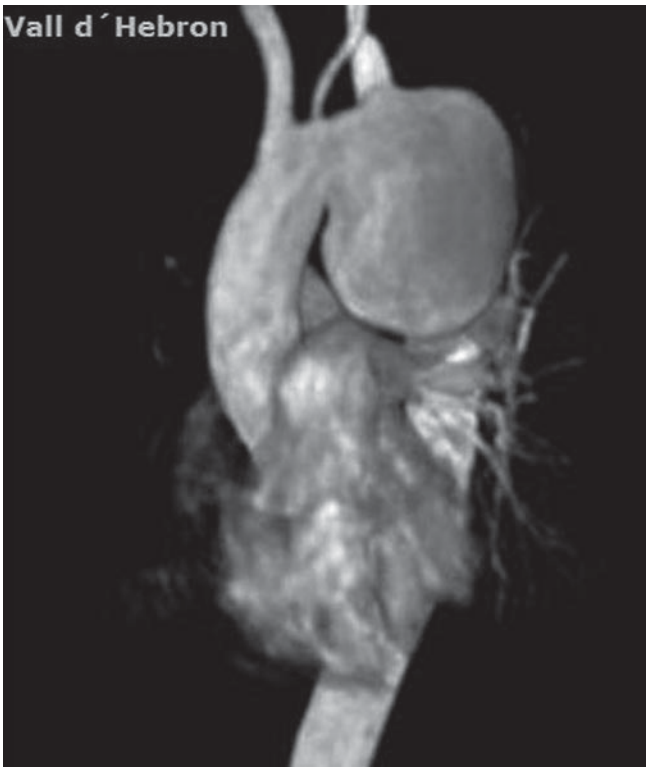

Fig. 33.3 Saccular atherosclerotic aneurysm. Volume rendering image from contrast-enhanced MR angiography (CE-MRA) shows a saccular aneurysm of the aortic arch and its relationship with the supra-aortic branches

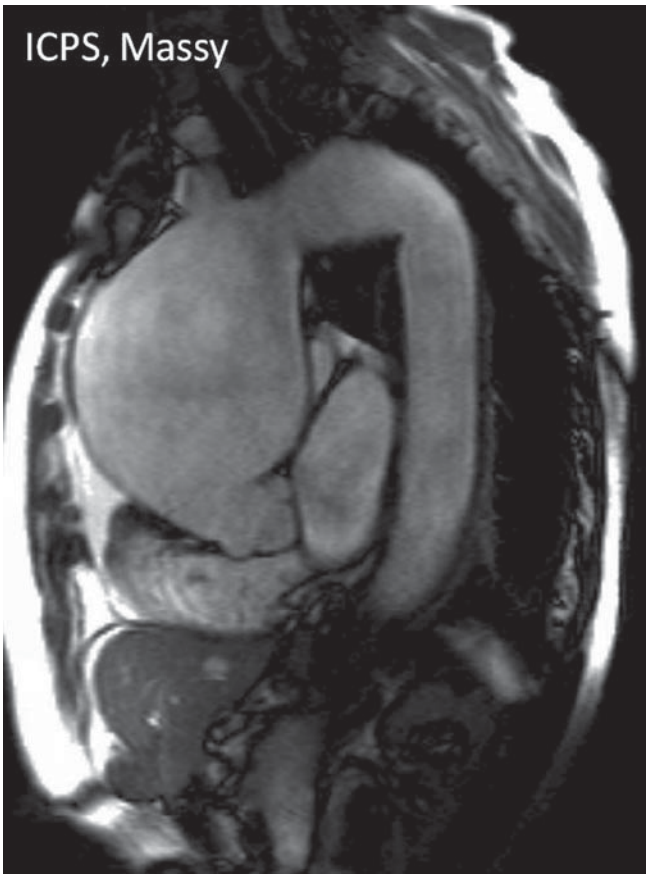

Fig. 33.4 Images extracted from a SSFP cine MR sequence of the thoracic aorta showing a huge aneurysm of the ascending aorta

spatial plane. Diameters of the aortic annulus, the sinus of Valsalva, the sino-tubular junction, and the ascending portion of the aorta should be measured in a standardized way. The sagittal plane permits more reproducible measurements to be taken.[8] Contrast-enhanced 3D MRA can provide precise topographic information on the extent of an aneurysm and its relationship with the aortic branches[9] (Fig. 33.3). The homogeneous enhancement of flowing blood within the lumen facilitates the delineation of thrombus. As reported in the literature, the capability of contrast MRA to visualize the Adamkiewicz artery represents an important advance in planning the surgical repair of a thoracic aneurysm, thereby avoiding post-operative neurological deficit secondary to spinal cord ischaemia. The combination of information obtained on aneurysm morphology and functional data provided by cine-MR sequences aids understanding of the physiopathology of aneurysmal dilatation.[1, 2] When the aneurysm affects the ascending aorta (Fig. 33.4), it is recommended to conduct a functional study through the aortic valve using cine-MR sequences to rule out associated valvular disease that may be related to aortic dilatation. The aortic cusps should be assessed as bicuspid or tricuspid, which has a significant impact when tailoring therapeutic strategy (Fig. 33.5). Recently, MRI has been established as an accurate non-invasive tool for the assessment of aortic distensibility and pulsed-wave velocity. These methods have been used to assess aortic elasticity in patients with Marfan syndrome, bicuspid aortic valve, or aortic aneurysms[10–12] Flow-wave velocity is calculated as the ratio of distance between two levels of the aorta and the time difference between the arrival of flow wave at these levels. Distensibility at different levels of the aorta is calculated by means of the following equation: $D=(A_{max}-A_{min})/A_{min} \times (P_{sys}-P_{dias})$, where D is distensibility, $A=$ aortic area, and P blood pressure in mmHg. Although some overlap in values for biophysical properties between patients with Marfan syndrome, bicuspid aortic valve, and matched control subjects is apparent, some studies showed that by using these methods, significantly increased flow wave velocity and decreased distensibility can be detected in these patients without dilatation of the aorta. Therefore, these methods could be of clinical value in the identification of patients who are especially at risk for aortic complications.

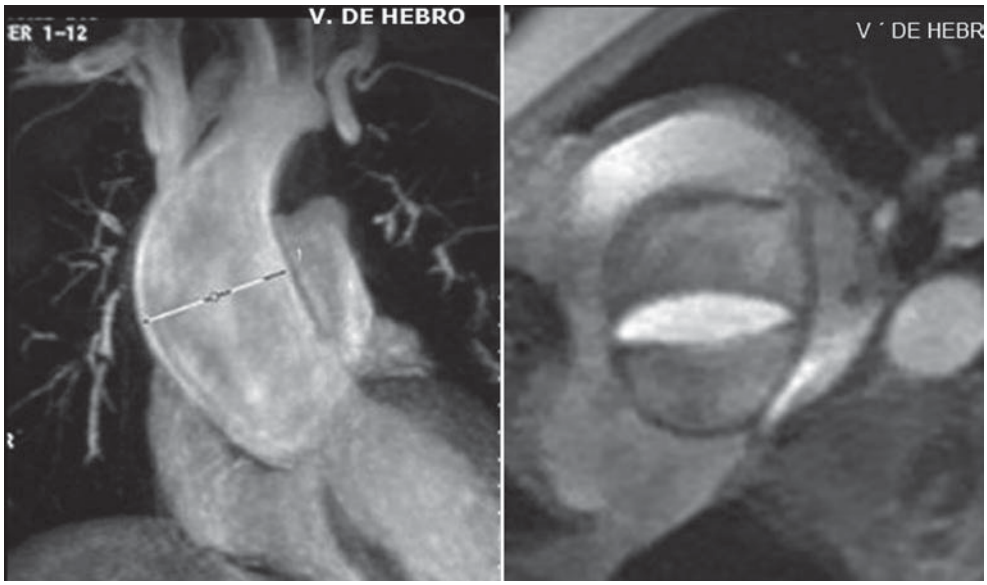

Fig. 33.5 Ascending aorta aneurysm (*left*) in a patient with bicuspid aortic valve (*right*) assessed by gradient echo MRI sequences

Acute Aortic Syndrome

Aortic Dissection

Aortic dissection is characterized by a laceration of the aortic intima and inner layer of the aortic media that allows blood to course through a false lumen in the outer third of the media. The diagnosis of aortic dissection is based on the demonstration of the intimal flap that separates the true from the false lumen (Fig. 33.6). In acute phase, MRI is limited by being less available, more time-consuming, and by patient claustrophobia. For unstable patients, TOE or CT is a better option. In a suspected aortic dissection, the standard MRI examination should begin with black-blood sequences. In the axial plane, the intimal flap is detected as a straight linear image inside the aortic lumen. The true lumen can be differentiated from the false by the anatomical features and flow pattern: the true lumen shows a signal void, whereas the false lumen has higher signal intensity. In addition, visualization of media remnants dissected as cobwebs adjacent to the outer wall of the lumen may help to identify the false lumen. A high signal intensity of a pericardial effusion indicates bloody components and is considered to be a sign of impending rupture of the ascending aorta into the pericardial space. Similarly, the presence of pleural effusion (PE) is an indicator of impending aortic rupture (Fig. 33.7). Detailed anatomical information of aortic dissection must indicate the extension of the dissection and the perfusion of branch vessels from the true or false channels. Therefore, a further spin-echo sequence in the sagittal plane should be performed, and, in stable patients, gradient-echo sequences or phase contrast images can be instrumental in identifying aortic regurgitation and entry or re-entry sites as well as in differentiating slow flow from thrombus in the false lumen.

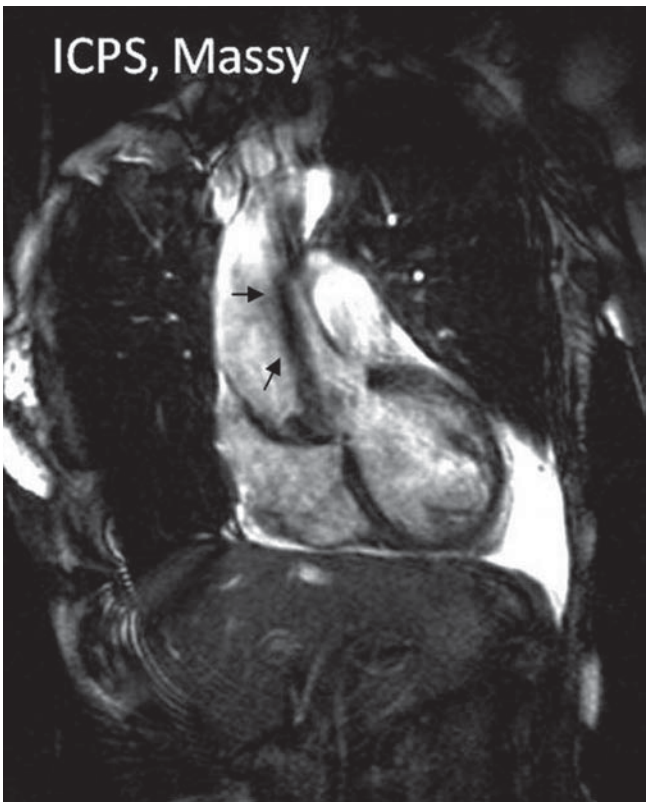

Fig. 33.6 Image extracted from a SSFP cine sequence in a patient with type A acute aortic dissection and an intimal flap (*arrows*)

Contrast CE-MRA has proved to be superior to black-blood sequences in the assessment of dissection extension and supra-aortic trunk involvement. However, owing to the limitation of this technique to visualize the aortic wall and adjacent structures, the study protocol of aortic dissection should

include black-blood sequences to rule out wall structure alterations.[13]

For planning surgery or endovascular repair, it is very useful to demonstrate the course of the flap, entry tear location, false lumen thrombosis, aortic diameter, and main arterial trunk involvement by post-processed techniques with MPR reconstructions, MIP, and volume rendering. It is mandatory to always visualize the image source of the CE-MRA since the flap may not be seen on volumetric reconstruction.[14] Above all, in Type B dissections, it is important to acquire images with wide field-of-view that include the whole aorta from the arch to the aortic bifurcation. Time-resolved MRA provides additional functional information compared to conventional MRA. The dynamic assessment of blood flow in entry tears is the main advantage of time-resolved MRA. The longer resolution times of conventional MRA, around 20 s, do not permit correct demonstration of dynamic changes in blood flow through the different entry tears. On the other hand, the different timing in contrast enhancement in both lumina implies that one of the lumina remains partially contrasted with the use of long resolution time sequences. By applying rapid MRA sequences, we obtain multiple continuous acquisitions, succeeding in visualizing both lumina with maximum contrast concentration in different phases, which facilitates their morphological assessment. Sub-second CE-MRA can demonstrate sequential filling of the true and false lumen and may help identify the entry and exit points of the dissection (Fig. 33.8). In ascending aorta dissections, it is recommendable to include cine-MRI sequences through the left ventricular outflow tract in the study protocol to rule out valvular regurgitation.

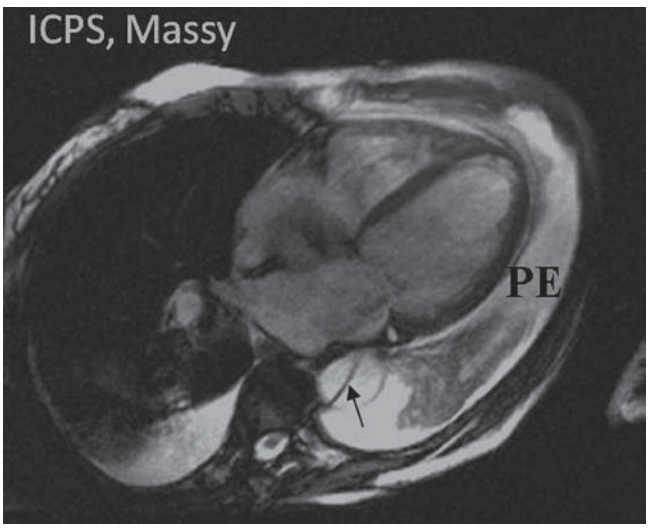

Fig. 33.7 Image extracted from an SSFP cine sequence acquired in the 4-chamber view in the same patient as in Fig. 33.6 with type A acute aortic dissection. The presence of pleural effusion (PE) is an indicator of impending aortic rupture. Note the intimal flap in descending aorta (*arrow*)

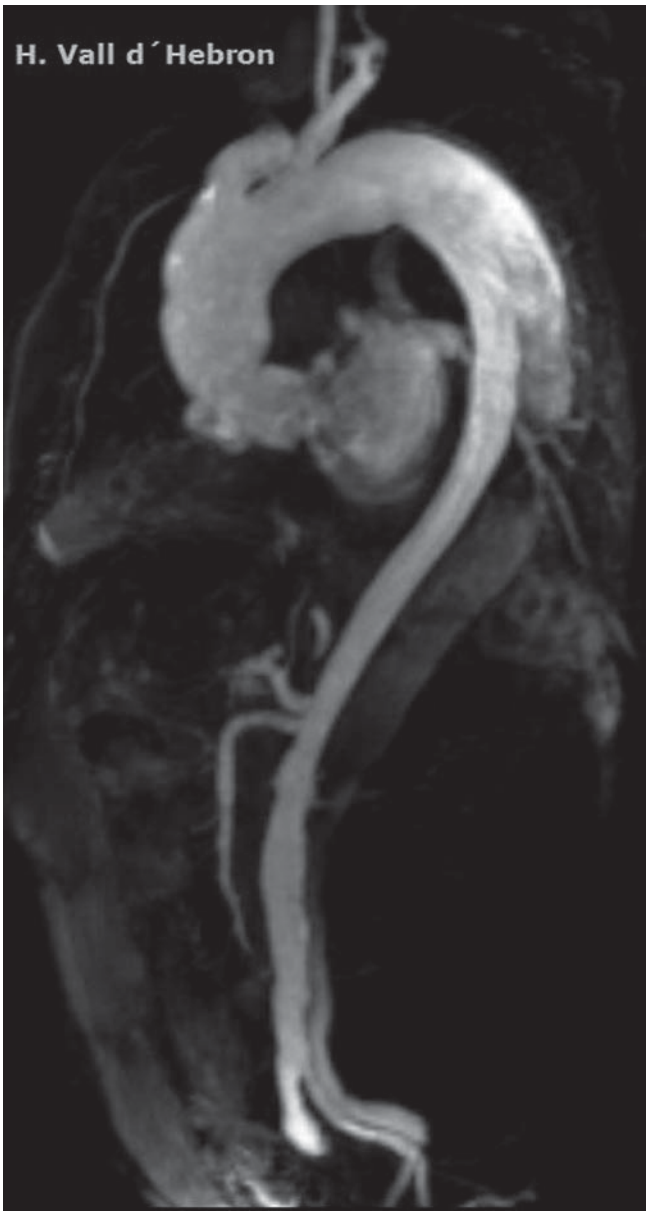

Fig. 33.8 Type B aortic dissection. Time-resolved sagittal maximum-intensity-projection angiograms show time course of enhancement of both lumina

Intra-mural Haematoma

Although greater availability and rapidity favour the use of CT in acute disease, MR plays a major role in the diagnosis of intra-mural haematoma. The greater contrast among tissues offered by MR often permits the depiction of small intra-mural haematomas, which may go unnoticed by CT.[15] The typical finding that permits diagnosis by MR is the presence of wall thickening of the hyper-intense aorta on T1-weighted black-blood sequences. In hyper-acute phase, the haematoma shows an isotense signal in T1-weighted images and a hyper-intense signal in T2-weighted images.

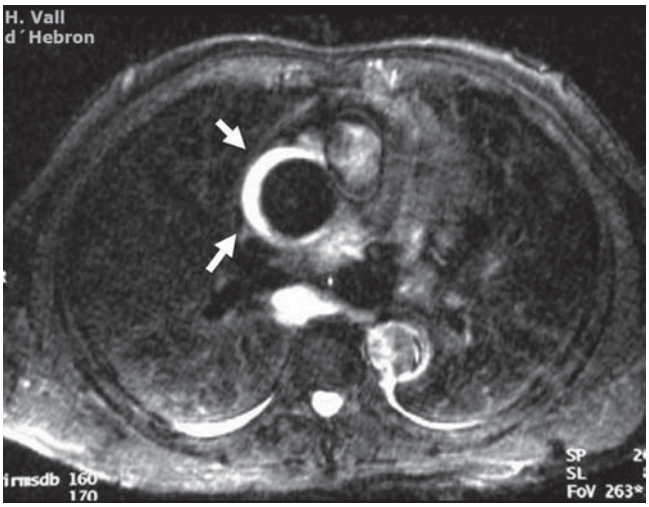

Fig. 33.9 Type A intra-mural haematoma. Axial T1-weighted black-blood image shows thickening of the aortic wall with increased signal intensity (*arrow*)

From the first 24–72 h, the change from oxyhaemoglobin to metahaemoglobin determines a hyper-intense signal in T1-and T2-weighted images (Fig. 33.9), which, with fat suppression, are useful to differentiate peri-aortic fat from intra-mural haematoma. On occasions, mural thrombi may present a semi-lumen morphology that mimics the morphology of the intra-mural haematoma, rendering the differential diagnosis by CT or TOE difficult. This differentiation is easier by MR since mural thrombosis shows a hypo or iso-intense signal in both T1- and T2-weighted sequences.

Penetrating Ulcer

The diagnosis of penetrating ulcer by MRI is based on the visualization of a crater-like ulcer located in the aortic wall. MRA is particularly suitable for depicting aortic ulcers along with the irregular aortic wall profile seen in diffuse atherosclerotic involvement. The aortic ulcer is easily recognized as a contrast-filled outpouching of variable extent with jagged edges (Fig. 33.10). Black-blood sequences may show disruption of the intima with extension of the ulcer to the media, which is thickened, and may be associated with the formation of an intra-mural haematoma. It may be difficult to differentiate penetrating ulcer from the typical forms of dissection. The differential diagnosis should be established between arteriosclerotic ulcers that penetrate the middle layer and ulcer-like images that develop from a localized dissection of an intra-mural haematoma that appears as a pseudoaneurysm located in the area of the former intra-mural haematoma. Prognosis of these ulcer-like images is clearly more benign than that of symptomatic arteriosclerotic ulcers.

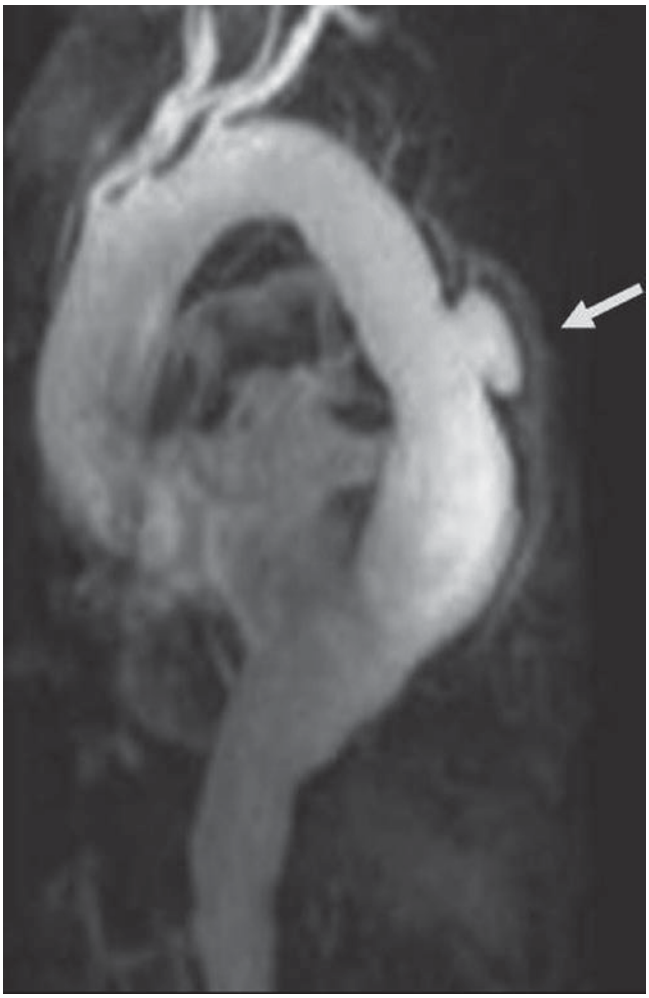

Fig. 33.10 Penetrating aortic ulcer in descending aorta shown by CE-MRA (*arrow*)

Aortic Trauma

The aortic segment subjected to the greatest strain by rapid deceleration forces is located just beyond the isthmus. Aortic rupture occurs 90% of times at this site. Other less common sites are the distal ascending aorta or distal segments of the descending aorta. The lesion is transverse and involves all or part of the aortic circumference, penetrating the aortic layers to various degrees with the formation of a false aneurysm. Intimal haemorrhage without any laceration has been described in pathological series, but was not easily recognized before the advent of high-resolution imaging modalities. Periaortic haemorrhage occurs irrespective of the type of lesion.

Long examination time and difficult access to the patient have been considered to be the main limitations of MRI in acute aortic diseases. The development of fast MRI techniques has shortened the examination time to a few minutes, and therefore, MRI can even be used in critically ill patients. The potential for MRI to detect the haemorrhagic component of a

lesion by its high signal intensity is beneficial in traumatized patients. On spin-echo images in the sagittal plane, a longitudinal visualization of the thoracic aorta makes it possible to distinguish a partial lesion from a lesion encompassing the entire aortic circumference. This discrimination is of prognostic significance since a circumferential lesion may be more likely to rupture. The presence of periadventitial haematoma and/or pleural and mediastinal haemorrhagic effusion may also be considered a sign of instability. In the same sequence used to evaluate the aortic lesion, without the need for any additional time, the wide field-of-view of MRI provides a comprehensive evaluation of chest trauma such as lung contusion and oedema, PE, and rib fractures. Furthermore, if delayed surgery is considered, MRI may be used to monitor thoracic and aortic lesions because it is non-invasive and repeatable.[16]

MRA provides an excellent display of the aortic lesion and its relationship with supra-aortic vessels. However, it does not add any diagnostic value to spin-echo MRI, and cannot supply information on parietal lesions and haemorrhagic fluids outside the aortic vessel.

Aortitis

Inflammatory diseases of the aorta can be classified into two major subgroups: aortitis of non-specific or unknown etiology (Takayasu's aortitis, Bechet disease, giant cell aortitis, Kawasaki disease, ankylosing spondylitis) and specific aortitis, in which the aortitis is the consequence of an inflammatory disease of known origin (e.g. syphilitic aortitis). Relevant ethnic differences have been observed in the epidemiological distribution of non-specific aortitis. They are more common in Asian countries. Typical findings are marked irregular thickening of the aortic wall and a fibrous lesion that are the result of the inflammatory process of the media, which can lead to stenotic lesions (Takayasu's disease), aneurysms of the aorta and its major branches, or aortic insufficiency as a consequence of dilatation of the aortic root.

Because of the high spatial and contrast resolution offered by newer MRI techniques, which permit assessment of the aortic wall, MRI is included as a routine test in the work-up of patients who have vasculitis, particularly in those who have vasculitis affecting larger vessels, giant cell arteritis, and Takayasu's arteritis. Contrast spin-echo in black-blood sequences is useful to identify the wall thickening produced in aortitis of various causes. In the initial stages of Takayasu's arteritis, short inversion-time, inversion-recovery (STIR), and post-contrast T1-weighted sequences are particularly useful. Inflammatory changes in initial phases are reflected with contrast uptake and hyper-intensity secondary to the wall oedema in STIR sequences (Fig. 33.11). Active inflammatory disease appears as variable thickening of the aortic wall and

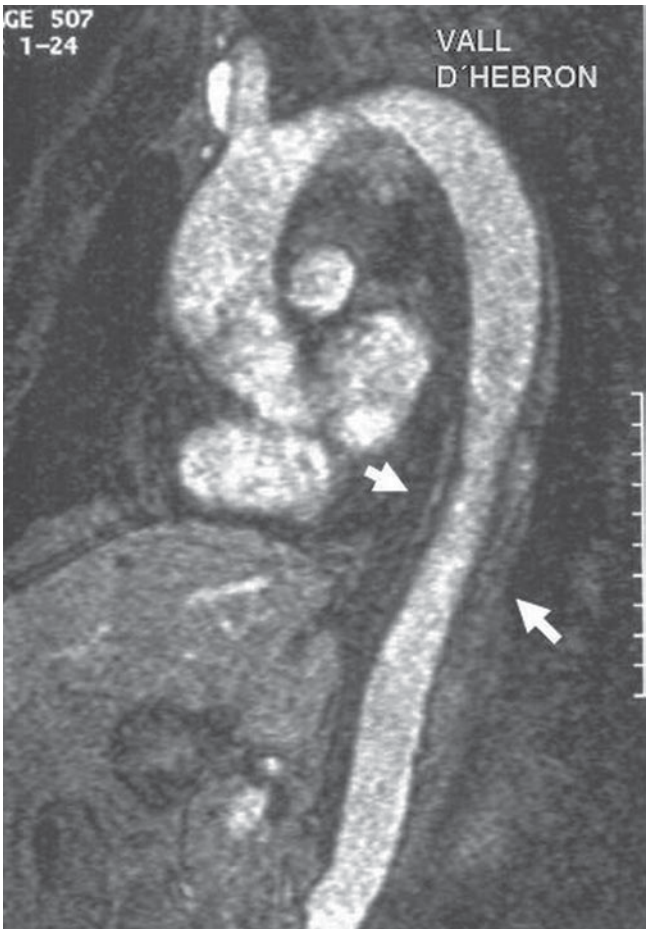

Fig. 33.11 Takayasu's arteritis. Sagittal STIR image shows thickening of the aortic wall with increased signal (*arrows*) suggesting wall oedema

delayed contrast-enhancement after gadolinium administration can characterize the degree of inflammation in the aortic wall of patients with Takayasu's arteritis.[17] In advanced stages of the disease, CE-MRA details the presence of stenosis in the aorta and its main branches secondary to the fibrous changes that appear in chronic phase. Recently, the capability of F-18 FDG hybrid camera PET combined with MRI to depict early stages of Takayasu's aortitis has been demonstrated.[18] Moreover, MRI can be useful in evaluating the response to medical treatment by depicting a decrease in wall thickness of the involved arteries.

Aortic Coarctation

Stenosis in the thoracic aorta is usually caused by atherosclerosis. It is commonly multi-focal and rarely flow-limiting. Coarctation of the aorta causes a more severe stenosis at the junction of the aortic arch and descending aorta, and may be

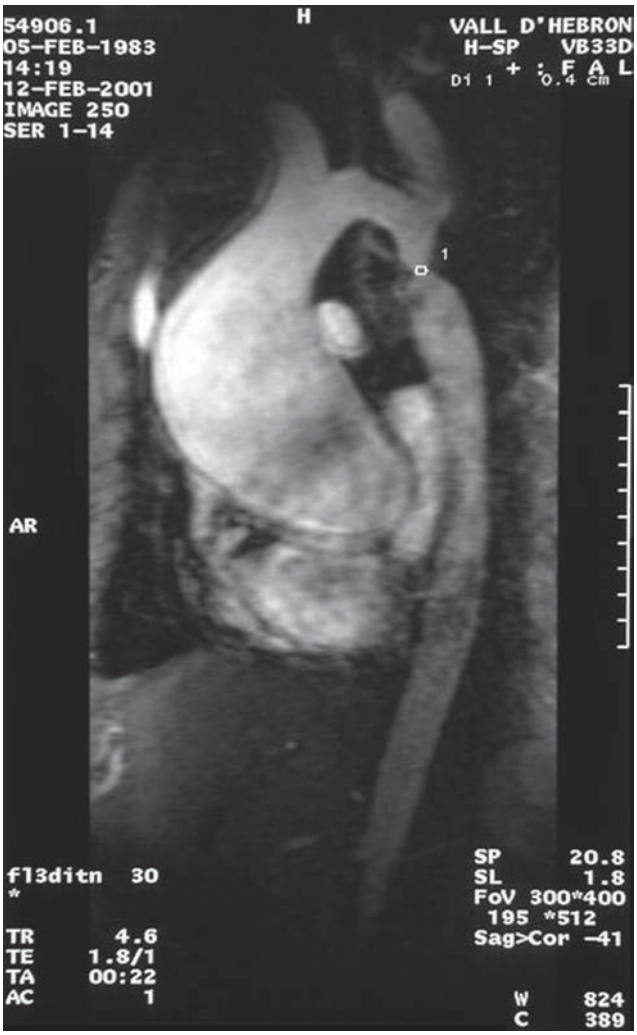

Fig. 33.12 Aortic coarctation with ascending aorta aneurysm in a patient with bicuspid valve aorta

focal or more diffuse (Fig. 33.12). Pseudocoarctation resembles a true coarctation, but is caused by aortic kinking just distal to the origin of the left subclavian artery. It is not haemodynamically flow-limiting, and, therefore, not associated with multiple collaterals. CE-MRA is the most useful technique for evaluating stenoses in the thoracic aorta. Temporally resolved sub-second CE-MRA can depict aortic stenoses, but it is particularly useful in haemodynamically significant lesions such as coarctation, where it demonstrates gradual filling of chest wall collaterals (Fig. 33.13). Phase contrast MRI can be used to measure velocity and flow, both proximal and distal to a stenosis, and helps assess the significance of a stenosis.[19] It may be more useful in monitoring disease progression over time; however, it is important to obtain measurements in similar anatomical locations to produce accurate and consistent results. MR is also very useful for serial follow-up imaging after surgery of the aortic aorta in this setting, with no radiation exposure (Fig. 33.14).

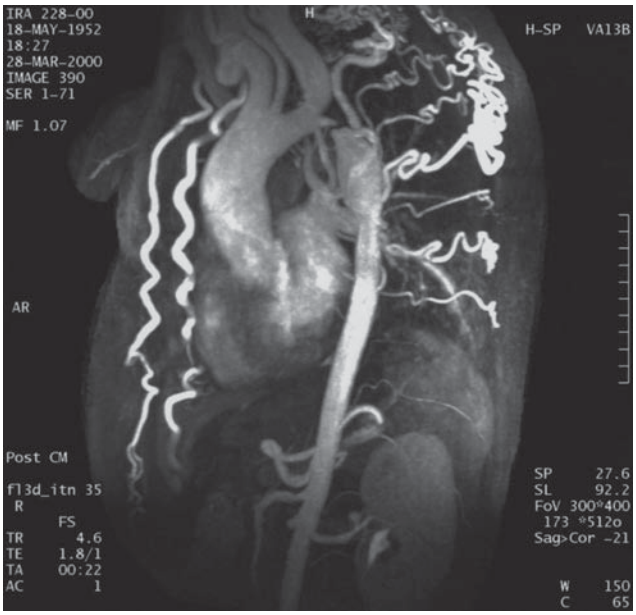

Fig. 33.13 Image extracted from a series of 3D MRA of the thoracic aorta in a patient with severe aortic coarctation, showing extensive collaterals

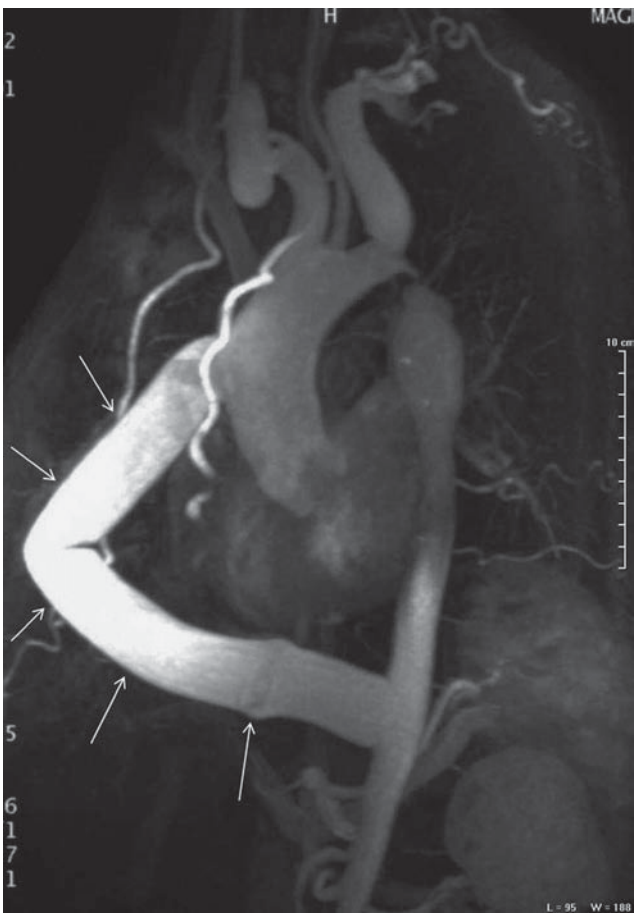

Fig. 33.14 Image extracted from 3D MRA in a patient followed by MR after bypass surgery (*arrows*) of the thoracic aorta for aortic coarctation

Pitfalls and Limitations

The main limitations of MRI imaging include its cost; patient claustrophobia; and the classical contraindications in patients with pacemakers/defibrillators, metallic ocular implants, and cerebral vascular clips. MRI is not contra-indicated in patients with mechanical prosthetic valves, but the valve induces a signal void artefact that precludes the study of the initial portion of the aorta. In acute aortic diseases, MRI is limited by lesser availability and is more time-consuming. For unstable patients, TOE or CT is usually a better option. The use of gadolinium chelates is not possible in patients with severe renal insufficiency (clearance < 30mL/min), even in those on haemodialysis, since it carries potential risk for the development of nephrogenic systemic fibrosis.[20]

MRI in Diagnostic Strategies

Aortic Atherosclerosis

TOE and MRI are powerful non-invasive tools for visualizing aortic atheromas. In patients with stroke or peripheral embolism, TOE is the technique of choice since it affords excellent assessment of the size and mobility of complicated plaques. MR imaging can non-invasively distinguish various components of the plaque such as fibrous cap, lipid core, and thrombus, thereby assessing plaque stability. In T2-weighted images, fibrous cap and thrombus are seen as a high-intensity signal, and lipid core is seen as a low-intensity signal.[21] Unlike TOE, MRI can visualize the entire thoracic aorta including the small section of ascending aorta, which is obscured by the tracheal air column. Also, serial MRI can be used to monitor progression and regression of atheromatous plaques after lipid-lowering therapy. Cine MRI may also permit the assessment of complex plaque and aortic debris mobility (Fig. 33.15). The advent of intra-oesophageal or intra-vascular MRI coils further enhances the spatial resolution by providing close proximity between the imaging coil and the vessel wall.[22]

Aortic Aneurysm

Aneurysms affecting the aortic root can be correctly assessed by TTE if the echocardiographic window is adequate. TOE will only be warranted when the acoustic window is poor or when the type of surgical treatment (repair or valve replacement) is considered. In contrast, both TTE and TOE have limitations for adequate measurement of distal ascending aorta diameters, aortic arch, and descending aorta (Fig. 33.16).

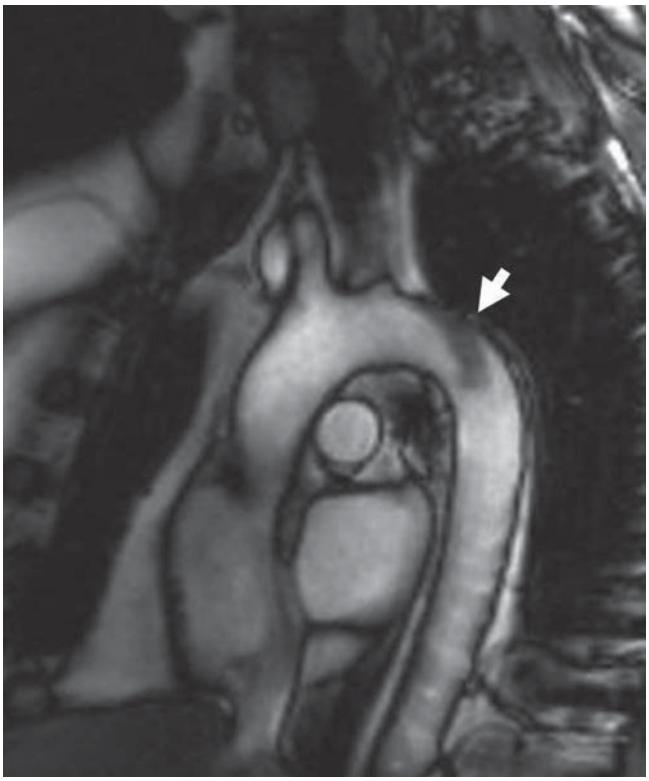

Fig. 33.15 Still frame extracted from SSFP cine MR showing extensive atherothrombotic debris (*arrow*) in a patient with aortic atheroma

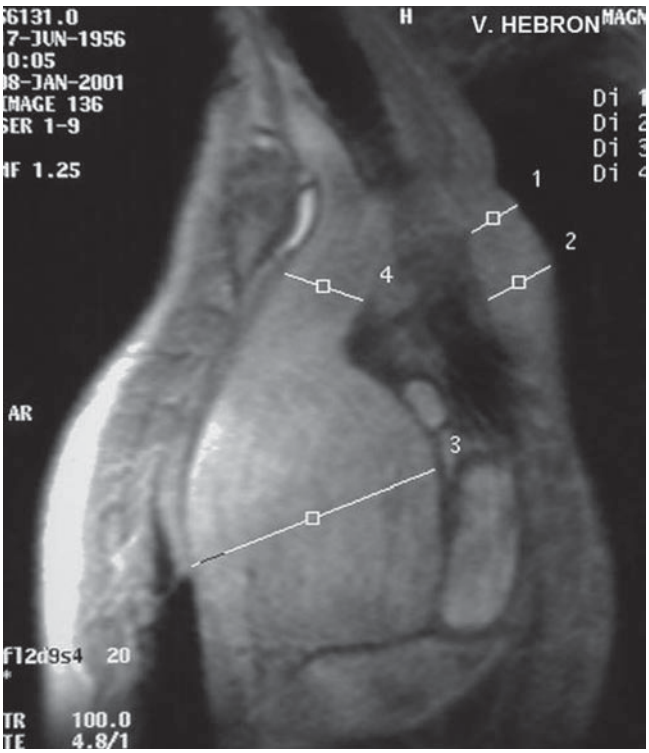

Fig. 33.16 Annuloaortic ectasia assessed by gradient-echo MR. Aortic diameter measurements can be obtained in different segments of the aorta

However, contrast-enhanced CT scanning and MRI very accurately detect the size of thoracic aortic aneurysms. Axial images often cut through the ascending aorta off-axis, resulting in a falsely large aortic diameter. Nevertheless, when the axial data are reconstructed into 3D images (CT angiography), one can measure the tortuous aorta in true cross section and obtain accurate measurement of aortic diameter. Such 3D imaging should then always be used to follow such patients over time. MRI may be preferred for the follow-up of patients because it avoids the need for ionizing radiation.[1, 2]

Acute Aortic Syndromes

A recently published meta-analysis[23] showed diagnostic accuracy to be practically the same (95–100%) for CT, TOE, and MRI. Most shortcomings are due to user interpretation errors, rather than the technique itself. The analysis of the International Registry of Aortic Dissection (IRAD)[24] showed that CT is the most frequently used imaging technique (61%), followed by echocardiography (33%), angiography (4%), and MRI (2%). The main advantage of CT is its wide availability, accuracy, and rapidity. In stable patients with doubtful intra-mural haematoma diagnosis by CT, MRI is the technique of choice as the hyper-intense signal in the aortic wall can facilitate a correct diagnosis. CT is better than TOE for detection of aortic ulcers, particularly if small. It is efficient for the evaluation of their penetration and bleeding in or outside the aortic wall. MRI is accurate for the investigation of aortic ulcers, especially for intra-mural haemorrhage complicating ulcers, and is indicated if renal failure is present.

TOE, CT, and MRI are also very useful in the diagnosis of traumatic aortic lesions, such as intimal dissection, medial laceration, pseudoaneurysm, or peri-aortic haemorrhage. Selection of the imaging test depends on the haemodynamic instability of the patient and the availability and experience of the centre. TOE offers excellent information on aortic wall lesions, but both CT and MR have an advantage owing to their wider field of view.

MRI in Prognosis and Follow-Up

Aortic Aneurysm

The size of the aorta is the principal predictor of aortic rupture or dissection. In a large retrospective study gathering thoracic aortic aneurysms of different aetiologies, the risk of rupture or dissection was 6.9% per year and, including death, was 15.6% per year for a size greater than 60 mm. The mean rate of growth for all thoracic aneurysms was 1 mm/year. The rate of growth was significantly greater for aneurysm of the descending aorta, 1.9 mm/year, than that of the ascending aorta, 0.7 mm/year. In addition, dissected thoracic aneurysms grew significantly more rapidly (1.4 mm/year) than non-dissected aneurysms (0.9 mm/year). In a more recent study, Davies et al[25] recommended elective operative repair before the patient enters the zone of moderate risk with an aortic size index greater than 2.75 cm/m^2.

The clinical importance of maximum aortic diameter in the indication for prophylactic surgical treatment implies taking measurements as accurately as possible. In studies comparing the reproducibility of the three techniques, echocardiography, CT, and MRI, inter-observer variability varies and increases with aortic diameter. It is essential for the same observer to compare measurements side by side using the same anatomical references. Tomographic scans in a situation where the aorta does not lay perpendicular to the scan plane produce an elliptical image with a major (maximum) and minor (minimum) diameter. In most natural history studies of aneurysm expansion, the minimum diameter has been reported to avoid the effect of convolution. However, MRI permits definition of a plane in any arbitrary space orientation, and easy location of plane orthogonal to the vessel walls (Fig. 33.17).

Acute Aortic Syndrome

Along with age, signs, and/or symptoms of organ malperfusion and clinical instability, fluid extravasation into the pericardium and peri-aortic haematoma have poor prognosis in acute phase. After discharge, variables related to greater aortic dilatation were entry tear size, maximum descending aorta diameter in sub-acute phase, and the high-pressure pattern in false lumen. Maximum aortic diameter in sub-acute phase was a significant predictor of progressive dilatation, since, according to Laplace's law, maximum aortic diameter is the main factor influencing increased wall stress.

After successful treatment of acute aortic syndrome, patients still remain at considerable risk for future complications. A persistent distal false lumen has been reported in 75–100% of cases. Secondary entry tears in the descending aorta or in the aortic arch are responsible for patency of the distal dissection, which is associated with unfavourable prognosis. Slight thickening around the graft caused by peri-graft fibrosis is a common finding. However, large or asymmetrical thickening around the tube-graft may represent localized haematoma caused by anastomotic leakage[26] (Fig. 33.18). A higher incidence of bleeding has been reported at the site of re-implanted coronary arteries. Gadolinium-enhanced MRI with standard spin-echo sequences can provide detailed information on suture

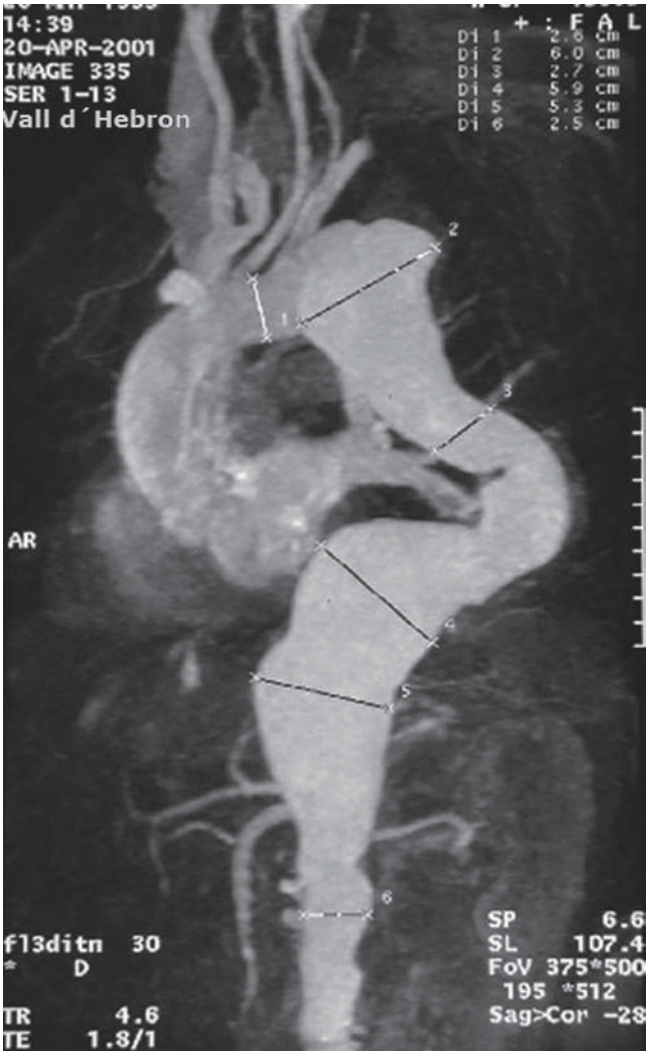

Fig. 33.17 Thoracoabdominal atherosclerotic aneurysms with significant aorta tortuosity. By gradient-echo, MR correct measurement of the aortic diameters perpendicular to the aortic walls can be performed

detachment; the site of bleeding appears as high-signal intensity within the haematoma. Moreover, gadolinium-enhanced MRA is particularly effective in the depiction of the complex post-operative anatomy and in elucidating the prosthetic tube, distal and proximal anastomoses and residual distal dissection, and, occasionally, dilated segments (Fig. 33.19).

MRI appears to be the technique of choice for following patients treated medically or surgically in acute aortic syndrome (Fig. 33.20). MRI avoids exposure to ionizing radiation or nephrotoxic contrast agents used for CT, and is less invasive than TOE. The large field-of-view of MRI permits visualization of anatomical landmarks for measurements to be taken at an identical level of the aorta. Furthermore, the integrated study of anatomy and physiology on blood flow can provide very interesting data to clarify the mechanisms responsible for aortic dilatation. Time-resolved MRA can provide additional dynamic information on blood flow in entry tears (Fig. 33.21). Velocity-encoded cine-MR sequences have a promising role in the functional assessment of aortic dissection through the quantification of flow in both lumina and the possibility of establishing haemodynamic patterns of progressive dilatation risk (Fig. 33.22). This technique, together with time-resolved MRA, should provide new and highly useful physiopathological understanding to determine the most tailored therapeutic management in each case. Increased false lumen pressure was another important factor implying false lumen enlargement. The high false lumen pressure was due, in the majority of cases, to a large entry tear without distal emptying flow or re-entry site of similar size. It is often difficult to identify the distal discharge communication; thus, indirect signs of high false lumen pressure such as true lumen compression, partial thrombosis of the false lumen,[27] or the velocity pattern of false lumen flow by phase contrast sequences should be considered.[28, 29]

The evolution of intra-mural haematoma may result in resorption, aneurysm formation, or dissection[30] (Fig. 33.23). Intra-mural haematoma may regress completely in 34% of patients, progress to aortic dissection in 12% and to aneurysm in 20%, and evolve to pseudoaneurysm in 24%

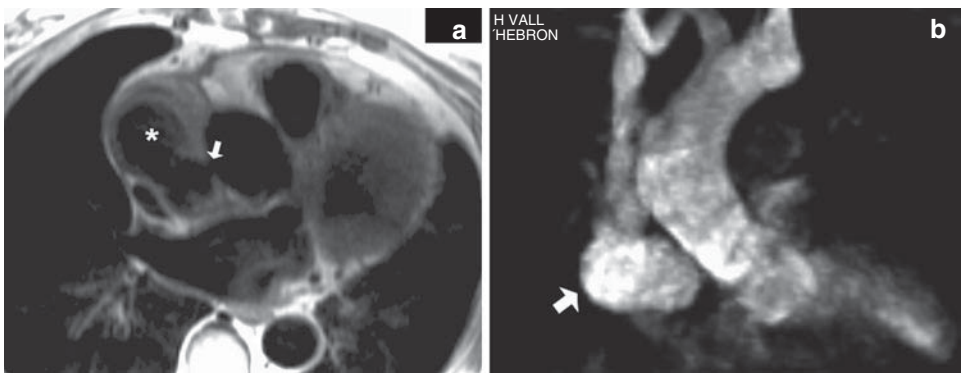

Fig. 33.18 Surgically treated Type A aortic dissection. **(a)** Axial T1-weighted black-blood image shows a pseudoaneurysm (*asterisk*) communicated (*arrow*) with the ascending aorta. **(b)** Sagittal maximum-intensity-projection image from CE-MRA shows contrast filling of the pseudoaneurysm

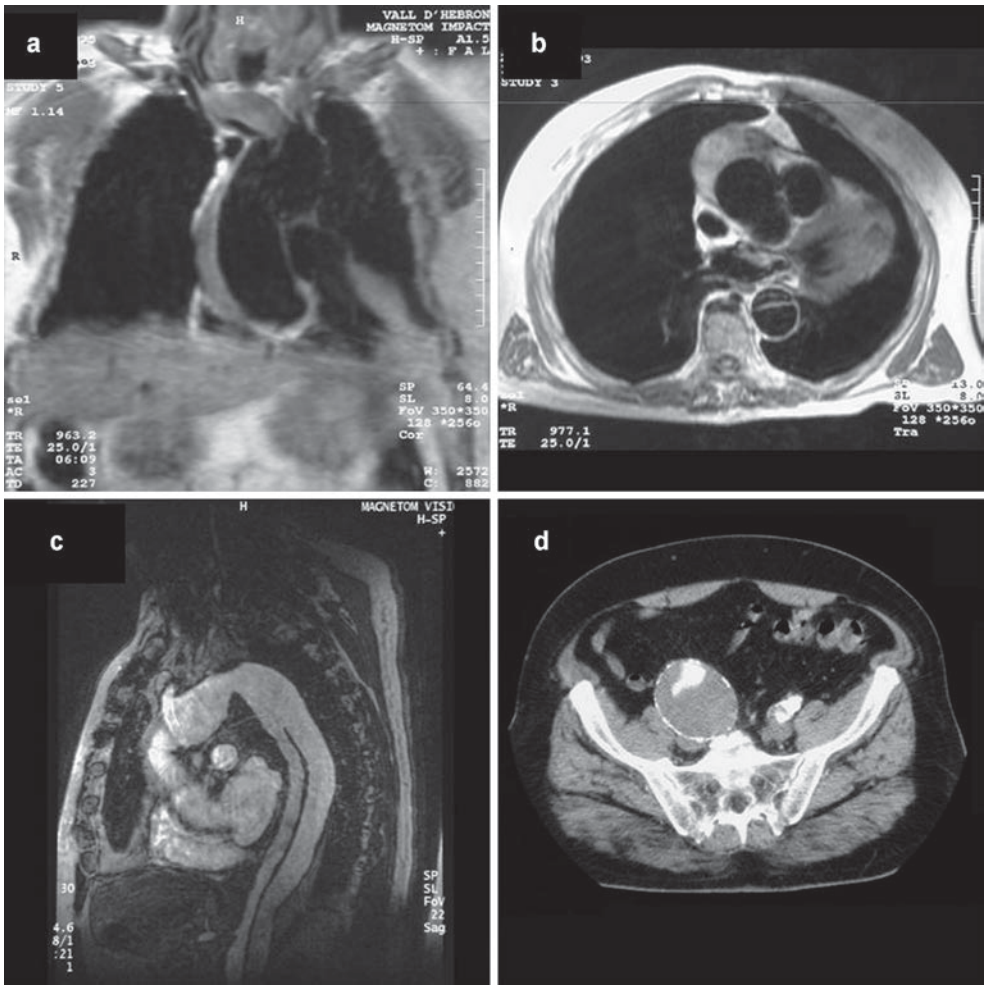

Fig. 33.19 Retrograde Type A dissection with total thrombosis of the false lumen in the ascending aorta. Spin-echo black blood in coronal view **(a)** and axial view **(b)**; note that the false lumen is patent in descending aorta. **(c)** After surgical treatment descending aorta dissection with patent false lumen persisted. **(d)**. Right iliac artery aneurysm with partial thrombosis was also diagnosed

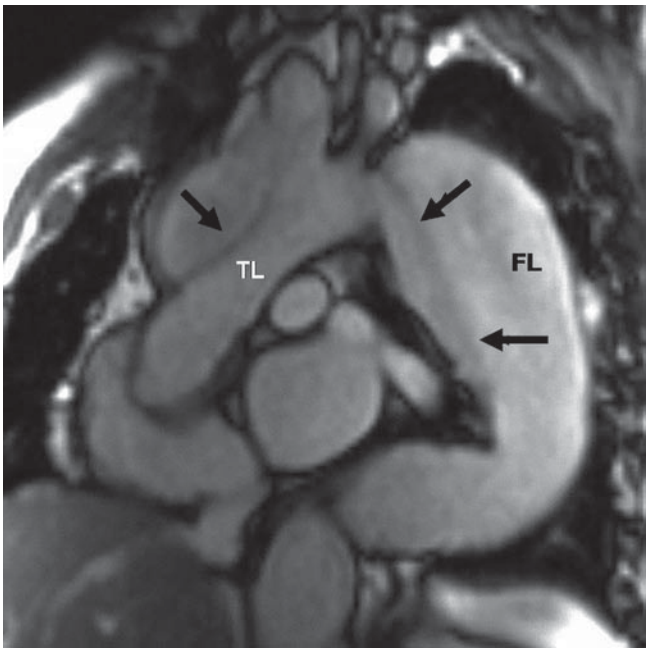

Fig. 33.20 Follow-up of a patient with a Type A aortic dissection treated surgically. Time-resolved sagittal maximum-intensity-projection angiograms show the intimal flap (*arrows*) and the time course of enhancement of both lumina

(Fig. 33.24). Given their wider field of view, MRI and CT are better than TOE for defining this dynamic evolution. MRI offers the possibility of monitoring the evolution of intra-mural bleeding and depicting new asymptomatic intra-mural re-bleeding episodes (Fig. 33.23).

The natural history of penetrating aortic ulcer is unknown. Like intra-mural haematoma, several evolutive possibilities have been described. Many patients with penetrating ulcer do not need immediate aortic repair, but do require close follow-up with serial imaging studies, by CT or MRI, to document disease progression (Fig. 33.25). Although many authors have documented the propensity of aortic ulcers to develop progressive aneurysmal dilatation, the progression is usually slow. MRI may be helpful to show incidental and asymptomatic bleeding of aortic ulcers. Spontaneous, complete aortic rupture may occur. Some aortic ulcers are incidental findings, similar to saccular aneurysms. In these cases, size and enlargement are the only predictors of complications.

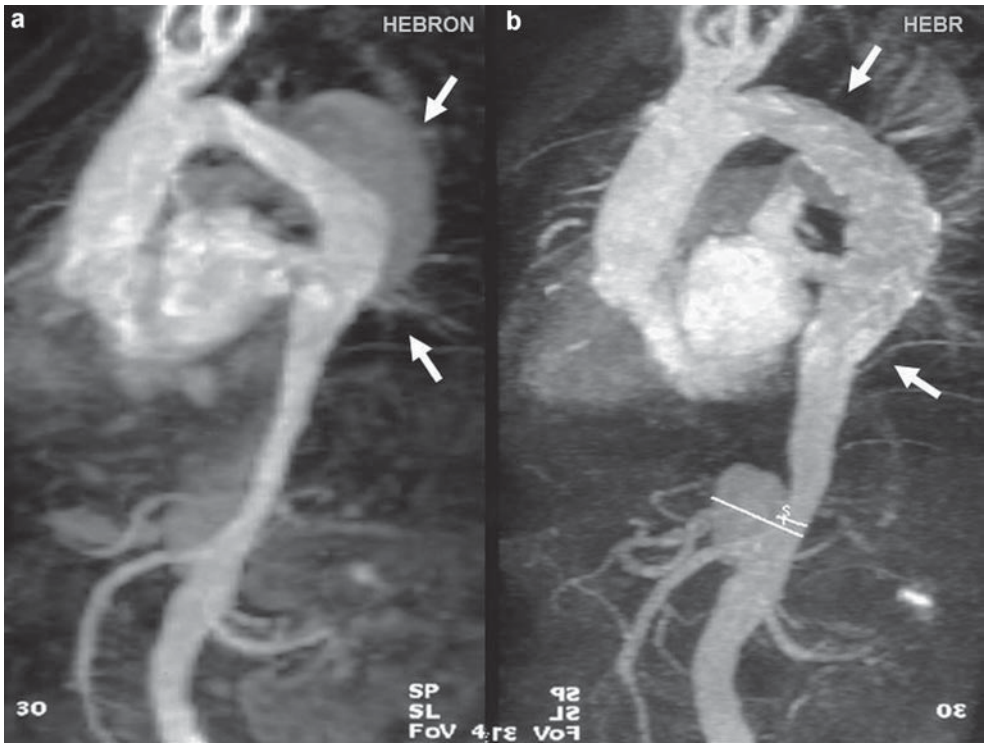

Fig. 33.21 **(a)** Type B aortic dissection with significant dilatation of the false lumen in proximal descending aorta (*arrows*). **(b)** Three months after endovascular therapy, MRI showed the correct implantation of the stent (*arrows*) with distal false lumen thrombosis up to visceral coeliac and mesenteric artery ostia (lines)

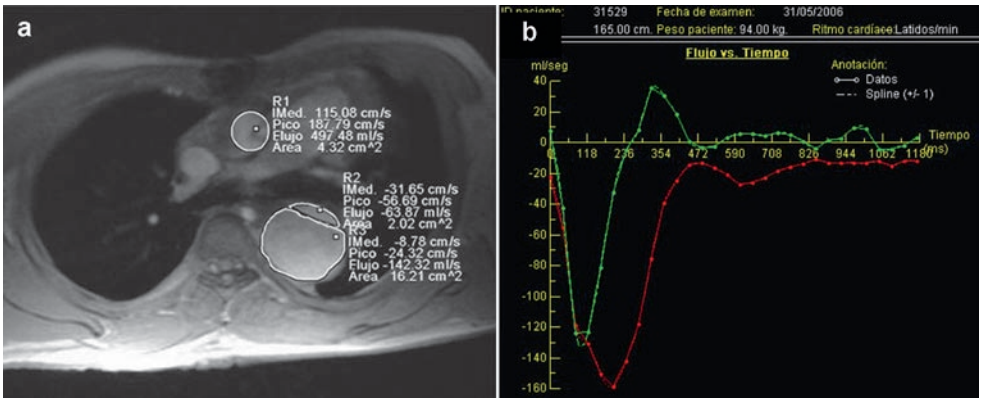

Fig. 33.22 Phase-contrast volumetric quantification of true and false lumen flows. **(a)** cross-sectional area of both lumina. **(b)** Flow volume curves of the true lumen (*red*) and false lumen (*green*)

Video 33.4

SSFP cine MR sequence of the thoracic aorta in a patient with a huge aneurysm of the ascending aorta

Video 33.7

SSFP cine MR in the 4-chamber view in a patient with Type A acute aortic dissection and pleural effusion

Video 33.6

Corresponding SSFP cine MR in the same patient with Type A acute aortic dissection and an intimal flap

Video 33.13

3D reconstructed view of MRA of the thoracic aorta in the same patient as in Fig. 33.13

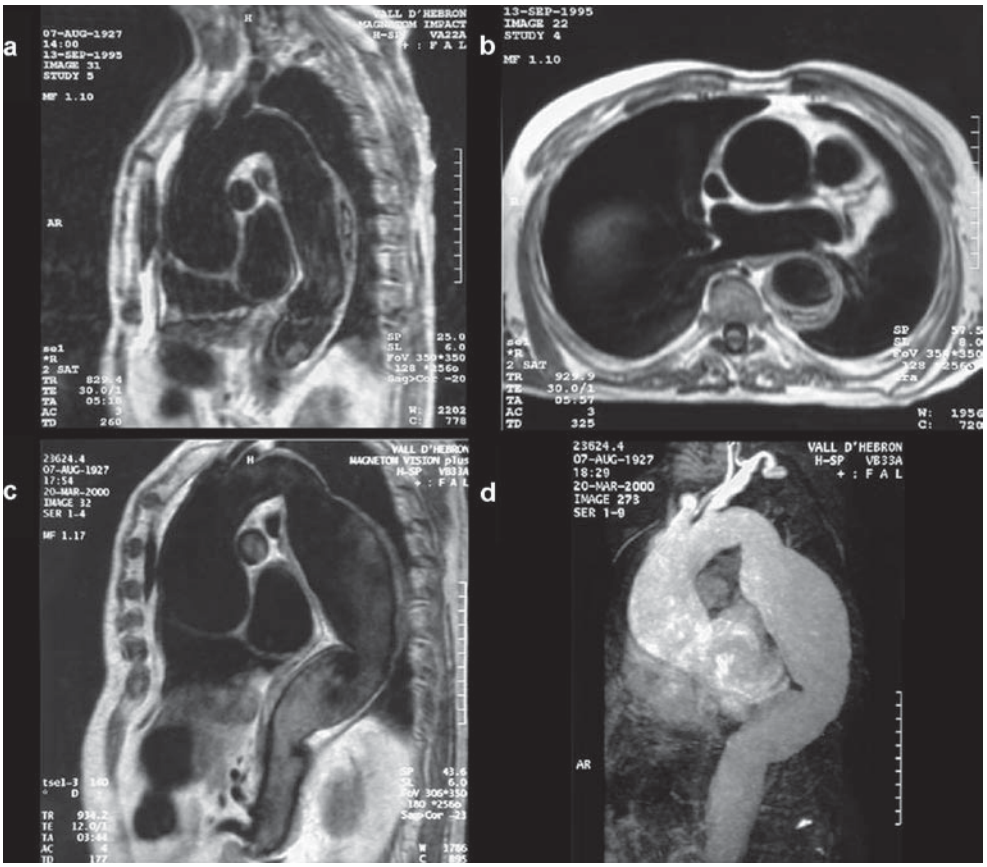

Fig. 33.23 Intra-mural haematoma in descending aorta in acute phase in sagittal **(a)** and axial **(b)** views. After a 5-year follow-up, a fusiform aneurysm was diagnosed by spin-echo black-blood **(c)** and gradient-echo MRI **(d)** sequences

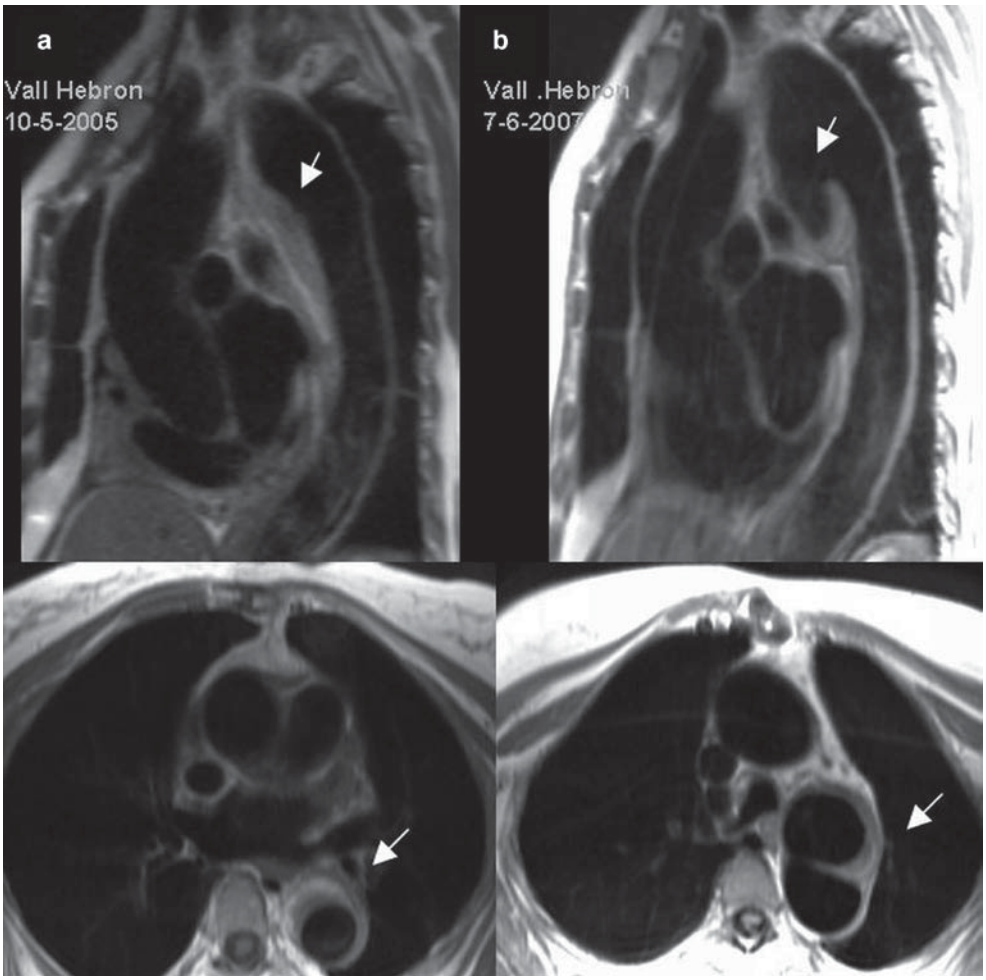

Fig. 33.24 Acute Type B intra-mural haematoma **(a)**, which evolved to localized dissection and pseudoaneurysm formation after a 2-year follow-up **(b)**

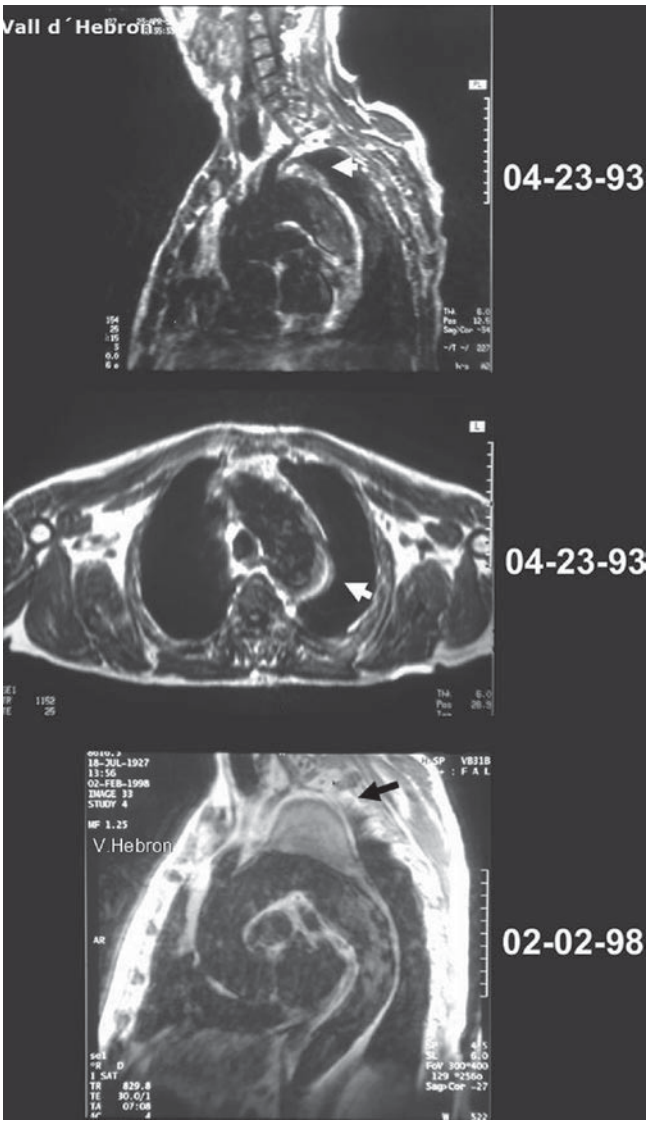

Fig. 33.25 Penetrating atherosclerotic ulcer with small intra-mural haemorrhage located in the upper part of the descending aorta. T1-weighted, in sagittal **(a)** and transversal views **(b)**, reveals this ulceration (*arrows*). **(c)** After 5 years of asymptomatic evolution, MRI shows a large saccular aneurysm formation (*arrow*). In the original site of the atherosclerotic ulcerated plaque

Acknowledgments The authors thank Pr Hervé Rousseau (CHU Rangueil, Toulouse), Pr Jean-Nicolas Dacher (CHU Rouen), and Dr. Victor Pineda (IDI, Hospital Vall d´Hebron, Barcelona) for their contribution to the iconographic data.

References

1. François CJ, Carr JC. MRI of the thoracic aorta. *Cardiol Clin*. 2007;25:171–184
2. Russo V, Renzulli, M Buttazzi K, et al Acquired of the thoracic aorta: role of MRI and MRA. *Eur Radiol*. 2006;16:852–865
3. Burman ED, Keegan J, Kilmer PJ. Aortic root measurement by cardiovascular magnetic resonance. *Circ Cardiovasc Imaging*. 2008;1:104–113
4. Fayad ZA, Nahar T, Fallon JT, et al In vivo magnetic resonance evaluation of atherosclerotic plaques in the human thoracic aorta. *Circulation*. 2000;101:2503–2509
5. Corti R, Fayad ZA, Fuster V, et al Effects of lipid–lowering by simvastatin on human atherosclerotic lesions. A longitudinal study by high-resolution, noninvasive magnetic resonance imaging. *Circulation*. 2001;104:249–252
6. Briley-Saebo KC, Shaw PX, Mulder WJ, et al Targeted molecular probes for imaging atherosclerotic lesions with magnetic resonance using antibodies that recognize oxidation-specific epitopes. *Circulation*. 2008;117:3206–3215
7. Briley-Saebo KC, Mulder WJ, Mani V, et al Magnetic resonance imaging of vulnerable atherosclerotic plaques: current imaging strategies and molecular imaging probes. *J Magn Reson Imaging*. 2007;26:460–479
8. Kawamoto S, Bluemke DA, Traill TA, et al Thoracoabdominal aorta in Marfan syndrome: MR imaging findings of progression of vasculopathy after surgical repair. *Radiology*. 1997;203:727–732
9. Krinsky G. Gadolinium-enhanced three-dimensional magnetic resonance angiography of the thoracic aorta and arch vessels. A review. *Invest Radiol*. 1998;33:587–605
10. Nollen GJ, Groenink M, Tijssen JGP, et al Aortic stiffness and diameter predict progressive aortic dilatation in patients with Marfan syndrome. *Eur Heart J*. 2004;25:1146–1152
11. Groeninck M, de Roos A, Mudder BJ, et al Changes in aortic distensibility and pulse wave velocity assessed with magnetic resonance imaging following beta-blocker therapy in the Marfan syndrome. *Am J Cardiol*. 1998;82:203–208
12. Grotenhuis HB, Ottenkamp J, Westenberg JM, et al Reduced aortic elasticity and dilatation are associated with aortic regurgitation and left ventricular hypertrophy in nonstenotic bicuspid aortic valve patients. *J Am Coll Cardiol*. 2007;49:1660–1665
13. Kunz RP, Oberholzer K, Kuroczynski W, et al Assessment of chronic aortic dissection: contribution of different ECG-gated breath-hold MRI techniques. *Am J Roentgenol*. 2004;182:1319–1326
14. Goldfarb JW, Holland AE, Heijstraten FM, et al Cardiac-synchronized gadolinium-enhanced MR angiography: preliminary experience for the evaluation of the thoracic aorta. *Magn Reson Imaging*. 2006;24;241–248
15. Nienaber CA, von Kodolitsch Y, Petersen B, et al Intramural hemorrhage of the thoracic aorta: diagnostic and therapeutic implications. *Circulation*. 1995;92:1465–1472
16. Fattori R, Celletti F, Descovich B, et al Evolution of post-traumatic aneurysm in the subacute phase: magnetic resonance imaging follow-up as a support of the surgical timing. *Eur J Cardiothorac Surg*. 1998;13:582–587
17. Choe YH, Kim DK, Koh EM, et al Takayasu arteritis: diagnosis with MR imaging and MR angiography in acute and chronic active stages. *J Magn Reson Imaging*. 1999;10:751–757
18. Meller J, Grabbe E, Becker W, et al Value of F-18 FDG hybrid camera PET and MRI in early Takayasu aortitis. *Eur Radiol*. 2003;13;400–405
19. Mohiaddin RH, Kilner PJ, Rees, et al Magnetic resonance volume flow and jet velocity mapping in aortic coarctation. *J Am Coll Cardiol*. 1993;22;1515–1521
20. Shellock FG, Spinazzi A. MRI safety update 2008: part 1, MRI contrast agents and nephrogenic systemic fibrosis. *Am J Roentgenol*. 2008;191:1129–1139
21. Shunk KA, Garot J, Atalar E, Lima JA. Transesophageal magnetic resonance imaging of the aortic arch and descending thoracic aorta in patients with aortic aterosclerosis. *J Am Coll Cardiol*. 2001;37:2031–2035
22. Farrar CT, Wedden VJ, Ackerman JL. Cylindrical meanderline radiofrequency coil for intravascular magnetic resonance studies of atherosclerotic plaque. *Magn Reson Med*. 2005;53:226–230
23. Shiga T, Wajima Z, Apfel CC, et al Diagnostic accuracy of transesophageal echocardiography, helical computed tomography, and magnetic resonance imaging for suspected thoracic aortic dissection. Systematic review and meta-analysis. *Arch Intern Med*. 2006;166:1350–1356

24. Hagan PG, Nienaber CA, Isselbacher EM, et al The international registry of acute aortic dissection (IRAD). *JAMA*. 2000;283:897–903
25. Davies RR, Goldstein LJ, Coady, et al Yearly ruptured or dissection rates for thoracic aortic aneurysms; simple prediction based on size. *Ann Thorac Surg*. 2002;73:17–27
26. Fattori R, Bacchi-Reggiani L, Bertaccini P, et al Evolution of aortic dissection after surgical repair. *Am J Cardiol*. 2000;86:868–872
27. Tsai TT, Evangelista A, Nienaber CA, et al Partial thrombosis of the false lumen in patients with acute type B aortic dissection. *N Engl J Med*. 2007;357:349–359
28. Inoue T, Watanabe S, Sakurada H, et al Evaluation of flow volume and flow patterns in the patent false lumen of chronic aortic dissection using velocity-encoded cine magnetic resonance imaging. *Jpn Circ J*. 2000;64:760–764
29. Strotzer M, Aebert H, Lehhart M, et al Morphology and hemodynamics in dissection of the descending aorta. Assessment with MR imaging. *Acta Radiologica*. 2000;41:594–600
30. Evangelista A, Domínguez R, Sebastià C, et al Long-term follow-up of aortic intramural hematoma. Predictors of outcome. *Circulation*. 2003;108:583–589

Chapter 34

ROLE OF MULTI-SLICE COMPUTED TOMOGRAPHY

Pedro Marcos-Alberca, José Luis Zamorano, and Raimund Erbel

CONTENTS

J. L. Zamorano et al. (eds.), *The ESC Textbook of Cardiovascular Imaging*
DOI: 10.1007/978-1-84882-421-8_34, © Springer-Verlag London Limited 2010

Introduction

Aortic disease is relatively uncommon. However, it has always been considered a serious and potentially fatal condition. The aorta is not easily accessible to direct physical examination. Imaging is essential for the diagnosis, treatment, stratification, and assessment of the short- and long-term follow-up. The most influential imaging technique developed in recent years that covers almost all aspects of aortic diseases is undoubtedly computed tomography (CT).

Traditional imaging techniques to visualize the aorta were chest radiography and invasive angiography at the catheterization laboratory.[1] The advent of the ultrasound marked the introduction of the non-invasive diagnosis of the aortic pathology. Shortly after the development or first commercial availability of CT scans, cardiac and great vessels anatomies were finely described.[2, 3] Normal findings are described, as well as aortic pathology: aortic aneurysm, dissection, traumatic lesions, etc.[4, 5] The introduction of helical multi-slice CT allows the achievement of impressive spatial resolutions, free of motion artefacts, of the aorta and main branches with equally impressive very short time acquisitions. Nowadays, CT scan is the leading imaging technique in the study of any aortic condition, congenital or acquired, acute or chronic, thoracic or abdominal. In the following sections, we will review the role of CT scan in the study of aortic diseases.

Technical Considerations

In adult patients, the recommended technique for high–resolution CT angiography of the cardiothoracic and abdominal vascular anatomy is retrospectively ECG-gated spiral acquisition.[6] It provides the highest resolution within breath-hold times accessible for the great majority of patients. In previous chapters, current helical technology and parameters for many instances of studies of cardiac tomography have been described. Nonetheless, comparing with CT of coronary arteries, aortic studies show differences.[7] In order to cover the thoracic or the abdominal aorta or both, protocols are optimized for the necessary large scan fields. When it is necessary to visualize thoracic and abdominal aorta, a two-step approach is usually used. The most frequent parameters for the analysis of great vessels are shown in Table 34.1.

Very low-pitch values are important to achieve a more than ideal spatial resolution and to shorten scan time and the prolonged apnea needed for aortic exploration (up to 300 mm of scan field in each step, thoracic, and abdominal). In order to reduce radiation exposure, it is important to adjust pitch values to rotation time.

For contrast administration, the catheter should be positioned in the right arm, if possible, to avoid opacification of the left brachiocephalic vein, which could result in a perivenous artefact that substantially degrades visualization of the origin of the brachiocephalic artery or generates confounding images in the aortic arch.

Current technology has allowed the development of fast, prospectively ECG-triggered protocols for CT angiography of the aorta. These protocols have poor spatial resolution and a limited use for coronary evaluation, but their results in aortic examinations are very promising, with a clear advantage in terms of radiation exposure, which is significantly lessened when compared with retrospective ECG gating helical CT examinations.[8]

Diagnostic accuracy of CT in aortic pathology can be affected by artefacts or errors in the acquisition of the study or in the reconstruction, processing, and inter-pretation of the data set. Among the most notable pitfalls are improper timing of contrast material administration relative to image acquisition, streak artefacts generated by high-attenuation material (i.e. sternal sutures), high-contrast interfaces or aortic wall motion blur due to bad apnea or phase artefacts, and adjacent anatomic structures (e.g. mediastinal veins, pericardial recess, thymus, atelectasis, pleural thickening, or effusion adjacent to the aorta).[9]

Congenital Diseases

Known or suspected congenital anomalies of the aortic arch and neighbouring structures constitute an indication of aortic CT.[10] Due to the exposure to radiation, CT is more limited to the adult patients and avoided in paediatric populations. Magnetic resonance imaging (MRI) competes with CT, and usually the choice depends more on the availability of one or another. When serial studies are scheduled, MRI is preferred since radiation effects are cumulative. However, in a medical emergency (i.e. severe respiratory insufficiency secondary to vascular rings), CT overcomes the logistics and time limitations of MRI.

Coarctation of the aorta is the most frequent aortic malformation found in adult patients. This lesion consists of a localized shelf in the postero-lateral aortic wall opposite the ductus arteriosus. In some patients who are diagnosed later in life, the shelf can be larger. Multi-planar reformatted reconstruction (MPR) images in two orthogonal planes depict the dimensional attributes of the coarctation, thereby helping the inter-ventionalist for planning balloon dilation and stent placement when indicated. Volume-rendered reconstructions

Table 34.1. Different scan parameters to perform aortography with retrospective ECG gating helical CT

	64-slice CT	32–40 slice CT	16-slice CT
Slice width (mm)	1.5–2.0	0.6–0.9	0.6–0.9
Increment (mm)	1.0–1.3	0.4–0.6	0.4–0.6
Rotation time (ms)	500	400	330
Temporal resolution (ms)	250	200	165
kV	120	120	120
mAs/slice	430–800	600–800	600–990
Pitch	0.25–0.35	0.20–0.30	0.20–0.30
Exposure (mSv)[a]	12–20	12–24	12–24
Scan time/apnea (s)	19–25	20–30	14–20
Contrast volume (mL)	120–150	120–150	100–120

[a]Exposure can vary in relation to specific vendor technology and patient characteristics. The specified values are activating tube current modulation

allow the surgeon to idealize the aortic isthmus architecture and its anatomic relations with neighbouring vessels (i.e. left subclavian artery or LSA), and can help in surgical management and evaluation of the final result. In the follow-up, when ultrasound or MRI is inconclusive or unavailable, CT allows to discard recoarctation, aneurysm formation at the site of the previous repair, pseudoaneurysm, or aortic dissection. Serial imaging in the asymptomatic patient would be indicated every 3–5 years, preferably with non-radiating imaging techniques.[11]

Aortic arch hypoplasia and aortic arch interruption involving the segment between the innominate artery and the ductus arteriosus usually present early on in life; they are ductus-dependent malformations associated with other left-sided anomalies, and require a prompt surgical management in the newborn. For initial evaluation, ultrasound and MRI are the preferred imaging techniques in order to avoid exposure to radiation.

Vascular rings are aortic malformations associated with abnormal anatomic relations with the trachea or the oesophagus and often cause respiratory symptoms (estridor) or dysphagia. Symptoms usually occur in the newborn or the young infant, and infrequently are diagnosed later in life. The most frequent vascular ring is a double aortic arch as a result of the persistence of the normal embryonic vascular anatomy of this area.[12] Volume-rendered reconstruction depicts images of the vascular anatomy of great visual effect which facilitate the understanding of these anomalies. Maximal pixel intensity (MPI) MPR images disclose two aortic arches, one left-sided and another right-sided. The left arch, distal to the exit of the LSA, is rarely patent. It is near always atretic and connects with the distal aorta through a fibrous ligament, closing the ring. In the right aortic arch, the next important vascular ring, the ligamentum arteriosum runs from the left pulmonary artery to the upper descending thoracic aorta in the right, closing the ring. Symptomatic patients normally associate a Kommerrell's diverticulum as a huge pouching in the point of arising of the LSA from the distal aortic arch (Fig. 34.1, Video 34.1). Anomalous origin of the right subclavian artery, when associated with a right-sided ligamentum arteriosum, is another sort of vascular ring.

When aortic dissection is suspected, the most important fact is to confirm the initial diagnosis and to characterize specific features, which allow defining the appropriate management of the patient: medical intervention or surgical therapy. Diagnostic tools have to have a high sensitivity and specificity for an accurate diagnosis, high availability, and fast performance to explore the whole aorta and main side branches in an emergency clinical setting. Of all the techniques, there is no doubt that multi-slice helical CT is the only one that meets all these conditions, and this makes it the first choice for this serious disease. The only exceptions would be those patients with a very unstable situation, who would be immediately transferred to the operating room and examined by trans-oesophageal echocardiography before surgery.

The first step is to define the location and extent (type A or type B acute aortic syndrome), and the second step is to classify the aortic dissection as classical (Class 1), intramural haematoma (Class 2), discrete dissection (Class 3), penetrating ulcer (Class 4), or traumatic (Class 5).[13]

Depending on the localization and extension, it is divided into two types: proximal and distal dissections. Proximal, or Standford's Type A aortic dissection, covers the ascending thoracic aorta, independently of the end of it. Distal, or

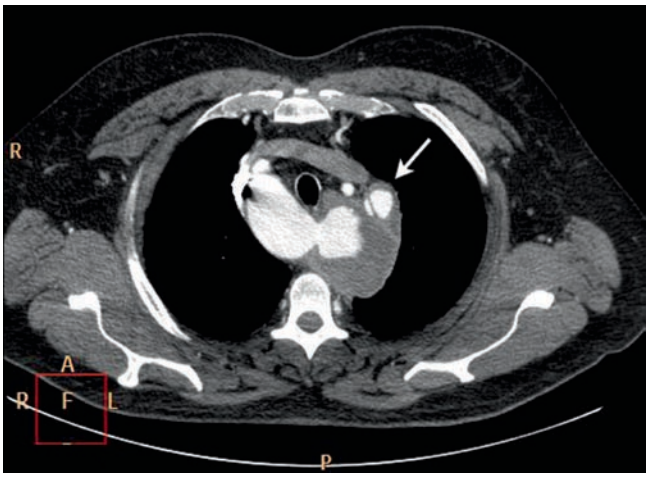

Fig. 34.1 Axial view of the upper thorax. The aortic arch is right sided and crossing to the left behind the trachea and the oesophagus. The left subclavian artery (*arrow*) clearly shows a flap into its lumen and a huge cavity in its vicinity partially filled with thrombus and corresponding to the Komerell's diverticulum

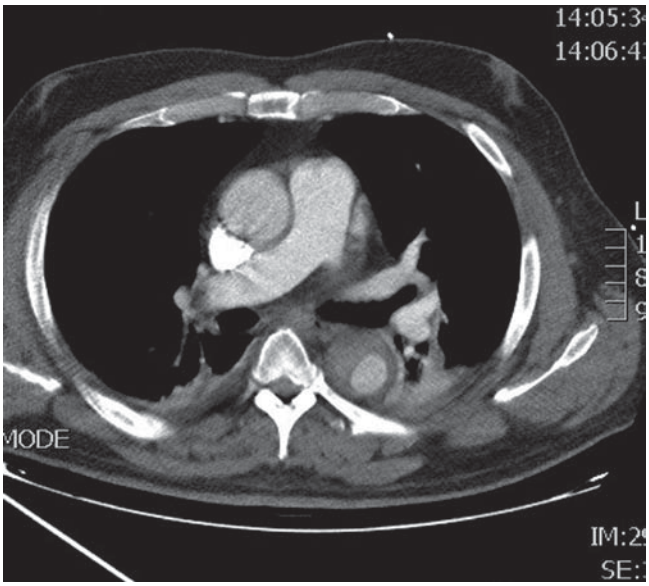

Fig. 34.2 Classical or Class 1 B-type acute aortic dissection. The axial view discloses the dual lumen into the descending thoracic aorta. There are stick artefacts into the ascending aorta caused by iodine contrast filling the superior cava vein. The tear was in the distal aortic arch (not showed). The false lumen unveils less attenuation than true ones secondary to a lesser degree of flow and contrast filling. If the tear is not clearly visible, differentiation with intra-mural haematoma could be challenging and another imaging technique (i.e. trans-oesophageal echocardiography) needed

Standford's Type B aortic dissection, does not affect the ascending aorta and begin immediately distal to the ligamentum arteriosum and the left sublcavian artery (LSA) (Fig. 34.2, Video 34.2). Sometimes, distal dissections have a retrograde progression and become Type A aortic dissection about 20 % of all type A as found by the Zurich and our group.

Class 1 Aortic Dissection: Classical Aortic Dissection

In classical or Class 1 aortic dissection, intimal tear is the common feature that underlies the origin of the aortic wall dissection. Blood dissects the aortic wall forming a novel lumen inside it, the false lumen. The final result is the appearance of a dual lumen (the *true* and the *false* lumens) in a sometimes normal non-dilated aorta. Tears are transversals or oblique, with well-defined edges from 4 to 5 cm in length. The dissection and false lumen can, in turn, affect a small segment of the circumference of the aorta or encircle it almost completely. It runs a variable distance, ranging from a few to several cm, sometimes reaching the iliac or femoral arteries. In their trajectory, they can dissect main branches, such as the aortic arch vessels, renal arteries, or mesenteric artery. Occasionally, there are re-entries towards the aortic lumen, generating new tears, more distal and usually smaller. The natural evolution of the dissection is usually the progressive dilation of the wall dissected, peri-adventitial bleeding, and rupture with extravasations of blood into cavities and adjacent organs, such as the pericardial, pleural, or peritoneal cavities.

Diagnostic findings in multi-slice CT of the aorta correlate well with the pathologic features previously described (Fig. 34.3).[13] High spatial resolution of modern CT and the versatility of multi-planar reformatting post-processing of the volumetric data set, allow precisely localizing the intimal tear and flap and describing their extensions and main vascular branch affectations. The intimal flap appears as a low attenuated well-defined line in the aortic true lumen. The entry tear is visualized around the 85–90% as a clear interruption of the intimal flap (Fig. 34.4). If the false lumen is thrombosed, or, similar to the IMH, there is no intimal tear to permit flow through the false lumen, a clearly distinct intimal flap may not be identified. The spiral trajectory, the inward displacement of the calcium, if present, and the well-defined contour help to differentiate dissection from atherothrombosis. Atypical configurations of the flap, such as seen with short dissections *(Class 3 or discrete aortic dissection)* or with complex flaps secondary to multiple false channels, and aortic anomalies are difficult diagnoses (Fig. 34.5). There are several signs to distinguish true from false lumen, a distinction that has gained importance with endovascular stent therapy. The false lumen shows area of less attenuation, its luminal area is greater, and on most contrast-enhanced CT scans, as an opposite of the true lumen, which may be identified by its continuity with an undissected portion of the aorta. The extension of the dissection to aortic arch branch and

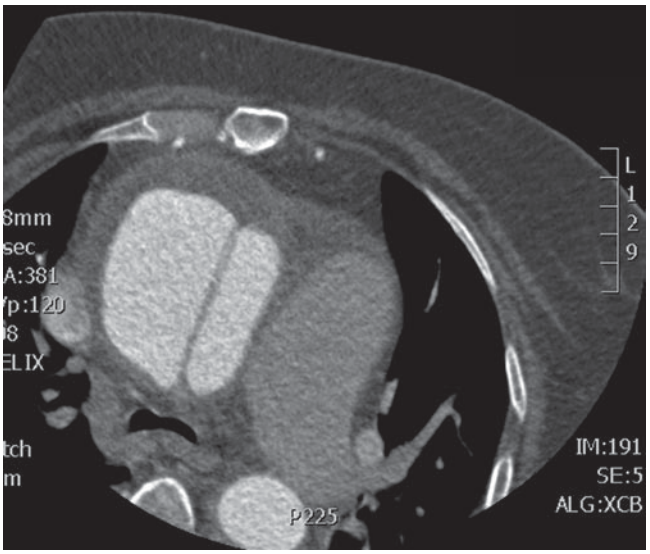

Fig. 34.3 Axial view of the great vessels, aorta, and pulmonary trunk. Ascending aorta is dilated and the intimomedial flap divides the lumen establishing the diagnosis of Stanford type-A Class 1 classical aortic dissection. The aortic wall is thickened and the attenuation reaches a value compatible with blood content. The descending thoracic artery shows a preserved lumen, indicating the dissection limited to the ascending segment

pericardial effusions in the Type A of aortic dissection diagnosed using CT is confirmed at surgery with an accuracy up to 95–100%.[14] In Type B aortic dissection, the intimal flap

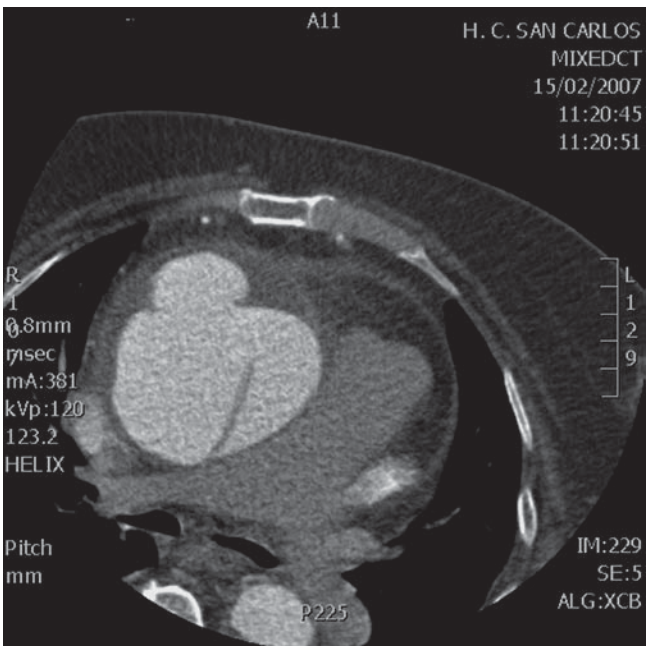

Fig. 34.4 Axial view of the great vessels at the level of the pulmonary bifurcation. The aortic contour is interrupted in its anterior part, being the rupture contained by the adventitia. The intimal tear is close to the contained rupture. The high flow across the tear makes the distinction between the true and the false lumen difficult. Owing to the preferential expansion, false lumen would correspond to the portion where the wall rupture is located

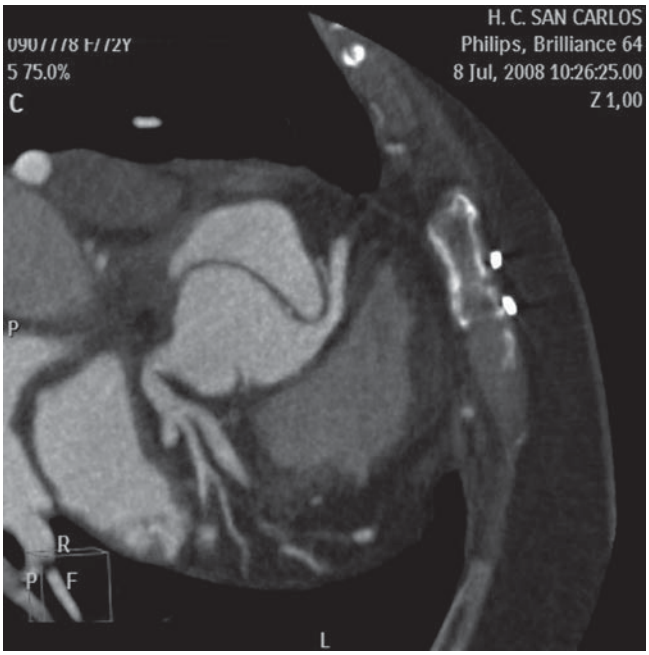

Fig. 34.5 Class 3 or discrete aortic dissection. Coronal modified view using multi-planar reformatted maximum pixel intensity showing a localized and non-propagating aortic dissection, the intimal tear, and a small pseudoaneurysm. Note the very close relation of the Intimal-medial flaps with the origin of the right coronary artery

usually discloses a spiral trajectory up to variable distances from the LSA. Medical treatment is the first choice in Type B aortic dissection, and CT offers important data for clinical management. Continuous chest pain, expansion with an increased size of the false lumen quantified through an area equal or greater than 900 mm^2, and extension with the involvement of branch-vessel (renal, mesenteric, etc) resulting in malperfusion make these patients prone to more complications during the hospitalization.[15]

In the follow-up of patients with chronic dissection of the descending thoracic aorta, CT provides an accurate assessment of serial expansion of the false lumen and, therefore, of the degree of dilation of the aorta, the main determinant of late aortic rupture, especially in patients with Type B aortic dissection and those who are non-operated.[16] Surveillance of aneurysm formation is especially important when the false lumen diameter is equal or greater than 22 mm at first scan examination, because in the mid-term (3–5 years), up to 75% of patients develop upper descending thoracic aorta aneurysm suitable for treatment (diameter equal or greater than 60 mm).[17]

The treatment with endovascular stents as an alternative to the surgical approach of Type B aortic dissection evolving towards severe dilation and aneurysm formation is currently evaluated, especially with the aim of preventing false lumen expansion and promoting aortic re-modelling. In contrast, in acute aortic rupture, stent placement can be live saving. Anyway, imaging with CT is a very useful tool for planning, assessing the result, and during the follow-up of patients submitted to this particular non-surgical invasive therapeutic strategy (Fig. 34.6).[18]

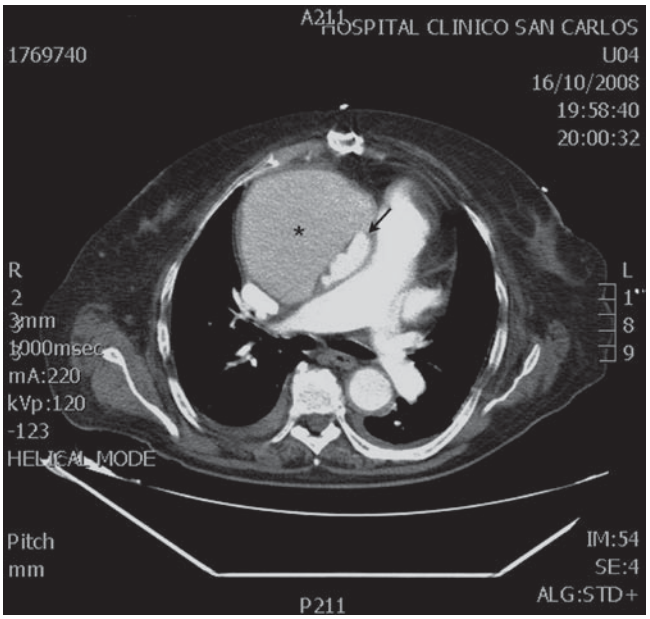

Fig. 34.6 Post-operative CT scan in a patient operated on 10 months earlier because of type A aortic dissection. Surgery consisted of the ascending aorta resection including the intimal tear and a graft interposition of the ascending aorta and hemiarch, with preservation of the native aortic valve. The axial image discloses a pseudoaneurysm (*asterisk*), which is filled by iodine contrast. The big mass compresses the graft and collapses it (*arrow*)

Only CT allows the visualization of the stent strut, its position, extension, and spatial orientation in relation to true and false lumen.

Class 2 Aortic Dissection: Intra-mural Haematoma

In the pathogenesis of aortic dissection, the intimal rupture is considered a crucial phenomenon in the origin of the dissecting haematoma of the aortic wall. In cases of autopsy, IMH was found, in greater or lesser extent, without clear existence of an intimal tear. The most widely accepted pathophysiological explanation is the bleeding from the vasa vasorum inside cystic degenerated media with expanded adventitia, preserving the lumen. The recognition of certain peculiarities in its natural history and some distinguishing features in its diagnosis and clinical management has led to the breakdown of IMH of the aorta from aortic dissection, while embracing the broadest concept of acute aortic syndromes.

Although the most accepted opinion is that the natural history of IMH is similar to that of the aortic dissection, there are subtle differences between the two entities. IMH can evolve into the intimal leakage as well, and its involution returned to the *restitution ad integrum* of the aortic wall.[19]

IMH appears as a crescent-shaped area unenhanced opposite the contrast filled aortic lumen; no intimal tear is seen. Differential diagnosis is established with the lumen in typical aortic dissection. The aortic dissection tends to spiral longitudinally around the aorta, whereas the IMH tends to maintain a constant circumferential relationship with the aortic wall (Fig. 34.7).[20] Some signs found in CT scan could be useful to anticipate the evolution of an IMH towards a classical aortic dissection, occurring in 25% of the patients. Among them, a maximum aortic diameter equal or greater than 50 mm in the initial CT scan is predictive of progression, especially in Type A IMH. Other predictors are a thick (>10 mm) haematoma with compression of the true lumen, pericardial effusion, or haemorrhagic pleural effusion. The recommended attitude in IMH is to proceed as in aortic dissection: in Type A IMH surgical treatment and in Type B medical treatment together with close clinical imaging follow-up.[13, 21]

The natural history of IMH can best be documented by serial CT scan. A normal aortic diameter in the acute phase is the best predictor of IMH regression without complications. The regression of the IMH is independent of location and has also been observed at locations in the proximal ascending aorta, although this observation does not need to change the actual recommendations of prompt surgical

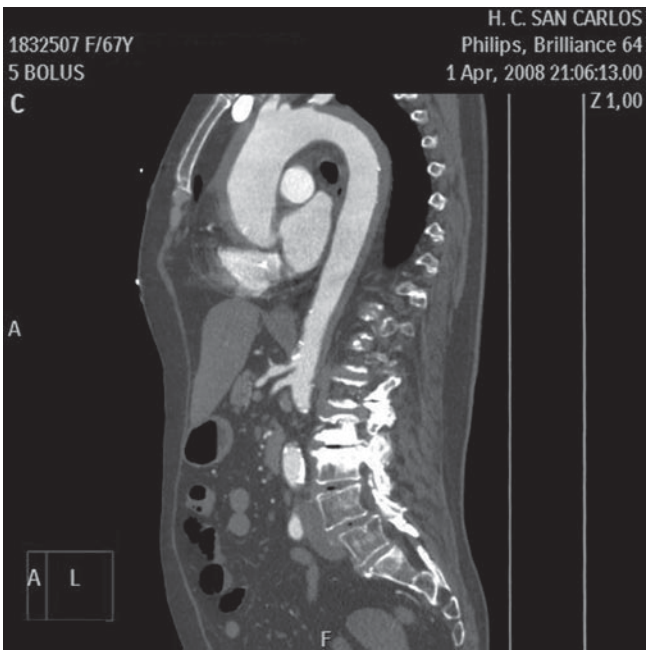

Fig. 34.7 Sixty-four-row multi-detector CT of a type A intra-mural aortic haematoma. Sagital modified view using multi-planar reformatted maximum pixel intensity depicting the non-spiral thickening of the aortic wall extending through the ascending aorta, the arch, and the descending thoracic aorta up to the exit of the celiac trunk and superior mesenteric artery. The haematoma includes the rise of the innominate artery

intervention in Type A IMH. Although patients with Type B IMH have better long-term prognosis than patients with aortic dissection, the appearance of an ulcer-like projection is predictive of progression to aortic dissection or late aneurysm in patients with Type B IMH, mainly older people.[22, 23]

Class 3 Aortic Dissection: Subtle-Discrete Aortic Dissection

Minor forms of aortic dissection can be diagnosed and assessed by means of helical CT scan. When the partial tear forms a scar, it is called an abortive, discrete dissection (Fig. 34.5).[13]

Class 4 Aortic Dissection: Penetrating Atherosclerotic Ulcer

Penetrating atherosclerotic ulcer (PAU) is an ulcerating atherosclerotic lesion of the descending thoracic aorta, or, less frequently, the aortic arch or even the ascending aorta, which penetrates the elastic lamina and can be associated with haematoma formation within the media of the aortic wall. There is controversy whether this lesion differs from classic acute Stanford Type B aortic dissection, based on its location, radiographic findings, natural history, and recommended therapeutic approach. It accounts for about 10% of the acute thoracic syndromes usually associated with intramural and non-propagating haematoma. The typical patient is elderly with multiple cardiac risk factors and presents with acute chest or back pain. Sometimes, PAU appears as an isolated and unexpected finding in CT examinations performed for other reasons.

At CT, PAU manifests as focal involvement with adjacent sub-intimal haemorrhage, and is often associated with aortic wall thickening or enhancement. Helical CT involves shorter examination times and allows high-quality image reconstruction. CT angiography can demonstrate complex spatial relationships, mural abnormalities, and extra-luminal pathologic conditions. They are described as a non-flap lesion demonstrating a crater extending from the aortic lumen into the space surrounding the lumen. Unlike classic dissection, PAU does not produce branch vessel compromise or occlusion and does not result in ischaemic manifestations in the extremities or visceral organs. PAU is more focal lesions and usually associated with severe aortic arteriosclerosis and calcification. PAU tends to occur in larger aortas and is strongly associated with aortic aneurysm, which is seen concomitantly in about 45% of PAU.[24]

Its natural history is controversial. Follow-up CT scans have shown asymptomatic and uneventful courses with total resolution of sub-intimal haematoma or some dilatation of the lumen, but no progression to rupture or aneurysm. The lack of pleural effusion correlates with clinical stability. Nonetheless, others stress the importance of differentiating symptomatic PAUs from Type B dissection aortic because of the higher incidence of rupture of penetrating ulcers, and therefore recommend early surgical intervention. The most convincing evidence points out the association of PAU and IMH as significantly associated with a progressive disease course and poor prognosis, which may occur within days or weeks. The traditional standard therapy for PAU is open operative repair with excision of the ulcerated aortic segment and graft interposition. Due to the high risk of the patients presenting with PAU because of coexisting severe cardiopulmonary abnormalities or other medical diseases, endovascular stent-graft technology provides an alternative to open surgery.[25]

Class 5 Aortic Dissection: Traumatic Aortic Lesion

Aortic traumatic lesions cover either blunt chest trauma, usually as a consequence of a traffic crash or owing to iatrogenic endovascular instrumentation, i.e. percutaneous trans-catheter coronary angioplasty, or extracorporeal renal lithotripsy. The latter is anecdotic nowadays, taking into account the high expertise achieved by interventionalists and the improvement of the technology, both of catheters and fluoroscopy.

The blunt chest trauma is the second leading cause of death after vehicular crashes only after head trauma. Up to 80% of patients die before their arrival at a hospital, and of those who survive, a majority will die without definitive treatment. Blunt aortic injury most often occurs after sudden deceleration. The descending aorta is fixed to the chest wall, whereas the heart and arch vessels are relatively mobile. Almost all patients who die due to aortic lesions have been involved in a crash in which the primary impact was against the side of the vehicle. The sudden deceleration causes a tear at the junction between the fixed and mobile portions of the aorta, usually near the isthmus. However, injury may also occur to the ascending aorta, the distal descending thoracic aorta, or the abdominal aorta. In addition to the stretching effect from sudden deceleration, there are further physiopathological theories: the so-called water-hammer effect, which combines simultaneous aortic occlusion and the rise in intra-aortic pressure, and the entrapment of the aorta between the anterior chest wall and the vertebral column. Approximately 90% of blunt traumatic aortic injuries occur

at the anteromedial side of the aortic isthmus, distal to the origin of the LSA. About 100% are located in the aortic root, often associated with aortic valve tears and severe acute aortic regurgitation, cardiac contusions or ruptures, coronary artery laceration, and cardiac tamponade secondary to haemopericardium. Less frequently, blunt traumatic lesions of the descending aorta occur at the level of the diaphragmatic crura, sometimes with simultaneous diaphragmatic ruptures.

The initial damage consists in the tear of the intimomedial layer and intimal flaps are detected. More severe injuries break deep medial layers resulting in fatal aortic transection, with massive haemorrhage into the mediastinum, pericardial, or pleural cavity or the abdomen. The time course is unpredictable, requiring close follow-up. CT is the diagnostic test of choice because of its availability, accuracy, and speed. Sensitivity and negative predictive values are as high as 100% in some series. Some fear to false positive scans due to artefacts can lead to referring the patient for additional trans-oesophageal echocardiography or even invasive angiography. At this point, we have to remark that isolated aortic bands or contour vessel abnormalities should be first considered as possible artefacts or related to non-traumatic etiologies, especially when mediastinal haematoma is absent.[26] The ability of helical CT to accurately diagnose blunt aortic injury as well other serious injuries has led to a wide use in nearly all patients with thoracic trauma after a traffic collision with velocities as low as 40 km/h (urban traffic).[27]

Problems exist concerning the detection of subtle or minimal intimal flaps. The term "minimal aortic injury" is often used to describe a lesion of the aorta associated with blunt injury that is believed to carry a relatively low risk of rupture. Minimal aortic injury can be present in approximately 10% of patients with blunt aortic injury. Minimal aortic lesion refers to an isolated intimal defect (intimal flap less than cm) not associated with pseudoaneurysm of any size, or periaortic haematoma the moment that it becomes an aortic rupture. The natural history of minimal aortic injury is unclear, but it should be followed using serial CT scan and, if the outcome becomes complicated (threatening rupture), prompt intervention is warranted.

There is a broad range of possible acute aortic syndromes, all diagnosed by means of thoracic helical scan. False aneurysm or pseudoaneurysm typically consists of a saccular outpouching demarcated from the aortic lumen by a collar. This pseudoaneurysm is limited externally by a thin layer of adventitia and neighbouring tissues. It is usually surrounded by a certain amount of haemomediastinum. If complete transection of the aorta happens, the tear extends from the intima and media into the adventitial layer, and there is a massive mediastinal haemorrhage that rapidly extends cranially, leading to left apical extra-pleural capping. The mediastinal haematoma may later rupture into the pleural space, resulting in a left-sided haemothorax. CT also accurately shows haemomediastinum and haemothorax. Haemorrhage surrounding the aorta and other vascular structures is more suggestive of vascular injury, opposite to blood confined to the retrosternal space secondary to a sternal fracture.

Aortic dissection is less commonly found in the setting of blunt thoracic trauma. While spontaneous dissections have typical spiral propagation, those resulting from trauma are longitudinally propagating. The imaging hallmark is the identification of the intimal flap, which separates the aorta into a true lumen and false lumen. It looks different from classical Class 1 aortic dissection because of a more irregular contour and a thicker flap. A distinct form of aortic dissection has been increasingly reported with modern helical CT techniques. This traumatic acute IMH shows a circular thickening of the aortic, well defined and without intimal tear. It weakens the aorta and may progress either to rupture the aortic wall externally or to inward disruption of the intimal layer, leading to a communicating aortic dissection.[28]

Acute traumatic aortic lesions, except the so-called minimal aortic injury, must be immediately repaired. Open surgery, excision, and graft interposition are the rules. Mortality is high, and there is a substantial risk of paraplegia. Spinal cord protection is of maximal importance. Endovascular grafting with specifically designed stents is an important progress in the treatment of acute traumatic aortic syndromes, especially the pseudoaneurysm or content rupture at the isthmus level. This live threatening condition can be cured by this novel technology. Results of several groups are very promising, and in some centres, the technique has replaced the surgery owing to lower mortality and hardly any risk of paraplegia secondary to spinal ischaemia.[29] Helical CT resumes a critical role in the follow-up of both operated and invasive endovascular treated patients. CT allows identifying poor apposition of the endovascular graft, leaks of the interposition or endovascular grafts, pseudoaneurysm formation and collapse of the graft, thrombosis or ischaemia of the upper extremity, or the territory perfused by the left vertebral artery secondary to coverage of the LSA.

It is noticeable that the durability of endovascular grafts is unknown. There are questions about long-term device integrity as well as the natural history of the repaired aorta. These issues are particularly important considering the relatively young age of trauma patients as compared with patients with aneurysmal disease. Close follow-up should include regular control and imaging. Although CT scan is very useful, for this purpose, aortic MRI may be regarded as the first option in order to minimize X-ray exposition in young people.

Aortic Aneurysm

The rupture of an aortic aneurysm is a dramatic event with very high mortality. Aortic aneurysms have a natural tendency to unlimited expansion and rupture. Less than 20% of

ruptured aneurysms reach the operating room, and their mortality jumps to about 50%. Prior to the rupture, they are very often asymptomatic or present with unspecific symptoms (i.e. peri- or infra-umbilical tenderness, chest discomfort, back pain). The diagnosis is usually made incidentally during the physical examination (pulsatile abdominal mass) or performing an imaging study indicated for another reason. In asymptomatic or mildly symptomatic patients, surgical total exclusion of the aortic aneurysm and graft interposition improve survival.

Angiography with CT has revolutionized the diagnosis, treatment, and follow-up of patients with suspected or known aortic aneurysm. CT angiography has replaced conventional catheter angiography. The advantages of CT are (1) high spatial resolution, which demonstrates mural changes, extraluminal pathologic conditions, and spatial relationships with adjacent organs; (2) high contrast resolution and sensitivity for detecting calcified lesions; (3) angiographic or 3D display of vascular structures and adjacent organs in any projection with a single spiral acquisition; and (4) demonstration of extrinsic causes of vascular compromise.[10, 30]

The aortic aneurysm is a dilation >4 cm or >2.1 cm/m^2 of the aortic lumen together with expansion or re-modelling, which evolves all aortic wall layers. Depending on their location, above or below the diaphragm, aortic aneurysms are classified as either thoracic (located at the ascending arch or descending thoracic aorta) or abdominal (supra or, most commonly, infra-renal abdominal aneurysm). Abdominal aneurysms are more common than thoracic ones. The prevalence of the aortic aneurysm increases with age, and they are five to six times more prevalent in men than women.

CT examination of the aorta in patients with suspected aortic aneurysm has to begin with a prospective unenhanced scan and be followed by a helical multi-detector contrast-enhanced examination with retrospective ECG-gated reconstruction for maximal spatial resolution and minimal motion blur. The importance of the unenhanced CT is crucial, so it allows detecting the peripheral expansion of the calcified intima helping to differentiate aneurysm from aortic dissection in which calcification is displaced inward, not outward. Blood extravasations and post-surgical periaortic attenuated thickenings are easily distinguished comparing findings between unenhanced and contrast-enhanced images. Since there is very frequent diffuse aortic affectation with aneurysm or another atherosclerotic lesion at other locations, CT has to cover the entire aorta, at least in the first examination and with the exception of follow-up of a previously imagined or corrected pathology.

The dilation of the aorta and its length, focal or diffuse, are visualized and quantified browsing the axial stacks. Mural thrombus formation is a very frequent finding in abdominal aneurysm, occasional in descending thoracic aortic aneurysm, and rarely formed in ascending aorta or aortic arch aneurysms (Fig. 34.8). Thrombus may be circumferential or

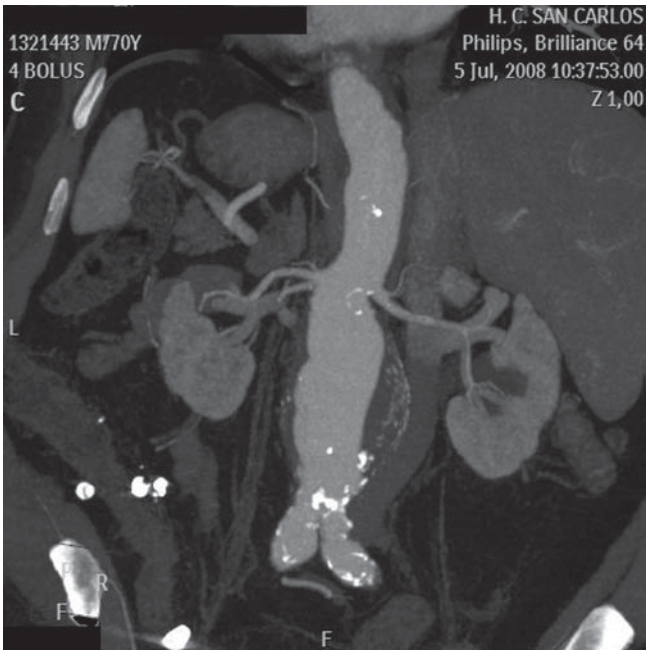

Fig. 34.8 MPI coronal view of an infrarenal abdominal aneurysm with its lumen partially occupied by a thrombus

crescentic. They imply differential diagnosis with aortic dissection. Fine indentations of the edge and the outward displacement of the intimal calcification indicate thrombus. Surgeons need to know the exact extension and amount of thrombus, especially in endovascular abdominal or thoracic stent placement. Multi-planar reformatting with variable thickness slice and curve-assisted multi-planar imaging allows to depict the anatomic and vascular relations of the aneurysm, such as the exit of the coronary arteries, aortic arch branches, renal arteries, celiac trunk, superior and inferior mesenteric arteries, and the iliac bifurcation (Fig. 34.9). CT clearly demonstrates the relationship of an aortic aneurysm to adjacent structures.

Subtle erosion of bone may be appreciated by adjusting the window width and level.

Compression of the tracheobronchial tree, the pulmonary arteries and veins, and the superior vena cava are easily identified. Oesophageal displacement and obstruction may also be seen.[30]

Atherosclerosis underlies in the genesis of abdominal aortic aneurysm. In the same way, other manifestations of atherosclerosis at the coronary, carotid, or peripheral artery beds are present in patients with abdominal aneurysms and observed in CT examinations (Figs. 34.10 and 34.11). The pathogenesis of thoracic aortic aneurysm differs from abdominal ones. Usually, cystic medial degeneration is the most important biological process that debilitates the aortic wall producing its expansion and dilation in the ascending aorta. The phenomenon is dramatic in some congenital conditions: Marfan syndrome or the Ehlers–Danlos syndrome

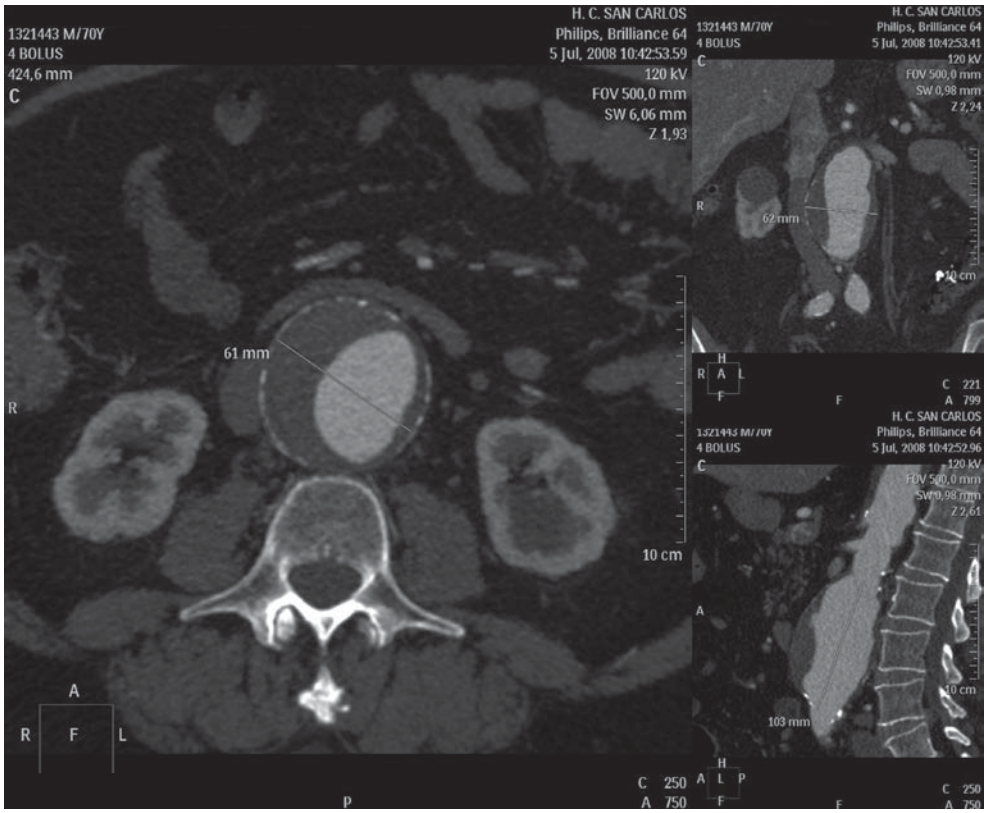

Fig. 34.9 Post-processing of a huge abdominal aneurysm in multi-planar reformatted maximum intensity pixel imaging displaying the correspondence in the three planes: axial (*left panel*), coronal (*right superior panel*), and sagital (*right inferior panel*). The aneurysm is partially filled by a crescent-shape thrombus. Note the outward location of the calcification, opposite to the aortic dissection, which calcification is displaced inward

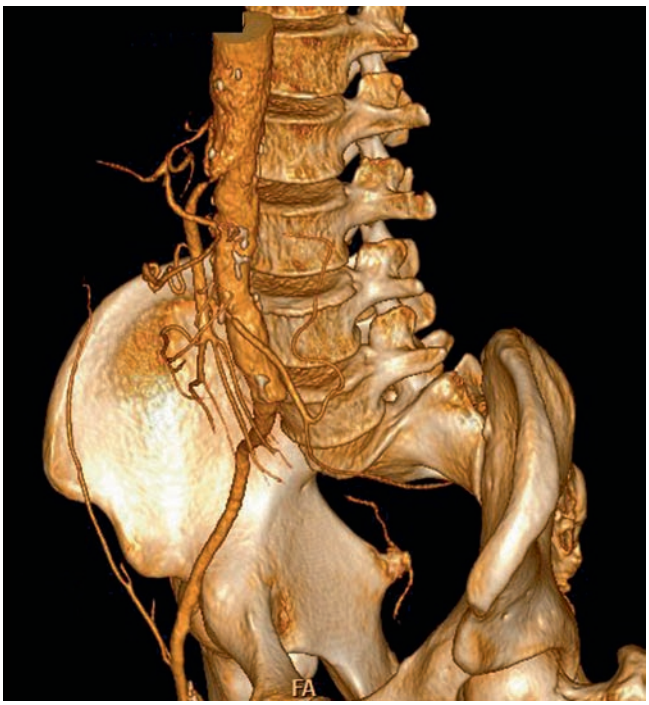

Fig. 34.10 Volume-rendered of the distal abdominal artery and iliac arteries. The left common iliac artery is occluded. Patients with thoracic aneurysm have frequently severe manifestations of atherosclerosis in another vascular bed. Screening is very important, especially when endovascular graft placement is being considered, so this lesion precludes the vascular access

(Fig. 34.12). Another classical condition associated with cystic medial degeneration and ascending aneurysm development is bicuspid aortic valve. Some patients have the dilation limited to the segment immediately above the aortic valve annulus. This ectasia of the ascending aorta is not unusual in patients with a previous vascular graft above the sinotubular junction who develop aneurysm of the sinus of Valsalva or the aortic arch (Figs. 34.13 and 34.14). Very infrequent causes of ascending aneurysm are syphilis and mycotic aneurysm, secondary to endocarditis or arteritis. Primary aneurysmatic dilation of the thoracic descending aorta is very uncommon. When present, it is due to atherosclerosis and accompanying of tortuousness and calcification of the entire aorta, and often is continued with abdominal aneurysm in up to 29% of cases (Figs. 34.15 and 34.16). The majority of atherosclerotic thoracic aneurysms are fusiform, but sometimes they are saccular.[31]

The prognosis and follow-up of patients with aortic aneurysm depend on its location, size, and clinical condition. For abdominal aortic aneurysm, surgical aneurysmectomy or replacement by vascular graft is indicated when the size is equal or greater than 5.5 cm of diameter. As an alternative, exclusion of the aneurysm by placing an endovascular stent has to balance the risk–benefit ratio in each patient and take into account the experience and surgical mortality of the referral centre. After the surgery, CT angiography plays an

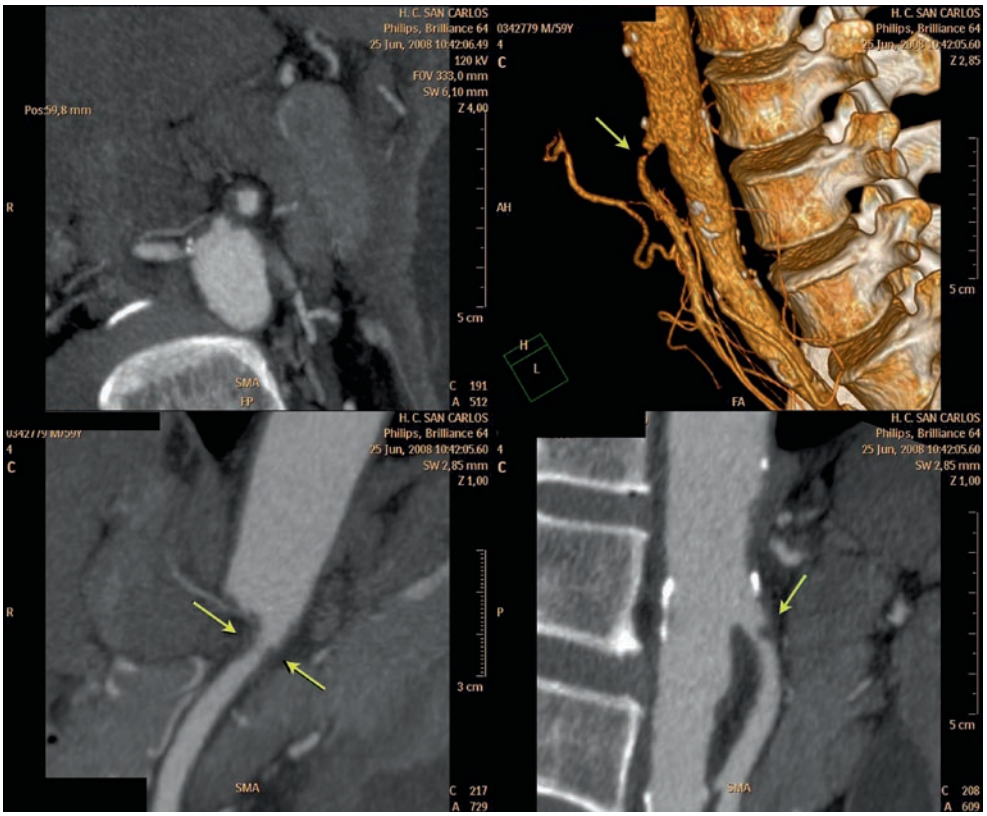

Fig. 34.11 Multi-task desktop capture of advanced software post-processing. Corresponding planes (axial, coronal, and sagital) showing a stenosis in the origin of the superior mesenteric artery (*arrows*). The incidental finding of these lesions is not anecdotic when examining patients diagnosed of thoracic and abdominal aneurysm and must be advised when aneurysm exclusion is planned

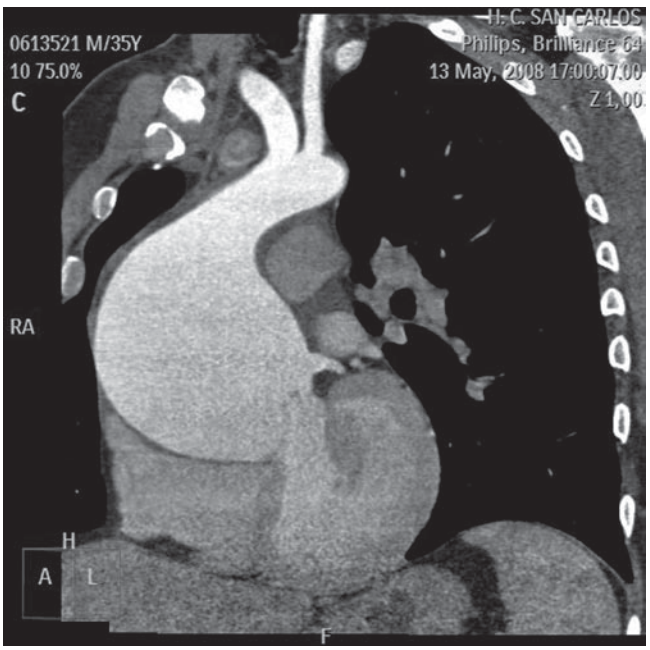

Fig. 34.12 Left anterior oblique projection obtained using MPR-MPI reconstruction of a 64-row multi-detector computed tomography (CT) in a 35-year-old man submitted because of diastolic heart murmur. There is a huge aneurysm of the ascending thoracic aorta which does not surpass the limits of the aortic arch

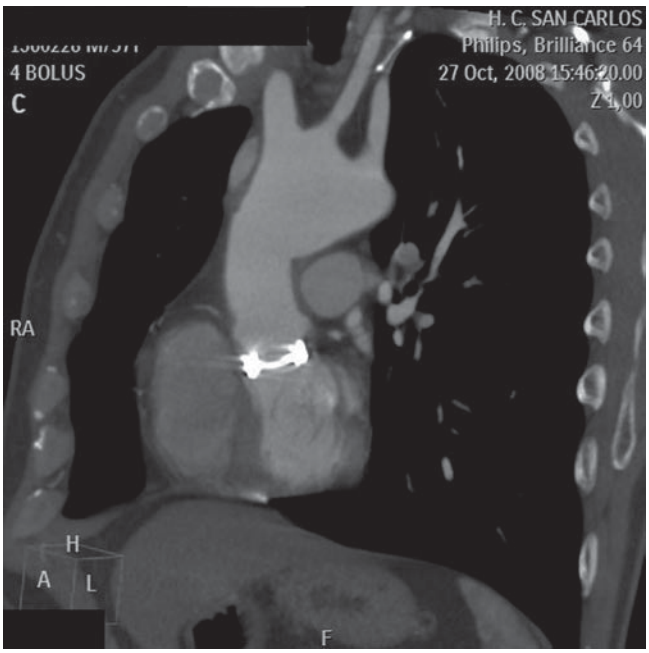

Fig. 34.13 Sixty-four-row multi-slice CT obtained in the follow-up of a 57-year-old man operated 5 years ago for a severe aortic annulectasia with a Bentall and DeBono procedure. There is a moderate dilation of the aortic arch (45 mm), which includes the exit of the main arterial branches of the arch. The high attenuation generated by the metallic prostheses is clearly visible

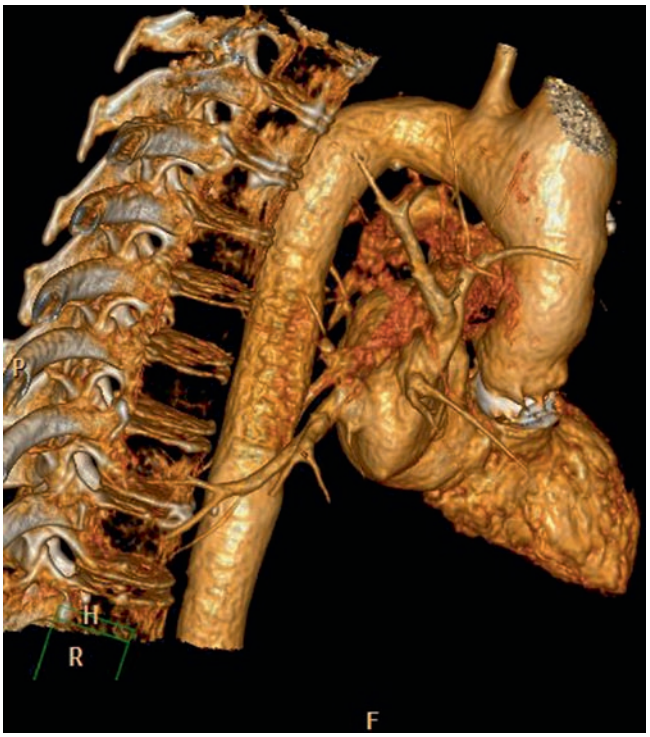

Fig 34.14 Volume-rendered reconstruction of the case described in Fig. 34.11. This way of post-processing offers a detailed vision of the anatomic vascular relations helping surgeon for clinical decision making

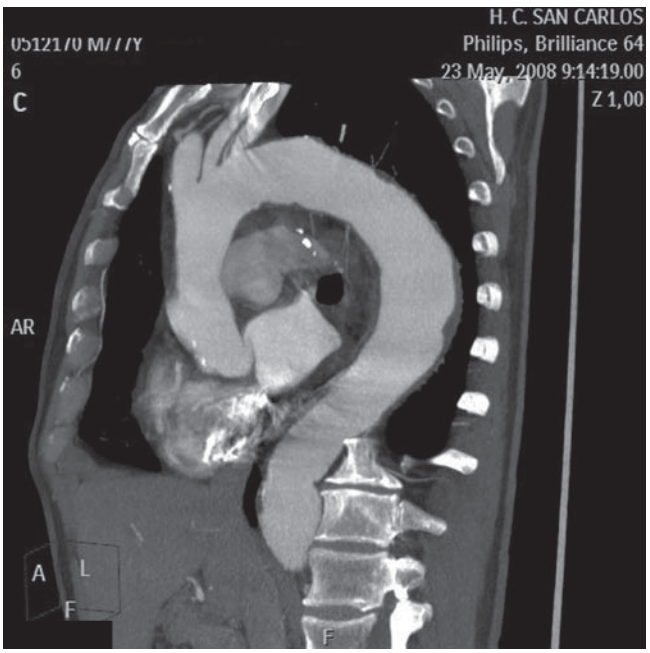

Fig. 34.15 Sagital view of a thoracic aneurysm. The dilation was moderate (45 mm). Note the tortuousness of the aorta and the mural thrombosis

important role in the follow-up, mainly to detect and promptly correct, if indicated, complications such as infection, leakage with peri-aortic haematoma, dislodgment, or late appearance

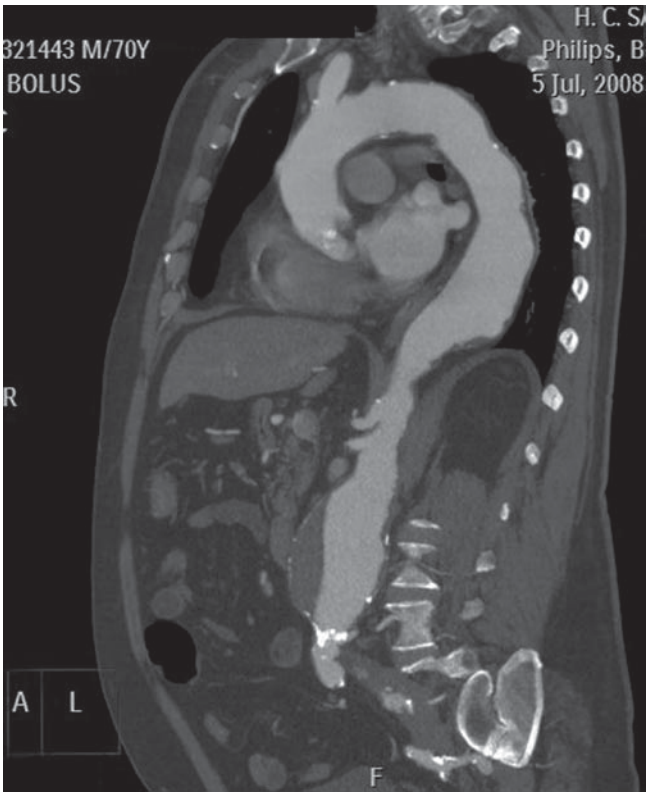

Fig. 34.16 Sixty-four-rows multi-slice CT of a patient with combined thoracic and abdominal aneurysms. This finding is relatively frequent because of the critical importance of the atherosclerosis in the origin of them in contrast with ascending aortic aneurysm in which cystic degeneration plays an important role

of a pseudoaneurysm. For thoracic aneurysm, the follow-up indicates surgical prophylactic treatment in the ascending aorta when the diameter surpasses 6.0 cm, except in patients with Marfan syndrome or familiar aortic dissection, in whom the limits decrease up to 5.5 cm (Figs. 34.17 and 34.18).[13] If affected, the aortic valve is replaced using a valve–tube graft. In a similar way, CT angiography is an excellent imaging tool to discard both early and late post-operative complications.[32] Aneurysm of the descending thoracic aorta is, by far, the most challenging. This is due to the very severe atherosclerotic process and calcification of the aortic wall and, on the other hand, the inherent difficulty in accessing this particular aortic segment by surgery. As result, great efforts have been made to develop a fine endovascular technique to offer a valid alternative to the high morbidity and mortality of surgery in these patients. Although clinical outcomes are controversial, everyone agrees on the essential role of the CT angiography in the follow-up, generally narrow, these patients need. Prerequisites for endovascular stent–graft placement are an adequate neck for graft attachment and adequate vascular access. When the ascending aorta or aortic arch is involved, surgical and endovascular procedures can be combined and performed simultaneously, allowing treatment of a wider range of cases.[33]

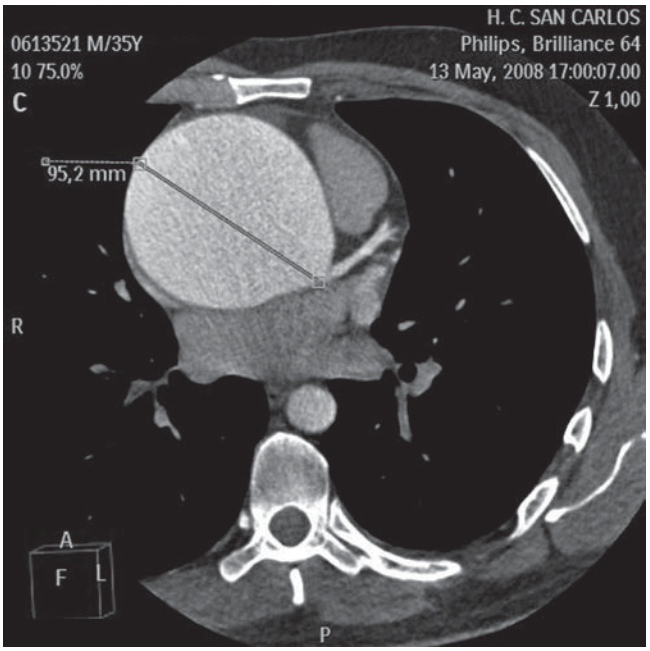

Fig. 34.17 Impressive dilation of the ascending aorta (95 mm). Note the exit of the left coronary artery

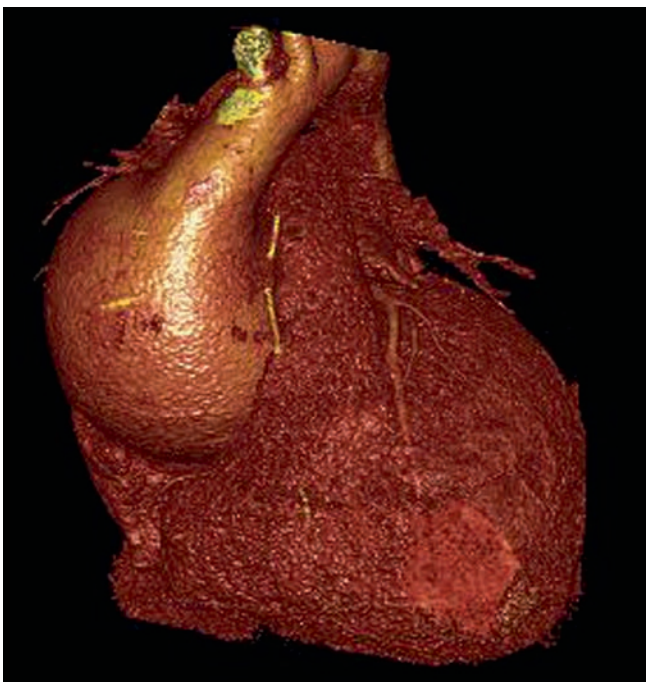

Fig. 34.18 Volume-rendered of the ascending aortic aneurysm. There is a close relation with the pulmonary trunk. Femoro-femoral external bypass or return from the pulmonary veins is frequently needed before any attempt of esternotomy because of the high risk to damage the dilated aorta

Awareness and understanding of possible complications of endovascular stent–graft implantation would ensure a safe procedure. Most common complications are leaks, graft thrombosis, and graft kinking. Infrequent complications are pseudoaneurysm secondary to graft infection, graft occlusion, distal embolism, aortic perforation due to inadvertent penetration of delivery system, colon necrosis, aortic dissection, and haematoma at the arteriotomy site. Since some of these complications are fatal, the specialist in cardiovascular imaging needs to instantly and accurately recognize them for prompt therapeutic and solving attitude.[34]

References

1. Dotter CT, Steinberg I. The angiocardiographic measurement of the normal great vessels. *Radiology*. 1949;52(suppl 3):353–358
2. Guthaner DF, Wexler L, Harell G. CT demonstration of cardiac structures. *AJR Am J Roentgenol*. 1979;133(suppl 1):75–81
3. Aronberg DJ, Glazer HS, Madsen K, et al Normal thoracic aortic diameters by computed tomography. *J Comput Assist Tomogr*. 1984;8(suppl 2):247–250
4. Pond GD, Hillman B. Evaluation of aneurysms by computed tomography. *Surgery*. 1981;89(suppl 2):216–223
5. Godwin JD, Korobkin M. Acute disease of the aorta. Diagnosis by computed tomography and ultrasonography. *Radiol Clin North Am*. 1983;21(suppl 3):551–574
6. Morgan-Hughes GJ, Marshall AJ, Roobottom CA. Refined computed tomography of the thoracic aorta: the impact of electrocardiographic assistance. *Clin Radiol*. 2003;58(suppl 8):581–588
7. Takahashi K, Stanford W. Multidetector CT of the thoracic aorta. *Int J Cardiovasc Imaging*. 2005;21(suppl 1):141–153
8. Roos JE, Willmann JK, Weishaupt D, et al Thoracic aorta: motion artifact reduction with retrospective and prospective electrocardiography-assisted multi-detector row CT. *Radiology*. 2002;222 (suppl 1):271–277
9. Batra P, Bigoni B, Manning J, et al Pitfalls in the diagnosis of thoracic aortic dissection at CT angiography. *Radiographics*. 2000; 20(suppl 2):309–320
10. Chung JW, Park JH, Im JG, et al Spiral CT angiography of the thoracic aorta. *Radiographics*. 1996;16(suppl 4):811–824
11. Becker C, Soppa C, Fink U, et al Spiral CT angiography and 3D reconstruction in patients with aortic coarctation. *Eur Radiol*. 1997;7(suppl 9):1473–1477
12. McLoughlin MJ, Weisbrod G, Wise DJ, et al Computed tomography in congenital anomalies of the aortic arch and great vessels. *Radiology.* 1981;138(suppl 2):399–403
13. Erbel R, Alfonso F, Boileau C, et al Diagnosis and management of aortic dissection. *Eur Heart J*. 2001;22(suppl 18):1642–1681
14. Yoshida S, Akiba H, Tamakawa M, et al Thoracic involvement of type A aortic dissection and intramural hematoma: diagnostic accuracy – comparison of emergency helical CT and surgical findings. *Radiology*. 2003;228(suppl 2):430–435
15. Chang CP, Liu JC, Liou YM, et al The role of false lumen size in prediction of in–hospital complications after acute type B aortic dissection. *J Am Coll Cardiol*. 2008;52(suppl 14):1170–1176
16. Kelly AM, Quint LE, Nan B, et al Aortic growth rates in chronic aortic dissection. *Clin Radiol*. 2007;62(suppl 9):866–875
17. Song JM, Kim SD, Kim JH, et al Long-term predictors of descending aorta aneurysmal change in patients with aortic dissection. *J Am Coll Cardiol*. 2007;50(suppl 8):799–804
18. Czermak BV, Waldenberger P, Fraedrich G, et al Treatment of Stanford type B aortic dissection with stent-grafts: preliminary results. *Radiology*. 2000;217(suppl 2):544–550
19. Song JK, Kim HS, Kang DH, et al Different clinical features of aortic intramural hematoma versus dissection involving the ascending aorta. *J Am Coll Cardiol*. 2001;37(suppl 6):1604–1610

20. Rubin GD. Helical CT angiography of the thoracic aorta. *J Thorac Imaging*. 1997;12(suppl 2):128–149
21. von Kodolitsch Y, Csosz SK, Koschyk DH, et al Intramural hematoma of the aorta: predictors of progression to dissection and rupture. *Circulation*. 2003;107(suppl 8):1158–1163
22. Kaji S, Akasaka T, Katayama M, et al Long-term prognosis of patients with type B aortic intramural hematoma. *Circulation*. 2003;108(suppl 1):II307–II311
23. Evangelista A, Dominguez R, Sebastia C, et al Long–term follow–up of aortic intramural hematoma: predictors of outcome. *Circulation*. 2003;108(suppl 5):583–589
24. Quint LE, Williams DM, Francis IR, et al Ulcerlike lesions of the aorta: imaging features and natural history. *Radiology*. 2001; 218(suppl 3):719–723
25. Eichhofer J, Mitchell AR, Banning AP. Emergency endovascular aortic stenting for the treatment of a ruptured atherosclerotic ulcer. *Heart*. 2004;90(suppl 7):793
26. Scaglione M, Pinto A, Pinto F, et al Role of contrast–enhanced helical CT in the evaluation of acute thoracic aortic injuries after blunt chest trauma. *Eur Radiol*. 2001;11(suppl 12):2444–2448
27. Neschis DG, Scalea TM, Flinn WR, et al Blunt aortic injury. *N Engl J Med*. 2008;359(suppl 16):1708–1716
28. Alkadhi H, Wildermuth S, Desbiolles L, et al Vascular emergencies of the thorax after blunt and iatrogenic trauma: multi-detector row CT and three–dimensional imaging. *Radiographics*. 2004;24 (suppl 5):1239–1255
29. Steingruber IE, Czermak BV, Chemelli A, et al Placement of endovascular stent–grafts for emergency repair of acute traumatic aortic rupture: a single–centre experience. *Eur Radiol*. 2007;17 (suppl 7):1727–1737
30. Posniak HV, Olson MC, Demos TC, et al CT of thoracic aortic aneurysms. *Radiographics*. 1990;10(suppl 5):839–855
31. Quint LE, Francis IR, Williams DM, et al Evaluation of thoracic aortic disease with the use of helical CT and multiplanar reconstructions: comparison with surgical findings. *Radiology*. 1996;201(suppl 1):37–41
32. Sundaram B, Quint LE, Patel HJ, et al CT findings following thoracic aortic surgery. *Radiographics*. 2007;27(suppl 6):1583–1594
33. Garzon G, Fernandez-Velilla M, Marti M, et al Endovascular stent–graft treatment of thoracic aortic disease. *Radiographics*. 2005;25(suppl 1):S229–S244
34. Mita T, Arita T, Matsunaga N, et al Complications of endovascular repair for thoracic and abdominal aortic aneurysm: an imaging spectrum. *Radiographics*. 2000;20(suppl 5):1263–1278

Index